JCTC Journal of Chemical Theory and Computation

PERSPECTIVE

pubs.acs.org/JCTC

Generalized Hartree−Fock Description of Molecular Dissociation

Carlos A. Jiménez-Hoyos,[†] Thomas M. Henderson,[†,‡] and Gustavo E. Scuseria*[,†,‡]

[†]Department of Chemistry, Rice University, 6100 Main Street, Houston, Texas 77005, United States

[‡]Department of Physics and Astronomy, Rice University, 6100 Main Street, Houston, Texas 77005, United States

ABSTRACT: An electronic structure method is said to be size-consistent if the energy of noninteracting fragments is the same when the fragments are treated in a supermolecule approach or are treated in isolation. Size consistency is often violated by Hartree−Fock when symmetries of the exact wave function are imposed on the Hartree−Fock determinant. Relaxing the requirement that the Hartree−Fock wave function be a spin eigenfunction leads to unrestricted Hartree−Fock, which is often (but not always) size-consistent. In this Perspective, we discuss the usually forgotten fact that imposing none of the exact symmetries in what is known as generalized Hartree−Fock allows Hartree−Fock to always be size-consistent and allows size extensive correlated methods such as coupled cluster theory to also be size-consistent. Furthermore, with all symmetries broken, dissociation curves connect the molecule to the fragments better than with symmetries imposed, although the curves are not smooth and show derivative discontinuities akin to unphysical phase transitions. In many cases, correlated dissociation curves based on this generalized Hartree−Fock reference are discontinuous.

1. INTRODUCTION

The past three decades have not been kind to the variational principle in quantum chemistry. Typical state-of-the-art correlated calculations employ some variant of coupled cluster theory,[1−4] which has many strengths but which in practice requires us to abandon the variational principle altogether. Typical mean-field calculations, on the other hand, use some form of Kohn−Sham density functional theory with an approximate exchange-correlation functional; though the variational principle does not hold for these functionals, we blithely apply it nonetheless. Meanwhile, such genuinely variational methods as Hartree−Fock (HF) and configuration interaction have all but disappeared from the computational toolkit, at least in practice.

On the other hand, it should not be forgotten that even in the case of Hartree−Fock, we have not historically taken the variational principle too seriously. That is, we have chosen to constrain the variation in Hartree−Fock by requiring the Hartree−Fock determinant to display at least some of the symmetries of the exact wave function, thereby abandoning full variational flexibility in favor of obtaining more qualitatively correct wave functions. Thus, the restricted Hartree−Fock (RHF) wave function is chosen to be an eigenfunction of the spin operators $\hat{S}^2$ and $\hat{S}_3$, as well as the time-reversal operator $\hat{\Theta}$ and generally the point-group operators $\hat{P}$. The wave function is also usually taken to be real (that is, it is an eigenfunction of the complex conjugation operator $\hat{K}$). The price we pay for preserving these symmetries is that RHF cannot dissociate a closed-shell molecule to the correct open-shell fragments. By this, we mean that RHF is not generally size-consistent, i.e., the energy of a dissociated molecule is not generally equal to the sum of the energies of the dissociation fragments. In unrestricted Hartree−Fock (UHF), we allow the wave function to break symmetry under $\hat{S}^2$ and $\hat{P}$ but not under $\hat{S}_3$ (in other words, we allow for spin contamination and spatial symmetry breaking, but we fix the number of spin-up and spin-down electrons). In simple cases, UHF is size-consistent, but it is not a panacea. The UHF dissociation limits for O_2 and CO_2, for example, are not size-consistent. Generally, UHF correctly dissociates a molecule to UHF fragments only if the open-shell electrons on a given fragment all have the same spin. Occasionally, we must allow the wave function to be complex, i.e., for the density matrix and the orbital coefficients to be complex, although the basis functions may remain real.

Our concern here is with generalized Hartree−Fock (GHF), in which we take the variational principle at face value and impose *none* of the correct symmetries on the Hartree−Fock wave function. The purpose of this paper is to remind the community that if we are willing to sacrifice all symmetries of the wave function by using GHF, then we can dissociate *any* molecule to GHF fragments. The GHF wave function of the dissociated molecule is just the product of the GHF wave functions of the fragments, and the dissociation curve is size-consistent. Generalized Hartree−Fock has seen only limited use, presumably because the wave functions it delivers can be qualitatively unreasonable and good quantum numbers are difficult to recover once lost. On the other hand, achieving size consistency while preserving the symmetries of the wave function is a difficult task.[5−8] Thus, there is a trade off as to what else one wants to do with these wave functions, and for many properties, it is better to keep some symmetries. For molecular dissociations, GHF allows us, in essence, to connect one UHF potential energy curve with another, thus obtaining an energetically reasonable zeroth-order dissociation curve for all bond lengths. The qualitative deficiencies in the GHF wave function can then in principle be corrected by the application of post-GHF correlated methods such as coupled cluster theory, though such corrections are not, as we shall see, without their own problems.

Received: May 21, 2011
Published: July 14, 2011

Table 1. Classification of Hartree−Fock Solutions According to the Symmetries of the Electronic Hamiltonian They Preserve[a]

Fukutome designation	Stuber−Paldus designation	symmetries preserved	structure of orbital coefficient matrix **C**
TICS[b]	real RHF	$\hat{S}^2, \hat{S}_3 \hat{K}, \hat{\Theta}$	$\begin{pmatrix} C_{\sigma\sigma} & 0 \\ 0 & C_{\sigma\sigma} \end{pmatrix}, C \in \mathbb{R}$
CCW[c]	complex RHF	$\hat{S}^2, \hat{S}_3$	$\begin{pmatrix} C_{\sigma\sigma} & 0 \\ 0 & C_{\sigma\sigma} \end{pmatrix}$
ASCW[d]	paired UHF	$\hat{S}_3 \hat{\Theta}$	$\begin{pmatrix} C_{\sigma\sigma} & 0 \\ 0 & C^*_{\sigma\sigma} \end{pmatrix}$
ASDW[e]	real UHF	$\hat{S}_3 \hat{K}$	$\begin{pmatrix} C_{\sigma\sigma} & 0 \\ 0 & C_{\sigma'\sigma'} \end{pmatrix}, C \in \mathbb{R}$
ASW[f]	complex UHF	$\hat{S}_3$	$\begin{pmatrix} C_{\sigma\sigma} & 0 \\ 0 & C_{\sigma'\sigma'} \end{pmatrix}$
TSCW[g]	paired GHF	$\hat{\Theta}$	$\begin{pmatrix} C_{\sigma\sigma} & C_{\sigma\sigma'} \\ -C^*_{\sigma\sigma'} & C^*_{\sigma\sigma} \end{pmatrix}$
TSDW[h]	real GHF	$\hat{K}$	$\begin{pmatrix} C_{\sigma\sigma} & C_{\sigma\sigma'} \\ C_{\sigma'\sigma} & C_{\sigma'\sigma'} \end{pmatrix}, C \in \mathbb{R}$
TSW[i]	complex GHF		$\begin{pmatrix} C_{\sigma\sigma} & C_{\sigma\sigma'} \\ C_{\sigma'\sigma} & C_{\sigma'\sigma'} \end{pmatrix}$

[a] We include the acronyms suggested by both Fukutome[10] and Stuber and Paldus[14] in each of these solutions. The structure of the matrix of orbital coefficients is also included for clarity along with any constraints in the matrix elements. [b] Time-reversal invariant closed-shell. [c] Charge current wave. [d] Axial spin current wave. [e] Axial spin density wave. [f] Axial spin wave. [g] Torsional spin current wave. [h] Torsional spin density wave. [i] Torsional spin wave.

2. GENERALIZED HARTREE−FOCK AND SYMMETRY

Elementary considerations make it clear that if a Hermitian operator $\hat{\Lambda}$ commutes with the Hamiltonian $\hat{H}$, then eigenstates $|\Psi\rangle$ of the Hamiltonian are also eigenstates of $\hat{\Lambda}$ (or can be chosen as such in the case of degeneracies). That is, we have

$$\hat{H}|\Psi\rangle = E|\Psi\rangle \tag{1a}$$

$$\hat{\Lambda}|\Psi\rangle = \lambda|\Psi\rangle \tag{1b}$$

where λ is the eigenvalue of $\hat{\Lambda}$ and is a good quantum number. In the case of the hydrogenic Hamiltonian, for example, the orbital angular momentum operators $\hat{L}^2$ and $\hat{L}_3$ commute with the Hamiltonian, as does the spin operator $\hat{S}_3$. [We have used $\hat{L}_3$ and $\hat{S}_3$ and not $\hat{L}_z$ and $\hat{S}_z$ essentially to indicate that the spatial direction of angular momentum quantization is irrelevant.] Thus, in addition to the principle quantum number n, which labels the energy, we obtain the familiar additional quantum numbers l, m_l, and m_s.

Approximate wave functions need not have all the symmetries of the real wave function (or, in other words, need not have the same good quantum numbers). Forcing an approximate wave function $|\Phi\rangle$ to be symmetry-adapted introduces constraints which reduce variational flexibility. One is forced to choose between finding the variationally optimal wave function and one which has the right symmetries. Löwdin was the first to point out this conundrum, which he called the symmetry dilemma.[9]

A common situation in which one faces the symmetry dilemma is in the dissociation of closed-shell molecules to open-shell fragments. If the Hartree−Fock wave function is optimized by preserving spatial and spin symmetry, then the predicted potential energy curve does not dissociate to the correct limit. On the other hand, allowing the Hartree−Fock wave function to break spatial and spin symmetry enables it to dissociate to the energetically correct limit with, however, a qualitatively incorrect wave function. When we can lower the energy by breaking a symmetry in the Hartree−Fock wave function, we say that the Hartree−Fock wave function is unstable with respect to that symmetry.

It is useful to classify the different solutions according to the self-consistent symmetries they preserve, an effort first undertaken by Fukutome.[10] To make this classification transparent, we must first discuss the symmetries of the electronic Hamiltonian. We note that if there is any symmetry present in the initial guess of the density matrix, then this symmetry will be preserved throughout the optimization procedure. That is, symmetries are self-consistent in the Hartree−Fock equations.

For any molecular system, the wave function $|\Psi\rangle$ must be an eigenfunction of the particle number operator $\hat{N}$. Solutions that break particle number symmetry are rare in quantum chemistry, but it is violated by the Bardeen−Cooper−Schrieffer (BCS) wave function.[11] For net repulsive interactions such as the Coulombic $1/r_{12}$ repulsion between electrons in quantum chemistry, the BCS wave function does not yield an energy lower than the HF wave function.[12] The standard electronic Hamiltonian is additionally invariant to spin rotations and time reversal. Finally, the point-group symmety determined by the nuclear framework is also preserved in exact solutions to the electronic Schrödinger equation.

The fact that the Hamiltonian is invariant to spin rotations implies that the exact eigenfunctions of the electronic Hamiltonian can always be labeled by the s and m_s quantum numbers, corresponding to the spin operators $\hat{S}^2$ and $\hat{S}_3$. The time reversal operator $\hat{\Theta}$ and the complex conjugation operator $\hat{K}$ also commute with the Hamiltonian, but the fact that they are antiunitary operators precludes their association with good quantum numbers.[13]

We will not discuss the group theoretical classification presented by Fukutome in great detail, but Table 1 does show the different Hartree−Fock solutions discussed by Fukutome, as well as the symmetries they preserve. We also include the designation recently suggested by Stuber and Paldus[14] in connection with each of Fukutome's solutions. We emphasize that the solutions we present are independent of the point group symmetry of the molecule; point group symmetry can be separately imposed on the Hartree−Fock wave function or not. Additionally, the classification is valid both for closed-shell and for open-shell wave functions.

Typically, we consider only the real RHF (or ROHF) and real UHF solutions. Complex solutions are known but are rarely sought.[15] While GHF solutions have been explored by Löwdin[16] and others, they are searched for more rarely still, even though Overhauser showed that in the uniform electron gas, the paramagnetic (RHF) state is always unstable with respect to the formation of helical spin density waves (which are GHF states).[17] In quantum chemistry, GHF solutions have been found, for example, in the beryllium atom in some basis sets, in BH, in H_4, and in a few other cases.[10,14,16]

3. HARTREE−FOCK STABILITY

The essence of Hartree−Fock is to find the single determinant which minimizes the expectation value of the Hamiltonian.

In practice, we solve

$$\frac{\partial}{\partial\langle\Phi|}\langle\Phi|\hat{H}|\Phi\rangle = 0 \tag{2}$$

subject to $|\Phi\rangle$ being a normalized determinant. This, of course, guarantees no more than that the energy is stationary. To determine whether or not the energy is a local minimum, we must check the second derivative as well.[18−20]

Determinants can be parametrized in terms of orbital rotations which mix occupied and virtual orbitals. The stationarity condition on the energy is simply

$$\langle\phi_a|\hat{\mathcal{F}}|\phi_i\rangle = 0 \tag{3}$$

where $\hat{\mathcal{F}}$ is the Fock operator and where, here and in the following, indices i and j will refer to occupied orbitals and a and b will refer to virtual orbitals. To check the second derivative of the Hartree−Fock energy, it suffices to check the eigenvalues of the Hartree−Fock orbital Hessian

$$\mathbf{H} = \begin{pmatrix} \mathbf{A} & \mathbf{B} \\ \mathbf{B}^* & \mathbf{A}^* \end{pmatrix} \tag{4}$$

where

$$A_{ia,jb} = \langle\phi_i\phi_b||\phi_a\phi_j\rangle + \langle\phi_b|\hat{\mathcal{F}}|\phi_a\rangle\delta_{ij} - \langle\phi_i|\hat{\mathcal{F}}|\phi_j\rangle\delta_{ab} \tag{5a}$$

$$B_{ia,jb} = \langle\phi_i\phi_j||\phi_a\phi_b\rangle \tag{5b}$$

in terms of the usual antisymmetrized two-electron integrals in Dirac notation. One can restrict the sectors of the Hessian one includes so as to test only for certain types of instabilities. For example, spin-adapting the Hessian searches only for so-called RHF instabilities (instabilities to states which are eigenfunctions of $\hat{S}^2$) and removing spin-flip blocks which mix spin-up occupied orbitals with spin-down virtual orbitals (and vice versa) tests only for RHF and UHF instabilities.

When the orbital Hessian has a negative eigenvalue, a lower energy Hartree−Fock solution exists, which typically displays lower symmetries. The eigenvector associated with this negative eigenvalue distorts the wave function in the direction of the broken symmetry solution. Having followed this eigenvector and obtained the self-consistent broken symmetry solution, we can repeat the stability analysis. At some point, we will converge to a Hartree−Fock solution which is at least locally stable within the manifold under consideration (i.e., has no negative eigenvalues). This solution will generally be one of several degenerate solutions which have broken the same symmetries in different ways. A fact usually unknown in quantum chemistry is that the Hessian corresponding to the broken symmetry solution will have zero eigenvalues, with eigenvectors pointing toward these degenerate solutions, usually known as Goldstone modes. By forming appropriate linear combinations of these broken symmetry solutions, one can restore the symmetry, though not at the single-determinant level.[21,22]

As pointed out by Piecuch et al., when the symmetry broken UHF state is spin projected, the projected wave function contains information about higher level excitations.[23] Presumably, the same is true in the case of projected GHF.

Closely related to the Hartree−Fock orbital Hessian is the random phase approximation (RPA), where one diagonalizes

$$\mathbf{R} = \begin{pmatrix} \mathbf{A} & \mathbf{B} \\ -\mathbf{B}^* & -\mathbf{A}^* \end{pmatrix} \tag{6}$$

to obtain excitation energies of the system. When the Hartree−Fock solution is unstable, the RPA will yield some complex eigenvalues. From the stable but broken symmetry Hartree−Fock state, the RPA matrix will contain zero eigenvalues associated with so-called collective motions that restore the broken symmetry, as already mentioned above.[21]

The much thornier question of whether one has obtained not a local minimum but a global minimum cannot generally be answered in a practical way.

4. MOLECULAR DISSOCIATION

Consider a molecule AB dissociating to well-separated fragments A and B. We will assume that in isolation, fragment A has a GHF wave function $|\Phi_A\rangle$ with energy E_A, and fragment B has a GHF wave function $|\Phi_B\rangle$ and corresponding energy E_B. For the well-separated AB system, we construct the wave function $|\Phi_{AB}\rangle = |\Phi_A\Phi_B\rangle$, which is still of the GHF form. It is not difficult to show (see the Appendix for details) that the energy corresponding to $|\Phi_{AB}\rangle$ is

$$E_{AB} = E_A + E_B + \frac{q_A q_B}{R_{AB}} \tag{7}$$

when the fragments are sufficiently far apart; here, q_A and q_B are the total charges on the two fragments and R_{AB} is the distance between the center of charges of the two fragments. Clearly, in the limit of infinite separation, our wave function $|\Phi_{AB}\rangle$ yields the correct dissociation limit, $E_{AB} = E_A + E_B$. In other words, nothing prevents the most general Hartree−Fock wave function from correctly dissociating to generalized Hartree−Fock fragments. Dissociation to multiple fragments is also shown to be correct by the foregoing, essentially in a recursive manner (i.e., $E_{ABC} = E_{AB} + E_C = E_A + E_B + E_C$).

That this result does not hold in general for RHF or UHF wave functions is well-known, and the reason for this failure is quite simple: the UHF and particularly the RHF wave functions enforce symmetries which exclude $|\Phi_{AB}\rangle$ from the variational space. In the case of H_2 at infinite separation, for example, $|\Phi_{AB}\rangle$ cannot be an RHF wave function because $|\Phi_{AB}\rangle = |\Phi_A\Phi_B\rangle$ is not an eigenfunction of $\hat{S}^2$. In the case of O_2 at infinite separation, as we shall see, UHF can only obtain the correct dissociation limit with $m_S = 0$ or $m_S = \pm 2$; neither of these connect to the UHF ground state wave function at equilibrium, which has $m_S = \pm 1$. The GHF wave function, however, simply reduces to the UHF triplet near equilbrium ($m_S = \pm 1$) and at dissociation to the UHF singlet ($m_S = 0$), because it does not conserve m_S.

5. RESULTS

The RHF, UHF, and GHF calculations shown in this work have been performed using a development version of the *Gaussian* suite of programs.[24,25] We have carried out correlated calculations at second order in perturbation theory (MP2), as well as with coupled cluster doubles[1,2] (CCD) and coupled cluster singles and doubles[26−30] (CCSD). Correlated calculations on

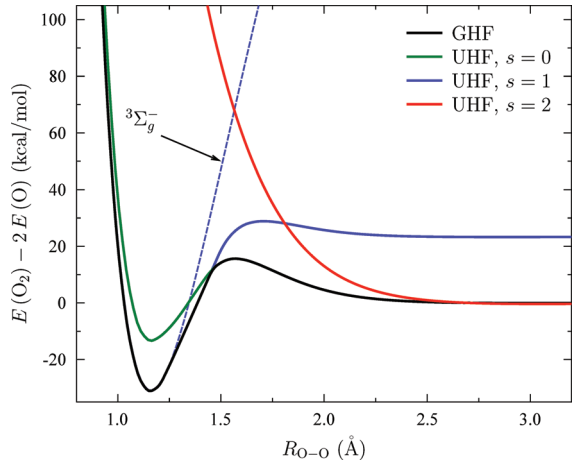

Figure 1. Dissociation curves of the oxygen molecule computed at the HF level. The zero of energy has been set at the energy of two triplet UHF oxygen atoms. We show the lowest energy UHF singlet, triplet, and quintet solutions, as well as the symmetric UHF triplet. The GHF curve connects the UHF triplet solution at equilibrium with the UHF singlet solution for $r \gtrsim 1.5$ Å.

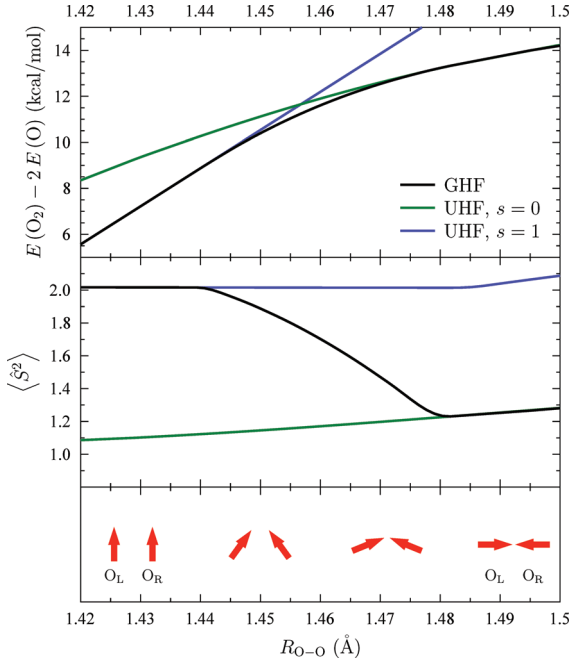

Figure 2. Top panel: Zoom-in of the region of the dissociation curve of O_2 where a GHF solution is lower than either of the UHF solutions. Middle panel: Expectation value of $\hat{S}^2$ for the broken symmetry UHF singlet, UHF triplet, and GHF solutions. Note that $\langle \hat{S}^2 \rangle$ diminishes for the GHF solution when it goes from the triplet UHF solution and merges into the spin-contaminated singlet solution. Bottom panel: Mulliken atomic densities of the two oxygen atoms (left and right) as a function of the bond length for the GHF solution. Observe how the spin densities rotate from being parallel for $r < 1.42$ Å to being antiparallel for $r > 1.5$ Å.

RHF and UHF references were done using *Gaussian*, while those calculations on GHF references were done using an in-house program which reads the GHF eigenvectors from *Gaussian* and which works in the spinorbital basis. We verified the correctness of this program by comparison to *Gaussian*'s MP2, CCD, and CCSD results for RHF and UHF references, as well as for rotated UHF references (i.e., UHF references in which the wave function is an eigenfunction of $\hat{S}_x$ rather than of $\hat{S}_z$).

All GHF solutions reported in this work are real GHF solutions, and we did not find any complex solutions with lower energy than the GHF solutions shown. *Gaussian* does not have the capability of analyzing the stability of GHF-type wave functions, though there is the capability to test whether UHF solutions are GHF-stable. Thus, we cannot guarantee that there are no GHF solutions other than those we are reporting. We did generate a variety of different initial guesses in an attempt to recover as many GHF solutions as possible. In selected cases, we have tested the stability of GHF solutions using our in-house program.

Throughout, we have used Dunning's cc-pvdz basis set[31] with Cartesian *d* functions. While this basis is of minimal utility for high-accuracy prediction of molecular properties using correlated wave functions, it should be adequate for our purpose, which is simply to show the qualitative features of GHF and post-GHF calculations.

5.1. Dissociation of O_2. Let us begin by considering O_2. In the ground state, O_2 dissociates through the $^3\Sigma_g^-$ surface into two ^3P oxygen atoms. Describing triplet O_2 at the UHF level requires us to have $m_S = \pm 1$, while describing two triplet oxygen atoms with UHF requires each atom to have $m_S = \pm 1$ and the overall system to therefore have $m_S = 0$ or $m_S = \pm 2$.

There are, then, three relevant broken symmetry UHF states for our purposes, shown in Figure 1 along with the symmetry preserving UHF solution $^3\Sigma_g^-$. The triplet UHF curve at equilibrium cannot properly dissociate into two triplet atoms. Both the broken-symmetry singlet ($m_S = 0$) and quintet ($m_S = \pm 2$) curves are excited states at equilibrium but correctly dissociate to two triplet atoms, which the singlet approaches from below and the quintet approaches from above. It is clear that the triplet curve must cross both the singlet and the quintet. What we might prefer is to follow the UHF triplet solution near equilibrium and the UHF singlet near dissociation. This is precisely what GHF delivers: the lowest energy GHF solution connects the broken symmetry UHF triplet solution at equilibrium with the broken symmetry UHF singlet solution for $r \gtrsim 1.5$ Å. In this case, the GHF dissociation curve is differentiable but not smooth. At dissociation, the orbitals are localized onto the atoms and become the GHF atomic orbitals, exactly as we would expect for a product wave function of the form $|\Phi_{AB}\rangle = |\Phi_A \Phi_B\rangle$.

Figure 2 zooms in on the region where the UHF triplet and singlet cross. There is a small region over which a GHF solution exists, connecting the two surfaces. In Figure 2, we show how the GHF solution rotates the spin densities on the oxygen atoms from being parallel for $r < 1.42$ Å to being antiparallel for $r > 1.5$ Å, where the GHF solution coincides with the broken symmetry singlet solution. The expectation value of $\hat{S}^2$ goes down until it merges with the curve corresponding to the spin-contaminated singlet solution.

In Figure 3, we show the coupled-cluster results for the dissociation of O_2 on the singlet and triplet UHF references and on the GHF reference, as well as the corresponding reference dissociation curves. Using the UHF triplet as a reference, coupled cluster is not size-consistent, but using the GHF curve as a reference, it is. In the case of CCD (as well as MP2, not shown) the curves are continuous using a GHF reference. However, the CCSD curve on the GHF reference appears to be discontinuous.

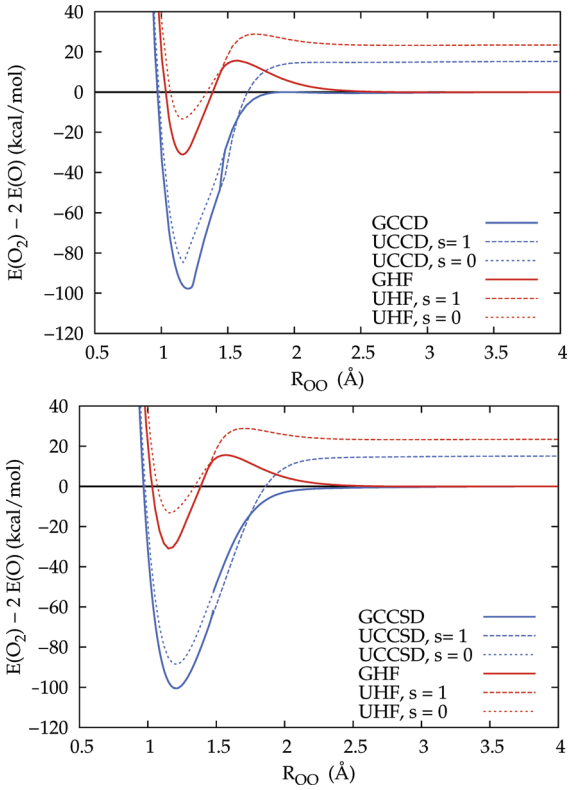

Figure 3. Top Panel: Coupled-cluster doubles and Hartree−Fock curves for the dissociation of O_2. Bottom Panel: Coupled-cluster singles and doubles and Hartree−Fock curves for the dissociation of O_2. The zero of energy has been set at the energy of two triplet oxygen atoms.

This can be readily understood in the following way: The effect of single excitations is simply to rotate the orbitals.[18] In the region of the potential energy curve where GHF is distinct from the UHF triplet, the single excitations will thus rotate the GHF reference toward the UHF triplet reference (and indeed, we see very little difference in their energy). Where the GHF joins the UHF singlet, however, the standard initial guess for the single excitation amplitudes forces CCSD to preserve $m_S = 0$. Since the CCSD curves based on the UHF singlet and triplet do not intersect at the same point as do the reference Hartree−Fock curves, we therefore see a discontinuity in the CCSD curve. The discontinuities in the CCSD curve appear to be, in other words, essentially due to abrupt changes in the character of the reference determinant and not due to the existence of multiple solutions to the CCSD equations *per se*. It may be that with a sufficiently clever initial guess that rotates the UHF singlet toward the UHF triplet, the CCSD curve can be made continuous, though we cannot guarantee this. The results of Li and Paldus[32] suggest that configuration interaction based on the GHF curve would quite probably be smoother, though no longer size-consistent. Because we use the lowest energy UHF solution as a reference at every geometry, the CCD and MP2 curves behave somewhat erratically where the UHF solution bifurcates.

If we were to continue to increase the level of correlation, the coupled-cluster curve based on the UHF triplet would improve, particularly near dissociation. Presumably the coupled-cluster curve based on the GHF reference would do likewise, provided with the correct initial guess. In Figure 4, we show the CCSD(T)[33] curves using the singlet and triplet UHF references.

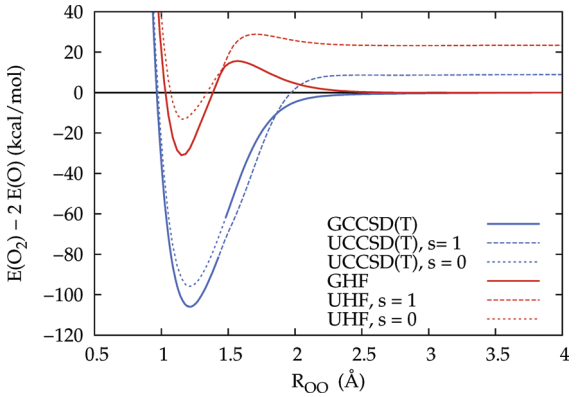

Figure 4. Hartree−Fock and CCSD(T) curves for the dissociation of O_2. The zero of energy has been set at the energy of two triplet oxygen atoms. Comparison with Figure 3 shows that CCSD(T) and CCSD have no qualitative differences in this case. The curve marked as the GHF-based CCSD(T) uses the UHF triplet as a reference for small R and the UHF singlet as a reference for large R.

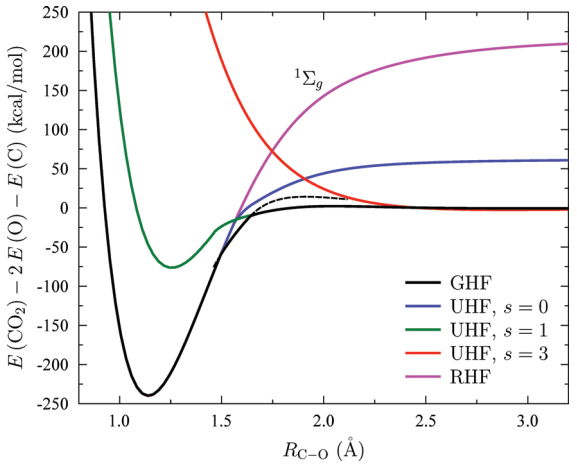

Figure 5. Dissociation curves of the CO_2 molecule into a carbon atom and a pair of oxygen atoms, computed at the HF level. The zero of energy has been set at the energy of UHF triplet atoms. We show the lowest energy UHF singlet, triplet, and septet solutions as well as the RHF solution and two GHF solutions. There are two kinks in the lowest energy GHF curve, as can be seen more clearly in Figure 6.

The curve marked as using the GHF reference in fact uses one of the two UHF states as a reference in the region where the GHF and UHF states are identical. We have not included data from the region where GHF is distinct from UHF, as we do not have a genuine GHF-based CCSD(T) implementation. Qualitatively, there is little distinction between the CCSD and CCSD(T) results, which is to be expected, though we note that indeed the difference between the singlet and triplet dissociation limits for CCSD(T) is less than the corresponding difference for CCD or CCSD. Eventually, as we reach full configuration interaction, the UHF-based and GHF-based coupled cluster curves would coincide. Finally, we point out that while GHF does go to the right limit, it does so with an artificial barrier to the formation of the bond in O_2. This is much in analogy with the behavior of UHF in N_2, which likewise goes to the proper limit but with an unphysical bump. Adding explicit correlations, as expected, eliminates the bump.

dx.doi.org/10.1021/ct200345a |J. Chem. Theory Comput. 2011, 7, 2667–2674

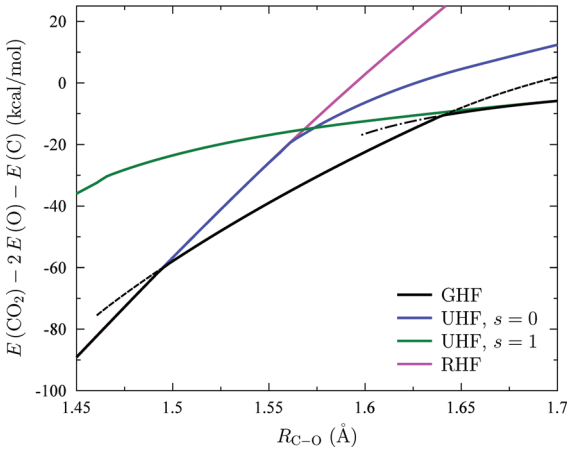

Figure 6. Zoom-in of the region of the symmetric dissociation curve of CO_2 where GHF solutions are lower than any of the UHF solutions. Three different GHF solutions were found in the interval 1.4 Å < r < 1.7 Å. None of the solutions connect smoothly with the RHF/UHF curve. We have succeeded in following the GHF solutions a short way past the point where they cross various UHF solutions.

5.2. Symmetric Dissociation of CO_2. Now, we turn to the description of the atomization of CO_2 by symmetric stretching of the C═O bonds. The ground state dissociation occurs through the $^1\Sigma_g$ surface into two ^3P oxygen atoms and a ^3P carbon atom. At the UHF level, the appropriate dissociation limit can then only be reached with $m_S = \pm 3$ and $m_S = \pm 1$, though at equilibrium the system must clearly have $m_S = 0$.

Dissociation curves computed at the HF level are shown in Figure 5. This figure includes the symmetric RHF solution $^1\Sigma_g$, which has a triplet instability for r > 1.6 Å, yielding the singlet UHF solution. Several broken symmetry triplet solutions were found, the lowest energy of which is included in the figure, as is the broken symmetry septet solution. The lowest energy GHF solution has two kinks, as explained below.

In Figure 6, we zoom in on the region of the potential energy curve where the various UHF solutions cross each other. Three different GHF solutions were found. The first (dashed in Figure 6) crosses the RHF solution near r = 1.5 Å; we can continue to follow this solution to $r \approx$ 1.46 Å, but no further. This same GHF solution crosses the UHF triplet near r = 1.64 Å and can be followed until $r \approx$ 2.1 Å. The second GHF solution (dashed-dotted in Figure 6) connects to the UHF broken-symmetry triplet and crosses the first GHF solution near r = 1.64 Å. A third solution can also be found in this vicinity, but it is slightly higher in energy.

While we can continuously follow various GHF curves from the RHF solution at equilibrium to the UHF triplet at dissociation, the result is not differentiable due to the kinks mentioned above. We looked for other GHF solutions near these kinks, to smooth the transition from one curve to another, but were unable to find any. Stability analyses every 0.005 Å between 1.5 Å and 1.65 Å revealed no GHF instabilities in our solutions. We have used a quadratically convergent algorithm[34] to follow solutions as far as possible.

In Figure 7, we show the results from MP2 based on the GHF reference. While the MP2 curve on the GHF reference is continuous in O_2, it is discontinuous here. This is simply because, unlike in O_2 where the GHF solution merges with the UHF triplet and UHF singlet, here in CO_2 the GHF solutions, as we have already noted, continue past the points where they cross the RHF and UHF triplet curves. Thus, unlike in O_2, the orbitals and orbital energies on the lowest-energy Hartree−Fock reference change abruptly at the curve crossings, and the MP2 becomes discontinuous. Coupled cluster will inherit these same deficiencies.

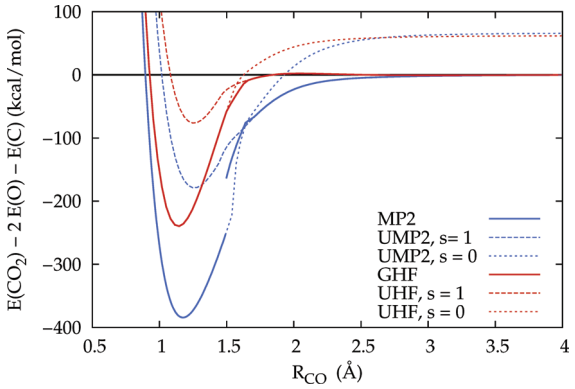

Figure 7. Second-order and Hartree−Fock curves for the dissociation of CO_2. The zero of energy has been set at the energy of isolated atoms. The GHF-based MP2 curve connects the two UHF-based curves, with a jump where the GHF and UHF singlet solution merge.

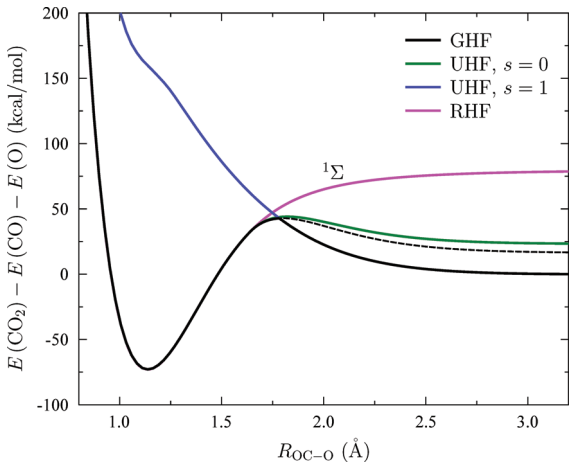

Figure 8. Dissociation curves of CO_2 molecule into an oxygen atom and the CO molecule, computed at the HF level. One of the C−O distances has been kept constant at r = 1.1621 Å. We show the symmetric RHF curve, the broken-symmetry UHF singlet and triplet, and two GHF solutions.

5.3. Asymmetric Dissociation of CO_2. The last example we consider corresponds to the asymmetric dissociation of the CO_2 into an oxygen atom and CO. In the ground state, this process occurs through the $^1\Sigma$ surface dissociating into a ^3P oxygen atom and a $^1\Sigma^+$ CO molecule. Thus, only a triplet solution will yield the right dissociation limit at the Hartree−Fock level.

Dissociation curves computed at the HF level are shown in Figure 8. We show the symmetric RHF solution $^1\Sigma$ along with a broken symmetry singlet UHF solution. Figure 8 also shows the lowest energy triplet UHF solution, which is unbound but which goes to the energetically correct dissociation limit. Finally, we include two GHF solutions. The lowest energy GHF curve shows a kink near r = 1.8 Å, where the triplet and UHF singlet cross. Note that there is another solution which is bound and has lower energy for small interatomic separations.

dx.doi.org/10.1021/ct200345a |J. Chem. Theory Comput. 2011, 7, 2667–2674

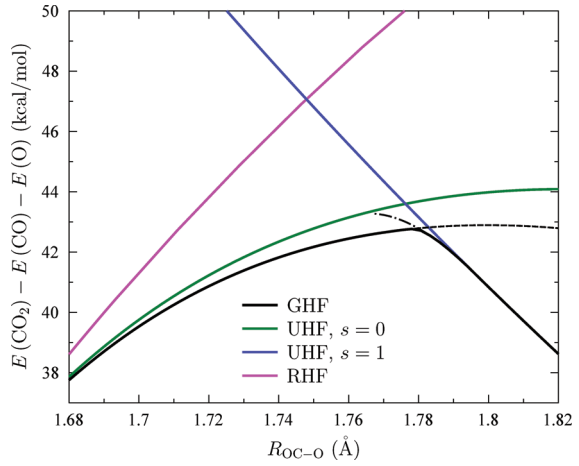

Figure 9. Zoom-in of the region of the asymmetric dissociation curve of CO_2 where GHF solutions are lower than any of the UHF solutions. Note how one of the GHF solutions merges with the singlet UHF solution for $r < 1.65$ Å. On the other hand, another GHF solution merges with the UHF triplet solution for $r > 1.8$ Å. At $r \approx 1.78$ Å, the two GHF solutions intersect.

Figure 9 zooms in on the region of the potential energy surface where GHF connects the singlet and triplet UHF states. Of our two GHF solutions, one connects to the singlet and the other to the triplet. These two solutions intersect at $r \approx 1.78$ Å, and we were unable to find other GHF solutions which connect them smoothly. Stability analysis of the lowest energy GHF solution every 0.005 Å between 1.77 Å and 1.80 Å revealed no GHF instabilities.

6. DISCUSSION

As we have seen, relaxing all of the symmetry constraints allows for Hartree−Fock to reach the energetically correct dissociation limit for several molecules for which RHF and UHF are not size-consistent. The price we pay for having the right behavior at equilibrium and size-consistent dissociation is that the GHF dissociation curve is not always smooth or even always differentiable. This is in analogy with UHF instabilities, where the wave function need not have continuous derivatives, but the situation appears to be somewhat exacerbated in GHF. We point out that due to the nonlinearity of the Hartree−Fock equations, this same phenomenon may exist in following the lowest energy RHF or UHF solution at each geometry. It is also worth noting that often one can find myriad GHF solutions which, however, cannot always be followed from one nuclear configuration to another. In other words, GHF is a rather tricky method. We point the interested reader to work by Fukutome[35] and Mestechkin[36] on the properties of the potential energy surface near a Hartree−Fock instability threshold and to work of Fukutome[37−39] on molecular dissociation.

Post-GHF correlated calculations inherit the same problems as does GHF. Worse, when GHF solutions cross rather than merge with higher symmetry solutions, correlated curves using the GHF reference may be discontinuous. Additionally, the inclusion of single excitations may be problematic, and one presumably needs a fairly clever initial guess to force solutions which carry the wave function from one symmetry to another (for example, changing the value of m_S from 0 to 1 in the dissociation of O_2). Configuration interaction may not inherit these same problems, simply because rather than solving nonlinear equations one merely diagonalizes the Hamiltonian in a restricted space which can be chosen to include spin flips. On the other hand, truncated configuration interaction is not size-extensive, and for all of their qualitative weaknesses, it should not be forgotten that size-extensive correlated techniques such as many-body perturbation theory or coupled cluster theory in combination with a size-consistent reference such as GHF result in size-consistent correlated methods, which is not generally the case when these same techniques are applied to a reference which is not size-consistent.

APPENDIX A. GHF AND SIZE CONSISTENCY

Let us return to our GHF-type wave function for the well-separated AB system, $|\Phi_{AB}\rangle = |\Phi_A\Phi_B\rangle$, where we recall that $|\Phi_A\rangle$ and $|\Phi_B\rangle$ are the GHF wave functions for the isolated fragments A and B, respectively. The total energy of the system, including the nuclear−nuclear repulsion energy, is then

$$\begin{aligned} E_{AB} &= E_{AB}^{nuc} + E_A^{nuc} + E_B^{nuc} + \sum\langle\phi_A|h|\phi_A\rangle \\ &\quad + \sum\langle\phi_B|h|\phi_B\rangle + \frac{1}{2}\sum\langle\phi_A\phi_{A'}||\phi_A\phi_{A'}\rangle \\ &\quad + \frac{1}{2}\sum\langle\phi_B\phi_{B'}||\phi_B\phi_{B'}\rangle + \sum\langle\phi_A\phi_B||\phi_A\phi_B\rangle \end{aligned} \tag{8}$$

where E_A^{nuc}, E_B^{nuc}, and E_{AB}^{nuc} are, respectively, the nuclear repulsion energy within fragment A within fragment B and between fragments A and B, and where ϕ_A and ϕ_B are molecular orbitals occupied in $|\Phi_A\rangle$ and $|\Phi_B\rangle$. $h = t + v_A + v_B$, where v_i represents interactions with the nuclei in fragment i, the total energy becomes simply

$$\begin{aligned} E_{AB} &= E_A + E_B + E_{AB}^{nuc} + \sum\langle\phi_A|v_B|\phi_A\rangle \\ &\quad + \sum\langle\phi_B|v_A|\phi_B\rangle + \sum\langle\phi_A\phi_B||\phi_A\phi_B\rangle \end{aligned} \tag{9}$$

The exchange energy between the two fragments vanishes since the orbitals do not overlap, and the remaining integrals can all be evaluated using the multipole expansion. The result is

$$E_{AB} = E_A + E_B + \frac{(Z_A - N_A)(Z_B - N_B)}{R_{AB}} + \mathcal{O}\left(\frac{1}{R_{AB}^2}\right) \tag{10}$$

where Z_i and N_i are, respectively, the total nuclear charge and the total number of electrons in fragment i. Recognizing $Z_i - N_i = q_i$ gives us eq 7.

AUTHOR INFORMATION

Corresponding Author
*E-mail: guscus@rice.edu.

ACKNOWLEDGMENT

This work was supported by the National Science Foundation (Grants CHE-0807194 and CHE-1110884) and the Welch Foundation (C-0036). We thank Juan Peralta for providing us with the code necessary for population analysis on a GHF wave function.

REFERENCES

(1) Čížek, J. *J. Chem. Phys.* **1966**, *45*, 4256.

(2) Čížek, J. *Adv. Chem. Phys.* **1969**, *14*, 35.
(3) Paldus, J.; Li, X. Z. *Adv. Chem. Phys.* **1999**, *110*, 1.
(4) Shavitt, I.; Bartlett, R. J. *Many-Body Methods in Chemistry and Physics*; Cambridge University Press: New York, 2009.
(5) Tsuchimochi, T.; Scuseria, G. E. *J. Chem. Phys.* **2009**, *131*, 121102.
(6) Scuseria, G. E.; Tsuchimochi, T. *J. Chem. Phys.* **2009**, *131*, 164119.
(7) Tsuchimochi, T.; Scuseria, G. E.; Savin, A. *J. Chem. Phys.* **2010**, *132*, 024111.
(8) Tsuchimochi, T.; Henderson, T. M.; Scuseria, G. E. *J. Chem. Phys.* **2010**, *133*, 134108.
(9) Löwdin, P.-O.; Lykos, P.; Pratt, G. W. *Rev. Mod. Phys.* **1963**, *35*, 496–501.
(10) Fukutome, H. *Int. J. Quantum Chem.* **1981**, *20*, 955–1065.
(11) Bardeen, J.; Cooper, L. N.; Schrieffer, J. R. *Phys. Rev.* **1957**, *108*, 1175–1204.
(12) Bach, V.; Lieb, E. H.; Solovej, J. P. *J. Stat. Phys.* **1994**, *76*, 3.
(13) Wigner, E. P. *J. Math. Phys.* **1960**, *1*, 409.
(14) Stuber, J. L.; Paldus, J. Symmetry Breaking in the Independent Particle Model. In *Fundamental World of Quantum Chemistry: A Tribute Volume to the Memory of Per-Olov Löwdin*; Brändas, E. J., Kryachko, E. S., Eds.; Kluwer Academic Publishers: Dordrecht, The Netherlands, 2003; Vol. 1, Chapter 4, pp 67−139.
(15) Benard, M. *J. Chem. Phys.* **1969**, *71*, 2546–2556.
(16) Löwdin, P.-O.; Mayer, I. *Adv. Quantum Chem.* **1992**, *24*, 79–114.
(17) Overhauser, A. W. *Phys. Rev.* **1962**, *128*, 1437–1452.
(18) Thouless, D. J. *Nucl. Phys.* **1960**, *21*, 225–232.
(19) Čížek, J.; Paldus, J. *J. Chem. Phys.* **1967**, *47*, 3976–3985.
(20) Seeger, R.; Pople, J. A. *J. Chem. Phys.* **1977**, *66*, 3045–3050.
(21) Blaizot, J.-P.; Ripka, G. *Quantum Theory of Finite Systems;* MIT Press: Cambridge, MA, 1985.
(22) Scuseria, G. E.; Jiménez-Hoyos, C. A.; Henderson, T. M.; Samanta, K.; Ellis, J. K. *Projected Quasiparticle Theory for Molecular Electronic Structure*. http://arxiv.org/abs/1106.0956. Submitted for publication.
(23) Piecuch, P.; Toboła, R.; Paldus, J. *Phys. Rev. A* **1996**, *54*, 1210.
(24) Frisch, M. J.; Trucks, G. W.; Schlegel, H. B.; Scuseria, G. E.; Robb, M. A.; Cheeseman, J. R.; Scalmani, G.; Barone, V.; Mennucci, B.; Petersson, G. A.; Nakatsuji, H.; Caricato, M.; Li, X.; Hratchian, H. P.; Izmaylov, A. F.; Bloino, J.; Zheng, G.; Sonnenberg, J. L.; Hada, M.; Ehara, M.; Toyota, K.; Fukuda, R.; Hasegawa, J.; Ishida, M.; Nakajima, T.; Honda, Y.; Kitao, O.; Nakai, H.; Vreven, T.; Montgomery, J. A., Jr.; Peralta, J. E.; Ogliaro, F.; Bearpark, M.; Heyd, J. J.; Brothers, E.; Kudin, K. N.; Staroverov, V. N.; Kobayashi, R.; Normand, J.; Raghavachari, K.; Rendell, A.; Burant, J. C.; Iyengar, S. S.; Tomasi, J.; Cossi, M.; Rega, N.; Millam, J. M.; Klene, M.; Knox, J. E.; Cross, J. B.; Bakken, V.; Adamo, C.; Jaramillo, J.; Gomperts, R.; Stratmann, R. E.; Yazyev, O.; Austin, A. J.; Cammi, R.; Pomelli, C.; Ochterski, J. W.; Martin, R. L.; Morokuma, K.; Zakrzewski, V. G.; Voth, G. A.; Salvador, P.; Dannenberg, J. J.; Dapprich, S.; Parandekar, P. V.; Mayhall, N. J.; Daniels, A. D.; Farkas, O.; Foresman, J. B.; Ortiz, J. V.; Cioslowski, J.; Fox, D. J. *Gaussian Development Version*, Revision H.01; Gaussian, Inc.: Wallingford, CT, 2009.
(25) Peralta, J. E.; Scuseria, G. E.; Frisch, M. J. *Phys. Rev. B* **2007**, *75*, 125119.
(26) Purvis, G. D., III; Bartlett, R. J. *J. Chem. Phys.* **1982**, *76*, 1910.
(27) Cullen, J. M.; Zerner, M. C. *J. Chem. Phys.* **1982**, *77*, 4088–4109.
(28) Scuseria, G. E.; Lee, T. J.; Schaeffer, H. F. *Chem. Phys. Lett.* **1986**, *130*, 236–239.
(29) Scuseria, G. E.; Schaeffer, H. F. *Chem. Phys. Lett.* **1988**, *146*, 23–31.
(30) Piecuch, P.; Paldus, J. *Int. J. Quantum Chem.* **1989**, *36*, 429.
(31) Dunning, T. H., Jr. *J. Chem. Phys.* **1989**, *90*, 1007.
(32) Li, X.; Paldus, J. *J. Chem. Phys.* **2009**, *130*, 084110.
(33) Raghavachari, K.; Trucks, G.; Pople, J. A.; Head-Gordon, M. *Chem. Phys. Lett.* **1989**, *157*, 479.
(34) Bacskay, G. B. *Chem. Phys.* **1981**, *61*, 385–404.
(35) Fukutome, H. *Prog. Theor. Phys.* **1975**, *53*, 1320–1336.
(36) Mestechkin, M. *THEOCHEM* **1988**, *181*, 231–236.
(37) Takabe, T.; Takahashi, M.; Fukutome, H. *Prog. Theor. Phys.* **1976**, *56*, 349.
(38) Takahashi, M.; Fukutome, H. *Prog. Theor. Phys.* **1978**, *59*, 1787.
(39) Igawa, A.; Fukutome, H. *Prog. Theor. Phys.* **1980**, *64*, 491.

JCTC Journal of Chemical Theory and Computation

LETTER

pubs.acs.org/JCTC

Bridging the Gap between Folding Simulations and Experiments: The Case of the Villin Headpiece

G. Saladino, M. Marenchino, and F. L. Gervasio*

Structural Biology and Biocomputing Programme, Spanish National Cancer Research Centre (CNIO), c/Melchor Fernandez Almagro 3, 28029, Madrid, Spain

Supporting Information

ABSTRACT: The increasing accuracy of molecular dynamics force fields parameters and the increasing resolution of experimental results allow one to carefully compare and complement in silico data with experimental observations. Here, we study the human villin headpiece C-terminal helical subdomain (HP35) with the recent highly optimized Amber99SB*-ILDN force field and compare the results with recent high resolution triplet−triplet energy transfer (TTET) experiments. The correct reproduction of the main structural features reveals a good agreement between experimental data and simulations.

1. INTRODUCTION

Understanding the mechanism of protein folding with high spatial and temporal resolution remains one of the most important and challenging goals of molecular biophysics and biophysical chemistry.[1] Thanks to the impressive progress in experimental techniques, such as as triplet−triplet energy transfer (TTET),[2] we now have access to very detailed information about the folding mechanisms. However, the atomistic interpretation of the spectroscopic observations can be complex and often requires the help of molecular modeling and simulations. Molecular dynamics (MD) simulations have been successfully used for studying complex biomolecular systems, providing an atomistic description of their structure and dynamics. Unfortunately, their predictive power has been so far hampered by the limited time-scale that they can routinely reach and by the accuracy of the force fields used. Recently, the development of advanced sampling algorithms,[3−5] the use of specialized hardware,[6] and the concomitant improvement of force fields[7−9] have extended the capability of MD simulations to the point that they can be directly used for interpreting and complementing the experiments. At the same time, a careful comparison of the simulation prediction with much more detailed experiments can be used to verify the quality of the latest force field.

Here, we take advantage of state-of-the-art simulation techniques to reinvestigate the mechanism of folding of the human villin headpiece C-terminal helical subdomain (HP35)[10] in water and compare it with high resolution spectroscopy experiments[2] and CD measurements. Our converged free energy surfaces agree surprisingly well with the experiments, showing a rather dynamic folded state and an unfolded ensemble that retains significant structure.

2. RESULTS

2.1. Different Conformations of HP35. HP35 has a well-defined secondary and tertiary structure, characterized by three α helices bundled together by a closely packed hydrophobic core involving three phenylalanines,[11] and is one of the smallest peptides that folds cooperatively.[12] Because of its small size and fast folding dynamics, HP35 has been the subject of several computational[13−19] and experimental[2,11,20−27] studies. We performed 1.5-μs-long unbiased fully atomistic MD simulations, massive bias exchange molecular dynamics simulations (BEMD)[28] at 298 and 320 K, and calorimetry and circular dichroism (CD) experiments. Fully atomistic MD simulations were performed at 298 K starting from the lowest energy NMR structure (PDB code: 1UNC).[10] We used the most recent Amber99SB*-ILDN[29] force field, including improved rotamer[7] and backbone corrections.[8]

During the simulation, we observed only partial unfolding and refolding events. The simulation spends most of the time in two folded structures that differ in the "compactness" of the hydrophobic core, while retaining all the secondary structure elements. This observation is in agreement with TTET experiments on HP35 folding, which have shown the presence of two folded states, N and N′, where the latter is less compact than the former.[2] Analysis of the conformations with the highest root mean square deviation (RMSD) from the NMR structure revealed the presence of a partially folded state, in which helixes 1 and 2 are correctly folded while helix 3 is largely unstructured. The higher stability of the region encompassing helixes 1 and 2 has been previously observed with both TTET and NMR.[2,23] It is worth noting that very long unbiased MD simulations at high temperature (380 K) performed with the same Amber99SB*-ILDN force field predicted that in the unfolded state the fraction of residues of helix 3 that are helical is larger than that of helix 1 and helix 2.[9]

To reconstruct a fully converged free-energy landscape of HP35 folding, we used massive BEMD simulations at 298 and 320 K, which is very close to the experimental melting temperature (see Supporting Information). Using BEMD, Piana et al.[19] were able to correctly predict the effects of a point mutation on HP35 in agreement with NMR and CD experiments. The BEMD runs were performed using the PLUMED[30] plug-in. The same

Received: April 12, 2011
Published: July 27, 2011

collective variables (CVs) of ref 19 were used. Each BEMD simulation required considerably longer sampling time than those used in ref 19 to converge (>300 ns). This is most probably due to the different version of the Amber force field used. Indeed, the folding time reported in ref 9 is 0.8 μs for Amber03 and 3.0 μs for Amber99*SB-ILDN. The free energy profiles were reconstructed from the unbiased probability distribution of the states of the neutral (unbiased) replica.

The existence of the two previously identified folded structures is confirmed by the free energy landscapes at 320 K. The representative structures of the two nearby free-energy basins correspond to the definition of the folded states N and N′ with the latter conformation, previously described as a "dry molten globule", being more open and more flexible (see Figure 1).[2] The solvent -accessible surface area (SASA) for the N′ conformation is 3109 Å^2, slightly more than the corresponding value (3056 Å^2) for the N state (Supporting Information, Figure S1). On average, the N′ state also shows an increase of the distance between the C- and N-termini compared to the N state (24.0 Å vs 18.7 Å), in agreement with experimental observations. As another point of agreement, half of the total SASA exposed during unfolding ($\Delta SASA_{N\rightarrow U}$ = 283 Å^2) is exposed during the N to N′ transition ($\Delta SASA^{max}_{N\rightarrow N'}$ = 123 Å^2).

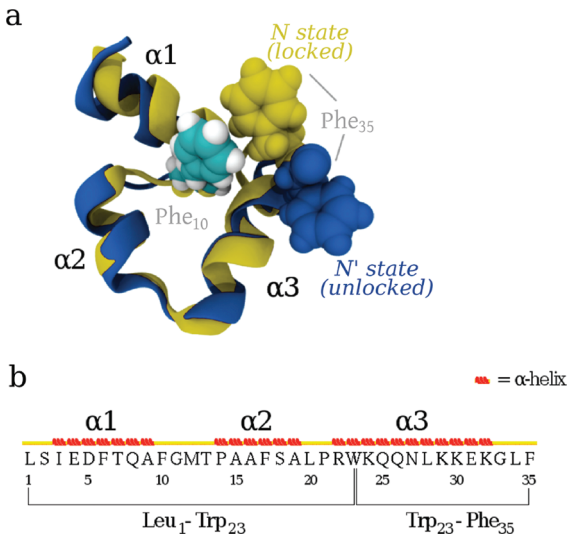

Figure 1. HP35 sequence and tridimensional structure. Two different folded states, N and N′, were observed. In agreement with ref 2, a locking mechanism exists involving the stacking of Phe_{10} and Phe_{35}.

For a punctual comparison with the high resolution experiment results, we calculated the free energy as a function of the set of distances measured in the TTET experiments and the C_α RMSD from the NMR structure. The distance between residues Trp_{23} and Phe_{35} was found to be the most suitable variable to discern the different conformations of HP35. The free energy at 320 K as a function of the Cα RMSD and the distance Trp_{23}—Phe_{35} is shown in Figure 2. Again two well-defined minima corresponding to the N and N′ states are observed: as opposed to the narrow N state minimum, the N′ state shows a wider free energy basin, confirming its increased flexibility. As suggested by Kiefhaber et al., the N and N′ conformations are very similar, reporting an overall Cα RMSD of 0.9 Å.

The calculation of relevant residues' distances and RMSDs for both conformations reveals that the structural differences between N and N′ are due to the stacking of the aromatic rings of Phe_{10} and Phe_{35}, responsible for the observed slightly more compact structure in which the orientation of helix 1 slightly changes (Figure 1).

Besides the clearly visible N and N′ states, a secondary partially folded minimum can be observed. This minimum, corresponding to a Trp_{23}—Phe_{35} distance of 9.85 Å, versus 15.22 Å of the native state, is populated by conformations in which helix 3 is partially unfolded (Supporting Information Figure S2). Its conformation strongly resembles the intermediate state I proposed in ref 2 and is consistent with the intermediate state proposed by Eaton et al.[26] and with the observed relative stability of the three helices.[23,25]

This confirms the observation done in the unbiased MD run at 298 K and is at odds with the results of unbiased MD runs at 380 K. The difference in relative helix stability could be due to the temperature. However, as we perform a biased MD simulation, we are only able to reconstruct the thermodynamics of the system, not the kinetics. Thus, we can only hypothesize that the I state that we observe is an off-path intermediate.

The free energy profile as a function of RMSD and the distance between residues Leu_1 and Trp_{23} shows once more two minima corresponding to the folded ensemble (low RMSD values and NMR Leu_1—Trp_{23} distance) together with a broad minimum corresponding to an unfolded structure (high RMSD and low Leu_1—Trp_{23} distance).

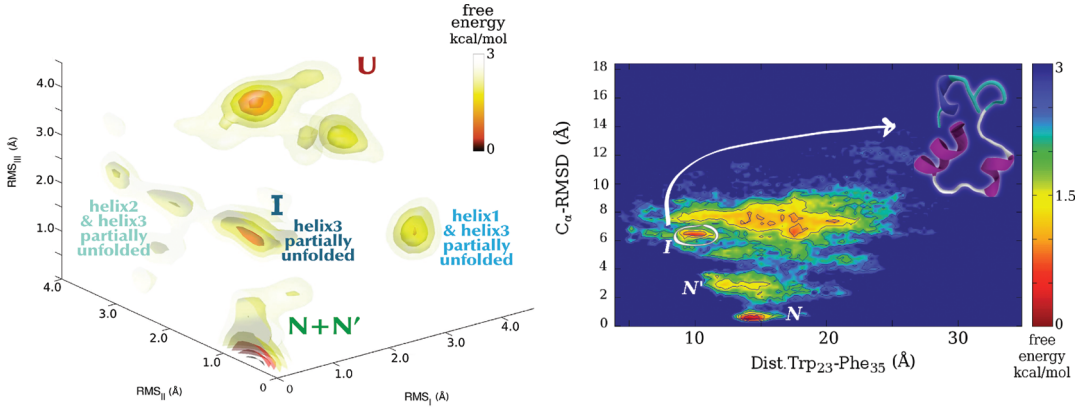

Figure 2. Left: HP35 free energy landscape at 320 K as a function of the RMSD from the ideal helical structure of the three helices. Right: Free energy landscape at 320 K projected on the distance between residues Trp_{23}-Phe_{35} and the RMSD of the Cα from the NMR native structure.

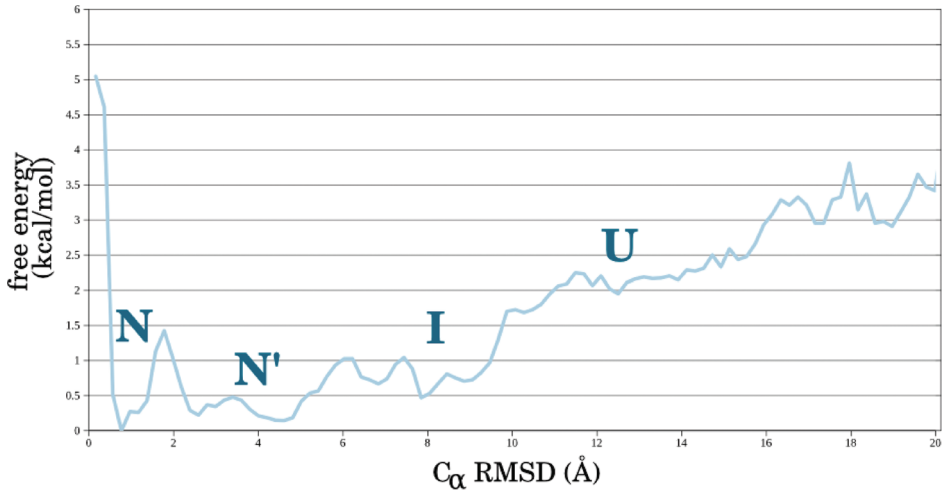

Figure 3. Free energy profile at 298 K as a function of the Cα RMSD. The relative stability of conformations N, N′, I, and U is very similar to that found in the experiments (see ref 2).

The structures found in the unfolded basin are consistent with the well-documented observations of residual helical structure in the unfolded ensemble of HP35.[23,25,31−33] The free energy as a function of the helical content (see Supporting Information Figure S3) shows two minima corresponding respectively to the value typical of the folded structure and to a higher helical content. The absence of a minimum corresponding to low helical content means that random coil structures are much higher in energy. This confirms the propensity of HP35 to adopt partially structured conformations in the unfolded ensemble instead of a random coil.

Overall, the conformations observed in TTET experiments are correctly identified in our simulations. However, at 320 K, the relative stability of the various conformations does not agree with that of the experiments, where the N and N′ states have almost the same stability, while the I state is scarcely populated (see Figure 2). Moreover, the stability order of the helices at 320 K does not correspond to that predicted at 380 K with very long unbiased MD simulations.

To assess whether these discrepancies are due to the different temperature of the simulations and the TTET experiments or to the force field, we repeated the BEMD simulation at 298 K. At this temperature, the main features of the FES, as well as the conformations of the N and N′ states, are conserved. On the contrary, the relative stability is now in better agreement with the experiments (as expected). The relative stability at 298 K is N < N′ ≪ I (see Figure 3).

While the agreement with experiments is recovered, not all is well with respect to the population of the I state as a function of the temperature. Indeed, TTET experiments suggest that, at higher temperatures, the population of the N′ state increases, while the I state remains scarcely populated, and the BEMD simulations predict that the population of the I state at 320 K is still significant, to the detriment of the N′ state.

We found that the calculated activation energies are lower that the experimental values. Nevertheless, the order observed in the experiments is reproduced, confirming that the N→N′ barrier is high (5.9 kJ/mol) and higher than the N′→I one (3.78 kJ/mol). Thus, the unfolding of helix α_3 is fast once the system reaches the unlocked N′ state and much faster than the N→N′ rearrangements, as observed experimentally. Our results suggest that the unfolding of HP35 should involve a three-step mechanism: unlocking (→N′), unfolding of helix α_3 (→I), and overall unfolding (→U). However, as mentioned, it is difficult to discern from BEMD simulations whether the unfolding of helix α_3 is part of the overall unfolding process or a competitive process leading to an off-path intermediate. Considering the kinetics of the process, these results are in agreement with ref 2, suggesting that the N→N′ conformational change can constitute a rate limiting step in fast-folder variants of HP35.

2.2. The Locking Mechanism for Native states N and N′. We carefully analyzed the differences between the states N and N′ performing two additional 100 ns unbiased MD simulations. No transitions were observed in either MD, confirming that the two structures are stable states and in agreement with the experimentally measured interconversion characteristic time of 900 ns (see ref 2). The unbiased MDs allowed for a better characterization of the differences between N and N′. As observed in the BEMD simulations, the stacking of Phe_{35} onto Phe_{10} is the most evident difference. However, the equilibrium MD revealed that Phe_{35} stacking is a faster movement compared to the N→N′ transition, as detachment and restacking of Phe_{35} was observed multiple times during the 100 ns. Hence, Phe_{35}−Phe_{10} interaction, while being a well-defined feature of the N state, seems to be involved in the locking mechanism but not univocally identifiable with it. In a previous work, Pande et al.[14] suggested that the stacking of Phe_{10} and Phe_{35} constitutes a kinetic trap since their strong interaction prevents HP35 from adopting a correct folding. However, it was proven experimentally[21] that mutation of residue Phe_{35} does not cause considerable alteration of folding kinetics. The fast kinetics of Phe_{35} observed in our simulations thus put into perspective the results previously obtained: while important and characteristic of the N state, the Phe_{35}−Phe_{10} interaction is fast enough not to be determinant for folding kinetics.

A deeper analysis of the interactions in the "lock region", where the terminal residues of helix α_1 are in contact with the C-terminal region belonging to helix α_3, comprising residues 8−11 and 32−35, respectively, revealed the presence of a complex network of hydrogen bonds. A highly populated (>42 %) H bond between Ala_9 and Leu_{34} was observed. This H bond is almost as strong as the *i*, *i* + 4 α-helical bonds, keeping

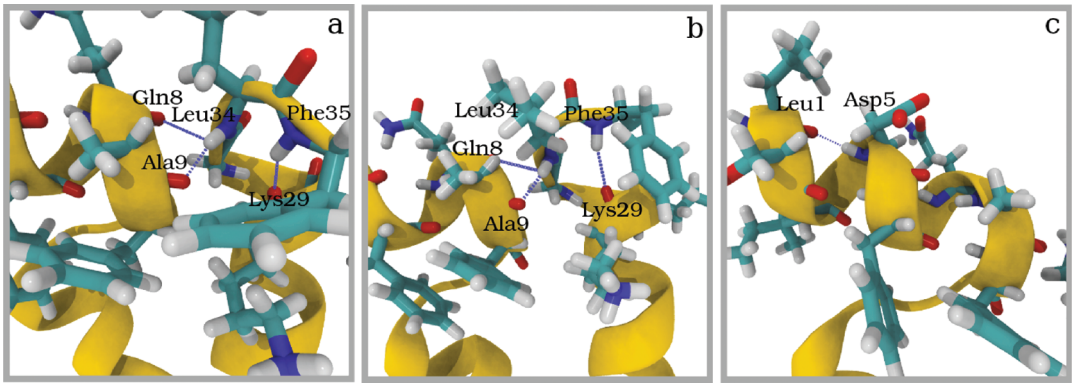

Figure 4. The residues involved in the locking mechanism. (a) H-bond network involving residues Gln_8, Ala_9, and Leu_{34}. (b) The strong H bonds are preserved even when Phe_{35} briefly detaches from the hydrophobic core. (c) As opposed to the N′ state, a strong *i*, *i* + 4 H bond is observed between residues Leu_1 and Asp_5 in the N state.

helices α_1 and α_3 close. Another strong H bond was observed between Gln_8 and Leu_{34}, with a population of 23.1 %. At least in 15% of the entire trajectory, Leu_{34} is involved in a bifurcated H bond involving both residues (see Figure 4, panel a).

A strong H bond was also observed between Phe_{35} and Lys_{29} (Figure 4, panel a); this *i*, *i* + 6 bond forces a particular conformation of the C terminus, where the backbone forms an additional "helix-like" turn. The identified H-bond network was never completely broken throughout our 100 ns simulation of the N state, even when Phe_{35} breifly undocks (see Figure 4, panel b), thus proving to be the slow-kinetic step involved in the "locking" mechanism. This is confirmed by the analysis of the N′ state conformations. In this case, none of the mentioned H bonds has a population higher then 1.8%, helices α_1 and α_3 are detached, and the C-terminal region is extremely more flexible, as observed in TTET experiments (see ref 2 and Supporting Information Figure S4).

The stacking of Phe_{35} onto Phe_{10} is not observed anymore, and Leu_{34} substitutes Phe_{35} in the strong HP35 hydrophobic core (see Supporting Information Figure S5). In the 75% of the conformations, Phe_{35} does not point toward the hydrophobic core, as in the N state, but toward the back side of helix α_1. Surprisingly, in this conformation Phe_{35} forms strong H-bonds with the residues left unpaired by Leu_{34}, Gln_8 (pop. 32.47%), and Ala_9 (pop. 7.99%; see Supporting Information Figure S6). Interestingly, the interaction of Phe_{35} with the side of helix α_3 destabilizes the first turn of helix α_1, as the population of the first *i*, *i* + 4 α-helical bond between Leu_1 and Asp_5 drops from the 57% of the N state to 31.8%. This gives rise to a quite different conformation of state N′ in the N-terminal region as well (see Supporting Information Figure S7).

Analyses of the N′ conformations also prompted an additional striking point toward the agreement with the experiments: conformations with a very low distance between residues Trp_{23} and Phe_{35} were observed, in which the C-terminal region unwinds on top of helix α_3 (see Supporting Information Figure S8). These conformations explain why TTET experiments observed more rapid exchanges between Nal23−Xan35 in the N′ state.

3. EXPERIMENTAL VALIDATION

So far, the simulations provided a very detailed view of the molecular structure and dynamics that at room temperature is in excellent agreement with spectroscopic observations. Still, as the temperature increases, the behavior seems to depart from that experimentally observed. To further investigate this issue, we performed thermodynamic and spectroscopic measurements. HP35 in water has a well-defined structure, as shown by the CD spectra with two minima at 208 and 222 nm and a positive band near 190 nm, characteristic of the α-helical structure (Figure 5). The ratio of those minima, $\theta_{222:208}$ has been used as a criterion in several proteins to evaluate the presence of coiled-coil helices. For a noninteracting α helix, the ratio has been shown to be 0.83, while for stranded coiled coils, the ratio was calculated to be >1.[34−38] HP35 in water exhibited a $\theta_{222:208}$ ratio above 1 up to 50 °C. Then, we exploited thermal and chemical denaturation to gain an in-depth thermodynamic description. Under all conditions tested, HP35 showed a cooperative, sigmoidal transition, and the data fit a two-state model with a transition temperature (T_m) of 44 °C. Chemical denaturation experiments using urea were also carried out at seven different temperatures ranging from 10 to 40 °C. The addition of urea resulted in the loss of secondary structure, and the denaturation curve, as determined by following the dichroic signal at 222 nm, also showed two-state unfolding behavior. At 25 °C, the midpoint of the urea-induced unfolding transition

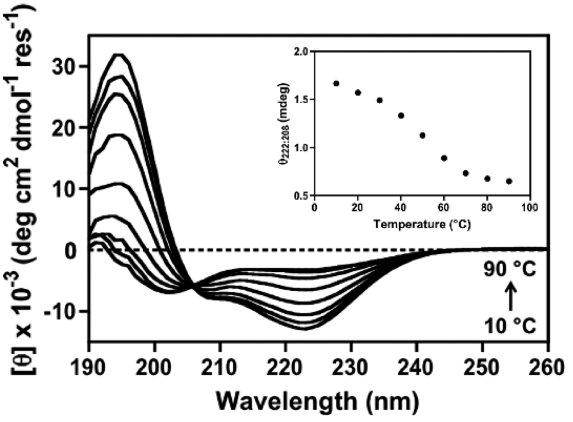

Figure 5. Far-UV CD spectra and $\theta_{222:208}$ ratio of HP35 in water as a function of temperature. Superimposition of the spectra acquired at different temperatures reveals the presence of an isodichroic point at 206 nm, indicative of a two-state unfolding of the protein.

Table 1. Thermodynamic Parameters for HP35 in Pure Water[a]

ΔH	ΔC_p	T_m (°C)	$\Delta G_{47°C}{}^{b}$	$\Delta G^{calc}_{47°C}{}^{c}$
24.8 ± 0.9	0.37 ± 0.06	44 ± 0.1	−0.24	−0.04

[a] Energies are in kcal mol^{-1}, C_p in kcal mol^{-1} K^{-1}, and temperature in °C. [b] Obtained from the experiments employing the Gibbs−Helmholtz equation. [c] Obtained by integration of the folded and unfolded basins in a tridimensional free energy projected as a function of the RMSD from a perfect α helix for the three helical segments of HP35.

is 2.9 M. From the combination of the change in Gibbs free energy upon thermal and chemical denaturation, we obtained the stability plot of HP35 (Supporting Information Figure S5), calculated the change of the unfolding free energy at 320 K, and compared it to the calculated value (Table 1). The agreement is surprisingly good, given reports of an overestimation of melting temperatures by various force fields.[6,8,39−45]

In conclusion, state-of-the-art simulations and recently improved force fields not only are able to reproduce the main structural features of HP35 folding in water but also to quantitatively predict the folding free energy landscape. Our simulations were able to interpret the postulated locking mechanism interconverting the two folded structures (open and closed), which involves the breaking of a strong hydrogen bond network involving residues Gln_8, Ala_9, and Leu_{34} and the stacking of Phe_{10} and Phe_{35} residues. Thermodynamics data obtained by CD were also found to be in surprisingly good agreement with the corresponding calculated values, showing that the latest correction to the Amber99SB*-ILDN force field does improve its predictive power in folding simulations. However, the relative stability of the three helices seems to be dependent on the temperature,[9] an issue that is worth analyzing in future studies.

■ ASSOCIATED CONTENT

Supporting Information. Computational and experimental methods, an experimental stability curve obtained through thermal and chemical denaturation, together with additional figures describing the main differences between the different conformations of HP35. This information is available free of charge via the Internet at http://pubs.acs.org/.

■ AUTHOR INFORMATION

Corresponding Author

*E-mail: flgervasio@cnio.es.

■ ACKNOWLEDGMENT

We acknowledge support by the Spanish Science and Innovation (MICINN) grant (BIO2010-20166, "AlteredDynamics"). G.S. acknowledges the European Commission Capacities Area - Research Infrastructures Initiative HPC-EUROPA2 (project number: 228398) for partial support. The Barcelona Supercomputing Center is acknowledged for a generous allocation of computer resources.

■ REFERENCES

(1) Shakhnovich, E. *Chem. Rev.* **2006**, *106*, 1559–88.
(2) Reiner, A.; Henklein, P.; Kiefhaber, T. *Proc. Natl. Acad. Sci. U.S.A.* **2010**, *107*, 4955–4960.
(3) Laio, A.; Gervasio, F. L. *Rep. Prog. Phys.* **2008**, *71*, 126601.
(4) Bonomi, M.; Branduardi, D.; Gervasio, F. L.; Parrinello, M. *J. Am. Chem. Soc.* **2008**, *130*, 13938–13944.
(5) Saladino, G.; Pieraccini, S.; Rendine, S.; Recca, T.; Francescato, P.; Speranza, G.; Sironi, M. *J. Am. Chem. Soc.* **2011**, *133*, 2897–2903.
(6) Shaw, D. E.; Maragakis, P.; Lindorff-Larsen, K.; Piana, S.; Dror, R. O.; Eastwood, M. P.; Bank, J. A.; Jumper, J. M.; Salmon, J. K.; Shan, Y.; Wriggers, W. *Science* **2010**, *330*, 341–346.
(7) Lindorff-Larsen, K.; Piana, S.; Palmo, K.; Maragakis, P.; Klepeis, J. L.; Dror, R. O.; Shaw, D. E. *Proteins: Struct. Funct. Bioinf.* **2010**, *78*, 1950–8.
(8) Best, R. B.; Buchete, N. V.; Hummer, G. *Biophys. J.* **2008**, *95*, L07–L09.
(9) Piana, S.; Lindorff-Larsen, K.; Shaw, D. E. *Biophys. J.* **2011**, *100*, L47–9.
(10) Vermeulen, W.; Vanhaesebrouck, P.; Troys, M. V.; Verschueren, M.; Fant, F.; Goethals, M.; Ampe, C.; Martins, J. C.; Borremans, F. A. M. *Protein Sci.* **2004**, *13*, 1276–1287.
(11) Chiu, T. K.; Kubelka, J.; Herbst-Irmer, R.; Eaton, W. A.; Hofrichter, J.; Davies, D. R. *Proc. Natl. Acad. Sci. U.S.A.* **2005**, *102*, 7517–22.
(12) McKnight, C. J.; Doering, D. S.; Matsudaira, P. T.; Kim, P. S. *J. Mol. Biol.* **1996**, *260*, 126–34.
(13) Duan, Y.; Kollman, P. A. *Science* **1998**, *282*, 740.
(14) Zagrovic, B.; Snow, C. D.; Shirts, M. R.; Pande, V. S. *J. Mol. Biol.* **2002**, *323*, 927–937.
(15) Ripoll, D.; Vila, J.; Scheraga, H. *J. Mol. Biol.* **2004**, *339*, 915–925.
(16) Mori, G. M. D.; Micheletti, C.; Colombo, G. *J. Phys. Chem. B* **2004**, *108*, 12267–12270.
(17) Lei, H.; Wu, C.; Liu, H.; Duan, Y. *Proc. Natl. Acad. Sci. U.S.A.* **2007**, *104*, 4925.
(18) Yang, J. S.; Wallin, S.; Shakhnovich, E. I. *Proc. Natl. Acad. Sci. U.S.A.* **2008**, *105*, 895–900.
(19) Piana, S.; Laio, A.; Marinelli, F.; Troys, M. V.; Bourry, D.; Ampe, C. *J. Mol. Biol.* **2008**, 460–470.
(20) Frank, B. S.; Vardar, D.; Buckley, D. A.; McKnight, C. J. *Protein Sci.* **2002**, *11*, 680–7.
(21) Kubelka, J.; Eaton, W. A.; Hofrichter, J. *J. Mol. Biol.* **2003**, *329*, 625–30.
(22) Wang, M.; Tang, Y.; Sato, S.; Vugmeyster, L.; McKnight, C.; Raleigh, D. *J. Am. Chem. Soc.* **2003**, *125*, 6032–6033.
(23) Tang, Y.; Rigotti, D.; Fairman, R.; Raleigh, D. *Biochemistry* **2004**, *43*, 3264–3272.
(24) Brewer, S. H.; Vu, D. M.; Tang, Y.; Li, Y.; Franzen, S.; Raleigh, D. P.; Dyer, R. B. *Proc. Natl. Acad. Sci. U.S.A.* **2005**, *102*, 16662–7.
(25) Havlin, R. H.; Tycko, R. *Proc. Natl. Acad. Sci. U.S.A.* **2005**, *102*, 3284–9.
(26) Kubelka, J.; Henry, E. R.; Cellmer, T.; Hofrichter, J.; Eaton, W. A. *Proc. Natl. Acad. Sci. U.S.A.* **2008**, *105*, 18655–62.
(27) Bunagan, M.; Gao, J.; Kelly, J.; Gai, F. *J. Am. Chem. Soc.* **2009**, *131*, 7470–7476.
(28) Piana, S.; Laio, A. *J. Phys. Chem. B* **2007**, *111*, 4553–4559.
(29) Hornak, V.; Abel, R.; Okur, A.; Strockbine, B.; Roitberg, A.; Simmerling, C. *Proteins: Struct. Funct. Bioinf.* **2006**, *65*, 712–725.
(30) Bonomi, M.; Branduardi, D.; Bussi, G.; Camilloni, C.; Provasi, D.; Raiteri, P.; Donadio, D.; Marinelli, F.; Pietrucci, F.; Broglia, R. A.; et al. *Comput. Phys. Commun.* **2009**, *180*, 1961–1972.
(31) Tang, Y.; Goger, M. J.; Raleigh, D. P. *Biochemistry* **2006**, *45*, 6940–6.
(32) Wickstrom, L.; Okur, A.; Song, K.; Hornak, V.; Raleigh, D. P.; Simmerling, C. L. *J. Mol. Biol.* **2006**, *360*, 1094–1107.
(33) Rajan, A.; Freddolino, P. L.; Schulten, K. *PLoS ONE* **2010**, *5*, e9890.
(34) Zhou, N.; Kay, C.; Hodges, R. *J. Biol. Chem.* **1992**, *267*, 2664–2670.
(35) Lau, S.; Taneja, A.; Hodges, R. *Biophys. J.* **1984**, *45*, A109–A109.
(36) Choy, N.; Raussens, V.; Narayanaswami, V. *J. Mol. Biol.* **2003**, *334*, 527–539.
(37) Thévenin, D.; Lazarova, T.; Roberts, M. F.; Robinson, C. R. *Protein Sci.* **2005**, *14*, 2177–2186.

(38) Marenchino, M.; Armbruster, D. W.; Hennig, M. *Protein Express. Purif.* **2009**, *63*, 112–119.
(39) Zhou, R. *Proc. Natl. Acad. Sci. U.S.A.* **2003**, *100*, 13280–5.
(40) Jas, G. S.; Kuczera, K. *Biophys. J.* **2004**, *87*, 3786–3798.
(41) Pitera, J. W.; Swope, W. *Proc. Natl. Acad. Sci. U.S.A.* **2003**, *100*, 7587–92.
(42) Nymeyer, H.; Garca, A. E. *Proc. Natl. Acad. Sci. U.S.A.* **2003**, *100*, 13934–9.
(43) Best, R. B.; Hummer, G. *J. Phys. Chem. B.* **2009**, *113*, 9004–15.
(44) Ghosh, T.; Garde, S.; Garca, A. E. *Biophys. J.* **2003**, *85*, 3187–93.
(45) Paschek, D.; Nymeyer, H.; Garca, A. E. *J. Struct. Biol.* **2007**, *157*, 524–33.

JCTC Journal of Chemical Theory and Computation

LETTER

pubs.acs.org/JCTC

Proton Wires via One-Dimensional Water Chains Adsorbed on Metallic Steps

R. Scipioni, D. Donadio, L. M. Ghiringhelli,*,† and L. Delle Site*

Max Planck Institut für Polymerforschung, Ackermannweg 10, D-55128 Mainz, Germany

ABSTRACT: The process of proton transfer is here analyzed for one-dimensional water chains adsorbed on metallic steps. When the water chain contains a hydronium and a hydroxyl ion, two different mechanisms are possible, depending on the metal substrate. On coinage metals (Ag, Au), recombination is observed through a spontaneous Grotthuss mechanism. On more reactive surfaces (Pd and Pt), the hydronium ion is unstable and releases a proton that adsorbs onto the metal, leaving the negatively charged OH^- unbalanced. In this case, the negative charge can be transferred along the wire with very low activation barriers.

1. INTRODUCTION

Metallic surfaces, due to their hydrophilicity, present fascinating possibilities to induce ordered two- and one-dimensional water networks stabilized by the adsorption interaction of water molecules onto the surface. Such networks may provide channels through which protons can move along paths of hydrogen bonds. Indeed, metal surfaces represent technologically relevant interfaces for water[1] and influence the proton transfer capabilities of adsorbed water.[2,3] However, on flat highly symmetric surfaces (e.g., the 111 cut of a fcc lattice), water builds 2D (or even 3D) networks, and the direction of proton transfer is not uniquely defined. This makes the experimental as well as the theoretical study more ambiguous, and the system remains of unclear technological utility.[4] It would be different instead to have 1D chains, where protons move along well-defined and controlled paths. (Quasi-)monodimensional chains of water molecules adsorbed on the step edge of Pt(111) terraces have been experimentally observed:[5] this initial finding obtained with STM was later confirmed with X-ray diffraction[6] and thermal desorption.[7] The edge of a step on a terraced metal surface represents an ideal model of a 1D system. In fact, the step consists of an aligned row of atoms, which are more reactive than the surface atoms laying in the terraces due to their lower coordination.[8−10] It follows that water molecules bind more strongly to the atoms along the step edge than to the atoms in the terraces, so that the formation of water wires is promoted: one-dimensional chains are only observed on steps and are stable up to 150 K.[5] This peculiar structural arrangement is such that the interaction of a hydrogen with the oxygen of the next molecule represents the only relevant degree of freedom for the proton transfer mechanism. Therefore, it is of major interest to explore the possibility of having proton transfer in water chains on stepped surfaces.

In this work, we report on a computational *ab initio* study about the proton transfer along water wires adsorbed on several different stepped metallic surfaces (namely, the 221 surfaces of Pt, Pd, Au, and Ag). We consider H_2O wires containing one hydronium and one hydroxyl ion, in order to trigger the proton transfer mechanism, yet enforcing charge neutrality. The main issue that we want to address is the ability of each metal species to promote different proton transfer mechanisms in the wire at low temperatures. To this aim, we perform a combination of density functional (DFT) *ab initio* static (geometry optimization) and molecular dynamics (MD) calculations and find two different mechanisms each occurring on specific metals. The results show the occurrence of spontaneous recombination of OH^- and H_3O^+ via a Grotthuss mechanism[11] on less reactive metals (Au, Ag), whereas on more reactive metals (Pt and Pd), the surface captures one excess proton from the H_3O^+, and the remaining negative charge is transferred along the wire by proton hopping. We interpret these qualitatively different behaviors as a consequence of the subtle balance between water/metal bonding and hydrogen bonding, which varies from one metal to another, and to the tendency of the metal to adsorb protons.

2. TECHNICAL DETAILS

We used the FEMD approach of Alavi et al.[12] within density functional theory (DFT). This is a state of the art method for treating metals and molecular adsorption on metal surfaces.[13,14] The method is implemented within the CPMD code.[15] In this method, the electron density and the Hellmann−Feynmann forces are calculated via a subspace diagonalization of a finite electronic temperature density matrix. We used the PBE functional.[16] All of the pseudopotentials are generated through the Troullier−Martins scheme,[17] and the plane-wave cutoff is set to 60 Ry. This setup has been extensively tested by some of us in previous work on the adsorption of molecules on metal surfaces.[14,18] We considered systems consisting of (221) metallic steps for Pt, Pd, Ag, and Au; the lattice constants of each metal are those obtained in previous studies.[14] The metal slabs consisted of four layers, where the bottom two were fixed. We have also checked that increasing the number of layers in the metal slab does not influence significantly the adsorption energy of a molecule. In fact, the difference in adsorption energy for a water molecule on a four- and five-layer slab is about 0.01 eV, which is within the accuracy of the method. The size of the lateral supercell was 6 × 1 (84 metal atoms) with a variable number of water molecules, from two to six, prearranged in a chain oriented along the step edge. The chains counting from two to

Received: May 13, 2011
Published: August 15, 2011

Table 1. Adsorption Energies E_{ads} for a Water Monomer and a Hydrogen Molecule onto the 221 Step of the Various Metals[a]

step (221)	E_{ads} (H_2O) [eV]	E_{ads} (H_2) [eV]	d_{abs} (H_2O) [Å]	d_{abs} (H_2) [Å]	d_{OH} [Å]	d_{HH} [Å]
Pt	−0.42	−0.50	2.30	1.74	2.00	0.92
Pd	−0.40	−0.35	2.35	1.84	2.10	0.85
Au	−0.23	−0.05	2.60	2.20	2.20	0.77
Ag	−0.20	−0.03	2.65	2.30	2.20	0.70

[a] The oxygen−metal and the H_2−metal distances are also reported, as well as the average hydrogen bond lengths O···H along the chain and H···H for the H_2.

five molecules had a (relatively) large interruption between periodic images and were prepared with the two charged defects at the chain ends. The chain with six molecules, even though there was no large interruption between the water molecules, had the hydrogen bond chain interrupted at one point. This is because there is no way to build a noninterrupted water chain (through boundary conditions) containing an OH defect. The six-membered chain was prepared with the defects according to the sequence: $H_2O-H_3O-3H_2O-OH$. The vacuum above the chain was at least 0.7−0.8 nm to make the interaction with the periodic images negligible, and a 1 × 3 × 1 mesh of K points was used. For the geometry optimizations, first the OH distance of the hydronium is constrained while relaxing the rest of the system. Next, we further relax the system after the release of the OH constraint. As a criterion of convergence, we chose a threshold of 10^{-3} au on the force components. The MD runs were performed with chains of five water molecules on a 6 × 1 (221) surface in the NVE ensemble for a maximum time of 0.5−1.0 ps, after a thermalization period of 0.1 ps at 50 K. The time step was chosen to be 10 au, which is standard for a Born−Oppenheimer type of dynamics for a system containing light nuclei such as hydrogens.

3. PROTON TRANSFER, AU AND AG

For the four metals considered here, we have found that the adsorption energies of water molecules (monomers) onto (221) metal steps are (see Table 1) either around −0.2 eV (Au, Ag) or −0.4 eV (Pd, Pt), i.e., on the order of one and two hydrogen bonds, respectively.[23] The adsorption energy for the monomer on the step is systematically larger than that on flat (111) surfaces of the corresponding metals.[10,24] This stems from the lower coordination of the metal atoms at the edge of the step, as previously discussed for the case of nickel.[8] When a water wire is formed, one has to consider also the effect of hydrogen bonding on the metal/water interaction. In previous works,[8,18,22] it was observed that in the adsorption of water networks onto metal surfaces, the water molecules that directly bind to metal atoms (via their oxygen atoms) have the strength of their hydrogen bonds modified. If a water donates two hydrogen bonds (HBs) to other molecules, the bonding to the metal will be stronger, while if it accepts bonds, the water−metal bond will be weaker even to the point of detaching from the metal.[9] This competition/cooperation between the adsorption strength onto the metal and strength of hydrogen bonds along the chain determines the nature of proton transport and the stability of defective species. Our results show that H_3O^+ is unstable on all of the metallic substrates considered here (independently from the chain length).

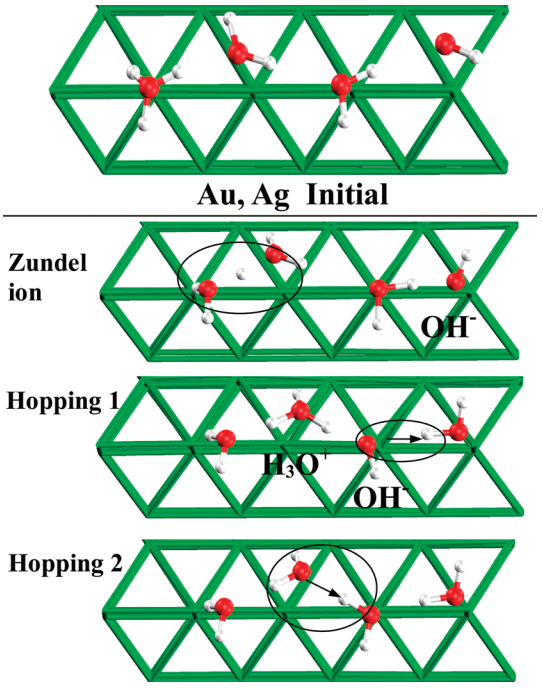

Figure 1. Proton transfer mechanism on Ag and Au (221). The top view of the initial configuration is shown in the top panel; the step edge is along the central sequence of metal atoms along the water chain. Below is illustrated the sequence of the different steps of the proton transfer. First, an intermediate Zundel ion (i.e., an excess proton shared by two water molecules) is formed, and then the proton is captured by the second water molecule, which in turn becomes a H_3O^+ ion. Next, the water molecule close to the OH^- ion releases its proton, becoming in turn an OH^-. This brings close the H_3O^+ and OH^-, which recombine in two neutral water molecules. The final configuration is that of a neutral chain of water molecules.

On Au and Ag, we found that H_3O^+ and OH^- recombine spontaneously. Recombination proceeds via a Grotthuss mechanism initiated from the hydronium H_3O^+, which acts as the starting point of a proton hopping along the chain (see Figure 1), toward the OH^- defect. This entails breaking and reforming of HBs, which in turn results in the proton being topologically transferred along the chain. However, MD runs performed on the coinage metals show that also the desorption barrier for the overall chain is very low (indeed, the chain typically desorbed, after the proton transfer completed). This observation seems to suggest that this Grotthuss mechanism on coinage metals may never be experimentally observed.

4. PROTON TRANSFER, PT AND PD

A different mechanism holds for Pt and Pd; in this case, one proton of the hydronium is captured by the surface. This dissociation is barrierless (see Figure 2) for all of the chains consisting of at least three molecules; when the system counts only one H_3O^+ and one OH^-, we observed a barrierless transfer of the excess proton between the two ions. The MD run shows that the water molecule remaining from the dissociation of hydronium is lifted from the surfaces but does not break the HBs with the neighboring water molecules. The readsorption of this water molecule is not seen within the time-span of our MD simulation, but we found that the readsorption of this water molecule needs to overcome a small barrier of 0.1−0.2 eV.

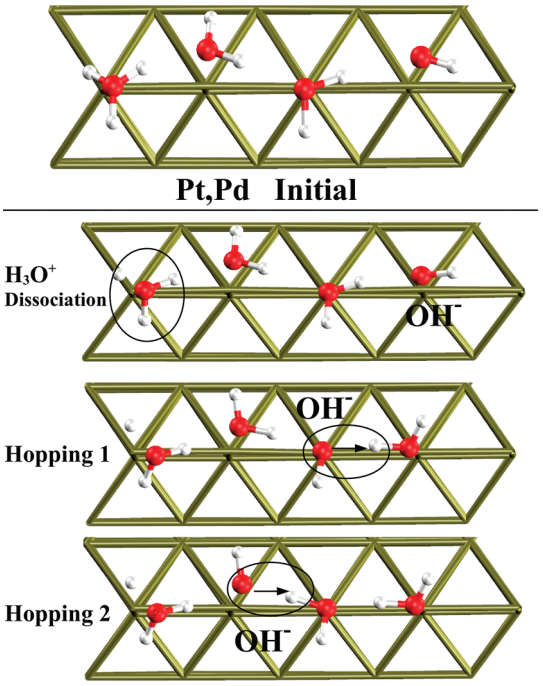

Figure 2. As in the previous figure, but for Pt and Pd. The first step is the dissociation of the H_3O^+, which donates a proton to the surface. The remaining chain is no more neutral and is characterized by the presence of a negative (OH^-) defect. The mechanism of traveling of this latter example happens in the following way: the molecule close to the OH^- releases a proton, and the proton is captured by the OH^-, which then becomes a water molecule. As a consequence, the donating molecule becomes in turn an OH^- ion. This mechanism is repeated along the chain. The hopping of the proton is characterized by low activation barriers, which can be overcome by thermal fluctuations.

This leads to a stable adsorbed chain with only one OH^- defect. Since Pt and Pd steps gain energy by capturing protons, the conclusion is that, for Pt(221) and Pd(221), the hydronium would rather donate the proton to the surface than promote a Grotthuss mechanism along the water chains (for chains with at least three molecules). Regarding the process of proton transfer along the chain, we have found that, after the adsorption of the excess proton on the surface, a hopping mechanism is initiated at the OH^- ions. Namely, the water molecule sitting next to the OH defect donates a proton to the OH, becoming in turn an OH, and the process, which involves overcoming activation barriers on the order of 0.10 eV is repeated. These values have been evaluated by means of constrained geometry optimizations for the system with the longer chain. The exact values depend on the distance between the defects and the orientation of the water molecules, but they were found to be at most 0.15 eV, that is, at worst, on the order of a hydrogen bond, which in turn implies that the overcoming of the barrier is not unlikely upon local rearrangement of the chain. The height of the barriers is size-independent; i.e., it does not vary systematically with the length of the chains, and this is a further indication that the proton hopping is somewhat local, i.e., does not depend on the relative positions of the defects along the chain.

5. COMPARISON BETWEEN THE SURFACES

In Table 1 are reported several quantities which explain the trend in affinity of the different surfaces for the excess proton of the hydronium. Pt and Pd show a clear trend, that is, strong interaction with the surface. In fact, adsorption energies for both the water and hydrogen molecules are rather large, bonding distances are short, and the ability of Pt and Pd in distorting the molecular structure is quite high. For Ag and Au, it is the opposite. In particular, for the coinage metals, the adsorption energy of molecular hydrogen is practically null, while for Pt and Pd, this energy is quite sizable. This explains the basic difference in the behavior of the excess proton of the H_3O^+ in the chains considered. Of course, further considerations need to be made because of the aspects neglected in this work. We have not adopted corrections to take into account dispersion forces, and these may play an important role regarding the stabilization of the chains on the surfaces.[20] However, given the energy differences in Table 1, it is unlikely that dispersions may convert the mechanism in Ag and Au to that for Pt and Pd. The interaction of the H_2 molecule with Ag and Au is by far too small compared to that of Pt and Pd, and it would be surprising if dispersion were on the order of 0.3−0.4 eV at short distances. Moreover, in ref 21, it was shown that dispersions do not play a significant role for water molecules in direct contact with the surface. In any case, even counting dispersion, the only difference would be an additional attractive force between the molecules and the metal and thus more stable chains on the surface. This actually would strengthen our conclusions about having stable one-dimensional systems along which the proton can diffuse. Another important phenomenon that would play a role in the mechanisms of transport is the delocalization of protons due to their quantum nature. In a very recent study of relatively small systems of H_2O on different metal surfaces,[3,19] it was observed that the delocalization of the proton is more relevant for metals with smaller lattice parameters. The effects of delocalization consist of a reduction in the free energy barrier for the transfer of the proton among water molecules compared to the case where this effect is not considered. We have not included quantum effects in our calculations because the computational costs would be prohibitive for large systems such as those considered in this work; however, on the basis of refs 3 and 19, what we may expect is simply that the barriers for the proton transfer are smaller. This would not change our conclusions about the mechanism of proton transport.

6. CONCLUSIONS

We have studied the dynamics of protons on water wires formed on the stepped surface of transition metals. We have identified two different mechanisms, one occurring on the more reactive metals (Pt and Pd) and one occurring on coinage metals (Au and Ag). Taken in perspective, there are potentially relevant implications for the mechanisms suggested above, at least for Pd and Pt step surfaces. A one-dimensional water wire represents, for example, a fascinating technological possibility that can be employed in disparate fields, for the process of protonation/deprotonation of molecules adsorbed on the surface, thus inducing a (at least partially) controlled functional change, fabrication of microcircuits, enhancing conductivity in ice, and several related technological realizations.[26−28] In this context, despite being at a basic theoretical level, these calculations propose a clear distinction between different metal species as possible candidates for building water wires and creating a proton current.

AUTHOR INFORMATION

Corresponding Author

*E-mail: luca@fhi-berlin.mpg.de; dellsite@mpip-mainz.mpg.de.

Present Addresses
[†]Fritz-Haber-Institut, Faradayweg 4−6, D-14195 Berlin-Dahlem, Germany

■ ACKNOWLEDGMENT

We thank K. Johnston for a critical reading of the manuscript. We acknowledge the RZG of the Max Planck Society for computational resources and the Multiscale Modeling of Materials initiative (MMM) of the Max Planck Society.

■ REFERENCES

(1) Michaelides, A. *Appl. Phys. A: Mater. Sci. Process.* **2006**, *84*, 415. Michelides, A.; Morgenstern, K. *Nat. Mater.* **2007**, *6*, 597. Carrasco, J.; Michaelides, A.; Forster, M.; Haq, S.; Raval, R; Hodgson, A. *Nat. Mater.* **2009**, *8*, 427.
(2) Hu, X. L.; Klimes, J.; Michaelides, A. *Phys. Chem. Chem. Phys.* **2010**, *12*, 3952.
(3) Li, X.-Z.; Probert, M. I. J.; Alavi, A.; Michaelidis, A. *Phys. Rev. Lett.* **2010**, *104*, 066102.
(4) Feibelman, P. J. *Phys. Rev. Lett.* **2003**, *90*, 186103.
(5) Morgenstern, M.; Michely, T.; Comsa, G. *Phys. Rev. Lett.* **1996**, *77*, 703.
(6) Nakamura, M.; Sato, N.; Hoshi, N.; Soon, J. M.; Sakata, O. *J. Phys. Chem. C* **2009**, *113*, 4538.
(7) Picolin, A.; Busse, C.; Redinger, A.; Morgenstern, M.; Michely, T. *J. Phys. Chem. C* **2009**, *113*, 691.
(8) Sebastiani, D.; Delle Site, L. *J. Chem. Theory Comput.* **2005**, *1*, 78. Murakhtina, T.; Delle Site, L.; Sebastiani, D. *ChemPhysChem* **2006**, *7*, 1215.
(9) Delle Site, L.; Sebastiani, D. *Phys. Rev. B* **2004**, *70*, 115401.
(10) Meng, S.; Wang, E. G.; Gao, S. *Phys. Rev. B* **2004**, *69*, 195404.
(11) de Grotthuss, C. J. T. *Ann. Chim.* **1806**, *LVIII*, 54.
(12) Alavi, A.; Kohanoff, J.; Parrinello, M.; Frenkel, D. *Phys. Rev. Lett.* **1994**, *73*, 2599.
(13) Lozovoi, A. Y.; Alavi, A.; Finnis, M. W. *Phys. Rev. Lett.* **2000**, *85*, 610. Benedek, R.; Alavi, A.; Seidman, D. N.; Yand, L. H.; Muller, D. A.; Woodward, C. *Phys. Rev. Lett.* **2000**, *84*, 3362. Michaelides, A.; Alavi, A.; King, D. A. *J. Am. Chem. Soc.* **2003**, *125*, 2746. Delle Site, L.; Alavi, A.; Abrams, C. F. *Phys. Rev. B* **2003**, *67*, 193406.
(14) Ghiringhelli, L. M.; Delle Site, L. *J. Am. Chem. Soc.* **2008**, *130*, 2634.
(15) *CPMD*, 3.13; IBM Corp.; MPI fur Festkorperforschung: Stuttgart, Germany, 1997−2004.
(16) Perdew, J. P.; Burke, K.; Erzerhorf, M. *Phys. Rev. Lett.* **1996**, *77*, 3865.
(17) Troullier, N.; Martins, J. L. *Phys. Rev. B* **1991**, *43*, 1993.
(18) Delle Site, L.; Ghiringhelli, L. M.; Andreussi, O.; Donadio, D.; Parrinello, M. *J. Phys.: Condens. Matter* **2007**, *19*, 242101.
(19) Davidson, E. R. M.; Alavi, A.; Michaelidis, A. *Phys. Rev. B* **2010**, *81*, 153410.
(20) Carrasco, J.; Santra, B.; Klimes, J.; Michaelides, A. *Phys. Rev. Lett.* **2011**, *106*, 026101.
(21) Hamada, I.; Lee, K.; Morikawa, Y. *Phys. Rev. B* **2010**, *81*, 115452.
(22) Schiros, T.; Ogasawara, H.; Naslund, L. A.; Andersson, K. J.; Ren, J.; Meng, S.; Karlberg, G. S.; Odelius, M.; Nilsson, A.; Petersson, L. G. M. *J. Phys. Chem. C* **2010**, *114*, 10240.
(23) Suresh, S. J.; Naik, V. M. *J. Chem. Phys.* **2000**, *113*, 9727.
(24) Michaelides, A.; Ranea, V. A.; De Andres, P. L.; King, D. A. *Phys. Rev. Lett.* **2003**, *90*, 216102.
(25) Marzari, N.; Vanderbilt, D. *Phys. Rev. B* **1997**, *56*, 12847.
(26) Chen, Y.; Liu, S.; Lei, M. *J. Phys. Chem. C* **2008**, *112*, 13524.
(27) Kapetanakis, E.; Douvas, A. M.; Velessiotis, D.; Makarona, E.; Argitis, P.; Glezos, M. *Org. Electron.* **2009**, *10*, 711.
(28) Moon, E.-S.; Lee, C.-W.; Kang, K. *Phys. Chem. Chem. Phys.* **2008**, *10*, 4814.

JCTC Journal of Chemical Theory and Computation

LETTER

pubs.acs.org/JCTC

Testing a Variety of Electronic-Structure-Based Methods for the Relative Energies of 5-Formyluracil Crystals

Matthew Habgood,[†] Sarah L. Price,[†] Gustavo Portalone,[‡] and Simona Irrera*[,†,§]

[†]Department of Chemistry, University College London, 20 Gordon Street, London, WC1H 0AJ United Kingdom

[‡]Dipartimento di Chimica, "Sapienza" Università di Roma, P.le Aldo Moro 5, 00185 Rome, Italy

Supporting Information

ABSTRACT: The lattice energies of the experimental and several hypothetical crystal structures of the RNA base uracil derivative 5-formyluracil are calculated with a range of methods, based either on the electronic structure of the molecule or the lattice. The explicit modeling of the polarization within the crystal in the model intermolecular potential and the inclusion of an empirical dispersion correction to the periodic density functional energy (DFT-D2) were the only methods able to calculate the energy balance between different conformations, hydrogen bonding, and $\pi-\pi$ stacking possibilities sufficiently accurately to give the observed structure as the most stable. Even these two methods underestimated the density of the room temperature structure, showing the need for improvement in the modeling of organic crystal structures.

The physical properties of organic molecular materials in the solid state are critically dependent upon the crystal structure that they adopt. This has led to an explosion of interest in modeling molecular crystals, driven by relevance to dyes, explosives, optics, electronics, and particularly to the pharmaceutical industry.[1−4] The propensity for a molecule to adopt multiple crystalline forms both threatens the manufacturer's control of the quality of their products[5] and provides the ability to select the solid state properties of a molecule. Accurate computational modeling of crystal structures and their relative energetic differences is essential to understanding existing crystalline forms and designing new ones.[6,7]

A wide variety of methods are available for evaluating the zero-temperature potential energy of crystal structures (lattice energy), ranging from computationally cheap but highly approximate analytical functions (e.g., atom-centered charges plus Lennard-Jones interactions)[8] through more sophisticated treatments of intermolecular forces (e.g., distributed multipole electrostatic models)[9] and density functional theory with analytical van der Waal's corrections[10−12] to sophisticated *ab initio* methods.[13−15] Different methods need to be used in a complementary fashion, according to their relative accuracy and computational cost,[16,17] as reliable crystal structure prediction will require both accurately ranking the energies of many thousands of plausible crystal structures and the ability to simulate the transformations that can occur with temperature and pressure.[18,19] It is notable that both of the methods that have been generally successful in the international blind tests of organic crystal structure prediction[20] rely on molecule-specific quantum mechanical calculations and the empirical fitting of part of the model to a range of organic crystal structures. The periodic DFT method has an empirically fitted damped C_6 atom−atom dispersion model.[21] The models that use a distributed multipole model of the *ab initio* molecular charge density for the electrostatic forces usually combine this with an empirically fitted *exp-6* atom−atom potential for the other contributions to the intermolecular lattice energy.[22] Since there has been considerable progress in the performance of electronic structure calculations for large molecular systems, it seemed timely to test these density-functional methods for modeling the balance of interatomic forces in organic crystal structures.

The chosen test molecule is 5-formyluracil ($C_5N_2O_3H_4$, Figure 1), a major oxidation product of thymine, which is fundamental to the investigation of DNA/RNA pairing and mispairing because it is known to be a major source for transition mutations.[23,24] The crystal structure[25] (Figure 2) is determined by the compromises between different hydrogen bonding, base stacking, and other intermolecular and intramolecular interactions, as the *syn* conformer is the only one to have been found in the crystalline phase, but the *anti* conformer is more stable in isolated molecule calculations (Figure 1).

A small set of the most stable hypothetical crystal structures for *syn* and *anti* 5-formyluracil was selected from a group generated using the program MOLPAK,[26] whose intermolecular lattice energies were within 4 kJ mol^{-1} of the most stable when optimized using the IMP model intermolecular potential. This comprised a distributed multipole[27] model (derived from the optimized MP2 6-31G(d,p) molecular charge density computed using GAUSSIAN[28]), for the electrostatic contribution to the intermolecular lattice energy U_{inter}, and an empirical *exp-6* potential for all other contributions. These, plus the corresponding experimental structure, cover a wide range of crystal packings, as has been found in the experimental and energetically competitive structures for other 5-substituted uracils.[29] The hypothetical 5-formyluracil structures have different hydrogen bonds (Supporting Information) involving the uracil and formyl groups from the observed structure (Figure 2).

Received: May 27, 2011
Published: July 13, 2011

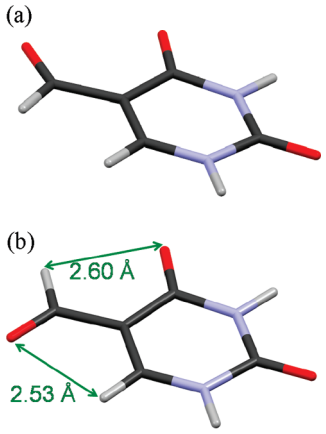

Figure 1. 5-Formyluracil in (a) the *syn* conformation found in the crystal structure and (b) the *anti* conformation showing the stabilizing intramolecular O···H close contacts.

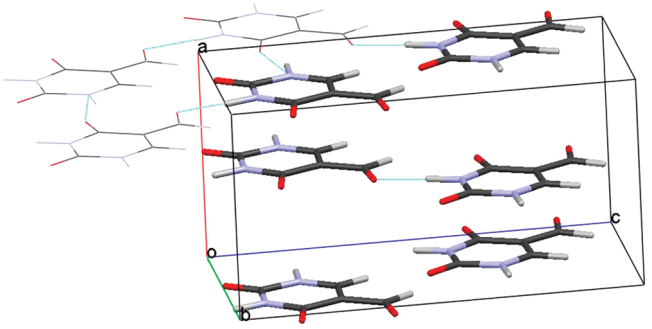

Figure 2. Layered experimental crystal structure of 5-formyluracil[25] (Cambridge Structural Database code GIMREA), showing the hydrogen-bonded network of the top layer with the molecules outside the conventional unit cell in wireframe. Hydrogen bonds are shown in light blue.

Three models based on separate evaluation of intermolecular and intramolecular energies were used to calculate the lattice energies of these 5-formyluracil crystal structures. To calculate the lattice energy, E_{latt}, of these crystal structures for the intermolecular potential model used in their derivation (IMP model), relative to infinitely separated molecules in their lowest energy conformation, the conformational energy penalty for the *syn* conformer, ΔE_{intra}, has to be added to the intermolecular lattice energy, U_{inter}, for the *syn* conformation crystal structures. The isolated molecule MP2 6-31G(d,p) calculations estimate ΔE_{intra} as 19.8 kJ mol^{-1}, so the loss of the O···H intramolecular interactions (Figure 1) significantly destabilizes the observed crystal structure. An improved lattice energy estimate (IMP+WSM) includes the intermolecular induction energy evaluated with an explicit polarization model, using distributed anisotropic dipole−dipole polarizabilities calculated using the Williams−Stone−Misquitta (WSM) scheme,[30−32] as implemented in the CamCASP suite of programs,[33] with the induced dipoles iterated to consistency using DMACRYS.[34] A more approximate method of simulating the average polarization of the molecule within the crystal structure[35] is to calculate the distributed multipoles and relative conformational energies using the polarized continuum model (PCM)[36] implemented in GAUSSIAN with $\varepsilon = 3$, a value typical of organic crystals. This model (IMP+PCM) provides a

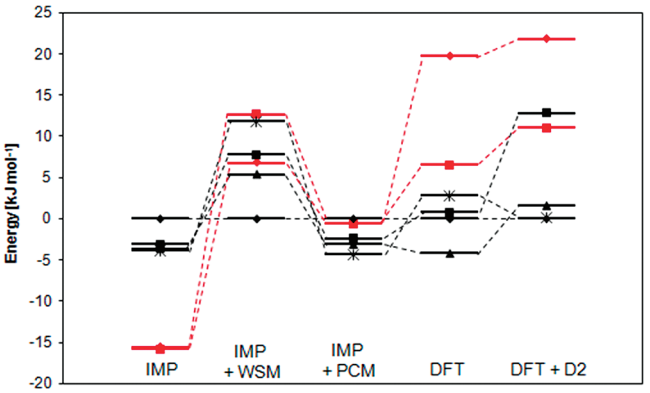

Figure 3. Lattice energies of the test set of four *syn* conformer structures (black) and two *anti* conformer structures (red) relative to the experimental structure. IMP = initial intermolecular potential model; IMP +WSM = intermolecular potential model with the addition of the induction energy; IMP+PCM = relaxed structures with average polarization from the PCM polarization model. DFT and DFT-D2 are the density functional theory relaxations without and with a dispersion correction. Some tie lines have been added to show significant changes in relative energy ordering between crystal structures with the same molecular conformation.

polarization effect that is not specific to the crystal structure, though the effect of the change in the charge distribution on the lattice energy minimized structure could be determined. Thus, these three models for the lattice energy which are based on *ab initio* calculations on a single molecule (to parametrize the electrostatic (and induction for WSM), model intermolecular potential, and provide the conformational energy difference (ΔE_{intra})) differ fundamentally in the treatment of the polarization of the molecule within the crystal structure.

Periodic electronic structure calculations have the advantage of not requiring separation into intermolecular and intramolecular interactions. The crystal structures were relaxed using periodic GGA-PW91 density functional theory (DFT) with the addition of an empirical dispersion correction, implemented using Grimme's method[37] (DFT-D2), within the QUANTUM ESPRESSO program package.[38] Problems of convergence of three of the structures led us to investigate the effect of annealing by DFT molecular dynamics. For three of the structures, the DFT-MD annealing led to a qualitative difference in the structures (shown in the Supporting Information) in terms of the atoms involved in hydrogen bonds and other close contacts, with the layers in one structure separating. The failure of MD using DFT without a dispersion correction to maintain the density of these structures is consistent with the considerable body of evidence pointing to the inadequate handling of long-range dispersion interactions by DFT.[39,40] The excessive expansion in DFT annealing allowed sufficient reorientation of the molecules in two cases to simulate a hypothetical phase transition to an alternative low energy structure.

The remaining six structures, two *anti* and four *syn* (including the experimental structure), did have a DFT minimum sufficiently close to the original [judged by the capacity to overlay a cluster of 15 nearest-neighbor molecules from the two structures to within distance tolerances of 20% and angle tolerances of 20°, as determined in the Crystal Packing Similarity module of Mercury[41] 2.4] for a meaningful comparison of lattice energies for all five computational methods (details in the Supporting Information, Table S1). The lattice energies relative to the

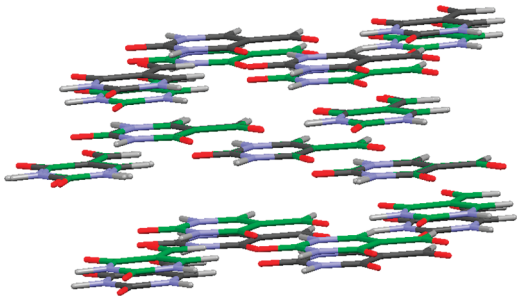

Figure 4. Overlay of three layers of the experimental structure, relaxed using uncorrected DFT (gray) and DFT-D2 (green). The closer interlayer spacing is more realistic for DFT-D2 but still overestimates the cell parameter in the stacking direction (*a*, Figure 2) by 9%, providing further evidence of deficiencies for π stacking.[11,13]

experimental structure, which can be reasonably assumed to be the most stable (Figure 3), show qualitative differences in the relative ordering and lattice energy differences in excess of the few kilojoules per mole usually associated with the experimental energy differences between polymorphs. The difference in the isolated molecule conformational energies results in the *anti* structures being considerably more stable than the *syn* structures with the initial intermolecular potential model (IMP), showing that this model does not balance the inter- and intramolecular interactions to give reasonable relative energies, despite giving the best match to the experimental structure. The PCM model reduces the difference between the two conformers considerably but, otherwise, results in little change in the energetic rankings of structures with the same conformer. It is perhaps not surprising that the redistribution of the *isolated* molecule charge densities as a response to an averaged electrostatic background does not accurately model the differences produced by the different hydrogen bonds in the crystalline environment. In contrast, lattice energies calculated using the WSM model yield a significant reranking, such that the most stable structures are those of the *syn* conformer, and the experimental crystal structure is the most stable overall. Hence, an intermolecular potential that includes the induction energy, representing how the charge density of the molecule adjusts to the specific crystalline environment (illustrated in the Supporting Information, Figure S1.3), is a considerable improvement over the initial model, which assumes that the isolated molecule electron density is undistorted in the crystal.

Following relaxation with DFT, the *syn* structures are the most stable overall, but the experimental structure is still less stable than another *syn* structure. With the inclusion of the empirical dispersion correction (DFT-D2), however, the experimental structure becomes the most stable. This can be related (Figure 4) to the dispersion correction having a significant effect on the interlayer distance in the lattice energy optimized experimental structure. However, the DFT-D2 method still significantly underestimates the density of the 298 K experimental structure, whereas the neglect of thermal expansion in all lattice energy models should result in an overestimate of the density by a few percent. Indeed, the density of all structures increases (Supporting Information, Table S1) in the order DFT, DFT-D2, IMP, IMP+PCM, (experiment), suggesting that improvements in the quality of the molecular or crystal charge density and the other approximations made in representing the intra- and intermolecular forces are needed before the neglect of thermal expansion becomes the dominant error.

Even without the dispersion correction, DFT resolves the apparent paradox of the *syn* conformer appearing in the solid state, whereas the *anti* conformer is the more stable in the gas phase. This is consistent with such methods treating all nuclei and electrons on the same footing, so that intra- and intermolecular polarization are both modeled well. This is in contrast to the intermolecular potential models when the polarization within the crystal is not modeled, although some average effect is absorbed in the empirically fitted *exp-6* potential. Explicit modeling of the differential polarizations in the different intermolecular hydrogen bonds is needed, through using a distributed polarizability model, for the observed structure to be calculated as the most stable. The stability of the *anti* conformer in the gas phase is partially the result of the close internal contacts between the carbonyl oxygens and hydrogen atoms (see Figure 1), which could be viewed as weak intramolecular hydrogen bonds. Thus, this study reinforces the finding[42] that the lattice energy differences between polymorphs of oxalyl dihydrazide and *o*-acetamidobenzamide, which differ in the number of intra- and intermolecular hydrogen bonds, were only plausible when the induction energy was explicitly modeled, or when a dispersion corrected periodic electronic structure method was used.

The crystal structure of 5-formyluracil is not unique in having a molecular conformation that is a high energy conformer for the isolated molecule, and in having alternative crystal structures with different hydrogen bonds that are close in energy. Thus, these structures of 5-formyluracil and the conformational polymorphs of oxalyl dihydrazide and *o*-acetamidobenzamide form a particularly stringent test of the ability to model condensed phases and complexes of uracils and peptides, respectively. The crystal structures of other uracils[29] and amino acids[43] have been successfully predicted, demonstrating the specificity of the challenge to the range of energetically competitive crystal structures. This study has demonstrated that the relative energies of conformational polymorphs can require modeling of both the polarization and dispersion interactions, which are often inadequately represented by readily evaluated model intermolecular potentials and periodic DFT calculations, respectively. The use of distributed polarizability models to improve the model intermolecular potentials, or the addition of dispersion to periodic DFT methods, appears to have the potential for systematically improving modeling of the balance between inter- and intramolecular forces in these challenging organic systems.

■ ASSOCIATED CONTENT

Ⓢ Supporting Information. Further details of the computational methods, crystal energy landscape, extent of polarization of molecules in the known crystal, diagrams of the 5-formyluracil crystal structures, a table comparing the crystal structures and energies calculated with the different methods, the nine crystal structures in .res format. This information is available free of charge via the Internet at http://pubs.acs.org/.

■ AUTHOR INFORMATION

Corresponding Author

*Tel.: +39 0649913819. E-mail: irrera@caspur.it.

Present Addresses

[§]Dipartimento di Chimica, "Sapienza" Università di Roma, P.le Aldo Moro 5, 00185 Rome, Italy.

■ ACKNOWLEDGMENT

This work has been supported by the Newton International Fellowship scheme (SI), the Ramsay Memorial Fellowships Trust (MH) and EPSRC via Control & Prediction of the Organic Solid State, www.cposs.org.uk (EP/F03573X). We thank Dr Alston Misquitta for assistance with determining the distributed polarizabilities of 5-formyluracil. Computing Support was provided by HECToR High Performance Computing resources via membership of the EPSRC-funded Materials Chemistry Consortium (EP/D504872).

■ REFERENCES

(1) Bernstein, J. *Cryst. Growth Des.* **2011**, *11*, 632–650.
(2) Bernstein, J. *Polymorphism in Molecular Crystals*; Clarendon Press: Oxford, United Kingdom, 2002; pp 240−296.
(3) Price, C. P.; Grzesiak, A. L.; Matzger, A. J. *J. Am. Chem. Soc.* **2005**, *127*, 5512–5517.
(4) Trask, A. V.; Shan, N.; Motherwell, W. D. S.; Jones, W.; Feng, S. H.; Tan, R. B. H.; Carpenter, K. J. *Chem. Commun.* **2005**, 880–882.
(5) Bauer, J.; Spanton, S.; Henry, R.; Quick, J.; Dziki, W.; Porter, W.; Morris, J. *Pharm. Res.* **2001**, *18*, 859–866.
(6) Price, S. L. *Acc. Chem. Res.* **2009**, *42*, 117–126.
(7) Lehmann, C. W. *Angew. Chem., Int. Ed.* **2011**, *50*, 5616–5617.
(8) Svard, M.; Rasmuson, A. C. *Ind. Eng. Chem. Res.* **2009**, *48*, 2899–2912.
(9) Day, G. M.; Motherwell, W. D. S.; Jones, W. *Cryst. Growth Des.* **2005**, *5*, 1023–1033.
(10) Asmadi, A.; Neumann, M. A.; Kendrick, J.; Girard, P.; Perrin, M. A.; Leusen, F. J. J. *J. Phys. Chem. B* **2009**, *113*, 16303–16313.
(11) Civalleri, B.; Zicovich-Wilson, C. M.; Valenzano, L.; Ugliengo, P. *CrystEngComm* **2008**, *10*, 405–410.
(12) Sorescu, D. C.; Rice, B. M. *J. Phys. Chem. C* **2010**, *114*, 6734–6748.
(13) Hongo, K.; Watson, M. A.; Sanchez-Carrera, R. S.; Iitaka, Y.; Aspuru-Guzik, A. *J. Phys. Chem. Lett.* **2010**, *1*, 1789–1794.
(14) Maschio, L.; Usvyat, D.; Civalleri, B. *CrystEngComm* **2010**, *12*, 2429–2435.
(15) Beran, G. J. O.; Nanda, K. *J. Phys. Chem. Letts* **2010**, *1*, 3480–3487.
(16) Guin, M.; Patwari, G. N.; Karthikeyan, S.; Kim, K. S. *Phys. Chem. Chem. Phys.* **2009**, *11*, 11207–11212.
(17) Maity, S.; Patwari, G. N.; Karthikeyan, S.; Kim, K. S. *Phys. Chem. Chem. Phys.* **2010**, *12*, 6150–6156.
(18) Gray, A. E.; Day, G. M.; Leslie, M.; Price, S. L. *Mol. Phys.* **2004**, *102*, 1067–1083.
(19) Karamertzanis, P. G.; Raiteri, P.; Parrinello, M.; Leslie, M.; Price, S. L. *J. Phys. Chem. B* **2008**, *112*, 4298–4308.
(20) Day, G. M.; Cooper, T. G.; Cruz-Cabeza, A. J.; Hejczyk, K. E.; Ammon, H. L.; Boerrigter, S. X. M.; Tan, J.; Della Valle, R. G.; Venuti, E.; Jose, J.; Gadre, S. R.; Desiraju, G. R.; Thakur, T. S.; van Eijck, B. P.; Facelli, J. C.; Bazterra, V. E.; Ferraro, M. B.; Hofmann, D. W. M.; Neumann, M.; Leusen, F. J. J.; Kendrick, J.; Price, S. L.; Misquitta, A. J.; Karamertzanis, P. G.; Welch, G. W. A.; Scheraga, H. A.; Arnautova, Y. A.; Schmidt, M. U.; van de Streek, J.; Wolf, A.; Schweizer, B. *Acta Crystallogr., Sect. B* **2009**, *65*, 107–125.
(21) Neumann, M. A.; Perrin, M. A. *J. Phys. Chem. B* **2005**, *109*, 15531–15541.
(22) Price, S. L. *Int. Rev. Phys. Chem.* **2008**, *27*, 541–568.
(23) Bjelland, S.; Eide, L.; Time, R. W.; Stote, R.; Eftedal, I.; Volden, G.; Seeberg, E. *Biochemistry* **1995**, *34*, 14758–14764.
(24) Bjelland, S.; Anensen, H.; Knaevelsrud, I.; Seeberg, E. *Mutat. Res.* **2001**, *486*, 147–154.
(25) Portalone, G.; Colapietro, M. *Acta Crystallogr., Sect. C* **2007**, *63*, O650–O654.
(26) Holden, J. R.; Du, Z. Y.; Ammon, H. L. *J. Comput. Chem.* **1993**, *14*, 422–437.
(27) Stone, A. J. *J. Chem. Theory Comput.* **2005**, *1*, 1128–1132.
(28) Frisch, M. J.; Trucks, G. W.; Schlegel, H. B.; Scuseria, G. E.; Robb, M. A.; Cheeseman, J. R.; Montgomery, J.; Vreven, T.; Kudin, K. N.; Burant, J. C.; Millam, J. M.; Iyengar, S. S.; Tomasi, J.; Barone, V.; Mennucci, B.; Cossi, M.; Scalmani, G.; Rega, N.; Petersson, G. A.; Nakatsuji, H.; Hada, M.; Ehara, M.; Toyota, K.; Fukuda, R.; Hasegawa, J.; Ishida, M.; Nakajima, T.; Honda, Y.; Kitao, O.; Nakai, H.; Klene, M.; Li, X.; Knox, J. E.; Hratchian, H. P.; Cross, J. B.; Bakken, V.; Adamo, C.; Jaramillo, J.; Gomperts, R.; Stratmann, R. E.; Yazyev, O.; Austin, A. J.; Cammi, R.; Pomelli, C.; Ochterski, J.; Ayala, P. Y.; Morokuma, K.; Voth, G. A.; Salvador, P.; Dannenberg, J. J.; Zakrzewski, V. G.; Dapprich, S.; Daniels, A. D.; Strain, M. C.; Farkas, O.; Malick, D. K.; Rabuck, A. D.; Raghavachari, K.; Foresman, J. B.; Ortiz, J. V.; Cui, Q.; Baboul, A. G.; Clifford, S.; Cioslowski, J.; Stefanov, B. B.; Liu, G.; Liashenko, A.; Piskorz, P.; Komaromi, I.; Martin, R. L.; Fox, D. J.; Keith, T.; Al Laham, M. A.; Peng, C. Y.; Nanayakkara, A.; Challacombe, M.; Gill, P. M. W.; Johnson, B.; Chen, W.; Wong, M. W.; Gonzalez, C.; Pople, J. A. *Gaussian 03*; Gaussian Inc.: Wallingford, CT, 2004.
(29) Barnett, S. A.; Hulme, A. T.; Issa, N.; Lewis, T. C.; Price, L. S.; Tocher, D. A.; Price, S. L. *New J. Chem.* **2008**, *32*, 1761–1775.
(30) Misquitta, A. J.; Stone, A. J. *J. Chem. Theory Comput.* **2008**, *4*, 7–18.
(31) Misquitta, A. J.; Stone, A. J.; Price, S. L. *J. Chem. Theory Comput.* **2008**, *4*, 19–32.
(32) Welch, G. W. A.; Karamertzanis, P. G.; Misquitta, A. J.; Stone, A. J.; Price, S. L. *J. Chem. Theory Comput.* **2008**, *4*, 522–532.
(33) Misquitta, A. J.; Stone, A. J. *CamCASP*; University of Cambridge: Cambridge, U. K., 2007. http://www-stone.ch.cam.ac.uk/programs.html#CamCASP (accessed Dec, 2009).
(34) Price, S. L.; Leslie, M.; Welch, G. W. A.; Habgood, M.; Price, L. S.; Karamertzanis, P. G.; Day, G. M. *Phys. Chem. Chem. Phys.* **2010**, *12*, 8478–8490.
(35) Cooper, T. G.; Hejczyk, K. E.; Jones, W.; Day, G. M. *J. Chem. Theory Comput.* **2008**, *4*, 1795–1805.
(36) Cossi, M.; Scalmani, G.; Rega, N.; Barone, V. *J. Chem. Phys.* **2002**, *117*, 43–45.
(37) Grimme, S. *J. Comput. Chem.* **2006**, *27*, 1787–1799.
(38) Giannozzi, P.; Baroni, S.; Bonini, N.; Calandra, M.; Car, R.; Cavazzoni, C.; Ceresoli, D.; Chiarotti, G. L.; Cococcioni, M.; Dabo, I.; Dal Corso, A.; de Gironcoli, S.; Fabris, S.; Fratesi, G.; Gebauer, R.; Gerstmann, U.; Gougoussis, C.; Kokalj, A.; Lazzeri, M.; Martin-Samos, L.; Marzari, N.; Mauri, F.; Mazzarello, R.; Paolini, S.; Pasquarello, A.; Paulatto, L.; Sbraccia, C.; Scandolo, S.; Sclauzero, G.; Seitsonen, A. P.; Smogunov, A.; Umari, P.; Wentzcovitch, R. M. *J. Phys.: Condens. Mat.* **2009**, *21*, 395502.
(39) Zhao, Y.; Truhlar, D. G. *J. Chem. Theory Comput.* **2007**, *3*, 289–300.
(40) Byrd, E. F. C.; Scuseria, G. E.; Chabalowski, C. F. *J. Phys. Chem. B* **2004**, *108*, 13100–13106.
(41) Macrae, C. F.; Bruno, I. J.; Chisholm, J. A.; Edgington, P. R.; McCabe, P.; Pidcock, E.; Rodriguez-Monge, L.; Taylor, R.; van de Streek, J.; Wood, P. A. *J. Appl. Crystallogr.* **2008**, *41*, 466–470.
(42) Karamertzanis, P. G.; Day, G. M.; Welch, G. W. A.; Kendrick, J.; Leusen, F. J. J.; Neumann, M. A.; Price, S. L. *J. Chem. Phys.* **2008**, *128*, 244708–244717.
(43) Day, G. M.; Cooper, T. G. *CrystEngComm* **2010**, *12*, 2443–2453.

■ NOTE ADDED AFTER ASAP PUBLICATION

This article was published ASAP on July 27, 2011 with an incorrect affiliation for the third author. The correct version was published on August 2, 2011.

JCTC Journal of Chemical Theory and Computation

LETTER

pubs.acs.org/JCTC

Derivation of an Electron−Proton Correlation Functional for Multicomponent Density Functional Theory within the Nuclear−Electronic Orbital Approach

Andrew Sirjoosingh, Michael V. Pak, and Sharon Hammes-Schiffer*

Department of Chemistry, 104 Chemistry Building, Pennsylvania State University, University Park, Pennsylvania 16802, United States

Supporting Information

ABSTRACT: Multicomponent density functional theory enables the quantum mechanical treatment of electrons and selected hydrogen nuclei. An electron−proton correlation functional is derived from the electron−proton pair density associated with a recently proposed ansatz for the explicitly correlated nuclear−electronic wave function. This ansatz allows the retention of all terms in the pair density, and the resulting functional is expected to scale properly and to be computationally efficient. Applications to model systems illustrate that it provides accurate nuclear densities.

Conventional density functional theory (DFT) relies on the Born−Oppenheimer separation of electrons and nuclei, and typically the nuclei move classically on adiabatic electronic surfaces. Nuclear quantum effects have been shown to be important for a broad range of systems, particularly those involving hydrogen bonding and hydrogen transfer.[1−3] In some cases, such as proton-coupled electron transfer reactions, nonadiabatic effects between the electrons and transferring protons have been shown to be significant.[4−6] Multicomponent DFT is a computationally practical method for incorporating these types of nuclear quantum effects into electronic structure calculations.[7−13] In the implementation of multicomponent DFT within the framework of the nuclear−electronic orbital (NEO) approach,[11,12,14] electrons and selected hydrogen nuclei are treated quantum mechanically without the Born−Oppeneheimer approximation. This NEO-DFT approach is designed for systems in which at least two nuclei are treated classically, eliminating difficulties associated with translations and rotations. Moreover, typically only a relatively small number of hydrogen nuclei, such as those involved in hydrogen bonding or hydrogen transfer, are treated quantum mechanically.

A major challenge of this approach is the development of electron−proton density functionals that accurately describe electron−proton correlation, which is highly significant because of the attractive interaction between the electron and proton and the disparity in the masses.[15,16] Previously, we devised a strategy for the development of electron−proton density functionals using the electron−proton pair density from an explicitly correlated nuclear−electronic wave function.[11] The initial electron−proton density functional developed with this strategy required the neglect of a large number of terms in the explicitly correlated electron−proton pair density. The objective of the present work is to derive an electron−proton density functional with a different ansatz for the explicitly correlated nuclear−electronic wave function, thereby enabling us to retain all of the terms in the electron−proton pair density. The resulting electron−proton functional has a similar form to that of the previous functional but is expected to be more reliable in terms of scaling with respect to the number of electrons and quantum protons. The application of this new functional to model systems illustrates that it provides accurate hydrogen nuclear densities. Moreover, the form of this functional is computationally practical for larger molecular systems.

We consider a multicomponent system comprised of N_e electrons and N_p protons that are treated quantum mechanically in a field of N_c fixed classical nuclei. Within the framework of multicomponent DFT, the ground state energy is the minimum of the energy functional

$$E[\rho^e,\rho^p] = \int d\mathbf{r}_1^e\, \rho^e(\mathbf{r}_1^e)\, v(\mathbf{r}_1^e) - \int d\mathbf{r}_1^p\, \rho^p(\mathbf{r}_1^p)\, v(\mathbf{r}_1^p) + F[\rho^e,\rho^p] \quad (1)$$

subject to the constraints $\int d\mathbf{r}_1^e\, \rho^e(\mathbf{r}_1^e) = N_e$ and $\int d\mathbf{r}_1^p\, \rho^p(\mathbf{r}_1^p) = N_p$. Here $\mathbf{r}^e$ and $\mathbf{r}^p$ denote the collective spatial coordinates of the electrons and quantum protons, respectively, $\rho^e(\mathbf{r}_1^e)$ and $\rho^p(\mathbf{r}_1^p)$ denote the one-particle electron and proton densities, respectively, and $v(\mathbf{r}_1)$ is the Coulomb interaction between the electron or proton and the classical nuclei, as defined in ref 12. Analogous to electronic DFT, we define a noninteracting reference system in which all quantum particles (i.e., electrons and quantum protons) do not interact with each other. The ground state nuclear−electronic wave function of this noninteracting reference system is given by the product of electronic and nuclear Slater determinants.

Following the Kohn−Sham procedure,[17,18] the universal functional $F[\rho^e,\rho^p]$ for the interacting system can be expressed as[11,12]

$$F[\rho^e,\rho^p] = T_s[\rho^e,\rho^p] + J_{ep}[\rho^e,\rho^p] + E_{epc}[\rho^e,\rho^p] + J_{ee}[\rho^e] + E_{exc}[\rho^e] + J_{pp}[\rho^p] + E_{pxc}[\rho^p] \quad (2)$$

where $T_s[\rho^e,\rho^p]$ is the total kinetic energy for the noninteracting system. The classical parts of the electron−proton and

Published: August 11, 2011

electron−electron Coulomb interactions are given by

$$J_{ep}[\rho^e, \rho^p] = -\iint d\mathbf{r}_1^e\, d\mathbf{r}_1^p \frac{\rho^e(\mathbf{r}_1^e)\,\rho^p(\mathbf{r}_1^p)}{|\mathbf{r}_1^e - \mathbf{r}_1^p|} \tag{3}$$

and

$$J_{ee}[\rho^e] = \frac{1}{2}\iint d\mathbf{r}_1^e\, d\mathbf{r}_2^e \frac{\rho^e(\mathbf{r}_1^e)\,\rho^e(\mathbf{r}_2^e)}{|\mathbf{r}_1^e - \mathbf{r}_2^e|} \tag{4}$$

and the proton−proton Coulomb interaction $J_{pp}[\rho^p]$ is defined analogously.

The terms $E_{epc}[\rho^e,\rho^p]$, $E_{exc}[\rho^e]$, and $E_{pxc}[\rho^p]$ are the electron−proton correlation functional, the electron exchange-correlation functional, and the proton exchange-correlation functional, respectively. In this formulation,[11,12] the definition of the electron exchange-correlation functional, $E_{exc}[\rho^e]$, is consistent with that from standard electronic DFT.[17−19] Thus, the traditional, well-established electron exchange-correlation functionals can be used, although these electronic functionals have been parametrized without the inclusion of nuclear quantum effects and electron−proton correlation. Furthermore, the contribution from the proton exchange-correlation functional, $E_{pxc}[\rho^p]$, is assumed to be negligible due to the localized nature of protons in typical molecular systems with only selected hydrogen nuclei treated quantum mechanically. For systems with multiple quantum nuclei, the quantum protons may be treated with a generalized Hartree−Fock approach, in which each proton can occupy a different localized spatial orbital, and the proton exchange-correlation functional may be chosen to be the diagonal proton exchange interaction terms to eliminate the self-interaction terms.[20] The present paper focuses on the development of a suitable electron−proton correlation functional, $E_{epc}[\rho^e,\rho^p]$.

Following the strategy devised in ref 11, we define the electron−proton correlation functional in terms of the electron−proton pair density, $\rho^{ep}(\mathbf{r}_1^e,\mathbf{r}_1^p)$, as

$$E_{epc}[\rho^e, \rho^p] = -\iint d\mathbf{r}_1^e\, d\mathbf{r}_1^p \frac{\rho^{ep}(\mathbf{r}_1^e, \mathbf{r}_1^p)}{|\mathbf{r}_1^e - \mathbf{r}_1^p|} - J_{ep}[\rho^e, \rho^p] \tag{5}$$

In ref 11, the electron−proton pair density was obtained from an explicitly correlated nuclear−electronic wave function defined as $\Psi_{gem} = (1 + G)\Phi^e\Phi^p$,[15] where Φ^e and Φ^p are electronic and nuclear Slater determinants, respectively, and

$$G(\mathbf{r}^e, \mathbf{r}^p) = \sum_{i=1}^{N_e}\sum_{i'=1}^{N_p} g(\mathbf{r}_i^e, \mathbf{r}_{i'}^p) \tag{6}$$

$$g(\mathbf{r}_i^e, \mathbf{r}_{i'}^p) = \sum_{k=1}^{N_{gem}} b_k\, e^{-\gamma_k|\mathbf{r}_i^e - \mathbf{r}_{i'}^p|^2} \tag{7}$$

Here, N_{gem} is the number of Gaussian type geminal functions used in the expansion, and b_k and γ_k are parameters that define these functions. Gaussian type geminal functions are used to ensure the tractable calculation of integrals over Gaussian basis functions.

In the present paper, we determine the electron−proton pair density from the alternative explicitly correlated nuclear−electronic wave function defined as[21]

$$\Psi_{gem} = \sqrt{1 + G}\Phi^e\Phi^p \tag{8}$$

The significant advantage of this alternative nuclear−electronic wave function ansatz over the previous ansatz is that all terms quadratic in the geminal functions are eliminated from the electron−proton pair density. Note that this alternative ansatz retains the important characteristics of a mixed nuclear−electronic wave function: it is antisymmetric with respect to the exchange of electrons or quantum protons, approaches the Hartree−Fock wave function at large electron−proton distances, and has the numerical flexibility to describe the correct linear behavior at small electron−proton distances. As a result of this alternative ansatz, in conjunction with a physically reasonable approximation for the two-particle electron and proton densities, all terms in the electron−proton pair density can be retained in the present treatment, compared to the neglect of 24 out of 26 terms in the electron−proton pair density in the previous treatment.[11,22] The remainder of this Letter presents the derivation of the new electron−proton density functional and an initial application to a model system.

Prior to the derivation, we define the geminal reduced densities, which are associated with the geminal wave function, and the auxiliary reduced densities, which are associated with the Slater determinants. The geminal one-particle and two-particle electron densities are defined as

$$\rho_1^e(\mathbf{r}_1^e) = \frac{N_e}{\langle\Psi_{gem}|\Psi_{gem}\rangle}\langle\Psi_{gem}|\Psi_{gem}\rangle_{-e_1} \tag{9}$$

$$\rho_2^e(\mathbf{r}_1^e, \mathbf{r}_2^e) = \frac{N_e(N_e - 1)}{2\langle\Psi_{gem}|\Psi_{gem}\rangle}\langle\Psi_{gem}|\Psi_{gem}\rangle_{-e_1e_2} \tag{10}$$

and the one-particle and two-particle proton densities are defined analogously. The geminal electron−proton pair density is defined as

$$\rho^{ep}(\mathbf{r}_1^e, \mathbf{r}_1^p) = \frac{N_eN_p}{\langle\Psi_{gem}|\Psi_{gem}\rangle}\langle\Psi_{gem}|\Psi_{gem}\rangle_{-e_1p_1} \tag{11}$$

In these expressions and those that follow, angular brackets without subscripts indicate integration over all coordinates, angular brackets with subscripts indicate the spatial coordinates of integration (i.e., $\langle\cdots\rangle_{e1}$ indicates integration over $\mathbf{r}_1^e$), and angular brackets with subscripts preceded by a minus sign denote integration over all coordinates except the specified spatial coordinate(s) (i.e., $\langle\cdots\rangle_{-e1}$ indicates integration over all coordinates except $\mathbf{r}_1^e$). The auxiliary one-particle and two-particle electron densities, $\tilde{\rho}_1^e(\mathbf{r}_1^e)$ and $\tilde{\rho}_2^e(\mathbf{r}_1^e,\mathbf{r}_2^e)$, are defined by substituting Φ^e for Ψ_{gem} in eqs 9 and 10, and the auxiliary proton densities are defined analogously with Φ^p. Note that the Slater determinants, Φ^e and Φ^p, are normalized because they are constructed with orthonormal spin orbitals, but the geminal wave function, Ψ_{gem}, is not normalized due to the geminal factor in eq 8.

The geminal electron−proton pair density corresponding to the ansatz given in eq 8 can be expressed in terms of the auxiliary densities as follows:

$$\begin{aligned}\rho^{ep}(\mathbf{r}_1^e, \mathbf{r}_1^p) = {} & \frac{1}{1 + \langle\tilde{\rho}_1^e(\mathbf{r}_1^e)\,\tilde{\rho}_1^p(\mathbf{r}_1^p)\,g(\mathbf{r}_1^e, \mathbf{r}_1^p)\rangle_{e_1p_1}}[\tilde{\rho}_1^e(\mathbf{r}_1^e)\,\tilde{\rho}_1^p(\mathbf{r}_1^p) \\ & \times\{1 + g(\mathbf{r}_1^e, \mathbf{r}_1^p)\} + 2\tilde{\rho}_1^p(\mathbf{r}_1^p)\langle\tilde{\rho}_2^e(\mathbf{r}_1^e, \mathbf{r}_2^e)\,g(\mathbf{r}_2^e, \mathbf{r}_1^p)\rangle_{e_2} \\ & + 2\tilde{\rho}_1^e(\mathbf{r}_1^e)\langle\tilde{\rho}_2^p(\mathbf{r}_1^p, \mathbf{r}_2^p)\,g(\mathbf{r}_1^e, \mathbf{r}_2^p)\rangle_{p_2} \\ & + 4\langle\tilde{\rho}_2^e(\mathbf{r}_1^e, \mathbf{r}_2^e)\,\tilde{\rho}_2^p(\mathbf{r}_1^p, \mathbf{r}_2^p)\,g(\mathbf{r}_2^e, \mathbf{r}_2^p)\rangle_{e_2p_2}]\end{aligned} \tag{12}$$

For comparison, the electron−proton pair density corresponding to the previous wave function ansatz, with the geminal factor of $(1+G)$ rather than $(1 + G)^{1/2}$, was comprised of 26 terms, as given by eq 32 in ref 22. Thus, the present electron−proton pair density is much simpler. In the previous derivation,[11] the geminal electron−proton pair density was truncated in a manner that eliminated all terms of order g^2 and all terms that included densities other than one-particle densities. As a result, the electron−proton pair density included only the first two terms, $\tilde{\rho}_1^e\tilde{\rho}_1^p(1 + g)$, in eq 12. This truncation required the renormalization of the electron−proton pair density so that $\langle\rho^{ep}(\mathbf{r}_1^e,\mathbf{r}_1^p)\rangle_{e_1p_1} = N_eN_p$, leading to an additional factor of $(N_eN_p)^{-1}$ in the second term of the denominator. In the present approach, the electron−proton pair density in eq 12 is already normalized properly because no terms have been eliminated. Note that the wave function ansatz with the geminal factor of $(1 + G)^{1/2}$ does not lead to any terms of order g^2 in the electron−proton pair density, and the terms including two-particle densities have been retained in eq 12.

To develop an effective electron−proton density functional, the electron−proton pair density given in eq 12 should depend on only one-particle densities. For this purpose, we assume that the auxiliary two-particle electron density can be approximated as

$$\tilde{\rho}_2^e(\mathbf{r}_1^e, \mathbf{r}_2^e) \approx \frac{1}{2}\frac{N_e - 1}{N_e}\tilde{\rho}_1^e(\mathbf{r}_1^e)\,\tilde{\rho}_1^e(\mathbf{r}_2^e) \tag{13}$$

This independent particle approximation is based on the assumption that the direct electron−electron exchange contributions included in the electron exchange-correlation functional, as defined in eq 2, are significantly greater than the indirect electron−electron exchange contributions in the electron−proton correlation functional. As a result, the indirect electron−electron exchange effects arising from the dependence of the electron−proton pair density on the two-particle electron density are neglected. We invoke the analogous approximation for the auxiliary two-particle proton density. These two-particle density terms were completely neglected in the previous treatment.[11]

Substituting these approximate auxiliary two-particle electron and proton densities into eq 12 leads to

$$\rho^{ep}(\mathbf{r}_1^e, \mathbf{r}_1^p) = \frac{\tilde{\rho}^e\tilde{\rho}^p}{1 + \langle\tilde{\rho}^e\tilde{\rho}^p g\rangle_{ep}}\left[1 + g + \frac{N_e - 1}{N_e}\langle\tilde{\rho}^e g\rangle_e + \frac{N_p - 1}{N_p}\langle\tilde{\rho}^p g\rangle_p + \frac{(N_e - 1)(N_p - 1)}{N_eN_p}\langle\tilde{\rho}^e\tilde{\rho}^p g\rangle_{ep}\right] \tag{14}$$

For notational convenience, we have dropped the dependence of the reduced densities on the coordinates, defined $g \equiv g(\mathbf{r}_1^e,\mathbf{r}_1^p)$, dropped the subscript on the one-particle densities, and simplified the subscripts on the brackets to denote the electron and/or proton spatial coordinates in the integrand. The analogous procedure for the geminal one-particle electron and proton densities leads to

$$\rho^e(\mathbf{r}_1^e) = \frac{\tilde{\rho}^e}{1 + \langle\tilde{\rho}^e\tilde{\rho}^p g\rangle_{ep}}\left[1 + \langle\tilde{\rho}^p g\rangle_p + \frac{N_e - 1}{N_e}\langle\tilde{\rho}^e\tilde{\rho}^p g\rangle_{ep}\right] \tag{15}$$

$$\rho^p(\mathbf{r}_1^p) = \frac{\tilde{\rho}^p}{1 + \langle\tilde{\rho}^e\tilde{\rho}^p g\rangle_{ep}}\left[1 + \langle\tilde{\rho}^e g\rangle_e + \frac{N_p - 1}{N_p}\langle\tilde{\rho}^e\tilde{\rho}^p g\rangle_{ep}\right] \tag{16}$$

Note that these densities satisfy the sum rules, $\rho^e(\mathbf{r}_1^e) = N_p^{-1}\langle\rho^{ep}(\mathbf{r}_1^e,\mathbf{r}_1^p)\rangle_p$ and $\rho^p(\mathbf{r}_1^p) = N_e^{-1}\langle\rho^{ep}(\mathbf{r}_1^e,\mathbf{r}_1^p)\rangle_e$.

The next step is to express the electron−proton pair density in eq 14 in terms of the one-particle densities given in eqs 15 and 16 by eliminating the auxiliary densities. To achieve this goal, expressions for the auxiliary one-particle densities in terms of the geminal one-particle densities must be determined. In principle, eqs 15 and 16 could be inverted to determine these expressions, but the exact analytical solution is not known. Instead, we follow the approximate procedure of ref 11 and replace $\tilde{\rho}^e(\mathbf{r}_1^e)$ with $\rho^e(\mathbf{r}_1^e)$ and $\tilde{\rho}^p(\mathbf{r}_1^p)$ with $\rho^p(\mathbf{r}_1^p)$ whenever they are multiplied by the geminal factor g in eqs 14, 15, and 16. These substitutions lead to the following expressions for the approximate geminal densities:

$$\rho^{ep}(\mathbf{r}_1^e, \mathbf{r}_1^p) = \frac{1}{1 + \langle\rho^e\rho^p g\rangle_{ep}}\left[\tilde{\rho}^e\tilde{\rho}^p + \rho^e\rho^p g + \frac{N_e - 1}{N_e}\rho^e\rho^p\langle\rho^e g\rangle_e + \frac{N_p - 1}{N_p}\rho^e\rho^p\langle\rho^p g\rangle_p + \frac{(N_e - 1)(N_p - 1)}{N_eN_p}\rho^e\rho^p\langle\rho^e\rho^p g\rangle_{ep}\right] \tag{17}$$

$$\rho^e(\mathbf{r}_1^e) = \frac{1}{1 + \langle\rho^e\rho^p g\rangle_{ep}}\left[\tilde{\rho}^e + \rho^e\langle\rho^p g\rangle_p + \frac{N_e - 1}{N_e}\rho^e\langle\rho^e\rho^p g\rangle_{ep}\right] \tag{18}$$

$$\rho^p(\mathbf{r}_1^p) = \frac{1}{1 + \langle\rho^e\rho^p g\rangle_{ep}}\left[\tilde{\rho}^p + \rho^p\langle\rho^e g\rangle_e + \frac{N_p - 1}{N_p}\rho^p\langle\rho^e\rho^p g\rangle_{ep}\right] \tag{19}$$

Note that these reduced densities still satisfy the sum rules given above and retain the property that $\lim_{r_{ep}\to\infty}\rho^{ep} = \tilde{\rho}^e\tilde{\rho}^p = \rho^e\rho^p$.

Substituting the expressions for the auxiliary one-particle electron and proton densities obtained from eqs 18 and 19 into the electron−proton pair density given in eq 17 leads to the final expression for the approximate pair density in terms of the one-particle densities:

$$\rho^{ep}(\mathbf{r}_1^e, \mathbf{r}_1^p) = \rho^e\rho^p\left[1 + \langle N_e^{-1}N_p^{-1}\rho^e\rho^p g\rangle_{ep} - \langle N_e^{-1}\rho^e g\rangle_e - \langle N_p^{-1}\rho^p g\rangle_p + \frac{g + \langle\rho^e g\rangle_e\langle\rho^p g\rangle_p}{1 + \langle\rho^e\rho^p g\rangle_{ep}}\right] \tag{20}$$

Equation 20 represents an approximate pair density derived from the explicitly correlated nuclear−electronic wave function given in eq 8 and defines an electron−proton correlation functional when substituted into eq 5. This expression is identical to the previous expression[11] derived from a different explicitly correlated nuclear−electronic wave function, except the last term, which differs by a factor of N_eN_p in the second term of both the numerator and denominator. These differences arise from the truncation of the electron−proton pair density and the subsequent renormalization in the previous treatment. Since the

present derivation includes all terms of the electron−proton pair density, whereas the previous derivation neglected a large number of terms, we expect the present functional to be more reliable in terms of scaling with respect to the number of electrons and protons. The computational cost is identical for the two functionals.

We applied the NEO-DFT approach with this electron−proton density functional to the model system, $[He-H-He]^+$, and the isotopomers $[He-D-He]^+$ and $[He-T-He]^+$. The two helium nuclei were treated classically at a fixed distance, and the central nucleus and four electrons were treated quantum mechanically. We studied these systems with the cc-pVDZ and cc-pVTZ electronic basis sets,[23,24] where the electronic basis functions corresponding to the central nucleus were placed at the midpoint between the two helium nuclei. The nuclear basis set was comprised of a single 1s nuclear basis function placed at the midpoint between the two helium nuclei, and the exponent was optimized variationally during the NEO-DFT calculation. Two Gaussian type geminal functions were used with geminal parameters obtained variationally with the wave function ansatz in eq 8 for a one-electron/one-proton model system.[21] To account for differences between the NEO-DFT and variational wave function approach, the geminal functions were scaled by a single constant factor to reproduce the hydrogen vibrational stretching frequency of $[He-H-He]^+$ with the cc-pVDZ electronic basis set. For all other systems and basis sets, these geminal parameters were fixed during the NEO-DFT calculations. Moreover, in this Letter, the electron exchange-correlation functional was chosen to be the Hartree−Fock exchange. Future studies will examine the effects of combining this electron−proton correlation functional with various electron exchange-correlation functionals. All calculations were performed with a modified version of the GAMESS program.[25]

The objective of this application is to provide evidence that this electron−proton functional can provide accurate hydrogen nuclear densities. The hydrogen vibrational stretching frequencies were determined from a Gaussian fit of the nuclear density along the He−He axis. These frequencies are compared to the corresponding splitting for the three-dimensional hydrogen vibrational states calculated with the Fourier grid Hamiltonian (FGH) method.[26] Since the nuclear basis set contains only a single 1s nuclear basis function, it is incapable of reproducing both the stretching and bending hydrogen vibrational frequencies. For these calculations, we determined the He−He distances at which the stretching and bending frequencies calculated with the FGH method are qualitatively similar. The resulting He−He distances for the cc-pVDZ and cc-pVTZ electronic basis sets were determined to be 1.955 and 1.945 Å, respectively. Future work will focus on studies with larger electronic and nuclear basis sets that will enable the calculation of bending as well as stretching frequencies.

The results of these calculations are provided in Table 1. The NEO-HF (Hartree−Fock) frequencies are much higher than the NEO-DFT frequencies, which are in qualitative agreement with the FGH frequencies. These values illustrate the importance of electron−proton correlation. In addition, these results indicate that the geminal parameters are reasonably transferable to larger electronic basis sets and to other isotopes of hydrogen for this model system. From a physical perspective, the geminal parameters are expected to be transferable because these terms are significant only at small electron−proton distances and should be relatively independent of the external chemical environment.

Table 1. Vibrational Frequencies in cm^{-1} Corresponding to the Hydrogen Vibrational Stretching Motion Calculated with the NEO-HF, NEO-DFT, and FGH Methods for the $[He-X-He]^+$ Systems with X = H, D, or T[a]

	cc-pVDZ			cc-pVTZ		
isotope	NEO-HF	NEO-DFT	FGH	NEO-HF	NEO-DFT	FGH
H	3098	1191	1191	3122	1103	1111
D	2284	820	801	2330	782	740
T	1903	660	633	1954	646	581

[a] The cc-pVDZ or cc-pVTZ electronic basis set was used as indicated. The NEO-HF and NEO-DFT calculations were performed using a single 1s nuclear basis function with a variationally optimized exponent, and the NEO-DFT calculations were performed using two geminals with parameters $(b_1,\gamma_1) = (0.3969,0.34)$ and $(b_2,\gamma_2) = (0.8912,2.47)$ for the electron−proton functional presented in this paper. Values of γ_k given in $bohr^{-2}$.

Future work will focus on optimizing the geminal parameters for applications to a wide range of chemical systems.

Qualitatively similar results are obtained for this model system with the previously derived electron−proton functional[11] using different geminal parameters, as given in the Supporting Information. Note that this previous functional may be derived from the ansatz given in eq 8 if the two-particle densities are neglected. The two electron−proton functionals will exhibit different scaling behaviors with respect to the number of electrons and protons, however, and the present functional is expected to be more reliable because fewer approximations were invoked in the derivation. Investigation of these scaling properties will require the study of systems with a larger number of quantum particles and is a direction for future research.

In this Letter, we derived an electron−proton density functional for use in multicomponent DFT calculations, where electrons and selected hydrogen nuclei are treated quantum mechanically. This functional was derived directly from the electron−proton pair density associated with a recently proposed ansatz for the explicitly correlated nuclear−electronic wave function. The advantage of this functional over the previously derived functional is that the new wave function ansatz, combined with the independent particle approximation for the auxiliary two-particle electron and proton densities, enabled us to retain all of the terms in the electron−proton pair density, whereas the previous derivation neglected a large number of terms. Thus, the present functional is based on a more rigorous derivation and therefore may be more robust, although further studies are required to assess both functionals. In particular, future work will focus on the further development of these types of electron−proton functionals with larger electronic and nuclear basis sets in conjunction with standard electron exchange-correlation functionals.

■ ASSOCIATED CONTENT

Supporting Information. Analog to Table 1 for the previously derived electron−proton functional. This material is available free of charge via the Internet at http://pubs.acs.org.

■ AUTHOR INFORMATION

Corresponding Author

*E-mail: shs@chem.psu.edu.

■ ACKNOWLEDGMENT

We thank Chet Swalina and Chaehyuk Ko for helpful discussions and technical assistance. We gratefully acknowledge funding from AFOSR Grant FA9550-10-1-0081 and NSF Grant CHE-10-57875. A.S. thanks the Natural Sciences and Engineering Research Council of Canada for a PGS scholarship.

■ REFERENCES

(1) Tuckerman, M. E.; Marx, D.; Klein, M. L.; Parrinello, M. *Science* **1997**, *275*, 817–820.
(2) Raugei, S.; Klein, M. L. *J. Am. Chem. Soc.* **2003**, *125*, 8992–8993.
(3) Cha, Y.; Murray, C. J.; Klinman, J. P. *Science* **1989**, *243*, 1325–1330.
(4) Hammes-Schiffer, S.; Stuchebrukhov, A. A. *Chem. Rev.* **2010**, *110*, 6939–6960.
(5) Sirjoosingh, A.; Hammes-Schiffer, S. *J. Phys. Chem. A* **2011**, *115*, 2367–2377.
(6) Georgievskii, Y.; Stuchebrukhov, A. A. *J. Chem. Phys.* **2000**, *113*, 10438–10450.
(7) Capitani, J. F.; Nalewajski, R. F.; Parr, R. G. *J. Chem. Phys.* **1982**, *76*, 568–573.
(8) Gidopoulos, N. *Phys. Rev. B* **1998**, *57*, 2146–2152.
(9) Kreibich, T.; Gross, E. K. U. *Phys. Rev. Lett.* **2001**, *86*, 2984–2987.
(10) Kreibich, T.; van Leeuwen, R.; Gross, E. K. U. *Phys. Rev. A* **2008**, *78*, 022501.
(11) Chakraborty, A.; Pak, M. V.; Hammes-Schiffer, S. *Phys. Rev. Lett.* **2008**, *101*, 153001.
(12) Chakraborty, A.; Pak, M. V.; Hammes-Schiffer, S. *J. Chem. Phys.* **2009**, *131*, 124115.
(13) Krishna, V. *Phys. Rev. Lett.* **2009**, *102*, 053002.
(14) Webb, S. P.; Iordanov, T.; Hammes-Schiffer, S. *J. Chem. Phys.* **2002**, *117*, 4106–4118.
(15) Swalina, C.; Pak, M. V.; Chakraborty, A.; Hammes-Schiffer, S. *J. Phys. Chem. A* **2006**, *110*, 9983–9987.
(16) Chakraborty, A.; Pak, M. V.; Hammes-Schiffer, S. *J. Chem. Phys.* **2008**, *129*, 014101.
(17) Kohn, W.; Sham, L. J. *Phys. Rev.* **1965**, *140*, A1133.
(18) Parr, R. G.; Yang, W. *Density Functional Theory of Atoms and Molecules*; Oxford University Press: New York, 1989.
(19) Ernzerhof, M.; Perdew, J. P.; Burke, K. Density functionals: where do they come from, why do they work? In *Density Functional Theory*; Nalewajski, R., Ed.; Springer-Verlag: Berlin, 1996.
(20) Auer, B.; Hammes-Schiffer, S. *J. Chem. Phys.* **2010**, *132*, 084110.
(21) Ko, C.; Pak, M. V.; Swalina, C.; Hammes-Schiffer, S. *J. Chem. Phys.* **2011**, *135*, 054106.
(22) Chakraborty, A.; Hammes-Schiffer, S. *J. Chem. Phys.* **2008**, *129*, 204101.
(23) Dunning, T. H., Jr. *J. Chem. Phys.* **1989**, *90*, 1007–1023.
(24) Woon, D. E.; Dunning, T. H., Jr. *J. Chem. Phys.* **1994**, *100*, 2975.
(25) Schmidt, M. W.; Baldridge, K. K.; Boatz, J. A.; Elbert, S. T.; Gordon, M. S.; Jensen, J. H.; Koseki, S.; Matsunaga, N.; Nguyen, K. A.; Su, S.; Windus, T. L.; Dupuis, M.; Montgomery, J. A. *J. Comput. Chem.* **1993**, *14*, 1347–1363.
(26) Webb, S. P.; Hammes-Schiffer, S. *J. Chem. Phys.* **2000**, *113*, 5214–5227.

JCTC Journal of Chemical Theory and Computation

LETTER

pubs.acs.org/JCTC

Photodynamics of All-*trans* Retinal Protonated Schiff Base in Bacteriorhodopsin and Methanol Solution

Xin Li, Lung Wa Chung,* and Keiji Morokuma*

Fukui Institute for Fundamental Chemistry, Kyoto University, Kyoto 606-8103, Japan

Supporting Information

ABSTRACT: Nonadiabatic ONIOM(CASSCF:AMBER) and CASSCF simulations elucidated different photodynamics of an all-*trans* retinal protonated Schiff base (RPSB) in bacteriorhodopsin and methanol as well as without an environment. The bR protein matrix holds RPSB tight via specific interactions and promotes bond-specific (along the C13═C14 bond), unidirectional, and ultrafast photoisomerization with a high quantum yield. In contrast, in methanol and for the twisted bare RPSB, photoisomerization is not bond-specific (mainly along the C11═C12 bond), is nonunidirectional, and is ineffective. Therefore, bR efficiently "catalyzes" photoisomerization and stores enough energy to promote the subsequent proton pumping and protein conformational changes.

Bacteriorhodopsin (bR) is a transmembrane protein in the purple membrane of *Halobacterium salinarium*.[1] An all-*trans* retinal protonated Schiff base (RPSB) is covalently linked to the Lys216 of the protein in the light-adapted bR. Absorption of a photon by RPSB can trigger a photocycle with several photostationary states (Scheme 1). The first step of this photocycle is photoisomerization of all-*trans* RPSB to give the 13-*cis* form in an ultrafast and efficient manner (quantum yield: ∼0.6−0.7),[2] which prompts vectorial proton transfer and protein conformational changes. Transient spectroscopic studies showed that, after photoexcitation in the Franck−Condon (FC) region, photoisomerization of RPSB was observed to rapidly give a twisted configuration in S_1 (>200 fs).[3]

In comparison, in a homogeneous methanol solution, photoisomerization of RPSB is slower, nonspecific, and inefficient, to give a mixture of different isomers, the 9-*cis* (0.02), 11-*cis* (0.14), and 13-*cis* (0.01) forms.[4] Also, the reaction time of photoisomerization is much slower in solutions (on the picosecond time scale).[5] The different reaction mechanisms and photodynamics of RPSB in bR and solutions are of great importance but still remain unclear. In this study, we report nonadiabatic (NA) ONIOM(CASSCF:AMBER) and CASSCF molecular dynamics (MD) simulations (mainly on S_1 and S_0 surfaces) to elucidate the effects of different environments on the photodynamics of RPSB. To our knowledge, it is the first NA CASSCF/AMBER MD simulation including all π bonds of RPSB as the QM part in bR as well as the first comparison of photodynamics in bR and in methanol.[6]

ONIOM(B3LYP/6-31G:AMBER) MD simulations with an electronic embedding (EE) scheme was performed to equilibrate the systems and then sample ground-state structures at 298 K. Afterward, ONIOM(CASSCF(12e,12o)/6-31G:AMBER) MD simulations in the constant energy ensemble were carried out. For the simulations in bR and methanol, around FC and fluorescent state regions, the ONIOM(CASSCF:AMBER)-EE method gives a wrong order of the covalent A_g-like excited state (S_2) and ionic B_u-like excited state (S_1).[6n] This problem can be remedied by using the computationally unaffordable MS-CASPT2 or MRCI method. To remedy this unrealistic situation, the mechanical embedding (ME) scheme was first used, and then the EE scheme was adopted when $\Delta E_{S1-S0} < \sim 35$ kcal/mol. As shown in Tables S1 and S3 (Supporting Information), time to access the crossing region is similar, when either we used the ONIOM-ME method only in S_1 or we switched to use the ONIOM-EE method. Therefore, the overall qualitative conclusions should not be affected by switching to the ONIOM-EE method.[7a]

In bR, as shown in Figures 1a,c and S1 (Supporting Information) and Table 1, photoexcited RPSB underwent ultrafast radiationless decay ($S_1 \rightarrow S_0$) exclusively via a torsional change along ϕ_{13} (Scheme 1). The mean excited-state (S_1) lifetime is about 114−162 fs (ranging from 75 to 334 fs) via nonadiabatic crossing (NC) and crossing seam (CS),[7b] which is shorter than the experimental values (>200 fs).[3] It is partly attributed to the over-repulsive potential of the CASSCF method.[8] Photoisomerization giving the 13-*cis* form is very efficient with a quantum yield ($\Phi_{photoiso}$) of 0.69−0.86, which is in good agreement with the experiments (∼0.6−0.7).[2] Moreover, photoisomerization in bR is always unidirectional (increasing ϕ_{13}, see also Figure S2, Supporting Information).

Additional CASSCF MD simulations for bare RPSB, with the same initial conditions but removing the protein matrix, were further performed. Notably, the equilibrium structure of RPSB in bR in S_0 is slightly twisted at ϕ_{13} (X-ray and ONIOM-optimized ones: ϕ_{13} = 203°).[9] *Although the chromophore is pretwisted, the unidirectional and bond-specific photoisomerization is lost in the absence of the protein matrix.* The rotations can take place in both directions (Figure S4, Supporting Information) and along the following torsions: ϕ_9 (6.25%), $\phi_9+\phi_{11}$ (6.25%), ϕ_{11} (56.25%), and ϕ_{13} (31.25%). Also, compared to bR, this twisted bare retinal model takes a longer time to access the crossing region (Table S1, Supporting Information). Therefore, the protein matrix is vital to efficiently channelling RPSB to the unique rotation (intramolecular vibrational redistribution) during the photoisomerization process. Comparatively, the protein matrix in rhodopsin (Rh) is not critical for the photoisomerization of the 11-*cis* retinal, which is partly driven by a steric repulsion between the C10−H and C13−Me moieties of the 11-*cis* retinal.[6ln]

Received: August 8, 2011
Published: August 09, 2011

Scheme 1. bR Protein, Key Events in the Photocycle, Retinal Protonated Schiff Base (QM Part in Bold), and Definition of the Key Torsions

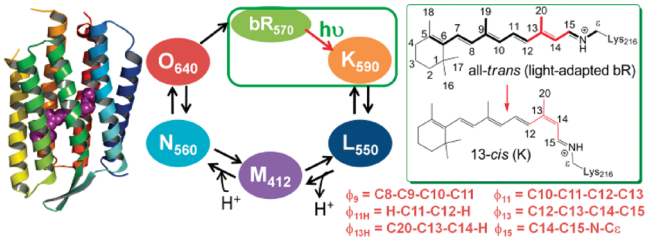

The bond-specific and unidirectional photoisomerization in bR is controlled by stereospecific chromophore−protein interactions. Namely, nearby residues (Trp86, Thr90, Met118, Ile119, Trp182, and Tyr185) sandwich RPSB except the C14C15N part (Figure 2a). Therefore, rotations around other bonds are suppressed by these residues, and the protein matrix specifically facilitates the rotation around the C13═C14 bond in a small preset cavity. The C14HC15-HNH part has the largest displacement at the crossings relative to the FC structure (Figure 2b). In contrast, photoisomerization of all-*trans* RPSB in bathorhodopsin (bathoRh) leads to the 11-*cis* form, presumably due to a lack of steric hindrance around the C11═C12 bond (Figure S5, Supporting Information).[10] In addition, C14H of RPSB in bR is in close contact with Trp86 (Figure 2a), which results in a pretwisted C13═C14 bond in S_0. Thus, photoisomerization occurs only toward one direction to avoid the repulsion with Trp86.[6b,c] It should be noted that the active sites of other microbial rhodopsin homologues (e.g., SRII and HR) are similar to bR (Figure S6, Supporting Information). We believe microbial rhodopsins may use a similar mechanism to control photoisomerization.

In methanol (compared to bR), the nearly planar RPSB takes a longer time to decay via one of three torsional changes: ϕ_9, ϕ_{11}, or ϕ_{13} (Scheme 1, Table 1, Figures 1b,c and S1, S3, and S7, Supporting Information). The mean S_1 lifetime is about 748 and 817 fs (ranging from 208 to 2488 fs) via NC or CS,[7b] respectively. Also, $\Phi_{photoiso}$ giving the 11-*cis* form is about 0.11 for NC, while that leading to the 11-*cis*, 9,11-di-*cis*, and 13-*cis* forms is 0.33, 0.07, and 0.07 for CS, respectively. It is qualitatively consistent with a smaller observed $\Phi_{photoiso}$.[4] Moreover, the rotation is not unidirectional in methanol (Figure 1b). Also, displacements of RPSB and nearby methanol molecules are larger at the crossing (Figure 2c), due to a more flexible solution cavity. Thus, solvent reorganization and a lack of the pretwisted RPSB (reactant destabilization) should increase the S_1 lifetime.

For most cases in bR, the twisting along ϕ_{13} and ϕ_{15} takes place in the opposite directions (Figure 3a). At the $S_1 \rightarrow S_0$ crossings, the former motion (average: ∼+61°) is more profound than the latter (∼−32°; Figures 1a and S2, S8, and S9, Supporting Information). These large torsional motions come mainly from motions of the C14H−C15H part, in particular, hydrogen atoms due to their lowest mass and size. Once the twisted system in S_1 makes the transition to S_0 and gives the 13-*cis* photoproduct, ϕ_{15} generally continues to twist until a maximum is reached and then turns back to the *trans* position (Figure 3a). Such an asynchronous crankshaft motion,[6h,i,k] which allows the rotation of the C13−C14−C15−N moiety in the limited protein cavity (Figures S8−S9, Supporting Information), is the main space-saving decay pathway in bR.

In methanol, torsions along ϕ_9 (average: ∼+36°) and ϕ_{11} (∼−74°) bonds are mostly twisted in the opposite directions at

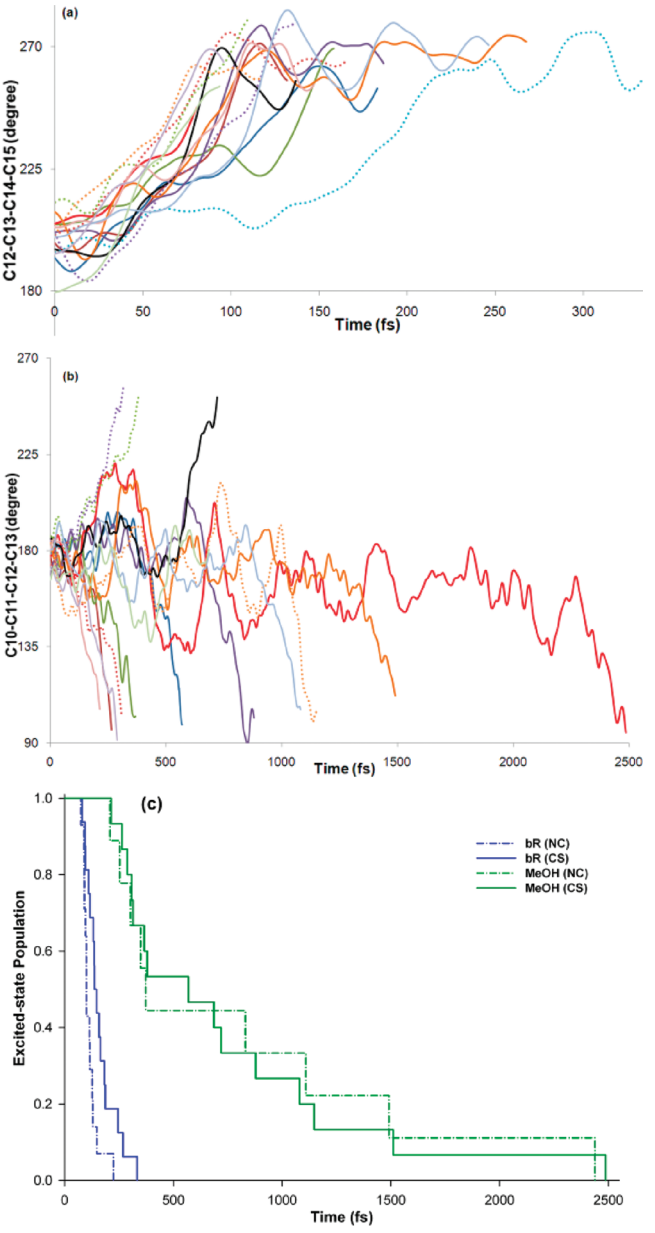

Figure 1. Changes of the rotating dihedral in S_1 until CS (ref 7b): (a) ϕ_{13} in bR and (b) ϕ_{11} in methanol (also see Figure S3, Supporting Information). (c) Excited-state population for photoisomerization in bR and methanol.

Table 1. The Mean S_1 Lifetime τ (fs) and Quantum Yield $\Phi_{photoiso}$ (Photoproducts) for Photoisomerization in bR and Methanol

	τ_{NC}[a]	$\Phi_{photoiso,NC}$[b]	τ_{CS}[c]	$\Phi_{photoiso,CS}$[b]
bR	114	0.86(13C)	162	0.69(13C)
Methanol	817	0.11(11C)	748	0.33(11C)[d]

[a] Nonadiabatic crossing (ref 7b). [b] 13-*cis* (13C) and 11-*cis* (11C) forms. [c] Crossing seam (ref 7b). [d] The formation of one 9,11-di-*cis* form and one 13-*cis* form was observed.

the S_1-S_0 crossings (Figures 1b and S3, S8, and S9, Supporting Information). The twisting along ϕ_{13} (∼+18°) is much smaller, except one case that led to the 13-*cis* form. Moreover, from the

dx.doi.org/10.1021/ct200549z |J. Chem. Theory Comput. 2011, 7, 2694–2698

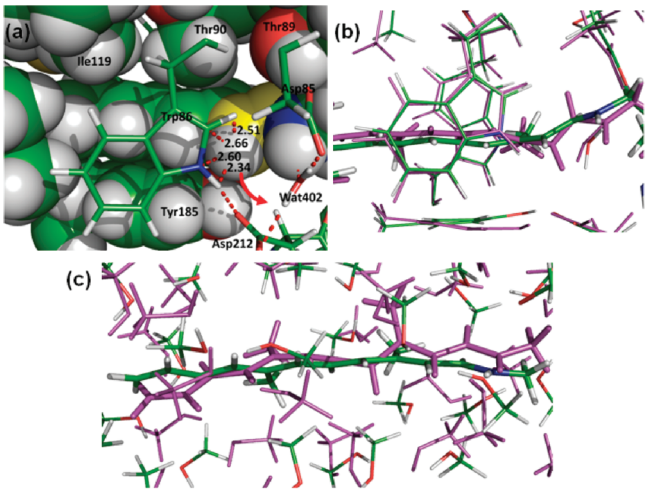

Figure 2. (a) ONIOM-optimized active-site structure of bR. The C14 and C15 are highlighted by a yellow color, and the close contacts between HC14 and Trp86 are given in Ångstroms. Superimposition of FC (green) and crossing (pink) structures in (b) bR and (c) methanol.

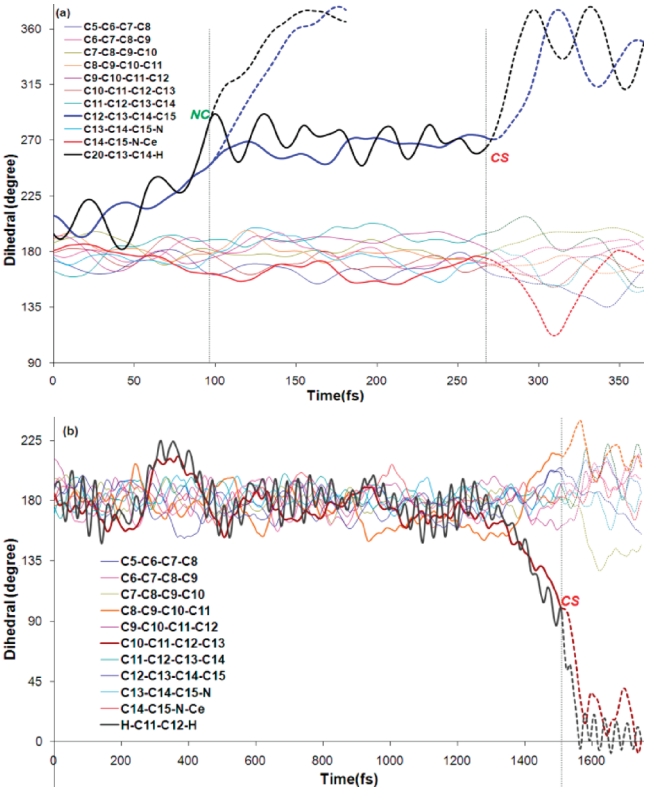

Figure 3. An example of the evolution of dihedrals for photoisomerizations of (a) all-*trans*→13-*cis* in bR and (b) all-*trans*→11-*cis* in a methanol solution.

twisted form in S_1 to the 11-*cis* photoproduct in S_0, ϕ_9 continues to twist to a maximum and then turns back (Figure 3b).[11] Again, the crankshaft motion is the main pathway for the decay in methanol. Overall, *the crankshaft motion is the major pathway for the decay and photoisomerization of RPSB in bR, Rh, methanol, and the gas phase*[6h,k−n] *and could also operate in the other retinal proteins or solutions*, although rotations at different angles/bonds can be involved.

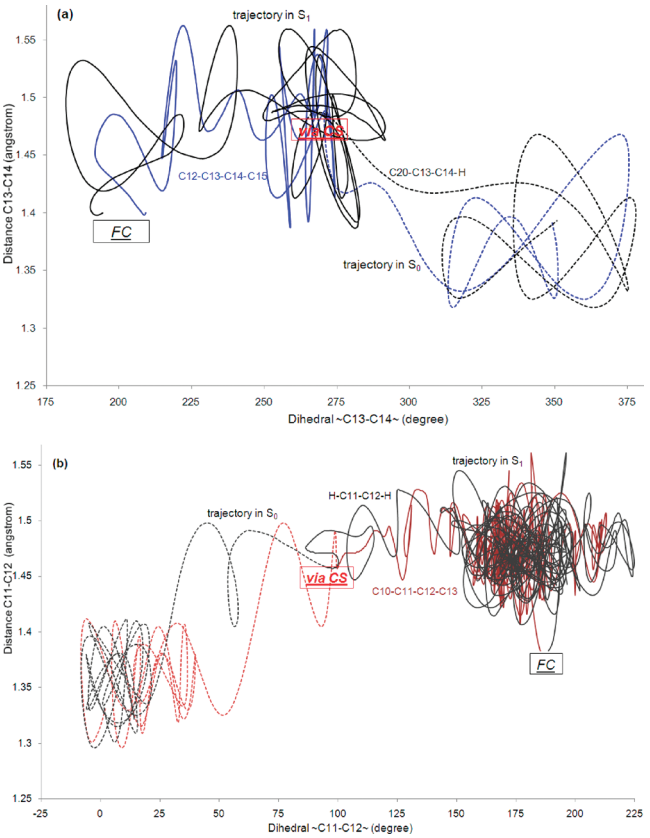

Figure 4. Dynamic changes of rotating torsions versus the bond length for photoisomerizations of (a) all-*trans*→13-*cis* in bR and (b) all-*trans*→11-*cis* in a methanol solution.

At all S_1-S_0 crossings, the largest twist involves hydrogen atoms, i.e., ϕ_{13H} (average: ∼81°) in bR and ϕ_{11H} (∼88°) in methanol (Scheme 1 and Figure S8, Supporting Information). A hydrogen-out-of-plane (HOOP) mode, the difference between ϕ_{13H} and ϕ_{13} torsions in bR or between ϕ_{11H} and ϕ_{11} torsions in methanol, oscillates around zero in S_1 (Figure S10, Supporting Information), indicating a small pyramidalization at these carbons. Pyramidalization, however, becomes important in some crossing regions, especially in bR.[6c] Just after the $S_1 \rightarrow S_0$ transition, ϕ_{13H} and ϕ_{11H} torsions generally move most rapidly (Figure S11, Supporting Information), due to the light-mass hydrogen atom. Interestingly, the larger and faster ϕ_{13H} torsional change can control the stereochemistry of the photoproduct.[6h,k] In comparison, a large-amplitude oscillation of the HOOP mode was found in the whole photoisomerization of highly twisted RPSB in bathoRh.[6h] The faster dynamics of torsions with hydrogen atom(s) was also observed in Dronpa and rhodopsin (Rh)[6h,12] and may operate in other photoisomerization systems.

Photoisomerization of RPSB generally follows a two-state, two-mode mechanism (Figure 4). However, an A_g-like (S_2) state occasionally mixes with the B_u-like S_1 state just after photoexcitation,[13] where ΔE_{S2-S1}(MS-CASPT2:MM-EE) is small (∼1−8 kcal/mol), due to electrostatic and polarization interaction of the QM part with the protein and solvent (Figure S12, Supporting Information). This has been found in a few trajectories in bR and methanol. Before reaching the $S_1 \rightarrow S_0$ crossing, ΔE_{S2-S1} oscillates around ∼20 kcal/mol, and the oscillation strength for $S_1 \rightarrow S_2$ is non-negligible. This is consistent with the

Scheme 2. Schematic Hydrogen Bonds (HB) of the Twisted Structures for bR, Retinal (In Methanol), GFP, and PYP Chromophores

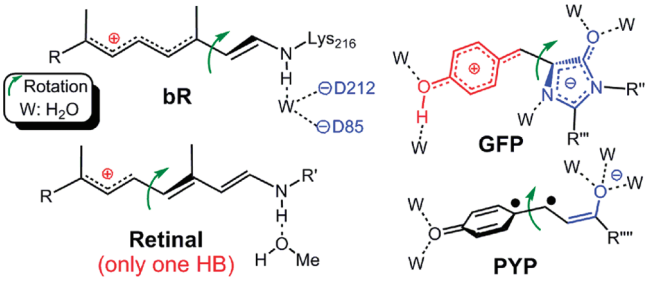

recently observed near-IR absorption.[5b] At the $S_1 \rightarrow S_0$ crossings in bR, large electrostatic and polarization interactions with the protein, mainly from Asp85 and Asp212,[14] can help reduce the energy gap by ~16 kcal/mol; this interaction is much smaller (~2−3 kcal/mol) in methanol.

Hydrogen bonding between the NH of RPSB and its nearby water molecule w402 in bR is weakened in the $S_1 \rightarrow S_0$ crossing region and is furthermore reduced during the *trans-cis* isomerization in S_0 (Figures 2a and S13, Supporting Information), due to translocation of the positive charge of RPSB and w402 being tightly held by Asp85 and Asp212. Notably, such a weaker hydrogen bond partly contributes to energy storage.[6d] However, in methanol solution, hydrogen bonding between RPSB and the nearby methanol molecule is not necessarily weakened during the *trans−cis* photoisomerization. In some trajectories, when the methanol molecule loses the hydrogen bond with RPSB, another (or two) nearby methanol molecule(s) can come and form new hydrogen bond(s) with RPSB (Figure S14, Supporting Information). Interestingly, multiple hydrogen bonds were suggested to promote the decay of GFP and PYP chromophores in water by preferentially stabilizing S_1 at the crossings (Scheme 2).[12,15] The weaker solvent effect at the crossings for RPSB in methanol is partly attributed to the existence of only one hydrogen bond with RPSB (Scheme 2).

In summary, our simulation has shown that the bR protein matrix is essential for catalyzing bond-specific, unidirectional, and efficient photoisomerization of RPSB. The protein environments specifically hold the chromophore tight for the controlled reaction. Bond specificity, unidirectionality, and efficiency are all lost for RPSB in methanol or for the twisted bare RPSB. The two-state, two-mode mechanism generally operates in bR and methanol, but an A_g-like state can occasionally mix with the B_u-like state in S_1 just after photoexcitation. Transition from S_1 to close-lying S_2 may account for the recently observed near-IR absorption in solution.[5b] The crankshaft motion is the dominant pathway that leads to internal conversion and isomerization ($S_1 \rightarrow S_0$). The hydrogen bond between RPSB and the nearby water molecule is weakened during the photoisomerization process in bR, but it is not necessarily weakened in methanol. Furthermore, at the crossings, there are strong electrostatic and polarization interactions on RPSB by the protein, but this is much smaller in methanol. These features tailored for bR are vital to efficiently converting the solar energy to drive proton transfer and protein conformational changes.

■ ASSOCIATED CONTENT

Supporting Information. Computational details, Figures S1−S15, Tables S1−S3, and Movies S1−S2. This material is available free of charge via the Internet at http://pubs.acs.org.

■ AUTHOR INFORMATION

Corresponding Author

*E-mail: morokuma@fukui.kyoto-u.ac.jp; chung@fukui.kyoto-u.ac.jp.

■ ACKNOWLEDGMENT

L.W.C. acknowledges FIFC Fellowship. This work is in part supported by Japan Science and Technology Agency with a Core Research for Evolutional Science and Technology grant in the Area of High Performance Computing for Multiscale and Multiphysics. Calculations in part at Research Center of Computer Science (Institute for Molecular Science) and Academic Center for Computing and Media Studies (Kyoto University) are also acknowledged.

■ REFERENCES

(1) Oesterhelt, D.; Stoechenius, W. *Nat. New Biol.* **1971**, *233*, 149–152.

(2) (a) Govindjee, R.; Balashov, S. P.; Ebrey, T. G. *Biophys. J.* **1990**, *58*, 597–608. (b) Tittor, J.; Oesterhelt, D. *FEBS Lett.* **1990**, *263*, 269–273.

(3) (a) Mathies, R. A.; Cruz, C. H. B.; Pollard, W. T.; Shank, C. V. *Science* **1988**, *240*, 777–779. (b) Gai, F.; Hasson, K. C.; McDonald, J. C.; Anfinrud, P. A. *Science* **1998**, *279*, 1886–1891. (c) Kobayashi, T.; Saito, T.; Ohtani, H. *Nature* **2001**, *414*, 531–534. (d) Herbst, J.; Heyne, K.; Diller, R. *Science* **2002**, *297*, 822–825. (e) Schenkl, S.; van Mourik, F.; van der Zwan, G.; Haacke, S.; Chergui, M. *Science* **2005**, *309*, 917–921. (f) Shim, S.; Dasgupta, J.; Mathies, R. A. *J. Am. Chem. Soc.* **2009**, *131*, 7592–7597.

(4) Koyama, Y.; Kubo, K.; Komori, M.; Yasuda, H.; Mukai, Y. *Photochem. Photobiol.* **1991**, *54*, 433–443.

(5) (a) Logunov, S. L.; Song, L.; El-Sayed, M. *J. Phys. Chem.* **1996**, *100*, 18586–18591. (b) Loevsky, B.; Wand, A.; Bismuth, O.; Friedman, N.; Sheves, M.; Ruhman, S. *J. Am. Chem. Soc.* **2011**, *133*, 1626–1629.

(6) (a) Humphrey, W.; Lu, H.; Logunov, I.; Werner, H. J.; Schulten, K. *Biophys. J.* **1998**, *75*, 1689–1699. (b) Tajkhorshid, E.; Baudry, J.; Schulten, K.; Suhai, S. *Biophys. J.* **2000**, *78*, 683–693. (c) Hayashi, S.; Tajkhorshid, E.; Schulten, K. *Biophys. J.* **2003**, *85*, 1440–1449. (d) Hayashi, S.; Tajkhorshid, E.; Kandori, H.; Schulten, K. *J. Am. Chem. Soc.* **2004**, *126*, 10516–10517. (e) Altoè, P.; Cembran, A.; Olivucci, M.; Garavelli, M. *Proc. Natl. Acad. Sci. U.S.A.* **2010**, *107*, 20172–20177. (f) Szymczak, J. J.; Barbatti, M.; Lischka, H. *J. Phys. Chem. A* **2009**, *113*, 11907–11918. (g) Phatak, P.; Ghosh, N.; Yu, H.; Cui, Q.; Elstner, M. *Proc. Natl. Acad. Sci. U.S.A.* **2008**, *105*, 19672–19677. (h) Schapiro, I.; Ryazantsev, M. N.; Frutos, L. M.; Ferré, N.; Lindh, N.; Olivucci, M. *J. Am. Chem. Soc.* **2011**, *133*, 3354–3364. (i) Warshel, A. *Nature* **1976**, *260*, 679–683. (j) Warshel, A.; Chu, Z. T. *J. Phys. Chem. B* **2001**, *105*, 9857–9871. (k) Polli, D.; Altoè, P.; Weingart, O.; Spillane, K. M.; Manzoni, C.; Brida, D.; Tomasello, G.; Orlandi, G.; Kukura, P.; Mathies, R. A.; Garavelli, M.; Cerullo, G. *Nature* **2010**, *467*, 440–443. (l) Weingart, O. *J. Am. Chem. Soc.* **2007**, *129*, 10618–10619. (m) Ishida, T.; Nanbu, S.; Nakamura, H. *J. Phys. Chem. A* **2009**, *113*, 4356–4366.(n) Hayashi, S.; Taikhorshid, E.; Schulten, K. *Biophys. J.* **2009**, *96*, 403−416 and references therein.

(7) (a) Detailed descriptions of the method and program citations are in the Supporting Information (SI). (b) Transition probability for NC and CS is >0.5 and assumed to be 1.0, respectively. See detailed definitions in the SI.

(8) Valsson, O.; Filippi, C. *J. Chem. Theory Comput.* **2010**, *6*, 1275–1292.

(9) Luecke, H.; Schobert, B.; Richter, H.-T.; Cartailler, J.-P.; Lanyi, J. K. *J. Mol. Biol.* **1999**, *291*, 899–911.

(10) (a) Spalink, J. D.; Reynolds, A. H.; Rentzepis, P. M.; Sperling, W.; Applebury, M. L. *Proc. Natl. Acad. Sci. U.S.A.* **1983**, *80*, 1887–1891. (b) Nakamichi, H.; Okada, T. *Angew. Chem., Int. Ed.* **2006**, *45*, 4270–4273.

(11) Torsional changes around terminal single bonds (e.g., C6−C7 and/or C8−C9) of vibrationally hot RPSB were large in S_0 in methanol, but they are suppressed by the protein.

(12) Li, X.; Chung, L. W.; Mizuno, H.; Miyawaki, A.; Morokuma, K. *J. Phys. Chem. Lett.* **2010**, *1*, 3328–3333.

(13) Three-state model: Hasson, K. C.; Gai, F.; Anfinrud, P. A. *Proc. Natl. Acad. Sci. U.S.A.* **1996**, *93*, 15124–15129 and refs 5b and 6a.

(14) Song, L.; El-Sayed, M. A.; Lanyi, J. K. *Science* **1993**, *261*, 891–894.

(15) (a) Boggio-Pasqua, M.; Robb, M. A.; Groenhof, G. *J. Am. Chem. Soc.* **2009**, *131*, 13580–13581.(b) Virshup, A. M.; Punwong, C.; Pogorelov, T. V.; Lindquist, B. A.; Ko, C.; Martínez, T. J. *J. Phys. Chem. B* **2009**, *113*, 3280−3291 and references therein.

JCTC Journal of Chemical Theory and Computation

ARTICLE

pubs.acs.org/JCTC

Efficient Sampling of a Dual-Resolution Ensemble by Means of Dragging

Elias Alphonsus Jozef Franciscus Peters* and Gijsbertus de With

Laboratory of Materials and Interface Chemistry, Eindhoven University of Technology, P.O. Box 513, 5600 MB Eindhoven, The Netherlands

Supporting Information

ABSTRACT: A method to simulate a dual-resolution ensemble for molecular systems is introduced. The dual-resolution system is characterized by an atomistic Hamiltonian and coarse coordinates connected by linear springs to this atomistic system. A 'dragging' update scheme based on an idea of Neal (Neal, R. M. *Taking Bigger Metropolis Steps by Dragging Fast Variables*; Technical Report; University of Toronto: Toronto, Canada, October, 2004; http://arxiv.org/PS_cache/math/pdf/0502/0502099v1.pdf) is proposed. It is theoretically proven that the scheme correctly samples the dual ensemble. As a proof-of-principle we show that in an one-dimensional barrier crossing simulation, the relaxation speeds up by a factor 80. In an asymmetric two-dimensional barrier crossing problem, the speedup is a factor 20. The application to molecular simulations is discussed.

1. INTRODUCTION

In this paper we consider the sampling of an equilibrium distribution of a molecular system. Computational methods, such as Monte Carlo sampling or molecular dynamics, can be inefficient due to the roughness of the energy landscape. A system might get stuck for a long time in a local energy minimum. A way to reduce the problem is to consider a coarse-grained description where many degrees of freedom are replaced by a single one.

An example of coarse graining is the use of united atoms instead of a fully atomistic description.[2] More progressive coarse grainings, i.e., beyond the united atom model, are also commonly applied nowadays (see, e.g., Marrink et al., ref 3). In the coarse-grained simulation the energy landscape will be much smoother as compared to the fine-grained one, and thus barriers can be more easily crossed. Besides this, there are less degrees of freedom to be simulated. All-in-all the process of equilibration in such a model will be much faster.

Accurate coarse-grained descriptions are hard to obtain. The results of a coarse-grain simulation will deviate from the underlying, fine grain, results. The loss of fine-grain information can be problematic if one is interested in the details. A strategy to overcome these drawback is to reintroduce fine-grain information into the coarse model. This reintroduction in turn induces its own set of problems. The problems are of two kinds, namely, efficiency and accuracy. One wants to spend as little as possible computational resources on the reintroduction. Ideally the state after the fine-graining procedure, i.e., the reintroduction, should be an equilibrium state. If the state is far from equilibrium, then computation time is spent on equilibrating the fine-grained system.

Reintroduction of the fine-grained information in molecular simulations is being actively researched.[4] Here we will highlight a recently proposed class of methods closely related to our method in what it aims to achieve. The first such method was named dual-resolution replica exchange.[5] Somewhat later a more efficient method called resolution exchange (ResEx) was proposed.[6] At present, the term 'ResEx' is used for a family of similar methods.[7]

ResEx methods consider an extended ensemble. In the dual case there are two subsystems, namely, the coarse-grain system characterized by an approximate coarse-grained Hamiltonian and the fine-grain atomistic model. The extended system exists of both the coarse- and fine-grain systems combined. The equilibrium distribution of the combined system is the product of the distributions of the coarse- and fine-grain systems. This means the different levels of description are considered as statistically independent.

The general idea of exchange simulations is to exchange values for variables between the subsystems in such a way that the equilibrium distribution of the extended system remains invariant. A well-known example of such a method is parallel tempering[8] in which the different subensembles have different temperatures and the positions of the particles are exchanged between the subsystems in equilibrium at different temperatures. For this approach Monte Carlo moves are accepted using a Metropolis rule.

In the case of ResEx the fine-grain coordinates are decomposed into coarse coordinates and high-resolution ones. The Monte Carlo move consists of exchanging the coarse part of the coordinates in the fine-grain system with the coordinates in the coarse-grained system. The method has some obvious difficulties associated with it.

Coarse coordinates are straightforward to define, e.g., as center-of-mass position of groups of atoms, while the high-resolution (fine-grain) coordinates relative to a center-of-mass are difficult to parametrize. The difficulty lies in defining them in such a way that, after exchange of the coarse-grained coordinates, the reconstructed fine-grain conformation is still a likely equilibrium conformation.

For the dual-resolution method[5] improvements of the reintroduction of fine-grain information can be found in Liu and Voth[9]

Received: February 2, 2011
Published: July 28, 2011

and Liu et al.[7] When the high-resolution coordinates are not relaxed, the conformation formed by an exchange will be far from equilibrium and will have a prohibitively low acceptance probability. A strategy to increase acceptance rates in ResEx is a construction of a ladder of intermediate systems.[10] Each subsystem is only a partial coarse graining of the level below. This means that the extended system is much expanded.

Motivated by the difficulties of exchanging the high-resolution degrees of freedom in ResEx, we propose an alternative approach. We will also make use of an extended ensemble. The fine-grain system is again determined by the atom positions. The coarse-grain beads are connected by means of linear springs to the atoms. This means that the total Hamiltonian of the extended system is the atomistic Hamiltonian, containing fine-grain variables only, plus a linear spring contribution coupling the fine-grain variables to the coarse-grain ones. Different from exchange ensembles, the systems are not statistically independent. However, after integration over the coarse-grain variables, the atomistic equilibrium distribution is recovered.

Instead of an exchange mechanism we will adopt a dragging scheme as proposed by Neal.[1] We will let the coarse-grained system evolve according to an approximate coarse-grain Hamiltonian. The fine-grain system is initially connected by linear springs to the old positions of the coarse system. Next, a set of springs is also connected to the new coarse coordinates. Initially these springs are of strength zero. The springs connecting the system to the old positions will be loosened, and the springs connecting it to the new positions tightened. The springs combined with the atomistic Hamiltonian drive the dynamics. Having created a new fine-grain configuration, we will accept it or not. Using the recipe of Neal this acceptance probability can be chosen such that detailed balance is obeyed, and the correct ensemble is sampled.

The paper is organized as follows. First our dual-resolution ensemble is introduced. Next, we provide the recipe for the dragging scheme and the proof it obeys detailed balance conditions. As a proof-of-principle, we will provide simulations on a simple one- and two-dimensional system. We will finalize with a discussion and an outlook on application to molecular simulations.

2. THEORY AND METHOD

The goal is to efficiently sample a canonical ensemble associated with a fine-grain, molecular system. This density associated with the fine-grain canonical ensemble is given by

$$\rho(\Gamma) = \frac{f(\Gamma)}{Z}, \text{ where}$$
$$f(\Gamma) = \exp[-\beta H(\Gamma)] \text{ and } Z = \int f(\Gamma)\mathrm{d}\Gamma \tag{1}$$

with the conventional $\beta = 1/kT$.

We will consider two levels of description, namely, a fine grain one indicated by Γ and a coarse-grain one indicated by X. In a typical molecular simulation Γ indicates positions of all atoms and possibly their momenta. A coarse graining consists of associating a lower dimensional state X to every Γ via a function $X(\Gamma)$. If the coarse graining consists of grouping atoms into effective particles, then X indicates, for example, the center-of-mass of these groups (and possibly the center-of-mass momenta).

A coarse-grained distribution is defined as

$$\rho_{\mathrm{cg}}(X) = \frac{f_{\mathrm{cg}}(X)}{Z}, \text{ where}$$
$$= \int \delta[X(\Gamma) - X] \exp[-\beta H(\Gamma)]\mathrm{d}\Gamma$$
$$f_{\mathrm{cg}}(X) \equiv \exp[-\beta H_{\mathrm{cg}}(X)] \tag{2}$$

This gives an expression for the effective coarse-grained Hamiltonian H_{cg}. If $H_{\mathrm{cg}}(X)$ is known, all kinds of thermodynamic quantities can be computed using this coarse-grained Hamiltonian, since the Helmholtz free energy is given by

$$\exp\left[-\frac{F}{kT}\right] = Z = \int f_{\mathrm{cg}}(X)\mathrm{d}X$$
$$= \int \exp[-\beta H_{\mathrm{cg}}(X)]\mathrm{d}X \tag{3}$$

One of the methods of computing the quantities is by using coarse-grain simulations where the Hamiltonian H_{cg} provides the forces or the Monte Carlo weights.

Usually the microscopic Hamiltonian $H(\Gamma)$ is a relatively simple expression, e.g., kinetic energy plus a sum of pair potentials. The nature of $H_{\mathrm{cg}}(X)$ is much more complicated. Therefore an analytic expression for H_{cg} is usually not available. In most coarse-graining procedures that are used in practice, an approximate Hamiltonian $H_{\mathrm{approx,cg}}$ is constructed that is close to H_{cg} but easier to handle. A common approach is to take $H_{\mathrm{approx,cg}}$ to consist of a kinetic energy and a pair potential part. A popular way to construct this pair potential is the inverse Boltzmann method,[11] but other approaches are also possible.[12]

The introduction of an approximate coarse-grained Hamiltonian gives rise to deviations. Furthermore one might be interested in quantities that depend on the fine-grain information. Therefore one would like to have the fine-grain system available, next to the coarse one. For this purpose we propose to sample a dual-resolution ensemble:

$$\rho_{\mathrm{dual}}(\Gamma, X) = \frac{\sqrt{(\beta/2\pi)^d \det K_0}}{Z} f_{\mathrm{dual}}(\Gamma, X), \text{ where}$$
$$f_{\mathrm{dual}}(\Gamma, X) = \exp\left[-\beta\left(H(\Gamma) + \frac{1}{2}(X - X(\Gamma))^T \cdot K_0 \cdot (X - X(\Gamma))\right)\right] \tag{4}$$

with Z the partition sum as defined in eq 1. The coarse degrees of freedom X are connected to $X(\Gamma)$ by means of linear springs with spring constants K_0. Note that integration over X gives the fine-grain canonical distribution:

$$\rho(\Gamma) = \int \rho_{\mathrm{dual}}(\Gamma, X)\mathrm{d}X \tag{5}$$

Integration of the dual distribution over the fine-grained coordinates gives

$$\rho_{\mathrm{cg}}^{(K_0)}(X) = \int \rho_{\mathrm{dual}}(\Gamma, X)\mathrm{d}\Gamma$$
$$= \sqrt{(\beta/2\pi)^d \det K_0} \int \rho_{\mathrm{cg}}(Y) \exp\left[-\frac{1}{2}\beta(X - Y)^T \cdot K_0 \cdot (X - Y)\right]\mathrm{d}Y \tag{6}$$

The distribution is a convolution of the coarse-grained distribution ρ_{cg}, given by eq 2, with a Gaussian with variance (matrix) $(\beta K_0)^{-1}$. An effective Hamiltonian can now be defined by

$$\exp[-\beta H_{cg}^{(K_0)}(X)] = \sqrt{(\beta/2\pi)^d \det K_0} \int \exp\left[-\beta\left(H_{cg}(Y) + \frac{1}{2}(X-Y)^T \cdot K_0 \cdot (X-Y)\right)\right] dY \quad (7)$$

For infinitely stiff springs, i.e., $K_0 \to \infty$, $\rho_{cg}^{(\infty)} = \rho_{cg}$ and $H_{cg}^{(\infty)} = H_{cg}$.

The procedure we propose to sample the dual-resolution ensemble is to use an approximate model to generate new coarse-grain variables X^* from the old ones X. Next, the fine-grain variables are dragged from an initial state Γ to a final state Γ^*. This is established by connecting the fine-grain state by means of springs to both X and X^* and changing the spring constants gradually. The configuration is dragged from X to X^* by loosening the springs connecting the fine-grain coordinates to X and tightening those connected to X^*. Finally the new dual-resolution state (Γ^*, X^*) is accepted or not. The acceptance rule should be such that the density described by eq 4 is sampled. The idea of *dragging* the fine-grained structure is borrowed from Neal.[1] The new elements in our approach are the addition of the extra variables X and the linear springs. A cartoon of this procedure is depicted in Figure 1.

In our computational method first X^* is generated from the previous position X. The new X^* is sampled by means of the conditional probability distribution $w(X^*|X)$. The equilibrium X needs to sample the Boltzmann distribution corresponding to the approximate coarse-grain Hamiltonian $H_{approx,cg}$:

$$\rho_{approx,cg}(X) = \frac{f_{approx,cg}(X)}{Z_{approx,cg}}, \text{ where}$$
$$f_{approx,cg}(X) = \exp[-\beta H_{approx,cg}(X)] \quad (8)$$

Therefore the detailed balance condition for $w(X^*|X)$ becomes

$$w(X^*|X)\rho_{approx,cg}(X) = w(X|X^*)\rho_{approx,cg}(X^*) \quad (9)$$

We will assume that X is generated using some Markovian simulation method [a Monte Carlo (MC) method, molecular dynamics (MD), or Brownian dyamics (BD)] that obeys this relation.

Having generated the final X^* we can start dragging the fine-grain model from X to X^*. During the dragging, the microscopic system evolves according to the Hamiltonian:

$$H_{drag}(\Gamma,\lambda) = H(\Gamma) + \frac{1}{2}K(\lambda) : (X(\Gamma) - X)^2 + \frac{1}{2}K^*(\lambda) : (X(\Gamma) - X^*)^2 \quad (10)$$

where the parameter λ is used to parametrize the magnitude of the spring constants. It is changed from 0 to 1 during the dragging procedure. We will take

$$K(0) = K_0, \quad K(1) = 0, \quad \text{and} \quad K^*(\lambda) = K(1-\lambda) \quad (11)$$

This means that for $\lambda = 0$, the fine-grain state is coupled by means of linear springs to the initial coarse-grain state X, while for $\lambda = 1$ the fine-grain state is coupled to the final coarse-grain state X^* and not connected to X anymore. The relation between K^* and K is such that the scheme can easily made to obey detailed balance.

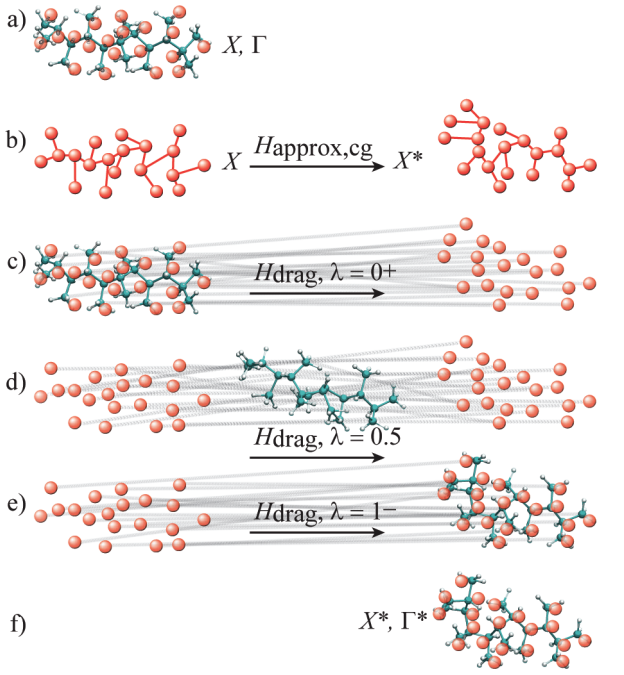

Figure 1. A cartoon of the dragging scheme. The fine-grain state Γ is depicted as a molecule. The coarse-grain state X is depicted as the larger (red) beads. These beads are connected by means of linear springs to the center-of-masses of groups of atoms (in this case carbon with its hydrogens). (a) The initial dual-resolution state consists of the atomistic model and the coarse beads connected to it. (b) The first step in the updating scheme is to move X to the new state X^* by using some approximate Hamiltonian. (c) Next the atomistic model is connected to both the old state X and the new state X^*. Each center-of-mass is connected to one bead in the old coarse-grain state X and one bead in the new coarse-grain state X^*. The magnitude of the spring constants is parametrized by a variable λ. Initially, for λ near to zero, the springs connecting the molecule to X are much stronger than the springs connected it to X^*. (d) Gradually λ is increased from 0 to 1. Simultaneously the molecule performs its natural dynamics. It is influenced by intra- and intermolecular forces as well as by the spring forces. Because the springs connected to X loosen and those connected to X^* become stiffer, the molecule will move toward X^*. (e) For λ near to 1 the molecule will be close to X^*. (f) The final dual-state is characterized by Γ^* and X^* and should be accepted or rejected according to the appropriate Metropolis rule.

At intermediate states where $\lambda \neq 0,1$, we define

$$\rho(\Gamma|X^*,X,\lambda) = c(X^*,X,\lambda) f(\Gamma,X^*,X,\lambda) \text{ with}$$
$$f(\Gamma,X^*,X,\lambda) = \exp[-\beta H_{drag}(\Gamma,\lambda)] \quad (12)$$

where $c(X^*,X,\lambda)$ is the normalization constant. This is the equilibrium distribution for the microscopic state Γ, for the case that the system would evolve according to the Hamiltonian with the value of λ fixed. In the scheme, however, the value of λ is changed from 0 to 1. Depending on the rate that λ changes, the distribution of Γ is close to $\rho(\Gamma|X^*,X,\lambda)$ or not. The fact that during the dragging the intermediate states are not in local equilibrium does not influence the validity of the scheme as will be discussed below.

The variable λ is changed in discrete steps $i = 1, ..., n$ from 0 to 1,

$$\lambda_i = i/(n + 1) \tag{13}$$

The microstate Γ_i is generated from the previous one at $i - 1$ by the transition probability $T(\Gamma_i|\Gamma_{i-1},X^*,X,\lambda_i)$. Here $\Gamma_0 = \Gamma$, and $\Gamma^* = \Gamma_n$. For each λ we take care that the conditional transition probability $T(\Gamma'|,X^*,X,\lambda)$, to go from state Γ to state Γ', obeys the detailed balance condition:

$$\begin{aligned} &T(\Gamma'|\Gamma, X^*, X, \lambda)\rho(\Gamma|X^*, X, \lambda) \\ &\quad = T(\Gamma|\Gamma', X^*, X, \lambda)\rho(\Gamma'|X^*, X, \lambda) \end{aligned} \tag{14}$$

This means that the transition probabilities can be generated using conventional simulation techniques, such as MC, MD, or BD using the Hamiltonian eq 10 with the appropriate value of λ for each step.

Finally, the path from initial state $(\Gamma_0 = \Gamma,X)$ to final state $(\Gamma^* = \Gamma_n,X^*)$ is accepted with a probability: $\mathrm{acc}(\Gamma_n, ..., \Gamma_1,X^*|\Gamma_0, X)$. The total probability density of this process becomes

$$\begin{aligned} &\rho(\Gamma_n, ..., \Gamma_0, X^*, X) \\ &\quad = \mathrm{acc}(\Gamma_n, \ldots, \Gamma_1, X^*|\Gamma_0, X) \\ &\quad \times w(X^*|X) \prod_{i=1}^{n} T(\Gamma_i|\Gamma_{i-1}, X^*, X, \lambda_i)\rho_{\mathrm{dual}}(\Gamma_0, X) \end{aligned} \tag{15}$$

By requiring that a detailed balance condition for the acceptance of the path is obeyed, we find that

$$\begin{aligned} &\frac{\mathrm{acc}(\Gamma_n, ..., \Gamma_1, X^*|\Gamma_0, X)}{\mathrm{acc}(\Gamma_0, ..., \Gamma_{n-1}, X|\Gamma_n, X^*)} \\ &\quad = \frac{w(X|X^*)}{w(X^*|X)} \prod_{i=1}^{n} \frac{T(\Gamma_{i-1}|\Gamma_i, X^*, X, \lambda_i)}{T(\Gamma_i|\Gamma_{i-1}, X^*, X, \lambda_i)} \frac{\rho_{\mathrm{dual}}(\Gamma_n, X^*)}{\rho_{\mathrm{dual}}(\Gamma_0, X)} \end{aligned} \tag{16}$$

Inserting the detailed balance conditions for the individual transition probabilities, eqs 14 and 9, results in

$$\begin{aligned} &\frac{\mathrm{acc}(\Gamma_n, ..., \Gamma_1, X^*|\Gamma_0, X)}{\mathrm{acc}(\Gamma_0, ..., \Gamma_{n-1}, X|\Gamma_n, X^*)} \\ &\quad = \frac{\rho_{\mathrm{approx,\,cg}}(X)}{\rho_{\mathrm{approx,\,cg}}(X^*)} \prod_{i=1}^{n} \frac{\rho(\Gamma_{i-1}|X^*, X, \lambda_i)}{\rho(\Gamma_i|X^*, X, \lambda_i)} \frac{\rho_{\mathrm{dual}}(\Gamma_n, X^*)}{\rho_{\mathrm{dual}}(\Gamma_0, X)} \\ &\quad = \frac{f_{\mathrm{approx,\,cg}}(X)}{f_{\mathrm{approx,\,cg}}(X^*)} \prod_{i=0}^{n} \frac{f(\Gamma_i, X^*, X, \lambda_{i+1})}{f(\Gamma_i, X^*, X, \lambda_i)} \\ &\quad = \exp\Big[\beta\{H_{\mathrm{approx,\,cg}}(X^*) - H_{\mathrm{approx,\,cg}}(X) \\ &\quad - \frac{1}{2}\sum_{i=0}^{n}((K(\lambda_{i+1}) - K(\lambda_i)) : (X(\Gamma_i) - X)^2 \\ &\quad + (K^*(\lambda_{i+1}) - K^*(\lambda_i)) : (X(\Gamma_i) - X^*)^2)\}\Big] \end{aligned} \tag{17}$$

This ratio of acceptance probabilities is used in a Metropolis rule by choosing the acceptance probability of the generated path as

$$\begin{aligned} &\mathrm{acc}(\Gamma_n, ..., \Gamma_1, X^*|\Gamma_0, X) \\ &\quad \equiv \min\left(1, \frac{\mathrm{acc}(\Gamma_n, ..., \Gamma_1, X^*|\Gamma_0, X)}{\mathrm{acc}(\Gamma_0, ..., \Gamma_{n-1}, X|\Gamma_n, X^*)}\right) \end{aligned} \tag{18}$$

This might seem a circular definition, but it is not. Clearly if one computes the ratio of these acceptance probabilities for the two paths, it will equal the ratio in the right-hand side, so the definition is consistent. It is, however, a further specification of the acceptance probability which is now, by construction, guaranteed to lie between 0 and 1. For the ratio appearing at the right-hand side, eq 17 needs to be substituted thus giving a closed definition for computing the acceptance probability.

The final result of the scheme is the generation of a path with probability density $\rho(\Gamma_n, ..., \Gamma_0,X^*,X)$, that gives rise the desired dual-resolution distribution for Γ^* and X^*, eq 4:

$$\rho_{\mathrm{dual}}(\Gamma^*, X^*) = \int \rho(\Gamma^*, ..., \Gamma_0, X^*, X)\mathrm{d}\Gamma_{n-1}, ..., \mathrm{d}\Gamma_0\mathrm{d}X \tag{19}$$

A derivation of the main result eq 16 is given in the Appendix A. The derivation is based on the work of Neal.[1]

It is probably worthwhile to point out some of the subtleties that might be overlooked otherwise. In the scheme, the index, i, on λ_i runs from 0 to $n + 1$ (including end points), while the index on Γ_i runs from 0 to n. If this were not the case, then the ratio of transition probabilities in eq 16 and the ratio of probability distributions in eq 17 normalization constants would not cancel. This means that for the transition Γ to Γ_1, the springs connecting Γ to X^* are already turned on by a small amount. Likewise for the last step Γ_{n-1} to Γ^*, the springs connecting Γ to X are still weakly turned on. These details are important for implementing the scheme, especially if n is not large.

In a dynamic simulation the time interval corresponding to a change of λ does not have to correspond to an integration time step of the equation of motion. One is allowed to divide a constant λ_i interval into more subintervals. Such a subdivision might be needed because the time step for integrating the equations of motion needs to be sufficiently small. When subdividing the constant λ intervals, some care has to be taken so that eq 35 remains valid.

Although eq 17 is expressed in terms of equilibrium distributions for Γ, this equilibrium does not have to be reached. The dragging is allowed to be performed out of equilibrium. The intermediate distributions in the expressions only arise because of eq 14. This gives a large flexibility to designing possible dragging schemes.

Equation 16 is a more generally valid expression than eq 17 since it can be used even if eq 14 is not valid. In many dynamical simulation methods, such as MD and BD, eq 14 is not exactly obeyed due to time discretization errors. In the BD simulation method the transition probabilities can often be exactly determined. In this case one can use eq 16 and prevent time discretization errors.

3. ANALYSIS OF METHOD AND SIMULATION RESULTS

In the previous section we gave a theoretical derivation of the dragging scheme. It remains to be proven that the scheme is useful in practice. We will consider some simple systems to provide a prove of principle. Besides this we want to develop an intuition for choosing the parameters of the scheme.

When the dragging has been performed, the newly generated state is accepted or rejected. For the scheme to be useful in practice, the acceptance probability should be reasonable. In Appendix B we consider the case of very slow dragging. If the number of subdivisions n is large enough and if also the approximate coarse-grain Hamiltonian $(H_{\mathrm{approx,cg}})$ is close to the real smoothed one $(H_{\mathrm{cg}}^{(K_0)})$, the acceptance ratio approaches 1.

The situation described in Appendix B is the optimal case. If the approximate Hamiltonian is not a good approximation or if the dragging is not slow, then the acceptance probabilities will

most likely drop. This is numerically investigated in the next two subsections. In both subsections a barrier crossing problem is considered. We think this is the archetypal situation where the dragging scheme can be useful. The barrier is so high that crossing it becomes a rare event when using conventional methods to simulate the dynamics.

The approximate Hamiltonian in the dragging scheme will be chosen such that the coarse-grain variable can relatively easily cross the barrier. By making the springs that connect the fine-grain variables to the coarse-grain ones stiff enough, the fine-grain variables can be pulled over the barrier. The hope is that parameters of the dragging scheme can be chosen in such a way that the acceptance probability is reasonable. If this is the case, then it means that barriers are crossed more easily. Since the barrier crossing is the rate-determining step, the system will equilibrate faster.

In both problems BD is used for generating the positions.[13,14] In BD only the particle positions are considered, not the momenta. The displacements of a particle have a fluctuating (stochastic) part that is characterized by the diffusion coefficient and a deterministic part that is driven by a potential U. Only the configurational part of the canonical distribution is relevant for BD. Therefore the potential U will play the same role as the Hamiltonian used in the general derivation of the previous section. This would also be the case for MC simulation. We choose BD, and not MC, because there is a natural time scale which makes it more straightforward to quantify the speedup of the dragging scheme.

3.1. The Double-Well Problem. The simplest barrier crossing problem is the one-dimensional double-well problem. We use the potential:

$$\beta U_h(x) = x^2(h\cdot(2x^2-3)x^2 - 2(1-x^2)^2) \qquad (20)$$

Here h is the barrier height expressed in units kT. The rationale for the functional form chosen is that the barrier height is exactly h, the wells are located at $x = -1$, a $x = 1$ irrespective of the barrier height and the curvature at the barrier is independent of h. In Figure 2 the potential is drawn for $h = 10$, which is the case studied. In the lower graph of the same figure we show the corresponding canonical equilibrium distribution. Also a simulation result obtained using the dragging scheme is shown.

In the one-dimensional case there is no real coarse-graining taking place. We do, however, introduce an approximate coarse-grain potential that has the same functional form as the fine-grain one, eq 20, but with a different barrier height. Values of $h = 1-4$ are considered. The reason is that now the coarse-grain position X will quite frequently cross its barrier. The starting and final coarse-grain positions, X and X^*, are connected to the fine-grain position, x, by means of two linear springs. The hope is that x will be dragged over the barrier and that the new configuration is accepted.

For the presented results both the units of length and time are taken to be 1. The energy scale is kT. The BD simulations of both x and X are performed with a diffusion coefficient of 1. The new position X^* is taken at a time $\Delta t = 5$ from the starting position X. The λ's are updated in $n = 100$ discrete steps during this time interval (see eq 13). The spring constants are varied linearly as $K(\lambda) = K_0\cdot(1-\lambda)$. The time step used to integrate the equations within the BD algorithm is a fraction of 0.05 such that discretization errors are negligible.

3.1.1. The Stuck Problem. In the upper graph of Figure 3, a typical time series of the dragging scheme is shown. A point is plotted once so many time steps. Initially the coarse-grain

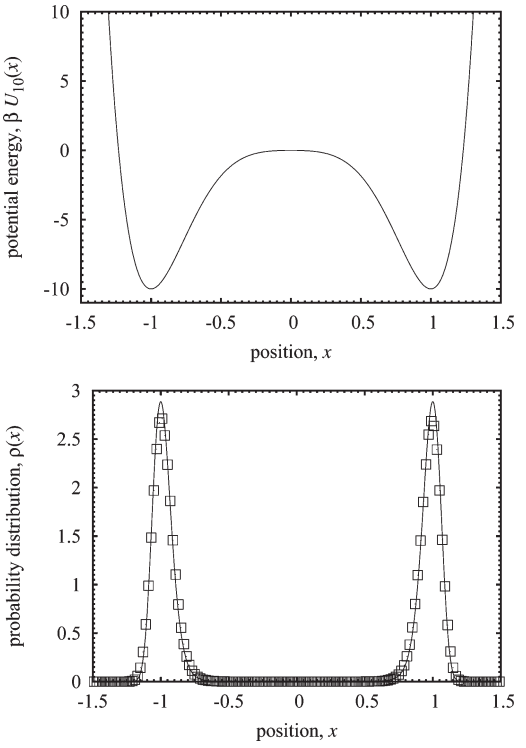

Figure 2. The upper graph shows the used double-well potential with a barrier height of $10kT$. The lower graph shows the corresponding canonical distribution. The symbols are the histogram found by means of the dragging scheme.

variable frequently hops from the $X = -1$ to the $X = 1$ position. The fine-grain variable x follows along. Quite often in the time series the positions X and x get stuck for a long time at a certain position. Such a position is typically far from the potential minimum. The simulation gets stuck because the acceptance ratio, eq 17, drops to nearly zero. The cause is the presence of the factor $\exp[\beta(H_{\text{approx,cg}}(X^*)]$ in the acceptance ratio. This factor is included to cancel the influence of the approximate coarse-grained dynamics on the final statistics.

In the Supporting Information a document is included in which this problem is analyzed. It turns out that the factor:

$$\exp[\beta(H_{\text{approx, cg}}(X^*) - H_{\text{cg}}(X^*))] \qquad (21)$$

determines the observed stuck behavior. If for large X^* this factor becomes very large, then this means that the approximate dynamics under samples this state compared to the real dynamics. To compensate for the fact that such a state is very rarely visited, the residence time, once the state is visited, should become very large. This means the simulation is stuck for a very long time. This gives rise to an ergodicity problem. The simulation time should be long compared to the time states are stuck. This time can be prohibitively long.

There is a simple remedy for this problem. An alternative way to sample the dual-resolution ensemble, eq 4, is to generate fine-grain states Γ (i.e., x for the system under consideration) and then connect the coarse-grain states X to it by means of drawing a Gaussian distributed displacement with a variance $(\beta K_0)^{-1}$. The sampling of Γ can straightforwardly be done by letting this state evolve according to its dynamics. If we apply this 'move' subsequent to a 'dragging move', then the coarse-grain position

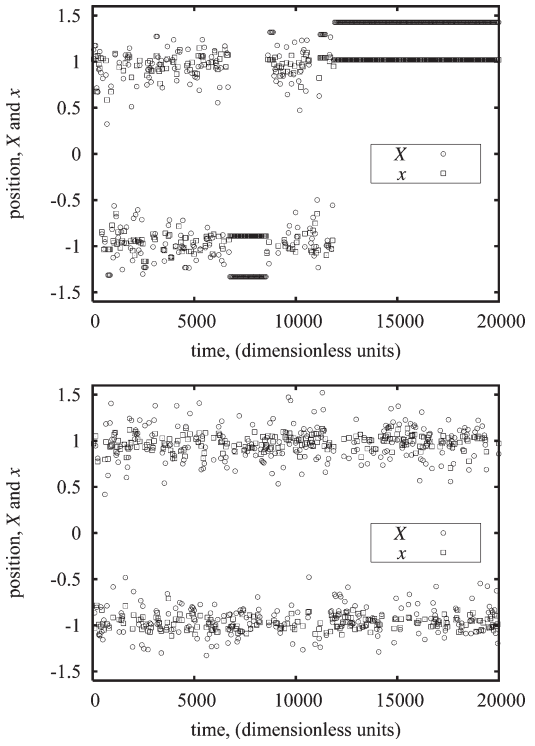

Figure 3. Time series of fine-grain positions x and coarse-grain positions X. The upper graph shows a time series generated by only using the dragging scheme. Configurations have the tendency to get stuck. In the lower graph, the dragging scheme and ordinary dynamics (with reconstruction of the coarse variables) are alternated. In this case configurations do not get stuck. The histogram in Figure 2 corresponds with this time series.

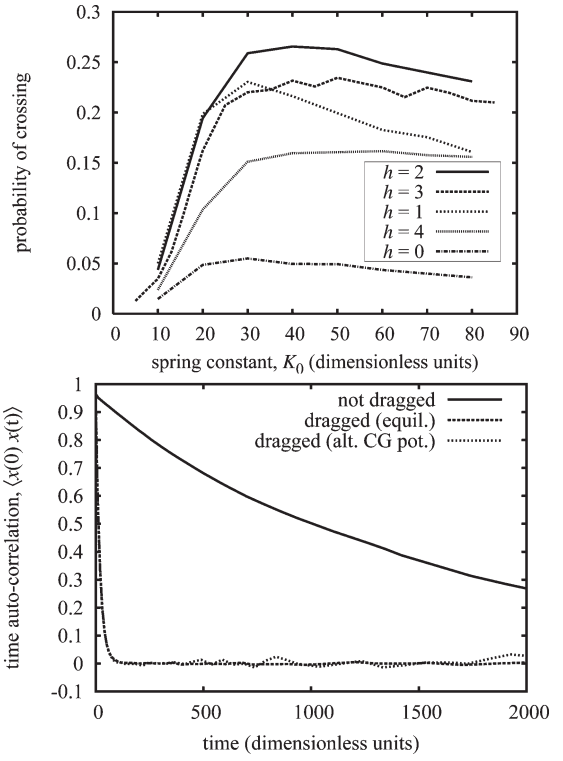

Figure 4. In the upper graph, crossing probabilities as a function of the spring constant K_0 are plotted. The crossing probability is the probability that the final positions, x, are at the other side of the $10kT$ barrier. The potentials used to generate coarse-grain position, i.e., eq 20, are labeled by their potential barrier height, h (in units kT). The lower graph shows the time autocorrelation of position, x. For the normal Brownian motion the decay is slow because a barrier of height $10kT$ needs to be crossed. For a dragged simulation, with well chosen parameters, the decay is much faster. Both the optimized potentials of functional forms eqs 20 and 22 give the same fast decay.

X will relax. Therefore the next application of the dragging scheme will not get stuck. The second graph in Figure 3 displays a time series generated by this method showing that configurations are no longer stuck, but both sides of the barrier are evenly sampled. The histogram shown in Figure 2 corresponds to this simulation.

In the example depicted in Figure 3 the approximate coarse-grained dynamics was generated with the potential eq 20 (with a low barrier). For large X, this potential diverges as $U_{\text{approx,cg}}(X) \propto X^6$. For the dual-resolution ensemble, eq 4, we expect that Γ is near one of the wells and that X is fluctuating in a Gaussian cloud around this position. Therefore we expect $U_{\text{cg}}(X) \propto X^2$. Clearly the factor given by eq 21 is very divergent in this case. This explains why the pure dragging simulation gets stuck. According to the reasoning this stuck problem can also be resolved by choosing $U_{\text{approx,cg}}(X)$ in such a way that eq 21 is well behaved. To test this, we also performed simulations with an approximate coarse-grained potential of the form:

$$\beta U_{\text{approx, cg}}(X) = -\ln\left(\exp\left[-\frac{\tilde{K}}{2}(X+1)^2\right] + \exp\left[-\frac{\tilde{K}}{2}(X-1)^2\right] + C\,\text{erfc}\left[\sqrt{\frac{\tilde{K}}{2}}(-X-1)\right]\text{erfc}\left[\sqrt{\frac{\tilde{K}}{2}}(X-1)\right]\right) \quad (22)$$

Here $\tilde{K}$ determines the curvature at the potential well. The error functions part can be used to lower the barrier by tuning the constant C. This potential increases as X^2 for large X. We indeed found that by using this potential for the approximate coarse-grained dynamics, the stuck problem does not occur (see below).

3.1.2. Tuning Parameters. One of the main parameters to be chosen when implementing the dragging scheme is the spring constant K_0. In the upper graph of Figure 4 the average probability of crossings is plotted as function of K_0. This is the probability that x and x^* lay on different sides of the barrier subsequent to a dragging move. The reason for considering this probability is that the barrier crossing is the rate-determining step for equilibration.

The acceptance probabilities will be such that the dual-resolution distribution, eq 4, is sampled. This means that if K_0 is large enough, then x lays almost always on the same side of the barrier as X. The probability that x crosses the barrier equals the probability that X crosses the barrier times the probability that x follows. This last probability is the acceptance probability, eq 18. In the case that X and the new position X^* are statistically independent, the probability that X crosses the barrier equals 0.5. Therefore 0.5 is an upper bound for the probability of crossing.

The acceptance probability can be of a reasonable magnitude only if K_0 is so large that x can be dragged over the barrier. This means that, approximately, $1/2 \cdot K_0 \cdot 1 > 10$, so

$$K_0 > 20 \quad (23)$$

We also expect that the dragging scheme works best if the potential that is used to sample X (i.e., eq 20 with, e.g., $h = 2$) resembles the smoothed coarse-grained potential of X, eq 6. In Appendix B we show that in the limit of slow dragging, the acceptance ratio approaches zero if the approximate Hamiltonian is close to the smoothed one. For the minimum of the local well, eq 20, we can approximate the region around a minimum by a harmonic potential. A spring constant $K_{well}(h) = 8\cdot(3h - 2)$ corresponds to this harmonic potential. The smoothed coarse-grain potential, $U_{cg}^{(K_0)}$, can be locally approximated by a harmonic potential with spring constant $K_{cg,well}^{(K_0)}$. This smoothed potential is obtained by coupling a spring to position x. The strength of the effective linear springs then follows as

$$\frac{1}{K_{cg,\,well}^{(K_0)}} = \frac{1}{K_{well}(10)} + \frac{1}{K_0} \tag{24}$$

By equating this spring constant to the one associated with the potential used to generate positions X, i.e., $K_{well}(h)$, an estimate for the optimal value of K_0 can be computed. For varying values of h we find: $h = 1 \rightarrow K_0 = 8.3$, $h = 2 \rightarrow K_0 = 37.3$, $h = 3 \rightarrow K_0 = 74.7$, and $h = 4 \rightarrow K_0 = 124.4$.

The probability for X crossing the barrier is larger if its barrier is lower. For low values of h, however, the optimal value of K_0 computed with eq 24 is too small to drag x over the barrier (see eq 23). Therefore the optimal value of h is expected to be a value that is just large enough such that the optimal K_0 can drag the fine-grain variable over the barrier.

In the lower graph of Figure 4, we find an optimal value of $K_0 \approx 40$ and a barrier of height of $2kT$ for the approximate dynamics of X using the potential eq 20. The probability for crossing is about $p_{cross} = 0.26$. The dragging of x from X to X^* is performed in a time $\Delta t = 50$. Slow dragging improves the acceptance probability. For very slow dragging, we find that the crossing probability increases to 0.31. For quicker dragging, $\Delta t = 10$, we have $p_{cross} = 0.17$, and $\Delta t = 5$ gives $p_{cross} = 0.11$.

The speedup in the computation due to the dragging scheme can be determined by comparing the CPU time needed for a conventional simulation and for a dragging simulation to approach equilibrium. In 'real' molecular simulations, the overhead due to the coarse-grain dynamics will be negligible. Also the extra spring forces will contribute little. Therefore the CPU time needed to equilibrate a system will be proportional to the simulated physical time of the fine-grain dynamics.

For determining the speedup in the equilibration due to dragging, we compare the time autocorrelation of the position x. The time plotted on the x-axis of the lower graph in Figure 4 is the physical time of the fine-grain dynamics. Time runs on irrespective of whether moves are accepted or not. The time autocorrelation of the normal BD is governed by the barrier crossing. Because the barrier height is $10kT$, this is a highly activated process. For the normal dynamics, we find a decay rate of 6.4×10^{-4}, while for the dragged simulation, with dragging time $\Delta t = 5$, the decay rate is 5.2×10^{-2}, so the speedup factor is 81. Note that the decay rate is expected to be proportional to $p_{cross}/\Delta t$. Since p_{cross} decreases with decreasing Δt, there is an optimal value for Δt. We found this value to be around $\Delta t = 5$.

When using eq 22 we see the same fast decaying behavior when we use $K_0 = 40$, $\tilde{K} = 20$, and $C = 0.04$ (potential barrier of about $1.9kT$). This shows that the behavior is quite robust. It does not seem to depend much on the details of the coarse-grained potential (except for the occurrence of the stuck problem). When independently varying K_0 between 25 and 60, $\tilde{K}$ between 10 and 50, and C between 0.01 and 0.25, we found essentially the same fast decaying behavior as depicted in Figure 4. The spring strength K_0 could be increased up to 120 if we simultaneously adapted $\tilde{K}$ such that eq 24 was obeyed. For parameters that deviated more, a noticeable deviation from the fastest possible decay was observed but still the dynamics was much faster than the nondragged case.

3.2. A Two-dimensional Case. In this section we will provide a proof-of-principle for a simple two-dimensional case. We will use the example also used in refs of Lyman and Zuckerman[10] and Liu and Voth[9] for proofs-of-principle. Compared to the one-dimensional example above, there are some additional features: In this case there will be a genuine coarse graining, namely, from two- to one-dimensional. This two-dimensional example has an asymmetric fine-grain potential and a symmetric approximate coarse-grain potential $U_{approx,cg}$.

The system considered is the canonical equilibrium corresponding to the potential energy:

$$\beta U(x,y) = 10(x^2 - 1)^2 + \frac{y^2}{1 + 250(\tanh(10x) + 1)} \tag{25}$$

In this potential there are two local minima, namely at $(x,y) = (-1,0)$ and $(x,y) = (1,0)$. At $(x,y) = (0,0)$ there is a saddle point. The height of the potential barrier to go from one minimum to the other one is $10kT$. Due to the presence of the 'tanh', the basin centered around $(1,0)$ is much more extended in the y-direction than the one centered around $(-1,0)$. The combination $\Gamma = (x,y)$ signifies the fine-grain state. The coarse graining is simply defined by $X(\Gamma) = x$. The coarse-grained potential, using eq 2, becomes

$$\beta U_{cg}(X) = 10(X^2 - 1)^2 - \frac{1}{2}\ln(1 + 250(\tanh(10X) + 1)) - \frac{1}{2}\ln \pi \tag{26}$$

To generate the dynamics for X, we use the same potential as in ref of Liu and Voth,[9] namely,

$$\beta U_{approx,\,cg}(X) = (X^2 - 1)^2 \tag{27}$$

This approximate potential does have a barrier that is much lower than the (smoothed) coarse-grained potential barrier and is therefore much easier crossed. Graphs of the canonical probability densities corresponding to the smoothed version of U_{cg} (with $K_0 = 10kT$) and eq 27 are shown in Figure 6.

As a method of simulation, BD is used with diffusion coefficients $D = 1$ for both the coarse- and fine-grain dynamics. The time interval from X to X^* is $\Delta t = 2$. The same time interval is used for the fine-grain dynamics.

For the spring constants we use

$$\beta K(\lambda) = 10(1 - \lambda) + 60\lambda(1 - \lambda) \tag{28}$$

The equilibrium distribution of X is governed by $K_0 = K(0) = 10kT$. This value of K_0 broadens the canonical distribution corresponding to the 'real' coarse-grained potential U_{cg}, eq 26, such that its peaks have widths comparable to the distribution associated with eq 27. Application of eq 24 gives a value of $K_0 = 8.9kT$. The value of $K_0 = 10kT$ is too small to drag the fine-grain position over the barrier. By adding the quadratic part we find that halfway $K(1/2) = 20kT$, which is strong enough. By means of

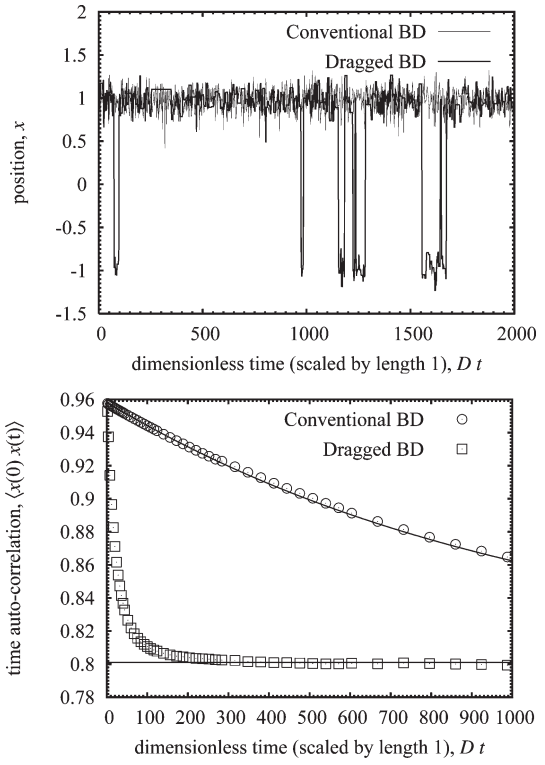

Figure 5. The upper graph shows a time series of the x-coordinate of a particle in the two-dimensional two-well problem. For conventional BD (thin line), the particle fluctuates around $x = 1$. For the dragging scheme (bold line), acceptance is lower, and the graph is sometimes flat. The dragging BD enhances barrier crossings, i.e., jumps to $x = -1$. The lower graph gives the autotime correlation for the time series. The simulation results of the dragging scheme relax much quicker to the long time limit value of 0.801.

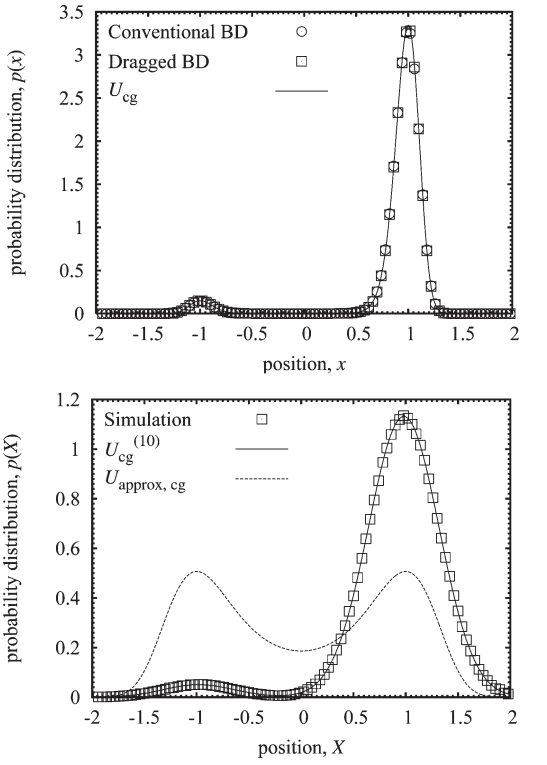

Figure 6. The upper graph shows the probability distribution of x as found in simulations. The dragging scheme samples the canonical distribution corresponding to U_{cg}, eq 26, to high accuracy. The lower graph shows the distribution for X. It samples the distribution corresponding to $U_{cg}^{(K_0)}$ with $K_0 = 10$ as it should. This distribution significantly deviates from the canonical distribution, eq 27, used to generate the moves.

trial-and-error, we determined that the choice eq 28 is close to optimal.

The upper graph in Figure 5 shows a sample time-series of positions $x(t)$. The thin line indicates simulation by conventional BD for the potential $U(x,y)$ given by eq 25. The initial position is $x = 1$ (and $y = 0$). Within the time interval simulated, the system does not cross the potential barrier. Only fluctuations around $x = 1$ are seen. For the dragging scheme, the time series is indicated by the bold line. This bold line does cross over to the local minimum around $x = -1$ several times.

The lower graph shows the time autocorrelation for $x(t)$. For $t = 0$, the equilibrium value is $\langle x^2 \rangle = 0.972$ according to eq 26. A small time later, local equilibrium has been established around $x = -1$ and 1. The equilibrium probability for $x < 0$ is $P_L = 0.0428$, while for $x > 0$ it is $P_R = 0.957$. For the average position inside the peak we find $\langle x \rangle_L = -0.979$ and for $\langle x \rangle_R = 0.979$. After local equilibration around the potential minima this gives

$$\langle x(0)x(0^+) \rangle \approx P_L \langle x \rangle_L^2 + P_R \langle x \rangle_R^2 = 0.958 \quad (29)$$

This is indeed the initial value seen in the time-correlation graph of Figure 5. For very long times, the barrier is crossed many times, so

$$\langle x(0)x(\infty) \rangle = \langle x \rangle^2 = (P_L \langle x \rangle_L + P_R \langle x \rangle_R)^2 = 0.801 \quad (30)$$

This value is indicated by means of a line in the graph.

For conventional BD, the decay of the time correlation from 0.958 to 0.801 is estimated to be a single exponential with a rate of 9.405×10^{-4}. This value is not fitted but computed by numerical determination of the lowest nonzero eigenvalue of the diffusion problem corresponding to the two-dimensional Brownian motion. The time-correlation graph shows that with the dragging scheme, decorrelation is about a factor 20 faster.

In Figure 6 the probability distributions for x and X, as obtained by the simulations, are given. The upper figure shows the histogram for x. The theoretical distribution is the canonical distribution corresponding to eq 26. Correspondence between simulation and theory is nearly perfect. The positions X are generated using the potential eq 27. The canonical probability distribution corresponding to this potential is also shown in the lower graph. The coarse variable X is, however, expected to be distributed according to eq 26 smoothed with $K_0 = 10kT$ as given by eq 6. It is clear that the difference between the 'generating' distribution and the sampled one is significant. The simulation results show that $\rho_{cg}^{(10)}$ is sampled accurately.

4. DISCUSSION AND CONCLUSIONS

We introduced a dual-resolution ensemble and implemented the Neal dragging idea for this ensemble. The dragging scheme was shown to significantly increase the efficiency of sampling the equilibrium distribution in a one- and two-dimensional potential barrier crossing problem. In the one-dimensional a large speedup factor of 81 was found, while in the two-dimensional case the speedup is a factor 20. When the scheme is generalized to

molecular simulations, this might give a significant speedup for these simulations also.

It was shown theoretically that the dragging scheme is sound, i.e., that the canonical ensemble remains invariant. This was achieved by applying the Metropolis rule such that the correct detailed balance condition for motion along a path is obeyed. In the two-dimensional example a symmetric Hamiltonian is used to generate the dynamics of the coarse-grain state. The 'real' coarse-grained Hamiltonian found by integrating out the fine-grain variables from the dual-resolution ensemble, however, is asymmetric. The corresponding asymmetric ensemble for X is well sampled by the scheme. This provides a practical example of the validity of the scheme. As a remark on the side, note that the smaller speedup factor of 20, as compared to 81, is partly due to the large mismatch between coarse-grain Hamiltonian used to generate the X and its true Hamiltonian. The scheme needs to correct for this mismatch by rejecting some of the moves. Because the potential generating the dynamics of X was given, the speedup could not be fully optimized. We used the less than optimal coarse-grain potential because it was also used proof-of-principle of ResEx methods.[9,10]

By means of analysis of the simulations of the simple systems we identified and also resolved a weakness of the dragging scheme. The problem is that the simulations get stuck because acceptance rates drop to zero. An analysis of this problem is available in the Supporting Information. It occurs if the approximate coarse-grain dynamics very rarely samples a region that should be sampled much more frequently, according to the real coarse-grain dynamics. One way to resolve the problem is to make sure this situation does not arise by choosing a suitable approximate coarse-grain Hamiltonian. It is not sure if this is always possible in practice.

A second way to resolve this stuck problem is by equilibrating the fine-grain system and regenerating the Gaussian springs. In this case the implementation of the dragging scheme alternates between two *moves*. In the dragging move the coarse-grain variables X move first and by means of dragging guide to fine-grain state Γ to a new favorable state. The second move is an equilibration move where the fine-grain system evolves according its natural dynamics. The coarse-grain variables are reconnected to the fine-grain state at the end. Both moves sample the dual-resolution ensemble correctly. By combining them, the system does not get stuck.

An envisioned application is to speedup molecular simulations. The idea is to use mesoscopic scale (coarse-grain) simulations to guide atomistic systems to sample phase space more efficiently. The mesoscopic system has the essential features of the molecular system. Configurations are, on a qualitative level, correct. Interactions are softer, and therefore, the barriers that determine the rate of equilibration are more easily crossed. A drawback of the mesoscopic level simulation is its lower accuracy due to the loss of atomistic detail. By dragging a atomistic model toward the mesoscopic configuration, it is force to cross the (higher) potential barriers. This means a speedup compared to atomistic simulation without dragging. The sampling of atomistic level means accuracy is high.

In the proof-of-principles and also in Appendix B, we found that the potentials used to generate the coarse-grain dynamics, $U_{\text{approx,cg}}$, should be close to $U_{\text{cg}}^{(K_0)}$. Most mesoscopic simulation techniques use approximate Hamiltonians that are aimed to be close to the real coarse-grained Hamiltonian defined by eq 2 corresponding to $K_0 \to \infty$. These are probably not the best potentials for performing the dragging scheme. Spring constants will be chosen such that barriers of say $10kT$ can be crossed. The conventional mesoscopic potentials are not that soft at all. They are probably too stiff. When applying the dragging scheme with these potentials, acceptance probabilities will be low. The simulation probably will get stuck. Note that in this case, the equilibration of the atomistic system and the redrawing of the Gaussian springs do not help. Because of the looseness of the springs compared to the stiffness of the mesoscopic potentials, the factor given by eq 21 remains small.

A solution might be to use softer mesoscopic potentials. The inclusion of a finite K_0 softens the coarse-grained potential $U_{\text{cg}}^{(K_0)}$. This is the potential that should be approximated by the potential, $U_{\text{approx,cg}}$, used mesoscopic simulation. It is, at least at this moment, not clear what values for the spring constants should be taken for molecular simulations. It would be best to be able to generate mesoscopic potentials corresponding to a chosen K_0. Therefore a dual-resolution simulation method for molecular systems that uses the dragging scheme is best combined with a on-the-fly coarse-graining procedure. In this case K_0 can be chosen optimally for the system at hand, and an appropriate coarse-grained potential can be generated. This is a topic of ongoing research.

Besides the factor that depends on the coarse-grained potential, there is also a second contribution to eq 17 due to the springs. How this factor scales with the dimensionality of the system is at present unclear. This factor needs to be kept in bounds also in the high dimensional case, if the scheme is to be useful to speedup molecular simulations. Whether this is possible remains to be seen and will determine the possible applicability in this domain. The large speedup factors of 80 for the one-dimensional case and 20 for the not fully optimized two-dimensional case are encouraging.

In a preliminary molecular study we investigated the dragging scheme to speedup trans−gauche transitions in butane. Here we found that the correct ensemble is sampled. Also high acceptance ratio's could be found by constructing approximate coarse-grained potentials that are well matched to the spring strengths K_0. However, to obtain these high acceptances, the dragging had to be performed so slowly that no effective speedup was achieved.

In the current paper we focused on crossing barriers. As one of the reviewers did point out, a useful application might lie elsewhere. In the coarse-grained dynamics of X, one takes large steps. This means that when dragging the fine-grain configuration, also large steps are taken because it is dragged along with X. This should be compared to local diffusive motion if the configuration is not dragged. Overall this could constitute a speedup in the sampling of phase space.

To a certain extent, the outlined method is a method in need of a good application. It is not clear yet if this application is the one envisioned in the current paper. We have good hopes that the dragging method, or a method derived from it, can be very useful in the realm of molecular simulations. The reason for these hopes is that the outlined method is very flexible, and many possible variants still need to be investigated. One of the flexibilities that is largely unexplored is the fact that during the dragging (i.e., $0 < \lambda < 1$), the used Hamiltonian $H_{\text{drag}}(\Gamma,\lambda)$ can be freely chosen. For example, one can choose to slowly turn of some of the interactions (and turn them on later) or temporarily raise the temperature. The general recipe given by the second line of eq 17 can then be used to generate the correct distribution at $\lambda = 0$ or 1.

APPENDIX

A. Proof of the Neal Dragging Method. We can write the probability density to sample a path in fine-grain phase space, when the initial state obeys the dual-resolution probability density, as

$$\rho(\Gamma_n\ ,\ ...,\ \Gamma_0, X^*, X)\ =\ w(\Gamma_n\ ,\ ...,\ \Gamma_1, X^*|\Gamma_0, X, \{\lambda_i\})\rho_{\text{dual}}(\Gamma_0, X) \tag{31}$$

Because all intermediate steps are Markovian processes, the conditional probability for the path can be decomposed as

$$\begin{aligned} &w(\Gamma_n,\ ...,\ \Gamma_1, X^*|\Gamma_0, X, \{\lambda_i\}) \\ &\quad =\ \text{acc}(\Gamma_n,\ ...,\ \Gamma_1, X^*|\Gamma_0, X) \\ &\quad \times w(X^*|X)\prod_{i=1}^{n} T(\Gamma_i|\Gamma_{i-1}, X^*, X, \lambda_i) \end{aligned} \tag{32}$$

Here we used the transition probabilities as introduced in eqs 9 and 14.

A detailed balance condition can be used to make sure that Γ_n (when averaging over initial and intermediate states) also obeys ρ_{dual}. This detailed balance condition is

$$\begin{aligned} &w(\Gamma_n,\ ...,\ \Gamma_1, X^*|\Gamma_0, X, \{\lambda_i\})\rho_{\text{dual}}(\Gamma_0, X) \\ &\quad =\ w(\Gamma_0,\ ...,\ \Gamma_{n-1}, X|\Gamma_n, X^*, \{\lambda_i\})\rho_{\text{dual}}(\Gamma_n, X^*) \end{aligned} \tag{33}$$

Here the states Γ_j are reversed, but the sequence of the λ_i's remains unchanged. Inserting eq 32 into this detailed balance condition gives

$$\begin{aligned} &\frac{\text{acc}(\Gamma_n\ ,\ ...,\ \Gamma_1, X^*|\Gamma_0, X)}{\text{acc}(\Gamma_0\ ,\ ...,\ \Gamma_{n-1}, X|\Gamma_n, X^*)} \\ &\quad =\ \frac{w(X|X^*)}{w(X^*|X)}\prod_{i=1}^{n}\frac{T(\Gamma_{n-i}|\Gamma_{n-i+1}, X, X^*, \lambda_i)}{T(\Gamma_i|\Gamma_{i-1}, X^*, X, \lambda_i)}\frac{\rho_{\text{dual}}(\Gamma_n, X^*)}{\rho_{\text{dual}}(\Gamma_0, X)} \\ &\quad =\ \frac{w(X|X^*)}{w(X^*|X)}\prod_{i=1}^{n}\frac{T(\Gamma_{i-1}|\Gamma_i, X, X^*, \lambda_{n-i+1})}{T(\Gamma_i|\Gamma_{i-1}, X^*, X, \lambda_i)}\frac{\rho_{\text{dual}}(\Gamma_n, X^*)}{\rho_{\text{dual}}(\Gamma_0, X)} \end{aligned} \tag{34}$$

The last line is obtained from the previous one by relabeling $i \rightarrow n - i + 1$ for the $T(\cdots|\cdots)$'s in the enumerator. This is not the same as the relation in eq 16. The relation of eq 16 is preferred because by means of eq 14, it allows for the transition of eqs 16 to 17. When making the transition to probability densities for the general relation, the normalization constants do not cancel. We want the normalization constants to cancel because these are unknown.

To obtain eq 16 we require that

$$T(\Gamma'|\Gamma, X^*, X, \lambda_{n-i+1})\ =\ T(\Gamma'|\Gamma, X, X^*, \lambda_i) \tag{35}$$

In the simulation we generate the transitions from one Γ to Γ' using the Hamiltonian eq 10. The coarse-grain states X and X^* and the λ's appear through the spring forces. The requirement eq 35 therefore gives that

$$K(\lambda_{n-i+1})\ =\ K^*(\lambda_i) \tag{36}$$

Since λ only provides a parametrization of K, we can take it to increase linearly from 0 to 1. Taking it in accordance with eq 13, we have $\lambda_{n-i+1} = 1 - \lambda_i$ and thus obtain the requirement eq 11.

B. The Slow Dragging Limit. In this appendix we analyze the dragging scheme for the case that dragging is performed (infinitely) slowly with (infinitesimally) small increments $\Delta\lambda$. In this case we can approximate the ratio of acceptance probabilities defined by eq 17 as

$$\begin{aligned} &\frac{f_{\text{approx, cg}}(X)}{f_{\text{approx, cg}}(X^*)}\prod_{i=0}^{n}\frac{f(\Gamma_i, X^*, X, \lambda_{i+1})}{f(\Gamma_i, X^*, X, \lambda_i)} \\ &\quad =\ \exp[\beta\Delta H_{\text{approx, cg}}]\prod_{i=0}^{n}\exp\left[-\beta(H_{\text{drag}}(\Gamma_i, \lambda_{i+1}) - H_{\text{drag}}(\Gamma_i, \lambda_i))\right] \\ &\quad \approx\ \exp[\beta\Delta H_{\text{approx, cg}}]\prod_{i=0}^{n}\exp\left[-\beta\Delta\lambda\frac{\partial H_{\text{drag}}(\Gamma_i, \lambda_i)}{\partial\lambda_i}\right] \end{aligned} \tag{37}$$

Because the dragging occurs so slowly, every Γ_i can be assumed to be statistically independent. For large n, many subsequent Γ_i's are sampled for a small increase in λ; this has an averaging effect:

$$\begin{aligned} &\exp[\beta\Delta H_{\text{approx, cg}}]\prod_{i=0}^{n}\exp\left[-\beta\Delta\lambda\frac{\partial H_{\text{drag}}(\Gamma_i, \lambda_i)}{\partial\lambda_i}\right] \\ &\quad \approx\ \exp[\beta\Delta H_{\text{approx, cg}}]\prod_{i=0}^{n}\left\langle\exp\left[-\beta\Delta\lambda\frac{\partial H_{\text{drag}}(\Gamma_i, \lambda_i)}{\partial\lambda_i}\right]\right\rangle \\ &\quad \approx\ \exp[\beta\Delta H_{\text{approx, cg}}]\prod_{i=0}^{n}\left[1 - \beta\Delta\lambda\left\langle\frac{\partial H_{\text{drag}}(\Gamma_i, \lambda_i)}{\partial\lambda_i}\right\rangle\right] \\ &\quad \approx\ \exp[\beta\Delta H_{\text{approx, cg}}]\prod_{i=0}^{n}\left[1\ +\ \Delta\lambda\frac{\partial \ln Z_{\lambda_i}}{\partial\lambda_i}\right] \\ &\quad \approx\ \exp[\beta\Delta H_{\text{approx, cg}}]\prod_{i=0}^{n}\exp\left[\Delta\lambda\frac{\partial \ln Z_{\lambda_i}}{\partial\lambda_i}\right] \\ &\quad \approx\ \exp[\beta\Delta H_{\text{approx, cg}}]\ \exp\left[\sum_{i=0}^{n}\Delta\lambda\frac{\partial \ln Z_{\lambda_i}}{\partial\lambda_i}\right] \\ &\quad \approx\ \exp[\beta\Delta H_{\text{approx, cg}}]\ \exp\left[\int_0^1 \text{d}\lambda\frac{\partial \ln Z_\lambda}{\partial\lambda}\right] \\ &\quad =\ \exp[\beta\Delta H_{\text{approx, cg}}]\ \exp[\ln Z_1 - \ln Z_0] \\ &\quad =\ \exp[\beta\Delta(H_{\text{approx, cg}} - H_{cg}^{(K_0)})] \end{aligned} \tag{38}$$

For every i, the expectation value is according to the canonical equilibrium distribution associated with $H_{\text{drag}}(\Gamma,\lambda_i)$. The corresponding partition sum, Z_λ, can be used to compute this expectation value. The Hamiltonian H_{drag} depends on X and X^* according to eq 10. For $\lambda = 0$, the system is only connected to X only and for $\lambda = 1$ only to X^*. In this the partitions sums are given by eq 7 (up to the prefactor which cancels in the computation above).

The final result indicates that, in the slow dragging limit, acceptance ratio's approach 1 when the approximate Hamiltonian used to generate the dynamics of X, i.e., $H_{\text{approx,cg}}$ is close to the real effective Hamiltonian $H_{\text{cg}}^{(K_0)}$. The most severe approximation used in the derivation above is the 'slowness'. At every instance the equilibrium distribution correspondig to λ needs to be sampled. Clearly we want to use the dragging scheme to speed-up computation and therefore not perform the dragging too slowly; hence in practical computations, the acceptance ratio is expected to deviate significantly from the optimal 100% acceptance case.

■ ASSOCIATED CONTENT

Supporting Information. A thorough analysis of the stuck problem is provided. This material is available free of charge via the Internet at http://pubs.acs.org.

■ AUTHOR INFORMATION

Corresponding Author
*E-mail: e.a.j.f.peters@tue.nl.

■ ACKNOWLEDGMENT

The authors wish to thank Dr. K. S. Lyakhova for fruitful discussions and feedback on earlier versions of the manuscript.

■ REFERENCES

(1) Neal, R. M. *Taking Bigger Metropolis Steps by Draggging Fast Variables*; Technical Report; University of Toronto: Toronto, Canada, October, 2005; http://arxiv.org/PS_cache/math/pdf/0502/0502099v1.pdf.
(2) Martin, M. G.; Siepmann, J. I. *J. Phys. Chem. B* **1998**, *102*, 2569–2577.
(3) Marrink, S. J.; Risselada, H. J.; Yefimov, S.; Tieleman, D. P.; de Vries, A. H. *J. Phys. Chem. B* **2007**, *111*, 7812–7824.
(4) Muller-Plathe, F. *ChemPhysChem* **2002**, *3*, 754–769.
(5) Lwin, T. Z.; Luo, R. *J. Chem. Phys.* **2005**, *123*, 10.
(6) Lyman, E.; Ytreberg, F. M.; Zuckerman, D. M. *Phys. Rev. Lett.* **2006**, *96*, 028105.
(7) Liu, P.; Shi, Q.; Lyman, E.; Voth, G. A. *J. Chem. Phys.* **2008**, *129*, 8.
(8) Frenkel, D.; Smit, B. *Understanding Molecular Simulation (From Algorithms to Applications)*; Academic Press: San Diego, CA, 2002.
(9) Liu, P.; Voth, G. A. *J. Chem. Phys.* **2007**, *126*, 6.
(10) Lyman, E.; Zuckerman, D. M. *J. Chem. Theory Comput.* **2006**, *2*, 656–666.
(11) Reith, D.; Putz, M.; Muller-Plathe, F. *J. Comput. Chem.* **2003**, *24*, 1624–1636.
(12) Izvekov, S.; Voth, G. A. *J. Phys. Chem. B* **2005**, *109*, 2469–2473.
(13) Gardiner, C. W. *Handbook of Stochastic Methods for Physics, Chemistry and the Natural Sciences*; Springer: Berlin, Germany, 1997.
(14) Öttinger, H. *Stochastic Processes in Polymeric Fluids*; Springer Verlag: Berlin, Germany, 1996.

JCTC Journal of Chemical Theory and Computation

ARTICLE

pubs.acs.org/JCTC

Flow-Dependent Unfolding and Refolding of an RNA by Nonequilibrium Umbrella Sampling

Alex Dickson, Mark Maienschein-Cline, and Allison Tovo-Dwyer

James Franck Institute, The University of Chicago, Chicago, Illinois 60637, United States

Jeff R. Hammond

Leadership Computing Facility, Argonne National Laboratory, Argonne, Illinois 60439, United States

Aaron R. Dinner*

James Franck Institute, The University of Chicago, Chicago, Illinois 60637, United States

ABSTRACT: Nonequilibrium experiments of single biomolecules such as force-induced unfolding reveal details about a few degrees of freedom of a complex system. Molecular dynamics simulations can provide complementary information, but exploration of the space of possible configurations is often hindered by large barriers in phase space that separate metastable regions. To solve this problem, enhanced sampling methods have been developed that divide a phase space into regions and integrate trajectory segments in each region. These methods boost the probability of passage over barriers and facilitate parallelization since integration of the trajectory segments does not require communication, aside from their initialization and termination. Here, we present a parallel version of an enhanced sampling method suitable for systems driven far from equilibrium: nonequilibrium umbrella sampling (NEUS). We apply this method to a coarse-grained model of a 262-nucleotide RNA molecule that unfolds and refolds in an explicit flow field modeled with stochastic rotation dynamics. Using NEUS, we are able to observe extremely rare unfolding events that have mean first passage times as long as 45 s (1.1×10^{15} dynamics steps). We examine the unfolding process for a range of flow rates of the medium, and we describe two competing pathways in which different intramolecular contacts are broken.

I. INTRODUCTION

Nonequilibrium measurements on biological macromolecules, such as mechanical force-induced unfolding[1] and flow-based analogs,[2] have emerged as a powerful complement to equilibrium studies. Indeed, it is now possible to follow the evolution of distances through fluorescence resonance energy transfer (FRET) simultaneously with forces through optical traps.[3] While these measurements provide unprecedented experimental data on the stochastic dynamics of individual molecules, they still only probe at most a few degrees of freedom among many. Molecular dynamics simulations, which provide complete information about the positions of all participating particles subject to the assumptions of the model, have proven to be a valuable tool for interpreting these data.[4] However, the time scales for conformational change are often long compared with elementary fluctuations, which makes waiting for the events of interest to occur spontaneously under conditions representative of experimental ones prohibitively computationally costly. To accelerate convergence, many simulation studies employ unrealistically extreme nonequilibrium conditions (see discussion in Hu et al.[5]).

Alternatively, enhanced sampling methods can be used to improve exploration of phase space and focus computational effort on low probability regions of mechanistic importance, such as transition states. The most widespread such methods[6−8] rely on the fact that the statistics of equilibrium systems are known *a priori*, which prevents the applicability of such methods to nonequilibrium situations. However, there now exist methods that can enhance the sampling of low probability regions without relying on equilibrium properties of the system.[9−20] Although these methods differ in detail, the essential idea in all of them is to harvest segments of unbiased dynamics trajectories such as to achieve relatively uniform sampling of different regions of a space of physically relevant degrees of freedom (order parameters). The acceleration of convergence follows from the fact that each trajectory segment need only traverse a small portion of the space of order parameters, across which the probability is relatively uniform.

We have been developing one such method: nonequilibrium umbrella sampling (NEUS).[13−16] In this paper, we present a streamlined version of the algorithm with improved convergence properties. The most significant change is the explicit association of a weight with each saved copy of the system, motivated by the weighted ensemble method.[17−20] The fact that many trajectory segments are integrated independently makes the method highly parallelizable, and we detail and implement a strategy that can provide excellent scaling to large numbers of processors.

We use the method to simulate partial unfolding and refolding of a coarse-grained model of a 262-nucleotide RNA molecule in

Received: June 2, 2011
Published: July 29, 2011

the presence of a flow field. Our interest in this system comes from single-molecule studies of FRET between probes on the L18 loop and 3′ terminus of the catalytic domain of the RNase P RNA from *Bacillus stearothermophilus*.[22−24] In these studies, the molecule was tethered in a microfluidic channel to enable relatively rapid changes in magnesium ion concentration, and this led to the question of whether flow contributed to the dynamics observed.[24] Specifically, we wondered whether there were dynamics like the quasi-periodic folding and unfolding observed in previous simulations of a homopolymer in a laminar flow field.[25] Here, we show that in the RNA under flow system there are two competing unfolding pathways, the likelihoods of which depend on the rate of flow of the solution. We compare these results with reversible unfolding simulations (without a net flow).

II. METHODS

II.A. Algorithm. As we show, the slowest degrees of freedom in the system examined here have relaxation times on the order of milliseconds to seconds, while straightforward simulations of the coarse-grained model are limited to tens of microseconds. Thus, enhanced sampling is needed. Here, we describe the version of nonequilibrium umbrella sampling (NEUS)[13−16] used in the present study. To this end, we summarize the overall strategy, and then we describe the phases of the simulation and parallelization; differences from earlier versions of the algorithm and competing methods are noted.

II.A.1. Overall Strategy. The sampling is guided by a set of physically relevant variables ("order parameters"). Ideally, these order parameters describe the slow dynamics in the system, and the remaining degrees of freedom relax relatively fast. In this work, we employ a single order-parameter that quantifies the total number of intramolecular contacts (section II.B). However, we explicitly separate the "forward" (unfolding) and "backward" (refolding) transition path ensembles as in Dickson et al.[15] This allows the sampling of the orthogonal degrees of freedom to differ between the two ensembles (i.e., allows for nonoverlapping unfolding and refolding transition path ensembles), and it enables the calculation of transition rates between basins.

For the simulations, we divide the space of order parameters into regions, which need not be uniform in size. Each region contains one or more copies of the system (walkers) that evolve independently according to the natural dynamics of the system, and we associate with that walker a weight for contributing to averages. When a walker of the system attempts to leave its region, the configuration is saved to a list of entry points for the neighboring region, along with the weight of the walker. When a neighboring list is full, the oldest saved configuration is overwritten, and its weight is distributed over the remaining points in the list in a manner that does not affect their relative probabilities of being chosen. The walker is then restarted from a saved configuration, i, which is chosen from one of its region's lists with a likelihood proportional to its weight (w_i). The weight of this point is then partitioned between the walker and the saved entry point: γw_i ($\gamma \in (0,1]$) is given to the walker, and the rest, $(1-\gamma)w_i$, remains associated with the saved entry point. Note that $\gamma = 1$ results in straightforward dynamics, or a single, continuous trajectory. Here, we use $\gamma = 0.9$. The incorporation of this feature in the NEUS algorithm is motivated by the (equal) partitioning of the probability when a trajectory branches in the weighted ensemble (WE) method;[17] it ensures conservation of the starting probability and suppresses artificial amplification of the probability of particular trajectories. As a result, we are able to obtain converged results with only one set (lattice) of regions in the extended space as opposed to two, as in previous work.[13−15]

II.A.2. Initialization. A common situation is that one is interested in studying a transition between two or more states, but one knows the configuration of the system in only one of the stable states. This situation applies here to the RNA-under-flow system, since we know the folded configuration but not the most likely unfolded configurations. Although in principle one could start the simulation in each region using any configuration consistent with the allowed order parameter values, in practice, it is best to start with a distribution of structures that is as consistent as possible with the physically weighted dynamics to avoid introducing unnecessary errors that take time to be corrected. To this end, we progressively activate the regions in a manner similar to forward flux sampling (FFS)[12] as follows.

We start by running an unconstrained simulation that is initialized in the known stable configuration. During this simulation, we record the configuration each time the system crosses a boundary of a region but do not reset the configuration. These configurations serve as the initial entry (i.e., resetting) points for the regions visited, and all such configurations are assigned equal weight. Following the unconstrained simulation, we begin the umbrella sampling simulation starting from saved entry points in each region that has at least one such point, employing and updating the copy weights as described above. Regions that were not visited previously are activated once entry points for them are obtained. As the simulations proceed, regions of lower and lower probability are activated by their neighbors, and trajectories emerge from the original stable state. Once all of the regions are activated, we are able to concurrently sample the entire order parameter space of interest, using only points that resulted directly from the starting distribution.

In the present study, the progressive initialization of regions accounts for about 2% of the total simulation time. The sampling procedure employed here further differs from FFS in that it does not explicitly require a notion of forward progress and thus can be used with sampling regions that are defined by an arbitrary number of order parameters. By the same token, trajectories are terminated when they cross any boundary, not only a forward one. This distinction is of practical importance when the dynamics do not lead rapidly back to the starting basin (see Dickson et al.[16] for further discussion).

II.A.3. Weight Redistribution. The algorithm as described is in principle complete. Indeed, it is very similar to the WE method except that (i) it permits strict control of the number of copies in a region (including only limiting it to one) and (ii) differs in the details of weight partitioning when resetting (branching) and redistributing when overwriting (pruning). However, the transfer of weight between regions of high probability can be very slow when the weight must pass through a bottleneck region of low probability. This is because a very large number of low probability walkers are required to add up to a significant change of weight in a high probability region. This convergence issue arises despite the fact that the time for initial exploration of the space decreases with an increasing number of regions, as in any umbrella sampling procedure.[8,26]

To accelerate convergence after the initialization phase, we periodically use the interface-to-interface crossing statistics to predict statistical weights for each region ($\{W_i\}$) and scale the weights of the entry points in each region, i, such that their sum is

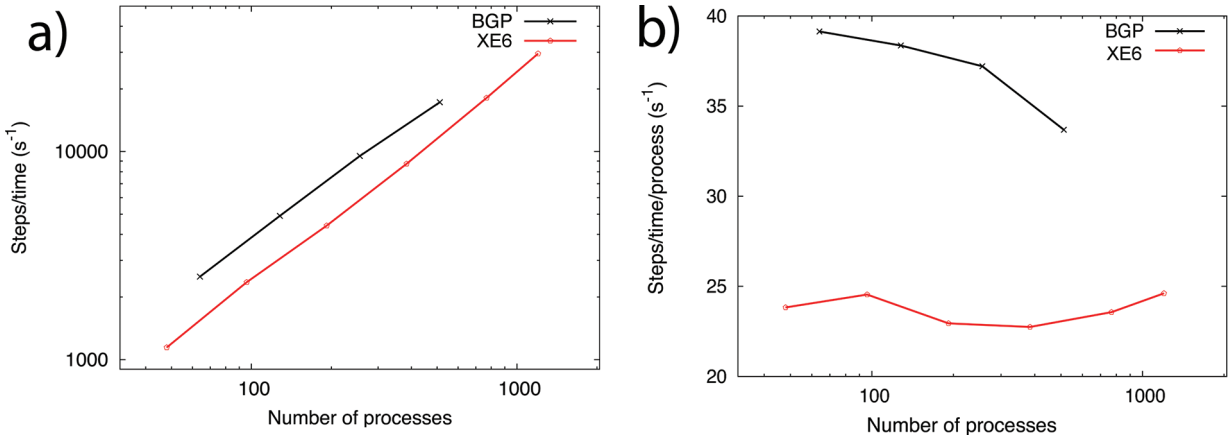

Figure 1. Scaling results on two parallel computing architectures: the Intrepid Blue Gene/P and the "Beagle" Cray XE6 supercomputers. Note that the code was not specifically optimized for performance on either machine. (a) Steps per unit time as a function of the number of processes on both machines. Perfect scaling on this plot is shown by a straight line with slope equal to 1. (b) Steps per unit time per process. Perfect scaling on this plot would be shown by a flat line. Note that here a process on the Blue Gene/P is composed of four cores, and a process on the Cray XE6 is composed of a single core.

equal to W_i. Here, the weights are obtained from a modified version of the scheme in Vanden-Eijnden and Venturoli,[27] where the total flux into a region is set equal to the total flux out of a region. To this end, we accumulate a transition matrix, **T**: each off-diagonal element t_{ij} is the number of transitions observed from region j to region i in the last weight update period, and each diagonal element $t_{ii} = -\sum_{j \neq i} t_{ji}$. We then solve the equation $\mathbf{TW} = 0$ for the weight vector **W** by using singular value decomposition to compute the nullspace of **T**, which is the single nontrivial solution **W**. Here, we perform this operation periodically throughout the simulation, as in previous NEUS studies;[15,27] this contrasts with the study by Bhatt et al.[19] in which a single such step is used to precondition the simulation and then flux balance is used to check convergence.

II.A.4. Parallelization. The simulations of the copies of the system require only limited communication. As such, NEUS and methods like it lend themselves well to parallelization. However, we find that they benefit from careful implementation on high performance computers. All simulations for the present study are run on parallel architectures using the Global Arrays toolkit,[28] which implements a global address space programming model in which processes can access remote data using one-sided communication. One-sided communication is particularly useful in this case, since the timing of boundary crossing events is not predictable. The global address space also enables one to distribute the storage of a large set of region entry points across the memory of many compute nodes. The entry points for each region, the region weights, boundary crossing statistics, and sampling histogram data are all stored as global arrays. These arrays can be modified by any process using "put" functions and "get" functions, where locks are used to enable atomic updates of global data (modifications of the entry point lists, for instance) that prevent processes from concurrently accessing the same region of a global array.

Although the dynamics of the copies are simulated essentially without communication once they are initialized, NEUS still periodically requires some collective operations, such as weight updates, and the computation of rates and probability distributions. To allow for such operations, we break down the simulation into "cycles" of computation, at the end of which all processes are synchronized. Within the cycles, the work is distributed among the processes as follows. When a process is finished running a trajectory segment, it queries how many steps have been run in each region k so far this cycle (N_k), and it uses the results to decide in which region to run the next trajectory segment. Specifically, it chooses to start a trajectory in region j with probability

$$P_j = \frac{N_{\text{steps}} - N_j}{\sum_k (N_{\text{steps}} - N_k)} \quad (1)$$

where N_{steps} is the number of steps to be run in each region per cycle. A trajectory is terminated if the counter in its region reaches N_{steps} (upon which the current configuration of the system is saved to the entry point list as a simple means of maintaining it), and a computational cycle ends when all counters reach N_{steps}. Here, N_{steps} is set to 2000.

Figure 1 shows preliminary scaling results obtained on two parallel architectures: Intrepid, a Blue Gene/P supercomputer, and Beagle, a Cray XE6 supercomputer. Each scaling test consisted of running 10 cycles (as defined above), and the wall-clock time elapsed between the beginning of the first cycle and the end of the last cycle was used to compute the number of dynamics steps per unit time. In each test, we use the RNA under flow system presented below, but we check for boundary crossings every 50 dynamics steps, as opposed to every five in the rest of the work presented here. Longer periods between boundary crossing checks results in better scaling since there is more time between communication events. On the Blue Gene/P, scaling tests are run on groups of 64, 128, 256, and 512 processes. In this case, each process is composed of four cores but acted as a single process in the NEUS algorithm, where three of the cores are used as OpenMP threads and one is used exclusively for communication. Figure 1a shows reasonable scaling up to 512 processes, but Figure 1b clearly reveals a loss in efficiency as the number of processes is increased. On Beagle, scaling tests were run on groups of 48, 96, 192, 384, 768, and 1200 processes. In this case, each process is composed of a single core; no OpenMP theading was used. Excellent scaling is observed for these numbers of processes, as seen in Figure 1, where the number of dynamics steps per unit time per process is roughly flat. The slight variation in Figure 1b reflects the specific compute nodes that are selected to run the job: nodes that are closer together in the machine

result in faster communication, and better scaling overall, which is expected.

II.B. Model. The system is a model of the catalytic domain of RNase P RNA from *Bacillus stearothermophilus*. To make the simulations tractable, we use a coarse-grained representation that averages over the atomic structure and dynamics, while taking into account the secondary and tertiary interactions that stabilize the native state: the self-organized polymer (SOP) model.[29] In the SOP model, each nucleotide of the RNA is treated as a bead, and the beads interact through potentials that depend on the known native structure. The potential defining the model is the sum of a finitely extensible nonlinear elastic (FENE) potential that connects adjacent beads[30] (V_{FENE}); a Lennard-Jones attraction between beads that has a minimum at the native structure distance ($V_{\mathrm{nb}}^{\mathrm{att}}$); pairwise nonbonded repulsions scaling as r^{-6}, which locally straighten the chain and mimic steric repulsions between nucleotides ($V_{\mathrm{nb}}^{\mathrm{rep}}$); and a Weeks−Chandler−Andersen[31] (WCA) repulsion between each bead and the wall at $y = 0$ (V^{wall}). The total potential function is

$$V_{\mathrm{T}} = V_{\mathrm{FENE}} + V_{\mathrm{nb}}^{\mathrm{att}} + V_{\mathrm{nb}}^{\mathrm{rep}} + V_{\mathrm{wall}}$$

with

$$V_{\mathrm{FENE}} = -\sum_{i=1}^{N-1} \frac{k}{2} R_0^2 \log\left(1 - \frac{(r_{i,i+1} - r_{i,i+1}^0)^2}{R_0^2}\right)$$

$$V_{\mathrm{nb}}^{\mathrm{att}} = \sum_{i=1}^{N-3} \sum_{j=i+3}^{N} \varepsilon_h \left[\left(\frac{r_{ij}^0}{r_{ij}}\right)^{12} - 2\left(\frac{r_{ij}^0}{r_{ij}}\right)^{6}\right] \Delta_{ij}$$

$$V_{\mathrm{nb}}^{\mathrm{rep}} = \sum_{i=1}^{N-2} \varepsilon_l \left(\frac{\sigma^*}{r_{i,i+2}}\right)^{6} + \sum_{i=1}^{N-3} \sum_{j=i+3}^{N} \varepsilon_l \left(\frac{\sigma}{r_{ij}}\right)^{6} (1 - \Delta_{ij})$$

$$V_{\mathrm{wall}} = \sum_{i=1}^{N} H(2^{1/6}\sigma_{\mathrm{WCA}} - y_i) \times 4\varepsilon_l \left[\left(\frac{\sigma_{\mathrm{WCA}}}{y_i}\right)^{12} - \left(\frac{\sigma_{\mathrm{WCA}}}{y_i}\right)^{6}\right] \quad (2)$$

where r_{ij} is the distance between residues i and j, and r_{ij}^0 is their distance in the native structure. We set the parameters in eq 2 to those in Hyeon and Thirumalai,[29] namely, $k = 20$ kcal/(mol × Å^2), $R_0 = 2$ Å, $\varepsilon_h = 0.7$ kcal/mol, and $\varepsilon_l = 1.0$ kcal/mol. We set $\sigma = 7$ Å to ensure noncrossing of the chain, and we set $\sigma^* = 3.5$ Å to prevent the flattening of helical structures. In V_{wall}, $\sigma_{\mathrm{WCA}} = 2$ Å, and $H(x)$ is a Heaviside function equal to 0 for $x < 0$ and 1 for $x > 0$. The size of the box was chosen such that the residues would interact only with the $y = 0$ surface. Consequently, repulsive potentials were not needed for the other walls of the box, and no collisions of the residues with those walls were observed in our simulations. The equation of motion for the polymer is integrated with the Velocity−Verlet algorithm with time step $\delta t = 40$ fs.

The native, folded structure was constructed from the crystal structure for the full RNase P RNA.[32] The coordinates of the catalytic domain (262 residues) were isolated from the full structure (417 residues), and coarse-graining into beads was carried out by replacing the coordinates of each residue with its center of mass. Unstructured residues, which did not have crystal structure coordinates (in Figure 2, residues 161−181 in P1, 15−20 in P15, 64−73 in P18, and 106−125 in P19), were added by introducing the appropriate number of beads into the sequence, separated by the average bead−bead distance (about 5 Å); these unstructured residues have no contacts. The structure was allowed to relax to its minimum energy by integrating without solvent so that the added unstructured residues form

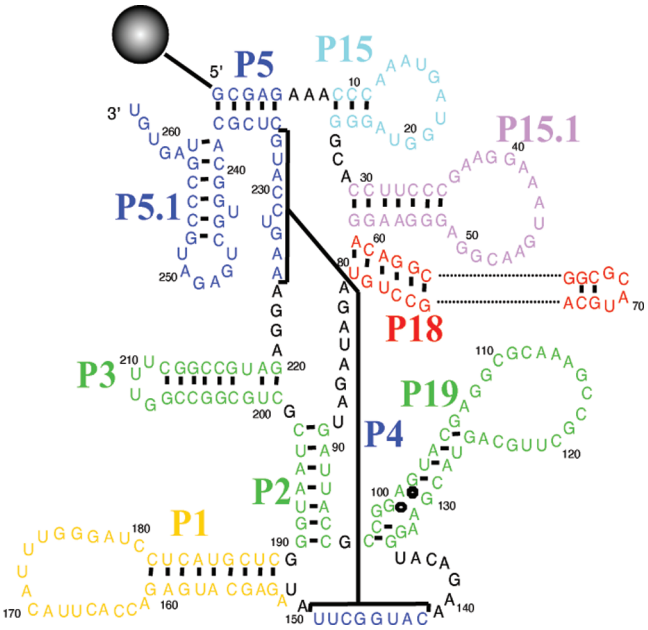

Figure 2. Secondary structure of the RNA molecule. In the simulation, the 5′ end of the molecule is attached to a tether (black sphere) that prevents the molecule from moving along with the flow. The index of every tenth residue is shown.

simple loops. Using this structure, we consider a native contact to exist ($\Delta_{ij} = 1$) between all pairs of residues i and j with $|i - j| > 2$ and a distance less than $R_{\mathrm{C}} = 14$ Å in the native structure; for all other pairs, $\Delta_{ij} = 0$.

The solvent in the simulation is modeled using the stochastic rotation dynamics method,[33−36] in which the solvent is represented by a large number (here, 503 200) of infinitesimal particles that are grouped into cubic "interaction cells". Each step of the algorithm comprises two parts: (1) free streaming, in which the position of particle i ($\mathbf{r}_i$) is updated according to $\mathbf{r}_i(t + \Delta t) = \mathbf{r}_i(t) + \mathbf{v}_i(t)\Delta t$, where $\mathbf{v}_i$ is the velocity at time t and $\Delta t = 150\delta t$ is the solvent time step, and (2) "collision", in which $\mathbf{v}_i(t + \Delta t) = \mathbf{v}_{\mathrm{cell}}(t) + \Omega[\mathbf{v}_i(t) - \mathbf{v}_{\mathrm{cell}}(t)]$, where $\mathbf{v}_{\mathrm{cell}}$ is the average velocity of particles in the cell containing i and Ω is a stochastic rotation matrix which rotates vectors around a random axis by $\pm\alpha$, a fixed angle, with equal likelihood. Here, we use $\alpha = 0.243\pi$, which in combination with the other parameters used here for the solvent gives a viscosity of 0.8 g/m/s, which is approximately the viscosity of liquid water at our simulation temperature (300 K). The viscosity was calculated using eqs 10 and 14 of Kikuchi et al.[37]

We allow the solvent to influence the RNA by including the polymer beads in the collisions, as in Webster and Yeomans.[38] This is done using

$$\mathbf{v}_{\mathrm{cell}}(t) = \frac{\sum_{\mathrm{solv} \in \mathrm{cell}} m\mathbf{v}_i(t) + \sum_{\mathrm{res} \in \mathrm{cell}} M\mathbf{V}_i(t)}{N_{\mathrm{cell}}^{\mathrm{solv}}(t)m + N_{\mathrm{cell}}^{\mathrm{poly}}(t)M} \quad (3)$$

where $m = 32$ amu is the mass of the solvent particles (chosen to make a solvent mass density of 1 g/mL) and $M = 300$ amu is the mass of the residues, compared with a range in mass for RNA nucleotides of 320−360 amu. $\mathbf{V}_i(t)$ is the velocity vector for residue i, and the sums on the left and right are over all the solvent particles in the cell and all the residues in the cell, respectively.

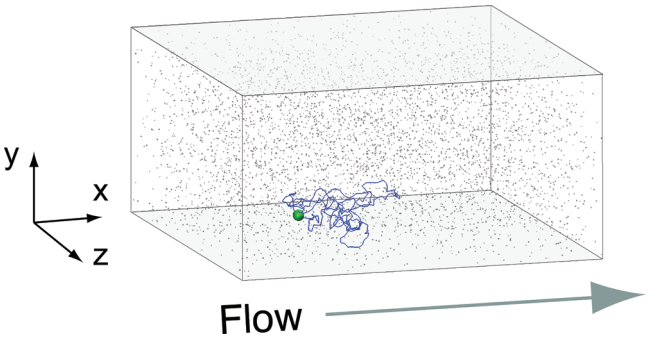

Figure 3. The simulation cell. The boundaries at $y = 0$ and $y = L_y$ have reflective boundary conditions, while the others are periodic. The tether point is shown as a green sphere, and the RNA molecule is in blue. A total of 5000 of the 503 200 solvent molecules are shown here. A flow is induced in the positive x direction by applying a constant acceleration to the solvent particles, which in turn causes extension of the RNA molecule in that direction.

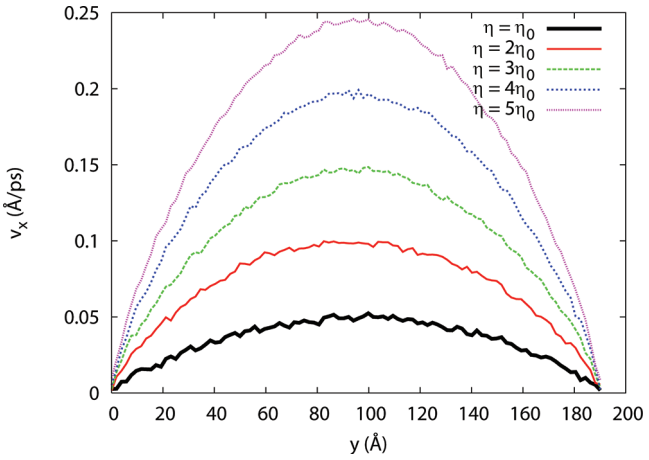

Figure 4. Flow velocity profiles. For each flow rate examined here, we plot the average velocity of solvent molecules in the x direction as a function of y. These were obtained without the polymer. The profiles are parabolic, due to the presence of reflective walls at $y = 0$ and $y = L_y$.

$N_{\text{cell}}^{\text{solv}}(t)$ and $N_{\text{cell}}^{\text{poly}}(t)$ are the number of solvent particles and residues in the cell, respectively, at time t. We then include the polymer beads in the collision step using $\mathbf{V}_i(t + \Delta t) = \mathbf{v}_{\text{cell}}(t) + \Omega[\mathbf{V}_i(t) - \mathbf{v}_{\text{cell}}(t)]$ where Ω is the same rotation matrix used for the solvent particles in the interaction cell.

We use periodic boundary conditions in the x and z directions and walls that reflect all components of the velocity of the solvent particles upon collision at $y = 0$ and $y = L_y$. We then drive the solvent to flow in the positive x direction (Figure 3). The dimensions of the box are $L_x = L_z = 384$ Å and $L_y = 192$ Å. The interaction cells are cubic with a side length of 8 Å, which was chosen to be comparable with the average distance traveled by a solvent particle in a time Δt. Following previous work, we shift the lattice periodically to avoid artifacts[34] and employ the generalized bounce back rule for partially filled cells along the $y = 0$ and $y = L_y$ edges.[35] An extra FENE interaction is added between the 5′ terminus and the tether point, located at (120, 25, 192 Å) to prevent the molecule from moving along with the flow.

The flow is introduced by accelerating each solvent particle that is not in the $y = 0$ or $y = L_y$ interaction cells in the x direction after every rotation step according to $v_x^i \rightarrow v_x^i + \eta\Delta t$, where η is an acceleration parameter. The η values used here range from η_0 to $5\eta_0$, where $\eta_0 = 625$ Å/fs^2. Figure 4 shows average flow profiles, obtained without the polymer. The Péclet number is the ratio of advective motion to thermal diffusive motion, given by

$$Pe = \frac{L\bar{v}_x}{D} \tag{4}$$

where $L = 8$ Å is the characteristic length, $\bar{v}_x$ is the average velocity of the solvent in the x direction, and D is the self-diffusion constant of a single residue calculated in zero flow. Here, Pe ranges from 7.5×10^{-3} to 3.9×10^{-2}, indicating that at all values of η we examined, thermal motion was much stronger than advective motion (i.e., $Pe \ll 1$). Prior to the start of the umbrella sampling simulation, the solvent was equilibrated without the polymer until the flow profiles converged; this required 40 ns, which corresponds to roughly 6700 streaming steps.

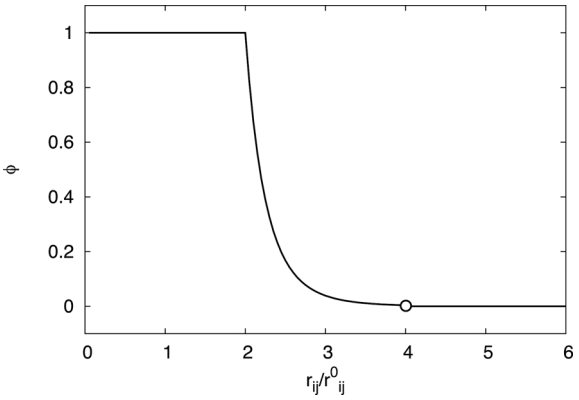

Figure 5. The function $\phi(r_{ij})$ that is used to calculate the order parameter N_c.

II.C. Order Parameter. The order parameter that we use here to distinguish between the folded and unfolded states is an estimate of the number of native contacts that are made in a given configuration:

$$N_c(t) = \sum_{i=1}^{N}\sum_{j\neq i}^{N} \Delta_{ij}\,\phi(r_{ij}(t)) \tag{5}$$

where $r_{ij}(t)$ is the distance between the two residues at time t, $\phi(r_{ij})$ is a function that is equal to 1 when the contact is satisfied ($r_{ij} < a_f r_{ij}^0$), is 0 when the contact is not satisfied ($r_{ij} > 2a_f r_{ij}^0$), and varies between 0 and 1 for intermediate values according to $(a_f r_{ij}^0/r_{ij})^8$, where the exponent was chosen to make the jump at $r_{ij} = 2a_f r_{ij}^0$ small, while being efficient to compute. The constant $a_f = 2.0$ was used here; we found that it provided a good balance between limiting sensitivity to fluctuations within stable states (large a_f) and detecting early unfolding activity (small a_f). A plot of $\phi(r_{ij})$ is shown in Figure 5.

We use this order parameter to define "folded" and "unfolded" basins as $N_c \geq N_{\text{fold}}$ and $N_c \leq N_{\text{unfold}}$, respectively. The choice of N_{fold} and N_{unfold} is discussed in section III. We separate the transition path ensemble into two subensembles: the unfolding ensemble and the refolding ensemble. The unfolding ensemble is composed of all trajectories that originate in the folded basin (regardless of whether they reach the unfolded basin or return to the folded one), and the refolding ensemble is composed of all trajectories that originate in the unfolded basin (regardless of whether they reach the folded basin or return to the unfolded one).

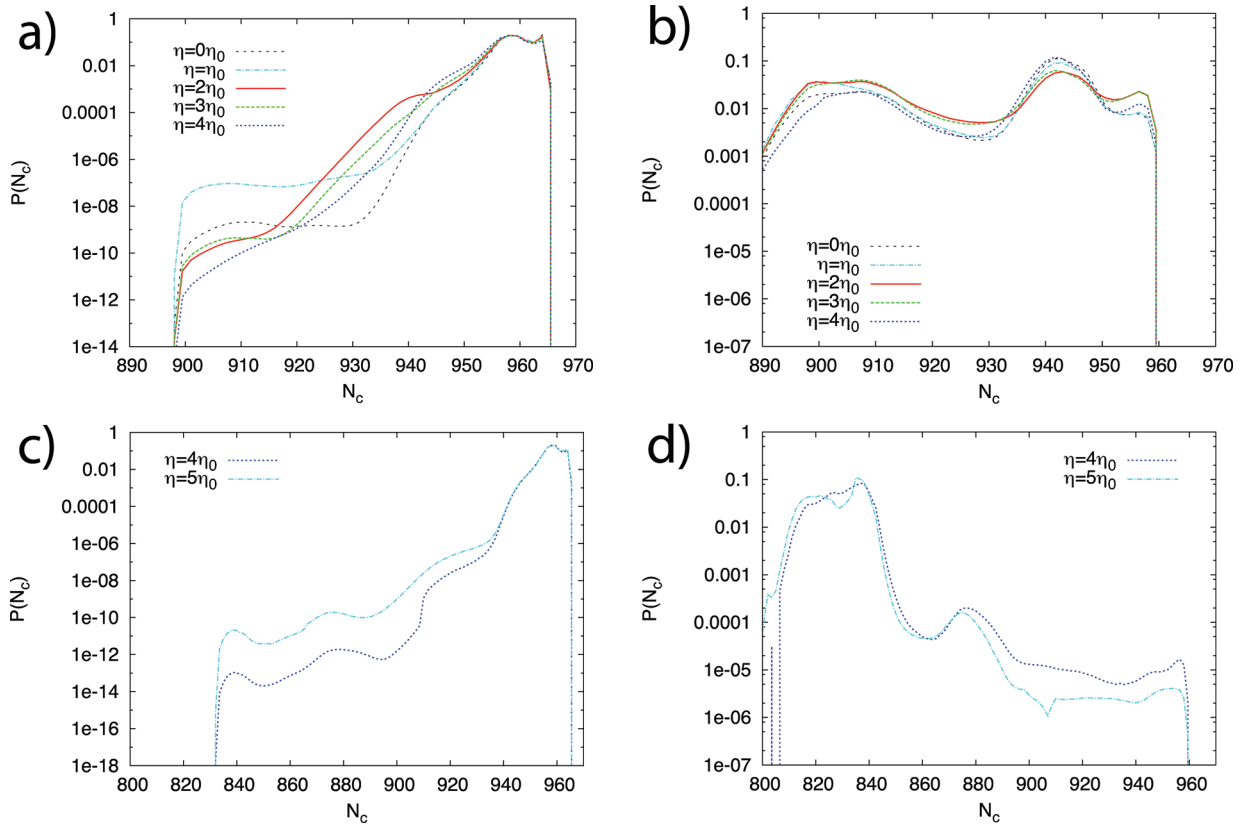

Figure 6. N_c histograms for both pathways. (a,b) The unfolding and refolding ensembles of path M, respectively. The histograms for all flow pressures are shown and share a similar shape. (c,d) The unfolding and refolding ensembles of path E, respectively. Flow pressures $\eta/\eta_0 = 4$ and 5 are shown. In all panels, the histograms are normalized such that the sum of the 200 points in each curve is equal to 1.

In other words, the ensembles are defined by the histories rather than futures of walkers. Each ensemble has its own set of regions that span the order parameter space. As shown in Dickson et al.,[15] the two sets of regions can be seen as a single set of nonoverlapping regions in an extended space, and transition rates between the basins can be obtained by calculating fluxes in this extended space.

II.D. Simulation Details. In the simulations presented here, the saved entry point lists for each region are divided into two lists of 250 points each. One list is dedicated to points coming from the right (higher N_c) and the other to points coming from the left (lower N_c). This helps ensure that the left and right ensembles are both well described. An element of a list consists of the positions and velocities of all the residues of the molecule, as well as forces from the previous step of the Velocity–Verlet algorithm. Along with these data, we store the weight of the trajectory and a time counter that is used to determine when to perform solvent streaming steps. We found it unnecessary to store the coordinates of the solvent along with the flux input point, since the solvent relaxes almost instantaneously to the presence of the polymer (data not shown), as there are no steric interactions between the polymer and solvent.

In the work below, 2000 RNA time steps in each active sampling region constitute a cycle. We allow 3000 cycles for progressive initialization (phase II) and another 3000 cycles with global weight updates (phase III). We perform a global weight update at the beginning of phase III and again every 600 cycles after that. As will be discussed below, the number of sampling regions used depends on the pathway observed and is either 40 or 84 in each direction, for a total of either 80 or 168 regions in the extended space. The total number of sampling steps depends on how fast regions are initialized in phase II, but it is less than 9.6×10^8 in the 40 region case and less than 2.02×10^9 in the 84 region case.

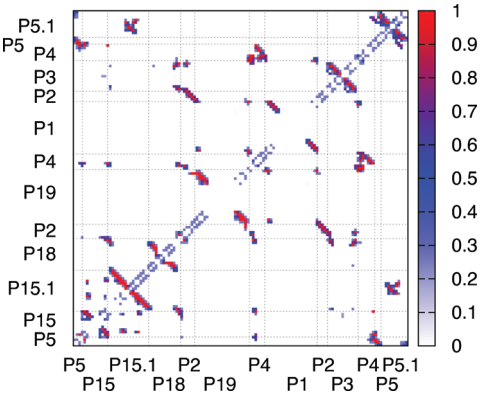

Figure 7. The contact map that is representative of the folded state for all flow rates examined here. This map was obtained using structures from entry points for the region in the unfolding ensemble with the highest value of N_c, at the end of a $\eta = 2\eta_0$ simulation.

III. RESULTS

The RNA-under-flow system was examined at five different flow accelerations: $\eta = \eta_0$, $2\eta_0$, $3\eta_0$, $4\eta_0$, and $5\eta_0$. These correspond to Péclet numbers of 7.5×10^{-3}, 1.5×10^{-2},

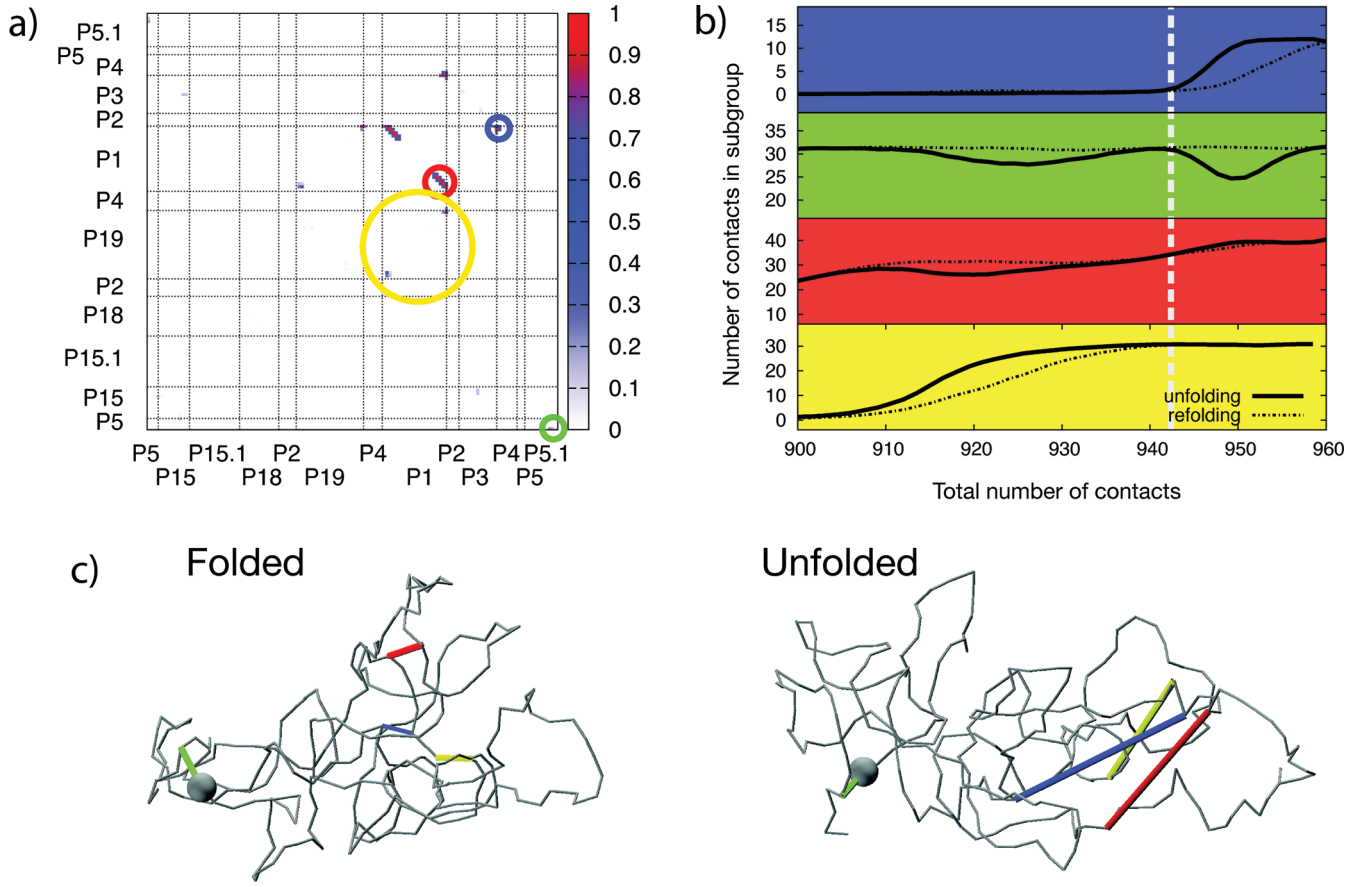

Figure 8. Analysis of path M. (a) Contact difference map obtained by subtracting the contact map of the unfolded state from the contact map of the folded state. This reveals the contacts which are broken along the pathway. The colored circles show the division of these contacts into subgroups. Note that although the contact map is symmetric, the colored circles are only shown in the lower right triangle for clarity. (b) The number of contacts in each subgroup is plotted as a function of the total number of contacts averaged over the $\eta = 2\eta_0$ ensemble of structures. These curves are computed using structures in the saved entry point lists for every region in both the unfolding and refolding ensembles, at many times throughout phase III of the simulation. The vertical line shows the metastable states along the refolding pathway. In the text, the subgroups are numbered 1 to 4, starting at the top. (c) Representative contacts from each group are shown on the RNA molecule for the folded and unfolded states.

2.3×10^{-2}, 3.0×10^{-2}, and 3.9×10^{-2}, respectively. These numbers indicate that thermal motion is much more important than advective motion (i.e., $Pe \ll 1$), but as we show, there are significant flow effects. We also examine the equilibrium case: $\eta = 0$. For each flow rate, we obtained folding and unfolding rates, probability distributions for the numbers of native contacts, and sets of input structures to each umbrella sampling region, from which we can reconstruct folding and unfolding pathways. As detailed below, the folded and unfolded basins were defined by our measure of the number of native contacts, N_c (section II.C).

III.A. Competing Unfolding Pathways. Interestingly, we found two competing reaction pathways for the molecule. One pathway ("path M") occurred by breaking contacts in the middle of the molecule, in and around the P1 loop (residues 150−190, see Figure 2), while the other ("path E") occurred by breaking contacts in and around the P5 region (residues 1−5 and 234−238), which is near the tethered end. We obtained pathways in duplicate for each value of η and found a dependence of the pathway on the flow pressure. For $\eta \leq 3\eta_0$, we observed path M in both trials. For $\eta = 5\eta_0$, we observed path E in both trials. And, for $\eta = 4\eta_0$, we observed path M and path E each once, which suggests that path E is more probable for higher flow rates, and that $\eta = 4\eta_0$ is close to a transition point where the relative probabilities of the two pathways cross over.

The folded basin for both pathways was located at $N_c \geq 960$, and the unfolded basin was placed at the first metastable unfolded structure we encountered along each unfolding pathway. Although these structures could be intermediates to further unfolded states, we will call these structures "unfolded" and their corresponding basins "unfolded basins". For path M, we set the unfolded basin to $N_c \leq 900$, and for path E we set the unfolded basin to $N_c \leq 834$. In both pathways, we define the regions in N_c with an even spacing of $\Delta N_c = 1.5$, giving us 40 regions for the unfolding pathway in path M and 84 regions for the unfolding pathway in path E. There are an equal number of regions in the refolding pathways in both cases, giving us a total of 80 and 168 regions in paths M and E, respectively.

III.B. Pathway Analysis. Probability distribution functions of the order parameter N_c are shown in Figure 6, for both pathways, and for both the unfolding and refolding ensembles. Histograms were saved every 50 cycles, and each curve shown in Figure 6 is an average of the last 20 histograms. For path M, we show histograms for $\eta \leq 4\eta_0$. In the unfolding ensemble (Figure 6a), there is a strong peak at $N_c = 960$ for all flow rates, corresponding to the native state. In the refolding ensemble (Figure 6b), there is

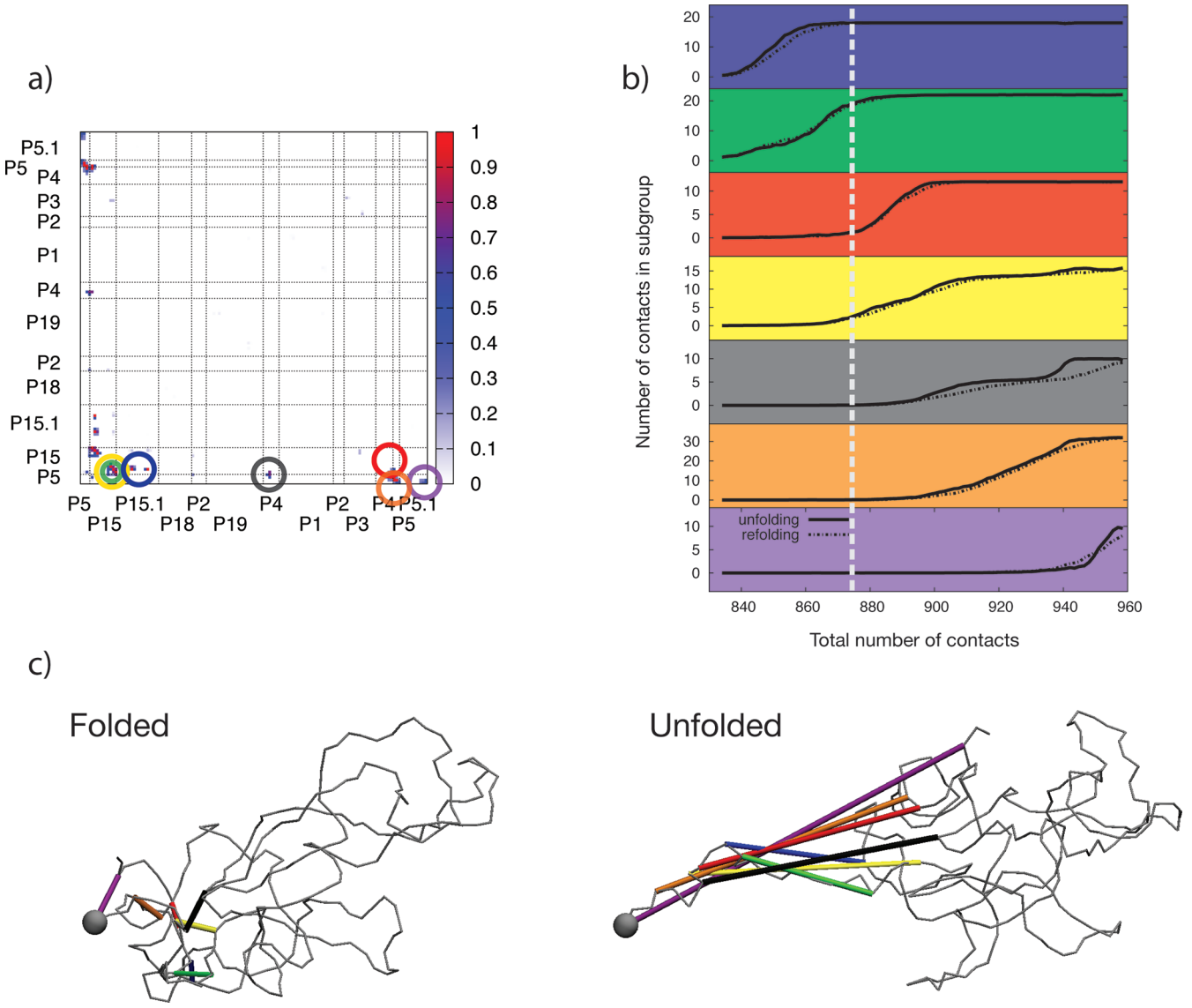

Figure 9. Analysis of path E. See descriptions of panels in Figure 8. (a) Contact difference map. The green and yellow circles define subgroups of secondary and tertiary contacts within the region, respectively. Although the contact map is symmetric, the colored circles are only shown in the lower right triangle for clarity. (b) Note in this pathway that there is a strong overlap between the unfolding and refolding ensembles.

a peak at $N_c = 907$ corresponding to the first metastable unfolded state and an intermediate unfolded state at $N_c = 942$. For path E, we show histograms for $\eta = 4\eta_0$ and $5\eta_0$. Here, the refolding ensemble (Figure 6d) shows that there are two metastable states near the unfolded basin with peaks at $N_c = 820$ and $N_c = 838$, as well as an intermediate at $N_c = 875$.

To characterize structures along the pathways, we construct contact difference maps by subtracting average contact maps for the unfolded states from that for the folded state shown in Figure 7. The contact maps for the unfolded states are computed using the structures from the saved entry point lists for the regions in the refolding ensembles with the lowest values of N_c, and similarly a contact map for the folded state is computed using structures from the saved entry point list for the region in the unfolding ensemble with the highest value of N_c. The contact difference maps are shown in Figures 8a and 9a along with characteristic structures of the folded and unfolded states (Figures 8c and 9c). On the basis of their kinetic behavior, we divide the contacts into groups and track the population of each group as a function of N_c (Figures 8b and 9b).

The vertical lines in Figures 8b and 9b show the metastable states along the refolding pathway. For path M, the local maximum at $N_c = 942$ is associated with the reformation of contacts in the P1 loop (subgroup 3, the third from the top in Figure 8b). For path E, the local maximum at $N_c = 875$ is associated with the reformation of contacts in the P15 loop (subgroups 2 and 4). For path M, we observe that the unfolding and refolding ensembles do not overlap. Specifically, contacts between the end points of the molecule (P5−P5.1 contacts) break and reform along the unfolding pathway but remain intact during the refolding pathway. In this regard, it is important to keep in mind that the unfolding ensemble, as defined in section II.C contains both folded-to-unfolded trajectories and folded-to-folded trajectories. The fact that the feature in question appears in analogous calculations for the reversible system ($\eta = 0$), where there can be no hysteresis, suggests that the P5−P5.1 contacts

Table 1. Unfolding and Refolding Mean First Passage Times for Path M, Obtained for $\eta = 0$, η_0, $2\eta_0$, $3\eta_0$, and $4\eta_0$[a]

η/η_0	unfolding (NEUS), in ms	refolding (NEUS), in ns	refolding (SF), in ns
0	29	1.4	1.7
1	0.60	1.4	0.8
2	140	0.40	1.4
3	170	0.48	0.6
4	3200	0.99	0.5

[a] For refolding pathways, the MFPTs from umbrella sampling (NEUS) and straightforward sampling (SF) are shown.

Table 2. Unfolding and Refolding Mean First Passage Times for Path E, Obtained for $\eta = 4\eta_0$ and $5\eta_0$[a]

η/η_0	unfolding (NEUS), in ms	refolding (NEUS), in μs	refolding (SF), in μs
4	45000	0.76	0.08
5	670	4.9	1.2

[a] For refolding pathways, the MFPTs from umbrella sampling (NEUS) and straightforward sampling (SF) are shown.

are broken along folded-to-folded trajectories and that this process is not a causal part of the path M unfolding mechanism.

There are variations in the contact subgroup projections between the $\eta = 2\eta_0$ ensemble (shown in Figure 8b) and the $\eta = 0$ and $\eta = \eta_0$ ensembles (not shown). Specifically, at N_c = 930, contacts in subgroup 4 are still mostly intact for $\eta = 2\eta_0$ but are mostly broken in the $\eta = 0$ and $\eta = \eta_0$ ensembles. This difference in the pathway coincides with the difference in shape of the unfolding N_c histograms shown in Figure 6a. For $\eta = 0$ and $\eta = \eta_0$, the major drop in probability has already occurred at N_c = 930 (going from right to left), where for the others, the probability continues to drop significantly for $N_c < 930$.

III.C. Transition Rates. The mean first passage times of the unfolding processes are given in Tables 1 and 2 for paths M and E, respectively. These range from 0.60 to 3200 ms for path M and 0.6 to 45 s for path E. As each dynamics step is 40 fs, these correspond to numbers of dynamics steps between 1.6×10^{10} and 1.1×10^{15}. The unfolding and refolding MFPTs are shown as functions of flow pressure in Figure 10.

Although we are only able to obtain unfolding rates for a small number of η values, the data suggests counterintuitive behavior for path M. For small flow rates, the MFPT decreases with increasing flow, which is intuitive, since one would expect the flow field to destabilize folded structures. However, for $\eta > \eta_0$, the MFPT increases with the flow rate; unfolding becomes more difficult as greater flow is applied to the system. Such behavior could be caused by larger flow gradients at the $y = 0$ boundary, causing nucleotides in the P1 loop to be pushed together rather than pulled apart. The difference in pathways between the $\eta \leq \eta_0$ flow rates and the $\eta \geq 2\eta_0$ flow rates described above could also explain the nonmonotonic rate behavior seen here, since the different pathways could involve different interactions with the flowing medium. Further sampling at intermediate flow rates, as well as isolated studies of the different intermediates, would be helpful to confirm this trend. For the two data points obtained for path E, the MFPT for unfolding decreases with increasing flow rate.

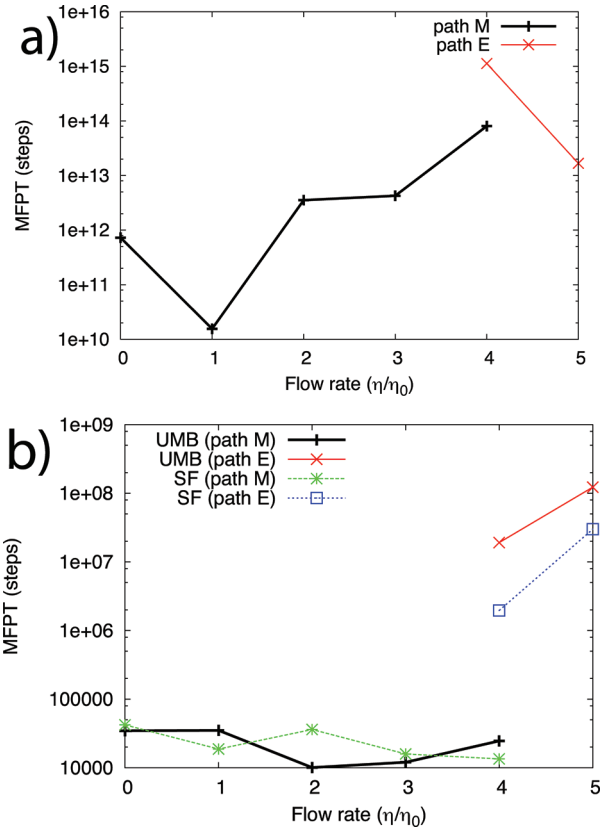

Figure 10. (a) Mean first passage times for unfolding events, as predicted by NEUS. For path M, this is the average number of steps required to go from N_c = 960 to N^c = 900, and for path E, this is the average number of steps to go from N_c = 960 to N_c = 834. (b) Mean first passage times for refolding events, comparing umbrella sampling (UMB) and straightforward trajectories (SF). These agree to within an order of magnitude.

We note that the MFPTs for path M and path E are not directly comparable, since the former measures the average amount of time to go from 960 to 900 contacts, and the latter measures the average amount of time to go from 960 to 834 contacts.

The rates of refolding are also given in Tables 1 and 2. They are much faster, which makes comparisons with straightforward trajectories possible. We use the umbrella sampling saved entry point lists to generate an initial unfolded ensemble for each flow rate, since umbrella sampling is our only access to physically weighted unfolded states. We compare refolding rates for both pathways and all flow pressures, which agree to within an order of magnitude. For path M, the refolding MFPT is short (~1 ns) and relatively constant with varying flow rate. For path E, the refolding MFPTs are longer, since the unfolded state is more stable, and increase with increasing flow rate: 0.76 μs for $\eta = 4\eta_0$ and 4.9 μs for $\eta = 5\eta_0$. The behavior suggests that, in this regime, higher flow fields stabilize the unfolded state.

To illustrate the importance of the enhanced sampling algorithm for the unfolding simulations, we computed 16 independent trajectories of 16 μs (4×10^8 dynamics steps) starting from structures taken from the folded basin. These trajectories were run using $\eta = 5\eta_0$, and "unfolding" was defined as reaching 900 contacts instead of the usual 834 for path E, in order to increase the probability of observing an unfolding event. Using NEUS, we found the MFPT for this process was 0.21 ms, making the length of

the straightforward trajectories 12.5% of the predicted MFPT, and no unfolding events were observed. These simulations required 30 days of computation on 16 2.5 GHz Intel Xeon processors. This also emphasizes the computational benefit of parallelization, as the $\sim 2 \times 10^9$ steps for the largest umbrella sampling simulations were completed in ~30 h of computation on 64 processors. However, even if a similar parallelization scheme using 64 processors was employed for straightforward trajectories, we predict that it would still take an average of ~1900 years to observe a single path E unfolding trajectory for $\eta = 4\eta_0$, and many times that to observe an ensemble of unfolding events.

IV. CONCLUSION

Here, we have presented a parallel version of NEUS and applied it to a coarse-grained macromolecular system driven far from equilibrium by flow. We obtained folding and unfolding rates and mechanisms for a range of flow speeds. This range was chosen to be physically reasonable yet result in significant flow effects. It is large compared to 1.6×10^{-5}, the Péclet number of the flow used to change the magnesium ion concentrations in the RNase P RNA single molecule experiments of Qu et al.,[23] and our simulations suggest that flow did not contribute to the dynamics discussed in refs 23 and 24, at least at moderately high magnesium ion concentrations, which strongly favor the folded state. A lack of knowledge of the structure of the RNA at low magnesium ion concentrations prevents us from assessing that situation.

Due to the stability of the native state, unfolding transitions were extremely slow, occurring as slowly as once in every 1.1×10^{15} dynamics steps, or every 45 s in real time. We observed two different unfolding pathways, one where secondary contacts were broken in the P1 loop, and another where contacts were broken in and around the P5 loop, which is near the tethered end point. We defined unfolded and folded states using an order parameter that measures the number of native contacts. If one were to use more than one order parameter, sampling could be enforced separately along these two pathways. This would allow for a more precise description of the competition between the two pathways for a given flow rate, and a description of the transition between the pathways of maximum probability as the flow rate changes. Work is currently underway to achieve this goal. The parallelization strategy presented here for piecewise sampling methods will enable treatment of increasingly complex order parameter spaces as large-scale computational architectures continue to grow in size.

AUTHOR INFORMATION

Corresponding Author

*E-mail: dinner@uchicago.edu.

ACKNOWLEDGMENT

We would like to thank Nicholas Guttenberg and Jonathan Weare for useful discussions on the algorithm and Glenna Smith and Norbert Scherer for help with the RNA model. We would also like to thank Lorenzo Pesce for help running NEUS on the Beagle Cray XE6 Supercomputer. This work was supported by National Science Foundation grant no. MCB-0547854, an Argonne−University of Chicago Strategic Collaborative Initiative Award, and the Natural Sciences and Engineering Research Council. Most of the calculations were run on "Fusion," a 320-node computing cluster operated by the Laboratory Computing Resource Center at Argonne National Laboratory, which is supported by the Office of Science of the U.S. Department of Energy under contract DE-AC02-06CH11357. Scaling data were obtained for Intrepid, a Blue Gene/P supercomputer at the Argonne Leadership Computing Facility at Argonne National Laboratory, which is supported by the Office of Science of the U.S. Department of Energy under contract DE-AC02-06CH11357, and for Beagle, a Cray XE6 supercomputer, which is supported in part by NIH through resources provided by the Computation Institute, University of Chicago and Argonne National Laboratory, under grant S10 RR029030-01.

REFERENCES

(1) Liphardt, J.; Onoa, B.; Smith, S. B.; Tinoco, I.; Bustamante, C. *Science* **2001**, *292*, 733–737.
(2) Lin, Y.; Zhao, T.; Jian, X.; Farooqui, Z.; Qu, X.; He, C.; Dinner, A. R.; Scherer, N. F. *Biophys. J.* **2009**, *96*, 1911–1917.
(3) Comstock, M. J.; Ha, T.; Chemla, Y. R. *Nat. Methods* **2011**, *8*, 335–340.
(4) Sotomayor, M.; Schulten, K. *Science* **2007**, *316*, 1144–1148.
(5) Hu, J.; Ma, A.; Dinner, A. R. *J. Chem. Phys.* **2006**, *125*, 114101.
(6) Dellago, C.; Bolhuis, P. G. *Advanced Computer Simulation Approaches for Soft Matter Sciences III*; Springer-Verlag: Berlin, 2009; Vol. 221, pp 167−233.
(7) Vanden-Eijnden, E. *Annu. Rev. Phys. Chem.* **2010**, *61*, 391–420.
(8) Frenkel, D.; Smit, B. *Understanding Molecular Simulation: From Algorithms to Applications*; Academic Press: London, 2002; pp 192−196; 389−397; 431−462.
(9) Allen, R. J.; Warren, P. B.; ten Wolde, P. R. *Phys. Rev. Lett.* **2005**, *94*, 018104.
(10) Allen, R. J.; Frenkel, D.; ten Wolde, P. R. *J. Chem. Phys.* **2006**, *124*, 024102.
(11) Allen, R. J.; Frenkel, D.; ten Wolde, P. R. *J. Chem. Phys.* **2006**, *124*, 194111.
(12) Allen, R. J.; Valeriani, C.; ten Wolde, P. R. *J. Phys.: Condens. Matter* **2009**, *21*, 463102.
(13) Warmflash, A.; Bhimalapuram, P.; Dinner, A. R. *J. Chem. Phys.* **2007**, *127*, 154112.
(14) Dickson, A.; Warmflash, A.; Dinner, A. R. *J. Chem. Phys.* **2009**, *130*, 074104.
(15) Dickson, A.; Warmflash, A.; Dinner, A. R. *J. Chem. Phys.* **2009**, *131*, 154104.
(16) Dickson, A.; Dinner, A. R. *Annu. Rev. Phys. Chem.* **2010**, *61*, 441–59.
(17) Huber, G. A.; Kim, S. *Biophys. J.* **1996**, *70*, 97–110.
(18) Zhang, B. W.; Jasnow, D.; Zuckerman, D. M. *Proc. Natl. Acad. Sci. U.S.A.* **2007**, *104*, 18043–18048.
(19) Bhatt, D.; Zhang, B. W.; Zuckerman, D. M. *J. Chem. Phys.* **2010**, *133*, 014110.
(20) Bhatt, D.; Zuckerman, D. M. *J. Chem. Theory Comput.* **2010**, *6*, 3527–3539.
(21) Zhang, B. W.; Jasnow, D.; Zuckerman, D. M. *J. Chem. Phys.* **2010**, *132*, 054107.
(22) Smith, G. J.; Lee, K. T.; Qu, X.; Xie, Z.; Pesic, J.; Sosnick, T. R.; Pan, T.; Scherer, N. F. *J. Mol. Biol.* **2008**, *378*, 943–953.
(23) Qu, X.; Smith, G. J.; Lee, K. T.; Sosnick, T. R.; Pan, T.; Scherer, N. F. *Proc. Natl. Acad. Sci. U.S.A.* **2008**, *105*, 6602–6607.
(24) Li, Y.; Qu, X. H.; Ma, A.; Smith, G. J.; Scherer, N. F.; Dinner, A. R. *J. Phys. Chem. B* **2009**, *113*, 7579–7590.
(25) Delgado-Buscaglioni, R. *Phys. Rev. Lett.* **2006**, *96*, 088303.
(26) Chandler, D. *Introduction to Modern Statistical Mechanics*; Oxford University Press: New York, 1987; pp 168−175.
(27) Vanden-Eijnden, E.; Venturoli, M. *J. Chem. Phys.* **2009**, *131*, 044120.
(28) Nieplocha, J.; Harrison, R. J.; Littlefield, R. J. *J. Supercomput.* **1996**, *10*, 169–189.

(29) Hyeon, C.; Thirumalai, D. *Biophys. J.* **2007**, *92*, 731–743.
(30) Kremer, K.; Grest, G. S. *J. Chem. Phys.* **1990**, *92*, 5057–5086.
(31) Weeks, J. D.; Chandler, D.; Andersen, H. C. *J. Chem. Phys.* **1971**, *54*, 5237.
(32) Kazantsev, A. V.; Krivenko, A. A.; Harrington, D. J.; Holbrook, S. R.; Adams, P. D.; Pace, N. R. *Proc. Natl. Acad. Sci. U.S.A.* **2005**, *102*, 13392–13397.
(33) Malevanets, A.; Kapral, R. *J. Chem. Phys.* **1999**, *110*, 8605–8613.
(34) Ihle, T.; Kroll, D. M. *Phys. Rev. E* **2001**, *63*, 020201.
(35) Lamura, A.; Gompper, G.; Ihle, T.; Kroll, D. M. *Europhys. Lett.* **2001**, *56*, 319–325.
(36) Allahyarov, E.; Gompper, G. *Phys. Rev. E* **2002**, *66*, 036702.
(37) Kikuchi, N.; Pooley, C. M.; Ryder, J. F.; Yeomans, J. M. *J. Chem. Phys.* **2003**, *119*, 6388–6395.
(38) Webster, M. A.; Yeomans, J. M. *J. Chem. Phys.* **2005**, *122*, 164903.

JCTC Journal of Chemical Theory and Computation

ARTICLE

pubs.acs.org/JCTC

Computing Alchemical Free Energy Differences with Hamiltonian Replica Exchange Molecular Dynamics (H-REMD) Simulations

Yilin Meng,[†] Danial Sabri Dashti,[‡] and Adrian E. Roitberg[*,§]

[†]Department of Biochemistry and Molecular Biology, University of Chicago, Chicago, Illinois 60637

[‡]Department of Physics and Quantum Theory Project, University of Florida, Gainesville, Florida 32611-8435

[§]Department of Chemistry and Quantum Theory Project, University of Florida, Gainesville, Florida 32611-8435

ABSTRACT: Alchemical free energy calculations play a very important role in the field of molecular modeling. Efforts have been made to improve the accuracy and precision of those calculations. One of the efforts is to employ a Hamiltonian replica exchange molecular dynamics (H-REMD) method to enhance conformational sampling. In this paper, we demonstrated that the H-REMD method not only improves convergence in alchemical free energy calculations but also can be used to compute free energy differences directly via the Free Energy Perturbation (FEP) algorithm. We show a direct mapping between the H-REMD and the usual FEP equations, which are then used directly to compute free energies. The H-REMD alchemical free energy calculation (replica exchange free energy perturbation, REFEP) was tested on predicting the pK_a value of the buried Asp26 in thioredoxin. We compare the results of REFEP with TI and regular FEP simulations. REFEP calculations converged faster than those from TI and regular FEP simulations. The final predicted pK_a value from the H-REMD simulation was also very accurate, only 0.4 pK_a units above the experimental value. Utilizing the REFEP algorithm significantly improves conformational sampling, and this in turn improves the convergence of alchemical free energy simulations.

INTRODUCTION

Free energy, especially the free energy difference between two states, is a crucial quantity in the study of chemical and biological systems.[1] Knowledge of the free energy differences can help us understand the behaviors of such systems. For example, the free energy of binding is one of the criteria used to evaluate the performance of drugs.[2] Therefore, one important aspect of molecular modeling is to yield accurate free energy differences efficiently. Many free energy calculation methodologies (such as free energy perturbation,[3] thermodynamic integration,[4] umbrella sampling,[5−7] and Jarzynski's equality[8]) as well as analysis techniques (such as the weighted histogram analysis method[9] and Bennett acceptance ratio method[10,11]) have been developed to achieve this goal. In general, free energy calculations could be divided into alchemical free energy and conformational free energy calculations. The alchemical free energy calculations are often employed when studying the free energy differences of processes that involve changes in noncovalent interactions. In an alchemical free energy simulation, a nonphysical reaction coordinate λ is generally adopted in order to connect the initial and final states. This reaction coordinate is usually expressed as an interpolation of the initial and final states. Thus, an alchemical process is achieved through a series of intermediate states having no direct physical meaning. Since the free energy difference between two states is a state function, the actual choice of coordinate cannot, in the limit of infinite sampling, affect qthe results. Free energy perturbation (FEP) and thermodynamic integration (TI) are two common methodologies that are utilized in alchemical free energy computations.

One important issue in alchemical free energy calculations is the convergence of the free energy difference versus computational cost. The convergence is particularly difficult in systems involving slow structural transition or large environmental reorganization as λ changes.[12−14] Therefore, conformational sampling is crucial in alchemical free energy calculations. Enhanced sampling methods, such as replica exchange molecular dynamics (REMD),[15] orthogonal space random walk (OSRW),[14] and accelerated molecular dynamics (AMD)[16] have been applied to free energy simulations in order to accelerate conformational sampling and, in turn, to yield accurate and converged free energy differences. Among the enhanced sampling methodologies, the REMD method is of particular interest because the weight of each state is a priori known (Boltzmann factor). The REMD algorithm was initially introduced by Sugita and Okamoto in 1999. In their REMD algorithm, N noninteracting copies (replicas) of a system are simulated at N different temperatures (one each). Regular MD is performed, and periodically an exchange of configurations between two (usually adjacent) temperatures is attempted. Many variants of the original REMD method have been developed. One of them is the so-called "Hamiltonian REMD (H-REMD)".[17−20] In the H-REMD algorithms, replicas differ in their potential energies but (usually) have the same temperature. In practice, different ways of assigning the potential energy function to replicas have been developed. For example, Fukunishi et al.[17] scaled hydrophobic interactions and van der Waals interactions. Protein−water as well as water−water interactions are scaled in the replica exchange with solute tempering (REST) algorithm.[18] Coarse-grained potential energy functions (low resolution) are combined with

Received: March 3, 2011
Published: July 28, 2011

all-atom force fields (high resolution) in the resolution REMD algorithm.[19−21]

Both temperature-based and Hamiltonian-based REMD have been applied to alchemical free energy calculations. Woods et al.[13,22] and Rick[23] have combined the temperature-based REMD with TI calculation. A temperature-based REMD simulation is conducted at each state along the reaction coordinate. Woods et al.[13,22] have also applied the H-REMD methodology to FEP and TI calculations. Each replica in the H-REMD simulation represents a state along the reaction coordinate λ, and a periodic swap in λ is attempted. Relative solvation free energy of water and methane as well as the relative binding free energies of halides to calis[4]pyrrole have been calculated in this way.[22] The Yang group has developed a dual-topology alchemical H-REMD (DTA-HREM) method.[24] Their method was tested on the free energy of mutating an asparagine amino acid (with two ends blocked) to leucine. More recently, the Roux group coupled the FEP methodology with the distributed replica technique (REPDSTR).[25,26] An additional acceleration in the sampling of the side-chain dihedral angle was also incorporated when Jiang and Roux utilized the FEP/H-REMD method to study the absolute binding free energy of *p*-xylene to the T4 lysozyme L99A mutant.[26] In all of those studies, the conformational sampling and convergence of free energy computations showed significant improvement when the REMD method was applied. The protocol presented here accelerates convergence but, of course, does not solve know problems in the field related to enhanced sampling of coordinates orthogonal to λ space, which would hamper many of the current methods.

In this paper, we will demonstrate that FEP is actually already incorporated in the H-REMD method in an elegant and formal way. The REFEP method is shown to be not only an enhanced sampling method but also a free energy calculation algorithm. We will apply the REFEP method to the pK_a prediction of thioredoxin Asp26. The experimental pK_a value of 7.5 has been shown to be one of the largest shifted from the intrinsic pK_a value[27,28] and, hence, makes it an interesting case to be studied theoretically. TI and FEP (regular molecular dynamics for conformational sampling) alchemical free energy simulations have been conducted in order to compare with REFEP simulations. A very accurate theoretical pK_a value is obtained from REFEP simulations. The convergence of the free energy difference and pK_a value is achieved in REFEP simulations much faster than that in the FEP and TI simulations. The advantage and simplicity of using the H-REMD simulation to compute the alchemical free energy difference is clearly shown.

THEORY AND METHOD

Free Energy Perturbation (FEP). The FEP method, which was initially introduced by Zwanzig in 1954,[3] is a well established method and is considered the most frequently employed methodology in alchemical free energy calculations.[12] The details of the FEP, as well as the TI, methodology and its applications have been extensively reviewed.[12,29−32] Therefore, only a very brief description of the FEP and TI methods will be given here. Consider two states (1 and 2) of a system in the canonical (NVT) ensemble, and their corresponding Helmholtz free energies A_1 and A_2. The Helmholtz free energy difference between two states can be expressed as

$$\Delta A_{1\rightarrow 2} = -k_B T \ln\langle e^{-[U_2(q) - U_1(q)]/k_B T}\rangle_1 \quad (1)$$

Here, k_B is the Boltzmann constant, T is the temperature, and q is the molecular structure. U_1 and U_2 are the potential energies of states 1 and 2, respectively. The bracket with subscript 1 stands for the average calculated over the structural ensemble generated by state 1. In order to compute $\Delta A_{1\rightarrow 2}$, one simulation of state 1 is performed. Once a configuration q is taken, the potential energy difference at configuration q is computed. The ensemble average, which is $\langle e^{-[U_2(q)-U_1(q)]/k_B T}\rangle_1$, can be calculated easily, and hence, $\Delta A_{1\rightarrow 2}$ is obtained. Although the Helmholtz free energies are utilized here, eq 1 can be extended to an isothermal−isobaric (NPT) ensemble and to the Gibbs free energy in the same manner.

When the fluctuations in ΔU in eq 1 are too large, FEP calculations are notoriously hard to converge. The convergence of the FEP calculation will be poor if the overlap in phase space between the two states is small. In order to compute the free energy difference between two states that are very different, intermediate states mixing the two end points are adopted in such a way that the differences between neighbors can be treated as perturbations. A frequently employed method to generate intermediate states is to interpolate potential energy functions linearly, as shown in eq 2. In eq 2, U_1 and U_2 are the potential energy functions of states 1 and 2, respectively. Free energy differences between neighboring states are then computed. The sum of individual free energy differences will be the targeted free energy difference between states 1 and 2 (eq 3). There are many ways of executing FEP calculations involving intermediate states. The double-ended, double-wide,[30,33] and overlap sampling algorithms[34] are among the most popular ones. A thorough description of different algorithms and their performance can be found in a recent review by Jorgensen and Thomas.[30]

$$U(\lambda) = (1-\lambda)U_1 + \lambda U_2 \quad (2)$$

$$\Delta A_{1\rightarrow 2} = -k_B T \sum_i \ln\langle e^{-(U(\lambda_{i+1}) - U(\lambda_i))/k_B T}\rangle_i \quad (3)$$

In practice, computing $\Delta A_{1\rightarrow 2}$ (forward free energy difference) is equally easy (or hard) as computing $\Delta A_{2\rightarrow 1}$ (backward free energy difference), and one is exactly the opposite of the other in principle. Evaluation of forward and backward free energy differences provides an indication of convergence. Furthermore, the potential energy differences generated from both directions can be utilized to reduce statistical error. The Bennett acceptance ratio (BAR) method is a frequently employed scheme to improve the precision of a free energy estimator.[10−12]

Thermodynamic Integration (TI). Another way of writing the free energy difference between two states 1 and 2 is

$$\Delta A_{1\rightarrow 2} = \int_0^1 \left(\frac{\partial A}{\partial \lambda}\right) d\lambda = \int_0^1 \left\langle \frac{\partial U}{\partial \lambda}\right\rangle_\lambda d\lambda \quad (4)$$

Here, λ is a reaction coordinate connecting states 1 and 2, and U is the potential energy of a state along the reaction coordinate. The bracket represents an ensemble average generated at a value of λ. The integration is often evaluated numerically via trapezoidal rule or Gaussian quadrature. If $U(\lambda)$ is constructed as in eq 2, the derivative of $U(\lambda)$ with respect to λ is

$$\frac{\partial U(\lambda)}{\partial \lambda} = U_2 - U_1 \quad (5)$$

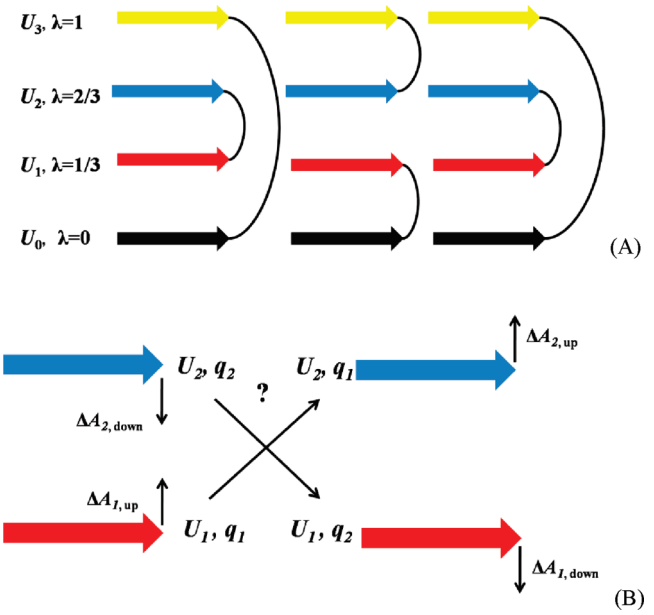

Figure 1. Diagrams displaying the H-REMD exchange algorithm and free energy calculation. (A) Exchange attempt orders. Replicas connected by a curve are neighbors, and attempts are made to exchange molecular configurations (q). (B) Free energy calculations in the H-REMD method. Each replica has two free energy differences: ΔA_{up} and ΔA_{down} from its attempting neighbor form a pair and are computed simultaneously, while ΔA_{down} and ΔA_{up} from its attempting neighbor form the other pair. In exchange attempts (regardless if the attempts are accepted or rejected), two pairs of free energy differences are computed in an alternating fashion utilizing eq 1.

And the free energy difference between states 1 and 2 can be expressed as

$$\Delta A_{1\rightarrow 2} = \int_0^1 \langle U_2 - U_1 \rangle_\lambda \, d\lambda \tag{6}$$

Hence, the ensemble average of potential energy gap between states 1 and 2 at each λ value is needed in a TI calculation. In this manuscript, we use the term TI to refer to constrained TI, in which the value of λ is not allowed to change at each window.

Hamiltonian Replica Exchange Molecular Dynamics (H-REMD). The original REMD method utilizes replicas having different temperatures (T-REMD). Replicas at high temperatures overcome potential energy barriers more easily than those at low temperatures. Another way to overcome potential energy barriers is simply to change the potential energy surface to reduce potential energy barriers. In the H-REMD algorithm, replicas differ in their Hamiltonians but have the same temperature. Regular MD is performed, and an exchange of configurations between two neighboring replicas is attempted periodically.

Figure 1 demonstrates the H-REMD algorithm and the free energy computation in an H-REMD simulation. Let us consider two replicas 1 and 2 with corresponding potential energies U_1 and U_2. By employing the detailed balance condition and Boltzmann weight of each molecular structure, the transition probability can be written as

$$w(q_1 \rightarrow q_2) = \min\{1, e^{-[(U_1(q_2) + U_2(q_1) - U_1(q_1) - U_2(q_2))/k_B T]}\} \tag{7}$$

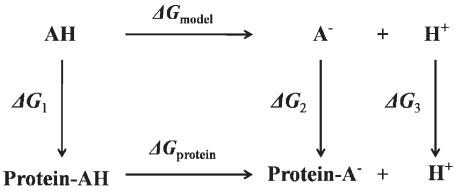

Figure 2. Thermodynamic cycle used to compute the pK_a shift. Both acid dissociation reactions occur in aqueous solution. The "protein-AH" represents the ionizable residue in a protein environment. The "AH" represents the model compound which is usually the same ionizable residue with capped terminii. In practice, a proton does not disappear but instead becomes a dummy atom. The proton still has its position and velocity. The bonded interactions involving the proton are still effective. However, there are no nonbonded interactions for that proton. The change in the ionization state is reflected by changes of partial charges in the ionizable residue.

where q_1 and q_2 are the molecular structures of replicas 1 and 2 before an exchange attempt, respectively. A Monte Carlo–Metropolis criterion[35] is used to evaluate whether the attempted swap of structures between two replicas should be accepted or not.

Equation 7 can be regrouped as

$$w(q_1 \rightarrow q_2) = \min\{1, e^{-[(U_2(q_1) - U_1(q_1) + U_1(q_2) - U_2(q_2))/k_B T]}\} \tag{8}$$

When comparing the exponential terms in eqs 1 and 8, it is clear that eq 8 incorporates all information necessary for a FEP calculation. $U_2(q_1) - U_1(q_1)$ is the potential energy difference computed on the basis of the structural ensemble generated by U_1, while $U_1(q_2) - U_2(q_2)$ is the potential energy difference computed on the basis of the structural ensembles generated by U_2. Every time the transition probability is computed, those potential energy differences can be utilized to compute the ensemble average shown in eq 1. Therefore, $\Delta A_{1\rightarrow 2}$ and $\Delta A_{2\rightarrow 1}$ can be computed on-the-fly utilizing the double-ended scheme. The ensemble average in eq 1 is computed regardless of whether an exchange attempt is accepted or rejected. When employing the H-REMD method to improve conformational sampling in the study of alchemical changes, H-REMD simulations are able to not only enhance conformational sampling but also yield the free energy difference directly. In fact, a regular FEP calculation can be thought of as an H-REMD calculation where no exchanges are allowed between replicas.

In practice, as shown in Figure 1, there are two free energy difference calculations (ΔA_{up} and ΔA_{down}) continuosly associated with each replica. Take replica 1 as an example: $\Delta A_{up} = \Delta A_{1\rightarrow 2}$ while $\Delta A_{down} = \Delta A_{1\rightarrow 0}$. In principle, when converged, $\Delta A_{1,up}$ should be equal to the negative of $\Delta A_{2,down}$:

$$\Delta A_{1,up} = -k_B T \ln\langle e^{-(U_2 - U_1)/k_B T}\rangle_1 = -\Delta A_{2,down} = k_B T \ln\langle e^{-(U_1 - U_2)/k_B T}\rangle_2 \tag{9}$$

Any difference (except for the sign) between the two is an indication of error or lack of convergence.

Convergence was gauged also by the time dependence of the predicted free energy differences, computing ΔG versus simulation length. This provides an asymptotically unbiased estimator for ΔG, and all methods presented here must eventually reach

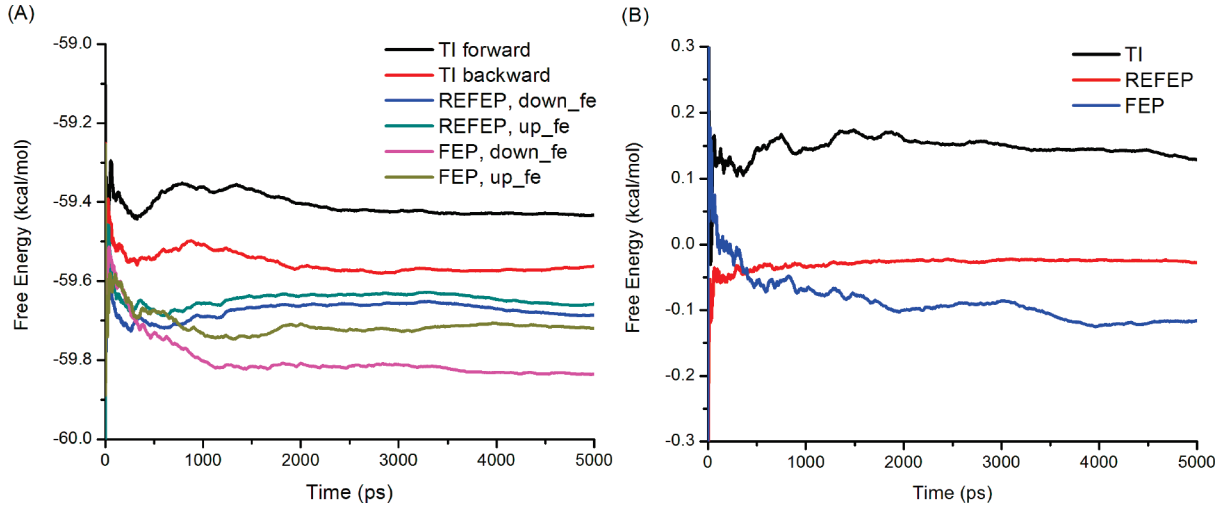

Figure 3. (A) Cumulative average free energy differences between protonated and deprotonated aspartic acid in the model compound (ΔG(AH→A$^-$)). (B) The differences between forward and backward ΔG(AH→A$^-$). (C) Cumulative average free energy differences between protonated and deprotonated Asp26 in thioredoxin (ΔG(proteinAH → proteinA$^-$)). (D) The differences between forward and backward(G-(proteinAH → proteinA$^-$).

Table 1. Free Energy Difference between Protonated and Deprotonated Aspartic Acids Obtained from TI, REFEP, and FEP Alchemical Free Energy Simulations[a]

		TI	REFEP	FEP
ASP model	forward	−59.43 (0.06)	−59.69 (0.05)	−59.84 (0.06)
compound	backward	−59.56 (0.06)	−59.66 (0.05)	−59.72 (0.06)
	average	−59.50 (0.08)	−59.68 (0.08)	−59.78 (0.08)
Asp26 in	forward	−54.35 (0.61)	−54.29 (0.17)	−54.23 (0.56)
thioredoxin	backward	- 55.82 (0.39)	−54.24 (0.14)	−53.84 (0.56)
	average	−55.09 (0.72)	−54.27 (0.22)	−54.04 (0.79)
	forward	5.08 (0.61)	5.40 (0.18)	5.61 (0.56)
ΔG difference	backward	3.74 (0.39)	5.42 (0.15)	5.88 (0.56)
	average	4.41 (0.72)	5.41 (0.23)	5.74 (0.79)
predicted	forward	7.7 (0.4)	7.9 (0.1)	8.1 (0.4)
$pK_{a,protein}$	backward	6.7 (0.3)	7.9 (0.1)	8.3 (0.4)
	average	7.2 (0.5)	7.9 (0.2)	8.2 (0.6)

[a] Free energy differences were calculated by utilizing all data points from a simulation (5 ns for the model compound and 4 ns for Asp26). The ΔG difference is given by ΔG(proteinAH → proteinA$^-$) − ΔG(AH → A$^-$). All backward free energy differences have positive signs and hence are multiplied by −1. Then, the average values of forward and backward free energy differences were computed and reported here. All free energies have units of kcal/mol. The numbers in parentheses are error bars. The error bars for forward and backward free energy differences of "model compound" and "Asp26 in thioredoxin" were calculated via block averages (a simulation was truncated into five blocks). The rest were obtained by error propagations.

the same final value (within error bars). REFEP is presented in this article as showing faster convergence toward the final value.

Simulation Details. Accurately determining the pK_a values of ionizable residues, especially those with large shifts from intrinsic pK_a values, is of great interest both experimentally and computationally.[27,28,36] In this paper, the pK_a calculation of Asp26 in thioredoxin has been selected as a test case in order to compare the performance of alchemical free energy simulations. Asp26 has been found deeply buried in thioredoxin and possesses one of the largest pK_a shifts among protein carboxylic groups.[27,28] Following the protocol employed in the paper of Simonson et al.,[36] the thermodynamic cycle utilized to compute the pK_a value of an ionizable residue is given in Figure 2. As can be seen in Figure 2, the use of a model compound as an auxiliary leg in the thermodynamic cycle makes ΔG_3 (proton to proton) equal to zero. Essentially, the pK_a shift relative to the intrinsic value (p$K_{a,model}$) is computed as

$$pK_a(\text{protein}) = pK_a(model) + \frac{1}{2.303k_BT}[\Delta G(\text{proteinAH} \rightarrow \text{proteinA}^-) - \Delta G(\text{AH} \rightarrow \text{A}^-)] \quad (10)$$

where ΔG(proteinAH → proteinA$^-$) and ΔG(AH → A$^-$) are the free energy differences between protonated and deprotonated aspartic acid in the protein environment and in aqueous solution, respectively. Alchemical free energy simulations were performed in order to yield those two terms. In eq 10, the Gibbs free energy differences are used because experiments determining pK_a values are generally conducted under an isobaric−isothermal condition.

Aspartic acid dipeptide in implicit water solvent was taken as the model compound with a pK_a value taken as 4.0.[37] The oxidized form of thioredoxin (PDB code 2TRX)[38] in implicit water was used in our simulation. Changes in ionization were represented by changes in the partial charges of the aspartic acid side chain (ASH→ASP in the AMBER terminology). Since the van der Waals radius of the proton in aspartic acid is zero for both protonated and deprotonated species, the free energy difference only contains the electrostatic interactions.

Three types of free energy simulations have been performed for both the model compound and the protein: TI (forward and backward), H-REMD-FEP (REFEP), and regular FEP simulations. Our regular FEP simulations were carried out via H-REMD simulations but with all exchange attempts rejected. Comparing the pK_a prediction and free energy convergence from FEP and REFEP simulations will directly indicate the effect of the

enhanced conformational sampling due to the exchanges. Linear interpolation of point charges was carried out in order to assign side chain charges for intermediate states. A seven-point Gaussian quadrature has been selected to compute total free energy difference for TI calculations. Therefore, eight λ values (one end point is needed in either direction) were utilized in the TI simulation. Due to the implementation of the TI algorithm in AMBER, 16 replicas were utilized to ensure the same amount of simulation time for all free energy simulations. A simulation time of 5 ns was used for each λ value and for each replica in the study of the model compound, while for thioredoxin, we used 4 ns runs. Structural swaps between neighboring replicas were attempted every 2 ps (1000 MD steps). No particular attempt was made in this work to optimize the number or location of the replicas, nor the exchange attempt frequency. Work in this area is in progress.

All simulations were done using the AMBER 10 molecular simulation suite,[39] locally modified to add H-REMD/REFEP capabilities. The AMBER ff99SB force field[40] was utilized in all of the simulations. The SHAKE algorithm[41] was used to constrain the bonds connecting hydrogen atoms with heavy atoms in all of the simulations, which allowed the use of a 2 fs time step. The OBC (Onufriev, Bashford, and Case) generalized Born implicit solvent model (*igb* = 5 in the AMBER terminology)[42] was used to model the water environment in all of our calculations. The cutoff for nonbonded interaction and the Born radii was set to 99 Å. This value is larger than the dimension of both systems. Langevin dynamics was employed in order to maintain the temperature at 300 K, using a friction coefficient of 3.0 ps^{-1}.

RESULTS AND DISCUSSIONS

Acceptance Ratio of H-REMD Simulations. The accuracy of FEP depends on the overlaps between phase spaces, which can be measured as overlaps between potential energy difference distributions.[12] The acceptance ratio in an H-REMD simulation is an indication of the overlap between two potential energy difference distributions.[24] Therefore, it could be utilized to monitor the convergence of free energy calculation qualitatively. In our study, large acceptance ratios were observed in both the model compound and protein H-REMD simulation. The acceptance ratio between two neighbors ranged from 0.7 to 0.9 in all H-REMD simulations. Those large acceptance ratios indicate that the overlap in phase space is large.

Aspartic Acid Model Compound Study. The free energy differences on the right-hand side of eq 10 were calculated as described in the Theory and Method section. The cumulative average free energy difference as a function of time is reported here. Figure 3A shows the $\Delta G(AH \rightarrow A^-)$ from TI, H-REMD, and FEP simulations (as mentioned before, a FEP simulation has been performed by rejecting all exchange attempts in an H-REMD simulation). The differences between forward and backward $\Delta G(AH \rightarrow A^-)$ are shown in Figure 3B. A converged alchemical free energy simulation should generate the same forward and backward free energy numerically (except for an opposite sign). Any nonzero value is an indication of free energy not converged.

For a simple system such as aspartic acid in implicit water, 5 ns of simulation time was long enough for $\Delta G(AH \rightarrow A^-)$ to stabilize in all three alchemical free energy simulations, as shown in Figure 3A. The forward and backward $\Delta G(AH \rightarrow A^-)$ at the end of each free energy calculation and the corresponding error bars are listed in Table 1. The forward and backward free energy differences are the same (within error bars) for both REFEP and FEP simulations. However, the TI simulations failed to do that, although the difference was very small (the difference between forward and backward $\Delta G(AH \rightarrow A^-)$ was only 0.13 kcal/mol). The average of forward and backward $\Delta G(AH \rightarrow A^-)$ was taken as the final value of $\Delta G(AH \rightarrow A^-)$ for the model compound and is also reported in Table 1. Clearly, as shown in Figure 3B, the REFEP simulations have converged much faster than the FEP calculations did.

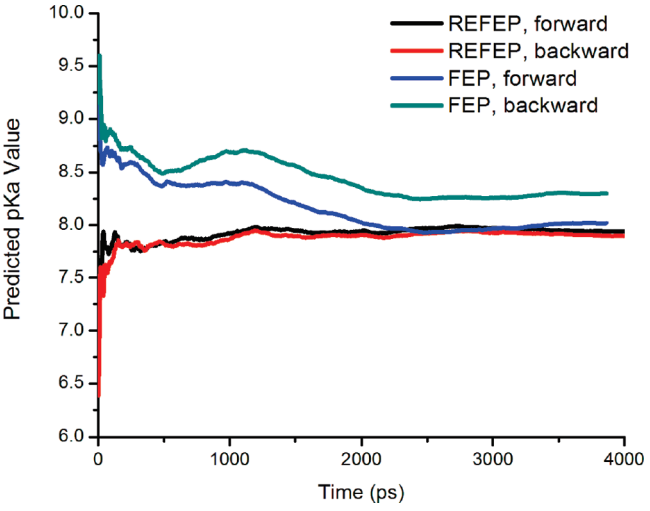

Figure 4. Predicted pK_a value of Asp26 in thioredoxin as a function of time. The $(\Delta G(AH \rightarrow A^-)$ values utilized in eq 10 were −59.68 and −59.78 kcal/mol for REFEP and FEP, respectively. The experimental value is 7.5.

Study on Asp26 in Thioredoxin. The free energy difference between protonated and deprotonated Asp26 is shown in Figure 3C and D. By analogy with the model compound plots, the cumulative average as a function of time is reported. The cumulative average was clearly not converged during the TI simulation, and neither was the difference between forward and backward $\Delta G(\text{proteinAH} \rightarrow \text{proteinA}^-)$. According to Table 1, after 4 ns of TI simulation, the difference between forward and backward free energy was 1.4 kcal/mol, while the uncertainty of the forward and backward free energy differences was 0.61 and 0.39 kcal/mol, respectively. Data not presented here show that TI requires roughly 40 ns of dynamics before converging to results comparable with FEP/REFP. It is worth noting that this comparison is slightly unfair to TI and deserves further explanation. First, we used eight intermediate states for TI versus 16 for FEP/REFEP. This setup, when executed within Amber, uses the same CPU time since the TI implementation is done with dual-topology methods. In fact, reusing the ensemble generated with the FEP Hamiltonians and computing TI values on that ensemble produces very fast-converging results.

For regular FEP free energy calculations, the cumulative averages stabilized after roughly 2.2 ns of simulation, while the cumulative averages for the REFEP simulation stabilized much faster (shown in Figure 3C). Furthermore, Figure 3D illustrates that the difference between forward and backward $\Delta G(\text{proteinAH} \rightarrow \text{proteinA}^-)$ in the REFEP reached a value very close to zero (~0.05 kcal/mol) very quickly. As described previously, the final value of $\Delta G(\text{proteinAH} \rightarrow \text{proteinA}^-)$ was calculated as the average of forward and backward free energy differences. Although the final free energy differences

computed from 4 ns of simulation were the same for REFEP and regular FEP, the calculations converged much faster in REFEP than in FEP simulation. Since the H-REMD and FEP calculations only differed in whether structures were allowed to be exchanged or not, the improvement in alchemical free energy convergence resulted from employing enhanced conformational sampling technique is significant. Data not presented here show that the histograms of $P_1(\Delta U)\exp(-\beta(\Delta U))$ for the calculation of the free energy difference between replicas 1 and 2 for different sampling times are slightly different for FEP and REFEP. The REFEP distributions converge faster with time and sample the left side of the distribution better. This helps rationalize the faster convergence of our technique.

pK_a Prediction for Asp26 in Thioredoxin. The pK_a value of Asp26 in thioredoxin can be computed by eq 10. The final value of $\Delta G(\text{proteinAH} \rightarrow \text{proteinA}^-)$ from the REFEP simulation was −54.3 kcal/mol, with a predicted pK_a value of 7.9, which is only 0.4 pK_a units above the experimental value. The predicted pK_a value with respect to time from REFEP simulations was plotted in Figure 4 in order to demonstrate the convergence of the pK_a prediction. Figure 4 shows that REFEP simulations not only yielded an accurate predicted pK_a value but also achieved convergence very fast. The regular FEP simulation predicted a pK_a value of 8.2, which is 0.7 pK_a units above the experimental value. The convergence in the regular FEP simulation was also worse than that in the REFEP simulation.

CONCLUSIONS

Conformational sampling is crucial in free energy calculations. In the case of alchemical free energy calculations, H-REMD is a useful and popular method to enhance the accuracy and convergence of free energy simulations. In this paper, we have demonstrated that REFEP not only improves conformational sampling in free energy calculations but also yields a free energy difference directly via the FEP algorithm. The implementation of REFEP is trival, once a H-REMD code is in place. The REFEP alchemical free energy calculation was tested on predicting the pK_a value of Asp26 in thioredoxin and compared with TI and regular FEP simulations. Free energy differences from the REFEP simulation converged faster than those from TI and regular FEP simulations. The final predicted pK_a value from the REFEP simulation was very accurate, only 0.4 pK_a unit above the experimental value. Utilizing the REFEP algorithm significantly improves conformational sampling, and this in turn improves the convergence of alchemical free energy simulations.

AUTHOR INFORMATION

Corresponding Author

*E-mail: roitberg@ufl.edu.

ACKNOWLEDGMENT

This work is supported from National Institute of Health under contract 1R01AI073674. Partial funding was provided by NSF award 1047919 to A.E.R. Computer resources and support were provided by the Large Allocations Resource Committee through grant TG-MCA05S010 and the University of Florida High-Performance Computing Center. We thank the reviewers for extremely useful comments that have made this manuscript better.

REFERENCES

(1) *Free energy calculations. Theory and applications in chemistry and biology*; Chipot, C., Pohorille, A., Eds.; Springer Verlag: Berlin, 2007.
(2) Bash, P. A.; Singh, U. C.; Brown, F. K.; Langridge, R.; Kollman, P. A. *Science* **1987**, *235*, 574–576.
(3) Zwanzig, R. W. *J. Chem. Phys.* **1954**, *22*, 1420–1426.
(4) Kirkwood, J. G. *J. Chem. Phys.* **1935**, *3*, 300–313.
(5) Mezei, M. *J. Comput. Phys.* **1987**, *68*, 237–248.
(6) Roux, B. *Comput. Phys. Commun.* **1995**, *91*, 275–282.
(7) Torrie, G. M.; Valleau, J. P. *J. Comput. Phys.* **1977**, *23*, 187–199.
(8) Jarzynski, C. *Phys. Rev. Lett.* **1997**, *78*, 2690–2693.
(9) Kumar, S.; Bouzida, D.; Swendsen, R. H.; Kollman, P. A.; Rosenberg, J. M. *J. Comput. Chem.* **1992**, *13*, 1011–1021.
(10) Bennett, C. H. *J. Comput. Phys.* **1976**, *22*, 245–268.
(11) Shirts, M. R.; Chodera, J. D. *J. Chem. Phys.* **2008**, *129*, 124105.
(12) Pohorille, A.; Jarzynski, C.; Chipot, C. *J. Phys. Chem. B* **2010**, *114*, 10235–10253.
(13) Woods, C. J.; Essex, J. W.; King, M. A. *J. Phys. Chem. B* **2003**, *107*, 13703–13710.
(14) Zheng, L. Q.; Chen, M. G.; Yang, W. *Proc. Natl. Acad. Sci. U. S. A.* **2008**, *105*, 20227–20232.
(15) Sugita, Y.; Okamoto, Y. *Chem. Phys. Lett.* **1999**, *314*, 141–151.
(16) Hamelberg, D.; Mongan, J.; McCammon, J. A. *J. Chem. Phys.* **2004**, *120*, 11919–11929.
(17) Fukunishi, H.; Watanabe, O.; Takada, S. *J. Chem. Phys.* **2002**, *116*, 9058–9067.
(18) Liu, P.; Kim, B.; Friesner, R. A.; Berne, B. J. *Proc. Natl. Acad. Sci. U. S. A.* **2005**, *102*, 13749–13754.
(19) Liu, P.; Voth, G. A. *J. Chem. Phys.* **2007**, *126*, 045106.
(20) Lyman, E.; Ytreberg, F. M.; Zuckerman, D. M. *Phys. Rev. Lett.* **2006**, *96*, 028105.
(21) Lwin, T. Z.; Luo, R. *J. Chem. Phys.* **2005**, *123*, 194904.
(22) Woods, C. J.; Essex, J. W.; King, M. A. *J. Phys. Chem. B* **2003**, *107*, 13711–13718.
(23) Rick, S. W. *J. Chem. Theory Comput.* **2006**, *2*, 939–946.
(24) Min, D. H.; Li, H. Z.; Li, G. H.; Bitetti-Putzer, R.; Yang, W. *J. Chem. Phys.* **2007**, *126*, 144109.
(25) Jiang, W.; Hodoscek, M.; Roux, B. *J. Chem. Theory Comput.* **2009**, *5*, 2583–2588.
(26) Jiang, W.; Roux, B. *J. Chem. Theory Comput.* **2010**, *6*, 2559–2565.
(27) Dyson, H. J.; Tennant, L. L.; Holmgren, A. *Biochemistry* **1991**, *30*, 4262–4268.
(28) Langsetmo, K.; Fuchs, J. A.; Woodward, C. *Biochemistry* **1991**, *30*, 7603–7609.
(29) Christ, C. D.; Mark, A. E.; van Gunsteren, W. F. *J. Comput. Chem.* **2010**, *31*, 1569–1582.
(30) Jorgensen, W. L.; Thomas, L. L. *J. Chem. Theory Comput.* **2008**, *4*, 869–876.
(31) Kollman, P. *Chem. Rev.* **1993**, *93*, 2395–2417.
(32) Straatsma, T. P.; Mccammon, J. A. *Annu. Rev. Phys. Chem.* **1992**, *43*, 407–435.
(33) Jorgensen, W. L.; Ravimohan, C. *J. Chem. Phys.* **1985**, *83*, 3050–3054.
(34) Lu, N. D.; Kofke, D. A.; Woolf, T. B. *J. Comput. Chem.* **2004**, *25*, 28–39.
(35) Metropolis, N.; Rosenbluth, A. W.; Rosenbluth, M. N.; Teller, A. H.; Teller, E. *J. Chem. Phys.* **1953**, *21*, 1087–1092.
(36) Simonson, T.; Carlsson, J.; Case, D. A. *J. Am. Chem. Soc.* **2004**, *126*, 4167–4180.
(37) Bashford, D.; Case, D. A.; Dalvit, C.; Tennant, L.; Wright, P. E. *Biochemistry* **1993**, *32*, 8045–8056.
(38) Katti, S. K.; Lemaster, D. M.; Eklund, H. *J. Mol. Biol.* **1990**, *212*, 167–184.
(39) Case, D. A.; Darden, T. A.; Cheatham, T. E.; Simmerling, C. L.; Wang, J.; Duke, R. E.; Luo, R.; Crowley, M.; Walker, R. C.; Zhang, W.; Merz, K. M.; B.;, W.; Hayik, S.; Roitberg, A. E.; Seabra, G.; Kolossváry, I.;

Wong, K. F.; Paesani, F.; Vanicek, J.; Brozell, S. R.; Steinbrecher, T.; Gohlke, H.; Yang, L.; Tan, C.; Mongan, J.; Hornak, V.; Cui, G.; Mathews, D. H.; Seetin, M. G.; Sagui, C.; Babin, V.; Kollman, P. A. *AMBER 10*; University of California: San Francisco, 2008.

(40) Hornak, V.; Abel, R.; Okur, A.; Strockbine, B.; Roitberg, A.; Simmerling, C. *Proteins: Struct., Funct., Bioinf.* **2006**, *65*, 712–725.

(41) Ryckaert, J. P.; Ciccotti, G.; Berendsen, H. J. C. *J. Comput. Phys.* **1977**, *23*, 327–341.

(42) Onufriev, A.; Case, D. A.; Bashford, D. *J. Comput. Chem.* **2002**, *23*, 1297–1304.

JCTC Journal of Chemical Theory and Computation

ARTICLE

pubs.acs.org/JCTC

Multisite λ Dynamics for Simulated Structure−Activity Relationship Studies

Jennifer L. Knight and Charles L. Brooks, III*

Department of Chemistry & Department of Biophysics, University of Michigan, 930 N. University Ave., Ann Arbor, Michigan 48109, United States

ABSTRACT: Multisite λ dynamics (MSλD) is a new free energy simulation method that is based on λ dynamics. It has been developed to enable multiple substituents at multiple sites on a common ligand core to be modeled simultaneously and their free energies assessed. The efficacy of MSλD for estimating relative hydration free energies and relative binding affinties is demonstrated using three test systems. Model compounds representing multiple identical benzene, dihydroxybenzene, and dimethoxybenzene molecules show that total combined MSλD trajectory lengths of ∼1.5 ns are sufficient to reliably achieve relative hydration free energy estimates within 0.2 kcal/mol and are less sensitive to the number of trajectories that are used to generate these estimates for hybrid ligands that contain up to 10 substituents modeled at a single site or five substituents modeled at each of two sites. Relative hydration free energies among six benzene derivatives calculated from MSλD simulations are in very good agreement with those from alchemical free energy simulations (with average unsigned differences of 0.23 kcal/mol and R^2 = 0.991) and the experiment (with average unsigned errors of 1.8 kcal/mol and R^2 = 0.959). Estimates of the relative binding affinities among 14 inhibitors of HIV-1 reverse transcriptase obtained from MSλD simulations are in reasonable agreement with those from traditional free energy simulations and the experiment (average unsigned errors of 0.9 kcal/mol and R^2 = 0.402). For the same level of accuracy and precision, MSλD simulations are achieved ∼20−50 times faster than traditional free energy simulations and thus with reliable force field parameters can be used effectively to screen tens to hundreds of compounds in structure-based drug design applications.

1. INTRODUCTION

Free energy calculations are fundamental to obtaining accurate theoretical estimates of hydration free energies and protein−ligand binding affinities.[1−5] Traditionally, free energy differences are calculated from alchemical free energy simulations, which are analyzed by free energy perturbation, thermodynamic integration, or Bennett acceptance ratio methods.[6,7] These traditional alchemical simulations mutate one compound into another in a stepwise fashion using several unphysical intermediates to compute relative free energies or, alternatively, grow a compound from nothing to obtain an absolute free energy. In practice, however, due to the number of intermediates that must be investigated and the length of the simulations, these methods are generally too computationally intensive to be used routinely in structure-based drug design or systematic exploration of chemical modifications of a lead compound.

λ dynamics is an alternative free energy method in which the transformation coordinate between the end states, the parameter "λ", is treated as a dynamic variable in the simulations and is propagated in a manner that is analogous to changes in the atomic coordinates.[8,9] In this way, instead of performing simulations for fixed λ values, all of the intermediate states are explored in a single simulation. λ dynamics has been used to compute hydration free energies[9,10] and binding free energies[11,12] and to identify ligand binding modes.[13−15] λ-dynamics simulation methods have stimulated the development of other theoretical approaches for a variety of applications in which the λ parameter scales the potential energy and dynamically varies throughout the course of a simulation. For example, constant pHMD (CPHMD) simulations account for accurate protonation states of protein residues,[16−18] Abrams et al.'s[19] adiabatic free energy dynamics (AFED) generates free energy profiles along a reaction path, and Zheng et al.'s orthogonal space random walk method enhances free energy simulations[20] and conformational sampling.[21] Bitetti-Putzer et al.[22] uses λ as a self-regulating sampling variable to efficiently traverse high-energy barriers and to thoroughly explore low-energy basins, and Tivado-Rives et al.'s[23] Just Add Water (JAWS) strategy identifies positions of water molecules in binding sites of protein−ligand complexes. Still other simulation methods use dynamic λ variables in discretized λ space, such as simulated scaling,[24] FEP/REMD,[25] and BEDAM.[5,26]

In traditional alchemical free energy calculations, the hybrid potential energy function is defined by

$$V(X,\{x\}) = V_{\mathrm{env}}(X) + (1-\lambda)\,V(X,x_1) + \lambda V(X,x_2) \qquad (1)$$

where X and x_i are the atomic coordinates associated with the environment and ligand i, respectively, V_{env} is the potential energy involving the environment atoms only, and $V(X,x_i)$ is the interaction energy computed between ligand i and the environment. In this formalism, a hybrid ligand can be constructed in which all atoms that are common to both ligands are represented once, while all atoms that are unique to each ligand are represented explicitly. Atoms in the common ligand core are then treated as part of the environment, while atoms that are unique to each ligand are modeled as substituents on this common core. In λ dynamics, the hybrid molecule is extended

Received: June 28, 2011
Published: August 10, 2011

to N ligands, and the corresponding hybrid potential energy function is constructed to be

$$V(X,\{x\},\{\lambda\}) = V_{\mathrm{env}}(X) + \sum_{i=1}^{N} \lambda_i (V(X,x_i) - F_i) \quad (2)$$

with the constraints

$$0 \le \lambda_i \le 1 \quad (3a)$$

$$\sum_{i=1}^{N} \lambda_i = 1 \quad (3b)$$

where λ_i is the coupling parameter associated with ligand i and F_i is a precalculated biasing potential that enhances the sampling of each $\lambda_i \approx 1$ state. The dynamics of the system are generated from the extended Hamiltonian:

$$H_o(X,\{x\},\{\lambda\}) = T_x + T_\lambda + V(X,\{x\},\{\lambda\}) \quad (4)$$

where T_x and T_λ are the kinetic energies of the atomic coordinates and λ variables, respectively (λ variables are treated as volumeless particles with mass m_λ). A ligand is defined to be "dominant" over other ligands when its corresponding λ value approaches 1. The difference in the changes in free energy in a given environment between ligands i and j is

$$\Delta\Delta G_{j\rightarrow i} = -k_B T \ln \frac{P(\lambda_i = 1, \{\lambda_{m\neq i} = 0\})}{P(\lambda_j = 1, \{\lambda_{m\neq j} = 0\})} \quad (5)$$

where $P(\lambda_i = 1,\{\lambda_{m\neq i} = 0\})$ corresponds to the amount of time ligand i has $\lambda_i = 1$ during the λ-dynamics simulation; in practice, the amount of time ligand i has $\lambda_i > 0.8$ during the simulation is counted. The relative binding affinities for each pair of ligands that are represented in the hybrid molecule can be estimated directly from simulations in the protein environment where the $\{F_i\}$ in eq 2 is assigned to be the relative free energy estimates for the solvent arm of the thermodynamic cycle. For a more detailed discussion of λ dynamics, the reader is referred to ref 9.

The original λ-dynamics methodology was implemented for modeling multiple substituents at a single site on a common ligand framework. By constrast, many experimental combinatorial chemistry approaches systematically vary substituents at multiple sites on a core compound. For example, structure−activity relationship studies often evaluate the efficacy of putative drug molecules that are chemical variants of a promising lead compound.

Here, we present a new version of λ dynamics that enables multiple substituents at multiple sites on a common ligand core to be modeled and demonstrate its usefulness for estimating series of relative hydration free energies and ligand binding affinities. With the ability to examine multiple substituents at multiple sites on a core molecule, this multisite λ-dynamics (MSλD) method has the potential to evaluate the relative free energies of many compounds simultaneously and further increase the efficiency of the λ-dynamics approach to free energy calculations. Furthermore, we have developed a strategy to implicitly satisfy the holonomic constraints on $\{\lambda\}$ that are defined in eq 3 and thus substantially improve the numerical stability of these simulations up to timesteps of 2 fs.[27]

First, using hybrid ligands that represent series of benzene, dihydroxybenzene, and dimethoxybenzene compounds, we demonstrate the robustness of MSλD for thorough sampling in vacuum and solvent environments. Second, we show that relative hydration free energies of six benzene derivatives that are estimated from MSλD compare very well with those obtained from traditional alchemical free energy simuations but at ∼1/20 the computational cost. Finally, we illustrate how estimates of the components of the relative binding affinities of 14 inhibitors of HIV-1 reverse transcriptase are computed about 50 times faster using MSλD relative to traditional free energy methods and yield comparable quality results. This study reveals the utility of MSλD as an effective sampling strategy in structure-based drug design to screen through on the order of tens to hundreds of variations of a lead compound in a reasonable amount of time.

2. METHODS

2.1. Multisite λ-Dynamics (MSλD) Theory. To enable multiple substituents at multiple sites to be sampled during λ dynamics, we have extended the hybrid potential energy function to be

$$V(X,\{x\},\{\lambda\}) = V_{\mathrm{env}}(X) + \sum_{S=1}^{M_{\mathrm{sites}}} \sum_{i=1}^{N_S} \lambda_{S,i}(V(X,x_{S,i}) - F_{S,i}) + \sum_{S=1}^{M_{\mathrm{sites}}-1} \sum_{i=1}^{N_S} \sum_{T=S+1}^{M_{\mathrm{sites}}} \sum_{j=1}^{N_T} \lambda_{S,i}\lambda_{T,j}(V(x_{S,i},x_{T,j})) \quad (6)$$

with the holonomic constraints:

$$0 \le \lambda_{\alpha,i} \le 1 \quad (7a)$$

$$\sum_{i=1}^{N_\alpha} \lambda_{\alpha,i} = 1 \quad (7b)$$

for each site α. M_{sites} is the total number of sites which contain multiple substituents, and N_S is the number of substituents at site S on the common ligand framework. The double summation in the second term of the hybrid potential accounts for the interactions between the environment and each substituent at each site in the system. The third term accounts for the interactions between each substituent and the substituents modeled at all other sites. Note that substituents at a given site do not "see" each other in these simulations. In this case, a ligand is now described to be "dominant" or "present" when the λ values associated with its constituent substituents are dominant at the same time. For systems with two substituent sites, the relative free energies between two distinct compounds are estimated via

$$\Delta\Delta G_{1,i;2,j\rightarrow 1,k;2,l} = -k_B T \ln \frac{P(\lambda_{1,k} = 1, \lambda_{2,l} = 1)}{P(\lambda_{1,i} = 1, \lambda_{2,j} = 1)} \quad (8)$$

Instead of using the Lagrange multiplier method to satisfy the holonomic constraints in eq 7 explicitly, in this new implementation, we implicitly satisfy the constraints by defining λ's for the N substituents at site α to be

$$\lambda_{\alpha,i} = \frac{e^{5.5\sin\theta_{\alpha,i}}}{\sum_{j=1}^{N_\alpha} \exp(5.5\sin\theta_{\alpha,j})} \quad (9)$$

Using this formalism for MSλD, it is the values of θ that have fictitious masses, m_θ, and are propagated through the equations of motion, not the λ values directly. Thus, the extended Hamiltonian is defined as

$$H_o(X,\{x\},\{\lambda(\theta)\}) = T_x + T_\theta + V(X,\{x\},\{\lambda(\theta)\}) \quad (10)$$

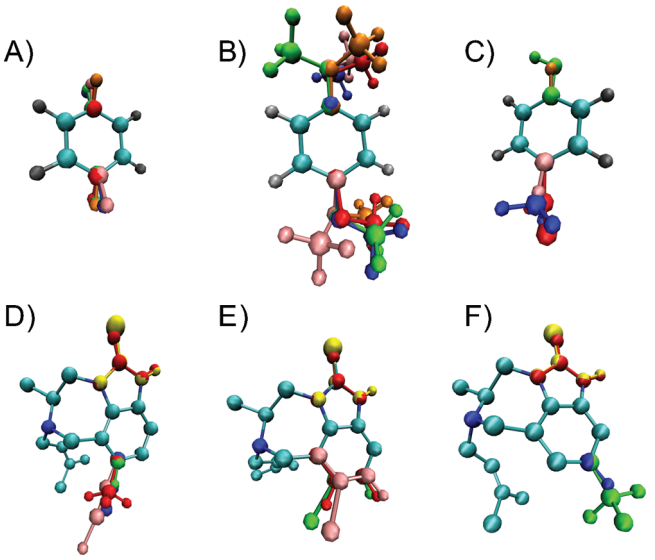

Figure 1. Schematic representation of three model systems that we have used to assess the quality of the MSλD implementation in CHARMM. Hybrid molecules representing multiple benzene molecules by modeling distinct sets of hydrogen and corresponding ipso carbon atoms at (A) site 1 and (B) sites 1 and 4 on a common benzene core. (C) A hybrid molecule representing six benzene derivatives modeled by three substituents at site 1 and two substituents on site 4 on a common benzene core. Hybrid TIBO molecules representing 14 inhibitors of HIV-1 reverse transcriptase containing both C═O and C═S variations at the X site and (D) variations involving nonhalides at the C-8 site or (E) halides at the C-8 site or (F) variations at the C-9 site.

Multisite λ dynamics has been implemented in the CHARMM macromolecular software package, version c36a4.[28,29]

2.2. Hybrid Ligands. Parameters and partial charges for the hybrid ligands were assigned from the recently developed CHARMM General Force Field (CGenFF).[30] Parameters and partial charge distributions for the TIBO compounds were optimized in our previous work[31] using our in-house parametrization tool MATCH[32] and quantum mechanical calculations and are included in that work's Supporting Information.

2.2.1. Model Compounds. Model hybrid ligands were constructed to represent multiple identical benzene, dihydroxybenzene, or dimethoxybenzene molecules. Each hybrid benzene molecule contained a single benzene ring with N distinct pairs of hydrogen and ipso carbon atoms at one or two sites on the common ring (see Figure 1A). Similarly, each hybrid dihydroxybenzene molecule consisted of a single benzene ring with N hydroxy groups and ipso carbon atoms at the *para* positions on the common ring, and each hybrid dimethoxybenzene molecule consisted of a single benzene ring with N methoxy groups and ipso carbon atoms at the *para* positions on the common ring (see Figure 1B). The hybrid molecules are identified in the text by the names "N_{site1} substituent × N_{site2} substituent" where substituents "h", "oh", and "och_3" designate the hydrogen atom, hydroxy, and methoxy moieties, respectively.

2.2.2. Benzene Derivatives. A hybrid ligand was constructed to represent six benzene derivatives: benzene, toluene, benzaldehyde, phenol, 4-methyl phenol, and 4-hydroxybenzaldehyde. At site 1, a hydrogen atom and methyl and aldehyde groups along with their corresponding ipso carbon atoms were modeled; at site 4, a hydrogen atom and hydoxyl group along with their corresponding ipso carbon atoms were modeled (see Figure 1C).

Table 1. Molecular Structures and the Corresponding Experimental IC_{50} and Binding Free Energies of the TIBO Analogues

compound	X	Y	IC_{50}[a] (μM)	ΔG_{bind}[b] (kcal/mol)	hybrid molecule
1	S	8-Br	0.0030	−12.09	E
2	S	8-CH_3	0.0136	−11.16	D
3	S	8-CCH	0.0296	−10.69	E
4	S	H	0.0440	−10.44	D, E, F
5	S	8-I	0.0474	−10.39	E
6	O	8-Br	0.0473	−10.39	E
7	S	8-CN	0.0563	−10.29	D
8	O	8-I	0.0880	−10.01	E
9	O	8-CCH	0.4376	−9.02	D
10	S	9-CF_3	0.4850	−8.96	F
11	O	8-CH_3	0.9890	−8.52	D
12	O	8-CN	1.1396	−8.43	D
13	O	H	3.1550	−7.81	D, E, F
14	O	9-CF_3	5.9190	−7.42	F

[a] Refs 34 and 35. [b] Calculated from $\Delta G_{bind}=RT \ln IC_{50}$ at 310 K.

Experimental hydration free energies were compiled from Cabini et al.;[33] the relative hydration free energies for all pairs of these compounds are listed in Table 2.

2.2.3. TIBO Compounds. Three hybrid TIBO molecules were constructed to represent a total of 14 unique inhibitors of HIV-1 reverse transcriptase. Figures 1D−F illustrate the hybrid ligands, and Table 1 summarizes the experimental binding free energies[34,35] of the TIBO compounds that were included in these calculations. Each hybrid molecule contained both C═O and C═S variations at the X site as well as variations involving nonhalides (Figure 1D) or halides (Figure 1E) at the C-8 site or variations at the C-9 site (Figure 1F). One TIBO pair (X═O→S, Y═H) is represented in each of the three hybrid molecules.

2.3. Simulation Details. In all MSλD simulations, the leapfrog Verlet algorithm was used to integrate the equations of motion and propagate the atomic coordinates and velocities as well as the θ values and their velocities. A nonbonded cutoff of 15 Å was used, and van der Waals switching and electrostatic shifting functions were implemented between 10 Å and 12 Å unless otherwise specified. Hydrogen bonds were restrained using the SHAKE[36] algorithm, and the time step was 2 fs unless otherwise specified. Each θ_i was assigned a fictious mass of 5 amu·Å^2, and λ values were saved every 10 steps. Linear scaling by λ was applied to all energy terms, except the bond and angle terms which were treated at full strength regardless of λ value. The threshold value for assigning $\lambda_{\alpha,i} \approx 1$ was $\lambda_{\alpha,i} \geq 0.8$ unless otherwise specified. To enhance transition rates between substituents, restraint functions were employed to superimpose the ipso carbons on one another at each site, and variable biases ($F^{variable}$) were added to the hybrid potential energy function in eq 6 for each $\lambda_{\alpha,i}$:

$$F_{\alpha,i}^{variable} = \begin{cases} k(\lambda_{\alpha,i} - 0.8)^2 \text{kcal/mol}; & \text{if } \lambda_{\alpha,i} < 0.8 \\ 0; & \text{otherwise} \end{cases} \quad (11)$$

with force constants, k, assigned between 0 and 7 kcal/mol. The temperature was maintained near 310 K by coupling to a Langevin heat bath using a frictional coefficient of 10 ps^{-1} for all nonprotein atoms and 5 ps^{-1} for each θ_i. Ten independent simulations using

different initial seed values of θ_i were performed unless otherwise stated, and the resulting averages and standard deviations were reported. All calculations and analyses were performed using the new implementation of multisite λ dynamics in the BLOCK module in CHARMM version c36a4 on dual 2.66 GHz Intel Quad Core Xeon processors.

In all FEP/BAR calculations, for each pair of compounds, 23 λ windows (λ = 0, 0.01, 0.025, 0.05, 0.075, 0.1, 0.15, 0.2, 0.25, 0.3, 0.4, 0.5, 0.6, 0.7, 0.75, 0.8, 0.85, 0.9, 0.925, 0.95, 0.975, 0.99, and 1.0) were used with soft-core potentials,[37] and the resulting trajectories were analyzed using the Bennett acceptance ratio (BAR) method.[38] Three independent series of simulations were performed for each pair, and the average and standard deviation over these three series are reported. All simuations were performed using the BLOCK module in CHARMM, and BAR analyses were performed using a modified version of pyMBAR.[39]

2.3.1. Model Compounds. Solvent simulations were performed using 351 TIP3P[40] water molecules in a water box of 22 Å^3 with periodic boundary conditions. Each θ_i was assigned a fictitious mass of 12 amu·Å^2. Heating and equilibration phases were 4 and 10 ps, respectively, and production runs were 25 and 3 ns for vacuum and solvation simulations, respectively, unless otherwise stated. A nonbonded cutoff of 15 Å was used, and van der Waals switching and electrostatic force shifting functions were implemented between 10 Å and 12 Å.

2.3.2. Benzene Derivatives. All relative hydration free energies were computed from the difference between relative free energy changes evaluated from solvated and vacuum simulations. Solvent simulations were performed using 351 TIP3P[40] water molecules in a water box of 22 Å^3 with periodic boundary conditions.

Only one set of MSλD simulations was required to compute the relative hydration free energies among all pairs of benzene derivatives. Relative free energies for each pair were averaged over results obtained from three independent trajectories. Initial biases $\{F_i\}$ for the six benzene derivatives were approximated in the solvent and vacuum simulations by the minimized GBMV[41,42] and vacuum energies for the individual ligands, respectively. Biases were optimized iteratively so that the final simulations in a given environment were projected to yield at least 50 transitions per site and at least 400 snapshots in which each unique compound was assigned to be "dominant", i.e., the substituent at site 1 and substituent at site 4 that corresponded to the compound had $\lambda_i \approx 1$. Heating and equilibration phases were 4 ps each. Production runs for the bias optimization stages were 200 and 20 ps for vacuum and solvent simulations, respectively, while the production runs for the final stage were 2 ns.

Nine series of traditional alchemical free energy simulations were performed for pairs of benzene derivatives that differed from one another at only one substituent site; from these simulations, relative hydration free energies for the remaining six pairs of compounds were inferred. Short heating and equilibration phases were performed, and production runs were 1 ns for both vacuum and solvent environments.

2.3.3. TIBO Compounds. Relative binding free energies were computed via thermodynamic cycles by performing MSλD simulations for subsets of TIBO compounds both in a solvent and while bound to the non-nucleoside reverse transcriptase inhibitor (NNRTI) binding pocket in HIV-1 RT. The same simulation parameters were used as was described in ref 31. For the solvation simulations, the hybrid molecules were solvated in a 20 Å^3 box of 244 TIP3P[40] water molecules, and periodic boundary conditions were employed. For the bound simulations, the PDB structure, 1TVR,[43] was truncated so that only residues within 20 Å of the crystallographic TIBO compound were retained, and the truncated protein−ligand system was solvated in a 20 Å sphere of 667 TIP3P[40] water molecules. Stochastic boundary conditions using a solvent boundary potential[44] of 22 Å with a 15 Å buffer region were employed. In addition to the bond and angle terms, the dihedral angle terms of the hybrid ligand were treated at full strength regardless of λ value.

Three sets of MSλD simulations were required to compute the relative binding free energies among the 14 TIBO compounds. Initial fixed biases $\{F_i\}$ in the solvent environment were estimated from the minimized energies of the individual ligands using the GBMV implicit solvent model[41,42] and were optimized iteratively using simulations of 200 ps in length such that the final simulations were projected to yield at least 50 transitions per site and 400 snapshots in which each unique ligand was assigned to be "dominant". Biases $\{F_i\}$ for the protein simulations were assigned from the MSλD-estimated $\Delta\Delta G_{solv}$ values. Final production runs were 2 and 1 ns for the solvated and bound simulations, respectively. Ligand populations from six 1 ns MSλD simulation trajectories were combined to compute relative free energies. The reported averages and standard deviations for MSλD simulations are calculated from three independent series of six MSλD trajectories.

Series of alchemical free energy simulations were performed for all 27 pairs of TIBO compounds, i.e., all pairs within the three hybrid molecules whose identities varied at only one site. Short heating and equilibration phases were performed, and production runs were 500 and 250 ps for solvent and bound environments, respectively.

2.4. Model Quality. All MSλD trajectories were analyzed using new routines that we have implemented in CHARMM. The fraction physical ligand (FPL) is a metric that describes the proportion of time that a full or physical ligand, as compared with only partial or unphysical ligands, is present during the course of a simulation. Transition rates ($\tau_{trans}(\alpha)$) among substituents on site α quantify the rate at which the identity of the "dominant" substituent changes throughout a simulation. The relative free energy difference for each pair of compounds (ij) in the hybrid molecules was estimated by averaging over results from multiple simulation trajectories. Alternatively, ligand populations from multiple trajectories were combined to compute the relative free energy difference by

$$\Delta\Delta G_k(ij) = -k_B T \ln \frac{\sum_{k=1}^{M} P(\lambda_j = 1)}{\sum_{k=1}^{M} P(\lambda_i = 1)} \quad (12)$$

3. RESULTS

A new version of λ dynamics, termed multisite λ dynamics (MSλD), has been implemented and is capable of simultaneously evaluating multiple chemical substituents at any number of sites on a common ligand core. The efficacy of this implementation of MSλD free energy simulations has been tested in three model systems. Figure 1 illustrates representative molecular structures of the alchemical hybrid molecule that are associated with each of these model systems. The first system includes a series of benzene, dihydroxybenzene, or dimethoxybenzene molecules in which multiple hydrogen atoms or hydroxy or methoxy groups

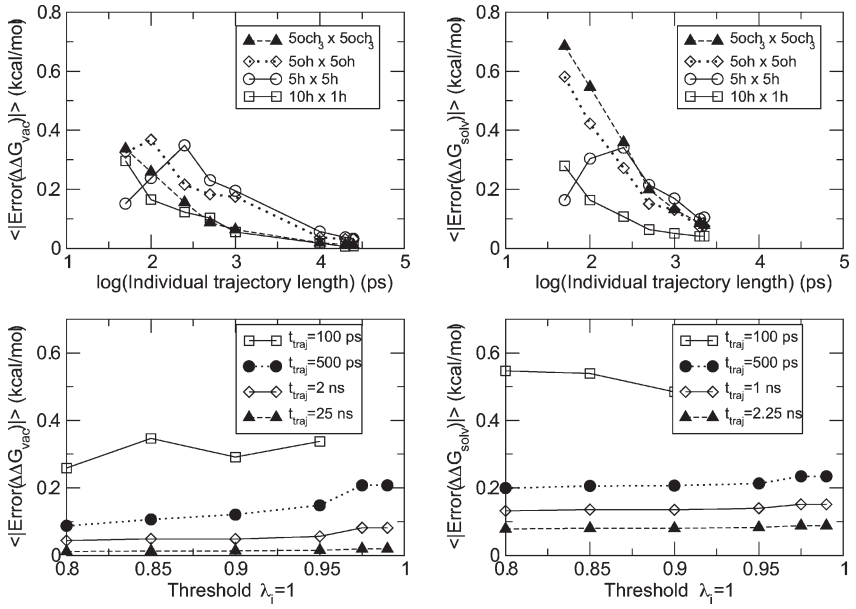

Figure 2. Sensitivity of MSλD simulations in estimating relative free energy differences based on hybrid ligands representing multiple, identical benzene (nh × nh) molecules, 25 dihydroxybenzene (5oh × 5oh) molecules, and 25 methoxybenzene ($5och_3 \times 5och_3$) molecules based on trajectory length in (A) vacuum and (B) solvent environments. Sensitivity of MSλD simulations for the 25 methoxybenzene ($5och_3 \times 5och_3$) molecules as a function of the threshold value used to assign $\lambda_{i,\alpha} \approx 1$ in (C) vacuum and (D) solvent environments. The reported unsigned errors were averaged over all ligand pairs whose individual relative free energies were obtained from data combined from 10 independent MSλD trajectories. Note: not all ligands were sampled as the "dominant" ligand in the 100 ps vacuum trajectories with threshold values $\lambda_{i,\alpha}$ >0.95 .

and their corresponding ipso carbon atoms are present at either site 1 or at site 1 and site 4 on a common benzene framework. The second system represents a series of six benzene derivatives: benzene, toluene, benzaldehyde, phenol, 4-methyl phenol, and 4-hydroxybenzaldehyde, for which experimental hydration free energies are available.[33] The third system represents a series of TIBO derivatives whose binding affinities to HIV-1 reverse transcriptase are known experimentally.[34,35] Since each substituent at each site interacts with each of the substituents at the other sites, a hybrid molecule with multiple substituents at two sites represents $N_{site1} \times N_{site2}$ distinct molecules where N_α is the number of substituents that are modeled at site α.

3.1. Relative Free Energies for Multiple Benzene, 1, 4-Dihydroxybenzene and 1,4-Dimethoxybenzene Molecules. In previous work,[27] we computed relative free energies in a vacuum and a solvent for pairs of identical benzene molecules that are represented in the model hybrid ligands. Given that each benzene molecule is assigned the same force field parameters, relative free energy differences of exactly 0 kcal/mol should theoretically be obtained in any environment; thus, any deviations in the simulation estimates from 0 kcal/mol can be understood as errors due to limitations in the MSλD sampling specifically. In addition, we considered the increasingly flexible and therefore more challenging systems of multiple, identical 1,4-dihydroxybenzene and 1,4-dimethoxybenzene compounds. For up to 10 substituents evaluated at a single site and five substituents evaluated at each of two sites, the average errors are on the order of 0.03 and 0.07 kcal/mol with maximum deviations of 0.12 and 0.28 kcal/mol for vacuum (25 ns) and solvent (2.25−3 ns) simulations, respectively.

Here, we characterize the sampling efficiency of MSλD in computing the free energy differences among these different hybrid ligands. First, the quality of results for the model compounds in vacuum environments is primarily dependent on the length of the simulation and is less affected by the complexity of the substituents which are being sampled, as demonstrated in Figure 2a. For each model system in a vacuum, the average unsigned error of the relative free energies estimated for all benzene, dihydroxybenzene, or dimethoxybenzene pairs that are averaged over 10 simulations each of length 250 ps are within 0.22 kcal/mol of the exact solution. The maximum observed errors for these short trajectory lengths are non-negligible, however, with deviations of up to 0.9 kcal/mol for any single ligand pair from simulations of the hybrid ligands representing 10 benzene, 25 benzene, 25 dihydroxybenzene, and 25 dimethoxybenzene molecules. However, within 10 ns (~8 CPU minutes on a single processor), the average unsigned error over all ligand pairs is 0.03 kcal/mol, and all ligand pairs have errors of less than 0.15 kcal/mol.

Benzene and dihydroxybenzene hybrid ligands experience similar transition rates among the "dominant" substituents at each site relative to one another and in both vacuum and explicit solvent environments. By contrast, transition rates for the dimethoxybenzene hybrid ligands are systematically slower than the benzene and dihydroxybenzene hybrid ligands and are systematically slower in a solvent than in a vacuum. This reduction in transition rates results in longer convergence times for simulations of the more flexible 1, 4-dimethoxybenzene relative to the corresponding benzene and dihydroxybenzene simulations, as shown in Figure 2b.

Finally, the quality of the relative free energy estimates is virtually insensitive to the specific threshold value that is used to define the presence of a "dominant" substituent, i.e., where $\lambda_{\alpha,i} \approx 1$ for the $\lambda_{\alpha,i}$ > threshold. While the actual ligand populations that are used in eq 8 to compute relative free energies depend on the threshold value, the ratio of the ligand populations is stable for threshold values between 0.8 and 0.95. For threshold values below 0.95, the accuracy of the relative free energies is primarily dependent on the length of the trajectory. Figure 2c,d

Table 2. Relative Hydration Free Energies ($\Delta\Delta G$) in kcal/mol for All Pairs of Six Benzene Derivatives Computed by MSλD and Alchemical Free Energy Perturbation Simulations Analyzed Using the Bennett Acceptance Ratio Method (FEP/BAR)[a]

		exptl	MSλD					FEP/BAR				
site1_site4		$\Delta\Delta G$[b]	$\Delta\Delta G_{vac}$		$\Delta\Delta G_{solv}$		$\Delta\Delta G$	$\Delta\Delta G_{vac}$		$\Delta\Delta G_{solv}$		$\Delta\Delta G$
react.	prod.		avg	σ	avg	σ	avg	avg	σ	avg	σ	avg
h_h	h_oh	−6.41	−10.58	0.07	−15.18	0.12	−4.60	−10.61	0.03	−15.15	0.04	−4.54
h_h	ch3_h	−0.02	−6.82	0.05	−7.29	0.13	−0.47	−6.76	0.03	−6.58	0.02	0.18
h_h	ch3_oh	*−5.88*	*−17.29*	*0.07*	*−22.34*	*0.14*	*−5.05*	*−17.24*	*0.05*	*−21.59*	*0.10*	*−4.34*
h_h	cho_h	−3.52	7.38	0.09	5.23	0.16	−2.14	7.39	0.01	5.78	0.04	−1.62
h_h	cho_oh	*−10.72*	*−2.41*	*0.20*	*−9.54*	*0.22*	*−7.12*	*−2.42*	*0.07*	*−8.77*	*0.08*	*−6.35*
h_oh	ch3_h	*6.39*	*3.76*	*0.08*	*7.89*	*0.13*	*4.12*	*3.85*	*0.06*	*8.56*	*0.07*	*4.72*
h_oh	ch3_oh	0.54	−6.71	0.04	−7.16	0.10	−0.45	−6.63	0.03	−6.44	0.06	0.20
h_oh	cho_h	*2.89*	*17.96*	*0.07*	*20.41*	*0.14*	*2.45*	*18.00*	*0.04*	*20.93*	*0.08*	*2.92*
h_oh	cho_oh	−4.30	8.17	0.16	5.64	0.19	−2.53	8.19	0.05	6.37	0.03	−1.81
ch3_h	ch3_oh	−5.85	−10.47	0.07	−15.04	0.09	−4.57	−10.51	0.03	−15.00	0.04	−4.50
ch3_h	cho_h	−3.50	14.20	0.10	12.52	0.10	−1.67	14.19	0.00	12.39	0.02	−1.81
ch3_h	cho_oh	*−10.69*	*4.41*	*0.19*	*−2.24*	*0.17*	*−6.65*	*4.24*	*0.06*	*−2.36*	*0.09*	*−6.61*
ch3_oh	cho_h	*2.35*	*24.67*	*0.05*	*27.57*	*0.09*	*2.90*	*24.80*	*0.03*	*27.54*	*0.07*	*2.73*
ch3_oh	cho_oh	−4.84	14.88	0.16	12.80	0.14	−2.08	14.85	0.03	12.79	0.05	−2.07
cho_h	cho_oh	−7.19	−9.79	0.16	−14.77	0.14	−4.98	−9.83	0.01	−14.56	0.02	−4.74

[a] Averages (avg) and standard deviations (σ) are calculated from three independent MSλD trajectories via eq 8 or a series of FEP/BAR trajectories. $\Delta\Delta G_{vac}$ and $\Delta\Delta G_{solv}$ represent the relative free energies estimated in the vacuum and solvent environments, respectively. FEP/BAR values in italics represent cases where the reactant and product differ at both sites, and thus $\Delta\Delta G$ estimates were obtained by combining results for the two FEP/BAR simulations evaluating changes at one site and then the other site. [b] Calculated from ref 33 at 310 K.

illustrate the quality of results in vacuum and solvent environments that are obtained for the dimethoxybenzene hybrid ligand which contained five substituents at each site as a function of the specific cutoff or threshold value that is used to define $\lambda_{\alpha,i} \approx 1$.

3.2. Relative Hydration Free Energies of Six Benzene Derivatives. Relative hydration free energies were computed for six benzene derivatives that differ from one another by the identity of the substituents in the para positions. To control for the influence of the force field parameters on the quality of the simulation results, MSλD results are first compared with those obtained from the Bennett acceptance ratio method analysis of traditional alchemical free energy simulations using the same ligand parameters (FEP/BAR; see Table 2). As shown in Figure 3a−c, the relative free energies estimated from MSλD and FEP/BAR agree very well with one another for each arm of the thermodynamic cycle (with R^2 values of 1.00 and 0.999 for the vacuum and solvent environments, respectively) and for the overall relative hydration free energies (with an R^2 value of 0.990 and slope of 1.0). The average unsigned difference between relative hydration free energies computed by FEP/BAR and MSλD for each pair of compounds is 0.29 kcal/mol with a maximum deviation of 0.56 kcal/mol.

The relative hydration free energies estimated from the MSλD simulations correlate well with those that were measured experimentally and have an average unsigned error (AUE) of 1.8 kcal/mol relative to experimental values and an R^2 of 0.959 (Figure 3d). The overall error, however, is dominated by contributions from pairs that include 4-hydroxybenzaldehyde; specifically, the five ligand pairs that include 4-hydroxybenzaldehyde have an AUE of 2.9 kcal/mol while the remaining 10 pairs have an AUE of 1.2 kcal/mol. The FEP/BAR results also yield an overall AUE of 1.8 kcal/mol with errors of 3.2 and 1.1 kcal/mol for pairs that include and exclude 4-hydroxybenzaldehyde, respectively.

We also explored the impact of averaging relative free energy changes obtained over multiple trajectories for a hybrid ligand. When multiple independent simulations initially explore different regions of phase space, the individual trajectories can be combined to give reasonable relative free energy estimates in a short amout of time. For example, ligand populations from 10 10-ps simulations were combined to give relative free energy estimates that are within 0.3 kcal/mol of the converged values, as shown in Figure 4a. However, the data from the explicit solvent simulation trajectory depicted in Figure 4b illustrate that longer trajectories are required to sufficiently explore the λ phase space. In fact, trajectory lengths of 100 ps are required for each of the 10 solvent simulations to sample all six distinct benzene derivatives. These results agree well with those that would be predicted from transition rates obtained in the previous section using model compounds. Using estimated transition rates for the model hybrid dimethoxybenzene compounds of 0.2−1.1 ps^{-1} that were reported in ref 27 and assuming that transitions are equally probable among each of the substituents at each site and that transitions at the two sites are not correlated, a minimum of 30 transitions or 30−150 ps would be required to sample each of the six distinct benzene derivatives five different times during a single trajectory. With total combined trajectory lengths of 1 ns, whether from a single simulation of 1 ns or 10 simulations of 100 ps, the relative free energy estimates are within 0.15−0.25 kcal/mol of the converged results.

3.3. Relative Binding Free Energies of 14 HIV-1 RT Inhibitors. In our previous study,[31] relative binding affinities for 44 pairs of TIBO compounds (among 21 unique TIBO compounds) were estimated from traditional alchemical free energy simulations analyzed by thermodynamic integration. In this current study, we are focusing on the ability of MSλD to estimate relative binding free energies when modeling different substituents at more than one site on a common ligand core simultaneously and so have only

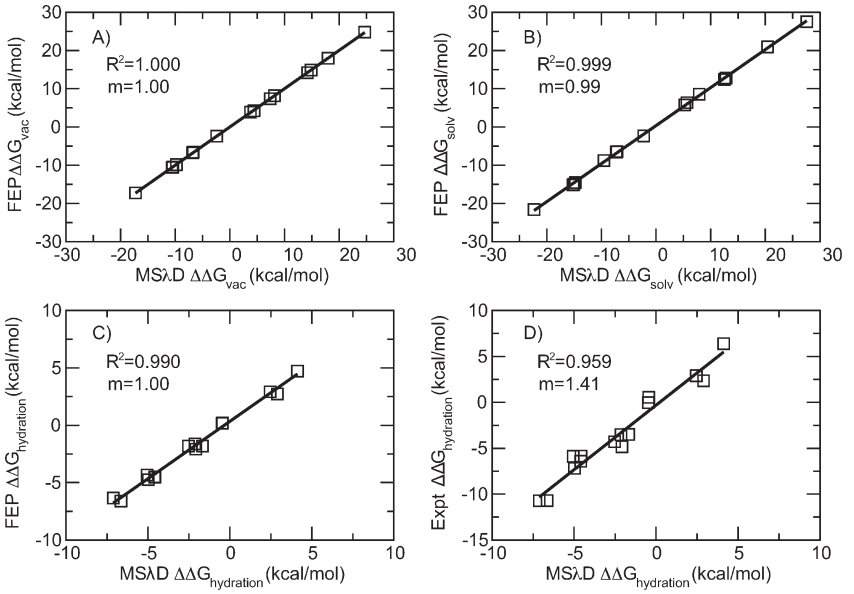

Figure 3. Correlation between MSλD-calculated and FEP/BAR-calculated relative free energies in (A) vacuum and (B) solvent environments for a series of six benzene derivatives and (C) the corresponding relative hydration free energies. (D) Correlation between MSλD-calculated and experimental relative hydration free energies.

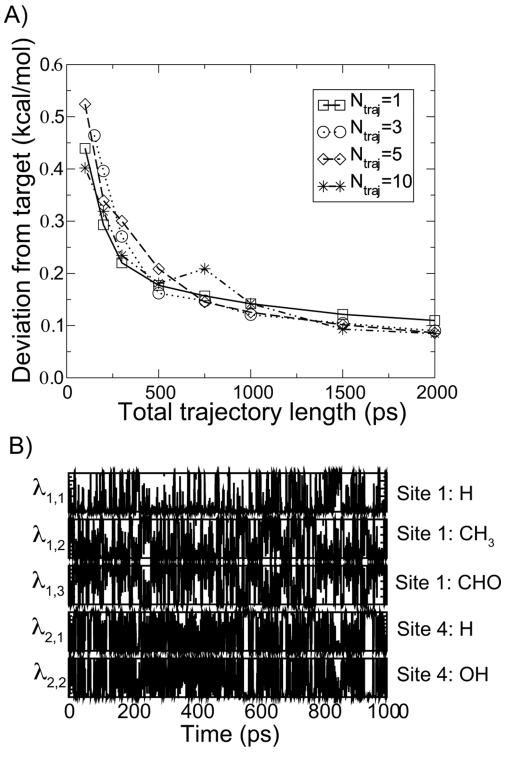

Figure 4. (A) Unsigned deviations for relative free energies in a solvent were averaged over N_{traj} simulations for all pairs in the hybrid ligand representing six benzene derivatives. The targets were defined for each pair by combining data from 10 independent trajectories each of 2 ns. (B) Representative data from an explicit solvent simulation trajectory for the hybrid benzene model.

included the 14 TIBO compounds for which experimental binding data are available for both X = O and X = S for a given substituent on site Y. In the previous study, we used different patch sizes (i.e., the number of atoms that were used to represent the substituents at each site) and scaled the dihedral angle terms by their corresponding $\{\lambda_i\}$; therefore, we repeated the free energy simulations so that we could compare each arm of the thermodynamic cycle with results obtained from the corresponding MSλD simulations. Free energy simulation trajectories were run for significantly longer than in our previous study, and soft-core potentials were used to ensure the convergence of the alchemical free energy simulations at the end points.

Table 3 and Figure 5 summarize the results for the relative free energies that have been computed for pairs of these TIBO compounds in solvent and protein environments by using either the new implementation of MSλD simulations or traditional alchemical free energy simulations analyzed by BAR. Transition rates at each site in the MSλD simulations are comparable to those observed for the model compounds and benzene derivatives modeled in a solvent and range from 0.02 to 0.9 ps^{-1}. The agreement between these two methods for estimates in the solvent environment is very good: the average unsigned difference and maximum difference are 0.55 and 1.30 kcal/mol, respectively. The R^2 is 0.998, and the slope of the regression line is 0.98. For the protein environment, the agreement in the relative free energies estimated with these two methods is also reasonably good: the average unsigned difference and maximum difference are 1.15 and 3.16 kcal/mol, respectively, while the R^2 and slope of the regression line are 0.987 and 0.96, respectively. In both solvent and protein environments, the difference between the relative free energies computed by FEP/BAR and MSλD tends to increase with the size differential of the pairs of compounds. For example, in solvent, the average unsigned difference in the relative free energies obtained from the two methods is 0.29, 0.67, and 0.96 kcal/mol for pairs of compounds whose substituents differ by 0, 1, and 2 heavy atoms, respectively. Similarly, in the protein environment, the average unsigned difference between the two methods is 0.73, 1.39, and 1.76 kcal/mol for

Table 3. Samping Characteristics of the Relative Free Energies for All Pairs of TIBO Compounds Estimated from Series of Alchemical Free Energy Simulations Analyzed by BAR (FEP/BAR) and from MSλD Simulations[a]

		FEP/BAR		MSλD				
hybrid ligand	pairs	$\langle\sigma\rangle$	FPL	τ_{trans}(X) (ps^{-1})	τ_{trans}(Y) (ps^{-1})	$\langle\sigma\rangle$	$\langle\Delta\rangle^b$	max Δ^c
				$\Delta\Delta G_{solv}$				
D	16	0.05	0.11	0.27	0.66	0.03	0.57	1.30
E	9	0.05	0.15	0.03	0.89	0.09	0.50	0.96
F	4	0.08	0.78	0.17	0.21	0.10	0.54	0.81
overall	*29*	*0.05*				*0.05*	*0.55*	*1.30*
				$\Delta\Delta G_{prot}$				
D	16	0.38	0.92	0.02	0.20	0.29	1.34	3.15
E	9	0.43	0.96	0.02	0.06	0.21	0.96	2.00
F	4	0.30	0.97	0.04	0.03	0.20	0.80	1.37
overall	*29*	*0.39*				*0.25*	*1.15*	*3.15*

[a] Averages and standard deviations (σ) are calculated from three independent series of six MSλD trajectories via eq 12 and three independent series of the FEP/BAR trajectories. $\Delta\Delta G_{solv}$ and $\Delta\Delta G_{prot}$ represent the relative free energies estimated in the solvent environment and binding pocket, respectively, and are reported in units of kcal/mol. The Fraction Physical Ligand (FPL) represents the fraction of time that a physical ligand is present during the simulation as opposed to several partial ligands. [b] $\langle|\Delta\Delta G^{MS\lambda D} - \Delta\Delta G^{FEP/BAR}|\rangle$. [c] Max $|\Delta\Delta G^{MS\lambda D} - \Delta\Delta G^{FEP/BAR}|$.

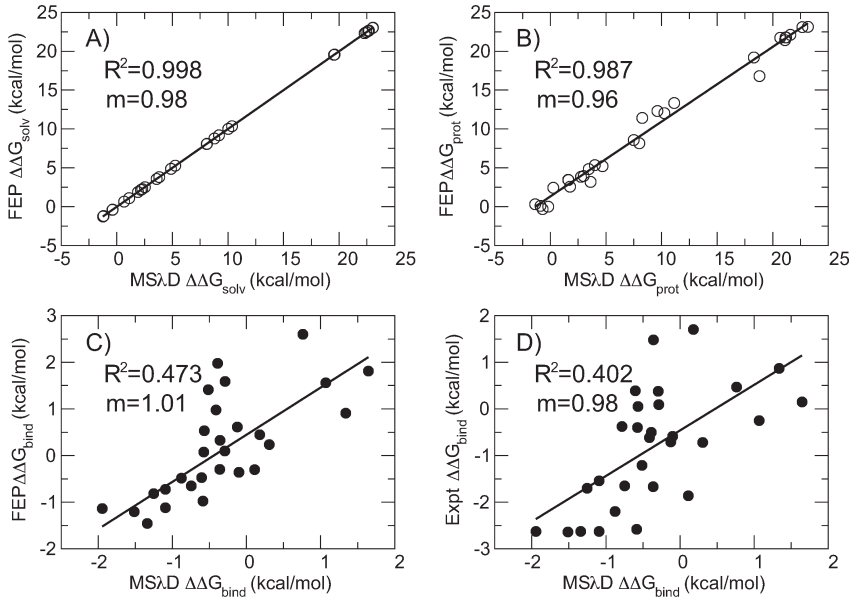

Figure 5. Correlation between MSλD-calculated and FEP/BAR-calculated relative free energies for 29 pairs of TIBO compounds that are inhibitors of HIV-1 reverse transcriptase in (A) solvent and (B) protein environments and (C) the corresponding relative binding affinities. (D) Correlation between MSλD-calculated and experimental relative binding free energies.

pairs of compounds whose substituents differ by 0, 1, and 2 heavy atoms, respectively.

As expected, in both methods, the uncertainty in the relative free energy estimates for the bound simulations is larger than that in the solvent environment. The average standard deviation of the free energy estimates from the three series of MSλD and FEP/BAR solvent simulations is 0.05 kcal/mol. By comparison, the average standard deviations for the protein simulations are 0.25 and 0.39 kcal/mol for the MSλD and FEP/BAR simulations, respectively. The average difference between the overall relative binding affinities for these pairs of TIBO inhibitors estimated by MSλD and FEP/BAR simulations is 0.7 kcal/mol, and the maximum difference is 2.4 kcal/mol. The range of predicted relative binding affinities for these pairs of TIBO inhibitors is quite small, so the R^2 of 0.473 between the relative binding affinities estimated from MSλD and FEP simulations is significantly lower than those obtained for relative free energy estimates in the solvent and bound environments.

Finally, the average unsigned error of the relative binding affinities for the 29 pairs of TIBO inhibitors is 0.9 and 1.3 kcal/mol for the MSλD and FEP/BAR simulations, respectively, and the largest errors are 2.0 and 2.6 kcal/mol, respectively (Table 4). The magnitudes of these errors are comparable to those that have been reported for FEP calculations of inhibitors bound to wild-type or mutant HIV-1 RT[45−49] and that may be considered reasonable for drug design applications. For example, in their recent paper, Chodera et al. state

Table 4. Average Unsigned Errors (AUE) and Maximum Errors (MaxE) in the Computed Relative Binding Affinities, $\Delta\Delta G_{bind}$ (in kcal/mol), for All Pairs of TIBO Compounds[a]

		FEP/BAR		MSλD	
hybrid ligand	pairs	AUE	MaxE	AUE	MaxE
D	16	1.42	2.62	0.77	1.97
E	9	1.23	2.38	1.05	1.99
F	4	1.00	1.17	1.14	1.84
overall	*29*	*1.30*	*2.62*	*0.91*	*1.97*

[a] Computed relative binding affinities are calculated from the differences in the $\Delta\Delta G_{prot}$ and $\Delta\Delta G_{solv}$ obtained from averaging three independent series of six MSλD trajectories via eq 12 and three independent series of the FEP/BAR trajectories.

Table 5. Percentage of Pairs of TIBO Compounds That Are Correctly Ranked with the Free Energy Methods and Force Field Parameters Used in This Work

$\Delta\Delta G^{expt}$ (kcal/mol)	# of pairs	FEP/BAR	MSλD
>2.0	6	100	100
>1.5	12	100	92
>1.0	14	93	93

that "statistical models of prediction-guided prioritization suggest that even moderate accuracy (RMS errors of 2 kcal/mol) could be sufficient to produce substantial efficiency gains in lead optimization campaigns."[4] The experimental relative binding affinities for these pairs of TIBO inhibitors are within 2.6 kcal/mol of each other, and thus the R^2 between MSλD-estimated and experimental relative binding affinities of 0.402 is quite encouraging. Perhaps a more interesting and relevant metric for the discriminatory ability of these free energy methods in structure-based drug design is the percentage of time that the better binder from a pair of compounds is correctly identified. Given that the experimental uncertainty associated with the binding affinity measurements are on the order of 0.5−1 kcal/mol[3], only pairs of compounds which have binding free energy differences above a certain threshold are examined. As demonstrated in Table 5, of the 14 pairs of TIBO compounds that have differences in their experimental binding affinities that are greater than 1 kcal/mol, FEP/BAR and MSλD correctly identify the more potent inhibitor 93% of the time. This percentage increases to 100 when the six pairs of compounds with experimental binding affinity differences of greater than 2 kcal/mol are considered.

4. DISCUSSION

4.1. Sampling Characteristics. Simulation results for the three model systems in this study clearly demonstrate the robustness of sampling using MSλD. The relative free energy differences between pairs of compounds that are estimated from MSλD agree well with theoretical values (in the case of the multiple identical benzene, dihydroxybenzene, and dimethoxybenzene compounds) and with traditional alchemical free energy methods (in the case of hydration free energies of the six benzene derivatives and binding free energies of the TIBO compounds). In MSλD simulations, the efficiency of the simulations is directly related to the proportion of time that a "dominant" ligand is represented relative to the partial, nonphysical ligands, and to the number of transitions or times that the identity of the "dominant" substituent at each site changes and more specifically, the number of times the identity of the "dominant" ligand changes. Thorough sampling enhances the convergence of the dominant ligands and thus the reliability of the relative free energies that are estimated from these populations using eq 8.

In the first model system, sampling convergence is most readily achieved for the smaller "h" and "oh" substituents since the substituents at each site sample very similar conformations at each time step. Given that each of these smaller substituents experiences comparable magnitudes of the unscaled interaction energies with the rest of environment at each time step, transitions between "dominant" substituents are relatively common. With the addition of the larger, more flexible methoxy moieties on the common benzene ring, however, the unscaled interaction energies between each substituent and the environment can be quite different from one another at a given point in time, which reduces the transition probabilities between dominant substituents for the dimethoxybenzene hybrid molecule relative to transition rates between the hybrid benzene and dihydroxybenzene molecules. This effect is magnified in the solvent simulations where systematically lower transition rates are observed. Visual inspection of the trajectories confirmed that the methoxy groups explore a wide variety of conformations. Thus, the extra volume that is explored by the methoxy groups relative to the smaller substituents suggests that more substantial solvent rearrangements are required to sample each of the 1,4-dimethoxybenzene ligands in the "dominant" ligand state.

Transitioning between dominant ligands can be even more challenging in the context of a binding pocket where substituent sites interact with distinct parts of the pocket. In solvent environments, local solvent configurations surrounding two substituent sites that are remote from one another can rearrange relatively independently from each other. By contrast, fluctuations in different parts of a given protein binding pocket influence one another due to their backbone connectivity and specific intermolecular interactions and thus are correlated at longer time scales with one another than are solvent configurations. By constucting hybrid ligands that contain substituents of similar molecular volume or polarity to one another, the extent of the rearrangement of the environment that is required to enable one substituent to replace the "dominant" substituent is minimized; therefore, the probability of transitions among substituents on a hybrid ligand will tend to increase, and the ability of each of the dominant ligands to be sampled will improve. If clusters of substituents are selected such that at least one ligand in each hybrid molecule overlaps with that of another hybrid molecule, the potency of each represented ligand can be localized on a single relative scale with one another. With at least one experimental measurement, these calculated estimates are able to be placed on an absolute scale.

Other simulation parameters can be varied to enhance the efficacy of MSλD simulations. For example, decreasing m_θ will tend to increase the mobility of the θ values and thus increase transition rates, though, in our experience, values of m_θ on the order of 5−20 amu·Å^2 are usually reasonable. Alternatively, adding biasing potentials associated with the θ values that take effect only when $\lambda_{\alpha,i} < 0.8$ as in eq 11 or increasing the magnitude of the force constant, k, on these biasing potentials will also tend to increase the transition rates. Though, with increasingly large force constants, there will be a concomitant increase in the amount

of time spent at intermediate λ values (data not shown) and lower populations for the free energy differences required in eq 8.

4.2. Computational Expense. The most significant difference between MSλD and alchemical free energy simulations lies in their relative computational expense. Results estimated from MSλD simulations for the hybrid molecule representing six benzene derivatives were achieved ~250 times faster than those for the reported FEP/BAR calculations. However, the triplicate FEP/BAR calculations were more precise, and so a more appropriate comparison would be for trajectory lengths that achieve a similar level of precision. FEP/BAR simulations in which each λ window for each pair was sampled for ~40 ps yield an average precision in the relative free energy estimates of 0.15 kcal/mol and require ~20 times more computational resources than MSλD simulations of comparable precision.

Similarly, relative binding affinity estimates for the TIBO compound series for comparable levels of precision are achieved by MSλD simulatons about 50 times faster than the corresponding series of alchemical free energy simulations. The 1 ns MSλD trajectories for the bound environment were sufficiently long to ensure that each physical ligand was sampled in the dominant state in all but a few simulations; however, significantly shorter simulations were sufficient to identify the most favorable binders. Arguably, in prospective drug-design applications, it is primarily the best binders that are sought and not necessarily a quantitative ranking of each ligand. Therefore, these relative times represent a lower bound on the computational efficiency of MSλD over traditional alchemical free energy simulations that are restricted to sampling individual pairs of ligands.

4.3. MSλD Applications. Application of MSλD simulations to structure-based drug design strategies is promising given its computational expediency relative to traditional alchemical free energy simulations for exploring multiple variants at multiple sites on a common ligand framework. However, the quality of the relative hydration free energies or binding affinities is also dependent on the quality of the underlying force field parameters. In this study, reasonable overall agreement is observed between experimental relative free energies and those obtained from MSλD simulations using CGenFF parameters. The overall average unsigned error for the relative hydration free energies of the series of benzene derivatives is 1.8 kcal/mol, while the average unsigned error for the relative binding affinities for pairs of TIBO compounds is 0.9 kcal/mol. However, it was also clear that some ligands were poorly modeled relative to the others and suggestive of errors in the underlying force field parameters associated with the corresponding functional groups. Specifically, the quality of the 4-hydroxybenzaldehye parameters yields systematically underestimated relative hydration free energies (by 1.2−2.9 kcal/mol) compared with the rest of the benzene derivatives. 4-Hydroxybenzaldehye has the largest dipole moment of the ligands in this series, and its electronic structure is arguably the most sensitive to the local solvent environment. Thus, the comparably poor quality associated with its calculated relative hydration free energies is not unexpected, and it is possible that more sophisticated polarizable charge models may be needed to capture its true solvation properties.

Given the uncertainties in the sampling on the order of 1 kcal/mol combined with inconsistencies in the force field parameters, MSλD is not the silver bullet that will reliably identify the best binder out of a pool of very good binders. The strength of MSλD simulations is likely to be in the lead optimization stage where a compound has been identified that binds at micromolar concentrations to a given macromolecular target. Different functional groups at various sites on this lead compound can be systematically screened for their ability to improve the binding affinity relative to the lead compound.[11] Thus, these MSλD simulations could bridge the gap between high-throughput docking studies that survey libraries of hundreds of thousands of diverse compounds and the much more expensive alchemical free energy calculations that are usually performed on only a handful of chemical variants of the lead compound. MSλD also appears to be a reasonable and rapid method for validating and optimizing force field parameters to reproduce available hydration free energy data or alternatively relative hydration free energies for series of functional groups that would be consistent for a given force field.

4.5. Functional Form of λ Values. In preparation for this study, we investigated various functional forms of the λ values that implicitly satisfy the holonomic constraints: $0 \le \lambda_{\alpha,i} \le 1$ and $\sum_{i=1}^{N} \lambda_{\alpha,i} = 1$. The functional form represented in eq 9 is used throughout this study and exhibits ideal characteristics for multisite λ dynamics simulations that mimick SAR strategies. First, it offers increased numerical stability at larger integration stepsizes over the original λ dynamics implementaion that used a simplified Lagrange multiplier method and renomalization at every time step.[27] Second, the periodicity of this functional form is oscillating in nature and so provides enhanced sampling of each of the $\lambda_i \approx 1$ states. Third, both the values of $\lambda_{\alpha,i}$ and the forces on $\lambda_{\alpha,i}$ are computationally inexpensive, and each $\lambda_{\alpha,i}$ has the same probability density function, so no further bias or correction is required to account for differences in effective phase space volume sampled. Finally, this functional form promotes rapid transitions between $\lambda_{\alpha,i} \approx 1$ and $\lambda_{\alpha,i} \approx 0$ such that (i) there is a significant fraction of θ-phase space in which a physical rather than unphysical ligand is present and (ii) it is relatively insensitive to the specific threshold that is used to define $\lambda_{\alpha,i} \approx 1$. The coefficient c in eq 7 can be tuned to describe the steepness of the switching between $\lambda_{\alpha,i} \approx 1$ and $\lambda_{\alpha,i} \approx 0$, and we have identified a "sweet spot" coefficient of 5.5 that seems optimal for MSλD simulations. Coefficients of less than 5.5 do not transition as quickly, so a larger fraction of θ space is restricted to intermediate λ values and so were less efficient for these simulations. Coefficients of greater than 5.5 demonstrate increased transition rates in vacuum and thus increased convergence rates; however, the rates of change in $\{\lambda\}$ near the end points are too abrupt in solvent simulations to retain the stability in the numerical integrator. Shorter timesteps and/or soft-core potentials could alleviate this problem; however, the functional form in eq 9 implicitly protects the system by implicitly restraining the upper bound of λ to be

$$\lambda_{\alpha,i}^{\max} \le \frac{e^{5.5}}{e^{5.5} + (N_\alpha - 1)e^{-5.5}} \tag{13}$$

or where $N = 5$ the boundaries are $0.000016 < \lambda_{\alpha,i} \le 0.99993$ on site α.

5. CONCLUSION

In the present study, we have presented the multisite λ dynamics method and its application in three model systems, including computing relative hydration free energies for a series of benzene derivatives and relative binding affinities for a series of TIBO inhibitors of HIV-1 reverse transcriptase. Results from our model compounds of multiple identical benzene, dihydroxybenzene, and dimethoxybenzene molecules demonstrate the robustness of sampling in MSλD simulations by achieving relative free energy

differences within 0.2 kcal/mol of the theoretical values in both vacuum and solvent environments for combined trajectory lengths of 1.5 ns.

The relative free energies estimated for individual arms of the thermodynamic cycle for calculating the relative hydration free energies for the benzene derivatives and the relative binding affinities for the TIBO compounds were in very good agreement with those obtained from traditional alchemical free energy calculations with R^2 values above 0.987. The primary difference between relative free energies estimated using MSλD and traditional free energy methods was the computational expense in which MSλD simulations achieved the same level of accuracy and precision as the traditional calculations ~20−50 times more quickly.

Overall, these results compared well with experimental results with an AUE of 1.8 kcal/mol for the 15 pairs of hydration free energies and an AUE of 0.9 kcal/mol for the 29 pairs of binding affinities. These simulations also highlighted potential inconsistencies in the CGenFF where the pairs involving 4-hydroxybenzaldehye yielded systematically poorer relative hydration free energies than the rest of the pairs of benzene derivatives.

Systematically evaluating a series of compounds mimics a chemical optimization strategy in structure-based drug design in which various substituents are evaluated at specific sites on a promising new therapeutic lead compound. These examples provide proof of concept of both the accuracy of MSλD simulation results that can be obtained and the efficiency of this approach relative to traditional alchemical free energy calculations that rely on fixed λ values and are limited to pairs of compounds. As generalized force field parametrization strategies for drug-like molecules continue to mature and methods for constructing hybrid ligand molecules become more automated, sampling using MSλD simulations should be effective for routinely screening on the order of tens to a hundred variations of a lead compound.

AUTHOR INFORMATION

Corresponding Author

*E-mail: brookscl@umich.edu.

ACKNOWLEDGMENT

This work was supported by the National Institutes of Health through grant (GM037554).

REFERENCES

(1) Beveridge, D. L.; DiCapua, F. M. Free energy via molecular simulation: applications to chemical and biomolecular systems. *Annu. Rev. Biophys. Biophys. Chem.* **1989**, *18*, 431–92.

(2) Foloppe, N.; Hubbard, R. Towards predictive ligand design with free-energy based computational methods? *Curr. Med. Chem.* **2006**, *13* (29), 3583–608.

(3) Gilson, M. K.; Zhou, H. Calculation of protein-ligand binding affinities. *Annu. Rev. Biophys. Biomol. Struct.* **2007**, *36*, 21–42.

(4) Chodera, J. D.; Mobley, D. L.; Shirts, M. R.; Dixon, R. W.; Branson, K.; Pande, V. S. Alchemical free energy methods for drug discovery: progress and challenges. *Curr. Opin. Struct. Biol.* **2011**, *21* (2), 150–160.

(5) Gallicchio, E.; Levy, R. M. Advances in all atom sampling methods for modeling protein-ligand binding affinities. *Curr. Opin. Struct. Biol.* **2011**, *21* (2), 161–166.

(6) Zwanzig, R. W. High-temperature equation of state by a perturbation method. 1. nonpolar gases. *J. Chem. Phys.* **1954**, *22* (8), 1420–1426.

(7) Straatsma, T. P.; Berendsen, H. J. C. Free-energy of ionic hydration - analysis of a thermodynamic integration technique to evaluate free-energy differences by molecular-dynamics simulations. *J. Chem. Phys.* **1988**, *89* (9), 5876–5886.

(8) Knight, J. L.; Brooks, C. L., III. λ-Dynamics free energy simulation methods. *J. Comput. Chem.* **2009**, *30*, 1692–1700.

(9) Kong, X.; Brooks, C. L., III. λ-dynamics: a new approach to free energy calculations. *J. Chem. Phys.* **1996**, *105* (6), 2414–2423.

(10) Guo, Z.; Brooks, C. L., III; Kong, X. Efficient and flexible algorithm for free energy calculations using the l-dynamics approach. *J. Phys. Chem. B* **1998**, *102*, 2032–2036.

(11) Guo, Z.; Brooks, C. L., III. Rapid screening of binding affinities: application of the l-dynamics method to a trypsin-inhibitor system. *J. Am. Chem. Soc.* **1998**, *120*, 1920–1921.

(12) Guo, Z. Y.; Durkin, J.; Fischmann, T.; Ingram, R.; Prongay, A.; Zhang, R. M.; Madison, V. Application of the lambda-dynamics method to evaluate the relative binding free energies of inhibitors to HCV protease. *J. Med. Chem.* **2003**, *46* (25), 5360–5364.

(13) Damodaran, K. V.; Banba, S.; Brooks, C. L., III. Application of multiple topology lambda-dynamics to a host-guest system: beta-cyclodextrin with substituted benzenes. *J. Phys. Chem. B* **2001**, *105* (38), 9316–9322.

(14) Banba, S.; Brooks, C. L., III. Free energy screening of small ligands binding to an artificial protein cavity. *J. Chem. Phys.* **2000**, *113* (8), 3423–3433.

(15) Banba, S.; Guo, Z.; Brooks, C. L., III. Efficient sampling of ligand orientations and conformations in free energy calculations using the l-dynamics method. *J. Phys. Chem. B* **2000**, *104*, 6903–6910.

(16) Lee, M. S.; Salsbury, F. R.; Brooks, C. L., III. Constant-pH molecular dynamics using continuous titration coordinates. *Proteins* **2004**, *56* (4), 738–752.

(17) Khandogin, J.; Brooks, C. L., III. Constant pH molecular dynamics with proton tautomerism. *Biophys. J.* **2005**, *89* (1), 141–57.

(18) Khandogin, J.; Brooks, C. L., III. Toward the accurate first-principles prediction of ionization equilibria in proteins. *Biochemistry* **2006**, *45* (31), 9363–9373.

(19) Abrams, J. B.; Rosso, L.; Tuckerman, M. E. Efficient and precise solvation free energies via alchemical adiabatic molecular dynamics. *J. Chem. Phys.* **2006**, *125* (7), 074115–074126.

(20) Zheng, L.; Chen, M.; Yang, W. Random walk in orthogonal space to achieve efficient free-energy simulation of complex systems. *Proc. Natl. Acad. Sci. U. S. A.* **2008**, *105* (51), 20227–20232.

(21) Zheng, L.; Chen, M.; Yang, W. Simultaneous escaping of explicit and hidden free energy barriers: Application of the orthogonal space random walk strategy in generalized ensemble based conformational sampling. *J. Chem. Phys.* **2009**, *130*, 234105–234114.

(22) Bitetti-Putzer, R.; Dinner, A.; Yang, W.; Karplus, M. Conformational sampling via a self-regulating effective energy surface. *J. Chem. Phys.* **2006**, *124* (17), 174901–174915.

(23) Michel, J.; Tirado-Rives, J.; Jorgensen, W. L. Prediction of the water content in protein binding sites. *J. Phys. Chem. B* **2009**, *113* (40), 13337–13346.

(24) Li, H.; Fajer, M.; Yang, W. Simulated scaling method for localized enhanced sampling and simultaneous "alchemical" free energy simulations: A general method for molecular mechanical, quantum mechanical, and quantum mechanical/molecular mechanical simulations. *J. Chem. Phys.* **2007**, *126* (2), 024106–024117.

(25) Jiang, W.; Hodoscek, M.; Roux, B. Computation of Absolute Hydration and Binding Free Energy with Free Energy Perturbation Distributed Replica-Exchange Molecular Dynamics. *J. Chem. Theory Comput.* **2009**, *5* (10), 2583–2588.

(26) Gallicchio, E.; Lapelosa, M.; Levy, R. M. Binding Energy Distribution Analysis Method (BEDAM) for Estimation of Protein Ligand Binding Affinities. *J. Chem. Theory Comput.* **2010**, *6* (9), 2961–2977.

(27) Knight, J. L.; Brooks, C. L., III. Applying efficient implicit non-geometric constraints in free energy simulations. *J. Comput. Chem.* **2011**.

(28) Brooks, B. R.; Bruccoleri, R. E.; Olafson, B. D.; States, D. J.; Swaminathan, S.; Karplus, M. CHARMM: A Program for

Macromolecular Energy, Minimization, and Dynamics Calculations. *J. Comput. Chem.* **1983**, *4*, 187–217.

(29) Brooks, B. R.; Brooks, C. L., III; Mackerell, A. D., Jr.; Nilsson, L.; Petrella, R. J.; Roux, B.; Won, Y.; Archontis, G.; Bartels, C.; Boresch, S.; Caflisch, A.; Caves, L.; Cui, Q.; Dinner, A. R.; Feig, M.; Fischer, S.; Gao, J.; Hodoscek, M.; Im, W.; Kuczera, K.; Lazaridis, T.; Ma, J.; Ovchinnikov, V.; Paci, E.; Pastor, R. W.; Post, C. B.; Pu, J. Z.; Schaefer, M.; Tidor, B.; Venable, R. M.; Woodcock, H. L.; Wu, X.; Yang, W.; York, D. M.; Karplus, M. CHARMM: the biomolecular simulation program. *J. Comput. Chem.* **2009**, *30* (10), 1545–614.

(30) Vanommeslaeghe, K.; Hatcher, E.; Acharya, C.; Kundu, S.; Zhong, S.; Shim, J.; Darian, E.; Guvench, O.; Lopes, P.; Vorobyov, I.; Mackerell, A. D., Jr. CHARMM General Force Field: A Force Field for Drug-Like Molecules Compatible with the CHARMM All-Atom Additive Biological Force Fields. *J. Comput. Chem.* **2009**, *00*, 1–20.

(31) Knight, J. L.; Brooks, C. L., III. Validating CHARMM parameters and exploring charge distribution models in structure-based drug design. *J. Chem. Theory Comput.* **2009**, *5*, 1680–1691.

(32) Yesselman, J. D.; Price, D. J.; Knight, J. L.; Brooks, C. L., III. MATCH: An Atom-Typing Toolset for Molecular Mechanics Force Fields. (submitted) 2011.

(33) Cabani, S.; Gianni, P.; Mollica, V.; Lepori, L. Group contributions to the thermodynamic properties of non-ionic organic solutes in dilute aqueous solution. *J. Sol. Chem.* **1981**, *10* (8), 563–595.

(34) Ho, W.; Kukla, M. J.; Breslin, H. J.; Ludovici, D. W.; Grous, P. P.; Diamond, C. J.; Miranda, M.; Rodgers, J. D.; Ho, C. Y.; De Clercq, E.; Pauwels, R.; Andries, K.; Janssen, M. A. C.; Janssen, P. A. J. Synthesis and anti-HIV-1 activity of 4,5,6,7-tetrahydro-5-methylimidazo-[4,5,1-jk][1,4]benzodiazepin-2(1H)-one (TlBO) derivatives. 4. *J. Med. Chem.* **1995**, *38* (5), 794–802.

(35) Smith, R. H., Jr.; Jorgensen, W. L.; Tirado-Rives, J.; Lamb, M. L.; Janssen, P. A.; Michejda, C. J.; Kroeger Smith, M. B. Prediction of binding affinities for TIBO inhibitors of HIV-1 reverse transcriptase using Monte Carlo simulations in a linear response method. *J. Med. Chem.* **1998**, *41* (26), 5272–86.

(36) van Gunsteren, W. F.; Berendsen, H. J. C. Algorithms for macromolecular dynamics and constrained dynamics. *Mol. Phys.* **1977**, *34*, 1311–1327.

(37) Zacharias, M.; Straatsma, T.; McCammon, J. Separation-shifted scaling, a new scaling method for Lennard-Jones interactions in thermodynamic integration. *J. Chem. Phys.* **1994**, *100* (12), 9025–9031.

(38) Bennett, C. H. Efficient Estimation of Free-Energy Differences from Monte-Carlo Data. *J. Comput. Phys.* **1976**, *22* (2), 245–268.

(39) Shirts, M. R.; Chodera, J. D. Statistically optimal analysis of samples from multiple equilibrium states. *J. Chem. Phys.* **2008**, *129* (12), 124105–124114.

(40) Jorgensen, W. L.; Chandrasekhar, J.; Madura, J. D.; Impey, R. W.; Klein, M. L. Comparison of simple potential functions for simulating liquid water. *J. Chem. Phys.* **1983**, *79* (2), 926–935.

(41) Lee, M. S.; Feig, M.; Salsbury, F. R., Jr.; Brooks, C. L., III. New analytic approximation to the standard molecular volume definition and its application to generalized Born calculations. *J. Comput. Chem.* **2003**, *24* (11), 1348–56.

(42) Lee, M. S.; Salsbury, F. R., Jr.; Brooks, C. L., III. Novel generalized Born methods. *J. Chem. Phys.* **2002**, *116* (24), 10606–10614.

(43) Das, K.; Ding, J.; Hsiou, Y.; Clark, A. D., Jr.; Moereels, H.; Koymans, L.; Andries, K.; Pauwels, R.; Janssen, P. A.; Boyer, P. L.; Clark, P.; Smith, R. H., Jr.; Kroeger Smith, M. B.; Michejda, C. J.; Hughes, S. H.; Arnold, E. Crystal structures of 8-Cl and 9-Cl TIBO complexed with wild-type HIV-1 RT and 8-Cl TIBO complexed with the Tyr181Cys HIV-1 RT drug-resistant mutant. *J. Mol. Biol.* **1996**, *264* (5), 1085–100.

(44) Brooks, C. L., III; Brunger, A.; Karplus, M. Active site dynamics in protein molecules: a stochastic boundary molecular-dynamics approach. *Biopolymers* **1985**, *24* (5), 843–65.

(45) Rizzo, R. C.; Wang, D. P.; Tirado-Rives, J.; Jorgensen, W. L. Validation of a model for the complex of HIV-1 reverse transcriptase with sustiva through computation of resistance profiles. *J. Am. Chem. Soc.* **2000**, *122* (51), 12898–12900.

(46) Wang, D.; Rizzo, R.; Tirado-Rives, J.; Jorgensen, W. Antiviral drug design: computational analyses of the effects of the L100I mutation for HIV-RT on the binding of NNRTIs. *Bioorg. Med. Chem. Lett.* **2001**, *11* (21), 2799–802.

(47) Udier-Blagovic, M.; Tirado-Rives, J.; Jorgensen, W. Structural and energetic analyses of the effects of the K103N mutation of HIV-1 reverse transcriptase on efavirenz analogues. *J. Med. Chem.* **2004**, *47* (9), 2389–92.

(48) Smith, M.; Smith, R.; Jorgensen, W. Assault on resistance: the use of computational chemistry in the development of anti-HIV drugs. *Curr. Pharm. Des.* **2006**, *12* (15), 1843–56.

(49) Smith, M. B. K.; Rader, L. H.; Franklin, A. M.; Taylor, E. V.; Smith, K. D.; Smith, R. H.; Tirado-Rives, J.; Jorgensen, W. L. Energetic effects for observed and unobserved HIV-1 reverse transcriptase mutations of residues L100, V106, and Y181 in the presence of nevirapine and efavirenz. *Bioorg. Med. Chem. Lett.* **2008**, *18* (3), 969–972.

JCTC Journal of Chemical Theory and Computation

ARTICLE

pubs.acs.org/JCTC

Can DFT Accurately Predict Spin Densities? Analysis of Discrepancies in Iron Nitrosyl Complexes

Katharina Boguslawski,[†] Christoph R. Jacob,*[,‡] and Markus Reiher*[,†]

[†]ETH Zurich, Laboratorium für Physikalische Chemie, Wolfgang-Pauli-Strasse 10, 8093 Zurich, Switzerland

[‡]Karlsruhe Institute of Technology (KIT), Center for Functional Nanostructures, Wolfgang-Gaede-Strasse 1a, 76131 Karlsruhe, Germany

Supporting Information

ABSTRACT: Iron nitrosyl complexes are a particularly challenging case for density functional theory. In particular, for the low-spin state, different exchange−correlation functionals yield very different spin densities [Conradie, J.; Ghosh, A. *J. Phys. Chem. B* **2007**, *111*, 12621−12624]. Here, we investigate the origin of these differences in detail by analyzing the Kohn−Sham molecular orbitals. Furthermore, to decide which exchange−correlation functionals yield the most accurate spin densities, we make comparisons to CASSCF calculations. To ensure that the spin densities are converged with respect to the size of the active space, this comparison is performed for $[Fe(NO)]^{2+}$ as a model system. We find that none of the investigated exchange−correlation functionals are able to reproduce the CASSCF spin densities accurately.

1. INTRODUCTION

Transition metal complexes are central to metal-mediated catalysis and bioinorganic chemistry.[1,2] For a detailed understanding of their function as catalytically active centers and of catalytic mechanisms, theoretical analysis has become indispensable.[3−12] However, to reliably accomplish such an analysis remains a challenge for theoretical chemistry.[13]

In quantum chemical studies of transition metal complexes, usually density functional theory (DFT) is employed. But, especially, the treatment of open-shell systems remains a challenge to DFT.[13,14] In particular, results regarding the relative energetic ordering of closely lying states of different spin multiplicities are difficult to obtain with sufficient accuracy.[13,15−26] The performance of different approximate exchange−correlation functionals was intensely discussed in the literature.[25−34] Recently, Conradie and Ghosh have identified a particularly difficult case. They studied the spin-state energetics for the spin-crossover complex Fe(salen)(NO) as well as the Fe(porphyrin)(NO) complex.[31] These compounds feature a noninnocent nitric oxide ligand, and the resulting nitrosyl complexes exhibit a complicated electronic structure.[30−32] In addition to the inconclusive prediction of the correct ground state, notable differences in the spin density distributions were found with different exchange−correlation functionals. A detailed analysis of the sources of these differences, however, was not undertaken. Here, we pursue closing this gap by analyzing their origin. Moreover, we expand the DFT studies of Conradie and Ghosh by considering the BP86, TPSS, TPSSh, and M06-L exchange−correlation functionals as well.

According to the Hohenberg−Kohn theorem,[35] only the total electron density is required to predict the electronic energy as well as all other molecular observables. In principle, the spin density is not needed. However, for open-shell molecules, one usually introduces the spin density as an additional variable, resulting in a spin-DFT formalism,[36] first proposed by von Barth and Hedin.[37] This allows one to construct better approximations for the exchange−correlation energy functional, since the additional information on the spin density is available and can be exploited. Within such a spin-DFT formalism, the exact spin-dependent exchange−correlation functional will (in addition to the exact electron density) also yield the exact spin density (see, e.g., ref 38), provided an unrestricted Kohn−Sham formalism is used.[39] Therefore, the spin density is one of the fundamental quantities in spin-DFT, and it is crucial to know which of the approximate exchange−correlation functionals yield accurate spin densities. Moreover, since electron paramagnetic resonance (EPR) parameters are explicitly dependent on the spin density,[40] reliable spin density distributions are an essential ingredient for an accurate calculation of EPR properties, which represents a difficult task for theoretical chemistry.[41−45]

With approximate exchange−correlation functionals, open-shell molecules in low-spin states are often treated in a broken-symmetry DFT formalism. In this case, the calculations do not yield the correct spin density. Instead, it has been argued that the Kohn−Sham reference system should represent the on-top pair density.[46] However, if properties depending on the spin-density such as EPR parameters are required, a broken-symmetry formalism is not useful. Therefore, we prefer the point of view that the need for a broken-symmetry treatment is an avoidable consequence of the insufficiencies of the currently available approximate exchange−correlation functionals and that instead one should aim at improved functionals that reproduce the exact spin-density.

To decide which exchange−correlation functional yields reliable spin densities, accurate benchmark calculations of the

Received: November 1, 2010
Published: August 15, 2011

spin density distribution are necessary. This requires multireference methods such as the multiconfigurational complete-active-space self-consistent-field (CASSCF) approach. The unfavorable scaling in computing time with the size of the active orbital space, however, disfavors the description of large molecular systems, and hence, such correlation methods are not frequently used in theoretical investigations of transition metal complexes (for counterexamples, see refs 32, 47, 48). Detailed CASSCF studies of the salen- as well as of different porphyrin-containing iron nitrosyl complexes were recently performed by Pierloot et al.[32,49] These studies provided important insight into the electronic structure of these compounds and the energetics of the different spin states. Furthermore, the problem of the inconclusive picture provided by DFT calculations for the spin densities was also addressed. A comparison of Mulliken spin populations and of spin density isosurface plots indicated that the nonhybrid functionals yield the most accurate spin densities.

However, a more detailed comparison of the DFT and the CASSCF calculations was not performed. Furthermore, the large size of the molecules under study restricts the dimension of the active space, and it is therefore not clear whether the spin densities are converged with respect to the size of the active space.

To circumvent these restrictions, one needs a small model system for which similar differences in the spin density distributions are found in DFT calculations, but where, due to the small size of this model system, one is still able to ascertain how the choice of the active space affects the resulting spin density distributions. Such an analysis of the spin density could then validate the corresponding CASSCF reference spin densities. Furthermore, a more detailed examination of the spin density distributions by considering the DFT−CASSCF spin density differences could be used as a representative benchmark of the approximate exchange−correlation functionals.

This work is organized as follows. In section 2, the computational details are presented. A detailed discussion of DFT spin densities of iron nitrosyl complexes is given in section 3. Then, section 4 introduces $[Fe(NO)]^{2+}$ as a small model system and validates the quality of CASSCF reference spin densities as a benchmark for the DFT results. Finally, a summary and concluding remarks are given in section 5.

2. COMPUTATIONAL METHODOLOGY

All unrestricted Kohn−Sham DFT calculations were performed with the quantum chemical program package ADF.[50] Eight popular exchange−correlation functionals were employed, from the widely used B3LYP hybrid exchange−correlation functional with 20% exact exchange[51] and TPSSh[52] with 10% Hartree−Fock exchange to five pure exchange−correlation functionals: OLYP,[53] OPBE,[54,55] BP86,[56,57] BLYP,[56,58] TPSS,[59] and M06-L.[60] For the molecular structures of Fe(salen)(NO) (in its two different conformations) and Fe(porphyrin)(NO), the optimized coordinates calculated by Conradie and Ghosh were taken.[31] For direct comparison, all DFT spin density profiles were obtained from single point calculations at these optimized structures. Since Slater-type orbitals give consistent and rapidly converging results for spin state splittings,[61] we applied a triple-ζ plus polarization Slater-type orbital basis set (TZP). The SCF algorithm was considered converged if the largest element of the commutator of the Fock matrix and the density matrix represented in the basis functions was lower than 10^{-6} Hartree. The

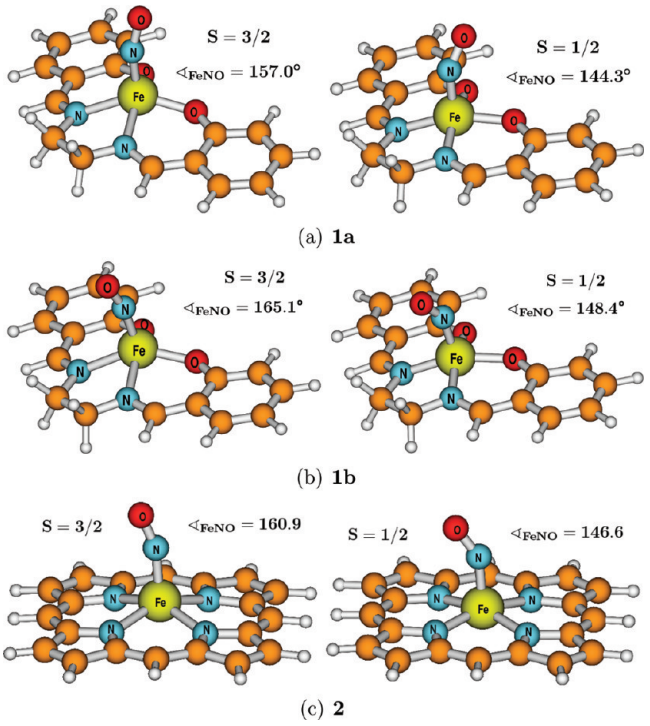

Figure 1. Structures of the iron nitrosyl complexes investigated in this work. (a) Conformation a of Fe(salen)(NO). (b) Conformation b of Fe(salen)(NO). (c) Fe(porphyrin)(NO). All structures are taken from ref 31.

spin density distributions were visualized using the ADF−GUI ADFVIEW program.[62]

All CASSCF calculations were performed with the program package Molpro[63] using Dunning's cc-pVTZ basis set for all atoms.[64,65] As an initial guess, an unrestricted Hartree−Fock calculation was performed. The natural orbitals from this unrestricted Hartree−Fock calculation are then used as starting orbitals for the CASSCF procedure. As convergence criteria, an orbital gradient threshold of 10^{-2} atomic units was chosen, and the threshold for the change in total energy was set to 10^{-6} Hartree in all calculations. As an optimization method, the method developed by Werner, Meyer, and Knowles[66−68] was used in all calculations. The CASSCF spin densities were visualized using the program Molekel.[69]

3. SPIN DENSITIES OF IRON NITROSYL COMPLEXES

Following the work of Ghosh and Conradie,[31] we investigate two iron nitrosyl complexes, denoted as $\{FeNO\}^7$ after Enemark and Feltham[70] (this notations indicates that seven electrons are distributed among the combinations of the NO π^* and the Fe 3d orbitals): Fe(salen)(NO) (**1**) and Fe(porphyrin)(NO) (**2**), whereby the former occurs in two different conformations named **1a** and **1b** (see Figure 1). The unpaired electron from the neutral NO species and the six d electrons of Fe(II) can be distributed over the combinations of the Fe 3d and NO π^* orbitals. The most favorable spin states resulting from this electronic structure are a doublet (one unpaired electron) and a quartet (three unpaired electrons) state. Experimentally, **2** is known to possess a doublet ($S = 1/2$) ground state,[71,72] while **1** exhibits a thermal spin-crossover from the doublet ($S = 1/2$) to the quartet state ($S = 3/2$) near 175 K.[73] Therefore, we

considered only the doublet and quartet spin states for all iron nitrosyl complexes in our theoretical study.

3.1. Energetics. We first analyze the relative spin-state energies of the iron nitrosyl complexes. These are listed, for the exchange−correlation functionals considered, in Table 1. For **1** (in both conformations), we found adiabatic energy splittings between the quartet and doublet state in the range of +12 and −10 kcal/mol. It is obvious that the energy splitting is largely dependent on the amount of exact exchange encoded in the exchange−correlation functional.[26] B3LYP (with 20% exact exchange) yields a quartet ground state favored by about 9 kcal/mol, while for TPSSh (with only 10% exact exchange), doublet and quartet spin states of almost the same energy are obtained. OLYP and OPBE behave similar to TPSSh and yield $S = 1/2$ and $S = 3/2$ spin states that are similar in energy. This is in agreement with the experimentally observed spin-crossover behavior. In contrast to the hybrid functionals, TPSS, BP86, and BLYP (all pure functionals without exact exchange) favor the doublet over the quartet state by approximately 10 kcal/mol. An exception is the meta-GGA functional M06-L (also a pure functional without exact exchange), which behaves similarly to B3LYP and favors the quartet state by about 9 kcal/mol. We note that the relative energies for OLYP, OPBE, and BLYP are consistent with the previous work presented by Conradie and Ghosh.[31] In general, only small deviations (<0.2 kcal/mol) can be observed. However, larger differences from the results of Conradie and Ghosh are found for **1b** for OPBE and B3LYP (2.1 and −11.1 kcal/mol, respectively). The reason for these differences can be revealed by inspecting the Mulliken spin populations and charges in our calculations (see Table 1 in the Supporting Information) and in ref 31. Note that since we use the same basis sets as in ref 31, these can be compared directly. The comparison indicates that Conradie and Ghosh have found a different state for $S = 3/2$ (OPBE) and $S = 1/2$ (B3LYP). Further, comparing the energies of these different states shows that those found in this work are lower in energy, and the corresponding Mulliken charges are physically more reasonable with no negative charges on the iron atom. For **1a**, larger differences can be observed for B3LYP. However, the Mulliken spin populations and charges in our calculations are similar to those in ref 31, and the origin of these differences remains unclear.

Table 1. Energy Differences ($E^{S=(3/2)} - E^{S=(1/2)}$) between Quartet and Doublet State (kcal/mol) in a TZP Basis Set for Selected Exchange−Correlation Functionals[a]

	OLYP	OPBE	BP86	BLYP	TPSS	TPSSh	B3LYP	M06-L
1a	−1.0	0.6	10.5	8.8	11.2	1.3	−9.0	−9.6
1a[31]	−1.2	0.5		8.8			−9.5	
1b	0.3	1.6	11.7	9.8	12.2	1.2	−9.7	−8.9
1b[31]	0.4	2.1		9.7			−11.1	
2	5.7	6.2	17.0	16.2	17.6	6.6	−3.1	−2.5
2[31]	5.9	6.5		16.6[b]			−4.6	

[a] A negative energy difference indicates that the quartet state ($S = 3/2$) is more stable, while for a positive value the doublet state ($S = 1/2$) is preferred. For comparison, the values reported by Conradie and Ghosh in ref 31 are also included. [b] Structure optimization.

For **2**, similar observations can be made. The adiabatic energy splittings follow the same trend as observed for **1**, except that the corresponding energy splittings are 6 kcal/mol higher in energy and, thus, found between −3 and +18 kcal/mol. B3LYP and M06-L predict a quartet ground state by about 3 kcal/mol. All other exchange−correlation functionals studied yield a doublet ground state, but with different relative energies. OLYP and OPBE as well as TPSSh favor the doublet state by 6 kcal/mol, while TPSS, BP86, and BLYP yield an energy gap of approximately 17 kcal/mol. As for **1**, our results for OLYP and OPBE are consistent with the previous work of Conradie and Ghosh,[31] and in general, only small deviations can be observed. Larger differences are only found for B3LYP. Again, inspection of the Mulliken spin populations (given in Table 2 of the Supporting Information) and charges indicates that a different state was converged for $S = 1/2$, and in comparison to ref 31, the one found by us is lower in energy.

3.2. Spin Density Distributions. It was already pointed out by Ghosh and Conradie[30,31] that the spin density distributions for the iron nitrosyl complexes are strongly dependent on the choice of the exchange−correlation functional. Let us first have a closer look at the spin density profiles before we continue to elaborate on the sources of these differences in detail.

The spin density distributions for **1b** are displayed in Figure 2. The spin densities for the quartet state do not depend on the exchange−correlation functional, where the iron atom carries an excess of α-electron density and the nitrosyl ligand an excess of

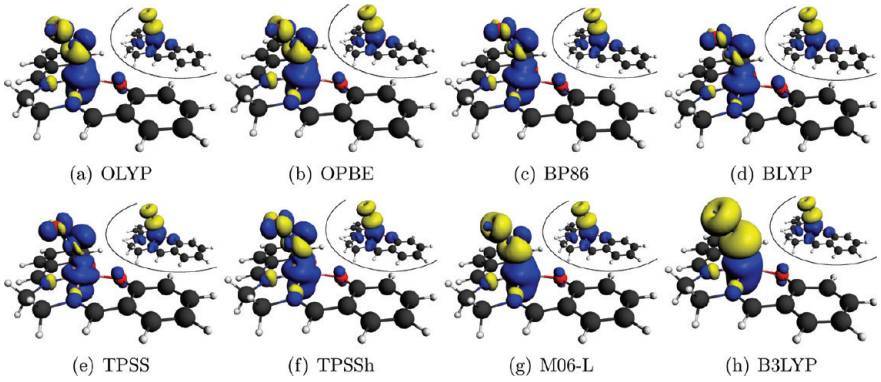

Figure 2. Spin density profiles for **1b** in a TZP basis set for selected density functionals. An isosurface value of 0.003 is chosen. The small picture in the upper right corner shows the quartet spin density for each exchange−correlation functional, while the large picture displays the sensitive doublet spin density. The blue surface (positive spin density) corresponds to an excess of α-electron density, while the yellow surface (negative spin density) corresponds to an excess of β-electron density.

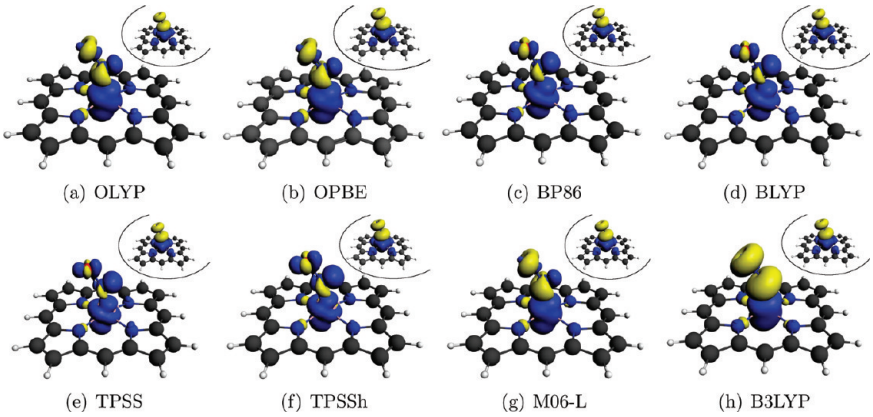

Figure 3. Spin density profiles for **2** in a TZP basis set for selected density functionals. An isosurface value of 0.003 is chosen. The small picture in the upper right corner shows the quartet spin density for each exchange−correlation functional, while the large picture displays the sensitive doublet spin density. The blue surface (positive spin density) corresponds to an excess of α-electron density, while the yellow surface (negative spin density) corresponds to an excess of β-electron density.

β-electron density. For the doublet state, however, notable differences in the spin density distributions can be observed. The spin densities can be ordered according to their associated energy splittings obtained for different exchange−correlation functionals. For BP86, BLYP, and TPSS, the spin densities are similar. OLYP, OPBE, and TPSSh yield different distributions around the nitrosyl ligand atoms with a larger amount of β-electron density. This excess of β-electron density further increases for M06-L. A completely different picture is obtained for B3LYP. While for all other functionals there is both α- and β-electron density on the nitrosyl ligand, with B3LYP, the ligand carries only β-electron density. In addition, the amount of β-electron density on the nitrosyl ligand is much larger with B3LYP than for all the other functionals, as is also obvious from the Mulliken spin populations (see Table 1 in the Supporting Information). For **1a**, similar spin density distributions are obtained, which are shown in Figure 1 in the Supporting Information.

Figure 3 shows the calculated spin densities for **2** as obtained with different exchange−correlation functionals. As already observed for **1**, BP86, BLYP, and TPSS yield similar results. One can recognize an increase in the α-electron density at the ligand atoms for TPSSh, and its decrease around the iron center. OLYP, OPBE, and M06-L yield a large amount of β-electron density located around the nitrosyl ligand atoms, which is missing for BP86, BLYP, TPSS, and TPSSh. As for **1**, an excess of β-electron density only on the nitrosyl ligand is found for B3LYP. But in contrast to **1**, we observe that calculations with different exchange−correlation functionals which yield similar energy splittings result in different spin density distributions (e.g., TPSSh which is comparable in relative energy, but not in spin density to OLYP/OPBE). M06-L, on the other hand, delivers a spin density similar to OLYP and OPBE but yields a very different energy gap (−2.5 kcal/mol with M06-L vs 6 kcal/mol with OLYP/OPBE).

3.3. Origin of Deviations in the Spin Density. To understand the origin of the differences in the spin densities of the doublet state, we investigate the Kohn−Sham molecular orbitals. For this, we choose **1b** and the three exchange−correlation functionals, BP86, OLYP, and B3LYP. To elucidate the subsequent analysis of the DFT orbitals, it is instructive to consider the qualitative molecular orbital diagram introduced by Hoffmann et al. for pentacoordinate metal complexes,[74,75] which we depict in Figure 4.

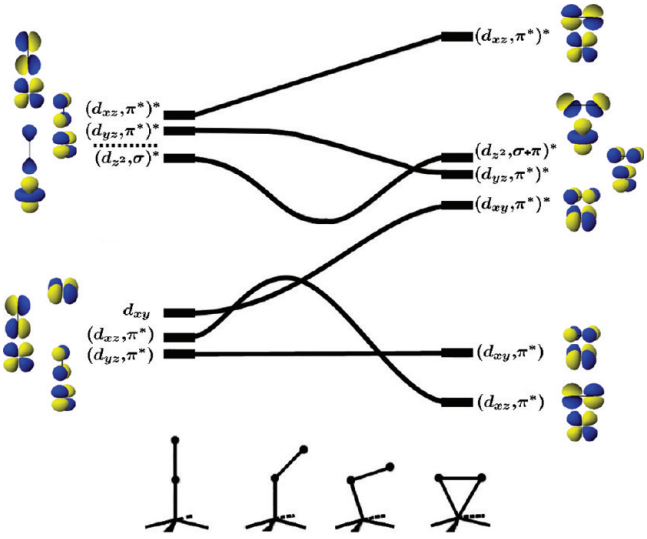

Figure 4. Hoffmann's correlation diagram for pentacoordinate metal complexes as presented in ref 74.

In their qualitative approach, they considered the iron d_{xy}, d_{z^2}, d_{xz}, and d_{yz} orbitals (the $d_{x^2-y^2}$-orbital is excluded because it is significantly higher in energy) as well as the NO σ and the two NO π^* orbitals. Four ligands (in our case, the nitrogen and oxygen donor atoms of the salen ligand and the nitrogen donor atoms of the porphyrin ligand) are arranged in the *xy* plane along the coordinate axes. Above this *xy* plane, the NO ligand is located between the *xz* and *yz* planes. For the bent structure present in **1** and **2**, these form (due to symmetry considerations) the molecular orbitals (d_{yz}, π^*), (d_{xz}, π^*), d_{xy}, $(d_{z^2}, \sigma)^*$, $(d_{yz}, \pi^*)^*$, and $(d_{xz}, \pi^*)^*$, which are occupied by seven electrons for the $\{FeNO\}^7$ complexes. For the doublet state, the (d_{yz}, π^*), (d_{xz}, π^*), and d_{xy} orbitals are doubly occupied, and the $(d_{z^2}, \sigma)^*$ orbital is singly occupied. These orbitals, in particular the singly occupied $(d_{z^2}, \sigma)^*$ orbital, determine the spin density distributions, and the corresponding differences in spin densities can be traced back to differing orbital patterns.

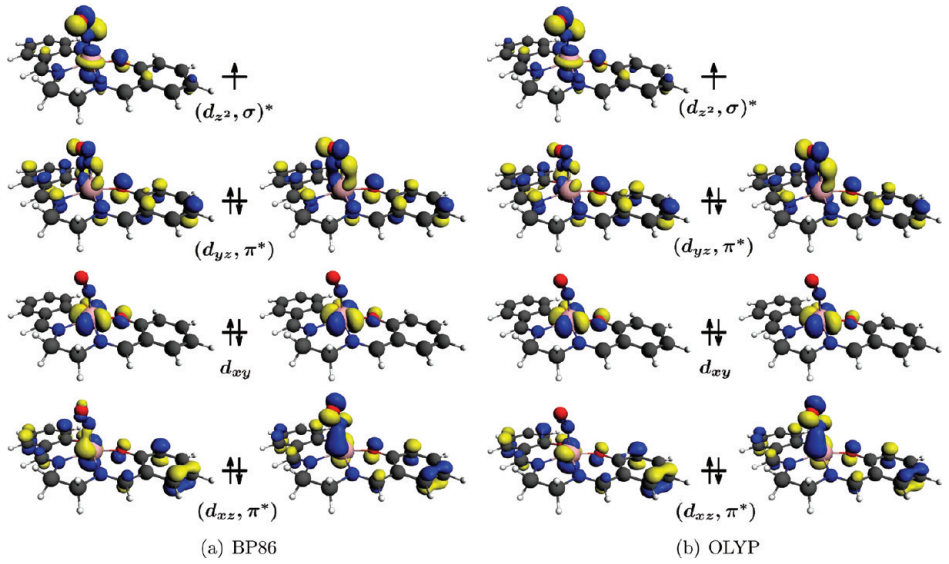

Figure 5. Valence orbitals for the doublet state of **1b** in a TZP basis set for selected exchange−correlation functionals. Those α and β orbitals which correspond to the same orbital combination are grouped together and ordered qualitatively according to the energy of the corresponding α orbital. An isosurface value of 0.05 is chosen. Only the orbitals which determine the spin density distribution are shown. Orbitals for α electrons are displayed on the left-hand side and orbitals for β electrons on the right-hand side.

For the quartet state, the (d_{yz}, π^*) and (d_{xz}, π^*) orbitals are doubly occupied. The remaining three electrons are then distributed over the singly occupied d_{xy}, (d_{z^2}, σ)*, and $d_{x^2-y^2}$ orbitals. Note that, in this case, the order of the molecular orbitals changes, and $d_{x^2-y^2}$, which is not shown in Figure 4, has to be included. The orbitals obtained in the DFT calculations for the quartet state are similar for all exchange−correlation functionals and qualitatively agree with Hoffmann's simplified picture. As a representative example, the relevant orbitals from the BP86 calculation are shown in Figure 2a in the Supporting Information.

Figure 5 shows the highest occupied molecular orbitals obtained for the doublet state with OLYP and BP86. All orbitals are described by Hoffmann's qualitative molecular orbital picture. However, in the unrestricted Kohn−Sham DFT calculations, α and β orbitals are different. In particular, the (d_{xz}, π^*) orbital contains no significant contribution from the NO π^* orbital to the corresponding α orbital. This induces an excess of β-electron density around the NO fragment. The same can be observed for the (d_{yz}, π^*) orbital, where the contribution of the NO π^* orbital to the α orbitals is reduced. The excess of α-electron density around the iron atom and nitrosyl fragment can be attributed to the singly occupied (d_{z^2}, σ)* orbital. Furthermore, there are also orbital contributions from the salen (and porphyrin) ligands, which, however, do not contribute to the spin density. In the case of OLYP, the α-spin (d_{yz}, π^*) orbital contains less contribution from the NO π^* orbital as compared to BP86, which increases the β-electron density around the nitrosyl fragment (see also Figure 2) and induces the divergent spin density distributions.

For B3LYP, we observe different orbital shapes for α and β electrons as compared to the former exchange−correlation functionals (see Figure 6). The α_1 and α_2 and the β_1 and β_2 orbitals result in very different orbital combinations, while the α_3 and α_4 and the β_3 orbitals can be related to Hoffmann's orbital diagram of Figure 4. The nonbonding d_{xy} orbital (α_2 and β_2) is replaced by different combinations of Fe d and NO π^* orbitals, which results in a stronger distribution of β-electron density into

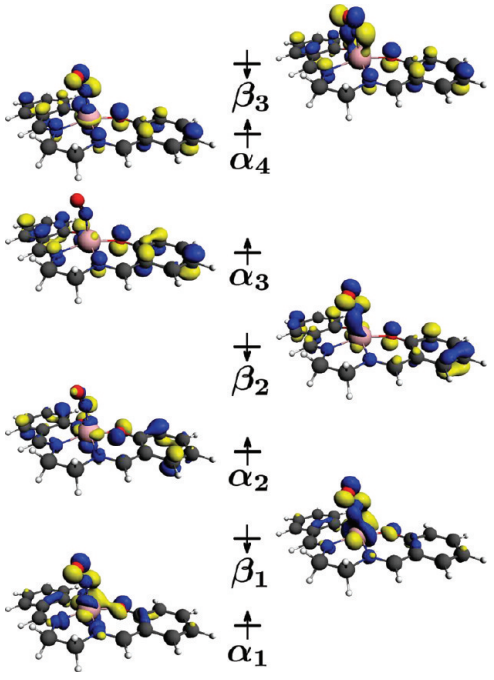

Figure 6. Valence orbitals for **1b** in a TZP basis set for B3LYP ordered qualitatively according to their energy. An isosurface value of 0.05 is chosen. Only the orbitals which determine the spin density distribution are shown. Orbitals for α electrons are displayed on the left-hand side and orbitals for β electrons on the right-hand side.

the NO π^* orbitals. While α electrons are preferentially distributed over the iron center and the salen fragment (α_2 and α_3), β electrons occupy the NO π^* orbitals (β_2 and β_3). This generates the characteristic cylindrical shape of the β electron density for B3LYP. Moreover, two singly occupied α orbitals and two different singly occupied β orbitals are obtained (compare α_1/α_2 and β_1/β_2, respectively).

Table 2. $\langle \hat{S}^2 \rangle$ Expectation Values in a TZP Basis Set for a Given Exchange−Correlation Functional

		OLYP	OPBE	BP86	BLYP	TPSS	TPSSh	B3LYP	M06-L	ideal
1a	$\langle \hat{S}_{hs}^2 \rangle$	4.40	4.42	4.21	4.18	4.27	4.57	4.75	4.62	3.75
	$\langle \hat{S}_{ls}^2 \rangle$	0.83	0.83	0.78	0.77	0.78	0.92	1.29	0.91	0.75
1b	$\langle \hat{S}_{hs}^2 \rangle$	4.40	4.42	4.21	4.19	4.27	4.58	4.75	4.63	3.75
	$\langle \hat{S}_{ls}^2 \rangle$	0.80	0.81	0.77	0.77	0.77	0.82	1.26	0.87	0.75
2	$\langle \hat{S}_{hs}^2 \rangle$	4.35	4.37	4.18	4.16	4.23	4.50	4.67	4.56	3.75
	$\langle \hat{S}_{ls}^2 \rangle$	0.81	0.82	0.77	0.77	0.77	0.80	1.20	0.86	0.75
3	$\langle \hat{S}_{hs}^2 \rangle$	4.49	4.53	4.35	4.30	4.41	4.68	4.82	4.68	3.75
	$\langle \hat{S}_{ls}^2 \rangle$	0.95	0.97	0.83	0.82	0.82	1.24	1.48	1.01	0.75

These different occupational patterns and orbital shapes result in a "broken-symmetry-like" solution for B3LYP, which can also be seen in the significantly larger $\langle \hat{S}^2 \rangle$ expectation value of 1.2 as compared to an ideal value of 0.75 in Hartree atomic units (see also Table 2; the same holds for 2). However, even though broken-symmetry solutions often yield accurate energetics, they result in incorrect spin density distributions. While this is obvious when broken-symmetry solutions are employed for singlet states (where the correct spin density vanishes[14]), for the doublet state considered here, it is less clear whether the spin density obtained from a particular solution is physically meaningful or not. Obviously, this is a serious problem if one is interested in the calculation of EPR properties. Note again that with the exact spin-dependent exchange−correlation functional, a broken-symmetry treatment should not be required, and unrestricted Kohn−Sham DFT would always yield the exact spin density.[38,39]

Finally, we note that the spin densities of **1** are comparable to those of **2** for a given exchange−correlation functional. Hence, similar spin densities are obtained for complexes with porphyrin or salen ligands. The iron nitrosyl moiety dominates the distribution of the α- and β-electron density, and we will have a closer look at this fragment in section 4.

4. DEFINING A SUITABLE MODEL FOR ACCURATE REFERENCE CALCULATIONS

Since the DFT spin densities are ambiguous, reference spin densities are required to decide which exchange−correlation functionals provide reliable spin densities. This task can be achieved by applying multireference *ab initio* methods. However, for the large salen and porphyrin complexes discussed above, such calculations are not feasible or require a restriction of the active space. Therefore, we construct a small model system for which CASSCF calculations are computationally feasible but which still shows similar differences in spin density distributions for the selected exchange−correlation functionals as the large iron nitrosyl complexes. As a model system, we choose $[FeNO]^{2+}$ (**3**), since the FeNO moiety dominates the distribution of α and β electrons in the full-fledged complexes. However, for the small $[FeNO]^{2+}$ molecule, a structure optimization of the bent structure results in a linear orientation of the nitrosyl group, suggesting an Fe(I) center and a positively charged NO^+ fragment. To ensure transferability, we need to enforce the occupation of the same orbitals as present in the large $\{FeNO\}^7$ complexes. These problems can be solved by considering the fixed geometry of the bent iron nitrosyl fragment present in the larger $\{FeNO\}^7$ complexes. Furthermore, we include four negative point charges of −0.5*e* each, which are located at a distance of 1.131 Å from the iron atom on the *x* and *y* axes, to model a square-planar ligand field and to obtain a similar electronic structure as present in the larger $\{FeNO\}^7$ complexes. All following CASSCF calculations are performed in C_1 symmetry and apply the OLYP optimized iron nitrosyl fragment of **1a**.

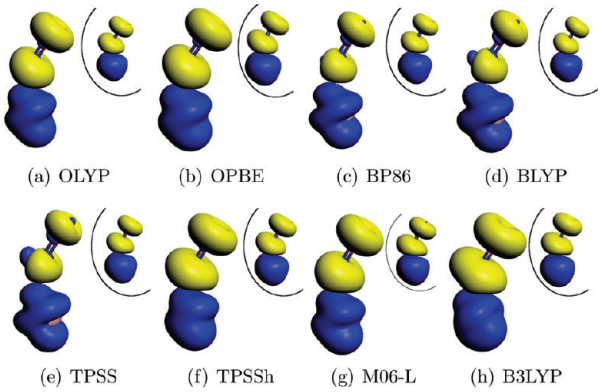

Figure 7. Spin density profiles for **3** in a TZP basis set for selected density functionals. An isosurface value of 0.003 is chosen. The small picture in the upper right corner shows the quartet spin density for each exchange−correlation functional, while the large picture displays the sensitive doublet spin density. The blue surface (positive spin density) corresponds to an excess of α-electron density, while the yellow surface (negative spin density) corresponds to an excess of β-electron density.

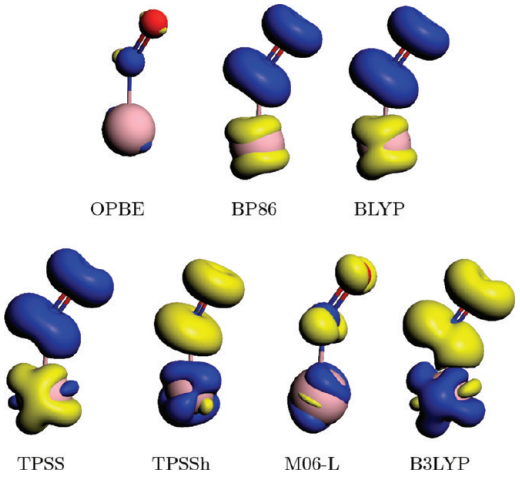

Figure 8. Spin density difference plots for **3** in a TZP basis set of the spin density profile for the corresponding exchange−correlation functional mentioned with respect to OLYP. An isosurface value of 0.003 is chosen. The blue surface corresponds to an excess of α-electron density, while the yellow surface corresponds to an excess of β-electron density with respect to OLYP.

4.1. DFT Calculations. First, we examine the influence of the exchange−correlation functional on the spin density distribution for the $[Fe(NO)]^{2+}$ model system. In Figure 7, the spin density profiles calculated for different exchange−correlation functionals are shown. As for the larger $\{FeNO\}^7$ complexes, the spin densities for the quartet configuration (shown in the inset on the right for each functional) are similar. The spin densities of the doublet state are shown in Figure 7 on the left for each functional. Compared to those of **1** and **2**, the differences between the different functionals appear smaller. However, there are considerable differences. To illustrate these more clearly, Figure 8

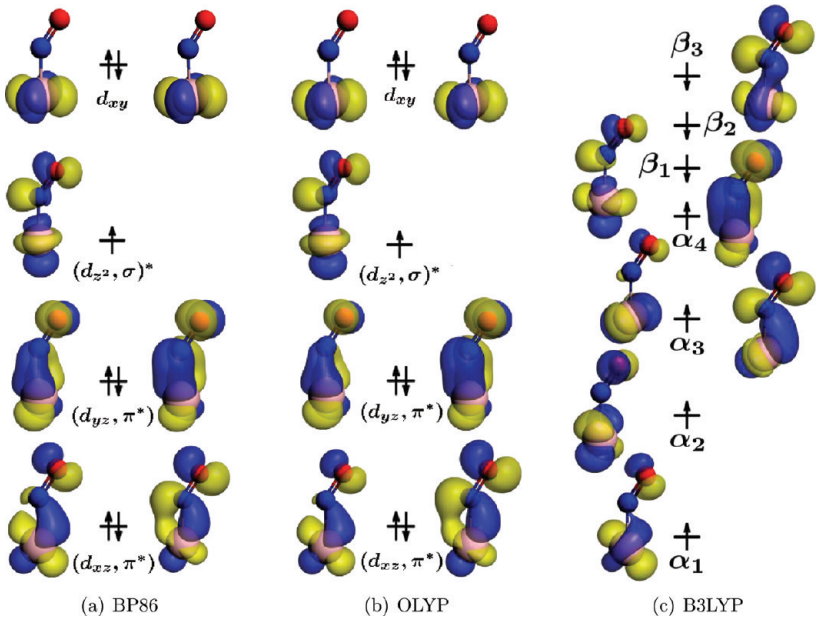

Figure 9. Valence orbitals of **3** in a TZP basis set for selected exchange−correlation functionals. An isosurface value of 0.05 is chosen. The orbitals are ordered qualitatively according to the energy of the corresponding α orbital. Orbitals which correspond to the same orbital combination are grouped together. All other orbitals turned out to be similar in shape for all exchange−correlation functionals. Orbitals for α electrons are displayed on the left-hand side and orbitals for β electrons on the right-hand side.

shows isosurface plots of the differences between the spin density obtained with OLYP and each of the other functionals. The isosurface value of 0.003 used in these plots of the spin density differences is the same as the one used for the spin densities themselves in Figure 7. Plots using larger isosurface values of 0.005 and 0.01 are shown in the Supporting Information (Figures 3 and 4) and are qualitatively similar to Figure 7.

The spin density difference plots reveal that for the $[Fe(NO)]^{2+}$ model system the spin densities can be arranged in two different groups, which are qualitatively similar to those found for **1** and **2**. For OLYP and OPBE, the spin density distributions are almost identical. The nonhybrid functionals BP86, BLYP, and TPSS lead to less β-electron density on the nitrosyl ligand compared to OLYP, i.e., a smaller overall spin polarization. For these functionals, one finds a region of α-electron density near the nitrogen atom in Figure 7. As for **1** and **2**, M06-L and the hybrid functionals TPSSh and B3LYP yield a stronger spin polarization compared to OLYP, corresponding to more α-electron density on the nitrosyl fragment in the difference plots of Figure 8. The magnitude of spin polarization, however, is dependent on the exchange−correlation functional and increases from M06-L to TPSSh and is largest for B3LYP.

In line with the spin density difference plot, the Mulliken spin populations given in Table 4 show the same increase in β-electron density on the nitrosyl ligand and in overall spin polarization. For BP86, BLYP, and TPSS, the β-spin population on the nitrosyl ligand is between 0.20 and 0.26. It increases to approximately 0.5 for OLYP and OPBE and to 0.55 for M06-L. For the hybrid functionals TPSSh and B3LYP, there is a β-spin population of 0.83 and 1.0, respectively, on the nitrosyl ligand. Note that the difference of ca. 0.3 between OLYP and OPBE on the one side and BP86, BLYP, and TPSS on the other is even larger than for the larger complexes, where the β-spin populations on the nitrosyl ligand differ only by approximately 0.2. Thus, the magnitude of the differences between the different functionals is comparable to those found for complexes **1** and **2**.

Note that for **3**, three different states can be optimized in the SCF procedure. In general, the state corresponding to 16 α and 15 β electrons in A′ and 4 α and β electrons in A″ represents the sought ground state that corresponds to the larger complexes, and all spin density distributions and in the following molecular orbitals are presented and discussed for this state. The energies obtained for all three possible states are given in Table 3 in the Supporting Information. Only with OPBE and B3LYP, the state corresponding to the larger complexes is not the ground state. Note that the point charges try to model a square planar ligand field in order to enforce similar occupation of orbitals in **3** as found in the larger $\{FeNO\}^7$ complexes. For OPBE and B3LYP, however, the modeled ligand field is not strong enough, leading to a physically unreasonable ground state.

But what is the origin of the observed differences in spin density distributions? For the quartet state, all orbitals are similar for all exchange−correlation functionals considered, and thus, no dependence of the spin density distribution on the exchange−correlation functional is found. Furthermore, for all functionals, the resulting orbitals qualitatively agree with Hoffmann's simplified molecular orbital diagram and with the results obtained for the larger complexes **1** and **2**. In particular, the spin density is determined by the three singly occupied orbitals, which can be described as d_{xy}, $(d_{z^2}, \sigma)^*$, and $d_{x^2-y^2}$. For the BP86 calculation, the relevant orbitals are shown in Figure 2b in the Supporting Information.

For the doublet configuration, the situation is different. An orbital analysis shows that the seven valence orbitals differ considerably for all selected exchange−correlation functionals. These seven orbitals determine the spin density distribution, which will be obvious if we refer to the orbital analysis of the larger $\{FeNO\}^7$ complexes. As an explicit example, the orbitals for B3LYP, OLYP, and BP86 are shown in Figure 9. As expected,

they represent a combination of the Fe d with the NO σ and NO π^* orbitals. The orbital shapes obtained for OLYP and BP86 are similar to those of the corresponding orbitals of the larger $\{FeNO\}^7$ complexes, and the divergent distributions of α and β electron density are due to similar occupation patterns. As for the larger complexes, α and β orbitals differ. While α electrons are centered on the iron atom, β electrons are more delocalized on the NO fragment. This leads to the separation of α- and β-electron density and results in weak spin polarization. The reduced β-electron density around the NO fragment obtained for BP86 is due to the enhanced delocalization of α electrons into the π^* orbital as compared to OLYP for the (d_{yz}, π^*) and (d_{xz}, π^*) orbitals.

In the case of B3LYP, different orbital combinations are obtained, as we have already observed in **1**. The α_1 and α_3 and the β_1 and β_3 orbitals contain additional contributions from different Fe d orbitals as compared to OLYP or BP86. Furthermore, α electrons preferentially occupy metal orbitals (α_1 to α_4), leading to an excess of α-electron density on the iron atom, while β electrons are distributed over ligand π^* orbitals (β_1 to β_3), resulting in the corresponding excess of β electron density. This occupation pattern produces strong spin polarization in the B3LYP case. Compared to OLYP and BP86, different α and β orbitals are obtained for B3LYP, resulting in a "broken-symmetry-like" solution, which we already observed for the larger $\{FeNO\}^7$ complexes and which is also indicated by the expectation value of $\langle \hat{S}^2 \rangle$ of 1.48 compared to the ideal value of 0.75 (see also Table 2).

In conclusion, one observes that the DFT electronic structures of all complexes studied are similar and correspond to the qualitative molecular orbital diagram by Hoffmann: Similar orbital combinations and occupations are obtained. We observe a similar dependence of the spin density on the approximate exchange−correlation functional for complex **3** as for complexes **1** and **2**, and we can arrange the spin density distributions of **3** according to their spin density patterns in a similar way to what we found for complexes **1** and **2**. Furthermore, the differences in spin density distributions are based on similar reasons and can be traced back to the same differences in Kohn−Sham molecular orbitals. Hence, the $[Fe(NO)]^{2+}$ complex **3** can serve as a representative model system for the larger complexes **1** and **2**.

4.2. CASSCF Calculations. As discussed in the previous paragraph, the spin density distributions obtained for the doublet state of **3** are—as those of the larger complexes—dependent on the exchange−correlation functional, and it remains unclear which functional describes the spin density most accurately. To investigate this question, we calculated CASSCF reference spin densities. Since we consider a small model system in which the salen or porphyrin ligands have been removed and replaced by point charges, we can choose an active space that contains all orbitals that are possibly relevant for a correct description of the spin density.

In a minimal active space, all orbitals present in the qualitative molecular orbital diagram by Hoffmann et al. (see Figure 4) have to be included. This results in an active space which is composed of four Fe 3d orbitals (d_{xy}, d_{xz}, d_{yz}, and d_{z^2}) and both NO π^* orbitals. In addition, the Fe $d_{x^2-y^2}$ orbital has to be included. Altogether, this results in a minimal active space of seven electrons correlated in seven orbitals. As a further step, we also consider both NO π orbitals, which further extends the minimal active space to 11 electrons correlated in nine orbitals. The natural orbitals obtained in these minimal CAS(7,7) and CAS(11,9) calculations are also shown in Figures 5 and 10 in the Supporting Information for the quartet and doublet states, respectively.

To guarantee that the spin density is converged with respect to the active space, we performed CASSCF calculations with different dimensions of the active space, which was systematically enlarged. In particular, it might be important to include an additional shell of Fe d orbitals (double-shell orbitals). The extension of the active orbital space by a second d-shell orbital for each metal 3d orbital represents a common procedure in CASSCF calculations.[49,76] However, it turns out that it is not trivial to identify these double-shell orbitals, because they mix considerably with antibonding ligand orbitals, and for this reason, additional antibonding ligand orbitals also have to be included in order to construct a stable active space.

For the quartet state, we proceed as follows. First, two virtual orbitals with contributions of Fe d_{xz} and d_{yz} were included in the CAS(11,9) active orbital space, resulting in the corresponding CAS(11,11) calculation. Yet, the d_{yz} double-shell orbital was rotated into an empty ligand orbital. To include this double-shell contribution, the active orbital space had to be extended by an additional virtual orbital, resulting in our CAS(11,12) calculation. The CAS(11,12) active space was further extended by an additional virtual orbital with a large contribution from the third Fe d_{z^2} orbital for the CAS(11,13) calculation. The fourth Fe d_{xy} double-shell orbital could be included in the active space in our CAS(11,15) calculation, which also contains an additional empty ligand orbital.

Similarly for the doublet state, first two virtual orbitals with contributions of Fe d_{xz} and d_{xy} were included in the CAS(11,9) described above, resulting in a CAS(11,11). Adding one additional virtual orbital with a contribution from Fe d_{yz} yields a CAS(11,12) active space. The fourth Fe d_{z^2} orbital could be included in our CAS(11,14) calculation, which contains an additional empty ligand orbital. Finally, we note that the contributions of the Fe double-shell orbitals to the natural orbitals are significantly larger for the doublet state than for the quartet state.

The CAS(11,15) and CAS(11,14) calculations for the quartet and doublet state, respectively, contain the four Fe d_{xz}, d_{xy}, d_{yz}, and d_{z^2} double-shell orbitals. Including the fifth (Fe $d_{x^2-y^2}$) double-shell orbital was, however, not feasible since its destabilization by the point charge environment requires the including of a number of additional ligand orbitals. For both the quartet and the doublet state, we also explored CASSCF calculations in which we extended the CAS(11,11) active space by one ligand σ orbital and the corresponding antibonding σ^* orbital, resulting in a CAS(13,13) containing the Fe d_{xz} and d_{xy} double-shell orbitals. However, including the remaining Fe double-shell orbitals in these calculations turned out to be problematic and would require the inclusion of additional ligand orbitals. Therefore, calculations with an active space containing the four Fe double-shell orbitals, which are included in the CAS(11,15) or CAS(11,14) calculations, were not possible. For this reason, we will only consider the CAS(11,x) calculations in the following. The converged natural orbitals for all employed active spaces can be found in the Supporting Information (Figures 5−9 and 10−14 for the quartet and doublet states, respectively).

The CASSCF spin densities of the quartet and doublet states are shown in Figures 10a and 11a, respectively. For the quartet state, one finds only a weak dependence of the spin density on the size of the active space chosen, and the CASSCF spin density

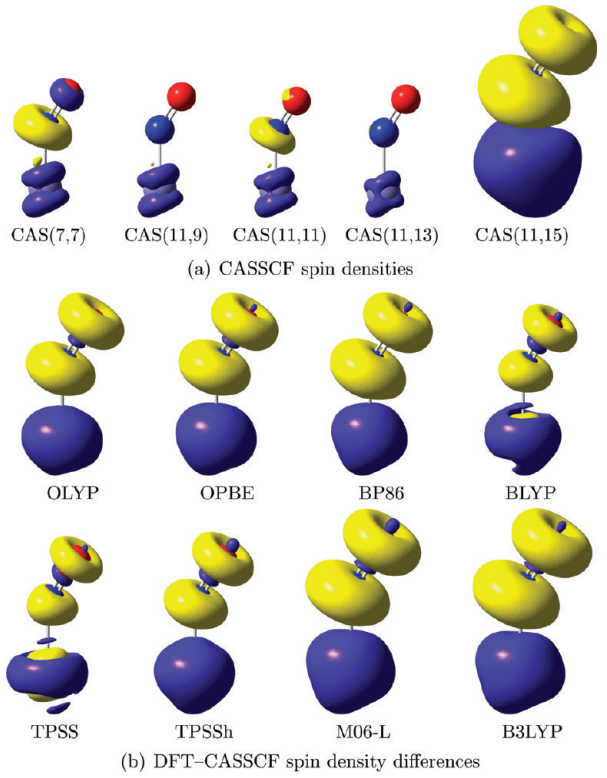

Figure 10. (a) CASSCF spin density difference plots for different dimensions of the active space with respect to the CAS(11,15) reference spin density for the quartet state of **3**. The CAS(11,15) spin density is shown on the right-hand side. The blue surface corresponds to an excess of α-electron density, while the yellow surface corresponds to an excess of β-electron density. (b) Difference plots of the spin density for the approximate exchange−correlation functionals and the CAS(11,15) reference spin density profile for the quartet state of $[Fe(NO)]^{2+}$. An isosurface value of 0.003 is used throughout. Similar plots using larger isosurface values are included in the Supporting Information (Figures 17 and 18).

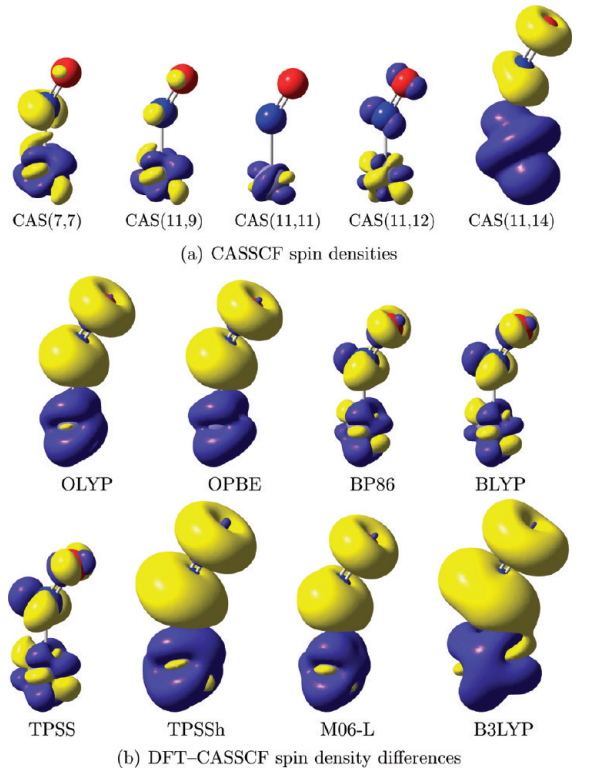

Figure 11. (a) CASSCF spin density difference plots for different active spaces with respect to the CAS(11,14) reference spin density for the doublet state of **3**. The CAS(11,14) reference spin density is shown on the right-hand side. The blue surface (positive spin density) corresponds to an excess of α-electron density, while the yellow surface (negative spin density) corresponds to an excess of β-electron density. (b) Difference plots of the spin density for the approximate exchange−correlation functionals and the CAS(11,14) reference spin density profile for the doublet state of $[Fe(NO)]^{2+}$. An isosurface value of 0.003 is used throughout. Similar plots using larger isosurface values are included in the Supporting Information (Figures 19 and 20).

profiles are similar for all active spaces considered. Therefore, the figures only show the CAS(11,15) spin density, while for the smaller active spaces, only the difference with respect to CAS(11,15) is shown. For the CAS(7,7) and CAS(11,9) calculations (i.e., without double-shell effect), the spin density distributions are qualitatively in good agreement with our converged CAS(11,15) reference spin density. Hence, already these minimal active spaces are sufficient to obtain an accurate spin density distribution. We note that also for the active spaces containing 13 active electrons, only small differences in the spin density are found (see the difference spin density plots in Figure 15 of the Supporting Information).

For the doublet state, larger deviations of the spin density distribution with respect to the size of the active space can be observed. Figure 11a shows the spin-density differences with respect to the CAS(11,14) reference, for which the active space contains the four most important double-shell d orbitals. When enlarging the active space, the spin density gradually converges toward the CAS(11,14) reference. We should note that the CAS(7,7) and CAS(11,9) spin densities, i.e., for active spaces without double-shell orbitals, are qualitatively similar to the CAS(11,14) reference spin density. These minimal active spaces are sufficient to obtain a *qualitative* estimate of the spin density distribution, while for quantitatively correct spin densities, Fe double-shell orbitals have to be included. Again, also for the active spaces containing 13 active electrons, very similar spin densities are obtained (see the difference spin density plots in Figure 16 of the Supporting Information.)

To analyze the origin of the spin densities in the CASSCF calculations, we will examine the natural orbitals and CASSCF configurations of **3** in detail. An in-depth discussion on the electronic structure of the larger $\{FeNO\}^7$ complexes can be found in ref 49. Concerning both the quartet and doublet states, the natural orbitals of different active spaces are in general similar; only some deviations in orbital shape and occupation numbers can be recognized when the active space is enlarged. The most important natural orbitals which correspond to those in the minimal active space of seven electrons in seven orbitals are shown in Figure 12. In general, the Fe d_{xy} orbital does not interact with the ligand orbitals for all active spaces considered. Moreover, we observe a strong covalent interaction between three Fe d orbitals (d_{yz}, d_{xz}, d_{z^2}) and the NO σ and π^* orbitals resulting in two bonding [(d_{yz},π^*) and (d_{xz},π^*)], two antibonding [(d_{yz}, π^*)* and (d_{xz}, π^*)*], and one nonbonding orbital [(d_{z^2},σ)*]. In general, the three highest bonding [(d_{yz}, π^*), (d_{xz}, π^*), and d_{xy}], the two lowest antibonding orbitals [(d_{yz}, π^*)* and (d_{xz}, π^*)*], and

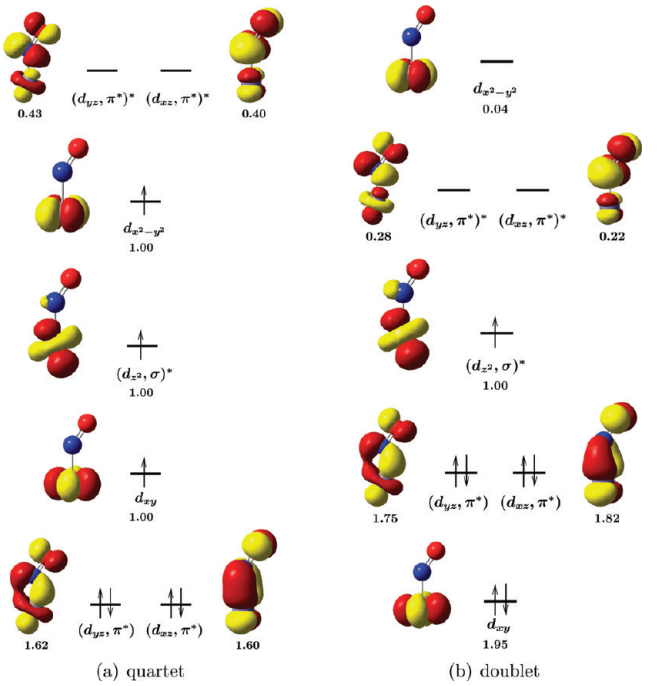

Figure 12. Natural orbitals and occupation numbers for the CAS(11,15) calculations of the quartet state and the CAS(11,14) calculation of the doublet configuration of **3**. An isosurface value of 0.05 was chosen. The natural orbitals are printed according to their occupation number. The arrows indicate the occupation in the principal configuration.

additionally the $(d_{z^2}, \sigma)^*$ orbital resemble qualitatively the orbital picture of Hoffmann et al., as given in Figure 4.

To identify how the spin density arises, one needs to investigate not only the (spin-independent) natural orbitals but also the corresponding wave functions. To this end, Table 3 lists the most important configurations for the quartet and the doublet states. For both the doublet and the quartet configuration, the CI coefficients are very similar for different active spaces, and therefore, only those obtained in the largest active spaces, CAS(11,15) for the quartet and CAS(11,14) for the doublet, are given in the table. For the quartet state, variations in CI coefficients are in general below 10%; only for the configuration with small CI weights can larger deviations be observed. Furthermore, there is a dominant contribution to the wave function (CI weight > 0.7) which corresponds to the quartet ground state; all other CI coefficients are smaller (<0.3). This principal configuration is also shown in Figure 12 and qualitatively corresponds to the orbitals obtained in the DFT calculations. The principal configuration, however, which contains three unpaired electrons on the iron atom, cannot explain the observed spin polarization (Figure 10a). The polarization can be accounted for by adding those configurations that contain excitations from the bonding (d_{yz}, π^*) and (d_{xz}, π^*) to the antibonding $(d_{yz}, \pi^*)^*$ and $(d_{xz}, \pi^*)^*$ orbitals, which shifts the β-electron density toward the ligand. All of these excitations correspond to medium-sized CI coefficients (>0.05) and are marked in bold face in Table 3. The distribution of β electrons in both NO π^* orbitals results in its characteristic cylindrical shape. Hence, these excited configurations lead to an excess of α-electron density on the iron atom and an excess of β-electron density on the NO fragment. It should be noted that in all of the configurations listed in Table 3, the $(d_{z^2}, \sigma)^*$, d_{xy}, and $d_{x^2-y^2}$ orbitals are each singly occupied by one α electron.

Table 3. Total Wave Function for the Quartet State for the CAS(11,15) and for the Doublet State for the CAS(11,14) Calculation of 3[a]

$S = (3/2)$		$S = (1/2)$	
22 aaa 00	0.7030268	2 22 a 00 0	0.8441848
20 aaa 20	−0.2427797	**2 ba a ba 0**	−0.1388339
02 aaa 02	−0.2329925	**2 ab a ab 0**	−0.1239105
2a aaa b0	0.2081849	**2 aa a bb 0**	0.1021302
a2 aaa 0b	0.1955026	**2 2a b a0 0**	−0.0859653
ab aaa ab	0.1355478	**2 bb a aa 0**	0.0844657
0a aaa b2	−0.0551488	**2 2a a b0 0**	0.0747853

[a] On the left-hand side, the configurations are printed; on the right hand-side, the corresponding CI coefficients are given. Only those natural orbitals which are important for the spin density are considered; all other bonding orbitals are doubly occupied and all other antibonding orbitals empty. The orbital ordering corresponds to the one in Figure 12: (d_{yz},π^*), (d_{xz},π^*), d_{xy}, $d_{x^2-y^2}$, $(d_{z^2},\sigma)^*$, $(d_{yz},\pi^*)^*$, and $(d_{xz},\pi^*)^*$ for the quartet state and d_{xy}, (d_{yz},π^*), (d_{xz},π^*), $(d_{z^2},\sigma)^*$, $(d_{yz},\pi^*)^*$, $(d_{xz},\pi^*)^*$, and $d_{x^2-y^2}$ for the doublet state, respectively. Further, those configurations which are important for the spin density and correspond to CI coefficients larger than 0.05 are considered and marked in bold face. A more detailed table can be found in the Supporting Information. 2: doubly occupied orbital. a: orbital occupied by an α electron. b: orbital occupied by a β electron. 0: empty orbital.

A similar observation can be made for the doublet configuration. As for the quartet state, there is one principal contribution to the wave function (CI weight > 0.8), which is included in Figure 12 and qualitatively corresponds to the orbitals obtained in the DFT calculations. In addition, we find configurations which correspond to excitations from the bonding (d_{yz}, π^*) and (d_{xz}, π^*) to the antibonding $(d_{yz}, \pi^*)^*$ and $(d_{xz}, \pi^*)^*$ orbitals. However, both α- and β-electron excitations are present in configurations with large CI weights for the doublet configuration, while for the quartet state, configurations containing only excitations of β electrons correspond to large CI coefficients. These excitations are marked in bold face in Table 3. Admixture of these configurations leads to a weaker spin polarization for the doublet state as compared to the quartet state. Furthermore, for most configurations with large CI coefficients, the $(d_{z^2}, \sigma)^*$ orbital remains singly occupied by an α electron, which induces the characteristic shape of the α-electron density around the Fe atom.

4.3. Comparison of CASSCF and DFT Results. The isosurface plot of the CASSCF reference spin densities in Figure 10a can be compared to those obtained from DFT calculations, shown in Figure 7. All considered exchange−correlation functionals favor spin polarization, and there is a good qualitative agreement between the DFT and CASSCF spin densities. However, a comparison of the isosurface plots might be misleading. Therefore, to consider a more quantitative benchmark of DFT spin density distributions as well, we additionally calculated difference plots of the DFT and CASSCF spin densities with respect to the CAS(11,15) spin density, which is shown in Figure 10b. Note that these difference plots employ the same isosurface value that was used for the spin densities themselves in Figures 7 and 10a. Plots using larger isosurface values are included in the Supporting Information. These spin density difference plots are very similar for all of the considered exchange−correlation functionals, but in all cases, there are non-negligible differences between DFT and CASSCF. At the

Table 4. Selected Mulliken Spin Populations for the Doublet State of 3

	$S = 1/2$		
method	Fe	N	O
OLYP	1.484	−0.259	−0.226
OPBE	1.520	−0.283	−0.237
BP86	1.259	−0.130	−0.129
BLYP	1.218	−0.105	−0.114
TPSS	1.208	−0.101	−0.107
TPSSh	1.831	−0.453	−0.378
M06-L	1.545	−0.294	−0.252
B3LYP	2.023	−0.559	−0.465
CAS(11,11)	1.168	−0.082	−0.086
CAS(11,12)	1.090	−0.036	−0.054
CAS(11,14)	1.144	−0.068	−0.076

nitrosyl ligand, all functionals predict a β-electron density that is too high, while at the Fe atom, there is a redistribution of the α-electron density. However, the shape of these spin density differences is comparable to that of the spin density itself, which indicates that the differences are mainly quantitative. While the shape of the spin density is qualitatively correct with all functionals, they all overestimate the spin polarization. This overestimation is the smallest for the BP86, BLYP, and TPSS functionals.

Similarly for the doublet state, a qualitative estimate of the accuracy of approximate exchange−correlation functionals can be obtained by comparing the DFT and CASSCF spin density isosurface plots in Figures 7 and 11a, respectively. In the CASSCF calculations, the α-electron density is located at the iron atom, while on the nitrosyl ligand, there is only β-electron density, with an almost cylindrical shape. By contrast, the spin densities obtained with BP86, BLYP, and TPSS contain α-electron density close to the nitrogen atom. Thus, the spin densities obtained with these functionals disagree with the accurate CASSCF spin density. For all other functionals, the isosurface plots qualitatively appear to agree with the CASSCF reference spin density.

However, in contrast to this apparently good agreement of the DFT and CASSCF isosurface plots for all functionals except BP86, BLYP, and TPSS, we can observe considerable differences in the corresponding DFT−CASSCF spin-density difference plots in Figure 11b. With OLYP, OPBE, and M06-L, there is a too large β-electron density on the nitrosyl ligand, and a too large α-electron density at the Fe atom; i.e., the spin polarization is overestimated. The magnitude of these differences is comparable to the one found for the quartet state. The hybrid functionals TPSSh and B3LYP yield an even larger excess of β electrons at the nitrosyl fragment and an overall larger spin polarization compared to the CASSCF reference. As discussed above, this is due to the "broken-symmetry-like" solutions obtained in this case. Finally, for BP86, BLYP, and TPSS, where already the isosurface plots of the spin density itself did qualitatively not agree with the CASSCF reference, the difference plots reveal a too large β-electron density on the nitrosyl ligand, with a redistribution of spin density close to the nitrogen. However, even though there is a qualitative disagreement close to the nitrogen atom, the smallest differences from the CASSCF reference spin density are found for the BP86, BLYP, and TPSS exchange−correlation functionals.

A similar picture can be obtained from comparing Mulliken spin populations of the DFT and CASSCF calculations given in Table 4. These also show that the functionals can be arranged in three groups: For BP86, BLYP, and TPSS, the Mulliken spin populations agree best. A slightly worse agreement is found for OLYP, OPBE, and M06-L. And, a much larger deviation from the CASSCF reference is found for B3LYP and TPSSh. Note, however, that a comparison of Mulliken spin populations obtained in different basis sets (Slater-type TZP basis set for DFT and Gaussian-type cc-pVTZ for CASSCF) is problematic. Despite the good agreement of the Mulliken spin populations for BP86, BLYP, and TPSS, the spin density difference plots show that for all functionals there are significant deviations from the CASSCF spin density.

These deviations in spin densities can also be related to differences in CASSCF and DFT orbitals. However, it is important to realize that such a comparison can be misleading: DFT and CASSCF both try to represent the same (spin) density in a different fashion (i.e., with integer and noninteger occupation numbers, respectively). Therefore, even with the exact exchange−correlation functional, the Kohn−Sham orbitals and the CASSCF natural orbitals would differ. The CASSCF natural orbitals are in general more delocalized than the corresponding DFT orbitals, in particular around the NO ligand (NO π^* orbitals), which decreases the α-electron density around the Fe atom. This can be observed as the blue surface in the spin density difference plots. The larger (or smaller) distribution of β electrons around the NO ligand with respect to the CASSCF reference can refer to the stronger (or weaker) delocalization of β electrons in the NO π^* orbitals. Note that the CASSCF excitation structure decreases the β-electron density around the NO ligand and simultaneously the α-electron density around the Fe atom.

In summary, the comparison of DFT and CASSCF spin densities shows that none of the exchange−correlation functionals considered here is able to predict the spin density distributions accurately. This view is supported by a comparison of the spin density isosurface plots, the spin density difference plots, and a comparison of the Mulliken spin populations. The size of the differences in the spin density is comparable for the quartet state and for the doublet state. For both the quartet and the doublet states, the smallest differences are found with the BP86, BLYP, and TPSS exchange−correlation functionals, even though for the doublet state these three functionals result in a qualitatively wrong spin density close to the nitrogen atom.

5. CONCLUSIONS

Since the spin density represents an essential quantity for the calculation of EPR parameters, it is important for quantum chemistry to be able to predict spin density distributions reliably. Recently, Conradie and Ghosh[31] discussed the difficulty in calculating accurate spin density distributions for $\{FeNO\}^7$ complexes employing DFT[31] where different exchange−correlation functionals yield qualitatively very different spin density distributions. In this work, we extend their studies by considering a large representative set of exchange−correlation functionals and by performing a detailed orbital analysis of the sources of the resulting differences in spin densities.

For the $\{FeNO\}^7$ complexes, the DFT description of the low-spin doublet state remains most challenging. The spin density distributions are sensitive to the chosen approximate exchange−correlation functional. Our orbital analysis shows that the

different spin densities can be traced back to different occupation patterns with respect to only a few orbitals. The seven highest molecular orbitals turn out to be crucial for the distribution of α and β electrons. Especially, the differences in the two (d,π^*) orbitals and the $(d_{z^2}, \sigma)^*$ orbital explain the spin density distribution obtained for nonhybrid exchange−correlation functionals. The hybrid functional B3LYP, however, results in a "broken-symmetry-like" solution. This shows that one has to be very careful when considering spin densities of low-spin states obtained from DFT calculations. If no "broken-symmetry-like" solution is obtained (as in the case of the nonhybrid functionals), the spin density can be interpreted as an approximation to the real spin density. If, on the other hand, a "broken-symmetry-like" solution is obtained, the DFT spin density does not correspond to the physical spin density. Instead, it could be interpreted as an approximation to the on-top pair density.[38] However, this precludes the calculation of properties depending on the spin density such as EPR parameters and is thus not desirable.

To decide which approximate exchange−correlation functionals yield accurate spin density distributions, multireference methods are required. Comparison to CASSCF results can serve as an accurate benchmark of exchange−correlation functionals. However, for the large complexes, it is not a priori clear whether the active spaces that are computationally feasible include all of the relevant orbitals. Therefore, we introduced a small model molecule, $[Fe(NO)]^{2+}$, which features the same electronic structure and exhibits a similar dependence of the spin density on the approximate exchange−correlation functional as the larger complexes. Due to its small size, we can efficiently apply the CASSCF approach. Furthermore, we can employ an active space that includes all relevant orbitals that have metal−ligand character as well as four of the five Fe double-shell d orbitals. This results in an active space of 11 electrons correlated in 15 or 14 active orbitals, which appears to be sufficient to obtain reliable reference spin densities.

Note that while such rather small active spaces are sufficient for the small $[Fe(NO)]^{2+}$ model system to obtain converged spin density distributions, this might not be the case for the salen and porphyrin complexes anymore. CASSCF calculations for different $\{FeNO\}^7$ complexes and medium-sized active spaces have already been presented in the literature,[49] giving first insights into the quality of DFT spin densities. However, studying the convergence of the spin density with respect to the dimension of the active space for these larger complexes remains challenging since additional ligand and iron orbitals should be included in the active space.[49] This renders such calculations infeasible with standard correlation methods. An efficient treatment of larger active spaces is possible with conceptually different electronic correlation methods such as the DMRG algorithm.[77−79] The DMRG study of the discussed $\{FeNO\}^7$ complexes is part of our future work.

A comparison of DFT and CASSCF spin density isosurface plots for the quartet state indicates that DFT provides qualitatively consistent spin densities for all exchange−correlation functionals studied. However, an inspection of DFT−CASSCF spin density difference plots shows non-negligible differences. These are similar for all exchange−correlation functionals, where the smallest differences are observed for the BP86, BLYP, and TPSS functionals. The deviations are mainly in the quantitative description of the amount of spin polarization, while qualitatively, the spin density is predicted correctly.

For the doublet state, the spin densities obtained with different exchange−correlation functionals are very different. The best agreement is again found for BP86, BLYP, and TPSS. However, these three functionals predict a qualitatively different spin density distribution at the ligand nitrogen atom. The spin densities obtained with the remaining nonhybrid functionals show larger deviations and predict a too large spin polarization, whereas the hybrid functionals B3LYP and TPSSh result in a "broken-symmetry-like" solution with a qualitatively wrong spin density. These results agree with those of earlier work by Pierloot et al.,[49] who found that for the doublet states of the larger $\{FeNO\}^7$ complexes, nonhybrid functionals yield spin densities which are (on the basis of a comparison of spin density isosurface plots and Mulliken spin populations) in closest agreement with the CASSCF reference.

In summary, we find that none of the tested exchange−correlation functionals is able to provide a satisfactory description of the spin densities in the considered iron nitrosyl complexes. Hence, improved exchange−correlation functionals that reliably predict the spin densities in transition metal complexes will have to be developed. Our results indicate that the currently available functionals do not take the spin density (which is, in addition to the total density, a basic variable in spin-DFT) properly into account. Therefore, we believe that considering the spin density more closely provides a promising route to improved exchange−correlation functionals for transition metal chemistry.

■ ASSOCIATED CONTENT

Supporting Information. Additional details on orbitals and active spaces are available and have been included. This information is available free of charge via the Internet at http://pubs.acs.org/.

■ AUTHOR INFORMATION

Corresponding Authors

*E-mail: christoph.jacob@kit.edu, markus.reiher@phys.chem.ethz.ch.

■ ACKNOWLEDGMENT

Financial support by the Swiss National Science Foundation (SNF) is gratefully acknowledged (project 200020-132542/1). C.R.J. acknowledges funding from the DFG-Center of Functional Nanostructures in Karlsruhe. K.B. thanks the Fonds der Chemischen Industrie for a Chemiefonds scholarship.

■ REFERENCES

(1) Carreira, E. M.; Kvaerno, L. *Classics in Stereoselective Synthesis*, 1st ed.; Wiley-VCH: Weinheim, Germany, 2009.

(2) Valentine, J. S.; Poulos, T. L.; Jameson, G. B.; Ibers, J. A.; Que, L., Jr.; Yoshikawa, S.; Lindley, P. F. Oxygen Metabolism. In *Biological Inorganic Chemistry: Structure and Reactivity*, 1st ed.; Gray, H. B., Stiefel, E. I., Valentine, J. S., Bertini, I., Eds.; University Science Book: Sausalito, CA, 2007; pp 319−442.

(3) Frenking, G.; Fröhlich, N. *Chem. Rev.* **2000**, *100*, 717.

(4) Ziegler, T.; Autschbach, J. *Chem. Rev.* **2005**, *105*, 2695.

(5) Neese, F. *Coord. Chem. Rev.* **2009**, *253*, 526.

(6) Rozanska, X.; Sauer, J. *J. Phys. Chem. A* **2009**, *113*, 11586.

(7) Sillar, K.; Hofmann, A.; Sauer, J. *J. Am. Chem. Soc.* **2009**, *131*, 4143.

(8) Trinh, C.; Timoshkin, A. Y.; Frenking, G. *J. Phys. Chem. A* **2009**, *113*, 3420.
(9) Duarte, F. J. S.; Cabrita, E. J.; Frenking, G.; Santos, A. G. *Chem.—Eur. J.* **2009**, *15*, 1734.
(10) Fan, J.; Autschbach, J.; Ziegler, T. *Inorg. Chem.* **2010**, *49*, 1355.
(11) Podewitz, M.; Reiher, M. *Adv. Inorg. Chem.* **2010**, *62*, 177.
(12) Podewitz, M.; Stiebritz, M. T.; Reiher, M. *Faraday Discuss.* **2011**, *148*, 119.
(13) Reiher, M. *Chimia* **2009**, *63*, 140.
(14) Reiher, M. *Faraday Discuss.* **2007**, *135*, 97.
(15) Reiher, M.; Sellmann, D.; Hess, B. A. *Theor. Chem. Acc.* **2001**, *106*, 379.
(16) Reiher, M. *Inorg. Chem.* **2002**, *41*, 6928.
(17) Herrmann, C.; Yu, L.; Reiher, M. *J. Comput. Chem.* **2006**, *27*, 1223.
(18) Zein, S.; Borshch, S. A.; Fleurat-Lessard, P.; Casida, M. E.; Chermette, H. *J. Chem. Phys.* **2007**, *126*, 014105.
(19) Fouqueau, A.; Casida, M. E.; Daku, L. M. L.; Hauser, A.; Neese, F. *J. Chem. Phys.* **2005**, *122*, 044110.
(20) Fouqueau, A.; Mer, S.; Casida, M. E.; Daku, L. M. L.; Hauser, A.; Mineva, T.; Neese, F. *J. Chem. Phys.* **2004**, *120*, 9473.
(21) Daku, L. M. L.; Vargas, A.; Hauser, A.; Fouqueau, A.; Casida, M. E. *ChemPhysChem* **2005**, *6*, 1393.
(22) Ganzenmüller, G.; Berkaine, N.; Fouqueau, A.; Casida, M. E.; Reiher, M. *J. Chem. Phys.* **2005**, *122*, 234321.
(23) Paulsen, H.; Trautwein, A. X. *Top. Curr. Chem.* **2004**, *235*, 197.
(24) Swart, M. *J. Chem. Theory Comput.* **2008**, *4*, 2057.
(25) Ye, S.; Neese, F. *Inorg. Chem.* **2010**, *49*, 772.
(26) Reiher, M.; Salomon, O.; Hess, B. A. *Theor. Chem. Acc.* **2001**, *107*, 48.
(27) Cramer, C. J.; Truhlar, D. G. *Phys. Chem. Chem. Phys.* **2009**, *11*, 10757.
(28) Salomon, O.; Reiher, M.; Hess, B. A. *J. Comput. Chem.* **2002**, *117*, 4729.
(29) Bachler, V.; Olbrich, G.; Neese, F.; Wieghardt, K. *Inorg. Chem.* **2002**, *41*, 4179.
(30) Ghosh, A. *J. Biol. Inorg. Chem.* **2006**, *11*, 712.
(31) Conradie, J.; Ghosh, A. *J. Phys. Chem. B* **2007**, *111*, 12621.
(32) Radon, M.; Pierloot, K. *J. Phys. Chem. A* **2008**, *112*, 11824.
(33) Jensen, K. P.; Cirera, J. *J. Phys. Chem. A* **2009**, *113*, 10033.
(34) Olah, J.; Harvey, J. N. *J. Phys. Chem. A* **2009**, *113*, 7338.
(35) Hohenberg, P.; Kohn, W. *Phys. Rev.* **1964**, *136*, B864.
(36) Parr, R. G.; Yang, W. Spin-density-functional theory. In *Density-Functional Theory of Atoms and Molecules*, 1st ed.; Breslow, R., Goodenough, J. B., Halpern, J., Rowlinson, J. S., Eds.; Oxford University Press, Inc.: New York, 1989; pp 169−174.
(37) von Barth, U.; Hedin, L. *J. Phys. C* **1972**, *5*, 1629.
(38) Perdew, J. P.; Ruzsinszky, A.; Constantin, L. A.; Sun, J.; Csonka, G. I. *J. Chem. Theory Comput.* **2009**, *5*, 902.
(39) Pople, J. A.; Gill, P. M. W.; Handy, N. C. *Int. J. Quantum Chem.* **1995**, *56*, 303.
(40) Munzarová, M. L.; Engels, B.; Rassolov, V. A.; Chipman, D. M.; Patchkovskii, S.; Schreckenbach, G.; Lushington, G. H.; Neese, F. EPR Parameters, Methodological Aspects. In *Calculation of NMR and EPR Parameters. Theory and Applications*, 1st ed.; Kaupp, M., Bühl, M., Malkin, V. G., Eds.; Wiley-VCH: Weinheim, Germany, 2004; pp 461−564.
(41) Munzarová, M. L.; Kubáček, P.; Kaupp, M. *J. Am. Chem. Soc.* **2000**, *122*, 11900.
(42) van Lenthe, E.; van der Avoird, A.; Wormer, P. E. S. *J. Comput. Chem.* **1998**, *108*, 4783.
(43) Neese, F. *J. Chem. Phys.* **2003**, *118*, 3939.
(44) Szilagyi, R. K.; Metz, M.; Solomon, E. I. *J. Phys. Chem. A* **2002**, *106*, 2994.
(45) Kossmann, S.; Kirchner, B.; Neese, F. *Mol. Phys.* **2007**, *105*, 2040.
(46) Perdew, J. P.; Savin, A.; Burke, K. *Phys. Rev. A* **1995**, *51*, 4531.
(47) Radon, M.; Broclawik, E. *J. Chem. Theory Comput.* **2007**, *3*, 728.
(48) Roos, B. O.; Veryazov, V.; Conradie, J.; Taylor, P. R.; Ghosh, A. *J. Phys. Chem. B* **2008**, *112*, 14099.
(49) Radon, M.; Broclawik, E.; Pierloot, K. *J. Phys. Chem. B* **2010**, *114*, 1518.
(50) Velde, G. T.; Bickelhaupt, F. M.; Baerends, E. J.; Guerra, C. F.; van Gisbergen, S. J. A.; Snijders, J. G.; Ziegler, T. *J. Comput. Chem.* **2001**, *22*, 931.
(51) Becke, A. D. *J. Chem. Phys.* **1993**, *98*, 5648.
(52) Perdew, J. P.; Tao, J.; Staroverov, V. N.; Scuseria, G. E. *J. Chem. Phys.* **2003**, *119*, 12129.
(53) Handy, N. C.; Cohen, A. J. *Mol. Phys.* **2000**, *99*, 403.
(54) Perdew, J. P.; Burke, K.; Ernzerhof, M. *Phys. Rev. Lett.* **1996**, *77*, 3865.
(55) Perdew, J. P.; Burke, K.; Ernzerhof, M. *Phys. Rev. Lett.* **1997**, *78*, 1396.
(56) Becke, A. D. *Phys. Rev. A* **1988**, *38*, 3098.
(57) Perdew, J. P. *Phys. Rev. B* **1986**, *33*, 8822.
(58) Lee, C.; Yang, W.; Parr, R. G. *Phys. Rev. B* **1988**, *37*, 785.
(59) Perdew, J. P.; Tao, J.; Staroverov, V. N.; Scuseria, G. E. *Phys. Rev. Lett.* **2003**, *91*, 146401.
(60) Zhao, Y.; Truhlar, D. G. *J. Chem. Phys.* **2006**, *125*, 194101.
(61) Güell, M.; Luis, J. M.; Solà, M.; Swart, M. *J. Phys. Chem. A* **2008**, *112*, 6384.
(62) *ADF-GUI*, version 2009.1; Scientific Computing and Modeling: Amsterdam, The Netherlands, 2009. See http://www.scm.com (accessed on July 31, 2011).
(63) Werner, H.-J.; Knowles, P. J.; Lindh, R.; Manby, F. R.; Schütz, M.; Celani, P.; Korona, T.; Mitrushenkov, A.; Rauhut, G.; Adler, T. B.; Amos, R. D.; Bernhardsson, A.; Berning, A; Cooper, D. L.; Deegan, M. J. O.; Dobbyn, A. J.; Eckert, F.; Goll, E.; Hampel, C.; Hetzer, G.; Hrenar, T.; Knizia, G.; Köppl, C.; Liu, Y.; Lloyd, A. W.; Mata, R. A.; May, A. J.; McNicholas, S. J.; Meyer, W.; Mura, M. E.; Nicklass, A.; Palmieri, P.; Pflüger, K.; Pitzer, R.; Reiher, M.; Schumann, U.; Stoll, H.; Stone, A. J.; Tarroni, R.; Thorsteinsson, T.; Wang, M.; Wolf, A. *MOLPRO*, version 2009.1; Cardiff University: Cardiff, United Kingdom; University of Stuttgart: Stuttgart, Germany, 2008.
(64) T. H. Dunning, J. *J. Chem. Phys.* **1989**, *90*, 1007.
(65) Balabanov, N. B.; Peterson, K. A. *J. Chem. Phys.* **2005**, *123*, 064107.
(66) Werner, H.-J.; Meyer, W. *J. Chem. Phys.* **1981**, *74*, 5794.
(67) Werner, H.-J.; Knowles, P. J. *J. Chem. Phys.* **1985**, *82*, 5053.
(68) Knowles, P. J.; Werner, H.-J. *Chem. Phys. Lett.* **1985**, *115*, 259.
(69) Varetto, U. *Molekel*, version 4.3; Swiss National Supercomputing Centre: Manno, Switzerland, 2000. See http://molkel.cscs.ch/wiki/pmwiki.php. (accessed on July 31, 2011).
(70) Westcott, B. L.; Enemark, J. L. Transition Metal Nitrosyls. In *Inorganic Electronic Structure and Spectroscopy*; Solomon, E. I., Lever, A. B. P., Eds.; Wiley: New York, 1999; Vol. 2, pp 403−450.
(71) Praneeth, V. K. K.; Neese, F.; Lehnert, N. *Inorg. Chem.* **2005**, *44*, 2570.
(72) Praneeth, V. K. K.; Nalther, C.; Peters, G.; Lehnert, N. *Inorg. Chem.* **2006**, *45*, 2795.
(73) Wells, F. V.; McCann, S. W.; Wickman, H. H.; Kessel, S. L.; Hendrickson, D. N.; Feltham, R. D. *Inorg. Chem.* **1982**, *21*, 2306.
(74) Hoffmann, R.; Chen, M.-L.; Thorn, D. L. *Inorg. Chem.* **1977**, *16*, 503.
(75) Hoffmann, R.; Chen, M.-L.; Elian, M.; Rossi, A. R.; Mingos, M. P. *Inorg. Chem.* **1974**, *13*, 2666.
(76) Chen, H.; Song, J.; Lai, W.; Wu, W.; Shaik, S. *J. Chem. Theory Comput.* **2010**, *6*, 940.
(77) Schollwöck, U. *Rev. Mod. Phys.* **2005**, *77*, 259.
(78) Chan, G. K.-L.; Dorando, J. J.; Ghosh, D.; Hachmann, J.; Neuscamman, E.; Wang, H.; Yanai, T. An Introduction to the Density Matrix Renormalization Group Ansatz in Quantum Chemistry. In *Frontiers in Quantum Systems in Chemistry and Physics*, 1st ed.; Wilson, S., Grout, P. J., Maruani, J., Delgado-Barrio, G., Piecuch, P., Eds.; Springer: Dordrecht, The Netherlands, 2008; Vol. 18, pp 49−65; e-print: arXiv:0711.1398v1.
(79) Marti, K. H.; Reiher, M. *Z. Phys. Chem.* **2010**, *224*, 583.

JCTC Journal of Chemical Theory and Computation

ARTICLE

pubs.acs.org/JCTC

Efficient and Accurate Methods for the Geometry Optimization of Water Clusters: Application of Analytic Gradients for the Two-Body:Many-Body QM:QM Fragmentation Method to $(H_2O)_n$, $n = 3-10$

Desiree M. Bates, Joshua R. Smith, and Gregory S. Tschumper*

Department of Chemistry and Biochemistry, University of Mississippi, University, Mississippi 38677, United States

Supporting Information

ABSTRACT: The structures of more than 70 low-lying water clusters ranging in size from $(H_2O)_3$ to $(H_2O)_{10}$ have been fully optimized with several different quantum mechanical electronic structure methods, including second-order Møller−Plesset perturbation theory (MP2) in conjunction with correlation consistent triple-ζ basis sets (aug-cc-pVTZ for O and cc-pVTZ for H, abbreviated haTZ). Optimized structures obtained with less demanding computational procedures were compared to the MP2/haTZ ones using both MP2/haTZ single point energies and the root-mean-square (RMS) deviations of unweighted Cartesian coordinates. Based on these criteria, B3LYP/6-31+G(d,2p) substantially outperforms both HF/haTZ and MP2/6-31G*. B3LYP/6-31+G(d,2p) structures never deviate from the MP2/haTZ geometries by more than 0.44 kcal mol^{-1} on the MP2/haTZ potential energy surface, whereas the errors associated with the HF/haTZ and MP2/6-31G* structures grow as large as 12.20 and 2.98 kcal mol^{-1}, respectively. The most accurate results, however, were obtained with the two-body:many-body QM:QM fragmentation method for weakly bound clusters, in which all one- and two-body interactions are calculated at the high-level, while a low-level calculation is performed on the entire cluster to capture the cooperative effects (nonadditivity). With the haTZ basis set, the MP2:HF two-body:many-body fragmentation method generates structures that deviate from the MP2/haTZ ones by 0.01 kcal mol^{-1} on average and not by more than 0.03 kcal mol^{-1}.

1. INTRODUCTION

Hydrogen bonding is widely studied, particularly in water, because of its key roles in biological phenomena as well as in a plethora of important chemical and physical processes.[1−7] The characterization of molecular clusters with sophisticated quantum mechanical (QM) electronic structure techniques is often highly desirable.[8−21] High-accuracy computational procedures are frequently necessary to reliably describe the properties (e.g., structures and energetics) of weakly bound clusters. Such computations can also help unravel the chemical physics of the noncovalent interactions that hold the clusters together. Unfortunately, the computational demands of the most reliable QM methods scale steeply with the size of the cluster, thereby prohibiting their routine application to large systems.

A wide variety of computational techniques have been introduced that partition a cluster into fragments (not necessarily monomers) in an attempt to extend high-accuracy computational methods to previously inaccessible size regimes.[22−42] The integrated QM:QM fragmentation methods being developed by our group fall into this category, and they facilitate the computation of not only energies but also properties. In this paper, we review the two-body:many-body fragmentation method and its analytic gradients. The technique is then used to optimize the geometries of more than 70 $(H_2O)_n$ clusters where $n = 3-10$. The errors associated with these two-body:many-body optimized structures are assessed and compared to those obtained with three other relatively inexpensive electronic structure methods.

2. THEORETICAL BACKGROUND

Through careful application of the inclusion−exclusion principle, integrated computational chemistry methods (QM:QM, QM:MM, ONIOM, etc.) have been extended from systems with a single chemically important subset (or reaction center) to systems with an arbitrary number of subsets that can overlap.[43,44] With this "multicentered" approach to integrated computations, the traditional many-body energy decomposition for weakly bound clusters has been recast[45,46] in the ONIOM formalism of Morokuma and co-workers.[47] The result is effectively a QM:QM fragmentation scheme for noncovalent clusters. This basic mathematical principle is also employed by other fragmentation methods, such as (cardinality guided) molecular tailoring,[35,48] generalized energy-based fragmentation,[49,50] and the molecules-in-molecules approach.[51]

In the original two-body:many-body implementation,[45,46] an accurate but computationally demanding high-level QM method is employed to compute the one- and two-body interactions within a cluster, while a less demanding low-level QM method is used to recover the higher-order (≥three-body) interactions, which are also commonly referred to as the cooperative or nonadditive effects. Consequently, a high-level calculation on the entire cluster $[f_1 f_2 \ldots f_n]$ can be avoided, and high-level computations only need to be performed on the fragments $[f_i]$ and unique pairs

Received: March 14, 2011
Published: August 02, 2011

of fragments $[f_i f_j]$ in the cluster. An expression for the total energy of the cluster can then be obtained by combining the high-level electronic energies with low-level computations on the entire cluster as well as the fragments and pairs:

$$E^{2bHi:Lo} = E_{Lo}[f_1 f_2 \ldots f_n] + \sum_{i=1}^{n}\sum_{j>i}^{n}(E_{Hi}[f_i f_j] - E_{Lo}[f_i f_j]) - (n-2)\sum_{i=1}^{n}(E_{Hi}[f_i] - E_{Lo}[f_i]) \quad (1)$$

When an appropriate low-level method is used (i.e., one that accurately reproduces the high-level ≥three-body effects), the method is quite accurate, and errors typically do not exceed 0.2 kcal mol^{-1}. It is also quite efficient because the demands of the high-level computations only increase quadratically with the size of the cluster and are ideally suited for coarse-grained parallelization. An analogous three-body:many-body procedure has also been developed to examine the convergence of the series:[52]

$$\Delta E^{3bHi:Lo} = E_{Lo}[f_1 f_2 \ldots f_n] + \sum_{i=1}^{n}\sum_{j>i}^{n}\sum_{k>j}^{n}(E_{Hi}[f_i f_j f_k] - E_{Lo}[f_i f_j f_k]) - (n-3)\sum_{i=1}^{n}\sum_{j>i}^{n}(E_{Hi}[f_i f_j] - E_{Lo}[f_i f_j]) + \frac{(n-2)(n-3)}{2}\sum_{i=1}^{n}(E_{Hi}[f_i] - E_{Lo}[f_i]) \quad (2)$$

For the three-body:many-body CCSD(T):MP2 approach, errors tend to decrease by an order of magnitude relative to the two-body:many-body method, suggesting that the series quickly converges and that the error can be systematically controlled.

These QM:QM fragmentation schemes have been developed within the ONIOM framework to facilitate the computation of properties, not just energies. An extremely important feature of the expression for cluster energies in eqs 1 and 2 is that they are linear with respect to the computed energies. Consequently for a linear operator like the gradient, one obtains analogous expressions for the gradient by taking linear combinations of the appropriate components from a series of high- and low-level gradient calculations. For example, the two-body:many-body gradient can be expressed in the following manner:

$$\nabla E^{2bHi:Lo} = \nabla E_{Lo}[f_1 f_2 \ldots f_n] + \sum_{i=1}^{n}\sum_{j>i}^{n}(\nabla E_{Hi}[f_i f_j] - \nabla E_{Lo}[f_i f_j]) - (n-2)\sum_{i=1}^{n}(\nabla E_{Hi}[f_i] - \nabla E_{Lo}[f_i]) \quad (3)$$

Evaluation of these two-body:many-body Cartesian gradients is fairly straightforward as long as all gradients are rotated into the same reference frame. The high- and low-level gradients for the fragments $[f_i]$ and pairs $[f_i f_j]$ in eq 3 only contribute to a few components of the composite Cartesian gradient. If atom a is contained in fragment j, then the only nonzero contributions to the component of the Cartesian gradient along the R coordinate ($R = x,y,z$) of atom a can be obtained with the following expression:

$$\frac{\partial E^{2bHi:Lo}}{\partial R_a} = \frac{\partial E_{Lo}[f_1 f_2 \ldots f_n]}{\partial R_a} + \sum_{i\neq j}^{n}\left(\frac{\partial E_{Hi}[f_i f_j]}{\partial R_a} - \frac{\partial E_{Lo}[f_i f_j]}{\partial R_a}\right) - (n-2)\left(\frac{\partial E_{Hi}[f_j]}{\partial R_a} - \frac{\partial E_{Lo}[f_j]}{\partial R_a}\right) \quad (4)$$

These analytic gradients were originally implemented in a stand-alone interface to the MPQC ab initio software package[53] and applied to the geometry optimization of 15 different hydrogen-bonded clusters of hydrogen fluoride, water, and methanol.[54] In the current implementation, Cartesian gradients are computed with MPQC, rotated into a common reference frame, and combined to form a composite two-body:many-body gradient that is then passed to the Gaussian 03 optimizer via the "external" keyword.

3. COMPUTATIONAL METHODS

All water clusters were optimized with the Hartree−Fock (HF) and second-order Møller−Plesset perturbation theory (MP2) methods, the MP2:HF QM:QM fragmentation method, and the B3LYP density functional. Residual Cartesian gradients of all optimized structures were smaller than 4.5×10^{-4} E_h a_0^{-1}. The 6-31+G(d,2p) basis set was used with the B3LYP optimizations because it has been shown that this methodology provides quite accurate structures for $(H_2O)_6$ isomers.[55] All B3LYP computations used a pruned grid, composed of 99 radial shells and 590 angular points per shell. Both HF and MP2 optimizations were performed with a triple-ζ correlation consistent basis set, aug-cc-pVTZ for O and cc-pVTZ for H (henceforth denoted haTZ). MP2 optimizations were also performed with the 6-31G* basis set, a prescription that has been used to accurately predict the energetics of cluster formation for the same range of water clusters that are the focus of this study.[56] The QM:QM fragmentation optimizations employed MP2/haTZ as the high-level method and HF/haTZ for the low-level calculations.

For all computations, the change in the root-mean-square (RMS) density between self-consistent field (SCF) iterations was converged to at least 1×10^{-8}, yielding energies converged to approximately 1×10^{-10} E_h. The 1s-like core orbitals of the oxygen atoms were frozen in all MP2 calculations. All atomic orbital basis sets employed in this work utilized spherical harmonic functions (5d, 7f) rather than their Cartesian counterparts (6d, 10f). MP2/haTZ single point energy calculations were performed on all optimized structures to compare the relative energies on the MP2/haTZ potential energy surface (PES). All calculations were performed with the Gaussian 03,[57] Gaussian 09,[58] and MPQC[53] software packages.

4. RESULTS AND DISCUSSION

Two independent means were used to compare the optimized structures obtained with the various computational methods. The first and more straightforward comparison utilized the minimal RMS deviation of the unweighted Cartesian coordinates optimized with the superpose program in TINKER.[59,60] The second metric is based on energetics. MP2/haTZ single point energies were computed for all optimized structures. By definition, the MP2/haTZ optimized structure corresponds to the lowest point associated with a particular minimum on the MP2/haTZ

Table 1. RMS Deviations (in Å) for Optimized Structures Relative to the MP2/haTZ Optimized Structures

method	HF	MP2	B3LYP	MP2:HF
basis Set	haTZ	6-31G*	6-31+G(d,2p)	haTZ
		$(H_2O)_3$		
C_1	0.121	0.127	0.010	0.004
C_3	0.160	0.186	0.012	0.004
C_{3h}	0.083	0.014	0.009	0.002
		$(H_2O)_4$		
S_4	0.131	0.059	0.017	0.006
C_i	0.146	0.093	0.010	0.007
C_4	0.204	0.150	0.010	0.007
C_{4h}	0.095	0.019	0.012	0.003
		$(H_2O)_5$		
C_1	0.160	0.126	0.041	0.013
C_5	0.243	0.136	0.014	0.011
C_{5h}	0.113	0.025	0.018	0.006
		$(H_2O)_6$		
prism	0.147	0.081	0.031	0.011
cage	0.180	0.115	0.040	0.008
book 1	0.203	0.076	0.020	0.008
book 2	0.262	[a]	0.081	0.017
bag	0.192	[b]	0.055	0.010
boat 1	0.297	0.332	0.078	0.038
boat 2	0.304	0.280	0.080	0.015
cyclic	0.154	0.134	0.017	0.012
		$(H_2O)_7$		
A	0.173	0.103	0.036	0.007
B	0.196	0.399	0.039	0.009
C	0.274	0.330	0.046	0.012
D	0.328	0.255	0.048	0.024
PR2	0.178	0.131	0.047	0.009
PR3	0.217	0.145	0.036	0.038
CA1	0.242	0.010	0.029	0.010
CA2	0.386	0.174	0.025	0.011
CH1	0.292	0.320	0.101	0.019
BI1	0.465	0.280	0.020	0.015
CH2	0.235	0.294	0.043	0.015
$(H_2O)_8$				
C_1a	0.166	0.073	0.029	0.010
C_1b	0.167	0.068	0.030	0.009
C_1c	0.173	0.070	0.029	0.007
C_2	0.186	0.021	0.050	0.006
C_i	0.200	0.050	0.031	0.004
C_s	0.179	0.076	0.032	0.007
D_{2d}	0.164	0.068	0.024	0.009
noncubic 1	0.272	0.308	0.184	0.013
S_4	0.165	0.069	0.026	0.008
		$(H_2O)_9$		
D_{2d}DDh	0.184	0.091	0.025	0.009
S_4Dah 1	0.185	0.092	0.024	0.008
S_4Dah 2	0.192	0.107	0.025	0.010
S_4DDh 1	0.184	0.103	0.026	0.010
S_4DDh 2	0.187	0.101	0.025	0.008
D_{2d}Dah	0.183	0.102	0.022	0.007
S_4Danh 1	0.185	0.125	0.023	0.008
S_4Danh 2	0.187	0.089	0.024	0.010
		$(H_2O)_{10}$		
PP1	[c]	0.073	0.029	0.013
PP2	0.185	0.076	0.026	0.007
PP3	0.186	0.087	0.027	0.021
PP4	0.191	0.084	0.028	0.007
PP5	0.185	0.086	0.026	0.009
OB1	0.200	0.096	0.026	0.011
OB2	0.202	0.094	0.028	0.008
OB3	0.201	0.089	0.028	0.010
DP1	[d]	0.102	0.028	0.008
OB4	0.202	0.083	0.034	0.015
OB5	0.200	0.203	0.023	0.012
DP2	0.190	0.109	0.033	0.008
OB6	0.204	0.106	0.037	0.017
OB7	0.205	0.070	0.033	0.016
OB8	0.205	0.073	0.032	0.014
DP3	0.204	0.203	0.060	0.010
DP4	0.210	0.081	0.102	0.025
DP5	0.204	0.089	0.050	0.014
DP6	0.198	0.199	0.022	0.009
OB9	0.220	0.221	0.031	0.012
DP7	0.225	0.143	0.032	0.011
DP8	0.208	0.120	0.052	0.013
OB10	0.199	0.318	0.030	0.006
OB11	0.284	0.279	0.043	0.018
DP10	0.210	0.103	0.065	0.022
DP11	0.212	0.118	0.026	0.014
C1	0.233	0.100	0.035	0.012
C2	0.199	0.101	0.033	0.024
C3	0.222	0.122	0.039	0.020

[a] Collapsed to prism structure. [b] Not located on the MP2/6-31G* PES. [c] Not located on the HF/haTZ PES. [d] Collapsed to DP2 structure.

PES. All other optimized structures lie above that minimum. Optimization procedures that most accurately reproduce the MP2/haTZ optimized structure will lie closest to the bottom of the well and, therefore, also have the smallest deviation from the MP2/haTZ//MP2/haTZ cluster energy.

All trimer, tetramer, and pentamer structures are commonly studied low-lying stationary points. Hexamer structures were taken from ref 21. Most initial heptamer, octamer, nonamer, and decamer structures came from MP2/6-31G* optimized geometries[56] with a few additional structures from HF/6-31G(d) optimizations.[60] The BI2, BI3, and CH3 isomers of $(H_2O)_7$ along with DP9 of the $(H_2O)_{10}$ have been omitted because they could not be located on the MP2/haTZ PES. We note, however, that exhaustive searches were not performed because they collapse to other structures on the PES. Because the number of possible

Table 2. Average and Maximum RMS Deviations (in Å) for Various Optimized Structures Relative to the MP2/haTZ Optimized Structures for Various $(H_2O)_n$ Clusters with $n = 3-10$

		HF/haTZ		MP2/6-31G*		B3LYP/ 6-31+G(d,2p)		MP2:HF/ haTZ	
n	no.	avg	max	avg	max	avg	max	avg	max
3	3	0.121	0.160	0.109	0.186	0.011	0.012	0.003	0.004
4	4	0.144	0.204	0.080	0.150	0.012	0.017	0.006	0.007
5	3	0.172	0.243	0.096	0.136	0.024	0.041	0.010	0.013
6	8	0.218	0.304	0.170[a]	0.332[a]	0.050	0.081	0.015	0.038
7	11	0.272	0.465	0.230	0.399	0.043	0.101	0.015	0.038
8	9	0.186	0.272	0.089	0.308	0.048	0.184	0.008	0.013
9	8	0.186	0.192	0.101	0.125	0.024	0.026	0.009	0.010
10	29	0.207[b]	0.284	0.125	0.318	0.037	0.102	0.013	0.025

[a] Excludes the bag and book 2 isomers. [b] Excludes the PP1 and DP1 isomers.

configurations grows very quickly with *n*, only structures within 5 kcal mol^{-1} of the lowest-lying isomer were examined in this study.

4.1. Comparison of Structures. Table 1 contains the minimal RMS deviations of the unweighted Cartesian coordinates for various optimized structures compared to MP2/haTZ optimized structures. The first column of data shows the deviations associated with the HF/haTZ structures. As expected, HF/haTZ structures have large deviations from the MP2/haTZ structures. The second column of data in Table 1 reports the RMS deviations for the MP2/6-31G* optimized structures. Overall, MP2/6-31G* has improved accuracy compared to HF/haTZ methodology. Occasionally however, the MP2/6-31G* RMS values exceed those for the HF/haTZ structures. The values in the last two columns of Table 1 are appreciably smaller, indicating that the B3LYP/6-31+G(d,2p) and MP2/haTZ:HF/haTZ optimized structures deviate only slightly from the MP2/haTZ ones. The two-body:many-body approach consistently reproduces the MP2/haTZ structures more accurately than any other procedure.

Table 2 summarizes the results of Table 1 with the average and maximum RMS deviations associated with each method for each value of *n*. The second column lists the number of isomers used to compute the average (unless otherwise noted) . For example, the largest RMS deviation between the HF/haTZ and MP2/haTZ structures is 0.465 Å (for isomer BI1 of the water heptamer). In general, the average and maxium RMS deviations of the HF/haTZ and MP2/6-31G* approaches are comparable, with the later exhibiting slightly better performance overall. The average values are roughly 1 order of magnitude smaller for the B3LYP/6-31+G(d,2p) optimized structures. The last two columns of Table 2 list the average and maximum RMS deviations associated with the two-body:many-body fragmentation method employing MP2/haTZ for the high-level calculation and HF/haTZ for the low-level calculations. Regardless of the size of the cluster, this QM:QM fragmentation procedure yields the smallest average errors relative to the MP2/haTZ optimized structures. In fact the RMS deviations never exceed 0.038 Å .

4.2. Comparison of Energetics. Table 3 is similar to Table 1, but it reports energetic, rather than structural, deviations from the MP2/haTZ optimized structures (i.e., from the MP2/haTZ//MP2/haTZ energies). For example, the first column of data reports the MP2/haTZ//HF/haTZ errors associated with the

Table 3. Errors Associated with MP2/haTZ Energies (in kcal mol^{-1}) Performed on Various Optimized Structures Relative to the MP2/haTZ//MP2/haTZ Values

method	HF	MP2	B3LYP	MP2:HF
basis set	haTZ	6-31G*	6-31+G(d,2p)	haTZ
		$(H_2O)_3$		
C_1	2.57	0.74	0.10	0.00
C_3	2.59	0.97	0.11	0.00
C_{3h}	2.27	0.25	0.10	0.00
		$(H_2O)_4$		
S_4	3.82	0.71	0.14	0.01
C_i	3.83	0.78	0.15	0.01
C_4	3.83	1.05	0.16	0.00
C_{4h}	3.25	0.37	0.16	0.00
		$(H_2O)_5$		
C_1	4.81	0.87	0.19	0.01
C_5	4.69	1.07	0.21	0.01
C_{5h}	4.16	0.51	0.21	0.00
		$(H_2O)_6$		
prism	6.47	0.79	0.25	0.01
cage	6.50	0.98	0.26	0.01
book 1	6.18	1.15	0.23	0.01
book 2	6.25	[a]	0.25	0.01
bag	6.32	[b]	0.24	0.01
boat 1	5.72	1.34	0.25	0.01
boat 2	5.64	1.22	0.25	0.01
cyclic	5.67	1.12	0.23	0.01
		$(H_2O)_7$		
A	7.77	1.14	0.30	0.01
B	7.64	2.36	0.29	0.01
C	7.21	0.28	0.28	0.01
D	6.89	1.58	0.25	0.01
PR2	7.82	1.02	0.31	0.01
PR3	7.21	1.07	0.30	0.01
CA1	7.07	1.09	0.28	0.01
CA2	6.53	1.26	0.28	0.01
CH1	7.20	1.21	0.28	0.01
BI1	6.82	1.44	0.25	0.01
CH2	7.20	2.20	0.27	0.01
		$(H_2O)_8$		
C_1a	9.29	1.05	0.34	0.01
C_1b	9.36	1.03	0.35	0.02
C_1c	9.32	1.03	0.35	0.01
C_2	9.65	0.78	0.39	0.01
C_i	9.73	0.86	0.35	0.01
C_s	9.53	1.01	0.35	0.02
D_{2d}	9.47	1.17	0.35	0.02
noncubic 1	9.13	1.83	0.41	0.02
S_4	9.50	1.19	0.36	0.02
		$(H_2O)_9$		
D_{2d}DDh	10.57	1.31	0.38	0.02
S_4Dah 1	10.69	1.30	0.38	0.02

Table 3. Continued

method	HF	MP2	B3LYP	MP2:HF
basis set	haTZ	6-31G*	6-31+G(d,2p)	haTZ
S_4Dah 2	10.66	1.35	0.38	0.02
S_4DDh 1	10.61	1.35	0.39	0.02
S_4DDh 2	10.60	1.36	0.39	0.02
D_{2d}Dah	10.65	1.34	0.37	0.02
S_4Danh 1	10.68	1.39	0.38	0.02
S_4Danh 2	10.66	1.35	0.38	0.02
		$(H_2O)_{10}$		
PP1	[c]	1.30	0.38	0.00
PP2	11.99	1.35	0.43	0.02
PP3	12.03	1.37	0.41	0.01
PP4	12.20	1.36	0.40	0.02
PP5	12.03	1.41	0.43	0.02
OB1	11.91	1.45	0.43	0.02
OB2	11.94	1.47	0.44	0.01
OB3	11.94	1.48	0.44	0.02
DP1	[d]	1.42	0.41	0.02
OB4	11.93	1.42	0.42	0.02
OB5	11.94	1.98	0.43	0.02
DP2	11.81	1.50	0.43	0.02
OB6	11.95	1.51	0.43	0.02
OB7	11.95	1.36	0.43	0.02
OB8	11.94	1.38	0.42	0.02
DP3	11.85	1.48	0.37	0.02
DP4	11.72	1.44	0.29	0.01
DP5	11.69	1.53	0.37	0.02
OB9	12.03	1.90	0.43	0.02
DP6	11.87	1.71	0.41	0.02
DP7	11.33	1.65	0.41	0.02
DP8	11.74	1.82	0.07	0.02
OB10	11.92	2.98	0.42	0.01
OB11	11.55	1.92	0.33	0.02
DP10	11.75	1.63	0.41	0.01
DP11	11.83	1.59	0.41	0.03
C1	11.84	1.48	0.40	0.02
C2	11.49	1.55	0.41	0.02
C3	11.63	1.42	0.41	0.02

[a] Collapsed to prism structure. [b] Not located on the MP2/6-31G* PES. [c] Not located on the HF/haTZ PES. [d] Collapsed to DP2 structure.

total cluster energy compared to the MP2/haTZ//MP2/haTZ energies. The MP2/haTZ//HF/haTZ errors are always the largest, which is entirely consistent with the RMS deviations. In contrast, the MP2/haTZ//MP2/6-31G* errors are much smaller despite having RMS deviations comparable to the HF/haTZ optimized structures. The errors associated with the B3LYP/6-31+G(d,2p) structures are listed in the penultimate column, and they are significantly smaller than the errors associated with the HF/haTZ and MP2/6-31G* optimized structures. The last column of data shows the energetic errors associated with the two-body:many-body scheme. Structures optimized with the MP2:HF QM:QM fragmentation method and the haTZ basis set are typically one or two hundredths of a kcal mol^{-1} above the MP2/haTZ optimized structures.

Table 4. Average and Maximum Errors for MP2/haTZ Energies (in kcal mol^{-1}) Performed on Various Structures Relative to MP2/haTZ//MP2/haTZ Values for $(H_2O)_n$ Clusters with n = 3−10

		HF/haTZ		MP2/6-31G*		B3LYP/6-31+G(d,2p)		MP2:HF/haTZ	
n	no.	avg	max	avg	max	avg	max	avg	max
3	3	2.48	2.59	0.65	0.97	0.10	0.11	0.00	0.00
4	4	3.68	3.83	0.73	1.05	0.15	0.16	0.00	0.01
5	3	4.55	4.81	0.81	1.07	0.21	0.21	0.01	0.01
6	8	6.09	6.50	1.10[a]	1.34[a]	0.24	0.26	0.01	0.01
7	11	7.21	7.82	1.45	2.36	0.28	0.31	0.01	0.02
8	9	9.44	9.73	1.11	1.83	0.36	0.41	0.01	0.02
9	8	10.64	10.69	1.34	1.39	0.38	0.39	0.02	0.02
10	29	11.84[b]	12.20	1.58	2.98	0.40	0.44	0.02	0.03

[a] Excludes the bag and book 2 isomers. [b] Excludes the PP1 and DP1 isomers.

Again, average and maximum errors are tabulated to help summarize all of the data in Table 3. For example, the data in Table 4 show that the errors associated with the HF/haTZ structures optimized structures increase with the size of the cluster and grow as large as 12.20 kcal mol^{-1} (for the PP4 isomer of the water decamer). The energetic errors associated with the MP2/6-31G* optimized structures also tend to increase with the value of n but do not exceed 2.98 kcal mol^{-1} (for isomer OB10 of the water decamer). The combination of the B3LYP density functional with the 6-31+G(d,2p) basis set appears to be a good way to quickly and reliably identify low-lying structures of $(H_2O)_n$ clusters. The largest MP2/haTZ//B3LYP/6-31+G(d,2p) error is only 0.44 kcal mol^{-1} (for both OB2 and OB3 structures of the water decamer). The two-body:many-body integrated fragmentation technique for noncovalent clusters provides even more accurate results. The errors associated with the structures optimized with the MP2:HF method and the haTZ basis set never exceed 0.03 kcal mol^{-1} (for DP11 isomer of the water decamer). The average error for the MP2:HF fragmentation method is 0.01 kcal mol^{-1} for all of 75 water clusters examined. These two-body:many-body results are particularly encouraging for certain pathological cases where water clusters are virtually isoenergetic and separated by less than 0.10 kcal mol^{-1}. For example, the MP2 complete basis set limit interaction energies for the prism and cage isomers of the water hexamer are separated electronically by only 0.06 kcal mol^{-1}.[10,21]

4.3. Efficiency and Convergence. In general, we have found that the convergence of geometry optimizations for the MP2:HF procedure is virtually identical to that of the MP2 method. For well-behaved cases, the MP2:HF optimization converges in a similar number cycles, typically ±10%, as the corresponding MP2 optimization (e.g., ± 2 iterations for a 20-step optimization). To demonstrate this behavior, both MP2 and MP2:HF geometry optimizations were started from the B3LYP/6-31+G(d,2p) optimized structure of the C_1a isomer of $(H_2O)_8$. The corresponding RMS gradients (in E_h a_0^{-1}) and relative electronic energies [in millihartree (mE_h) with respect to the optimized structures] are shown in Figure 1. For this system, the MP2 optimization converges quickly (within 20 iterations), and the progression of the MP2:HF procedure is virtually identical. Only for iterations 8 and 9 is there any noticible difference between the MP2 and MP2:HF optimizations. It should be noted, however, that when it is difficult to

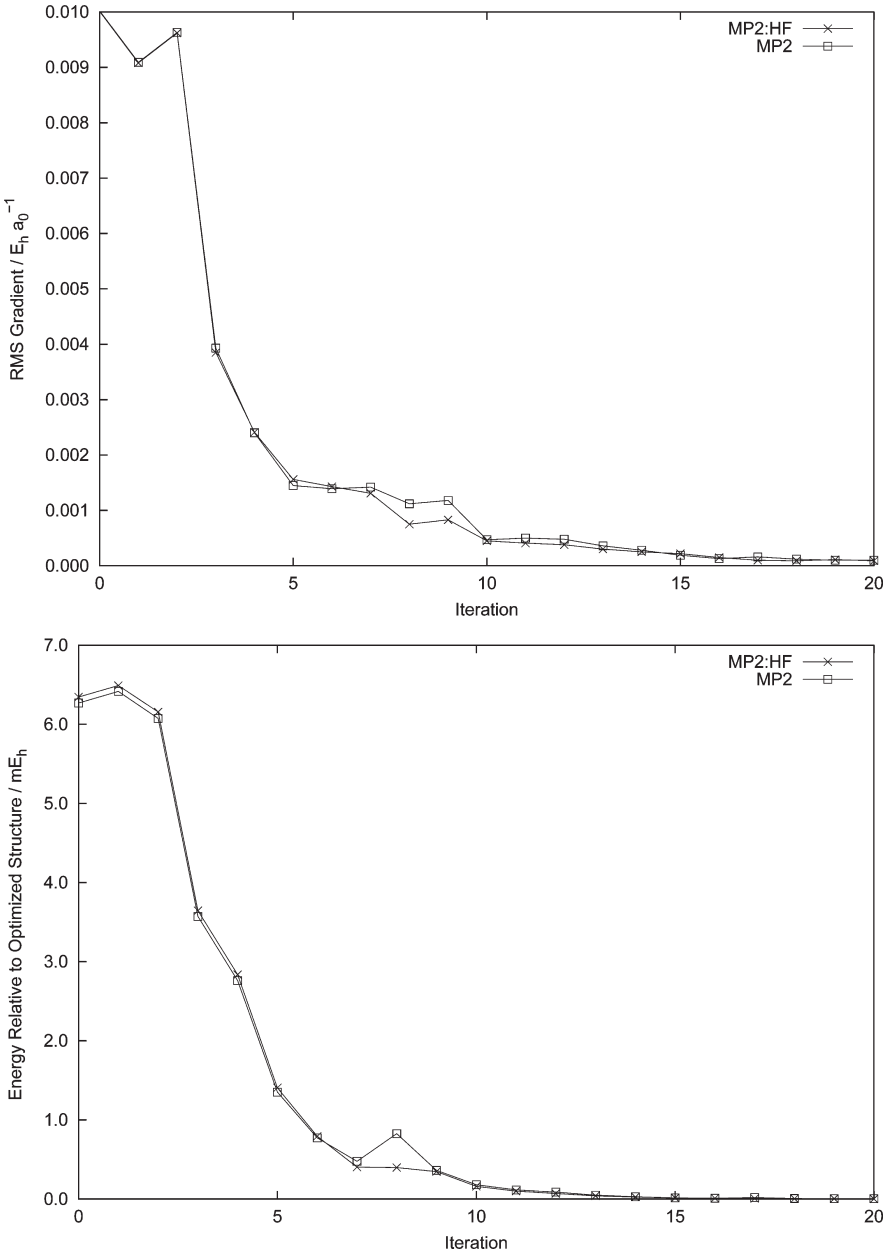

Figure 1. RMS gradients and relative energies during MP2 and MP2:HF geometry optimizations of the C_1a isomer of the water octamer.

converge the high-level geometry optimization, as is common for weakly bound noncovalent clusters, the same problem should be expected for the corresponding two-body:many-body QM:QM geometry optimization.

The efficiency of the two-body:many-body gradient computations relative to the high-level method depends not only on the size and nature of the cluster being examined but also on the methods, basis sets, and software programs used for the high- and low-level calculations. To provide some measurement of the efficiency of our approach, we recomputed the MP2 and MP2:HF gradients for the C_1a isomer of $(H_2O)_8$ and the PP1 isomer of $(H_2O)_{10}$ with the MPQC program on a workstation equipped with two quad-core Opteron 2.4 GHz 2378 processors and 32 GB of memory. The wall times (in minutes) are reported in Table 5. (Note that no timings reported here were obtained with Gaussian.) The first column of data has been labeled "MPQC:MPQC" to denote that both the MP2 and HF computations were perfomed with the MPQC software package. When computed in this manner, the MP2:HF gradient is approximately twice as fast as the canonical MP2 gradient calculation. Roughly 70% of the wall time in these MP2:HF computations is spent evaluating the low-level gradient for the complex. Efficiency can be further improved by using a program with faster parallel HF first derivatives. The last column of data (with the "MPQC:PQS" heading) contains the wall times obtained when PQS[61] is used to compute the HF gradients and MPQC is only used for the MP2 gradients. PQS dramatically decreases the time for the HF gradients (by a factor of $\approx$8), which increases the speedups associated with the MP2:HF computations by a factor of 3. In both columns, the efficiency of the two-body:many-body procedure increases with the size of the cluster. Spatial and energetic thresholds are expected to further improve efficiency because distance-based cutoffs have yielded

Table 5. Typical Wall Times (in minutes) Associated with the Two-Body:Many-Body MP2:HF Gradient Calculations and Speedups Relative to the MP2 Gradient Computed with MPQC

		MP2:HF	MP2:HF
calculation(s)		MPQC: MPQC	MPQC: PQS
	C_1a Isomer of $(H_2O)_8$		
lo-level	8 fragments	<1	<1
hi-level	8 fragments	1	1
lo-level	28 pairs	23	6
hi-level	28 pairs	47	47
lo-level	1 complex	144	18
total		215	72
speedup (relative to 376 min)[a]		1.7	5.2
	PP1 Isomer of $(H_2O)_{10}$		
lo-level	8 fragments	<1	<1
hi-level	8 fragments	1	1
lo-level	28 pairs	36	9
hi-level	28 pairs	72	72
lo-level	1 complex	267	34
total		376	115
speedup (relative to 887 min)[a]		2.4	7.7

[a] Wall time for MP2 gradient with MPQC.

very promising results for the closely related molecules-in-molecules method.[51]

5. CONCLUSIONS

Analytic gradient techniques for the two-body:many-body fragmentation method for weakly bound clusters were used to optimize the geometries of more than 70 water clusters ranging in size from $(H_2O)_3$ to $(H_2O)_{10}$. In this application, MP2/haTZ was used as the high-level method to compute the one- and two-body interactions, while HF/haTZ was employed as the low-level method to recover the higher-order ($\geq$three-body) interactions. This procedure proved to be quite efficient because the largest MP2 computations associated with the MP2:HF calculations involve a pair of water molecules (i.e., a dimer), regardless of the size of the cluster. Consequently, the HF/haTZ computation on the entire cluster was always the rate determining step in these two-body:many-body fragmentation calculations. Structures optimized with this QM:QM fragmentation procedure were compared to those obtained from conventional MP2/haTZ optimizations using two different metrics, the minimum RMS deviation of unweighted Cartesian coordinates and the MP2/haTZ energy. The two-body:many-body optimized structures were virtually identical to those from the MP2/haTZ optimizations. On average, the structures optimized with these two methods were within 0.01 kcal mol^{-1} of each other on the MP2/haTZ PES, and they never differed by more than 0.03 kcal mol^{-1} . For comparison, HF/haTZ and MP2/6-31G* optimized structures deviated by as much as 12.20 and 2.98 kcal mol^{-1}, respectively, from the MP2/haTZ structures. This work also demonstrated that the B3LYP/6-31+G(d,2p) structures did not differ from the MP2/haTZ ones by more than 0.44 kcal mol^{-1} on the MP2/haTZ PES.

■ ASSOCIATED CONTENT

Supporting Information. Tables of Cartesian coordinates for the MP2/haTZ-optimized structures from this work are included. This material is available free of charge via the Internet at http://pubs.acs.org.

■ AUTHOR INFORMATION

Corresponding Author
*E-mail: tschumpr@olemiss.edu.

■ ACKNOWLEDGMENT

We acknowledge the Mississippi Center for Super Computing Research for CPU time and the National Science Foundation for funding (CHE-0957317 and EPS-0903787).

■ REFERENCES

(1) Castleman, A.; Bowen, K. *J. Phys. Chem.* **1996**, *100*, 12911–12944.
(2) Bačić, Z.; Miller, R. E. *J. Phys. Chem.* **1996**, *100*, 12945–12959.
(3) Jeffrey, G. A. *An Introduction to Hydrogen Bonding*; Oxford University Press: Oxford, England, 1997.
(4) Schuster, P.; Wolschann, P. *Monat. Chem.* **1999**, *130*, 947–960.
(5) Ludwig, R. *Angew. Chem., Int. Ed. Engl.* **2001**, *40*, 1808–1827.
(6) Steiner, T. *Angew. Chem., Int. Ed. Engl.* **2002**, *41*, 48–76.
(7) Černý, J.; Hobza, P. *Phys. Chem. Chem. Phys.* **2007**, *9*, 5281–5388.
(8) Klopper, W.; Schuetz, M. *Ber. Bunsen. Phys. Chem.* **1995**, *99*, 469–473.
(9) Klopper, W.; Quack, M.; Suhm, M. A. *Mol. Phys.* **1998**, *94*, 105–116.
(10) Xantheas, S. S.; Burnham, C. J.; Harrison, R. J. *J. Chem. Phys.* **2002**, *116*, 1493–1499.
(11) Sinnokrot, M.; Valeev, E.; Sherrill, C. *J. Am. Chem. Soc.* **2002**, *124*, 10887–10893.
(12) Hobza, P. *Annu. Rep. Prog. Chem., Sect. C: Phys. Chem.* **2004**, *100*, 3–27.
(13) Zhao, Y.; Truhlar, D. G. *J. Chem. Theory Comput.* **2005**, *1*, 415–432.
(14) Jurečka, P.; Šponer, J.; Černý, J.; Hobza, P. *Phys. Chem. Chem. Phys.* **2006**, *8*, 1985–1993.
(15) Boese, A.; Martin, J.; Klopper, W. *J. Phys. Chem. A* **2007**, *111*, 11122–11133.
(16) Tschumper, G. S.; Leininger, M. L.; Hoffman, B. C.; Valeev, E. F.; Schaefer, H. F.; Quack, M. *J. Chem. Phys.* **2002**, *116*, 690–701.
(17) Anderson, J. A.; Crager, K.; Fedoroff, L.; Tschumper, G. S. *J. Chem. Phys.* **2004**, *121*, 11023–11029.
(18) Hopkins, B. W.; Tschumper, G. S. *J. Phys. Chem. A* **2004**, *108*, 2941–2948.
(19) Copeland, K. L.; Anderson, J. A.; Farley, A. R.; Cox, J. R.; Tschumper, G. S. *J. Phys. Chem. B* **2008**, *112*, 14291–14295.
(20) ElSohly, A. M.; Hopkins, B. W.; Copeland, K. L.; Tschumper, G. S. *Mol. Phys.* **2009**, *107*, 923–928.
(21) Bates, D. M.; Tschumper, G. S. *J. Phys. Chem. A* **2009**, *113*, 3427–3708.
(22) Christie, R. A.; Jordan, K. D. *n*-Body Decomposition Approach to the Calculation of Interaction Energies of Water Clusters. In *Intermolecular Forces and Clusters II*; Wales, D. J., Ed.; Springer: Germany, 2005; Vol. 116, pp 27−41.
(23) Kitaura, K.; Ikeo, E.; Asada, T.; Nakano, T.; Uebayasi, M. *Chem. Phys. Lett.* **1999**, *313*, 701–706.
(24) Nakano, T.; Kaminuma, T.; Sato, T.; Akiyama, Y.; Uebayasi, M.; Kitaura, K. *Chem. Phys. Lett.* **2000**, *318*, 614–618.
(25) Fedorov, D. G.; Kitaura, K. *J. Phys. Chem. A* **2007**, *111*, 6904–6914.
(26) Fedorov, D. G.; Ishimura, K.; Ishida, T.; Kitaura, K.; Pulay, P.; Nagase, S. *J. Comput. Chem.* **2007**, *28*, 1476–1484.

(27) Hirata, S.; Valiev, M.; Dupuis, M.; Xantheas, S. S.; Sugiki, S.; Sekino, H. *Mol. Phys.* **2005**, *103*, 2255–2265.
(28) Sakai, S.; Morita, S. *J. Phys. Chem. A* **2005**, *109*, 8424–8429.
(29) Dahlke, E.; Truhlar, D. *J. Chem. Theory Comput.* **2007**, *3*, 46–53.
(30) Dahlke, E.; Truhlar, D. *J. Chem. Theory Comput.* **2007**, *3*, 1342–1348.
(31) Dahlke, E.; Leverentz, H.; Truhlar, D. *J. Chem. Theory Comput.* **2008**, *4*, 33–41.
(32) Imamura, A.; Aoki, Y.; Maekawa, K. *J. Chem. Phys.* **1991**, *95*, 5419–5431.
(33) Zhang, D. W.; Zhang, J. Z. H. *J. Chem. Phys.* **2003**, *119*, 3599–3605.
(34) Jiang, N.; Ma, J.; Jiang, Y. *J. Chem. Phys.* **2006**, *124*, 114112.
(35) Gadre, S. R.; Shirsat, R. N.; Limaye, A. C. *J. Chem. Phys.* **1994**, *98*, 9103–9169.
(36) Sæbø, S.; Pulay, P. *Chem. Phys. Lett.* **1985**, *113*, 13–18.
(37) Day, P. N.; Jensen, J. H.; Gordon, M. S.; Webb, S. P.; Stevens, W. J.; Krauss, M.; Garmer, D.; Basch, H.; Cohen, D. *J. Chem. Phys.* **1996**, *105*, 1968–1986.
(38) Rauhut, G.; Pulay, P.; Werner, H. J. *J. Comput. Chem.* **1998**, *19*, 1241–1254.
(39) Li, S.; Ma, J.; Jiang, Y. *J. Comput. Chem.* **2002**, *23*, 237–244.
(40) Min, D.; Yang, W. *J. Chem. Phys.* **2008**, *128*, 094106.
(41) Li, W.; Piecuch, P.; Gour, J. R.; Li, S. *J. Chem. Phys.* **2009**, *131*, 114109.
(42) Gordon, M. S.; Mullin, J. M.; Pruitt, S. R.; Roskop, L. B.; Slipchenko, L. V.; Boatz, J. A. *J. Phys. Chem. B* **2009**, *113*, 9646–9663.
(43) Hopkins, B. W.; Tschumper, G. S. *J. Comput. Chem.* **2003**, *24*, 1563–1568.
(44) Hopkins, B. W.; Tschumper, G. S. *Mol. Phys.* **2005**, *103*, 309–315.
(45) Hopkins, B. W.; Tschumper, G. S. *Chem. Phys. Lett.* **2005**, *407*, 362–367.
(46) Tschumper, G. S. *Chem. Phys. Lett.* **2006**, *427*, 185–191.
(47) Maseras, F.; Morokuma, K. *J. Comput. Chem.* **1995**, *16*, 1170–1179.
(48) Ganesh, V.; Dongare, R. K.; Balanarayan, P.; Gadre, S. R. *J. Chem. Phys.* **2006**, *125*, 104109.
(49) Li, W.; Li, S.; Jiang, Y. *J. Phys. Chem. A* **2007**, *111*, 2193–2199.
(50) Hua, W.; Fang, T.; Li, W.; Yu, J.-G.; Li, S. *J. Phys. Chem. A* **2008**, *112*, 10864–10872.
(51) Mayhall, N. J.; Raghavachari, K. *J. Chem. Theory Comput.* **2011**, *7*, 1336–1343.
(52) Bates, D. M.; Janowski, T.; Smith, J. R.; Tschumper, G. S. *J. Chem. Phys.* **2011**, *135*, 012345.
(53) Janssen, C. L.; Nielsen, I. B.; Leininger, M. L.; Valeev, E. F.; Seidl, E. T. *The Massively Parallel Quantum Chemistry Program (MPQC)*, version 2.3.1; Sandia National Laboratories: Livermore, CA, 2004; http://www.mpqc.org.
(54) ElSohly, A. M.; Shaw, C. L.; Guice, M. E.; Smith, B. D.; Tschumper, G. S. *Mol. Phys.* **2007**, *105*, 2777–2782.
(55) Dahlke, E. E.; Olson, R. M.; Leverentz, H. R.; Truhlar, D. G. *J. Phys. Chem. A* **2008**, *112*, 3976–3984.
(56) Shields, R. M.; Temelso, B.; Archer, K. A.; Morrell, T. E.; Shields, G. C. *J. Phys. Chem. A* **2010**, *114*, 11725–11737.
(57) Frisch, M. J.; Trucks, G. W.; Schlegel, H. B.; Scuseria, G. E.; Robb, M. A.; Cheeseman, J. R.; Montgomery, J. R., Jr.; Vreven, T.; Kudin, K. N.; Burant, J. C.; Millam, J. M.; Iyengar, S. S.; Tomasi, J.; Barone, V.; Mennucci, B.; Cossi, M.; Scalmani, G.; Rega, N.; Petersson, G. A.; Nakatsuji, H.; Hada, M.; Ehara, M.; Toyota, K.; Fukuda, R.; Hasegawa, J.; Ishida, M.; Nakajima, T.; Honda, Y.; Kitao, O.; Nakai, H.; Klene, M.; Li, X.; Knox, J. E.; Hratchian, H. P.; Cross, J. B.; Bakken, V.; Adamo, C.; Jaramillo, J.; Gomperts, R.; Stratmann, R. E.; Yazyev, O.; Austin, A. J.; Cammi, R.; Pomelli, C.; Ochterski, J. W.; Ayala, P. Y.; Morokuma, K.; Voth, G. A.; Salvador, P.; Dannenberg, J. J.; Zakrzewski, V. G.; Dapprich, S.; Daniels, A. D.; Strain, M. C.; Farkas, O.; Malick, D. K.; Rabuck, A. D.; Raghavachari, K.; Foresman, J. B.; Ortiz, J. V.; Cui, Q.; Baboul, A. G.; Clifford, S.; Cioslowski, J.; Stefanov, B. B.; Liu, G.; Liashenko, A.; Piskorz, P.; Komaromi, I.; Martin, R. L.; Fox, D. J.; Keith, T.; Al-Laham, M. A.; Peng, C. Y.; Nanayakkara, A.; Challacombe, M.; Gill, P. M. W.; Johnson, B.; Chen, W.; Wong, M. W.; Gonzalez, C.; Pople, J. A. *Gaussian 03*, revision E.01; Gaussian, Inc.: Wallingford, CT, 2003.
(58) Frisch, M. J.; Trucks, G. W.; Schlegel, H. B.; Scuseria, G. E.; Robb, M. A.; Cheeseman, J. R.; Scalmani, G.; Barone, V.; Mennucci, B.; Petersson, G. A.; Nakatsuji, H.; Caricato, M.; Li, X.; Hratchian, H. P.; Izmaylov, A. F.; Bloino, J.; Zheng, G.; Sonnenberg, J. L.; Hada, M.; Ehara, M.; Toyota, K.; Fukuda, R.; Hasegawa, J.; Ishida, M.; Nakajima, T.; Honda, Y.; Kitao, O.; Nakai, H.; Vreven, T.; Montgomery, J. A., Jr.; Peralta, J. E.; Ogliaro, F.; Bearpark, M.; Heyd, J. J.; Brothers, E.; Kudin, K. N.; Staroverov, V. N.; Kobayashi, R.; Normand, J.; Raghavachari, K.; Rendell, A.; Burant, J. C.; Iyengar, S. S.; Tomasi, J.; Cossi, M.; Rega, N.; Millam, J. M.; Klene, M.; Knox, J. E.; Cross, J. B.; Bakken, V.; Adamo, C.; Jaramillo, J.; Gomperts, R.; Stratmann, R. E.; Yazyev, O.; Austin, A. J.; Cammi, R.; Pomelli, C.; Ochterski, J. W.; Martin, R. L.; Morokuma, K.; Zakrzewski, V. G.; Voth, G. A.; Salvador, P.; Dannenberg, J. J.; Dapprich, S.; Daniels, A. D.; Farkas, O.; Foresman, J. B.; Ortiz, J. V.; Cioslowski, J.; Fox, D. J. *Gaussian 09*, revision A.2; Gaussian, Inc.: Wallingford, CT, 2009.
(59) Ponder, J. W. *TINKER - Software tools for molecular design*, version 5.1.09; Washington University School of Medicine: Saint Louis, MO, 2009.
(60) Qian, P.; Song, W.; Lu, L.; Yang, Z. *Int. J. Quantum Chem.* **2010**, *110*, 1923–1937.
(61) *PQS*, version 4.0; Parallel Quantum Solutions: Fayetteville, Arkansas;http://www.pqs-chem.com.

JCTC Journal of Chemical Theory and Computation

ARTICLE

pubs.acs.org/JCTC

Stability of Hydrocarbons of the Polyhedrane Family: Convergence of ab Initio Calculations and Corresponding Assessment of DFT Main Approximations

J. C. Sancho-García*

Departamento de Química Física, University of Alicante, E-03080 Alicante, Spain

ABSTRACT: Highly accurate coupled-cluster (CC) calculations with large basis sets have been performed to study the binding energy of the $(CH)_{12}$, $(CH)_{16}$, $(CH)_{20}$, and $(CH)_{24}$ polyhedral hydrocarbons in two, cage-like and planar, forms. We also considered the effect of other minor contributions: core-correlation, relativistic corrections, and extrapolations to the limit of the full CC expansion. Thus, chemically accurate values could be obtained for these complicated systems. These nearly exact results are used to evaluate next the performance of main approximations (i.e., pure, hybrid, and double-hybrid methods) within density functional theory (DFT) in a systematic fashion. Some commonly used functionals, including the B3LYP model, are affected by large errors, and only those having reduced self-interaction error (SIE), which includes the last family of conjectured expressions (double hybrids), are able to achieve reasonable low deviations of 1−2 kcal/mol especially when an estimate for dispersion interactions is also added.

1. INTRODUCTION

The stability of the polyhedrane family of hydrocarbons $(CH)_{2n}$ (n = 6, 8, 10, 12; see Figures 1 and 2) has recently attracted much attention[1−6] due to the subtle interplay found between intramolecular short-, medium-, and long-range (in the weak overlap region) physical effects when increasing the size of the system. The field of computational organic chemistry[7,8] is expected to face a compromise between accuracy and computational cost in these cases; thus, the assessment of efficient yet accurate methods for this kind of systems is a topic of ongoing research. To do so appropriately, benchmarking always needs highly accurate and/or experimental results for the systematic validation of less costly methods. Furthermore, we note that two of the $(CH)_{12}$ possible isomers are also part of the DC9 subset of the stringent GMTKN24 general benchmark database,[9] which was recently developed to facilitate a nonbiased comparison between different theoretical methods, intrinsically proving the current interest on these molecules as complicated and thus challenging systems.

In this context and as it has been done before,[4,5] we carefully calculate the binding energies (BE) of polyhedranes relative to the number of constituing acetylene units

$$\Delta E(\mathrm{BE}) = \frac{1}{n}E[(CH)_{2n}] - E(C_2H_2) \quad (1)$$

Before any attempt to assess the accuracy of an approximate model (i.e., DFT) to deal with these and related systems, we will calculate these energies with the current standard for covalent and noncovalent interactions of medium-size molecules:[10,11] high-level coupled-cluster (CC) theory with singles, doubles, and perturbatively estimated triple excitations, the CCSD(T) method. Note the extraordinary effort needed for a method formally scaling as N^7, where N can be related to the size of the systems, to the whole $(CH)_{2n}$ family of compounds shown in Figures 1 and 2. These calculations are 2 orders of magnitudes more demanding than those obtained before, based on spin-scaled variants of the Møller−Plesset perturbation theory up to second order (MP2), and subsequently used to benchmark a large number of density functionals.[4] Additionally, the latter authors have recently corrected their benchmark values due to some inadvertent overestimation of the original numbers.[5] Thus, at this stage, our objective is 2-fold: (i) to provide first highly accurate reference values for binding energies of the members of the $(CH)_{2n}$ family and (ii) to further use these numbers to carefully benchmark the results of density functional theory (DFT).

2. TECHNICAL DETAILS

The ab initio final energy for each system was calculated as follows

$$E^{\mathrm{CBS}}_{\mathrm{CCSD(T)}} \approx E^{\text{cc-pVQZ//cc-pVTZ}}_{\mathrm{MP2}} + \left(E^{\text{cc-pVTZ}}_{\mathrm{CCSD(T)//MP2}} - E^{\text{cc-pVTZ}}_{\mathrm{MP2}}\right) \quad (2)$$

where the first term tries to saturate the correlation effects at the second order of the Møller−Plesset perturbation theory with respect to the space expanded by the basis sets, the slowest converging step, while the second term, denoted for the sake of simplicity ΔCCSD(T) in the following, adds the remaining correlation effects which have commonly a less marked dependence with respect to the basis sets. Note that these terms are single-point corrections at the sufficiently converged MP2/cc-pVTZ geometries. This strategy intends to estimate the correlation effects at the complete basis sets (CBS) limit. The family of cc-pVnZ basis sets (n = D, T, Q) has been consequently used along the study. All single-point ab initio calculations were performed keeping frozen the core orbitals, a minor effect that

Received: March 23, 2011
Published: July 21, 2011

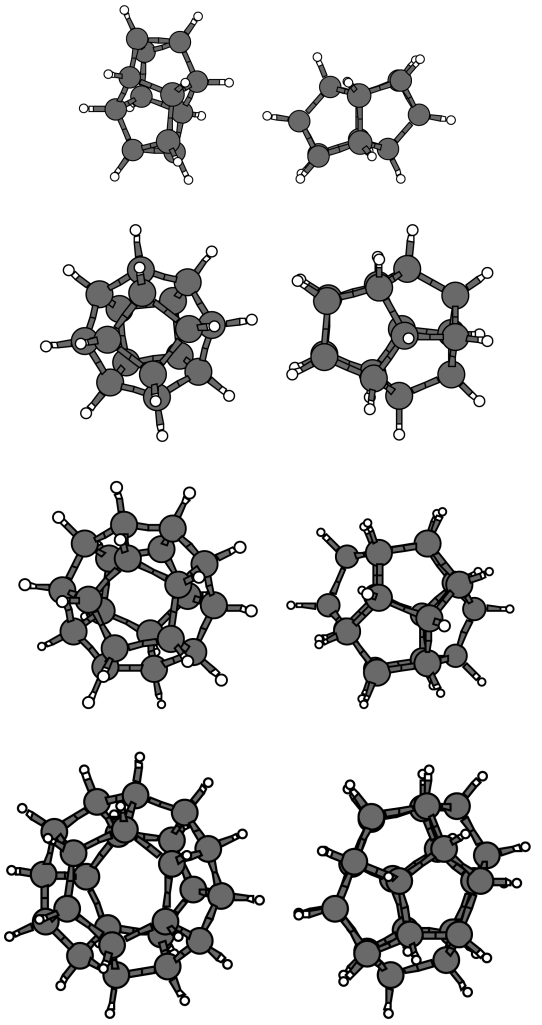

Figure 1. Representation of the molecular geometries of cage-like $(CH)_{2n}$ (n = 6, 8, 10, 12) compounds **1a**−**4a** (from top to bottom) in two views. Figure created with XMakemol (see http://www.nongnu.org/xmakemol/).

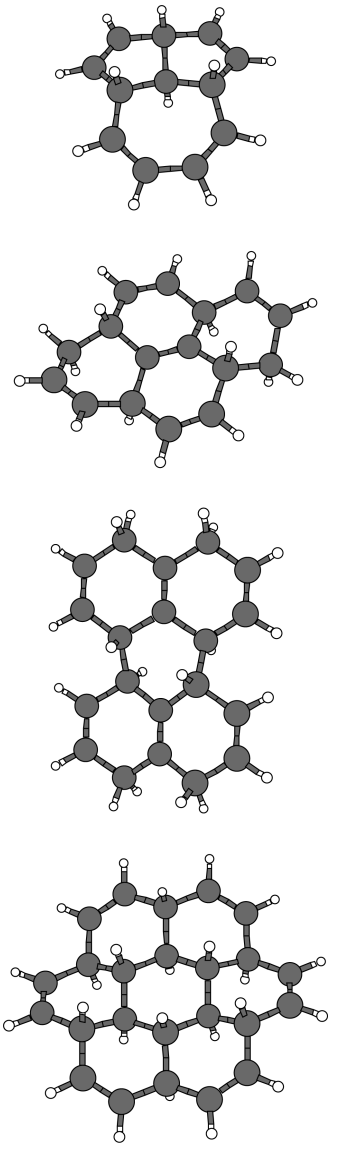

Figure 2. Representation of the molecular geometries of planar $(CH)_{2n}$ (n = 6, 8, 10, 12) compounds **1b**−**4b** (from top to bottom). Figure created with XMakemol (see http://www.nongnu.org/xmakemol/).

will however be further investigated at the MP2 level, and without the counterpoise correction for basis sets superposition error, which facilitates comparison with previous results.

The 2.8.0 version of the ORCA quantum-chemical package[12] was consistently used for all calculations reported here. Concerning the use of DFT-based methods, note that (i) we significantly increased all the default thresholds (i.e., integration grid or convergence of self-consistent resolution of the Kohn−Sham equations) to reduce numerical errors and (ii) the geometries of the compounds are fully optimized with the cc-pVTZ basis set, which seems enough to ensure nearly converged results with respect to the one-particle space. Additionally, the resolution-of-the-identity (RI) and chain-of-spheres (COSX) techniques[13,14] were employed if needed to alleviate the computational cost of the more demanding steps. The auxiliary basis functions were taken from the corresponding basis set library.

3. POLYHEDRANE FAMILY $(CH)_{2N}$: AB INITIO RESULTS

We will investigate first the convergence of the MP2 values with respect to the basis sets: Increasing the level from cc-pVDZ to cc-pVTZ reduces the values of ΔE(BE) by 2.0−2.5 (1.5−1.8) kcal/mol for the **1a**−**4a** (**1b**−**4b**) compounds along the $(CH)_{2n}$ series, whereas going from cc-pVTZ to cc-pVQZ leaves the values almost unaltered (maximum deviation less than 0.1 kcal/mol for both cage-like and planar forms). Thus, the first term of eq 2 can be considered as practically converged at this stage. Before analysis of the complete CCSD(T)/CBS results for the entire $(CH)_{2n}$ family, let us focus first on further envisioned computational savings. We see two strategies to reduce the cost of the more demanding ΔCCSD(T) contribution: (i) to employ the cc-pVDZ basis sets, which reduces the number of two-electron integrals, and (ii) to employ the CCSD level, which reduces the formal scaling of the procedure by an order of magnitude. However, this last strategy is discouraged due to csome compensation of errors between the convergence of CCSD and (T) contributions.[15] We will thus investigate next the efficiency of the first possibility for the $(CH)_{12}$ (**1a**) case: ΔE(BE) only

Table 1. Binding Energies, ΔE(BE) in kcal/mol, of the $(CH)_{2n}$ (n = 6, 8, 10, 12) Family of Compounds Calculated at the Approximate CCSD(T)/CBS Level

	$(CH)_{12}$		$(CH)_{16}$		$(CH)_{20}$		$(CH)_{24}$	
compound	**1a**	**1b**	**2a**	**2b**	**3a**	**3b**	**4a**	**4b**
ΔE(BE)	−47.36	−42.28	−51.85	−45.86	−56.38	−48.81	−54.93	−49.60

varies (in kcal/mol) from −47.27 ($\Delta CCSD(T) = E^{cc\text{-}pVTZ}_{CCSD(T)//MP2} - E^{cc\text{-}pVTZ}_{MP2}$) to −47.36 ($\Delta CCSD(T) = E^{cc\text{-}pVDZ}_{CCSD(T)//MP2} - E^{cc\text{-}pVDZ}_{MP2}$), which completely validates the use of this approximation in the following. Therefore, the possible impact of further basis sets extension is not expected to significantly influence the conclusions reached up to here.

Further investigation of these results, expectedly taken as benchmarks, is carried out next again for compound **1a**, taken again as example. To do so, we invoke the technique called valence "focal-point analysis" (FPA)[16,17] to study again the dual convergence of both basis sets and methods toward nearly exact results. The asymptotic value is estimated as follows: (i) the binding energy provided by zeroth-order energy (RHF) is calculated with the cc-pVnZ (n = D, T, Q) sequence and extrapolated to its CBS limit by a n^{-5} function;[18] (ii) the remaining correlation contributions to ΔE(BE) employing CC-based methods (δ_{CCSD} and $\delta_{CCSD(T)}$, respectively) are included at the extrapolated values; and (iii) the CC series is extrapolated toward completeness (δ_{FCC}) thanks to the availability of a continued fraction approximation.[19] Among all the available extrapolation techniques for CC-based correlation energies, E_c, we choose the expression[20]

$$E_c(\infty) = [E_c(n+1) - E_c(n)]F + E_c(n) \quad (3)$$

where F is a coefficient for extrapolation depending on n and n + 1 and $E_c(\infty)$ is the final extrapolated value. Application of the aforesaid scheme to $(CH)_{12}$ (**1a**) brings a final value of −47.39 kcal/mol, in complete agreement with calculations based on eq 2; δ_{CCSD}, $\delta_{CCSD(T)}$, and δ_{FCC} contributing, respectively, with −8.36, −0.30, and −0.09 kcal/mol to the initial RHF/cc-pV∞Z value of −38.63 kcal/mol. As a byproduct of this FPA result, we confirm again the hypothesis implicit in eq 2 about the negligible impact on further basis sets extension.

Additionally, one needs to complementarily address other effects which are normally overlooked when trying to reach errors in the subchemical accuracy range (best estimates deviating the most with respect to the exact value by 1 kcal/mol): core correlation effects and scalar relativistic corrections. The former is calculated here by the difference between MP2/cc-pCVTZ//MP2/cc-pVTZ and MP2/cc-pVTZ energies and amounts to less than 0.1 kcal/mol (in absolute value) for the whole $(CH)_{2n}$ set. The latter correction employs the Douglas−Kroll−Hess (DKH) Hamiltonian[21] and is estimated as the difference between MP2-DKH/cc-pVTZ//MP2/cc-pVTZ and MP2/cc-pVTZ energies, which thus gives a value around 0.1 kcal/mol for all compounds. We have not evaluated the impact of other minor effects yet, i.e., the influence of the CCSDT−CCSD(T) correction, although they are expected to be negligibly small according to the FPA value obtained for δ_{FCC} of the smallest compound. To summarize, our best-estimates (nonrelativistic) core-correlation corrected CCSD(T)/CBS binding energies for compounds **1a**−**4a** (cage-like) and **1b**−**4b** (planar) are gathered in Table 1 and will be used next to benchmark the results obtained by other methods such as density functional theory (DFT) using mainly hybrid and double-hybrid models.[22−28] Note that orbital-dependent density functionals are called to play a major role in next decades[29] and further applications to chemically interesting systems are largely envisioned.

Table 2. Mean Unsigned Error, MUE in kcal/mol, for Binding Energies of the $(CH)_{2n}$ (n = 6, 8, 10, 12) Family of Compounds at Various MP2 and DFT Levels

method		MUE	
		1a−**4a**	**1b**−**4b**
ab initio[a]	MP2	2.4	0.9
	SCS-MP2	1.7	2.2
DFT[b]	BLYP	13.1	9.4
	BLYP-D	8.0	5.2
	B3LYP	7.4	5.0
	B3LYP-D	2.8	1.3
	BHHLYP	2.0	0.9
	BHHLYP-D	0.7	0.2
	B2-PLYP	3.6	2.7
	B2-PLYP-D	1.2	0.8
	B2GP-PLYP	1.0	0.9
	B2GP-PLYP-D	0.7	0.5

[a] With the cc-pVQZ basis set at the corresponding cc-pVTZ-optimized geometry. [b] At the cc-pVTZ-optimized geometry.

4. POLYHEDRANE FAMILY $(CH)_{2N}$: DFT RESULTS

In this context, we present in Table 2 the results of the systematic analysis performed; the mean unsigned error (MUE) will be used to judge the quality of the approximations. Before analyzing the DFT-based results, we would like to underline first that spin-component-scaled MP2 models (as SCS-MP2[30]) are still an approximation to the CCSD(T) values yet certainly an improvement with respect to unscaled MP2 upon inspection (vide infra) of the corresponding values; thus, previous claims[4,5] should also benefit from the current CCSD(T)/CBS values.

We start with the discussion with systems **1a**−**4a**. Table 2 also shows that whereas BLYP and B3LYP behave inaccurately, a MUE of 13.1 and 7.4 kcal/mol is obtained, respectively, a higher value of exact-like exchange (BHHLYP) clearly improves the results and reduces the corresponding MUE to 2.0 kcal/mol. However, further steps in this direction (i.e., increasing the value of the exact-like exchange weight in an hybrid-like model) is not recommended, and in fact, the HF-LYP model, with full exact-like exchange together with a coupled correlation potential in a self-consistent fashion, drops an MUE of 10.2 kcal/mol. On the other hand, the double hybrids selected (B2-PLYP and B2GP-PLYP) are undoubdtedly a major improvement with respect to the golden standard (B3LYP) since the corresponding MUE is at least halved. Concerning compounds **1b**−**4b**, simply speaking, the trends found are the same as before. Dispersion-uncorrected MUE values are 9.4, 5.0, 0.9, and 8.6 kcal/mol for BLYP, B3LYP, BHHLYP, and HF-LYP models, lower than for cage-like forms; note that double-hybrid forms behave very respectably again.

There is still room for further improvement if one couples the dispersion energy (-D) to any of the calculated DFT values.[31] To do that, at essentially no extra computational cost, we resort to a

Table 3. Mean Unsigned Error, MUE in kcal/mol, for Isomerization Energies between 1a−4a and 1b−4b Members of the $(CH)_{2n}$ (n = 6, 8, 10, 12) Family of Compounds at Various MP2 and DFT Levels

	method	MUE
ab initio[a]	MP2	12.2
	SCS-MP2	3.8
DFT[b]	BLYP	32.9
	BLYP-D	23.8
	B3LYP	20.6
	B3LYP-D	12.5
	BHHLYP	9.4
	BHHLYP-D	7.0
	B2-PLYP	8.0
	B2-PLYP-D	3.7
	B2GP-PLYP	1.7
	B2GP-PLYP-D	1.5

[a] With the cc-pVQZ basis set at the corresponding cc-pVTZ-optimized geometry. [b] At the cc-pVTZ-optimized geometry.

first-order function which explicitly depends on the well-known R^{-6} decay of these interactions

$$E = s_6 \sum_{AB} f_d(R_{AB}) \frac{C_6^{AB}}{R_{AB}^6} \quad (4)$$

where s_6 is a scaling parameter used to efficiently couple the exchange-correlation and dispersion energies, $f_d(R_{AB})$ is a damping function of the interatomic distance (R_{AB}), and C_6^{AB} is a dispersion coefficient for the atomic pair AB.[32−34] Table 2 nicely shows how the MUE is dramatically altered in the right direction after addition of the dispersion term to the final values, independently of the model chosen.

If one averages now the MUE obtained for both sets of compounds, **1a**−**4a** and **1b**−**4b**, a range of hybrid (BHHLYP-D) and double-hybrid (B2-PLYP-D, B2GP-PLYP-D, and B2GP-PLYP-D) methods are able to be obtained now, in some cases by far the target of "chemical accuracy" (a maximum error of ±1 kcal/mol with respect to energy reference values). Note that even in the worst possible scenario any double hybrid would at least halve the MUE with respect to B3LYP, a somehow superseded method now.

In addition, concerning these nonrelativistic all-core DFT-based calculations, we would like to remark first that a large set of calculated key properties of organic systems is known to be mostly affected by the self-interaction error (SIE) of common density functionals[35] (i.e., the spurious self-interaction of an electron with itself). Generally speaking, functionals having minimal SIE should be used for theoretical studies of organic systems.[36] As commonly admitted in the field and far from being trivial,[37] the SIE is very often used interchangeably with the concept of delocalization error, which is maybe more intuitive: a functional with large SIE would overstabilize delocalized densities while giving too high energies for localized densities. Note that this effect would strongly manifest when computing the energy differences between cage-like (**1a**−**4a**) and planar (**1b**−**4b**) isomer forms.

In this respect, Table 3 presents the values of the MUE obtained for isomerization energies $E(na) - E(nb)$ (n = 1−4) with respect to the reference values given again by eq 2. The

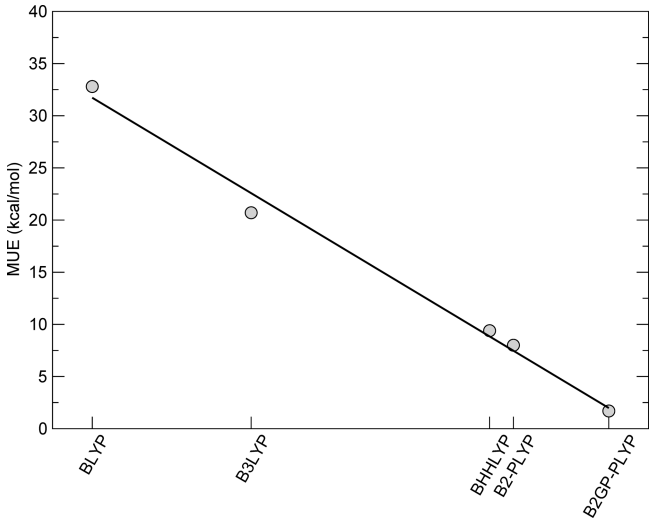

Figure 3. Evolution of MUE (in kcal/mol) for the isomerization energies of cage-like vs planar forms as a function of the exact-like exchange term introduced into the functional.

striking decrease of the MUE values with the weight of exact-like exchange introduced into the (double-)hybrid form is shown in Figure 3; we remind that the exact-like exchange is, by definition, SIE free, which helps to interpret the trend found with a correlation coefficient r^2 = 0.991. It is maybe also illustrative to compare these numbers with other modern methods belonging to the Minnesota family of functionals,[38] as M06-L and M06-2X. The numbers taken from ref 4 lead to a MUE of 8.0 and 4.4 kcal/mol, respectively, which can be considered as competitive too. All in all, we would like to warn about the marked influence of SIE and/or dispersion corrections here and some strategies to cope with the former among others: high weights of exact-like exchange (i.e., BHHLYP), double-hybrid models (i.e., B2-PLYP or B2GP-PLYP), or long-range-corrected functionals (i.e., CAM-B3LYP or LC-BLYP, the latter drops a MUE of 8.2 kcal/mol according to the values taken from ref 4). The latter effect can be efficiently and accurately taken into account by the correction given by eq 4 or related.[39]

5. CONCLUSIONS

We briefly remind here that our main purpose was to convincingly establish a set of benchmark values for the stability energy of two forms, cage-like and planar, of polyhedrane hydrocarbons, which have recently attracted much interest. In the pursuit of the greatest possible accuracy, we relied on CCSD(T) calculations at the estimated basis sets limit together with some minor corrections in an attempt to successfully reach the subchemical accuracy range. Having done that, further assessment of less costly methods, such as spin-component-scaled MP2 variants (SCS-MP2) as well as hybrid and double-hybrid functionals, was carried out. Since there exists in the literature a plethora of density functionals, our intention was not to extensively cover all of them; we selected examples from the main existing categories (pure, hybrid, and double-hybrid methods) without changing the exchange and correlation density kernels: BLYP, B3LYP, BHHLYP, B2-PLYP, and B2GP-PLYP. A dispersion correction (-D) was then added to each functional form to test its influence on the final results. One can clearly observe upon inspection of the results and independently of the isomer type (cage-like or

planar) how standard methods such as B3LYP keep unacceptably large errors and a higher weight of exact-like exchange in the composition of the hybrid functional definitively helps. Note that double hybrids normally have, by default, larger weights of exact-like exchange, and thus, they have also shown excellent behavior. This seems to indicate the large influence of SIE, especially for isomerization energies, although intramolecular dispersion interactions are also important mostly for binding energies. Overall, to be always on the safer side due to the possible existing interplay between SIE and intramolecular dispersion interactions, we believe that older functionals should be progressively discarded, for a routine use in the field of computational organic chemistry, and double hybrids might be routinely applied if the computational cost does not become a serious bottleneck.

AUTHOR INFORMATION

Corresponding Author

*E-mail: jc.sancho@ua.es.

REFERENCES

(1) Schreiner, P. R.; Fokin, A. A.; Pascal, R. A., Jr.; de Meijere, A. *Org. Lett.* **2006**, *8*, 3635.
(2) Schreiner, P. R. *Angew. Chem., Int. Ed.* **2007**, *46*, 4217.
(3) Shamov, G. A.; Budzelaar, P. H. M.; Schreckenbach, G. *J. Chem. Theory Comput.* **2010**, *6*, 477.
(4) Shamov, G. A.; Schreckenbach, G.; Budzelaar, P. H. M. *J. Chem. Theory Comput.* **2001**, *6*, 3442.
(5) Shamov, G. A.; Schreckenbach, G.; Budzelaar, P. H. M. *J. Chem. Theory Comput.* **2011**, *7*, 804.
(6) Swart, M.; Solá, M.; Bickelhaupt, M. *J. Comput. Chem.* **2011**, *32*, 1117.
(7) Bachrach, S. *Computational Organic Chemistry*; Wiley: New York, 2007.
(8) Bachrach, S. *Annu. Rep. Prog. Chem. Sect. B* **2008**, *104*, 394.
(9) Goerigk, L.; Grimme, S. *J. Chem. Theory Comput.* **2010**, *6*, 107.
(10) Černý, J.; Hobza, P. *Phys. Chem. Chem. Phys.* **2007**, *9*, 5291.
(11) Riley, K. E.; Pitoňák, M.; Jurečka, P.; Hobza, P. *Chem. Rev.* **2010**, *110*, 5023.
(12) Neese, F. *ORCA 2.8.0*; University of Bonn: Bonn, Germany; http://www.thch.uni-bonn.de/tc/orca/
(13) Neese, F. *J. Comput. Chem.* **2003**, *24*, 1740.
(14) Neese, F.; Wennmohs, F.; Hansen, A.; Becker, U. *Chem. Phys.* **2009**, *356*, 98.
(15) Pitoňák, M.; Riley, K. E.; Neogrady, P.; Hobza, P. *ChemPhysChem* **2008**, *9*, 1636.
(16) Császár, A. G.; Allen, W. D.; Schaefer, H. F., III *J. Chem. Phys.* **1998**, *108*, 9751.
(17) Sancho-Garca, J. C. *Chem. Phys. Lett.* **2009**, *468*, 138.
(18) Parthiban, S.; Martin, J. M. L. *J. Chem. Phys.* **2001**, *114*, 6014.
(19) Goodson, D. Z. *J. Chem. Phys.* **2002**, *116*, 6948.
(20) Schwenke, D. W. *J. Chem. Phys.* **2005**, *122*, 014107.
(21) Neese, F.; Wolf, A.; Fleig, T.; Reiher, M.; Hess, B. A. *J. Chem. Phys.* **2005**, *122*, 204107.
(22) Becke, A. D. *J. Chem. Phys.* **1993**, *98*, 5648.
(23) Becke, A. D. *J. Chem. Phys.* **1993**, *98*, 1372.
(24) Grimme, S. *J. Chem. Phys.* **2006**, *124*, 034108.
(25) Schwabe, T.; Grimme, S. *Phys. Chem. Chem. Phys.* **2006**, *8*, 4398.
(26) Tarnopolsky, A.; Karton, A.; Sertchook, R.; Vuzman, D.; Martin, J. M. L. *J. Phys. Chem. A* **2008**, *112*, 3.
(27) Karton, A.; Tarnopolsky, A.; Lamère, J. F.; Schatz, G. C.; Martin, J. M. L. *J. Phys. Chem. A* **2008**, *112*, 12868.
(28) Zhang, Y.; Xu, X.; Goddard, W. A., III *Proc. Natl. Acad. Sci. U.S.A.* **2009**, *106*, 4963.
(29) Kummel, S.; Kronik, L. *Rev. Mod. Phys.* **2008**, *3*, 80.
(30) Grimme, S. *J. Chem. Phys.* **2003**, *118*, 9095.
(31) Burns, L. A.; Vázquez-Mayagoitia, A.; Sumpter, B. A.; Sherrill, C. D. *J. Chem. Phys.* **2011**, *134*, 084107.
(32) Wu, Q.; Yang, W. *J. Chem. Phys.* **2002**, *116*, 515.
(33) Grimme, S. *J. Comput. Chem.* **2006**, *27*, 1787.
(34) Jurečka, P.; Černý, J.; Hobza, P.; Salahub, D. R. *J. Comput. Chem.* **2007**, *28*, 555.
(35) Mori-Sánchez, P.; Cohen, A. J.; Yang, W. *J. Chem. Phys.* **2006**, *125*, 201102.
(36) Johnson, E. R.; Mori-Sánchez, P.; Cohen, A. J.; Yang, W. *J. Chem. Phys.* **2008**, *129*, 204112.
(37) Körzdörfer, T. *J. Chem. Phys.* **2011**, *134*, 094111.
(38) Zhao, Y.; Truhlar, D. G. *Acc. Chem. Res.* **2008**, *41*, 157.
(39) Grimme, S.; Antony, J.; Ehrlich, S.; Krieg, H. *J. Chem. Phys.* **2010**, *132*, 154104.

JCTC Journal of Chemical Theory and Computation

ARTICLE

pubs.acs.org/JCTC

Accuracy of Effective Core Potentials and Basis Sets for Density Functional Calculations, Including Relativistic Effects, As Illustrated by Calculations on Arsenic Compounds

Xuefei Xu and Donald G. Truhlar*

Department of Chemistry and Supercomputing Institute, University of Minnesota, Minneapolis, Minnesota 55455-0431, United States

Supporting Information

ABSTRACT: For molecules containing the fourth-period element arsenic, we test (i, ii) the accuracy of all-electron (AE) basis sets from the def2-*x*ZVP and ma-*x*ZVP series (where *x*Z is S, TZ, or QZ), (iii) the accuracy of the 6-311G series of AE basis sets with additional polarization and diffuse functions, and (iv) the performance of effective core potentials (ECPs). The first set of tests involves basis-set convergence studies with eleven density functionals for five cases: equilibrium dissociation energy (D_e) of As_2, vertical ionization potential (VIP) of As_2, IP of As, acid dissociation of H_3AsO_4, and D_e of FeAs. A second set of tests involves the same kinds of basis-set convergence studies for the VIP and D_e values of As_3 and As_4 clusters. Both relativistic and nonrelativistic calculations are considered, including in each case both AE calculations and calculations with ECPs. Convergence and accuracy are assessed by comparing to relativistic AE calculations with the cc-pV5Z-DK or ma-cc-pV5Z-DK basis and to nonrelativistic AE calculations with the cc-pV5Z or ma-cc-pV5Z basis. The primary objective of this study is to evaluate the abilities of ECPs with both their recommended basis sets and other basis sets to reproduce the results of all-electron relativistic calculations. The performance of the def2 and ma series basis sets is consistent with their sizes, and quadruple-ζ basis sets are the best. The def2-TZVP basis set performs better than most of the 6-311G series basis sets, which are the most commonly used basis sets in the previous studies of arsenic compounds. However, relativistic def2-TZVP calculations are not recommended. The large-core ECPs, which are the only available ECPs for arsenic in the popular Gaussian program, have average errors of 9−12 kcal/mol for the arsenic systems studied; therefore, these ECPs are not recommended. The triple-ζ small-core relativistic ECP (RECP) basis set cc-pVTZ-PP is found to have performance better than that of the def2-TZVP basis set, and it is highly recommended for arsenic-containing systems. The double-ζ RECP basis set ma-sc-SVP is recommended for large arsenic systems for which the def2-TZVP and cc-pVTZ-PP basis sets are unaffordable, if a basis-set error of ∼2 kcal/mol can be tolerated.

1. INTRODUCTION

An effective core potential (ECP) is a potential energy function added to an electronic structure calculation to replace the explicit treatment of core electrons. ECPs have two main advantages in quantum chemistry: they reduce the cost of calculations by decreasing the size of the basis set required for a given accuracy (core basis functions are not needed), and—by using a relativistic ECP (RECP)—they allow the inclusion of relativistic effects on the size and shape of core orbitals without using a relativistic treatment of the wave function. A third benefit is that using ECPs reduces basis set superposition errors. The use of ECPs is now well-established for calculating wave functions of systems containing many-electron atoms, and ECPs developed with Hartree−Fock (HF) wave functions have been found to be "very reliable and highly transferable"[1] for such calculations. The valence orbitals in a calculation employing an ECP differ from the valence orbitals in an all-electron (AE) calculation and are called pseudo-orbitals.

However, when one proceeds from wave function theory (WFT) to Kohn−Sham (KS) density functional theory (DFT), new issues arise because of the nonlinear dependence of the exchange−correlation (xc) functional on density.[2,3] This is widely recognized in solid-state physics, and so-called nonlinear core corrections (NLCCs) are widely employed in plane wave codes for density functional calculations of extended systems. (Despite its name, an NLCC is not an add-on correction but rather constitutes a more elaborate method for defining and using an ECP by changing the treatment of the core density.) In calculations with plane wave basis sets, the ECP is usually called a pseudopotential (PP), and it is more approximate than the ECPs usually used in quantum chemistry for calculations with Gaussian basis functions because one attempts to find a compromise between high accuracy in representing the effect of core electrons and the need to include high-momentum plane waves to represent the pseudo-orbitals. Perhaps for this reason it has not been recognized that NLCCs may also be needed for calculations with Gaussian basis sets, and in fact, NLCCs are not employed in popular Gaussian-based electronic structure packages.

The need for NLCCs in Gaussian-based DFT calculations has been studied by van Wüllen,[4] who wrote, "Since the xc potential is nonlinear,... one cannot expect that an ECP adjusted at the HF level performs necessarily well when doing a density functional calculation on the pseudosystem with a lesser electron number and an electron density resulting from the valence orbitals alone. On the other hand, much work has been invested in the

Received: April 6, 2011
Published: June 30, 2011

development of ECPs at the HF level.... Gaussian basis sets suitable for the expansion of valence orbitals have been developed together with the core potentials. It would be very desirable to profit from this work in KS calculations." Indeed ECPs developed at the HF level and often validated only at the HF level are present in most popular quantum chemistry software and are widely used for KS calculations. However, there is only a handful of systematic work validating this.[4−7] Van Wüllen also pointed out that "To assess the validity of using ECPs, an 'internal' consistency check is more important than is a comparison with experiment." He used large basis sets for his tests "to avoid any bias introduced by different quality basis sets in the all-electron and ECP calculations." He found, in a systematic set of nonrelativistic calculations with large basis sets and small-core nonrelativistic ECPs (NRECPs), that ECP calculations agree with AE calculations on average to 0.012 Å for bond lengths and 0.9 kcal/mol for bond energies, whereas these values change to 0.007 Å and 2.5 kcal/mol for KS calculations, which he judged satisfactory. Han and Hirao[6] extended this kind of systematic test to one-component relativistic ECPs (RECPs) and found "little loss of accuracy" in using ECPs with DFT if one uses flexible basis sets and appropriate contraction coefficients; in particular, they found accuracies of 0.001 Å and 1 kcal/mol for bond lengths and bond energies.

But questions remain: (1) Are the conclusions valid for a wider variety of systems? (2) Are the conclusions valid if one uses the basis sets recommended by the ECP developers as widely used with standard quantum chemistry programs rather than the large, flexible basis sets in the kind of test summarized above? (3) What new considerations arise when one compares calculations with RECPs to calculations with NRECPs for the same system? In this paper we explore these questions, in particular for systems containing arsenic.

Arsenic and its compounds are well-known for their toxicity for most life forms and their potent physiological properties, and they have been used medicinally for thousands of years.[8] Now, arsenic is under the spotlight due to the report[9] of a protebacterium from Mono Lake that reportedly can substitute arsenic for phosphorus to sustain its growth. This finding is highly controversial,[10−12] and it will stimulate further experimental and theoretical investigations on arsenic's role in living systems. Before one starts a computational study of the biological role or other properties of arsenic compounds, it is important to choose a suitable basis set and—to efficiently include relativistic effects on core orbitals and to keep the overall cost of the calculation for a given accuracy as low as possible—to choose an accurate RECP. Exploring these choices for arsenic is of interest not only for calculations on arsenic-containing systems but also for the study's implications for other elements, especially those in the fourth through sixth periods of the periodic table.

Motivated by the discussion above, we focus in this paper on the choice of ECP for As, along with the choice of corresponding basis set, for density-functional electronic-structure calculations on arsenic-containing compounds. To sort out the special needs for DFT as compared to those of WFT, we carry out HF calculations as well as KS calculations. To be sure that our results for DFT are not biased by the choice of a particular xc functional, all conclusions about DFT calculations are averaged over 11 different xc functionals.

In the literature,[13] the most commonly used all-electron (AE) basis sets for the theoretical study of small arsenic compounds are the 6-311G triple-ζ basis set[14] with polarization functions and sometimes augmented with diffuse functions. Although less widely used for As, the popular correlation consistent basis sets (cc-pVxZ)[15] by Dunning and the most recent collection of basis sets (def2-xZVP)[16] from the Ahlrichs group can be used to improve the accuracy of AE calculations by increasing the size of the basis set. However, the 6-311-type, cc-pVxZ, and def2 basis sets are AE basis sets and, as such, are inefficient for the simulation of large systems. In addition, arsenic belongs to the fourth period of the elements, for which the scalar relativistic effects have been found to be very important for some properties. Calculations including relativistic effects that use AE basis sets involve higher costs for accurate results, e.g., the CPU time can be much larger than that of nonrelativistic calculations at a comparable level for large systems. Therefore, using effective core potentials fitted to relativistic atomic calculations to replace the inner shell electrons of arsenic may be a good choice for large systems, because it allows one to incorporate the most important scalar relativistic effect (the changes in size of s and p core orbitals) in formally nonrelativistic (NR) calculations while simultaneously reducing the need for basis functions to expand the core orbitals. This raises another issue, namely, the number of core electrons to be replaced by an ECP. Large-core ECPs that replace 28 electrons have been employed for As,[13e,17] but medium-core (18 electrons) and small-core (10 electrons) ECPs are potentially better choices. The accuracy of all these choices needs to be investigated more systematically than has been done in previous work, especially in the context of DFT.

In the present work, the performance of popular basis sets and ECPs (large-core, medium-core, and small-core) for HF and KS calculations of equilibrium bond dissociation energies (D_e) and vertical ionization potentials (VIP) of prototype As-containing compounds will be investigated. In particular, we consider the ionization potential (IP) of As; the D_e and VIP of As_2, As_3, and As_4; the energy of the first acid dissociation of H_3AsO_4 (i.e., the energy to remove a proton); and the D_e of FeAs.

The choice of FeAs is motivated in part by the recent finding that solid iron arsenide is a novel superconductor material.[18] Furthermore, as a 3d metal in the fourth period, the choice of basis set and RECP for Fe raises some of the same questions we have raised for As; therefore, by calculating the bond dissociation energy of the diatomic molecule FeAs, we test whether our choices of basis set and ECP for As are general, by examining whether we can use the same basis set choice for Fe as for As.

2. COMPUTATIONAL DETAILS

Although most xc functionals have similar basis set requirements, we need to recognize that the requirements do vary. Therefore, one strategy that we employ for many of our tests of basis sets and ECPs is to consider 11 xc functionals for a given property, for example, an equilibrium bond energy (D_e) or vertical ionization potential (VIP), and for each functional we use a large-basis relativistic AE calculation with a basis set specifically optimized for relativistic calculations to obtain a reference value for that xc functional and property. For brevity, this reference value is labeled NCBS-DK (NCBS denotes "nearly complete basis set" and "DK" is explained below). Then, for a given smaller basis, employed in an AE or ECP calculation with the rest of the Hamiltonian either relativistic or nonrelativistic, we calculate a deviation from the relativistic NCBS-DK value; we will call this the complete error. The complete mean unsigned error (C-MUE) is the mean unsigned deviation of the 11 calculated values of the property, each from its NCBS-DK reference value. Similarly, we use a large-basis nonrelativistic AE calculation

with a basis set specifically optimized for nonrelativistic calculations to obtain a nearly complete basis set nonrelativistic reference value, labeled NCBS-NR, for each functional and that property. The mean unsigned deviation from the NCBS-NR reference value is calculated for the 11 calculated values of the property with a given smaller basis set, and this error measure is called the nonrelativistic mean unsigned error (NR-MUE). The NR-MUE is a measure of how well a nonrelativistic basis set approaches the nonrelativistic limit, whereas the C-MUE is a measure of how well the whole treatment approaches the complete basis set limit including relativistic effects.

Following the above protocol, for our first set of tests, the D_e of the diatomic molecules As_2 ($^1\Sigma_g^+$) and FeAs ($^2\Delta$), the VIP of As_2 ($^1\Sigma_g^+$), the IP of As atom, and the energy of the first acid dissociation of $H_3AsO_4 \rightarrow H_2AsO_4^- + H^+$ have been calculated using 11 popular and high-performance xc functionals (M05,[19] M06-L,[20] M06,[21] BLYP,[22] ωB97X-D,[23] τHCTHhyb,[24] G96LYP,[22b,25] mPWLYP,[22b,26] B3LYP,[22,27] X3LYP,[28] and BPBE[22a,29]), with different basis sets and ECPs. For each given xc functional, we will compare our relativistic and nonrelativistic AE calculations and our nonrelativistic RECP and NRECP calculations to Douglas−Kroll−Hess second-order scalar relativistic calculation[30] (sometimes called DKH and sometimes called DK) results with the nearly complete basis set NCBS-DK, and we will also compare our nonrelativistic AE calculations to nonrelativistic results with the NCBS-NR basis set for a given xc functional. By looking at such comparisons, one can largely decouple the errors that are intrinsic to a given xc functional and treatment of relativistic effects from those resulting from the choice of basis set and ECP.

For the bond dissociation energy calculations of As_2 and FeAs and the VIP calculations on As_2 and IP calculations on the As atom, the cc-pV5Z-DK and cc-pV5Z basis sets[15c,d] have been chosen as NCBS-DK and NCBS-NR basis sets, respectively. For D_e of As_2, relativistic and nonrelativistic calculations with the uncontracted cc-pV5Z basis set were also performed to confirm that the cc-pV5Z-DK and cc-pV5Z basis sets are good enough to serve as the reference basis set in our investigations. There are no diffuse functions in the NCBS basis sets for these calculations, because they were previously found to be unimportant in most density functional calculations of bond dissociation energy and ionization energy of neutral molecules.[31] In the calculations of the energy of reaction of the first acid dissociation of H_3AsO_4, the minimally augmented cc-pV5Z-DK basis set (ma-cc-pV5Z-DK) is used as the NCBS-DK basis set, and the minimally augmented cc-pV5Z (ma-cc-pV5Z) is used as the NCBS-NR basis set. In these minimally augmented basis sets, a set of diffuse s and p functions has been added to the cc-pV5Z-DK or cc-pV5Z basis set for non-hydrogen elements, with the exponents of the most diffuse s or p functions of cc-pV5Z-DK or cc-pV5Z basis set divided by a factor of 3, as recommended previously.[31]

In addition, the relativistic effects of these five cases have been respectively calculated as the difference between the results of the relativistic DKH calculations and nonrelativistic calculations with a given AE basis set and the 11 xc functionals. The value of the relativistic effect on each property is calculated as the difference between the NCBS-DK and NCBS-NR values of that property with a given xc functional, and this is taken as the NCBS relativistic effect for that property and that functional. The NCBS relativistic effect is averaged over the eleven functionals to obtain a nominal reference value for relativistic effect of that property. For each property obtained with a given smaller AE basis set and a given xc functional, we calculate a deviation from the NCBS relativistic effect of that property with that functional; the mean unsigned deviation from the NCBS relativistic effect, with the mean obtained by averaging over the absolute values of the deviations for the 11 xc functionals, is called the mean unsigned error (MUE) of the relativistic effect for that property and that AE basis set.

In this first set of tests, the tested AE basis sets are the def2 basis sets, with size increasing from double-ζ to quadruple-ζ; the minimally augmented diffuse def2 basis sets[31] (which are called ma-*x*ZVP basis sets); and the 6-311G basis set series with various polarization functions and in some case with diffuse functions. Note that "double-ζ valence" is labeled as "split valence" (SV) rather than DZV in the def2 series and ma series. The "def2" basis sets were developed as a second generation of default basis sets for the popular TURBOMOLE program, and they constitute balanced economical basis sets of graded quality from partially polarized (P) double-ζ to heavily polarized (PP) quadruple-ζ for all elements up to radon (Z = 86). The P-type basis sets of the "def2" series, def2-SVP, def2-TZVP, and def2-QZVP, were recommended for DFT calculations.[16] In general, basis sets containing diffuse functions are called augmented. Recently, we[31] enhanced the def2 basis sets by adding a minimal set of diffuse functions to a subset of the elements for certain kind of calculations, and the new basis sets were labeled by "ma" (which stands for minimally augmented"). The new ma-TZVP basis set has been suggested for general-purpose applications of DFT.[31] However, the tested elements in the previous study do not include any elements of the fourth period, for which the omission of scalar relativistic effects could be a significant omission. Therefore, the performance of the def2-*x*ZVP and ma-*x*ZVP basis sets for both nonrelativistic and relativistic DKH calculations is tested in the present study, and all results are compared with those obtained from relativistic DKH calculations or nonrelativistic calculations with NCBS basis sets. We also provide limited testing of the cc-pVTZ and cc-pVTZ-DK basis sets.[15c]

The tested ECP basis sets (i.e., basis sets to be used with ECPs) and ECPs are

(i) cc-pV*x*Z-PP (x = D, T, Q, 5),[32] which are correlation-consistent-type basis sets used with the small-core (10 electrons) multiconfiguration-Dirac−Hartree−Fock (MDF) adjusted fully relativistic Stuttgart ECP, denoted MDF10;[33]
(ii) the MDF10 RECP with its own basis set;[33]
(iii) the CRENBL medium-core (18e) RECP[34] with its own basis set; and
(iv−vii) the large-core (28e) ECPs and corresponding ECP basis sets implemented in the Gaussian program.

The large-core ECP basis sets and ECPs are

(iv) the Wood−Boring quasirelativistic Stuttgart large-core ECP, labeled MWB28 (also sometimes called SDD);[35]
(v) the compact effective potential, labeled CEP,[36] which is an RECP [and which is also sometimes called the Stevens−Basch−Krauss−Jasien (SBKJ) potential];
(vi) the LANL2DZ[37] potential, which is a large-core NRECP for As and a small-core NRECP for Fe; and
(vii) the relatively new large-core (28e) MDF-adjusted fully relativistic Stuttgart ECP, denoted MDF28,[1] with its own basis set.

In addition, we also tested some combinations of modified and unmodified def2 and ma basis sets with the MDF10 RECP. The main motivation for choosing the def2 and ma basis sets for these

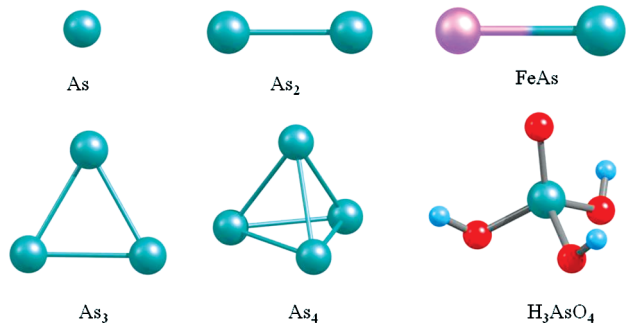

Figure 1. Structures.

combinations is that, as we already mentioned, the def2 basis sets are available for all elements up to radon.

For comparison to the ECP calculations of arsenic compounds with DFT, we also performed calculations with these ECPs by the HF method for four of the cases in the first test set: D_e and VIP of As_2, IP of As, and the first acid dissociation energy of H_3AsO_4. (The D_e of FeAs was excluded in the HF test in order to avoid complicating the comparison by having to consider transferability of ECPs for iron.) For each calculated HF property obtained with each combination of ECP and corresponding basis set, we computed the deviation from the NCBS-DK reference value of that property (obtained by relativistic HF calculations), and the mean unsigned deviation over these properties for each ECP and associated basis set was labeled MUE.

For the second set of tests, the performance of several selected basis sets and RECPs has been further tested by calculating VIPs and D_e values of arsenic clusters As_n (n = 3 and 4). The NCBS-DK and NCBS-NR basis sets are again respectively taken as cc-pV5Z-DK and cc-pV5Z.

For the third set of tests, we carried out nonrelativistic cc-pVTZ[15c] calculations and relativistic cc-pVTZ-DK[15c] calculations for D_e and VIP of As_2 and for the IP of As. These all-electron basis sets are de-emphasized because they are not of primary relevance to our goal of testing ECPs. Furthermore, we note that the cc-pVxZ and cc-pVxZ-DK basis sets employ general contraction schemes in which a primitive Gaussian is used in more than one contracted function. Although general contractions have some theoretical advantages over the segmented contraction schemes that the def2-xZVP, ma-xZVP, and 6-311G series basis sets use, efficient integral calculations with general contractions are not implemented in most popular ab initio packages, which effectively increases the number of primitive functions.

When we perform ECP calcuations in this paper, the electrons treated explicitly are always treated nonrelativistically, although the ECP may be an RECP or an NRECP. We do not test explicitly relativistic calculations that also include effective core potentials.[38]

Taking As_2 as an example, it has been confirmed that all 11 of the xc functionals considered here can predict reasonable geometrical structures, and the calculated properties, such as D_e values for As_2, are not very sensitive to reasonable choices of molecular geometries. (See Tables S1 and S2 of Supporting Information for this confirmation.) Therefore, in all calculations, for each molecule, the same reasonable geometry was used, which has the advantage that we are directly comparing electronic energies without the complication of using different geometries, and this strategy simplifies the interpretation of the results.

For As_2, the experimental bond length[39] of 2.1026 Å was used. The D_{3h} structure was used for arsenic trimer, as obtained from Igel-Mann et al.[40] with each bond length equal to 2.3284 Å. The experimental structure[41] was used for arsenic tetramer; it is a tetrahedron with each bond length equal to 2.4353 Å. The structures of FeAs, H_3AsO_4, and $H_2AsO_4^-$ were optimized by nonrelativistic calculations with the M05 xc functional, with the def2-TZVP basis set for FeAs, and with the ma-TZVP basis set for H_3AsO_4 and $H_2AsO_4^-$. The structures of the six molecules involved in the present article are shown in Figure 1.

All calculations are carried out using the Gaussian 09 electronic structure package.[42]

3. RESULTS AND DISCUSSION

3.1. Performance of All-Electron Basis Sets. Table 1 shows the mean unsigned errors (C-MUE and NR-MUE) for five cases (D_e and VIP of As_2, IP of As, and D_e of H_3AsO_4 and FeAs) averaged over 11 xc functionals with the def2, ma, and 6-311G-type basis sets. The corresponding average of the C-MUEs or NR-MUEs (A-C-MUE or A-NR-MUE) over three or five cases for each basis set is also listed in Table 1. In addition, the mean unsigned deviations of D_e for As_2 from the relativistic or nonrelativistic calculations with uncontracted cc-pV5Z basis set are also shown in Table 1. Comparing these results to the MUEs calculated with relativistic cc-pV5Z-DK or nonrelativistic cc-pV5Z results, we confirm that cc-pV5Z-DK and cc-pV5Z are reasonable reference basis set for As.

3.1.1. def2 and ma Basis Sets. 3.1.1.1. VIP of As_2, D_e of As_2, and IP of As. For the calculations of D_e of H_3AsO_4 and FeAs, the basis set choice for other elements (H, O, or Fe) could have an impact on the conclusions. Therefore, we first analyze the calculated VIP of As_2, D_e of As_2, and IP of As, based on their average C-MUE [A-C-MUE(3)] values, which are based on comparison to the NCBS-DK reference values.

As shown in rows 16 and 17 of Table 1, for nonrelativistic calculations, the def2-QZVP basis set has a similar, slightly lower A-C-MUE(3) value than the larger cc-pV5Z basis set (which is the NCBS-NR reference basis). The errors in the def2-TZVP nonrelativistic calculations (row 18) are comparable with those of def2-QZVP. The A-C-MUE(3) for the smaller def2-SVP basis set (row 20) is 0.4 kcal/mol larger than that of def2-TZVP. The def2-SVP basis set is worse for D_e values than for VIP and IP values. This indicates that the double split valence basis is not sufficiently flexible for a good description of the electron distribution of bonds; a triple-ζ or more accurate basis set is needed for calculations of bond dissociation energy.

When relativistic calculations are performed (rows 1−15), the average performance of both def2-QZVP and def2-SVP for the three cases is improved, while the results for the def2-TZVP basis set get worse. Examining Table 1 in more detail, we see that the complete mean unsigned errors, C-MUEs, of ionization potentials are decreased in relativistic calculations with all three def2 basis sets as compared to those of the nonrelativistic calculations with the same basis sets, while for D_e calculations on As_2, only the def2-QZVP results are improved. That is because the relativistic effects will contract the inner core and cause a more efficient screening of the nuclear charge for the outer shells, thus leading (in this case) to an expansion of the valence orbitals.[43] Although the shape changes of the valence orbitals are weak, the important role of valence orbitals in molecular bonding apparently requires that, to get more accurate D_e values in relativistic calculations,

Table 1. Mean Unsigned Errors (C-MUE and NR-MUE, kcal/mol) in All-Electron Calculations of D_e and VIP of As_2 ($^1\Sigma_g^+$), IP of As, D_e of H_3AsO_4 ($H_3AsO_4 \rightarrow H_2AsO_4^- + H^+$), and D_e of FeAs ($^2\Delta$) Averaged over 11 xc Functionals, Based on Comparisons to the NCBS-DK Reference Value and NCBS-NR Reference Value of the Given Functional

		C-MUE						
basis set	type	D_e, As_2	VIP, As_2	IP, As	D_e, H_3AsO_4[a]	D_e, FeAs	A-C-MUE(3)[b]	A-C-MUE(5)[a,c]
NCBS-DK[d]	DK	0/0.17[e]	0	0	0	0	0	0
def2-QZVP	DK	0.55/0.69[e]	0.15	0.16	1.04	0.21	0.29	0.42
def2-TZVP	DK	2.63/2.75[e]	0.79	0.58	2.01	0.23	1.33	1.25
def2-TZVPxf	DK	0.35/0.52[e]				0.40[f]		
def2-SVP	DK	2.11/2.11[e]	0.84	0.50	10.53	3.80	1.15	3.56
def2-SVP+f	DK	1.80/1.84[e]						
ma-QZVP	DK	0.45/0.58[e]	0.22	0.21	0.07	0.13	0.29	0.22
ma-TZVP	DK	2.14/2.27[e]	1.27	0.76	1.58	0.35	1.39	1.22
ma-SVP	DK	2.75/2.62[e]	1.64	1.13	5.33	2.81	1.84	2.73
6-311++G(3df,3pd)	DK	1.17/1.33[e]	0.60	0.44	0.78	0.60	0.74	0.72
6-311+G(2d,p)	DK	1.23/1.14[e]	0.92	0.47	2.87	0.26	0.87	1.15
6-311+G(d,p)	DK	1.75/1.65[e]	0.99	0.43	4.39	0.30	1.06	1.57
6-311G(3df,3pd)	DK	1.35/1.51[e]	0.46	0.37	5.67	2.91	0.73	2.15
6-311G(2d,p)	DK	1.21/1.11[e]	0.65	0.40	5.32	5.03	0.75	2.52
6-311G(d,p)	DK	1.86/1.76[e]	0.76	0.35	5.79	8.02	0.99	3.36
NCBS-NR	NR	0.69/0.78[e]	1.42	0.82	0.34	2.28	0.98	1.11
def2-QZVP	NR	0.70/0.80[e]	1.37	0.81	1.32[0.99]	2.14	0.96	1.27 [1.20]
def2-TZVP	NR	0.78/0.94[e]	1.56	0.85	2.27[1.25]	2.00	1.06	1.49 [1.29]
def2-TZVPxf	NR	1.58/1.42[e]				1.65[g]		
def2-SVP	NR	1.67/1.62[e]	1.97	0.73	10.72[1.53]	1.87	1.46	3.39 [1.55]
def2-SVP+f	NR	1.50/1.61[e]						
ma-QZVP	NR	0.79/0.88[e]	1.46	0.88	0.24	2.10	1.04	1.09
ma-TZVP	NR	0.88/1.04[e]	2.15	1.07	1.27	2.13	1.37	1.50
ma-SVP	NR	2.34/2.22[e]	3.12	1.50	5.03	1.14	2.32	2.63
6-311++G(3df,3pd)	NR	1.24/1.41[e]	1.81	0.75	0.53	2.66	1.27	1.40
6-311+G(2d,p)	NR	1.43/1.33[e]	2.17	0.63	2.57	2.19	1.41	1.80
6-311+G(d,p)	NR	1.85/1.75[e]	2.21	0.80	4.11	1.82	1.62	2.16
6-311G(3df,3pd)	NR	1.35/1.52[e]	1.62	0.61	5.94	2.14	1.19	2.33
6-311G(2d,p)	NR	1.44/1.34[e]	1.81	0.48	5.55	2.86	1.24	2.43
6-311G(d,p)	NR	2.05/1.92[e]	1.93	0.66	6.05	5.55	1.55	3.25

		NR-MUE						
basis set	type	D_e, As_2	VIP, As_2	IP, As	D_e, H_3AsO_4[a]	D_e, FeAs	A-NR-MUE(3)[b]	A-NR-MUE(5)[a,c]
NCBS-NR[h]	NR	0/0.17[i]	0	0	0	0	0	0
def2-QZVP	NR	0.15/0.19[i]	0.07	0.07	0.98[1.33]	0.18	0.10	0.29 [0.36]
def2-TZVP	NR	0.51/0.65[i]	0.54	0.36	1.99[1.59]	0.42	0.47	0.76 [0.68]
def2-SVP	NR	1.57/1.44[i]	0.94	0.65	10.38[1.87]	4.14	1.05	3.54 [1.83]
ma-QZVP	NR	0.14/0.24[i]	0.13	0.10	0.11	0.20	0.12	0.14
ma-TZVP	NR	0.47/0.60[i]	0.73	0.33	1.61	0.28	0.51	0.68
ma-SVP	NR	2.27/2.13[i]	1.70	0.77	5.38	3.18	1.58	2.66
6-311++G(3df,3pd)	NR	0.87/1.03[i]	0.44	0.37	0.84	0.40	0.56	0.58
6-311+G(2d,p)	NR	1.46/1.36[i]	0.77	0.40	2.91	0.18	0.88	1.14
6-311+G(d,p)	NR	1.89/1.76[i]	0.84	0.36	4.45	0.46	1.03	1.60
6-311G(3df,3pd)	NR	1.00/1.17[i]	0.34	0.33	5.60	3.76	0.56	2.21
6-311G(2d,p)	NR	1.47/1.37[i]	0.52	0.40	5.71	5.00	0.80	2.62
6-311G(d,p)	NR	2.01/1.91[i]	0.63	0.31	5.21	7.83	0.98	3.20

[a] The values in square brackets are obtained using the ma-TZVP basis set for O and the def2-TZVP basis set for H. [b] A-C-MUE(3) [A-NR-MUE(3)] is the average of C-MUE (NR-MUE) for three cases (VIP and D_e of As_2, IP of As). [c] A-C-MUE(5) [A-NR-MUE(5)] is the average of C-MUE (NR-MUE) for all five cases. [d] The NCBS-DK reference value is the relativistic result with the cc-pV5Z-DK basis set for D_e and VIP of As_2, IP of As, and D_e of FeAs, and it is the relativistic result with ma-cc-pV5Z-DK for D_e of H_3AsO_4. [e] For comparison, the mean unsigned deviation of D_e of As_2 from the relativistic result with uncontracted cc-pV5Z-DK basis set is shown after the slash. [f] The def2-TZVPxf on As and def2-TZVP on Fe yields 0.38. [g] The def2-TZVPxf on As and def2-TZVP on Fe yields 1.71. [h] The NCBS-NR reference value is the nonrelativistic result with the cc-pV5Z basis set for D_e and VIP of As_2, IP of As, and D_e of FeAs, and it is the nonrelativistic result with ma-cc-pV5Z for D_e of H_3AsO_4. [i] For comparison, the mean unsigned deviation of D_e of As_2 from the nonrelativistic result with uncontracted cc-pV5Z basis set is shown after the slash.

dx.doi.org/10.1021/ct200234r |J. Chem. Theory Comput. 2011, 7, 2766–2779

Table 2. Mean Unsigned Error (MUE, kcal/mol) in the Value of the Relativistic Effect[a] Averaged over 11 xc Functionals

	MUE					
basis set	D_e, As_2[b]	VIP, As_2	IP, As	D_e, H_3AsO_4	D_e, FeAs	AMUE(5)
def2-QZVP	0.58	0.15	0.14	0.06	0.35	0.26
def2-TZVP/def2-TZVPxf	2.11/1.45	0.60	0.55	0.03	0.53	0.76
def2-SVP/def2-SVP+f	0.82/0.82	0.32	0.36	0.15	0.96	0.52
ma-QZVP	0.50	0.14	0.14	0.05	0.29	0.22
ma-TZVP	1.67	0.53	0.51	0.03	0.50	0.65
ma-SVP	0.78	0.10	0.46	0.05	0.90	0.46
6-311++G(3df,3pd)	0.40	0.18	0.22	0.06	0.20	0.21
6-311+G(2d,p)	0.17	0.41	0.21	0.04	0.23	0.21
6-311G(d,p)	0.37	0.16	0.22	0.06	0.19	0.20
6-311G(3df,3pd)	0.43	0.16	0.20	0.08	1.27	0.43
6-311G(2d,p)	0.43	0.15	0.19	0.10	1.27	0.43
6-311G(d,p)	0.41	0.14	0.21	0.08	1.26	0.42

[a] The relativistic effect is calculated as the difference between the value obtained in an all-electron relativistic DKH calculation and the value obtained in an all-electron nonrelativistic calculation with the same basis set. The error is the deviation from the NCBS relativistic effect, which is obtained with two different NCBS basis sets, one for the relativistic calculation and one for the nonrelativistic calculation; in particular, the NCBS relativistic effect for a given property and a given xc functional is the difference between the relativistic DKH result using the cc-pV5Z-DK basis set (ma-cc-pV5Z-DK for H_3AsO_4) and the nonrelativistic result with the cc-pV5Z basis set (ma-cc-pV5Z for H_3AsO_4). [b] The values after the slash are obtained with def2-TZVPxf or def2-SVP+f basis sets.

one must use valence basis functions specifically optimized for relativistic calculations or use relatively complete valence basis sets that can accommodate the change of shape. The parameters of the def2 basis sets were obtained from nonrelativistic calculations; therefore, the incomplete def2-TZVP and def2-SVP basis sets cannot accurately represent the valence orbitals in relativistic calculations. At the same time, we notice that the relativistic def2-SVP results are relatively better than those of def2-TZVP, and they have a 0.5 kcal/mol lower C-MUE for D_e of As_2.This is probably due to cancellation of errors in def2-SVP relativistic calculations.

The relativistic def2-TZVP calculations overestimate the D_e values; this could be an indication that the def2-TZVP basis set is overpolarized for relativistic valence orbitals. Therefore, we deleted the f polarization subshell of def2-TZVP to get what we call def2-TZVPxf basis set, where "xf" denotes excluding f functions. The nonrelativistic def2-TZVPxf calculations give a larger C-MUE for D_e of As_2 than does def2-TZVP, but the relativistic def2-TZVPxf calculations have improved performance compared to def2-TZVP, even better than def2-QZVP. This confirms that the def2-TZVP basis set is overpolarized for relativistic valence orbitals. On the contrary, the f subshell added to def2-SVP basis set slightly improves the relativistic results of def2-SVP.

Previous investigations showed that the diffuse functions are usually not important for D_e and IP calculations by DFT.[31] Due to the relative completeness of the def2-QZVP basis set, the ma-QZVP basis has similar A-C-MUE(3) values to those of the def2-QZVP basis set for both relativistic and nonrelativistic calculations. The ma-TZVP and ma-SVP basis sets perform worse than the correspondingly sized def2 basis sets, especially for ma-SVP. This implies that augmented small basis sets might be unbalanced for D_e and IP calculations.

3.1.1.2. D_e of H_3AsO_4. Table 1 shows that, when the same basis sets are used for all the atoms of H_3AsO_4, the C-MUEs of the def2-TZVP and def2-SVP basis sets are respectively 2 or 10 times larger than that of def2-QZVP, for both relativistic and nonrelativistic calculations of the energy of acid dissociation of H_3AsO_4 (which is denoted as D_e even though we are considering dissociation to ions, i.e., proton detachment). Due to the small relativistic effect on D_e of H_3AsO_4 (the relativistic effect will be discussed in section 3.2), the relativistic and nonrelativistic calculations with def2 basis sets have similar C-MUE values.

The products of the first acid dissociation reaction of H_3AsO_4 are a proton and $H_2AsO_4^-$. Because a negative ion is involved, diffuse functions play an important role in getting an accurate D_e value for H_3AsO_4. As shown in Table 1, the diffuse ma basis sets improve the calculated results for D_e of H_3AsO_4 remarkably. The C-MUE of the relativistic ma-QZVP results is only 0.07 kcal/mol, showing that ma-QZVP is very close to the complete basis set. The improvement due to adding diffuse functions is most dramatic for the double-ζ basis set; the C-MUE of ma-SVP is 5 kcal/mol lower than that of the def2-SVP basis set for both relativistic and nonrelativistic calculations.

In the calculations of D_e of H_3AsO_4, the choice of basis sets for oxygen and hydrogen could also affect the accuracy of the results, especially for oxygen, because the negative charge is mainly distributed on oxygen atoms. However, here we are concerned more with the choice of basis set for As. Therefore, we tested the performance of different sizes of def2 basis sets for As in nonrelativistic calculations in which the ma-TZVP basis set is used for O and H. In contrast to the large improvement discussed in the previous paragraph, when the same basis set is used for all elements, only ~0.3 kcal/mol of improvement is observed when the size of basis set increases from double-ζ to triple-ζ or from triple-ζ to quadruple-ζ. Hence, the basis set of As is less important than that of oxygen in the acid dissociation reaction of H_3AsO_4, and diffuse functions are not needed for As but are very important for O; using def2-TZVP or using ma-TZVP for As gives almost the same MUE (C-MUE or NR-MUE) values if the ma-TZVP basis set is used for oxygen in both cases.

3.1.1.3. D_e of FeAs. The relativistic def2-QZVP and def2-TZVP calculations have similar C-MUE values, which are very small (~0.2 kcal/mol), for D_e of FeAs. The nonrelativistic

Table 3. Details of the Basis Sets and ECPs for As

basis set	contracted functions	numbers of basis functions	numbers of primitive Gaussians	ECP	core[a]	l^b
cc-pV5Z-DK(cc-pV5Z)	8s,7p,5d,3f,2g,1h	104	309 (306)			
def2-QZVP	11s,7p,4d,2f,1g	75	179			
def2-TZVP	6s,5p,4d,1f	48	114			
def2-SVP	5s,4p,3d	32	80			
ma-QZVP	12s,8p,4d,2f,1g	79	183			
ma-TZVP	7s,6p,4d,1f	52	118			
ma-SVP	6s,5p,3d	36	84			
6-311++G(3df,3pd)	9s,8p,5d,1f	65	116			
6-311+G(2d,p)	9s,8p,4d	53	100			
6-311+G(d,p)	9s,8p,3d	48	94			
6-311G(3df,3pd)	8s,7p,5d,1f	61	112			
6-311G(2d,p)	8s,7p,4d	49	96			
6-311G(d,p)	8s,7p,3d	44	90			
cc-pV5Z-PP	7s,6p,5d,3f,2g,1h	100	236	MDF10	10	0−3
cc-pVQZ-PP	6s,5p,4d,2f,1g	64	178	MDF10	10	0−3
cc-pVTZ-PP	5s,4p,3d,1f	39	133	MDF10	10	0−3
cc-pVDZ-PP	4s,3p,2d	23	87	MDF10	10	0−3
MDF10	6s,6p,4d	44	126	MDF10	10	0−3
CRENBL	3s,3p,4d	32	36	CRENBL	18	0−∞
SDD	2s,2p	8	16	MWB28	28	0−3
MDF28	4s,4p	16	24	MDF28	28	0−3
CEP	2s,2p	8	20	CEP	28	0−∞
LANL2DZ	2s,2p	8	12	LANL2DZ	28	0−∞
ma-sc-SVP	5s,5p,3d	35	78	MDF10	10	0 − 3

[a] This column shows the number of core electrons, that is, the number of electrons replaced by the ECP. [b] This column shows the range of l in the ECPs.

calculations with the two basis sets give similar C-MUE, which are ∼1.8−1.9 kcal/mol higher than those of the relativistic calculations. It seems that the relativistic def2-TZVP calculation is good enough for calculating the D_e of FeAs. However, based on our analysis in the previous section, the def2-TZVP basis set is overpolarized for relativistic valence orbitals of As. Hence, the good results of the relativistic def2-TZVP could be fortuitous. There is only one σ bond in the $^2\Delta$ state of FeAs, and it is formed by a 4p orbital of As and the 4s orbital of Fe. Table 1 shows that f functions have only a small effect on D_e for FeAs, which indicates that the σ bond is not strongly affected by the polarization afforded by f functions.

The nonrelativistic calculations of def2-SVP have a lower C-MUE value than those of def2-QZVP and def2-TZVP, as a result of cancellation of errors. The relative incompleteness of def2-SVP can be confirmed from the NR-MUE of nonrelativistic calculations with def2-SVP and from C-MUE for relativistic def2-SVP calculations, which are shown in Table 1.

On the basis of the C-MUE and NR-MUE values of all calculations with ma basis sets for D_e of FeAs, the diffuse functions are not needed for the larger def2 basis set, but they can improve the results of def2-SVP.

3.1.1.4. The Overall Performance of def2 and ma Basis Sets for the Five Cases. Consider the overall performance for the five cases, which can be evaluated through the A-C-MUE(5) in Table 1. The relativistic ma-QZVP calculations give the best results, and they have a 0.2 kcal/mol of improvement compared to the relativistic def2-QZVP results. The relativistic calculations do not systematically increase the accuracy of def2-TZVP and def2-SVP basis sets for As.

3.1.2. The 6-311G Series of Basis Sets. Although they are the most commonly used basis sets in studies of arsenic compounds, when the relativistic effect is ignored, all 6-311G-type basis sets have worse performance than def2-TZVP for VIP and D_e of As_2; however, they have a slightly better performance for the IP of As. Except for the 6-311++G(3df,3pd) calculation of D_e for H_3AsO_4 and the 6-311+G(d,p) calculation of D_e for FeAs, nonrelativistic calculations with basis sets of the 6-311G series also perform worse than def2-TZVP for D_e of H_3AsO_4 and FeAs. Relativistic calculations improve the accuracy of 6-311G-type basis sets for the VIP and D_e of As_2 and IP of As, but they have less effect on D_e of H_3AsO_4. For D_e of FeAs, only augmented 6-311G-type basis sets, such as 6-311++G(3df,3pd) [which is the same as 6-311+G(3df) for FeAs], 6-311+G(2d,p) [which is the same as 6-311+G(2d) for FeAs], and 6-311+G(d,p) [which is the same as 6-311+G(d) for FeAs], can give results comparable to def2-TZVP, and the others perform very badly. The p functions of the 6-311G basis set for iron are too tight (the smallest p exponent is 0.592684) compared with the p functions of the def2 series (the smallest p exponent is 0.134915 for def2-SVP and def2-TZVP and 0.028000 for def2-QZVP). Therefore, adding diffuse functions is helpful for D_e calculations on FeAs with 6-311G-type basis sets. This is in agreement with the recommendation of Raghavachari and Trucks[14e] that diffuse functions are needed when using 6-311G-type (Wachters−Hay) basis sets[14a,b] for first row transition metals. As shown in Table 1, based on the overall results for the five tested cases, only the very large 6-311++G(3df,3pd) basis set and 6-311+G(2d,p) basis set (with relativistic treatment) perform better than the smaller def2-TZVP basis set.

Table 4. Complete Mean Unsigned Errors (C-MUE, kcal/mol) for D_e and VIP of As_2 ($^1\Sigma_g^+$), IP of As, D_e of H_3AsO_4 ($H_3AsO_4 \rightarrow H_2AsO_4^- + H^+$), and D_e of FeAs ($^2\Delta$) Averaged over 11 xc Functionals, with Standard ECPs with Individual Optimized Valence Basis Sets, Compared to the NCBS-DK Reference Value[a] for the Given Functional

		C-MUE							
basis set	ECP for As	D_e, As_2	VIP, As_2	IP, As	D_e, H_3AsO_4[b]	D_e, FeAs	A-C-MUE(3)[c]	A-C-MUE(4)[b,d]	A-C-MUE(5)[b,e]
cc-pV5Z-PP	MDF10	0.57/0.44	0.60	0.61	0.75	2.35	0.59	0.63	0.98
cc-pVQZ-PP	MDF10	0.70/0.57	0.69	0.68	2.32	2.51	0.69	1.10	1.38
cc-pVTZ-PP	MDF10	0.74/0.62	0.36	0.71	5.49 (0.87) [1.44]	2.80	0.60	1.83 (0.67) [0.81]	2.02 (1.10) [1.21]
cc-pwCVTZ-PP	MDF10	0.66/0.53	0.42	0.77			0.62		
cc-pVDZ-PP	MDF10	3.64/5.51	1.03	1.13	10.82	3.52	1.93	4.16	4.03
MDF10	MDF10	2.69/2.56	0.21	0.58	0.65[f] [1.91]	2.78	1.16	1.03[f] [1.35]	1.38[f] [1.63]
CRENBL	CRENBL	20.84/21.35	6.95	4.19	9.37	8.30	10.66	10.34	9.93
SDD	MWB28	21.48/20.71	8.65	4.32	7.91 [1.74]	6.43	11.48	10.59 [9.05]	9.76 [8.52]
MDF28	MDF28	23.92/23.79	4.62	3.90	[1.57]	9.37	10.81	[8.50]	[8.68]
CEP	CEP	25.12/24.99	9.67	2.99	13.83	7.73	12.59	12.90	11.87
LANL2DZ	LANL2DZ	30.10/29.97	11.54	4.35	6.23 [1.52]	2.87	15.33	13.06 [11.88]	11.02

[a] The NCBS-DK reference value is the relativistic result with the cc-pV5Z-DK basis set for D_e and VIP of As_2, IP of As, and D_e of FeAs, and it is the relativistic result with ma-cc-pV5Z-DK for D_e of H_3AsO_4. For comparison, the mean unsigned deviation of D_e of As_2 from the relativistic result with uncontracted cc-pV5Z-DK basis set is shown after the slash. [b] The values in parentheses are obtained using the ma-cc-pVTZ-PP basis set for As and the ma-cc-pVTZ basis set for O and H; the values in square brackets are obtained using the ma-TZVP basis set for O and H. [c] The A-C-MUE(3) is the average of C-MUE for VIP and D_e of As_2 and IP of As. [d] The A-C-MUE(4) is the average of C-MUE for VIP and D_e of As_2, IP of As, and D_e of H_3AsO_4. [e] The A-C-MUE(5) is the average of C-MUE for VIP and D_e of As_2, IP of As, D_e of H_3AsO_4, and D_e of FeAs. [f] The MDF10 basis set is used for As; the aug-cc-pVTZ basis set is used for O and H.

3.2. Relativistic Effects. So far we have discussed both relativistic and nonrelativistic calculations but we have not discussed the relativistic effect itself, that is, the difference between the two kinds of calculation. To estimate the magnitude of the relativistic effect, we calculated this difference with each of the eleven xc functionals and averaged the eleven results. These calculations show that the average absolute value of relativistic effect, calculated with the two NCBS basis sets, is respectively 1.42, 0.69, 0.82, 0.34, and 2.28 kcal/mol for VIP of As_2, D_e of As_2, IP of As, D_e of H_3AsO_4, and D_e of FeAs. For each small AE basis set, the mean unsigned deviation (MUE) of the relativistic effects obtained with eleven xc functionals from the NCBS relativistic effects and their average MUE over the five cases (AMUE(5)) are summarized in Table 2.

As shown in Table 2, the def2-TZVP has the worst performance of all tested basis sets for calculating relativistic effects, especially for D_e of As_2, as a result of overpolarized valence orbitals in relativistic calculations. The 6-311G series of basis sets is more appropriate for describing relativistic effects than def2-TZVP and def2-SVP in most of the cases, although the 6-311G series without diffuse functions fails in the case of D_e for FeAs. Table 2 shows that diffuse functions are usually beneficial for calculations of relativistic effects. Therefore, ma basis sets perform better than the corresponding def2 basis sets. Augmented 6-311G basis sets and the ma-QZVP basis set have the smallest average mean unsigned error for calculating the relativistic effect itself.

The present investigations show that the relativistic effect is usually not very large for arsenic compounds, but it is more than 2 kcal/mol in one case. Unless there is cancellation of errors, all nonrelativistic calculations have an error equal at least to the relativistic effect; therefore, the error of nonrelativistic calculations with the best AE basis sets could be more than 2 kcal/mol. Although def2-TZVP (or ma-TZVP when diffuse functions are needed) is a good basis set for nonrelativistic studies, it fails in relativistic calculations, as we have seen. Only the relativistic calculations with the larger basis sets, def2-QZVP, ma-QZVP, 6-311+G(2d,p), or 6-311++G(3df,3pd), can give accurate results for describing the properties of arsenic compounds. However, for large systems, such basis sets could be unaffordable; even nonrelativistic def2-TZVP calculations could be hard. A good ECP (especially an RECP) and corresponding valence basis set is potentially a better choice for large systems, and we will study this next.

3.2.1. DFT Calculations with Standard ECP Basis Sets. Next we consider the use of ECPs in DFT calculations. Table 3 compares the size of the AE basis sets considered in this work to basis sets used in combination with ECPs. Whereas AE basis sets for As involve 32−104 contracted basis functions (80−309 primitive Gaussians), with ECPs we can reduce this to as few as eight basis functions (12 primitive Gaussians) for a large-sized core or 32 basis functions (36 primitive Gaussians) for a medium-sized core; ECP basis sets for a small core have 23−100 contracted basis functions (78−236 primitive Gaussians). The computational effort of DFT calculations usually scales as N^3 or N^4 as the number of atoms N in the system is increased, while HF calculations scale as N^4, and these scaling laws may be combined with the numbers of basis functions and primitive Gaussians in Table 3 for rough estimates of relative computational savings when using ECPs. (Specific timing examples will be given in section 3.6.) We should keep in mind though that the purpose of an ECP is not just to decrease the number of basis functions. As mentioned in the Introduction, another purpose that is important to us is to introduce scalar relativistic effects by using relativistic ECPs without requiring a fully relativistic calculation.

In general, the ECP on an atom is written as[44]

$$U = U_{L+1}(r) + \sum_{l=0}^{L} \sum_{m=-l}^{l} [U_l(r) - U_{L+1}(r)]|lm\rangle\langle lm| \qquad (1)$$

where r is the distance from the nucleus, and $|lm\rangle$ is a spherical harmonic. When $U_{L+1}(r) \neq 0$, the ECP affects all symmetries (l = 0−∞), whereas when $U_{L+1}(r) = 0$, it affects only l = 0−L.

Table 5. Complete Mean Unsigned Errors (C-MUE, kcal/mol), Averaged over 11 xc Functionals, Using the Relativistic Small-Core RECP (MDF10) Combined with Different Valence Basis Sets, Compared to the NCBS-DK Reference Value [a] for the Given Functionals

		C-MUE							
basis set	RECP	D_e, As_2 [b]	VIP, As_2	IP, As	D_e, H_3AsO_4 [c]	D_e, FeAs	A-C-MUE(3) [d]	A-C-MUE(4) [c,e]	A-C-MUE(5) [c,f]
ma-sc-SVP	MDF10	0.77 (0.81)	1.59	2.07	4.58 [0.80]	1.42	1.48	2.25 [1.31]	2.09 [1.33]
ma-SVP	MDF10	1.11 (1.06)	0.66	3.04	4.70	1.67	1.60	2.38	2.24
def2-SVP	MDF10	0.90 (1.07)	1.07	3.72	11.09 [0.93]	2.99	1.90	4.20 [1.66]	3.95 [1.92]
def2-TZVP/def2-TZVPxf	MDF10	3.30/1.99 (3.43/1.86)	4.05	4.60	2.67 [1.01]	9.11	3.98/3.55	3.66 [3.24]	4.75 [4.41]
def2-QZVP	MDF10	0.95 (1.09)	4.12	4.43	2.01 [0.95]	2.29	3.17	2.88 [2.61]	2.76 [2.55]

[a] The NCBS-DK reference value is the relativistic result with the cc-pV5Z-DK basis set for D_e and VIP of As_2, IP of As, and D_e of FeAs, and it is the relativistic result with ma-cc-pV5Z-DK for D_e of H_3AsO_4. For comparison, the mean unsigned deviation of D_e of As_2 from the relativistic result with uncontracted cc-pV5Z-DK basis set is shown in parentheses. [b] The values after the slash are obtained with def2-TZVPxf as valence basis set [c] The corresponding ma-SVP or def2-*x*ZVP basis sets are used for O and H. The values in square brackets are obtained using the ma-TZVP basis set for O and H. [d] The A-C-MUE(3) is the average of C-MUE for VIP and D_e of As_2 and IP of As. [e] The A-C-MUE(4) is the average of C-MUE for VIP and D_e of As_2, IP of As, and D_e of H_3AsO_4. [f] The A-C-MUE(5) is the average of C-MUE for all five cases.

The last column of Table 3 shows the range of l in all of the ECPs considered in this work.

The complete mean unsigned errors (C-MUE) of calculations with the standard combinations of ECP basis sets and ECPs listed in Table 3 are given in Table 4, where, as in earlier sections, the mean is over 11 xc functionals. Since these errors are with respect to the relativistic NCBS-DK (cc-pV5Z-DK or ma-cc-pV5Z-DK) results, they include both basis set incompleteness and any errors due to the ECP being an inexact substitute for an explicit relativistic core.

As shown in Table 4, the results obtained with cc-pV*x*Z-PP ($x \geq$ T) basis sets are in good agreement with those of the relativistic NCBS-DK (cc-pV5Z-DK) basis set, with an average C-MUE [A-C-MUE(3)] of less than 0.7 kcal/mol for VIP and D_e of As_2 and IP of As, better than either the relativistic or nonrelativistic calculations with any of the AE triple-ζ basis sets and even better than nonrelativistic calculations with quadruple- and quintuple-ζ sets. The MDF10 RECP with its own basis set is also reasonably accurate with an A-C-MUE(3) of 1.2 kcal/mol. The large-core and medium-core ECPs usually are not good choices, because they could lead to misestimating of valence electron correlation and polarization energies compared to AE calculations because of a nodeless valence pseudo-orbital in the core region and core penetration effects, as well as inadequate Pauli repulsion between valence electrons on one center with the pseudopotential core on another.[43] Therefore, as expected, they have a very large A-C-MUE(3) (>10 kcal/mol) for the three homonuclear cases. LANL2DZ is the only tested NRECP generated from nonrelativistic AE numerical HF atomic wave functions for As; that could be one of reasons that it has the largest C-MUEs for the three cases.

In the case of H_3AsO_4, if the cc-pV*x*Z AE basis set is used for oxygen and hydrogen and the cc-pV*x*Z-PP basis set is used for As, all the tests, except for that using the quintuple-ζ basis set, give worse results than those with the def2 basis set at the same level. We took cc-pVTZ-PP as an example and tested its performance when the diffuse ma-cc-pVTZ or ma-TZVP basis set is used for O and H. The C-MUE for D_e of H_3AsO_4 is respectively decreased from 5.5 to 0.9 or to 1.4 kcal/mol. Even when a large-core ECP basis set is used for As, but with ma-TZVP for O and H, the C-MUE could be around 1.5 kcal/mol. This confirms that the choice of basis set for oxygen is more important than the As basis for the H_3AsO_4 acid dissociation reaction.

In the calculations of D_e for FeAs, unpublished cc-pV*x*Z-PP basis sets for iron were kindly provided by Peterson.[45] For the tests of large-core ECP basis sets for As, the corresponding small-core (10 electrons) ECP is used for iron. Table 4 shows that only cc-pV*x*Z-PP ($x \geq$ T), MDF10, and LANL2DZ (which is small-core NRECP for Fe) give reasonably accurate results for D_e of FeAs.

Considering all five cases, the cc-pVTZ-PP ECP basis set and the MDF10 RECP with its own basis set are recommended for arsenic, and their A-C-MUE(5) are smaller than or similar to that of the AE def2-TZVP basis. In addition, the latest new cc-pwCVTZ-PP basis set[46] that considers core−valence correlation effect is also tested for the VIP and D_e of As_2 and the IP of As. It yields a similar result to that for cc-pVTZ-PP. This indicates that the effect of core−valence correlation effect is slight for the arsenic compounds tested.

3.2.2. DFT Calculations with Nonstandard RECP Basis Sets. Sufficiently accurate optimized valence basis sets are as important as the ECPs themselves because the radial shape of the pseudo-valence orbitals in the core region is different from the shape of AE valence orbitals as a result of the underlying pseudovalence orbital transformation.[43] The shape and size extent of pseudo-valence orbitals depend on the choice of ECP, so that the exponents of basis functions from AE nonrelativistic basis sets are not necessarily applicable for ECP calculations, nor are the contraction coefficients. For each ECP, a particular valence basis set is usually recommended by the creators of the ECP. Nevertheless, in this section we test some new combinations of def2 basis sets with the reasonably successful MDF10 small-core RECP. Selected results are presented in Table 5.

From the investigations above, we know that the def2-SVP or ma-SVP basis sets are relatively better at calculations of the relativistic effect than def2-TZVP; thus, it is not very surprising that Table 5 shows that the combinations of def2-SVP or some modified basis sets based on def2-SVP with MDF10 perform relatively well, in despite of having less basis functions than def2-TZVP. One modification that we considered is deleting the first contracted s basis function from def2-SVP to make it more compatible with the MDF10 RECP. We label the modified def2-SVP basis in which this 1s contracted function is excluded the sc-SVP basis, where "sc" denotes its intended use with a small-core RECP. The best combination that we found employs the MDF10 RECP combined with a minimally augmented sc-SVP basis set,

Table 6. Deviation (kcal/mol) from Relativistic NCBS-DK Reference Value[a] of HF Calculations and Mean Unsigned Deviation (MUEs in kcal/mol)

basis set	RECP	D_e, As_2	VIP, As_2	IP, As	D_e, H_3AsO_4[b]	MUE(3)[c]	MUE(4)[b,d]
cc-pV5Z-PP	MDF10	0.41	−0.07	0.01	0.28	0.16	0.19
cc-pVQZ-PP	MDF10	0.32	−0.02	0.06	1.15	0.13	0.39
cc-pVTZ-PP	MDF10	−0.23	0.53	0.40	3.30	0.38	1.11
cc-pVDZ-PP	MDF10	−3.33	1.78	0.56	4.65	1.89	2.58
MDF10	MDF10	−1.91	1.15	0.14	−0.37[e]	1.07	0.89[e]
CRENBL	CRENBL	−22.86	12.72	1.77	−13.85	12.45	12.80
SDD	MWB28	−28.15	9.41	5.70	−16.02	14.42	14.82
MDF28	MDF28	−29.16	5.90	−1.44	[-1.56]	12.17	[9.51]
CEP	CEP	−29.74	9.63	4.50	−21.08	14.62	16.23
LANL2DZ	LANL2DZ	−35.06	8.02	6.07	−14.47	16.38	15.90
ma-sc-SVP	MDF10	−0.60	1.23	−1.41	−5.42	1.08	2.16
ma-SVP	MDF10	−1.73	−0.01	−2.34	−5.54	1.36	2.41
def2-SVP	MDF10	−1.05	0.03	−2.51	4.66	1.20	2.06
def2-TZVP	MDF10	4.86	−4.67	−3.96	0.93	4.50	3.61
def2-QZVP	MDF10	1.17	−4.18	−3.64	1.34	2.99	2.58

[a] The NCBS-DK reference value is the HF relativistic result with the cc-pV5Z-DK basis set for D_e and VIP of As_2 and IP of As, and it is the relativistic result with ma-cc-pV5Z-DK for D_e of H_3AsO_4. [b] The values in square brackets are obtained using the ma-TZVP basis set for O and H. [c] The MUE(3) is the mean unsigned deviation from relativistic NCBS-DK reference value for VIP and D_e of As_2 and IP of As. [d] The MUE(4) is the mean unsigned deviation from relativistic NCBS-DK reference value for VIP and D_e of As_2, IP of As, and D_e of H_3AsO_4. [e] The MDF10 basis set is used for As; the aug-cc-pVTZ basis set is used for O and H.

where the minimal augmentation is performed in the usual[31] way. We label this combination of basis set and RECP as ma-sc-SVP. The ma-sc-SVP basis set has a little worse performance than MDF10 when only three cases (VIP and D_e of As_2 and IP of As) are considered; however, when all five tested properties are considered, it has comparable accuracy to MDF10 and is only 0.1 kcal/mol worse than cc-pVTZ-PP (in the case of H_3AsO_4, the ma-TZVP basis set is used for O and H). As shown in Table 3, ma-sc-SVP has less basis functions than cc-pVTZ-PP and MDF10. In addition, in contrast to cc-pVTZ-PP (which is unpublished for 3d metal elements from Sc to Ni), ma-sc-SVP is published for all 3d metals. It could be a good compromise to use ma-sc-SVP in calculations for large arsenic systems containing 3d metals. The ma-sc-SVP basis needs to be tested further and validated, if possible, for 3d metals.

As shown in Table 5, the combination of def2-TZVP with the MDF10 RECP, denoted as def2-TZVP-MDF10, is the worst combination due to overpolarized pseudovalence orbitals. The def2-TZVPxf-MDF10, which is def2-TZVP-MDF10 without f functions, has a substantially improved performance for D_e of As_2 as compared to def2-TZVP-MDF10. The larger def2-QZVP-MDF10 (def2-QZVP in conjunction with the MDF10 RECP) is worse than the combination of def2-SVP and MDF10 (def2-SVP-MDF10) or than ma-sc-SVP. We hypothesize that the better performance of double-ζ basis sets with MDF10 could be a result of cancellation of two kinds of errors: one is the intrinsic error of small basis sets; the other is the error resulting from the radial shape change of pseudovalence orbitals in the core region.

3.2.3. HF Calculations with ECPs. Table 6 lists the deviation and mean unsigned deviation (MUE) of HF calculations with the ECPs tested above from relativistic NCBS-DK HF reference values for D_e of As_2, VIP of As_2, IP of As, and D_e of H_3AsO_4. Comparing Table 6 with Tables 4 and 5 shows that, in most of the cases, the small-core MDF10 RECP with the basis sets optimized for it (the original MDF10 basis set and the cc-pV*x*Z-PP basis) have better performance for HF calculations than for DFT, especially with the cc-pV*x*Z-PP ($x \geq$ T) basis set. The nonstandard combinations of MDF10 with def2-SVP, ma-SVP, or ma-sc-SVP basis sets always perform better for IP of As in HF calculations, and when considering all four cases, these nonstandard combinations also have a smaller MUE(4) for HF calculations than for DFT calculations. The relatively worse performance in DFT confirms that the transferability of HF-based ECPs is reduced in DFT calculations because of the nonlinear nature of the xc functional's dependence on the density.

Although DFT calculations with the MDF10 RECP for arsenic have larger deviations from relativistic NCBS-DK reference values than do HF calculations, the deviations still are within an acceptable error range. Therefore, NLCCs will be helpful but are not very important for As.

All of the large- and medium-core ECPs have even larger errors for HF calculations than DFT calculations, as shown in Tables 4 and 6. This probably occurs because the errors introduced by using a large core dominate the total error of the large-core ECP calculations, so that the nonlinear error is drowned out by the large-core error.

3.3. Further Tests for def2-TZVP, cc-pVTZ-PP, ma-sc-SVP, and MDF10 for Arsenic Clusters. On the basis of the above investigations, the preferred basis sets and ECPs for arsenic in DFT calculations of relatively large arsenic-containing systems are RECP calculations with the cc-pVTZ-PP, ma-sc-SVP, and MDF10 basis sets and nonrelativistic def2-TZVP all-electron calculations. In this section, we test these four choices further by comparing their performance for 10 D_e and three VIP calculations of arsenic clusters As_n ($n = 2-4$) plus the IP of As atom to NCBS-DK reference values. The calculated C-MUEs and the average C-MUE of the 14 properties (A-C-MUE(14)) over 11 xc functionals are listed in Table 7, along with (for comparison) the relativistic results obtained with the def2-TZVP and 6-311+G(2d,p) basis sets. We note that previous studies[47] of arsenic

Table 7. Complete Mean Unsigned Errors (C-MUE, kcal/mol) for D_e Values of 10 Dissociation Reactions and IP or VIPs of Four Ionization Reactions over 11 xc Functionals, with cc-pV5Z, def2-TZVP, cc-pVTZ-PP, ma-sc-SVP, and MDF10, Compared to NCBS-DK Reference Values for the Given Functional

	NCBS-DK[a]	NCBS-NR[b]	6-311+G(2d,p)	def2-TZVP	def2-TZVP	cc-pVTZ-PP	ma-sc-SVP	MDF10
type	DK	NR	DK	DK	NR	RECP	RECP	RECP
				For D_es of 10 Dissociation Reactions				
$As_2 \rightarrow As + As$	0	0.65	1.23	2.63	0.78	0.74	0.77	2.69
$As_3 \rightarrow As_2 + As$	0	0.27	2.30	1.70	0.84	0.35	0.76	2.58
$As_4 \rightarrow As_3 + As$	0	0.35	2.07	3.23	1.36	0.26	3.77	2.89
$As_4 \rightarrow 2As_2$	0	0.62	3.54	2.30	1.76	0.54	2.87	2.79
$As_2^+ \rightarrow As + As^+$	0	0.66	1.75	2.46	0.50	1.19	3.44	3.16
$As_3^+ \rightarrow As_2 + As^+$	0	0.33	2.46	1.51	0.39	0.58	2.37	2.37
$As_3^+ \rightarrow As_2^+ + As$	0	0.40	1.54	1.67	0.93	0.20	1.30	1.90
$As_4^+ \rightarrow As_3 + As^+$	0	0.99	3.17	2.38	0.62	0.67	1.41	3.26
$As_4^+ \rightarrow As_2 + As_2^+$	0	0.48	3.73	1.62	0.57	0.45	1.39	2.68
$As_4^+ \rightarrow As_3^+ + As$	0	0.41	3.02	2.57	0.23	0.46	0.44	3.47
				For IP or VIPs of Four Ionization Reactions				
$As \rightarrow As^+$	0	0.82	0.47	0.58	0.85	0.71	2.07	0.58
$As_2 \rightarrow As_2^+$	0	1.42	0.92	0.79	1.56	0.36	1.59	0.21
$As_3 \rightarrow As_3^+$	0	1.40	0.25	0.86	1.48	0.55	0.98	0.88
$As_4 \rightarrow As_4^+$	0	2.11	1.10	1.43	2.80	0.39	3.07	0.41
A-C-MUE(14)[c]	0	0.78	1.98	1.84	1.05	0.53	1.87	2.13
A-C-MUE(16)[d]	0	0.85	1.92	1.75	1.19	0.98	2.01	2.08

[a] NCBS-DK reference value is the relativistic result with cc-pV5Z-DK basis set. [b] NCBS-NR reference value is the nonrelativistic result with cc-pV5Z basis set. [c] A-C-MUE(14) is the average C-MUE of the 14 properties, each of which is calculated with 11 xc functionals, for a total of 154 comparisons to NCBS-DK results for each entry in the second last row. [d] A-C-MUE(16) is the average C-MUE for the five quantities in Tables 1 (or Table 3 or 4) and the 14 quantities in this table, counting the three quantities that appear in both tables only once. Therefore, each entry in the last row is an average over 16 × 11 = 176 comparisons to NCBS-DK results.

Table 8. Mean Unsigned Errors (C-MUE and NR-MUE, kcal/mol) of cc-pVTZ and cc-pVTZ-DK Basis Sets for D_e and VIP of As_2 and IP of As Averaged over 11 xc Functionals, Based on Comparisons to the NCBS-DK Reference Value and NCBS-NR Reference Value of the Given Functional[a]

		C-MUE			
basis set	type	D_e, As_2	VIP, As_2	IP, As	A-C-MUE(3)[b]
cc-pVTZ-DK	DK	0.61	0.13	0.32	0.35
cc-pVTZ	DK	7.99			
cc-pVTZ	NR	0.28	1.35	0.53	0.72
		NR-MUE			
basis set	type	D_e, As_2	VIP, As_2	IP,As	A-NR-MUE(3)[b]
cc-pVTZ	NR	0.63	0.14	0.31	0.36

[a] The NCBS-DK reference value is the relativistic result with cc-pV5Z-DK basis set; the NCBS-NR reference value is the nonrelativistic result with the cc-pV5Z basis set. All results in this table are for all-electron calculations. [b] A-C-MUE(3) [A-NR-MUE(3)] is the average of C-MUE (NR-MUE) for the three cases.

clusters showed that the def2-TZVPP basis set gives reliable results for both nonrelativistic density functional and wave function calculations. Here we restrict attention to density functional calculations, and we study the def2-TZVP basis set and compare the results to a more diverse set of other approaches, including relativistic effects.

Table 9. Complete Error (kcal/mol) for IP of As

basis set	def2-TZVP	6-311++G(3df,3pd)
Type	NR	NR
M05	0.87	0.99
M06-L	2.37	0.00
M06	1.26	0.43
BLYP	0.36	0.87
ωB97X-D	1.20	1.12
τHCTHhyb	0.46	0.57
G96LYP	0.92	0.85
mPWLYP	0.06	0.81
B3LYP	0.63	0.87
X3LYP	0.55	0.86
BPBE	0.70	0.83

Table 7 shows the clear superiority of cc-pVTZ-PP when errors are averaged over the 14 properties, and it has a smaller A-C-MUE(14) than nonrelativistic calculations with the cc-pV5Z (NCBS-NR) basis set, although A-C-MUE(16), which is our most comprehensive figure of merit, is worse. The nonrelativistic def2-TZVP calculations also show reasonably good performance. As we expected, the relativistic def2-TZVP calculations are worse with an A-C-MUE(14) of 1.8 kcal/mol and a similar value for A-C-MUE(16). This confirms again that the def2-TZVP basis set should only be used in nonrelativistic calculations. Although the relativistic calculations with the 6-311+G(2d,p) basis set perform

Table 10. Relative Computational Cost Required for Single-Point Energy Calculations with Various Basis Sets for an As_{20} Cluster, Using the HF and BLYP Methods

	type	number of basis functions	number of primitive Gaussians	HF[a]	BLYP[a]
cc-pVTZ-DK	DK	43	197	5.95	4.52
cc-pVTZ	NR	43	196	5.68	4.15
cc-pVTZ-PP	RECP	39	133	4.81	3.28
def2-TZVP	NR	48	114	2.76	1.32
ma-sc-SVP	RECP	35	78	1.00	0.63

[a] The relative computational cost is estimated by dividing the CPU time required for each calculation by the CPU time for HF/ma-sc-SVP calculations.

well for the first test set, they have slightly worse A-C-MUE(14) value than the relativistic def2-TZVP results in this larger test set. The performances of ma-sc-SVP and of MDF10 with its own basis set are found to be inconsistent. For some cases they perform well, but in other cases they perform poorly. The ma-sc-SVP has a general performance worse than that of relativistic def2-TZVP calculations, and MDF10 is even worse. Therefore, although ma-sc-SVP is a relatively good RECP basis set, considering its small size and its availability for 3d metals, one must be careful about using it, and MDF10 cannot be recommended.

3.4. cc-pVTZ and cc-pVTZ-DK. Table 8 shows a few results for all-electron calculations with the cc-pVTZ and cc-pVTZ-DK basis sets. First we see, as already seen earlier, that the use of contracted AE basis sets in relativistic calculations where contraction coefficients are optimized for nonrelativistic calculations can lead to very large errors; in particular, the relativistic calculations with the cc-pVTZ basis set (optimized for nonrelativistic calculations) has a C-MUE of 7.99 kcal/mol for D_e of As_2. For the same size and type of basis set, the results are much better when a nonrelativistically optimized basis is used nonrelativistically or when a relativistically optimized basis is used relativistically.

3.5. Method Dependence. We emphasize that all results presented so far are averaged over 11 choices of xc functional. To remind the reader that the results depend on the functional, Table 9 presents some results for individual functionals. Table 9 takes the IP of As as an example. The table shows the calculated complete error in the IP of As for each of the 11 xc functionals with def2-TZVP and 6-311++(3df,3pd) [it is the same as 6-311+G(3df) for As], in each case comparing to the relativistic cc-pV5Z-DK result for that functional. We see that M06-L has the smallest basis set error with 6-311++G(3df,3pd) and the largest basis set error for the def2-TZVP basis set. The mPWLYP functional is best with def2-TZVP (error = 0.06 kcal/mol) but has an error of 0.81 kcal/mol with the other basis for which results are shown.

3.6. Timings. The CPU time for calculating integrals depends on both the number of Gaussian primitives and the number of contracted Gaussians, while all other steps depend on only the number of contracted basis functions. Some AE basis sets and ECP basis sets have been chosen to illustrate the computational cost of HF and BLYP methods for a large arsenic cluster As_{20}, and the corresponding CPU times are shown in Table 10. The time saving of using ECPs is confirmed. Furthermore, we note that the all-electron cc-pVTZ-DK BLYP calculation takes 7.2 times longer than the ma-sc-SVP one employing an ECP.

4. SUMMARY

Before summarizing the conclusions, we remind the reader that the present study is concerned with effective core potentials (ECPs) and basis-set incompleteness, not with the accuracy of density functionals. Therefore, all errors are relative to the nearly complete basis set all-electron limit for a given property and given density functional, not with respect to experiment.

We know from previous work that basis set requirements for electronic structure calculations are different for DFT and for wave function theory. We also know that scalar relativistic effects become significant for chemical accuracy for fourth-period elements. Here we test strategies for reproducing the basis-set limit of relativistic calculations on the fourth-period element As. We test four kinds of strategies for reproducing nearly complete basis set relativistic calculations: all-electron (AE) relativistic calculations; AE nonrelativistic calculations; formally nonrelativistic calculations in which a small, medium, or large core is replaced by a relativistic effective core potential (RECP); and formally nonrelativistic calculations with a nonrelativistic ECP (NRECP). All relativistic calculations are carried out by employing the Douglas–Kroll–Hess second-order scalar relativistic Hamiltonian.

The performance of AE basis sets from the def2-*x*ZVP and ma-*x*ZVP series and from the 6-311G series with additional polarization and diffuse functions was first tested by relativistic and nonrelativistic density functional calculations for five cases: VIP of As_2, D_e of As_2, IP of As, acid dissociation of H_3AsO_4, and D_e of FeAs. Overall, relativistic ma-QZVP and def2-QZVP calculations, with average mean unsigned errors of 0.2 and 0.4 kcal/mol, perform better than relativistic 6-311++G(3df,3pd) calculations, which have an average mean unsigned error of 0.7 kcal/mol. The def2-TZVP and ma-TZVP basis sets are good for nonrelativistic calculations, with average mean unsigned errors relative to nearly converged relativistic calculations of 1.3–1.5 kcal/mol, but using them in relativistic calculations does not decrease their errors. Therefore, it is not recommended to do relativistic calculations with the def2-TZVP or ma-TZVP basis set. The relativistic calculations with the 6-311+G(2d,p) basis set perform significantly better than nonrelativistic calculations with this basis set, and they perform slightly better than the def2-TZVP basis set, with an averaged mean unsigned error of ~1.2 kcal/mol. The other tested 6-311G-type basis sets [6-311G(3df,3pd), 6-311G(2d,p), 6-311G(d,p), and 6-311+G(d,p)], which are commonly used in previous studies of arsenic compounds, perform worse than def2-TZVP for both relativistic and nonrelativistic calculations, with average mean unsigned errors in the range 1.6–3.4 kcal/mol. As expected, the smallest basis set, def2-SVP, performs worst of all tested AE basis sets, except 6-311G(d,p). However, when a good basis set, ma-TZVP, is used for oxygen, the use of def2-SVP for As only has an average mean unsigned error over the five cases that is only 0.3 kcal/mol larger than using def2-TZVP. Due to the ionic product $H_2AsO_4^-$, the use of diffuse functions can significantly improve the results for acid dissociation of H_3AsO_4. For the case of FeAs, diffuse functions have less effect on the def2-TZVP and def2-QZVP basis sets, but they are helpful for the smaller def2-SVP basis set and the 6-311G-type basis set with tighter p functions for iron. The inclusion of diffuse functions does not improve the results for the other cases and may even lead to worse results.

Several ECPs available for arsenic were also investigated in the present work. First we considered the same five cases as in the previous paragraph. The cc-pV*x*Z-PP ($x \geq$ T) basis in which valence basis functions are specifically optimized for the

small-core MDF10 RECP was found to give very good results; this combination, denoted simply as cc-pVTZ-PP, has an average mean unsigned error of 1.1 kcal/mol (when the ma-cc-pVTZ augmented basis set is used for O in the case of H_3AsO_4). The small-core MDF10 RECP with its own basis set also performs well, with an average mean unsigned error of 1.4 kcal/mol. All of the medium-core and large-core ECPs perform poorly, with average mean unsigned errors of 8.5−11.9 kcal/mol. In the popular Gaussian program, only large-core ECPs are implemented for arsenic, so one must expect large deviations from the relativistic nearly complete basis set limit.

We also introduced a very efficient nonstandard combination of basis set and RECP that is called ma-sc-SVP; this denotes the ma-SVP basis set with the first contracted s function removed and used in conjunction with the small-core MDF10 RECP. This combination has a comparable performance with MDF10, but with many less basis functions. The application of ma-sc-SVP to the rest of the fourth period needs to be validated.

The performances of small-core ECPs and associated basis sets for DFT calculations are a little worse than but still comparable to those for HF calculations for four cases: D_e of As_2, VIP of As_2, IP of As, and D_e of H_3AsO_4. Therefore, NLCCs in DFT calculations for arsenic will be helpful, but are not particularly necessary.

We selected seven of the methods for further DFT tests on a larger test set with 11 additional cases (D_e and VIP for various As_n with n = 3 and 4), and we computed an average mean unsigned error for all 16 cases. Since each case is already averaged over 11 xc functionals, this final error estimate is an average over 176 basis set convergence tests. The final error for nearly complete basis set nonrelativistic calculations is 0.9 kcal/mol, and the final error for def2-TZVP nonrelativistic calculations is 1.2 kcal/mol. The latter number increases to 1.8 kcal/mol if the calculation is instead carried out relativistically. The relativistic calculations with the 6-311+G(2d,p) basis set give a slightly larger error than def2-TZVP relativistic calculations and therefore are not recommended. A much more efficient and more accurate way to include relativistic effects is with an RECP, and such a calculation with cc-pVTZ-PP has a final basis-set-incompleteness error of 1.0 kcal/mol. A very efficient but slightly less accurate option is ma-sc-SVP, with a final error of 2.0 kcal/mol.

On the basis of the present investigations, for small arsenic-containing systems, we recommend relativistic def2-QZVP (or ma-QZVP when diffuse functions are needed) calculations for getting accurate results. If the relativistic effect is insignificant for the property under consideration, nonrelativistic def2-TZVP (or ma-TZVP when diffuse functions are needed) calculations are good enough. The triple-ζ RECP basis set cc-pVTZ-PP is recommended for larger arsenic systems. However, if 3d metals are involved in the arsenic-containing system, the double-ζ RECP basis set ma-sc-SVP may be tested. The use of ma-sc-SVP for As could lead to basis-set errors up to ∼2 kcal/mol.

■ ASSOCIATED CONTENT

Ⓢ Supporting Information. Bond length tests and NCBS-DK reference values. This material is available free of charge via the Internet at http://pubs.acs.org/.

■ AUTHOR INFORMATION

Corresponding Author
*E-mail: truhlar@umn.edu.

■ ACKNOWLEDGMENT

This work was supported in part by the National Science Foundation by grant no. CHE09-56776 and by the Air Force Office of Scientific Research.

■ REFERENCES

(1) Stoll, H.; Metz, B.; Dolg, M. *J. Comput. Chem.* **2002**, *23*, 767.
(2) Louie, S. G.; Froyen, S.; Cohen, M. L. *Phys. Rev. B* **1982**, *26*, 1738.
(3) Porezag, D.; Pederson, M. R.; Liu, A. Y. *Phys. Rev. B* **1999**, *60*, 14132.
(4) van Wüllen, C. *Int. J. Quantum Chem.* **1996**, *58*, 147.
(5) Russo, T. V.; Martin, R. L.; Hay, P. J. *J. Phys. Chem.* **1995**, *99*, 17085.
(6) Han, Y-K; Hirao, K. *Chem. Phys. Lett.* **2000**, *324*, 453.
(7) Lovallo, C. C.; Klobukowski, M. *J. Comput. Chem.* **2004**, *25*, 1206.
(8) Dhubhghaill, O. M. Ni; Sadler, P. J. *Struct. Bonding (Berlin)* **1991**, *78*, 129 and references cited therein.
(9) Wolfe-Simon, F.; Blum, Jodi S.; Kulp, T. R.; Gordon, G. W.; Hoeft, S. E.; Pett-Ridge, J.; Stolz, J. F.; Webb, S. M.; Weber, P. K.; Davies, P. C. W.; Anbar, A. D.; Oremland, R. S. dx.doi.org/10.1126/science.1197258 (accessed March 28, 2011)
(10) Katsnelson, A. dx.doi.org/10.1038/news.2010.645 (accessed March 28, 2011)
(11) Bortman, H. http://www.space.com/9631-arsenic-eating-bacteria-opens-possibilities-alien-life.html (accessed March 28, 2011)
(12) Silver, S.; Phung, L. T. *FEMS Microbiol. Lett.* **2011**, *315*, 79.
(13) (a) Miqueu, K.; Sotiropoulos, J. M.; Pfister-Guillouzo, G.; Ranaivonjatovo, H.; Escudié, J. *J. Mol. Struct.* **2001**, *545*, 139. (b) Tossell, J. A. *Geochem. Trans.* **2003**, *4*, 28. (c) Xu, W. G.; Jin, B. *J. Mol. Struct.: THEOCHEM* **2005**, *731*, 61. (d) Xu, W. G.; Jin, B. *J. Mol. Struct.: THEOCHEM* **2006**, *759*, 101. (e) Urban, D. R.; Wilcox, J. *J. Phys. Chem. A* **2006**, *110*, 5847. (f) Tossell, J. A.; Zimmermann, M. D. *Geochim. Cosmochim. Acta* **2008**, *72*, 5232. (g) Ahmed, A. B.; Feki, H.; Abid, Y.; Minot, C. *Spectrochim. Acta, Part A* **2010**, *75*, 1315. (h) Ramírez-Galicia, G.; Peñ-Méndez, E. M.; Pangavhane, S. D.; Alberti, M.; Havel, J. *Polyhedron* **2010**, *29*, 1567.
(14) (a) Wachters, A. J. H. *J. Chem. Phys.* **1970**, *52*, 1033. (b) Hay, P. J. *J. Chem. Phys.* **1977**, *66*, 4377. (c) Raghavachari, K.; Binkley, J. S.; Seeger, R.; Pople, J. A. *J. Chem. Phys.* **1980**, *72*, 650. (d) McLean, A. D.; Chandler, G. S. *J. Chem. Phys.* **1980**, *72*, 5639. (e) Raghavachari, K.; Trucks, G. W. *J. Chem. Phys.* **1989**, *91*, 1062. (f) Binning, R. C., Jr.; Curtiss, L. A. *J. Comput. Chem.* **1990**, *11*, 1206. (g) McGrath, M. P.; Radom, L. *J. Chem. Phys.* **1991**, *94*, 511. (h) Curtiss, L. A.; McGrath, M. P.; Blaudeau, J.-P.; Davis, N. E.; Binning, R. C., Jr.; Radom, L. *J. Chem. Phys.* **1995**, *103*, 6104.
(15) (a) Dunning, T. H., Jr. *J. Chem. Phys.* **1989**, *90*, 1007. (b) Woon, D. E.; Dunning, T. H., Jr. *J. Chem. Phys.* **1993**, *98*, 1358. (c) Wilson, A. K.; Woon, D. E.; Peterson, K. A.; Dunning, T. H., Jr. *J. Chem. Phys.* **1999**, *110*, 7667. (d) Balabanov, N. B.; Peterson, K. A. *J. Chem. Phys.* **2005**, *123*, 064107.
(16) Weigend, F.; Ahlrichs, R. *Phys. Chem. Chem. Phys.* **2005**, *7*, 3297.
(17) (a) Billes, F.; Mitsa, V.; Fejes, I.; Mateleshko, N.; Fejsa, I. *J. Mol. Struct.* **1999**, *513*, 109. (b) Ozeki, M.; Iwasa, Y.; Shimizu, Y. *Appl. Surf. Sci.* **2007**, *253*, 5914. (c) Lu, H.-L.; Chen, W.; Ding, S.-J.; Zhang, D. W.; Wang, L.-K. *Chem. Phys. Lett.* **2007**, *445*, 188. (d) Zimmermann, M. D.; Tossell, J. A. *J. Phys. Chem. A* **2009**, *113*, 5105. (e) Yang, S.; Adjaye, J.; McCaffrey, W. C.; Nelson, A. E. *J. Mol. Catal. A* **2010**, *321*, 83.
(18) Chu, J .-H.; Analytis, J. G.; Greve, De. K.; McMahon, P. L.; Islam, Z.; Yamamoto, Y.; Fisher, I. R. *Science* **2010**, *329*, 824.
(19) Zhao, Y.; Schultz, N. E.; Truhlar, D. G. *J. Chem. Phys.* **2005**, *123*, 161103.
(20) (a) Zhao, Y.; Truhlar, D. G. *J. Chem. Phys.* **2006**, *125*, 194101. (b) Zhao, Y.; Truhlar, D. G. *Acc. Chem. Res.* **2008**, *41*, 157.

(21) Zhao, Y.; Truhlar, D. G. *Theor. Chem. Acc.* **2008**, *120*, 215.
(22) (a) Becke, A. D. *Phys. Rev. A* **1988**, *38*, 3098. (b) Lee, C. T.; Yang, W. T.; Parr, R. G. *Phys. Rev. B* **1988**, *37*, 785.
(23) Chai, J.-D.; Head-Gordon, M. *Phys. Chem. Chem. Phys.* **2008**, *10*, 6615.
(24) Boese, A. D.; Handy, N. C. *J. Chem. Phys.* **2002**, *116*, 9559.
(25) (a) Gill, P. M. W. *Mol. Phys.* **1996**, *89*, 433. (b) Adamo, C.; Barone, V. *J. Comput. Chem.* **1998**, *19*, 418.
(26) Adamo, C.; Barone, V. *J. Chem. Phys.* **1998**, *108*, 664.
(27) Stephens, P. J.; Devlin, F. J.; Chabalowski, C. F.; Frisch, M. J. *J. Phys. Chem.* **1994**, *98*, 11623.
(28) Xu, X.; Goddard, W. A., III *Proc. Natl. Acad. Sci. U. S. A.* **2004**, *101*, 2673.
(29) (a) Perdew, J. P.; Burke, K.; Ernzerhof, M. *Phys. Rev. Lett.* **1996**, *77*, 3865. (b) Perdew, J. P.; Burke, K.; Ernzerhof, M. *Phys. Rev. Lett.* **1997**, *78*, 1396.
(30) (a) Douglas, M.; Kroll, N. M. *Ann. Phys. (NY)* **1974**, *82*, 89. (b) Hess, B. A. *Phys. Rev. A* **1985**, *32*, 756. (c) Hess, B. A. *Phys. Rev. A* **1986**, *33*, 3742. (d) Jansen, G.; Hess, B. A. *Phys. Rev. A* **1989**, *39*, 6016. (e) Barysz, M.; Sadlej, A. J. *J. Mol. Struct.: THEOCHEM* **2001**, *573*, 181. (f) deJong, W. A.; Harrison, R. J.; Dixon, D. A. *J. Chem. Phys.* **2001**, *114*, 48.
(31) Zheng, J.; Xu, X.; Truhlar, D. G. *Theor. Chem. Acc.* **2011**, *128*, 295.
(32) Peterson, K. A. *J. Chem. Phys.* **2003**, *119*, 11099.
(33) (a) Metz, B.; Stoll, H.; Dolg, M. *J. Chem. Phys.* **2000**, *113*, 2563. (b) Dolg, M.; Wedig, U.; Stoll, H.; Preuss, H. *J. Chem. Phys.* **1987**, *86*, 866.
(34) Hurley, M. M.; Pacios, L. F.; Christiansen, P. A.; Ross, R. B.; Ermler, W. C. *J. Chem. Phys.* **1986**, *84*, 6840.
(35) Bergner, A.; Dolg, M.; Kuechle, W.; Stoll, H.; Preuss, H. *Mol. Phys.* **1993**, *80*, 1431.
(36) Stevens, W. J.; Krauss, M.; Basch, H.; Jasien, P. G. *Can. J. Chem.* **1992**, *70*, 612.
(37) (a) Hay, P. J.; Wadt, W. R. *J. Chem. Phys.* **1985**, *82*, 270. (b) Hay, P. J.; Wadt, W. R. *J. Chem. Phys.* **1985**, *82*, 284. (c) Hay, P. J.; Wadt, W. R. *J. Chem. Phys.* **1985**, *82*, 299.
(38) Dyall, K. G. *Theor. Chem. Acc.* **2006**, *115*, 441.
(39) Huber, K, P.; Herzberger, G. *Molecular Spectra and Molecular Structure IV. Constants of Diatomic Molecules*; Van Nostrand: Princeton, 1979.
(40) Igel-Mann, G.; Stoll, H.; Preuss, H. *Mol. Phys.* **1993**, *80*, 325.
(41) Morino, Y.; Ukaji, T.; Ito, T. *Bull. Chem. Soc. Jpn.* **1966**, *39*, 64.
(42) Frisch, M. J.; Trucks, G. W.; Schlegel, H. B.; Scuseria, G. E.; Robb, M. A.; Cheeseman, J. R.; Scalmani, G.; Barone, V.; Mennucci, B.; Petersson, G. A.; Nakatsuji, H.; Caricato, M.; Li, X.; Hratchian, H. P.; Izmaylov, A. F.; Bloino, J.; Zheng, G.; Sonnenberg, J. L.; Hada, M.; Ehara, M.; Toyota, K.; Fukuda, R.; Hasegawa, J.; Ishida, M.; Nakajima, T.; Honda, Y.; Kitao, O.; Nakai, H.; Vreven, T.; Montgomery, Jr., J. A.; Peralta, J. E.; Ogliaro, F.; Bearpark, M.; Heyd, J. J.; Brothers, E.; Kudin, K. N.; Staroverov, V. N.; Kobayashi, R.; Normand, J.; Raghavachari, K.; Rendell, A.; Burant, J. C.; Iyengar, S. S.; Tomasi, J.; Cossi, M.; Rega, N.; Millam, N. J.; Klene, M.; Knox, J. E.; Cross, J. B.; Bakken, V.; Adamo, C.; Jaramillo, J.; Gomperts, R.; Stratmann, R. E.; Yazyev, O.; Austin, A. J.; Cammi, R.; Pomelli, C.; Ochterski, J. W.; Martin, R. L.; Morokuma, K.; Zakrzewski, V. G.; Voth, G. A.; Salvador, P.; Dannenberg, J. J.; Dapprich, S.; Daniels, A. D.; Farkas, Ö.; Foresman, J. B.; Ortiz, J. V.; Cioslowski, J.; Fox, D. J. *Gaussian 09,* Revision A.02, Gaussian, Inc., Wallingford CT, 2009.
(43) Dolg, M. *Relativistic Elecronic Structure Theory, Part 1: Fundamentals Theoretical and Computational Chemistry*; Schwerdtfeger, P., Ed.; Theoretical and Computational Chemistry Series 11; Elsevier: Amsterdam, 2002; 793.
(44) Kahn, L. R.; Baybutt, P.; Truhlar, D. G. *J. Chem. Phys.* **1976**, *65*, 3826.
(45) The cc-pV*x*Z-PP basis sets for iron element were obtained from Kirk Peterson. The cc-pV*x*Z-PP basis sets are matched with the new RECP optimized by Dolg in 2005. See: Dolg, M. *Theor. Chem. Acc.* **2005**, *114*, 297.
(46) Peterson, K. A.; Yousaf, K. E. *J. Chem. Phys.* **2010**, *133*, 174116.
(47) Nava, P.; Ahlrichs, R. *Chem.—Eur. J.* **2008**, *14*, 4039.

JCTC Journal of Chemical Theory and Computation

ARTICLE

pubs.acs.org/JCTC

Natural Orbitals for Wave Function Based Correlated Calculations Using a Plane Wave Basis Set

Andreas Grüneis,*[,†] George H. Booth,[‡] Martijn Marsman,[†] James Spencer,[§] Ali Alavi,[‡] and Georg Kresse[†]

[†]Faculty of Physics and Center for Computational Materials Science, University Vienna, Sensengasse 8/12, A-1090 Vienna, Austria

[‡]Department of Chemistry, University of Cambridge, Lensfield Road, Cambridge CB2 1EW, U.K.

[§]Department of Physics and Department of Materials, Imperial College London, Exhibition Road, London SW7 2AZ, U.K.

ABSTRACT: We demonstrate that natural orbitals allow for reducing the computational cost of wave function based correlated calculations, especially for atoms and molecules in a large box, when a plane wave basis set under periodic boundary conditions is used. The employed natural orbitals are evaluated on the level of second-order Møller−Plesset perturbation theory (MP2), which requires a computational effort that scales as $O(N^5)$, where N is a measure of the system size. Moreover, we find that a simple approximation reducing the scaling to $O(N^4)$ yields orbitals that allow for a similar reduction of the number of virtual orbitals. The MP2 natural orbitals are applied to coupled-cluster singles and doubles (CCSD) as well as full configuration interaction Quantum Monte Carlo calculations of the H_2 molecule to test our implementation. Finally, the atomization energies of the LiH molecule and solid are calculated on the level of MP2 and CCSD.

INTRODUCTION

Correlated methods such as coupled-cluster theory and Møller−Plesset perturbation theory are common practice in the field of quantum chemistry. However, in their canonical formulation these methods are hard to apply to large systems and require huge computational resources. Reducing the computational cost is therefore one of the main goals in the development of correlated methods. Local correlation methods,[1−4] pair-natural orbitals,[5−7] explicitly correlated methods,[8−11] optimized virtual orbitals,[12] and natural orbitals[13−17] are among the most popular approaches to reduce the computational cost of wave function based methods. In the canonical formulation of wave function based methods, the computational cost arises in large part from the virtual orbital space. Therefore, many attempts aim at minimizing the number of virtual orbitals. Natural orbitals allow for a reduction of the virtual orbital space without compromising accuracy and are obtained easily from diagonalization of the virtual−virtual orbital block of the one-electron reduced density matrix, which can be calculated at the level of second-order Møller-Plesset perturbation theory (MP2):

$$D_{ab}^{(2)} = \sum_{cij} \frac{2\langle cb|ij\rangle\langle ij|ca\rangle - \langle cb|ji\rangle\langle ij|ca\rangle}{\Delta_{ij}^{cb}\Delta_{ij}^{ca}} \quad (1)$$

where

$$\Delta_{ij}^{cb} = \varepsilon_i + \varepsilon_j - \varepsilon_c - \varepsilon_b$$

The indices i, j and a, b, c denote occupied and unoccupied one-electron spatial orbitals, respectively, and are understood to be shorthands for both the band index and the Bloch wave vector. The ε_n correspond to one-electron Hartree−Fock eigenvalues and $\langle ij|ab\rangle$ are two-electron-four-orbital integrals. Note that the evaluation of eq 1 scales as $O(N^5)$ for atoms and molecules, where N is a measure of the system size. In ref 17, Aquilante et al. proposed to approximate the density matrix by

$$D_{ab}^{(2)} \approx \sum_{ci} \frac{\langle cb|ii\rangle\langle ii|ca\rangle}{\Delta_{ii}^{cb}\Delta_{ii}^{ca}} \quad (2)$$

This allows for calculating an *approximate MP2 density matrix* with a computational effort that scales as $O(N^4)$ only.

Eigenvectors and eigenvalues of the density matrix are called (approximate) MP2 natural orbitals and occupation numbers, respectively. The occupation numbers lie between 0 and 1, and those extreme values imply that the corresponding natural orbital occurs in none or all configurations (excited Slater determinants), respectively.[13] We stress that only virtual orbitals are mixed by $D_{ab}^{(2)}$.

If Gaussian-type orbitals (GTOs) are used, natural orbitals allow for a reduction of the virtual orbital space by about one-half without significantly compromising accuracy.[14−16] But Gaussian-type orbitals are already spatially confined to the regions around the atoms, and much larger reductions are possible if a spatially delocalized, unbiased basis set is used to capture correlation effects.

Plane waves (PWs) fall into this category. They have undeniable advantages; in particular, their precision and completeness can be arbitrarily improved by increasing a single parameter, the PW energy cutoff. Plane waves are very efficient for conventional density functional theory or Hartree−Fock calculations if iterative algorithms are used to determine the occupied orbitals only.[19] Similar iterative algorithms are not yet available for many-electron wave function based methods. The advantages of plane waves then turn into a severe handicap: the number of virtual orbitals becomes intractable very quickly. Fortunately, most of the variational degrees of freedom are irrelevant for the description of the many-electron wave function, in particular, for

Received: April 16, 2011
Published: July 05, 2011

atoms or molecules in a large box, where several thousand plane waves are required to achieve total energy convergence. A large part of this variational space is unnecessary, because it describes regions in the vacuum far away from the nucleus, where the true many-electron wave function vanishes. In the following, it is shown that one can lift this problem by means of natural orbitals that are calculated at the level of MP2 or in an even more approximate fashion. This allows for the efficient calculation of the electronic correlation energy using highly sophisticated many-electron methods, such as coupled-cluster or full configuration interaction quantum Monte Carlo (FCIQMC) methods, which have previously been limited to more compact basis sets such as GTOs.

COMPUTATIONAL DETAILS

The density matrix in eq 1 is calculated using the Vienna ab initio simulation package (VASP) in the framework of the projector-augmented wave (PAW) method.[18−20] In the PAW method, the one-electron orbitals ψ are derived from the pseudo-orbitals $\tilde{\psi}$ by means of a linear transformation

$$|\psi\rangle = |\tilde{\psi}\rangle + \sum_i (|\phi_i\rangle - |\tilde{\phi}_i\rangle)\langle\tilde{p}_i|\tilde{\psi}\rangle \quad (3)$$

The pseudo-orbitals $\tilde{\psi}$ are the variational quantities of the PAW method and are expanded in reciprocal space using plane waves. The index i is a shorthand for the atomic site $\mathbf{R}_i$, the angular momentum quantum numbers l_i and m_i, and an additional index ε_i denoting the linearization energy.[19] The all-electron partial waves ϕ_i are the solution to the radial Schrödinger equation for the non-spin-polarized reference atom at specific energies ε_i and specific angular momentum l_i. The pseudopartial waves, $\tilde{\phi}_i$, are equivalent to the all-electron partial waves outside a core radius r_c and match continuously onto ϕ_i inside the core radius. The partial waves ϕ_i and $\tilde{\phi}_i$ are represented on radial logarithmic grids. The projector functions $\tilde{p}_i$ are constructed in such a way that they are dual to the pseudopartial waves, i.e.,

$$\langle\tilde{p}_i|\tilde{\phi}_j\rangle = \delta_{ij} \quad (4)$$

As a result of the transformation, any local operator (e.g., density) can be expressed as a sum of three terms:

$$A = \langle\tilde{\psi}|A|\tilde{\psi}\rangle - \sum_{ij}[\langle\tilde{\phi}_i|A|\tilde{\phi}_j\rangle\langle\tilde{\psi}|\tilde{p}_i\rangle\langle\tilde{p}_j|\tilde{\psi}\rangle + \langle\phi_i|A|\phi_j\rangle\langle\tilde{\psi}|\tilde{p}_i\rangle\langle\tilde{p}_j|\tilde{\psi}\rangle] \quad (5)$$

The first term is a pseudized contribution evaluated on a plane wave grid, whereas the second and third terms are corrections to account for the shape difference between the pseudized orbitals $|\tilde{\psi}\rangle$ and the exact all-electron orbitals $|\psi\rangle$. They are calculated separately for each atomic site using atom centered grids (i.e., only one-center contributions are required). The terms $\langle\tilde{\phi}_i|A|\tilde{\phi}_j\rangle$ and $\langle\phi_i|A|\phi_j\rangle$ are the expectation values of the operator A in an LCAO (linear combination of atomic orbitals) basis, where the first and second basis set describes the pseudized orbitals and the exact all-electron orbitals, respectively. The efficiency of the method relates to the fact that only one-center corrections are required, since all long-range contributions are (exactly) described by the first term. Similar expressions are obtained for the two-electron integrals (see ref 21 for details). Since a more detailed introduction to the PAW method is beyond the scope of this work, we refer the reader to the seminal paper of Blöchl[18] and the work of Kresse and Joubert.[20]

The evaluation of the two-electron−four-orbital integrals $\langle ij|ab\rangle$ in the PAW method is thoroughly discussed in ref 21 and requires two plane wave basis sets: (i) the basis set for the one-electron orbitals $\psi_i(\mathbf{r})$, $\psi_j(\mathbf{r})$, $\psi_a(\mathbf{r})$, and $\psi_b(\mathbf{r})$ as well as (ii) the auxiliary basis set used in the construction of the overlap density between two orbitals $\psi_i^*(\mathbf{r})\psi_a(\mathbf{r})$. These basis sets are determined by all PWs $e^{i\mathbf{G}\mathbf{r}}$ with wavevectors $\mathbf{G}$ satisfying the equations

$$(\hbar^2/2m_e)|\mathbf{G}|^2 < E_{cut}$$

and

$$(\hbar^2/2m_e)|\mathbf{G}|^2 < E_\chi$$

respectively.

As such, the energy cutoff E_{cut} determines the basis set for the one-electron orbitals, whereas the cutoff E_χ defines a basis set for densities (products of two orbitals) that is analogous to auxiliary basis sets used in density fitting.[22] For the evaluation of $D_{ab}^{(2)}$ we set E_χ close to E_{cut} because we find a fast convergence of the natural orbitals with respect to E_χ. The correlation energy in the complete basis set limit, however, is extrapolated by systematically increasing E_χ at fixed E_{cut}. The exact extrapolation procedure is outlined in ref 21.

In this work, we used a newly developed coupled-cluster singles and doubles (CCSD) module in VASP and the FCIQMC code from ref 23 that was interfaced with VASP. Coupled-cluster theory[24−26] is a very successful method for describing electronic correlation in atoms and molecules.[27] In particular, CCSD(T) is known for achieving chemical accuracy (1 kcal/mol) in the prediction of atomization and reaction energies for a wide class of molecules.[27] We apply the CCSD method to three-dimensional fully periodic systems. Our CCSD implementation employs the working equations published in refs 28−30 and reduces the memory requirements by evaluating all two-electron−four-orbital integrals on-the-fly. The FCIQMC method by Booth et al.[23] constitutes a recently developed and very efficient way to calculate the exact full CI ground state energy of a many-electron system by solving the imaginary-time Schrödinger equation stochastically. We will not repeat the expressions of the CCSD and FCIQMC methods, but we refer the reader to refs 28−30 and 23, 31−33 for details, respectively.

Natural orbitals with an occupation number close to zero are expected to contribute only little to the correlation energy.[13] Therefore, we introduce a threshold, ξ, that defines a subspace of the natural orbitals by truncating them according to their occupation number. Only natural orbitals with an occupation number larger than ξ are included in this subspace.

Unlike HF orbitals, natural orbitals do not diagonalize the HF Hamiltonian. Therefore, noncanonical formulations of the employed correlated methods would be required. We use a standard recanonicalization to avoid the necessity for noncanonical implementations by carrying out the following procedure subsequent to the underlying Hartree−Fock (HF) calculation: (i) calculate the natural orbitals (NOs), (ii) order the natural orbitals according to their occupation numbers (eigenvalues of $D_{ab}^{(2)}$), (iii) recalculate the HF Hamiltonian in the basis of NOs, and (iv) diagonalize the HF Hamiltonian in a truncated subspace defined by those natural orbitals with occupation numbers above a threshold ξ. These "canonicalized" orbitals diagonalize

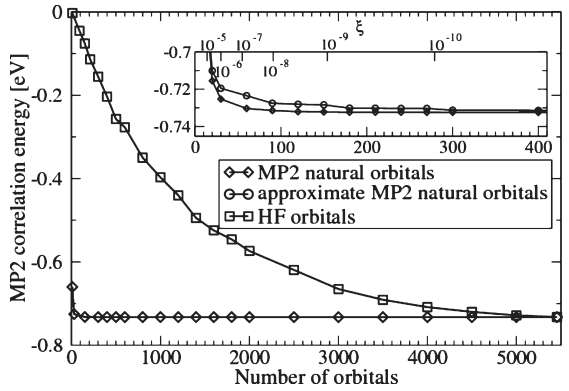

Figure 1. Convergence of the MP2 correlation energy of the Li atom in a $6 \times 6 \times 6$ Å^3 box with respect to the number of natural and HF orbitals per spin-channel. The inset shows the convergence on a different scale. The top axis in the inset shows the occupation number threshold, ξ, of the MP2 natural orbitals for the spin-up channel.

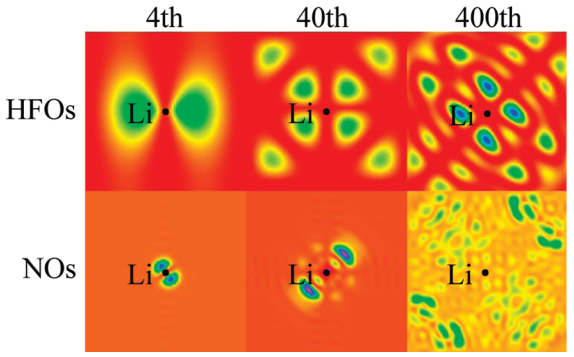

Figure 2. Charge densities of the Hartree−Fock orbitals (HFOs) in the top row and natural orbitals (NOs) in the bottom row of a Li atom in a $6 \times 6 \times 6$ Å^3 box. The fourth, 40th, and 400th orbitals have been plotted.

the Hartree−Fock Hamiltonian in the truncated subspace and can be used in a subsequent canonical wave function based correlated calculation. We stress that the correlation energy is not changed by the diagonalization in the subspace of NOs since the occupied orbital space is always unchanged.

In the calculations of the atomization energies of the molecular systems (H_2 and LiH), we minimize the interaction between the periodic images by extrapolating the contribution from the correlation energy according to a $1/V^2$ behavior to $V \rightarrow \infty$, where V corresponds to the unit cell volume. This procedure has already been outlined in ref 21. To obtain the atomization energies of solids, we use large cubic boxes with 9 Å length in the calculations of the isolated atoms.

RESULTS

Natural MP2 Orbitals. As a first example, we study the convergence of the MP2 correlation energy of a spin polarized Li atom in a $6 \times 6 \times 6$ Å^3 box. The correlation energy was not extrapolated to the complete basis set limit; instead, a fixed kinetic energy cutoff of $E_\chi = 400$ eV was used. The kinetic energy cutoff for the one-electron orbitals was set to $E_{cut} = 500$ eV. Figure 1 shows the MP2 correlation energy of the Li atom with respect to the number of orbitals per spin channel. For the given cutoff and box size, 5450 orbitals span the complete space of

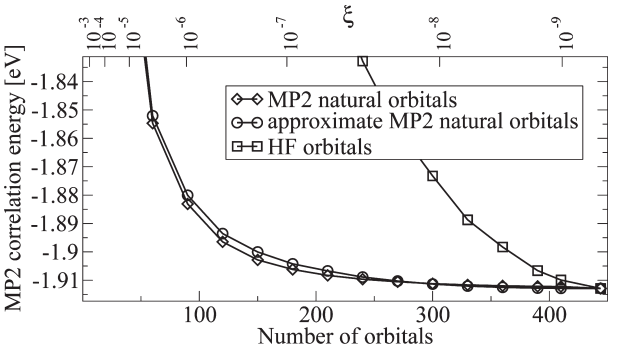

Figure 3. Convergence of the MP2 correlation energy of the LiH solid using a $4 \times 4 \times 4$ k-point mesh with respect to the number of natural and HF orbitals per k-point. The top axis shows the occupation number threshold, ξ, of the MP2 natural orbitals at the Γ-point.

one-electron Hartree−Fock orbitals (HFOs). The convergence of the correlation energy with respect to the number of HFOs is extremely slow. Even 4000 HFOs yield an MP2 correlation energy that deviates by more than 10 meV from the correlation energy obtained using the full space (733 meV). In contrast, 30 natural orbitals (NOs) already suffice to obtain an agreement that is within 10 meV of the converged value. The top axis of the inset in Figure 1 shows the corresponding occupation number threshold, ξ, of the MP2 natural orbitals, indicating that 30 natural orbitals correspond to an occupation number threshold of 10^{-6}. The occupation numbers quickly decay to zero, which illustrates the insignificance of the neglected natural orbitals and the "redundancy" present in the PW basis set in the description of many-electron properties. Approximate MP2 natural orbitals (eigenvectors of the approximate density matrix given by eq 2) reduce the convergence rate only slightly (see inset of Figure 1). In fact, both types of natural orbitals allow for reducing the number of virtuals compared to Hartree−Fock by at least an order of magnitude.

Figure 2 shows the charge densities of the fourth, 40th, and 400th natural and Hartree−Fock orbital of a Li atom in a $6 \times 6 \times 6$ Å^3 box. Hartree−Fock orbitals and natural orbitals are ordered by their increasing one-electron HF eigenvalues and decreasing occupation numbers, respectively. The HF orbitals become essentially plane waves at higher energies and greater band indices, since the kinetic energy operator dominates at sufficiently high energies. The natural orbitals with large occupation numbers maximize the overlap with the occupied orbitals, whereas the natural orbitals with small occupation numbers exhibit only very little density at the Li atom, as can be clearly seen for the 400th NO.

Figure 3 shows the convergence of the MP2 correlation energy of the face-centered-cubic LiH crystal with a unit cell volume of 17.03 Å^3. The first Brillouin zone was sampled using a $4 \times 4 \times 4$ k-point mesh and the same cutoffs as for the Li atom were employed ($E_\chi = 400$ eV, $E_{cut} = 500$ eV). In the case of solids, the reduction of the virtual orbital space using natural orbitals is less significant than for a single atom in a box. This is not unexpected, because in contrast to an atom in a box, the electrons of the solid are delocalized over the entire unit cell and almost all degrees of freedom supplied by the plane wave basis set are required to describe the many-electron wave function. Nevertheless, it is possible to remove about half of the full HF virtual orbital space without introducing an error larger than 10 meV. Note that a

Table 1. Atomization Energies of the LiH Molecule in the HF, MP2, and CCSD Approximation Using Natural and HF Orbitals[a]

	this work	ref 21	GAMESS
basis set type	PWs	PWs	aug-cc-pV[TQ]Z
orbitals	NOs	HFOs	HFOs
ΔE^{HF}	1.084	1.084	1.085
ΔE_c^{MP2}	0.823	0.822	0.818
ΔE_c^{CCSD}	1.039		1.034

[a] Plane-waves (PWs) as well as aug-cc-pVXZ(X=T,Q) basis sets were used in the calculations. The results obtained using aug-cc-pVXZ basis sets were extrapolated to $X \rightarrow \infty$ assuming a functional form of $1/X^3$ for the correlation energy. All energies in eV.

reduction in the number of virtual orbitals by a factor of 2 reduces the computational cost in MP2 calculations by a factor of 4. The approximate and exact MP2 natural orbitals show a very similar convergence rate. The top axis in Figure 3 shows the corresponding occupation number thresholds, ξ, for the MP2 natural orbitals. An error smaller than 10 meV in the correlation energy can be achieved by including all NOs with $\xi = 10^{-7}$.

Natural MP2 orbitals for CCSD and FCIQMC. As a first test of our implementation we calculate the dissociation energy of the H_2 molecule with a bond length of 0.75 Å using 80 natural orbitals. Both the CCSD as well as the FCIQMC method were applied. Since for a two-electron system CCSD accounts for all possible excitations from the HF determinant into excited Slater determinants, it should yield exact results, as does the full CI quantum Monte Carlo method. Indeed, our FCIQMC and CCSD results agree exactly. We obtain a HF and FCIQMC contribution to the dissociation energy of 3.619 and 1.112 eV, respectively. Likewise, the resulting dissociation energy of 4.731 eV agrees with the experimental value of 4.73 eV.[34]

As a second test of our implementation we have calculated the dissociation energy of the LiH molecule at the level of MP2 as well as CCSD using NOs. The bond length was set to 2.042 Å. This bond length corresponds to the nearest neighbor distance in the LiH solid at the unit cell volume of 17.03 Å^3. Table 1 summarizes the HF, MP2, as well as CCSD contributions to the atomization energies of the LiH molecule. The column on the right lists the results that have been obtained using the GTO GAMESS code.[35−37] The middle column summarizes the HF and MP2 results that were calculated using a PW basis set and Hartree−Fock orbitals in ref 21. The column on the left summarizes the HF, MP2, as well as CCSD contributions obtained using PWs and NOs. The PW and GTO results agree to within a few millielectronvolts. The discrepancy between the PW MP2 results obtained using NOs and HFOs is 1 meV and originates from the truncation of the virtual orbitals in the natural orbital basis. A total of 200 and 58 NOs were used in the calculations of the molecule and atom, respectively corresponding to an occupancy threshold ξ of approximately 10^{-7}. For comparison, we note that the aug-cc-pVQZ basis set consists of 126 and 80 orbitals in the LiH molecule and Li atom, respectively. The agreement of the CCSD result calculated using PWs with the one obtained using the GTO basis is very good as well, with the PW result being approximately 5 meV lower in energy than the GTO result. This is excellent considering that VASP employs the PAW method and is not a conventional GTO all-electron code.

Table 2. Contributions of the MP2 Correlation Energy to the Atomization Energy of the LiH Crystal Calculated According to eq 6[a]

m_{NOs}	m_3	m_4	ΔE_c^{MP2}
192	16	16	1.192
256	16	16	1.195
192	32	16	1.203
192	48	16	1.189
192	54	16	1.189
192	64	16	1.205
192	54	32	1.185
192	54	48	1.187

[a] All energies in eV.

Table 3. HF, MP2, and CCSD Contributions to the Atomization Energy of the LiH Crystal Using Different Orbitals Compared to Quantum Chemical Calculations Deducing the Atomization Energy from LiH Clusters Using an Incremental Approach (ref 40)[a]

	this work	ref 21	ref 40
orbitals	NOs	HFOs	HFOs
ΔE^{HF}	3.583	3.583	3.589
ΔE_c^{MP2}	1.187	1.188	1.182
ΔE_c^{CCSD}	1.326		1.329

[a] The MP2 contribution to the atomization energy of the LiH crystal from ref 21 corresponds to a calculation using a $4 \times 4 \times 4$ k-point mesh. All energies in eV.

At this point we want to stress that the calculations of the LiH molecule summarized above and in ref 21 were not carried out at the experimental equilibrium bond length (1.596 Å).[38] MP2 and CCSD calculations using NOs at the experimental bond length of the LiH molecule yield an atomization energy of 2.33 and 2.52 eV, respectively. The experimental dissociation energy corrected for the zero-point energy amounts to 2.52 eV.[38] As expected, CCSD corrects for the underestimation present in MP2 and deviates from experiment by less than 10 meV.

As a last application, we calculate the atomization energy of the LiH solid on the level of MP2 as well as CCSD. Even with natural orbitals, it would be impossible to perform a CCSD calculation of the LiH crystal with a k-point mesh denser than $2 \times 2 \times 2$, because of the large number of virtual orbitals and the unfavorable scaling of the computational effort of CCSD with respect to the system size. Therefore, we use an approach similar to the progressive downsampling technique of Ohnishi et al. in ref 39, relying on the observation that the long-range behavior of the correlation energy depends mostly on the low-lying excitations. We approximate the correlation energy, $\hat{E}_c$, of a solid for $(K \times K \times K)$ k-points and m_{full} orbitals per k-point with

$$\hat{E}_c(K \times K \times K, m_{full}) = E_c(2 \times 2 \times 2, m_{full}) + \sum_{k=3}^{K} C_k \quad (6)$$

$E_c(2 \times 2 \times 2, m_{full})$ is the calculated correlation energy using a $(2 \times 2 \times 2)$ k-point mesh and a converged basis set. C_k are correction terms that account for the difference between

$(2 \times 2 \times 2)$ and denser k-point grids. Those corrections are calculated according to

$$C_k = E_c(k \times k \times k, m_k) - E_c((k-1) \times (k-1) \times (k-1), m_k)$$

In practice, we find a fast convergence of C_k with respect to m_k. This allows the denser k-point meshes to be calculated with fewer bands per k-point since only the energy *difference* between the k-point meshes is required.

Evidently eq 6 becomes exact for $m_k \rightarrow m_{full}$, but typically m_k is chosen significantly smaller than m_{full} and decreases with an increasing number of k-points, k. Moreover, we note that $E_c(2 \times 2 \times 2, m_{full})$ is calculated using m_{NOs} natural orbitals at each k-point.

Table 2 summarizes the convergence of the MP2 atomization energy with respect to m_{NOs} and m_i for all k. We find that the convergence with respect to m_k is fairly noisy. From the noise, we estimate an error bar of approximately 10 meV for the correlation energy given by eq 6. To attain this accuracy, it suffices to use $m_{NOs} = 192$, $m_3 = 54$, and $n_4 = 32$ to reproduce straightforward MP2 calculations.

These values are then employed in a CCSD calculation. Table 3 summarizes the resulting HF, MP2, and CCSD contributions to the atomization energy of the LiH crystal. The results are compared to previous calculations obtained using Gaussian type orbitals and standard quantum chemical methods combined with the incremental approach, which extrapolates the correlation energy from LiH clusters of increasing size.[40] For MP2, the agreement between refs 21 and 40 was already discussed in ref 21. The first important observation is that the extrapolation procedure eq 6 works reliably for the MP2 contribution to the atomization energy of the LiH crystal. Our MP2 results deviate by less than 10 meV from those of ref 21. In passing, we note that periodic local MP2 results for the cohesive energy of the LiH crystal published in ref 41 also agree to within 10 meV with our values. Moreover, our CCSD results are in very good agreement with ref 40, which gives us confidence in the correct implementation of the CCSD code for periodic boundary conditions.

The resulting MP2 and CCSD atomization energies deviate from the experimental atomization energy corrected for zero point vibrations (4.974 eV[42]) by 204 and 65 meV, respectively. As such, CCSD clearly outperforms MP2 and is likely to capture more of the correct physics in the case of the LiH solid.

CONCLUSIONS AND OUTLOOK

In summary, we have shown that MP2 natural orbitals allow for a tremendous reduction of the virtual orbital space, compared to HF orbitals for calculations of atoms or molecules in a box using a PW basis set. For the atoms and molecules considered here, the basis set is typically reduced by a factor of 10−100 compared to untruncated canonical HF plane wave orbitals. The reduction allows for calculations of atoms and small molecules using highly accurate quantum-chemical methods such as CCSD and even FCIQMC in a PW basis set. In the case of solids, the virtual orbital space can be reduced approximately by half without compromising the accuracy significantly. Note that in CCSD calculations, a reduction of the virtual orbital space by half corresponds to a speed-up of an order of magnitude. Although the computational cost of evaluating natural orbitals scales as $O(N^5)$, we can approximate the MP2 NOs by a simpler expression that scales only as $O(N^4)$. The approximated NOs perform only slightly worse than the exact MP2 NOs. This even allows us to reduce the computational cost of MP2 calculations for large systems. But natural orbitals will not only help in expanding the applicability of our MP2 or CCSD implementation. Many other correlated methods that are implemented in a PW basis will benefit as well. It is straightforward to apply the presented procedures to other methods such as the random-phase approximation plus second-order screened exchange[43] or GW-BSE.[44] We hope to use this formalism to greatly expand the scope of wave function based periodic methods in a PW basis set. Moreover, future prospects shall include the development of an FCIQMC algorithm that will enable us to treat solid-state systems using complex orbitals and arbitrary k-point meshes.

AUTHOR INFORMATION

Corresponding Author
*E-mail: ag618@cam.ac.uk.

ACKNOWLEDGMENT

This work was supported by the Austrian Fonds zur Förderung der wissenschaftlichen Forschung (FWF) within the SFB ViCom (F41) and the START grant. Most of the calculations have been performed in the Vienna Scientific Cluster (VSC).

REFERENCES

(1) Pulay, P.; Saebø, S. *Theor. Chim. Acta* **1986**, *69*, 357.
(2) Saebø, S.; Pulay, P. *Annu. Rev. Phys. Chem.* **1993**, *44*, 213.
(3) Schütz, M.; Hetzer, G.; Werner, H.-J. *J. Chem. Phys.* **1999**, *111*, 5691.
(4) Subotnik, J.; Head-Gordon, M. *J. Chem. Phys.* **2005**, *123*, 064108.
(5) Meyer, W. *Int. J. Quantum Chem.* **1971**, *S5*, 341.
(6) Meyer, W. *J. Chem. Phys.* **1973**, *58*, 1017.
(7) Nesse, F.; Wennmohs, F.; Hansen, A. *J. Chem. Phys.* **2009**, *130*, 114108.
(8) Hättig, C.; Tew, D. P.; Köhn, A. *J. Chem. Phys.* **2010**, *132*, 231102.
(9) Klopper, W.; Samson, C. C. M. *J. Chem. Phys.* **2002**, *116*, 6397.
(10) Werner, H. J.; Adler, T. B.; Manby, F. R. *J. Chem. Phys.* **2007**, *126*, 164102.
(11) Shiozaki, T.; Hirata, S. *J. Chem. Phys.* **2010**, *132*, 151101.
(12) Neogrády, P.; Pitonák, M.; Urban, M. *Mol. Phys.* **2005**, *103*, 2141.
(13) Löwdin, P.-O. *Phys. Rev.* **1995**, *97*, 1474.
(14) Taube, A. G.; Bartlett, R. J. *Collect. Czech. Chem. Commun.* **2005**, *70*, 837.
(15) Taube, A. G.; Bartlett, R. J. *J. Chem. Phys.* **2008**, *128*, 164101.
(16) Rolik, Z.; Kállay, M. *J. Chem. Phys.* **2011**, *132*, 124111.
(17) Aquilante, F.; Todorova, T. K.; Gagliardi, L.; Pedersen, T. B.; Roos, B. O. *J. Chem. Phys.* **2009**, *131*, 034113.
(18) Blöchl, P. E. *Phys. Rev. B* **1994**, *50*, 17953.
(19) Kresse, G.; Furthmüller, J. *Phys. Rev. B* **1996**, *54*, 11169.
(20) Kresse, G.; Joubert, D. *Phys. Rev. B* **1999**, *59*, 1758.
(21) Marsman, M.; Grüneis, A.; Paier, J.; Kresse, G. *J. Chem. Phys.* **2009**, *130*, 184103.
(22) Maschio, L.; Usvyat, D.; Manby, F. R.; Casassa, S.; Pisani, C.; Schütz, M. *Phys. Rev. B* **2007**, *76*, 075101.
(23) Booth, G. H.; Thom, A. J. W.; Alavi, A. *J. Chem. Phys.* **2009**, *131*, 054106.
(24) Coester, F. *Nucl. Phys.* **1958**, *1*, 421.
(25) Coester, F.; Kümmel, H. *Nucl. Phys.* **1960**, *17*, 477.
(26) Čížek, J. *J. Phys. Chem.* **1966**, *45*, 4256.
(27) Bartlett, R. J.; Musial, M. *Rev. Mod. Phys.* **2007**, *79*, 291.

(28) Hirata, S.; Grabowski, I.; Tobita, M.; Bartlett, R. J. *Chem. Phys. Lett.* **2001**, *345*, 475.
(29) Hirata, S.; Podeszwa, R.; Tobita, M.; Bartlett, R. J. *J. Chem. Phys.* **2004**, *120*, 2581.
(30) Hirata, S. *J. Phys. Chem. A* **2003**, *107*, 9887.
(31) Cleland, D.; Booth, G. H.; Alavi, A. *J. Chem. Phys.* **2010**, *132*, 041103.
(32) Booth, G. H.; Alavi, A. *J. Chem. Phys.* **2010**, *132*, 174104.
(33) Cleland, D. M.; Booth, G. H.; Alavi, A. *J. Chem. Phys.* **2011**, *134*, 024112.
(34) Huber, K.P.; Herzberg, G.*Molecular Spectra and Molecular Structure. Constants of Diatomic Molecules*; Van Nostrand Reinhold: New York, 1979; Vol. IV, 716 pp.
(35) http://www.msg.chem.iastate.edu/GAMESS/GAMESS.html, 4.7.2011
(36) Schmidt, M. W.; Baldridge, K. K.; Boatz, J. A.; Elbert, S. T.; Gordon, M. S.; Jensen, J. H.; Koseki, S.; Matsunaga, N.; Nguyen, K. A.; Su, S. J.; Windus, T. L.; Dupuis, M.; Montgomery, J. A. *J. Comput. Chem.* **1993**, *14*, 1347.
(37) Gordon, M. S.; Schmidt, M. W. In *Theory and Applications of Computational Chemistry: The First Forty Years*; Elsevier: New York, 2005; Chapter 41, pp 1167−1189.
(38) Trail, J. R.; Needs, R. J. *J. Chem. Phys.* **2008**, *128*, 204103 and references therein.
(39) Ohnishi, Y.-y.; Hirata, S. *J. Chem. Phys.* **2010**, *133*, 034106.
(40) Nolan, S. J.; Gillan, M. J.; Alfé, D.; Allan, N. L.; Manby, F. R. *Phys. Rev. B* **2009**, *80*, 165109.
(41) Usvyat, D.; Civalleri, B.; Maschio, L.; Dovesi, R.; Pisani, C.; Schütz, M. *J. Chem. Phys.* **2011**, *134*, 214105.
(42) Schimka, L.; Harl, J.; Kresse, G. *J. Chem. Phys.* **2011**, *134*, 024116.
(43) Grüneis, A.; Marsman, M.; Harl, J.; Schimka, L.; Kresse, G. *J. Chem. Phys.* **2009**, *131*, 154115.
(44) Albrecht, S.; Reining, L.; Del Sole, R.; Onida, G. *Phys. Rev. Lett.* **1998**, *80*, 4510.

JCTC Journal of Chemical Theory and Computation

ARTICLE

pubs.acs.org/JCTC

Variational Monte Carlo Method with Dirichlet Boundary Conditions: Application to the Study of Confined Systems by Impenetrable Surfaces with Different Symmetries

Antonio Sarsa*,† and Claude Le Sech‡

†Departmento de Física, Campus de Rabanales Edif. C2, Universidad de Córdoba, E-14071 Córdoba, Spain

‡Institut des Sciences Moleculaires d'Orsay-ISMO (UMR 8214), Université Paris Sud 11, CNRS, 91405, Orsay Cedex, France

ABSTRACT: Variational Monte Carlo method is a powerful tool to determine approximate wave functions of atoms, molecules, and solids up to relatively large systems. In the present work, we extend the variational Monte Carlo approach to study confined systems. Important properties of the atoms, such as the spatial distribution of the electronic charge, the energy levels, or the filling of electronic shells, are modified under confinement. An expression of the energy very similar to the estimator used for free systems is derived. This opens the possibility to study confined systems with little changes in the solution of the corresponding free systems. This is illustrated by the study of helium atom in its ground state ^{1}S and the first ^{3}S excited state confined by spherical, cylindrical, and plane impenetrable surfaces. The average interelectronic distances are also calculated. They decrease in general when the confinement is stronger; however, it is seen that they present a minimum for excited states under confinement by open surfaces (cylindrical, planes) around the radii values corresponding to ionization. The ground ^{2}S and the first ^{2}P and ^{2}D excited states of the lithium atom are calculated under spherical constraints for different confinement radii. A crossing between the ^{2}S and ^{2}P states is observed around $r_c = 3$ atomic units, illustrating the modification of the atomic energy level under confinement. Finally the carbon atom is studied in the spherical symmetry by using both variational and diffusion Monte Carlo methods. It is shown that the hybridized state sp^3 becomes lower in energy than the ground state ^{3}P due to a modification and a mixing of the atomic orbitals s, p under strong confinement. This result suggests a model, at least of pedagogical interest, to interpret the basic properties of carbon atom in chemistry.

1. INTRODUCTION

Bound states of free atoms or molecules are associated with wave functions that are quadratically integrable when the spatial integration extends over all space. As a consequence, the eigenfunction of the Schrödinger equation tends to zero when one of the particles belonging to the system goes to infinity. When the atoms or the molecules are confined by impenetrable surfaces, the wave function vanishes on these repulsive surfaces. When the atom is inside an impenetrable sphere, this corresponds to an ideal model related to an approximation of the physical reality. The solutions of the Schrödinger equation fulfill the so-called Dirichlet boundary conditions. The model of a spatially confined atom is not just of pedagogic interest. The properties of atoms and molecules undergo drastic changes when they are spatially confined in either penetrable or impenetrable surfaces. This topic has been attracting a lot of attention, and it has become a field of active research. During the last 70 years this model has proved to be quite useful in a number of fields of physics: the effect of pressure on properties, such as the atomic compressibility, the filling of the energy levels, the polarizability or the ionization threshold of atoms and molecules,[1−3] and artificial atoms like quantum dots[4] and in several other areas, like astrophysics and chemistry.[5] Since then many studies investigating various aspects of confined hydrogen atom by employing different approaches have been reported in the literature. We refer the reader to the reviews.[6−8]

The resolution of the Schrödinger equation with Dirichlet boundary conditions is a difficult problem, and to the best of our knowledge, accurate results exist only for low-Z atoms and few-electrons diatomic molecules. The Rayleigh−Ritz variational method is one of the most popular method for calculating accurately the ground- or excited-state energy of an atomic or a molecular system. Its extension to confined systems with more electrons is an important point.

Within the variational approximation, the variational Monte Carlo (VMC) method has been extensively applied to study free complex atoms and molecules obtaining accurate results.[9,10] In the most widely employed implementations, the trial wave function is written as the product of two factors. One factor is completely antisymmetric to account for the fermionic character of the electrons, while the other is symmetric and is tailored to describe the electronic correlations. A third correlation mechanism,[10] based on nonhomogeneous backflow transformations that introduces a dependence of the orbitals in the position of the other electrons, has been employed obtaining very accurate results in atomic, molecular, and extended systems.[11−13]

It is tempting to introduce in the second function a factor to take into account the Dirichlet boundary condition that the wave function vanishes on the impenetrable surfaces. Several forms for such cutoff function to satisfy the Dirichlet boundary condition have been proposed and employed in different works. External potentials, like harmonic oscillator potentials,

Received: April 25, 2011
Published: August 04, 2011

have been used to describe confined quantum system in different symmetries, including oblate symmetries when confined molecules are studied.[14,15]

The purpose of this paper is to extend the VMC method to study confined systems. Taking explicitly into account the Dirichlet boundary condition, we will derive a functional which is quasi identical to the functional used for nonconfined systems. The present work opens the possibility to start from the available function for unbound systems and to analyze the changes of these systems under confinement in a straightforward and flexible manner with little changes in the VMC codes. We illustrate the applicability of this approach by calculating ground- and excited-state energy of confined atoms in different symmetries.

The remaining of the paper is organized in the following manner. In Section 2 the theoretical methods employed in this paper are presented. Section 3 is devoted to the discussion of the results. The paper is concluded in Section 4. Atomic units are used throughout this work.

2. THEORY

2.1. Dirichlet Boundary Conditions and VMC Approach. Let us consider a general Hamiltonian, H, of a quantum system of n interacting particles:

$$H = -\frac{1}{2}\sum_{i=1}^{n}\nabla_i^2 + V(\mathbf{r}_1, ..., \mathbf{r}_n)$$

where the first sum is the kinetic energy operator and V stands for the potential energy operator of the n particles.

The VMC method is based on the variational approach with expectation values calculated by using random walks. The variational approach starts from a judicious choice for the ansatz of a many-body wave function satisfying various properties in accordance with the system under consideration. For unbounded systems, the integration volume in the spatial coordinates is R^{3n}, and the trial wave function vanishes at the infinity. In order to account for confinement by impenetrable surfaces a cutoff factor, w, vanishing at the boundary surface, $\partial\tau$, is included in the variational ansatz:

$$\Psi_t(\mathbf{r}_1, ..., \mathbf{r}_n) = \Psi_f(\mathbf{r}_1, ..., \mathbf{r}_n)w(\mathbf{r}_1, ..., \mathbf{r}_n) \quad (1)$$

where Ψ_f is a trial function for the unbound system.

For brevity, in the following we will use the notation, $\Psi_t(\mathbf{r}_i) = \Psi_t(\mathbf{r}_1, ..., \mathbf{r}_n)$, $\Psi_f(\mathbf{r}_i) = \Psi_f(\mathbf{r}_1, ..., \mathbf{r}_n)$, $w(\mathbf{r}_i) = w(\mathbf{r}_1, ..., \mathbf{r}_n)$ and $\nabla_{3n} = \sum_i \nabla_i$ so that the expressions $\nabla_{3n}^2 w(r_i)$ and $\nabla_{3n} w(r_i)$ stand for the $3n$ dimension laplacian and the gradient, respectively, of the $3n$ variables function $w(r_i)$ or $\Psi_f(\mathbf{r}_i)$. The expectation value of the Hamiltonian with properly normalized trial functions can be written as follows:

$$\langle H\rangle_{\Psi_t} = \int_{\tau(\partial\tau)}\left[-\frac{w(\mathbf{r}_i)^2\Psi_f(\mathbf{r}_i)\nabla_{3n}^2\Psi_f(\mathbf{r}_i)}{2} - \frac{\Psi_f^2(\mathbf{r}_i)w(\mathbf{r}_i)\nabla_{3n}^2 w(\mathbf{r}_i)}{2} - \Psi_f(\mathbf{r}_i)w(\mathbf{r}_i)\nabla_{3n}\Psi_f(\mathbf{r}_i)\cdot\nabla_{3n}w(\mathbf{r}_i) + \Psi_t^2(\mathbf{r}_i)V(\mathbf{r}_i)\right]d\tau \quad (2)$$

where $\tau(\partial\tau)$ represents the volume enclosed by the surface $\partial\tau$. The term with the gradients can be simplified by using

$$\int_{\tau(\partial\tau)}[\Psi_f(\mathbf{r}_i)\nabla_{3n}\Psi_f(\mathbf{r}_i)]\cdot[w(\mathbf{r}_i)\nabla_{3n}w(\mathbf{r}_i)]d\tau = \frac{1}{4}\int_{\tau(\partial\tau)}\nabla_{3n}w^2(\mathbf{r}_i)\cdot\nabla_{3n}\Psi_f^2(\mathbf{r}_i)d\tau$$

and applying a Green transformation:

$$\int_{\tau(\partial\tau)}\nabla_{3n}w^2(\mathbf{r}_i)\cdot\nabla_{3n}\Psi_f^2(\mathbf{r}_i)d\tau = \int_{\partial\tau}\Psi_f^2(\mathbf{r}_i)\nabla_{3n}w^2(\mathbf{r}_i)\cdot d\mathbf{s} - \int_{\tau(\partial\tau)}\Psi_f^2(\mathbf{r}_i)\nabla_{3n}^2w^2(\mathbf{r}_i)d\tau$$

In the latter equation the surface term vanishes because of the Dirichlet condition, $w(r_i) = 0$ when $r_i \in \partial\tau$, and the volume term can be rewritten as follows

$$\int_{\tau(\partial\tau)}\Psi_f^2(\mathbf{r}_i)\nabla_{3n}^2w^2(\mathbf{r}_i)d\tau = 2\int_{\tau(\partial\tau)}\Psi_f^2(\mathbf{r}_i)w(\mathbf{r}_i)\nabla_{3n}^2w(\mathbf{r}_i)d\tau + 2\int_{\tau(\partial\tau)}\Psi_f^2(\mathbf{r}_i)\nabla_{3n}w(\mathbf{r}_i)\cdot\nabla_{3n}w(\mathbf{r}_i)d\tau$$

the first integral cancels out when substituted in the expectation value of the Hamiltonian, eq 2, obtaining

$$\langle H\rangle_{\Psi_t} = \int_{\tau(\partial\tau)}|\Psi_f(\mathbf{r}_i)|^2\left\{w(\mathbf{r}_i)^2E_L^f(\mathbf{r}_i) + \frac{1}{2}[\nabla_{3n}w(\mathbf{r}_i)]^2\right\}d\tau \quad (3)$$

$$= \int_{\tau(\partial\tau)}|\Psi_t(\mathbf{r}_i)|^2\left\{E_L^f(\mathbf{r}_i) + \frac{1}{2}[\nabla_{3n}\ln w(\mathbf{r}_i)]^2\right\}d\tau \quad (4)$$

where

$$E_L^f(\mathbf{r}_i) \equiv \frac{H\Psi_f(\mathbf{r}_i)}{\Psi_f(\mathbf{r}_i)}$$

These expressions provide the energy for a system under constrains defined by the choice of the cutoff function w. The estimator for unbound systems is recovered by making $w(\mathbf{r}_i) \equiv 1$ and extending the surface to infinity

$$\langle H\rangle_{\Psi_f} = \int_{\tau(\infty)}|\Psi_f(\mathbf{r}_i)|^2E_L^f(\mathbf{r}_i)d\tau$$

Extension of these equations to non-normalized trial wave functions is straightforward. Equations 3 and 4 are specially suited for VMC calculations. Calculations for bounded systems can be carried out starting from these equations with minor changes in a VMC code.

2.2. Dirichlet Boundary Conditions and Diffusion Monte Carlo (DMC) Approach. To improve the energies of the atoms, in particular for the carbon atom calculated below, with the wave functions proposed in this work, we have also used them as trial functions in a quantum Monte Carlo calculation. The results are presented below in Section 3.4. More specifically, we shall use in this work the so-called diffusion Monte Carlo (DMC) method. We recall briefly here the main ideas underlying the DMC approach. Further details relative to this powerful approach to solve the

Schrödinger by simulating the Green's function of the system in question by statistical methods can be found in, e.g., refs 9 and 10.

DMC method starts from the time-dependent Schrödinger equation in imaginary time that becomes the classical diffusion equation. To determine the random walk that simulates the diffusion, the Green's function at short time approximation is invoked. Then a step of the random walk consists in an isotropic Gaussian diffusion and branching processes of the walkers. After a large number of iterations, the excited-state contributions are projected out from the initial ensemble, converging to the ground-state wave function, and the ground-state energy can be deduced.

Fermi systems, as those studied in this work, are affected by sing problems resulting from the required antisymmetry of the wave function. Here we will employ the fixed node approximation that uses a prefix nodal surface, including the Dirichlet boundary conditions, in the configuration space of the system. For fermions systems, the fixed node diffusion DMC can be thought of as a super variational approach with an energy which is guaranteed to be closer than the value given by the VMC with the same wave function to the exact one. The results so calculated are not exact anymore, instead an upper bound for the energy is obtained. The accuracy of such bound is governed by the quality of the nodal surface employed in the simulation. This is the most commonly used approach in the literature.

The algorithm, as described above, is in general very inefficient due to the large fluctuations in the ensemble along the random walk introduced by the interaction potential. Practical implementations usually make use of the Monte Carlo technique known as importance sampling that greatly reduces these fluctuations. This method requires an analytical trial function that is used to bias the random walk. However, very involved parametrizations, which generally are time-consuming, will slow down the calculation due to the fact that in each step the gradient and the laplacian must be calculated for each walker. Hence, compact and concise and still accurate wave functions are ideal. The choice of an adequate trial wave function that affects the statistical error in the calculation is very important. For fermion systems, the trial wave function not only affects the statistical error of the calculation but also to the value obtained for the energy. This comes from the fact that the trial wave function also determines the location of the nodal surface. In general, very little is known about the exact location of the nodes in fermion systems. The quality of the nodes structure induced by the trial wave function will determine how close one can come to the exact result. This is usually established a posteriori for those systems for which exact or quasi-exact solutions are available by other methods.

2.3. Determination of the Wave Function and the Energy for Confined Few-Electron Atoms. The atomic Hamiltonian considered here is

$$H = -\frac{1}{2}\sum_{i=1}^{n}\nabla_i^2 - \sum_{i=1}^{n}\frac{Z}{r_i} + \sum_{i<j}\frac{1}{r_{ij}} \tag{5}$$

Bound states are calculated within the variational approximation starting from the trial wave function given in eq 1, i.e., the product of a trial function for the unbound system times a cutoff factor. For the trial function of the unbound system, we use

$$\Psi_f(\mathbf{r}_i) = \Phi_0(\mathbf{r}_i)J(\mathbf{r}_i) \tag{6}$$

The function $\Phi_0(\mathbf{r}_i)$ is the model function and takes into account the antisymmetry of this fermionic system. The $J(\mathbf{r}_i)$ factor describes the correlation between the electrons and is chosen to be positive. This correlation factor usually includes variational parameters and different functional forms are available in the literature to describe accurately the electronic correlation up to relatively large systems.[16,17] In the present work we will use a simple wave function including only three parameters. The main advantage of employing a simple few-parameters wave function is to provide an easy physical insight on the behavior of interelectronic correlation with the variation in the confinement parameter.

In all of the different applications of this work, the model function $\Phi_0(\mathbf{r}_i)$ is chosen such that it satisfies the Schrödinger equation for n noninteracting electrons moving in a nuclear potential with electric charge Z:

$$\left[\sum_{i=1}^{n}\left(-\frac{1}{2}\nabla_i^2 - \frac{Z}{r_i}\right)\right]\Phi_0(r_i) = E_0\Phi_0(\mathbf{r}_i) \tag{7}$$

Then the expression for the energy, eq 4 reduces to

$$\langle H\rangle_{\Psi_t} = E_0 + \int_{\tau(\partial\tau)}|\Psi_t(\mathbf{r}_i)|^2\left\{\frac{1}{2}[\nabla_{3n}\ln(J(\mathbf{r}_i)w(\mathbf{r}_i))]^2 + \sum_{i<j}\frac{1}{r_{ij}}\right\}d\tau \tag{8}$$

The total energy of a n-electron atomic system is decomposed into two parts: E_0 representing the energy of the free n noninteracting electrons moving in an attractive potential of nucleus with charge Z and a second term accounting for the electron−electron repulsion energy, electronic correlations, and cutoff conditions. This expression is convenient for carrying out variational calculations. In the following we apply it to study confined helium, lithium, and carbon atoms with different boundary conditions.

2.4. Explicit Wave Function for Few-Electron Systems. *2.4.1. Helium Atom.* Three different confinements, spherical, two planes, and cylindrical, have been considered for the helium atom. This is done by using different forms of the confinement function $w(\mathbf{r}_i)$. Different expressions for the cutoff function, linear, quadratic, step-like function, have been considered in the literature.[18] The functional form for the cutoff function $w(r_i)$ used in this work was proposed by Laughlin and Chu.[19] It is extended here to the different geometries considered. In a recent work[20] the accuracy of this choice for the cutoff on the confined ground state of hydrogen atom has been studied. The exact solution of the latter atom is known under Dirichlet boundary conditions, and this allows a check of the accuracy of the different forms of the cutoff functions. Additional calculations made on the confined helium atom in spherical surfaces show also the validity of this choice for the cutoff function.

For an atom located at the center of an impenetrable sphere of radius r_c, the cutoff function is taken as

$$w_{\text{spherical}}(r_i) = \prod_{i=1}^{n}\left(1 - \frac{r_i}{r_c}\right)\exp\left(\frac{r_i}{r_c}\right) \tag{9}$$

When the atom is located on the z axis of a impenetrable cylinder, axial symmetry, of radius ρ_c, $w_{cylindical}$ is

$$w_{\text{cylindrical}}(\rho_i) = \prod_{i=1}^{n}\left(1-\frac{\rho_i}{\rho_c}\right)\exp\left(\frac{\rho_i}{\rho_c}\right) \tag{10}$$

where $\rho_i^2 = x_i^2 + y_i^2$. Finally, to describe an helium atom confined between two parallel impenetrable planes located at $\pm z_c$ the following cutoff function is employed

$$w_{\text{planar}}(z_i) = \prod_{i=1}^{n}\left(1-\frac{|z_i|}{z_c}\right)\exp\left(\frac{|z_i|}{z_c}\right) \tag{11}$$

We study both, the ground state and the first ^{3}S excited state. For both states Φ_0 is written as a Slater determinant

$$\Phi_0^{1S} = \frac{1}{\sqrt{2!}}\det\{\varphi_{100}|\uparrow\rangle, \varphi_{100}|\downarrow\rangle\}$$

$$\Phi_0^{3S} = \frac{1}{\sqrt{2!}}\det\{\varphi_{100}|\uparrow\rangle, \varphi_{200}|\uparrow\rangle\}$$

with $|\uparrow\rangle$ and $|\downarrow\rangle$ the electronic spin part and

$$\varphi_{nlm}(\mathbf{r}) = R_{nl}(r)Y_{lm}(\Omega)$$

with $Y_{lm}(\Omega)$ the spherical harmonic and R_{nl}

$$R_{10}(r) = 2Z^{3/2}e^{-Zr}, \quad R_{20}(r) = \frac{Z^{3/2}}{\sqrt{2}}\left(1-\frac{Z}{2}r\right)e^{-Z/2r}$$

has already been proposed in a previous paper .[21]

For the correlation factor, we use the following form

$$J(\mathbf{r}_1,\mathbf{r}_2) = [\cosh(\lambda r_1) + \cosh(\lambda r_2)]\exp\left(\frac{br_{12}}{1+ar_{12}}\right) \tag{12}$$

so that the trial function, eq 1, for these two states of the confined helium atom is

$$\Psi_t(\mathbf{r}_i) = [\Phi_0^{1S} \text{ or } \Phi_0^{3S}]J(\mathbf{r}_i)w(\mathbf{r}_i)$$

with w any of the three cutoff factors given in eqs 9, 10, or 11. This function satisfies the electron−electron cusps conditions governing the interaction for the short interelectronic distances and the electron−nucleus cusps conditions. The parameter λ is interpreted as a screening constant for one electron when it is located far away from the nucleus. The relevant part of the wave function representing the latter property is

$$\cosh(\lambda r_i)\exp(-Zr_i) \approx \exp[-(Z-\lambda)r_i]r_i \gg 1 \tag{13}$$

Such function, though very simple, is accurate and convenient for the calculation.

The expectation value of the energy has been calculated by using eq 8. The integral has been evaluated by using the VMC method with Metropolis sampling. Analytical expressions for $|\nabla(Jw)|^2$ can be obtained in a straightforward manner.

2.4.2. Lithium Atom. The wave function for the lithium atom ground, $1s^22s\ ^2S$ and $1s^22p\ ^2P$, and, $1s^23d\ ^2D$, excited states is a direct extension to the three-electron system of the previous one. For this atom we will consider spherical confinement only.

The Slater determinant part is built starting from hydrogenic orbitals ϕ_{nlm}

$$\Phi_0^{2S} = \frac{1}{\sqrt{3!}}\det\{\varphi_{100}|\uparrow\rangle, \varphi_{100}|\downarrow\rangle, \varphi_{200}|\uparrow\rangle\}$$

$$\Phi_0^{2P} = \frac{1}{\sqrt{3!}}\det\{\varphi_{100}|\uparrow\rangle, \varphi_{100}|\downarrow\rangle, \varphi_{210}|\uparrow\rangle\}$$

$$\Phi_0^{2D} = \frac{1}{\sqrt{3!}}\det\{\varphi_{100}|\uparrow\rangle, \varphi_{100}|\downarrow\rangle, \varphi_{320}|\uparrow\rangle\}$$

The spherical confinement, eq 9, is used for the cutoff function w. For the correlation factor, a product of two terms, one depending on the interelectronic distance and the other on the electron−nucleus distance, is employed

$$J(\mathbf{r}_i)w(\mathbf{r}_i) = \left\{\sum_{i<j}^{3}[\cosh(\lambda r_i)\cosh(\lambda r_j)]\prod_{i<j}^{3}\exp\left(\frac{br_{ij}}{1+ar_{ij}}\right)\right\}\left\{\prod_{i=1}^{3}\left(1-\frac{r_i}{r_c}\right)e^{r_i/r_c}\right\} \tag{14}$$

The trial wave functions for these three states Φ_0^{2S}, Φ_0^{2P}, and Φ_0^{2D} of the lithium atom under spherical confinement read

$$\Psi_t(\mathbf{r}_i) = [\Phi_0^{2S} \text{ or } \Phi_0^{2P} \text{ or } \Phi_0^{2D}]J(\mathbf{r}_i)w(\mathbf{r}_i) \tag{15}$$

Note that the factor depending on the interelectronic distance is of the same form as that employed for the helium atom. For the other factor, a pair product form employed in a previous work[22] is used because it provides a better performance from the variational point of view.

2.4.3. Carbon Atom. We focus on the carbon atom in order to study the effect of the spherical confinement on the electronic configuration. In particular we aim to compare the behavior under confinement of the ground state ^{3}P wave function of carbon atom with that of the hybridized configuration sp^3. The hybridized atomic orbitals are employed in quantum chemistry calculations to account for the valence of this atom. In doing so, two different orbital sets to build Φ_0 are considered.

In order to describe the ^{3}P ground state a single Slater determinant can be used

$$\Phi_0^{3P} = \frac{1}{\sqrt{6!}}\det\{\varphi_{100}|\uparrow\rangle, \varphi_{100}|\downarrow\rangle, \varphi_{200}|\uparrow\rangle, \varphi_{200}|\downarrow\rangle, \varphi_{211}|\uparrow\rangle, \varphi_{210}|\uparrow\rangle\} \tag{16}$$

with the form of the orbitals given above and

$$R_{21}(r) = \frac{Z^{3/2}}{2\sqrt{6}}Zre^{-Z/2r}$$

Hybrid orbitals are symmetry adapted atomic orbitals because they are constructed to provide a basis of atomic orbitals consistent with the observed structure of the molecules, e.g., ref 23. This is done by taking linear combinations to form a basis for a representation of the point symmetry group of the

Table 1. Ground-State Energy and Radial Expectation Values for the Helium Atom under Different Constraints for Some Values of the Constraint Distance [a]

d_c	const	λ	E	E_{Hyll}	$\langle r \rangle$	$\langle r_{ij} \rangle$
1.0	3D	0.00	1.01866(4)	1.015755	0.44279(2)	0.64795(4)
	2D	0.05	−0.52859(7)		0.55925(5)	0.83369(9)
	1D	0.50	−1.86606(6)		0.71691(8)	1.0825(1)
1.1	3D	0.50	0.01077(3)		0.47795(2)	0.70122(4)
	2D	0.45	−1.14577(7)		0.59531(5)	0.8891(1)
	1D	0.60	−2.14097(6)		0.74635(9)	1.1284(2)
1.2	3D	0.70	−0.70744(2)		0.51274(2)	0.75411(5)
	2D	0.575	−1.58350(7)		0.62662(5)	0.9373(3)
	1D	0.65	−2.33433(7)		0.76839(9)	1.1627(2)
1.3	3D	0.825	−1.22999(2)		0.54636(3)	0.80542(5)
	2D	0.675	−1.90036(6)		0.65777(6)	0.9855(1)
	1D	0.70	−2.47314(6)		0.79125(9)	1.1986(2)
1.4	3D	0.90	−1.61647(2)		0.57798(3)	0.85338(5)
	2D	0.75	−2.13348(6)		0.68731(6)	1.0315(1)
	1D	0.725	−2.57454(6)		0.80819(9)	1.2250(2)
1.5	3D	0.95	−1.90621(2)		0.60783(3)	0.89991(6)
	2D	0.80	−2.30743(6)		0.71376(7)	1.0727(1)
	1D	0.75	−2.64948(5)		0.82477(9)	1.2511(2)
2.0	3D	1.05	−2.60303(2)	−2.604038	0.73327(4)	1.09582(7)
	2D	0.90	−2.72192(4)		0.81224(7)	1.2275(1)
	1D	0.80	−2.82508(4)		0.87972(9)	1.3379(2)
3.0	3D	1.0	−2.87060(2)	−2.872495	0.87392(7)	1.3228(1)
	2D	0.875	−2.88044(3)		0.89839(8)	1.3660(1)
	1D	0.80	−2.89118(3)		0.9231(1)	1.4075(2)
4.0	3D	0.9	−2.89883(2)	−2.900485	0.91761(9)	1.3964(2)
	2D	0.825	−2.89856(2)		0.9237(1)	1.4078(2)
	1D	0.775	−2.89954(2)		0.9325(1)	1.4229(2)
5.0	3D	0.85	−2.90188(2)	−2.903410	0.93475(9)	1.4258(2)
	2D	0.80	−2.90127(2)		0.9347(1)	1.4262(2)
	1D	0.75	−2.90114(2)		0.9314(1)	1.4211(2)
6.0	3D	0.85	−2.90121(2)	−2.903696	0.9538(1)	1.4578(2)
	2D	0.775	−2.90179(2)		0.9353(1)	1.4274(2)
	1D	0.75	−2.90152(2)		0.9361(1)	1.4289(2)
10.0	3D	0.75	−2.90196(2)	−2.903724	0.9355(1)	1.4279(2)
	2D	0.725	−2.90185(2)		0.9291(1)	1.4173(2)
	1D	0.725	− 2.90177(2)		0.9325(1)	1.4229(2)
20.0	3D	0.75	− 2.90179(2)	−2.903724	0.9333(1)	1.4242(2)
	2D	0.725	−2.90178(2)		0.9340(1)	1.4255(2)
	1D	0.725	−2.90178(2)		0.9348(1)	1.4267(2)

[a] 3D stands for spherical, 2D for cylindrical, and 1D for two plane impenetrable surfaces. The energy in the 3D case is compared with the highly accurate value, E_{Hyll}, of Laughlin and Chu[19] calculated by using Hylleraas-type basis functions. In parentheses we show the statistical error in the last digit.

molecule. For example, the four sp^3 hybrid orbitals of the carbon atom form a basis for a representation of the group T_d and are given as

$$\varphi_1 = \frac{1}{2}(2s + 2p_x + 2p_y + 2p_z),$$
$$\varphi_2 = \frac{1}{2}(2s + 2p_x - 2p_y - 2p_z) \quad (17)$$
$$\varphi_3 = \frac{1}{2}(2s - 2p_x + 2p_y - 2p_z),$$
$$\varphi_4 = \frac{1}{2}(2s - 2p_x - 2p_y + 2p_z) \quad (18)$$

where p_x, p_y, and p_z are the real spherical harmonics. The spatial distribution of the sp^3 orbitals is such that the directions of maximum density point from the center of the tetrahedron to its corners. Therefore, these atomic hybrid orbitals of the carbon atom are specially suited to build molecular orbitals of compounds like methane.

Starting from the hybrid sp^3 orbitals given in eq 18 a Slater determinant $\Phi_0^{sp^3}$ is built

$$\Phi_0^{sp^3} = \frac{1}{\sqrt{6!}} \det\{\varphi_{100}|\uparrow\rangle, \varphi_{100}|\downarrow\rangle, \varphi_1|\uparrow\rangle, \varphi_2|\downarrow\rangle, \varphi_3|\uparrow\rangle, \varphi_4|\uparrow\rangle\} \quad (19)$$

To study the performance of both set of orbitals for confined carbon atom, the spherical confinement is considered. For the correlation and confinement factors, the following form is employed

$$J(\mathbf{r}_i)w(\mathbf{r}_i) = \left\{\prod_{i=1}^{6} \cosh(\lambda r_i) \prod_{i<j}^{6} \exp\left(\frac{br_{ij}}{1 + ar_{ij}}\right)\right\}\left\{\prod_{i=1}^{6}\left(1 - \frac{r_i}{r_c}\right)e^{r_i/r_c}\right\} \quad (20)$$

The two trial wave functions employed for the ground state of the carbon atom under spherical confinement are

$$\Psi_t = [\Phi_0^{3p} \text{ or } \Phi_0^{sp^3}]J(\mathbf{r}_i)w(\mathbf{r}_i) \quad (21)$$

3. RESULTS AND DISCUSSION

This section presents the results obtained with the correlated wave function proposed in the previous section. They are compared with the data in the literature when available. The present trial wave function has only three variational parameters. They have been first optimized for the free systems. When the constraint is added we have also optimized these parameters. We found that among the three parameters a, b, and λ, the optimized values of the parameters a and b do not vary significantly along the confinement radius r_c in all the atoms studied here. For this reason we present in the tables the results obtained with fixed values for a and $b = 0.5$ determined at once for the free system. The λ parameter is optimized for the different values of the constraint distances r_c, ρ_c, or z_c.

This suggests that for the atoms studied here the interelectronic correlation remains almost unaffected by the confining potential, and the major contribution of this part of the energy comes from close interelectronic distances, cusps conditions, that are favored by the strong confining conditions. For the atoms studied here this is in agreement with the observation made by Ludeña who noted that the correlation energy is largely independent of the size of the enclosing sphere .[24] This conclusion cannot be straightforwardly extended to confined heavier atoms where[2] first relativistic effects are important, and second the use

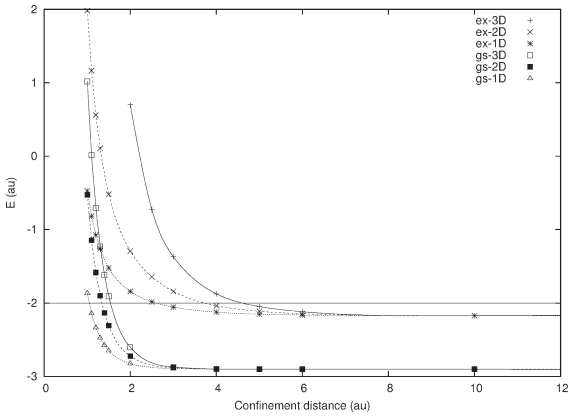

Figure 1. Total energy at different confinement distances for the He atom ground state, *gs* values, and 2^3S excited state, *ex* values. The 3D stands for spherical, 2D for cylindrical, and 1D for two plane impenetrable surfaces. The lines are for guiding the eyes. Statistical error is smaller than the symbol size.

of the Dirichlet boundary condition to model confinement is not relativistically consistent.

3.1. Confined Helium Ground State. The energy values for helium ground state under different constrains: spherical (3D), axial (2D), and planar (1D) are reported in Table 1. The corresponding values are plotted in Figure 1. In all of the cases, it can be remarked that the energies are increased when the constraint is stronger. The raise in energy is more important when the atom is located at the center of a impenetrable sphere than on the axis of a impenetrable cylinder or in the middle between two impenetrable planes. The assumption that the atom lies at the center of a repulsive sphere is an exact result in this case, but it should not be extended when the surface is attractive, like a fullerene surface. The values for ground state in the 3D constraint are in good agreement with the highly accurate energies obtained from expansions in terms of Hylleraas-type basis functions, results included in Table 1, and also with other data available in the literature, see ref 19 and references therein. In this respect it is very useful to evaluate and test a new approach. To the best of our knowledge, no other data are presently available for 2D or 1D constrains. It might be of interest to note that in the latter constrains (2D, 1D), the space allowed to the atom is still infinite and, however, a significant effect of the confinement results. Such constraint is similar to the constraint for excitons in quantum wire (2D) or quantum well (1D). In Table 1 the radial expectation values $\langle r\rangle$ and $\langle r_{ij}\rangle$ calculated in the different constraints are also reported. It can be seen that for the ground state, both $\langle r\rangle$ or $\langle r_{ij}\rangle$ decrease with the constraint distance for all kind of confinements. The effect of confinement on these quantities is larger for the 3D than the 2D and 1D constraints.

3.2. Confined Helium Excited State ^{3}S. For excited states the wave function is more diffuse in the space, and the raise in energy is expected to be significant at larger values of the constraint than in the case of the ground state. In Table 2 we report the values of the energies for the helium He(1s,2s) ^{3}S excited state. These results are plotted in Figure 1. The raise in energy is significant at $r_c = 6$ au for 3D constraint and around ρ_c, $z_c = 4$ au for cylindrical and planar constrains, respectively. The ionization of the excited helium atom occurs when the energy of this atom is equal to the energy of the compressed ion $He(1s)^+$, which is practically equal to $E = -2$ au in this range of r_c, ρ_c, z_c values. With the help of the results shown in Figure 1 it can be obtained that this energy value is reached for $r_c \approx 4.5$ au, $\rho_c \approx 4$ au and $z_c \approx 3$ au.

In Figure 2 the expectation value $\langle r_{ij}\rangle$ determined for the different constraints are plotted. For the closed 3D constraint the $\langle r_{ij}\rangle$ values decrease obviously at all the values of r_c. But for 2D and 1D constraint, the space is still infinite, and $\langle r_{ij}\rangle$ decreases down to $\rho_c = 4$ au and $z_c = 3$ au and increases again. These values should be related to the corresponding values of these parameters for the ionization as determined above. The situation is significantly different for the ground state.

Table 2. Total Energy and Radial Expectation Values of the 2^3S Excited State of the Helium Atom under Different Constraints for Some Values of the Constraint Distance[a]

d_c	const	λ	E	$\langle r\rangle$	$\langle r_{ij}\rangle$
1.0	3D				
	2D	0.675	1.9839(4)	2.915(2)	5.343(4)
	1D	0.475	−0.4736(2)	2.3696(6)	4.179(1)
1.1	3D				
	2D	0.7	1.1636(4)	3.159(2)	5.808(4)
	1D	0.475	−0.8189(2)	2.3754(6)	4.182(1)
1.2	3D				
	2D	0.7	0.5604(3)	3.167(2)	5.810(4)
	1D	0.475	−1.0717(1)	2.3819(6)	4.187(1)
1.3	3D				
	2D	0.7	0.1053(3)	3.173(2)	5.806(4)
	1D	0.5	−1.2610(1)	2.4925(6)	4.396(1)
1.5	3D				
	2D	0.7	−0.5205(2)	3.179(2)	5.796(4)
	1D	0.5	−1.52170(9)	2.5035(6)	4.407(1)
2.0	3D	0	0.7004(2)	0.93115(3)	1.46115(6)
	2D	0.6	−1.2916(1)	2.4285(9)	4.279(2)
	1D	0.475	−1.84207(6)	2.4180(5)	4.221(1)
2.5	3D	0	−0.72776(7)	1.0919(4)	1.73303(8)
	2D	0.55	−1.64206(8)	2.2050(6)	3.822(1)
	1D	0.45	−1.98126(3)	2.3449(4)	4.0692(8)
3.0	3D	0	−1.36873(2)	1.22921(5)	1.97062(8)
	2D	0.5	−1.83986(5)	2.0632(5)	3.5342(9)
	1D	0.45	−2.05443(2)	2.3657(4)	4.1031(8)
4.0	3D	0.4	−1.87388(1)	1.51565(6)	2.4750(1)
	2D	0.45	−2.03480(2)	2.0360(3)	3.4668(6)
	1D	0.45	−2.12324(1)	2.4141(4)	4.1899(8)
5.0	3D	0.475	−2.04758(1)	1.75936(8)	2.9210(1)
	2D	0.45	−2.11193(1)	2.1447(3)	3.6683(6)
	1D	0.45	−2.15081(1)	2.4645(4)	4.2844(7)
6.0	3D	0.5	−2.11740(1)	1.9631(1)	3.3035(2)
	2D	0.475	−2.14463(1)	2.3067(3)	3.9769(5)
	1D	0.45	−2.16287(1)	2.5124(4)	4.3761(8)
10.0	3D	0.5	−2.17191(1)	2.4563(2)	4.2545(4)
	2D	0.45	−2.17235(1)	2.5157(3)	4.3804(6)
	1D	0.425	−2.17290(1)	2.6387(4)	4.6204(7)
20.0	3D	0.45	−2.17442(1)	2.6045(4)	4.5457(8)
	2D	0.425	−2.17410(1)	2.5927(4)	4.5309(8)
	1D	0.425	−2.17400(1)	2.6159(4)	4.5762(7)

[a] 3D stands for spherical, 2D for cylindrical, and 1D for two plane impenetrable surfaces. In parentheses we show the statistical error in the last digit.

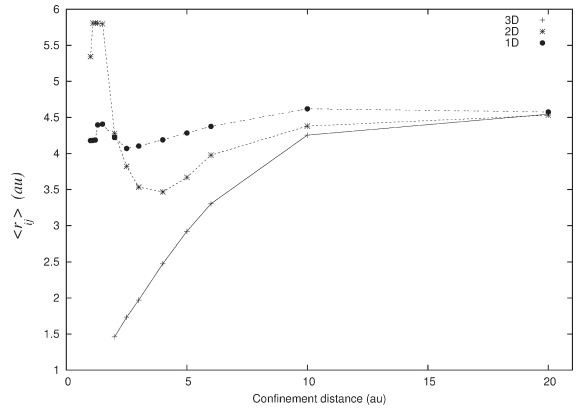

Figure 2. Expectation value of the interelectronic distance as a function of the confinement parameter for the 2^3S excited state of the He atom. The 3D stands for spherical, 2D for cylindrical, and 1D for two planes impenetrable surfaces. The lines are for guiding the eyes. Statistical error is smaller than the symbol size.

3.3. Confined Lithium Atom. The results for this three-electron system, ground state ^2S and excited states ^2P and ^2D, confined in an impenetrable sphere are determined by using fully correlated wave function given by eq 15 are presented in Table 3 and also displayed in Figure 3. The results have been obtained with $a = 0.7$, which has been fixed by performing a calculation for a very large value of r_c. Like two-electron systems we do not observe any significant change in the optimized value of the parameter a when r_c is varied, and consequently we use the same value of parameter a ($a = 0.7$) for all the calculations. Only few calculations are available in the literature for the ground state and to the best of our knowledge none exist for excited states. The ground-state energies of ref 24 obtained by using the Hartree–Fock approach are reported in Table 3. We note from Table 3 and Figure 3 that our results for the energy are significantly lower than the Hartree–Fock ones for $r_c > 2$ au. In order to check the accuracy of the correlated wave function, the energy of a confined Li atom with $r_c = \infty$ (uncompressed atom) has been calculated. The ground-state energy obtained with the simple wave function of eq 15 $E = -7.47360(3)$ au is in very a good agreement with the high-precision variational results of Yan and Drake[25] $E = -7.478060$ au calculated by using multiple basis sets in Hylleraas coordinates. As stated above, the optimized value of the parameter a remains constant at all confinement radii. This suggests that the electron–electron interaction is almost independent of the confinement. This finding is in agreement with a conclusion already drawn by Gimarc[26] who noted that in the case of helium the correlation energy is largely independent of the size of the enclosing sphere.

The λ values are strongly dependent on the confinement as illustrated by the changes in the values of λ in Table 3. Like the confined H^- ion and the He atom, the value of the parameter λ also tends to zero for a strongly confined Li atom. Thus the electronic screening of the nuclear charge by the electrons decreases when the confinement radius becomes small.

The results for the confined lithium atom in the excited state ^2P are reported in Table 3 and plotted in the Figure 3. The energy of the free atom in this state obtained by the present method is $E = -7.40315(4)$ au to be compared to the accurate value[25] $E = -7.410157$ au. When the confinement is stronger, the energy increases. A crossing with the ground state occurs at $r_c = 3.3$ au.

Table 3. Total Energy and Radial Expectation Values of the Ground State $(1s^22s)\ ^2S$ and $(1s^22p)\ ^2P$ and $(1s^23d)\ ^2D$ Excited State in Spherical Confinement as a Function of the Radius[a]

r_c	λ	$\langle r \rangle$	$\langle r_{ij} \rangle$	E	E_{SCF}
			$(1s^22s)\ ^2S$		
1.5	0	0.61113(2)	0.93871(3)	−1.9805(3)	−2.2281
2.0	0.3	0.72939(3)	1.13934(4)	−5.1305(2)	−5.1782
3.0	0.675	0.94861(4)	1.52472(7)	−6.83046(6)	−6.8027
4.0	0.775	1.12640(6)	1.8524(1)	−7.24481(4)	−7.2046
5.0	0.8	1.26424(8)	2.1143(2)	−7.38155(4)	−7.3395
6.0	0.825	1.3853(1)	2.3469(2)	−7.43428(3)	−7.3925
8.0	0.825	1.5370(2)	2.6430(3)	−7.46581(3)	−7.4249
10.0	0.825	1.6289(2)	2.8215(4)	−7.47176(3)	
∞	0.775	1.6855(3)	2.9380(5)	−7.47360(3)	−7.4327
∞	Hyll	1.66317	2.88947	−7.478060	
			$(1s^22p)\ ^2P$		
1.5	0.48	0.60585(2)	0.93232(4)	−3.9142(2)	
2.0	0.7	0.73002(3)	1.13783(4)	−5.7740(1)	
3.0	0.83	0.93032(4)	1.48703(7)	−6.85948(6)	
4.0	0.88	1.09853(7)	1.7956(1)	−7.16837(3)	
5.0	0.92	1.2542(1)	2.0890(2)	−7.28902(3)	
6.0	0.94	1.3888(1)	2.3471(2)	−7.34415(4)	
8.0	0.96	1.6028(2)	2.7628(3)	−7.38536(3)	
10.0	0.96	1.7366(2)	3.0256(5)	−7.39724(4)	
∞	0.95	1.9918(5)	3.5303(9)	−7.40315(4)	
∞	Hyll	1.95712	3.47070	−7.410157	
			$(1s^23d)\ ^2D$		
2.0	0	0.77719(3)	1.21442(5)	−3.6126(3)	
3.0	0	0.97962(4)	1.58763(7)	−5.9095(1)	
4.0	0.35	1.18591(6)	1.9778(1)	−6.61559(9)	
5.0	0.46	1.39216(7)	2.3754(1)	−6.92147(6)	
6.0	0.52	1.5925(1)	2.7664(2)	−7.07723(6)	
8.0	0.60	1.9887(2)	3.5457(4)	−7.21916(5)	
10.0	0.63	2.3322(3)	4.2261(5)	−7.27530(4)	
∞	0.65	3.825(2)	7.201(3)	−7.32579(4)	
∞	Hyll	3.87641	7.28852	−7.335524	

[a] The ground-state results are compared with the self consistent field energy, E_{SCF} of Ludeña,[24] and the results for the unconfined state ($r_c = \infty$) are compared with the very precision values of Yan and Drake,[25] Hyll, calculated by using multiple basis set in Hylleraas coordinates.

Changes of the order of the atomic levels and the ordering of filling of the shells are observed in compressed atoms as already found by different authors, see refs 1 and 3 and references therein.

The results for the confined lithium atom in the excited state ^2D are reported in Table 3 and plotted in the Figure 3. The energy of the free atom in this state obtained form the variational wave function of this work is $E = -7.32579(4)$ au to be compared to the accurate value[25] $E = -7.335524$ au. It is interesting to remark that the rise in energy versus r_c is important and becomes significant at relatively large values of $r_c \simeq 8$ au.

3.4. Confined Carbon Atom. It is well-known that the carbon atom needs a rearrangement of its electronic ground-state configuration $2s^22p^2$ in order to account for molecules such as CH_4. In basic text books an ad hoc hypothesis is made that consists to mix the 2s and 2p orbitals to form four new hybridized

orbitals sp^3, where the four electrons can be placed to form the right number of chemical bounds. This hypothesis is often said to be a purely mathematical device, but necessary, to describe the basic chemical properties of the carbon atom.

We propose here an analysis that might be of pedagogical interest and gives some more physical insight of mechanism of this electronic rearrangement. In this section we show that the mixing of the 2s and 2p orbitals to form the four sp^3 orbitals could be interpreted as a natural consequence of the constraints induced by the surrounding of the carbon, i.e., the protons of hydrogen atoms close to this atom.

The present approach, not dependent on the self consistent field approach, is convenient to calculate the consequence of the confinement by impenetrable sphere on the ground state C $(1s^2 2s^2 2p^2)$ ^{3}P or hybridized C $(1s^2(2sp^3)^4)$ on the same footing. The values of the energies of the carbon atom in the ^{3}P and hybridized state sp^3 using the VMC approach are reported at different values of the confinement radii r_c in Table 4. For the free system (no constraint) the ground-state energy of the ^{3}P calculated with the present simple wave function of eq 21 is $E(^3\mathrm{P}) = -37.6786(2)$ au to be compared to the self consistent field energy $E = -37.6886$ au, and the estimated exact energy[27] is $E = -37.8450$ au. The energy of the hybridized configuration sp^3 calculated by the present approach is $E(sp^3) = -37.4793(2)$ au, i.e., 0.199 au above the ground-state energy. When confinement, measured by the cutoff radius r_c, becomes stronger, the energies are raised.

In order to improve the energy of the carbon atom obtained through the VMC approach, we made further calculations using the DMC approach both for the ground state $(1s^2 2s^2 2p^2)$ ^{3}P and the hybridized C $(1s^2(2sp^3)^4)$ under confinement. The results are displayed in Table 4. It can be noticed that within this approach, the energies are significantly improved respectively $E(^3\mathrm{P}) = -37.7996(9)$ au and $E(sp^3) = -37.6333(5)$ au for the free systems, i.e., 0.166 au above the ground-state energy.

In Figure 4 the energy difference $\Delta E = E(^3\mathrm{P}) - E(^3sp^3)$, i.e., the threshold of the transition from the ground state to the hybridized one deduced with the VMC and the DMC methods, is plotted versus r_c. A crossing $(\Delta E = 0)$ is found in the neighborhood of $r_c = 1.6$ au. It can be said that the differences between both approaches are small, and the VMC method is able to describe correctly the behavior of the carbon atom under

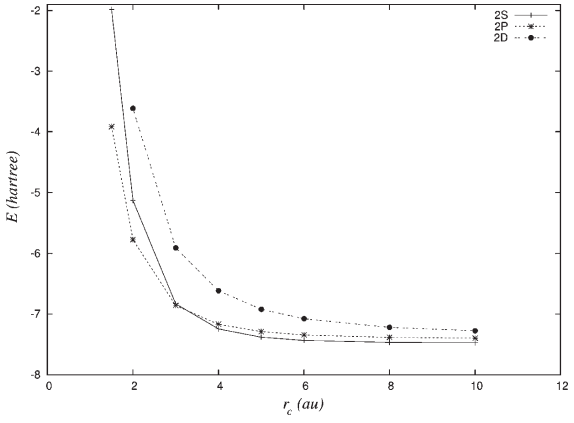

Figure 3. Ground- and excited-state energies of the lithium atom under spherical as a function of the confinement radius, r_c. The lines are for guiding the eyes. Statistical error is smaller than the symbol size.

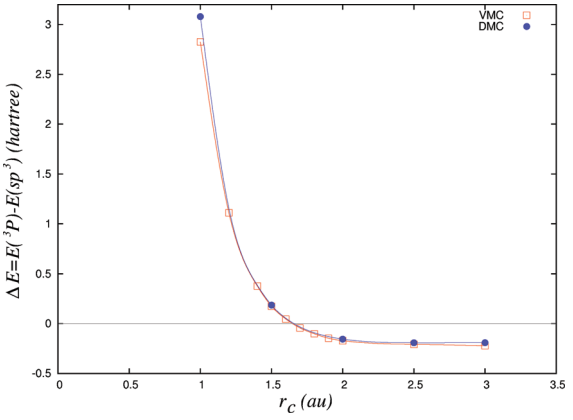

Figure 4. Difference of energy obtained from wave functions built from atomic and orbitals hybrid orbitals for the ground state of the carbon atom surrounded by a nonpenetrable spherical surface of radius r_c. The lines are for guiding the eyes. Statistical error is smaller than the symbol size.

Table 4. Ground-State Energy of the Carbon Atom in Spherical Confinement As a Function of the Radius[a]

r_c	$E_{SCF}(^3\mathrm{P})$	$E_{VMC}(^3\mathrm{P})$	$E_{DMC}(^3\mathrm{P})$	$E_{VMC}(sp^3)$	$E_{DMC}(sp^3)$	$\lambda(^3\mathrm{P})$	$\lambda(sp^3)$
1.0	−10.9178	−10.9832(4)	−11.1042(5)	−13.8081(5)	−14.183(1)	0.008	0.026
1.2		−22.3683(3)		−23.4792(3)		0.040	0.070
1.4		−28.3927(2)		−28.7694(2)		0.25	0.41
1.5	−30.2169	−30.3303(2)	−30.3856(6)	−30.5048(5)	−30.572(3)	0.43	0.52
1.6		−31.8184(2)		−31.8647(2)		0.57	0.62
1.7		−32.9704(2)		−32.9269(2)		0.63	0.69
1.8		−33.8709(4)		−33.7692(2)		0.70	0.74
1.9		−34.5829(8)		−34.4364(2)		0.74	0.79
2.0	−35.0588	−35.1435(2)	−35.2084(6)	−34.9722(2)	−35.0526(9)	0.79	0.83
2.5	−36.6548	−36.6681(3)	−36.7939(6)	−36.4604(3)	−36.6023(8)	0.89	0.93
3.0	−37.2570	−37.2441(3)	−37.3906(7)	−37.0227(3)	−37.200(1)	0.92	0.96
∞	−37.6885	−37.6786(2)	−37.7996(9)	−37.4793(2)	−37.6333(5)	0.84	0.88

[a] In column ^{3}P column we report the results obtained from Coulomb orbitals, while in sp^3 column we show the energy obtained from hybridized orbitals. In parentheses we show the statistical error in the last figure. The λ parameter in the correlation factor in each calculation is reported. The results are compared with the self consistent field energy, E_{SCF}, of Ludeña.[24]

confinement. The present model, based on a simple impenetrable sphere confinement, shows that the carbon hybridization sp^3 might be understood as due to the confinement by the surrounding atoms when it becomes sufficiently strong. Briefly stated, the spherical confinement has induced a raise in the energy, corresponding to the symmetry group of the ^3P state, equal to the energy of carbon atom in the symmetry group T_d at r_c around 1.6 au.

As explained previously the choice of pure hydrogenic orbitals in the present wave function allows a direct calculation of the nonspectroscopic state. However for the carbon atom the energy calculated within the VMC is a little bit degraded. For the ground state of the unconfined atom, the VMC obtained by using self consistent field orbitals and a more complex correlation factor[11] is $E = -37.8064(3)$, and the fixed node DMC value is $E = -37.8297(2)$.

It is of interest to recall here that the first spectroscopic excited state $2s2p^3\ ^5S^o$ with four unpaired electrons in the carbon atom is about 0.1537 au above the ground state,[28] and it could be a candidate to account for the electronic rearrangement in the carbon atom. However the spin value, $S = 2$, of this term precludes the transition from the, $S = 1$, ground state. The nearest triplet states with four unpaired electrons are[28] the, $2s2p^3\ ^3D^o$ and $2s2p^3\ ^3P^o$, terms with excitation energies of $E = 0.2920$ and 0.3429 au, respectively. Thus as a consequence of this energy gap they cannot easily be populated from the ground state.

The present model suggests that the constraint by the surrounding atoms induces first a transitory state in the carbon atom, the hybridized state, followed by the chemical binding resulting in a stable four bond molecule.

4. CONCLUSIONS

In the present work a functional of the energy has been derived in the framework of the VMC method to study confined systems by nonpenetrable surfaces of different symmetries. The functional has been applied to study ground and excited states of some atoms under different constraints. In all cases the energies of the systems, He, Li, and C, are raised when the confinement parameter becomes stronger. Average values of the interparticle distances (electron−nucleus $\langle r \rangle$ and electron−electron $\langle r_{ij} \rangle$) are also determined.

It is observed that for the first excited ^3S of helium atom, the values of $\langle r_{ij} \rangle$ versus the constraint parameter present a minimum when the confinement results from impenetrable cylinder or planes at values corresponding to the ionization threshold of this excited atom.

The study of the confined carbon atom suggests a possible mechanism responsible of the hybridization of the s,p orbitals of this atom in order to explain the four chemical bonds generally observed with the carbon atom.

We hope that the present extension of the VMC to confined nonrelativistic systems will be useful to study larger systems including molecules. In particular the confinement might play an important role in the chemical reactivity of molecules, even in biology, for example, in enzymatic reactions when the substrate is enclosed in the active site of the enzyme.

AUTHOR INFORMATION

Corresponding Author

*E-mail: fa1sarua@uco.es.

ACKNOWLEDGMENT

A.S. thanks partial support for this work to the Spanish Dirección General de Investigación Cientfica y Técnica (DGICYT) and FEDER under contract FIS2009--07390 and by the Junta de Andalucía.

REFERENCES

(1) Connerade, J.-P.; Dolmatov, V.; Lakshmi, P. *J. Phys. B: At. Mol. Phys.* **2000**, *33*, 251.
(2) Connerade, J.-P.; Semaoune, R. *J. Phys. B: At. Mol. Phys.* **2000**, *33*, 3467.
(3) Dolmatov, V.; Baltenkov, A.; Connerade, J.-P.; Manson, S. *Radiat. Phys. Chem.* **2004**, *70*, 417–433.
(4) Sako, T.; Diercksen, G. *J. Phys. B: At. Mol. Phys.* **2003**, *36*, 1681–1702.
(5) Sarkar, U.; Giri, S.; Chattaraj, P. K. *J. Phys. Chem. A* **2009**, *113*, 10759–10766.
(6) Jaskolski, W. *Phys. Rep.* **1996**, *27*, 1–66.
(7) Cruz, S. In *Advances in Quantum Chemistry*; Sabin, J., Brandas, E., Ed.; Elsevier: San Diego, CA, 2009; Vol. 57; pp 255−283.
(8) Connerade, J.-P.; Kengkan, P. *Idea-Finding Symposium*; EP Systema: Frankfurt, Germany, 2003; pp 35−46.
(9) Hammond, B. L.; Lester, W. A., Jr.; Reynolds, P. J. *Monte Carlo Methods in ab initio Quantum Chemistry*; World Scientific: Singapore, 1994.
(10) Foulkes, W. M. C.; Mitáš, L.; Needs, R. J.; Rajagopal, G. *Rev. Mod. Phys.* **2001**, *73*, 33.
(11) López-Ríos, P.; Ma, A.; Drummond, N.; Towler, M. D.; Needs, R. J. *Phys. Rev. E* **2006**, *74*, 066701.
(12) Parker, W.; Wilkins, J.; Hennig, R. *Phys. Status Solidi B* **2011**, *248*, 267.
(13) Seth, P.; López-Ríos, P.; Needs, R. J. *J. Chem. Phys.* **2011**, *134*, 084105.
(14) Sako, T.; Diercksen, G. *J. Phys.: Condens. Matter* **2005**, *17*, 5159–5178.
(15) Pupyshev, V. I.; Bobrikov, V. *Int. J. Quantum Chem.* **2004**, *100*, 528–538.
(16) Drummond, N.; Towler, M. D.; Needs, R. J. *Phys. Rev. B* **2004**, *70*, 235119.
(17) Buendía, E.; Gálvez, F. J.; Sarsa, A. *Chem. Phys. Lett.* **2008**, *465*, 190–192.
(18) Flores-Riveros, A.; Rodríguez-Contreras, A. *Phys. Lett. A* **2008**, *372*, 6175–6183.
(19) Laughlin, C.; Chu, S.-I. *J. Phys. A: Math. Theor.* **2009**, *42*, 265004.
(20) Le Sech, C.; Banerjee, A. *J. Phys. B: At. Mol. Phys.* **2011**, *44*, 105003.
(21) Banerjee, A.; Kamal, C.; Chowdhury, A. *Phys. Lett. A* **2006**, *350*, 121–125.
(22) Le Sech, C.; Sarsa, A. *Phys. Rev. A* **2001**, *63*, 022501.
(23) Weissbluth, M. *Atoms and Molecules*; Academic Press: San Diego, CA, 1978.
(24) Ludeña, E. *J. Chem. Phys.* **1978**, *69*, 1770–1775.
(25) Yan, Z.-C.; Drake, G. *Phys. Rev. A* **1995**, *52*, 3711–3717.
(26) Gimarc, B. *J. Chem. Phys.* **1967**, *47*, 5110–5115.
(27) Chakravorty, S. J.; Gwaltney, S. R.; Davidson, E. R.; Parpia, F.; Fischer, C. F. *Phys. Rev. A* **1993**, *47*, 3649–3670.
(28) Ralchenko, Y.; Kramida, A. E.; Reader, J. *NIST Atomic Spectra Database*, version 4.0.1; NIST ASD Team: Gaithersburg, MD, 2011. Accessed April 11, 2011.

JCTC Journal of Chemical Theory and Computation

ARTICLE

pubs.acs.org/JCTC

Intra- and Interatomic Spin Interactions by the Density Functional Theory plus *U* Approach: A Critical Assessment

Yachao Zhang and Hong Jiang*

Beijing National Laboratory of Molecular Sciences, State Key Laboratory of Rare Earth Materials Chemistry and Applications, College of Chemistry and Molecular Engineering, Peking University, Beijing, 100871, China

Supporting Information

ABSTRACT: Accurate evaluation of the total energy difference between different spin states in molecular magnetic systems is currently a great challenge in theoretical chemistry. In this work we assess the performance of the density functional theory plus the Hubbard *U* (DFT+*U*) approach for the first-principles description of the high spin-low spin (HS-LS) splitting and the exchange coupling constant, corresponding to the intra- and interatomic spin interactions, respectively. The former is investigated using a set of mononuclear ion complexes with different HS-LS splitting, including seven spin-crossover (SCO) compounds, while the latter is investigated in a series of binuclear copper complexes covering both ferromagnetic and antiferromagnetic interactions. We find that the DFT+*U* approach can reproduce experimental data as accurately as the hybrid functionals approach but with much lower computational efforts. We further analyze the effect of *U* in terms of spin density on magnetic centers, and we find that the main effect of the *U* correction can be attributed to the enhanced localization of magnetic orbitals. Even taking the uncertainty related to the determination of *U* into account, we think the DFT+*U* approach is an efficient and predictive first-principles method for the SCO phenomenon and interatomic magnetic interactions.

1. INTRODUCTION

Recent years have seen a remarkable revival of interest in molecular magnetism[1,2] due to the unique role it plays in molecule-based spintronics.[3,4] By exploiting electronic charge and spin degrees of freedom simultaneously at the molecular level, molecular spintronics holds great hope on a wide range of applications, such as molecule-based memory,[5] switches,[6] and quantum computation.[7,8] A large number of molecular magnetic systems have been discovered and brought under intensive investigation. Among them two kinds of materials, spin-crossover (SCO)[9] compounds and single-molecule magnets (SMMs),[10] are of particular interest. Their unique magnetic bistable states and spin transition (reversal) behavior make them promising candidates for data storage materials, switching devices, displays, and sensors.[5,6,11,12] A SCO compound is one in which an intra-atomic, reversible low spin-high spin (LS-HS) transition, often occurring in octahedral coordinated d^4–^{7} transition-metal complexes, can be readily induced by a variety of external stimuli, such as temperature, pressure, and light irradiation. The necessary condition for the spin transition to occur is that the perturbation energy is approximately equal to the energy splitting between the LS and the HS states:

$$\Delta E_{\text{H-L}} \equiv E_{\text{HS}} - E_{\text{LS}} \tag{1}$$

The energy splitting $\Delta E_{\text{H-L}}$ largely determines the critical parameter characterizing the transition, such as the spin transition temperature (T_c).[9,13] Physically $\Delta E_{\text{H-L}}$ is mainly determined by the two competing factors, the effective electron-pairing energy (P) of the d electrons and the crystal-field splitting (Δ_o), which, when dominant, favors HS and LS ground states, respectively.[14] The magnitude of $\Delta E_{\text{H-L}}$ in typical SCO compounds is usually quite small, falling in the range of 0–0.3 eV (i.e., 0–30 kJ/mol).[13] An accurate evaluation of this quantity is therefore highly challenging from a theoretical point of view. While the SCO phenomenon is mainly determined by the intra-atomic spin coupling, a SMM is characterized by a strong interatomic spin interaction, which gives rise to a large collective ground-state spin (S). When the large spin is combined with a large magnetic anisotropy as a result of the spin–orbit coupling (SOC), the spin-reversal process between spin-up and spin-down configurations will be blocked by an energy barrier DS^2 (D, axial zero-field splitting parameter), which eventually determines the blocking temperature (T_B).[10,15] A room-temperature T_B is required for a SMM system to be practically useful, for which a large S and/or a large D are needed. Large ground-state spins can be formed from strong collective interactions among local magnetic moments in polynuclear molecular clusters (e.g., $Mn_{12}O_{12}$).[10] The interatomic spin–spin interaction is usually described by a phenomenological Heisenberg Hamiltonian:[16]

$$\hat{H} = -J\hat{S}_i \cdot \hat{S}_j \tag{2}$$

Here $\hat{S}_i$ and $\hat{S}_j$ represent the spin operators of the coupling magnetic centers i and j, respectively, and J is the intersite exchange coupling constant that characterizes the type [positive J, ferromagnetic (FM); negative J, antiferromagnetic (AFM)] and the strength of the magnetic interactions between neighboring magnetic centers. Compared to S, it is even more challenging to attain a large D, which depends on both strong spin–orbit coupling and constructive alignment of individual anisotropy axes on different magnetic centers. To make things

Received: May 2, 2011
Published: August 01, 2011

more complicated, there is clear evidence from both theory and experiment that the total magnetic anisotropy of a polynuclear cluster can often be dramatically reduced as a result of mutual cancellation of the local anisotropies so that a large ground-state spin S is often accompanied by a very small zero-field splitting.[17]

Accurate evaluation of the two key parameters, $\Delta E_{\text{H-L}}$ and J, is currently a great challenge in theoretical chemistry. Both quantities are determined by the energy difference between different spin configurations of open-shell (i.e., with unpaired electrons) systems, for which theoretical chemistry is much less well developed than that of closed-shell systems. For open-shell systems, the electronic ground state in general cannot be described based on the single Slater determinant-based approaches, like Hartree−Fock (HF) or Kohn−Sham (KS) density functional theory (DFT). A theoretically rigorous treatment of them requires using correlated wave function-based approaches, such as the multireference perturbation theory (e.g., CASPT2), configuration interaction (MRCI), or coupled cluster (MRCC) methods.[18−22] They are, however, too expensive to be applied routinely for practically interesting molecular magnetic systems with tens or even hundreds of atoms. It is even more difficult to apply the correlated wave function-based approaches to crystalline systems, the form in which molecular magnetic systems are usually studied experimentally. Currently most first-principles studies of molecular magnetic systems are based on HF or KS DFT. As a result of their single-determinant framework, additional approximations are often needed to relate theoretically calculated quantities to $\Delta E_{\text{H-L}}$ and J.

Although sharing a similar single-configuration framework, HF and DFT exhibit very different performances in terms of their descriptions of magnetic properties, owing to their different treatment of the exchange−correlation (xc) interaction. Due to the lack of dynamic Coulomb correlation, electrons in HF tend to get too close to each other so that the electron-pairing energy (denoted as P henceforth) is often overestimated. Therefore, HF favors the HS ground state.[13] On the other hand, KS DFT in the local density or generalized gradient approximation (LDA or GGA, respectively) to the xc energy functionals suffers from the self-interaction error (SIE) problem.[23] As a result, electrons tend to repel each other artificially, leading to a tendency to stabilize the LS state,[24,25] and the local magnetic orbitals (singly occupied molecular orbitals) are delocalized, thus overestimating the magnetic interactions.[26] The SIE problem of LDA or GGA can be partially remedied by mixing a fraction of the HF (exact) exchange with the standard LDA or GGA xc functionals,[27,28] hence termed the hybrid functionals approach, which has become the most successful DFT method for molecular systems.[29] The hybrid functionals approach has also been applied to molecular magnetic systems recently, and the overall performance is very promising.[30−32] It has, however, at least two drawbacks. The results often depend quite sensitively on the parameters used in these functionals, including in particular the percentage of the exact exchange that is included. Different materials (or properties) need different parameters to obtain optimal results.[30−32] From a practical point of view, the hybrid functionals approach, when implemented with the periodic boundary condition that is used in most popular first-principles DFT packages, is computationally much more expensive than standard LDA or GGA. Therefore, although the hybrid functionals approach has become popular in computational chemistry since two decades ago,[29] its use in computational materials science is much more limited, and it becomes available in popular DFT packages only very recently.[33,34]

For systems with partially occupied d- or f-states, a simple and effective approach that can overcome the major failure of LDA or GGA is to introduce a local correction characterized by the Hubbard Coulomb interaction term U,[35] hence termed LDA (GGA)+U (or more generally DFT+U).[36−38] Physically the U correction has the effect of introducing a penalty for fractional occupation that is favored by LDA or GGA. DFT+U was originally developed to describe Mott insulators[39] properly in the band theory framework and has become a popular first-principles method for strongly correlated materials during the past decade.[40] Only recently have a few attempts been made to apply the approach in molecular magnetic systems.[41−45] It was found that the DFT+U method can in general improve the description of magnetic interactions considerably, but its overall performance is still inconclusive.[41−45] Rivero et al.[44] applied the plane wave-based DFT+U approach to investigate magnetic coupling constants of a series of binuclear copper complexes. They showed that the description of AFM systems was significantly improved by DFT+U but that of FM ones was still quite poor.

The main goal of this work is to investigate the performance of the DFT+U method for the evaluation of $\Delta E_{\text{H-L}}$ and J in a systematic manner. For $\Delta E_{\text{H-L}}$, we consider a set of mononuclear iron complexes including seven SCO compounds. For J, we study a group of binuclear copper complexes that cover both FM and AFM intersite interactions. The paper is organized as follows. In the next section, Section 2, we present the method used in our investigation and some computational details. In Section 3, we first show that the DFT+U method is able to describe the SCO phenomenon and exchange interactions with an accuracy that is comparable to the state-of-the-art hybrid functionals approaches. Then the physical effect of U is analyzed in terms of the variation of local spin density projected on magnetic centers, from which we argue that the Hubbard U correction can effectively induce localization of magnetic orbitals to eliminate their erroneous overlap with other orbitals. In Section 4 we conclude the work with a few general remarks regarding the limitation of the DFT +U approach for molecular magnetic systems.

2. COMPUTATIONAL DETAILS

To investigate the performance of DFT+U for the description of intra-atomic spin interaction, we consider seven iron(II) complexes[46−50] with different ground spin states and seven iron SCO compounds[51−64] for which experimental data for the enthalpy difference ΔH between different spin states (iron(II): LS, $S = 0$; HS, $S = 2$ and iron(III): LS, $S = 1/2$; HS, $S = 5/2$) are available. We calculate $\Delta E_{\text{H-L}}$ in terms of eq 1, where the total energies in the HS and LS states are obtained from standard spin-unrestricted KS DFT calculations with fully optimized molecular structures.

For the calculation of J that characterizes the interatomic spin coupling, we use the "broken symmetry" (BS) approach:[65,66] J is related to the total energy difference between the HS state, in which the neighboring magnetic ions have parallel spin alignment ($\uparrow\uparrow$) and a constructed BS state with the corresponding antiparallel spin alignment ($\uparrow\downarrow$). By assuming fully localized magnetic orbitals and using the Heisenberg Hamiltonian (eq 2),[66] one obtains

$$E_{\text{BS}} - E_{\text{HS}} = \langle\uparrow\downarrow| - J\hat{S}_i\cdot\hat{S}_j|\uparrow\downarrow\rangle - \langle\uparrow\uparrow| - J\hat{S}_i\cdot\hat{S}_j|\uparrow\uparrow\rangle = 2JS_iS_j \quad (3)$$

where S_i and S_j are the spin quantum numbers of the two interacting local magnetic centers. We consider only binuclear

copper(II) complexes,[67−77] which have $S_i = S_j = 1/2$, so that the exchange coupling constant can be calculated by

$$J = 2(E_{BS} - E_{HS}) \quad (4)$$

We use the molecular structures extracted from the crystal data without further structural optimization, which is a common practice in the studies of exchange coupling constants to avoid additional uncertainty.[26]

All calculations are performed using the SIESTA code[78,79] (with the DFT+U extension[80]), which is based on numerical atomic basis[78] and norm-conserving pseudopotentials (NCPPs).[81] The capability of the code to treat molecular magnetic systems has been well verified by Ruiz et al.[82] We use the triple-ζ plus polarization (TZP) basis for magnetic ions (Fe, Cu), and the double-ζ plus polarization (DZP) basis for the other atoms. Both LDA[23] and Perdew−Burke−Erzernhof (PBE)[83] GGA functionals are used in our calculations.

The DFT+U calculations are based on the simplified rotationally invariant scheme by Dudarev et al.[37] in which the parameter U corresponds to $U-J$ in the original formulas proposed by Anisimov et al.,[36] with J here being the onsite exchange interaction. Considering the important role of U, a few comments on the choice of U are in order. U is defined physically as the effective on-site Coulomb interaction among localized electrons in partially occupied d- or f-shells, which is determined mainly by the nature of localized d or f electrons and their chemical environments. The Hubbard U correction is introduced in DFT+U mainly to overcome the severe SIE among localized d or f electrons. In practice, however, U is often regarded as an adjustable parameter, whose value is determined by fitting to experiment. This is in some sense to use U to correct not only SIE but also all other errors of a particular LDA or GGA functional. Such empiricism in the DFT+U approach is certainly useful to greatly enhance its applicability to a wide range of complicated materials for which more accurate and theoretically more rigorous methods are infeasible. On the other hand, the predictive power of DFT+U can be impaired, and more importantly, the physical significance of U can be lost if the adjustability of U is overused. Using different target properties for fitting may result in significantly different values of U, and the situation can become more complicated if the experimental data used for fitting have significant uncertainty (error bar). Therefore, we think U should be chosen based on physical considerations, either by fitting to the experimental data that carry the information of on-site Coulomb interaction, such as photoemission spectroscopic (PES) data,[84,85] or calculated from first-principles approaches, such as the constrained DFT.[38,86−88] Although a unique determination of U is difficult, a physical range of U can be easily established for a particular transition-metal ion. Guided by these considerations, we use in this work U = 4.0 eV for Fe(II) and Fe(III) and U = 6.5 eV for Cu(II) based on previous constrained DFT calculations and PES experimental data for some simple Fe(II)[38,85,88] and Cu(II)[85,89] inorganic materials. Rigorously speaking, the value of U should depend on the oxidation state and the chemical environments of the transition-metal ion, which are, however, secondary factors. We leave further investigation of this issue to the future. Finally we note that although the dependence on U introduces uncertainty when interpreting the results from DFT+U, we can also take advantage of such dependence in the spirit of a Gendanken experiment; since U characterizes the strength of onsite Coulomb interaction, we can obtain insights on physical mechanisms underlying different spin interactions by investigating how physical properties under study depend on the value of U.

Table 1. Assessment of the Pseudopotentials and Basis Used in This Work by Comparing the Calculated $\Delta E_{H\text{-}L}$ (kJ/mol)[a] of $[Fe(2\text{-}A)_3]^{2+}$ with That Obtained Using ECP and All-Electron Basis

basis[b]	TZP	Lanl2dz	6-311+G(d)
LDA	544	533	552
GGA	447	428	450

[a] Structures determined at 12 and 298 K are used as in LS and HS states, respectively. [b] Different basis sets are employed for iron: TZP in SIESTA (DZP for the other atoms) and Lanl2dz and 6-311+G(d) in GAUSSIAN09 (6-31G(d) for the others).

We use the NCPPs taken from ABINIT's pseudopotential database,[90] as provided by the SIESTA group,[80] for all elements involved in our calculations except for iron. For the latter, a NCPP with nonlinear core correction (NLCC)[81] is generated based on the nonrelativistic spin-polarized atomic calculations ($[Ar]3d^64s^2$) with a cutoff radius of 2.0 Bohr for all the angular components. The inclusion of NLCC in the pseudopotential is found to be crucial for the accurate description of the Fe 3d states.

To check the accuracy of the pseudopotentials as well as the numerical atomic basis functions used in our calculations, we compare $\Delta E_{H\text{-}L}$ of $[Fe(2\text{-}A)_3]^{2+}$ (2-A = 2-picolylamine)[58] calculated by SIESTA with that by GAUSSIAN09[91] using both all-electron and effective core potential (ECP) basis (see Table 1). The results from SIESTA are in excellent agreement with all-electron and small-core ECP results, which confirms the accuracy of the method used in our calculations.

3. RESULTS AND DISCUSSION

3.1. Spin-Crossover of Iron Complexes. We begin the analysis by inspecting a series of iron(II) complexes with significantly different ground-state spin properties (Table 2). This list of compounds is ordered in terms of the magnitude of Δ_o that is determined by the coordination nature of the ligands. Since $\Delta E_{H\text{-}L}$ depends on Δ_o linearly, the results are expected to change from large positive values for the compounds coordinated with NO^+ and CO to negative ones for those with NH_3 and H_2O. This trend is indeed well delivered by all theoretical methods except GGA+U, which overstabilizes the HS state dramatically such that it completely loses the ability to distinguish between HS and LS states. We note that GGA+U with a significantly smaller U (∼ 1.0 eV) would give much improved results, but using such a small U is physically not well founded. A more quantitative assessment is however not straightforward, since the only experimental information available is the nature (HS or LS) of the ground state, i.e., the sign of $\Delta E_{H\text{-}L}$. We will therefore take the results obtained from CASPT2[18] as the benchmark. In general, GGA yields quite accurate results, but its performance is not systematic. In particular, for $[Fe(N_2H_4)(NHS_4)]$ and $[Fe(NH_3)(NHS_4)]$ (NHS_4^{2-} = 2,2′-bis(2-mercaptophenylthio)),[49] $\Delta E_{H\text{-}L}$ calculated by GGA is about ten times larger than that by CASPT2. Compared to GGA, LDA tends to favor the LS states more strongly, and therefore, $\Delta E_{H\text{-}L}$ is significantly overestimated. Overall the best performance is obtained by LDA+U, which gives results closely comparable with those from the

Table 2. Calculated $\Delta E_{H\text{-}L}$ (kJ/mol) Compared with Results Obtained by TPSSh and CASPT2

compound	LDA	LDA+U	GGA	GGA+U	TPSSh[a]	CASPT2[b]	expt[c]	ref
$[Fe^{II}(NO^{+})(NHS_4)]$[d]	204	71	123	−42	102	178	LS	46
$[Fe^{II}(CO)(NHS_4)]$	236	73	139	−35	103	122	LS	47
$[Fe^{II}(PMe_3)(NHS_4)]$	208	36	92	−81	63	81	LS	48
$[Fe^{II}(N_2H_4)(NHS_4)]$	155	3	49	−104	5	4	HS	49
$[Fe^{II}(NH_3)(NHS_4)]$	145	−5	40	−107	−53	5	HS	49
$[Fe^{II}(NH_3)_6]^{2+}$	93	−32	−21	−134	−24	−86	HS	–
$[Fe^{II}(H_2O)_6]^{2+}$	−76	−153	−163	−232	−114	−195	HS	50

[a] Ref 92. [b] Ref 18. [c] Experimental ground spin states: LS, $S = 0$; HS, $S = 2$. [d] NHS_4^{2-} = 2,2′-bis(2-mercaptophenylthio) diethylamine dianion.

Table 3. Calculated $\Delta E_{H\text{-}L}$ (kJ/mol) in Comparison with the Enthalpy Difference ΔH (kJ/mol) Obtained from TPSSh and Experiment

	$\Delta E_{H\text{-}L}$ (kJ/mol)				ΔH (kJ/mol)[a]		
compound	LDA	LDA+U	GGA	GGA+U	TPSSh[b]	expt	ref
$[Fe^{III}(acac)_2trien]^{+}$	126	18	32	−68	33	7−17	51 and 52
$[Fe^{II}(papth)_2]^{2+}$	177	23	51	−95	15	16	53 and 54
$[Fe^{II}(tacn)_2]^{2+}$	141	5	30	−94	16	21−24	55 and 56
$[Fe^{II}(2\text{-}A)_3]^{2+}$	174	20	46	−98	14	18−25	57 and 58
$[Fe^{II}(HB(pz)_3)_2]$	218	47	75	−80	51	16−22	59 and 60
$[Fe^{II}(py(bzimH))_3]^{2+}$	191	28	55	−96	26	20−21	61 and 62
$[Fe^{II}(tppn)]^{2+}$	186	29	58	−88	31	25−30	63 and 64

[a] $\Delta H = \Delta E_{H\text{-}L} + \Delta E_{vib} + p\Delta V$, where the vibrational part ΔE_{vib} contributes to the enthalpy difference a few kJ/mol (negative) but is basically independent of the system; the last term $p\Delta V$ can be ignored. [b] Ref 31.

hybrid functional (TPSSh) approach reported by Ye and Neese.[92]

We further investigate the performance of the DFT+U approach in describing $\Delta E_{H\text{-}L}$ of real SCO complexes. Table 3 shows $\Delta E_{H\text{-}L}$'s of the seven iron SCO compounds obtained from LDA(+U) and GGA(+U), together with the results from TPSSh[31] and the enthalpy differences determined experimentally. Rigorously speaking, ΔH contains, in addition to the electronic energy change $\Delta E_{H\text{-}L}$, the contributions from the change of volume ($p\Delta V$) and the vibrational part (ΔE_{vib}). While the former is expected to be marginal, the latter, mainly the difference in zero-point energies between LS and HS states, is non-negligible because of significantly different metal−ligand (M−L) binding strength in LS and HS states. Nevertheless, the contribution of ΔE_{vib} is typically a few kJ/mol,[31] which is smaller than $\Delta E_{H\text{-}L}$ in typical SCO compounds and comparable to the uncertainty (error bar) in the experimental data of ΔH. Most importantly, ΔE_{vib} is nearly constant for different systems.[25] It is therefore reasonable to compare theoretical results of $\Delta E_{H\text{-}L}$ to experimental ΔH. For these SCO compounds, $\Delta E_{H\text{-}L}$'s from LDA are overestimated dramatically, by nearly 1 order of magnitude. GGA results, however, are only slightly overestimated. The U correction added to GGA again results in qualitatively wrong ground states for all SCO compounds considered. On the other hand, the LDA+U approach gives results very similar to those from TPSSh, both in good agreement with experimental enthalpy differences. We note that for $[Fe(HB(pz)_3)_2]$ ($HB(pz)_3$ = hydro-tris(1-pyrazolyl)-borato),[60] both LDA+U and TPSSh overestimate $\Delta E_{H\text{-}L}$ significantly. On the whole, the LDA+U approach delivers a comparable accuracy as the hybrid functionals approach for the description of the SCO phenomenon.

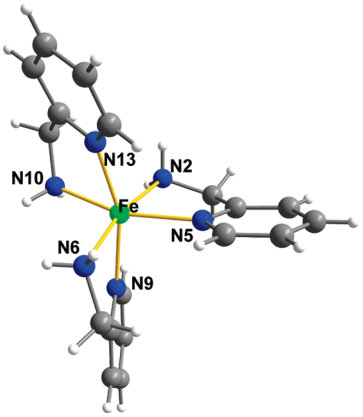

Figure 1. Molecular structure of $[Fe(2\text{-}A)_3]^{2+}$.

Besides an accurate evaluation of $\Delta E_{H\text{-}L}$, a reliable prediction of equilibrium molecular structures in different spin states is also of great importance for the simulation of SCO compounds. To assess the performance of the DFT+U approach for that, we consider $[Fe(2\text{-}A)_3]^{2+}$ (Figure 1), whose experimental crystal structural data in both LS and HS states are available.[58] We note that crystal and finite-temperature effects are not taken into account in our calculations, a common practice in theoretical studies of SCO compounds.[13,31] Optimized M−L bond lengths obtained from different theoretical approaches are compared to experimental ones in Table 4. In the LS state, which is stable at low temperature, the M−L bonds from LDA are systematically shorter than those from experiment, a feature that has been well recognized for transition-metal complexes.[29] LDA+U

Table 4. Experimental and Optimized M−L Bond Lengths (Å) of $[Fe(2\text{-}A)_3]^{2+}$ in the LS and HS States

	LS (S = 0)					HS (S = 2)				
M−L bond	crystal	LDA	LDA+U	GGA	GGA+U	crystal	LDA	LDA+U	GGA	GGA+U
$Fe-N_{10}$	2.024	1.975	2.018	2.030	2.082	2.179	2.220	2.232	2.265	2.303
$Fe-N_{13}$	1.991	1.924	1.975	1.978	2.049	2.196	2.100	2.162	2.191	2.242
$Fe-N_2$	2.020	1.976	2.017	2.033	2.088	2.180	2.218	2.237	2.290	2.280
$Fe-N_5$	2.004	1.936	1.982	2.001	2.061	2.220	2.113	2.164	2.204	2.292
$Fe-N_6$	2.034	1.966	2.011	2.024	2.084	2.183	2.210	2.225	2.250	2.272
$Fe-N_9$	1.998	1.927	1.978	1.990	2.049	2.213	2.097	2.160	2.193	2.258
MAE[a]		0.061	0.015	0.009	0.057		0.071	0.049	0.051	0.079

[a] MAE with respect to the corresponding experimental structures (12 K, LS; 298 K, HS).

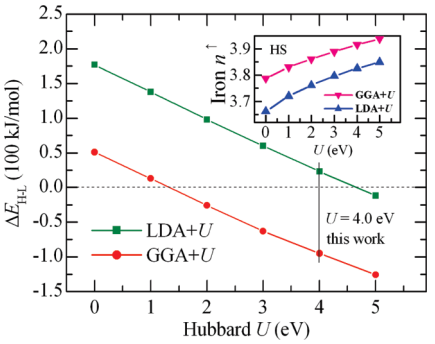

Figure 2. Calculated ΔE_{H-L} of $[Fe(papth)_2]^{2+}$ as a function of U employing LDA+U [green line, solid squares (■)] and GGA+U [red line, solid circles (●)]. Dash line: bottom line of qualitatively correct results. The vertical line refers to the U value used in this work. Inset: spin density $n^{\uparrow}$ of iron (Mulliken population analysis) in HS state versus U [blue line, triangle (▲), LDA+U; pink line, inverse-triangle (▼), GGA+U].

significantly improves the LDA results, reducing the mean absolute error (MAE) from 0.061 to 0.015 Å. On the other hand, since pure GGA already describes M−L bond lengths quite well, the inclusion of the U correction, which tends to increase the M−L bond lengths, results in systematically overestimated bond lengths with a MAE of 0.057 Å with respect to experiment. For the HS state, the overall trend is still similar: LDA+U gives results that are generally in better agreement with experiment than LDA, and GGA+U tends to overestimate the M−L bond lengths systematically. On the other hand, the agreement between theory (LDA+U and GGA) and experiment is noticeably poorer in the HS state than that in the LS state. A likely cause for this is that the experimental data for the HS state are obtained from crystallographic structures measured at room temperature, in contrast to those for the LS state, which is measured at low temperature. We can therefore expect that structural data in the HS state are influenced by crystal and finite-temperature effects more strongly than those in the LS state.

Optimized M−L bond lengths for other SCO compounds considered in this work can be found in the Supporting Information, and they exhibit very similar features. Overall, both PBE-GGA and LDA+U give equilibrium structures with an accuracy comparable to that from BP86-GGA. The latter was shown to give optimal structural properties of transition-metal complexes.[31] Therefore, by using LDA+U, both electronic and structural properties of SCO systems can be described accurately by the same theoretical approach. In contrast, GGA (BP86 or PBE) can only describe structural properties accurately but not electronic properties.

In the following we will take $[Fe(papth)_2]^{2+}$ (papth = 2-(pyridin-2-ylamino)-4-(pyridin-2-yl)thiazole)[54] as an example to analyze how the Hubbard U works. According to the crystal field theory, ΔE_{H-L} can be roughly determined by the difference between the crystal field splitting Δ_o and the mean electron pairing energy P among the localized d electrons,[14] the latter being closely related to the on-site Coulomb repulsion U. This simplified picture is confirmed in Figure 2, which shows that ΔE_{H-L} from LDA+U and GGA+U both decrease linearly as a function of U, but GGA+U results are systematically smaller by a constant difference of ∼125 kJ/mol. These features can be rationalized from the viewpoint of chemical bonding. Pure LDA (i.e., U = 0) dramatically favors the LS state characterized by the fully occupied t_{2g} (bonding) orbitals and strong M−L bonds. This tendency along with the underestimation of the M−L bond lengths can be attributed to two drawbacks of LDA:[29] one is the local formulation based on the uniform electron gas, which poorly describes coordination bonds, and the other is the SIE that causes artificial delocalization. The U term tackles the on-site Coulomb interaction to eliminate the severe SIE among localized d-electrons.[39] By increasing U, a large portion or the whole part of the artificial delocalization contribution can be removed from the real hybridization responsible for the M−L bonding. As shown in the inset of Figure 2, the local spin density projected on the iron center increases as a function of U, indicating enhanced localization of the magnetic orbitals. The latter in turn tends to weaken the M−L bonding and reduce the energy bias for the LS states. When an appropriate U (4.0 eV) is used, LDA+U reproduces experimental geometries (in Table S1, Supporting Information) as well as the SCO behavior of the compound. On the other hand, a too large U (> ∼ 5.0 eV) would bring unphysical localization error and therefore overstabilize the HS state.

In the case of GGA+U, the pure GGA (U = 0) already gives results in a good agreement with experiment. This is likely due to the fact that the first drawback of LDA has been largely overcomed by introducing the gradient correction.[29] It also means that GGA+U is vulnerable to overcorrection. With U = 4.0 eV, indeed GGA+U gives qualitatively wrong ground-state spin (negative ΔE_{H-L}) and significantly overestimated M−L bond lengths. Using a smaller U, GGA+U would also be able to give reasonable results. Lebègue et al.[43] reproduced the experimental adiabatic ΔE_{H-L} of a prototype SCO compound $[Fe(phen)_2(NCS)_2]$ using GGA+U with U = 2.5 eV. For our molecular model system, GGA+U with U = ∼1.0 eV gives ΔE_{H-L} and the

Table 5. $Cu^{II}-Cu^{II}$ Exchange Coupling Constants J (cm^{-1})[a] of the Model Compounds

compound	LDA	LDA+U	GGA	GGA+U	B3LYP	expt	ref
$[Cu_2(bpy)_2(H_2O)_2(C_2O_4)]^{2+}$	−2951	−908	−1765	−464	−634[d]	−382	67
$[Cu_2(petdien)_2(C_2O_4)]^{2+}$	−207	−79	−121	−63	−21[d]	−19	68
$[Cu_2(H_2O)_2(AcO)_4]$	−1374	−433	−863	−230	−429[d]	−286	69
$[Cu_2(dmen)_2(\mu\text{-OMe})(O_2C\text{-}L^b)]^{2+}$	132	36	150	−71	−61[d]	−11	70
$[Cu_2(dpt)_2(O_2C\text{-}L^b)_2]^{2+}$	28	13	20	−5	4[d]	2	71
$[Cu_2(phen)_2(AcO)(\mu\text{−}OH)(\mu\text{−}OH_2)]^{2+}$	408	173	223	84	194[d]	111	72
$[Cu_2(O_2CEt)_2{}^c(\mu\text{−}OH)(dpyam)_2]^{+}$	207	102	117	44	198[e]	24	73
$[Cu_2(O_2CEt)(\mu\text{−}OH)(\mu\text{−}OH_2)(bpy)_2]^{2+}$	341	164	239	90	353[e]	149	74
$[Cu_2(Et_5dien)_2(C_2O_4)]^{2+}$	−1003	−321	−622	−149	−266[f]	−75	75
$[Cu_2(bpm)_2(\mu\text{−}OH)_2]^{2+}$	159	184	115	94	224[f]	114	76
$[Cu_2(DMPTD)(\mu\text{-}N_3)(\mu\text{-Cl})Cl_2]$	−181	101	−4	185	226[f]	168	77

[a] Heisenberg Hamiltonian $\hat{H} = -J\hat{S}_i\cdot\hat{S}_j$, where $J = 2(E_{BS} - E_{HS})$. [b] L=(η^5-C_5H_4)Fe^{II}(η^5-C_5H_5). [c] One of the propionato ligands is in the monatomic bridging mode (μ-OCOEt). [d] Ref 96. [e] Ref 97. [f] Ref 98.

local spin density (see the inset in Figure 2) that are close to those from LDA+U with U = 4.0 eV.

From a physical point of view, the Hubbard U plays a similar role as the weight of the exact (HF) exchange in the hybrid functionals approach in the sense that both can correct the severe SIE among localized d-electrons. The connection between DFT+U and the hybrid functionals approach is clearly demonstrated in the recent work by Tran et al.,[93] in which the hybrid functional is implemented only for strongly correlated electrons in localized d or f states as in DFT+U, and it gives results very similar to those from DFT+U. For SCO compounds, inclusion of the HF exchange stabilizes the HS state, so the accuracy of the hybrid functionals approach for $\Delta E_{H\text{-}L}$ depends on the percentage of the HF exchange. The popular B3LYP including 20% exact exchange fails to predict the correct ground spin states of the SCO compounds,[13,92] while its modified variant, B3LYP*, which reduces the HF percentage to 15%, delivers reasonable $\Delta E_{H\text{-}L}$ values.[94,95]

3.2. Exchange Interactions of Binuclear Copper Complexes. Table 5 shows the calculated exchange interaction constants J of the selected binuclear copper complexes in comparison with the results by B3LYP[96−98] and experiment.[67−77] Neither LDA nor GGA can provide acceptable results since the deviations are far beyond the uncertainty in the experimental data ($\sim$ 10 cm^{-1}). In particular, they even predict the wrong interaction types for some compounds. In contrast, B3LYP generally yields qualitatively correct values, indicating clearly the importance of the HF exchange for the description of the intersite exchange interactions. Consistent with the preceding observation on the relation between the U correction and the HF exchange, LDA+U and GGA+U systematically improve the predictions of LDA and GGA, respectively, and give results that are very similar to those of B3LYP. We note in particular that GGA+U is able to describe magnetic interactions of both AFM and FM dicopper complexes.

In a plane-wave based study, Rivero et al.[44] reported that J in FM complexes could not be properly described by DFT+U, which contradicts the finding in this work. They found that the U correction reduced the overestimated results obtained using both LDA and PW91 by no more than 20% (with U = 6.0 eV), resulting in J still 3−8 times larger than experimental values. A precise explanation for this discrepancy is difficult without more detailed information. Here we give some speculation on the possible causes. The BS state in a FM system is metastable and therefore more difficult to reach than that in the AFM case. To find the metastable BS state, it is necessary to start the calculation from a tailored initial guess and caution is needed to ensure the true BS state is found when the self-consistent field (SCF) iteration converges. This issue has been paid particular attention in our calculations. As far as we know, the DFT+U approach has been widely used to study exchange coupling constants of bulk inorganic magnetic systems, where comparable accuracy has been reached for FM and AFM systems (see, e.g., ref 99). We see no particular reasons that molecular magnetic systems should be different in this aspect.

We use $[Cu_2(bpy)_2(H_2O)_2(\mu\text{-}C_2O_4)]^{2+}$ (bpy = 2, 2′-bipyridyl)[67] as a model system to investigate the effect of U in more detail. Figure 3a shows J from LDA (GGA)+U as a function of U. LDA overestimates the absolute value of J by a factor of 7, and GGA only shows a slight improvement, overestimating the result by more than four times. This is again associated with the unphysical delocalization of magnetic orbitals that can be characterized by the local spin density projected on copper centers (see Figure 3b). In fact, the BS approach to the evaluation of J (eqs 3 and 4) is formulated based on the strict localization limit,[100] which can, however, be partly invalidated by the delocalization error of LDA and GGA. The Hubbard U correction included in LDA (GGA)+U improves the situation by suppressing the delocalization, as indicated by the increase of the local spin density on copper ions (Figure 3b). This is reminiscent of Kahn's valence bond model,[101,102] which goes back to the Heitler−London's view of the chemical bond and formulates the exchange coupling constant in terms of natural magnetic orbitals:[26]

$$J = J_{FM} + J_{AFM} \approx 2K_{ab} + 4h_{ab}S_{ab} \quad (5)$$

where K_{ab}, h_{ab}, and S_{ab} refer to the exchange, one-electron, and overlap integrals in terms of certain fragment orbitals (denoted as a and b), respectively.[26] The constant J is therefore governed by the competition between the two terms: the positive FM part $2K_{ab}$ (denoted as J_{FM}) and the negative AFM part $4h_{ab}S_{ab}$ (denoted as J_{AFM}). Increasing localization of the magnetic orbitals lowers absolute values of both terms, thus in most cases reducing the absolute value of J whatever the interaction type may be.

We can also interpret the effects of the U correction in terms of the error cancellation. According to the BS model, J is obtained

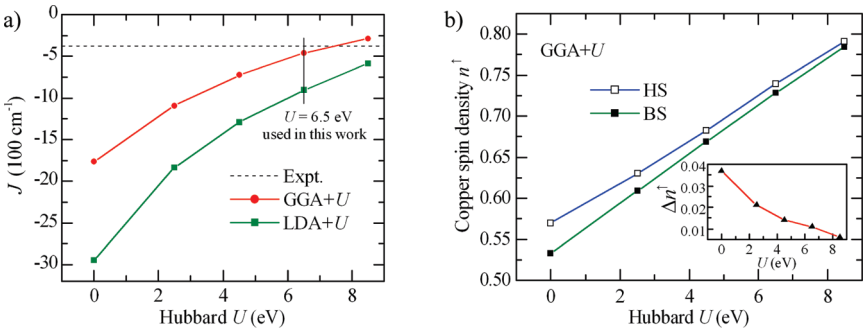

Figure 3. (a) Calculated J [red line, solid circles (●), GGA+U; green line, solid squares (■), LDA+U] under different U values, compared with the experiment (horizontal dash line). The vertical line refers to the value of U used in this work. (b) Spin density $n^{\uparrow}$ (Mulliken population analysis) of one copper center both in HS and BS states obtained using GGA+U for several U values. Inset: spin density difference between HS and BS state $\Delta n^{\uparrow}$ ($n^{\uparrow}_{HS} - n^{\uparrow}_{BS}$) versus U.

from the energy difference between the HS and BS states, which will benefit from extensive cancellation of the errors, including, in particular, the SIE. The extent of the spurious spin delocalization originating from the SIE is slightly different for the HS (↑↑) and the BS (↑↓) states. As shown in Figure 3b, the local spin density on the copper center in the HS state is larger than that in the BS state, implying, in some sense, the incomplete cancellation of the SIE in the two states. The inclusion of U reduces the difference significantly. In the localization limit, the local spin density on Cu(II) in the HS and BS states would become identical, which could be reached by using a very large U. The latter, however, is also unphysical considering that in reality the magnetic moments in these transition-metal complexes are not really local. In other words, the intersite magnetic interaction characterized by the finite J originates from the chemical bonding that relies on the overlap of orbitals on neighboring atoms, i.e., delocalization of electrons. An alternative approach to cancel the SIE is proposed by Rudra et al.[98] in a constrained DFT formalism, in which a binuclear magnetic molecule is divided into two fragments, and J is obtained in terms of eq 4 with the total spin in each fragment fixed to the same value in the HS and BS states. We note, however, that this approach, although physically very sound, might suffer from the drawback that the selection of fragments is not uniquely defined.

4. CONCLUDING REMARKS

In summary, we have investigated the performance of the DFT+U method for the description of both intra-atomic and interatomic spin interaction, the former characterized by the low spin-high spin energy splitting ($\Delta E_{H\text{-}L}$) and the latter by the exchange coupling constant J. We found that LDA+U can reproduce the experimental results in both the electronic and the structural aspects of the SCO compounds. GGA+U approach consistently predicts the exchange coupling constants that are well in agreement with experiment. The comparison with more sophisticated hybrid functionals further confirms the reliability and the applicability of DFT+U approach for the simulation of the SCO systems and the exchange couplings. In addition, we have interpreted the effect of U through the local spin density analysis. The Hubbard U imposes the localization of magnetic orbitals and therefore reduces the overestimated energy splitting between different spin states provided by LDA or GGA.

We close the paper by a few general comments on the DFT+U approach for molecular magnetic systems. As we have shown in this work, the DFT+U approach is quite effective to overcome the delocalization error of LDA or GGA for the description of localized d states in transition-metal complexes. It has the advantage of giving a clear physical picture as well as delivering reasonable accuracy for both intra- and interatomic spin interactions that is comparable to the hybrid functionals approaches. On the other hand, the results from DFT+U depend on U quite strongly. By varying U, electronic states on magnetic centers can change from strongly localized to significantly delocalized. In practice, it is often tempting to use U as an adjustable parameter that makes up for all the possible limitations and uncertainties arising from theoretical models, xc functionals, geometries, and basis sets as well as error bars in experimental data. We adopt a different strategy and choose U based on physical consideration without fitting the target properties under study. In other words, the Hubbard U is introduced mainly to correct the SIE among localized d-electrons. The performance of DFT+U with a particular choice of LDA or GGA then depends not only on the value of U but also on the accuracy of the LDA or GGA for other aspects than the description of localized d states. In this case, it is crucial to establish the overall performance of the DFT+U approach for the properties of interest, based on which reliable prediction can be made, and possible errors can also be estimated. In this work, we have chosen a fixed U for the same transition-metal ion disregarding the different nature of ligands and oxidation states. This is a reasonable first approximation, but a more accurate treatment requires considering the effects of changing chemical environments on the value of U, which can be taken into account by using the constrained DFT approach for the determination of U.[38,86−88]

■ ASSOCIATED CONTENT

Supporting Information. Optimized metal−ligand bond lengths of the iron compounds investigated in this work. This material is available free of charge via the Internet at http://pubs.acs.org.

■ AUTHOR INFORMATION

Corresponding Author
*E-mail: h.jiang@pku.edu.cn.

■ ACKNOWLEDGMENT

We thank Professors Song Gao and Bingwu Wang for helpful discussions. We gratefully thank Prof. Kasper Planeta Jensen,

Technical University of Denmark, and Prof. Francesc Illas, Universitat de Barcelona, for providing us with the crystal data of the model compounds. And we also acknowledge the kind help offered by Dr. Wei Xue and Dr. Jun Jiang. This work is partly supported by the National Natural Science Foundation of China (project no. 20973009).

REFERENCES

(1) Kahn, O. *Molecular Magnetism*; Wiley-VCH: New York, 1993.
(2) Gatteschi, D.; Bogani, L.; Cornia, A.; Mannini, M.; Sorace, L.; Sessoli, R. *Solid State Sci.* **2008**, *10*, 1701.
(3) Sanvito, S.; Rocha, A. R. *J. Comput. Theor. Nanosci.* **2006**, *3*, 624.
(4) Bogani, L.; Wernsdorfer, W. *Nat. Mater.* **2008**, *7*, 179.
(5) Mannini, M.; Pineider, F.; Sainctavit, P.; Danieli, C.; Otero, E.; Sciancalepore, C.; Talarico, A. M.; Arrio, M. A.; Cornia, A.; Gatteschi, D.; Sessoli, R. *Nat. Mater.* **2009**, *8*, 194.
(6) Misiorny, M.; Barnaś, J. *Phys. Rev. B* **2007**, *75*, 134425.
(7) Leuenberger, M. N.; Loss, D. *Nature* **2001**, *410*, 789.
(8) Lehmann, J.; Gaita-Ariño, A.; Coronado, E.; Loss, D. *J. Mater. Chem.* **2009**, *19*, 1672.
(9) Gütlich, P.; Goodwin, H. A. *Top. Curr. Chem.* **2004**, *233*, 1.
(10) Gatteschi, D.; Sessoli, R.; Villain, J. *Molecular Nanomagnets;* Oxford University Press: New York, 2006.
(11) Sato, O.; Tao, J.; Zhang, Y. Z. *Angew. Chem., Int. Ed.* **2007**, *46*, 2152.
(12) Wende, H. *Nat. Mater.* **2009**, *8*, 165.
(13) Paulsen, H.; Trautwein, A. X. *Top. Curr. Chem.* **2004**, *235*, 197.
(14) Cotton, F. A.; Wilkinson, G. *Advanced Inorganic Chemistry*; John Wiley & Sons: Hoboken, NJ, 1988; Chapter 17, pp 625−648.
(15) Sessoli, R.; Gatteschi, D.; Caneschi, A.; Novak, M. A. *Nature* **1993**, *365*, 141.
(16) Van Vleck, J. H. *The Theory of Electric and Magnetic Susceptibilities*; Oxford University Press: Oxford, U.K., 1932.
(17) Neese, F.; Pantazis, D. A. *Faraday Discuss.* **2011**, *148*, 229.
(18) Pierloot, K.; Vancoillie, S. *J. Chem. Phys.* **2008**, *128*, 034104.
(19) Kepenekian, M.; Robert, V.; Guennic, B. L.; Graaf, C. D. *J. Comput. Chem.* **2009**, *30*, 2327.
(20) Vancoillie, S.; Zhao, H.; Radoń, M.; Pierloot, K. *J. Chem. Theory Comput.* **2010**, *6*, 576.
(21) Guennic, B. L.; Amor, N. B.; Maynau, D.; Robert, V. *J. Chem. Theory Comput.* **2009**, *5*, 1506.
(22) Paulovič, J.; Cimpoesu, F.; Ferbinteanu, M.; Hirao, K. *J. Am. Chem. Soc.* **2004**, *126*, 3321.
(23) Perdew, J. P.; Zunger, A. *Phys. Rev. B* **1981**, *23*, 5048.
(24) Harvey, J. N. *Struct. Bonding (Berlin, Ger.)* **2004**, *112*, 151.
(25) Wolny, J. A.; Paulsen, H.; Trautwein, A. X.; Schünemann, V. *Coord. Chem. Rev.* **2009**, *253*, 2423.
(26) Ruiz, E.; Alvarez, S.; Rodriguez-Fortea, A.; Alemany, P.; Pouillon, Y.; Massobrio, C. In *Magnetism: Molecules to Materials*; Miller, J. S., Drillon, M., Ed.; Wiley-VCH: Weinheim, Germany, 2001; Chapter 7, pp 227−279.
(27) Becke, A. D. *J. Chem. Phys.* **1993**, *98*, 1372.
(28) Becke, A. D. *J. Chem. Phys.* **1993**, *98*, 5648.
(29) Koch, W.; Holthausen, M. C. *A Chemist's Guide to Density Functional Theory*; Wiley-VCH: Weinheim, Germany, 2001.
(30) Neese, F. *Coord. Chem. Rev.* **2009**, *253*, 526.
(31) Jensen, K. P.; Cirera, J. *J. Phys. Chem. A* **2009**, *113*, 10033.
(32) Valero, R.; Costa, R.; de, P. R.; Moreira, I.; Truhlar, D. G.; Illas, F. *J. Chem. Phys.* **2008**, *128*, 114103.
(33) Hafner, J. *J. Comput. Chem.* **2008**, *29*, 2044.
(34) Paolo Giannozzi, P.; Baroni, S.; Bonini, N.; Calandra, M.; Car, R.; Cavazzoni, C.; Ceresoli, D.; Chiarotti, G. L.; Cococcioni, M.; Dabo, I.; Corso, A. D.; de Gironcoli, S.; Fabris, S.; Fratesi, G.; Gebauer, R.; Gerstmann, U.; Gougoussis, C.; Kokalj, A.; Lazzeri, M.; Martin-Samos, L.; Marzari, N.; Mauri, F.; Mazzarello, R.; Paolini, S.; Pasquarello, A.; Paulatto, L.; Sbraccia, C.; Scandolo, S.; Sclauzero, G.; Seitsonen, A. P.; Smogunov, A.; Umari, P.; Wentzcovitch, R. M. *J. Phys.: Condens. Matter* **2009**, *21*, 395502.
(35) Hubbard, J. *Proc. R. Soc. A* **1963**, *276*, 238.
(36) Anisimov, V. I.; Zaanen, J.; Andersen, O. K. *Phys. Rev. B* **1991**, *44*, 943.
(37) Dudarev, S. L.; Botton, G. A.; Savrasov, S. Y.; Humphreys, C. J.; Sutton, A. P. *Phys. Rev. B* **1998**, *57*, 1505.
(38) Cococcioni, M.; de Gironcoli, S. *Phys. Rev. B* **2005**, *71*, 035105.
(39) Anisimov, V. I.; Aryasetiawan, F.; Lichtenstein, A. I. *J. Phys.: Condens. Matter* **1997**, *9*, 767.
(40) Karlsson, K.; Aryasetiawan, F.; Jepsen, O. *Phys. Rev. B* **2010**, *81*, 245113.
(41) Boukhvalov, D. W.; Lichtenstein, A. I.; Dobrovitski, V. V.; Katsnelson, M. I.; Harmon, B. N.; Mazurenko, V. V.; Anisimov, V. I. *Phys. Rev. B* **2002**, *65*, 184435.
(42) Scherlis, D. A.; Cococcioni, M.; Sit, P.; Marzari, N. *J. Phys. Chem. B* **2007**, *111*, 7384.
(43) Lebègue, S.; Pillet, S.; Ángyán, J. G. *Phys. Rev. B* **2008**, *78*, 024433.
(44) Rivero, P.; Loschen, C.; de, P. R.; Moreira, I.; Illas, F. *J. Comput. Chem.* **2009**, *30*, 2316.
(45) Gangopadhyay, S.; Masunov, A. E.; Poalelungi, E.; Leuenberger, M. N. *J. Chem. Phys.* **2010**, *132*, 244104.
(46) Sellman, D.; Kunstmann, H.; Moll, M.; Knoch, F. *Inorg. Chim. Acta* **1988**, *154*, 157.
(47) Sellmann, D.; Kunstmann, H.; Knoch, F.; Moll, M. *Inorg. Chem.* **1988**, *27*, 4183.
(48) Sellmann, D.; Hofmann, T.; Knoch, F. *Inorg. Chim. Acta* **1994**, *224*, 61.
(49) Sellmann, D.; Soglowek, W.; Knoch, F.; Ritter, G.; Dengler, J. *Inorg. Chem.* **1992**, *31*, 3711.
(50) Hagen, K. S. *Inorg. Chem.* **2000**, *39*, 5867.
(51) Dose, E. V.; Murphy, K. M. M.; Wilson, L. J. *Inorg. Chem.* **1976**, *15*, 2622.
(52) Sinn, E.; Sim, G.; Dose, E. V.; Tweedle, M. F.; Wilson, L. J. *J. Am. Chem. Soc.* **1978**, *100*, 3375.
(53) Beattie, J. K.; Binstead, R. A.; West, R. J. *J. Am. Chem. Soc.* **1978**, *100*, 3044.
(54) Baker, A. T.; Goodwin, H. A.; Rae, A. D. *Aust. J. Chem.* **1984**, *37*, 443.
(55) Turner, J. W.; Schultz, F. A. *Inorg. Chem.* **1999**, *38*, 358.
(56) Boeyens, J. C. A.; Forbes, A. G. S.; Hancock, R. D.; Wieghardt, K. *Inorg. Chem.* **1985**, *24*, 2926.
(57) Chum, H. L.; Vanin, J. A.; Holanda, M. I. D. *Inorg. Chem.* **1982**, *21*, 1146.
(58) Chernyshov, D.; Hostettler, M.; Tornroos, K. W.; Burgi, H. B. *Angew. Chem., Int. Ed.* **2003**, *42*, 3825.
(59) Jesson, J. P.; Swiatoslaw, T.; Eaton, D. R. *J. Am. Chem. Soc.* **1967**, *89*, 3158.
(60) Oliver, J. D.; Mullica, D. F.; Hutchinson, B. B.; Milligan, W. O. *Inorg. Chem.* **1980**, *19*, 165.
(61) Reeder, K. A.; Dose, E. V.; Wilson, L. J. *Inorg. Chem.* **1978**, *17*, 1071.
(62) Peng, S. M.; Chen, H. F. *Bull. Inst. Chem. Acad. Sin.* **1990**, *37*, 49.
(63) McGarvey, J. J.; Lawthers, I.; Heremans, K.; Toftlund, H. *Inorg. Chem.* **1990**, *29*, 252.
(64) McCusker, J. K.; Rheingold, A. L.; Hendrickson, D. N. *Inorg. Chem.* **1996**, *35*, 2100.
(65) Noodleman, L. *J. Chem. Phys.* **1981**, *74*, 5737.
(66) Ruiz, E.; Cano, J.; Alvarez, S.; Alemany, P. *J. Comput. Chem.* **1999**, *20*, 1391.
(67) Castillo, O.; Muga, I.; Luque, A.; Gutierrez-Zorrilla, J. M.; Sertucha, J.; Vitoria, P.; Roman, P. *Polyhedron* **1999**, *18*, 1235.
(68) Julve, M.; Verdaguer, M.; Gleizes, A.; Philoche-Levisalles, M.; Kahn, O. *Inorg. Chem.* **1984**, *23*, 3808.
(69) de Meester, P.; Fletcher, S. R.; Skapski, A. C. *J. Chem. Soc., Dalton Trans.* **1973**, 2575.
(70) López, C.; Costa, R.; Illas, F.; de Graaf, C.; Turnbull, M. M.; Landee, C. P.; Espinosa, E.; Mata, I.; Molins, E. *Dalton Trans.* **2005**, 2322.

(71) López, C.; Costa, R.; Illas, F.; Molins, E.; Espinosa, E. *Inorg. Chem.* **2000**, *39*, 4560.
(72) Tokii, T.; Hamamura, N.; Nakashima, M.; Muto, Y. *Bull. Chem. Soc. Jpn.* **1992**, *65*, 1214.
(73) Youngme, S.; Chailuecha, C.; van Albada, G. A.; Pakawatchai, C.; Chaichit, N.; Reedijk, J. *Inorg. Chim. Acta* **2005**, *358*, 1068.
(74) Chailuecha, C.; Youngme, S.; Pakawatchai, C.; Chaichit, N.; van Albada, G. A.; Reedijk, J. *Inorg. Chim. Acta* **2006**, *359*, 4168.
(75) Felthouse, T. R.; Laskowski, E. J.; Hendrickson, D. N. *Inorg. Chem.* **1977**, *16*, 1077.
(76) Munno, G. D.; Julve, M.; Lloret, F.; Faus, J.; Verdaguer, M.; Caneschi, A. *Inorg. Chem.* **1995**, *34*, 157.
(77) Tandon, S. S.; Thompson, L. K.; Manuel, M. E.; Bridson, J. N. *Inorg. Chem.* **1994**, *33*, 5555.
(78) Soler, J. M.; Artacho, E.; Gale, J. D.; García, A.; Junquera, J.; Ordejón, P.; Sánchez-Portal, D. *J. Phys.: Condens. Matter* **2002**, *14*, 2745.
(79) Its accuracy and efficiency is mainly controlled by two key parameters: (a) energy shift, defining the cutoff radii of the numerical basis functions used, corresponds to the energy increase due to the confinement of the basis; (b) mesh cutoff controlling the real-space grid, onto which the electron density is to be projected, is equivalent to the plane wave cutoff for the spacing grid. We use 50 meV for the energy shift and 160 Ry for the mesh cutoff.
(80) Artacho, E.; Gale, J. D.; García, A.; Junquera, J.; Martin, R. M.; Ordejón, P.; Sánchez-Portal, D.; Soler, J. M. *SIESTA*, v. LDAU; Universidad Autónoma de Madrid (UAM): Madrid, Spain; http://www.icmab.es/siesta/. (Accessed August 1, 2010).
(81) Martin, R. M. *Electronic Structure: Basic Theory and Practical Methods*: Cambridge University Press: Cambridge, U.K., 2004; Chapter 11, pp 204−231.
(82) Ruiz, E.; Rodríguez-Fortea, A.; Tercero, J.; Cauchy, T.; Massobrio, C. *J. Chem. Phys.* **2005**, *123*, 074102.
(83) Perdew, J. P.; Burke, K.; Ernzerhof, M. *Phys. Rev. Lett.* **1996**, *77*, 3865.
(84) Hüfner, S. *Photoelectron Spectroscopy: Principles and Applications*. 3rd ed. Springer: Berlin, 2003.
(85) Hüfner, S. *Adv. Phys.* **1994**, *43*, 183.
(86) Anisimov, V. I.; Gunnarsson, O. *Phys. Rev. B* **1991**, *43*, 7570.
(87) Nakamura, K.; Arita, R.; Yoshimoto, Y.; Tsuneyuki, S. *Phys. Rev. B* **2006**, *74*, 235113.
(88) Jiang, H.; Gomez-Abal, R. I.; Rinke, P.; Scheffler, M. *Phys. Rev. B* **2010**, *82*, 045108.
(89) Liechtenstein, A. I.; Anisimov, V. I.; Zaanen, J. *Phys. Rev. B* **1995**, *52*, R5467.
(90) Gonze, X. *ABINIT*; Université catholique de Louvain: Louvain-la-Neuve, BELGIUM; http://www.abinit.org/. (Accessed July 1, 2010).
(91) Frisch, M. J.; Trucks, G. W.; Schlegel, H. B.; Scuseria, G. E.; Robb, M. A.; Cheeseman, J. R.; Scalmani, G.; Barone, V.; Mennucci, B.; Petersson, G. A.; Nakatsuji, H.; Caricato, M.; Li, X.; Hratchian, H. P.; Izmaylov, A. F.; Bloino, J.; Zheng, G.; Sonnenberg, J. L.; Hada, M.; Ehara, M.; Toyota, K.; Fukuda, R.; Hasegawa, J.; Ishida, M.; Nakajima, T.; Honda, Y.; Kitao, O.; Nakai, H.; Vreven, T.; Montgomery, J. A., Jr.; Peralta, J. E.; Ogliaro, F.; Bearpark, M.; Heyd, J. J.; Brothers, E.; Kudin, K. N.; Staroverov, V. N.; Kobayashi, R.; Normand, J.; Raghavachari, K.; Rendell, A.; Burant, J. C.; Iyengar, S. S.; Tomasi, J.; Cossi, M.; Rega, N.; Millam, J. M.; Klene, M.; Knox, J. E.; Cross, J. B.; Bakken, V.; Adamo, C.; Jaramillo, J.; Gomperts, R.; Stratmann, R. E.; Yazyev, O.; Austin, A. J.; Cammi, R.; Pomelli, C.; Ochterski, J. W.; Martin, R. L.; Morokuma, K.; Zakrzewski, V. G.; Voth, G. A.; Salvador, P.; Dannenberg, J. J.; Dapprich, S.; Daniels, A. D.; Farkas, O.; Foresman, J. B.; Ortiz, J. V.; Cioslowski, J.; Fox, D. J. *Gaussian 09*, revision A. 01; Gaussian, Inc.: Wallingford, CT, 2009.
(92) Ye, S.; Neese, F. *Inorg. Chem.* **2010**, *49*, 772.
(93) Tran, F.; Blaha, P.; Schwarz, K.; Novák, P. *Phys. Rev. B* **2006**, *74*, 155108.
(94) Shiota, Y.; Sato, D.; Juhász, G.; Yoshizawa, K. *J. Phys. Chem. A* **2010**, *114*, 5862.
(95) Conradie, J.; Ghosh, A. *J. Phys. Chem. B* **2007**, *111*, 12621.
(96) de, P. R.; Moreira, I.; Costa, R.; Filatov, M.; Illas, F. *J. Chem. Theory Comput.* **2007**, *3*, 764.
(97) Costa, R.; de, P. R.; Moreira, I.; Youngme, S.; Siriwong, K.; Wannarit, N.; Illas, F. *Inorg. Chem.* **2010**, *49*, 285.
(98) Rudra, I.; Wu, Q.; Voorhis, T. V. *J. Chem. Phys.* **2006**, *124*, 024103.
(99) Larson, P.; Lambrecht, W. R. L. *J. Phys.: Condens. Matter* **2006**, *18*, 11333.
(100) Caballol, R.; Castell, O.; Illas, F.; de, P. R.; Moreira, I.; Malrieu, J. P. *J. Phys. Chem. A* **1997**, *101*, 7860.
(101) Girerd, J. J.; Journaux, Y.; Kahn, O. *Chem. Phys. Lett.* **1981**, *82*, 534.
(102) Kahn, O. *Inorg. Chim. Acta* **1982**, *62*, 3.

JCTC Journal of Chemical Theory and Computation

ARTICLE

pubs.acs.org/JCTC

The Role of Anharmonicity in Hydrogen-Bonded Systems: The Case of Water Clusters

Berhane Temelso and George C. Shields*

Dean's Office, College of Arts and Sciences, Department of Chemistry, Bucknell University, Lewisburg, Pennsylvania 17837, United States

Supporting Information

ABSTRACT: The nature of vibrational anharmonicity has been examined for the case of small water clusters using second-order vibrational perturbation theory (VPT2) applied on second-order Møller−Plesset perturbation theory (MP2) potential energy surfaces. Using a training set of 16 water clusters $(H_2O)_{n=2-6,8,9}$ with a total of 723 vibrational modes, we determined scaling factors that map the harmonic frequencies onto anharmonic ones. The intermolecular modes were found to be substantially more anharmonic than intramolecular bending and stretching modes. Due to the varying levels of anharmonicity of the intermolecular and intramolecular modes, different frequency scaling factors for each region were necessary to achieve the highest accuracy. Furthermore, new scaling factors for zero-point vibrational energies (ZPVE) and vibrational corrections to the enthalpy (ΔH_{vib}) and the entropy (S_{vib}) have been determined. All the scaling factors reported in this study are different from previous works in that they are intended for hydrogen-bonded systems, while others were built using experimental frequencies of covalently bonded systems. An application of our scaling factors to the vibrational frequencies of water dimer and thermodynamic functions of 11 larger water clusters highlights the importance of anharmonic effects in hydrogen-bonded systems.

1. INTRODUCTION

It has long been recognized that comparison of calculated harmonic vibrational frequencies (ω) with observed fundamental frequencies (ν) requires an empirical correction to account for vibrational anharmonicity and inherent errors in the electronic structure calculations.[1−12] There are three main reasons for scaling calculated harmonic vibrational frequencies to approximate experimental frequencies. First, scaling corrects for deviation from the harmonic oscillator model as a consequence of anharmonicity. The deviation could be mild in the case of high-frequency stretching modes where the vibrational potential around the equilibrium geometry of the molecule is deep and well-described by a harmonic oscillator potential. The difference between this harmonic potential and the more appropriate Morse potential is small, and a simple scaling factor goes a long way in reducing the disparity between the two. However, there are extreme cases of anharmonicity where the "vibrational" potential has multiple shallow minima and the motion is better described as an internal rotation, ring inversion, or a pseudorotation.[13−17] This is most common in low-frequency modes and cannot be easily remedied by introducing scaling factors. In cases where the harmonic approximation works well, a second reason for using scaling factors is that they can correct for the incompleteness of the basis set and electron correlation treatment that is inherent in the most practical quantum mechanical calculations. Scaling factors allow one to perform vibrational frequency analysis using a modest basis set and electron correlation method and to improve the quality of the calculated frequencies by scaling with a prescribed multiplicative factor. A third source of error in harmonic vibrational frequencies is the coupling of different modes, but accounting for these requires the calculation of coupled (as opposed to independent normal mode) vibrational wave functions. In principle, methods like vibrational configuration interaction (VCI)[18−20] and the Huang−Braams−Bowman (HBB)[21] potential can give exact vibrational wave functions, but they are not practical for systems with more than 10 atoms.

Anharmonic correction for rigid and semirigid systems typically amounts to 3−5% of harmonic frequencies computed using second-order Møller−Plesset perturbation theory (MP2) and Becke, three-parameter, Lee−Yang−Parr (B3LYP) methods and about 10% using Hartree−Fock (HF) methods with modest basis sets. Errors in harmonic vibrational frequencies are systematic, and it is possible to determine scaling factors by comparing calculated frequencies with experimental ones. Most scaling factors reported in the literature make use of large databases of experimental vibrational frequencies to systematically improve harmonic frequencies. By least-squares fitting of harmonic frequencies to experimental frequencies, many scaling factors have been suggested for a host of methods and basis sets. Radom et al.[4,7] have obtained scaling factors for vibrational frequencies, zero point vibrational energies (ZPVE) and vibrational enthalpies (ΔH_{vib}) and entropies (S_{vib}). They suggested different scaling factors for high- and low-frequency modes, with the high modes being scaled by 0.95−0.97 and the inverse of the low modes being scaled by 1.01−1.04 for MP2 theory with aug-cc-pVNZ basis sets where $N = D - Q$. A similar work by Sinha et al.[5] suggests split scaling of fundamental modes and low-frequency modes. The recommended fundamental and inverse low-frequency scaling factors for MP2 theory were 0.9604 and 1.0999 for the aug-cc-pVDZ basis set, 0.9557 and 1.0634 for the aug-cc-pVTZ basis set, and 0.9601 and 1.0698 for the aug-cc-pVQZ basis set. Halls et al.[12] have determined frequency scaling factors for various

Received: May 15, 2011
Published: July 15, 2011

methods along with the Sadlej pVTZ electric property basis set and found that dual scaling improves agreement between computed and observed vibrational frequencies better than a single uniform scaling. Wong[11] has looked at the performance of different density functionals and recommended scaling factors for each. As noted by Irikura et al.,[6,8,9] even though the uncertainty in most scaling factors is larger than typically acknowledged, empirical scaling of frequencies almost universally marks an improvement over plain harmonic ones. Nevertheless, the effectiveness of emipirical scaling is still being debated in the literature.[22−25]

While the works discussed above introduce uniform or separate scaling factors for different regions of the vibrational spectrum to correct harmonic vibrational frequency, Borowski's effective scaling frequency factor (ESFF)[26−28] method and Pulay's scaled quantum mechanical (SQM)[29] force field approaches scale individual vibrational frequencies or force constants depending on the nature of the local modes (ESFF) or the internal coordinates (SQM) contributing to each vibrational mode. Both ESFF and SQM have been shown to reduce the root-mean-square (RMS) deviation between scaled vibrational frequencies and experimental frequencies impressively when applied for density functional methods with various basis sets.[26−28,30,31] Even though SQM has been successfully applied to hydrogen-bonded acid dimers,[30−33] its use has been limited to date.

All the empirical scaling schemes described so far are derived from training sets of small covalently bound molecules for which experimental frequencies are readily available. None of these training sets include the experimental vibrational frequencies of even water dimers: the prototypical hydrogen-bonded system with a resolved vibrational spectrum. Thus, their applicability to hydrogen-bonded systems, like water clusters, is highly questionable even though they have been routinely employed in the literature.[34−38]

Each water cluster $(H_2O)_n$ has $3n$ high-frequency intramolecular vibrational modes corresponding to the symmetric stretch, asymmetric stretch and bending of each monomer. As water clusters form from individual monomers, the $6n - 6$ translational and rotational degrees of freedom of the monomers turn into low-frequency intermolecular vibrational modes. Experimental intramolecular vibrational frequencies are available for $(H_2O)_n$, however the intermolecular modes remain murky due to the coupling of low-frequency vibrational modes with each other and rotational degrees of freedom. Moreover, the experimental spectra are taken with the water clusters in different matrices that shift and broaden the spectral lines of the clusters in ways that are difficult to interpret. Perhaps the one exception is the water dimer whose 12 experimental vibrational frequencies have been resolved with the help of theoretical calculations.[37,39−41] Therefore, in the absence of reliable experimental intermolecular frequencies, it is imperative that one relies on theoretical anharmonic calculations to correct harmonic vibrational frequencies.

Many approaches have been developed to incorporate anharmonic effects in vibrational wave function calculations. One popular approach is vibrational second-order perturbation theory (VPT2) where anharmonic corrections are calculated from higher (third and fourth) order derivatives of the potential energy surface along the normal mode coordinates. The cubic and semidiagonal quartic force constants are calculated by finite differentiation of the Hessian along the normal mode coordinates.[42,43] It has the advantage of being affordable (albeit substantially more expensive than a harmonic calculation), and it is often the only practical approach for most systems of interest. If one has analytical second derivatives of the energy, then the necessary third and fourth derivatives can be computed easily using finite differentiation. For a system with N_m normal modes, the cost is $2N_m + 1$ times that of a single harmonic vibrational calculation. Because each of the Hessian calculations on the $2N_m + 1$ displaced geometries can be run separately, VPT2 calculations are amenable to parallelization. The main drawback of VPT2 is that it is subject to the problem of near degeneracies (resonances) just like all other perturbation theory.

In a manner analogous to electronic wave function methods, grid-based methods start with the vibrational self-consistent field (VSCF) approach, where each normal mode couples with all other modes in an average way.[44−46] Higher order correlation between the modes is included via second-order perturbation theory (VMP2), configuration interaction (VCI), or coupled-cluster (VCC) theory. These methods give good anharmonic frequencies for fundamental modes and overtones resulting from them, and they can account for coupling of different modes. They can however be expensive as they scale nonlinearly with the number of normal modes and the number of modes being correlated.[47] The cost of a VPT2 calculation scales linearly with the number of normal modes, and it is typically at least an order of magnitude cheaper than VSCF and its correlation corrected analogs. Another downside of VSCF is that it often gives unreasonable anharmonic frequencies for large amplitude, low-frequency modes, like the intermolecular modes of hydrogen-bonded systems.[48−50] Aside from these two popular schemes, harmonically coupled anharmonic oscillator (HCAO),[51] ab initio molecular dynamics,[52] P_VMWCI2,[53] and HBB[54] have been used to account for anharmonicity in hydrogen-bonded systems.

Most of the literature on the vibrational frequencies of water clusters attempts to look at the red shift in the bonded O−H stretching modes of gas-phase water clusters relative to the gas-phase monomer.[36,55,56] Aside from the water dimer,[57] there has been little work done on the effect of anharmonicity on vibrational modes of water clusters. Diri at al.[58] have evaluated the effect of anharmonic correction of the binding energy and ZPVE of $(H_2O)_{n=2-6}$ using MP2 and B3LYP theories with VPT2. Dunn et al.[37] showed that harmonic frequencies calculated using HF theory are more amenable to scaling than those computed using MP2. Njegic and Gordon[50] have looked at the effect of the anharmonicity of vibrational modes on thermodynamic functions of small- and medium-size molecules, including the water dimer using VSCF. They concluded that vibrational anharmonicity and coupling of modes have a substantial effect on the ZPVE as well as thermodynamic functions. They suggest expressing the normal mode displacement vectors in internal instead of Cartesian coordinates to get reasonable VSCF anharmonic frequencies for modes that involve bending and torsional motion. For the case of the water dimer, casting the potential energy surface in internal coordinates improves the agreement between calculated and experimental low-frequency modes remarkably. Correlation corrected vibrational mean field theory (cc-VSCF) has also been applied to hydrogen-bonded systems.[48,49] Kjaergaard at al.[57] have examined the performance of VPT2, VSCF, cc-VSCF, and HCAO for the water dimer. Their results show that VSCF, cc-VSCF, and HCAO perform well for O−H stretches but are somewhat erratic for intermolecular modes. VPT2 works well for all vibrational modes, even though it does not perform as well as HCAO for O−H stretching frequencies. Begue et al.[53] have benchmarked different anharmonic approaches and found VPT2 to be consistently applicable to water clusters, while other approaches had many pitfalls. Similarly, Torrent-Sucarrat et al.[59] have studied the role of vibrational anharmonicity in hydrogen-bonded complexes formed between the hydroperoxyl radical and formic, acetic, nitric, and sulfuric acids. They conclude that VPT2 anharmonic frequencies computed over

B3LYP/6-31+G(d,p) and B3LYP/6-311+G(2d,2p) PES agree well with experiment. Watanabe et al.[60] used a scaled hypersphere search (SHS) by polynomial fitting of the intramolecular potential energy function of water clusters to get fundamental frequencies that were very close to experimental values. A recent application of these different anharmonic treatments to $(HF)_{n=2-4}$ showed that VPT2, VSCF, and cc-VSCF perform comparably for high-frequency stretching modes, but the latter two were unreliable for low-frequency intermolecular modes.[47] Dykstra has looked at anharmonic effects on zero point energies of weakly bound molecular clusters including the water dimer and trimer and concluded that the effect is large when there are multiple minima on the intermolecular potential energy surface.[61]

Low-frequency modes are generally much more anharmonic than high-frequency ones. They also couple with each other as well as rotational degrees of freedom, thus making theoretical treatments and experimental spectral resolutions daunting. Since low-frequency modes contribute the most to the thermal correction to the enthalpy and entropy of a system, even small deviations in these modes lead to large errors in free energies. As a result, researchers have been somewhat reluctant to use calculated harmonic frequencies to estimate free energies of weakly bound clusters, particularly at high temperatures where the errors would be most pronounced.[62]

On the basis of existing literature, VPT2 is the most appropriate and affordable approach for evaluating the role of anharmonicity in large water clusters. Even though recent works by Barone et al.[63,64] advocate the use of density functional methods with modest basis sets to calculate VPT2 anharmonic frequencies, we chose to use an MP2 wave function because it has been shown to be the most affordable and accurate method for studying water clusters. The aug-cc-pVDZ basis set has the necessary diffuse and polarization functions to describe hydrogen bonding well, and it is often used to determine optimal geometries and harmonic vibrational frequencies. MP2 calculations with correlation consistent basis sets, when extrapolated to the CBS limit, capture all the important features of small water clusters.[65−80] MP2/aug-cc-pVDZ harmonic vibrational frequencies have been used for benchmark quality works on water clusters as large as $(H_2O)_{17}$ due to their affordability.[80] Therefore, appropriate scaling factors for the MP2/aug-cc-pVDZ level of theory are especially important.

In this paper, we demonstrate the need to use separate scaling factors for intermolecular vibrational modes of hydrogen-bonded clusters. For the commonly used MP2/aug-cc-pVDZ level of theory, we provide a set of frequency scaling factors for harmonic frequencies as well as the ZPVE and vibrational corrections to the enthalpy and entropy. Using 723 VPT2 anharmonic frequencies calculated for $(H_2O)_{n=2-6,8,9}$, scaling factors for the harmonic vibrational frequencies have been determined. The intermolecular modes (ω < 1100 cm^{-1}) are found to be substantially more anharmonic than intramolecular bending (1100 cm^{-1} < ω <1800 cm^{-1}) and stretching modes (ω > 1800 cm^{-1}), suggesting that the use of different frequency scaling factors for each region in correcting the harmonic vibrational modes is appropriate. Similarly, by comparing the harmonic and anharmonic ZPVE, vibrational contribution to the enthalpy (ΔH_{vib}) and entropy (S_{vib}), scaling factors are calculated. These different scaling approaches are applied to the water dimer system in order to evaluate the importance of anharmonicity and the validity of the rigid rotor-harmonic oscillator (RRHO) model. The transferability of the recommended scaling factors to other levels of theory and hydrogen-bonded systems is also discussed.

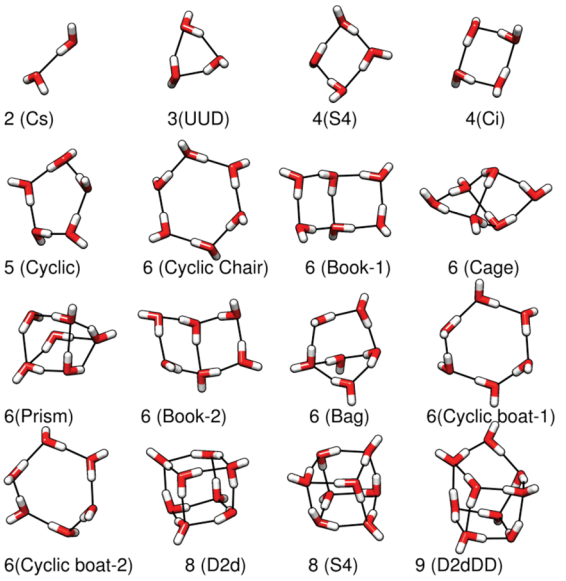

Figure 1. The 16 water clusters included in this study.

2. METHODOLOGY

The clusters included in this study are the water dimer (2-C_s), trimer (3-UUD), tetramers (4-S_4, 4-C_i), pentamer (5-Cyclic), hexamers (6-Cyclic-chair, 6-Book-1, 6-Cage, 6-Prism, 6-Book-2, 6-Bag, 6-Cyclic-boat-1, 6-Cyclic-boat-2), octamers (8-D_{2d}, 8-S_4), and one nonamer (9-D_{2d}DD). The optimized structures are shown in Figure 1. These 16 clusters have a total of 723 harmonic vibrational modes. The geometry optimizations and harmonic vibrational frequencies were computed using MP2/aug-cc-pVDZ with analytical gradients and Hessians. To avoid numerical problems in subsequent anharmonic frequency calculations, tight convergence criteria was enforced for both the geometry optimization and the Hessian calculations. We denote VPT2 anharmonic calculations on MP2/aug-cc-pVDZ potential energy function as VPT2/MP2/aVDZ for the sake of brevity. For these anharmonic calculations, the necessary third and fourth derivatives were determined by finite differentiation of analytic Hessians with respect to nuclear displacements along each normal mode. The default 0.0250 Å[43] step size is appropriate for rigid and semirigid systems, but it gives erratic anharmonic frequencies for the larger water clusters even after our geometries and energies were converged very tightly. A step size that gave the most reasonable anharmonic frequencies for $(H_2O)_{n=2-6,8,9}$ is 0.0050 Å.

One unintended consequence of using small step sizes is that it reduced the number of resonances encountered in VPT2 calculation. One of the shortcomings of VPT2 is that it suffers in handling Fermi (that affect modes coupled by cubic force constants) and Darling−Dennison resonances (which affect modes coupled by quartic force constants and Coriolis coupling constants).[81] We used the default cutoffs for Fermi and Darling−Dennison resonances. Gaussian 09 A.02[82] removes resonances in an automated way as prescribed by Martin et al.[83,84] All computations are performed using the Gaussian 09 A.02[82] software package on a 128-core SGI Altix 3700 Bx2. There are differences in anharmonic frequencies calculated using Gaussian 03 B.02,[85] Gaussian 09 A.02, and CFOUR.[86] In the interest of consistency, all our calculations are performed using Gaussian 09 A.02.[82]

Of the 16 clusters we studied, 4 hexamers had one or more anharmonic frequencies that are abnormally small compared to

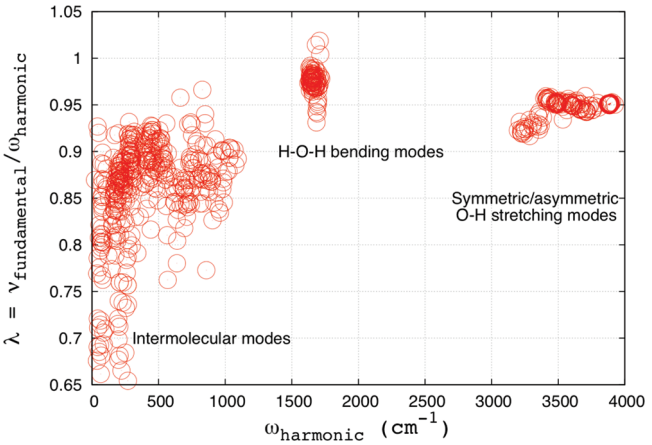

Figure 2. The differing anharmonicity in the three classes of VPT2/MP2/aug-cc-pVDZ vibrational modes of water clusters $(H_2O)_{2-6,8,9}$.

the harmonic analog. These outliers have individual scaling factors ($\lambda_i = \nu_i/\omega_i$) that lie outside of three standard deviations (σ) from the average λ of each class. Since these anomalous frequencies introduce large uncertainty, they have been removed from the scaling scheme. Scaling factors are calculated in a manner that is partly different from previous works.[3−5,7] First, while others have used the inverse of frequencies to calculate scaling factors for low-frequency modes, we find such an approach to massively skew the scaling factors toward those of the lowest (and most error prone) frequency modes. Scaling the inverse of the frequency may be appropriate for covalently bonded systems where the anharmonicity rarely exceeds 10% even for low-frequency modes, but it gives unreasonably low-scaling factors and large errors when applied to the highly anharmonic intermolecular modes of our water clusters. Since we preemptively separate low-frequency intermolecular modes into their own class, deriving the frequency scaling factors using the normal frequencies works reasonably well. Second, the ZPVE scaling factors in our case are determined by scaling the harmonic ZPVE against an estimate of the true ZPVE in a manner suggested by Barone et al.[42] Third, to get scaling factors for ΔH_{vib} and S_{vib}, previous works used least-squares fitting of frequencies to minimize the residual between the experimental and theoretical ΔH_{vib} and S_{vib}. We have looked at two approaches: (a) scaling the harmonic ΔH_{vib} and S_{vib} against their anharmonic analogs directly and (b) determining frequency scaling factors that minimize the residual of ΔH_{vib} and S_{vib}. The merits and downsides of both approaches are discussed.

3. RESULTS AND DISCUSSION

3.1. Classification of Vibrational Frequencies. Each water cluster $(H_2O)_n$ has $2n$ high-frequency intramolecular stretching modes, n intramolecular bending modes, and $6n - 6$ low-frequency intermolecular modes. In this study, there are 723 vibrational modes of which 182 correspond to monomer stretching, 91 to monomer bending, and 450 to low-frequency intermolecular motion. Removing a few anomalous anharmonic frequencies leaves us with 703 vibrational frequencies of which 435, 271, 88, and 178 are intermolecular, intramolecular, bending, and stretching modes, respectively. As illustrated in Figure 2, the distribution of the ratio of anharmonic to harmonic frequencies ($\lambda = \nu^f/\omega^h$) for the water clusters in this study shows three distinct groupings. The stretching modes which lie above 3000 cm^{-1} are not particularly anharmonic; as can be seen from the $\lambda \sim 0.95$, one would need to match the harmonic frequencies to the fundamentals. The bending modes are even less anharmonic, needing a scaling factor of $\lambda \sim 0.97$ to match fundamentals. In contrast, the low-frequency intermolecular modes have a larger and more spread anharmonicity. Figure 2 demonstrates the need to use separate multiplicative factors to scale the different classes of frequencies. Johnson et al.[9] outline the three conditions that need to be met to form a class of frequencies as "(1) the bias (λ) for the target frequency is believed to be of similar value to those in the class; (2) the (estimated) biases in the class have an approximately normal and acceptably narrow distribution; (3) the number of vibrational frequencies in the class is reasonably large." Our grouping of the water clusters frequencies into two or three classes satisfies the conditions listed above. The frequencies can be classified into intermolecular (ω^h < 1100 cm^{-1}) and intramolecular (ω^h > 1100 cm^{-1}) modes, and that scheme will be designated as two-split scaling. Alternatively, the frequencies can be grouped into intermolecular (ω^h < 1100 cm^{-1}), bending (1100 cm^{-1} < ω^h < 1800 cm^{-1}), and stretching (ω^h > 1800 cm^{-1}) modes, in a scheme we will call three-split scaling. A comparison of uniform scaling with the two- and three-split scaling schemes is performed below.

3.2. Scaling Vibrational Frequencies. Given N MP2/aVDZ harmonic frequencies (ω^h) and VPT2/MP2/aVDZ anharmonic fundamental frequencies (ν^f), an optimal scaling factor, λ can be found by using the least-squares procedure minimizing the residual (Δ) which is defined as

$$\Delta = \sum_{i=1}^{N} (\lambda \omega_i^h - \nu_i^f)^2 \tag{1}$$

The λ that minimizes the residual is

$$\lambda = \frac{\sum_{i=1}^{N} \omega_i^h \nu_i^f}{\sum_{i=1}^{N} (\omega_i^h)^2} \tag{2}$$

How well this scaling factor improves the harmonic frequencies is assessed by evaluating the root-mean-square error (RMSE) of the scaled frequency relative to the anharmonic fundamental:

$$RMSE = \sqrt{\frac{1}{N} \sum_{i=1}^{N} (\lambda \omega_i^h - \nu_i^f)^2}$$
$$RMSE = \sqrt{\frac{\Delta}{N}} \tag{3}$$

The uncertainty associated with the scaling factor λ is a critical measure of the confidence and applicability of the scaling scheme, as shown repeatedly by Irikura et al.[6,8,9] The uncertainty $\sigma(\lambda)$ is defined as

$$\sigma(\lambda) = \sqrt{\frac{\Delta}{\sum_{i=1}^{N} (\omega_i^h)^2}} \tag{4}$$

As noted already, there are many ways to calculate frequency scaling factors. Table 1 shows the scaling factors for uniform, two- and three-split scaling schemes for each separate water

Table 1. Individual Scaling Factors for MP2/aug-cc-pVDZ Harmonic Frequencies Relative to VPT2/MP2/aug-cc-pVDZ Anharmonic Frequencies of $(H_2O)_{n=2-6,8,9}$

	uniform	two-split scaling		three-split scaling		
	λ (all)	λ (ω < 1100)	λ (ω > 1100)	λ (ω < 1100)	λ (1100 < ω < 1800)	λ (ω > 1800)
2-C_s	0.954	0.831	0.955	0.831	0.972	0.953
3-UUD	0.951	0.811	0.955	0.811	0.970	0.953
4-C_i	0.952	0.875	0.955	0.875	0.976	0.952
4-S_4	0.952	0.878	0.954	0.878	0.980	0.952
5-Cyclic	0.950	0.880	0.952	0.880	0.972	0.950
6-Cyclic-chair[a]	0.950	0.876	0.953	0.876	0.971	0.951
6-Book-1	0.950	0.880	0.953	0.880	0.979	0.950
6-Cage	0.948	0.864	0.951	0.864	0.974	0.949
6-Prism	0.947	0.872	0.950	0.872	0.983	0.946
6-Book-2[a]	0.947	0.878	0.949	0.878	0.969	0.947
6-Bag	0.947	0.876	0.950	0.876	0.975	0.947
6-Cyclic-boat-1[a]	0.949	0.864	0.952	0.864	0.967	0.951
6-Cyclic-boat-2[a]	0.949	0.863	0.952	0.863	0.964	0.950
8-S_4	0.944	0.888	0.946	0.888	0.982	0.943
8-D_{2d}	0.944	0.885	0.947	0.885	0.983	0.943
9-D_{2d}DD [a]	0.944	0.884	0.946	0.884	0.978	0.943
overall	0.948	0.876	0.950	0.876	0.975	0.949

[a] Have individual scaling factors ($\lambda_i = \nu_i / \omega_i$) that lie outside 3σ of the average λ.

Table 2. Collective Scaling Factors for MP2/aug-cc-pVDZ Harmonic Frequencies Relative to VPT2/MP2/aug-cc-pVDZ Anharmonic Frequencies of $(H_2O)_{n=2-6,8,9}$[a]

	nature of mode	scaling factor (λ)	uncertainty [$\sigma(\lambda)$]	RMSE (cm^{-1})
		Uniform Scaling		
λ (all)	all	0.948	0.019	39
		Two-Split Scaling		
λ (ω < 1100)	intermolecular	0.876	0.036	17
λ (ω > 1100)	intramolecular	0.950	0.012	36
		Three-Split Scaling		
λ (ω < 1100)	intermolecular	0.876	0.036	17
λ (1100 < ω < 1800)	intramol. bending	0.975	0.010	17
λ (ω > 1800)	intramol. stretching	0.949	0.007	25

[a] Using 703, 435, 271, 88, and 178 frequencies for all, intermolecular, intramolecular, bending, and stretching modes, respectively, after removing outlying frequencies from an initial set of 723, 450, 273, 91, and 182 modes.

cluster and all 15 clusters combined. The individual scaling factors do not vary substantially among the clusters, with the dimer and the trimer being slight outliers. The overall scaling factors are given in Table 2. Applying a uniform scaling factor of 0.948 ± 0.019 leads to an RMSE of 39 cm^{-1}. It is clear that the high-frequency stretching modes are dominating this scaling factor, as evidenced by the scaling factor of 0.949 ± 0.007 we get just for the stretching modes alone. In the two-split scaling scheme, we get a scaling factor of 0.876 ± 0.036 for the 435 intermolecular modes and 0.950 ± 0.012 for the 271 intramolecular modes. The larger uncertainty in the intermolecular scaling factor is due to the diverse range of anharmonicity in the low-frequency modes, as can be seen in the frequency range ω^h < 1100 cm^{-1} in Figure 2. The RMSE of the two-split scaling scheme is lower than that of the uniform scaling. In the three-split scaling, we derive values of 0.876 ± 0.036 for the 435 intermolecular modes, 0.975 ± 0.010 for the 88 intramolecular bending modes, and 0.949 ± 0.007 for the 178 intramolecular stretching modes. The RMSE for this scheme is lower than that of the uniform and two-split scaling approaches. The distribution of the error in each scheme, defined as the difference between the scaled harmonic and anharmonic frequency, is shown in Figure 3. Figure 3a shows that the harmonic frequencies exceed anharmonic ones by as much as 260 cm^{-1}, and the error distribution is large. Applying the scaling schemes substantially improves the agreement with the anharmonic frequencies, as illustrated in Figure 3b. The three-split scaling has the lowest average error and narrowest error distribution.

Our scaling factors for the intramolecular modes (0.950 ± 0.012) in the two-split scaling scheme are comparable to those in the literature which are constructed by least-squares fitting of theoretical

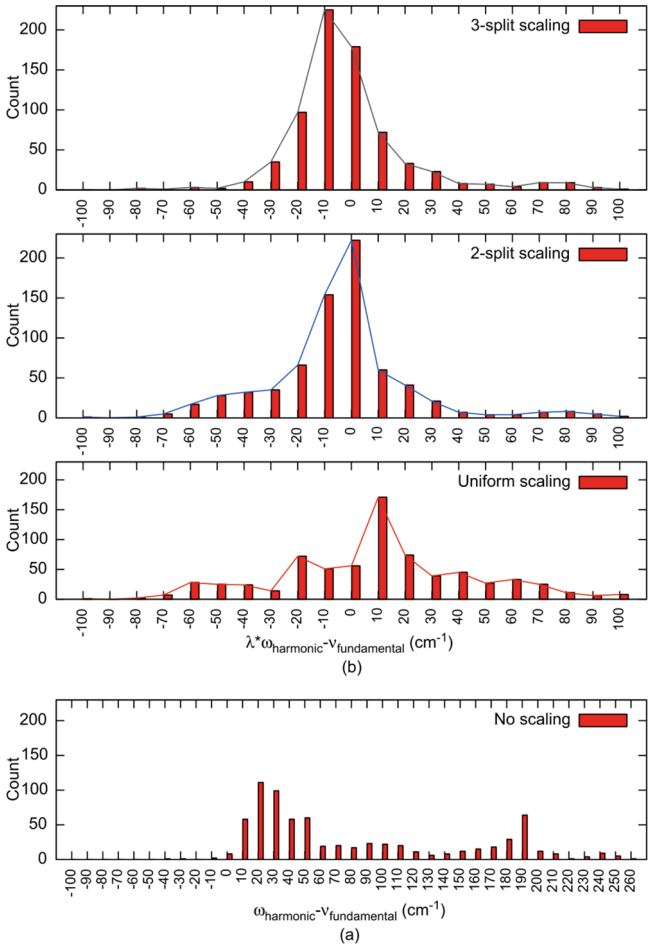

Figure 3. Error distribution of unscaled (a) and scaled (b) MP2/aVDZ harmonic vibrational frequencies of $(H_2O)_{2-6,8,9}$ relative to VPT2/MP2/aVDZ anharmonic frequencies. Please note that different abscissa scales are used in (a) and (b).

harmonic vibrational frequencies to experimental fundamental frequencies of covalently bonded molecules. For the MP2/aVDZ level of theory, Merrick et al. report scaling factors of 0.9615 and 0.9614 for fundamental frequencies using the F1 and F1″ set of frequencies.[7] Sinha et al. similarly recommend a scaling factor of 0.9604 based on a database of 41 common organic molecules.[5] There are two reasons for the slight differences between our scaling factors and those from the literature. First, we are comparing harmonic frequencies against calculated anharmonic frequencies, while the literature references compare against experimental fundamental frequencies. Second, we are using a database of hydrogen-bonded water clusters, while those in the literature rely on a set of small covalently bonded molecules.

The most stark difference between our scaling scheme and others is the scaling factor for the low-frequency intermolecular modes. Merrick et al. use inverse frequency scaling and obtain scaling factors of 1.0418 and 1.0338 for the F1 and F1″ set of frequencies for the MP2/aVDZ level of theory.[7] Using the same approach on a database of 41 organic molecules, Sinha at al. get scaling factors for MP2/aVDZ low frequencies ($\omega^h < 1000\ cm^{-1}$) of 1.0999.[5] We did not use inverse frequency scaling because it is unduly biased toward the lowest frequency modes which are very anharmonic and error prone. For the database of covalently bonded molecules that Merrick and Sinha used, the level of anharmonicity in the lowest frequency modes is not as severe as ours. So, it would make sense to use an inverse frequency scaling factor to overcome the dominance of the high-frequency modes in the direct scaling scheme. We circumvent that dominance by grouping our frequencies into three classes and determining separate scaling factors for each class.

3.3. Scaling of ZPVE. Provided how important quantum mechanical ZPVE corrections are to most chemical systems, a proper scaling factor for ZPVEs is crucial. As demonstrated by Grev et al.,[2] ZPVE scaling factors are different from plain frequency scaling factors due to the presence of anharmonicity. The harmonic and fundamental ZPVE for a molecule with N_m vibrational modes are given by

$$ZPVE^h = \frac{1}{2}\sum_{i=1}^{N_m} \omega_i^h \tag{5}$$

$$ZPVE^f = \frac{1}{2}\sum_{i=1}^{N_m} \nu_i^f \tag{6}$$

Since our calculated anharmonic fundamental corresponds to the $\nu(0\rightarrow1)$ transition frequency and not the energy of $\nu(0)$, we cannot get the anharmonic ZPVE by simply plugging the fundamental frequency into the ZPVE expression in eq 6. The true ZPVE lies somewhere in between $ZPVE^h$ and $ZPVE^f$ and various approximations to it have been given in the literature.[2,87] A commonly used estimate of the true ZPVE is

$$ZPVE = \chi_0 + \frac{1}{2}(ZPVE^h + ZPVE^f) - \frac{1}{4}\sum_{i=1}^{N_m} \chi_{ii} \tag{7}$$

where χ_0 is a small anharmonic correction and χ_{ii} are the diagonal elements of the anharmonicity matrix. With an estimate of the true ZPVE in hand, we can derive a scaling factor that maps the harmonic ZPVE to it. For a database of N_{mols} molecules, the residual of the harmonic and true ZPVE is

$$\Delta = \sum_{i=1}^{N_{mols}} (\lambda(ZPVE_i^h) - ZPVE_i)^2 \tag{8}$$

The λ that minimizes the residual is

$$\lambda = \frac{\sum_{i=1}^{N_{mols}} (ZPVE_i^h)(ZPVE_i)}{\sum_{i=1}^{N_{mols}} (ZPVE_i^h)^2} \tag{9}$$

The RMSE and uncertainty are then given by

$$RMSE = \sqrt{\frac{\Delta}{N_{mols}}} \tag{10}$$

$$\sigma(\lambda) = \sqrt{\frac{\Delta}{\sum_{i=1}^{N_{mols}} (ZPVE_i^h)^2}} \tag{11}$$

The anharmonic fundamental (ν_i^f), χ_0, and χ_{ii} terms can be determined from the quadratic, cubic, and semidiagonal quartic force constants calculated using VPT2. Of the 16 clusters in our training set, we have removed 5 because they had one or more abnormally low anharmonic frequencies. For the remaining 11 water clusters, Table 3 shows the scaling factor for each cluster and the set overall. All the scaling factors are in a narrow range

Table 3. Scaling Factors for the MP2/aug-cc-pVDZ Harmonic ZPVE of Water Clusters[a,b]

	$ZPVE^{harmonic}$	$ZPVE^{anharmonic\ c}$	$ZPVE^{anharmonic}/ZPVE^{harmonic}$
2-C_s	28.88	28.23	0.978
3-UUD	45.50	44.31	0.974
4-C_i	61.59	60.19	0.977
4-S_4	61.78	60.27	0.976
5-Cyclic	77.36	75.40	0.975
6-Book-1	93.59	91.20	0.974
6-Cage	93.96	91.48	0.974
6-Prism	94.16	91.78	0.975
6-Bag	93.38	90.95	0.974
8-S_4	127.57	124.76	0.978
8-D_{2d}	127.57	124.90	0.979
λ			0.976
$\sigma(\lambda)$			0.002
RMSE/cluster			0.18

[a] Four hexamers (Cyclic-chair, Book-2, Cyclic-boat-1, and Cyclic-boat-2) and the $D_{2d}DD$ nonamer are excluded because they had individual scaling factors ($\lambda_i = \nu_i/\omega_i$) that lie outside 3σ of the average λ. [b] In kcal/mol. [c] Estimate of the true ZPVE calculated using eq 7.

Table 4. Scaling Factors for the MP2/aug-cc-pVDZ Harmonic ΔH_{vib}(298.15 K) of Water[a]

	$\Delta H_{vib}{}^{h}$ (298.15 K)[a]	$\Delta H_{vib}{}^{f}$ (298.15 K)[a]	$\Delta H_{vib}{}^{f}/\Delta H_{vib}{}^{h}$ (298.15 K)
2-C_s	1.92	2.10	1.096
3-UUD	3.03	3.49	1.154
4-C_i	4.51	5.01	1.112
4-S_4	4.40	4.82	1.096
5-Cyclic	6.27	6.95	1.109
6-Book-1	7.74	8.49	1.096
6-Cage	7.51	8.39	1.118
6-Prism	7.46	8.33	1.117
6-Bag	7.82	8.70	1.112
8-S_4	9.75	10.71	1.098
8-D_{2d}	9.75	10.69	1.097
λ_H			1.106
$\sigma(\lambda_H)$			0.011
RMSE/cluster[b]			0.07

[a] Four hexamers (Cyclic-chair, Book-2, Cyclic-boat-1, and Cyclic-boat-2) and the D_{2d}DD nonamer are excluded because they had individual scaling factors ($\lambda_i = \nu_i/\omega_i$) that lie outside 3σ of the average λ. [b] In kcal/mol.

between 0.97 and 0.98. Our overall scaling factor of 0.976 ± 0.002 is close to the 0.9675[5] and 0.9878[7] reported in the literature from databases of small covalently bonded molecules. Considering that ZPVE is dominated by high-frequency modes, the proximity between our scaling factors and those from the literature (which have a larger number of high-frequency modes) is not surprising.

3.4. Scaling of Vibrational Corrections to the Enthalpy and Entropy. Given the vibrational energy levels of a molecule, we can calculate the vibrational partition function $Q_{vib}(T)$ and the finite temperature vibrational correction to the enthalpy $[\Delta H_{vib}(T) = H_{vib}(T) - H_{vib}(0)]$ and entropy $[S_{vib}(T)]$. The vibrational and rotational contributions to the partition function employ the canonical rigid rotor-harmonic oscillator (RRHO) equations.[15,88] In the harmonic oscillator model, the vibrational energy levels of each mode are evenly spaced, and we can get compact expressions for $Q_{vib}(T)$ and the finite temperature corrections:

$$Q_{vib} = \prod_i \left(\frac{1}{1 - e^{-\mu_i}}\right) \tag{12}$$

$$\Delta H_{vib}(T) = RT \sum_i \left(\frac{\mu_i}{e^{\mu_i} - 1}\right) \tag{13}$$

$$S_{vib}(T) = R \sum_i \left[\frac{\mu_i}{e^{\mu_i} - 1} - \ln(1 - e^{-\mu_i})\right] \tag{14}$$

where $\mu_i = \hbar c\omega_i/k_B T$, R is the universal gas constant, $\hbar$ is Planck's constant, c is the speed of light, and ω_i is the harmonic frequency in wavenumbers. The anharmonic partition function is not amenable for such simplifications, and it has terms that include the anharmonicity constant. Anharmonic energy levels are not evenly spaced as is the case for a harmonic oscillator. One would need to sum over all the anharmonic energy levels to calculate the partition function, but the perturbation theory is prone to failures in predicting higher vibrational energy levels. To overcome these limitations, Truhlar and Isaacson[89] have proposed an approximation called simple perturbation theory (SPT) which retains a form like the harmonic expression above but uses anharmonic frequencies and ZPVEs:

$$Q_{vib} = \frac{\exp\left(\frac{-ZPVE}{k_B T}\right)}{\prod_i (1 - e^{-\mu_i})} \tag{15}$$

where $\mu_i = \hbar c\nu_i/k_B T$, $\hbar$ is Planck's constant, c is the speed of light, ν_i is the anharmonic frequency in wavenumbers, and ZPVE is the true zero point vibrational energy correction shown in eq 7. SPT has been shown to compare well with methods summing over anharmonic energy levels for linear and nonlinear molecules in the small anharmonicity limit.[81,89−91] In modes like torsions, ring inversions, and internal rotations where the vibrational potential differs markedly from that of a single well harmonic oscillator, the SPT approximation will not work well. Kurtén et al.[92] have recently generalized the solution to a one-dimensional system in the small anharmonicity limit to n-dimensions and successfully applied it to $(H_2SO_4)(H_2O)_{n=1-2}$ and $(HSO_4^-)(H_2O)_{n=1-2}$. Their more complicated anharmonic expressions contain terms including the anharmonicity constant, and they do predict vibrational enthalpies and entropies that differ substantially from those of SPT for hydrogen-bonded systems. Nevertheless, since their expressions have not been rigorously tested on a variety of systems, we will use the SPT approximation here. The SPT thermal corrections to the enthalpy and the entropy look similar to their harmonic analogs except we use the fundamental frequency ($\mu_i = \hbar c\nu_i/k_B T$) in this case:

$$\Delta H_{vib}(T) = RT \sum_i \left(\frac{\mu_i}{e^{\mu_i} - 1}\right) \tag{16}$$

$$S_{vib}(T) = R\sum_i \left[\frac{\mu_i}{e^{\mu_i}-1} - \ln(1-e^{-\mu_i})\right] \quad (17)$$

There are two approaches to determine appropriate scaling factors for $\Delta H_{vib}(T)$ and $S_{vib}(T)$. One can calculate the harmonic and anharmonic $\Delta H_{vib}(T)$ and $S_{vib}(T)$ for each molecule first and seek scaling factors (λ_H and λ_S) that minimize the residuals:

$$\Delta_H = \sum_{i=1}^{N_{mols}} [\lambda_H \Delta H_{vib,i}(T,\omega^h) - \Delta H_{vib,i}(T,\nu^f)]^2 \quad (18)$$

$$\Delta_S = \sum_{i=1}^{N_{mols}} [\lambda_S S_{vib,i}(T,\omega^h) - S_{vib,i}(T,\nu^f)]^2 \quad (19)$$

This method is easy to apply, and below is an analytic form for the scaling factors:

$$\lambda_H = \frac{\sum_{i=1}^{N_{mols}} \Delta H_{vib,i}(T,\omega^h)\Delta H_{vib,i}(T,\nu^f)}{\sum_{i=1}^{N_{mols}} [\Delta H_{vib,i}(T,\omega^h)]^2} \quad (20)$$

$$\lambda_S = \frac{\sum_{i=1}^{N_{mols}} S_{vib,i}(T,\omega^h)S_{vib,i}(T,\nu^f)}{\sum_{i=1}^{N_{mols}} [S_{vib,i}(T,\omega^h)]^2} \quad (21)$$

The RMSE and uncertainty in the scaling factors are calculated simply:

$$RMSE_H = \sqrt{\frac{\Delta_H}{N_{mols}}} \quad (22)$$

$$RMSE_S = \sqrt{\frac{\Delta_S}{N_{mols}}} \quad (23)$$

$$\sigma(\lambda_H) = \sqrt{\frac{\Delta_H}{\sum_{i=1}^{N_{mols}} [\Delta H_{vib,i}(T,\omega^h)]^2}} \quad (24)$$

$$\sigma(\lambda_S) = \sqrt{\frac{\Delta_S}{\sum_{i=1}^{N_{mols}} [S_{vib,i}(T,\omega^h)]^2}} \quad (25)$$

Please note that the thermal correction to the enthalpy here excludes the ZPVE, since the ZPVE has been scaled separately in the previous subsection. Here $\Delta H_{vib}(T) = H_{vib}(T) - H_{vib}(0)$. Since the ZPVE makes up a large part of the $H_{vib}(T)$ at most relevant temperatures, scaling $H_{vib}(T)$ would closely resemble scaling of the ZPVE. Thus, we are scaling the vibrational correction to the enthalpy excluding the ZPVE.

Table 4 shows the scaling factors for $\Delta H_{vib}(T)$ determined using the procedure above. With the exception of the water trimer, the ratio of anharmonic to harmonic $\Delta H_{vib}(298.15\ K)$ is between 1.09 and 1.11. A scaling factor exceeding unity makes sense here because harmonic vibrational frequencies and $\Delta H_{vib}(T)$ have an inverse relationship; as we scale down the harmonic frequencies, the $\Delta H_{vib}(T)$ is scaled up. The overall scaling factor of 1.106 ± 0.011 works well as evidenced by the RMSE of 0.07 kcal/mol for the 11 clusters in this study. Table 5 shows the scaling factor for $S_{vib}(298.15\ K)$ for the individual clusters and the collective group. All the scaling factors lie within the range of 1.12−1.21. Considering how sensitive the entropy is to the low-frequency modes (which are scaled down by 0.876), it should not come as a surprise that the entropy is scaled up by 10−20%. The overall scaling factor for this scheme is 1.150 ± 0.021 with an RMSE of 0.95 cal/mol/K.

Table 5. Scaling Factors for the MP2/aug-cc-pVDZ Harmonic $S_{vib}(298.15\ K)$ of Water Clusters[a,b]

	$S_{vib}^h(298.15\ K)^b$	$S_{vib}^f(298.15\ K)^b$	$S_{vib}^f(298.15\ K)/S_{vib}^h(298.15\ K)$
2-C_s	12.17	13.95	1.147
3-UUD	17.59	21.24	1.207
4-C_i	29.16	33.16	1.137
4-S_4	27.37	30.63	1.119
5-Cyclic	43.06	50.06	1.163
6-Book-1	52.37	59.84	1.143
6-Cage	48.19	56.21	1.166
6-Prism	47.44	55.44	1.169
6-Bag	52.94	62.54	1.181
8-S_4	61.33	69.49	1.133
8-D_{2d}	61.20	68.87	1.125
λ_S			1.150
$\sigma(\lambda_S)$			0.021
RMSE			0.945

[a] Four hexamers (Cyclic-chair, Book-2, Cyclic-boat-1, and Cyclic-boat-2) and the D_{2d}DD nonamer are excluded because they had individual scaling factors ($\lambda_i = \nu_i/\omega_i$) that lie outside 3$\sigma$ of the average λ. [b] In cal/mol/K.

The approach just outlined for scaling $\Delta H_{vib}(T)$ and $S_{vib}(T)$ has the advantage that it gives a simple multiplicative factor that can be applied directly to harmonic $\Delta H_{vib}(T)$ and $S_{vib}(T)$. An alternative approach that has been advocated in the literature seeks frequency scaling factors that minimize the residuals:

$$\Delta_H = \sum_{i=1}^{N} [\Delta H_{vib}(T,\lambda_H\omega_i^h) - \Delta H_{vib}(T,\nu_i^f)]^2 \quad (26)$$

$$\Delta_S = \sum_{i=1}^{N} [S_{vib}(T,\lambda_S\omega_i^h) - S_{vib}(T,\nu_i^f)]^2 \quad (27)$$

There is no analytic expression for the scaling factors, and they have to be determined numerically. The RMSE and uncertainty in the scaling factors are calculated in the same way as frequencies and ZPVEs. Along the same lines, it would make sense to separate the vibrational modes into three classes and scale each group independently. However, the vibrational corrections to both the enthalpy and entropy are overwhelmingly dominated by the low-frequency modes. Figure 4 shows a plot of $\Delta H_{vib}(298.15\ K)$ and $S_{vib}(298.15\ K)$ as a function of vibrational frequency. Vibrational modes of frequency exceeding 1100 cm^{-1} (i.e., intramolecular modes) make a very minimal contribution to $\Delta H_{vib}(298.15\ K)$ and $S_{vib}(298.15\ K)$. The contribution of the intramolecular modes to the enthalpy and entropy for small water clusters is typically around 1%, which is below 0.1 kcal/

mol. So, it is not necessary to separate the frequencies into classes and scale them differently.

Since low-frequency modes are the dominant contributors to ΔH_{vib} and S_{vib}, the frequency scaling factors that minimize ΔH_{vib} and S_{vib} residuals are similar to the scaling factor for low-frequency modes. Tables 6 and 7 show the frequency scaling factors for ΔH_{vib} and S_{vib} at temperatures ranging from 50 K to 373.15 K. At low temperatures, there is only enough thermal energy to populate all the ground vibrational levels of all the modes and the excited vibrational levels of the low-frequency modes. So, we see ΔH_{vib} and S_{vib} frequency scaling factors that reflect the scaling factor for low-frequency modes (0.876). As more thermal energy is available at higher temperatures, the excited vibrational levels of more modes start contributing, and the ΔH_{vib} and S_{vib} frequency scaling factors increase. At temperatures below 373.15 K, the ΔH_{vib} and S_{vib} frequency scaling factors are less than 0.870 and 0.845, respectively.

The uncertainty in the ΔH_{vib} frequency scaling factors is large, particularly at low temperatures, but the RMSE is very small. For the S_{vib} frequency scaling factors, both the uncertainty and the RMSE are small. Our scaling factors differ significantly from those in the literature which are intended for covalently bonded systems. Unlike our ΔH_{vib}(298.15 K) frequency scaling factor of 0.866 ± 0.040, Sinha et al.[5] and Merrick et al.[7] report values of 0.9473 and 1.0359, respectively. Our S_{vib}(298.15 K) frequency scaling factor of 0.841 ± 0.016 is different from Sinha et al.'s[5] 0.9049 and Merrick et al.'s[7] 1.0452, respectively. Our RMSE is in general comparable to the two cited above.

The two approaches we have used to scale ΔH_{vib} and S_{vib} (scaling ΔH_{vib} and S_{vib} themselves or the vibrational frequencies that enter the ΔH_{vib} and S_{vib} expressions) are equivalent, but scaling the frequencies is advocated in this case because that approach is more rigorous. It also happens to be the approach taken by others in the literature.[4,5,7]

3.5. Assessment of the Scaling Factors. The performance of the scaling factors reported above is evaluated in two ways. First, the vibrational scaling factors are applied to the water dimer, and the resulting vibrational frequencies are compared with experimental, harmonic, and anharmonic frequencies. While the small RMSEs reported in Table 2 and the narrow error distribution shown in

Table 6. Frequency Scaling Factors for $\Delta H_{vib}(T)$ for Water Clusters at the MP2/aug-cc-pVDZ Level of Theory[a]

T (K)	scaling factor (λ_H)	uncertainty [$\sigma(\lambda_H)$]	RMSE (kcal/mol)
50	0.806	0.117	0.00
100	0.835	0.087	0.00
150	0.851	0.069	0.01
200	0.860	0.055	0.01
250	0.865	0.045	0.01
273.15	0.866	0.042	0.01
298.15	0.868	0.039	0.01
300	0.868	0.039	0.01
350	0.871	0.034	0.01
373.15	0.872	0.033	0.01

[a] Using 703 frequencies after removing outliers from an initial set of 723 frequencies.

Table 7. Frequency Scaling Factors for $S_{vib}(T)$ for Water Clusters at the MP2/aug-cc-pVDZ Level of Theory[a]

T (K)	scaling factor (λ_S)	uncertainty [$\sigma(\lambda_S)$]	RMSE (cal/mol/K)
50	0.790	0.040	0.06
100	0.815	0.028	0.08
150	0.828	0.023	0.09
200	0.836	0.020	0.10
250	0.841	0.018	0.10
273.15	0.843	0.017	0.11
298.15	0.844	0.016	0.11
300	0.844	0.016	0.11
350	0.847	0.015	0.11
373.15	0.848	0.014	0.11

[a] Using 703 frequencies after removing outliers from an initial set of 723 frequencies.

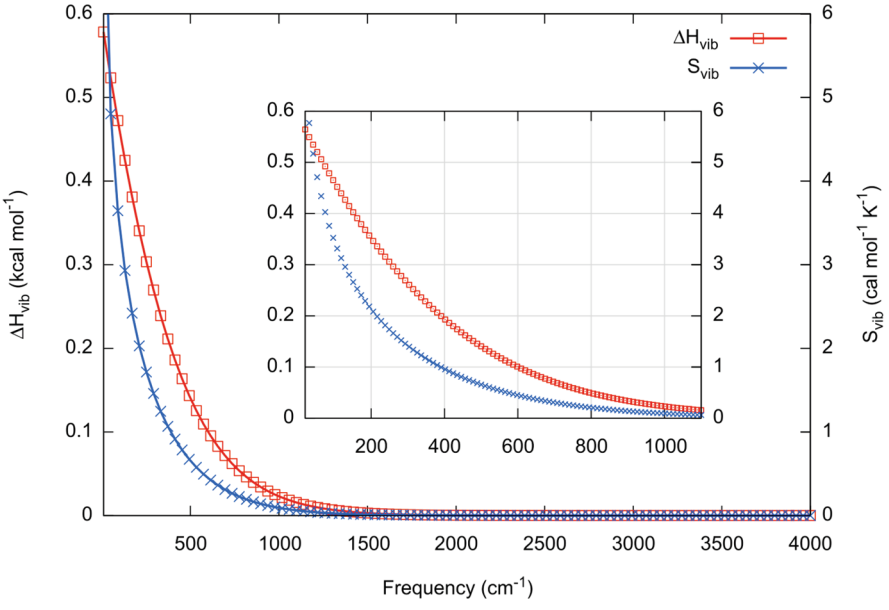

Figure 4. ΔH_{vib} and S_{vib} as a function of frequency at T = 298.15 K. Low-frequency modes contribute most greatly to ΔH_{vib} (left axis) and S_{vib} (right axis).

Table 8. Comparison of Calculated Harmonic,[a] Scaled Harmonic,[b−d] and Anharmonic[e] Frequencies[f] with Experimental[g] Values for the Water Dimer

		scaled				
mode[h]	harmonic[a]	uniform[b]	two-split[c]	three-split[d]	anharmonic[e]	experiment[g]
donor torsion	127	121	112	112	108	88
acceptor wag	148	140	130	130	123	103
acceptor twist	151	143	132	132	124	108
intermol. stretch	184	174	161	161	152	143
in-plane bend	358	339	313	313	328	311
out-of-plane bend	639	605	560	560	514	523
ν_2(a)	1624	1539	1543	1583	1581	1599
ν_2(d)	1643	1557	1561	1601	1593	1616
ν_1(d)	3704	3511	3520	3515	3554	3601
ν_1(a)	3796	3597	3607	3602	3614	3660
ν_3(d)	3904	3700	3710	3705	3720	3735
ν_3(a)	3925	3720	3730	3725	3730	3745
RMSE	98	53	41	36	**25**	

[a] MP2/aug-cc-pVDZ harmonic frequencies. [b] MP2/aug-cc-pVDZ harmonic frequencies scaled by 0.948. [c] MP2/aug-cc-pVDZ harmonic frequencies scaled by 0.876 and 0.950 for the inter- and intramolecular modes, respectively. [d] MP2/aug-cc-pVDZ harmonic frequencies scaled by 0.876, 0.975, and 0.949 for the intermolecular, bending, and stretching modes, respectively. [e] VPT2/MP2/aug-cc-pVDZ anharmonic frequencies. [f] In cm^{-1}. [g] See ref 37 and references therein. [h] ν_1 for symmetric stretching; ν_2 for bending; and ν_3 for asymmetric stretching. The use of (a) signifies hydrogen-bond acceptor water, and the (d) signifies the hydrogen-bond donor water.

Figure 3 speak to the reliability of our scaling approach, a comparison with experimental frequencies answers questions about the validity of using calculated anharmonic frequencies as proxies for experimental ones. Second, the ZPVE, ΔH_{vib}, and S_{vib} scaling factors are applied to 11 water clusters, and their effectiveness in reproducing anharmonic numbers is assessed.

3.5.1. Vibrational Scaling Factors Applied to $(H_2O)_2$. The water dimer is a prototypical hydrogen-bonding system that has been the subject of extensive theoretical and experimental investigations. It remains the only water cluster for which all the experimental vibrational frequencies are available. Thus, it serves as an ideal system for assessing the performance of the harmonic, anharmonic, and scaled harmonic approaches outlined in Section 3.2.

A comparison of the theoretical harmonic and anharmonic frequencies and intensities of the water dimer against the experimental analogs has been performed by the research groups of Shields,[37] Jordan,[58] and Kjaergaard[57] among others. We perform a similar assessment on the MP2/aVDZ frequencies and scaling schemes in Table 8. The RMSE in the harmonic frequencies relative to experiment is large (98 cm^{-1}), but scaling it by different factors brings sizable improvements. As discussed earlier, using uniform scaling factors does not correct for the varying anharmonicity in the harmonic frequencies. Using the two- and three-split scalings gives substantially better agreement with experiment, with RMSEs of 41 and 36 cm^{-1}, respectively. The experimental frequencies are closer to the anharmonic frequencies (RMSE = 25 cm^{-1}) than they are to the harmonic ones (RMSE = 98 cm^{-1}). That observation further validates our decision to use calculated anharmonic frequencies as proxies for experimental frequencies. In the case of larger water clusters whose vibrational spectra are not resolved fully, calculated anharmonic frequencies serve an indispensible role.

3.5.2. ZPVE, ΔH_{vib}, and ΔS_{vib} Scaling Factors Applied to $(H_2O)_{n=2-6,8}$. Here, we want to evaluate: (a) the ability of our scaling factors to map harmonic values onto anharmonic ones and (b) the magnitude of the anharmonic correction to the ZPVE, ΔH_{vib}, and S_{vib}. The scaled harmonic ZPVE is calculated by multiplying the harmonic ZPVE by 0.976 (see Table 3), while the harmonic and anharmonic values are determined using eqs 5 and 7, respectively. For ΔH_{vib} and S_{vib}, the harmonic and anharmonic values are computed using eqs 16 and 17. The scaled harmonic values require proper frequency factors for T = 298.15 K. Looking at Tables 6 and 7, those factors are λ_H = 0.868 and λ_S = 0.844 for ΔH_{vib} and S_{vib}. The harmonic frequencies are scaled by these factors before being input into eqs 16 and 17 to get the scaled harmonic ΔH_{vib} and S_{vib}.

Figure 5a−c displays a comparison of ZPVE, ΔH_{vib}(298.15 K), and S_{vib}(298.15 K) for 11 water clusters. It is quite evident that application of our scaling factors works remarkably well in mapping the harmonic values to their anharmonic analogs. Starting with the ZPVE, the largest absolute difference between the scaled harmonic and anharmonic value is only 0.39 kcal/mol for the S_4 octamer. This difference is small compared to the largest absolute difference between the harmonic and anharmonic ZPVE, which is 2.82 kcal/mol for the same S_4 octamer. The absolute difference between the scaled harmonic and anharmonic ZPVE ranges from 0.05 to 0.39 kcal/mol, while that between the harmonic and anharmonic values is 0.65 to 2.82 kcal/mol. Considering the magnitude of the ZPVE spans ∼28 kcal/mol for the water dimer to ∼125 kcal/mol for the octamer, the scaled harmonic value is matching the anharmonic one within 0.5% or less.

For ΔH_{vib}(298.15 K), we again see that our scaled harmonic value agrees remarkably well with the anharmonic value. The absolute difference between the scaled harmonic and anharmonic values ranges from 0.01 to 0.16 kcal/mol, while that between the harmonic and anharmonic values is 0.18 to 0.96 kcal/mol. Likewise, our scaled harmonic S_{vib}(298.15 K) is in great agreement with the anharmonic values. The absolute difference between the scaled harmonic and anharmonic value is in the range of 0.01−2.68 cal/mol/K, while the harmonic and anharmonic values differ by as much as 9.60 cal/mol/K.

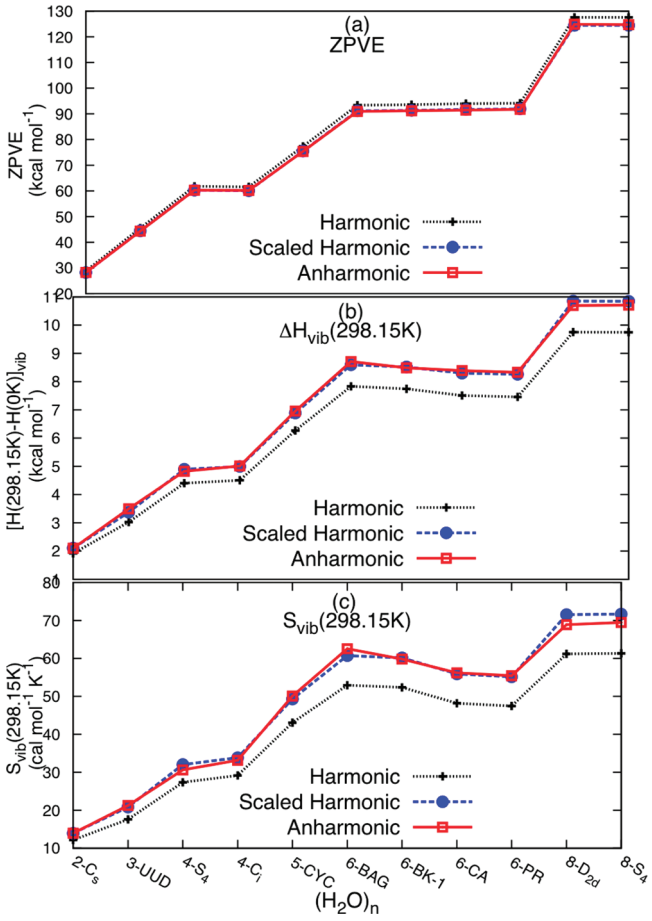

Figure 5. Comparison of harmonic, scaled harmonic and anharmonic ZPVE(a), ΔH_{vib}(b) and S_{vib}(c) for 11 water clusters at 298.15 K. The harmonic and anharmonic frequencies are calculated using [VPT2]/MP2/aug-cc-pVDZ level of theory. We used a scaling factor of 0.976 to get the scaled harmonic ZPVE. The scaled harmonic ΔH_{vib} and S_{vib} are calculated using harmonic vibrational frequencies scaled by 0.868 and 0.844, respectively.

The apparent gap between the harmonic and anharmonic values for ZPVE and ΔH_{vib} and S_{vib} in Figure 5 is indicative of the importance of anharmonicity. The anharmonic correction, which we define as the difference between the harmonic and anharmonic values as a percentage of the anharmonic value, is 1.8−2.7% for the ZPVE, 8.7−13.4% for the ΔH_{vib}, and 10.7−17.2% for the S_{vib}. Given such large anharmonic corrections, it is very important that one accounts for them. More importantly, when scaling factors are used to correct for anharmonicity, it is essential that the proper scaling factors are used. Applying scaling factors intended for covalently bonded systems to hydrogen-bonded clusters could lead to large errors, even though we have not attempted to quantify them here.

3.6. Transferability of the Scaling Factors. The vibrational scaling factors we have determined are strictly intended for application to the MP2/aVDZ harmonic vibrational frequencies of water clusters. Even though our training set contains vibrational frequencies for $(H_2O)_{n=2-6,8,9}$, the scaling factors should be applicable to larger water clusters. At the very least, they should perform better than conventional frequency scaling factors that are based on training sets of covalently bonded systems. The transferability of these scaling factors to other hydrogen-bonded systems requires further investigation. Our preliminary look at sulfuric acid hydrates, $H_2SO_4(H_2O)_{n=1-2}$ yielded reasonable VPT2 fundamental frequencies (see Tables S17 and S18 of the Supporting Information) indicating that a scaling scheme similar to that we devised for water clusters can be developed. However, it is not as trivial to partition the vibrational frequencies into physically meaningful classes (such as intramolecular stretching, intramolecular bending, and intermolecular modes) as it is for water clusters. That is because nine of H_2SO_4 vibrational modes lie below 1000 cm^{-1}, which is in the same region as the hydrogen-bonded intermolecular modes. Thus, one would need to develop an algorithm to determine whether certain low-frequency modes are primarily intramolecular H_2SO_4 modes or intermolecular modes. While such an approach is certainly possible, it borders on the territory of other scaling methods like SQM and ESFF which are better equipped to handle such cases.

4. CONCLUSION

Using a training set of 16 water clusters with a combined 723 vibrational frequencies, we have determined scaling factors for vibrational frequencies, ZPVEs, $\Delta H_{vib}(T)$, and $S_{vib}(T)$ at the MP2/aug-cc-pVDZ level of theory. Our scaling factors were determined by comparing harmonic vibrational frequencies with VPT2 anharmonic fundamentals. For vibrational frequencies, it is important to separate the modes into different classes because of the varying range of anharmonicities. The disparity between our scaling factors and those derived from databases of covalently bonded systems highlights the need to use different scaling factors for hydrogen-bonded systems. The application of our scaling factors to the water dimer binding energy illustrates the importance of accounting for anharmonic effects. Our scaling factors can readily be applied to calculations on water clusters using the MP2/aug-cc-pVDZ level of theory, but their applicability to other hydrogen-bonded systems has yet to be tested. While VPT2 or the three-split scaling methods are the most reliable techniques for calculating anharmonic frequencies, the relatively good agreement using a single scaling factor supports the conclusions obtained from past studies of water cluster free energies.[93,94]

■ ASSOCIATED CONTENT

Supporting Information. All the MP2/aVDZ optimized geometries, energies, VPT2/MP2/aVDZ harmonic and fundamental frequencies for $(H_2O)_{n=2-6,8,9}$ and $H_2SO_4(H_2O)_{n=1-2}$. This information is available free of charge via the Internet at http://pubs.acs.org/.

■ AUTHOR INFORMATION

Corresponding Author
*E-mail: george.shields@bucknell.edu.

■ ACKNOWLEDGMENT

Acknowledgment is made to the NSF and Bucknell University for their support of this work. This project was supported in part by NSF grant CHE-0848827 and by NSF grants CHE-0116435, CHE-0521063, and CHE-0849677 as part of the MERCURY high-performance computer consortium (http://mercuryconsortium.org). We thank Drs. Theo Kurten and Madis Noppel for helpful discussions and the reviewers for useful comments.

REFERENCES

(1) Hehre, W. J. *Ab Initio Molecular Orbital Theory*; Wiley: New York, 1986.

(2) Grev, R. S.; Janssen, C. L.; Schaefer, H. F., III Concerning Zero-point Vibrational Energy Corrections to Electronic Energies. *J. Chem. Phys.* **1991**, *95*, 5128.

(3) Pople, J.; Scott, A.; Wong, M.; Radom, L. Scaling Factors For Obtaining Fundamental Vibrational Frequencies And Zero-Point Energies From HF/6-31G* And MP2/6-31G* Harmonic Frequencies. *Isr. J. Chem.* **1993**, *33*, 345.

(4) Scott, A. P.; Radom, L. Harmonic Vibrational Frequencies: An Evaluation of Hartree-Fock, Moller-Plesset, Quadratic Configuration Interaction, Density Functional Theory, and Semiempirical Scale Factors. *J. Phys. Chem.* **1996**, *100*, 16502.

(5) Sinha, P.; Boesch, S. E.; Gu, C. M.; Wheeler, R. A.; Wilson, A. K. Harmonic Vibrational Frequencies: Scaling Factors for HF, B3LYP, and MP2Methods in Combination with Correlation Consistent Basis Sets. *J. Phys. Chem. A* **2004**, *108*, 9213.

(6) Irikura, K. K.; Johnson, R. D.; Kacker, R. N. Uncertainties in Scaling Factors for ab Initio Vibrational Frequencies. *J. Phys. Chem. A* **2005**, *109*, 8430.

(7) Merrick, J. P.; Moran, D.; Radom, L. An Evaluation of Harmonic Vibrational Frequency Scale Factors. *J. Phys. Chem. A* **2007**, *111*, 11683.

(8) Irikura, K. K.; Johnson, R. D., III; Kacker, R. N.; Kessel, R. Uncertainties in Scaling Factors for Ab Initio Vibrational Zero-point Energies. *J. Chem. Phys.* **2009**, *130*, 114102.

(9) Johnson, R. D., III; Irikura, K. K.; Kacker, R. N.; Kessel, R. Scaling Factors and Uncertainties for ab Initio Anharmonic Vibrational Frequencies. *J. Chem. Theory Comput.* **2010**, *6*, 2822.

(10) Alecu, I. M.; Zheng, J.; Zhao, Y.; Truhlar, D. G. Computational Thermochemistry: Scale Factor Databases and Scale Factors for Vibrational Frequencies Obtained from Electronic Model Chemistries. *J. Chem. Theory Comput.* **2010**, *6*, 2872.

(11) Wong, M. W. Vibrational Frequency Prediction using Density Functional Theory. *Chem. Phys. Lett.* **1996**, *256*, 391.

(12) Halls, M. D.; Velkovski, J.; Schlegel, H. B. Harmonic Frequency Scaling Factors for Hartree-Fock, S-VWN, B-LYP, B3-LYP, B3-PW91 and MP2 with the Sadlej pVTZ Electric Property Basis Set. *Theor. Chem. Acc.* **2001**, *105*, 413.

(13) Pitzer, K. S.; Gwinn, W. D. Energy Levels and Thermodynamic Functions for Molecules with Internal Rotation I. Rigid Frame with Attached Tops. *J. Chem. Phys.* **1942**, *10*, 428.

(14) Ayala, P. Y.; Schlegel, H. B. Identification and Treatment of Internal Rotation in Normal Mode Vibrational Analysis. *J. Chem. Phys.* **1998**, *108*, 2314.

(15) East, A. L. L.; Radom, L. Ab initio Statistical Thermodynamical Models for the Computation of Third-law Entropies. *J. Chem. Phys.* **1997**, *106*, 6655.

(16) Katzer, G.; Sax, A. F. Identification and Thermodynamic Treatment of Several Types of Large-amplitude Motions. *J. Comput. Chem.* **2005**, *26*, 1438.

(17) Fabian, W. M. F. Accurate Thermochemistry from Quantum Chemical Calculations? *Monatsh. Chem.* **2008**, *139*, 309.

(18) Bowman, J. M.; Christoffel, K. M.; Tobin, F. Application of SCF-SI Theory to Vibrational Motion in Polyatomic Molecules. *J. Phys. Chem.* **1979**, *83*, 905.

(19) Christoffel, K. M.; Bowman, J. M. Application of SCF-SI Theory to Vibrational Motion in Polyatomic Molecules. *Chem. Phys. Lett.* **1982**, *85*, 220.

(20) Carter, S.; Bowman, J. M.; Handy, N. C. Extensions and Tests of "multimode": a Code to Obtain Accurate Vibration/rotation Energies of Many-mode Molecules. *Theor. Chim. Acta* **1998**, *100*, 191.

(21) Huang, X.; Braams, B. J.; Bowman, J. M. Ab Initio Potential Energy and Dipole Moment Surfaces of (H2O)2. *J. Phys. Chem. A* **2005**, *110*, 445.

(22) Teixeira, F.; Melo, A.; Cordeiro, M. N. D. S. Calibration sets and the accuracy of vibrational scaling factors: A case study with the X3LYP hybrid functional. *J. Chem. Phys.* **2010**, *133*, 114109.

(23) Pernot, P.; Cailliez, F. Comment on "Uncertainties in scaling factors for ab initio vibrational zero-point energies" [J. Chem. Phys. **130**, 114102 (2009)] and "Calibration sets and the accuracy of vibrational scaling factors: A case study with the X3LYP hybrid functional" [J. Chem. Phys. **133**, 114109 (2010)]. *J. Chem. Phys.* **2011**, *134*, 167101.

(24) Irikura, K. K.; Johnson, R. D.; Kacker, R. N.; Kessel, R. Response to "Comment on 'Uncertainties in scaling factors for ab initio vibrational zero-point energies' and 'Calibration sets and the accuracy of vibrational scaling factors: A case study with the X3LYP hybrid functional'" J. Chem. Phys. 134, 167101 (2011). *J. Chem. Phys.* **2011**, *134*.

(25) Teixeira, F.; Melo, A.; Natalia, M.; Cordeiro, D. S. Response to "Comment on 'Uncertainties in scaling factors for ab initio vibrational zero-point energies' and 'Calibration sets and the accuracy of vibrational scaling factors: A case study with the X3LYP hybrid functional'" J. Chem. Phys. 134, 167101 (2011). *J. Chem. Phys.* **2011**, *134*.

(26) Borowski, P.; Fernandez-Gomez, M.; Fernandez-Liencres, M.; Ruiz, T. P. An Effective Scaling Frequency Factor Method for Scaling of Harmonic Vibrational Frequencies: Theory and Preliminary Application to Toluene. *Chem. Phys. Lett.* **2007**, *446*, 191.

(27) Borowski, P.; Drzewiecka, A.; Fernandez-Gomez, M.; Fernandez-Liencres, M.; Ruiz, T. P. An Effective Scaling Frequency Factor Method for Harmonic Vibrational Frequencies: The Factors' Transferability Problem. *Chem. Phys. Lett.* **2008**, *465*, 290.

(28) Borowski, P.; Drzewiecka, A.; Fernandez-Gomez, M.; Ferandez-Liencres, M. P.; Ruiz, T. P. A new, reduced set of scaling factors for both SQM and ESFF calculations. *Vib. Spectrosc.* **2010**, *52*, 16.

(29) Rauhut, G.; Pulay, P. Transferable Scaling Factors for Density Functional Derived Vibrational Force Fields. *J. Phys. Chem.* **1995**, *99*, 3093.

(30) Wolfs, I.; Desseyn, H. O. Modelling the vibrational behaviour of the cyclic carboxylic acid dimer. SQM force field of the formic acid dimer. *J. Mol. Struct. (Theochem)* **1996**, *360*, 81.

(31) Fabri, C.; Szidarovszky, T.; Magyarfalvi, G.; Tarczay, G. Gas-Phase and Ar-Matrix SQM Scaling Factors for Various DFT Functionals with Basis Sets Including Polarization and Diffuse Functions. *J. Phys. Chem. A* **2011**, *115*, 4640.

(32) Fernandez, L. E.; Marigliano, A. C. G.; Varetti, E. L. The vibrational properties of formic acid as monomer and dimer: a DFT study. *Vib. Spectrosc.* **2005**, *37*, 179.

(33) Kocevski, V.; Pejov, L. On the Assessment of Some New Meta-Hybrid and Generalized Gradient Approximation Functionals for Calculations of Anharmonic Vibrational Frequency Shifts in Hydrogen-Bonded Dimers. *J. Phys. Chem. A* **2010**, *114*, 4354.

(34) Karthikeyan, S.; Singh, J. N.; Park, M.; Kumar, R.; Kim, K. S. Structures, Energetics, Vibrational Spectra of NH4+(H2O)(n=4,6) Clusters: Ab Initio Calculations and First Principles Molecular Dynamics Simulations. *J. Chem. Phys.* **2008**, *128*, 244304.

(35) Pickard, F. C.; Pokon, E. K.; Liptak, M. D.; Shields, G. C. Comparison of CBS-QB3, CBS-APNO, G2, and G3 Thermochemical Predictions with Experiment for Formation of Ionic Clusters of Hydronium and Hydroxide Ions Complexed with Water. *J. Chem. Phys.* **2005**, *122*, 024302.

(36) Lee, H. M.; Suh, S. B.; Lee, J. Y.; Tarakeshwar, P.; Kim, K. S. Structures, Energies, Vibrational Spectra, and Electronic Properties of Water Monomer to Decamer. *J. Chem. Phys.* **2000**, *112*, 9759.

(37) Dunn, M. E.; Evans, T. M.; Kirschner, K. N.; Shields, G. C. Prediction of Accurate Anharmonic Experimental Vibrational Frequencies for Water Clusters, (H2O)(n), n=2−5. *J. Phys. Chem. A* **2006**, *110*, 303.

(38) Losada, M.; Leutwlyer, S. Water Hexamer Clusters: Structures, Energies, and Predicted Mid-infrared Spectra. *J. Chem. Phys.* **2002**, *117*, 2003.

(39) Braly, L. B.; Liu, K.; Brown, M. G.; Keutsch, F. N.; Fellers, R. S.; Saykally, R. J. Terahertz Laser Spectroscopy of the Water Dimer Intermolecular Vibrations. II. (H2O)(2). *J. Chem. Phys.* **2000**, *112*, 10314.

(40) Ceponkus, J.; Uvdal, P.; Nelander, B. Intermolecular Vibrations of Different Isotopologs of the Water Dimer: Experiments and Density Functional Theory Calculations. *J. Chem. Phys.* **2008**, *129*, 194306.

(41) Ceponkus, J.; Uvdal, P.; Nelander, B. Far-Infrared Band Strengths in the Water Dimer: Experiments and Calculations. *J. Phys. Chem. A* **2008**, *112*, 3921.
(42) Barone, V. Vibrational Zero-point Energies and Thermodynamic Functions Beyond the Harmonic Approximation. *J. Chem. Phys.* **2004**, *120*, 3059.
(43) Barone, V. Anharmonic Vibrational Properties by a Fully Automated Second-order Perturbative Approach. *J. Chem. Phys.* **2005**, *122*, 014108.
(44) Bowman, J. M. The Self-consistent-field Approach to Polyatomic Vibrations. *Acc. Chem. Res.* **1986**, *19*, 202.
(45) Gerber, R. B.; Ratner, M. A. A Semiclassical Self-consistent Field (SC SCF) Approximation for Eigenvalues of Coupled-Vibration Systems. *Chem. Phys. Lett.* **1979**, *68*, 195.
(46) Ratner, M. A.; Gerber, R. B. Excited Vibrational States of Polyatomic Molecules: the Semiclassical Self-consistent Field Approach. *J. Phys. Chem.* **1986**, *90*, 20.
(47) Xantheas, S. S. Anharmonic Vibrational Spectra of Hydrogen Bonded Clusters: Comparison between Higher Energy Derivative and Mean-field Grid Based Methods. *Int. Rev. Phys. Chem.* **2006**, *25*, 719.
(48) Jung, J.; Gerber, R. B. Vibrational Wave Functions and Spectroscopy of (H2O)n, n= 2, 3, 4, 5: Vibrational Self-consistent Field with Correlation Corrections. *J. Chem. Phys.* **1996**, *105*, 10332.
(49) Chaban, G. M.; Jung, J. O.; Gerber, R. B. Anharmonic Vibrational Spectroscopy of Hydrogen-Bonded Systems Directly Computed from ab Initio Potential Surfaces: (H2O)n, n = 2, 3; Cl-(H2O)n, n = 1, 2; H+(H2O)n, n = 1, 2; H2O-CH3OH. *J. Phys. Chem. A* **2000**, *104*, 2772.
(50) Njegic, B.; Gordon, M. S. Exploring the Effect of Anharmonicity of Molecular Vibrations on Thermodynamic Properties. *J. Chem. Phys.* **2006**, *125*, 224102.
(51) Child, M. S.; Lawton, R. T. Local and Normal Vibrational States: A Harmonically Coupled Anharmonic-oscillator Model. *Faraday Discuss. Chem. Soc.* **1981**, *71*, 273.
(52) Lee, M. S.; Baletto, F.; Kanhere, D. G.; Scandolo, S. Far-infrared Absorption of Water Clusters by First-principles Molecular Dynamics. *J. Chem. Phys.* **2008**, *128*, 214506.
(53) Begue, D.; Baraille, I.; Garrain, P. A.; Dargelos, A.; Tassaing, T. Calculation of IR Frequencies and Intensities in Electrical and Mechanical Anharmonicity Approximations: Application to Small Water Clusters. *J. Chem. Phys.* **2010**, *133*, 034102.
(54) Huang, X.; Braams, B. J.; Bowman, J. M.; Kelly, R. E. A.; Tennyson, J.; Groenenboom, G. C.; van der Avoird, A. New Ab initio Potential Energy Surface and the Vibration-rotation-tunneling Levels of (H2O)2 and (D2O)2. *J. Chem. Phys.* **2008**, *128*, 034312.
(55) Su, J. T.; Xu, X.; Goddard, W. A. Accurate Energies and Structures for Large Water Clusters using the X3LYP Hybrid Density Functional. *J. Phys. Chem. A* **2004**, *108*, 10518.
(56) Ohno, K.; Okimura, M.; Akai, N.; Katsumoto, Y. The Effect of Cooperative Hydrogen Bonding on the OH Stretching-band Shift for Water Clusters Studied by Matrix-isolation Infrared Spectroscopy and Density Functional Theory. *Phys. Chem. Chem. Phys.* **2005**, *7*, 3005.
(57) Kjaergaard, H. G.; Garden, A. L.; Chaban, G. M.; Gerber, R. B.; Matthews, D. A.; Stanton, J. F. Calculation of Vibrational Transition Frequencies and Intensities in Water Dimer: Comparison of Different Vibrational Approaches. *J. Phys. Chem. A* **2008**, *112*, 4324.
(58) Diri, K.; Myshakin, E. M.; Jordan, K. D. On the Contribution of Vibrational Anharmonicity to the Binding Energies of Water Clusters. *J Phys. Chem. A* **2005**, *109*, 4005.
(59) Torrent-Sucarrat, M.; Anglada, J. M.; Luis, J. M. Role of Vibrational Anharmonicity in Atmospheric Radical Hydrogen-bonded Complexes. *Phys. Chem. Chem. Phys.* **2009**, *11*, 6377.
(60) Watanabe, Y.; Maeda, S.; Ohno, K. Intramolecular Vibrational Frequencies of Water Clusters (H2O)(n) (n=2−5): Anharmonic Analyses using Potential Functions Based on the Scaled Hypersphere Search Method. *J. Chem. Phys.* **2008**, *129*, 074315.
(61) Dykstra, C. E.; Shuler, K.; Young, R. A.; Bacic, Z. Anharmonicity Effects on Zero Point Energies of Weakly Bound Molecular Clusters. *J. Mol. Struct. (Theochem)* **2002**, *591*, 11.
(62) Isayev, O.; Gorb, L.; Leszczynski, J. Theoretical Calculations: Can Gibbs Free Energy for Intermolecular Complexes be Predicted Efficiently and Accurately? *J. Comput. Chem.* **2007**, *28*, 1598.
(63) Carbonniere, P.; Barone, V. Performances of Different Density Functionals in the Computation of Vibrational Spectra Beyond the Harmonic Approximation. *Chem. Phys. Lett.* **2004**, *399*, 226.
(64) Biczysko, M.; Panek, P.; Scalmani, G.; Bloino, J.; Barone, V. Harmonic and Anharmonic Vibrational Frequency Calculations with the Double-Hybrid B2PLYP Method: Analytic Second Derivatives and Benchmark Studies. *J. Chem. Theory Comput.* **2010**, *6*, 2115.
(65) Xantheas, S.; Dunning, T. Ab-Initio Studies Of Cyclic Water Clusters (H2o)N, N = 1−6 0.1. Optimal Structures And Vibrational-Spectra. *J. Chem. Phys.* **1993**, *99*, 8774.
(66) Xantheas, S. S. Ab initio Studies of Cyclic Water Clusters (H2O)n, n=1−6. II. Analysis of Many-body Interactions. *J. Chem. Phys.* **1994**, *100*, 7523.
(67) Xantheas, S. S. Ab initio Studies of Cyclic Water Clusters (H2O)n, n=1−6. III. Comparison of Density Functional with MP2 Results. *J. Chem. Phys.* **1995**, *102*, 4505.
(68) Xantheas, S. S. On the Importance of the Fragment Relaxation Energy Terms in the Estimation of the Basis Set Superposition Error Correction to the Intermolecular Interaction Energy. *J. Chem. Phys.* **1996**, *104*, 8821.
(69) Xantheas, S. S. Significance of Higher-order Many-body Interaction Energy Terms in Water Clusters and Bulk Water. *Philos. Mag. B* **1996**, *73*, 107.
(70) Xantheas, S. S. Cooperativity and Hydrogen Bonding Network in Water Clusters. *Chem. Phys.* **2000**, *258*, 225.
(71) Burnham, C. J.; Xantheas, S. S. Development of Transferable Interaction Models for Water. IV. A Flexible, All-atom Polarizable Potential (TTM2-F) Based on Geometry Dependent Charges Derived from an Ab initio Monomer Dipole Moment Surface. *J. Chem. Phys.* **2002**, *116*, 5115.
(72) Burnham, C. J.; Xantheas, S. S. Development of Transferable Interaction Models for Water. I. Prominent Features of the Water Dimer Potential Energy Surface. *J. Chem. Phys.* **2002**, *116*, 1479.
(73) Burnham, C. J.; Xantheas, S. S. Development of Transferable Interaction Models for Water. III. Reparametrization of an All-atom Polarizable Rigid Model (TTM2-R) from First Principles. *J. Chem. Phys.* **2002**, *116*, 1500.
(74) Burnham, C. J.; Xantheas, S. S.; Miller, M. A.; Applegate, B. E.; Miller, R. E. The Formation of Cyclic Water Complexes by Sequential Ring Insertion: Experiment and Theory. *J. Chem. Phys.* **2002**, *117*, 1109.
(75) Xantheas, S. S.; Burnham, C. J.; Harrison, R. J. Development of Transferable Interaction Models for Water. II. Accurate Energetics of the First Few Water Clusters from First Principles. *J. Chem. Phys.* **2002**, *116*, 1493.
(76) Bulusu, S.; Yoo, S.; Apra, E.; Xantheas, S.; Zeng, X. C. Lowest-energy structures of water clusters (H2O)(11) and (H2O)(13). *J Phys. Chem. A* **2006**, *110*, 11781.
(77) Xantheas, S. S.; Apra, E. The Binding Energies of the D2d and S4 Water Octamer Isomers: High-level Electronic Structure and Empirical Potential Results. *J. Chem. Phys.* **2004**, *120*, 823.
(78) Xantheas, S. S. Interaction Potentials for Water from Accurate Cluster Calculations. In *Intermolecular Forces and Clusters II*; Pacific Northwest National Laboratory: Richland, WA, 2005; Vol. 116; p 119.
(79) Yoo, S.; Kirov, M. V.; Xantheas, S. S. Low-Energy Networks of the T-Cage (H2O)(24) Cluster and Their Use in Constructing Periodic Unit Cells of the Structure I (sl) Hydrate Lattice. *J. Am. Chem. Soc.* **2009**, *131*, 7564.
(80) Yoo, S.; Apra, E.; Zeng, X. C.; Xantheas, S. S. High-Level Ab Initio Electronic Structure Calculations of Water Clusters (H2O)16 and (H2O)17: A New Global Minimum for (H2O)16. *J. Phys. Chem. Lett.* **2010**, *1*, 3122.
(81) Isaacson, A. D. Removing Resonance Effects from Quantum Mechanical Vibrational Partition Functions Obtained from Perturbation Theory. *J. Chem. Phys.* **1998**, *108*, 9978.
(82) Frisch, M. J.; Trucks, G. W.; Schlegel, H. B.; Scuseria, G. E.; Robb, M. A.; Cheeseman, J. R.; Montgomery, J. A.; Vreven, T.;

Kudin, K. N.; Burant, J. C.; Millam, J. M.; Iyengar, S. S.; Tomasi, J.; Barone, V.; Mennucci, B.; Cossi, M.; Scalmani, G.; Rega, N.; Petersson, G. A.; Nakatsuji, H.; Hada, M.; Ehara, M.; Toyota, K.; Fukuda, R.; Hasegawa, J.; Ishida, M.; Nakajima, T.; Honda, Y.; Kitao, O.; Nakai, H.; Klene, M.; Li, X.; Knox, J. E.; Hratchian, H. P.; Cross, J. B.; Bakken, V.; Adamo, C.; Jaramillo, J.; Gomperts, R.; Stratmann, R. E.; Yazyev, O.; Austin, A. J.; Cammi, R.; Pomelli, C.; Ochterski, J. W.; Ayala, P. Y.; Morokuma, K.; Voth, G. A.; Salvador, P.; Dannenberg, J. J.; Zakrzewski, V. G.; Dapprich, S.; Daniels, A. D.; Strain, M. C.; Farkas, O.; Malick, D. K.; Rabuck, A. D.; Raghavachari, K.; Foresman, J. B.; Ortiz, J. V.; Cui, Q.; Baboul, A. G.; Clifford, S.; Cioslowski, J.; Stefanov, B. B.; Liu, G.; Liashenko, A.; Piskorz, P.; Komaromi, I.; Martin, R. L.; Fox, D. J.; Keith, T.; Al-Laham, M. A.; Peng, C. Y.; Nanayakkara, A.; Challacombe, M.; Gill, P. M. W.; Johnson, B.; Chen, W.; Wong, M. W.; Gonzalez, C.; Pople, J. A. *Gaussian 09*, revision A.02; Gaussian, Inc.: Wallingford, CT, 2009.

(83) Martin, J. M. L.; Lee, T. J.; Taylor, P. R.; Francois, J. P. The Anharmonic Force Field of Ethylene, C2H4 by Means of Accurate Ab initio Calculations. *J. Chem. Phys.* **1995**, *103*, 2589.

(84) Boese, A. D.; Martin, J. M. L. Vibrational Spectra of the Azabenzenes Revisited: Anharmonic Force Fields. *J. Phys. Chem. A* **2004**, *108*, 3085.

(85) Frisch, M. J.; Trucks, G. W.; Schlegel, H. B.; Scuseria, G. E.; Robb, M. A.; Cheeseman, J. R.; Montgomery, J. A.; Vreven, T.; Kudin, K. N.; Burant, J. C.; Millam, J. M.; Iyengar, S. S.; Tomasi, J.; Barone, V.; Mennucci, B.; Cossi, M.; Scalmani, G.; Rega, N.; Petersson, G. A.; Nakatsuji, H.; Hada, M.; Ehara, M.; Toyota, K.; Fukuda, R.; Hasegawa, J.; Ishida, M.; Nakajima, T.; Honda, Y.; Kitao, O.; Nakai, H.; Klene, M.; Li, X.; Knox, J. E.; Hratchian, H. P.; Cross, J. B.; Bakken, V.; Adamo, C.; Jaramillo, J.; Gomperts, R.; Stratmann, R. E.; Yazyev, O.; Austin, A. J.; Cammi, R.; Pomelli, C.; Ochterski, J. W.; Ayala, P. Y.; Morokuma, K.; Voth, G. A.; Salvador, P.; Dannenberg, J. J.; Zakrzewski, V. G.; Dapprich, S.; Daniels, A. D.; Strain, M. C.; Farkas, O.; Malick, D. K.; Rabuck, A. D.; Raghavachari, K.; Foresman, J. B.; Ortiz, J. V.; Cui, Q.; Baboul, A. G.; Clifford, S.; Cioslowski, J.; Stefanov, B. B.; Liu, G.; Liashenko, A.; Piskorz, P.; Komaromi, I.; Martin, R. L.; Fox, D. J.; Keith, T.; Al-Laham, M. A.; Peng, C. Y.; Nanayakkara, A.; Challacombe, M.; Gill, P. M. W.; Johnson, B.; Chen, W.; Wong, M. W.; Gonzalez, C.; Pople, J. A. *Gaussian 03*, revisions D.01 and E.01); Gaussian, Inc.: Wallingford, CT, 2004.

(86) Stanton, J. F.; Gauss, J.; Harding, M. E.; Szalay, P. G.; Auer, A. A.; Bartlett, R. J.; Benedikt, U.; Berger, C.; Bernholdt, D. E.; Bomble, Y. J.; Christiansen, O.; Heckert, M.; Heun, O.; Huber, C.; Jagau, T. -C.; Jonsson, D.; J. Jusèlius; Klein, K.; Lauderdale, W. J.; Matthews, D.; Metzroth, T.; D. P. O'Neill; Price, D. R.; Prochnow, E.; Ruud, K.; Schiffmann, F.; Stopkowicz, S.; Varner, M. E.; J. Vázquez; Watts, J. D.; Wang, F.; Almlöf, J.; Taylor, P. R.; Helgaker, T.; Jørgensen, P.; Jensen, H. J. A.; Olsen, J.; Mitin, A. V.; Wüllen, C. v. *CFOUR (Coupled Cluster Techniques for Computational Chemistry), a quantum-chemical program package*; The University of Texas at Austin, Johannes Gutenberg-Universität Mainz, and Eötvös-Lorand-University Budapest: Austin, TX, Mainz, Germany, and Budapest, Hungary, 2010.

(87) Csonka, G. I.; Ruzsinszky, A.; Perdew, J. P. Estimation, Computation, and Experimental Correction of Molecular Zero-point Vibrational Energies. *J Phys. Chem. A* **2005**, *109*, 6779.

(88) McQuarrie, D. A. *Statistical Thermodynamics*; Harper & Row: New York, 1973.

(89) Truhlar, D. G.; Isaacson, A. D. Simple Perturbation Theory Estimates of Equilibrium Constants from Force Fields. *J. Chem. Phys.* **1991**, *94*, 357.

(90) Isaacson, A. D. Anharmonic Effects on the Transition State Theory Rate Constant. *J. Chem. Phys.* **2002**, *117*, 8778.

(91) Isaacson, A. D. Including Anharmonicity in the Calculation of Rate Constants. 1. The HCN/HNC Isomerization Reaction. *J. Phys. Chem. A* **2006**, *110*, 379.

(92) Kurten, T.; Noppel, M.; Vehkamaki, H.; Salonen, M.; Kulmala, M. Quantum Chemical Studies of Hydrate Formation of H2SO4 and HSO4. *Boreal Environ. Res.* **2007**, *12*, 431.

(93) Dunn, M. E.; Pokon, E. K.; Shields, G. C. Thermodynamics of Forming Water Clusters at Various Temperatures and Pressures by Gaussian-2, Gaussian-3, Complete Basis Set-QB3, and Complete Basis Set-APNO Model Chemistries; Implications for Atmospheric Chemistry. *J. Am. Chem. Soc.* **2004**, *126*, 2647.

(94) Morrell, T. E.; Shields, G. C. Atmospheric Implications for Formation of Clusters of Ammonium and 1−10 Water Molecules. *J. Phys. Chem. A* **2010**, *114*, 4266.

JCTC Journal of Chemical Theory and Computation

ARTICLE

pubs.acs.org/JCTC

Local MP2 with Density Fitting for Periodic Systems: A Parallel Implementation

Lorenzo Maschio*

Dipartimento di Chimica IFM and Centre of Excellence NIS (Nanostructured Interfaces and Surfaces), Università di Torino, via P. Giuria 5, I-10125 Torino, Italy

ABSTRACT: A parallel implementation is presented for the evaluation of local second-order Møller−Plesset perturbation theory (LMP2) energies in periodic, nonconducting crystalline systems with a density-fitting approximation of two-electron repulsion integrals. Peculiarities of the periodic case with respect to parallel LMP2 implementations in molecular codes, such as the use of translational and point symmetry, impose different strategies in order to achieve good parallel performance. The implementation is benchmarked on a few systems, representing a choice of the most interesting solid state quantum-chemistry problems where the MP2 approach can be decisive. Good parallel efficiency of the algorithms is demonstrated for up to 54 processors. Test systems include a metal organic framework (MOF-5) 3D crystalline structure with a triple-ζ-quality basis set: this is the largest calculation performed so far with 106 atoms, 532 correlated electrons, and 2884 atomic orbitals per unit cell.

1. INTRODUCTION

Molecular quantum chemistry has undergone a significant revolution in recent years. Thanks to the implementation of fast electron correlation techniques in modern quantum chemistry codes,[1,2] accurate post-Hartree−Fock methods are now applicable to very large molecular complexes[3] at a reasonable computational cost, thus becoming a serious competitor to DFT also for routine calculations. This has become possible after the assessment of fast integral evaluation techniques, like multipole-based screening,[4−6] resolution of identity (RI),[7] or density fitting (DF),[8−10] and due to the introduction of approximate yet efficient variants of the traditional quantum chemistry methods, like local correlation[11−13] and Laplace transform[14] techniques. The efficient parallelization of the algorithms had, and still has, a central role in this process,[15−24] following the growing availability of cheap and powerful multicore machines.

The progress of solid state quantum chemistry along this path is a few years behind. Several groups, in the past decade, have proposed different and often complementary approaches, successfully taking up the challenge of evaluating *ab initio* electron correlation in periodic systems.[25−31] Still, the application of such methods has mainly played a benchmark role, since it has been limited, up to date, to the study of simple model systems, with a small number of atoms in the reference cell.[32−34]

The present work presents a step forward in the direction of the assessment of a powerful and usable tool for real-life quantum chemical calculations at the correlated level for crystalline solids. The Cryscor program,[35] jointly developed by the theoretical chemistry groups of Torino and Regensburg, is part of a project aimed at implementing local correlation methods for the study of crystalline periodic systems. The first public (serial) version of the code[36] implements density-fitted local Møller-Plesset perturbative correction at second order (DF-LMP2) to the Hartree−Fock (HF) solution provided by the Crystal code.[37,38] Both programs adopt a local basis set consisting of Gaussian-type atomic orbitals.

The implemented method is an adaptation to the periodic case of the LMP2 method first proposed by Pulay[11,13] and then efficiently implemented for molecules by Schütz and Werner in the Molpro code.[1,39,40] Periodic LMP2 relies on a localized solution of the HF equations, expressed in terms of symmetry-adapted Wannier functions (WF),[41,42] and on a representation of the virtual space by projected atomic orbitals (PAO; *vide infra*). The adoption of approximate integrals evaluation techniques like the DF approximation allows one to speed up the calculation by several orders of magnitude.[43] The serial periodic LMP2 code has already been successfully applied to the study of cohesive energy of molecular crystals[44−46] and rare gas crystals,[34] surface adsorption,[47,48] the relative stability of crystalline polymorphs,[49] pressure-induced phase transitions,[50] and simulation of Compton scattering experiments.[51] The largest calculations performed so far with Cryscor on a single processor have been a CO_2 bulk crystal with the aug(d,f)-cc-pVQZ basis set (12 atoms, 696 basis functions in the reference cell)[45] and a sodalite crystal with a triple-ζ-quality basis set[52] (36 atoms, 1128 basis functions in the reference cell).

A great amount of literature exists concerning implementation of electronic structure methods for molecules, a good review of which can be found in ref 21. In particular, a number of parallel MP2 implementations have been reported in the past 10 years.[53−56] Among these, a massively parallel implementation of the local MP2 method for molecules, which is of particular relevance to the scopes of the present work, has been presented by Nielsen and Janssen.[20] In that work, it is shown that due to peculiarities of the local approach, it is very difficult to obtain a good parallel efficiency. Earlier work on local MP2 parallel implementation, using nonorthogonal occupied orbitals, has been reported by Nakao and Hirao.[55] Finally, parallel implementation of canonical MP2 with RI approximation of two-electron repulsion integrals

Received: May 26, 2011
Published: August 01, 2011

```
STEP1:
Define N segments
Set up N empty buckets
Loop over all blocks
 read integral block
 put block into appropriate bucket n
 If n full then
     write n to disk
     empty bucket n
 EndIf
End Loop
Flush to disk partly filled buckets
STEP2:
Loop N segments
    gather all buckets of this segment
    sort the segment and write to disk
End Loop segments
```

Figure 1. Standard scheme of bucket sort algorithm.

has been proposed by Hättig et al.[56] and by Katouda and Nagase.[24]

The presentation of the periodic LMP2 algorithms is structured as follows: In section, 2 the main strategies for parallel efficiency and I/O are presented. In section 3, the structure of the parallel implementation is described and discussed in detail, with reference to the main formalism of the periodic LMP2 method. In section 4, benchmark calculations are reported; the performance of the different parts of the parallel code is analyzed.

2. PARALLELIZATION STRATEGIES AND I/O

The main priority, when implementing a parallel version of a quantum chemistry algorithm, is to extend its applicability to larger and more complex systems. In this sense, saving memory resources is the most important goal to achieve. General principles, which have been followed in the development, are as follows. (i) Code linearity: parallel instructions should not be too invasive—only the outermost loops of very complex routines are parallelized. (ii) Code maintainability: when possible the parallel code source is the same as the serial, and parallel libraries can be linked or not at the compilation stage. (iii) Code portability: pure MPI instructions have been used throughout, with no use of OpenMP.

Since the periodic DF-LMP2 code is very heterogeneous, with distinct features and peculiarities in its different parts, different strategies have been followed for distributing CPU load and memory:

- *Distributed memory linear algebra*. The use of Scalapack routines has been necessary in the PAO generation step, where the size of the matrices involved scales quadratically with the number of atoms in the unit cell. In all other parts, the peculiarities of the local method allow for the use of matrices whose size is not closely related to the number of atoms in the system (though it depends on basis set choice and local domain definition).
- *Parallelization according to atomic index in the unit cell*. This is the strategy followed for the parallelization of the different steps of the Periodic Density Fitting code and in the evaluation of integrals for the multipolar expansion. The advantages of such a coarse grain parallelization are a clean and straightforward implementation and a good efficiency (see section 4). Drawbacks such as load unbalancing arise if the number of processors is larger than the number of atoms in the unit cell, or in the case of atoms with very different numbers of electrons.
- *Parallelization according to pair index*. The LMP2 equations can be conveniently factorized in terms of WF pair contributions. Given the large number of WF pairs involved in a fairly large calculation (several thousands), load balancing issues are not likely to appear at this stage.

```
 STEP1:
 Define N segments
 Set up N empty buckets
*classified=false
 Loop over irreducible blocks b
p  If ( my b) then
     read integral block
p  EndIf
*  Loop over all symm.  operators V
*    Obtain rotated block b'=V b
*    If (classified(b')) skip
*    If (not needed(b')) skip
*    classified(b')= true
p    If (my b) then
*       obtain rotated (b')
p       If( my b') then
          put block into bucket
          if bucket full write to disk
p       Else
p         send (b') to processor which wants it
p       EndIf
p    Else if (I want b' ) then
p      recv (b')
       put block into bucket
       if bucket full write to disk
p    EndIf
   End Loop V
 End Loop blocks
 Flush to disk partly filled buckets
 STEP2:  same as the serial one
```

Figure 2. Modified bucket sort algorithm with symmetry exploitation and data redistribution. The lines colored in red and marked by a p letter on the left are specific of the parallel implementation. The instruction lines colored in blue and marked by an asterisk on the left perform exploitation of symmetry.

Local post-Hartree−Fock methods are characterized by the huge amount of intermediate data produced, especially if density fitting techniques are adopted. Data (i.e., integrals, MP2 amplitudes) is by far too large to be kept in memory even for fairly simple calculations. Efficient strategies have to be devised in order to keep the I/O overhead under control and, at the same time, reduce communication among processors. Discussion of such strategies will be covered in the remainder of this section.

2.1. Bucket Sort Algorithm. As will become clear in the remainder of this paper, the parallelized bucket sort plays a central role in the implementation of periodic density fitting.

Bucket sort, also known in quantum chemistry as the bin sort, is a standard, well-known algorithm that allows one to efficiently sort arrays, which must be kept on disk because it is considerably larger than the available system memory. For a recent discussion on this algorithm, see for instance ref 57. Bucket sort was first introduced in electron correlation theory by Yoshimine,[58] and a

parallel implementation was described in 2002 by Baker and Pulay in the context of canonical MP2 energy calculation.[54] In the present LMP2 implementation, a new parallel version of this algorithm is introduced, which features redistribution of data among processors and exploitation of symmetry at the same time.

The serial algorithm, which has been adapted from the corresponding one in the Molpro code, is sketched in Figure 1. A set of N "segments" is defined such that the length of a single segment is equal to the available memory. A buffer is allocated and formally divided in a set of N empty "buckets". In a first step, atomic integral blocks are read from the disk, one at a time, and assigned to the corresponding destination bucket. When a bucket is full, it is written to disk and emptied. After all blocks have been processed, the second step is performed: all buckets corresponding to the first segment are loaded in memory, sorted, and written to disk. By repeating the process for all segments, the file with the sorted elements is generated. If memory is large enough to hold full segments, no intermediate buckets are written to disk. In this case, the sort is $\mathcal{O}(n)$ scaling (since the final order is known *a priori*); otherwise the scaling depends on the amount of available memory.

The parallel version of this algorithm is reported in Figure 2; instructions which are specific for symmetry and parallelization are highlighted as explained in the caption. After the processor, which has computed *symmetry irreducible* block $\mathfrak{b}$, has read it, all symmetry operators are applied to it (this includes identity), generating several $\mathfrak{b}'$ new objects. It is checked whether $\mathfrak{b}'$ is actually needed or if it has already been obtained by some other rotation. $\mathfrak{b}'$ is then sent to the processor to which it is assigned according to memory distribution strategies (this happens only if the target processor is not the same as $\mathfrak{b}$). The target processor receives $\mathfrak{b}'$ and puts it in its bucket. The routine proceeds as for the serial one: step 2 is performed by each processor on the quantities it holds, and no further communication takes place.

Note that parallel step 1 is not *globally blocking*, since only one-to-one (or one-to-many) communications take place, and processors which are neither owners of a given $\mathfrak{b}$ nor targets for the rotated $\mathfrak{b}'$ are allowed to proceed independently. Still, it is not completely *asynchronous* like the algorithm outlined by Baker and Pulay, who achieved this result through spawning of additional "listening" processes per each node, dedicated to I/O.

In the present context, the bucket sort is used in two parts of the DF procedure. The symmetry is applied only in the second sort.

2.2. Paging Algorithm. A paging strategy has been implemented to deal with matrices that are too large to fit into the available memory. A buffer, as large as the available memory, is allocated. The big matrix is divided in *blocks*, having the size of all shells belonging to a pair of atoms. Initially, the buffer is empty. During the program execution, when a block is needed, it is loaded in memory and fills an empty part of this buffer. If the buffer is full and a new block must be loaded, a suitable portion of it is freed by discarding one block. The choice is made according to a scoring system: every time a block is used, it gains one point. The block, currently in memory, which has the lowest score is discarded. If this block has changed in the meantime (this is the case of the updated LMP2 amplitudes), it is written back to disk; otherwise (most frequently), its memory slot is just overwritten. The blocks used more frequently are thus always kept in memory, if possible.

2.3. Disk Sharing. In addition to the paging algorithm just described, a further scheme has been set up to efficiently handle large, replicated matrices. If two or more nodes share the same disk space, the disk itself can be used as a communication medium among them instead of message passing. The CPUs are classified according to groups, where each group is formed by those processors sharing the same disk, and one processor of each group is nominated the "leader" of the group. The processors automatically recognize if they are sharing the disk with others (no input is required by the user in this sense).

Direct writes can be done, within a group, to the same physical file, and information is accessible by all processors of that group. Replication of data on the disk is avoided, and all-to-all communication steps are reduced to a communication among group leaders. In the case of the SP6 AIX machine, used for the benchmark calculations in this work, all of the processors share the same disk. As a consequence, message passing instructions are avoided when this scheme is applied. Although not as advanced as the Array Files system,[59] this very simple technique can be quite effective in achieving good overall parallel performance. The disk sharing strategy is adopted for the two-index density fitting integrals (section 3.3.1) and for excitation amplitudes (section 3.4). In combination with the paging algorithm described in section 2.2, it represents a powerful tool to improve the parallel efficiency of the LMP2 equations.

3. THE PARALLEL CODE AND PERIODIC LMP2 ESSENTIAL FORMALISM

The general scheme of the Cryscor code has been outlined in our previous works[28,60] but will be reported here for ease of reference and to support the discussion of the parallel algorithms. After a preliminary stage, in which information of the system is recovered from Crystal (geometry, symmetry data, basis set, HF solution expressed in terms of Wannier functions), the main computational steps of a local MP2 calculation are (i) generation of the localized functions used to represent the virtual space, that is projected atomic orbitals (PAO),[13] (ii) integrals evaluation via multipolar expansion and density fitting techniques, and (iii) periodic LMP2 iterative equations.

The notation adopted in the following is meant to be consistent with previous papers:[28,35]

- Greek letters μ, ν, etc. represent an atomic orbital, i.e., a basis function.
- Letters *i*, *j*, etc. represent an occupied orbital, i.e., a Wannier function.
- Letters *a*, *b*, etc. represent a virtual orbital, i.e., a PAO.
- Capital letters *P*, *Q*, etc. indicate an auxiliary basis function, used for density fitting.
- Calligraphic capital letters $\mathcal{J}$,$\mathcal{A}$,$\mathcal{P}$, etc. indicate a lattice vector label, while symbols such as $\mathbf{R}_{\mathcal{J}}$, $\mathbf{R}_{\mathcal{A}}$, and $\mathbf{R}_{\mathcal{P}}$ will indicate the corresponding vectors. Where no lattice vector label is indicated, the reference cell is implicitly understood. Primed lattice vectors $\mathcal{J}'$,$\mathcal{A}'$,$\mathcal{P}'$, etc. indicate that the corresponding index has been shifted to take advantage of translational symmetry. The entity of the shifting is always clear from the context (e.g., $(P\mathcal{P}|Q\mathcal{Q}) = (P|Q\mathcal{Q}')$ where $\mathcal{Q}' = \mathcal{Q}\ominus\mathcal{P}$).

The algorithms will be presented in the order they are executed by the code. For this reason, evaluation of preliminary quantities and integrals will be discussed before the LMP2 energy calculation.

3.1. Generation of Local Virtual Space and Related Matrices. Wannier functions are used to represent the occupied

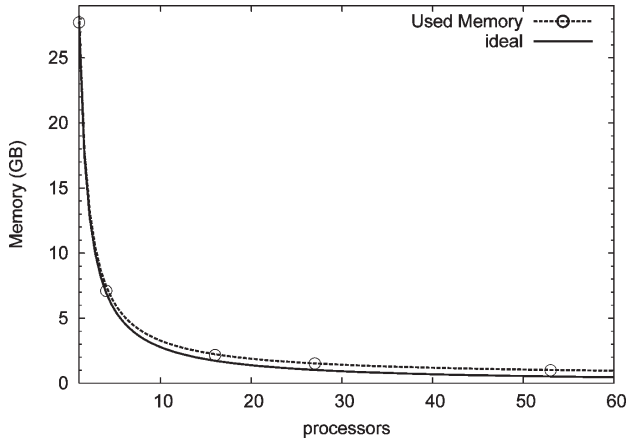

Figure 3. Use of memory in the PAO generation step, for the largest test case of this work (MOF-5).

space. These symmetry-adapted and well-localized objects are calculated by the Crystal program.[37,38] To describe the virtual manifold, following the proposal of Saebø and Pulay,[13] atomic orbitals projected out from the occupied space (PAO) have to be generated. Each PAO $\chi_a(\mathbf{r})$ is described by a linear combination of the AO basis set: $\chi_a(\mathbf{r}) = \Sigma_{\mu_{\mathscr{M}}} c_a^{\mu\mathscr{M}} \phi_{\mu\mathscr{M}}$. They form a redundant nonorthogonal set but at the same time are appreciably well localized and have the symmetry of the parent AOs. The projection that produces the coefficients of a reciprocal space image of a PAO, $\chi_a{}^{\mu}(\mathbf{k})$, can be cast as

$$c_a^{\mu}(\mathbf{k}) = \sum_{\nu}[\delta_{\mu,\nu} - \sum_i |u_{\mathbf{k}}^{i,\mu}\rangle\langle u_{\mathbf{k}}^{i,\mu}|]S_{\nu,\mu}^*(\mathbf{k}) \quad (1)$$

where $|u_{\mathbf{k}}^{i,\mu}\rangle$ are the occupied Fock eigenvectors and $S_{\nu,\mu}(\mathbf{k})$ is the overlap matrix in the AO basis, both expressed in reciprocal space. The PAOs in direct space are obtained through a back Fourier transform:

$$c_a^{\mu,\mathscr{M}} = \sum_{\mathbf{k}} c_a^{\mu}(\mathbf{k})\, e^{i\mathbf{k}\cdot\mathbf{R}_{\mathscr{M}}} \quad (2)$$

The most demanding steps within this part of the code are the orbital transformation of overlap (**S**) and Fock (**F**) matrices from the AO to the PAO basis, which is also performed in reciprocal space,

$$X_{a,b,\mathscr{B}} = \sum_{\mathbf{k}} X_{a,b}(\mathbf{k})\, e^{i\mathbf{k}\cdot\mathbf{R}_{\mathscr{B}}} = \sum_{\mathbf{k}}[\sum_{\mu} c_a^{\mu}(\mathbf{k})[\sum_{\nu} X_{\mu,\nu}(\mathbf{k})\, c_b^{*\nu}(\mathbf{k})]]e^{i\mathbf{k}\cdot\mathbf{R}_{\mathscr{B}}} \quad (3)$$

where $X = S, F$.

This step represents mainly a memory bottleneck, since square matrices having the full size of the basis functions in the unit cell are involved. For small and medium-sized systems, eqs 2 and 3 might be conveniently factorized according to the **k**-mesh sampling points. This approach would imply just a little communication (a global sum for the inverse Fourier transform at the end) but would limit the number of processors that can be used to be equal or less than the number of **k** points and cause load balancing problems, without solving the problem of square matrices to be kept in memory.

When the system grows large, the number of needed **k** points reduces considerably, while the user almost certainly strives for a larger number of CPUs to handle the computational expense of the calculation. For this reason, this step is parallelized, according to a *distributed memory* strategy by means of standard parallel distributed linear algebra routines.[61] All matrices in eqs 2 and 3 are distributed among all processors. In Figure 3, the use of memory is reported for a test case: deviation of the memory distribution from ideal behavior is small, showing that 96% of the allocated arrays are handled through distributed linear algebra routines.

Thanks to the features of the local approach, the other steps of the LMP2 code exhibit a need for memory that can be made independent of the size of the system.

3.2. Fast Integral Evaluation: The Multipolar Expansion. The main bottleneck of the LMP2 method is constituted by the calculation of the four index two-electron repulsion integrals in the basis of WFs and PAOs:

$$K_{a\mathscr{A},b\mathscr{B}}^{ij\mathscr{J}} = (ia\mathscr{A}|j\mathscr{J}b\mathscr{B}) = \int d\mathbf{r}_1 \int d\mathbf{r}_2\, \chi^i(\mathbf{r}_1)\, \chi^a(\mathbf{r}_1 - \mathbf{R}_{\mathscr{A}}) \frac{1}{|\mathbf{r}_2 - \mathbf{r}_1|} \chi^j(\mathbf{r}_2 - \mathbf{R}_{\mathscr{J}})\, \chi^b(\mathbf{r}_2 - \mathbf{R}_{\mathscr{B}}) \quad (4)$$

Approximate techniques for the evaluation of such integrals must be devised, which are described in this subsection and the following.

An efficient multipolar expansion can be applied if the two $\rho_{ia\mathscr{A}}$ and $\rho_{jb\mathscr{B}}$ product distributions are distant enough that they can be considered as enclosed in separate spheres. This is a well-known and widely used technique in quantum chemistry (see for instance ref 62). The integrals are obtained through the interaction of two sets of point multipoles:

$$K_{a\mathscr{A},b\mathscr{B}}^{ij\mathscr{J}} \approx \sum_{\ell,\ell'} Q_{ia\mathscr{A}}^{\ell} V_{i,j\mathscr{J}}^{\ell,\ell'} Q_{jb\mathscr{B}'}^{\ell'} \quad (5)$$

where the interaction operator $V_{i,j\mathscr{J}}^{\ell\ell'}$ is an interaction matrix which depends only on the relative position $\mathbf{r}_j + \mathbf{R}_{\mathscr{J}} - \mathbf{r}_i$ of the two centers and is easily calculated. The evaluation of the multipole moments of each product distribution with respect to its WF centroid $\mathbf{r}_i$,

$$Q_{ia\mathscr{A}}^{\ell} = \sum_{\nu,\mathscr{N}} c_a^{\nu,\mathscr{N}} [\sum_{\mu,\mathscr{M}} c_i^{\mu\mathscr{M}} \phi_{\mu\mathscr{M},\nu\mathscr{N}}^{\ell}(\mathbf{r}_i)] \quad (6)$$

becomes the most demanding step. The index ℓ indicates the multipole order, and by default it runs up to 4 (hexadecapoles): a total of 25 multipole moments have to be evaluated for each $ia\mathscr{A}$ product distribution. Note that the multipole moments $\phi_{\mu\mathscr{M},\nu\mathscr{N}}^{\ell}(\mathbf{r}_i)$ are not, in general, translationally invariant, since they are computed with respect to a center $\mathbf{r}_i$. A suitable translation operator must be applied.[63]

Parallelization of eq 6 is performed according to the ν index: each processor computes only a subset of the $\phi_{\mu,\nu\mathscr{N}}^{\ell}$ shell multipoles and uses them to compute a partial result for *all* of the $Q_{ia\mathscr{A}}^{\ell}$ objects. No intermediate communications are needed, and through a global sum after the end of the algorithm, all processors hold all computed multipole moments. The time required by eq 5 is negligible. The load is distributed according to the same strategy as in the LMP2 equation (see below), so that no further redistribution of the K integrals is required.

3.3. Fast Integral Evaluation: The Density Fitting Approximation. Density fitting (DF) approximation[9,10] is a powerful technique that allows one to speed up the calculation of two electron repulsion integrals of eq 4 by orders of magnitude, with

Table 1. Different Steps of the Periodic Density Fitting Parallel Code[a]

section	step	order of indices	parallelization index
3.3.1	two-index integrals	$\mathcal{Q}$, P, Q	$\mathcal{Q}$
3.3.1	three-index integrals	P, i, a, $\mathcal{A}$, $\mathcal{P}$	P
2.1	bucket sort		
3.3.2	solve for $d^{P\mathcal{P}}_{ia\_\mathcal{A}}$ coefficients	i, a, $\mathcal{A}$, P, $\mathcal{P}$	i, a, $\mathcal{A}$
2.1	bucket sort with symmetry		
3.3.3	assembly	P, i, a, $\mathcal{A}$, $\mathcal{P}$	P

[a] In the first column, reference is made to the section in the text where the corresponding algorithm is discussed. Column 3 reports the order according to which the quantities are evaluated/handled, from slowest to fastest index. The last column explicitly reports the index according to which the parallelization is made. In all cases, this coincides with the slowest index. Bucket sort routines redistribute the quantities among processors.

negligible errors.[43,60] The simple idea is to expand each product distribution between a PAO and a WF in a set of *auxiliary basis functions* $\{\Xi_P\}$:

$$\rho_{ia\_\mathcal{A}} = \chi_i(\mathbf{r})\,\chi_a(\mathbf{r}-\mathbf{R}_\mathcal{A}) \approx \sum_{P\mathcal{P}} d^{P\mathcal{P}}_{i,a\_\mathcal{A}}\Xi_P(\mathbf{r}-\mathbf{R}_\mathcal{P}) \tag{7}$$

A mixed auxiliary basis of Gaussian and Poisson functions[64] is used in this work.

Different flavors of the DF approximation have been developed and implemented for LMP2 in periodic systems (see ref 52 for a complete discussion). Among these, the local direct-space approach is the most similar to the approach adopted in molecular codes and in some of its aspects is similar to the one implemented by Scuseria and Izmaylov.[65] This is the simplest periodic DF approach, and at the same time, it is the most suitable for large unit cell systems. Thus, it was the method of choice in the parallel implementation of the LMP2 code.

The different steps of the implementation are outlined in Table 1. For each step, the corresponding strategy of parallelization is sketched and will be discussed in detail in the following. As can be seen, parallelization is always performed on the slowest running index, and MPI communications are almost entirely enclosed within the bucket sort steps.

3.3.1. Three- and Two-Index Integrals Calculation. Evaluation of three-index integrals of the type $(ia\_\mathcal{A}|P\mathcal{P})$ is distributed according to blocks containing all integrals sharing the same P index. Each processor computes independently all the needed $(\mu\nu\_\mathcal{N}|P\mathcal{P})$ three-index integrals in the AO basis, which are selected by each CPU through prescreening of the set of $(ia\_\mathcal{A}|P\mathcal{P})$ owned.[35] This coarse grain parallelization totally avoids communication among processors at this stage.

The number of computed integrals is huge, so they are kept on disk. Once computed and stored, integrals must be resorted: in the solve step, the index running the P atom has to be the fastest index, since to obtain a coefficient d^P_{ia} (eq 8) all fitting functions in a fitting domain are needed at once. This is achieved through the bucket sort algorithm described in section 2.1. The atomic object handled by the routine (a *block*) includes all $(ia|P)$ integrals where all PAOs a belong to the same atom, and all fitting functions P belong to the same atom. Redistribution of the integrals among processors takes place contextually. No symmetry operators are applied at this stage.

```
Loop over all P fitting functions
   If (my P) Then
     read integrals (iaA|PP) for all i, all aA, all P
     read coefficients d^{PP'}_{j,bB'} for all j, all bB', all P'
     Loop over all i,j,J pairs
       add contribution from atom P to K local buffer
       local sum K on processor who owns K(i,j,J)
     End Loop i,j,J pairs
   EndIf
End Loop P
```

Figure 4. Parallel algorithm for the density fitting assembly step.

Two-index integrals of the type $(P|Q\_\mathcal{Q})$ are treated differently. These simple objects are evaluated quickly but are large, so the costly part is to store them on disk. Calculation is distributed according to the cell index of the second function, following a disk-sharing strategy (section 2.3), so that all unit cells are computed by processors of one *group*. This avoids replication of this matrix on disk, which can be very large, and totally avoids communication.

3.3.2. The Solve Step. The coefficients $d^{P\mathcal{P}}_{ia\_\mathcal{A}}$ of eq 7 are defined by the linear equation system

$$\sum_{P\mathcal{P}} d^{P\mathcal{P}}_{ia\_\mathcal{A}}(P|Q\_\mathcal{Q}') = (ia\_\mathcal{A}|Q\_\mathcal{Q}) \tag{8}$$

Both the indices $P\mathcal{P}$ and $Q\_\mathcal{Q}$ run over all fitting functions in the fit-domain, which is *specific for each separate set of* i, a, and $\mathcal{A}$ indices, that is, for all PAOs on a same atom. This allows for fairly small matrices in eq 8, leading at the same time to a greater number of different coefficients to be calculated and handled. A linear equation solver allows one to solve eq 8 efficiently and stably, given that no linear dependency issues arise in the $(P|Q\_\mathcal{Q})$ matrix. The eigenvalues of this matrix are thus always computed beforehand: if they are all above a threshold (10^{-5} by default), the linear equation solver is invoked; otherwise, inversion is carried out through a much more costly singular value decomposition procedure. Such linear dependency issues are likely to appear in periodic systems, which are considerably more closely packed than molecules, since molecular fitting basis sets are adopted.

After the solve step, a second bucket sort procedure is needed, in which point symmetry is exploited in order to obtain all objects needed for the assembly step in eq 10. This is applied twice, to the integrals $(ia\_\mathcal{A}|P\mathcal{P})$ file and to the coefficients $d^{P\mathcal{P}}_{ia\_\mathcal{A}}$ file. Once more, redistribution of data among processors takes place.

At this stage, $d^{P\mathcal{P}}_{ia\_\mathcal{A}}$ coefficients are in memory and distributed in the most convenient order, so that the following intermediate quantities are conveniently evaluated:

$$D^{P\mathcal{P}}_{ia\_\mathcal{A}} = \sum_{Q\mathcal{Q}} d^{Q\mathcal{Q}}_{ia\_\mathcal{A}}(Q|P\mathcal{P}') \tag{9}$$

These quantities are needed in the assembly step described in the next subsection. They are written on disk, and the bucket sort routine with symmetry and redistribution is applied in the same way as for three-index integrals and coefficients.

3.3.3. The Assembly Step. According to Dunlap's robust expression,[9] which guarantees that the error in the integral is second order with respect to the error in the fitting, the four-index two-electron integrals are approximated as

$$K^{ij,\mathcal{J}}_{a\_\mathcal{A},b\mathcal{B}} \approx \sum_{P\mathcal{P}}(ia\_\mathcal{A}|P\mathcal{P})d^{P\mathcal{P}'}_{jb\mathcal{B}'} + \sum_{P\mathcal{P}} d^{P\mathcal{P}}_{ia\_\mathcal{A}}[(P\mathcal{P}'|jb\mathcal{B}') - D^{P\mathcal{P}'}_{jb\mathcal{B}'}] \tag{10}$$

with $D^{P\mathscr{P}'}_{jb\mathscr{B}'}$ factors as defined in eq 9. The three-index integrals (and coefficients), after the preceding bucket sort step, are stored on disk with the fitting function center as the slowest index and distributed among processors according to the same index. Symmetry has been exploited as well, so no rotations are needed at this stage.

The parallel implementation of the algorithm for the first term of eq 10 is sketched in Figure 4. Each processor performs *one* single complete read of integrals and coefficients, thus loading in memory all the quantities having the same set of P indices in common. The K integrals, at the end of the procedure, are distributed among CPUs according to the same strategy as in the LMP2 equations (next section). A partial sum is performed by each processor, and an all-to-one global sum is needed for each pair. This allows each processor to allocate only one K buffer, which is reused for each pair, and the number of such global sums depends on the size of the fitting basis set.

The parallel algorithm for the second term is identical, with "corrected" $[(P\mathscr{P}'|jb\mathscr{B}') - D^{P\mathscr{P}'}_{jb\mathscr{B}'}]$ integrals instead of normal ones. This algorithm guarantees a reasonable memory occupation: three buffers are allocated by each CPU, one for the three index integrals, one for the coefficients (these have the size of one fitting function "block"), and one for the K integrals.

3.4. Local MP2 Equations. Once all of the ingredients are available (integrals, Fock, and overlap matrices in the PAO basis) the orbital invariant local MP2 energy per unit cell can computed. It is expressed as a sum over pair contributions:

$$E^{\mathrm{LMP2}}_{\mathrm{cell}} = \sum_{i,j_c\mathscr{J}} E^{\mathrm{LMP2}}_{i,j_c\mathscr{J}} \tag{11}$$

Each pair contribution is obtained as

$$E^{\mathrm{LMP2}}_{i,j_c\mathscr{J}} = \sum_{a,\mathscr{A},b,\mathscr{B}} K^{ij,\mathscr{J}}_{a\mathscr{A},b\mathscr{B}}[2T^{ij,\mathscr{J}}_{a\mathscr{A},b\mathscr{B}} - T^{ij,\mathscr{J}}_{b\mathscr{B},a\mathscr{A}}] \tag{12}$$

where $T^{ij\mathscr{J}}$ is the amplitude corresponding to a two-electron excitation from a pair of WFs to a pair of PAOs.

Summations over $a\mathscr{A}$ and $b\mathscr{B}$ indices are truncated through the selection of non-negligible excitations according to the *locality Ansatz*. To the general WF i, a *domain* $\mathscr{D}_i$ is associated, consisting of a number of atoms close to it. $\mathscr{D}_i$ is usually defined through a Boughton−Pulay criterion.[66] A *pair-domain* $\mathscr{D}_{(ij)}$, assigned to a WF pair ij, is defined as the union of the corresponding WF domains. Only those excitations are retained for which, first, both PAOs a and b belong to atoms in $\mathscr{D}_{(ij)}$ and, second, the distance d_{ij} between the centers of the two WFs is within a certain value D. Following the so-called *frozen core* approximation, only *valence* WFs are usually considered.

The unknown amplitudes $T^{ij,\mathscr{J}}_{b\mathscr{B},a\mathscr{A}}$ are obtained solving a set of linear equations which imposes on the $R^{ij,\mathscr{J}}_{a\mathscr{A},b\mathscr{B}}$ residuals to be zero:

$$R^{ij,\mathscr{J}}_{a\mathscr{A},b\mathscr{B}} = K^{ij,\mathscr{J}}_{a\mathscr{A},b\mathscr{B}} + A^{ij,\mathscr{J}}_{a\mathscr{A},b\mathscr{B}} + B^{ij,\mathscr{J}}_{a\mathscr{A},b\mathscr{B}} = 0 \tag{13}$$

where the matrices **A** and **B** incorporate *internal* and *external* contributions to the residual, respectively, and are defined as follows:

$$A^{i,j\mathscr{J}}_{a\mathscr{A},b\mathscr{B}} = \sum_{c\mathscr{C},d\mathscr{D}} [F^{\mathscr{C}'}_{ac} T^{i,j,\mathscr{J}}_{c\mathscr{C},d\mathscr{D}} S^{\mathscr{B}'}_{db} + S^{\mathscr{C}'}_{ac} T^{i,j,\mathscr{J}}_{c\mathscr{C},d\mathscr{D}} F^{\mathscr{B}'}_{db}] \tag{14}$$

$$B^{i,j,\mathscr{J}}_{a\mathscr{A},b\mathscr{B}} = \sum_{c\mathscr{C},d\mathscr{D}} S^{\mathscr{C}'}_{ac} \sum_{k\mathscr{K}} [T^{i,k\mathscr{K}}_{c\mathscr{C},d\mathscr{D}} F^{\mathscr{J}'}_{kj} + F^{\mathscr{K}}_{ik} T^{k,j,\mathscr{J}'}_{c\mathscr{C}',d\mathscr{D}'}] S^{\mathscr{B}'}_{db} \tag{15}$$

S_{ab} (F_{ab}) denotes the element of the overlap (Fock) matrix between functions a and b, and the simplifications due to translational symmetry are implicitly introduced. The range of the $k\mathscr{K}$ summation is suitably truncated according to *locality* criteria in order to include only significant contributions.

The condition expressed by eq 13 is reached iteratively by minimizing a suitable Hylleraas functional. At each step of the iterative procedure, the residuals are used to update the amplitudes. Due to the redundant character of PAOs, the update must be performed in the orthogonal basis proper of the pair $i,j\mathscr{J}$, the so-called local orthonormal (LON) basis. The matrices to perform this unitary transformation are obtained by diagonalizing the Fock matrix in the local pair domain. The set of transformations, one for each WF pair, is generated once before entering the iterative procedure and stored on disk.

The update is then expressed as

$$\Delta\tilde{T}^{i,j\mathscr{J}}_{a\mathscr{A},b\mathscr{B}} = \frac{\tilde{R}^{i,j\mathscr{J}}_{a\mathscr{A},b\mathscr{B}}}{\varepsilon_a + \varepsilon_b - f_{ii} - f_{jj}} \tag{16}$$

with the tilde symbol indicating that $\tilde{T}$ and $\tilde{R}$ are in the LON basis representation. Only symmetry irreducible amplitudes are computed, updated, and stored during the procedure. The amplitudes needed in eq 14 are obtained on the fly from the irreducible ones by applying suitable symmetry operators.

Parallelization of the iterative LPM2 equations is conveniently performed by distributing the workload according to $i,j\mathscr{J}$ pairs (eq 11), but an efficient parallel algorithm is difficult to achieve. In fact, in the evaluation of *external* residuals, term B in eq 14, which accounts for the majority of the time spent in the iterative procedure, amplitudes from different WF pairs contribute to each $i,j\mathscr{J}$ pair. Nielsen and Janssen[20] have proposed two different parallel algorithms for the molecular LMP2 equations: (i) based on replication of the amplitudes and (ii) based on distribution of the amplitudes according to a smart assignment of the workload for each processor. They conclude that scheme i is more load-balanced but less efficient, since it involves a global summation step, while scheme ii is more efficient, since only a redistribution of amplitudes is needed but suffers from load imbalance when a large number of processors is used. A 60% performance has been demonstrated for scheme i when 50 processors are used.

A fundamental feature of periodic LMP2 equations is the extensive use of translational and point symmetry. This makes algorithm ii of Nielsen and Janssen not practicable, since a huge number of additional, globally blocking, communications would be needed, along with a significant overhead for the bookkeeping of all these operations. A replicated memory (scheme i) strategy has therefore been adopted, with a difference: communication among processors takes place only at the end of one iteration, and not after each update. This has some drawbacks: the updates performed by a single processor cannot take advantage of already updated amplitudes (Gauss−Siedel), and therefore the convergence can be slower. Thanks to the use of disk sharing (and paging) strategies for the amplitudes, this problem is softened,

since all processors within a group can read from disk amplitudes that other members of the group have updated and stored.

Regarding the distribution of data, LON transformation matrices, **R** residuals, and **K** integrals are distributed according to the pair index, while **T** amplitudes are replicated—but buffered. Parallelization is straightforward, since no communication is needed during one iteration.

The implemented algorithm (Figure 5) contains also instructions to avoid one processor sending the data to its own group leader. As a consequence of that, in the case of all CPUs sharing the same disk, no MPI communications are needed but rather a final I/O step in which all processors write to disk (all in the same file) the updated amplitudes.

```
Loop over all i, j, 𝒥 pairs
  If (my i, j, 𝒥 pair) then
    If (not in memory) then
      read T_{i,j 𝒥}
    Else
      write T_{i,j 𝒥}
    End If
    send T_{i,j 𝒥} to leaders of other CPU groups
  Else if (I am a group leader) then
    receive T_{i,j 𝒥}
    write T_{i,j 𝒥}
  EndIf
End i, j, 𝒥 loop
```

Figure 5. Scheme of the communication algorithm for the updated amplitudes in LMP2 equations.

Thanks to paging routines, only the amplitudes that can fit in memory are loaded. As a limiting case, in case of very small memory or a very large basis set, only a block of each matrix is kept in memory at once, and each of these blocks has the size of the number of functions *in a local domain* squared—which is constant with the increasing number of atoms in the unit cell.

4. RESULTS

As discussed in the previous section, the periodic LMP2 program is complex and formed by several parts. The parallel efficiency of these different parts has been benchmarked on a small but significative set of periodic crystalline systems, representing a choice of interesting problems, in the field of solid state quantum chemistry, in which the LMP2 method can give

Table 2. Information on the Crystalline Systems Used As a Benchmark[a]

system	$n_{\text{atoms}}^{\text{cell}}$	$n_{\text{elec}}^{\text{cell}}$	basis set	$n_{\text{ao}}^{\text{cell}}$	n_{pairs}
MgO slab with "F" center	54	210	Mg: [4s3p2d1f] O: [4s3p3d2f]	1916	15663
double-walled nanotube	144	360	aug(p,d)-cc-pVDZ	1944	14439
aspirin on SiO_2	141	652	slab: 88-31G* molecule: TZP	2465	72426
MOF-5	106	532	cc-pVTZ	2884	28562

[a] $n_{\text{elec}}^{\text{cell}}$ is the number of correlated electrons per unit cell. $n_{\text{ao}}^{\text{cell}}$ is the number of basis functions in a unit cell; n_{pairs} is the number of Wannier function pairs included in the calculation with the chosen thresholds for the LMP2 truncations.

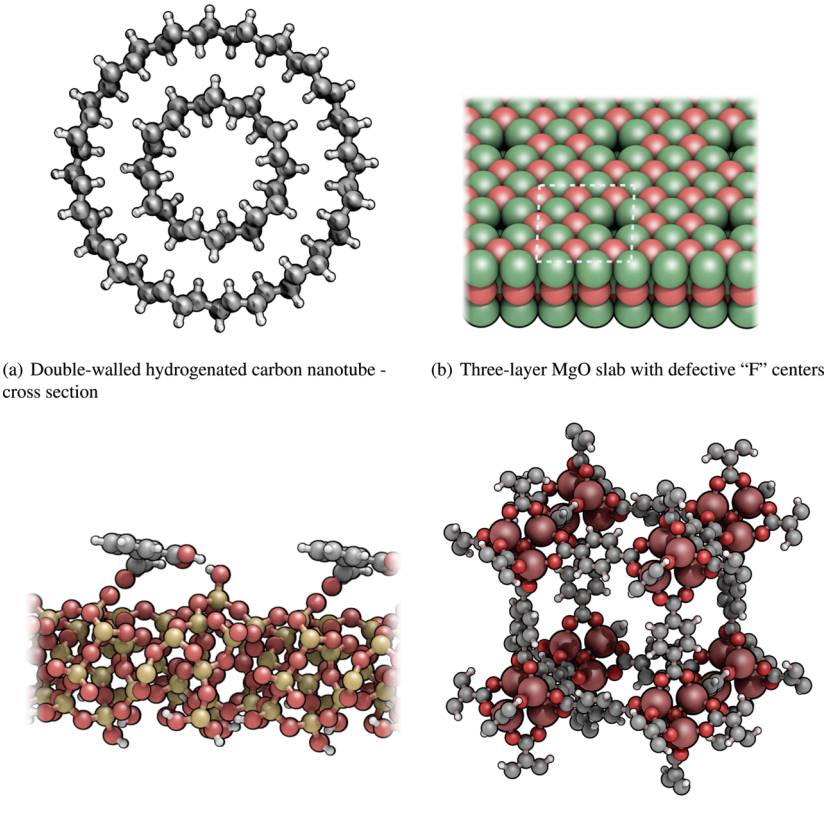

(a) Double-walled hydrogenated carbon nanotube - cross section

(b) Three-layer MgO slab with defective "F" centers

(c) Aspirin adsorbed on Silica slab

(d) MOF-5 - conventional unit cell

Figure 6. The systems used for benchmark calculations. In panel b, the repetitive unit is marked by a dashed white box.

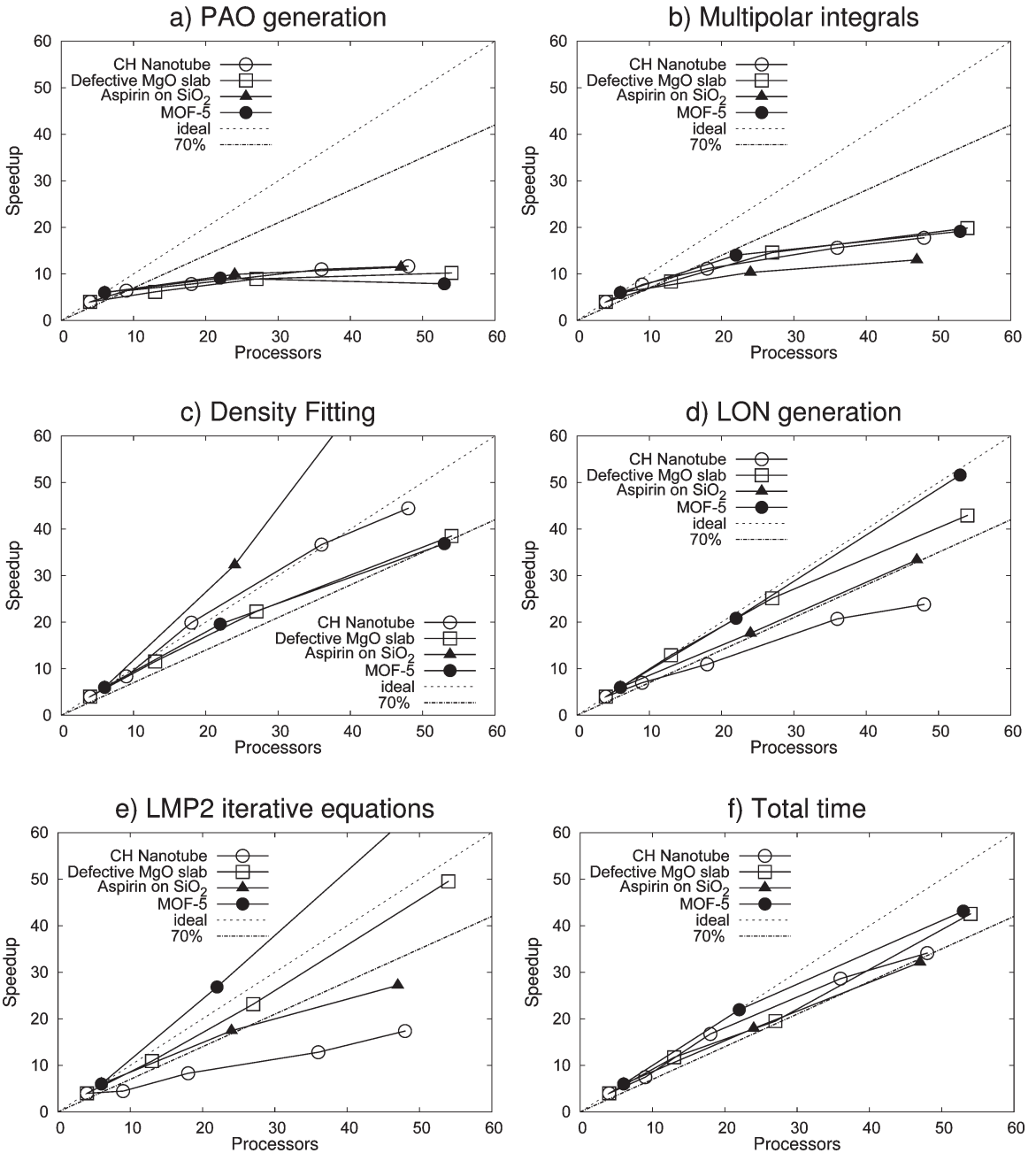

Figure 7. Parallel performance of the different parts of the LMP2 algorithm. Dotted lines indicate the ideal performance (100%) and the 70% performance, considered as an optimal target for the present work.

important answers. The efficiency and features of the scalar algorithm have been discussed in previous works[35] and will not be addressed here. In particular, quasi-linear scaling behavior has been demonstrated with respect to the number of atoms in the unit cell.[52]

4.1. The Test Systems. The set of test systems has been defined in order to cover many of the several geometrically and chemically different situations that can be encountered when dealing with periodic crystals. Systems periodic in one, two, and three dimensions have been considered. Ionic, covalent, and weakly bound, closely packed, as well as microporous materials are included. Let us discuss more in detail the features of each benchmark system. Pictures of the crystalline structure can be found in Figure 6, and some reference data about each test case are reported in Table 2.

Double-Walled Hydrogenated Carbon Nanotube. Graphene and carbon nanotubes (CNTs) are among the "hot" nanomaterials in today's science. One way to tune the chemical and physical properties of CNTs is by means of chemical functionalization, for example, by hydrogenation.[67] A double-walled CNT, composed of two fully hydrogenated tubes, has been chosen as an interesting test case, because of the dispersive interactions that take place among the two tubes. The unit cell of this 1D periodic system is made of 144 atoms and represents the section perpendicular to the tube length (see Figure 6a). The basis set adopted is a cc-pVDZ[68] augmented with polarization functions for high angular momenta.

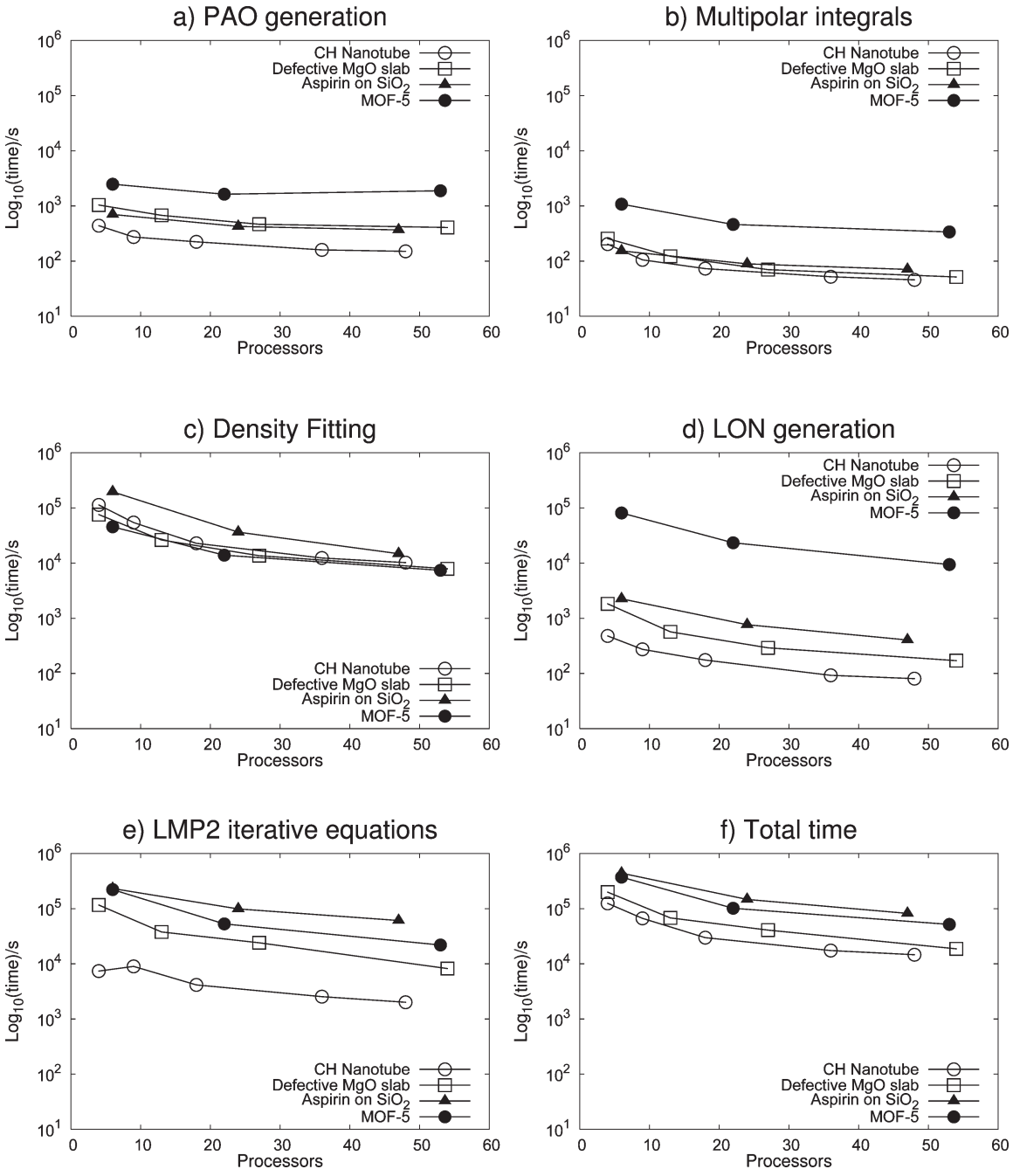

Figure 8. Total wall clock timings (reported in logarithmic scale, in seconds) of the different parts of the LMP2 parallel algorithm.

MgO Three-Layer Slab with a Defective "F" Center. Magnesium oxide, as a bulk crystalline system or as a modeled surface, is and has been a favorite system for periodic *ab initio* calculation, both for its simple crystalline structure and for its interesting chemical properties. In particular, defective sites on the surface are the key to many catalysis processes, of great relevance in modern industry. When modeling a defect in a periodically repeated structure, one has to define a supercell in order to mimic the defect concentration of a real sample. In this way, the computational cost of the calculation is greatly increased. The thickness of the slab is an important factor as well, since one wants generally to reproduce the features of a semi-infinite system. The test case used in this work is a three-layer slab, commonly recognized as a reasonable thickness for the modeling of many surface properties, with a 3 × 3 supercell, resulting in 54 atoms per cell. One oxygen atom of the upper surface is then removed and replaced by two paired electrons, thus creating a diamagnetic F center, one of the most well-known widely diffused defects in rocksalt structures. The basis set is also a good one, with [4s3p2d1f] functions on Mg and [4s3p3d2f] on oxygen,[52] and cc-pVTZ for hydrogen on the F center.

Aspirin Molecule on Silica Substrate. Adsorption of molecules on surfaces is both a technologically interesting process and a challenge for quantum chemistry, since it is ruled mainly by dispersive interactions. A particular case is that of the adsorption of organic or pharmaceutical molecules on biocompatible

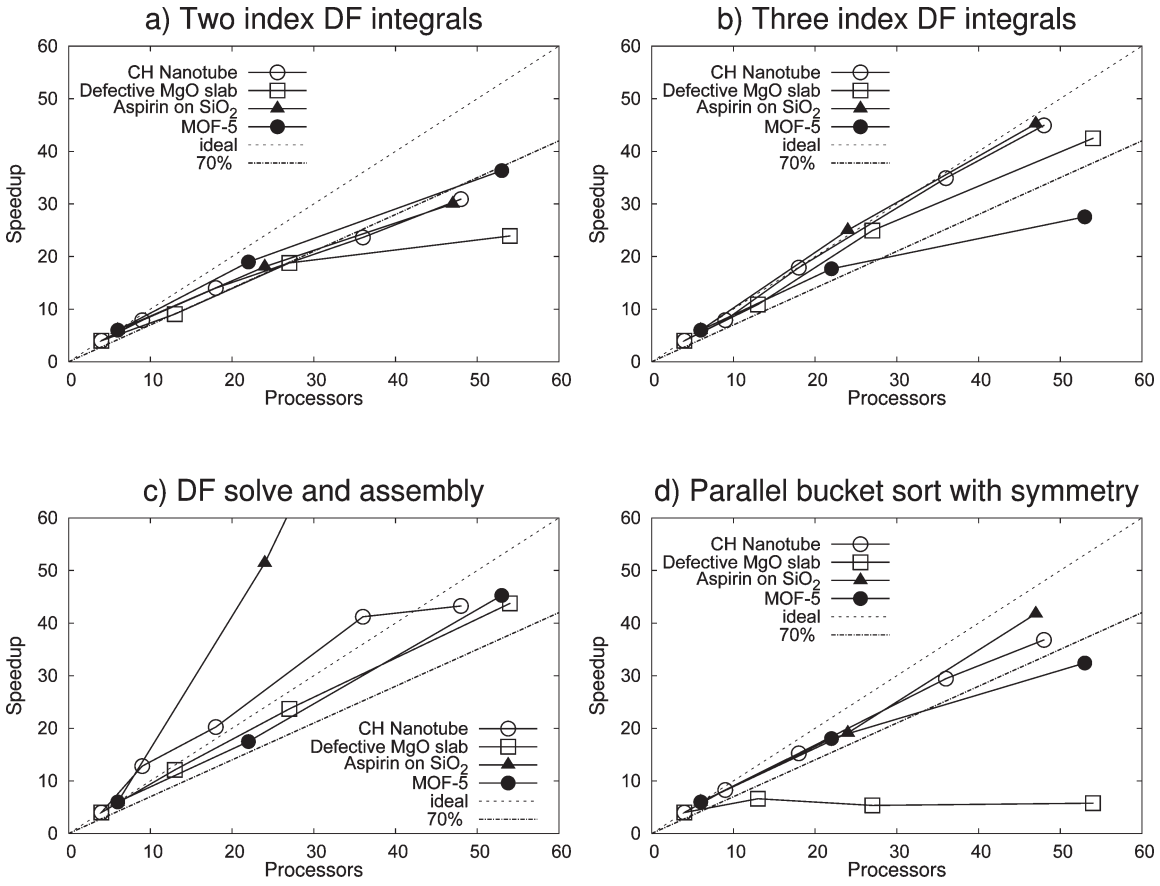

Figure 9. Detail of parallel performance in different steps of the periodic density fitting procedure. See caption of Figure 7 for details.

substrates.[69] In the present test, kindly provided by Piero Ugliengo, the substrate is represented by a ∼10-Å-thick slab of SiO_2, with 141 atoms in the unit cell, and the adsorbate is a molecule of aspirin, a well-known pharmaceutical compound. A good basis set has been used: 88−31G* on Si and O atoms in the slab, TZP on the molecule's atoms.

Metal−Organic Framework (MOF-5). Storage of small gases like hydrogen or CO_2 inside microporous materials is presently one of the main technological challenges. In the past few years, MOFs have become universally popular and recognized as one of the most promising classes of porous materials, with surface areas higher than that of commonly used zeolites.[70] Sillar et al., in 2009, wrote: "...use of even the simplest of [post Hartree-Fock methods], second-order Møller-Plesset perturbation theory (MP2), is far beyond present computational resources for periodic structures with large unit cells, such calculations are performed only on finite-sized models that represent individual structural elements of the whole MOF framework".[71] It is here demonstrated that this is now feasible, with a basis set such as cc-pVTZ with Stuttgart−Dresden ECPs on the Zn atom, at a reasonable computational cost. Problems have been encountered though, trying to reach Hartree−Fock SCF convergence with the unmodified molecular cc-pVTZ basis; since it is beyond the scope of the present work to optimize a suitable basis set for periodic calculations, Wannier functions obtained through a B3LYP Hamiltonian have been used instead of HF ones. The energy results are not to be discussed in this paper, and since this procedure is totally equivalent from a computational point of view, this detail is not relevant to the conclusions on code performance.

4.1.1. Computational Parameters. The parameters relevant to the following discussion—that is, with a significant impact on the cost of the LMP2 calculation—are those related to the local treatment of electron correlation. In all test cases, parameters compatible with real-life calculations have been chosen. Only valence electrons are correlated, according to the commonly accepted *frozen core* approximation. WF pairs are explicitly included up to 10 Å in the smallest cases, 9 Å in the largest. Integrals are evaluated through density fitting for pairs up to 6 Å and through multipolar expansion beyond that. Excitation domains are always defined according to a Boughton−Pulay parameter[66] of 0.990, larger than the commonly used value of 0.985.

4.2. Benchmark Calculations. Computations reported in this section were performed on the IBM SP Power 6 cluster at CINECA supercomputing facilities in Bologna, Italy. The system features 4.7 GHz cores, Infiniband network connection, and shared disk file system. In all calculations, 8 GB of RAM memory have been made available to each processor, independently from the number of processors used.

In Figure 7, the parallel performance of the different parts of the code is reported. The speedup is defined, for a given number of processors N, as $(t_{ref} \times N_{ref})/t_N$. The reference number of processors is for all systems set to 4 or 6, since it is not possible to run these calculations on a smaller number of processors (this comes out quite clearly from the use of memory in Figure 3). In Figure 8, the wall clock timings are reported, on a logarithmic scale, for the same pieces of code, in order to highlight the different calculation weights and to give a feeling of the relative cost of the same algorithm on different systems, which can be quite different.

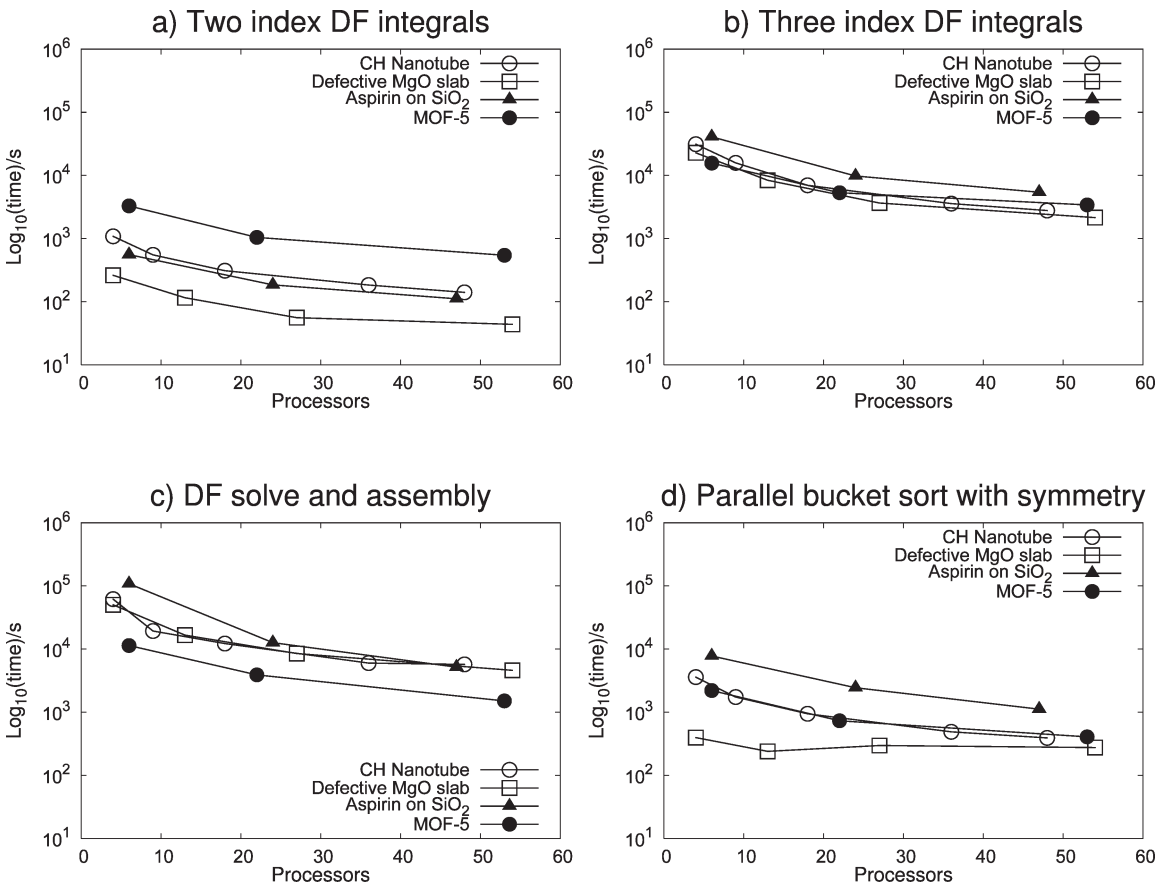

Figure 10. Total wall clock timings (reported in logarithmic scale, in seconds) of the different steps of periodic density fitting procedure.

At first glance, the reader can notice that the four different test systems show a very different behavior in the different parts, especially in panels c, d, and e, which cover most of the execution time. Despite these differences, the global performance of the code, evaluated on wall clock timings, is very similar for all the systems and is comprised between 70% and 80% at the highest number of processors. Correspondingly, the total execution times are reduced by almost an order of magnitude.

The first two panels concern the generation of PAOs and related matrices and the multipolar integrals calculation. The poor parallel scaling behavior is explained by the small elapsed time of these pieces of code, since serial code and I/O take a leading role when the cost of the parallelized part is minor. Besides, it is known that Scalapack routines do not have an ideal scaling for this matrix size. As a matter of fact, as already discussed the purpose of this piece of code is to mostly distribute the memory load, which is achieved quite efficiently (Figure 3).

Evaluation of integrals through the density fitting approximation is definitely more relevant to the present discussion. The cost on a low number of processors ranges from half a day to two days but is generally very similar, if compared with the large differences (several order of magnitude) which are observed in the elapsed time of other parts of the code. The largest calculation, MOF-5, has the lowest time since in this microporous lattice the prescreenings are very efficient, and thus the number of integrals to be computed is reduced. The behavior of the test set when increasing the number of processors is very heterogeneous, even showing superlinear scaling phenomena, and it needs more careful examination.

In Figures 9 and 10, speedups and total timings are reported for the most significant steps of the DF algorithm, in analogy with Figures 6 and 7. Two-index integrals are quite cheap, and no worries come from some nonoptimal speedup, which is actually observed when the CPUs outnumber the unit cells to be computed. The performance of the three-index integrals code is generally very good and deteriorates at a high number of processors only for MOF-5. This system contains different elements such as zinc and hydrogen and suffers from load-balancing problems, due to the coarse grain parallelization according to the atomic center, as discussed in section 3.3.1. The most expensive step, solve and assembly, shows superlinear scaling behavior for two of out the four systems. The two-index auxiliary integrals are here handled through a paging strategy (see section 2.2), and the algorithm greatly benefits from the larger amount of total memory available.

The analysis of the parallel bucket sort with symmetry exploitation is quite surprising. First, its cost is non-negligible, though generally an order of magnitude lower than the most important DF steps. Second, it scales very well in three out of the four test cases, with speedups up to 90% at 50 CPUs. This is in fact a combination of different factors: (i) the better performance of the algorithm due to the increasing of the total available memory, which brings superlinear scaling, (ii) sublinear scaling due to concurrent access to the disk and locally blocking steps, and (iii) the fact that no all-to-all communications take place, but always one-to-one, making this step non-globally-blocking. In the case of a globally blocking algorithm, the speedup would be constant. In the case of MgO, the overall cost is small, thus making irrelevant point i above and point ii dominant.

The last two steps of the LMP2 algorithm to be discussed are the LON generation and the LMP2 iterative equations, reported in panels d and e of Figures 6 and 7. The first is important only in the case of MOF-5; this fact is a consequence of a very good basis set (cc-pVTZ) and large excitation domains, since the diagonalization of matrices of the size of the number of basis functions in the domain is involved—which scales as $\mathcal{O}(n^3)$. Fortunately, the parallel performance is close to ideal for this system, while it is worse for others only due to the fact that, since the elapsed time is small, serial parts of the code or noise become significant.

The LMP2 equations, described in section 3.4, are the most delicate and complex part of the parallel implementation, and the same experience is reported for nonperiodic implementations.[20] Again, a very heterogeneous behavior is observed in this case, ranging from superlinear scaling to sublinear. For this reason, let us analyze separately the four test cases: (i) The CH double-walled nanotube has a small basis set and is not a dense system. The pair excitation domains contain few centers and few functions per center; the number of external contributions to the update of a single amplitude is also small. As a consequence, the cost of the iterations is not very significant and is mainly dominated by I/O. (ii) The aspirin on SiO_2 two-dimensional system is rather dense, and the calculation involves a high number of WF−WF pairs (Table 2), but excitation domains are constituted of few centers, since WFs are very localized, and the cost of evaluating a single residual is small. A large part of the time resides also in this case in the I/O. (iii) MgO is the most dense among the test cases, and the number of external contributions in eq 14 is very large. The cost of computing residuals then dominates with respect to I/O, so the performance is close to ideal. (iv) MOF-5 is a microporous system, so even if it is periodic in three dimensions, not many pairs are included in the calculation. The WFs are not well localized though, due to aromatic rings, so large excitation domains are defined by the chosen Boughton−Pulay threshold. The local approach is then not at its peak efficiency, and large matrices have to be handled. For this reason, the paging algorithm is intensively used, and as already observed for the solve step of the DF procedure, superlinear scaling is observed due to the increasing of the global amount of memory when the number of processors is increased. We recall here that, thanks to the disk-sharing strategy described in section 2.3, no communication among processors takes place in all of the LMP2 iterations, since this is substituted by writing on the disk unit shared by all processors.

As mentioned above, all of the different parts of the code, behaving differently on the different systems, do average in the end, resulting in quite similar speedups for all of the test systems. The performance is satisfactory in all cases, and the total time required to complete a job ranges from 4 h in the smallest case (CH nanotube) to 23 h (MOF-5).

5. CONCLUSION AND PROSPECTS

A parallel implementation of the periodic local MP2 code of the Cryscor program has been presented and thoroughly tested. It is seen that scaling with the number of processors is favorable up to more than 50 processors, with parallel performance up to 70−80% with respect to the ideal behavior.

The challenges posed by the full exploitation of symmetry at different levels present throughout the code have been overcome by adopting simple yet powerful strategies: (i) to enclose all communication in well-defined and separate pieces of code, thus relying on coarse-grain parallelization, and (ii) to fruitfully use the disk, as far as it is possible, as a communication medium among CPUs who share the same disk space.

The behavior of the four periodic systems in the test set, chosen to be different as concerns the number of periodic dimensions, density, and chemical composition, is very heterogeneous in specific parts of the code, while the speedups evaluated on the total wall clock time are very similar. This can be a good indication that this general purpose code will perform reasonably well on any kind of crystalline system.

As a final result, the calculation of MP2 energy of a MOF-5 three-dimensional periodic crystal with a cc-pVTZ basis (106 atoms, 2884 basis functions in the unit cell) is achieved in less than 24 h on 53 processors. The parallelized LMP2 code will be soon released as an update to the Cryscor program, making this work available to the scientific community.

A massive parallel implementation, i.e., capable of efficiently running on hundreds of processors, would require a complete recoding of the LMP2 procedure, extending the use of linear algebra routines (Scalapack) to the whole code. As a perspective, the power of implementations taking advantage of GPU cores is emerging nowadays,[72] which opens the way to an innovative concept of the parallelization codes.

AUTHOR INFORMATION

Corresponding Author

*E-mail: lorenzo.maschio@unito.it.

ACKNOWLEDGMENT

The author is grateful to Prof. Cesare Pisani, Dr. Ian J. Bush, Dr. Denis Usvyat, and Prof. Martin Schütz for fruitful discussions. Mikko Linnolahti, Piero Ugliengo, and Bartolomeo Civalleri have kindly provided the input structures for the double walled nanotube, the aspirin adsorbed on silica, and MOF-5 test systems, respectively. 3D images of crystalline structures have been realized with Qutemol.[73] Calculations have been performed at the CINECA facilities thanks to grants HP10C5J7E1-QCECSSC and HP10CNWQPB-TPC.

REFERENCES

(1) Werner, H.-J. et al. *MOLPRO*, version 2010.1; University College Cardiff Consultants Limited: Cardiff, Wales, 2010. See http://www.molpro.net (accessed Aug 2011).

(2) *TURBOMOLE*, V6.2; University of Karlsruhe and Forschungszentrum Karlsruhe GmbH: Karlsruhe, Germany, 2010. Available from http://www.turbomole.com (accessed Aug 2011).

(3) Doser, B.; Zienau, J.; Clin, L.; Lambrecht, D. S.; Ochsenfeld, C. *Z. Phys. Chem.* **2010**, *224*, 397–412.

(4) Lambrecht, D. S.; Ochsenfeld, C. *J. Chem. Phys.* **2005**, *123*, 184101.

(5) Lambrecht, D. S.; Doser, B.; Ochsenfeld, C. *J. Chem. Phys.* **2005**, *123*, 184102.

(6) Izmaylov, A.; Scuseria, G. E.; Frisch, M. J. *J. Chem. Phys.* **2006**, *125*, 104103.

(7) Feyereisen, M.; Fitzgerald, G.; Komornicki, A. *Chem. Phys. Lett.* **1993**, *208*, 359.

(8) Pedersen, T. B.; Aquilante, F.; Lindh, R. *Theor. Chem. Acc.* **2009**, *124*, 1–10.

(9) Dunlap, B. *Phys. Chem. Chem. Phys.* **2000**, *2*, 2113–2116.

(10) Werner, H.; Manby, F.; Knowles, P. *J. Chem. Phys.* **2003**, *118*, 8149.

(11) Pulay, P. *Chem. Phys. Lett.* **1983**, *100*, 151.

(12) Saebø, S.; Pulay, P. *Chem. Phys. Lett.* **1985**, *113*, 13.
(13) Saebø, S.; Pulay, P. *Annu. Rev. Phys. Chem.* **1993**, *44*, 213.
(14) Häser, M.; Almlöf, J. *J. Chem. Phys.* **1992**, *96*, 489.
(15) Schütz, M.; Lindh, R. *Theor. Chem. Acc.* **1997**, *95*, 13–34.
(16) Mitin, A.; Baker, J.; Wolinski, K.; Pulay, P. *J. Comput. Chem.* **2003**, *24*, 154–160.
(17) Aikens, C.; Gordon, M. *J. Phys. Chem. A* **2004**, *108*, 3103–3110.
(18) Fossgard, E.; Ruud, K. *J. Comput. Chem.* **2006**, *27*, 326–333.
(19) Ishimura, K.; Pulay, P.; Nagase, S. *J. Comput. Chem.* **2006**, *27*, 407–413.
(20) Nielsen, I. M. B.; Janssen, C. L. *J. Chem. Theory Comput.* **2007**, *3*, 71–79.
(21) Lotrich, V.; Flocke, N.; Ponton, M.; Yau, A. D.; Perera, A.; Deumens, E.; Bartlett, R. J. *J. Chem. Phys.* **2008**, *128*, 194104.
(22) Janowski, T.; Pulay, P. *J. Chem. Theory Comput.* **2008**, *4*, 1585–1592.
(23) Harding, M. E.; Metzroth, T.; Gauss, J.; Auer, A. A. *J. Chem. Theory Comput.* **2008**, *4*, 64–74.
(24) Katouda, M.; Nagase, S. *Int. J. Quantum Chem.* **2009**, *109*, 2121–2130.
(25) Ayala, P.; Kudin, K.; Scuseria, G. *J. Chem. Phys.* **2001**, *115*, 9698.
(26) Stoll, H. *Phys. Rev. B* **1992**, *46*, 6700–6704.
(27) Paulus, B. *Phys. Rep.* **2006**, *428*, 1–52.
(28) Pisani, C.; Busso, M.; Capecchi, G.; Casassa, S.; et al. *J. Chem. Phys.* **2005**, *122*, 094113.
(29) Manby, F.; Alfè, D.; Gillan, M. *Phys. Chem. Chem. Phys.* **2006**, *8*, 5178–5180.
(30) Hirata, S. *J. Chem. Phys.* **2008**, *129*, 204104.
(31) Marsman, M.; Grüneis, A.; Paier, J.; Kresse, G. *J. Chem. Phys.* **2009**, *130*, 184103.
(32) Gruneis, A.; Marsman, M.; Kresse, G. *J. Chem. Phys.* **2010**, *133*, 074107.
(33) Hermann, A.; Schwerdtfeger, P. *Phys. Rev. Lett.* **2008**, *101*, 183005.
(34) Halo, M.; Casassa, S.; Maschio, L.; Pisani, C. *Chem. Phys. Lett.* **2009**, *467*, 294–298.
(35) Pisani, C.; Maschio, L.; Casassa, S.; Halo, M.; Schütz, M.; Usvyat, D. *J. Comput. Chem.* **2008**, *29*, 2113–2124.
(36) Pisani, C.; Casassa, S.; Maschio, L.; Schütz, M.; Usvyat, D. CRYSCOR09. See www.cryscor.unito.it (accessed Aug 2011).
(37) Dovesi, R.; Saunders, V. R.; Roetti, C.; Orlando, R.; Zicovich-Wilson, C. M.; Pascale, F.; Doll, K.; Harrison, N. M.; Civalleri, B.; Bush, I. J.; D'Arco, P.; Llunell, M. CRYSTAL09 User's Manual. http://www.crystal.unito.it/Manuals/crystal09.pdf (accessed Aug 2011).
(38) Dovesi, R.; Orlando, R.; Civalleri, B.; Roetti, C.; Saunders, V.; Zicovich-Wilson, C. *Z. Kristallogr.* **2005**, *220*, 571–573.
(39) Schütz, M.; Werner, H. *J. Chem. Phys.* **2001**, *114*, 661.
(40) Schütz, M.; Hetzer, G.; Werner, H. *J. Chem. Phys.* **1999**, *111*, 5691.
(41) Zicovich-Wilson, C.; Dovesi, R.; Saunders, V. *J. Chem. Phys.* **2001**, *115*, 9708.
(42) Casassa, S.; Zicovich-Wilson, C.; Pisani, C. *Theor. Chem. Acc.* **2006**, *116*, 726–733.
(43) Maschio, L.; Usvyat, D. *Phys. Rev. B* **2008**, *78*, 73102.
(44) Maschio, L.; Usvyat, D.; Civalleri, B. *CrystEngComm* **2010**, *12*, 2429–2435.
(45) Maschio, L.; Usvyat, D.; Schütz, M.; Civalleri, B. *J. Chem. Phys.* **2010**, *132*, 134706.
(46) Erba, A.; Pisani, C.; Casassa, S.; Maschio, L.; Schütz, M.; Usvyat, D. *Phys. Rev. B* **2010**, *81*, 165108.
(47) Martinez-Casado, R.; Mallia, G.; Usvyat, D.; Maschio, L.; Casassa, S.; Schütz, M.; Harrison, N. M. *J. Chem. Phys.* **2011**, *134*, 014706.
(48) Halo, M.; Casassa, S.; Maschio, L.; Pisani, C.; Dovesi, R.; Ehinon, D.; Baraille, I.; Rèrat, M.; Usvyat, D. *Phys. Chem. Chem. Phys.* **2011**, *13*, 4434–4443.
(49) Halo, M.; Pisani, C.; Maschio, L.; Casassa, S.; Schütz, M.; Usvyat, D. *Phys. Rev. B* **2011**, *83*, 035117.
(50) Erba, A.; Maschio, L.; Salustro, S.; Casassa, S. *J. Chem. Phys.* **2011**, *134*, 074502.
(51) Erba, A.; Itou, M.; Sakurai, Y.; Ito, M.; Casassa, S.; Maschio, L.; Terentjevs, A.; Pisani, C. *Phys. Rev. B* **2011**, *83*, 125208.
(52) Schütz, M.; Usvyat, D.; Lorenz, M.; Pisani, C.; Maschio, L.; Casassa, S.; Halo, M. Density fitting for correlated calculations in periodic systems. In *Accurate Condensed-Phase Quantum Chemistry*; Manby, F. R., Ed.; CRC Press: Boca Raton, FL, 2010; pp 29−56.
(53) Ishimura, K.; Pulay, P.; Nagase, S. *J. Comput. Chem.* **2006**, *27*, 407.
(54) Baker, J.; Pulay, P. *J. Comput. Chem.* **2002**, *23*, 1150.
(55) Nakao, Y.; Hirao, K. *J. Chem. Phys.* **2004**, *120*, 6375.
(56) Hättig, C.; Hellweg, A.; Köhn, A. *Phys. Chem. Chem. Phys.* **2006**, *8*, 1159.
(57) Shutler, P. M. E.; Sim, S. W.; Lim, W. Y. S. *Comput. J.* **2008**, *51*, 451–469.
(58) Yoshimine, M. *J. Comput. Phys.* **1973**, *11*, 449.
(59) Ford, A. R.; Janowski, T.; Pulay, P. *J. Comput. Chem.* **2006**, *28*, 1215.
(60) Maschio, L.; Usvyat, D.; Manby, F.; Casassa, S.; Pisani, C.; Schütz, M. *Phys. Rev. B* **2007**, *76*, 75101.
(61) Blackford, L. S.; Choi, J.; Cleary, A.; D'Azevedo, E.; Demmel, J.; Dhillon, I.; Dongarra, J.; Hammarling, S.; Henry, G.; Petitet, A.; Stanley, K.; Walker, D.; Whaley, R. C. *ScaLAPACK User's Guide*; Society for Industrial and Applied Mathematics: Philadelphia, PA, 1997.
(62) Hetzer, G.; Pulay, P.; Werner, H. *Chem. Phys. Lett.* **1998**, *290*, 143.
(63) Helgaker, T.; Jørgensen, P.; Olsen, J. *Molecular Electronic-Structure Theory*; Wiley: New York, 2000; pp 410−416.
(64) Manby, F.; Knowles, P. *Phys. Rev. Lett.* **2001**, *87*, 163001.
(65) Izmaylov, A.; Scuseria, G. *Phys. Chem. Chem. Phys.* **2008**, *10*, 3421–3429.
(66) Boughton, J. W.; Pulay, P. *J. Comput. Chem.* **1993**, *14*, 736–740.
(67) Tanskanen, J.; Linnolahti, M.; Karttunen, A. J.; Pakkanen, T. A. *ChemPhysChem* **2008**, *9*, 2390–2396.
(68) Kendall, R.; T.H. Dunning, J.; Harrison, R. *J. Chem. Phys.* **1992**, *96*, 6796.
(69) Rimola, A.; Civalleri, B.; Ugliengo, P. *Phys. Chem. Chem. Phys.* **2010**, *12*, 6357–6366.
(70) Civalleri, B.; Napoli, F.; Noel, Y.; Roetti, C. *CrystEngComm* **2006**, *8*, 364–371.
(71) Sillar, K.; Hofmann, A.; Sauer, J. *J. Am. Chem. Soc.* **2009**, *131*, 4143–4150.
(72) Vogt, L.; Olivares-Amaya, R.; Kermes, S.; Shao, Y.; Amador-Bedolla, C.; Aspuru-Guzik, A. *J. Phys. Chem. A* **2008**, *112*, 2049–2057.
(73) Tarini, M.; Cignoni, P.; Montani, C. *IEEE Trans. Visualization Comput. Graphics* **2006**, *12*, 1237–1244.

JCTC Journal of Chemical Theory and Computation

ARTICLE

pubs.acs.org/JCTC

Diabatization Schemes for Generating Charge-Localized Electron−Proton Vibronic States in Proton-Coupled Electron Transfer Systems

Andrew Sirjoosingh and Sharon Hammes-Schiffer*

Department of Chemistry, 104 Chemistry Building, Pennsylvania State University, University Park, Pennsylvania 16802, United States

Supporting Information

ABSTRACT: A scheme for the rigorous construction of charge-localized diabatic electron−proton vibronic states for proton-coupled electron transfer (PCET) reactions is presented. The diabatic electronic states are calculated using an adiabatic-to-diabatic transformation designed to ensure that the first-order nonadiabatic couplings with respect to a specified one-dimensional reaction coordinate vanish exactly. This scheme is applied to both symmetric and asymmetric PCET systems with several different one-dimensional reaction coordinates, including the hydrogen transfer coordinate, a normal mode coordinate, and the intrinsic reaction coordinate. This approach is also extended to describe the three-dimensional motion of the transferring hydrogen. The diabatic electronic states exhibit relatively invariant charge distributions along the reaction coordinate and are in excellent agreement with the analogous states obtained from the generalized Mulliken−Hush and Boys localization methods. Furthermore, these diabatic electronic states are combined with the associated proton vibrational wave functions to generate charge-localized electron−proton vibronic states that describe one- or three-dimensional hydrogen motion. These electron−proton vibronic states can be used to calculate the vibronic couplings, rate constants, and kinetic isotope effects of PCET reactions.

I. INTRODUCTION

Proton-coupled electron transfer (PCET) reactions are prevalent in many facets of biology, chemistry, and physics.[1−5] Concerted PCET reactions, which are characterized by simultaneous electron and proton transfer without a stable intermediate, have been observed in a wide variety of systems, including enzymatic, photoinduced, and electrochemical processes. Typically, PCET reactions are characterized as vibronically nonadiabatic because the subsystem comprised of the electrons and transferring proton does not respond instantaneously to the motions of the solvent and other solute nuclei. Within this nonadiabatic framework, PCET theories require the identification of the charge-localized reactant and product diabatic electron−proton vibronic states corresponding to the transferring electron and proton localized on their donors and acceptors, respectively.[2,6] These diabatic electron−proton vibronic states can be used to calculate the vibronic couplings, which are key quantities in the nonadiabatic PCET rate constant expressions derived with the golden rule formalism.[7,8] Combined with the solute and solvent reorganization energies, as well as the vibronic energy level splittings, these vibronic couplings can be used to calculate experimentally accessible quantities such as rate constants and kinetic isotope effects.

The objective of this paper is to develop a methodology for the rigorous construction of the charge-localized diabatic electron−proton vibronic states that form the basis of nonadiabatic PCET theories. A variety of schemes have been developed to generate diabatic electronic states, particularly for electron transfer reactions.[9−31] Diabatic electronic states can be defined mathematically as states with vanishing first-order nonadiabatic couplings at all possible nuclear configurations. In the context of electron transfer reactions, the diabatic electronic states are associated with the physically meaningful reactant and product states corresponding to the electron localized on the donor and acceptor, respectively. These diabatic electronic states are usually characterized by charge invariance in that the electronic charge distribution does not change significantly with nuclear motion. Schemes that have been developed to generate charge-localized diabatic electronic states for electron transfer reactions include the minimization of first-order nonadiabatic couplings using an adiabatic electronic state basis,[10−12] the generalized Mulliken−Hush method[13,14] and extensions using Boys localization,[25,26] block diagonalization methods,[19,20] approaches enforcing configurational uniformity,[9,16,17,22] constrained density functional theory,[29,30] and valence bond theory approaches.[15,24]

In a previous study,[23] we devised a scheme to calculate charge-localized diabatic electronic states for PCET reactions. In particular, we used an adiabatic-to-diabatic transformation[10] to generate diabatic electronic states constructed to ensure that the first-order nonadiabatic couplings with respect to the one-dimensional transferring hydrogen coordinate vanish exactly. When this diabatization approach was applied to the phenoxyl−phenol self-exchange PCET reaction, the diabatic electronic states were shown to exhibit physically meaningful charge-localized electronic charge distributions. Moreover, we showed that this diabatization scheme provides quantitative diagnostics for the degree of electron−proton nonadiabaticity in PCET systems.[23] Identifying the degree of electron−proton nonadiabaticity is important because this property impacts the form of

Received: May 27, 2011
Published: July 28, 2011

the vibronic coupling and the rate constant and provides insight into the fundamental mechanism. Specifically, electronically adiabatic proton transfer is associated with the hydrogen atom transfer mechanism, which does not involve significant electronic charge redistribution, and electronically nonadiabatic proton transfer is associated with the PCET mechanism, which involves significant electronic charge redistribution.[32,33]

In the present study, we expand this diabatization scheme in several directions. We extend this approach to general asymmetric PCET reactions and to other one-dimensional reaction coordinates, such as a normal mode coordinate or the intrinsic reaction coordinate (IRC). We also expand the previous treatment to describe three-dimensional hydrogen motion, where the component of the first-order nonadiabatic coupling vector along a specified one-dimensional reaction coordinate vanishes rigorously for all points on the three-dimensional diabatic electronic surfaces. In addition, we devise a strategy that utilizes the diabatic electronic states, along with the associated proton vibrational wave functions, to construct electron−proton vibronic states that describe either one-dimensional or three-dimensional hydrogen motion. These electron−proton vibronic states form the basis of nonadiabatic PCET theories and enable the calculation of vibronic couplings, rate constants, and kinetic isotope effects.

In addition to developing these extensions of the diabatization method for PCET reactions, we compare the diabatic electronic states obtained with this approach to those obtained with the generalized Mulliken−Hush (GMH) method[13,14] and extensions using Boys localization.[25,26] These alternative diabatization methods generate the diabatic electronic states from the dipole moments associated with the ground and excited adiabatic electronic states rather than the first-order nonadiabatic couplings. The application of the GMH and Boys localization diabatization methods to PCET reactions is straightforward but, to our knowledge, has not been explored previously. The similarities among the diabatic electronic states generated with these three different diabatization methods provide a degree of validation for the underlying assumptions of the theoretical treatments.

An outline of this paper is as follows. Section II.A describes the adiabatic-to-diabatic transformation along a one-dimensional hydrogen coordinate utilized to generate diabatic electronic states. In section II.B, we discuss modifications of this diabatization protocol to generate diabatic electronic states along general one-dimensional reaction coordinates, including a normal mode coordinate and the IRC. Section II.C describes the construction of diabatic electron−proton vibronic states for both one-dimensional and three-dimensional hydrogen motion. Section II.D summarizes the GMH and Boys localization methods that are implemented for comparison. In section III, we provide the details of the computational methods used to study three model PCET systems: the phenoxyl−phenol self-exchange reaction, the asymmetric phenoxyl−quinol reaction, and the amidinium−carboxylate system representing an experimentally studied photoinduced PCET reaction.[34−36] Section IV.A describes the generation of the diabatic electronic states for these three model systems, illustrating the extensions to asymmetric systems and to alternative one-dimensional reaction coordinates. Section IV.B presents the strategy for combining the diabatic electronic states with the associated proton vibrational states to construct diabatic electron−proton vibronic states. In section IV.C, we provide a comparison of this diabatization method to the GMH and Boys localization methods for generating diabatic electronic states. Finally, conclusions and future direction are discussed in section V.

II. THEORY

II.A. Adiabatic-to-Diabatic Transformation. Consider a system comprised of N_e electrons, N_p protons, and N_s slow nuclei with coordinates $\mathbf{r}_e$, $\mathbf{r}_p$, and $\mathbf{R}$ and masses m_e, m_p, and $\{M_I\}$, respectively, and with potential energy $V(\mathbf{r}_e,\mathbf{r}_p,\mathbf{R})$. The Hamiltonian for the "fast" degrees of freedom (i.e., the electron−proton subsystem) is

$$H_q = -\sum_{i'=1}^{N_p}\frac{\hbar^2}{2m_p}\nabla_{i'}^2 + H_e \tag{1}$$

where the electronic Hamiltonian is

$$H_e = -\sum_{i=1}^{N_e}\frac{\hbar^2}{2m_e}\nabla_i^2 + V(\mathbf{r}_e,\mathbf{r}_p,\mathbf{R}) \tag{2}$$

For fixed $\mathbf{R}$, the eigenfunctions $\{\Phi_k(\mathbf{r}_e;\mathbf{r}_p;\mathbf{R})\}$ of H_q are calculated by solving

$$H_q\Phi_k(\mathbf{r}_e,\mathbf{r}_p;\mathbf{R}) = E_k(\mathbf{R})\,\Phi_k(\mathbf{r}_e,\mathbf{r}_p;\mathbf{R}) \tag{3}$$

The adiabatic electronic states for fixed $(\mathbf{r}_p,\mathbf{R})$ are determined by solving

$$H_e\psi_i(\mathbf{r}_e;\mathbf{r}_p,\mathbf{R}) = \varepsilon_i(\mathbf{r}_p,\mathbf{R})\,\psi_i(\mathbf{r}_e;\mathbf{r}_p,\mathbf{R}) \tag{4}$$

Assuming N electronic states, we define $\vec{\psi}$ to be a column vector of the N electronic eigenfunctions $\{\psi_i(\mathbf{r}_e;\mathbf{r}_p,\mathbf{R})\}$ of eq 4. Then, we define an $N \times N$ transformation matrix $\mathbf{A}(\mathbf{r}_p;\mathbf{R})$ such that

$$\vec{\xi}(\mathbf{r}_e;\mathbf{r}_p,\mathbf{R}) = \mathbf{A}(\mathbf{r}_p;\mathbf{R})\,\vec{\psi}(\mathbf{r}_e;\mathbf{r}_p,\mathbf{R}) \tag{5}$$

where $\vec{\xi}$ is a column vector of functions satisfying the condition

$$\langle\xi_i|\nabla_{\mathbf{r}_p}\xi_j\rangle_e = 0 \text{ for all } i,j \tag{6}$$

Thus, the transformed electronic states $\{\xi_i(\mathbf{r}_e;\mathbf{r}_p,\mathbf{R})\}$ satisfy the standard definition of diabatic states with respect to the proton coordinate $\mathbf{r}_p$.

As discussed in refs 10 and 23, for a one-dimensional proton coordinate r_p and $N = 2$ electronic states, the matrix $\mathbf{A}$ is given by

$$\mathbf{A}(r_p;\mathbf{R}) = \begin{pmatrix}\cos\gamma & -\sin\gamma\\ \sin\gamma & \cos\gamma\end{pmatrix} \tag{7}$$

where

$$\gamma(r_p;\mathbf{R}) = \gamma(r_0;\mathbf{R}) - \int_{r_0}^{r_p} d_{12}^{(ep)}(r;\mathbf{R})\,dr \tag{8}$$

In this expression,

$$d_{12}^{(ep)}(r_p;\mathbf{R}) = \left\langle\psi_1\left|\frac{\partial\psi_2}{\partial r_p}\right.\right\rangle_e = \frac{\left\langle\psi_1\left|\frac{\partial H_e}{\partial r_p}\right|\psi_2\right\rangle_e}{\varepsilon_2-\varepsilon_1} \tag{9}$$

is the first-order nonadiabatic coupling between adiabatic electronic states 1 and 2, and $\gamma(r_0;\mathbf{R})$ is an additive constant that must be specified at some proton coordinate $r_p = r_0$. The diabatic potential energy matrix is given by $\mathbf{W} = \mathbf{AUA}^{-1}$, where $U_{ij} = \varepsilon_i(r_p,\mathbf{R})\delta_{ij}$

is the adiabatic potential energy matrix. Here, $W_{11}(r_p,\mathbf{R})$ and $W_{22}(r_p,\mathbf{R})$ are the diabatic electronic energies and $W_{12}(r_p,\mathbf{R})$ is the diabatic electronic coupling.

Previously, we applied this approach to symmetric systems. In this case, we chose $r_0 = 0$, corresponding to the transition state geometry, and set $\gamma(r_0) = -\pi/4$. This choice ensures that the adiabatic electronic states mix maximally and the diabatic electronic states cross at the transition state geometry, where the nonadiabatic coupling is a maximum. Moreover, the magnitude of the diabatic electronic coupling, W_{12}, is exactly half the splitting between the adiabatic electronic energies at this geometry. In the present paper, we extend this treatment to asymmetric systems, for which the nonadiabatic coupling is not necessarily a maximum at the transition state geometry. For the general case, we choose r_0 to be the hydrogen position at which the nonadiabatic coupling is maximum and set $\gamma(r_0) = -\pi/4$. This choice ensures that the diabatic states cross at $r_p = r_0$ and that the adiabatic states mix maximally at the hydrogen position corresponding to the largest nonadiabatic coupling.

II.B. Diabatization along Other One-Dimensional Reaction Coordinates. This approach may be extended to other one-dimensional reaction coordinates, such as a normal mode coordinate or an IRC. In this subsection, we discuss the generation of the diabatic electronic states along these types of alternative one-dimensional reaction coordinates, which typically are comprised of combinations of the motions of the transferring hydrogen and other heavy nuclei in the system. The objective is to calculate diabatic electronic states for which the first-order nonadiabatic coupling vanishes exactly along a general one-dimensional reaction coordinate. These diabatic electronic states will not be used to generate electron−proton vibronic states.

First, we discuss the generation of diabatic electronic states along a single normal mode coordinate, q, with corresponding effective mass μ. In this case, we can still utilize eqs 1−4 by replacing r_p with q and m_p with μ, where the adiabatic and diabatic electronic energies depend explicitly on q rather than r_p. In PCET reactions, the relevant normal mode describing the proton transfer reaction is expected to be dominated by proton motion, so typically $\mu \approx m_p$. The adiabatic-to-diabatic transformation given in eq 5 ensures that the component of the nonadiabatic coupling vector along the normal mode coordinate q vanishes. Since the normal mode coordinate is a linear combination of Cartesian displacements of all nuclei, the nonadiabatic coupling with respect to the normal mode coordinate can be calculated analytically as a linear combination of the nonadiabatic couplings with respect to the Cartesian coordinates of all nuclei.

An alternative one-dimensional reaction coordinate is the IRC, which is generated numerically by following the minimum energy path from a transition state to the corresponding reactant and product state minima. In this case, the theoretical formalism described above is no longer rigorous, but we are able to define the adiabatic-to-diabatic transformation given in eq 5 so that the component of the first-order nonadiabatic coupling vector along the IRC vanishes. Since the IRC is generally not a linear combination of Cartesian coordinates, the nonadiabatic coupling in eq 9 cannot be calculated analytically. Instead, the component of the nonadiabatic coupling vector along the IRC can be calculated numerically as the scalar product of the nonadiabatic coupling vector with respect to the Cartesian coordinates of all nuclei and the instantaneous displacement vector of these coordinates with respect to the IRC approximated at each point using central-point differentiation. The formal treatment of the IRC in terms of eqs 1−4 is not rigorously valid because the IRC is not associated with a specific mass and is not defined to have vanishing kinetic energy couplings with respect to other nuclear coordinates. As shown below, however, physically reasonable charge-localized diabatic electronic states for which the first-order nonadiabatic coupling vanishes along the IRC can be generated with this approach. Similarly, this approach may be used to generate these types of diabatic electronic states along any specified one-dimensional coordinate, such as the reaction path generated by a series of constrained optimizations, where the relative hydrogen position is constrained while all other nuclear coordinates are optimized.

II.C. Construction of Electron−Proton Vibronic States. The diabatic electronic energies and couplings may be used to construct the electron−proton vibronic states that form the basis of nonadiabatic PCET theories. In the case of one-dimensional hydrogen motion with fixed heavy nuclei $\mathbf{R}$, the proton vibrational states for diabatic electronic state i are obtained by solving

$$\left(-\frac{\hbar^2}{2m_p}\frac{\partial^2}{\partial r_p^2} + W_{ii}(r_p,\mathbf{R})\right)\varphi_\mu^{(i)}(r_p;\mathbf{R}) = \tilde{\varepsilon}_\mu^{(i)}(\mathbf{R})\,\varphi_\mu^{(i)}(r_p;\mathbf{R}) \tag{10}$$

where $\tilde{\varepsilon}_\mu^{(i)}(\mathbf{R})$ is the energy of the electron−proton vibronic state (i,μ). The diabatic electron−proton vibronic states $\{\zeta_{i\mu}(\mathbf{r}_e,r_p;\mathbf{R})\}$ are then defined as products of the diabatic electronic wave functions and associated proton vibrational wave functions:

$$\zeta_{i\mu}(\mathbf{r}_e,r_p;\mathbf{R}) = \xi_i(\mathbf{r}_e;r_p,\mathbf{R})\,\varphi_\mu^{(i)}(r_p;\mathbf{R}) \tag{11}$$

In the electronically nonadiabatic limit, the vibronic coupling between the reactant and product diabatic vibronic states $\zeta_{1\mu}$ and $\zeta_{2\nu}$ is[23,33,37]

$$V_{\mu\nu}^{(\mathrm{na})} = \langle\varphi_\mu^{(1)}|W_{12}|\varphi_\nu^{(2)}\rangle_p \tag{12}$$

which reduces to the familiar form of the diabatic electronic coupling multiplied by the Franck−Condon overlap between the reactant and product proton vibrational wave functions when the diabatic electronic coupling $W_{12}(r_p,\mathbf{R})$ is independent of r_p. In principle, a similar procedure could be applied to the diabatic electronic states generated along a normal mode coordinate when this normal mode is dominated by the hydrogen motion.

This treatment can be extended to construct three-dimensional electron−proton vibronic states that include the three-dimensional motion of the transferring hydrogen. In this case, the adiabatic and diabatic electronic states depend on the three-dimensional proton coordinate $\mathbf{r}_p = (r_p,s_p,t_p)$. The diabatic electronic states are constructed so that the component of the first-order nonadiabatic coupling vector along r_p, as given in eq 9, vanishes exactly for all points on a three-dimensional proton coordinate grid. Thus, the adiabatic-to-diabatic transformation can be expressed as

$$\vec{\xi}(\mathbf{r}_e;r_p,s_p,t_p,\mathbf{R}) = \mathbf{A}(r_p,s_p,t_p;\mathbf{R})\,\vec{\psi}(\mathbf{r}_e;r_p,s_p,t_p,\mathbf{R}) \tag{13}$$

but only the component of the first-order nonadiabatic coupling vector along r_p is used to determine $\mathbf{A}(r_p,s_p,t_p;\mathbf{R})$. In practice, the component of the first-order nonadiabatic coupling vector along r_p is calculated at each grid point (r_p,s_p,t_p). For each value of (s_p,t_p), r_0 is chosen to be the proton position along the r_p slice at which this nonadiabatic coupling is maximum, and $\gamma(r_p,s_p,t_p)$ is determined by calculating the line integral in eq 8 with $\gamma(r_0,s_p,t_p) = -\pi/4$. This procedure ensures that the first-order

nonadiabatic couplings with respect to r_p vanish exactly for all points on the three-dimensional proton coordinate grid.

The resulting three-dimensional diabatic potential energy matrix is given by $\mathbf{W} = \mathbf{AUA}^{-1}$, where $U_{ii} = \varepsilon_i(r_p,s_p,t_p,\mathbf{R})$ are the three-dimensional adiabatic potential energy surfaces and $W_{ii}(r_p,s_p,t_p,\mathbf{R})$ are the three-dimensional diabatic potential energy surfaces. For fixed heavy nuclei $\mathbf{R}$, the three-dimensional proton vibrational wave functions for diabatic electronic state i are calculated using the three-dimensional analog of eq 10 with potential energies $W_{ii}(r_p,s_p,t_p,\mathbf{R})$. These wave functions can then be combined with the associated diabatic electronic states, as in eq 11, to form three-dimensional electron−proton vibronic states.

We also explored an alternative more approximate formulation in which the adiabatic-to-diabatic transformation matrix $\mathbf{A}$ defined in eq 7 depends explicitly on only the one-dimensional proton coordinate r_p [i.e., $\gamma(r_p)$ is independent of the orthogonal coordinates (s_p,t_p)]. The advantage of this alternative formulation is that it only requires the calculation of the first-order nonadiabatic couplings along the one-dimensional r_p axis corresponding to $s_p = t_p = 0$ (i.e., the proton donor−acceptor axis in the applications discussed below). As a result, however, the first-order nonadiabatic couplings with respect to r_p vanish only along the one-dimensional r_p axis and do not vanish exactly for the other points on the three-dimensional proton coordinate grid.

II.D. Generalized Mulliken−Hush and Boys Localization. The GMH method[13,14] generates diabatic electronic states using the adiabatic electronic state dipole moments. These dipole moments are defined in terms of the adiabatic electronic states as $\vec{\mu}_{ij} = \langle\psi_i|\hat{\mu}|\psi_j\rangle$ for $i \in \{1,2\}$, where $\hat{\mu}$ is the dipole moment operator. The GMH method utilizes an adiabatic-to-diabatic transformation matrix analogous to eq 7:

$$\mathbf{A}^{\mathrm{GMH}}(r_p;\mathbf{R}) = \begin{pmatrix} \cos\theta & -\sin\theta \\ \sin\theta & \cos\theta \end{pmatrix} \tag{14}$$

In this case, $\theta(r_p;\mathbf{R})$ depends on the adiabatic electronic state dipole moments:

$$\tan(2\theta) = \frac{2\vec{\mu}_{12}\cdot\vec{v}}{|\vec{v}|^2} \tag{15}$$

where $\vec{v} = \vec{\mu}_{11} - \vec{\mu}_{22}$ and typically $\vec{\mu}_{12}$ and $\vec{v}$ are assumed to be parallel. Analogous to eq 5, the diabatic electronic states are determined by

$$\vec{\xi}^{\mathrm{GMH}}(\mathbf{r}_e;r_p,\mathbf{R}) = \mathbf{A}^{\mathrm{GMH}}(r_p;\mathbf{R})\,\vec{\psi}(\mathbf{r}_e;r_p,\mathbf{R}) \tag{16}$$

The GMH expression for the mixing angle in eq 15 is derived by defining $\mathbf{A}^{\mathrm{GMH}}$ as the transformation that diagonalizes the adiabatic dipole moment matrix, ensuring that the diabatic transition dipole moment is exactly zero, i.e., $\langle\xi_1^{\mathrm{GMH}}|\hat{\mu}|\xi_2^{\mathrm{GMH}}\rangle = 0$.

Subotnik et al. demonstrated that the GMH procedure can be extended to arbitrary geometries and multiple charge centers using Boys localization.[26] The more general expression for θ in eq 14 is given as[26]

$$\cos(4\theta) = \frac{-F}{\sqrt{F^2+G^2}} \tag{17}$$

where

$$F = |\vec{\mu}_{12}|^2 - \frac{|\vec{\mu}_{11}-\vec{\mu}_{22}|^2}{4} \tag{18}$$

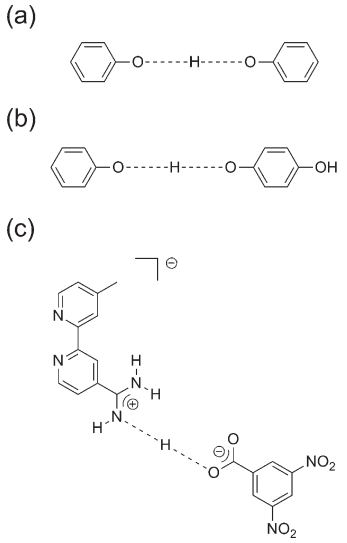

Figure 1. Three model systems studied: (a) phenoxyl−phenol, (b) phenoxyl−quinol, and (c) amidinium−carboxylate systems. The phenoxyl−phenol and phenoxyl−quinol systems are neutral, while the amidinium−carboxylate system has an overall charge of −1.

and

$$G = \vec{\mu}_{12}\cdot(\vec{\mu}_{11}-\vec{\mu}_{22}) \tag{19}$$

Invoking the assumption that $\vec{\mu}_{12}$ and $\vec{v}$ are parallel in eqs 17−19 leads to an expression for θ that coincides with the GMH expression given in eq 15.

III. COMPUTATIONAL METHODS

We used three systems to test the theoretical methods developed above. We studied the self-exchange reaction between the phenoxyl radical and the phenol molecule depicted in Figure 1a. We also studied the analogous reaction between the phenoxyl radical and the 1,4-benzenediol (quinol) molecule depicted in Figure 1b. The transition state geometries for these systems were calculated using density functional theory (DFT) with the B3LYP functional[38,39] and the 6-31G* basis set.[40] We also examined the amidinium−carboxylate system depicted in Figure 1c. We followed a similar but not identical geometry optimization procedure as that described in ref 36. In our procedure, we optimized the complete neutral amidinium−carboxylate system at the RHF/6-31G** level of theory, maintaining planarity of the system except for the three methyl group hydrogen atoms. The adiabatic and diabatic electronic states were calculated for the PCET reaction in the negatively charged complex with the lower proton in Figure 1c being transferred. The geometry optimizations were performed using Gaussian 09.[41]

We generated the adiabatic and diabatic electronic energy curves for the phenoxyl−phenol and phenoxyl−quinol systems along three different types of one-dimensional reaction coordinates. In the first scheme,[23] all nuclei except the transferring hydrogen atom were fixed at the transition state geometry, and the hydrogen was displaced along a one-dimensional grid spanning the hydrogen donor−acceptor axis. In the second scheme, all nuclei were displaced according to the normal mode coordinate corresponding to the negative frequency identified at the transition state geometry. In the third scheme, all nuclei were displaced according to the IRC calculated using the same level of

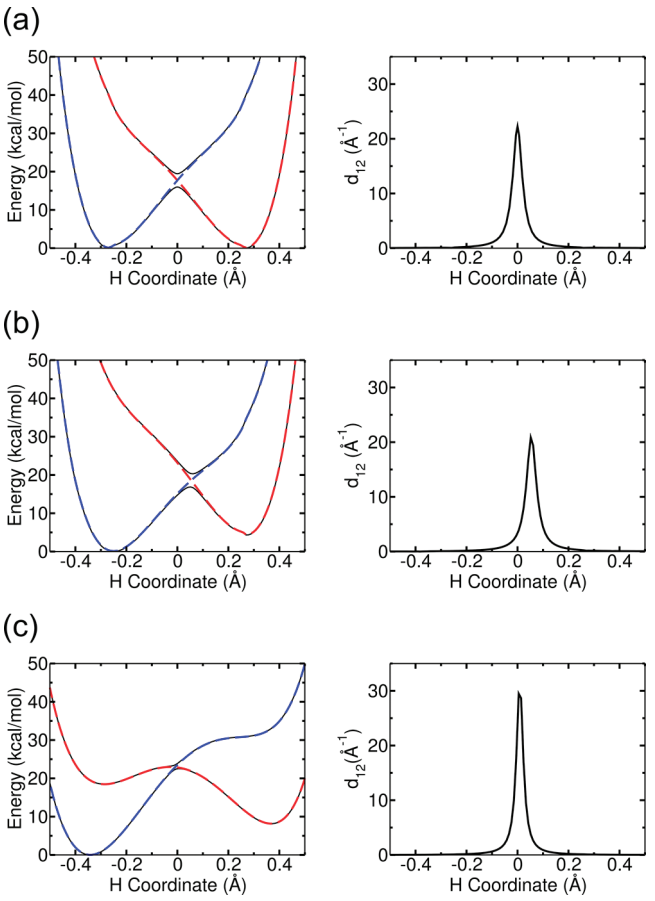

Figure 2. Adiabatic and diabatic electronic state properties as functions of the transferring hydrogen coordinate for the (a) phenoxyl−phenol, (b) phenoxyl−quinol, and (c) amidinium−carboxylate systems. The left panels depict the electronically adiabatic and diabatic potential energy curves. The solid black curves are the ground and first excited adiabatic state energies $\varepsilon_1(r_p,\mathbf{R})$ and $\varepsilon_2(r_p,\mathbf{R})$, respectively, calculated with the CASSCF method, and the dashed blue and red curves are the diabatic electronic energies $W_{11}(r_p,\mathbf{R})$ and $W_{22}(r_p,\mathbf{R})$, respectively, where the choice of $\gamma(r_0)$ is described in the text. The right panels depict the component of the first-order nonadiabatic coupling vector along the hydrogen donor−acceptor axis, as defined in eq 9.

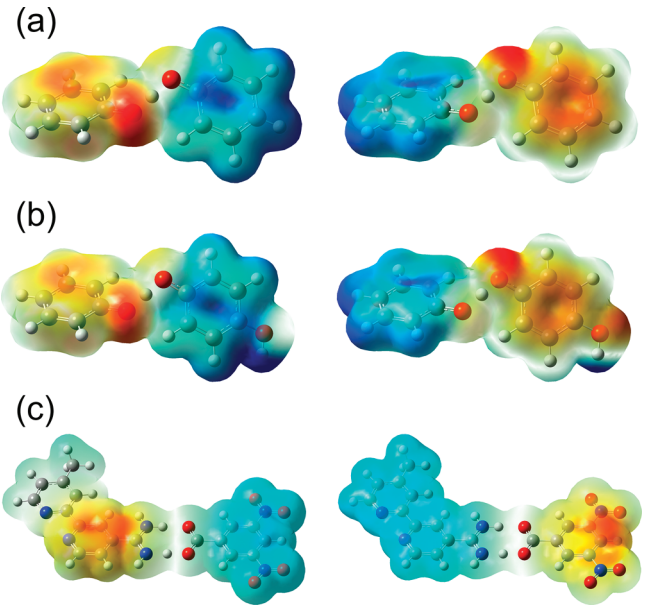

Figure 3. Electrostatic potential maps for the diabatic electronic states ξ_1 (left) and ξ_2 (right) corresponding to a density isosurface value of 0.005 for the (a) phenoxyl−phenol, (b) phenoxyl−quinol, and (c) amidinium−carboxylate systems at $r_p = r_0$. Negatively and positively charged regions are indicated by red and blue coloring, respectively. The maps for the amidinium−carboxylate system are difference electrostatic potential maps with respect to the neutral complex, as described in the text.

theory as described above. For all three schemes, we generated 128 geometries along the reaction coordinate. We used only the first scheme, which is based on the one-dimensional hydrogen coordinate along the hydrogen donor−acceptor axis with all other nuclei fixed, to study the amidinium−carboxylate system.

For each system, we calculated the two lowest-energy electronically adiabatic potential energy curves using the complete active space self-consistent field (CASSCF) method. The CASSCF calculations of the phenoxyl−phenol and phenoxyl−quinol systems were performed with the 6-31G* basis set and an active space of three electrons in six orbitals, state-averaging over the ground and first excited electronic states with equal weighting. The CASSCF calculations of the amidinium−carboxylate system were performed with the 6-31G** basis set and an active space of one electron in three orbitals, state-averaging over the lowest three electronic states with equal weighting.[36] We also calculated the two lowest-energy electronically adiabatic potential energy surfaces in three dimensions by displacing the hydrogen on a three-dimensional grid consisting of 16 points in each direction, with all other nuclei remaining fixed. In addition, we obtained the nonadiabatic coupling vectors with respect to the Cartesian coordinates of all nuclei directly from the CASSCF calculations. The GAMESS electronic structure package[42] was used to perform all CASSCF calculations. Note that these calculations were performed at a relatively low level of theory because our goal is to examine only the qualitative features of the various theoretical approaches.

We constructed the electron−proton vibronic states for one-dimensional or three-dimensional hydrogen motion with all other nuclei fixed. This procedure utilized the diabatic electronic states generated with the first scheme described above. We calculated one-dimensional proton vibrational wave functions describing the proton motion on the diabatic electronic energy surfaces by solving the one-dimensional Schrödinger equation given in eq 10. These calculations were performed with the Fourier grid Hamiltonian (FGH) method[43] using 128 grid points along the hydrogen donor−acceptor axis. We calculated three-dimensional proton vibrational wave functions using the three-dimensional analog of eq 10. These calculations were performed with the FGH−FCI (full configuration interaction) method[44] on the three-dimensional diabatic electronic energy surfaces mentioned above.

To examine the charge transfer properties, we calculated the dipole moments, atomic charges, and electrostatic potential maps as functions of the one-dimensional reaction coordinate for the adiabatic and diabatic electronic states. The properties of the adiabatic electronic states were calculated directly from the CASSCF wave functions with GAMESS. For the diabatic electronic states, we modified a local version of GAMESS to calculate these properties for the appropriate linear combination of configuration interaction states following the transformation

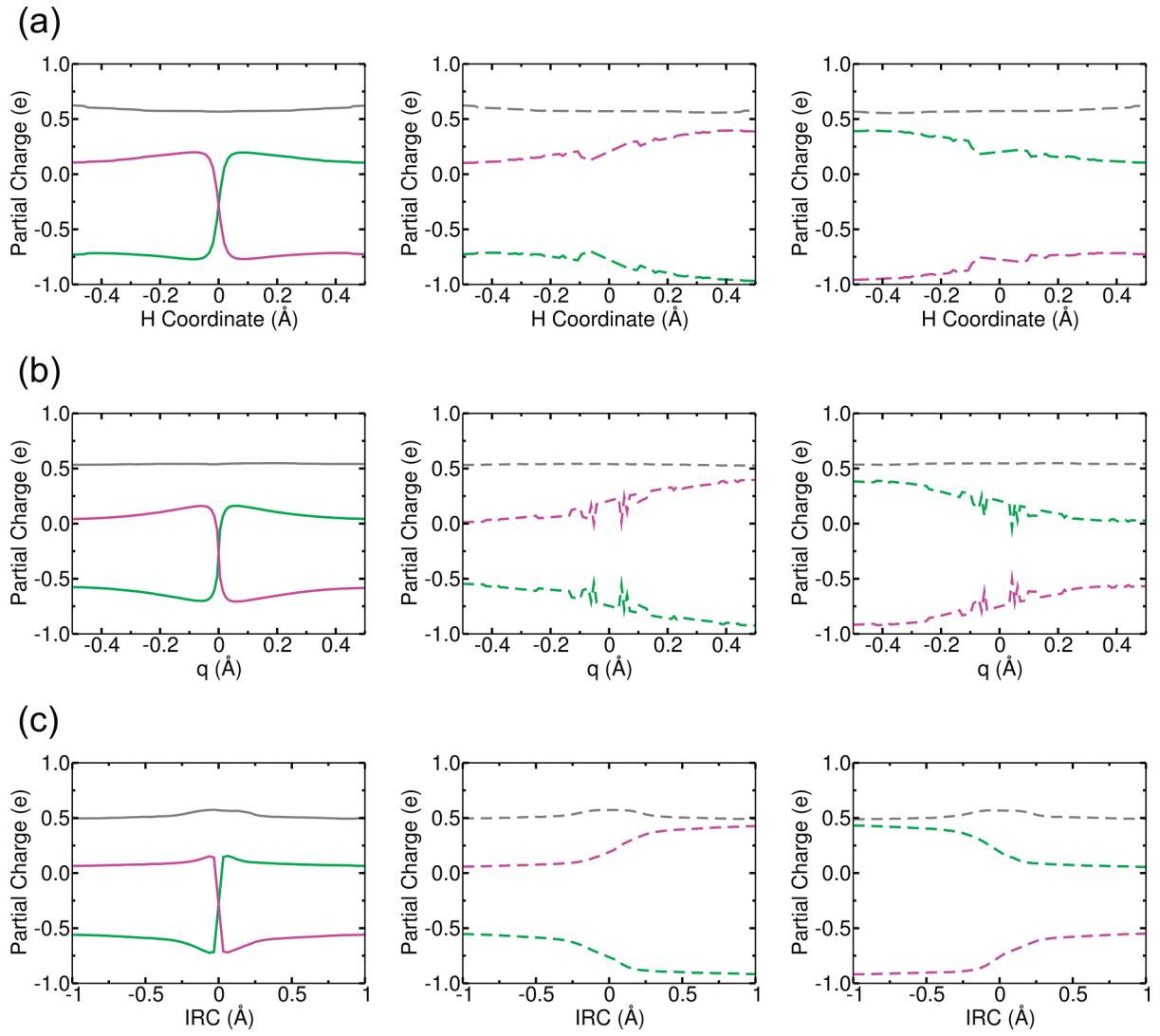

Figure 4. Partial charges determined from electrostatic potential-derived atomic charges for the ground adiabatic electronic state (left), the diabatic electronic state ξ_1 (center), and the diabatic electronic state ξ_2 (right) for the phenoxyl−phenol system calculated using various reaction coordinates: (a) the one-dimensional hydrogen coordinate, (b) the normal mode coordinate corresponding to the negative frequency at the transition state geometry, and (c) the IRC. Partial charges are shown for the donor molecule (green), acceptor molecule (purple), and transferring hydrogen (gray). Calculated values of the partial charges for the diabatic electronic states around $r_p = r_0$ are omitted due to numerical noise in this region.

given in eq 5. The atomic charges were obtained by fitting to the electrostatic potential calculated at points on the Connolly surface[45] under the constraint of reproducing the total charge and dipole moment of the electronic state under consideration.[46]

IV. RESULTS

IV.A. Generating Diabatic Electronic States. In this study, we applied the adiabatic-to-diabatic transformation methodology[23] to the more general case of asymmetric PCET reactions, as depicted in Figures 1b and c. For each system, we calculated the ground and first excited adiabatic electronic states and the nonadiabatic couplings along the one-dimensional hydrogen coordinate using the CASSCF method. As shown in Figures 2 and 3, the adiabatic-to-diabatic transformation successfully generated physically meaningful charge-localized diabatic electronic states for all three systems. In all cases, the diabatic electronic energies, $W_{11}(r_p,\mathbf{R})$ and $W_{22}(r_p,\mathbf{R})$ (dashed blue and red lines, respectively, in the left panels of Figure 2) are virtually identical to the adiabatic electronic energies, $\varepsilon_1(r_p,\mathbf{R})$ and $\varepsilon_2(r_p,\mathbf{R})$ (solid black lines in the left panels of Figure 2), over all hydrogen positions except near $r_p = r_0$, where they smoothly cross. All three systems exhibit a relatively localized region of strong nonadiabatic coupling, as shown in the right panels of Figure 2.

Figures 2b and c illustrate that the phenoxyl−quinol and the amidinium−carboxylate systems possess significantly asymmetric adiabatic electronic energies and nonadiabatic couplings. In particular, these systems exhibit an energy bias between geometries corresponding to the hydrogen localized on the donor molecule and the hydrogen localized on the acceptor molecule. Furthermore, the maximum of the nonadiabatic coupling along the donor−acceptor axis is shifted from the donor−acceptor midpoint, which is chosen to be at $r_p = 0$ for all systems. This shift is more noticeable for the phenoxyl−quinol system. As mentioned above, we chose r_0 to be the hydrogen position at which the nonadiabatic coupling is maximum and set

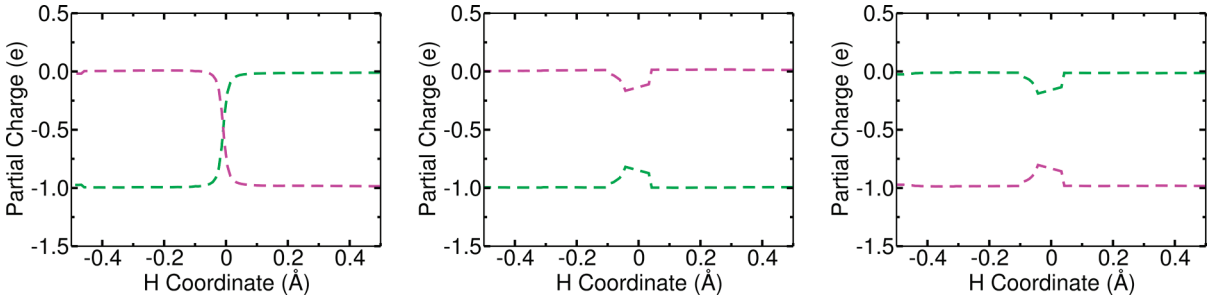

Figure 5. Partial charges determined from electrostatic potential-derived atomic charges for the ground adiabatic electronic state (left), the diabatic electronic state ξ_1 (center), and the diabatic electronic state ξ_2 (right) as functions of the transferring hydrogen coordinate for the amidinium−carboxylate system. Partial charges are shown for the donor molecule (green) and the acceptor molecule (purple). The partial charges on the donor and acceptor molecules are obtained after subtracting the corresponding partial charges of the neutral complex, as described in the text. Due to this subtraction, the transferring hydrogen has no significant charge, although it has a nearly constant charge of ∼0.58*e* for the adiabatic and diabatic electronic states prior to this subtraction. Calculated values of the partial charges for the diabatic electronic states around $r_p = r_0$ are omitted due to numerical noise in this region.

$\gamma(r_0) = -\pi/4$ in eq 8 to ensure that the diabatic states cross at $r_p = r_0$ and that the adiabatic states mix maximally at the hydrogen position corresponding to the largest nonadiabatic coupling. Figure 2 illustrates that the resulting diabatic potential energies correspond to the transferring hydrogen localized on the donor molecule in $W_{11}(r_p,\mathbf{R})$ and the acceptor molecule in $W_{22}(r_p,\mathbf{R})$.

The electrostatic potential maps for diabatic states ξ_1 and ξ_2 at $r_p = r_0$ are depicted in Figure 3. These electrostatic potential maps illustrate that the diabatic electronic states possess localized electronic charge distributions. The corresponding electrostatic potential maps for other positions of the transferring hydrogen are provided in the Supporting Information (Figures S1−S3) and indicate that these electronic charge distributions are relatively invariant along the transferring hydrogen coordinate. The amidinium−carboxylate system is negatively charged, and the electrostatic potential maps are strongly influenced by the charge separation at the hydrogen-bonding interface (see Figure 1c). To clarify the charge localization of the diabatic electronic states with respect to the transferring electron, the electrostatic potential of the neutral amidinium−carboxylate complex was subtracted from that of the negatively charged complex. The resulting difference electrostatic potential maps plotted in Figure 3 clearly demonstrate charge localization with respect to the transferring electron.

Figures 4a and 5 depict the partial charges on the donor (green) and acceptor (purple) molecules for the adiabatic (left panels) and diabatic (center and right panels) electronic states for the phenoxyl−phenol and amidinium−carboxylate systems, respectively. The corresponding figure for the phenoxyl−quinol system is provided in Supporting Information Figure S4. For all three systems, the partial charges on the donor and acceptor molecules change significantly along the reaction coordinate for the adiabatic electronic states but remain relatively constant for the diabatic electronic states. Analogous to the procedure used for the electrostatic potential maps, the partial charges for the donor and acceptor molecules in the amidinium−carboxylate system are determined by subtracting the corresponding partial charges calculated for the neutral complex. The partial charges prior to this subtraction are provided in Supporting Information Figure S5. As shown in Figure 5, the resulting plots clearly demonstrate the charge localization of the diabatic electronic states with respect to the transferring electron. Thus, this adiabatic-to-diabatic transformation method provides physically

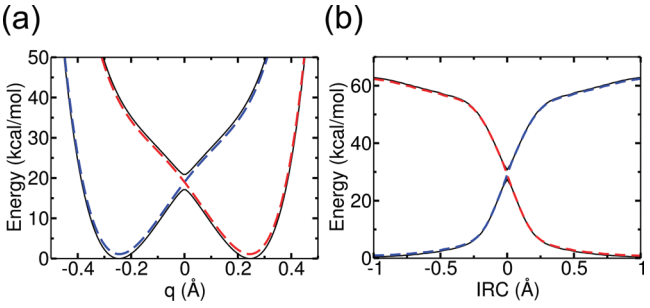

Figure 6. Electronically adiabatic and diabatic potential energy curves for the phenoxyl−phenol system as functions of (a) the normal mode coordinate corresponding to the negative frequency at the transition state geometry and (b) the IRC. The solid black curves are the ground and first excited adiabatic state energies, and the dashed blue and red curves are the diabatic electronic energies.

meaningful diabatic electronic states with localized electronic charge distributions that are relatively invariant along the transferring hydrogen coordinate for both symmetric and asymmetric systems.

We also calculated the diabatic electronic states along two other types of reaction coordinates: the normal mode coordinate associated with the negative frequency at the transition state and the IRC. We present the results for the phenoxyl−phenol system, although the corresponding results for the asymmetric phenoxyl−quinol system are qualitatively similar to those for the symmetric case and are included in Supporting Information Figure S6. Figure 6 depicts the adiabatic and diabatic electronic energies calculated along the normal mode coordinate and the IRC. We observed that the normal mode coordinate is dominated by the motion of the transferring hydrogen (i.e., the mass associated with this normal mode was ∼1.12 amu). For this reason, the adiabatic and diabatic electronic energies calculated along the normal mode coordinate (Figure 6a) are very similar to those calculated along the one-dimensional hydrogen coordinate (Figure 2a). The adiabatic and diabatic electronic energies calculated along the IRC (Figure 6b) are qualitatively similar to those calculated along the one-dimensional hydrogen coordinate near the transition state but plateau in the outer regions after the IRC reaches the minimum energy geometries.

Figure 4 compares the partial charges on the donor (green) and acceptor (purple) molecules for the adiabatic (left panels)

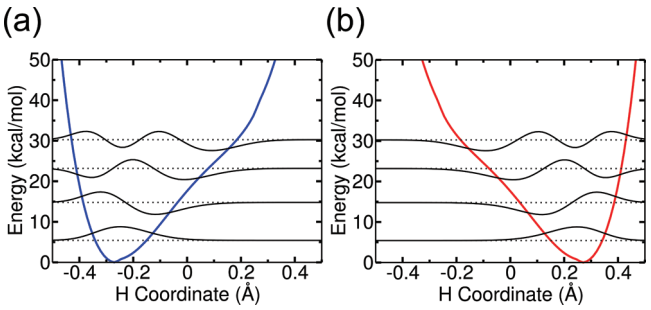

Figure 7. Four lowest-energy one-dimensional proton vibrational wave functions (black solid lines) calculated using eq 10 for the diabatic electronic potential (a) W_{11} and (b) W_{22} for the phenoxyl−phenol system.

and diabatic (center and right panels) electronic states for the three different types of reaction coordinates. The partial charges for the one-dimensional hydrogen coordinate and the normal mode coordinate, as depicted in Figures 4a and b, respectively, are very similar. The results for the IRC are also qualitatively similar. In all cases, the partial charges on the donor and acceptor molecules remain relatively constant along the reaction coordinate for the diabatic electronic states. Thus, the adiabatic-to-diabatic transformation method provides charge-localized diabatic electronic states with electronic charge distributions that are relatively invariant along all three types of reaction coordinates.

IV.B. Constructing Electron−Proton Vibronic States. We constructed the electron−proton vibronic states corresponding to the diabatic electronic states generated along the one-dimensional hydrogen coordinate with all other nuclei fixed. For this purpose, we calculated the one-dimensional proton vibrational wave functions by solving eq 10 with each of the diabatic electronic energies, $W_{11}(r_p,\mathbf{R})$ and $W_{22}(r_p,\mathbf{R})$, shown in Figure 2a. The four lowest-energy proton vibrational wave functions corresponding to each diabatic electronic state for the phenoxyl−phenol system are depicted in Figure 7. These proton vibrational wave functions can be combined with the diabatic electronic wave functions, ξ_1 and ξ_2, by forming products as in eq 11 to obtain the electron−proton vibronic states that comprise the basis of nonadiabatic PCET rate theories. In particular, these vibronic states can be used directly to calculate vibronic couplings, which are essential for the calculation of experimentally accessible quantities such as rate constants and kinetic isotope effects. The vibronic couplings calculated using eq 12 will be discussed below.

We also calculated three-dimensional diabatic potential energy surfaces and the associated proton vibrational wave functions. For this purpose, we applied the adiabatic-to-diabatic transformation given by eq 13, where the transformation matrix depends on the three-dimensional proton coordinate, and the component of the nonadiabatic coupling vector along r_p vanishes exactly for all points on the three-dimensional proton coordinate grid. The resulting partial charges for the phenoxyl−phenol system are given in Table 1. For comparison, we also applied the more approximate adiabatic-to-diabatic transformation, where the transformation matrix depends explicitly on only the one-dimensional proton coordinate r_p, and the component of the nonadiabatic coupling vector along r_p vanishes exactly only for points on the one-dimensional proton donor−acceptor axis. The resulting partial charges are given in Table S1 of the

Table 1. Average Electrostatic Potential-Derived Partial Charges Calculated for the Three-Dimensional Ground Adiabatic and Diabatic Electronic States Reported with Standard Deviations for the Phenoxyl−Phenol System[a]

electronic state	donor charge	acceptor charge	H charge
ψ_1	-0.2 ± 0.4	-0.2 ± 0.4	0.5 ± 0.1
ξ_1	-0.7 ± 0.2	0.3 ± 0.2	0.4 ± 0.1
ξ_2	0.3 ± 0.2	-0.7 ± 0.2	0.4 ± 0.1

[a] The tabulated results were computed by averaging over the 16^3 hydrogen positions on the three-dimensional grid, where points around $r_p = r_0$ were omitted due to numerical noise in this region. All charges are given in units of e. Deviation of the total charge from zero is due to numerical noise and round-off error. The diabatic electronic states were calculated using eq 13, ensuring that the component of the first-order nonadiabatic coupling vector along r_p vanishes exactly for all points on the three-dimensional grid.

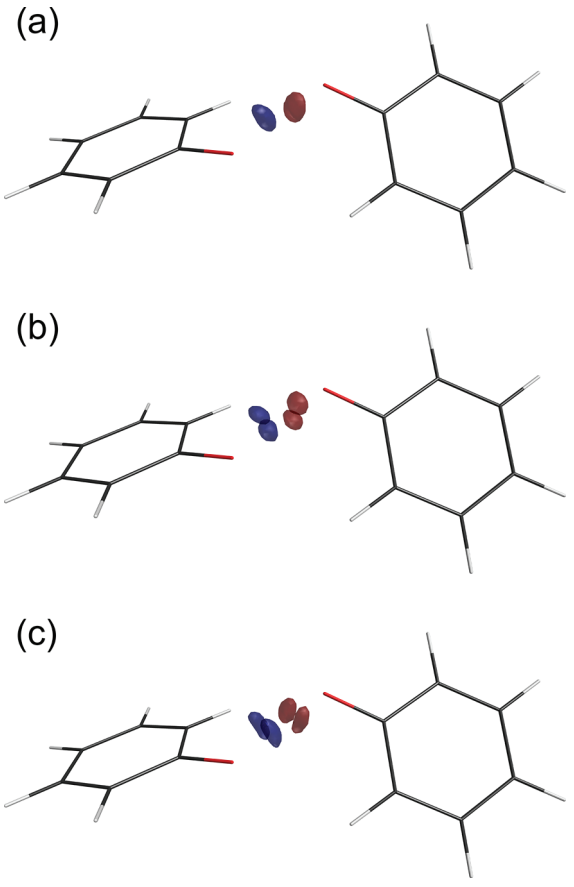

Figure 8. Three lowest-energy three-dimensional proton vibrational wave functions corresponding to a density isosurface value of 0.002 for the three-dimensional diabatic potential energy surfaces W_{11} (blue wave functions) and W_{22} (red wave functions) for the phenoxyl−phenol system. The top figure corresponds to the lowest-energy proton vibrational state.

Supporting Information and are qualitatively similar to those provided in Table 1. This more approximate approach may be useful for larger systems because the computational expense is significantly lower.

Table 1 demonstrates that the three-dimensional diabatic electronic states generated for the phenoxyl−phenol system

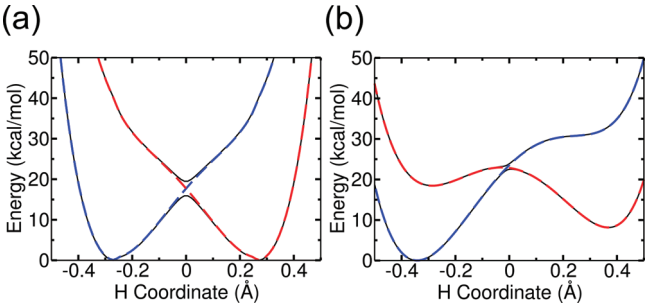

Figure 9. Electronically adiabatic and diabatic potential energy curves for (a) the phenoxyl−phenol system and (b) the amidinium−carboxylate system as functions of the hydrogen coordinate calculated using the GMH method. The solid black curves are the ground and first excited adiabatic state energies, and the dashed blue and red curves are the diabatic electronic energies.

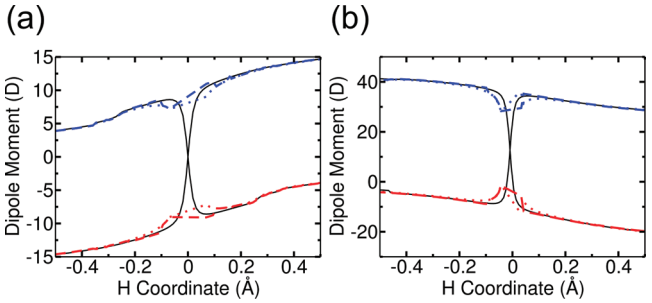

Figure 10. Component of the dipole moment vector along the hydrogen donor−acceptor axis for the ground and first excited adiabatic electronic states (solid black curves) and the diabatic electronic states ξ_1 (blue) and ξ_2 (red) for the (a) phenoxyl−phenol system and (b) amidinium−carboxylate system calculated using the GMH method (dotted) and the adiabatic-to-diabatic transformation method described in section II.A (dashed). A positive (negative) dipole moment indicates a dipole moment vector pointing toward the acceptor (donor). The origin was chosen to be $r_p = 0$ for the amidinium−carboxylate system.

are charge-localized. This table provides the partial charges on the donor and acceptor molecules, as well as the transferring hydrogen, averaged over all hydrogen positions on the three-dimensional grid. As expected, the average donor and acceptor partial charges for the three-dimensional adiabatic electronic ground state are identical, and the standard deviations reflect the changes in the donor and acceptor partial charges that are consistent with those observed along the one-dimensional hydrogen coordinate depicted in the left panel of Figure 4a. In contrast, the three-dimensional diabatic electronic states exhibit charge-localization: the average charge on the donor is negative (positive) and the average charge on the acceptor is positive (negative) when averaged over all hydrogen positions for the diabatic electronic state ξ_1 (ξ_2). These results are also consistent with the partial charges along the one-dimensional hydrogen coordinate depicted in the center and right panels of Figure 4a. The standard deviations are slightly larger than would be predicted from Figure 4 because of numerical fluctuations near the transition state geometry.

We used these three-dimensional diabatic potential energy surfaces to calculate the associated three-dimensional proton vibrational wave functions with the FGH−FCI method. The three lowest-energy proton vibrational wave functions corresponding to each diabatic electronic state for the phenoxyl−phenol system are depicted in Figure 8. The proton vibrational wave functions associated with the diabatic state ξ_1 (blue) are localized near the donor molecule, while the proton vibrational wave functions associated with the diabatic state ξ_2 (red) are localized near the acceptor molecule. These results are consistent with the corresponding one-dimensional proton vibrational wave functions along the donor−acceptor axis depicted in Figure 7. The three-dimensional proton vibrational wave functions can be combined with the corresponding diabatic electronic wave functions to generate three-dimensional diabatic electron−proton vibronic states, which can be used to calculate vibronic couplings, rate constants, and kinetic isotope effects of nonadiabatic PCET reactions.

IV.C. Comparison to Generalized Mulliken−Hush and Boys Localization. We also used the GMH procedure to generate charge-localized diabatic electronic states for the phenoxyl−phenol and amidinium−carboxylate systems. The adiabatic state dipole moments were calculated directly from the CASSCF wave functions. The GMH diabatization produced qualitatively similar diabatic electronic states to those generated using the diabatization procedure described in section II.A. In particular, the diabatic electronic energies depicted in Figures 9a and b are virtually identical to those depicted in Figures 2a and c, respectively. Moreover, Figure 10 illustrates that the calculated diabatic state dipole moments are very similar for the two diabatization schemes. Thus, these two fundamentally different diabatization approaches lead to nearly identical diabatic electronic states. In principle, proton vibrational wave functions could be calculated using the GMH diabatic potential energies and combined with the associated diabatic electronic wave functions to form electron−proton vibronic states, as described above.

In addition, we used the Boys localization scheme to generate diabatic electronic states for the phenoxyl−phenol and amidinium−carboxylate systems. The Boys localization method produced results that are virtually identical to the GMH results presented in Figures 9 and 10. This high level of agreement is attributed to the observation that the vectors $\vec{\mu}_{12}$ and $\vec{\mu}_{11} - \vec{\mu}_{22}$ were essentially parallel for all positions of the transferring hydrogen. In particular, for all r_p such that $|r_p| \leq 0.5$ Å, $|(\vec{\mu}_{12})^u \cdot (\vec{\mu}_{11} - \vec{\mu}_{22})^u| \geq 0.998$ for the phenoxyl−phenol system and $|(\vec{\mu}_{12})^u \cdot (\vec{\mu}_{11} - \vec{\mu}_{22})^u| \geq 0.992$ for the amidinium−carboxylate system, where the u superscript indicates the unit vector in the specified direction. Thus, the GMH and Boys localization methods are in excellent agreement with the diabatization method presented in section II.A for the systems studied.

Finally, we calculated the electronic coupling at the geometry corresponding to the crossing point of the diabatic potential energy curves for the three systems studied. This quantity, $W_{12}(r_0;\mathbf{R})$, is calculated as the off-diagonal element of the diabatic potential energy matrix obtained from transforming the adiabatic potential energy matrix at $r_p = r_0$. Table 2 demonstrates that the electronic couplings calculated using the GMH and Boys localization methods agree very well with those obtained from the diabatization procedure described in section II.A. Table 2 also provides the vibronic couplings between the ground electron−proton vibronic states calculated using eq 12 for $\mu = \nu = 0$. These vibronic couplings are significantly smaller than the corresponding electronic couplings because of the relatively small overlap

Table 2. Electronic and Vibronic Couplings Calculated at the Geometry Corresponding to the Crossing Point of the Diabatic Potential Energy Curves Using the Various Diabatization Methods[a]

system	V_{el}^{GMH}	V_{el}^{Boys}	V_{el}	$V_{00}^{(na)}$
phenol	606	606	606	7.2
quinol	610	610	611	8.7
amidinium−carboxylate	205	205	206	0.44

[a] The electronic couplings were calculated as the off-diagonal element of the diabatic potential energy matrix at $r_p = r_0$ using the GMH method, the Boys localization method, and the method described in Section IIA for V_{el}^{GMH}, V_{el}^{Boys}, and V_{el}, respectively. The vibronic couplings $V_{00}^{(na)}$ between ground electron−proton vibronic states were calculated with V_{el} using eq 12 for $\mu = \nu = 0$. All couplings are given in units of cm^{-1}.

between the reactant and product ground state proton vibrational wave functions.

V. CONCLUSIONS

In this paper, we developed a scheme to generate charge-localized diabatic electronic states for a wide range of PCET systems. These charge-localized diabatic electronic states are obtained from standard electronic structure calculations using an adiabatic-to-diabatic transformation designed to ensure that the first-order nonadiabatic couplings with respect to a specified one-dimensional reaction coordinate vanish exactly. We applied this protocol to both symmetric and asymmetric PCET systems with several different one-dimensional reaction coordinates, including the hydrogen transfer coordinate, a normal mode coordinate, and the IRC. This approach was also extended to construct three-dimensional charge-localized diabatic electronic surfaces corresponding to the three-dimensional motion of the transferring hydrogen. We demonstrated that this methodology leads to physically meaningful charge-localized diabatic electronic states with relatively invariant charge distributions along the reaction coordinate. These diabatic electronic states are in excellent agreement with those obtained from the GMH and Boys localization methods.

In addition, we combined these diabatic electronic states with the associated proton vibrational wave functions to generate electron−proton vibronic states that describe one- or three-dimensional hydrogen motion. These electron−proton vibronic states can be used to calculate the vibronic couplings that enter the nonadiabatic rate constant expressions for PCET reactions. Within the golden rule formalism, each term in the nonadiabatic PCET rate constant expression is proportional to the square of the electron−proton vibronic coupling for a pair of reactant and product vibronic states. As a result, the vibronic couplings strongly impact the rate constants and kinetic isotope effects of PCET reactions. Thus, the construction of charge-localized electron−proton vibronic states is essential for the calculation of experimentally measurable quantities such as the rate constants and kinetic isotope effects of PCET reactions.

■ ASSOCIATED CONTENT

Supporting Information. Electrostatic potential maps corresponding to the diabatic electronic states at different positions of the transferring hydrogen for all three systems studied; partial charges of the donor molecule, acceptor molecule, and transferring hydrogen for the adiabatic and diabatic electronic states of the phenoxyl−quinol system and of the amidinium−carboxylate system prior to subtraction of the corresponding charges for the neutral system; adiabatic and diabatic electronic state energies along a normal mode coordinate and the IRC for the phenoxyl−quinol system; average partial charges of the donor molecule, acceptor molecule, and transferring hydrogen for the three-dimensional adiabatic and diabatic electronic states of the phenoxyl−phenol system using the alternative more approximate approach; coordinates of the phenoxyl−quinol and amidinium−carboxylate systems. This material is available free of charge via the Internet at http://pubs.acs.org.

■ AUTHOR INFORMATION

Corresponding Author
*E-mail: shs@chem.psu.edu.

■ ACKNOWLEDGMENT

We thank Alexander Soudackov and Anirban Hazra for helpful discussions and advice. We gratefully acknowledge funding from NSF grants CHE-07-49646 and CHE-10- 57875. A.S. thanks the Natural Sciences and Engineering Research Council of Canada for a PGS scholarship.

■ REFERENCES

(1) Cukier, R. I.; Nocera, D. G. *Annu. Rev. Phys. Chem.* **1998**, *49*, 337–369.
(2) Hammes-Schiffer, S.; Soudackov, A. V. *J. Phys. Chem. B* **2008**, *112*, 14108–14123.
(3) Hammes-Schiffer, S.; Stuchebrukhov, A. A. *Chem. Rev.* **2010**, *110*, 6939–6960.
(4) Huynh, M. H. V.; Meyer, T. J. *Chem. Rev.* **2007**, *107*, 5004–5064.
(5) Mayer, J. M. *Annu. Rev. Phys. Chem.* **2004**, *55*, 363–390.
(6) Hammes-Schiffer, S. *Acc. Chem. Res.* **2001**, *34*, 273–281.
(7) Soudackov, A.; Hammes-Schiffer, S. *J. Chem. Phys.* **2000**, *113*, 2385–2396.
(8) Soudackov, A.; Hatcher, E.; Hammes-Schiffer, S. *J. Chem. Phys.* **2005**, *122*, 014505.
(9) Atchity, G. J.; Ruedenberg, K. *Theor. Chem. Acc.* **1997**, *97*, 47–58.
(10) Baer, M. *Chem. Phys. Lett.* **1975**, *35*, 112–118.
(11) Baer, M. *Mol. Phys.* **1980**, *40*, 1011–1013.
(12) Baer, M. *Phys. Rep.-Rev. Sec. Phys. Lett.* **2002**, *358*, 75–142.
(13) Cave, R. J.; Newton, M. D. *Chem. Phys. Lett.* **1996**, *249*, 15–19.
(14) Cave, R. J.; Newton, M. D. *J. Chem. Phys.* **1997**, *106*, 9213–9226.
(15) Cembran, A.; Song, L. C.; Mo, Y. R.; Gao, J. L. *J. Chem. Theory Comput.* **2009**, *5*, 2702–2716.
(16) Nakamura, H.; Truhlar, D. G. *J. Chem. Phys.* **2001**, *115*, 10353–10372.
(17) Nakamura, H.; Truhlar, D. G. *J. Chem. Phys.* **2002**, *117*, 5576–5593.
(18) Newton, M. D. *Chem. Rev.* **1991**, *91*, 767–792.
(19) Pacher, T.; Cederbaum, L. S.; Koppel, H. *J. Chem. Phys.* **1988**, *89*, 7367–7381.
(20) Pacher, T.; Cederbaum, L. S.; Koppel, H. *Adv. Chem. Phys.* **1993**, *84*, 293.
(21) Papas, B. N.; Schuurman, M. S.; Yarkony, D. R. *J. Chem. Phys.* **2008**, *129*, 124104.
(22) Ruedenberg, K.; Atchity, G. J. *J. Chem. Phys.* **1993**, *99*, 3799–3803.
(23) Sirjoosingh, A.; Hammes-Schiffer, S. *J. Phys. Chem. A* **2011**, *115*, 2367–2377.
(24) Song, L. C.; Mo, Y. R.; Gao, J. L. *J. Chem. Theory Comput.* **2009**, *5*, 174–185.

(25) Subotnik, J. E.; Cave, R. J.; Steele, R. P.; Shenvi, N. *J. Chem. Phys.* **2009**, *130*, 234102.
(26) Subotnik, J. E.; Yeganeh, S.; Cave, R. J.; Ratner, M. A. *J. Chem. Phys.* **2008**, *129*, 244101.
(27) Thiel, A.; Koppel, H. *J. Chem. Phys.* **1999**, *110*, 9371–9383.
(28) Van Voorhis, T.; Kowalczyk, T.; Kaduk, B.; Wang, L. P.; Cheng, C. L.; Wu, Q. *Annu. Rev. Phys. Chem.* **2010**, *61*, 149–170.
(29) Wu, Q.; Van Voorhis, T. *J. Chem. Phys.* **2006**, *125*, 164105.
(30) Wu, Q.; Van Voorhis, T. *J. Chem. Theory Comput.* **2006**, *2*, 765–774.
(31) Zhu, X. L.; Yarkony, D. R. *J. Chem. Phys.* **2010**, *132*, 104101.
(32) Hammes-Schiffer, S. *ChemPhysChem* **2002**, *3*, 33–42.
(33) Skone, J. H.; Soudackov, A. V.; Hammes-Schiffer, S. *J. Am. Chem. Soc.* **2006**, *128*, 16655–16663.
(34) Kirby, J. P.; Roberts, J. A.; Nocera, D. G. *J. Am. Chem. Soc.* **1997**, *119*, 9230–9236.
(35) Roberts, J. A.; Kirby, J. P.; Nocera, D. G. *J. Am. Chem. Soc.* **1995**, *117*, 8051–8052.
(36) Soudackov, A.; Hammes-Schiffer, S. *J. Am. Chem. Soc.* **1999**, *121*, 10598–10607.
(37) Georgievskii, Y.; Stuchebrukhov, A. A. *J. Chem. Phys.* **2000**, *113*, 10438–10450.
(38) Becke, A. D. *J. Chem. Phys.* **1993**, *98*, 5648–5652.
(39) Lee, C. T.; Yang, W. T.; Parr, R. G. *Phys. Rev. B* **1988**, *37*, 785–789.
(40) Hariharan, P. C.; Pople, J. A. *Theor. Chim. Acta* **1973**, *28*, 213–222.
(41) Frisch, M. J.; Trucks, G. W.; Schlegel, H. B.; Scuseria, G. E.; Robb, M. A.; Cheeseman, J. R.; Scalmani, G.; Barone, V.; Mennucci, B.; Petersson, G. A.; Nakatsuji, H.; Caricato, M.; Li, X.; Hratchian, H. P.; Izmaylov, A. F.; Bloino, J.; Zheng, G.; Sonnenberg, J. L.; Hada, M.; Ehara, M.; Toyota, K.; Fukuda, R.; Hasegawa, J.; Ishida, M.; Nakajima, T.; Honda, Y.; Kitao, O.; Nakai, H.; Vreven, T.; Montgomery, J. A.; Peralta, J. E.; Ogliaro, F.; Bearpark, M.; Heyd, J. J.; Brothers, E.; Kudin, K. N.; Staroverov, V. N.; Kobayashi, R.; Normand, J.; Raghavachari, K.; Rendell, A.; Burant, J. C.; Iyengar, S. S.; Tomasi, J.; Cossi, M.; Rega, N.; Millam, J. M.; Klene, M.; Knox, J. E.; Cross, J. B.; Bakken, V.; Adamo, C.; Jaramillo, J.; Gomperts, R.; Stratmann, R. E.; Yazyev, O.; Austin, A. J.; Cammi, R.; Pomelli, C.; Ochterski, J. W.; Martin, R. L.; Morokuma, K.; Zakrzewski, V. G.; Voth, G. A.; Salvador, P.; Dannenberg, J. J.; Dapprich, S.; Daniels, A. D.; Farkas; Foresman, J. B.; Ortiz, J. V.; Cioslowski, J.; Fox, D. J. *Gaussian 09*, Revision B.01; Gaussian Inc.: Wallingford, CT, 2009.
(42) Schmidt, M. W.; Baldridge, K. K.; Boatz, J. A.; Elbert, S. T.; Gordon, M. S.; Jensen, J. H.; Koseki, S.; Matsunaga, N.; Nguyen, K. A.; Su, S. J.; Windus, T. L.; Dupuis, M.; Montgomery, J. A. *J. Comput. Chem.* **1993**, *14*, 1347–1363.
(43) Marston, C. C.; Balint-Kurti, G. G. *J. Chem. Phys.* **1989**, *91*, 3571–3576.
(44) Webb, S. P.; Hammes-Schiffer, S. *J. Chem. Phys.* **2000**, *113*, 5214–5227.
(45) Connolly, M. L. *J. Appl. Crystallogr.* **1983**, *16*, 548–558.
(46) Singh, U. C.; Kollman, P. A. *J. Comput. Chem.* **1984**, *5*, 129–145.

JCTC Journal of Chemical Theory and Computation

ARTICLE

pubs.acs.org/JCTC

Accurate Interaction Energies for Problematic Dispersion-Bound Complexes: Homogeneous Dimers of NCCN, P_2, and PCCP

Edward G. Hohenstein,[†] Heather M. Jaeger,[‡] Emily J. Carrell,[‡] Gregory S. Tschumper,[*,‡] and C. David Sherrill[*,†]

[†]Center for Computational Molecular Science and Technology, School of Chemistry and Biochemistry, and School of Computational Science and Engineering, Georgia Institute of Technology, Atlanta, Georgia 30332, United States

[‡]Department of Chemistry and Biochemistry, University of Mississippi, University, Mississippi 38677, United States

Supporting Information

ABSTRACT: All intermolecular interactions involve London dispersion forces. The accurate treatment of dispersion is essential for the computation of realistic interaction potentials. In general, the most reliable method for computing intermolecular interactions is coupled-cluster singles and doubles with perturbative triples [CCSD(T)] in conjunction with a sufficiently flexible Gaussian atomic orbital basis set, a combination which is not routinely applicable due to its excessive computational demands (CPU time, memory, storage). Recently, many theoretical methods have been developed that attempt to account for dispersion in a more efficient manner. It is well-known that dispersion interactions are more difficult to compute in some systems than others; for example, $\pi-\pi$ dispersion is notoriously difficult, while alkane−alkane dispersion is relatively simple to compute. In this work, numerous theoretical methods are tested for their ability to compute reliable interaction energies in particularly challenging systems, namely, the P_2, PCCP, and NCCN dimers. Symmetry-adapted perturbation theory (SAPT) is applied to these dimers to demonstrate their sensitivity to the treatment of dispersion. Due to the small size of these systems, highly accurate CCSD(T) potential energy curves could be estimated at the complete basis set limit. Numerous theoretical methods are tested against the reliable CCSD(T) benchmarks. Methods using a treatment of dispersion that relies on time-dependent density functional theory (TDDFT) response functions are found to be the most reliable.

1. INTRODUCTION

Molecules with large, delocalized π orbitals are ubiquitous throughout chemistry. Not surprisingly, noncovalent interactions involving these types of molecules are important in the stacking of bases in DNA,[1−8] interactions between graphene sheets,[9] the structure and energetics of certain organic crystals,[10−13] and some side chain interactions within proteins.[14−18] Unfortunately, the interactions between these highly polarizable molecules are notoriously difficult to study. Even seemingly simple systems, such as the benzene dimer or indole−benzene complex, can prove extremely challenging for all but the most robust quantum mechanical methods.[19−21] The most reliable standard method for treating these types of systems is coupled-cluster singles and doubles with perturbative triples [CCSD(T)].[22,23] However, due to the computational expense associated with this method, it can only be applied to systems roughly the size of a nucleic acid base pair (with a medium-sized basis set).

The difficulty, in many cases, is to accurately capture London dispersion forces, which are critical for the study of noncovalent interactions. For even a qualitatively correct description of the interaction of neutral, nonpolar molecules, a reasonable treatment of dispersion is required. Of the four interaction components (electrostatics, induction, dispersion, and exchange-repulsion), the dispersion interaction is the most difficult for quantum mechanical methods to include in a reliable, yet computationally efficient manner. The quantum mechanical treatment of electrostatics, exchange-repulsion, and induction proves effective, at least semiquantitatively, via Hartree−Fock (HF) or density functional theory (DFT).[24−26] Focusing on wave-function-based methods, second-order Møller−Plesset perturbation theory (MP2) is the simplest method that contains some account of dispersion. However, in many cases (especially those involving delocalized π orbitals), MP2 grossly overestimates the magnitude of dispersion interactions.[27,28] The usually robust coupled-cluster singles and doubles (CCSD) method[22] also struggles to describe dispersion in difficult cases, usually underestimating its magnitude in the cases where MP2 overestimates.[29] The inclusion of a perturbative triples correction is required for quantitatively correct results.[29]

There are many approximate methods that attempt to correct the description of dispersion by MP2 or CCSD. The spin-component scaled (SCS) methods, originally introduced by Grimme, attempt to correct the correlation energy by empirically scaling the same- and opposite-spin components.[30,31] There are several different parametrizations of MP2, including some specifically for noncovalent interactions;[32,33] unfortunately, it is not clear that any one set of parameters is reliable for all types of interactions.[21,26,34] The SCS-CCSD method[31] has been shown to be much more reliable than SCS-MP2 for treating all types of noncovalent interactions.[26] However, this method requires an iterative $\mathcal{O}(N^6)$ procedure to compute an interaction energy, which limits its applicability. The MP2.5 method of Hobza and

Received: June 3, 2011
Published: July 27, 2011

co-workers[35] is comparable to SCS-CCSD with regard to accuracy and only requires a noniterative $\mathcal{O}(N^6)$ energy evaluation. Of the reliable, approximate wave-function-based methods, the least computationally expensive [noniterative $\mathcal{O}(N^5)$] and the most physically justified is the MP2C method of Hesselmann.[36,37] This method attempts to correct the behavior of MP2 by evaluating dispersion with frequency-dependent polarizabilities from time-dependent density functional theory (TDDFT).

For the study of molecular interactions in even larger systems, much lower-scaling methods need to be applied. One very popular and effective approach is to augment traditional density functionals with a damped R^{-6} term.[38−41] This DFT-D approach uses the density functional to account for short-range electron correlation and the empirical correction to capture the long-range correlation that the functional neglects. The recently developed -D3 correction[42] includes R^{-6} and R^{-8} terms computed with atomic dispersion coefficients that depend on the chemical environment (through the steric numbers of the atoms). A possible improvement to DFT-D methods is to apply the dispersion correction to long-range corrected functionals that are parametrized in the presence of the dispersion correction; ωB97X-D is such a functional[43] and appears to be particularly robust for noncovalent interactions when used with augmented triple-ζ basis sets.[44] The so-called "double hybrid" functionals contain an MP2-like term that accounts for dispersion. These functionals also appear well suited to describe noncovalent interactions. The B2PLYP and XYG3 functionals are two examples of double hybrid functionals that have been shown to perform well.[44−48]

The methods described above are *supermolecular* approaches to computing an interaction energy. It is also possible to compute interaction energies directly through a *perturbative* approach; the most rigorous of these methods is the symmetry-adapted perturbation theory (SAPT).[49] At this point, it should be noted that MP2C is a hybrid of supermolecular and perturbative approaches. SAPT exists in both wave-function-based and DFT-based forms [with the latter termed SAPT(DFT)]. The wave-function-based SAPT, which relies on a many-body perturbation theory (MBPT) expansion, has traditionally been too expensive to apply to large systems, since it scales as $\mathcal{O}(N^7)$ when all second-order intramonomer correlation terms are included. However, through density-fitting (DF) and natural orbital (NO) based approximations, it can be applied to systems with roughly 50 atoms.[50,51] The simplest SAPT method, SAPT0, consists of a Hartree−Fock interaction energy and an MP2-like dispersion term; this method can be applied to systems with over 100 atoms.[52] The SAPT(DFT) method[53−57] scales as $\mathcal{O}(N^5)$ after DF approximations are applied.[58−60] SAPT(DFT) is quickly becoming the preferred method for describing dispersion in difficult systems with as many as 72 atoms.[9]

One of the most accurate methods for obtaining a dispersion energy via a perturbative approach was developed in the mid-1990s by Williams et al.[61] Their CCD-based approach is similar to the supermolecular CCD+ST(CCD) method developed by Raghavachari.[62] The evaluation of CCD+ST(CCD) dispersion requires the iterative solution of five sets of doubles amplitudes, all of which scale as $\mathcal{O}(N^6)$. Finally, these amplitudes are used to evaluate a perturbative triples correction scaling $\mathcal{O}(N^7)$. Due to the expense of this method, it has remained virtually unused since its development. Recently, we have implemented the CCD+ST(CCD) dispersion while taking advantage of modern DF and NO approximations.[63] These approximations allow CCD+ST(CCD) dispersion energies to be computed for systems that are orders of magnitude larger than those which were previously accessible. A similarly accurate method for computing dispersion energies, due to Korona and Jeziorski, exists; however, it also scales as $\mathcal{O}(N^7)$ (if density fitting approximations are applied).[64−66]

With the number of recently developed methods aimed at describing noncovalent interactions, it is important to have reliable and challenging benchmarks available. One of the most popular is the S22 test set of Hobza and co-workers.[6] This set of benchmark interaction energies has been used extensively to test and train new methods.[24] For most wave-function-based methods, two of the most difficult systems in this test set are the stacked benzene dimer and indole−benzene complexes.[21,67] Even the original benchmark energy for the stacked indole−benzene differs by approximately 15% from the best estimates currently available.[21,67] It is useful to study systems that contain dispersion interactions similar to the stacked aromatic $\pi-\pi$ complexes in the S22 test set, but for which more accurate benchmarks can be established.

In this work, we examine NCCN, P_2, and PCCP dimers as such model systems. All three of these systems are much smaller than the benzene dimer or indole−benzene, allowing for the computation of the nonrelativistic, electronic interaction energy in the complete basis set limit. We apply our new CCD+ST(CCD) SAPT program to examine the nature of the dispersion interactions present in NCCN, P_2, and PCCP dimers compared to those in stacked aromatic $\pi-\pi$ complexes. Through this analysis, the problems encountered by finite-order perturbation theory are explored. Furthermore, we compare the molecular interaction between an extensive set of the aforementioned methods and our new benchmark data over multiple slices of the interaction potential for these three dimers.

2. METHODS

Rigid, linear monomer geometries were adopted for all computations. Experimental bond lengths were taken from Herzberg[68,69] for P_2 and NCCN [R(PP) = 1.8943 Å, R(CC) = 1.3839 Å, and R(CN) = 1.1578 Å]. Although PCCP has been observed experimentally, structural characterization was not feasible, and no experimentally inferred geometrical parameters were reported.[70] As such, the bond lengths for PCCP used in this study [R(CC) = 1.35560 Å and R(CP) = 1.58597 Å] were obtained from a low-level geometry optimization (details in the Supporting Information). These values, however, are entirely consistent with CCSD(T) optimizations with correlation consistent triple-ζ basis sets.[71]

Potential energy curves (PECs) of the dimer structures were computed in three different configurations: cross (X), parallel-displaced (PD), and T-shaped (T) that belong to the D_{2d}, C_{2h}, and C_{2v} point groups, respectively. These configurations are depicted in Figure 1 for $(PCCP)_2$, but the general definitions of the intermolecular geometrical parameters also apply to $(P_2)_2$ and $(NCCN)_2$. The D_{2d} cross configuration is depicted in Figure 1a, where the arrow indicates the intermolecular distance (R) between the midpoints of the central bond of each monomer. For the C_{2v} T-shaped structures, the arrow shown in Figure 1b denotes the intermolecular distance (R) from the midpoint of the central bond that is perpendicular to the C_2 rotational axis of symmetry to the nearest atom in the other monomer that lies on the C_2 axis of symmetry. The C_{2h} parallel displaced structures are defined by two intermolecular parameters. R is again used to indicate the

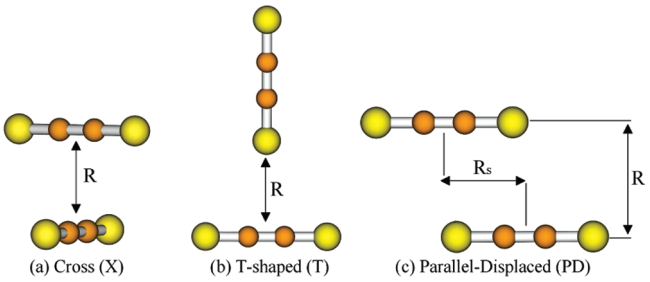

Figure 1. Three prototypical dimer configurations of NCCN, PCCP, and P_2 dimers included in this study.

separation between the monomers, specifically the distance between the two parallel lines defined by the linear monomers (denoted by the vertical arrow in Figure 1c). The other intermolecular geometrical parameter for the PD configurations is the displacement of the monomers along the aforementioned parallel lines relative to a rectangular (or sandwich) D_{2h} structure. In Figure 1c, this "horizontal slip" distance is labeled R_S and denoted by the horizontal arrow. The R_S coordinate was fixed at a value of 2.80 Å for $(NCCN)_2$, 2.31 Å for $(P_2)_2$, and 2.66 Å for $(PCCP)_2$. These values roughly correspond to the average of MP2 and CCSD(T) optimized R_S parameters (details in the Supporting Information).

The PECs in this work were generated by scanning over R for each configuration of the three homogeneous dimers. HF, MP2, CCSD, and CCSD(T) electronic energies were computed at each point along the curve with the aug-cc-pVDZ, aug-cc-pVTZ, and aug-cc-pVQZ basis sets. Larger, aug-cc-pV(X+d)Z-type basis sets were determined to provide nearly identical results (details in the Supporting Information). The 1s-like core orbitals of C and N were constrained to be doubly occupied during the electron correlation computations, whereas this constraint was applied to the 1s-, 2s-, and 2p-like core orbitals of P (i.e., the frozen core approximation). The electronic energies were converged to at least 1×10^{-10} E_h for the SCF and 1×10^{-8} E_h for the coupled-cluster procedures. The single point energy computations were performed using both the 2006.1 and 2010.1 versions of the Molpro software package.[72]

Electronic interaction energies were computed at the complete basis set (CBS) limit along the PECs for the X, PD, and T configurations of $(NCCN)_2$, $(P_2)_2$, and $(PCCP)_2$ by extrapolating the energy with respect to the cardinal number of the basis set. Within the supermolecular approach, CBS-limit interaction energies are computed by subtracting the extrapolated monomer electronic energies from the extrapolated electronic energies of the complex. Extrapolations were performed for the monomer energies in the monomer basis and for the dimer energies in the dimer basis. The electronic energy was separated into Hartree–Fock and correlation energies. HF energies were extrapolated with aug-cc-pVDZ, aug-cc-pVTZ, and aug-cc-pVQZ according to a three-parameter formula.[73,74] The correlation energies were extrapolated to the CBS limit using the two-point formula of Halkier et al. with aug-cc-pVTZ and aug-cc-pVQZ basis sets.[75]

The simplest wave-function-based methods tested in this work are the spin-component scaled MP2 methods. These methods have been shown to be capable of accurately computing noncovalent interactions with a triple-ζ quality basis.[30,33,34] In this work, the original parametrization, SCS-MP2, and a molecular interaction specific parametrization, SCS(MI)-MP2, are tested.[30,33] The SCS- and SCS(MI)-MP2 computations in this work use the cc-pVTZ basis;[76,77] the HF and MP2 computations are performed under the DF approximation using the cc-pVTZ-JK and cc-pVTZ-RI auxiliary basis sets, respectively.[78,79] The spin-component scaled CCSD method of Takatani et al., SCS-CCSD,[31] and its recent reparameterization for molecular interactions, SCS-(MI)-CCSD,[80] are also tested. The SCS-CCSD method has been found to yield excellent results with large basis sets;[26] in the present work, SCS-CCSD/aug-cc-pVQZ and SCS(MI)-CCSD/aug-cc-pVQZ interaction energies are computed. The SCS parameters for these methods can be found in the Supporting Information. The midground in terms of computation expense between SCS-MP2 and SCS-CCSD is the scaled MP3 method (MP2.5) of Pitoňak et al.[35] This method includes half of the third-order correction to MP2 (or, equivalently, averages MP2 and MP3 energies). Similarly to SCS-CCSD, this method performs well with large basis sets, and MP2.5/aug-cc-pVQZ interaction energies are reported. The counterpoise correction is applied to these wave-function-based methods.[81] These computations are performed with Molpro.[72]

We also test the promising MP2C method.[36,37] This method is a composite of a counterpoise corrected MP2 interaction energy and dispersion energies from intermolecular perturbation theory. The uncoupled Hartree–Fock (UCHF) dispersion energy contained in MP2 is replaced with a dispersion energy computed with time-dependent density functional theory (TDDFT) response functions.

$$E_{\mathrm{MP2C}} = E_{\mathrm{MP2}} - E_{\mathrm{disp}}(\mathrm{UCHF}) + E_{\mathrm{disp}}(\mathrm{TDDFT}) \qquad (1)$$

The E_{disp}(TDDFT) term would be exact if the exact exchange-correlation potential could be used to evaluate the response functions.[55] In lieu of the exact exchange-correlation potential, the PBE0 functional in conjuction with the adiabatic local density approximation (ALDA) kernel has been shown to yield highly accurate dispersion energies.[37] The MP2C interaction energies are computed with an aug-cc-pVQZ basis and use aug-cc-pVQZ-JK and aug-cc-pVQZ-RI auxiliary basis sets (details in the Supporting Information). For the PCCP dimer, aug-cc-pVTZ, aug-cc-pVTZ-JK, and aug-cc-pVTZ-RI basis sets were used. A related method (in terms of its description of dispersion) is density-functional-based symmetry-adapted perturbation theory, SAPT(DFT).[53−57] Here, we use PBE0 with local HF exchange to describe the monomers. One caveat of SAPT(DFT) is that the monomer DFT computations need to be asymptotically corrected in order to produce accurate interaction energies; this requires the ionization potential of the monomers, which we compute at the PBE0/TZVPP level. The SAPT(DFT) computations use the DF approximation and the same basis sets as the MP2C computations. The MP2C and SAPT(DFT) computations are performed with Molpro.[72]

Many DFT methods have been developed in recent years that attempt to accurately describe noncovalent interactions.[82] Here, we test two hybrid meta-GGA functionals, M05-2X and M06-2X.[83−85] These functionals have been found to perform well when paired with the aug-cc-pVDZ and aug-cc-pVTZ basis sets, respectively.[44] Meta-GGA's are known to be susceptible to numerical errors related to the integration grid.[86] For this reason, we use a large, 100 302 (radial points, angular points) grid for the M05-2X and M06-2X computations. The ωB97X-D method of

Chai and Head-Gordon[43] and Grimme's B97-D3 method[40] are both evaluated with aug-cc-pVTZ basis sets.[44] A dense numerical integration grid was employed for the ωB97X-D computations, a pruned grid composed of 99 radial shells and 590 angular points per shell. We also test two double-hybrid DFT methods that include a perturbative MP2-like correlation correction, specifically, B2PLYP-D3/aug-cc-pVTZ and XYG3/6-311+G(3df,2p).[44,45,47] The XYG3 functional is evaluated with B3LYP orbitals and densities.[87] Only the ωB97X-D interaction energies are counterpoise-corrected. The M05-2X and M06-2X computations were performed with QChem 3.2.[88] The ωB97X-D computations were performed with the Gaussian 09 software package.[89] The B97-D3, B2PLYP-D3, and XYG3 computations were performed with NWChem 6.0.[90]

Wave-function-based SAPT computations were performed with a development version of the PSI4 program.[52,91] All SAPT computations use the density fitting approximation. SAPT computations were performed with the aug-cc-pVQZ basis and use the aug-cc-pVQZ-RI auxiliary basis (with the exception of the PCCP dimer, where aug-cc-pVTZ and aug-cc-pVTZ-RI sets were used). To reduce the expense of including triple excitations, a truncated virtual space constructed from MP2 natural orbitals is used. This approximation has been shown to greatly improve efficiency without introducing significant errors.[51] A similar approximation can be applied to the evaluation of the CCD dispersion energy and will be discussed in a forthcoming publication.[63] The highest level of SAPT applied in this work is denoted SAPT2+3(CCD), which is defined as follows:

$$\begin{aligned} E_{\mathrm{SAPT2+3(CCD)}} = {} & E^{(10)}_{\mathrm{elst,resp}} + E^{(12)}_{\mathrm{elst,resp}} + E^{(13)}_{\mathrm{elst,resp}} \\ & + E^{(10)}_{\mathrm{exch}} + E^{(11)}_{\mathrm{exch}}(S^2) + E^{(12)}_{\mathrm{exch}}(S^2) \\ & + E^{(20)}_{\mathrm{ind,resp}} + E^{(20)}_{\mathrm{exch-ind,resp}}(S^2) \\ & + E^{(30)}_{\mathrm{ind}} + E^{(30)}_{\mathrm{exch-ind}}(S^2) + {}^{t}E^{(22)}_{\mathrm{ind}} \\ & + {}^{t}E^{(22)}_{\mathrm{exch-ind}} \\ & + \varepsilon^{(2)}_{\mathrm{disp}}[\mathrm{CCD} + \mathrm{ST(CCD)}] \\ & + E^{(30)}_{\mathrm{disp}} + E^{(20)}_{\mathrm{exch-disp}} + E^{(30)}_{\mathrm{exch-disp}} \\ & + E^{(30)}_{\mathrm{ind-disp}} + E^{(30)}_{\mathrm{exch-ind-disp}} \end{aligned} \quad (2)$$

The supermolecular HF interaction energy is not included in the SAPT energy, since the third-order treatment of induction is expected to be sufficient when nonpolar monomers are considered. A thorough discussion of the supermolecular HF interaction energy in the context of SAPT can be found in ref 92. Approximate exchange terms are scaled according to $E^{(10)}_{\mathrm{exch}}/E^{(10)}_{\mathrm{exch}}(S^2)$ in order to account for higher-order exchange effects that are neglected in the S^2 approximation. At equilibrium, this scaling adds, at most, 0.03 kcal mol^{-1} of exchange to the interaction energy. At shorter intermolecular separations, for the first repulsive configuration considered (the potential energy curves are computed in 0.1 Å increments), this scaling can add as much as 1 kcal mol^{-1} to the exchange energy; the largest contributions come from scaling the $E^{(30)}_{\mathrm{exch-ind}}(S^2)$ term.

Table 1. Magnitude of the Dispersion Energy Relative to the Total SAPT2+3(CCD) Interaction Energy at Estimated CCSD(T)/CBS Limit Equilibrium Geometries

	NCCN	PCCP	P_2
cross	333%	205%	240%
PD	116%	216%	250%
T-shaped	96%	194%	234%

3. RESULTS

3.1. SAPT Analysis of the Dispersion Energy. The SAPT computations on the NCCN, PCCP, and P_2 dimers allow the dispersion energy to be analyzed separately from the total interaction energy. The dependence of interaction energies on the theoretical treatment of dispersion can be estimated from the relative importance of the dispersion component. To identify which systems would most likely be sensitive to the treatment of dispersion, Table 1 shows the magnitude of the dispersion energy relative to the total SAPT2+3(CCD) interaction energy computed at the estimated CCSD(T)/CBS limit equilibrium geometry. In the cross configurations of the NCCN, PCCP, and P_2 dimers, for example, the magnitude of the dispersion energy is 2−3 times larger than the total interaction energy. The relative contribution from dispersion is appreciably smaller for the PD and T-shaped configurations of the NCCN dimer but remains large for P_2 and PCCP dimers. From this simple analysis, one would expect the PCCP and P_2 dimers to be more sensitive to the treatment of dispersion than the NCCN dimer.

A more detailed analysis of the dispersion energy in these complexes can be found in Table 2. Here, the dispersion energy is reported as computed at various truncations of the MBPT expansion. For the moment, we will consider only the $E_{\mathrm{disp}}(2)$, $E_{\mathrm{disp}}(4)$, and $E_{\mathrm{disp}}(\mathrm{CCD})$ treatments of the dispersion energy. The $E_{\mathrm{disp}}(2)$ term is an MP2-like (UCHF) dispersion energy. The $E_{\mathrm{disp}}(4)$ term contains perturbative intramonomer correlation corrections to dispersion through second order. The $E_{\mathrm{disp}}(\mathrm{CCD})$ dispersion is the most reliable and uses CCD wave functions to correct the dispersion energy for intramonomer correlation. The dispersion energies are also presented as a percentage of the $E_{\mathrm{disp}}(2)$ dispersion energy. These percentages can be used as a means of gauging how difficult the dispersion energies in a given complex are to compute. For simple systems, there will be little change between $E_{\mathrm{disp}}(2)$ and $E_{\mathrm{disp}}(\mathrm{CCD})$. For more difficult systems, there will be a significant difference between $E_{\mathrm{disp}}(2)$ and $E_{\mathrm{disp}}(4)$, but not $E_{\mathrm{disp}}(4)$ and $E_{\mathrm{disp}}(\mathrm{CCD})$. For the most difficult systems, there will be large differences between all three of these treatments of dispersion.

For the sake of comparison with more commonly studied systems, the methane dimer, methane−benzene, and benzene dimer dispersion energies are also presented in Table 2. For typical interactions, such as these, the $E_{\mathrm{disp}}(4)$ treatment of dispersion has been found previously to be quite reliable.[50] The dispersion interactions between alkanes can be treated accurately with $E_{\mathrm{disp}}(2)$. The interactions involving π orbitals are more difficult and require, at least, the $E_{\mathrm{disp}}(4)$ treatment of dispersion. Dispersion within the NCCN dimer is comparable to the dispersion in the benzene dimer. There is a large difference between $E_{\mathrm{disp}}(2)$ and $E_{\mathrm{disp}}(4)$ and a small difference between $E_{\mathrm{disp}}(4)$ and $E_{\mathrm{disp}}(\mathrm{CCD})$. The P_2 dimer differs in that there is an even larger difference between $E_{\mathrm{disp}}(2)$ and $E_{\mathrm{disp}}(4)$, but the $E_{\mathrm{disp}}(\mathrm{CCD})$ correction is unimportant.

Table 2. Dispersion Energies Computed with Various Levels of SAPT[a]

	$E_{disp}(2)^b$	$E_{disp}(3)^c$	$E_{disp}(2.5)^d$	$E_{disp}(4)^e$	$E_{disp}(CCD)^f$
$(NCCN)_2$ cross	−2.3	−1.5 (65%)	−1.9 (83%)	−2.0 (85%)	−1.9 (81%)
$(NCCN)_2$ PD	−2.9	−1.8 (65%)	−2.4 (82%)	−2.5 (87%)	−2.3 (82%)
$(NCCN)_2$ T-shaped	−2.5	−1.6 (66%)	−2.1 (83%)	−2.3 (92%)	−2.2 (87%)
$(PCCP)_2$ cross	−8.0	−3.9 (49%)	−6.0 (74%)	−6.3 (79%)	−5.8 (72%)
$(PCCP)_2$ PD	−7.9	−3.7 (47%)	−5.8 (73%)	−6.5 (82%)	−5.8 (73%)
$(PCCP)_2$ T-shaped	−4.7	−2.6 (55%)	−3.7 (77%)	−4.0 (85%)	−3.7 (78%)
$(P_2)_2$ cross	−3.2	−1.9 (58%)	−2.5 (79%)	−2.4 (74%)	−2.4 (75%)
$(P_2)_2$ PD	−3.6	−2.1 (58%)	−2.8 (79%)	−2.8 (78%)	−2.8 (78%)
$(P_2)_2$ T-shaped	−2.0	−1.2 (58%)	−1.6 (79%)	−1.7 (82%)	−1.6 (79%)
$(CH_4)_2$	−1.3	−1.2 (97%)	−1.2 (99%)	−1.3 (103%)	−1.3 (106%)
CH_4−Bz	−2.9	−2.4 (82%)	−2.7 (91%)	−2.7 (93%)	−2.7 (93%)
$(Bz)_2$ PD	−7.9	−5.2 (65%)	−6.6 (83%)	−6.7 (84%)	−6.5 (82%)

[a] Dispersion energies are given in kcal mol^{-1} and as percentages of $E_{disp}(2)$. [b] $E_{disp}(2) = E_{disp}^{(20)}$. [c] $E_{disp}(3) = E_{disp}^{(20)} + E_{disp}^{(30)} + E_{disp}^{(21)}$. [d] $E_{disp}(2.5) = E_{disp}^{(20)} + (1)/(2)(E_{disp}^{(30)} + E_{disp}^{(21)})$. [e] $E_{disp}(4) = E_{disp}^{(20)} + E_{disp}^{(30)} + E_{disp}^{(21)} + E_{disp}^{(22)}$. [f] $E_{disp}(CCD) = E_{disp}^{(2)}(CCD) + E_{disp}^{(22)}(ST)(CCD)$.

The PCCP dimer has the most difficult dispersion interactions to compute. In this case, not only is the difference between $E_{disp}(2)$ and $E_{disp}(4)$ large, but the difference between $E_{disp}(4)$ and $E_{disp}(CCD)$ can be as large as 0.7 kcal mol^{-1}. This analysis shows that only the most robust methods will be capable of accurately computing dispersion interactions within the PCCP dimer.

3.2. Performance of Supermolecular Methods. The methods tested in this work can be grouped in terms of their treatments of the dispersion interaction. We test four methods that contain highly parametrized dispersion corrections (M05-2X, M06-2X, B97-D3, and ωB97X-D). We test four methods that contain empirically corrected MP2-like dispersion terms (SCS-MP2, SCS(MI)-MP2, XYG3, and B2PLYP-D3). The other methods compute dispersion with more robust techniques than MP2: MP2.5 contains contributions from MP3; SCS- and SCS(MI)-CCSD contain a CCSD treatment of dispersion; and MP2C and SAPT(DFT) use TDDFT-based dispersion corrections.

First, we will consider the M05-2X and M06-2X density functionals. Although these functionals do not contain the correct physics to describe long-range dispersion interactions, through extensive parametrization, they appear to capture "medium-range" dispersion (up to perhaps 4−5 Å).[44,84,93−96] This deficiency is evident in Figures 3−5; M05-2X tends to predict reasonable interaction energies near equilibrium and underbinds at long range. M06-2X often predicts reasonable interaction energies but equilibrium distances that are too short; at long range, the performance of M06-2X degrades quickly. The PD PCCP dimer (Figure 4) is an example of typical behavior for M05-2X and M06-2X. Although lacking long-range dispersion interactions, these functionals can provide reasonable interaction energies for small, closely interacting complexes with relatively low computational expense. In Figure 2, the average errors of each method are presented for the equilibrium configurations of the nine dimers considered in this work. For these equilibrium geometries, the performance of M05-2X and M06-2X is slightly better than the DFT-D methods. Their performance for the difficult dispersion interactions included in this work is similar to their performance for less difficult dispersion bound systems included in other test sets (e.g., the S22 and NBC10 test sets).[44] The fact that the accuracy of these functionals does not degrade for more difficult systems is a desirable characteristic. These functionals can be a practical solution for studying near-equilibrium configurations of dispersion bound complexes.

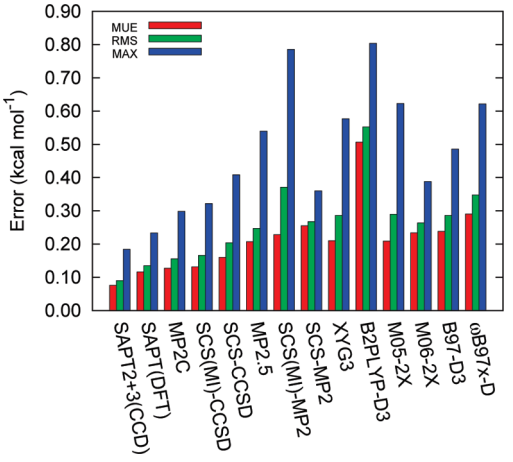

Figure 2. Errors in interaction energies for NCCN, PCCP, and P_2 dimers computed at equilibrium with various methods.

The B97-D3 and ωB97X-D methods rely entirely on pairwise C_6R^{-6} terms to account for dispersion. Therefore, the accuracy of these functionals for dispersion-bound complexes is tied to the empirical parametrization of these -D terms. B97-D3 uses C_6 coefficients that provide some information about the chemical environment of each atom.[42] This is done through a rather ingenious atom-typing procedure that is completely black-box and varies continuously with the molecular geometry. The performance of these DFT-D methods at equilibrium is not as good as that for the M0N-2X methods; however, at long range, the behavior of these functionals improves rather than degrades (see Figure 3−5). ωB97X-D tends to be underbound relative to the CCSD(T) benchmark, which could be indicative of C_6 coefficients that are not optimal for these highly polarizable molecules. Overall, the B97-D3 functional outperforms ωB97X-D for the dimers considered in this work. This is a useful result, since the B97-D3 functional exhibits $\mathcal{O}(N^3)$ scaling as opposed to the $\mathcal{O}(N^4)$ scaling of the hybrid ωB97X-D method.

Two promising double hybrid density functionals, XYG3 and B2PLYP-D3, were applied to the NCCN, P_2, and PCCP dimers.

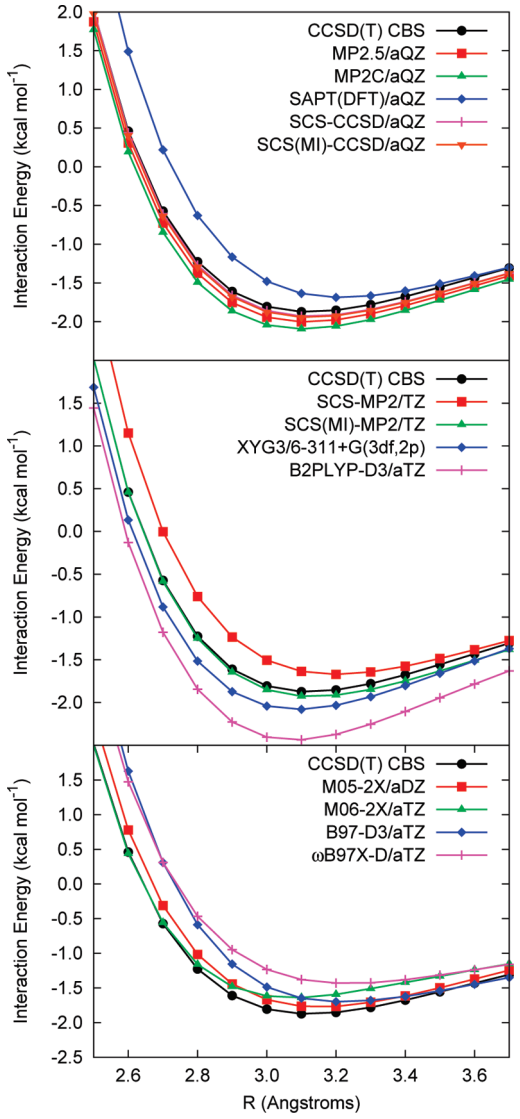

Figure 3. T-shaped NCCN dimer potential energy curves computed with various methods.

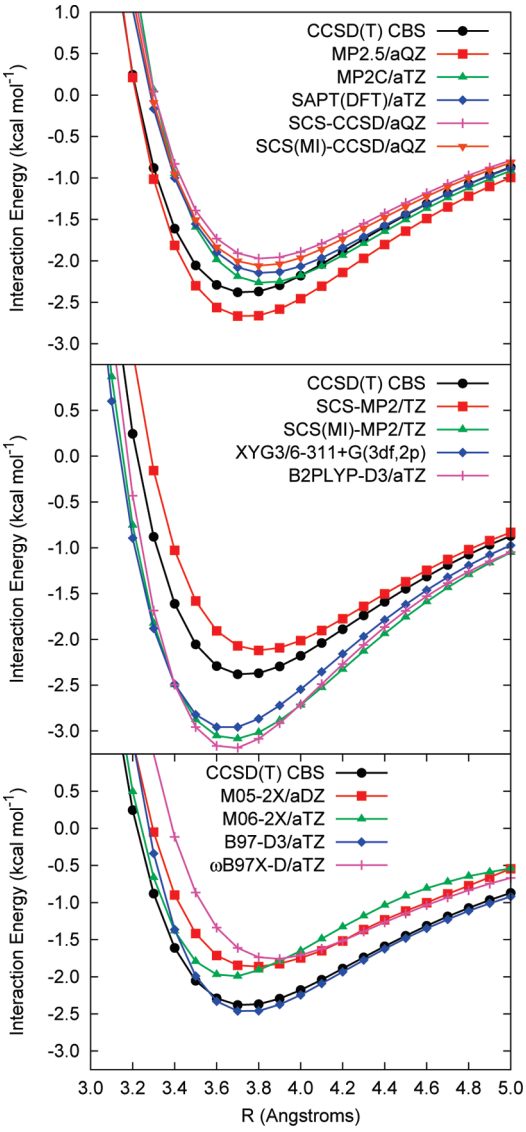

Figure 4. Parallel-displaced PCCP dimer potential energy curves computed with various methods.

XYG3 accounts for dispersion with an MP2-like term that is evaluated using B3LYP orbitals and scaled by 0.3211. This small scaling parameter is required because short-range correlation is included elsewhere in the functional; additionally, the DFT orbitals have, relative to Hartree−Fock orbitals, a smaller HOMO−LUMO gap, resulting in a larger perturbative correction. The B2PLYP functional contains a similar scaled perturbative correction but still requires a small empirical dispersion correction in order to provide accurate results for dispersion bound complexes. The results for B2PLYP-D3 for these dimers is very poor. Perhaps the limited data set used to parametrize this functional, which contains no third row elements, contributes to this failing. This poor performance is unusual, as the B2PLYP-D3 method is typically reliable for treating dispersion dominated interactions.[44] XYG3 performs as well as any DFT-based method that was tested; this is consistent with previous findings for other test sets.[44,48] Unfortunately, it merely equals the performance of M05-2X and M06-2X, which both scale as $\mathcal{O}(N^5)$, whereas XYG3 scales as $\mathcal{O}(N^5)$ due to the perturbative correction. An important observation is that XYG3 does not inherit the poor performance of MP2 in its own perturbative correction, even for these particularly difficult cases. This can be attributed to the small fraction of the perturbative correction that needs to be included.

The SCS-MP2 methods we tested offer tremendous improvement over unscaled MP2 interaction energies. However, their performance is erratic; SCS(MI)-MP2, which was parametrized against the S22 test set, performs brilliantly for NCCN and P_2 dimers but severely overbinds the PCCP dimer. The SCS-MP2 method is more consistent but underbinds every dimer considered. It is probable that SCS-MP2/aug-cc-pVTZ would provide better results than SCS-MP2/cc-pVTZ, which is tested here. However, SCS-MP2 methods have an underlying problem that prevents any single parametrization from providing accurate results for a wide variety of dispersion bound complexes. The leading dispersion term, $E_{\mathrm{disp}}^{(20)}$, which is included in MP2, is composed of 1/2 same-spin and 1/2 opposite-spin correlation (assuming a closed shell reference). For an SCS-MP2 method, this means that the scaling of the dispersion term is effectively an

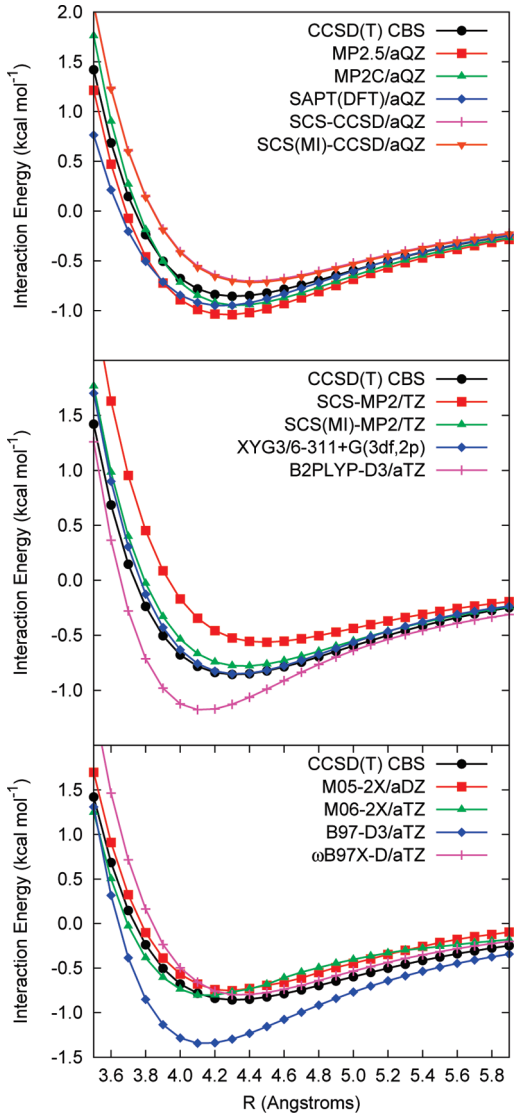

Figure 5. Cross P_2 dimer potential energy curves computed with various methods.

average of the same-spin and opposite-spin parameters, i.e.,

$$E_{\mathrm{disp}}^{(20)}(\mathrm{SCS{-}MP2}) = \frac{S_{\mathrm{os}} + S_{\mathrm{ss}}}{2} E_{\mathrm{disp}}^{(20)}(\mathrm{MP2}) \qquad (3)$$

With this in mind, the percentages of $E_{\mathrm{disp}}^{(20)}$ in Table 2 given for $E_{\mathrm{disp}}(\mathrm{CCD})$ represent nearly ideal values of $(S_{\mathrm{os}} + S_{\mathrm{ss}})/2$ for each dimer considered. For the dimers in Table 2, the ideal value for $(S_{\mathrm{os}} + S_{\mathrm{ss}})/2$ ranges from 1.06 to 0.72. In SCS-MP2 and SCS-(MI)-MP2, these averaged values are 0.77 and 0.96, respectively. The use of a nonaugmented basis set, cc-pVTZ, essentially has the same effect as scaling the dispersion energy. The realization that the dispersion energy is scaled by a single parameter shows that it is not possible to find one set of SCS parameters that will provide consistent results for a diverse set of nonbonded interactions.

The problems encountered by SCS-MP2 methods are a result of the inconsistent behavior of MP2 for treating dispersion interactions. The SCS-CCSD methods circumvent this problem by attempting to correct a method that behaves in a much more consistent manner. Previous benchmarking of SCS-CCSD has shown that the only drawback is the $\mathcal{O}(N^6)$ scaling of CCSD; admittedly, this is a considerable limitation. The tests of SCS- and SCS(MI)-CCSD for the NCCN dimer were consistent with previous results; indeed, the SCS-CCSD methods provide interaction energies within the uncertainties of the CCSD(T) benchmarks. For the P_2 and PCCP dimers, however, their performance was not as good. Both parametrizations of SCS-CCSD consistently underbind both of these dimers. Despite this slight problem, the overall performance of both SCS-CCSD methods was still excellent. The new SCS(MI) parametrization outperforms the original SCS-CCSD parameters for nearly all of the test cases, but, on average, only by a few hundredths of 1 kcal mol^{-1}. The parameters themselves are very similar: the original opposite- and same-spin scaling parameters of 1.27 and 1.13, respectively, and the SCS(MI) parameters of 1.11 and 1.28. The apparent insensitivity of SCS-CCSD methods to the choice of parameters is an obvious advantage of SCS-CCSD over SCS-MP2 and a desirable trait in general for an SCS method to possess.

In a similar spirit to SCS-MP2 and SCS-CCSD, MP2.5 attempts to correct the behavior of MP2 and MP3 by combining their energies in an empirical manner. MP2.5 is an average of MP2 and MP3 interaction energies; equivalently, it is also MP2 plus half of the third-order correction. The motivation for this method is obvious from the results in Table 2. The third-order dispersion energy $[E_{\mathrm{disp}}(3)]$ is always higher than the second-order dispersion energy $[E_{\mathrm{disp}}(2)]$. In the cases where the second-order dispersion energy is a good estimate of the CCD dispersion energy $[E_{\mathrm{disp}}(\mathrm{CCD})]$, the third-order correction to the dispersion energy is small. Where there is a large difference between the second-order dispersion energy and the CCD dispersion energy, there is an even larger difference between the second-order and third-order dispersion energies. We also report the second-order dispersion energy with half of the third-order correction included $[E_{\mathrm{disp}}(2.5)]$. There is excellent agreement between $E_{\mathrm{disp}}(2.5)$ and our best estimate of the dispersion energy, $E_{\mathrm{disp}}(\mathrm{CCD})$; this is the origin of the excellent performance of MP2.5 for dispersion-bound complexes. For the complexes considered in this work, the performance of MP2.5 is slightly better than SCS-MP2 methods and slightly worse than SCS-CCSD methods. MP2.5 tends to overbind somewhat relative to the CCSD(T) benchmark. For more typical interactions, the simple averaging of MP2 and MP3 in the MP2.5 method provides rather accurate results.[26] For these more difficult dispersion bound complexes, a larger fraction of MP3 would need to be included for similar accuracy.

The least empirical method tested for these complexes is the MP2C method of Hesselmann.[36,37] This method uses TDDFT response functions to correct the account of dispersion in MP2. The initial tests of this method have been very promising.[26,37] Here, we apply MP2C to more difficult systems than were included in the previous tests. The performance of this method, however, does not degrade for these systems. The performance of MP2C is slightly better than the SCS-CCSD methods at greatly reduced cost. A related method, in terms of the treatment of dispersion, SAPT(DFT) also performs extremely well for these complexes. These methods perform better than any of the other approximate methods tested in this work. Additionally, both MP2C and SAPT(DFT) scale as $\mathcal{O}(N^5)$, which is better than or equivalent to all but the DFT methods (excluding the double hybrids). SAPT(DFT) is slightly better than MP2C, and this is likely due to a more accurate treatment of dispersion and a more rigorous treatment of exchange-dispersion. Both of these methods contain a treatment of the dispersion energy that does not degrade for more difficult systems. They can both be

recommended as generally applicable for the study of nonbonded interactions.

4. CONCLUSIONS

We have introduced the NCCN, P_2, and PCCP dimers as model systems for dispersion dominated $\pi-\pi$ interactions. These dimers involve dispersion interactions that are problematic to study computationally. Dispersion interactions of this type are typically found in much larger complexes (e.g., benzene dimer or indole−benzene). SAPT computations show that the dispersion in the NCCN dimer is similar in nature to the dispersion in the benzene dimer, while dispersion in P_2 and PCCP dimers is potentially more difficult to accurately characterize. The advantage of these model systems lies in their relatively small size; near complete basis set limit CCSD(T) interaction energies were obtained for NCCN, P_2, and PCCP dimers.

The performance of many recently developed quantum mechanical methods was tested for the NCCN, P_2, and PCCP dimers. DFT-based methods provide reasonable results at relatively low computational expense. An advantage of these methods is that their performance does not degrade for these more difficult systems. Spin-component scaled methods perform much better than their unscaled, parent methods; although generally good, the performance of SCS methods can be somewhat erratic. The best results for the NCCN, P_2, and PCCP dimers come from the methods that use TDDFT response functions to describe dispersion interactions, MP2C and SAPT(DFT). These methods provide accuracy that could otherwise only be achieved through the inclusion of the effect of triple excitations on the dispersion energy. However, there are some limitations for general applicability of MP2C and SAPT(DFT) due to their roots in intermolecular perturbation theory (i.e., the need to fragment the system and the current lack of analytic gradients). Despite this, both methods are very promising for accurately characterizing $\pi-\pi$ dispersion interactions in extended systems.

■ ASSOCIATED CONTENT

Ⓢ Supporting Information. Additional information regarding the monomer and dimer geometries, testing of aug-cc-pV(X+d)Z basis sets, and all nine of the PCCP, P_2 and NCCN dimer potential energy curves computed with various methods is available. This information is available free of charge via the Internet at http://pubs.acs.org/.

■ AUTHOR INFORMATION

Corresponding Author

*E-mail: tschumpr@olemiss.edu; sherrill@gatech.edu.

■ ACKNOWLEDGMENT

This work was supported in part by the National Science Foundation through grants to CDS (Grant No. CHE-1011360) and to GST (Grant No. CHE-0957317 and EPS-0903787). The Center for Computational Molecular Science and Technology is funded through an National Science Foundation CRIF award (Grant No. CHE-0946869) and by Georgia Tech. Some of the computations were performed using resources at the Mississippi Center for Supercomputing Research.

■ REFERENCES

(1) Saenger, W. *Principles of Nucleic Acid Structure*; Springer-Verlag: New York, 1984.
(2) Shieh, H.-S.; Berman, H. M.; Dabrow, M.; Neidle, S. *Nucleic Acids Res.* **1980**, *8*, 85–97.
(3) Šponer, J.; Leszczynski, J.; Hobza, P. *J. Phys. Chem.* **1996**, *100*, 5590–5596.
(4) Elstner, M.; Hobza, P.; Frauenheim, T.; Suhai, S.; Kaxiras, E. *J. Chem. Phys.* **2001**, *114*, 5149–5155.
(5) Jurečka, P.; Hobza, P. *J. Am. Chem. Soc.* **2003**, *125*, 15608–15613.
(6) Jurečka, P.; Šponer, J.; Černý, J.; Hobza, P. *Phys. Chem. Chem. Phys.* **2006**, *8*, 1985–1993.
(7) Langner, K. M.; Kedzierski, P.; Sokalski, W. A.; Leszczynski, J. *J. Phys. Chem. B* **2006**, *110*, 9720–9727.
(8) Li, S.; Cooper, V. R.; Thonhauser, T.; Lundqvist, B. I.; Langreth, D. C. *J. Phys. Chem. B* **2009**, *113*, 11166–11172.
(9) Podeszwa, R. *J. Chem. Phys.* **2010**, *132*, 044704.
(10) Collings, J. C.; Roscoe, K. P.; Robins, E. G.; Batsanov, A. S.; Stimson, L. M.; Howard, J. A. K.; Clark, S. J.; Marder, T. B. *New J. Chem.* **2002**, *26*, 1740.
(11) Ringer, A. L.; Sherrill, C. D. *Chem.—Eur. J.* **2008**, *14*, 2542–2547.
(12) Podeszwa, R.; Rice, B. M.; Szalewicz, K. *Phys. Rev. Lett.* **2008**, *101*, 115503.
(13) Podeszwa, R.; Rice, B. M.; Szalewicz, K. *Phys. Chem. Chem. Phys.* **2009**, *11*, 2241.
(14) Meyer, E. A.; Castellano, R. K.; Diederich, F. *Angew. Chem., Int. Ed. Engl.* **2003**, *42*, 1210–1250.
(15) Burley, S. K.; Petsko, G. A. *Science* **1985**, *229*, 23–28.
(16) Braun, J.; Neusser, H. J.; Hobza, P. *J. Phys. Chem. A* **2003**, *107*, 3918–3924.
(17) Ringer, A. L.; Figgs, M. S.; Sinnokrot, M. O.; Sherrill, C. D. *J. Phys. Chem. A* **2006**, *110*, 10822–10828.
(18) Ringer, A. L.; Senenko, A.; Sherrill, C. D. *Protein Sci.* **2007**, *16*, 2216–2223.
(19) Sinnokrot, M. O.; Sherrill, C. D. *J. Phys. Chem. A* **2006**, *110*, 10656–10668.
(20) Geng, Y.; Takatani, T.; Hohenstein, E. G.; Sherrill, C. D. *J. Phys. Chem. A* **2010**, *114*, 3576–3582.
(21) Takatani, T.; Hohenstein, E. G.; Malagoli, M.; Marshall, M. S.; Sherrill, C. D. *J. Chem. Phys.* **2010**, *132*, 144104.
(22) Purvis, G. D.; Bartlett, R. J. *J. Chem. Phys.* **1982**, *76*, 1910–1918.
(23) Raghavachari, K.; Trucks, G. W.; Pople, J. A.; Head-Gordon, M. *Chem. Phys. Lett.* **1989**, *157*, 479–483.
(24) Riley, K. E.; Pitoňák, M.; Jurečka, P.; Hobza, P. *Chem. Rev.* **2010**, *110*, 5023–5063.
(25) Riley, K. E.; Pitonak, M.; Cerny, J.; Hobza, P. *J. Chem. Theory Comput.* **2010**, *6*, 66–80.
(26) Gráfová, L.; Pitoňák, M.; Řezáč, J.; Hobza, P. *J. Chem. Theory Comput.* **2010**, *6*, 2365–2376.
(27) Hobza, P.; Selzle, H. L.; Schlag, E. W. *J. Phys. Chem.* **1996**, *100*, 18790–18794.
(28) Sinnokrot, M. O.; Valeev, E. F.; Sherrill, C. D. *J. Am. Chem. Soc.* **2002**, *124*, 10887–10893.
(29) Hopkins, B. W.; Tschumper, G. S. *J. Phys. Chem. A* **2004**, *108*, 2941–2948.
(30) Grimme, S. *J. Chem. Phys.* **2003**, *118*, 9095–9102.
(31) Takatani, T.; Hohenstein, E. G.; Sherrill, C. D. *J. Chem. Phys.* **2008**, *128*, 124111.
(32) Hill, J. G.; Platts, J. A. *J. Chem. Theory Comput.* **2007**, *3*, 80–85.
(33) Distasio, R. A.; Head-Gordon, M. *Mol. Phys.* **2007**, *105*, 1073–1083.
(34) Takatani, T.; Sherrill, C. D. *Phys. Chem. Chem. Phys.* **2007**, *9*, 6106–6114.
(35) Pitoňák, M.; Neogrády, P.; Černý, J.; Grimme, S.; Hobza, P. *ChemPhysChem* **2009**, *10*, 282–289.
(36) Hesselmann, A. *J. Chem. Phys.* **2008**, *128*, 144112.

(37) Pitonak, M.; Hesselmann, A. *J. Chem. Theory Comput.* **2010**, *6*, 168–178.
(38) Wu, Q.; Yang, W. *J. Chem. Phys.* **2002**, *116*, 515–524.
(39) Grimme, S. *J. Comput. Chem.* **2004**, *25*, 1463–1473.
(40) Grimme, S. *J. Comput. Chem.* **2006**, *27*, 1787–1799.
(41) Jurečka, P.; Černý, J.; Hobza, P.; Salahub, D. R. *J. Comput. Chem.* **2007**, *28*, 555–569.
(42) Grimme, S.; Antony, J.; Ehrlich, S.; Krieg, H. *J. Chem. Phys.* **2010**, *132*, 154104.
(43) Chai, J.; Head-Gordon, M. *Phys. Chem. Chem. Phys.* **2008**, *10*, 6615.
(44) Burns, L. A.; Vázquez-Mayagoitia, Á.; Sumpter, B. G.; Sherrill, C. D. *J. Chem. Phys.* **2011**, *134*, 084107.
(45) Grimme, S. *J. Chem. Phys.* **2006**, *124*, 034108.
(46) Schwabe, T.; Grimme, S. *Phys. Chem. Chem. Phys.* **2007**, *9*, 3397–3406.
(47) Zhang, Y.; Xu, X.; Goddard, W. A. *Proc. Natl. Acad. Sci. U.S.A.* **2009**, *106*, 4963–4968.
(48) Vazquez-Mayagoitia, A.; Sherrill, C. D.; Apra, E.; Sumpter, B. G. *J. Chem. Theory Comput.* **2010**, *6*, 727–734.
(49) Jeziorski, B.; Moszynski, R.; Szalewicz, K. *Chem. Rev.* **1994**, *94*, 1887–1930.
(50) Hohenstein, E. G.; Sherrill, C. D. *J. Chem. Phys.* **2010**, *133*, 014101.
(51) Hohenstein, E. G.; Sherrill, C. D. *J. Chem. Phys.* **2010**, *133*, 104107.
(52) Hohenstein, E. G.; Sherrill, C. D. *J. Chem. Phys.* **2010**, *132*, 184111.
(53) Williams, H. L.; Chabalowski, C. F. *J. Phys. Chem. A* **2001**, *105*, 646–659.
(54) Misquitta, A. J.; Szalewicz, K. *Chem. Phys. Lett.* **2002**, *357*, 301–306.
(55) Misquitta, A. J.; Jeziorski, B.; Szalewicz, K. *Phys. Rev. Lett.* **2003**, *91*, 033201.
(56) Hesselmann, A.; Jansen, G. *Phys. Chem. Chem. Phys.* **2003**, *5*, 5010.
(57) Misquitta, A. J.; Podeszwa, R.; Jeziorski, B.; Szalewicz, K. *J. Chem. Phys.* **2005**, *123*, 214103.
(58) Bukowski, R.; Podeszwa, R.; Szalewicz, K. *Chem. Phys. Lett.* **2005**, *414*, 111–116.
(59) Hesselmann, A.; Jansen, G.; Schütz, M. *J. Chem. Phys.* **2005**, *122*, 014103.
(60) Podeszwa, R.; Bukowski, R.; Szalewicz, K. *J. Chem. Theory Comput.* **2006**, *2*, 400–412.
(61) Williams, H.; Szalewicz, K.; Moszynski, R.; Jeziorski, B. *J. Chem. Phys.* **1995**, *103*, 4586.
(62) Raghavachari, K. *J. Chem. Phys.* **1985**, *82*, 4607.
(63) Hohenstein, E. G.; Sherrill, C. D. Manuscript in Preparation.
(64) Korona, T.; Jeziorski, B. *J. Chem. Phys.* **2008**, *128*, 144107.
(65) Korona, T. *J. Chem. Theory Comput.* **2009**, *5*, 2663–2678.
(66) Korona, T. Coupled cluster treatment of intramonomer correlation effects in intermolecular interactions. In *Recent Progress in Coupled Cluster Methods*, 1st ed.; Cársky, P., Paldus, J., Pittner, J., Eds.; Springer-Verlag: The Netherlands, 2010; Vol. 11, pp 267−298.
(67) Podeszwa, R.; Patkowski, K.; Szalewicz, K. *Phys. Chem. Chem. Phys.* **2010**, *12*, 5974–5979.
(68) Herzberg, G. *Molecular Spectra and Molecular Structure: Spectra of Diatomic Molecules*; R.E. Krieger Pub. Co: Malabar, FL, 1989; Vol. 1.
(69) Herzberg, G. *Molecular Spectra and Molecular Structure: Electronic Spectra and Electronic Structure of Polyatomic Molecules*; Van Nostrand: Princeton, NJ, 1950; Vol. 3.
(70) Bronstrup, M.; Gottfriedsen, J.; Kretzschmar, I.; Blanksby, S. J.; Schwarz, H.; Schumann, H. *Phys. Chem. Chem. Phys.* **2000**, *2*, 2245–2250.
(71) Hajgato, B.; Pham-Tran, N.-N.; Veszpremi, T.; Nguyen, M. T. *Phys. Chem. Chem. Phys.* **2001**, *3*, 5158–5164.
(72) Werner, H.-J.; Knowles, P. J.; Knizia, G.; Manby, F. R.; Schütz, M.; Celani, P.; Korona, T.; Lindh, R.; Mitrushenkov, A.; Rauhut, G.; Shamasundar, K. R.; Adler, T. B.; Amos, R. D.; Bernhardsson, A.; Berning, A.; Cooper, D. L.; Deegan, M. J. O.; Dobbyn, A. J.; Eckert, F.; Goll, E.; Hampel, C.; Hesselmann, A.; Hetzer, G.; Hrenar, T.; Jansen, G.; Köppl, C.; Liu, Y.; Lloyd, A. W.; Mata, R. A.; May, A. J.; McNicholas, S. J.; Meyer, W.; Mura, M. E.; Nicklass, A.; O'Neill, D. P.; Palmieri, P.; Pflüger, K.; Pitzer, R.; Reiher, M.; Shiozaki, T.; Stoll, H.; Stone, A. J.; Tarroni, R.; Thorsteinsson, T.; Wang, M.; Wolf, A. *MOLPRO*, version 2010.1, see http://www.molpro.net.
(73) Halkier, A.; Helgaker, T.; Jorgensen, P.; Klopper, W.; Olsen, J. *Chem. Phys. Lett.* **1999**, *302*, 437–446.
(74) Feller, D. *J. Chem. Phys.* **1993**, *98*, 7059–7071.
(75) Halkier, A.; Helgaker, T.; Jørgensen, P.; Klopper, W.; Koch, H.; Olsen, J.; Wilson, A. K. *Chem. Phys. Lett.* **1998**, *286*, 243–252.
(76) Dunning, T. H. *J. Chem. Phys.* **1989**, *90*, 1007–1023.
(77) Kendall, R. A.; Dunning, T. H.; Harrison, R. J. *J. Chem. Phys.* **1992**, *96*, 6796–6806.
(78) Weigend, F. *Phys. Chem. Chem. Phys.* **2002**, *4*, 4285–4291.
(79) Weigend, F.; Köhn, A.; Hättig, C. *J. Chem. Phys.* **2002**, *116*, 3175–3183.
(80) Pitoňák, M.; Řezác, J.; Hobza, P. *Phys. Chem. Chem. Phys.* **2010**, *12*, 9611–9614.
(81) Boys, S. F.; Bernardi, F. *Mol. Phys.* **1970**, *19*, 553–566.
(82) Grimme, S. *WIREs Comput. Mol. Sci.* **2011**, *1*, 211–228.
(83) Zhao, Y.; Schultz, N. E.; Truhlar, D. G. *J. Chem. Phys.* **2005**, *123*, 161103.
(84) Zhao, Y.; Schultz, N. E.; Truhlar, D. G. *J. Chem. Theory Comput.* **2006**, *2*, 364–382.
(85) Zhao, Y.; Truhlar, D. G. *J. Chem. Phys.* **2006**, *125*, 194101.
(86) Johnson, E. R.; Becke, A. D.; Sherrill, C. D.; DiLabio, G. A. *J. Chem. Phys.* **2009**, *131*, 034111.
(87) Goerigk, L.; Grimme, S. *J. Chem. Theory Comput.* **2011**, *7*, 291.
(88) Shao, Y.; Molnar, L. F.; Jung, Y.; Kussmann, J.; Ochsenfeld, C.; Brown, S. T.; Gilbert, A. T. B.; Slipchenko, L. V.; Levchenko, S. V.; O'Neill, D. P.; R. A., D., Jr.; Lochan, R. C.; Wang, T.; Beran, G. J. O.; Besley, N. A.; Herbert, J. M.; Lin, C. Y.; Voorhis, T. V.; Chien, S. H.; Sodt, A.; Steele, R. P.; Rassolov, V. A.; Maslen, P. E.; Korambath, P. P.; Adamson, R. D.; Austin, B.; Baker, J.; Byrd, E. F. C.; Dachsel, H.; Doerksen, R. J.; Dreuw, A.; Dunietz, B. D.; Dutoi, A. D.; Furlani, T. R.; Gwaltney, S. R.; Heyden, A.; Hirata, S.; Hsu, C.-P.; Kedziora, G.; Khalliulin, R. Z.; Klunzinger, P.; Lee, A. M.; Lee, M. S.; Liang, W.; Lotan, I.; Nair, N.; Peters, B.; Proynov, E. I.; Pieniazek, P. A.; Rhee, Y. M.; Ritchie, J.; Rosta, E.; Sherrill, C. D.; Simmonett, A. C.; Subotnik, J. E.; Woodcock, H. L.; Zhang, W.; Bell, A. T.; Chakraborty, A. K.; Chipman, D. M.; Keil, F. J.; Warshel, A.; Hehre, W. J.; Schaefer, H. F.; Kong, J.; Krylov, A. I.; Gill, P. M. W.; Head-Gordon, M. *Phys. Chem. Chem. Phys.* **2006**, *8*, 3172–3191.
(89) Frisch, M. J.; Trucks, G. W.; Schlegel, H. B.; Scuseria, G. E.; Robb, M. A.; Cheeseman, J. R.; Scalmani, G.; Barone, V.; Mennucci, B.; Petersson, G. A.; Nakatsuji, H.; Caricato, M.; Li, X.; Hratchian, H. P.; Izmaylov, A. F.; Bloino, J.; Zheng, G.; Sonnenberg, J. L.; Hada, M.; Ehara, M.; Toyota, K.; Fukuda, R.; Hasegawa, J.; Ishida, M.; Nakajima, T.; Honda, Y.; Kitao, O.; Nakai, H.; Vreven, T.; Montgomery, J. A., Jr.; Peralta, J. E.; Ogliaro, F.; Bearpark, M.; Heyd, J. J.; Brothers, E.; Kudin, K. N.; Staroverov, V. N.; Kobayashi, R.; Normand, J.; Raghavachari, K.; Rendell, A.; Burant, J. C.; Iyengar, S. S.; Tomasi, J.; Cossi, M.; Rega, N.; Millam, N. J.; Klene, M.; Knox, J. E.; Cross, J. B.; Bakken, V.; Adamo, C.; Jaramillo, J.; Gomperts, R.; Stratmann, R. E.; Yazyev, O.; Austin, A. J.; Cammi, R.; Pomelli, C.; Ochterski, J. W.; Martin, R. L.; Morokuma, K.; Zakrzewski, V. G.; Voth, G. A.; Salvador, P.; Dannenberg, J. J.; Dapprich, S.; Daniels, A. D.; Farkas, Ö.; Foresman, J. B.; Ortiz, J. V.; Cioslowski, J.; Fox, D. J. *Gaussian 09*, revision B.01; Gaussian Inc.: Wallingford, CT, 2009.
(90) Valiev, M.; Bylaska, E.; Govind, N.; Kowalski, K.; Straatsma, T.; van Dam, H.; Wang, D.; Nieplocha, J.; Apra, E.; Windus, T.; de Jong, W. *Comput. Phys. Commun.* **2010**, *181*, 1477.
(91) Crawford, T. D.; Sherrill, C. D.; Valeev, E. F.; Fermann, J. T.; King, R. A.; Leininger, M. L.; Brown, S. T.; Janssen, C. L.; Seidl, E. T.; Kenny, J. P.; Allen, W. D. *J. Comput. Chem.* **2007**, *28*, 1610–1616.

(92) Patkowski, K.; Szalewicz, K.; Jeziorski, B. *J. Chem. Phys.* **2006**, *125*, 154107.
(93) Zhao, Y.; Truhlar, D. G. *J. Chem. Theory Comput.* **2007**, *3*, 289–300.
(94) Sherrill, C. D.; Takatani, T.; Hohenstein, E. G. *J. Phys. Chem. A* **2009**, *113*, 10146–10159.
(95) Hohenstein, E. G.; Chill, S. T.; Sherrill, C. D. *J. Chem. Theory Comput.* **2008**, *4*, 1996–2000.
(96) Thanthiriwatte, K. S.; Hohenstein, E. G.; Burns, L. A.; Sherrill, C. D. *J. Chem. Theory Comput.* **2011**, *7*, 88–96.

JCTC Journal of Chemical Theory and Computation

ARTICLE

pubs.acs.org/JCTC

Obtaining Good Performance With Triple-ζ-Type Basis Sets in Double-Hybrid Density Functional Theory Procedures

Bun Chan* and Leo Radom*

School of Chemistry and ARC Center of Excellence for Free Radical Chemistry and Biotechnology, University of Sydney, Sydney, NSW 2006, Australia

Supporting Information

ABSTRACT: A variety of combinations of B-LYP-based double-hybrid density functional theory (DHDFT) procedures and basis sets have been examined. A general observation is that the optimal combination of exchange contributions is in the proximity of 30% Becke 1988 (B88) exchange and 70% Hartree−Fock (HF) exchange, while for the correlation contributions, the use of independently optimized spin-component-scaled Møller−Plesset second-order perturbation theory (SCS-MP2) parameters (MP2OS and MP2SS) is beneficial. The triple-ζ Dunning aug′-cc-pVTZ+d and Pople 6-311+G(3df,2p)+d basis sets are found to be cost-effective for DHDFT methods. As a result, we have formulated the DuT-D3 DHDFT procedure, which employs the aug′-cc-pVTZ+d basis set and includes 30% B88 and 70% HF exchange energies, 59% LYP, 47% MP2OS, and 36% MP2SS correlation energies, and a D3 dispersion correction with the parameters s_6 = 0.5, $s_{r,6}$ = 1.569, and s_8 = 0.35. Likewise, the PoT-D3 DHDFT procedure was formulated with the 6-311+G(3df,2p)+d basis set and has 32% B88 and 68% HF exchange energies, 63% LYP, 46% MP2OS, and 27% MP2SS correlation energies, and the D3 parameters s_6 = 0.5, $s_{r,6}$ = 1.569, and s_8 = 0.30. Testing using the large E3 set of 740 energies demonstrates the robustness of these methods. Further comparisons show that the performance of these methods, particularly DuT-D3, compares favorably with the previously reported DSD-B-LYP and DSD-B-LYP-D3 methods used in conjunction with quadruple-ζ aug′-pc3+d and aug′-def2-QZVP basis sets but at lower computational expense. The previously reported ωB97X-(LP)/6-311++G(3df,3pd) procedure also performs very well. Our findings highlight the cost-effectiveness of appropriate- and moderate-sized triple-ζ basis sets in the application of DHDFT procedures.

INTRODUCTION

The appearance of the B2-PLYP method[1] has sparked considerable interest in the further development of double-hybrid density functional theory (DHDFT) procedures[2−13] due to their superior performance when compared with conventional DFT methods.[12,14] The DHDFT procedures contain wave function-type components, namely Hartree−Fock exchange and Møller−Plesset second-order perturbation theory (MP2) correlation. For instance, the energy given by B2-PLYP is evaluated with exchange energies from Becke 1988 (B88, E_X^{B88}) and Hartree−Fock (HF, E_X^{HF}) and correlation energies from Lee−Yang−Parr (LYP, E_C^{LYP}) and MP2 (E_C^{MP2}), according to eq 1:

$$E_{B2\text{-}PLYP} = c_{B88}E_X^{B88} + c_{HF}E_X^{HF} + c_{LYP}E_C^{LYP} + c_{MP2}E_C^{MP2} \quad (1)$$

The coefficients for the various components were determined[1] by fitting to the heats of formation in the G2/97 training set,[15] with the conditions $c_{B88} + c_{HF} = 1$ and $c_{LYP} + c_{MP2} = 1$. The values recommended for B2-PLYP are c_{B88} = 0.47, c_{HF} = 0.53, c_{LYP} = 0.73, and c_{MP2} = 0.27. A variety of DHDFT procedures have been subsequently developed with the aim of further improving the accuracy and the versatility.[2−12] These include the recently reported DSD-B-LYP procedure.[11] It makes use of the spin-component-scaled MP2 (SCS-MP2)[16] methodology, in which opposite-spin (MP2OS) and same-spin (MP2SS) contributions to the MP2 correlation energy are treated separately and includes an empirical correction (E_D)[17] for dispersion interactions:

$$E_{DSD\text{-}B\text{-}LYP} = c_{B88}E_X^{B88} + c_{HF}E_X^{HF} + c_{LYP}E_C^{LYP} + c_{OS}E_C^{MP2OS} + c_{SS}E_C^{MP2SS} + E_D \quad (2)$$

The five scaling coefficients and the parameter in E_D in eq 2 were obtained, with the condition $c_{B88} + c_{HF} = 1$, by fitting to a collection of six training sets, comprising atomization energies (W4/08),[4] main-group reaction barriers (DBH24),[18] weak interactions (S22),[19] artificially generated species (MB08)[20] and transition-metal chemistry (Pd[21] and Grubbs).[22] We will refer to this collection as the DSD set hereafter. The recommended scaling coefficients for DSD-B-LYP are c_{B88} = 0.31, c_{B88} = 0.69, c_{LYP} = 0.54, c_{OS} = 0.46, and c_{SS} = 0.37. Recently, a slightly modified DSD-B-LYP method (DSD-B-LYP-D3)[12] has been shown to perform well on the diverse and sizable GMTKN30 test set.[12] This variant uses the D3 scheme[23] for the dispersion term.

The optimized parameters for DHDFT methods have often been obtained using quadruple-ζ basis sets of different styles. For instance, the coefficients for the original B2-PLYP[1] were obtained in combination with QZV3P, which is a modified first-generation Ahlrichs basis set.[24] The variants B2T-PLYP,[3] B2K-PLYP,[3] and B2GP-PLYP[4] were derived mainly from a quadruple-ζ polarization-consistent (Jensen) basis set,[25] namely aug-pc3. A correlation-consistent (Dunning) basis set,[26] cc-pVQZ, was used

Received: June 10, 2011
Published: August 23, 2011

for ROB2-PLYP.[7] The ωB97X-2 procedure[6] was developed with the complete-basis-set limit using triple- and quadruple-ζ Dunning sets for extrapolation. A mixture of aug′-pc3 (aug′ denotes the inclusion of diffuse functions on nonhydrogen atoms) and second-generation Ahlrichs basis sets,[27] def2-QZVP and def2-QZVPP, were the major basis sets employed for the development of DSD-B-LYP.[11] The recently proposed PTPSS[12] and PW-PB95[12] procedures were optimized mainly with the def2-QZVP basis set. Nonetheless, smaller triple-ζ basis sets have also been employed for the development of DHDFT procedures, but the resulting procedures show variable performance. Thus, the B2−P3LYP method[5] was optimized for cc-pVTZ, and this combination leads to a mean absolute deviation (MAD) from benchmark values of 13.0 kJ mol^{-1} for the G2/97 set of atomization energies.[15] The Pople basis set 6-311+G(3df,2p)[28] was employed in deriving XYG3,[8] and it has an MAD of 7.6 kJ mol^{-1} for the G3/99 set of heats of formation (ΔH_f).[29] In addition, the ωB97X-2(LP) procedure[6] was parametrized with the 6-311++G(3df,3pd) basis set and yields a very impressive MAD of 6.4 kJ mol^{-1} for G3/99 ΔH_f.

The large variety of mostly quadruple-ζ basis sets employed in the development of DHDFT procedures begs the following questions: (1) Is a quadruple-ζ basis set required for good performance, or can one utilize more manageable triple-ζ basis sets without significantly sacrificing accuracy? (2) Do basis sets of similar size but of different types give comparable results, or is one type of basis set particularly suitable for DHDFT methods?

Goerigk and Grimme have attempted to answer the first question by testing a variety of DHDFT procedures on the GMTKN30 set with the (aug-)def2-TZVPP and (aug-)def2-QZVP basis sets.[12] They find that, for the PW-PB95-D3 procedure for which the basis set dependence is the smallest, the MAD from benchmark values for the triple-ζ basis set is greater than that for the quadruple-ζ basis set by 0.2 kcal mol^{-1} (∼0.8 kJ mol^{-1}).[30] Because DHDFT contains exchange and correlation components from both DFT and wave function methods, the second question is particularly interesting. Does DHDFT work better with the Jensen basis sets, which are designed for DFT procedures, or with the Dunning sets that are tailored for wave function correlation methods? How about the performance of the Ahlrichs sets that are often used in the development of DHDFT or the popular Pople basis sets?

The aim of the present study is to address these questions. We also attempt to identify other important components of the calculations that contribute to the good performance of DHDFT procedures and features that would broaden their applicability. In particular, we strive to identify triple-ζ basis sets that yield results of comparable quality to the larger quadruple-ζ basis sets, thus reducing the computational cost for performing DHDFT calculations and enabling their use in situations where the use of a quadruple-ζ basis set is computationally too demanding.

COMPUTATIONAL DETAILS

Standard wave function and DFT calculations[31] were carried out with Gaussian 03[32] and Gaussian 09.[33] D3 dispersion corrections were obtained with the dftd3 program.[23] Unless otherwise noted, geometries were optimized using BMK[34] with the 6-31+G(2df,p) basis set. This level of theory has previously been shown to represent a cost-effective means for obtaining reliable geometries.[35] Energies at 0 K incorporate zero-point vibrational energies, obtained with scaled (0.9770) BMK/6-31+G(2df,p) frequencies, while 298 K enthalpies additionally include thermal corrections derived from frequencies scaled by 0.9627.[35,36]

While more detailed descriptions of the various basis sets employed in the present study will be given within the main text, for convenience we provide a brief summary here. For the sake of simplicity, in the tables we abbreviate the Dunning basis sets cc-pV*n*Z as V*n*Z, and the aug-cc-pV*n*Z basis sets as AV*n*Z, where *n* = T and Q. The use of ′ in a basis set, for example, in aug′-cc-pVTZ+d and def2-TZVPD′+d, indicates the use of diffuse functions only on nonhydrogen atoms. The aug′-def2-TZVP basis set represents the def2-TZVP basis set augmented with diffuse functions taken from aug′-cc-pVTZ. We have also employed the aug′-def2-QZVP basis set, in which diffuse functions from aug′-cc-pVQZ are added to the def2-QZVP basis set. Our baseline basis set for the purpose of comparison is the Dunning (aug-)cc-pVTZ basis set, in which (aug-) denotes the inclusion of diffuse functions only for the calculation of electron affinities. The corresponding selectively augmented triple-ζ Pople, Ahlrichs, and Jensen basis sets are denoted 6-311(++)G(3df,2p), def2-TZVP(D), and (aug-)pc2, respectively. They are derived from the combinations 6-311G(3df,2p)/6-311++G(3df,2p), def2-TZVP/def2-TZVPD,[37] and pc2/aug-pc2.

Basis sets that are external to the Gaussian 03 and 09 programs were obtained from the Environmental Molecular Sciences Laboratory (EMSL) basis set library.[38] The inclusion of tight d functions for the elements Al−Ar is indicated by the suffix +d, as, for example, in aug′-cc-pVTZ+d and 6-311+G(3df,2p)+d. We derived the tight d functions for use in the aug′-pc2+d and aug′-pc3+d basis sets according to the recommendation by Martin.[39] Thus, the exponents were obtained by scaling the existing largest d exponents by 2.5. We also employ the same approach for obtaining tight d functions for use in the def2-TZVPD′+d, aug′-def2-TZVP+d, and 6-311+G(3df,2p)+d basis sets.

The frozen-core approximation is employed in the evaluation of the MP2 correlation energy, unless otherwise noted. Parameters for the quantum mechanical DHDFT procedures that were reoptimized in the present study were obtained by fitting to the G2/97 training set, while the parameters for the empirical D3 dispersion correction were determined by adjustment for the larger E3 set, as we find that this is necessary in order to provide further robustness for a more diverse range of systems. Following previous practice,[35] our optimization procedures involved minimizing the average of the mean absolute deviation (MAD) from benchmark values and the standard deviation (SD) of these deviations. All relative energies are reported in kJ mol^{-1}.

RESULTS AND DISCUSSION

In the present study, we focus on the B-LYP functional as the DFT component, as this is by far the most commonly employed functional in DHDFT procedures.[1,3−5,7−11] For most of the study, we examine three forms of DHDFT methods: (1) B2-PLYP-type procedures where the DHDFT energy is derived from eq 1 and satisfies the conditions $c_{B88} + c_{HF} = 1$ and $c_{LYP} + c_{MP2} = 1$. Included in this category are B2-PLYP, B2T-PLYP, B2GP-PLYP, and B2K-PLYP, which offer increasing wave function contributions to the DHDFT energy in the above order. We term such procedures STD-DHDFT, where STD denotes "standard"; (2) DHDFT procedures that are similar to B2-PLYP but with c_{MP2} reoptimized independently of the default value of c_{LYP}, which means that $c_{LYP} + c_{MP2}$ is no longer constrained to be equal to 1. We term such procedures UCMP-DHDFT, where UCMP

Table 1. MADs From Experimental Values (kJ mol^{-1}) for Various DHDFT Procedures with a Variety of Basis Sets for the G2/97 Set and its Subsets

	1	2	3	4	5	6	7	8	9	10	11	12
DHDFT	B2-PLYP	B2-PLYP[c]	B2-PLYP	B2-PLYP	B2-PLYP	B2-PLYP	B2-PLYP	B2-PLYP	B2-PLYP	B2T-PLYP	B2GP-PLYP	B2K-PLYP
basis set[a]	(A)VTZ	(A)VTZ	(A)VTZ+d	(A)VQZ	AVTZ	A′VTZ	6-311(++)G (3df,2p)	def2-TZVP(D)	(aug-)pc2	(A)VTZ	(A)VTZ	(A)VTZ
						STD-DHDFT						
G2/97[b]	16.7	12.6	15.2	9.8	14.3	14.7	14.3	20.4	13.4	19.9	19.8	22.3
ΔH_f	22.2	14.1	19.4	10.2	19.0	19.7	16.1	27.4	16.3	28.9	29.5	34.5
IE	14.9	14.6	14.9	11.9	11.8	11.9	15.9	14.3	13.5	13.9	12.9	12.2
EA	7.1	7.0	6.7	6.5	7.1	7.3	8.3	14.1	7.1	8.0	7.9	8.7
PA	4.8	4.7	4.2	3.7	5.9	6.0	7.3	4.2	3.4	5.0	5.2	5.6
						UCMP-DHDFT[d]						
G2/97	10.2	10.2	9.1	8.7	9.2	9.3	12.0	11.7	9.3	9.0	8.7	8.7
ΔH_f	10.4	10.1	8.4	8.4	9.6	9.8	13.0	12.4	9.0	9.0	8.8	9.1
IE	12.4	13.3	12.6	11.2	10.3	10.3	14.2	11.3	12.1	10.9	10.1	9.1
EA	6.9	6.5	6.4	6.4	6.7	6.8	6.9	11.6	6.7	6.8	7.0	7.4
PA	4.7	4.6	3.9	3.8	6.4	6.5	7.2	4.6	3.5	4.8	4.8	5.0
						SCS-DHDFT[e]						
G2/97	10.1	10.2	9.0	8.7	9.1	9.2	11.1	10.8	9.3	9.0	8.7	8.5
ΔH_f	10.3	10.1	8.1	8.4	9.6	9.7	11.0	10.6	9.0	8.9	8.8	8.9
IE	12.5	13.3	12.6	11.2	10.2	10.2	14.5	11.3	12.0	10.9	10.1	9.1
EA	6.7	6.4	6.3	6.3	6.6	6.7	6.9	11.5	6.6	6.8	6.8	7.2
PA	4.5	4.6	3.9	3.6	6.1	6.2	6.7	3.5	3.4	4.7	4.7	5.0
timing[f]	1.0	1.1	1.0	12.1	4.6	2.8	0.9	0.6	1.0	1.0	1.0	1.0

[a] (A), (++), (D) and (aug-) indicate inclusion of diffuse functions only for the calculation of electron affinities, V*n*Z = cc-pV*n*Z, AV*n*Z = aug-cc-pV*n*Z, A′V*n*Z = V*n*Z for hydrogen and AV*n*Z for other elements. [b] ΔH_f = heat of formation (298 K), IE = ionization energy (0 K), EA = electron affinity (0 K), and PA = proton affinity (0 K). [c] All electrons are correlated for the MP2 treatment. [d] Each c_{MP2} parameter is optimized for the specific procedure and basis set. [e] The c_{OS} and c_{SS} parameters are optimized for each method. [f] Relative to the total time for B2-PLYP/(A)VTZ calculations for the G2/97 set.

signifies "unconstrained MP2 correlation"; and (3) DSD-B-LYP-like procedures[11] in which the energy is given by eq 2 with c_{OS} and c_{SS} optimized but without the D correction. We term such procedures SCS-DHDFT. While we will examine the effect of dispersion corrections at a later stage, we attempt initially to recover the maximum amount of long-range effects using quantum mechanics and employ the dispersion correction to provide further improvement to the procedure.

Important Components for DHDFT Procedures. In this section, we use frozen-core B2-PLYP/(aug-)cc-pVTZ as our baseline method to examine a variety of options for improving the performance. The (aug-)cc-pVTZ basis set includes diffuse functions only for the evaluation of electron affinities (EAs), which we deem a minimal requirement for obtaining reliable energies. The MADs for the G2/97 set and its subsets are given in Table 1.

We first note that, regardless of the basis set used, the MADs for the three different types of DHDFT procedures generally decrease in the order STD-DHDFT > UCMP-DHDFT ~ SCS-DHDFT. In particular, STD-DHDFT generally yields significantly poorer performance for ΔH_f than is obtained for the corresponding UCMP-DHDFT and SCS-DHDFT procedures. We have examined the values of the reoptimized c_{MP2} parameters in the UCMP-DHDFT procedures (Supporting Information, Table S1) and find that they are all larger than their originally recommended values. In other words, the imposed constraint of $c_{LYP} + c_{MP2} = 1$ in the original B2-PLYP formalism appears to lead to insufficient incorporation of electron correlation. Grimme has suggested that the inclusion of a relatively large amount of nonlocal correlation is the major contributing factor for the good performance of the XYG3 procedure.[12] Our finding of an optimal correlation energy in excess of $c_{LYP} + c_{MP2} = 1$ is consistent with such a proposition. It is also noteworthy that the added flexibility in the SCS-DHDFT scheme does not lead to a significant improvement over UCMP-DHDFT in most cases.

We now examine the various options for improving frozen-core B2-PLYP, UCMP-B2-PLYP, and SCS-B2-PLYP with the (aug-)cc-pVTZ basis set for which the MADs are 16.7, 10.2, and 10.1 kJ mol^{-1}, respectively (Table 1, column 1). We find that, while correlating all electrons for MP2 (column 2) appears to be beneficial for B2-PLYP, it provides little improvement for UCMP-B2-PLYP and SCS-B2-PLYP. On the other hand, the inclusion of tight d functions for second-row atoms leads to somewhat lower overall MADs for all three variants of B2-PLYP (column 3). When the quadruple-ζ basis set is used (column 4), the MADs are all lowered substantially, with values of ~8.5–10 kJ mol^{-1} for the overall G2/97 set. A small overall improvement is also achieved when one includes diffuse functions for the calculation of heats of formation, ionization energies (IEs), and proton affinities (PAs) as well as for electron affinities (EAs)

Table 2. MADs from Experimental Values (kJ mol^{-1}) for the G2/97 Set and its Subsets for B2-PLYP-Type and B2K-PLYP-Type Procedures with a Variety of Basis Sets[a]

	1	2	3	4	5	6	7	8	9	10
DHDFT	B2-PLYP	B2-PLYP	B2-PLYP	B2-PLYP	B2-PLYP	B2K-PLYP	B2K-PLYP	B2K-PLYP	B2K-PLYP	B2K-PLYP
basis set	def2-TZVPD′+d	6-311+G(3df,2p)+d	aug′-pc2+d	aug′-def2-TZVP+d	A′VTZ+d	def2-TZVPD′+d	6-311+G(3df,2p)+d	aug′-pc2+d	aug′-def2-TZVP+d	A′VTZ+d
					STD-DHDFT					
G2/97	19.6	13.8	11.5	16.3	13.3	26.0	18.5	14.9	21.9	17.6
ΔH_f	25.6	17.1	13.1	22.8	17.0	39.3	27.2	20.6	34.7	26.7
IE	12.9	12.4	12.2	12.2	11.8	10.9	10.2	10.1	10.1	9.5
EA	16.2	8.7	7.2	7.2	7.0	17.8	10.4	9.1	8.9	8.5
PA	6.4	5.8	4.8	7.2	5.2	6.5	5.8	4.8	7.2	5.2
					UCMP-DHDFT[b]					
G2/97	11.5	10.1	8.9	10.0	8.4	10.4	8.8	7.5	9.2	6.6
ΔH_f	11.8	11.0	8.6	11.4	8.1	10.8	9.6	7.0	10.9	5.7
IE	10.3	10.9	11.2	10.1	10.3	8.1	8.4	8.6	8.0	7.9
EA	13.4	6.9	6.8	6.5	6.3	13.7	7.9	7.6	7.2	7.0
PA	7.2	6.3	5.0	7.9	5.7	7.0	6.2	5.0	7.8	5.5
					SCS-DHDFT[c]					
G2/97	10.8	9.5	8.7	9.2	8.3	8.4	7.5	7.2	6.8	6.1
ΔH_f	10.4	10.0	8.3	9.9	8.1	6.6	7.0	6.4	6.3	5.0
IE	10.2	10.9	11.2	10.0	10.2	7.9	8.3	8.6	7.8	7.7
EA	13.5	6.7	6.6	6.3	6.3	13.9	8.0	7.4	6.7	6.7
PA	5.7	4.9	4.4	6.3	5.1	5.5	4.8	4.4	6.2	4.9
timing[d]	1.0	1.1	2.9	2.0	2.8	1.0	1.2	3.0	2.0	2.8

[a] Augmented in each case with diffuse functions for heavy atoms and tight d functions for second-row group 13−18 elements. [b] Each c_{MP2} parameter is optimized for the specific procedure and basis set. [c] The c_{OS} and c_{SS} parameters are optimized for each method. [d] Relative to the total time for B2-PLYP/(A)VTZ calculations for the G2/97 set.

(column 5). Thus, the MADs for the G2/97 set for B2-PLYP, UCMP-B2-PLYP and SCS-B2-PLYP, with aug-cc-pVTZ, are 14.3, 9.2, and 9.1 kJ mol^{-1}, respectively. The lowering of the MADs for ΔH_f and IEs is small but significant, while the performance for PAs is slightly worse. We find that exclusion of diffuse functions on hydrogen atoms from the aug-cc-pVTZ basis set, i.e., aug′-cc-pVTZ (column 6), does not lead to a significant deterioration of performance.

Turning our attention to timing comparisons (Table 1), we find that, for the G2/97 set, the use of all electrons for the MP2 correlation treatment (column 2) and the inclusion of tight d functions (column 3) does not significantly affect the timings when compared with frozen-core (aug-)cc-pVTZ (column 1). Increasing the basis set size to (aug-)cc-pVQZ (column 4) is significantly more expensive (12.1×). The use of the aug-cc-pVTZ basis set (column 5) leads to a less substantial increase in timing (4.6×), while the omission of diffuse functions for hydrogen in aug′-cc-pVTZ (column 6) further reduces the time required (2.8×). Given that (aug-)cc-pVQZ, aug-cc-pVTZ, and aug′-cc-pVTZ basis sets lead to similar results for UCMP-B2-PLYP and SCS-B2-PLYP, we consider the use of aug′-cc-pVTZ a more cost-effective means for improving the performance than (aug-)cc-pVQZ. We also deem the inclusion of tight d functions cost-effective, as it leads to a small but noticeable improvement in performance, with minimal increase in computational cost.

We next examine the performance of four different families of partially augmented triple-ζ basis sets (columns 1 and 7−9) used in conjunction with the three types of DHDFT procedures, namely B2-PLYP, UCMP-B2-PLYP, and SCS-B2-PLYP (Table 1). These basis sets include diffuse functions only for the calculation of EAs. We can see that 6-311(++)G(3df,2p) (column 7) performs somewhat better than (aug-)cc-pVTZ for B2-PLYP but does slightly less well for UCMP-B2-PLYP and SCS-B2-PLYP. The partially augmented Ahlrichs set def2-TZVP(D) (column 8) comprises the def2-TZVP basis set for neutral molecules and cations and the recently developed def2-TZVPD basis set for anions,[37] in which a small set of diffuse functions is added, and they are optimized for the calculation of polarizability. The use of the def2-TZVP(D) basis set yields larger MADs for B2-PLYP when compared with (aug-)cc-pVTZ. Its performance versus the Dunning (aug-)cc-pVTZ set appears to be only slightly worse when combined with UCMP-B2-PLYP and SCS-B2-PLYP. The use of the Jensen set (aug-)pc2 (column 9) gives MADs that are lower than those for (aug-)cc-pVTZ, regardless of the type of DHDFT procedure employed. We also note that the (aug-)pc2 basis set yields MADs that are not too different from those obtained with aug-cc-pVTZ (column 5) and aug′-cc-pVTZ (column 6).

We now examine the effect of the amount of wave function contribution on the performance of the DHDFT procedures with the (aug-)cc-pVTZ basis set (Table 1, columns 1 and 10−12).

We find that, for STD-DHDFT-type procedures, the overall MADs for the G2/97 set increase in the order B2-PLYP (column 1) < B2T-PLYP (column 10) ~ B2GP-PLYP (column 11) < B2K-PLYP (column 12), i.e., the MADs increase as the wave function fraction becomes larger. This is mainly associated with the variation in the performance for ΔH_f. For UCMP-DHDFT and SCS-DHDFT, however, the MADs decrease slightly with increasing wave function contribution.

Favorable Combinations of DHDFT Procedures and Basis Sets. While the results presented in Table 1 have provided a useful indication of the variation in the performance of a DHDFT procedure with respect to its form and the basis set employed, the most favorable combination is not yet clear. In search of the optimal and most cost-effective combination of a DHDFT procedure with a specific basis set, we have further examined B2-PLYP- and B2K-PLYP-type procedures combined with the four families of triple-ζ basis sets, in each case augmented with diffuse functions for nonhydrogen atoms and with tight d functions for second-row group 13−18 elements.

We choose B2-PLYP and B2K-PLYP as they represent the two extremes of the DHDFT methods considered, with the former having the smallest and the latter having the largest wave function contributions. For the Ahlrichs def2-TZVP basis set, we have considered two types of diffuse augmentation: (1) the def2-TZVPD′ basis set, which makes use of the def2-TZVPD diffuse functions on nonhydrogen atoms; and (2) the aug′-def2-TZVP basis set, where diffuse functions are taken from the Dunning aug′-cc-pVTZ set. The MADs for the G2/97 set for these combinations are shown in Table 2.

A comparison between Tables 1 (columns 1 and 7−9) and 2 (columns 1−5) shows that the inclusion of additional diffuse functions and tight d functions leads to somewhat lower MADs for the B2-PLYP, UCMP-B2-PLYP, and SCS-B2-PLYP procedures, with small but noticeable improvements for ΔH_f and IE found in most cases. We again find that the MADs decrease in the order STD-DHDFT > UCMP-DHDFT ~ SCS-DHDFT, which is similar to the trends in Table 1. We also see that the performance of STD-DHDFT for ΔH_f is significantly poorer than those of the corresponding UCMP-DHDFT and SCS-DHDFT procedures. We note that the slightly lower MADs for SCS-DHDFT compared with UCMP-DHDFT are somewhat more obvious in these cases.

We now compare the performance of the different basis sets. It can be seen that, for the STD-DHDFT procedures B2-PLYP (columns 1−5) and B2K-PLYP (columns 6−10), the MADs decrease in the order def2-TZVPD′+d (columns 1 and 6) > aug′-def2-TZVP+d (columns 4 and 9) > 6-311+G(3df,2p)+d (columns 2 and 7) > aug′-cc-pVTZ+d (columns 5 and 10) > aug′-pc2+d (columns 3 and 8). Thus, while (aug-)cc-pVTZ performs less well than the 6-311(++)G(3df,2p) basis set (Table 1, columns 1 and 7), the inclusion of extra functions in the aug′-cc-pVTZ+d basis set leads to comparable results to the corresponding Pople set. In fact, when we make the comparison for UCMP-DHDFT and SCS-DHDFT, we find that, although all basis sets lead to respectable MADs, the Dunning set (columns 5 and 10) somewhat outperforms the other types of basis sets. It is also noteworthy that the aug′-def2-TZVP+d basis set (columns 4 and 9) yields lower MADs than those for the def2-TZVPD′+d basis set (columns 1 and 6). Rappoport and Furche have pointed out the potential difficulty of the smaller set of diffuse functions in def2-TZVPD for describing more demanding systems, such as anions.[37] Our observation is consistent with such a proposition.

Table 3. MADs from Experimental Values (kJ mol^{-1}) for the G2/97 Set and its Subsets for B2K-PLYP-Type Procedures

	frozen core		all electron	
	A′VTZ+d	AVQZ+d	A′VTZ+d	AVQZ+d
		B2K-PLYP		
G2/97	17.6	9.5	9.7	7.7
ΔH_f	26.7	11.2	10.8	7.7
IE	9.5	8.5	9.2	8.3
EA	8.5	7.4	8.4	7.3
PA	5.2	5.2	4.8	4.9
		UCMP-B2K-PLYP[a]		
G2/97	6.6	6.6	7.8	7.7
ΔH_f	5.7	5.8	7.5	7.7
IE	7.9	7.9	8.5	8.3
EA	7.0	6.7	7.7	7.3
PA	5.5	5.3	4.8	5.0
		SCS-B2K-PLYP[b]		
G2/97	6.1	6.4	7.5	7.6
ΔH_f	5.0	5.5	7.0	7.5
IE	7.7	7.9	8.6	8.3
EA	6.7	6.6	7.7	7.3
PA	4.9	4.9	4.6	4.7
timing[c]	2.8	64.5	3.2	70.6

[a] Each c_{MP2} parameter is optimized for the specific basis set and core-correlation options. [b] The c_{OS} and c_{SS} parameters are optimized for each method. [c] Relative to the total time for B2-PLYP/(A)VTZ calculations for the G2/97 set.

While the aug′-cc-pVTZ+d basis set yields the lowest MADs for SCS-DHDFT, and we deem its use sufficiently economical for a wide range of applications, we note that the use of the 6-311+G(3df,2p)+d basis is also cost-effective. It offers further savings in computational resources over the Dunning set, but its performance is slightly worse.

Turning our attention to the effect of the amount of wave function contribution on the performance of the DHDFT procedures (Table 2), we find that B2-PLYP gives lower MADs than those for B2K-PLYP. On the other hand, it can be seen that UCMP-B2K-PLYP outperforms UCMP-B2-PLYP, and likewise SCS-B2K-PLYP yields lower MADs than those for SCS-B2-PLYP. These observations are also consistent with the results in Table 1 (columns 1 and 12). Overall, we find the combination of SCS-B2K-PLYP and aug′-cc-pVTZ+d (Table 2, column 10) gives the lowest MAD of 6.1 kJ mol^{-1} for the G2/97 set of energies. At the other end of the spectrum, it is striking that if one employs B2K-PLYP with the def2-TZVPD′+d basis set (column 6), a substantially larger MAD of 26.0 kJ mol^{-1} is obtained! This emphasizes the importance of carefully choosing the combination of method and basis set.

At this point it is instructive to summarize our observations so far. We find that the use of diffuse functions is beneficial not only for EAs but also for the calculation of ΔH_f and IE. In addition, we notice that the inclusion of excess correlation is favorable. Combining these two main ingredients and other minor details, we find that the frozen-core SCS-B2K-PLYP/aug′-cc-pVTZ+d procedure offers a cost-effective means for obtaining reliable results, with an MAD of 6.1 kJ mol^{-1} for the G2/97 test set.

Table 4. MADs from Experimental Values (kJ mol^{-1}) of Various Combinations of c_{OS} and c_{SS} Parameters, Core-Correlation Options[a] and Basis Sets for SCS-B2K-PLYP on the G2/97 Set

parameter optimization level	basis set and core-correlation options: A′VTZ+d (FC)	AVQZ+d (FC)	A′VTZ+d (FU)	AVQZ+d (FU)
		G2/97		
A′VTZ+d (FC)	6.1	12.6	15.3	17.8
AVQZ+d (FC)	13.0	6.4	8.8	10.1
A′VTZ+d (FU)	13.8	6.5	7.5	9.6
AVQZ+d (FU)	17.8	9.5	8.3	7.6
		ΔH_f		
A′VTZ+d (FC)	5.0	18.2	24.0	28.7
AVQZ+d (FC)	18.1	5.5	9.9	13.0
A′VTZ+d (FU)	19.6	5.6	7.0	12.0
AVQZ+d (FU)	27.1	11.1	8.2	7.5
		IE, EA, and PA		
A′VTZ+d (FC)	7.2	7.2	6.9	7.3
AVQZ+d (FC)	8.1	7.3	7.7	7.2
A′VTZ+d (FU)	8.2	7.3	8.0	7.3
AVQZ+d (FU)	8.9	7.8	8.5	7.7

[a] FC = frozen-core, and FU = full, i.e., all electrons.

On the other hand, from Table 1, we see that the use of (aug-)cc-pVQZ (column 4) offers a noteworthy improvement over (aug-)cc-pVTZ. It is reasonable to ask: are we able to further improve the performance by using aug-cc-pVQZ+d instead of aug′-cc-pVTZ+d? In order to address this question, we have carried out investigations in which we have examined both frozen-core and all-electron B2K-PLYP-type procedures. The results are shown in Table 3.

We can see that, for frozen-core B2K-PLYP, there is a substantial improvement in going from aug′-cc-pVTZ+d to aug-cc-pVQZ+d. This can mainly be attributed to poor ΔH_f predictions with frozen-core B2K-PLYP when the aug′-cc-pVTZ+d basis set is used. The corresponding improvement for all-electron B2K-PLYP is much smaller. In particular, all-electron B2K-PLYP/aug′-cc-pVTZ+d gives an MAD for ΔH_f (10.8 kJ mol^{-1}) that is somewhat larger than that for all-electron B2K-PLYP/aug-cc-pVQZ+d (7.7 kJ mol^{-1}) but much smaller than that for frozen-core B2K-PLYP/aug′-cc-pVTZ+d (26.7 kJ mol^{-1}). For UCMP-B2K-PLYP and SCS-B2K-PLYP with either frozen-core or all-electron MP2, the use of aug-cc-pVQZ+d yields results that are very similar to those obtained with aug′-cc-pVTZ+d. In comparing the performance of the frozen-core calculations with their all-electron counterparts, we find that, for B2K-PLYP, the use of all electrons in the MP2 treatment leads to lower MADs. On the other hand, the performance in fact slightly deteriorates for UCMP-B2K-PLYP and SCS-B2K-PLYP when one employs all-electron MP2. This is consistent with the observations in Table 1 (columns 1 and 2). Remarkably, the best combination of correlation treatment, theoretical method, and basis set remains frozen-core SCS-B2K-PLYP/aug′-cc-pVTZ+d.

Dependence of Performance on Optimized Parameters. When the empirical parameters in a procedure are optimized under a certain set of conditions, one potential pitfall is that the resulting method may not be able to adapt to a different set of conditions. For example, does the performance of the SCS-B2K-PLYP/aug′-cc-pVTZ+d procedure change significantly when a different basis set is used, but the c_{OS} and c_{SS} parameters optimized for aug′-cc-pVTZ+d are retained? Indeed, the desirability of using a basis set for which a DHDFT method is parametrized has been emphasized previously.[5,6,11] To this end, we have assessed the sensitivity of the performance of SCS-B2K-PLYP to different combinations of core-correlation options (frozen-core or all-electron) and basis sets (aug′-cc-pVTZ+d or aug-cc-pVQZ+d), with parameters optimized for the various core-correlation options and basis sets (Table 4).

We find that there is a large variation in the MADs for the G2/97 set for the different combinations, in which the performance of the procedure can deteriorate significantly when a set of mismatched parameters is used with certain combinations of core-correlation and basis-set options. The situation is worst when one stretches such "incompatibility" the most. Thus, the overall G2/97 MAD is largest (17.8 kJ mol^{-1}) when one employs parameters optimized for frozen-core aug′-cc-pVTZ+d but uses them in combination with all-electron aug-cc-pVQZ+d, and (coincidentally) vice versa. However, such large variations are mainly due to the differences in the performance for ΔH_f, where the use of matched parameters for frozen-core aug′-cc-pVTZ+d gives an MAD of 5.0 kJ mol^{-1}, but the use of this set of parameters for all-electron aug-cc-pVQZ+d yields the largest MAD of 28.7 kJ mol^{-1}.

On the other hand, the variation in performance for other thermochemical properties in G2/97 (IE, EA, and PA) is small, with MAD values that span a range of just 2 kJ mol^{-1}. We note that the smallest MAD for the IE, EA, and PA set of energies corresponds to the use of parameters optimized for frozen-core aug′-cc-pVTZ+d, applied to energies obtained from all-electron aug′-cc-pVTZ+d calculations. Upon inspection of the c_{OS} and c_{SS} parameters for the four procedures (Supporting Information, Table S1), we find that there is a larger variation in c_{OS} than in c_{SS}. In addition, c_{OS} is larger in magnitude than c_{SS}, and E_C^{MP2OS} is, in general, about three times larger than E_C^{MP2SS}. Thus, it appears that the variation in the $c_{OS}E_C^{MP2OS}$ term is a major contributing factor to the overall differences in the procedures.

New DuT-D3 Procedure and its Performance. Based on what we have learned from the previous sections, we have reoptimized the parameters c_{B88}, c_{HF}, c_{LYP}, c_{OS}, and c_{SS} for a B-LYP-based frozen-core SCS-DHDFT with the aug′-cc-pVTZ+d basis set. The new procedure will be referred to as DS-B-LYP/aug′-cc-pVTZ+d, owing to its similarity to DSD-B-LYP but without the D correction for dispersion.

$$E_{DS\text{-}B\text{-}LYP} = c_{B88}E_X^{B88} + c_{HF}E_X^{HF} + c_{LYP}E_C^{LYP} + c_{OS}E_C^{MP2OS} + c_{SS}E_C^{MP2SS} \quad (3)$$

Within the DS label, the D relates to the double-hybrid DFT procedure, while the S relates to the use of SCS-MP2 correlation. We then supplement this method with a D3 dispersion correction and term this procedure DS-B-LYP/aug′-cc-pVTZ+d-D3. We have also optimized the parameters for the 6-311+G(3df,2p)+d basis set,[40] and the resulting methods are denoted DS-B-LYP/6-311+G(3df,2p)+d and DS-B-LYP/6-311+G(3df,2p)+d-D3. For the sake of simplicity, we will refer to DS-B-LYP/aug′-cc-pVTZ+d,

Table 5. Scale Coefficients and Parameters for the D3 Corrections for the B2K-PLYP, SCS-B2K-PLYP, DuT-D3, PoT-D3, and DSD-B-LYP-D3 Procedures

DHDFT	B2K-PLYP[a]	SCS-B2K-PLYP[b,c]	DuT-D3[b,c]	PoT-D3[c,d]	DSD-B-LYP-D3[e]
c_{B88}	0.28	0.28	0.30	0.32	0.30
c_{HF}	0.72	0.72	0.70	0.68	0.70
c_{LYP}	0.58	0.58	0.59	0.63	0.56
c_{OS}	0.42	0.48	0.47	0.46	0.46
c_{SS}	0.42	0.39	0.36	0.27	0.40
s_6	–	–	0.5	0.5	0.5
$s_{r,6}$	–	–	1.569	1.569	1.569
s_8	–	–	0.35	0.30	0.705

[a] Ref 3. [b] Optimized in conjunction with the aug′-cc-pVTZ+d basis set. [c] Frozen-core approximation for MP2 correlation. [d] Optimized for 6-311+G(3df,2p)+d. [e] Scale coefficient values for frozen-core DSD-B-LYP from ref 11 and D3 parameters from ref 12.

DS-B-LYP/aug′-cc-pVTZ+d-D3, DS-B-LYP/6-311+G(3df,2p)+d, and DS-B-LYP/6-311+G(3df,2p)+d-D3 as the DuT, DuT-D3, PoT, and PoT-D3 procedures. The DuT denotes that the first two procedures are matched to the Dunning triple-ζ basis set, and PoT signifies the use of the Pople triple-ζ basis set in the latter two.

For DHDFT procedures, the D3 correction has three adjustable parameters, namely s_6, $s_{r,6}$, and s_8.[12,23] For the DuT-D3 and PoT-D3 procedures, we initially chose the parameters determined for the DSD-B-LYP-D3 procedure,[12] with values of 0.5, 1.569, and 0.705 for s_6, $s_{r,6}$, and s_8, respectively. Examination of the effect of modifying the three D3 parameters for the DuT-D3 and PoT-D3 procedures shows that the performance of the method is relatively insensitive to the values of s_6 and $s_{r,6}$. We have therefore adopted the DSD-B-LYP-D3 s_6 and $s_{r,6}$ values for both DuT-D3 and PoT-D3. On the other hand, altering the s_8 parameter has a greater influence on the results obtained with DuT-D3 and PoT-D3. In particular, we find that a smaller value of s_8 gives a more uniformly satisfactory description for the range of thermochemical properties considered in the present study. Thus, we have chosen values for s_8 of 0.35 and 0.30 for the DuT-D3 and PoT-D3 procedures, respectively.

We have also examined the effect of using the new D3(BJ) form[41] of dispersion correction. It makes use of the damping function of Becke and Johnson,[42] instead of the form of Chai and Head-Gordon[43] that is employed in the original D3 formulation. We find that, in general, D3 and D3(BJ) give comparable results when used in conjunction with DuT and PoT. The use of D3(BJ) gives a more noticeable improvement for the MB08 set, but this comes at the expense of a small but evidently worse performance on the S22 and Grubbs sets. Taking these results into account, we have opted for the original Chai and Head-Gordon approach for the DuT-D3 and PoT-D3 procedures.

While our discussion will mainly focus on DuT-D3 due to its higher accuracy, we note that, for the largest E3 test set that we used in the present study (see below), the DuT-D3 procedure is 3.4 times more expensive than the PoT-D3 procedure, while the latter has an MAD that is only 0.7 kJ mol^{-1} larger than that for the former. We thus repeat our recommendation for the use of 6-311+G(3df,2p)+d, i.e., the PoT-D3 procedure, when the use of aug′-cc-pVTZ+d in DuT-D3 becomes computationally too demanding. The optimized parameters for DuT-D3 and PoT-D3 are shown in Table 5, together with those for B2K-PLYP, frozen-core SCS-B2K-PLYP/aug′-cc-pVTZ+d, and frozen-core DSD-B-LYP-D3 for comparison.

Table 6. Performance of the DuT-D3 Procedure for the E3 Test Set[a,b]

statistics	MAD	MD	LD	SD	NO
E3	7.9	−4.4	−60.9	11.3	183
E2[c]	5.9	−1.7	−49.0	8.7	88
E0	6.5	−2.8	−49.0	10.0	26
W4/08	8.5[d]	−4.3	−49.0	11.7	25
DBH24	3.7	−0.3	10.6	4.4	1
HB16	2.0	1.9	4.7	1.4	0
WI9/04	0.8	−0.6	−2.0	0.8	0
G2/97′	6.2	−1.2	−42.1	8.7	45
ΔH_f	4.6	−1.0	−21.3	6.4	12
IE	7.7	−2.5	−42.1	10.6	23
EA	6.5	1.0	39.8	9.1	9
PA	4.9	−4.1	−10.8	4.6	1
E1	4.7	−1.6	−28.7	7.0	17
G3/99′	6.5	−2.4	−28.7	8.8	17
ADD	2.0	1.3	7.2	2.5	0
ABS	1.6	−0.1	−4.7	2.0	0
PR8	6.5	−6.5	−9.8	2.5	0
DSD′[e]	12.7	−10.8	−60.9	14.0	95
S22	2.1	2.1	9.2	2.9	0
MB08	15.9	−14.4	−60.9	14.1	95
Pd[f]	2.2	−1.1	−7.4	2.6	0
Grubbs[f]	3.8	3.3	8.6	3.9	0

[a] MAD = mean absolute deviation, MD = mean deviation, LD = largest deviation, and SD = standard deviation (kJ mol^{-1}); and NO = number of outliers (deviations >10 kJ mol^{-1}). [b] Geometries were obtained at the BMK/6-31+G(2df,p) level, unless otherwise noted. [c] See ref 35 for the definition of the E2 set and its subsets E0, G2/97′, and E1. [d] MAD for nonmultireference systems is 6.2 kJ mol^{-1}. [e] Literature geometries were used, see refs 19−22. [f] The aug-cc-pVTZ-PP basis set and the corresponding ECP were employed for the elements Pd and Ru.

It is noteworthy that the parameters c_{B88} and c_{HF} are very similar for all these methods, despite the fact that they are determined in combination with different basis sets and fitted to different training sets. Thus, it appears that the optimal c_{B88} and c_{HF} parameters vary within a relatively narrow range for a wide variety of thermochemical properties, with values of 0.30 ± 0.02 and 0.70 ± 0.02, respectively. We can see that there is a similar proportional variation for the c_{LYP} parameter, with optimum values in the range 0.60 ± 0.04. A comparison of SCS-B2K-PLYP, DuT-D3, PoT-D3, and DSD-B-LYP-D3 shows that the optimal value for c_{OS} lies in a relatively narrow range of 0.46−0.48, but there is a larger variation for the coefficient for the same-spin component of the MP2 correlation energy. Thus, c_{SS} has values that lie between 0.27 (PoT-D3) and 0.40 (DSD-B-LYP-D3).

We now assess the performance of DuT-D3 for a wider range of systems. We employ the E2 set[35] of 526 energies as the main benchmark set. The E2 set includes the W4/08 and the DBH24 sets that are also part of the DSD set. We have also included the remaining subsets of DSD, namely the S22,[44] MB08, Pd, and Grubbs sets, in our benchmark. While the Pd and Grubbs sets represent two important applications in

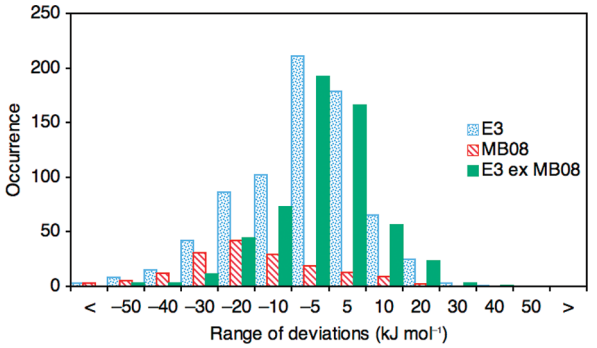

Figure 1. Distribution of the deviations (kJ mol^{-1}) for DuT-D3 for the E3, MB08, and E3 sets, excluding MB08.

transition-metal chemistry, we caution that generalization requires further investigations, especially for 3d transition metals that are not covered in the present study. The S22, MB08, Pd, and Grubbs sets comprise 214 energies, and we will refer to this collection as the DSD′ set. Thus, we have assessed the new procedure for a total of 740 energies, and we refer to this compilation of energies as the E3 set. For Pd and Ru, we have employed the aug-cc-pVTZ-PP basis set with the corresponding effective core potentials (ECPs),[45] in conjunction with aug′-cc-pVTZ+d for all the other elements. The results are shown in Table 6.

We can see that, with the exception of MB08, the MADs for all the subsets of E3 are less than 10 kJ mol^{-1}. Likewise, DuT-D3 affords SDs below 10 kJ mol^{-1} for most sets except W4/08, G2/97′ IE, and MB08. We find that the MD values for the PR8 and MB08 sets have magnitudes that are larger than 5 kJ mol^{-1}. In particular, the MB08 set is associated with an MD of −14.4 kJ mol^{-1}. This indicates systematic deviations for these sets. There are a total of 183 outliers in which the deviations are larger than 10 kJ mol^{-1}. These are dominated by outliers from the MB08 set, which account for 95 out of the total.

Figure 1 shows the distribution of the deviations for the E3, MB08, and E3 sets, excluding MB08. We can see that there are indeed systematic deviations for the MB08 set. On the other hand, the deviations for the rest of the subsets in E3 are normally distributed around zero. Thus, we find that the MD for the E3 set when MB08 is excluded is −1.5 kJ mol^{-1}, compared with −4.4 kJ mol^{-1} when MB08 is included in the analysis. Other subsets that represent substantial challenges to the DuT-D3 procedure, in terms of the number of outliers and largest deviations, include W4/08 (atomization energies), G2/97′ ΔH_f, G3/99′ ΔH_f, G2/97′ IE, and G2/97′ EA.

Comparison of DuT-D3, PoT-D3, DuT, and PoT with DSD-B-LYP and its Variants. In a recent study,[12] Goerigk and Grimme have formulated the DSD-B-LYP-D3 method and found it to be one of the best performing DHDFT procedures for the extensive GMTKN30 test set. In the present study, we employ DSD-B-LYP and DSD-B-LYP-D3 as yardsticks to further scrutinize the performance of the DuT-D3 and PoT-D3 procedures and their pure quantum mechanical variants, i.e., DuT and PoT. We have also examined the effect of removing the dispersion term in DSD-B-LYP altogether, and we refer to this method as DSD-B-LYP(ex D).

We have employed two quadruple-ζ basis sets, namely aug′-pc3+d and aug′-def2-QZVP, for the calculation of the quantum mechanical component of DSD-B-LYP and DSD-B-LYP-D3. The aug′-pc3+d basis set was chosen because it is one of the major basis sets employed in the original parametrization of DSD-B-LYP.[11] The remaining basis sets utilized in the formulation of DSD-B-LYP are Ahlrichs-style basis sets def2-TZVP, def2-QZVP, and def2-QZVPP. Among these, the def2-QZVP basis set was also used for the evaluation of DSD-B-LYP-D3, and this combination shows promising results.[12] In the present study, we augment the def2-QZVP basis set with diffuse functions from aug′-cc-pVQZ to arrive at the aug′-def2-QZVP basis set, and we examine its performance when used in conjunction with DSD-B-LYP and DSD-B-LYP-D3. The frozen-core approximation was applied, as the inclusion of all electrons for SCS-MP2 correlation in the context of the DHDFT procedure has been shown to lead to only a small improvement in performance (ref 11 and Table 3). The MADs for the E3 set and its subsets are summarized in Table 7.

We first note that, in general, all combinations of methods and basis sets perform comparably. Among the two basis sets employed for the DSD-B-LYP-type procedures, the use of the aug′-def2-QZVP basis set (columns 6, 8, and 10) typically yields results that are slightly better than those for aug′-pc3+d (columns 5, 7, and 9). In addition, the use of the aug′-def2-QZVP basis set offers a notable saving in computational resources compared with aug′-pc3+d, with timing ratios of 26.4× and 45.9× relative to PoT, for aug′-def2-QZVP and aug′-pc3+d, respectively, for the E2 set. While a generalization of the above observations would require further investigations, nonetheless the aug′-def2-QZVP basis set appears to be a more suitable and cost-effective quadruple-ζ basis set for DSD-B-LYP-type procedures than aug′-pc3+d.

A comparison of DuT-D3 with PoT-D3 and DuT with PoT shows that, for each subset, the DuT procedures (columns 1 and 3) generally outperform the PoT variants (columns 2 and 4), with MAD values that are lower than those for the corresponding PoT procedures by up to 2 kJ mol^{-1}. Cases where PoT-D3 and PoT gives MADs that are larger than those for the respective DuT procedures by more than 2 kJ mol^{-1} include W4/08, G3/99′, and the Grubbs set. Among these three sets, the largest MADs occur for the W4/08 set, in which DuT-D3 yields an MAD of 8.5 kJ mol^{-1}, while the corresponding value for PoT-D3 is 10.8 kJ mol^{-1}. On the other hand, PoT-D3 performs better than DuT-D3 for the PR8 and MB08 sets. In general, we find that the inclusion of D3 corrections (columns 1 and 2) leads to comparable or lower MADs than those for DuT and PoT (columns 3 and 4). Only very minor deterioration in the performance is observed for the DBH24, G2/97′ ΔH_f, and PR8 sets when dispersion corrections are included. Nonetheless, we emphasize the general good performance of all four DS-B-LYP-type procedures, namely DuT-D3, PoT-D3, DuT, and PoT, such that a large part of the chemistry can be captured with quantum mechanics without the requirement for additional dispersion corrections.

We now compare the performance of DuT-D3 and DuT with the performances of the three variants of DSD-B-LYP (Table 7). We find that the procedures that do not include a dispersion correction, i.e., DuT (column 3) and DSD-B-LYP(ex D) (columns 9 and 10) generally give MAD values that are similar to one another for each subset, with the G2/97′ ΔH_f, G3/99′, S22, and Grubbs sets being notable exceptions. Likewise, the two dispersion-corrected variants of DSD-B-LYP (columns 5 and 6 for DSD-B-LYP and columns 7 and 8 for DSD-B-LYP-D3) have performances that are comparable, except for the G3/99′ and Grubbs sets. However, there are more substantial differences

Table 7. Comparison of MADs from Benchmark Values (kJ mol^{-1}) for the E3 Test Set for DuT-D3, PoT-D3, DuT, PoT, DSD-B-LYP, DSD-B-LYP-D3, and DSD-B-LYP(ex D)[a]

	1	2	3	4	5	6	7	8	9	10
DHDFT	DuT-D3	PoT-D3	DuT	PoT	DSD-B-LYP		DSD-B-LYP-D3		DSD-B-LYP(ex D)	
basis set	A′VTZ +d[b]	6-311+G (3df,2p)+d[c]	A′VTZ +d[b]	6-311+G (3df,2p)+d[c]	aug′-pc3 +d	aug′-def2-QZVP	aug′-pc3 +d	aug′-def2-QZVP	aug′-pc3 +d	aug′-def2-QZVP
D Correction	D3	D3	nil	nil	D		D3		nil	
E3	7.9	8.6	8.4	9.0	9.3	9.0	9.0	8.7	9.2	9.1
E2	5.9	7.3	6.0	7.4	8.4	7.9	7.8	7.4	6.9	6.7
E0	6.5	8.2	6.5	8.2	6.7	6.5	6.6	6.4	6.5	6.3
W4/08	8.5	10.8	8.5	10.8	8.9	8.4	8.8	8.3	8.7	8.3
DBH24	3.7	3.7	3.5	3.7	3.2	3.7	3.2	3.7	3.1	3.4
HB16	2.0	2.6	1.6	2.2	1.8	2.0	1.6	1.8	0.9	1.1
WI9/04	0.8	0.8	1.0	1.0	0.8	0.8	0.8	0.8	1.0	1.0
G2/97′	6.2	7.4	6.1	7.4	8.0	7.6	7.7	7.3	7.0	6.8
ΔH_f	4.6	6.5	4.4	6.4	9.2	8.5	8.4	7.7	6.7	6.3
IE	7.7	8.4	7.7	8.4	8.0	7.7	8.0	7.7	8.0	7.7
EA	6.5	7.7	6.5	7.7	6.4	6.3	6.4	6.3	6.4	6.3
PA	4.9	5.0	4.9	5.0	4.4	4.8	4.6	5.1	4.6	5.1
E1	4.7	5.9	5.1	6.4	11.0	10.2	9.4	8.7	7.0	6.9
G3/99′	6.5	8.8	7.0	9.3	17.4	16.0	14.8	13.4	10.1	9.8
ADD	2.0	3.1	3.1	4.3	2.0	2.1	1.8	1.8	3.9	3.8
ABS	1.6	1.5	1.7	1.7	1.6	1.7	1.6	1.6	1.9	1.8
PR8	6.5	1.9	5.4	1.7	9.2	9.6	7.6	8.0	5.5	5.9
DSD′	12.7	11.9	14.4	13.2	11.8		11.8		15.0	
S22	2.1	2.5	4.9	4.8	1.3[d,g,h]		1.7[d,i,h]		6.5[d,j,h]	
MB08	15.9	14.4	17.5	15.6	14.6[e,g]		14.5[e,i]		17.7[e,j]	
Pd	2.2	3.9	2.5	4.1	2.8[f,g]		2.9[f,i]		3.2[f,j]	
Grubbs	3.8	7.5	7.2	11.0	3.6[d,g]		6.1[d,i]		13.4[d,j]	
timing (E2)[k]	2.8	1.0	2.8	1.0	46.4	26.4	46.4	26.4	46.4	26.4
timing (E3)[k]	3.4	1.0	3.4	1.0	–	–	–	–	–	–

[a] The frozen-core approximation is employed for all methods. [b] The aug-cc-pVTZ-PP basis set was used for Pd and Ru. [c] The aug-def2-TZVP basis set was used for Pd and Ru. [d] Values for the def2-TZVP basis set. [e] Values for the def2-QZVP basis set. [f] Values for the def2-QZVPP basis set. [g] Obtained from literature deviations reported in the Supporting Information of ref 11. [h] Revised for updated benchmark values from ref 19b. [i] Deviations obtained by adding the D3 − D contributions to the literature values (ref 11). [j] Deviations obtained by subtracting the D contributions from the literature values (ref 11). [k] Relative to the total time for PoT calculations for the designated test set.

between DSD-B-LYP(ex D) (columns 9 and 10) and DSD-B-LYP (columns 5 and 6), notably for the G3/99′, S22, and Grubbs sets. These results highlight the significant contribution of empirical dispersion corrections to the relative energies in the DSD-B-LYP method. Overall, we find that there are large variations for the G3/99′, PR8, S22, and Grubbs sets between the various methods.

What factors contribute to the more significant variations in these sets? The G3/99′ set contains ΔH_f values for medium-sized molecules. One can expect large variations in the performance of different methods for ΔH_f, and that the differences grow with the size of the molecules. In addition, the dispersion correction for ΔH_f would also grow with the size of the molecule, as the product atoms contain a zero dispersion term. For instance, there is a D correction (for DSD-B-LYP) of −26.1 kJ mol^{-1} and a D3 correction (for DSD-B-LYP-D3) of −17.3 kJ mol^{-1} for the ΔH_f of *n*-octane.[46] Therefore, we see large variations for G3/99′, and the inclusion of the particular dispersion corrections appears to lead to larger MADs for DSD-B-LYP and DSD-B-LYP-D3.

The S22 set includes complexation energies between large monomers, while the PR8 and Grubbs sets comprise barriers and reaction energies with large reactants. In these cases, we also see the sizable contributions of large empirical dispersion corrections to the DSD-B-LYP energies, which lead to larger MADs for PR8 but smaller MADs for the S22 and the Grubbs sets. To illustrate the large dispersion corrections for some of the species in the S22 set, for example, for DSD-B-LYP and DSD-B-LYP-D3, the adenine-thymine stacked dimer has a D correction of −18.0 kJ mol^{-1} and a D3 correction of −15.2 kJ mol^{-1} to the binding energy.[47] In this case, the dispersion corrections lead to improved results. In addition, for the Grubbs set, 6 out of the 7 entries in the set have D contributions to relative energies that exceed 10 kJ mol^{-1}, and these D corrections contribute significantly to the difference in the MADs of the DSD-B-LYP(ex D) and DSD-B-LYP methods.

We now rank the performance of these methods. Overall, DuT-D3 yields the smallest MAD for the complete E3 set, although the other procedures follow closely. When compared with the DSD-B-LYP variants, the better performance of

Table 8. Comparison of MADs from Benchmark Values (kJ mol^{-1}) for Selected Subsets of the E3 Test Set for ωB97X-2(LP), DuT-D3, PoT-D3, DSD-B-LYP(ex D), DSD-B-LYP, and DSD-B-LYP-D3

	1[a]	2	3	4	5	6	7	8	9
DHDFT	ωB97X-2(LP)	DuT-D3	PoT-D3	DSD-B-LYP(ex D)		DSD-B-LYP		DSD-B-LYP-D3	
basis set	6-311++G (3df,3pd)	A′VTZ +d	6-311+G (3df,2p)+d	aug′-pc3 +d	aug′-def2-QZVP	aug′-pc3 +d	aug′-def2-QZVP	aug′-pc3 +d	aug′-def2-QZVP
D Correction	nil	D3	D3	nil		D		D3	
G2/97 and G3/99 ΔH_f	6.4	5.6	7.7	8.1	7.7	11.6	10.7	10.4	9.6
G2-1 IE	7.2	7.0	7.8	7.3	6.8	7.3	6.8	7.3	6.8
G2-1 EA	6.5	5.8	9.2	6.0	5.4	6.0	5.4	6.0	5.4
G2/97 PA	4.6	4.9	5.0	4.6	5.1	4.4	4.8	4.6	5.1
S22	1.0[b]	2.3	2.7	6.7	6.7	1.2	1.2	1.7	1.7

[a] MAD values obtained from ref 6. [b] Value corresponds to deviations from benchmark values from ref 19a.

DuT-D3 can primarily be attributed to the much smaller deviations for the G3/99′ set, while maintaining its robustness for the other sets. It is thus important to note that, for DHDFT procedures, the use of appropriate triple-ζ basis sets, such as aug′-cc-pVTZ+d and 6-311+G(3df,2p)+d in this instance, can yield results that are of comparable reliability to those obtained with quadruple-ζ basis sets but at considerably lower computational expense.

We have also compared (Table 8) the performance of the very promising ωB97X-2(LP)/6-311++G(3df,3pd) procedure with the performances for the methods, listed in Table 7, on a selected subset of E3, namely G2/97 and G3/99 ΔH_f, the G2-1 subsets[15] of G2/97 IE and G2/97 EA, G2/97 PA, and S22. It can be seen that all three procedures that employ triple-ζ basis sets (columns 1−3) are competitive in performance with the DSD-B-LYP variants (columns 4−9) that use quadruple-ζ basis sets. This provides further support for the use of appropriate triple-ζ basis sets for DHDFT calculations.

It can be seen (Table 8) that the procedures that do not include an explicit dispersion correction or those that include dispersion corrections with smaller s_8 contributions (columns 1−5) are characterized by smaller MADs for the G2/97 and G3/99 ΔH_fs and, in general, by larger MADs for the S22 set. On the other hand, the procedures that include a larger dispersion correction (columns 6−9) are characterized by larger MADs for the G2/97 and G3/99 ΔH_fs and smaller MADs for the S22 set. It is notable that ωB97X-2(LP)/6-311++G(3df,3pd) performs well for both the ΔH_f sets and the S22 set, presumably because of the incorporation of long-range corrections through its range-separation scheme.[6]

CONCLUDING REMARKS

In the present investigation, we have examined a variety of B-LYP-based DHDFT procedures used in conjunction with a range of basis sets, particularly triple-ζ basis sets. The following important points emerge from our study:

(1) We find that the optimal $\%E_X^{B88}$ and $\%E_X^{HF}$ are ∼30 and 70%, respectively, and these values are relatively insensitive to the thermochemical properties of interest. We also find that it is beneficial to include correlation energy in excess of the amount constrained by the requirement of $\%E_C^{LYP} + \%E_C^{MP2} = 100\%$. For the energies in the G2/97 set, the use of SCS-MP2 yields comparable or slightly better results than the use of conventional MP2. We find the optimal $\%E_C^{MP2OS}$ to be ∼47%, while $\%E_C^{MP2SS}$ lies between 27 and 40%.

(2) Regarding the basis set, the use of diffuse functions on nonhydrogen atoms appears to be important not only for the evaluation of EAs but also for other thermochemical properties, such as ΔH_f and IE. However, the inclusion of diffuse functions on hydrogen is not essential. On the other hand, we deem the use of tight d functions on second-row atoms a cost-effective improvement. Among the different styles of augmented triple-ζ-type basis sets examined, namely the Pople 6-311+G(3df,2p)+d, Dunning aug′-cc-pVTZ+d, Jensen aug′-pc2+d, and Ahlrichs def2-TZVPD′+d and aug′-def2-TZVP+d sets, the aug′-cc-pVTZ+d basis set emerges as the best-performing basis set for B-LYP-based DHDFT methods. The use of the 6-311+G(3df,2p)+d basis set gives slightly less accurate results but offers notable savings in computer time. When used in conjunction with UCMP-B2K-PLYP and SCS-B2K-PLYP procedures, aug′-cc-pVTZ+d somewhat outperforms the larger aug-cc-pVQZ+d basis set for the G2/97 set.

(3) We find that when a set of SCS parameters is optimized for a specific basis set, its use with a different basis set can lead to large deviations for heats of formation, while other relative energies are less sensitive to the combination of parameters and basis set. We recommend the use in general of matching optimum parameters and basis sets.

(4) Using aug′-cc-pVTZ+d, we have formulated the DuT-D3 and DuT DHDFT procedures. For the larger E2 and E3 test sets, DuT-D3 and DuT perform comparably to DSD-B-LYP-D3 and DSD-B-LYP when the latter are used in conjunction with the quadruple-ζ basis sets for which they are developed, namely aug′-pc3+d and aug′-def2-QZVP. However, the computational expense of DuT-D3 and DuT is significantly lower. This supports the use of appropriate and cost-effective triple-ζ basis sets for DHDFT calculations.

(5) We have also formulated the PoT-D3 and PoT DHDFT procedures with the 6-311+G(3df,2p)+d basis set. These are only slightly less accurate than the DuT variants, but the smaller basis set enables calculations on larger systems.

The previously formulated ωB97X-2(LP)/6-311++G-(3df,3pd) method also performs particularly well.

■ ASSOCIATED CONTENT

Supporting Information. Optimized MP2 parameters for the various DHDFT procedures (Table S1), total DuT and PoT electronic energies and associated D3 corrections (Tables S2−S17), and deviations from benchmark values for DuT-D3 and PoT-D3 (Tables S18−S32). Also included are the aug′-cc-pVTZ+d (for the DuT procedure) and 6-311+G(3df,2p)+d) (for the PoT procedure) basis sets in Gaussian 09 format, along with input examples for performing DuT and PoT calculations with Gaussian 09. This material is available free of charge via the Internet at http://pubs.acs.org.

■ AUTHOR INFORMATION

Corresponding Author

*E-mail: chan_b@chem.usyd.edu.au; radom@chem.usyd.edu.au.

■ ACKNOWLEDGMENT

We gratefully acknowledge the award of an Australian Professorial Fellowship and funding from the ARC Centre of Excellence for Free Radical Chemistry and Biotechnology (L.R.) and generous allocations of computer time from the National Computational Infrastructure (NCI) National Facility and Intersect Australia Ltd.

■ REFERENCES

(1) Grimme, S. *J. Chem. Phys.* **2006**, *124*, 034108.
(2) Grimme, S.; Schwabe, T. *Phys. Chem. Chem. Phys.* **2006**, *8*, 4398.
(3) Tarnopolsky, A.; Karton, A.; Sertchook, R.; Vuzman, D.; Martin, J. M. L. *J. Phys. Chem. A* **2008**, *112*, 3.
(4) Karton, A.; Tarnopolsky, A.; Lamere, J. F.; Schatz, G. C.; Martin, J. M. L. *J. Phys. Chem. A* **2008**, *112*, 12868.
(5) Benighaus, T.; Lochan, R. C.; Chai, J.-D.; Head-Gordon, M. *J. Phys. Chem. A* **2008**, *112*, 2702.
(6) Chai, J.-D.; Head-Gordon, M. *J. Chem. Phys.* **2009**, *131*, 174105.
(7) Graham, D. C.; Menon, A. S.; Goerigk, L.; Grimme, S.; Radom, L. *J. Phys. Chem. A* **2009**, *113*, 9861.
(8) Zhang, Y.; Xu, X.; Goddard, W. A., III *Proc. Natl. Acad. Sci. U.S.A.* **2009**, *106*, 4963.
(9) Zhang, I. Y.; Luo, Y.; Xu, X. *J. Chem. Phys.* **2010**, *132*, 194105.
(10) Zhang, I. Y.; Luo, Y.; Xu, X. *J. Chem. Phys.* **2010**, *133*, 104105.
(11) Kozuch, S.; Gruzman, D.; Martin, J. M. L. *J. Phys. Chem. C* **2010**, *114*, 20801The DSD label relates to double-hybrid, SCS-MP2 correlation, and a dispersion correction.
(12) Goerigk, L.; Grimme, S. *J. Chem. Theory Comput.* **2011**, *7*, 291.
(13) Sharkas, K.; Toulouse, J.; Savin, A. *J. Chem. Phys.* **2011**, *134*, 064113.
(14) Grimme, S.; Schwabe, T. *Acc. Chem. Res.* **2008**, *41*, 569.
(15) (a) Curtiss, L. A.; Redfern, P. C.; Raghavachari, K.; Pople, J. A. *J. Chem. Phys.* **1997**, *106*, 1063. (b) Curtiss, L. A.; Redfern, P. C.; Raghavachari, K.; Pople, J. A. *J. Chem. Phys.* **1998**, *109*, 42.
(16) Grimme, S. *J. Chem. Phys.* **2003**, *118*, 9095.
(17) Grimme, S. *J. Comput. Chem.* **2004**, *25*, 1463.
(18) (a) Zheng, J.; Zhao, Y.; Truhlar, D. G. *J. Chem. Theory Comput.* **2007**, *3*, 569. (b) Zheng, J.; Zhao, Y.; Truhlar, D. G. *J. Chem. Theory Comput.* **2009**, *5*, 808.
(19) (a) Jurecka, P.; Sponer, J.; Cerny, J.; Hobza, P. *Phys. Chem. Chem. Phys.* **2006**, *8*, 1985. (b) Takatani, T.; Hohenstein, E. G.; Malagoli, M.; Marshall, M. S.; Sherrill, C. D. *J. Chem. Phys.* **2010**, *132*, 144104.
(20) Schwabe, T.; Grimme, S. *J. Phys. Chem. A* **2009**, *113*, 3005.
(21) Quintal, M. M.; Karton, A.; Iron, M. A.; Boese, A. D.; Martin, J. M. L. *J. Phys. Chem. A* **2006**, *110*, 709.
(22) Zhao, Y.; Truhlar, D. G. *J. Chem. Theory Comput.* **2009**, *5*, 324.
(23) Grimme, S.; Antony, J.; Ehrlich, S.; Krieg, H. *J. Chem. Phys.* **2010**, *132*, 154104.See also: http://toc.uni-muenster.de/DFTD3/index.html (accessed January 27, 2011).
(24) Weigend, F.; Furche, F.; Ahlrichs, R. *J. Chem. Phys.* **2003**, *119*, 12753.
(25) Jensen, F. *J. Chem. Phys.* **2002**, *116*, 7372.
(26) Dunning, T. H., Jr. *J. Chem. Phys.* **1999**, *90*, 1007.
(27) Weigend, F.; Ahlrichs, R. *Phys. Chem. Chem. Phys.* **2005**, *7*, 3297.
(28) Hehre, W. J.; Radom, L.; Schleyer, P. v. P.; Pople, J. A. *Ab Initio Molecular Orbital Theory*; Wiley: New York, 1986, pp 65−88.
(29) Curtiss, L. A.; Raghavachari, K.; Redfern, P. C.; Pople, J. A. *J. Chem. Phys.* **2000**, *112*, 7374.
(30) For other DHDFT procedures examined in ref 12, a larger basis set effect (∼0.4−0.5 kcal mol^{-1}, i.e., ∼1.6−2.1 kJ mol^{-1}) is found, with the quadruple-ζ basis set again performing better.
(31) See for example: (a) Hehre, W. J.; Radom, L.; Schleyer, P. v. P.; Pople, J. A. *Ab Initio Molecular Orbital Theory*; Wiley: New York, 1986. (b) Koch, W.; Holthausen, M. C. *A Chemist's Guide to Density Functional Theory*, 2nd ed.; Wiley: New York, 2001. (c) Jensen, F. *Introduction to Computational Chemistry*, 2nd ed.; Wiley: Chichester, U.K., 2007.
(32) Frisch, M. J.; Trucks, G. W.; Schlegel, H. B.; Scuseria, G. E.; Robb, M. A.; Cheeseman, J. R.; Montgomery, J. A., Jr.; Vreven, T.; Kudin, K. N.; Burant, J. C.; Millam, J. M.; Iyengar, S. S.; Tomasi, J.; Barone, V.; Mennucci, B.; Cossi, M.; Scalmani, G.; Rega, N.; Petersson, G. A.; Nakatsuji, H.; Hada, M.; Ehara, M.; Toyota, K.; Fukuda, R.; Hasegawa, J.; Ishida, M.; Nakajima, T.; Honda, Y.; Kitao, O.; Nakai, H.; Klene, M.; Li, X.; Knox, J. E.; Hratchian, H. P.; Cross, J. B.; Bakken, V.; Adamo, C.; Jaramillo, J.; Gomperts, R.; Stratmann, R. E.; Yazyev, O.; Austin, A. J.; Cammi, R.; Pomelli, C.; Ochterski, J. W.; Ayala, P. Y.; Morokuma, K.; Voth, G. A.; Salvador, P.; Dannenberg, J. J.; Zakrzewski, V. G.; Dapprich, S.; Daniels, A. D.; Strain, M. C.; Farkas, O.; Malick, D. K.; Rabuck, A. D.; Raghavachari, K.; Foresman, J. B.; Ortiz, J. V.; Cui, Q.; Baboul, A. G.; Clifford, S.; Cioslowski, J.; Stefanov, B. B.; Liu, G.; Liashenko, A.; Piskorz, P.; Komaromi, I.; Martin, R. L.; Fox, D. J.; Keith, T.; Al-Laham, M. A.; Peng, C. Y.; Nanayakkara, A.; Challacombe, M.; Gill, P. M. W.; Johnson, B.; Chen, W.; Wong, M. W.; Gonzalez, C.; Pople, J. A. *Gaussian 03*, revision E.01; Gaussian, Inc.: Wallingford, CT, 2004.
(33) Frisch, M. J.; Trucks, G. W.; Schlegel, H. B.; Scuseria, G. E.; Robb, M. A.; Cheeseman, J. R.; Scalmani, G.; Barone, V.; Mennucci, B.; Petersson, G. A.; Nakatsuji, H.; Caricato, M.; Li, X.; Hratchian, H. P.; Izmaylov, A. F.; Bloino, J.; Zheng, G.; Sonnenberg, J. L.; Hada, M.; Ehara, M.; Toyota, K.; Fukuda, R.; Hasegawa, J.; Ishida, M.; Nakajima, T.; Honda, Y.; Kitao, O.; Nakai, H.; Vreven, T.; Montgomery, J. A., Jr.; Peralta, J. E.; Ogliaro, F.; Bearpark, M.; Heyd, J. J.; Brothers, E.; Kudin, K. N.; Staroverov, V. N.; Kobayashi, R.; Normand, J.; Raghavachari, K.; Rendell, A.; Burant, J. C.; Iyengar, S. S.; Tomasi, J.; Cossi, M.; Rega, N.; Millam, N. J.; Klene, M.; Knox, J. E.; Cross, J. B.; Bakken, V.; Adamo, C.; Jaramillo, J.; Gomperts, R.; Stratmann, R. E.; Yazyev, O.; Austin, A. J.; Cammi, R.; Pomelli, C.; Ochterski, J. W.; Martin, R. L.; Morokuma, K.; Zakrzewski, V. G.; Voth, G. A.; Salvador, P.; Dannenberg, J. J.; Dapprich, S.; Daniels, A. D.; Farkas, Ö.; Foresman, J. B.; Ortiz, J. V.; Cioslowski, J.; Fox, D. J. *Gaussian 09*, revision A.02; Gaussian, Inc.: Wallingford, CT, 2009.
(34) Boese, A. D.; Martin, J. M. L. *J. Chem. Phys.* **2004**, *121*, 3405.
(35) Chan, B.; Deng, J.; Radom, L. *J. Chem. Theory Comput.* **2011**, *7*, 112.
(36) Merrick, J. P.; Moran, D.; Radom, L. *J. Phys. Chem. A* **2007**, *111*, 11683.
(37) Rappoport, D.; Furche, F. *J. Chem. Phys.* **2010**, *133*, 134105.
(38) (a) Feller, D. *J. Comput. Chem.* **1996**, *17*, 1571. (b) Schuchardt, K. L.; Didier, B. T.; Elsethagen, T.; Sun, L.; Gurumoorthi, V.; Chase, J.; Li, J.; Windus, T. L. *J. Chem. Inf. Model* **2007**, *47*, 1045.
(39) Martin, J. M. L. *J. Mol. Struct. (Theochem)* **2006**, *771*, 19.

(40) For the calculations that include Pd and Ru, we have employed the def2-TZVP basis set for these two elements, augmented with diffuse functions from the aug-cc-pVTZ-PP basis set. The def2-TZVP ECPs are used for Pd and Ru. This basis set is chosen as its performance and computational cost are close to those for 6-311+G(3df,2p)+d (Table 2).
(41) Grimme, S.; Ehrlich, S.; Goerigk, L. *J. Comput. Chem.* **2011**, *32*, 1456.
(42) (a) Becke, A. D.; Johnson, E. R. *J. Chem. Phys.* **2005**, *122*, 154101. (b) Johnson, E. R.; Becke, A. D. *J. Chem. Phys.* **2005**, *123*, 024101. (c) Johnson, E. R.; Becke, A. D. *J. Chem. Phys.* **2006**, *124*, 174104.
(43) Chai, J.-D.; Head-Gordon, M. *Phys. Chem. Chem. Phys.* **2008**, *10*, 6615.
(44) Unless otherwise noted, for the S22 set, we have employed the revised values from ref 19b.
(45) Peterson, K. A.; Figgen, D.; Dolg, M.; Stoll, H. *J. Chem. Phys.* **2007**, *126*, 124101.
(46) The calculated ΔH_f values for *n*-octane are −214.0 (DuT-D3), −207.8 (PoT-D3), −204.8 (DuT), −199.7 (PoT), −227.3 (DSD-B-LYP/aug′-def2-QZVP), −218.5 (DSD-B-LYP-D3/aug′-def2-QZVP), and −201.2 (DSD-B-LYP(ex D)/aug′-def2-QZVP) kJ mol^{-1}, compared with the experimental value of −208.8 kJ mol^{-1}.
(47) The reference value for the adenine-thymine stacked dimer binding energy is −48.8 kJ mol^{-1}. The calculated values are −45.6 (DuT-D3), −44.1 (PoT-D3), −36.9 (DuT), −36.4 (PoT), −48.5 (DSD-B-LYP/def2-TZVP), −45.6 (DSD-B-LYP-D3/def2-TZVP), and −30.4 (DSD-B-LYP(ex D)/def2-TZVP) kJ mol^{-1}. The values for DSD-B-LYP, DSD-B-LYP-D3, and DSD-B-LYP(ex D) were evaluated using data given in the Supporting Information of ref 11.

JCTC Journal of Chemical Theory and Computation

ARTICLE

pubs.acs.org/JCTC

Effects of Spin−Orbit Coupling on Covalent Bonding and the Jahn−Teller Effect Are Revealed with the Natural Language of Spinors

Tao Zeng,[†] Dmitri G. Fedorov,[‡] Michael W. Schmidt,[§] and Mariusz Klobukowski*[,†]

[†]Department of Chemistry, University of Alberta, Edmonton, Alberta, Canada, T6G 2G2

[‡]NRI, National Institute of Advanced Industrial Science and Technology (AIST), Central 2, Umezono 1-1-1, Tsukuba, 305-8568, Japan

[§]Department of Chemistry and Ames Laboratory USDOE, Iowa State University, Ames, Iowa 50011, United States

ABSTRACT: The orbital-based natural language describing the complexity of chemistry (Stowasser, R.; Hoffmann, R. *J. Am. Chem. Soc.* **1999**, *121*, 3414) was extended by us recently to the definition of spin−orbit natural spinors (Zeng, T. et al. *J. Chem. Phys.* **2011**, *134*, 214107). This novel method gives chemical insights into the role of spin−orbit coupling in covalent bonding and in the Jahn−Teller effect. The natural spinors are used to explain antibonding spin−orbit effects on TlH and Tl_2: it is found that the spin−orbit induced charge transfer from the bonding to the nonbonding or antibonding orbitals has a large effect on the bond strength. The natural spinors are also used to explain the spin−orbit quenching of the Jahn−Teller effect in WF_5: the spin−orbit interaction can stabilize the totally symmetric electron distribution so that the high-symmetry molecular structure becomes more stable than its distortions. A general discussion of the role of the spin−orbit coupling in covalent bonding and Jahn−Teller effect is given in terms of the competition between the rotational nature of the spin−orbit coupling and the directionality of the two effects. The natural spinors offer the advantage of providing a simple and clear pictorial explanation for the profound relativistic spin-dependent interactions in chemistry often appearing as a black box answer.

1. INTRODUCTION

The special theory of relativity leads to very profound effects in chemistry.[1−4] The relativistic effects can be divided into two categories: the scalar-relativistic and the spin-relativistic effects. The manifestations of the former effect are, for example, the liquid state of mercury under ambient temperature and pressure,[5] the golden color of gold,[6−8] and the inertness of the $6s^2$ electron pair.[9] Since the operators describing the scalar-relativistic effects do not introduce new symmetry, they are relatively easy to implement in the conventional quantum chemistry programs, and their interpretation is facilitated by that. The spin-relativistic effect, however, introduces the double group symmetry[10,11] related to the electron spin of 1/2, forms one of the obstacles in current development of quantum chemistry, and presents difficulties in the conceptual interpretation of the "black box" results. The importance of a tool giving a simple representation of a complex phenomenon cannot be overestimated; a chemist wants to understand not only what happens but also why and be able to form a mental picture of the complex chemical processes caused by complicated physical concepts. Among the spin-related operators, the spin−orbit coupling typically has the largest magnitude.[12] The circulation of an electron around a nucleus in the reference frame of the electron can be considered a circulating motion of the nucleus around the electron, which creates a magnetic field. On the other hand, the electronic spin creates a magnetic dipole moment. The coupling between the magnetic field and the magnetic dipole moment leads to the spin−orbit coupling (see section 1.3.3 of ref 13 for a detailed discussion). The spin−orbit coupling manifests itself in several phenomena in chemistry:[12,14] the fine structure splitting, intersystem crossing, and spin-forbidden radiative transition. Because this interaction increases with the nuclear charge,[15,16] a proper study of the heavy element chemistry often requires taking this interaction into account.

There are two strategies for spin−orbit coupling calculations: the so-called one-step[17−19] and two-step methods.[20−25] The advantage of the one-step coupling scheme is that the spin−orbit effects are included in the orbital optimization yielding $j-j$ spinors. The influence of this interaction on the wave function can be directly analyzed, which is important as the orbitals provide a *natural language*[26] for the complexity of chemistry. In contrast, the two-step coupling first generates a set of states (Russell−Saunders terms) with a definite total spin quantum number S for the spin part and a point group symmetry label Γ for the spatial part of the wave function. Subsequently, the spin−orbit coupling effect is added at a post-Hartree−Fock level taking the Russell−Saunders terms (Γ-S states) as the multielectron basis functions.[16,27] In this way, the two-step coupling scheme can be easily implemented in typical nonrelativistic quantum-chemical programs, so their impressive development of the electron correlation methodology can be easily incorporated into spin−orbit calculations. However, the action of the spin−orbit operator on the wave function is represented by the mixing of the Russell−Saunders terms, and the orbital-based analysis cannot be applied. Recently, we developed an algorithm[28] to calculate the natural orbitals for two-step coupled wave functions, and these natural spinors have been shown to closely mimic the corresponding $j-j$ spinors. This new technique allows one to obtain a $j-j$ spinor analogue in a two-step coupled wave function, and the advantages of both coupling schemes are then combined.

Following our recent derivation and algorithm of the natural spinor methodology, we present here the first chemical applications of this new technique. There are two interesting problems related to spin−orbit interaction that have fascinated chemists

Received: June 30, 2011
Published: August 05, 2011

for a long time: the interplay between the spin−orbit and the bonding interactions[29−39] and the interplay between the spin−orbit and the Jahn−Teller effect.[40−51] Spin−orbit interaction often lifts the electronic degeneracy and transforms the Jahn−Teller effect into a pseudo-Jahn−Teller effect. In the present work, we apply the natural spinors to illuminate the details of these two phenomena. As shown below, the natural spinors capture the role of spin−orbit coupling both in the covalent bonding and in the Jahn−Teller effect and provide deep chemical insights. Although discussions in this work are based mainly on case studies, the approach based on natural spinor analysis is general and can be applied to other systems. To be more specific, the term "bonding" only means covalent bonding interaction in this work.

This paper is arranged as follows. In section 2, we present a short review of the natural spinors and some computational details in this work. In section 3, we use the natural spinors to explain the spin−orbit antibonding effect, taking TlH and Tl_2 as examples. In section 4, we use the natural spinors to explain the spin−orbit quenching of the Jahn−Teller distortion, taking WF_5 as an example. Section 5 summarizes this work. Unless further specified, all units used in this paper are atomic units (a.u.) and "term" and "level" are used to denote the multielectron states without and with the spin−orbit interaction being considered, respectively.

2. METHODOLOGY

The concept of natural orbitals dates back well into the past.[52−54] In our recent application[28] of this concept to a two-step spin−orbit coupled wave function, the natural spinors are obtained as the eigenfunctions of the two-step spin−orbit coupled density operator. The two-step coupled wave functions are generally complex-valued and mix different spin multiplicities. As a reflection of this nature, the natural spinors are also generally complex-valued and mix the two spin components (α and β) of an electron. If all of the components of a multidimensional irreducible representation of the associated double group are equally averaged to produce the one-electron reduced density, the associated density operator is of the totally symmetric irreducible representation and commutes with all of the symmetry operators.[28,54] Consequently, its eigenvectors (natural spinors) must belong to the irreducible representations of the same double group, i.e., they must have the same symmetry properties as the $j-j$ spinors. Since the natural spinors contain the information of the two-step coupled wave function and are symmetry adapted, they are perfect candidates for wave function analysis. The details of the algorithm and test cases of the natural spinors are given in the previous publication.[28]

For general polyatomic molecules, the one-electron effective spin−orbit operator is[12]

$$\sum_{iA} \hat{V}_{iA}\, \hat{\vec{l}}_{iA} \cdot \hat{\vec{s}}_i \qquad (1)$$

where i labels the electrons, A labels the nuclei, $\hat{V}_{iA}$ stands for the coupling strength and is a function of the distance r_{iA} between electron i and nucleus A in the spatial representation, $\hat{\vec{l}}_{iA}$ is the orbital angular momentum operator of electron i around nucleus A, and $\hat{\vec{s}}_i$ is the electron spin operator. Since the two-electron spin−orbit interaction does not change the symmetry properties of the one-electron analogue,[13] eq 1 can be taken to represent both one- and two-electron operators for the symmetry analysis, with the two-electron shielding effect stored in the effective coupling strength V_{iA}. The operator $\hat{\vec{l}}_{iA}$ determines that the spin−orbit interaction exerts its effect (either lowering or raising the energy) by the electron rotation around each nucleus, since the angular momentum operator is the generator for rotation.[55]

An important concept in the present work is the spin−orbit induced electron transfer between molecular orbitals. This terminology stems from the interpretation of the matrix element $\langle \mu\lambda|\hat{V}_{iA}\, \hat{\vec{l}}_{iA} \cdot \hat{\vec{s}}_i|\nu\sigma\rangle$, where μ and ν are the spatial molecular orbitals and λ and σ are the spin components (α or β). Such matrix elements are responsible for the spin−orbit splitting in the two-step coupling scheme,[56] and they can be written as $\langle \mu|\hat{V}_{iA}\, \hat{\vec{l}}_{iA}|\nu\rangle \cdot \langle \lambda|\hat{\vec{s}}_i|\sigma\rangle$. The spin part (the matrix element after the dot) determines the spin magnetic dipole, and the spatial part (the matrix element before the dot) determines the effective magnetic field, which stems from the relative nucleus A rotation around electron i. In the space-fixed (nuclei-fixed) frame, such a relative rotation appears as the electron i rotation around nucleus A, and this explains the appearance of $\hat{\vec{l}}_{iA}$, not $\hat{\vec{l}}_{Ai}$, in eq 1. Here, we would like to emphasize that $\hat{\vec{l}}_{iA}$ is the angular momentum operator of electron i around nucleus A while $\hat{\vec{l}}_{Ai}$ is the analogue for the motion of nucleus A around electron i. For the real orbitals usually used in chemistry, only the off-diagonal matrix elements of $\langle \mu|V_{iA}\, \hat{\vec{l}}_{iA}|\nu\rangle$ are nonzero,[56,57] which means that the spin−orbit effect cannot be realized by keeping the electron in the same spatial orbital; i.e., it has to come as an electron transition between spatial orbitals.

Next, it is well-known that, in the two-step methods,[56,57] doubly occupied orbitals alone do not contribute to spin−orbit coupling, and nonzero spin−orbit matrix elements must couple Slater determinants with occupancy discoincidence of one or two orbitals, i.e., transferring electrons from occupied to virtual orbitals. This charge transfer is a manifestation of the direction change of the electron spatial distribution around a nucleus induced by the electron rotation in the spin−orbit effect. A similar notation was employed by Turro et al.[31] to visualize the action of spin−orbit coupling. We also note that, for atoms, the charge transfer can be visualized by rotations more directly, as the atomic orbitals have well-defined rotational properties suitable for this interpretation, while in molecules, the anisotropic nature of the Coulomb interaction leads to molecular orbitals with various distributions which obstruct the orbital rotation interpretation. Therefore, we refer to the action of spin−orbit coupling as electron (or charge) transfer.

Let us consider a charge (electron) transfer from an occupied orbital $\mu\sigma$ to a virtual orbital $\nu\lambda$ induced by spin−orbit coupling. By employing the second order perturbation theory formulas, the magnitude (not considering the sign) of the spin−orbit energy and wave function contributions from a transfer between a pair of orbitals can be expressed, respectively, as

$$\frac{\left|\left\langle \mu\lambda|\hat{V}_{iA}\, \hat{\vec{l}}_{iA} \cdot \hat{\vec{s}}_i|\nu\sigma\right\rangle\right|^2}{|E^0_{\nu\sigma} - E^0_{\mu\lambda}|} \text{ and } \frac{\left|\left\langle \mu\lambda|\hat{V}_{iA}\, \hat{\vec{l}}_{iA} \cdot \hat{\vec{s}}_i|\nu\sigma\right\rangle\right|}{|E^0_{\nu\sigma} - E^0_{\mu\lambda}|} \qquad (2)$$

where the denominator is the energy gap between the states in which $\mu\lambda$ or $\nu\sigma$ is occupied. This energy gap can then be approximated as the orbital energy difference between $\mu\lambda$ and

$\nu\sigma$, which leads to the explanation that the larger the energy gap between the two orbitals, the less significant the spin−orbit induced electron transfer between them.

At this point, it is necessary to compare our natural spinors and the canonical $j-j$ spinors in the one-step spin−orbit coupled calculation. The canonical spinors are obtained by diagonalizing the two-component Fock operator that has included the spin−orbit effect, and therefore, they have the associated spinor energies[17] (analogues of orbital energies in calculations without spin−orbit), which are the eigenvalues of the Fock operator. However, those canonical $j-j$ spinors in the active space have unknown occupation numbers. In contrast, our natural spinors diagonalize the density matrix of a spin−orbit wave function and have a definite occupation number for each spinor but do not have the associated orbital energy. Therefore, the natural spinors and the $j-j$ canonical spinors provide complementary information about a spin−orbit coupled wave function.

We implemented the natural spinor algorithm into GAMESS-US[58,59] and employed this open-source quantum chemistry program package to perform all of the electronic structure calculations in this work. The basis sets and the relativistic treatment are described below. The electron correlation is treated at the complete active space configuration interaction (CASCI) levels, and the corresponding SO-CASCI treatment[50] is employed to account for the spin−orbit interaction. The natural spinors are obtained from the SO-CASCI wave functions.

All orbital pictures in this work are prepared using graphical program MacMolPlt.[60] We developed a program that can create MacMolPlt data files for the complex natural spinors by dividing each of the complex spinors into four real-valued "orbitals", and the spinor's occupation number is assigned to each of the pseudo-orbitals. This program is employed to make images of the electron density for natural spinors. The four pseudo-orbitals correspond to the four phases of a spinor: real-valued function with α spin, real-valued function with β spin, imaginary-valued function with α spin, and imaginary-valued function with β spin. For example, the $p_{1/2,-1/2}$ spinor (we use the notation $l_{j,jz}$, see Table S.II in the Supporting Information of ref 28 for the definition of these prototypical atomic spinors):

$$p_{1/2,-1/2} = \sqrt{\frac{1}{3}}p_x\alpha - i\sqrt{\frac{1}{3}}p_y\alpha + \sqrt{\frac{1}{3}}p_z\beta \qquad (3)$$

requires three "orbitals" to visualize: a real α "orbital" for $(1/3)^{1/2}p_x\alpha$, an imaginary α "orbital" for $-i(1/3)^{1/2}p_y\alpha$, and a real β "orbital" for $(1/3)^{1/2}p_z\beta$. Each of the pseudo-orbitals are unnormalized, and if this $p_{1/2,-1/2}$ spinor is occupied by x ($x \leq 1$) electrons, x is assigned to the three pseudo-orbitals. One should notice that the natural spinors in this work may not have the same mathematical expression as used elsewhere, because they follow the phase convention and coordinate system of the program we use, which may not be identical to those in other programs. In the discussions below, the term "natural orbital" is reserved for the eigenvectors that diagonalize the one-electron density matrix of a non-spin−orbit wave function, while "natural spinor" is used for the spin−orbit analogues. One should be aware of the difference between the two terms.

3. HOW SPIN−ORBIT COUPLING CHANGES THE COVALENT BOND STRENGTH IN DIATOMIC MOLECULES

According to Ruedenberg et al.,[61,62,64,65] a covalent bond is formed in two steps. First, the electron sharing between atoms leads to an attenuation of the kinetic energy pressure and the associated lower ratio between kinetic and potential energies ($T/|V|$). Second, the nonequilibrium $T/|V|$ ratio leads to a wave function relaxation together with an increase of the kinetic and a decrease of the potential energy until the equilibrium $T/|V|$ ratio is attained (1/2 for the pure Coulomb interaction according to the virial theorem). The kinetic pressure attenuation when the bonded atoms approach is the ultimate reason for the covalent bonding, and an orbital deformation (polarization and contraction) and the electron correlation are important in the subsequent step. The electron occupation in a bonding orbital (with no node along the bonding direction) is the signature for kinetic pressure attenuation in the bonding region and the formation of a covalent bond.

It is known that the spin−orbit effect can alter the bond strength of molecules (see section 22.3 of ref 66 and the references therein). Two typical examples are TlH[38] and Tl_2[67] molecules, whose bond energies are greatly weakened when the spin−orbit effect is included. Conceptually, one may explain this phenomenon by the fact that the spin−orbit effect lowers the energy of the Tl $6p_{1/2}$ orbital and thus stabilizes the Tl atom at the dissociation limit. In this section, we explain this antibonding spin−orbit effect in terms of the population analysis using the natural spinors. To this end, we perform the two-step spin−orbit coupling calculations for the two molecules with the active space of the valence spin-free one-component natural orbitals and investigate the change of their electron occupation numbers. This change of occupation numbers reflects the change of the bond strength. Before going into the details, we need to emphasize that we focus on the qualitative wave function analysis by studying the natural spinors, as accurate quantitative energetics are not pursued here.

We employ a very simple model for the TlH calculation, and since this is a qualitative study, the simple model can tell us what we need to know without the entanglement of other nondetermining factors. In this model, we completely contract the well-tempered basis functions (WTBS)[68] using the atomic orbital coefficients (calculated at the relativistic level of the third order of Douglas−Kroll−Hess (DKH3) Hamiltonian[69,70]) to make the basis set for Tl and completely contract the s primitives of the aug-cc-pV5Z basis set[71] to make the basis set for H. No additional diffuse or polarization functions are added. The construction of these basis sets is similar to that of the MINI basis set,[72] providing no polarization and only near-degeneracy (often called strong) correlation within the valence orbital space, for a simple qualitative analysis illustrating the concepts. We note here that our analysis is based on occupation numbers of natural orbitals (NOs), and *the NO occupation numbers are stable quantities that do not vary much when a wave function is improved, once a wave function has been defined that includes the most important NOs.*[73] We do not involve any dynamic electron correlation in this model since correlation does not dominate in a conventional covalent bond.[62] Neglecting this effect helps to disentangle this complex interaction from the rest and focus on the interplay between spin−orbit and covalent interactions.

Using these basis sets and the active space of two electrons in the σ, σ^*, and π orbitals, we perform a complete active space self-consistent field (CASSCF) geometry optimization to find the equilibrium internuclear distance of 2.062 Å. This rather long bond length as compared to the experimental value of 1.872 Å[63] is as expected because of the unpolarized basis set used and the missing dynamic correlation. For this structure, CASCI is performed to obtain one-component natural orbitals of the ground state $^1\Sigma^+$ term, and those orbitals are depicted in Figure 1a−c with their

occupation numbers listed in Table 1. Obviously, the π orbitals are the nonbonding $6p_{x,y}$ orbitals of Tl, and the asterisk of the σ^* orbital denotes its antibonding charater. Subsequently, all Γ-S terms generated by the CASCI distributing two electrons in the four natural orbitals are included in the spin−orbit CI calculation to produce the ground state spin−orbit wave function, the 0^+ level.

Employing this active space, the 0^+ level's natural spinors can be represented by the one-component natural orbitals of the $^1\Sigma^+$ term, and their expressions and occupation numbers are:

$$\frac{1}{2} = 0.993885\sigma\alpha - 0.001369\sigma^*\alpha - 0.078072(\pi_x\beta + i\pi_y\beta), \text{occup} : 0.9641 \quad (4)$$

$$\frac{1'}{2} = -0.022310\sigma\alpha + 0.976810\sigma^*\alpha - 0.150574(\pi_x\beta + i\pi_y\beta), \text{occup} : 0.0355 \quad (5)$$

$$\frac{3}{2} = \sqrt{\frac{1}{2}}\pi_x\alpha + i\sqrt{\frac{1}{2}}\pi_y\alpha, \text{occup} : 0.0002 \quad (6)$$

$$\frac{1''}{2} = 0.108142\sigma\alpha + 0.214105\sigma^*\alpha + 0.686464(\pi_x\beta + i\pi_y\beta), \text{occup} : 0.0002. \quad (7)$$

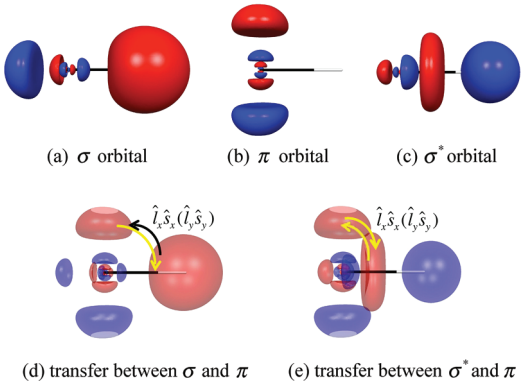

Figure 1. One-component natural orbitals from CASCI without spin−orbit coupling (a−c) for TlH, as well as the spin−orbit coupling induced electron transfer (d,e) among them. The Tl atom is on the left (black), and hydrogen on the right (white). The $\hat{l}_x$ and $\hat{l}_y$ operators are centered on the Tl atom. In d and e, if the shown π orbital is the π_y component, then the $\hat{l}_x\hat{s}_x$ operator applies and similarly for π_x and $\hat{l}_y\hat{s}_y$. Substantial electron transfers (typically, from occupied to unoccupied orbitals) are denoted by a black arrow, while the negligible ones are denoted by yellow ones.

Here, we use the ω value (the eigenvalue of the $\hat{j}_z$ operator on the left-hand side of the expressions above) to label the natural spinors and prime and double prime to differentiate the orbitals with the same ω. Since the Kramers pairs[74] (with negative ω) of the listed natural spinors have the same eigenvalues, they are omitted here, and one can apply the time-reversal operator on the listed spinors to generate them.[66,75] The effect of the time-reversal operator is to change α to β and β to $-\alpha$ and take the complex conjugate for its operand. Despite its simplicity, this model includes the primary covalent and spin−orbit interactions and serves as a good model to study the interplay between these two interactions.

To compare the one-component natural orbitals (σ, σ^*, and π) to the natural spinors of the spin−orbit 0^+ wave function, we can calculate the averaged occupation numbers (diagonal density matrix elements) for each of the natural spinors according to

$$\text{occ}_i = \sum_j \text{occ}_j |C_{ij}|^2 \quad (8)$$

where i labels the one-component natural orbitals, j labels the natural spinors, C_{ij} are the coefficients in eqs 4−7, and the summation runs over all of the natural spinors. The calculated average occupation numbers are listed in Table 1. The comparison of the occupation numbers for the $^1\Sigma^+$ and 0^+ wave functions indicates that the spin−orbit interaction causes a substantial electron transfer (0.0285) from the bonding σ orbital to the nonbonding π and antibonding σ^* orbitals. This electron transfer weakens the bond, and if we use the effective bond order model,[73,76] in which the bond order equals one-half of the total occupation number of bonding orbitals less the total occupation number of antibonding orbitals, then the TlH bond order is lowered from 0.9336 to 0.9184. Most of the depleted electron from the σ orbital (0.0270) is deposited in the nonbonding π orbitals, and this can be explained considering the detailed spin−orbit interaction. For the TlH molecule, the spin−orbit effect at the Tl nucleus is overwhelming and, focusing on the interaction around this nucleus, we label the orbital angular momentum operators centered on Tl as $\hat{\vec{l}}$. In the ground state, the spin−orbit effect must lower the energy,[12] and this stabilization is the driving force for the electron transfer.

The relevant spin−orbit induced electron transfer is illustrated in Figure 1d. Since only the σ orbital is substantially occupied in the original $^1\Sigma^+$ wave function, the net result observed is electron transfer from σ to π orbitals. Likewise, any charge originally occupying the π orbitals can be transferred to the σ^* orbital and vice versa, as illustrated in Figure 1e. Because of the insignificant occupations of the σ^* and π orbitals, the transfer between them is negligible. As $\hat{l}_z$ can only couple the two π orbitals and the electron transfer between these two nonbonding orbitals does not change the bond strength, the effect of $\hat{l}_z$ is not shown. One

Table 1. Electron Occupation Numbers in TlH and Tl_2 of the Spin-Free Natural Orbitals Induced by the Spin−Orbit Coupling and the Electric Dipole Moments μ (Debye) in TlH

	TlH				Tl_2			
spin−orbit coupling	σ	σ^*	π^a	μ^b	σ_g	σ_u	π_u	π_g
neglected	1.9332	0.0661	0.0003 × 2	1.2958	1.8746	0.0432	0.0409 × 2	0.0002 × 2
included	1.9047	0.0678	0.0138 × 2	1.1821	1.8340	0.0447	0.0406 × 2	0.0202 × 2
Δ^c	−0.0285	0.0017	0.0135 × 2	−0.1137	−0.0406	0.0015	−0.0003 × 2	0.0200 × 2

[a] The multiplication by 2 for π orbitals reflects the degenerate occupation of the π_x and π_y components. [b] The dipoles are pointing from H to Tl. [c] The values with spin−orbit coupling included minus those where it is neglected.

dx.doi.org/10.1021/ct200457q |J. Chem. Theory Comput. 2011, 7, 2864–2875

should notice that both σ and σ^* orbitals have $m_{lz} = 0$ (where m_{lz} is the projection value of the orbital angular momentum along the z axis) and $\langle\sigma|\{\hat{l}_x, \hat{l}_y, \hat{l}_z\}|\sigma^*\rangle = 0$. Therefore, no electron can be directly transferred between the two orbitals by rotation, and any possible transfer has to be mediated by a transfer to a π orbital. This secondary electron promotion explains the negligible increase of the σ^* orbital occupation in the 0^+ wave function, so the weakened bond in TlH is due to the loss of the bonding, rather than a direct increase in the antibonding effect. The electric dipole moments for the $^1\Sigma^+$ and 0^+ wave functions are calculated and the reduction of the dipole by 0.1137 D is consistent with the fact that more electrons are located at the Tl center of the molecule by the electron transfer from the bonding to the nonbonding orbitals, and the positive charge of the region near Tl is reduced.

A similar investigation is also performed for Tl_2. For computational efficiency, we employed our newly developed ZFK3[77] model core potential and basis set for Tl, and the spin−orbit effect in this potential is at the level of DKH1.[78,79] The active space includes six orbitals with two electrons distributed among them. CASSCF geometry optimization for the first $^1\Sigma_g^+$ term gives the equilibrium internuclear distance of 3.507 Å. The $^1\Sigma_g^+$ term is of interest because it has the σ_g^2 electron configuration, which is similar to the σ^2 configuration of TlH that we just discussed, and the two cases can be compared. One should note that several studies[67,80−82] determined that the actual spin−orbit ground state of Tl_2 is the 0_u^- level stemming from the $^3\Pi_u$ term. Therefore, the $^1\Sigma_g^+$ term considered here is not the overall ground state but only the lowest $^1\Sigma_g^+$ term, used here for illustrative purposes.

At the equilibrium internuclear distance, CASCI is used to generate the $^1\Sigma_g^+$ wave function and the associated six one-component natural orbitals, σ_g, π_u, σ_u, and π_g, which are depicted in Figure 2a−d, and their occupation numbers are listed in Table 1. All of the *gerade* Γ-S terms generated with the active space of distributing two electrons in the six natural orbitals are used as the multielectron basis for the subsequent spin−orbit CI calculation to produce the spin−orbit 0_g^+ wave function. Only the gerade (g) terms are considered because the spin−orbit operator conserves parity, and we focus mainly on the spin−orbit influence on the $^1\Sigma_g^+$ term. The averaged occupation numbers of the one-component natural orbitals are obtained through the same procedure as the TlH case, and they are also listed in Table 1. As in the TlH case, the electron occupation in the bonding σ_g orbital is substantially depleted (0.0406), and most of this depletion is deposited into the antibonding π_g orbitals. Because of the even parity of the spin−orbit operator, only orbitals with the same parity can be coupled, which explains the correspondence between the electron depletion of the σ_g and the electron deposition on the π_g orbital. The electron transfer between the π_u and σ_u orbitals is insignificant, since they are barely occupied in the $^1\Sigma_g^+$ wave function. Employing the aforementioned effective bond order model, we calculate the bond order of Tl_2 to be 0.9564 for the $^1\Sigma_g^+$ and 0.9150 for the 0_g^+ wave function. Apparently, the decrease of the bond order for Tl_2 (0.0414) is greater than that for TlH (0.0152), consistent with the increase of the number of heavy atoms (Tl). However, considering the different basis sets used for the two molecules (without polarization functions for TlH, with polarization functions for Tl_2), this bond order change comparison is only qualitative.

Figure 2e,f demonstrates the electron transfer induced by the $\hat{l}_i\hat{s}_i$ components ($i = x, y$) of the spin−orbit operator. Similar arguments as for Figure 1d,e can be made, except that the inversion

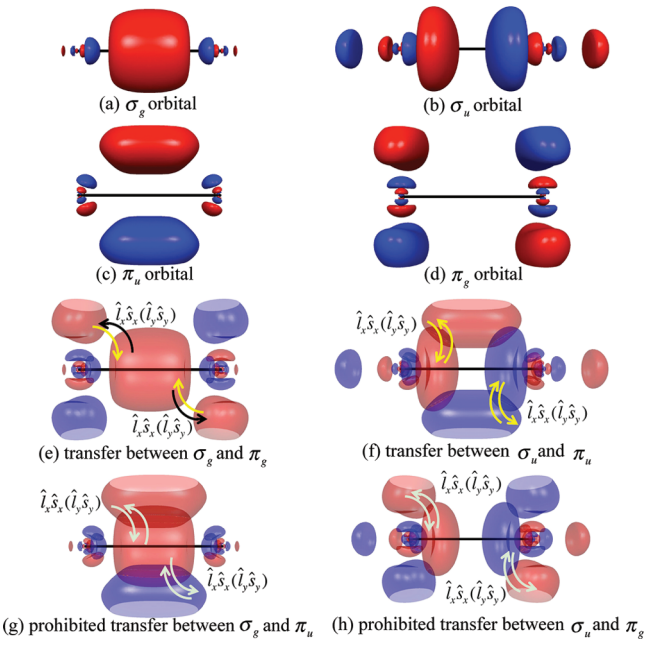

Figure 2. One-component natural CASCI orbitals (a−d) of Tl_2 and the spin−orbit coupling induced electron transfer (e−h) among them. In e−h, the $\hat{l}_x$ and $\hat{l}_y$ operators centered on the two Tl centers cause the electron transfer to (or from) the π_y and π_x orbitals, respectively. The substantial transfers are denoted by a black arrow, the negligible ones by yellow, and the prohibited ones by gray.

symmetry adds to the correlated electron rotation (transfer) around the two Tl nuclei, which is reflected in the inversion-symmetric pairwise arrangement of the curved arrows in Figure 2e,f. Actually, Figure 2e−h provides a graphical description of the even parity of the spin−orbit interaction. If the spin−orbit induced in-phase rotation (red to red or blue to blue) is energetically favorable, then the inversion-symmetrically correlated electron motion guarantees that this effect at the two Tl centers adds up in Figure 2e,f. This accumulation effect also applies if the out-of-phase (red to blue or blue to red) is energetically favorable instead. In contrast, in Figure 2g,h, an in-phase rotation on one side of the molecule must correspond to an out-of-phase rotation on the other side, and the spin−orbit effects cancel out. Therefore, any g−u electron transfer results in a null energy gain, and the spin−orbit effect must conserve the parity of the orbitals.

One might argue that the spin−orbit antibonding effect leads to a very substantial reduction of the dissociation energy (D_e), incommensurate with the reduction of bond order presented in this work. For example, in our recent study of TlH,[38] the reduction of the dissociation energy is about 0.4 eV at the CI level, 1/5 of the D_e of the $^1\Sigma^+$ state, while the reduction of bond order in the present work is just 1.6%. Furthermore, the 0_g^+ level of Tl_2 was predicted to be purely repulsive,[80] but our natural orbital analysis still predicts substantial bonding. This is because we focus only on the wave function change induced by the spin−orbit interaction without considering the explicit energy effects. At the dissociation limits for both TlH and Tl_2, the Tl 6p orbitals are all degenerate, and there is no energy cost for the spin−orbit induced electron transfer among them. Therefore, the spin−orbit stabilization leads to its maximum energy lowering at the dissociation limits. However, the degeneracy of the 6p orbitals is lifted as the covalent

bonds are formed, and the bonding electron pair tends to occupy the orbitals with lower energies (σ for TlH and σ_g for Tl_2). Consequently, the spin−orbit induced rotation will have to promote the electron from the low-energy orbitals to the high-energy orbitals, and this additional energy cost quenches the spin−orbit interaction and consequently reduces the amount of the spin−orbit energy lowering. This can also be understood as the covalent interaction hindering the spin−orbit induced electron transfer. The R-dependent spin−orbit stabilizations cause the large reduction of D_e for the 0^+ level of TlH and the purely repulsive potential energy curve for the 0_g^+ level of Tl_2. This effect cannot be revealed by considering only the wave functions at the equilibrium internuclear distances. In fact, there are many factors that together determine the bond energy, and it has been pointed out[73] that in general there is no direct correlation between bond order and bond energy.

Although only diatomic molecules are considered in this section, the concept presented here can be straightforwardly generalized to other molecules. For polyatomic molecules, there could be mixed bonding, antibonding, and nonbonding character in each one-component natural orbital, and this may complicate the analogous analysis. To solve this problem, one may use Weinhold's natural bond orbitals,[83−86] which have clear bonding, antibonding, or nonbonding character, as the basis to obtain the natural spinors. Before closing this section, we would like to once again emphasize that the computational methods and basis sets for TlH and Tl_2 were chosen to produce two bonding models that manifest interplay between covalent and spin−orbit interactions. One can use our analysis at higher levels such as the natural spinors from the energetically accurate multireference CI method.

4. HOW SPIN−ORBIT COUPLING QUENCHES THE JAHN−TELLER DISTORTION

In qualitative terms (see Figure 2.9 of ref 87), the Jahn−Teller distortion is caused by a nontotally symmetric electronic distribution in one of the degenerate electronic states. Under that circumstances, the symmetry of the Coulomb interactions between the nuclei and electrons is lowered, and the molecular structure is distorted correspondingly.[87,88] It has been reported that the spin−orbit interaction can quench the Jahn−Teller effect, and two simple but enlightening examples are Pb_3^+ [42] and WF_5.[41] Without considering the spin−orbit effect, the excited states of Pb_3^+ and the ground state of WF_5 suffer a strong Jahn−Teller distortion and change their structures from D_{3h} to C_{2v} symmetry. When the spin−orbit coupling is considered, however, those energetic minima are shifted back to the D_{3h} structure. This can be explained either by the fact that the spin−orbit interaction splits the electronic degeneracy and removes the driving force for the distortion or that the spin−orbit interaction introduces new symmetry operations of the double group, and the distortion based on point group arguments may not happen in the double group context.[43,89] To the best of our knowledge, the studies of this quenching effect have so far been based on the multielectron wave functions, with the focus placed on the spin−orbit and vibronic coupling between different electronic terms. Although this multielectron picture is natural for physicists, it does not serve as a good illustration in terms of the orbital picture of interactions. Therefore, an orbital-based explanation of this quenching would be informative, and in the present section we will use the natural spinors to illustrate

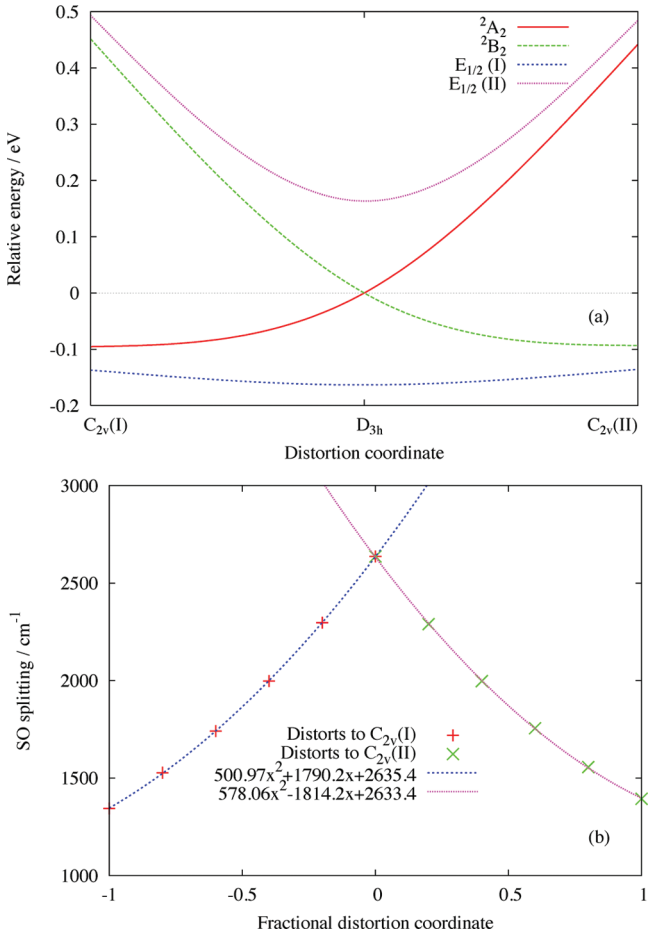

Figure 3. (a) Energetic profile of the Jahn−Teller distortion of WF_5. The term and level symbols are labeled as in the C_{2v} point group and double group. The curves are obtained by cubic-splines fitting to the energies calculated at the three labeled structures. (b) The spin−orbit splitting along the fractional distortion coordinate. From 0 to −1 is the $^2A_2$ distortion channel to the C_{2v}(I) structure and from 0 to 1 is the $^2B_2$ distortion channel to the C_{2v}(II) structure. The equations of the two fitted quadratic curves are also shown.

this quenching effect, with WF_5 as an example. In this work, we only focus on the traditional Jahn−Teller distortion that is induced by the electrostatic interaction. The recently formulated spin−orbit induced Jahn−Teller effect[48,49] is not considered here.

For computational efficiency, we employed the SBKJC effective core potentials (ECP) and basis sets.[90−92] Correspondingly, the spin−orbit adapted effective charges[93,94] were used for the spin−orbit CI calculations. We optimized the WF_5 structure both in D_{3h} and in the C_{2v} symmetry. In the D_{3h} optimization, the CASSCF calculation with one electron being distributed in the e'' degenerate orbitals is performed to calculate energy, while in the C_{2v} optimization the restricted open-shell Hartree−Fock (ROHF) is employed (which is equivalent to the CASSCF in D_{3h}, because there is only one occupied orbital instead of two). There are two distorted C_{2v} structures, whose ground states are $^2A_2$ and $^2B_2$, and we label them as C_{2v} (I) and C_{2v} (II), respectively. The $^2A_2$ and $^2B_2$ states cross at the D_{3h} symmetry and form the two components of the $^2E''$ state. The energetic profile of the distortion is illustrated in Figure 3a. The relative energies of these states and structural parameters of the three

Table 2. Bond Lengths (in Å), Angles (in Degrees) and Relative State Energies (eV) of the D_{3h} and the Two C_{2v} Structures of WF_5[a]

	W_1-F_3	W_1-F_6	W_1-F_5	$F_4-W_1-F_5$	$^2A_2$	$^2B_2$	$E_{1/2}$(I)	$E_{1/2}$(II)
D_{3h}	1.902	1.841	1.841	120.00	0.000	0.000	−0.163	0.163
C_{2v} (I)	1.904	1.826	1.846	109.80	−0.095	0.452	−0.137	0.493
C_{2v} (II)	1.904	1.854	1.831	129.53	0.442	−0.093	−0.136	0.484

[a] Term symbols are assigned according to the C_{2v} point group and its double group. The energy of the $^2E''$ state for the D_{3h} structure is taken to be the zero energy.

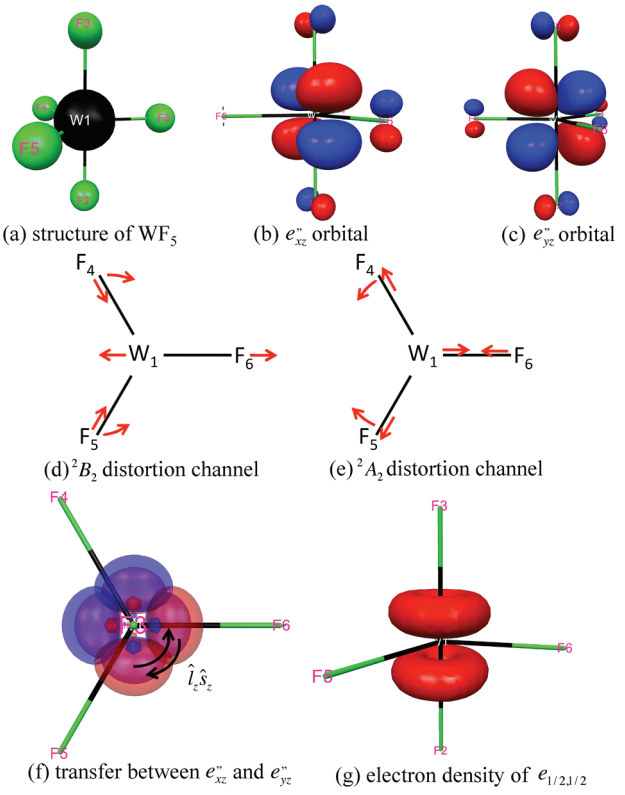

Figure 4. Structure (a), CASCI natural orbitals (b,c), distortions (d,e), spin−orbit induced electron transfer (f), and natural spinor electron density (g) of WF_5. The $\hat{l}_z$ operator in g is centered on W.

structures are listed in Table 2. The atoms are labeled according to Figure 4a. In this discussion, the $F_3-W_1-F_2$ and F_6-W_1 axes are the principal axes for the D_{3h} and C_{2v} structures, respectively.

Going from the C_{2v}(I) to D_{3h} and to C_{2v}(II) structures, the W_1-F_6 bond is lengthened. The W_1-F_4 and W_1-F_5 bonds are shrunk equivalently, and the $F_4-W_1-F_5$ angle opens up. This is the Jahn−Teller distortion coordinate. The structural parameters in Table 2 indicate that the $F_4-W_1-F_5$ angle changes more substantially than all of the W−F bond lengths in the distortion. Therefore, the distortion coordinate is mainly of a bending nature. The $^2A_2$ and $^2B_2$ terms ($^2E''$ term at the D_{3h} structure) are included in the spin−orbit coupling, and the energies of the resultant spin−orbit wave functions ($E_{1/2}$ and $E_{3/2}$ levels at the D_{3h} structure and $E_{1/2}$(I) and $E_{1/2}$(II) levels at the C_{2v} structures) are also listed in Table 2. The results from our calculations are qualitatively consistent with those of the previous DFT study of Dyall,[41] with the correct term symbols (see ref 95) and structural parameters slightly different by about 0.01 Å. The lack of interelectron correlation in the present study suggests that Dyall's B3LYP structural parameters and energies are more reliable. However, the energy profile in Figure 3a indicates that our simple model captures all of the essences of the distortion and its spin−orbit quenching.

All of the atomic labels in this discussion follow Figure 4a. The electronic configuration of WF_5 at the D_{3h} structure is predicted to be $(e'')^1$, and the e'' orbitals are shown in Figure 4b and c. Taking the $F_3-W_1-F_2$ and F_6-W_1 axes to be z and x axes, we call the two orbitals e''_{xz} and e''_{yz} orbitals, characterizing their main d components at the W center. Taking the F_6-W_1 axis as the C_{2v} principal axis, the e''_{xz} and e''_{yz} orbitals correspond to the b_2 and a_2 orbitals. Obviously, the e''_{xz} orbital has antibonding character for the W_1-F_6 bond, and increasing the population in the e''_{xz} orbital (forming the $^2B_2$ term) elongates the bond. As a consequence of this elongation, the reduced repulsion between F_6 and the remaining equatorial fluorine atoms (F_4 and F_5), with each of the equatorial fluorine atoms carrying Mulliken charge of −0.457 a.u., leads to shorter F_4-W_1 and F_5-W_1 bonds, and consequently, the stronger F_4-F_5 repulsion leads to the larger $F_4-W_1-F_5$ angle. This distortion is illustrated by Figure 4d. The e''_{yz} orbital has antibonding character for the F_4-W_1 and F_5-W_1 bonds, and putting an electron in this orbital (forming the $^2A_2$ term) elongates the two bonds. Meanwhile, the $F_4-W_1-F_5$ angle tends to be smaller to reduce the out-of-phase overlap between the p_z orbitals on F_4 and F_5 and the d_{yz} orbital on W. Smaller repulsion between the two equatorial atoms F_4 and F_5 and the remaining equatorial atom F_6 leads to a shorter F_6-W_1 bond. This distortion is illustrated in Figure 4e. Since both e'' orbitals have the same antibonding character along the $F_2-W_1-F_3$ axis, the F_2-W_1 and F_3-W_1 bond lengths are unchanged along the distortion. This orbital analysis based on antibonding characters and electrostatic repulsion fully explains the distortion coordinate mentioned in the previous paragraph. Obviously, this distortion coordinate is a component of the e' vibrational normal mode of the D_{3h} point group, and hence, this Jahn−Teller distortion is a typical $E'' \otimes e'$ problem.[87]

The spin−orbit CI calculation for the $^2E''$ term produces two levels, each having a pair of Kramers doublets. The natural spinors of the two lower states are calculated to be

$$e_{1/2,1/2} = \frac{1}{\sqrt{2}} e''_{xz}\beta + \frac{i}{\sqrt{2}} e''_{yz}\beta;$$
$$e_{1/2,-1/2} = \frac{1}{\sqrt{2}} e''_{xz}\alpha - \frac{i}{\sqrt{2}} e''_{yz}\alpha \quad (9)$$

and those of the two higher states are

$$e_{3/2,3/2} = \frac{1}{\sqrt{2}} e''_{xz}\alpha + \frac{i}{\sqrt{2}} e''_{yz}\alpha;$$
$$e_{3/2,-3/2} = \frac{1}{\sqrt{2}} e''_{xz}\beta - \frac{i}{\sqrt{2}} e''_{yz}\beta \quad (10)$$

dx.doi.org/10.1021/ct200457q |J. Chem. Theory Comput. 2011, 7, 2864–2875

Each of them is singly occupied in the corresponding levels. We can assign the symmetry label $e_{1/2,1/2}$ to the first spinor easily, as the $XZ\beta + iYZ\beta$ combination only exists in the $d_{3/2,1/2}$ and $d_{5/2,1/2}$ spinors (Table S.II of ref 28) and it has $j_z = 1/2$, and all functions with $j_z = 1/2$ must be of the $E_{1/2}$ irreducible representation of the D_{3h} double group.[96] The remaining orbitals follow the same argument. Here "XZ" and "YZ" represent any functions sharing the same symmetry properties as the d_{xz} and d_{yz} spherical harmonics, and similar notation is used below without further specification. Obviously, this labeling is consistent with the decomposition of the direct product between the orbital and spin representations in the D_{3h} double group:

$$E'' \otimes E_{1/2} = E_{1/2} \oplus E_{3/2} \tag{11}$$

This relationship demonstrates the usefulness of Table S.II of ref 28 for fast symmetry labeling of the natural spinors. However, this trick can be used only when there are basis functions on the principal axis, although one may put ghost functions on the principal axis to meet this requirement. Also, one has to check whether the m_{jz} values can be uniquely associated with the double group irreducible representations. Despite all of these constraints, the tentative symmetry labeling by using this trick serves as a good starting point for the more rigorous labeling by checking the double group character tables.

The like spins in each of the natural spinors suggest that only the $\hat{l}_z\hat{s}_z$ component of the spin−orbit operator is involved. This is consistent with the fact that $\langle XZ|\hat{l}_z|YZ\rangle$ is the only nonzero matrix element of $\langle XZ|\{\hat{l}_x, \hat{l}_y, \hat{l}_z\}|YZ\rangle$. Because of the much larger spin−orbit interaction around the W nucleus, the orbital angular momentum operators discussed here are centered on W. The spin−orbit induced electron transfer from the e_{xz}'' to e_{yz}'' orbitals and vice versa are illustrated in Figure 4f. Using the concept of spherical tensors,[55] one can easily associate the combinations of $e_{xz}'' + ie_{yz}''$ and $e_{xz}'' - ie_{zy}''$ to the eigenfunctions of $\hat{l}_z$ with eigenvalues of +1 and −1. Thus, the associated spin functions of eqs 9 and 10 indicate the two $e_{1/2}$ orbitals are of antiparallel coupling nature, while the two $e_{3/2}$'s are of parallel coupling, and this explains the spin−orbit stabilization of the $E_{1/2}$ and destabilization of the $E_{3/2}$ level. Contrary to the $\hat{l}_x\hat{s}_x$ and $\hat{l}_y\hat{s}_y$ induced electron transfer in the TlH and Tl_2 cases discussed above, the two orbitals involved in the $\hat{l}_z\hat{s}_z$ induced electron transfer in WF_5 are degenerate, and therefore the transfer is not hindered energetically. This free rotation leads to equivalent contributions from the two e'' orbitals in the $e_{1/2}$ and $e_{3/2}$ orbitals, in strong contrast to the unequal orbital contributions in eqs 4 and 5. Equations 6 and 7 have the same contributions from the π_x and π_y orbitals, as they are also degenerate and the $\hat{l}_z\hat{s}_z$ induced electron transfer is also without hindrance. When the symmetry is broken to C_{2v} and the two e'' orbitals are split to a_2 and b_2 with different energies, the rotation is hindered. The natural spinors for the $E_{1/2}(\mathrm{I})$ state at the $C_{2v}(\mathrm{I})$ structure are calculated to be

$$\begin{aligned} e_{1/2} &= 0.966440a_2\alpha + 0.256892b_2\beta \\ &\approx 0.966440e_{yz}''\alpha + 0.256892e_{xz}''\beta \end{aligned} \tag{12}$$

and its Kramers pair, with each of them singly occupied for the two $E_{1/2}$ components. The label $e_{1/2}$ is assigned since $E_{1/2}$ is the only Fermion irreducible representation of the C_{2v} double group and the approximate equality in eq 12 associates the orbital labels to those of D_{3h} symmetry. (The a_2 and b_2 orbitals at this structure cannot be identical to the e'' orbitals at the D_{3h} structure since orbitals are relaxed in the course of distortion.) The dominance of $a_2\alpha$ reflects the difficulty of the spin−orbit induced electron transfer, which is also seen in the small amount of spin−orbit energy lowering (0.042 eV) compared to that at the D_{3h} symmetry (0.163 eV).

The hindering of the spin−orbit induced electron transfer is also reflected by the smaller spin−orbit splitting at the distorted structures. Figure 3b illustrates the decrease of the spin−orbit splitting along the distortions to the two C_{2v} structures from the D_{3h} reference. In this figure, the spin−orbit splitting is estimated as

$$|E_{E_{1/2}(II)}(\underline{R}) - E_{E_{1/2}(I)}(\underline{R})| - |E_{2A_2}(\underline{R}) - E_{2B_2}(\underline{R})| \tag{13}$$

i.e., subtracting the splitting between the $^2A_2$ and $^2B_2$ terms from the splitting between the $E_{1/2}(\mathrm{I})$ and $E_{1/2}(\mathrm{II})$ levels at a given structure $\underline{R}$. The molecular structures between the D_{3h} reference and the two C_{2v} limits are obtained by fractional interpolation. For example, a structure between the D_{3h} and $C_{2v}(\mathrm{II})$ structures is given by

$$\underline{R}(f) = \underline{R}(D_{3h}) + f(\underline{R}(C_{2v}(\mathrm{II})) - \underline{R}(D_{3h})) \tag{14}$$

where $\underline{R}$ stands for coordinate vector of all six atoms and f is the fractional distortion coordinate ranging from 0 to 1. For the convenience of comparison between the two panels of Figure 3, we plot the spin−orbit splittings along the $^2A_2$ distortion (i.e., $C_{2v}(\mathrm{I})$) channel versus the negative values of the fractions. The two fitted curves in Figure 3b indicate a linear decrease of the spin−orbit splitting in the vicinity of the D_{3h} structure along each direction of the distortion. This can be understood by considering a Taylor expansion of the energy with respect to the distortion coordinate at the vicinity of the D_{3h} structure. The linear term is given by the energy gradient. Let us examine the symmetry properties of the gradient terms of matrix elements of the spin−orbit operator between two states. The symmetry of the spin−orbit operator derivative is of the E' irreducible representation, i.e., the symmetry of the distortion coordinate. The three possible direct products of the two states for the matrix elements are

$$A_1' \notin E_{1/2} \otimes E' \otimes E_{1/2} \tag{15}$$

$$A_1' \notin E_{3/2} \otimes E' \otimes E_{3/2} \tag{16}$$

$$A_1' \in E_{1/2} \otimes E' \otimes E_{3/2} \tag{17}$$

We can conclude that the coupling between the $E_{1/2}$ and $E_{3/2}$ states is allowed by symmetry (A'_1 is the totally symmetric irreducible representation of the D_{3h} double group), and it is this interaction that results in the nonzero gradient and thus linear terms in the Taylor series describing the dependence of the spin-orbit splitting as a function of the distortion coordinate.

As a side issue, it is worthwhile to discuss why the $\hat{l}_z\hat{s}_z$ operator in Figure 4f can couple different spins (mixing α and β in eq 12) when the structure is distorted. The reason is that in the calculation at the C_{2v} structure, the z axis has been reoriented along the F_6−W_1 bond and so is the quantization of the spin. Consequently, the $\hat{l}_z\hat{s}_z$ operator in Figure 4f becomes a $\hat{l}_y\hat{s}_y$ operator. The original e_{zy}'' and e_{xz}'' orbitals become of symmetry XY and YZ, and they are only coupled by $\hat{l}_y$ in the new coordinates. Thus, the flipping of spin is the result of choosing the new coordinate. To justify this reasoning, we carry out the calculation again, this time choosing the same coordinate

frame as the one for the D_{3h} structure, and produce the natural spinors to be

$$e_{1/2} = 0.966440a_2\alpha + i0.256892b_2\alpha \approx 0.966440e''_{yz}\alpha + i0.256892e''_{xz}\alpha \quad (18)$$

and its Kramers pair. Obviously, the electron transfer in this new coordinate is induced by the $l_z s_z$ component of the spin−orbit interaction, and the spin-flipping is removed. This side issue reminds us of the importance of choosing the right coordinate for a meaningful discussion. It is often troublesome to switch between coordinate systems when using several different point groups for the same system because of the convention most programs use to define the principal and secondary axis orientations, and tedious care should be exercised in discussing the symmetry labels and following their interrelation when the symmetry is changed.

As a result of the unhindered electron transfer at the D_{3h} symmetry and equivalent contributions from the two e'' orbitals, the spatial part of the electron densities of all of the natural spinors has the symmetry $(X^2 + Y^2)Z^2$, and this cylindrically symmetric electron density is plotted in Figure 4g. Obviously, the Coulomb potential stemming from this cylindrical distribution belongs to the totally symmetric irreducible representation (A_1') of the D_{3h} point group. Hence, there is no nontotally symmetric force exerted by the electrons to the nuclei around W that can distort the D_{3h} symmetric nuclear configuration so the Jahn−Teller distortion is quenched. One may argue that as the two e'' orbitals are degenerate, even without the spin−orbit effect, we may freely combine them as eq 9 and have a totally symmetric electron density, and the Jahn−Teller distortion could be avoided from the beginning. However, if this totally symmetric electron distribution is not stabilized by the spin−orbit interaction, it can be easily distorted by any perturbation induced by the nontotally symmetric molecular vibration, and the Jahn−Teller distortion would be turned on. Actually, if the spin−orbit stabilization of the totally symmetric electron distribution is not strong enough, despite the degeneracy removal, the energy gain from the vibronic coupling can still recouple the $e_{1/2}$ and $e_{3/2}$ orbitals to produce nontotally symmetric electron distribution, leading to the so-called pseudo-Jahn−Teller distortion. In such a case, the D_{3h} minimum on the blue curve of Figure 3a would become a maximum, a transition state connecting two stable C_{2v} structures. This distortion originates from the vibronic mixing of two (or more) nondegenerate electronic states under nuclear displacements. The ratio between the square of the vibronic coupling constant and the energetic gap between the electronic states determines whether the distortion is allowed.[87,88] In the context of this work, the energetic gap is proportional to the strength of the spin−orbit interaction, and the stronger the spin−orbit interaction, the less likely the vibronic distortion. The relative energies in Table 2 indicate that the spin−orbit stabilization (0.163 eV) is more substantial than the Jahn−Teller stabilization (0.093 and 0.095 eV) and that is why the D_{3h} structure is stable. Generally, the competition between the spin−orbit stabilization and the vibronic stabilization determines whether the high symmetry structure can stably exist.[43] The comparison between the strong and weak spin−orbit interactions in the stabilization of the high-symmetry nuclear configuration is illustrated by Figure 5.

The discussion of the simple WF_5 example can be generalized as follows. In the high symmetry structure with electronic degeneracy, the spin−orbit induced electron transfer among the degenerate orbitals is unhindered and the spin−orbit effect is maximized. Whenever this electron transfer produces a totally symmetric electron distribution that provides a totally symmetric Coulomb interaction with the nuclei, and the spin−orbit stabilization of this distribution is more significant than the possible energy lowering induced by the vibronic coupling, the Jahn−Teller distortion is quenched and the stable high-symmetry structure will exist. In other words, the spin−orbit interaction has an inherent symmetry-driven tendency to quench the electrostatic Jahn−Teller distortion, but it may not always have the strength to do so by sufficiently lowering the energy (clearly demonstrated in Figure 5, where the central high symmetry structure can have a higher or lower energy than the lower symmetry ones, depending on the magnitude of the splitting). Paradoxically, the electronic degeneracy that leads to the Jahn−Teller distortion also enlarges the spin−orbit interaction that quenches the distortion. One should note that although the spin−orbit interaction cannot split the degeneracy induced by the time-reversal symmetry (Kramers degeneracy), but neither can the vibronic coupling.[87,88] In this sense, for a system with an odd number of electrons, as long as the spin−orbit interaction splits all the electronic degeneracy into the double-valued Fermion irreducible representation of the corresponding double group and provides enough stabilization, the Jahn−Teller distortion is quenched. We would also like to emphasize that the spin−orbit effect may not completely split all of the electronic degeneracy to the Kramers 2-fold degeneracy, as for the T, O, and I type double groups, 4-fold Fermion irreducible representations are present.[89] For the molecules whose structures are of the corresponding point groups, the Jahn−Teller distortion can still occur with a spin−orbit coupled electronic wave function.

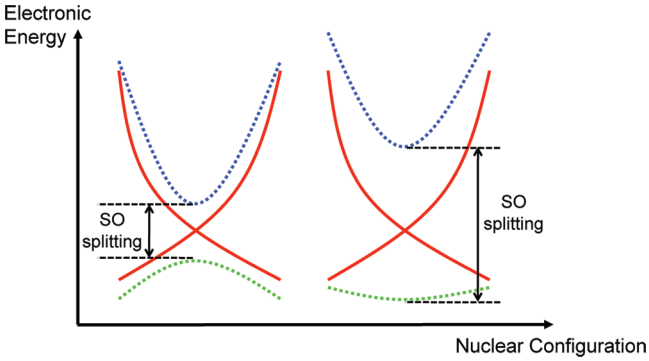

Figure 5. A schematic energy profile of the interplay between the spin−orbit (SO) interaction and the Jahn−Teller distortion. The red curves represent adiabatic potential energy curves without spin−orbit interaction, whereas the blue and green are with the interaction. On the left panel, the spin−orbit splitting is not strong enough to completely quench the Jahn−Teller distortion, resulting in the pseudo-Jahn−Teller distortion. On the right panel, the spin−orbit interaction is strong enough to stabilize the high-symmetry nuclear configuration. One should notice the similarity between Figure 3a and the right panel here.

A common typical feature of covalent bonding and Jahn−Teller effects is their anisotropy (directionality): covalent bonds are directional as the kinetic pressure of the valence electrons of one bonding atom is attenuated in the direction of the other bonding atom;[61,64] the Jahn−Teller distortion proceeds along the specific direction (molecular vibrational mode) that favors a bonding interaction. It is for this reason that since the dawn of quantum chemistry, the Cartesian basis functions like p_x, p_y, and p_z are convenient, as they are the best

representations for such directional interactions, and the *rotational* analogues like p_{+1}, p_0, and p_{-1} are almost never used. Consequently, directional terminologies like "head-to-head" (for a σ bond) and "side-to-side" (for a π bond) have been used widely in chemistry education and research. In contrast, the spin−orbit interaction is intrinsically rotational, as the presence of angular momentum $\hat{\vec{l}}_{iA}$ in eq 1 shows, and its exertion is through a change of direction. The discussions in sections 3 and 4 reveal that the interplay between the spin−orbit and the bonding effect and Jahn−Teller distortion is caused by the competition between the rotational nature and the directional nature of the different interactions. This conclusion can be readily obtained from the orbital picture of the spin−orbit interaction, which is provided by the natural spinors.

To the best of our knowledge, this direction/rotation competition is proposed for the first time and can be extensively used to explain experimental or computational results in future studies of the spin−orbit effect in chemistry. For example, it can be used to quantitatively interpret the spin−orbit coupling in a metal pair of trinuclear copper complexes bridged by an oxygen ligand (Scheme 4 of ref 4) through the analysis of one-component orbital coefficients in the natural spinor expressions; also, it can be applied to quantitatively investigate the different Jahn−Teller distortion channels of the Tl_6^- cluster anion, which distorts from a cube to a parallelepiped when not considering spin−orbit interaction, but to a tetrahedral star otherwise.[98] There is one special advantage of using natural spinors in wave function analysis. Since the spinors are composed of the orbitals obtained in calculations without spin−orbit, they provide information about the changes induced by spin−orbit coupling to the wave function. In this sense, natural spinors are the natural language to explain any nontrivial spin−orbit effects in chemistry, and their potential utility should be more extensive than what was shown in the present paper.

5. CONCLUSION

In this work, we explored the utility of our newly developed natural spinors based on illustrative case studies. Two examples of TlH and Tl_2 molecules are presented to demonstrate how to use the natural spinors in order to rationalize the spin−orbit effect on bonding interactions (section 3). We demonstrated that the spin−orbit interaction will induce electron transfer among orbitals with different bonding, antibonding, and nonbonding characters (Figures 1 and 2 and Table 1) and affect the bond strength. A graphical description of the parity-conservation of the spin−orbit operator is also presented, connecting the conservation to the accumulation or cancellation of the spin−orbit effect. In section 4, we also used the natural spinors of the $E_{1/2}$ ground state of WF_5 to explain the spin−orbit quenching of the Jahn−Teller distortion (Figures 3 and 4 and Table 2). We demonstrated that the unhindered spin−orbit induced electron transfer among the degenerate orbitals can produce a totally symmetric electron distribution. If the spin−orbit stabilization of this distribution is large enough, the Jahn−Teller distortion is quenched (Figure 5). These illustrative cases demonstrate the power of natural spinors and the methods of analysis. The conclusions can be extended to general cases.

Davidson made the following comment about the natural orbitals in his comprehensive review of natural orbitals:[54] *the real advantage of natural orbitals is in getting maximum understanding for a fixed cost.* The results of the present work demonstrate that the understanding brought about by describing the spin-dependent relativistic effects with the aid of natural spinors can reach far beyond its original scope of electron correlation and lead us to a new vision of spin−orbit coupling. On the basis of the simple pictorial representations of natural spinors, we propose the hypothesis that any unexpected role that the spin−orbit interaction plays in chemistry is rooted in the competition between the rotational nature of the spin−orbit operator and the anisotropic interactions. This supposition provides the basis for the understanding of spin−orbit effects in chemistry.

AUTHOR INFORMATION

Corresponding Author

*E-mail: Mariusz.Klobukowski@ualberta.ca.

ACKNOWLEDGMENT

T.Z. expresses his gratitude to the Alberta Ingenuity Funds, Killam Trusts, and Alberta Scholarship Program for the student scholarships. M.K. thanks the Natural Sciences and Engineering Research Council of Canada for the support of the present project under Research Grant No. G121210414. M.W.S. acknowledges support by the DOE Chemical Physics program. The calculations were performed on the Linux clusters at the Department of Chemistry and Department of Academic Information and Communication Technologies at the University of Alberta. We are grateful to Professor M. S. Gordon for his continuing support of the development of the GAMESS-US program suite.

REFERENCES

(1) Desclaux, J. P.; Pyykkö, P. *Recherche* **1980**, *11*, 592–594.
(2) Pyykkö, P. *Chem. Rev.* **1988**, *88*, 563–594.
(3) Pyykkö, P.; Desclaux, J. P. *Acc. Chem. Res.* **1979**, *12*, 276–281.
(4) Pyykkö, P.; Desclaux, J. P. *C. R. Acad. Sci. Paris* **1981**, *292*, 1513–1515.
(5) Norrby, L. *J. Chem. Educ.* **1991**, *68*, 110–113.
(6) Pyykkö, P. *Angew. Chem., Int. Ed.* **2004**, *43*, 4412–4456.
(7) Pyykkö, P. *Inorg. Chim. Acta* **2005**, *358*, 4113–4130.
(8) Pyykkö, P. *Chem. Soc. Rev.* **2008**, *37*, 1967–1997.
(9) Schwerdtfeger, P.; Heath, G. A.; Dolg, M.; Bennet, M. A. *J. Am. Chem. Soc.* **1992**, *114*, 7518–7527.
(10) Visscher, L. *Chem. Phys. Lett.* **1996**, *253*, 20–26.
(11) Fedorov, D. G.; Gordon, M. S. Symmetry in Spin-Orbit Coupling. In *Low-lying Potential Energy Surfaces*; Hoffmann, M. R., Dyall, K. G., Eds.; American Chemical Society: Washington, DC, 2002; Vol. 828, pp 276−297.
(12) Marian, C. M. Spin-Orbit Coupling in Molecules. In *Reviews in Computational Chemistry*; Lipkowitz, K. B., Boyd, D. B., Eds.; WILEY-VCH: New York, 2001; Vol. 17, pp 99−204.
(13) Zeng, T. Ph.D. thesis, University of Alberta, Alberta, Canada, 2010
(14) Marian, C. M. Fine and hyperfine structure: Spin properties of molecules. In *Problem Solving in Computational Molecular Science: Molecules in Different Environments*; Wilson, S., Diercksen, H. F., Eds.; Kluwer Academic Publishers: Dordrecht, The Netherlands, 1997; pp 291−351.
(15) Fedorov, D. G.; Koseki, S.; Schmidt, M. W.; Gordon, M. S. *Int. Rev. Phys. Chem.* **2003**, *22*, 551–592.
(16) Fedorov, D. G.; Schmidt, M. W.; Koseki, S.; Gordon, M. S. Spin-orbit coupling methods and applications to chemistry. In *Recent Advances in Relativistic Molecular Theory*; Hirao, K., Ishikawa, Y., Eds.; World Scientific: Singapore, 2004; pp 107−136.

(17) Armbruster, M. K.; Weigend, F.; van Wüllen, C.; Klopper, W. *Phys. Chem. Chem. Phys.* **2008**, *10*, 1748–1756.
(18) Takahashi, O.; Saito, K.; Yabushita, S. *Int. J. Quantum Chem.* **1999**, *74*, 515–530.
(19) Bearpark, M. J.; Handy, N. C.; Palmieri, P.; Tarroni, R. *Mol. Phys.* **1993**, *80*, 479–502.
(20) Vallet, V.; Maron, L.; Teichteil, C.; Flament, J.-P. *J. Chem. Phys.* **2000**, *113*, 1391–1402.
(21) Das, K. K.; Petsalakis, I. D.; Liebermann, H.-P.; Alekseyev, A. B. *J. Chem. Phys.* **2002**, *116*, 608–616.
(22) Barandiarán, Z.; Seijo, L. *J. Chem. Phys.* **2003**, *118*, 7439–7456.
(23) Sánchez-Sanz, G.; Barandiarán, Z.; Seijo, L. *Chem. Phys. Lett.* **2010**, *498*, 226–228.
(24) Danilo, C.; Vallet, V.; Flament, J.-P.; Wahlgren, U. *J. Chem. Phys.* **2008**, *128*, 154310.
(25) Brozell, S. R.; Shepard, R. *J. Phys. Chem. A* **2009**, *113*, 12741.
(26) Stowasser, R.; Hoffmann, R. *J. Am. Chem. Soc.* **1999**, *121*, 3414–3420.
(27) Alekseyev, A. B.; Liebermann, H.-P.; Buenker, R. J. Spin-orbit multireference configuration interaction method and applications to systems containing heavy atoms. In *Recent Advances in Relativistic Molecular Theory*; Hirao, K., Ishikawa, Y., Eds.; World Scientific: Singapore, 2004; pp 65−105.
(28) Zeng, T.; Fedorov, D. G.; Schmidt, M. W.; Klobukowski, M. *J. Chem. Phys.* **2011**, *134*, 214108.
(29) Dagdigian, P. J.; Campbell, M. L. *Chem. Rev.* **1987**, *87*, 1–18.
(30) Bersuker, I. B.; Budnikov, S. S.; Leizerov, B. A. *Int. J. Quantum Chem.* **1977**, *11*, 543–559.
(31) Khudyakov, I. V.; Serebrennikov, Y. A.; Turro, N. J. *Chem. Rev.* **1993**, *93*, 537–570.
(32) Danovich, D.; Shaik, S. *J. Am. Chem. Soc.* **1997**, *119*, 1773–1786.
(33) van Koppeh, P. A. M.; Bowers, M. T.; Haynes, C. L.; Armentrout, P. B. *J. Am. Chem. Soc.* **1998**, *120*, 5704–5712.
(34) Roos, B. O.; Malmqvist, P. A.; Gagliardi, L. *J. Am. Chem. Soc.* **2006**, *128*, 17000–17006.
(35) Graves, C. R.; Yang, P.; Kozimore, S. A.; Vaughn, A. E.; Clark, D. L.; Conradson, S. D.; Schelter, E. J.; Scott, B. L.; Thompson, J. D.; Hay, P. J.; Morris, D. E.; Kiplinger, J. L. *J. Am. Chem. Soc.* **2008**, *130*, 5272–5285.
(36) Wang, X.; Andrews, L.; Malmqvist, P. A.; Roos, B. O.; Goncalves, A. P.; Pereira, C. C. L.; Marcalo, J.; Godart, C.; Villeroy, B. *J. Am. Chem. Soc.* **2010**, *132*, 8484–8488.
(37) Zeng, T.; Fedorov, D. G.; Klobukowski, M. *J. Chem. Phys.* **2009**, *131*, 124109.
(38) Zeng, T.; Fedorov, D. G.; Klobukowski, M. *J. Chem. Phys.* **2010**, *132*, 074102.
(39) Truflandier, L. A.; Brendler, E.; Wagler, J.; Autschbach, J. *Angew. Chem., Int. Ed.* **2011**, *50*, 255–259.
(40) Samet, C.; Rose, J. L.; Piepho, S. B.; Laurito, J.; Andrews, L.; Schatz, P. N. *J. Am. Chem. Soc.* **1994**, *116*, 11109–11119.
(41) Dyall, K. G. *J. Phys. Chem. A* **2000**, *104*, 4077–4083.
(42) Balasubramanian, K.; Majumdar, D. *J. Chem. Phys.* **2001**, *115*, 8795.
(43) Balasubramanian, K. *Mol. Phys.* **2010**, *107*, 797–807.
(44) Hisashima, T. A.; Matsushita, T.; Asada, T.; Koseki, S.; Toyota, A. *Theor. Chem. Acc.* **2008**, *120*, 85–94.
(45) Poluyanov, L. V.; Domcke, W. *J. Chem. Phys.* **2008**, *129*, 224102.
(46) Poluyanov, L. V.; Mishra, S.; Domcke, W. *Mol. Phys.* **2007**, *105*, 1471–1485.
(47) Poluyanov, L. V.; Mishra, S.; Domcke, W. *Chem. Phys.* **2007**, *332*, 243–248.
(48) Opalka, D.; Segado, M.; Poluyanov, L. V.; Domcke, W. *Phys. Rev. A* **2010**, *81*, 042501.
(49) Poluyanov, L. V.; Domcke, W. *Chem. Phys.* **2010**, *374*, 86–93.
(50) David, J.; Geurra, D.; Restrepo, A. *Inorg. Chem.* **2011**, *50*, 1480–1483.
(51) Pérez-Villa, A.; David, J.; Fuentealba, P.; Restrepo, A. *Chem. Phys. Lett.* **2011**, *507*, 57–62.
(52) Löwdin, P.-O. *Phys. Rev.* **1955**, *97*, 1474–1489.
(53) Löwdin, P.-O.; Shull, H. *Phys. Rev.* **1956**, *101*, 1730–1739.
(54) Davidson, E. R. Natural orbitals. In *Adv. Quantum Chem.*; Löwdin, P.-O., Ed.; Academic Press, Inc: New York, 1972; Vol. 6, pp 235−266.
(55) Zare, R. N. *Angular Momentum: Understanding Spatial Aspects in Chemistry and Physics*; John Wiley and Sons, Inc.: New York, 1988.
(56) Fedorov, D. G.; Gordon, M. S. *J. Chem. Phys.* **2000**, *112*, 5611–5623.
(57) Fedorov, D. G. Ph.D. thesis, Iowa State University, Ames, IA, 1999
(58) Schmidt, M. W.; Baldridge, K. K.; Boatz, J. A.; Elbert, S. T.; Gordon, M. S.; Jensen, J. H.; Koseki, S.; Matsunaga, N.; Nguyen, K. A.; Su, S.; Windus, T. L.; Dupuis, M.; Montgomery, J. A., Jr. *J. Comput. Chem.* **1993**, *14*, 1347–1363.
(59) Gordon, M. S.; Schmidt, M. W. Advances in electronic structure theory: GAMESS a decade later. In *Theory and Applications of Computational Chemistry: The First Forty Years*; Dykstra, C. E., Frenking, G., Kim, K. S., Scuseria, G. E., Eds.; Elsevier: Amsterdam, The Netherlands, 2005; pp 1167−1189.
(60) Bode, B. M.; Gordon, M. S. *J. Mol. Graphics Model.* **1998**, *16*, 133–138.
(61) Ruedenberg, K.; Schmidt, M. W. *J. Comput. Chem.* **2007**, *28*, 391–310.
(62) Bitter, T.; Ruedenberg, K.; Schwarz, W. H. E. *J. Comput. Chem.* **2007**, *28*, 411–422.
(63) Grundström, B.; Valberg, P. *Z. Phys.* **1938**, *108*, 326–337.
(64) Ruedenberg, K.; Schmidt, M. W. *J. Phys. Chem. A* **2009**, *113*, 1954–1968.
(65) Bitter, T.; Wang, S. G.; Ruedenberg, K.; Schwarz, W. H. E. *Theor. Chem. Acc.* **2010**, *127*, 237–257.
(66) Dyall, K. G.; Fægri, K., Jr. *Introduction to Relativistic Quantum Chemistry*; Oxford University Press: Oxford, U.K., 2007.
(67) Lee, Y. S. Two-component relativistic effective core potential calculations for molecules. In *Relativistic electronic structure theory: Part 2. Applications*; Schwerdtfeger, P., Ed.; Elsevier: Amsterdam, The Netherlands, 2004; pp 352−416.
(68) Klobukowski, M. *Chem. Phys. Lett.* **1993**, *214*, 166–174.
(69) Nakajima, T.; Hirao, K. *Chem. Phys. Lett.* **2000**, *329*, 511–516.
(70) Nakajima, T.; Hirao, K. *J. Chem. Phys.* **2000**, *113*, 7786–7789.
(71) Dunning, T. H. *J. Chem. Phys.* **1989**, *90*, 1007–1023.
(72) Huzinaga, S.; Andzelm, J.; Klobukowski, M.; Radzio-Andzelm, E.; Sakai, Y.; Tatewaki, H. *Gaussian basis sets for molecular calculations*; Huzinaga, S., Ed.; Elsevier: Amsterdam, The Netherlands, 1984.
(73) Roos, B. O.; Borin, A. C.; Gagliardi, L. *Angew. Chem., Int. Ed.* **2007**, *46*, 1469–1472.
(74) Kramers, H. A. *Proc. Acad. Sci. Amsterdam* **1936**, *33*, 959.
(75) Bethe, H. A.; Salpeter, E. E. *Quantum Mechanics of One- and Two-Electron Atoms*; Dover Publications, Inc.: Mineola, NY, 2008.
(76) Frenking, G.; Tonner, R. *Nature* **2007**, *446*, 276–277.
(77) Zeng, T.; Fedorov, D. G.; Klobukowski, M. *J. Chem. Phys.* **2010**, *133*, 114107.
(78) Hess, B. A. *Phys. Rev. A* **1986**, *33*, 3742.
(79) Jansen, G.; Hess, B. A. *Phys. Rev. A* **1989**, *39*, 6016.
(80) Pitzer, K. S. *Int. J. Quantum Chem.* **1984**, *25*, 131–148.
(81) Ermler, W. C.; Lee, Y. S.; Christiansen, P. A.; Pitzer, K. S. *Chem. Phys. Lett.* **1981**, *81*, 70–74.
(82) Ermler, W. C.; Ross, R. B.; Christiansen, P. A. Spin-orbit coupling and other relativistic effects in atoms and molecules. In *Advances in Quantum Chemistry*; Löwdin, P.-O., Ed.; Academic Press, Inc.: San Diego, CA, 1988; Vol. 19, pp 139−182.
(83) Foster, J. P.; Weinhold, F. *J. Am. Chem. Soc.* **1980**, *102*, 7211–7218.
(84) Read, A. E.; Curtiss, L. A.; Weinhold, F. *Chem. Rev.* **1988**, *88*, 899–926.
(85) Weinhold, F. Natural bond orbital methods. In *Encyclopedia of Computational Chemistry*; Schleyer, P. v. R., Ed.; John Wiley and Sons, Ltd.: Athens, GA, 1998; Vol. 3, pp 1792−1811.
(86) Weinhold, F.; Landis, C. R. *Chem. Educ. Res. Pract. Eur.* **2001**, *2*, 91–104.

(87) Bersuker, I. B. *The Jahn-Teller Effect*; Cambridge University Press: Cambridge, U.K., 2006.
(88) Bersuker, I. B. *The Jahn-Teller Effect and Beyond*; The Academy of Sciences of Moldova: Chişinău, Moldova; The University of Texas at Austin: Austin, TX, 2008.
(89) Balasubramanian, K. *Relativistic Effects in Chemistry Part A*; John Wiley and Sons, Inc.: New York, 1997.
(90) Stevens, W. J.; Basch, H.; Krauss, M. *J. Chem. Phys.* **1984**, *81*, 6026–6033.
(91) Stevens, W. J.; Krauss, M.; Basch, H.; Jasien, P. G. *Can. J. Chem.* **1992**, *70*, 612–630.
(92) Cundari, T. R.; Stevens, W. J. *J. Chem. Phys.* **1993**, *98*, 5555–5565.
(93) Koseki, S.; Gordon, M. S.; Schmidt, M. W.; Matsunaga, N. *J. Chem. Phys.* **1995**, *99*, 12764–12772.
(94) Koseki, S.; Schmidt, M. W.; Gordon, M. S. *J. Phys. Chem. A* **1998**, *102*, 10430–10435.
(95) We repeated the same DFT calculation in ref 41 and found that the $^2A_2$ and $^2B_2$ label assignments in Figure 1 of the reference should be swapped.
(96) Jacobs, P. *Group Theory with Applications in Chemical Physics*; Cambridge University Press: Cambridge, U.K., 2005.
(97) Yoon, J.; Mirica, L. M.; Daniel, T.; Stack, P.; Solomon, E. I. *J. Am. Chem. Soc.* **2004**, *126*, 12586–12595.
(98) Wedig, U.; Saltykov, V.; Nuss, J.; Jansen, M. *J. Am. Chem. Soc.* **2010**, *132*, 12458–12463.

JCTC Journal of Chemical Theory and Computation

ARTICLE

pubs.acs.org/JCTC

First Step in the Reaction of Zerovalent Iron with Water

František Karlický* and Michal Otyepka*

Regional Centre of Advanced Technologies and Materials, Department of Physical Chemistry, Faculty of Science, Palacky University Olomouc, tr. 17 listopadu 12, 771 46 Olomouc, Czech Republic

ABSTRACT: Here we present a comprehensive quantum chemical study of the simplest model system for the reactions of nanoscale zerovalent iron, i.e., the gas-phase reaction of an iron atom with water, to identify a theoretical method that provides reasonably accurate geometries and thermochemical data for selected iron compounds along the reaction path (Fe, FeO, HFeOH, $Fe(OH)_2$). The energies of selected stationary points on the ground electronic potential energy surface were systematically studied using HF and post-HF methods (MP2, MP3, MP4, CCSD, CCSD(T), CASSCF, MRCI) and selected DFT functionals (B3LYP, B97-1, BPW91, M06, M06-HF, M06-L, M06-2X and MPW1K) using various basis sets up to the complete basis set. Scalar relativistic effects were modeled using the Douglas−Kroll−Hess Hamiltonian up to the fourth order, and the effects of valence plus outer-core electronic correlation were also evaluated. The calculations showed that (i) dynamic electron correlation is crucial for accurate modeling of the reactions in question, (ii) the PES around the stationary points along the reaction path is rather flat, (iii) the single-point energies calculated at the CCSD(T)/CBS level are in reasonably good agreement with experimental measurements, (iv) it is difficult to interpret DFT energies in the absence of benchmarking against experimental data or results obtained at a level of theory that is known to accurately reproduce experimental results, (v) relativistic effects are relatively modest in this system but should be included if chemical accuracy is desired, and (vi) careful analysis of the multireference character of the system and potential spin contamination is important. The CCSD(T)-3*s*3*p*-DKH2/CBS method can be considered the gold standard for this reaction because calculations at this level are in good agreement with experimental atomic excitation energies and thermochemical data. The gas-phase activation energy of the reaction between Fe and H_2O is 23.6 kcal/mol including the ZPVE correction ($\Delta G^{\ddagger}_{298K}$ = 29.2 kcal/mol), and HFeOH is a stable intermediate lying −31.2 kcal/mol below the reactants (ΔG_{298K} = −25.4 kcal/mol).

I. INTRODUCTION

In recent years, reductive technologies for the decontamination of ground and wastewater using zerovalent iron (ZVI) and nanoscale zerovalent iron (nZVI) have become popular.[1−4] The high reductive capacity of ZVI has been known for some time.[5−23] A detailed understanding of the mechanisms by which reduction with nZVI proceeds will make it possible to optimize these processes and identify other potential uses of this material. In this respect, theoretical methods can provide relatively cheap and unique information on an atomic resolution.

However, the theoretical study of nZVI is complicated by the fact that is difficult to identify reasonable model systems. An nZVI particle with a radius of ∼5 nm contains $\sim 10^4-10^5$ iron atoms; such large systems are computationally intractable. As such, it is necessary to model the nZVI particle either as a cluster of a few iron atoms[24,25] or as a solid phase using Bloch's approach.[26,27] Unfortunately, both approaches have some drawbacks and limitations; in particular, the sizes of the systems involved and the need for periodic boundary conditions and simulation of electron correlation mean that it is necessary to use DFT methods, typically LDA or GGA functionals. This is a potentially serious issue because DFT functionals do not always provide systematic results for transition metal (TM) compounds, and the accuracy of their results is highly system dependent.[28−30] Moreover, even the best theoretical methods can generally only predict the thermochemistry of transition metal complexes with an accuracy of ±3 kcal/mol,[28,31,32] whereas the goal of chemical accuracy (i.e., predictions that are within ±1 kcal/mol of the experimental value) can be realized for main group compounds.

A better understanding of the reactivity of nZVI and iron in general would be useful because it could provide new insights into processes such as corrosion and steel production. However, there are numerous difficulties associated with computational studies of the reactivity of iron-containing compounds. First, the compounds may have several spin states; as such, it is necessary to identify the correct ground state[33−36] and to account for the possibility of crossing between states of different multiplicities along the reaction path.[35] Moreover, it is necessary to consider dynamic electron correlation to accurately model the behavior of iron compounds;[37,38] if a high degree of accuracy is required, scalar relativistic effects should also be considered[28,39−41] and it may be difficult to identify a suitable basis set.[42] Other complications may arise from the multireference character of certain iron-containing compounds. It is well known that unrestricted single-reference methods give rise to spin-contamination issues when applied to open-shell systems. In such cases, the unrestricted Hartree−Fock (uHF) wave function is not an eigenfunction of the total spin operator, S^2, and so the expectation value $\langle S^2\rangle$ may not be equal to $S(S + 1)$; as such, the obtained energies may be inaccurate. On the other hand, restricted open-shell Hartree−Fock (roHF) calculations with the right $\langle S^2\rangle$ are more computationally demanding, can generate unphysical results due to symmetry breaking artifacts, and do not allow correct spin polarization.[43] Therefore, it is sometimes necessary to use multi-reference methods for highly spin-contaminated systems,

Received: June 3, 2011
Published: July 18, 2011

especially for their transition states.[38] DFT methods are usually capable of predicting the properties of open-shell systems quite satisfactorily because they model correlation effects in a different way.[43] Finally, quantitative inconsistencies between DFT, CCSD(T), and CASPT2 results can be reconciled using quantum diffusion Monte Carlo theory.[44]

We present here a systematic quantum chemical study conducted to identify a method that provides reasonably accurate geometries and thermochemical data for selected iron compounds along the reaction coordinate for reaction of an iron atom with a water molecule (Fe + H_2O). This reaction was chosen because it was expected that the data obtained would be useful in future studies of the reactions of nZVI with organic and inorganic pollutants. The chosen reaction represents the simplest model of nZVI reaction with water, but on the other hand, it allows one to benchmark considered quantum chemical methods against golden standards of quantum chemistry, e.g., CCSD(T)/CBS. The approach adopted in this work has previously been used to study the reaction of iron atoms with CCl_4[45] and cross validated with experimental data.[46] The considered reaction has previously been studied using both theoretical and experimental methods.[47−51]

The paper is organized as follows: the theoretical approaches and methods used are briefly described in section II. The results obtained are presented and discussed in section III. There are described systematic studies of the excitation energies of iron (section III.A) and the thermochemistry of FeO and $Fe(OH)_2$ (section III.B); the results obtained were compared to experimental data, in order to identify optimal methods and basis sets for modeling the reactions in question. Studies of the potential energy surfaces of the reaction between Fe and H_2O using various methods are discussed in section III.C, and the conclusions of the study are presented in section IV.

II. METHODS

A set of calculations using selected ab initio methods was performed to identify important effects in the description of the model system. Dynamic electron correlation, which is important in molecular systems containing iron atoms,[38] was modeled using standard post-HF methods where possible. Both restricted and unrestricted open-shell variants were examined to avoid the problems mentioned in section I. Møller−Plesset perturbation theory, which is sometimes very sensitive to spin contamination,[43] was tested up to the fourth order. The coupled cluster methods (especially CCSD(T))[28,39,52] are quite efficient at reducing uHF spin contamination to acceptable levels,[53] so the results of uHF- and roHF-based coupled cluster calculations are often very similar. Because of the inherently multireference nature of many TM species, such single-reference computations can provide an inaccurate description of both static and dynamic electron correlation and it is necessary to check their legitimacy. Thus, not only spin contamination, but also T_1 diagnostic,[54,55] which is a mathematically rigorous indication of the quality of an open-shell coupled cluster wave function, was monitored. A T_1 diagnostic greater than 0.05 usually indicate some multireference character to the wave function.[28,56] For the simplest molecular system considered, FeO, higher correlation effects were investigated by comparison to results obtained using the complete active space SCF (CASSCF) and multireference CI (MRCI) methods. In the multireference calculations, the $1\sigma-6\sigma$ and $1\pi-2\pi$ orbitals were doubly occupied and kept in the inactive space as was the 7σ orbital because of its almost pure oxygen 2s character. The remaining 12 valence electrons were distributed between the 9 (MRCI(12,9)) valence orbitals ($8\sigma-10\sigma, 3\pi-4\pi, \delta$) corresponding to the iron 3d and 4s orbitals and the oxygen 2p orbital or between a set of 12 valence orbitals (MRCI(12,12), CASSCF(12,12)) consisting of the previous nine with additional 11σ and 5π orbitals. This resulted in 270 and 49 285 configurations, respectively. Scalar relativistic effects were studied using the Douglas−Kroll−Hess (DKH) Hamiltonian; calculations of the zeroth (DKH0), second (DHK2), and fourth order (DKH4) were performed.

We also sought to identify a less computationally demanding quantum chemical method that could accurately describe the model system for use in future studies and therefore examined the performance of various DFT methods. A limited set of functionals was considered; those selected have often been used for studying TM compounds or recommended as being particularly useful for studying the thermochemistry of TM complexes and the transition structures encountered in their reactions. The hybrid B3LYP functional[57] has been used in many studies of this kind, having been used to study the reaction between Fe and H_2O by Plane et al.,[47,51] Mebel and Hwang,[48] and Zhang et al.[49] Gutsev et al. used the BPW91 exchange-correlation functional[58,59] to study the interactions of small iron clusters with individual molecules of water[50] and nitrogen monoxide[60] and with a carbon atom;[61] these authors also used this functional to study FeO_n and FeO_n^- clusters.[62] The B97-1 functional has been used to model the interactions of molecules with water and in small water clusters.[63,64] Recently, Zhao and Truhlar developed a new set of functionals called the M06 suite for the study of the thermochemistry, thermochemical kinetics, noncovalent interactions, and excited states of main group and transition metal compounds.[65] We examined the performances of the hybrid meta exchange-correlation M06 and M06-2X functionals, the full Hartree−Fock M06-HF functional, and the M06-L local functional.[66] The older hybrid-GGA MPW1K functional,[67] which was designed for accurate computation of reaction barriers, was also considered.

Previous studies in this area[47−49,51] used Pople's basis sets, i.e., 6-31G**, 6-311G**, 6-311+G(3df,2p). These sets were also used in this work, but we performed a major part of our calculations using the correlation-consistent basis sets (cc-pV*n*Z, aug-cc-pV*n*Z, n = D, T, Q), which were recently extended to cover the 3d elements by Balabanov and Peterson.[52] The basis sets recommended by Balabanov and Peterson for iron (cc-pV*n*Z-DK, aug-cc-pV*n*Z-DK; cc-pwCV*n*Z-DK)[52] were employed in scalar relativistic calculations and calculations of valence plus outer-core (3s3p3d4s) electron correlation; these sets were obtained from the basis set exchange database.[68] Correlation-consistent basis sets can be used to extrapolate to the complete basis set (CBS) limit. Although the DFT methods are much less basis set dependent and this convergence is not necessarily guaranteed for DFT, it has been shown (see, e.g., ref 31 or 32 and references therein) that for some molecules quadruple-ζ or higher basis sets are required for saturation in DFT, and CBS extrapolation has been used successfully. Two CBS extrapolation schemes were utilized here. In the first (CBS1), the HF and correlation energies are extrapolated separately, as is usually done when studying main group species. The HF energy was extrapolated using the two-point scheme described by Halkier et al.[69]

$$E_\infty^{HF} = E_n^{HF} - \frac{E_n^{HF} - E_{n+1}^{HF}}{1 - \exp(-B)} \quad (1)$$

This scheme has also been recommended for use with TMs, albeit with a different value for parameter B.[70] The correlation

Table 1. Calculated Excitation Energies of Iron (kcal/mol) for the $^5D \rightarrow {}^5F$ (a), $^5D \rightarrow {}^3F$ (b), and $^5D \rightarrow {}^7D$ (c) Transitions[a]

method	uCCSD(T)	uCCSD(T)-DKH2	uCCSD(T)-3*s*3*p*-DKH2
basis set	cc-pV*n*Z	cc-pV*n*Z-DK	cc-pwCV*n*Z-DK
	(a) ^5D ($4s^23d^6$) → ^5F ($4s^13d^7$)		
n = T	22.6	28.5	25.9
n = Q	20.2	26.1	23.0
CBS1	18.5	24.4	21.0
CBS2	18.4	24.3	20.9
exp.[b]			20.1
	(b) ^5D ($4s^23d^6$) → ^3F ($4s^13d^7$)		
n = T	31.5	37.8	36.4
n = Q	29.0	35.4	33.4
CBS1	27.3	33.7	31.3
CBS2	27.2	33.6	31.2
exp.[b]			34.0
	(c) ^5D ($4s^23d^6$) → ^7D ($4s^13d^64p^1$)		
n = T	52.5	54.4	56.0
n = Q	53.5	55.4	57.0
CBS1	54.3	56.2	57.7
CBS2	54.3	56.2	57.7
exp.[b]			54.7
		$^5D \rightarrow {}^5F$	$^5D \rightarrow {}^3F$	$^5D \rightarrow {}^7D$
	(d) uCCSD(T) calculations for smaller basis sets		
6-31G**		73.6	79.6	58.3
6-311G**		41.4	48.5	135.7
6-311G(3df,2p)		20.7	29.6	53.5
cc-pVDZ		29.3	37.6	49.5

[a] Results for other basis sets tested in this work are also shown (d). [b] Reference 76; the spin−orbit effect has been removed using the experimental fine-structure splitting.

energy was extrapolated from two points using the following expression[71]

$$E_{\infty}^{\mathrm{corr}} = \frac{n^3 E_n^{\mathrm{corr}} - m^3 E_m^{\mathrm{corr}}}{n^3 - m^3} \quad (2)$$

E_∞ and E_n denote the extrapolated energy and energy for a basis set of n-ζ cardinality, respectively. Equation 2 was also used in the second extrapolation scheme (CBS2) using the total energies only as in ref 52. CBS extrapolations were performed from bases of triple-ζ and quadruple-ζ cardinality (i.e., $n = 3$, $m = 4$).

Most of the calculations reported in this work were performed using the Gaussian 09 package;[72] the Molpro 2006 package[73] was used for multireference calculations. The stability of the obtained wave functions was always checked. In cases of bad SCF convergence, which is often caused by a small HOMO−LUMO gap, we used the "level-shifting" method,[74] which shifts the virtual orbitals to a higher energy to increase the HOMO−LUMO gap, and/or techniques that fractionally occupy orbitals around the Fermi energy during the SCF cycles (Fermi broadening).[75] The quadratically convergent SCF algorithm (which can only be employed with unrestricted methods in Gaussian 09) was generally more effective at forcing SCF convergence than the direct inversion in the iterative subspace (DIIS) algorithm. The nature of all identified stationary points on the PES was tested by examining the eigenvalues of the Hessian matrix, and the intrinsic reaction coordinate method was used to verify the correspondence of transition structures to their adjacent minima.

III. RESULTS AND DISCUSSION

III.A. Excitation Energies of Atomic Iron. In order to asses the quality of the CCSD(T) method, which we intended to use as our benchmark, we computed selected excitation energies of the iron atom. The calculated energies for the $^5D \rightarrow {}^5F$, $^5D \rightarrow {}^3F$, and $^5D \rightarrow {}^7D$ transitions are shown along with the experimental values[76] in Table 1. The high quality of the coupled cluster wave functions for the ^5D and ^5F states was demonstrated by their $\langle S^2 \rangle$ and T_1 diagnostic values, which were less than 6.02 and 0.03, respectively. For the CBS limit energies, inclusion of scalar relativity through the DKH2 Hamiltonian and cc-pV*n*Z-DK basis set worsened the agreement with experiment; the calculated relativistic effect was 5.9 kcal/mol. On the other hand, inclusion of 3s3p electron correlation (with the cc-pwCV*n*Z-DK basis set) reduced the calculated $^5D \rightarrow {}^5F$ excitation energy by 3.4 kcal/mol, giving very good agreement with the experimental value; the difference between the calculated and measured values in this case is only 0.8 kcal/mol. It is worth noting that our results (obtained with Gaussian09 using the uCCSD(T) method) are consistent with those of previous calculations[39] using the open-shell variant of CCSD(T) implemented in MOLPRO; the differences between the two sets of calculated results were 0.7 kcal/mol and less than 0.1 kcal/mol appear for calculations including valence correlation and 3s3p3d4s correlation, respectively.

The calculated excitation energies for the $^5D \rightarrow {}^3F$ and $^5D \rightarrow {}^7D$ transitions do not exhibit such good agreement with the experimental data as was the case for the $^5D \rightarrow {}^5F$ transition (see Table 1) but are still within the chemical accuracy for TM (3 kcal/mol). This may be due to high-spin contamination for the ^3F state, for which $\langle S^2 \rangle \approx 3$ (although the value of the T_1 diagnostic in this case remained within acceptable limits, <0.03); the ^7D state wave function is not contaminated ($\langle S^2 \rangle = 12.00$, $T_1 = 0.01$). We also calculated the excitation energies using Pople's basis sets which have been used in previous studies (cf. Methods) and the cc-pVDZ basis set. The smaller basis sets (6-31G**, 6-311G**, and cc-pVDZ) perform significantly poor (Table 1d).

III.B. Heats of Formation of FeO and $Fe(OH)_2$. We also compared the calculated thermochemical data to available experimental data for FeO and $Fe(OH)_2$. Theoretical heats of formation ΔH_f at $T = 0$ K were calculated by subtracting the calculated atomization energies from the known heats of formation of isolated atoms. Atomic ΔH_f values were taken from NIST-JANAF tables.[77] It should be noted that the experimental heat of formation for FeO in the gas phase is not well established at the present time, as can be seen from the last lines of Table 2. CCSD and the various DFT methods considered here give very different results (column 5 of Table 2) for the quintet ground state[78,79] of FeO ($^5\Delta$; $Fe(4s^{0.5}3d^{6.4}4p^{0.2})$ $O(2s^{1.9}2p^{4.9})$). However, the CCSD(T)/CBS values for ΔH_f calculated as single-point energies for the same geometries are surprisingly consistent and reasonably close to the experimental values.[77,80,81] This implies that the CCSD(T) ΔH_f values are insensitive to the length of the Fe−O bond (cf. the second and last columns of Table 2: a difference of 0.021 Å in the Fe−O distance

Table 2. Bond Lengths [Å], Vibrational Frequencies [cm^{-1}], $\langle S^2\rangle$, and Heats of Formation ΔH_f [kcal/mol] of FeO at 0 K, Calculated Using Unrestricted Methods and the cc-pVTZ Basis Set (the geometry of FeO was fully optimized)[a]

method	b(Fe−O)	freq	$\langle S^2\rangle$	ΔH_f[b]	ΔH_f[c]
CCSD	1.6184	832	6.791	86.9	67.6 (69.7, 68.1)
B3LYP	1.6095	911	6.038	57.7	67.7
B97-1	1.6124	903	6.030	59.9	67.7
BPW91	1.6047	922	6.018	34.9	67.7
M06	1.6118	926	6.037	72.4	67.7
M06-L	1.6130	915	6.130	53.4	67.7
M06−2X	1.6257	955	6.523	88.9	67.8
MPW1K	1.6125	901	6.018	82.2	67.7
exp.	1.616[d]	880[e]			60.0 ± 5.0[h]
	1.57[f]	965[f]			61.9 ± 4.8[I]
		882[g]			65.5 ± 3.0[j]
					64.8 ± 3.0[k]

[a] The rightmost column shows the heats of formation calculated using the uCCSD(T)/CBS2 method for the same geometries. Values obtained using the CCSD(T)-DKH2/CBS2 method using the cc-pV*n*Z-DK basis sets and additional 3s3p electron correlation are shown in parentheses in the rightmost column of the first row. [b] Values calculated using the methods indicated in the first column. [c] Values calculated using the CCSD(T)/CBS2 method for geometries obtained by optimization using the method indicated in the first column. [d] Reference 79. [e] Reference 78. [f] Reference 77. [g] Reference 84. [h] Reference 77; adopted from several values cited therein (47.2, 65.7 ± 23.1, 60.1 ± 11.6, 59.8 ± 5, and 52.2 kcal/mol at 298.15 K). [I] Reference 80. [j] Reference 81. [k] Reference 47 (revised data from ref 81; see ref 47 Table 5, footnote *i*).

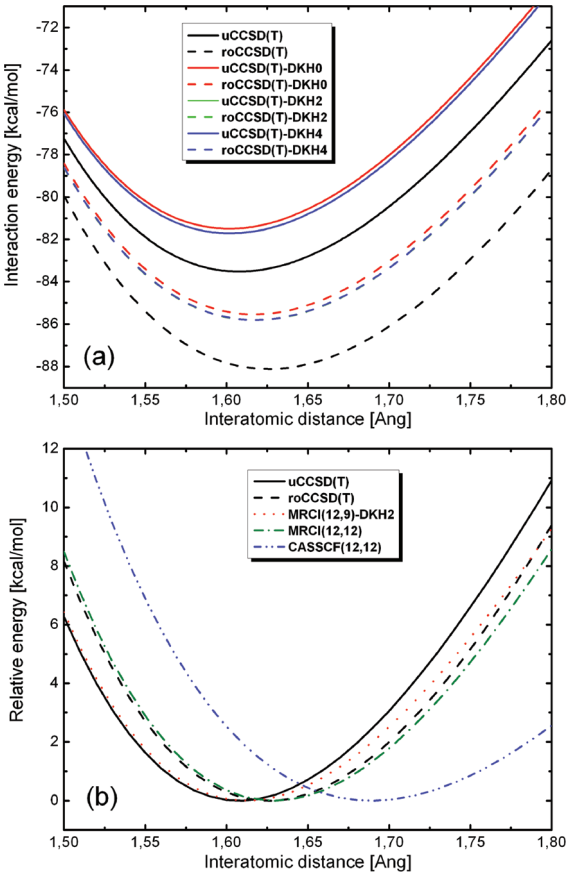

Figure 1. (a) Quintet FeO interaction potentials constructed from 30 points for unrestricted (solid lines) and restricted open-shell (dashed lines) CCSD(T) methods with the cc-pVTZ basis set using several Hamiltonians: nonrelativistic (black lines), scalar relativistic DKH0 (red lines), DKH2 (green lines; these are coincident with the blue lines), and DKH4 (blue lines). (b) Relative energies reported with respect to the minima of the individual curves obtained using multireference methods. The nonrelativistic unrestricted (black line) and restricted open (dashed black line) CCSD(T) data from a are included for comparative purposes; in addition, MRCI(12,12), MRCI(12,9)-DKH2, and CASSCF(12,12) curves are also shown (green dot−dashed, red dotted, and blue dash−dot−dotted lines, respectively).

corresponds to a 0.1 kcal/mol difference in the CCSD(T)/CBS energies). This finding suggests that the potential energy surface (PES) is flat in the vicinity of the minimum. In addition, we also checked the influence of the basis set on the geometry of the FeO molecule. Bond lengths optimized with methods of Table 2 were very similar when cc-pVTZ or aug-cc-pVQZ basis sets were used: differences were typically smaller than 0.003 Å. This shows that the cc-pVTZ basis set is adequate for geometry optimizations and that the error in bond length associated with the use of a finite basis of triple-ζ cardinality is much less than the uncertainty associated with the choice of DFT functional.

The potential energy curve around the minimum on the FeO potential energy curve (Figure 1) was calculated using various methods in order to compare the performance of single and multireference methods, to evaluate the differences between the restricted open-shell and unrestricted approaches, to assess the influence of scalar relativistic effects calculated on various levels, and to confirm the expected flatness around the minimum. For the uHF wave function an $\langle S^2\rangle$ value of ∼6.7 was obtained (compared to an expected $S(S+1)$ of 6; cf. Table 2), and the CC T_1 diagnostic was ∼0.1 (values above 0.05 indicate that the wave function may have multireference character[28]). On the other side, the MRCI(12,12) leading configuration for $S = 2$ was $(\text{core})8\sigma^2 3\pi^4 9\sigma 1\delta^3 4\pi^2$, with weight 82%, 78%, 75%, and 71% for bond length 1.5, 1.62, 1.7, and 1.8 Å, respectively; this corresponds to the $^5\Delta$ state (in the $C_{\infty v}$ group, i.e., $^5A_1$ or $^5A_2$ for C_{2v}) in agreement with a recent theoretical study.[82] The geometries corresponding to ro-methods are slightly more diffuse than geometries calculated by u-methods. However, this difference is energetically insignificant because the increase in length of around 0.03 Å magnitude at the minima of the depicted curves is associated with energy differences of 0.5 kcal/mol or less (Figure 1a). The bond lengths obtained using the multireference CASSCF(12,12) method, which lacks dynamic electron correlation, are noticeably greater than those obtained in MRCI calculations (Figure 1b), which account for both static and dynamic electron correlation. This observation illustrates the point that inclusion of dynamic electron correlation is important for reliable geometry optimization. Inclusion of scalar relativistic effects did not alter the position of the energy minima (Figure 1a). We also note that using the DKH2 Hamiltonian introduced a systematic reduction in all of the calculated energies of around 2.1 kcal/mol, while introduction of additional 3s3p electron correlation made all of the calculated energies about 1.6 kcal/mol higher (see also Table 2).

We also carried out similar benchmark calculations for Fe(OH)$_2$. The experimental heats of formation for Fe(OH)$_2$ in the gas phase seem to be more precisely determined than for FeO (see Table 3), although the accuracy of the reported experimental error of 0.5 kcal/mol has been questioned.[83] Table 3 reports the heats of

Table 3. Bond Lengths [Å], Dihedral Angles [deg], $\langle S^2 \rangle$, and Heats of Formation ΔH_f [kcal/mol] of $Fe(OH)_2$ at 0 K[a]

method	b(Fe−O)	b(O−H)	d(HOO′H′)	$\langle S^2 \rangle$	ΔH_f^b	ΔH_f^c
CCSD	1.804	0.953	95.42	6.017	−45.1	−72.3 (−69.6)
B3LYP	1.791	0.957	89.48	6.010	−66.7	−72.5
B97-1	1.792	0.956	88.90	6.011	−65.4	−72.5
BPW91	1.787	0.967	−85.26	6.008	−75.1	−72.4
M06	1.780	0.954	86.76	6.021	−59.5	−72.1
M06-L	1.788	0.955	87.23	6.016	−65.4	−72.5
M06-2X	1.809	0.953	98.92	6.014	−63.7	−72.3
MPW1K	1.788	0.946	95.90	6.013	−50.0	−73.6
exp.	1.8[d]	0.96[d]				−77.2 ± 0.5[d]

[a] All calculations reported in this table were performed using unrestricted methods and the cc-pVTZ basis set except for those reported in the last column, which shows the uCCSD(T)/CBS2 values for the same geometries. Values obtained using the CCSD(T)-DKH2/CBS2 method using the cc-pV*n*Z-DK basis set are reported in parentheses in the first row (rightmost column). [b] Values calculated using the methods indicated in the first column. [c] Values calculated using the CCSD(T)/CBS2 method for geometries obtained by optimization at the level indicated in the first column. [d] Reference 77.

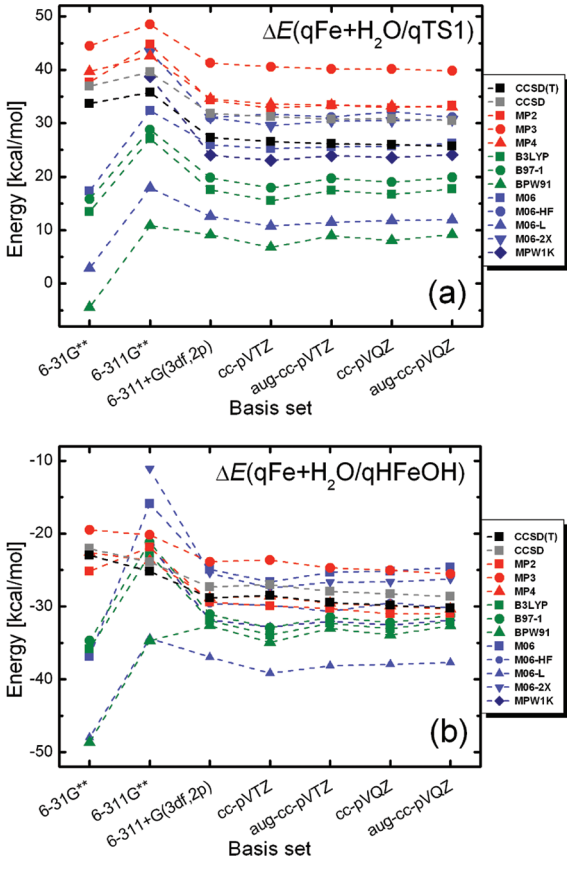

Figure 2. Single-point energy differences (in kcal/mol, calculated using unrestricted methods) for three quintet configurations (Fe + H_2O, TS1, and HFeOH) optimized using the B3LYP functional and their dependences on the chosen basis set: (a) qFe+H_2O/qTS1, (b) qFe+H_2O/qHFeOH.

formation of $Fe(OH)_2$ calculated using various methods. Overall, the trends in these data are similar to those observed in the case of

Table 4. Single-Point Energy Differences (in kcal/mol, calculated using unrestricted methods) for Three Quintet Configurations (Fe + H_2O, TS1, and HFeOH) Optimized Using the B3LYP Functional

	ΔE(qFe+H_2O/qTS1)		ΔE(qFe+H_2O/qHFeOH)	
method	cc-pVTZ	cc-pVQZ	cc-pVTZ	cc-pVQZ
CCSD(T)	26.6	26.0	−28.5	−29.9
CCSD	31.2	30.8	−27.0	−28.3
MP2	32.8	32.9	−29.9	−31.0
MP3	40.6	40.1	−23.6	−25.0
MP4	33.6	33.2	−28.6	−29.9
B3LYP	15.5	16.7	−33.9	−31.1
B97-1	17.9	19.0	−32.9	−32.2
BPW91	6.8	8.0	−35.0	−33.9
M06	25.2	25.7	−26.6	−25.2
M06-HF	31.7	32.2	−29.8	−29.5
M06-L	10.7	11.8	−39.2	−38.0
M06-2X	29.5	30.5	−27.5	−26.7
MPW1K	23.0	23.6	−32.8	−32.5

FeO. Once again, the ΔH_f values obtained with the different methods are somewhat inconsistent, but the energies obtained from single-point CCSD(T) calculations at the various optimized geometries are all very similar. We therefore believe that the region surrounding the global minimum on the PES of $Fe(OH)_2$ is very flat. Inclusion of the DKH2 Hamiltonian reduces all of the calculated energies by 2.3−2.9 kcal/mol.

In general, it is not so surprising that different DFT functionals will exhibited varied performance when predicting the thermochemical data of TM compounds. Recently, Yang et al.[30] studied 94 systems containing first-row TMs from Ti to Zn with 12 different functionals. The best mean unsigned error (MUE; the difference between the experimental and calculated values of ΔH_f) for systems containing iron atoms was 12.2 kcal/mol; the worst was 43.5 kcal/mol (see Table 4 of ref 30).

III.C. Reaction of Fe with H_2O. A systematic study of the energies of selected stationary points on the ground state electronic quintet PES of the Fe + H_2O system was conducted, and the energy differences between the stationary points were calculated to complete the benchmark thermochemical data discussed in sections III.A and III.B. We focused on the most important stationary points in the reaction mechanism, namely, those corresponding to the reactants (qFe+H_2O), the global minimum (qHFeOH), and the transition state between them (qTS1). We carried out single-point unrestricted calculations on B3LYP-optimized geometries using various basis sets. Figure 2 shows how varying the basis set affects the energy differences encountered along the reaction pathway. The smaller basis sets used in some previous studies[47−49,51] (6-31G** and 6-311G**) do not provide reliable results for the studied reaction (cf. also ref 42). Table 4 compares the energy differences calculated using unrestricted methods with the cc-pVTZ and cc-pVQZ basis sets. All methods perform rather poorly (with respect to CCSD(T)) for the TS (MUE = 8.3 and 7.9 kcal/mol for the TZ and QZ basis sets, respectively) but are significantly better at the minima (MUE = 3.6 and 3.0). In the case of FeO, accurate results could be obtained without having to use augmented basis sets; to verify that this remained true, we computed CBS2 energies for basis sets

Table 5. Energy Differences (in kcal/mol) for Stationary Points on the Ground Quintet Surface of the Fe + H_2O Reaction[a]

	ΔE (without ZPE correction)				ZPE corr.	ΔE (with ZPE correction)				ΔG_{corr}	ΔG
method	first column	CCSD(T)	CCSD(T)-DKH2	CCSD(T)-3*s*3*p*-DKH2	first column	first column	CCSD(T)	CCSD(T)-DKH2	CCSD(T)-3*s*3*p*-DKH2	first column	CCSD(T)-3*s*3*p*-DKH2
basis set on Fe	cc-pVTZ	cc-pV*n*Z	cc-pV*n*Z-DK	cc-pwCV *n*Z-DK	cc-pVTZ	cc-pVTZ	cc-pV*n*Z	cc-pV*n*Z-DK	cc-pwCV *n*Z-DK	cc-pVTZ	cc-pwCV *n*Z-DK
					$\Delta E(qFe+H_2O/qFe\cdots OH_2)$						
B3LYP	−10.2	−3.7	−2.7	−2.9	1.0	−9.1	−2.7	−1.6	−1.8	6.3	3.4
B971	−8.7	−3.7	−2.7	−2.9	1.1	−7.7	−2.7	−1.6	−1.8	6.3	3.4
BPW91	−10.2	−3.5	−2.5	−2.7	0.9	−9.3	−2.6	−1.6	−1.8	6.1	3.4
M06	−7.7	−3.7	−2.7	−2.9	0.9	−6.7	−2.7	−1.8	−2.0	6.1	3.2
M06-HF	−6.1	−3.4	−2.5	−2.6	0.8	−5.3	−2.6	−1.7	−1.8	5.7	3.0
M06-L	−12.4	−3.7	−2.7	−2.9	0.8	−11.6	−2.9	−1.9	−2.1	5.9	3.0
M06-2X	−5.3	−3.7	−2.8	−2.9	0.9	−4.4	−2.9	−1.9	−2.1	6.0	3.0
MPW1K	−5.6	−3.8	−2.8	−2.9	1.2	−4.3	−2.5	−1.5	−1.7	6.4	3.4
average	−8.3	−3.6	−2.7	−2.8	1.0	−7.3	−2.7	−1.7	−1.9	6.1	3.2
MUE	2.1	0.1	0.1	0.1	0.1	2.1	0.1	0.1	0.1	0.2	0.2
					$\Delta E(qFe+H_2O/qTS1)$						
B3LYP	15.5	25.6	27.2	26.8	−3.2	12.3	22.4	24.0	23.7	2.3	29.2
B971	17.9	25.6	27.2	26.9	−3.5	14.4	22.1	23.7	23.4	2.3	29.2
BPW91	6.7	26.0	27.6	27.2	−3.0	3.8	23.0	24.7	24.2	2.5	29.7
M06	24.3	25.3	26.9	26.6	−4.0	20.3	21.2	22.8	22.5	2.1	28.7
M06-HF	30.3	25.9	27.7	27.8	−3.3	27.0	22.6	24.5	24.6	1.5	29.3
M06-L	10.9	25.8	27.5	27.1	−3.7	7.2	22.1	23.8	23.4	2.3	29.4
M06-2X	28.7	25.6	27.3	27.2	−3.4	25.4	22.2	24.0	23.9	1.8	29.1
MPW1K	22.9	25.6	27.2	26.9	−3.5	19.5	22.2	23.7	23.4	2.1	29.0
average	19.7	25.7	27.3	27.1	−3.4	16.2	22.2	23.9	23.6	2.1	29.2
MUE	6.9	0.2	0.2	0.3	0.2	6.8	0.3	0.4	0.5	0.2	0.2
					$\Delta E(qFe+H_2O/qHFeOH)$						
CCSD	−27.1	−30.9	−29.2	−28.4	−2.8	−29.9	−33.7	−32.0	−31.2	3.0	−25.4
B3LYP	−34.0	−30.9	−29.2	−28.4	−3.0	−37.0	−33.9	−32.1	−31.4	2.7	−25.7
B971	−33.0	−30.9	−29.2	−28.4	−3.1	−36.0	−34.0	−32.2	−31.5	2.6	−25.8
BPW91	−35.3	−30.2	−28.5	−27.9	−2.7	−38.0	−32.9	−31.2	−30.6	3.0	−24.9
M06	−26.7	−30.7	−29.0	−28.3	−3.1	−29.8	−33.9	−32.1	−31.4	2.5	−25.8
M06-HF	−30.7	−30.3	−28.2	−27.2	−2.8	−33.5	−33.1	−31.0	−30.1	3.1	−24.1
M06-L	−39.2	−30.8	−29.1	−28.3	−3.1	−42.3	−33.9	−32.2	−31.5	2.4	−25.9
M06-2X	−28.1	−30.8	−28.9	−28.0	−2.9	−30.9	−33.7	−31.8	−30.9	3.0	−25.1
MPW1K	−32.8	−30.9	−29.2	−28.4	−3.7	−36.5	−34.6	−32.9	−32.1	2.1	−26.3
average	−31.9	−30.7	−28.9	−28.2	−3.0	−34.9	−33.7	−32.0	−31.2	2.7	−25.4
MUE	3.3	0.2	0.3	0.3	0.2	3.4	0.3	0.4	0.4	0.3	0.5
					$\Delta E(qFe+H_2O/qTS2)$						
CCSD	55.2	39.2	43.0	41.1	−4.7	50.6	34.6	38.3	36.4	0.9	42.0
B3LYP	26.5	39.1	42.6	40.7	−4.7	21.8	34.4	37.9	36.0	0.9	41.6
B971	27.6	38.9	42.5	40.6	−4.7	23.0	34.3	37.9	35.9	0.9	41.5
BPW91	11.3	39.1	42.2	40.6	−4.7	6.6	34.3	37.5	35.9	0.8	41.5
M06	37.6	39.0	42.5	40.6	−4.6	33.0	34.5	37.9	36.1	1.0	41.6
M06-HF	58.9	38.6	42.7	41.3	−3.5	55.4	35.2	39.3	37.9	1.9	43.3
M06-L	18.5	39.0	42.3	40.8	−4.9	13.6	34.1	37.4	35.9	0.7	41.5
M06-2X	50.3	37.0	41.1	38.7	−4.1	46.1	32.8	36.9	34.6	1.4	40.1
MPW1K	43.6	38.4	42.5	40.6	−4.3	39.3	34.2	38.2	36.3	1.2	41.8
average	36.6	38.7	42.4	40.6	−4.5	32.2	34.3	37.9	36.1	1.1	41.6
MUE	13.9	0.5	0.3	0.4	0.3	14.1	0.4	0.4	0.5	0.3	0.5

dx.doi.org/10.1021/ct200372y |*J. Chem. Theory Comput.* 2011, 7, 2876–2885

Table 5. Continued

	ΔE (without ZPE correction)				ZPE corr.	ΔE (with ZPE correction)				ΔG_{corr}	ΔG
method	first column	CCSD(T)	CCSD(T)-DKH2	CCSD(T)-3*s*3*p*-DKH2	first column	first column	CCSD(T)	CCSD(T)-DKH2	CCSD(T)-3*s*3*p*-DKH2	first column	CCSD(T)-3*s*3*p*-DKH2
basis set on Fe	cc-pVTZ	cc-pV*n*Z	cc-pV*n*Z-DK	cc-pwCV *n*Z-DK	cc-pVTZ	cc-pVTZ	cc-pV*n*Z	cc-pV*n*Z-DK	cc-pwCV *n*Z-DK	cc-pVTZ	cc-pwCV *n*Z-DK
					Δ*E*(qFe+H_2O/qH_2FeO)						
CCSD	36.6	22.0	24.3	22.9	−3.2	33.4	18.8	21.1	19.7	2.6	25.4
B3LYP	10.6	21.8	24.1	22.6	−3.8	6.8	18.0	20.3	18.8	2.2	24.8
B971	14.8	21.8	24.0	22.5	−3.9	10.9	17.9	20.1	18.6	2.0	24.6
BPW91	−9.7	25.8	27.4	25.4	−3.4	−13.1	22.4	24.0	22.0	2.1	27.6
M06	24.1	21.8	24.0	22.4	−4.1	20.0	17.8	19.9	18.3	1.8	24.2
M06-HF	54.0	24.9	27.2	25.9	−3.6	50.4	21.2	23.5	22.3	1.3	27.2
M06-L	−0.5	26.2	27.7	25.8	−3.4	−4.0	22.8	24.2	22.3	2.1	27.9
M06-2X	41.6	23.6	26.0	24.7	−3.9	37.7	19.7	22.1	20.8	0.8	25.5
MPW1K	−76.5	22.2	24.5	23.1	−4.5	−81.1	17.7	20.0	18.6	1.5	24.6
average	10.5	23.3	25.5	23.9	−3.8	6.8	19.6	21.7	20.2	1.8	25.8
MUE	26.3	1.6	1.4	1.4	0.3	26.3	1.7	1.6	1.5	0.4	1.2
					Δ*E*(qFe+H_2O/qFeO+H_2)						
CCSD	41.7	32.5	34.3	33.3	−6.1	35.5	26.3	28.1	27.2	−6.1	27.2
B3LYP	16.6	32.4	34.2	33.1	−5.7	10.8	26.6	28.4	27.4	−5.6	27.5
B971	22.0	32.4	34.2	33.2	−5.8	16.2	26.6	28.4	27.4	−5.7	27.4
BPW91	−1.4	32.3	34.0	32.9	−5.5	−6.9	26.7	28.5	27.4	−5.4	27.5
M06	33.6	32.4	34.2	33.2	−6.1	27.5	26.3	28.1	27.1	−6.0	27.2
M06-HF	61.1	42.4	36.3	35.7	−5.8	55.2	36.5	30.5	29.8	−5.8	29.8
M06-L	12.8	32.4	34.2	33.2	−4.9	7.9	27.5	29.3	28.3	−5.9	27.3
M06-2X	48.9	41.0	40.4	40.2	−6.0	42.9	35.0	34.4	34.2	−5.9	34.2
MPW1K	38.7	32.4	34.2	33.2	−6.0	32.7	26.4	28.2	27.2	−5.9	27.3
average	30.4	34.4	35.1	34.2	−5.8	24.7	28.7	29.3	28.4	−5.8	28.4
MUE	15.9	3.2	1.5	1.6	0.3	15.7	3.1	1.4	1.6	0.2	1.6

[a] Calculations presented in this table were performed using unrestricted methods; methods used for geometry optimization and frequency calculations are specified in the first column (the results of these calculations are shown in columns 2, 6, 7, and 11). Additional single-point energies were obtained using the CBS2 scheme with bases of triple-ζ and quadruple-ζ cardinality (i.e., n = 3 and 4).

with (augmented) and without diffuse functions (aug-cc-pV*n*Z vs cc-pV*n*Z) for all methods listed in Table 4. The average differences between the CBS2 energies calculated with the two basis sets were 0.4 and 0.3 kcal/mol for qFe+H_2O/qTS1 and qFe+H_2O/qHFeOH, respectively. For the post-HF methods the differences were less than 0.2 kcal/mol. This shows that reasonable accuracy with respect to the CBS limit and computational demands can be using basis sets without diffusion functions. It is worth noting that double-ζ basis sets do not provide sufficiently accurate results (Figure 2), and so the CBS limit should be calculated from TZ and QZ basis sets at least.

The final goal of our study was to explore the potential energy surfaces of the reaction between Fe and H_2O as accurately as possible. In light of the results reported in the preceding paragraphs and sections III.A and III.B, we adopted the following scheme: (1) geometry optimization was performed using all of the considered DFT methods with the cc-pVTZ basis set, (2) frequencies and zero-point energy corrections using the harmonic approximation were obtained at the same levels of theory, (3) single-point uCCSD(T) energy calculations using CBS extrapolation from the cc-pVTZ and cc-pVQZ basis sets were carried out, or, alternatively, (4) the scalar relativistic uCCSD(T)-DKH2 and valence plus outer-core (3s3p3d4s) electronic correlation CCSD(T)-3*s*3*p*-DKH2 calculations were also performed using the CBS limit and the cc-pV*n*Z-DK or cc-pwCV*n*Z-DK basis sets, respectively. In order to verify that the ground electronic state of the Fe + H_2O reaction coordinate retained the quintet multiplicity[47−49,51] and that no crossing occurred, we also performed calculations for different multiplicities. Figure 3 shows the lowest energies for the quintet state and that there is no crossing between the quintet and triplet surfaces. The only limitation of our approach is the single-reference description; some stationary points on the PES (specifically, the TS) may have some multireference character. Bias in the energies attributable to this can be measured using the T_1 diagnostic for coupled cluster methods. Problems due to spin contamination can also be partially relieved by using coupled cluster methods, which are quite effective at reducing uHF spin contamination to acceptable levels.[53] In this context, the results obtained for Fe and FeO with coupled cluster methods (including $\langle S^2 \rangle$ and T_1 values) are discussed in sections III.A and III.B, respectively. For a single-point energy calculation at the uCCSD(T)-3*s*3*p*-DKH2 level on

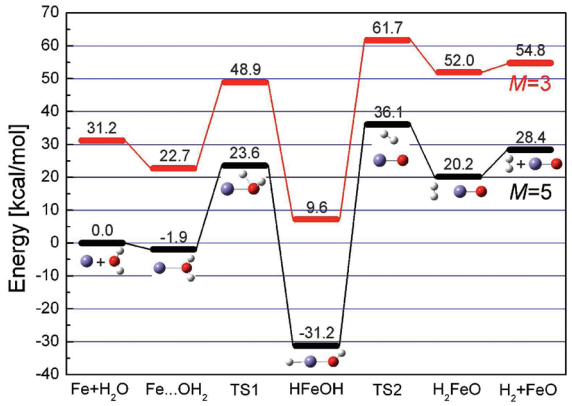

Figure 3. Reaction scheme showing the stationary points on the quintet (multiplicity $M = 5$) and triplet ($M = 3$) PES along the path of the Fe + H_2O reaction in the gas phase, with ZPVE corrections. The reported energies are the averages of the CCSD(T)-3*s*3*p*-DKH2/CBS2 values reported in the 10th column of Table 5 for $M = 5$.

the transition state qTS1, we obtained $\langle S^2 \rangle \approx 6.7$ (vs expected $S(S + 1) = 6$) for the uHF wave function; however, the T_1 diagnostic had an acceptable value (below 0.03). The single-reference description is fully adequate for the global minimum (qHFeOH), for which $\langle S^2 \rangle \approx 6.03$ and $T_1 < 0.022$. The only potentially problematic stationary point could be transition state TS2; for the uHF wave function for this species, $\langle S^2 \rangle \approx 6.9$ and $T_1 < 0.12$. The value of the T_1 diagnostic indicates that this transition state has some multireference character. However, the accuracy of energy corresponding to this transition state is not crucial for practical purposes and the final goal of this study, to explore the kinetics and the thermodynamics of the reaction between Fe and H_2O. In terms of the performance of the different methods used, the trends shown in Table 5 for the Fe + H_2O reaction mirror those observed in Tables 3 and 4, which report the thermochemical data for FeO and $Fe(OH)_2$; the different density functionals all afford very different energies, but all of the single-point CCSD(T) energies obtained at the different DFT geometries are very similar. This again suggests that the regions surrounding the stationary points on the PES of the Fe + H_2O reaction are quite flat.

The results obtained by examining all the stationary points on the Fe + H_2O potential energy surface using the method described above are collected in Table 5 and visualized in Figure 3 (the energies reported in this figure are an average of the CCSD(T)-3*s*3*p*-DKH2/CBS2 energies from the 10th column of Table 5 for $M = 5$; for $M = 3$ only three values for such average were used). In the computed reaction mechanism, the iron atom forms a noncovalent complex with the water molecule. The two react via transition state qTS1 ($Fe(4s^{1.1}3d^{6.3}4p^{0.1})$ $H(1s^{0.9})$ $O(2s^{1.8}2p^{5.2})$ $H(1s^{0.5})$) to form the highly stable qHFeOH intermediate ($H(1s^{1.5})$ $Fe(4s^{0.5}3d^{6.2}4p^{0.2})$ $O(2s^{1.8}2p^{5.3})$ $H(1s^{0.5})$), which is expected to be the dominant reaction intermediate. We also identified a local minimum labeled qH_2FeO that was not mentioned in ref 48 but is discussed in refs 49 and 51. The overall mechanism of the Fe + H_2O reaction is in qualitative agreement with that reported in previous publications.[48,49,51] However, in quantitative terms, there are various inconsistencies in the literature data on this reaction. A wide range of values (all of which include the ZPE correction) have been reported for the energy barrier that is most important in understanding the reaction's kinetics, qFe+H_2O/qTS1. Specifically, this barrier has been calculated to be 14.8[48] (B3LYP/6-311+G(3df,2p)), 32.7[48] (CCSD(T)/6-311G**), 8.6[49] (B3LYP/6-311++G(d,p)), and 14.3 kcal/mol[51] (B3LYP/6-311+G(2d,p)) compared with our benchmark value (including ZPE correction) of 23.6 kcal/mol (the average of the CCSD(T)- 3*s*3*p*-DKH2/CBS2 values in the 10th column of Table 5). The large deviations can be attributed to the small basis sets and DFT methods used in the previous literature studies (cf. Figure 2 and Table 4). Similarly, literature values for the energy difference between the reactants and the global minimum on the PES (qFe+H_2O/qHFeOH) are very different, although the deviation between the literature data and our benchmark is less pronounced in this case: previous results include −34.2[48] (B3LYP/6-311+G(3df,2p)), −26.2[48] (CCSD(T)/6-311G**), −41.1[49] (B3LYP/6-311++G(d,p)), and −35.6 kcal/mol[51] (B3LYP/6-311+G(2d,p)) compared with our value of −31.2 kcal/mol (CCSD(T)-3*s*3*p*-DKH2/CBS2).

IV. CONCLUSIONS

The quantum chemical study reported herein examined the simplest model system for studying the reaction of nZVI with water, i.e., the gas-phase reaction of an iron atom with a water molecule. This simple model was used to compare the performance of various widely used DFT functionals to that of highly accurate post-HF methods and multireference quantum chemical methods that can properly account for electron correlation and scalar relativistic effects. The calculations illustrate the following. (i) Inclusion of dynamic electron correlation is essential for a proper description of this reaction. (ii) The PES around the stationary points along the reaction path is rather flat; various methods that account for dynamic electron correlation can be used for geometry optimizations, and scalar relativistic effects do not significantly affect the calculated geometries. (iii) The only single-point energies that were in reasonable agreement with the experimental data were those calculated at the CCSD(T)/CBS level; the DFT and post-HF single reference methods gave inaccurate results. (iv) Direct interpretation of DFT energies can be unproductive in the absence of either benchmark data obtained at the recommended level of theory or experimental data, (v) Scalar relativistic effects are small in this system, but their magnitude is still in the same sort of range as chemical accuracy (±1 kcal/mol). (vi) The multireference character of intermediates and potential spin contamination should always be carefully examined. The CCSD(T)-3*s*3*p*-DKH2/CBS2 method can be considered a gold standard for the reaction in question because results obtained at this level are in good agreement with experimental atomic excitation energies and thermochemical data. The gas-phase activation energy (including the ZPVE correction) of the Fe + H_2O reaction is 23.6 kcal/mol ($\Delta G^{\ddagger}_{298K} = 29.2$ kcal/mol); HFeOH is a stable intermediate lying −31.2 kcal/mol below reactants ($\Delta G_{298K} = -25.4$ kcal/mol).

AUTHOR INFORMATION

Corresponding Author

*E-mail: frantisek.karlicky@upol.cz (F.K.), michal.otyepka@upol.cz (M.O.).

ACKNOWLEDGMENT

Financial support from the Czech Science Foundation (GACR P208/11/P463), the Operational Program Research

and Development for Innovations-European Regional Development Fund (CZ.1.05/2.1.00/03.0058), and the Operational Program Education for Competitiveness-European Social Fund (CZ.1.07/2.3.00/20.0017) is gratefully acknowledged. We thank Dana Nachtigallova (IOCHB, Prague) for critical comments and helpful discussions.

REFERENCES

(1) Tratnyek, P. G.; Johnson, R. L. *Nano Today* **2006**, *1*, 44–48.
(2) Zhang, W. X. *J. Nanopart. Res.* **2003**, *5*, 323–332.
(3) Li, X. Q.; Elliott, D. W.; Zhang, W. X. *Crit. Rev. Solid State* **2006**, *31*, 111–122.
(4) Cundy, A. B.; Hopkinson, L.; Whitby, R. L. D. *Sci. Total Environ.* **2008**, *400*, 42–51.
(5) Amonette, J. E.; Sarathy, V.; Linehan, J. C.; Matson, D. W.; Wang, C.; Nurmi, J. T.; Pecher, K.; Penn, R. L.; Tratnyek, P. G.; Baer, D. R. *Geochim. Cosmochim. Acta* **2005**, *69*, A263–A263.
(6) Arnold, W. A.; Roberts, A. L. *Environ. Sci. Technol.* **2000**, *34*, 1794–1805.
(7) Bandstra, J. Z.; Miehr, R.; Johnson, R. L.; Tratnyek, P. G. *Environ. Sci. Technol.* **2005**, *39*, 230–238.
(8) Gillham, R. W.; Ohannesin, S. F. *Ground Water* **1994**, *32*, 958–967.
(9) Johnson, T. L.; Fish, W.; Gorby, Y. A.; Tratnyek, P. G. *J. Contam. Hydrol.* **1998**, *29*, 379–398.
(10) Kim, J. H.; Tratnyek, P. G.; Chang, Y. S. *Environ. Sci. Technol.* **2008**, *42*, 4106–4112.
(11) Nam, S.; Tratnyek, P. G. *Water Res.* **2000**, *34*, 1837–1845.
(12) Roberts, A. L.; Totten, L. A.; Arnold, W. A.; Burris, D. R.; Campbell, T. J. *Environ. Sci. Technol.* **1996**, *30*, 2654–2659.
(13) Sarathy, V.; Salter, A. J.; Nurmi, J. T.; Johnson, G. O.; Johnson, R. L.; Tratnyek, P. G. *Environ. Sci. Technol.* **2010**, *44*, 787–793.
(14) Sayles, G. D.; You, G. R.; Wang, M. X.; Kupferle, M. J. *Environ. Sci. Technol.* **1997**, *31*, 3448–3454.
(15) Wang, C. B.; Zhang, W. X. *Environ. Sci. Technol.* **1997**, *31*, 2154–2156.
(16) Alowitz, M. J.; Scherer, M. M. *Environ. Sci. Technol.* **2002**, *36*, 299–306.
(17) Darab, J. G.; Amonette, A. B.; Burke, D. S. D.; Orr, R. D.; Ponder, S. M.; Schrick, B.; Mallouk, T. E.; Lukens, W. W.; Caulder, D. L.; Shuh, D. K. *Chem. Mater.* **2007**, *19*, 5703–5713.
(18) Miehr, R.; Tratnyek, P. G.; Bandstra, J. Z.; Scherer, M. M.; Alowitz, M. J.; Bylaska, E. J. *Environ. Sci. Technol.* **2004**, *38*, 139–147.
(19) Ponder, S. M.; Darab, J. G.; Bucher, J.; Caulder, D.; Craig, I.; Davis, L.; Edelstein, N.; Lukens, W.; Nitsche, H.; Rao, L. F.; Shuh, D. K.; Mallouk, T. E. *Chem. Mater.* **2001**, *13*, 479–486.
(20) Ponder, S. M.; Darab, J. G.; Mallouk, T. E. *Environ. Sci. Technol.* **2000**, *34*, 2564–2569.
(21) Ponder, S. M.; Ford, J. R.; Darab, J. G.; Mallouk, T. E., Ferragels: A new family of materials for remediation of aqueous metal ion solutions. In *Scientific Basis for Nuclear Waste Management XXII*; Wronkiewicz, D. J., Lee, J. H., Eds.; Materials Research Society: Warrendale, PA, 1999; Vol. 556, pp 1269−1276.
(22) Su, C. M.; Puls, R. W. *Environ. Sci. Technol.* **2001**, *35*, 4562–4568.
(23) Su, C. M.; Puls, R. W. *Environ. Sci. Technol.* **2001**, *35*, 1487–1492.
(24) Lanzani, G.; Nasibulin, A. G.; Laasonen, K.; Kauppinen, E. I. *Nano Res.* **2009**, *2*, 660–670.
(25) Lanzani, G.; Nasibulin, A. G.; Laasonen, K.; Kauppinen, E. I. *J. Phys. Chem. C* **2009**, *113*, 12939–12942.
(26) Lim, D. H.; Lastoskie, C. M. *Environ. Sci. Technol.* **2009**, *43*, 5443–5448.
(27) Lim, D. H.; Lastoskie, C. M.; Soon, A.; Becker, U. *Environ. Sci. Technol.* **2009**, *43*, 1192–1198.
(28) DeYonker, N. J.; Peterson, K. A.; Steyl, G.; Wilson, A. K.; Cundari, T. R. *J. Phys. Chem. A* **2007**, *111*, 11269–11277.
(29) Schultz, N. E.; Zhao, Y.; Truhlar, D. G. *J. Phys. Chem. A* **2005**, *109*, 11127–11143.
(30) Yang, Y.; Weaver, M. N.; Merz, K. M. *J. Phys. Chem. A* **2009**, *113*, 9843–9851.
(31) Li, S. G.; Hennigan, J. M.; Dixon, D. A.; Peterson, K. A. *J. Phys. Chem. A* **2009**, *113*, 7861–7877.
(32) Tekarli, S. M.; Drummond, M. L.; Williams, T. G.; Cundari, T. R.; Wilson, A. K. *J. Phys. Chem. A* **2009**, *113*, 8607–8614.
(33) Hubner, O.; Sauer, J. *J. Chem. Phys.* **2002**, *116*, 617–628.
(34) Hubner, O.; Sauer, J. *Collect. Czech. Chem. Commun.* **2003**, *68*, 405–422.
(35) Roithová, J.; Schröder, D. *Chem. Rev.* **2010**, *110*, 1170–1211.
(36) Schröder, D. *J. Phys. Chem. A* **2008**, *112*, 13215–13224.
(37) Knowles, P. J.; Werner, H. J. *Chem. Phys. Lett.* **1985**, *115*, 259–267.
(38) Zilberberg, I.; Gora, R. W.; Zhidomirov, G. M.; Leszczynski, J. *J. Chem. Phys.* **2002**, *117*, 7153–7161.
(39) Balabanov, N. B.; Peterson, K. A. *J. Chem. Phys.* **2006**, *125*, 074110.
(40) Cundari, T. R.; Leza, H. A. R.; Grimes, T.; Steyl, G.; Waters, A.; Wilson, A. K. *Chem. Phys. Lett.* **2005**, *401*, 58–61.
(41) Ilias, M.; Kello, V.; Urban, M. *Acta Phys. Slovaca* **2010**, *60*, 259–391.
(42) Martin, J.; Baker, J.; Pulay, P. *J. Comput. Chem.* **2009**, *30*, 881–883.
(43) Bally, T.; Borden, W. T. Calculations on Open-Shell molecules: A Beginner's Guide. In *Reviews in Computational Chemistry*; Lipkowitz, K. B., Boyd, D. B., Eds.; Wiley: New York, 1999; Vol. 13, pp 1−97.
(44) Matxain, J. M.; Mercero, J. M.; Irigoras, A.; Ugalde, J. M. *Mol. Phys.* **2004**, *102*, 2635–2637.
(45) Camaioni, D. M.; Ginovska, B.; Dupuis, M. *J. Phys. Chem. C* **2009**, *113*, 1830–1836.
(46) Parkinson, G. S.; Dohnalek, Z.; Smith, R. S.; Kay, B. D. *J. Phys. Chem. C* **2009**, *113*, 1818–1829.
(47) Rollason, R. J.; Plane, J. M. C. *Phys. Chem. Chem. Phys.* **2000**, *2*, 2335–2343.
(48) Mebel, A. M.; Hwang, D. Y. *J. Phys. Chem. A* **2001**, *105*, 7460–7467.
(49) Zhang, L. N.; Zhou, M. F.; Shao, L. M.; Wang, W. N.; Fan, K. N.; Qin, Q. Z. *J. Phys. Chem. A* **2001**, *105*, 6998–7003.
(50) Gutsev, G. L.; Mochena, M. D.; Bauschlicher, C. W. *Chem. Phys.* **2005**, *314*, 291–298.
(51) Self, D. E.; Plane, J. M. C. *Phys. Chem. Chem. Phys.* **2003**, *5*, 1407–1418.
(52) Balabanov, N. B.; Peterson, K. A. *J. Chem. Phys.* **2005**, *123*, 064107.
(53) Stanton, J. F. *J. Chem. Phys.* **1994**, *101*, 371–374.
(54) Lee, T. J. *Chem. Phys. Lett.* **2003**, *372*, 362–367.
(55) Lee, T. J.; Taylor, P. R. *Int. J. Quantum Chem.* **1989**, 199–207.
(56) Janssen, C. L.; Nielsen, I. M. B. *Chem. Phys. Lett.* **1998**, *290*, 423–430.
(57) Becke, A. D. *J. Chem. Phys.* **1993**, *98*, 5648–5652.
(58) Becke, A. D. *Phys. Rev. A* **1988**, *38*, 3098–3100.
(59) Perdew, J. P.; Wang, Y. *Phys. Rev. B* **1992**, *45*, 13244–13249.
(60) Gutsev, G. L.; Mochena, M. D.; Johnson, E.; Bauschlicher, C. W. *J. Chem. Phys.* **2006**, *125*, 194312.
(61) Gutsev, G. L.; Bauschlicher, C. W. *Chem. Phys.* **2003**, *291*, 27–40.
(62) Gutsev, G. L.; Khanna, S. N.; Rao, B. K.; Jena, P. *J. Phys. Chem. A* **1999**, *103*, 5812–5822.
(63) Vitek, A.; Kalus, R.; Paidarova, I. *Phys. Chem. Chem. Phys.* **2010**, *12*, 13657–13666.
(64) Sousa, S. F.; Fernandes, P. A.; Ramos, M. J. *J. Phys. Chem. A* **2007**, *111*, 10439.
(65) Zhao, Y.; Truhlar, D. G. *Theor. Chem. Acc.* **2008**, *120*, 215–241.
(66) Zhao, Y.; Truhlar, D. G. *J. Chem. Phys.* **2006**, *125*, 194101.

(67) Lynch, B. J.; Fast, P. L.; Harris, M.; Truhlar, D. G. *J. Phys. Chem. A* **2000**, *104*, 4811–4815.
(68) Schuchardt, K. L.; Didier, B. T.; Elsethagen, T.; Sun, L. S.; Gurumoorthi, V.; Chase, J.; Li, J.; Windus, T. L. *J. Chem. Inf. Model* **2007**, *47*, 1045–1052.
(69) Halkier, A.; Helgaker, T.; Jorgensen, P.; Klopper, W.; Olsen, J. *Chem. Phys. Lett.* **1999**, *302*, 437–446.
(70) Williams, T. G.; DeYonker, N. J.; Wilson, A. K. *J. Chem. Phys.* **2008**, *128*, 044101.
(71) Halkier, A.; Helgaker, T.; Jorgensen, P.; Klopper, W.; Koch, H.; Olsen, J.; Wilson, A. K. *Chem. Phys. Lett.* **1998**, *286*, 243–252.
(72) Frisch, M. J.; Trucks, G. W.; Schlegel, H. B.; Scuseria, G. E.; Robb, M. A.; Cheeseman, J. R.; Scalmani, G.; Barone, V.; Mennucci, B.; Petersson, G. A.; Nakatsuji, H.; Caricato, M.; Li, X.; Hratchian, H. P.; Izmaylov, A. F.; Bloino, J.; Zheng, G.; Sonnenberg, J. L.; Hada, M.; Ehara, M.; Toyota, K.; Fukuda, R.; Hasegawa, J.; Ishida, M.; Nakajima, T.; Honda, Y.; Kitao, O.; Nakai, H.; Vreven, T.; J. A. Montgomery, J.; Peralta, J. E.; Ogliaro, F.; Bearpark, M.; Heyd, J. J.; Brothers, E.; Kudin, K. N.; Staroverov, V. N.; Kobayashi, R.; Normand, J.; Raghavachari, K.; Rendell, A.; Burant, J. C.; Iyengar, S. S.; Tomasi, J.; Cossi, M.; Rega, N.; Millam, J. M.; Klene, M.; Knox, J. E.; Cross, J. B.; Bakken, V.; Adamo, C.; Jaramillo, J.; Gomperts, R.; Stratmann, R. E.; Yazyev, O.; Austin, A. J.; Cammi, R.; Pomelli, C.; Ochterski, J. W.; Martin, R. L.; Morokuma, K.; Zakrzewski, V. G.; Voth, G. A.; Salvador, P.; Dannenberg, J. J.; Dapprich, S.; Daniels, A. D.; Farkas, Ö.; Foresman, J. B.; Ortiz, J. V.; Cioslowski, J.; Fox, D. J. *Gaussian 09*, Revision A.02; Gaussian, Inc.: Wallingford. CT, 2009.
(73) Werner, H.-J.; Knowles, P. J.; Lindh, R.; Manby, F. R.; Schütz, M.; Celani, P.; Korona, T.; Mitrushenkov, A.; Rauhut, G.; Adler, T. B.; Amos, R. D.; Bernhardsson, A.; Berning, A.; Cooper, D. L.; Deegan, M. J. O.; Dobbyn, A. J.; Eckert, F.; Goll, E.; Hampel, C.; Hetzer, G.; Hrenar, T.; Knizia, G.; Köppl, C.; Liu, Y.; Lloyd, A. W.; Mata, R. A.; May, A. J.; McNicholas, S. J.; Meyer, W.; Mura, M. E.; Nicklass, A.; Palmieri, P.; Pflüger, K.; Pitzer, R.; Reiher, M.; Schumann, U.; Stoll, H.; Stone, A. J.; Tarroni, R.; Thorsteinsson, T.; Wang, M.; Wolf, A. *MOLPRO, version 2006.1, a package of ab initio programs*; University College Cardiff Consultants Limited: Cardiff, UK, 2006; http://www.molpro.net.
(74) Saunders, V. R.; Hillier, I. H. *Int. J. Quantum Chem.* **1973**, *7*, 699–705.
(75) Rabuck, A. D.; Scuseria, G. E. *J. Chem. Phys.* **1999**, *110*, 695–700.
(76) Sansonetti, J. E.; Martin, W. C.; Young, S. L. *Handbook of Basic Atomic Spectroscopic Data* (version 1.1.2); National Institute of Standards and Technology: Gaithersburg, MD, 2005; http://physics.nist.gov/Handbook.
(77) Chase, M. W. *NIST-JANAF Thermochemical Tables*, 4th ed. *(J. Phys. Chem. Ref. Data, Monograph No. 9)*; American Chemical Society and American Institute of Physics: Woodbury, NY, 1988.
(78) Cheung, A. S. C.; Gordon, R. M.; Merer, A. J. *J. Mol. Spectrosc.* **1981**, *87*, 289–296.
(79) Cheung, A. S. C.; Lee, N.; Lyyra, A. M.; Merer, A. J.; Taylor, A. W. *J. Mol. Spectrosc.* **1982**, *95*, 213–225.
(80) Jensen, D. E.; Jones, G. A. *J. Chem. Soc., Faraday Trans. 1* **1973**, *69*, 1448–1454.
(81) Murad, E. *J. Chem. Phys.* **1980**, *73*, 1381–1385.
(82) Sakellaris, C. N.; Miliordos, E.; Mavridis, A. *J. Chem. Phys.* **2011**, *134*, 234308.
(83) Kellogg, C. B.; Irikura, K. K. *J. Phys. Chem. A* **1999**, *103*, 1150–1159.
(84) Drechsler, G.; Boesl, U.; Bassmann, C.; Schlag, E. W. *J. Chem. Phys.* **1997**, *107*, 2284–2291.

JCTC Journal of Chemical Theory and Computation

ARTICLE

pubs.acs.org/JCTC

Refinement of the Cornell et al. Nucleic Acids Force Field Based on Reference Quantum Chemical Calculations of Glycosidic Torsion Profiles

Marie Zgarbová,[†] Michal Otyepka,[†,‡] Jiří Šponer,[†,‡] Arnošt Mládek,[‡] Pavel Banáš,[†,‡] Thomas E. Cheatham, III,[§] and Petr Jurečka*[,†]

[†]Regional Centre of Advanced Technologies and Materials, Department of Physical Chemistry, Faculty of Science, Palacky University, 17 listopadu 12, 77146 Olomouc, Czech Republic

[‡]Institute of Biophysics, Academy of Sciences of the Czech Republic, Královopolská 135, 612 65 Brno, Czech Republic

[§]Departments of Medicinal Chemistry and Pharmaceutics and Pharmaceutical Chemistry, University of Utah, 2000 East 30 South Skaggs 201, Salt Lake City, Utah 84112, United States

Supporting Information

ABSTRACT: We report a reparameterization of the glycosidic torsion χ of the Cornell et al. AMBER force field for RNA, χ_{OL}. The parameters remove destabilization of the anti region found in the ff99 force field and thus prevent formation of spurious ladder-like structural distortions in RNA simulations. They also improve the description of the syn region and the syn−anti balance as well as enhance MD simulations of various RNA structures. Although χ_{OL} can be combined with both ff99 and ff99bsc0, we recommend the latter. We do not recommend using χ_{OL} for B-DNA because it does not improve upon ff99bsc0 for canonical structures. However, it might be useful in simulations of DNA molecules containing syn nucleotides. Our parametrization is based on high-level QM calculations and differs from conventional parametrization approaches in that it incorporates some previously neglected solvation-related effects (which appear to be essential for obtaining correct anti/high-anti balance). Our χ_{OL} force field is compared with several previous glycosidic torsion parametrizations.

INTRODUCTION

The relevance of sampled structures and conformational dynamics of molecules in molecular dynamics (MD) simulations critically depends on the quality and accuracy of the applied empirical force fields. Among force-field terms, the torsion parameters are known to strongly influence the molecular structures. This creates a considerable problem since the torsions are the least "physics-based" parameters in the sense that they cannot be *directly* derived from either experimental data or quantum mechanics (QM). Further, the sampled torsions depend not only on the values of all of the other parameters but also on the applied simulation methods (for example, whether or not all bonds, only bonds with hydrogen atoms, or no bonds are constrained). Bond and angle parameters can be straightforwardly derived from crystal data, IR and microwave spectroscopy, and/or high-level QM. Relatively straightforward procedures or protocols are also available to determine intermolecular parameters, such as van der Waals radii and well depths by matching experimental densities and atomic charges through fits to QM-derived electrostatic potentials or energetics. In contrast, fitting of the torsional parameters is largely an art and often rather ad hoc. The results strongly depend on the choice of model systems and approach, including the means used to fit the QM data, the level of QM calculations, the QM optimization methodology, and inclusion of solvation. For nucleic acids, a particularly difficult problem is parametrization of the flexible and anionic sugar−phosphate backbone, as the force field must simultaneously reproduce properties of canonical nucleic acid forms and numerous noncanonical topologies.[1−7]

Most of the current generation of nucleic acid force fields were initially designed to reproduce properties of isolated nucleosides in vacuo. This residue-based parametrization approach relies on investigations of small molecule model systems under the assumption that the parameters are transferable and applicable to nucleosides and larger nucleic acid structures in solution.[8,9] A significant issue at the time of writing is that these model systems were primarily studied in the early 1990s when higher level QM investigations of full models representative of the nucleotides or nucleotides were not possible. Understanding the deficiencies, the initial nucleic acid force fields were then tweaked—arguably with limited success—through a series of designed, automated, or ad hoc torsional potential modifications aiming to reproduce B-DNA and A-RNA helix structures in solution. Other target properties included (inter alia) the subtle balance of the A−B DNA conformational equilibrium and the B-DNA helical twist.[10−20]

Despite improvements, cryptic deficiencies remained and tend to remain undiscovered except through prolonged MD or enhanced sampling simulations and investigations of larger numbers of noncanonical structures, such as various G-DNA and RNA structures. For example, although unexpected and persistent γ = trans backbone conformational transitions in B-DNA simulations were reported

Received: March 8, 2011
Published: August 02, 2011

in the early 2000s,[21−23] it took time (and longer simulations) to convince the research community that the most widely used nucleic acid force field, the AMBER force field (ff94) presented by Cornell et al.,[8] and its basic variants ff98[17] and ff99[20] (collectively termed the AMBER ff9X force fields) significantly overstabilized the γ = trans backbone state. As a result, the initially infrequently populated γ = trans state sampled in α/γ conformational transitions becomes the global minimum in B-DNA. Given sufficiently long MD simulations this overstabilization leads to complete degradation of the B-DNA structure. To overcome this deficiency, several approaches based on high-level QM calculations of larger and more representative model systems were applied to improve mapping of the α/γ energy surfaces, leading to the bsc0 refinement of the AMBER ff9X force fields.[24,25] The ff99bsc0 force field is the best currently available for modeling B-DNA,[26,27] but it still has potential inaccuracies. For example, the B-DNA helical twist remains underestimated, the occasional γ = trans flips in B-DNA simulations are still probably too frequent,[28] and for modeling DNA hairpin loops, although the refinement improves the overall force-field performance, an experimentally known γ = trans state is incorrectly eliminated.[29] On the other hand, all of the AMBER ff9X force fields, with or without bsc0 modifications, provide similar simulations of the behavior of RNA helices, since in all cases the γ = trans backbone flip is reversible.[30] This indicates that force-field modifications for DNA and RNA simulations might be pursued independently, in contrast to earlier perceptions that the parameters should be transferable across the nucleic acids.

Considerably more challenging than simply maintaining canonical helical structure is achieving a balanced description of the various noncanonical and/or unfolded nucleic acid structures, which are especially important in analyses of RNA functions, catalysis, dynamics, and drug targeting.[31−35] Although simulations of such structures may be improved by straightforward adjustment of a particular parameter (as for the γ = trans backbone states), some problems will likely require simultaneous or concerted modification of numerous parameters, which is demanding. Finally, considering the severity of the overall physical approximations of the pairwise additive force fields, some problems might be entirely beyond the capabilities of simple force-field approximations. Thus, it is not surprising that different force fields often provide remarkably different descriptions of the same structure, a phenomenon termed "force-field-dependent polymorphism".[36−40] A large part of this undesirable variability can likely be attributed to the inaccurate or nonoptimal description of the torsion space. Hence, the torsion parameters used in the various force-field treatments have been continuously refined.[8,19,20,24,41,42]

In nucleic acids one of the most distinctive torsions is the glycosidic torsion, χ, describing rotation about the bond that links the base to the sugar moiety and determines the relative orientation of the nucleobase and sugar moieties in DNA and RNA (Figure 1). It is believed to be involved in the equilibrium of the A and B forms of DNA as well as the C2′-endo and C3′-endo equilibrium. The χ torsion is linked to many base pair and helical parameters that are modeled rather inaccurately by current force fields, including the helical twist (underestimated),[17] base pair propeller twist (also underestimated), and size of the DNA grooves. Recent work also suggests that it is important for the correct description of complex RNA folds.[43] In the two most widely used sets of biomolecular force fields for nucleic acids, AMBER and CHARMM, several reparameterizations of the χ torsion have appeared in recent years,[7,17,19,41,42,44,45] indicating that deriving its torsion potential is a particularly difficult task.

The focus of this work is on the χ torsion in the Cornell et al. ff9X force-field family. Before reviewing previous parametrizations, we should note that the χ angle is tightly coupled to sugar puckering. Therefore, when corrections to the χ parameters are made in a particular force field they are often accompanied by adjustments to the ribose/deoxyribose parameters. The parameters for χ and sugar pucker in the most commonly used force field for NA simulations, AMBER ff94, originally presented by Cornell et al.,[8] have already been revised at least four times. In the AMBER ff98 force field[17] both the χ torsion and sugar puckers were changed, followed by minor readjustments of the sugar pucker parameters in the AMBER ff99 force field.[20] Although not fully described in the literature, these modifications were largely based on ad hoc changes to the parameters with assessment by relatively long (for the time) MD simulations to ascertain their influences on the DNA structure, twist, and sugar puckering. This contrasts with a more physically based approach involving better QM calculations based on more relevant model systems. The main aim of the rather subtle tunings in ff98 was to reduce the ff94 force field's quite pronounced underestimation of helical twist in B-DNA. However, the improvement afforded by the reparameterization was modest, and all the ff9X force fields are usually assumed to have similar strengths, weaknesses, and ranges of applicability. While the ff94 force field underestimates χ values, sugar pucker, and helical twist[17] in B-DNA simulations, the ff98 twist is closer to experimental values. Even with the latest ff99 force field, the description of the structural parameters coupled to the χ angle is not fully satisfactory. For DNA, the helical twist is still somewhat underestimated, and the average χ and pucker values are probably still too far from values obtained from X-ray and solution analyses. We emphasize that this assessment concerns primarily B-DNA, which has been the main target of the force-field parametrization efforts. Assessment and validation of the performance of force fields for other types of nucleic acid structures has been much less systematic, and the results have often been difficult to interpret due to a lack of both unambiguous target experimental structures and published or disseminated data regarding simulation failures.[29,38,43,46−49] The above-mentioned critical α/γ torsional reparameterization (bsc0) was primarily designed as a complement to ff99.[24]

In 2008 Ode et al. attempted a new χ parametrization based on QM calculations.[44] This parametrization can be combined with either ff99 or ff99-parmbsc0, but assessing the effects of the new parameters on the performance of these force fields is difficult since the original testing was limited to analysis of the progression of rmsd values in a few very short MD trajectories. More recently, we tested the modifications in simulations of guanine quadruplex (G-DNA) loops, which are known to be described poorly with standard ff9X parametrizations. However, the Ode et al. modifications did not have any clear advantages with respect to the original force fields for the G-DNA loops; the simulation outcomes were not significantly influenced by the choice of χ potential but were strongly influenced by the choice of ff99 versus ff99-parmbsc0.[29] Recently, another χ reparameterization was presented by Yildirim et al.[45] This reparameterization (tested solely in combination with ff99, in RNA simulations) was shown to improve the concordance of syn−anti populations of isolated RNA nucleosides with NMR data, but no simulations of nucleic acids were presented.

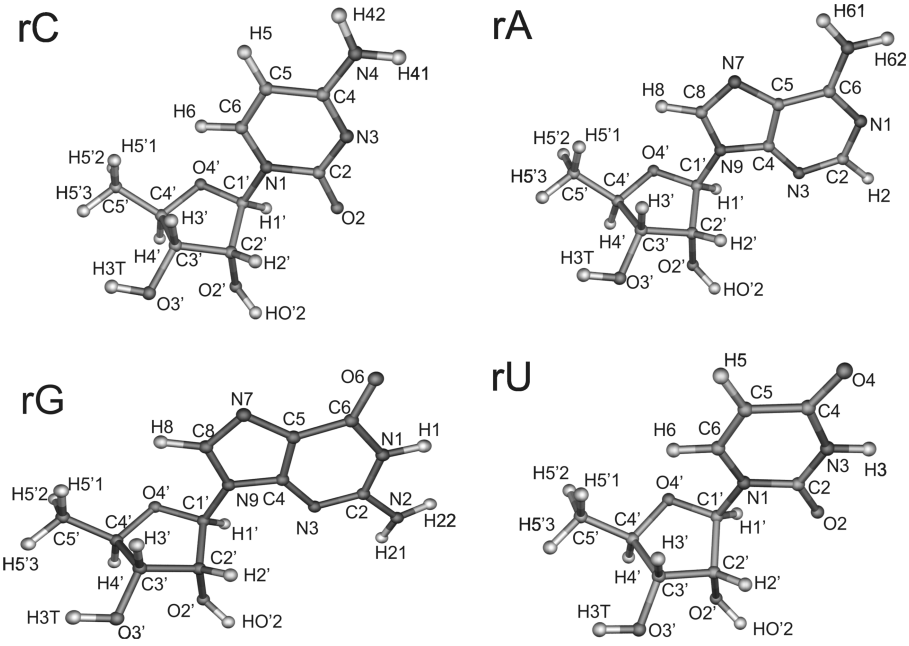

Figure 1. Chemical structures and atom-naming conventions for the model ribonucleosides used in our derivation of χ torsion parameters for cytosine (C), adenine (A), guanine (G), and uracil (U). The dihedral angle χ is defined by the O4′−C1′−N1−C2 atoms for C and U and by the O4′−C1′−N9−C4 atoms for A and G (this definition is used throughout this work). Note, however, that in ff94, ff98, and ff99 force fields the χ parameters are actually assigned to the complementary angle, specifically O4′−C1′−N1−C6 for C and U and O4′−C1′−N9−C8 for A and G.

In simulations of RNA, a major failure of the ff99 force field recently reported by Mlynsky et al.[43] is the generation of large "ladder-like" structural distortions in one stem of the hairpin ribozyme.[43] These distortions are characterized by a shift of χ toward the region typical for the B form (high-anti, ∼270°), loss of helical twist, a change of the sugar pucker from C3′-endo to C2′-exo, and increases in slide and P−P distances in their radial distribution function. According to our experience, deformations of this type are actually fairly common in MD simulations of smaller RNA fragments.[46] Hence, they may have appeared in some previously published investigations, including RNA tetraloop folding studies, and results of these simulations should be viewed with care.

It should be noted that the "ladder-like" artifact would not have appeared in most previous RNA simulation studies, since it usually takes at least several tens of nanoseconds to emerge, depending on the system (for several examples see our recent study, in which we found that between 20 and 95 ns is required for some RNA tetraloop structures[46]). However, collectively through the large sets of RNA simulations performed by the collaborating groups we accumulated quite strong evidence that the "ladder-like" structure is preferentially favored over traditional A-RNA helices by both the ff99 and the ff99bsc0 force fields. Thus, we expect the ladder-like structure artifact to appear, eventually, in all sufficiently long RNA MD simulations. In other words, we hypothesize that the "ladder-like" structure is the global RNA minimum and its appearance (and accompanying structural changes in the simulated RNA molecule) is solely dependent on the simulation time scale, even for folded RNAs. Finally, we note that deficiencies in the χ potential are not unique to the AMBER force fields since χ parameters of the CHARMM all22 and all27 force fields have been revised,[19,50] and subsequent studies suggest that further revision is required.[7,41]

Since transition to the ladder-like structures is accompanied by a large shift of the χ value toward the high-anti region, the distortions could be attributed to the χ torsion parametrization. Removing the tendency of force fields to generate unnatural ladder-like structures in RNA simulations through reparameterization of the glycosidic torsion was one of the main motivations of the work presented here.

To derive new χ torsion parameters, we decided to base the parametrization procedure on better quantum-chemical (QM) reference data obtained from more relevant model systems. Here, we compare the most frequently used QM methods, including HF/6-31G*, MP2/6-31G*, DFT-based computations, etc., with the best available reference QM method, here denoted CBS(T). CBS(T) is the MP2 method extrapolated to the complete basis set (CBS) limit of atomic orbitals with a correction by the CCSD(T) method using a smaller basis set.[51] Further, we carefully evaluate errors arising from other commonly applied methodological assumptions. The first is the choice of the geometries for deriving the parameters, namely, the assumption that the same QM-optimized geometries can be used for both the QM and the MM single-point calculations. The second assumption is that solvation effects can be ignored, i.e., that in vacuo parameters for torsion can be reliably applied. Hypothesizing that both approximations may lead to substantial errors, we suggested a new protocol that takes both effects into account, derived new χ torsion parameters, and compare them here to other available parametrizations, in terms of the shape of the torsion profiles with regard to the A/B form equilibrium, syn/anti relative energies, and transition barriers. In addition, we tested various χ profiles in MD simulations of a B-DNA helical structure and three A-RNA structures. Finally, after the preliminary tests, we ran extensive MD simulations (dozens of microseconds) of numerous other systems with various force fields. The results of these more extensive simulations are briefly mentioned here and described (or will be

described) in more detail in separate publications, such as our recent study of RNA tetraloops.[46]

METHODS

Selection of Model Molecules. In our attempts to improve modeling of the χ potential, we used almost complete ribo- and deoxyribonucleoside models with the 5′-OH group replaced by a hydrogen (Figure 1; only the ribo compounds are shown). We omitted the 5′-OH group to avoid its contacts with the nucleobases (for instance, the contact of 5′-OH with H6 of pyrimidines), which would bias the parameters. Note that the value of the pseudorotation angle was fixed in all calculations (see below), and therefore, neglect of the anomeric effect of the missing 5′-OH group should not influence our results. We refer to the compounds in Figure 1 as ribo/deoxyribonucleosides or simply dN/rN hereafter to facilitate discussion, noting that in this work these terms always refer to the nucleosides with the 5′-OH replaced by a hydrogen. These molecules are probably the smallest models that could be reasonably used for our purpose as they include all the intramolecular contacts that occur upon rotation about the torsion angle. The intramolecular contacts are very important because they make major contributions to the torsion energy. For instance, the repulsive O4′···O2 and O4′···N3 contacts in purines and pyrimidines, respectively, correspond to the highest rotation barriers on the potential energy surface. Note also that increasing the complexity of the model beyond certain limits does not necessarily improve the quality of the results as some long-range interactions and contacts might introduce considerable additional problems.[25,52] As described below, to assess the influence of the sugar pucker, the calculations were performed for two sugar conformations in deoxyribonucleosides, C2′-endo and C3′-endo. For the ribonucleosides only the C3′-endo conformation was considered.

Levels of Theory. The single-point calculations were performed at various levels of theory. The most accurate are the MP2/CBS + ΔCCSD(T) calculations, which approximate CCSD(T)/CBS quality and are denoted CBS(T) hereafter. The complete basis set (CBS) extrapolations were obtained through the scheme of Helgaker and Halkier[53,54] (HF and MP2 energies were extrapolated separately) using cc-pVTZ and cc-pVQZ basis sets. Turbomole 5.10[55,56] was used to calculate the MP2 energies with the RI approximation. The correction term for higher order correlation effects, ΔCCSD(T), was calculated using the cc-pVDZ basis set in Molpro 06.[57] For more details, see Jurecka and Hobza.[51] To derive the DFT-based parameters we used the PBE density functional, 6-311++G(3df,3pd)[58−61] basis set (LP hereafter), and empirical dispersion corrections (DFT-D, 1.06-23).[62] For some of the geometry optimizations described below we also used smaller basis sets, TZVP and TZVPP.[63]

Geometry Optimizations and Constraints. In the QM calculations, the starting structures corresponding to either C2′-endo or C3′-endo forms were first relaxed at the PBE/TZVPP level with the continuum solvent model COSMO[64] in the TurboMole 5.10[55,56] software suite (water, ε_r = 78.4). Then, several constraints were applied in the TurboMole program. The O4′−C4′−C3′−C2′ angle was constrained at the value taken from the PBE/TZVPP/COSMO optimal structure to keep the sugar pucker close to C2′-endo or C3′-endo, i.e., for dA, dT, dG, and dC at 28.1°, 26.0°, 25.2°, and 25.4° and for rA, rU, rG, and rC at −34.7°, −38.9°, −39.6°, and −39.2°, respectively. The C4′−C3′−O3′−H3T angle was constrained at −60° to prevent H bonding with the O2′ oxygen, and for ribonucleosides, the C3′−C2′−O2′−HO′2 torsion was constrained at −120° to prevent any sugar···base H-bond formation or intramolecular H-bond formation with O2′. Then, the χ angle was increased with 10° increments and the geometries relaxed using the PBE DFT functional and the LP basis set (see above) in the COSMO continuum solvent. The same constraints were applied in the MM optimizations, which were performed in the Gaussian software suite[65] using the "external" function and the ff99 force field. The external program for MM geometries was the sander module of AMBER[66] and a Poisson−Boltzmann (PB) continuum solvent was used.

Solvent Models. The COSMO continuum solvent model[64] was used in the QM calculations, while a Poisson−Boltzmann (PB) continuum solvent model[67,68] was applied in the MM calculations. The COSMO calculations were performed with TurboMole 5.10[55,56] with default scaled Bondi radii (scaling factor, 1.17) and default water parameters (ε_r = 78.4). The PB calculations were carried out with Gaussian 03 software using the "external" function and in-house scripts linking Gaussian to the sander module of AMBER 9.[66] In sander the grid spacing was set to 0.2 Å, while default water parameters (ε_r = 78.4) and default radii were used (see also refs 67 and 68). The nonpolar terms were included in the PB optimizations, but only the PB electrostatic component was considered in dihedral parameter development (see discussion below).

Obtaining the Torsion Profiles. Usually the torsion angle parameters ($E_{\mathrm{dih},\chi}^{\mathrm{vac}}$ here) are determined by the difference between the MM single-point energy ($E_{-\chi}^{\mathrm{MM//QM,vac}}$) and QM single-point energy ($E^{\mathrm{QM//QM,vac}}$) obtained in vacuo using the same (QM) geometry for both the MM and the QM calculations (eq 1):

$$E_{\mathrm{dih},\chi}^{\mathrm{vac}} = E^{\mathrm{QM//QM,\,vac}} - E_{-\chi}^{\mathrm{MM//QM,\,vac}} \quad (1)$$

Here, we use a different scheme that takes into account certain solvation-related effects (eq 2). In this approach, the geometry optimizations are carried out at the QM and MM levels separately (see below) in continuum solvents (COSMO and PB, respectively) and are followed by single-point calculations including solvation energies ($E^{\mathrm{QM//QM,COSMO}}$ and $E_{-\chi}^{\mathrm{MM//MM,PB}}$, respectively). Note that similar techniques have been used before. For instance, independent relaxation of the QM and MM structures is used in CHARMM (see, e.g., ref 69 and references therein). Solvation by the IEFPCM model (QM calculation only) was used, e.g., in ref 70.

$$E_{\mathrm{dih},\chi}^{\mathrm{solv}} = E^{\mathrm{QM//QM,\,COSMO}} - E_{-\chi}^{\mathrm{MM//MM,\,PB}} \quad (2)$$

With this approach, only the difference between the COSMO and the PB solvation energies enters the resulting torsion parameters (not the total solvation energy). In this way double counting of solvation energy is prevented, while some desirable terms (such as solute polarization) are included. The force field can subsequently be used in simulations with explicit solvent molecules. Our approach can also be justified by the observed improvements in the performance of the force field. Note that for consistency we use full solvent treatment in all our calculations, i.e., for both MM and QM and for both optimizations and single-point energy evaluations. In the PB calculations (single point) only the electrostatic component is considered, in accordance with the COSMO calculations.

Derivation of χ Parameters. In the Cornell et al. force field, the force-field energy (without the PB solvation energy) is a sum

of the bond stretching (E_{bond}), angle bending (E_{angle}), dihedral (E_{dih}), nonbonded electrostatic (E_{elst}), and nonbonded van der Waals (E_{vdW}) terms (eq 3).

$$E = E_{bond} + E_{angle} + E_{dih} + E_{elst} + E_{vdW} \quad (3)$$

The dihedral term is described as a cosine series (eq 4), where n is the periodicity of the torsion, V_n is the rotational barrier, ϕ is the torsion angle, and γ is the phase angle.

$$E_{dih} = \sum_{torsions} \sum_{n} \frac{V_n}{2}[1 + \cos(n\phi - \gamma)] \quad (4)$$

The QM-MM difference obtained in eq 2 is approximated (fitted) by eq 4 (V_n and γ are varied). Upon torsion rotation all force-field components (eq 3) contribute to torsion potential energy, not only the dihedral term (eq 4). To differentiate between the total energy of the torsion and the dihedral contribution to the torsion energy we call the former the "χ torsion profile" and the latter the "χ dihedral term" hereafter. To better understand the various contributions to the χ parameters two parametrizations were derived and tested.

(1) $\chi_{OL\text{-}DFT}$: The first parametrization, $\chi_{OL\text{-}DFT}$, was fully based on the DFT-D QM profile. Only the deoxyribonucleosides (dA, dT, dC, and dG) in a C2′-endo conformation were considered. After DFT optimization (PBE/LP in continuum solvent) the single-point calculations were performed at the DFT-D level (PBE-D-1.06-23/LP). Solvent effects were introduced according to eq 2. In the fitting procedure, double weight factors were assigned to the five points around the important χ values of 200° and 260° to improve the fit in the anti and high-anti regions. The total χ dihedral term was distributed among three of the six torsions contributing to χ (C2−N1−C1′−X in pyrimidines and C4−N9−C1′−X in purines). Since χ dihedral parameters derived for dA and dG were quite similar, only one set of parameters was fitted (i.e., both dG and dA curves were used in a single fitting). This parametrization is presented only for comparison and is not intended to be used for NA simulations. However, although the $\chi_{OL\text{-}DFT}$ parameter set is not recommended for simulations, we provide the respective parameters in the Supporting Information. The abbreviation "OL" in the force-field name stands for the city of Olomouc (see affiliations).

(2) χ_{OL}: In the second parametrization, χ_{OL}, the MP2/CBS data were taken as a reference. The MP2/CBS method was used instead of CBS(T) because both methods provide very similar profiles (see below) but MP2/CBS is much less computationally demanding. Both the deoxyribonucleosides (C2′-endo) and ribonucleosides (C3′-endo) were considered. For the deoxyribonucleosides single-point calculations were also carried out at the DFT-D (PBE-D-1.06-23/LP) level. The difference between the MP2/CBS and PBE-D-1.06-23/LP calculations for deoxyribonucleotides was then added to the PBE-D-1.06-23/LP results for ribonucleosides to save computer time (assuming that the MP2/CBS correction is similar for ribonucleosides and deoxyribonucleosides). Then, continuum solvent terms were introduced according to eq 2 using the PBE-D-1.06-23/LP method. The final QM values were then obtained as combinations of the COSMO PBE-D-1.06-23/LP data adjusted by the above-mentioned MP2/CBS correction. The reference curve for the fit was obtained by combining the data for the ribo- and deoxyribonucleosides. For the region between 210° and 330°, we took the reference curve for the deoxyribonucleosides (C2′-endo) while the ribonucleoside (C3′-endo) curve was used for the remaining χ range. Double weights were assigned to χ values of 180°, 190°, 200°, 210°, and 220° and 240°, 250°, 260°, 270°, and 280° to improve the accuracy of the fit in the important anti and high-anti regions, respectively. The parameters obtained in this manner (our final parameters) are listed in Table 1.

Table 1. Dihedral Parameters for χ_{OL} Parameterization[a]

		χ_{OL} parameter		
nucleoside	torsion (atom types)	n	$V_n/2$	ϕ
A	O4′−C1′−N9−C8	1	0.9656	68.79
	(OS-CT-N*-C2)	2	1.0740	15.64
		3	0.4575	171.58
		4	0.3092	19.09
G	O4′−C1′−N9−C8	1	0.7051	74.76
	(OS-CT-N*-CK)	2	1.0655	6.23
		3	0.4427	168.65
		4	0.2560	3.97
C	O4′−C1′−N1−C6	1	1.2251	146.99
	(OS-CT-N*-C1)	2	1.6346	16.48
		3	0.9375	185.88
		4	0.3103	32.16
U(T)	O4′−C1′−N1−C6	1	1.0251	149.88
	(OS-CT-N*-CM)	2	1.7488	16.76
		3	0.5815	179.35
		4	0.3515	16.00

[a] C1 and C2 are new atom types for C introduced to distinguish A from G and C from U (T). The parameters can be downloaded from http://fch.upol.cz/en/rna_chi_ol/.

MD Simulations of RNA and DNA Duplexes. Initial structures of RNA and DNA duplexes were taken from X-ray data. The ions and water molecules were removed from the original PDB files. The 1RNA tetradecamer duplex r(U(AU)$_6$A)[71] and 1BNA dodecamer duplex d(CGCGAATTCGCG)[72] were taken without any further modifications. In the brominated tridecamer r(GCGUU-5BUGAAACGC) (PDB ID 2R20)[73] the brominated uracil was replaced with uracil, and this structure is hereafter denoted 2R20′. The decamer r(GCACCGUUGG) was excised from the 1QC0[74] structure and is hereafter denoted 1QC0′. In all simulations the total charge was neutralized by Na^+ ions.[75] A TIP3P[76] water box was used to solvate the nucleic acid molecules (equilibrium box sizes 59 × 68 × 65 Å with 8428 water molecules for 1RNA, 51 × 55 × 68 Å with 6145 water molecules for 1BNA, 65 × 60 × 60 Å with 7502 water molecules for 2R20′, and 54 × 51 × 58 Å with 5121 water molecules for 1QC0′). Simulations were carried out with the pmemd code from the AMBER 9 program suite[66] under NPT conditions with default temperature and pressure settings (tautp = 1.0 ps and taup = 1.0 ps), a 2 fs time step, a 9 Å nonbonded cutoff, and SHAKE on bonds to hydrogen atoms with default tolerance (0.00001). Nonbonded pairlist was updated every 25 steps. PME was used with default grid settings and default tolerance (dsum_tol = 0.00001). Default scaling factors were used to scale nonbonded and Coulomb interactions (scnb = 2.0 and scee = 1.2, respectively).

Averages of several structural parameters were taken from the last 20 ns of 100 ns simulations, and snapshots were stored every 1 ps. In the case of B-DNA simulation we ran only 50 ns simulations (the last 20 ns were taken for analysis), because this was enough to demonstrate the large deviations for the χ_{OL} parametrization.

Two terminal base pairs at both ends of the modeled structures were omitted from the analyses. All analyses were performed using X3DNA code.[77] For the 2R20′ structure, the base pair parameters of the noncanonical GG pair and base pair step parameters of the steps including this noncanonical pair were filtered off in order to focus solely on the canonical base pair geometries (and thus avoid averaging of bimodal distributions). Mass-weighted rmsd values were calculated with respect to the initial structure (all atoms), again omitting the two terminal base pairs at both ends.

Further force-field assessments included very extensive simulations of numerous other RNA species, including UUCG and GNRA RNA tetraloops (up to 1 μs trajectories), short A-RNA duplexes, and reverse kink-turns (see below). Simulations of sarcin-ricin domains of 23S rRNA, ribozymes, riboswitch, kink-turns, C-loops, and other selected molecules are in progress. A detailed report of the RNA tetraloop calculations has already been published.[46]

RESULTS AND DISCUSSION

Choice of the Method for Geometry Optimization. In order to derive reliable data for force-field parametrization, it is first necessary to determine the level of computations required. Several levels of theory for geometry optimization were tested for the dC nucleoside with the C2′-endo pucker. The dC nucleoside has the largest steric clashes of all nucleosides (the highest rotational barrier) and thus should theoretically be the most sensitive probe regarding the level of theory.

We used DFT-based methods for geometry optimizations, due to their advantageous balance between quality and speed. The utility of HF and MP2 methods for deriving geometries has not been specifically tested for the following reasons. The HF method is highly unreliable due to the lack of electron correlation, and the MP2 method is known to exhibit very large intramolecular basis set superposition errors (BSSEs) when manageable basis sets are used.[78−80] The following DFT functional/basis set combinations were tested: BLYP/TZVP, B3LYP/TZVP, PBE/TZVP, PBE/TZVPP, and PBE/LP. All optimizations were carried out in COSMO implicit solvent[64] (water, $\varepsilon = 78.4$). We assumed that the last combination, the PBE functional with the largest LP basis set, would be the most reliable because it is known to provide the best results for polar molecular complexes[62] (note that the potential energy surface is shaped mainly by the polar contacts in dC). The other optimization methods were judged according to rmsd values of 36 optimized geometries (χ profiles) with respect to the PBE/LP geometries. The BLYP/TZVP and PBE/TZVP combinations yielded the largest rmsd values (1.26 and 0.91 Å, respectively, all atoms) relative to the PBE/LP geometries, and the RSMD between the geometries they generated was also large (1.48 Å). The B3LYP/TZVP gave a better rmsd of 0.76 Å. These results are consistent with the results found for molecular complexes.[62] To test whether a smaller basis set could be used, PBE results were also calculated using the TZVP and TZVPP basis sets. While the results for TZVPP were very close to the PBE/LP results (total rmsd 0.48 Å), the PBE/TZVP optimization exhibited rather large structural deformations for several geometries (rmsd 0.76 Å).

Considering these results we decided to use the largest LP basis set (6-311++G(3df,3pd)) together with the PBE density functional in all optimizations carried out in this study to ensure quality of the results. The LP basis set is already fairly efficient at eliminating intramolecular BSSE, while the large BSSE of smaller basis sets could compromise the results. Hence, we strongly recommend use of large basis sets for geometry derivation in force-field parametrization. Although the lower level methods, such as the popular HF/6-31G* method (used for example by Yildirim et al.[45] to derive their χ parametrization), may sometimes provide acceptable results based on fortuitous error cancellation, in general they are likely to introduce bias. The HF/6-31G* method for geometry derivation was justified in the mid-1990s, when better methods were not feasible, but it does not reflect contemporary standards in the field.

Brief comment is needed regarding the use of the empirical dispersion correction for the DFT optimizations. We did not use the dispersion correction for the DFT optimizations carried out in solvent to avoid an imbalanced description of the solute−solute and solute−solvent interactions. However, it is possible that when larger and more compact molecules are modeled the intramolecular dispersion correction of DFT might become necessary. Note, however, that it is still necessary to include dispersion correction in the single-point QM calculations in eq 2.

Choice of Method for Single-Point Calculations. As mentioned in the Introduction, even very small changes in the torsion potential can cause substantial discrepancies in MD simulations. Therefore, it is important to determine the sensitivity of the torsion profile to the level of theory. The best available reference method for systems containing tens of atoms is the CCSD(T)/CBS (coupled clusters singles and doubles with perturbative treatment of triple excitations/complete basis set limit) method.[51] However, since CCSD(T)/CBS calculation is not tractable, we used the MP2/CBS level with CCSD(T)/cc-pVDZ correction, here denoted CBS(T). Figure 2 compares profiles obtained with several frequently used methods with the CBS(T) reference profile for nucleosides.

Although the torsion profiles presented in Figure 2 may seem fairly similar at first sight, differences from the reference CBS(T) curve are often greater than 1 kcal/mol, especially those obtained using less computationally demanding methods. For instance, the MP2/6-31G* method predicts the modeled structure to be significantly less stable (by about 0.6 kcal/mol) than does the reference CBS(T) method at the key energy minimum in the high-anti region (χ = 250°). Furthermore, MP2/6-31G* yields an incorrect balance of the anti and high-anti regions (torsion angles 210° and 250°) and somewhat overestimates the height of the lower barrier. Given the requirements for the χ profile discussed in this paper, we conclude that use of MP2 with a small basis set would not yield sufficiently accurate data for parameter development.

The data shown in Figure 2 also suggest that the DFT description of the χ profile is quite inaccurate. Although the profile generated using the PBE-D-1.06-23 method with a large LP basis set is somewhat closer to the reference curve than the MP2/6-31G* profile around the anti minimum, it still exhibits sizable errors around the energy barriers. As we show below, such deviations in the χ potential lead to substantial deviations of certain structural parameters in MD simulations of RNA duplexes (compare the results for $\chi_{OL\text{-}DFT}$ and χ_{OL} below). Similar conclusions can also be drawn regarding the M06 and M06-2X DFT functionals recently presented by Zhao and Truhlar,[81] both of which are overly repulsive in the high-anti region, overestimate the lower transition barrier, and provide inaccurate balances between the syn and the anti minima (note, the LP basis set used here is similar to the basis set used for the M06 functional

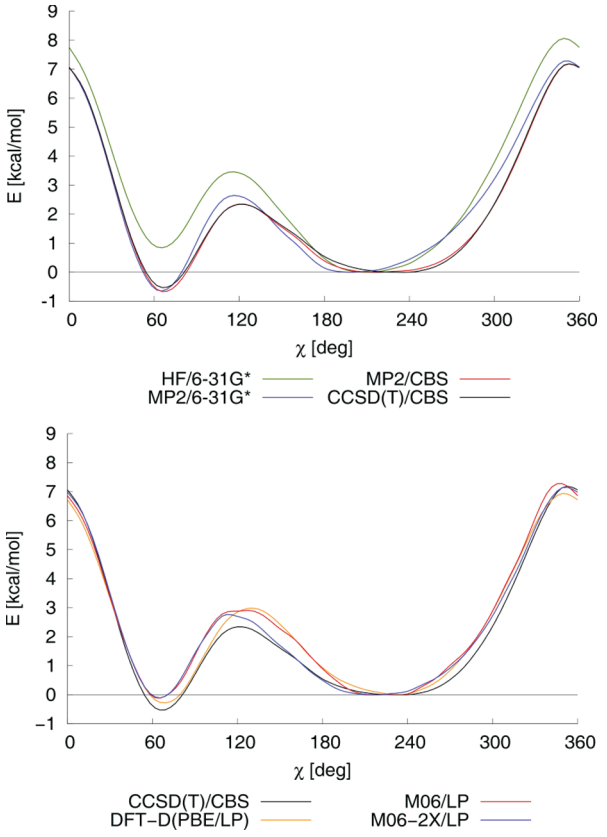

Figure 2. Torsion profiles for guanine nucleoside (dG) calculated at various levels of theory in vacuo. The reference method is CBS(T). (Top) Profiles obtained with the wave function methods: CBS(T) (black), HF/6-31G* (green), MP2/6-31G* (blue), and MP2/CBS (red). (Bottom) Profiles obtained with the DFT methods: DFT-D (PBE/6-311++G-(3df,3pd)/1.06-23) (orange), M06 (red), M06-2X (blue), and the reference CBS(T) profile (black). Energies are offset to the anti minimum structure.

development). Given the accuracy required for the χ dihedral parameters, none of the applied DFT-based methods can be recommended for their derivation. This is an important methodological finding of our study, which is corroborated by our recent benchmark study of another model of nucleic acid backbone, in which a broader set of DFT methods was tested.[52]

In contrast, the MP2/CBS level provides results that are very close to those obtained using the reference CBS(T) method, with differences of merely ca. 0.1 kcal/mol around the minima. We hypothesize that the MP2/CBS method is sufficiently accurate to serve as a reference level of theory, and our final parameters (χ_{OL}, presented below) are based on MP2/CBS data because they are significantly less computationally demanding to handle than CBS(T) reference data. We do not recommend using any level of theory lower than MP2/CBS for torsion profile derivation.

Dependence of the χ Profile and Dihedral Term on Sugar Conformation and Type. To assess the effect of sugar pucker on the derived dihedral parameters we calculated the χ torsion profiles for two different puckers of the A, T, C, and G deoxyribonucleoside models (C2′-endo and C3′-endo) and for the C3′-endo pucker of the A, U, C, and G ribonucleoside models. Figure 3 displays results of the PBE-D-1.06-23/LP calculations both in vacuo (left panel) and in COSMO continuum solvent (middle panel) for cytosine. The χ dihedral term contributions (i.e., the QM profile minus the MM profile without the respective χ terms) derived from the continuum solvent data are shown on the right. The results for the other nucleosides are similar and can be found in the Supporting Information (Figure S3).

To differentiate between the total potential energy of the torsion (as in eq 3, including PB solvation energy for calculations in solvent) and the dihedral contribution to the total torsion energy (E_{dih} only, eq 4) we call the former the "χ torsion profile" and the latter the "χ dihedral term" hereafter.

The results presented in Figure 3 suggest that in vacuum the χ torsion profile is quite strongly modulated by the sugar conformation and the presence of the 2′-OH group. Comparing the deoxy C2′-endo and ribo C3′-endo compounds, the maximum difference is almost 3 kcal/mol, and around the anti minimum the differences are as large as 2 kcal/mol.

When a COSMO continuum treatment of the solvation energy is included, the χ profiles differ from those obtained in vacuum. The higher energy barrier is lowered, the lower barrier increases, and both the syn/anti equilibrium and the shape of the profile in the anti minimum region are also affected. Profiles obtained at the force-field level with PB continuum solvent show very similar patterns in these respects (see Supporting Information, Figure S3). Clearly, the in vacuo and in-solvent profiles of the torsion potentials differ markedly. Consequently, comparing, for instance, the relative stability of two minima in vacuum and in solvent can lead to quite different conclusions. We hypothesize that in-solvent profiles are more likely to be representative of NAs in solution than corresponding profiles obtained in vacuo because the continuum mimics the screening of the electrostatic component that occurs with hydrated nucleoside structures in solution. If so, in-solvent profiles rather than in vacuo profiles should be considered (although the latter are commonly used) in attempts to link torsion curves to the outcomes of in-solvent MD simulations.

Interestingly, when solvation is included, the profiles show less dependence on the pucker or presence of the 2′-OH and overall become strikingly more similar. The maximum difference between the deoxy C2′-endo and the ribo C3′-endo compounds drops to less than 1.5 kcal/mol, and around minima the differences are smaller than 1 kcal/mol. These differences are mainly due to variation of the van der Waals (vdW) and electrostatic interactions of the sugar and base atoms as the χ torsion rotates. For different sugar puckers the interacting parts of the sugar and base moieties approach each other at different distances, thus providing different energy profiles. However, the major components of this variation cancel out when the MM single-point energies (with χ dihedral terms set to zero) are subtracted from the QM energies; see the χ dihedral terms derived from these data (Figure 3, right).

The derived χ dihedral terms (Figure 3, right) display a maximum difference between the curves corresponding to the different puckers/2′-hydroxylation of about 2 kcal/mol. If we consider only the two most relevant dC C2′-endo and rC C3′-endo conformations, the maximum difference drops to about 1 kcal/mol and around the minima it is even smaller. When average parameters are used as a compromise, the corresponding errors drop to about one-half of the averaged differences between the curves (if two conformations are considered, as in the case of χ_{OL}). This gives an estimate of the errors intrinsic to our parametrization. These errors cannot be eliminated if a universal set of torsion parameters is required for DNA and RNA. Note, however, that there is still the possibility of reducing the errors by

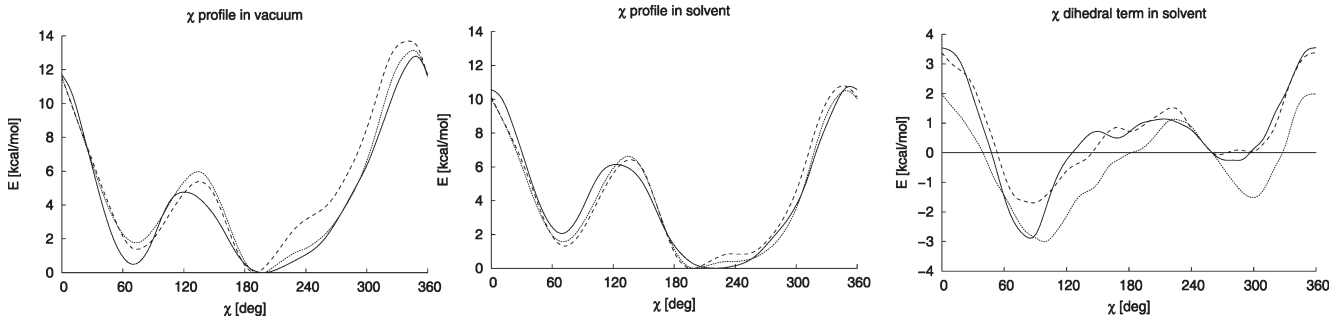

Figure 3. Torsion profiles for cytosine calculated in vacuo (left), with COSMO continuum solvent (middle), and the χ dihedral term's contribution to the torsion derived from the continuum solvent data (right) of the cytosine 2-deoxyribonucleoside with C2′-endo and C3′-endo sugar puckers and the ribonucleoside with C3′-endo sugar pucker (full, dotted, and dashed lines, respectively).

simultaneously adjusting another (coupled) component of the force field, for instance, the torsions determining the sugar pucker, but this was not attempted in the work presented here.

Effects of Geometry Relaxation. The effects of geometry relaxation on the resulting torsion parameters are rarely discussed. Usually, the following procedure is used to obtain new parameters. First, a model molecule with constrained dihedral angle is relaxed at the QM level and the QM energy, $E^{\mathrm{QM//QM}}$, is obtained. Then single-point MM energy is calculated, based on the QM geometry with the parametrized torsion set to zero, $E_{-\chi}{}^{\mathrm{MM//QM}}$, and the torsion parameters are determined according to eq 5.

$$E_{\mathrm{dih},\chi} = E^{\mathrm{QM//QM}} - E_{-\chi}{}^{\mathrm{MM//QM}} \tag{5}$$

However, more adequate parameters may be obtained when a MM optimization is also carried out and the MM energy, $E_{-\chi}{}^{\mathrm{MM//MM}}$, is calculated based on the MM relaxed geometry rather than the QM geometry. Then, the resulting parameters are determined according to eq 6. This scheme is used, for instance, in the CHARMM force field (see, e.g., ref 69 and references therein), and a very similar scheme was applied by Ode et al.[44]

$$E_{\mathrm{dih},\chi}{}^{\mathrm{relaxed}} = E^{\mathrm{QM//QM}} - E_{-\chi}{}^{\mathrm{MM//MM}} \tag{6}$$

The rationale underlying eq 6 is that the MM potential energy surface (PES) derived in this manner is more similar to the QM PES than when eq 5 is used, in terms of the relative energies of key PES regions, such as minima and transition states. The relative energies of minima and transition states are of primary interest in empirical modeling; hence, they need to be as similar as possible to reference QM values on the QM PES. The key to understanding which of the approaches (eq 5 or 6) is more adequate in this sense is to realize that eq 6 corresponds to situations where the system samples the MM geometries and acquires MM energies, as in molecular dynamics, while eq 5 corresponds to situations where the system samples the QM geometries but acquires MM energies. The latter is clearly artificial, critically dependent on the other intra- and intermolecular MM force-field parameters, and may substantially bias parametrization of force fields. Thus, the former approach (i.e., eq 6) is preferable.

Equation 5 can also be understood as an approximation to eq 6, which can be reasonably justified in two cases: (i) when the optimal QM and MM geometries are very similar, especially in terms of distances between the 1−4, 1−5, etc. atoms or (ii) when the remaining force-field contributions, namely, the Coulombic and wdW terms, and the bond, angle, and other dihedral angle terms do not contribute significantly to the torsion profile. Note that the Coulomb and vdW terms codetermine the 1−4 distances. This also holds for the bond, angle, and other dihedral terms that may be deformed when the given torsion is rotated. Many of those terms are quite inaccurate in the force fields (and likely parametrized for different geometries than the QM-optimized geometries). Using eq 6 can partially correct for these inaccuracies by including them in the parametrized torsion.

To illustrate the differences between relaxed and nonrelaxed conditions we show torsion profiles calculated using the QM method based on QM-optimized geometries ($E^{\mathrm{QM//QM,COSMO}}$, full line) and compare them with the MM$_{-\chi}$ profiles based on QM-optimized geometries ($E_{-\chi}{}^{\mathrm{MM//QM,PB}}$, dashed line) and MM-optimized geometries ($E_{-\chi}{}^{\mathrm{MM//MM,PB}}$, dotted line) for dC in Figure 4 (top). The derived χ parameters correspond to the differences between the dashed and full lines (eq 5) and dotted and full lines (eq 6) and are also shown in Figure 4 (bottom). Clearly, the resulting dihedral terms differ markedly. For example, consider the torsion barrier (around 360°) between the high-anti and syn regions. When dihedral parameters are derived from eq 5 (illustrated by the difference between the full and dotted lines), they will be positive for the transition region but much smaller (by about 2.5 kcal/mol) compared to those derived from eq 6 (illustrated by the difference between the full and dashed lines). In a MD simulation the molecule will follow the MM PES on its way from the high-anti region to the syn region. If we added the underestimated dihedral penalty obtained from eq 5 to the MM energy, the total barrier would be underestimated as well. Similar errors appear in other parts of the PES and influence the relative stability of the anti and syn forms, the low-anti to syn transition barrier, and the shape of the resulting MM potential curve.

It is important to note that the magnitude of the errors associated with using the QM geometries for the MM single-point calculations is not marginal; the differences in this case reach almost 3 kcal/mol, comparable to the amplitude of the dihedral torsion itself. Deviations are significant for both the barrier heights (∼2.5 and 0.7 kcal/mol for the lower and upper barriers, respectively) and the region around $\chi \approx 70°$ characteristic of the Z-form of DNA and many nucleotides in folded RNA structures (∼1 kcal/mol). Interestingly, in the context of this study, there are also differences in the shape of the curves in the anti region, which might contribute to the relative stability of the A and B forms of nucleic acids (see also the $\Delta E_{\mathrm{anti/high\text{-}anti,dih}}$ criterion described below).

Regarding the origin of the observed differences, we can hypothesize that they are mainly due to the short-ranged vdW contacts that occur upon dihedral rotation. For instance, in the

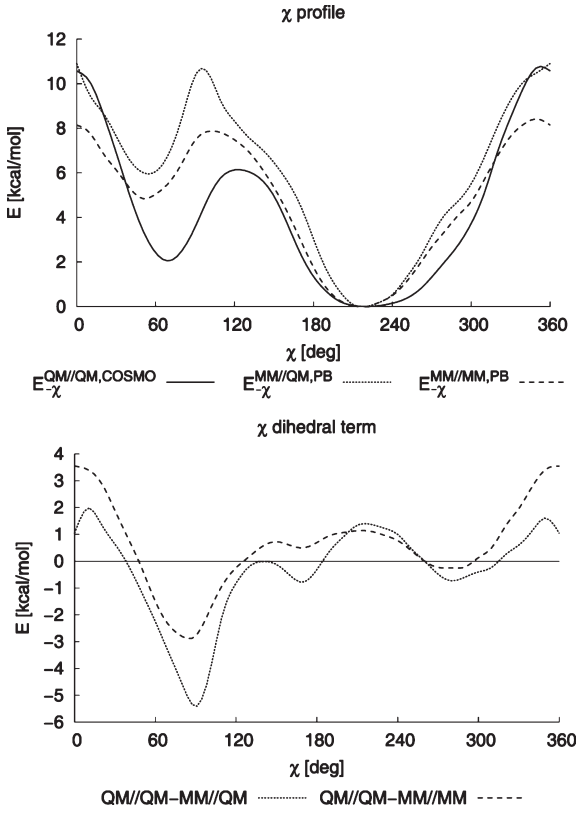

Figure 4. (Top) Torsion profiles for dC calculated as QM energy based on QM-optimized geometry ($E^{QM//QM,COSMO}$, full line), $MM_{-\chi}$ energy based on MM-optimized geometry ($E_{-\chi}^{MM//MM,PB}$, dashed line), and $MM_{-\chi}$ energy based on QM-optimized geometry ($E_{-\chi}^{MM//QM,PB}$, dotted line). (Bottom) χ dihedral terms $E_{dih,\chi}^{solv}$ derived from $E^{QM//QM,COSMO} - E_{-\chi}^{MM//MM,PB}$ (QM//QM-MM//MM, dashed line) and $E^{QM//QM,COSMO} - E_{-\chi}^{MM//QM,PB}$ (QM//QM-MM//QM, dotted line) normalized to $\chi = 250°$. The ff99bsc0 force field was used in all cases, and energies are in kcal/mol.

cytosine nucleoside the O4′ and O2 oxygen atoms approach each other closely (this contact corresponds to the higher torsion barrier, $\chi = 0°$) and upon rotation the O2 and H2′ atoms also approach each other (the lower barrier, $\chi = 120°$). The optimal QM distances for these interactions differ from the optimal MM distances. For instance, in dC the distances between the O4′ and O2 atoms for $\chi = 0°$ are 2.72 Å in QM and 2.66 Å in MM and those between the O2 and H2′ atoms for $\chi = 120°$ are 2.31 Å in QM and 2.44 Å in MM. Since the vdW and Coulomb energies depend strongly on distance, especially at short separations,[82] the associated errors may be significant. Other geometry differences between the QM and MM structures are probably less important. In MM structures the pseudorotation angle P (for definition see below, section MD Simulations of A-RNA Duplexes) is systematically underestimated by about 5° compared to QM, and this underestimation somewhat increases for $\chi = 0°$, 90°, and 180° (note that only the O4′−C4′−C3′−C2′ angle was constrained, therefore the ribose was partly flexible). The next difference is the slightly different value of pyramidalization on the N1 atom in QM and MM (around the anti minimum they differ by less than 3°). In other parameters the MM and QM structures are very similar.

For the above reasons we recommend using relaxed MM geometries for calculating MM single-point energies in attempts to derive torsion parameters that perform well in MD simulations.

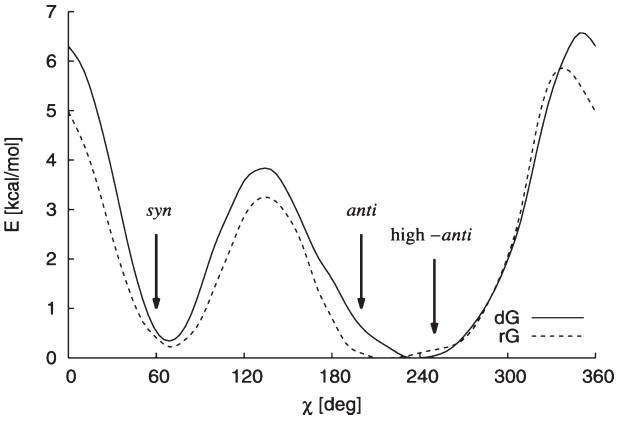

Figure 5. χ torsion profiles for dG (full line) and rG (dashed line), indicating typical average X-ray values for A-RNA, B-DNA, and Z-DNA. PBE/LP data including solvent effects.

However, it is possible that relaxation of the MM geometries may lead to a significantly different structure than QM relaxation (due to differences between the MM and the QM PES). If so, using suitable constraints to keep the MM geometry close to expectations would probably cause a smaller error than using eq 5.

Finally, we compare the fully relaxed structures of rA, rG, rC, and rU obtained with the ff99bsc0 and ff99bsc0 χ_{OL} force fields with the QM reference geometries (PBE with LP basis set). All optimizations are carried out in solvent (COSMO in QM and PB in MM) without any constraints. The OH group on C2′ is oriented such that it forms a hydrogen bond with the OH group on C3′ atom in order to prevent formation of hydrogen bonds with the NA bases. The optimal χ values are 201° (QM), 217° (ff99bsc0), and 194° (ff99bsc0χ_{OL}) for rC and 201° (QM), 204° (ff99bsc0), and 196° (ff99bsc0χ_{OL}) for rU. These values are quite similar, and the small differences between the QM reference and the ff99bsc0χ_{OL} force field can be attributed to geometry constraints used in parameter derivation and to inaccuracies of the fit. For purines the optimal χ values are 200° (QM), 266° (ff99bsc0), and 189° (ff99bsc0χ_{OL}) for rG and 198° (QM), 261° (ff99bsc0), and 183° (ff99bsc0χ_{OL}) for rA. Here, the ff99bsc0χ_{OL} values are again quite similar to the QM reference; however, the ff99bsc0 values are significantly higher, closer to the high-anti region. The relatively large shift in the minimum position of rG and rA is in line with the observed propensity to formation of the ladder-like structures in the ff99bsc0 force field.

Comparing χ Parameters. Before comparing effects of various parametrizations on the behavior of modeled systems in the anti region we discuss relevant experimental data. In crystal structures,[83] RNA is typically found in the A form with the χ population peaking at around 200° (anti). For DNA the B form is prevalent with $\chi \approx 250°$ (high-anti), but in DNA χ can also adopt values characteristic of the A and Z forms. In the Z form χ is in the syn region ($\chi \approx 60°$) for dG and the high-anti region ($\chi \approx 250°$) for dC. Typical values of χ are indicated and compared with the χ torsion profiles of dG and rG nucleosides, calculated at the PBE/LP level (including COSMO continuum solvation energy to improve comparability with nucleic acids in real environments), in Figure 5.

The data displayed in Figure 5 show that in the anti region the energy minimum of the dG potential is shifted more toward the high-anti ($\chi \approx 250°$) while the rG minimum is closer to the anti configuration ($\chi \approx 200°$). The same trend is also found for other

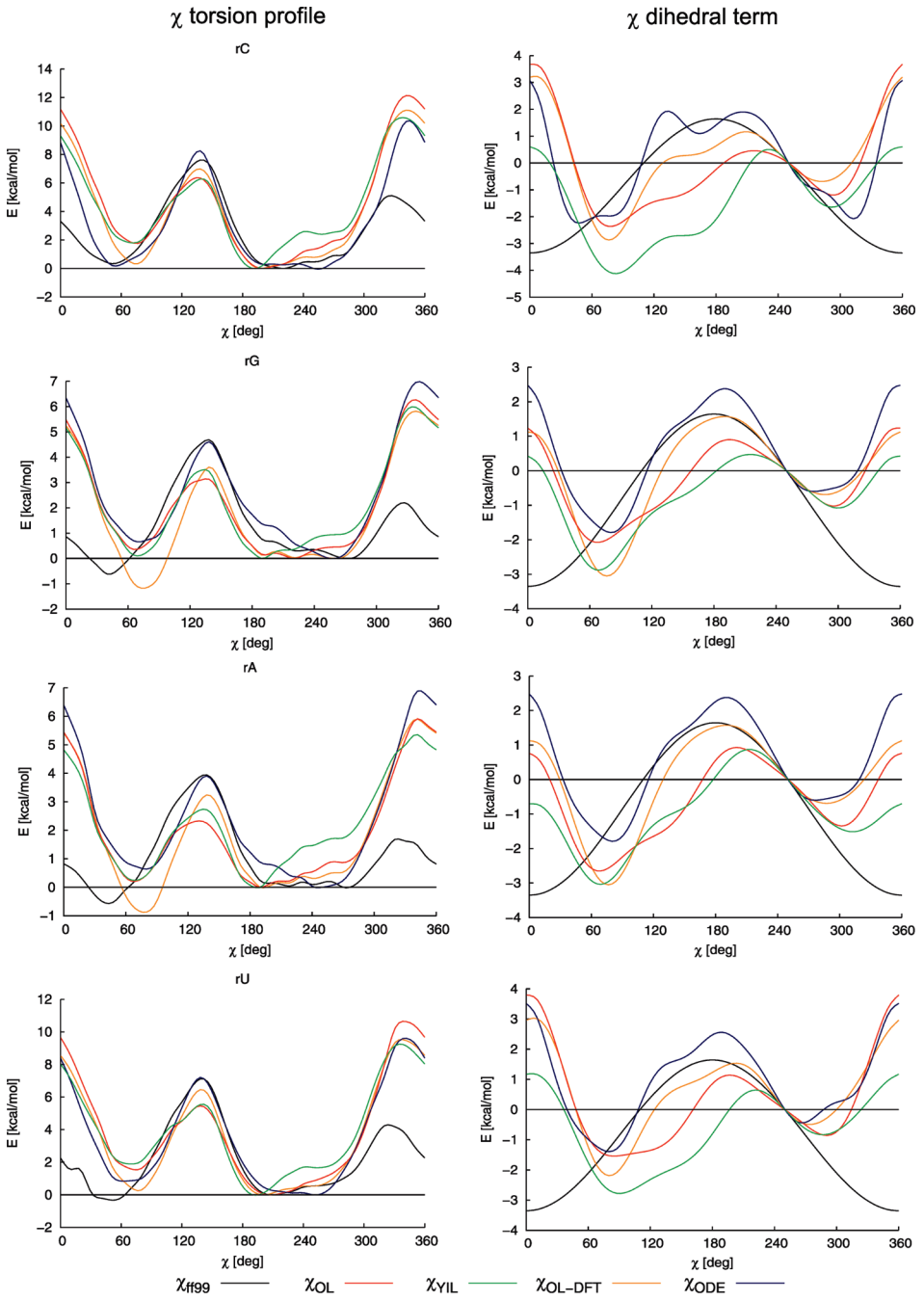

Figure 6. Torsion profiles for the χ angle (on the left, ff99-optimized geometries) and the χ dihedral terms (on the right) of ff99 (black), Ode et al. (blue), Yildirim et al. (green), and parameters derived herein ($\chi_{OL\text{-}DFT}$ orange, χ_{OL} red) for ribonucleosides. The dihedral term was offset to $\chi = 250°$, and idealized geometries were used to calculate the χ dihedral terms on the right to facilitate comparison with published data (see also text).

nucleosides (see Figure S1 in the Supporting Information). Therefore, it seems that the shape of the χ potential profile drives the ribo- and deoxyribonucleosides toward their typical A and B forms (anti and high-anti configurations, respectively). Note, however, that in the X-ray structures of B-DNA (for instance) the χ distribution is relatively broad and very high values of χ may also appear, much higher than those corresponding to the energy minima in Figure 5. This indicates that either our theoretical potentials are still inaccurate, or the environment (surrounding bases and the sugar−phosphate backbone) contribute strain to the χ torsion and significantly influence the actual values of χ.

Here it is worth noting that the MM-derived χ profiles exhibit the same systematic anti/high-anti propensities for dN/rN compounds as the QM profiles (compare Figure 6 below and Figure S2 in Supporting Information), although the same χ dihedral parameters were used for both dN and rN nucleosides. Therefore, the A/B propensities of ribo/deoxyribo compounds must come partially from the nonbonded interactions or dihedral contributions associated with the 2′-OH group of ribose and not from the χ parametrization.

In the following text we compare the available χ parametrizations and discuss their influence on the main features of χ torsion

dx.doi.org/10.1021/ct200162x |J. Chem. Theory Comput. 2011, 7, 2886–2902

Table 2. χ Contribution to Anti/High-Anti Relative Stability, $\Delta E_{anti/high\text{-}anti,dih} = E_{dih}(\chi = 210°) - E_{dih}(\chi = 250°)$, for Several χ Parameterizations[a]

	$\Delta E_{anti/high\text{-}anti,dih}$ [kcal/mol]				
parameterization	A	G	C	U(T)	average
ff94	1.9	1.9	1.9	1.9	1.9
ff98/99	1.3	1.3	1.3	1.3	1.3
χ_{ODE}	2.0	2.0	1.8	1.8	1.9
χ_{YIL}	0.8	0.5	0.0	0.5	0.5
χ_{vac}[b]	1.8	1.7	1.1	1.9	1.6
$\chi_{OL\text{-}DFT}$	0.5	0.5	0.8	1.2	0.8
χ_{OL}	0.9	0.8	0.4	0.9	0.8

[a] The more positive the anti/high-anti value, the stronger the stabilization of the high-anti conformation. Results with and without bsc0 correction are identical. [b] The χ dihedral term was derived in the same way as in $\chi_{OL\text{-}DFT}$, but based on gas phase QM data; see text.

profiles. Figure 6 compares χ torsion profiles (on the left) and the corresponding dihedral terms (on the right) calculated using ff99 (black), Ode et al. (blue), and Yildirim et al. (green) parametrizations and parameters derived herein, i.e., $\chi_{OL\text{-}DFT}$ (orange) and the final χ_{OL} parameters (red). All energies were calculated using the same force-field-optimized geometry (ff99), and only the profiles for ribonucleosides are shown (for dN profiles see Supporting Information, Figure S2). In order to make the profiles as comparable as possible to those of hydrated NA structures, PB solvation energy (identical for all parametrizations) was included in the calculations.

It should be noted that the differences between the χ torsion profiles (on the left) do not fully correspond to the differences between the derived dihedral terms (on the right). This is because the latter were calculated using cosine formulas assuming idealized geometries (i.e., C1′ was assumed to be an ideal tetrahedron, the O4′−C1′−N1−C6 dihedral was assumed to be O4′−C1′−N1−C2 + 180°, etc.), whereas MM-optimized geometries were used to generate the profiles on the left. The MM-optimized geometries slightly differ from the idealized geometries because all the nonconstrained dihedrals and angles deform upon torsion rotation, for example, the C1′ is not perfectly tetrahedral. Consequently, differences in energy are found mainly for the χ torsion parametrizations that involve terms including C2′ and H1′ of ribose, such as $\chi_{OL\text{-}DFT}$, χ_{ODE}, and χ_{YIL}. This also means that the $\Delta E_{anti/high\text{-}anti,dih}$ values (see below) that would be obtained from the right part of Figure 6 differ somewhat from those given in Table 2, because the latter were determined using optimized geometries. The dihedral terms are presented for the idealized geometries to facilitate their comparison with published data.

Anti Minimum and Relative Anti/High-Anti Stability. Figure 6 shows that the profiles generated using the compared parametrizations differ significantly in the anti minimum region. While the minima of curves obtained using the parametrization of Yildirim et al. are located strictly in the anti region, the parameters presented by Ode et al. shift the minimum to the high-anti region. Minima of profiles generated using the ff99, χ_{OL} (and $\chi_{OL\text{-}DFT}$) parameters appear somewhere between those two extremes but closer to the anti region. Further, the profiles differ not only in the position of the minimum but also in its shape. This is also very important because the distribution of the χ angle in real NA structures is usually quite broad; thus, the steepness of changes in the potential across a wide range of angles matters.

χ Contribution to Relative Anti/High-Anti Stability and Ladder-Like Structures. The link between emergence of the ladder-like structures in RNA simulations and the glycosidic angle χ was first pointed out by Mlynsky et al.[43] Since the transition to the ladder-like structure is accompanied by a significant shift of the χ angle from the anti region ($\chi \approx 210°$) toward the high-anti region ($\chi \approx 250°$), the χ potential must clearly affect the simulated behavior of RNA (the values of $\chi \approx 210°$ and 250° were chosen arbitrarily and provide stable results for our purposes). In order to assess the contribution of χ to formation of the ladder-like structures quantitatively, we need a suitable measure. A convenient one could be the energy difference between anti ($\chi = 210°$) and high-anti ($\chi = 250°$) orientations, $\Delta E_{anti/high\text{-}anti} = E(\chi = 210°) - E(\chi = 250°)$. However, this would also incorporate electrostatic, vdW, and other contributions to high-anti propensity. An alternative measure is the χ dihedral term's contribution to the anti/high-anti equilibrium, $\Delta E_{anti/high\text{-}anti,dih} = E_{dih}(\chi{=}210°) - E_{dih}(\chi = 250°)$. This measure enables assessment of the available χ parametrizations—ff94, ff98/99, χ_{YIL}, χ_{ODE}, $\chi_{OL\text{-}DFT}$, and χ_{OL}—with regard to their propensity to lead to high-anti conformation (Table 2).

Table 2 shows $\Delta E_{anti/high\text{-}anti,dih}$ values for all nucleosides and all parametrizations shown in Figure 6 plus the ff94 parametrization. All values in Table 2 are positive, which means that all dihedral terms considered destabilize the anti ($\chi \approx 210°$) region typical for RNA. However, they do so to varying extents. We suggest that decreasing the stability of the anti region will increase the likelihood of formation of high-anti ladder-like structures in MD simulations. Thus, the propensity of the parametrizations to lead to formation of ladder-like structures should increase in the following order: $\chi_{YIL} < \chi_{OL\text{-}DFT} \approx \chi_{OL} <$ ff99 $< \chi_{ODE}$. If so, the bottom three parametrizations in Table 2 (χ_{YIL}, $\chi_{OL\text{-}DFT}$, and χ_{OL}) have the potential to eliminate (or at least reduce) formation of ladder-like structures in RNA simulations because they destabilize the anti orientation less than ff98/99. In contrast, the parametrization of Ode et al. should promote laddering behavior more than ff99.

Extensive testing of different force fields has confirmed this expectation.[46,84] The ff99 and χ_{ODE} parametrizations lead to predictions of the ladder-like structure as the global minimum of the A-RNA stem, the latter actually accelerating its formation in simulations, while the χ_{YIL}, $\chi_{OL\text{-}DFT}$, and χ_{OL} parametrizations appear to eliminate ladder formation.[46] However, the χ_{YIL} parametrization seems to do so excessively, which introduces other irregularities into the simulations (see below). Note that the particularly large anti/high-anti value for χ_{YIL} stems from significant destabilization of the high-anti region connected with the rapid onset of the high-anti penalty manifested in the "bumps" in the profiles in Figure 6 (left). In part this could be attributed to use of the insufficiently large 6-31G* basis set of atomic orbitals in the MP2 calculations, which contributes to destabilization in the high-anti region (e.g., by about 0.6 kcal/mol in the case of guanine, see Figure 2).

It should be noted that solvation-related effects also contribute to the relative anti/high-anti stability. To assess the magnitude of this contribution we derived another set of parameters in the same way as for χ_{OL} except that solvation was not included (using eq 1 instead of eq 2). Comparison of these vacuum-derived parameters (denoted χ_{vac} in Table 2) with χ_{OL} shows that including the solvation effects destabilizes the high-anti region by about

0.8 kcal/mol on average, thus increasing preference for the anti conformation typical for A-RNA. Thus, neglecting the solvation effects may introduce substantial bias in the χ potential. Note that the lack of solvent-induced stabilization is also apparent when the χ_{ODE} parameters (which were also derived in vacuo) are used. Interestingly, the same effect is not found in the χ_{YIL} modification, probably as a result of the error compensation (χ_{YIL} parameters represent a compromise between four structures with rather different torsion profiles; therefore, substantial uncertainties connected with the fitting procedure are to be expected).

Note that the $\Delta E_{anti/high\text{-}anti,dih}$ values presented in Table 2 were derived using the relaxed geometries with fixed χ angle value, while plots in the right part of Figure 6 were derived using idealized geometries (assuming a perfect tetrahedron on C1′ and planarity of the bases). Therefore, the results shown in Figure 6 may not fully correspond with the values in Table 2.

At this point, one might question the assumption that such small differences (on the order of tenths of a kcal/mol) between the parameters could be responsible for major structural distortions. However, such energy contributions may have strong cumulative effects since they reflect interactions that are present at numerous sites in regular DNA and RNA structures.[85] Furthermore, the dihedral terms are "hard wired" in the force fields and are not diminished by competing interactions with water, unlike Coulomb and vdW interactions. Therefore, even small errors can have profound consequences. The strong effects of small changes to torsional potentials have also been considered and addressed in parametrizations of the ϕ/ψ parameters of proteins, for example, in both the AMBER ff99SB[86] modifications of ff99 and the CMAP corrections to the CHARMM all22 force field.[87] It is also worth noting that the position of the energy minimum and the anti/high-anti criterion are not sufficient to fully characterize the anti minimum; the detailed shape and derivatives of the χ profile around the anti and high-anti regions are also probably very important for correctly describing nucleic acid structure, as also pointed out by Bosh et al.[41]

To conclude, the χ_{OL} parameters provide greater stabilization of the anti region than the ff99 force-field parameters. This is desirable as it helps to avoid the known tendency for ladder-like structures to form in RNA simulations. χ_{YIL} stabilizes the anti region even more than $\chi_{OL\text{-}DFT}$ and χ_{OL}. The χ_{YIL} parameters also stabilize the anti region, even more than $\chi_{OL\text{-}DFT}$ and χ_{OL} parameters, but probably excessively. Our tests (see also ref 46) suggest that the χ_{OL} parameters perform best for RNA structures.

Syn Region. The local minimum in the syn region, around $\chi \approx 70°$, is mainly associated with guanosine residues in Z-DNA but also occurs in the stems of antiparallel DNA quadruplexes. It is also often populated in RNA structures, UNCG hairpin tetraloops, for example,[46] and various other recurrent RNA motifs. Figure 6 clearly shows that use of the available torsion parameters leads to quite significant differences in the syn region and that these differences are not always systematic among different nucleosides. Let us first consider the position of the syn minima. Our best references are the QM/COSMO curves shown in Figure S1 in the Supporting Information. Compared to the QM reference, ff99 shifts the minimum to low angles, around 50°, while the other force fields mostly tend to shift it to higher angles, around 70−75°, that are more consistent with the QM data. As we have shown in reference simulations of the UUCG RNA tetraloop,[46] the imbalanced ff99 syn region destabilizes the tetraloop structure while the reparameterized χ torsions are apparently able to maintain the stable structure of the tetraloop over at least the ∼100+ ns time scale, with the χ force-field modifications in combination with the parmbsc0 α/γ correction providing the best performance in this respect. In fact, the advantages of the parmbsc0 modifications over ff99 for RNA simulations can only be fully appreciated after tuning the χ profile.

Regarding the energy of the syn minimum relative to that of the anti minimum, the χ_{YIL} and χ_{OL} parametrizations provide similar results, both of which agree fairly well with our QM data. The χ_{YIL} parametrization has been tested against syn/anti populations of C and U ribonucleosides as detected in NMR experiments and shows notable improvement compared to ff99, which tends to overstabilize syn conformation for C and U.[45] Because χ_{OL} parametrization is similar to χ_{YIL} in this respect, we can expect the same improvement for χ_{OL} as well. Note that our preliminary $\chi_{OL\text{-}DFT}$ version also exhibits certain tendency to overstabilize syn, mainly because ribonucleosides were not included in the $\chi_{OL\text{-}DFT}$ fitting.

Torsion Barriers. Figure 6 shows that various χ parametrizations differ considerably in the resulting torsion barrier heights, most obviously ff99 gives a reversed order of torsion barrier heights, relative to those in the QM profile. Since our best estimates for the torsion barrier heights are the latter, we suggest that ff99 gives qualitatively incorrect descriptions of the torsion energetics. The other parametrizations appear to be more accurate, but the spread of the torsion barriers is still quite wide. Compared to the QM data, χ_{YIL} and χ_{OL} seem to provide the best agreement.

MD Simulations of A-RNA Duplexes. Several A-RNA MD simulations were carried out to compare the available χ parametrizations: ff99, ff99χ_{YIL}, ff99$\chi_{OL\text{-}DFT}$, ff99χ_{OL}, and the corresponding χ combinations with bsc0. The χ_{ODE} parametrization was not included in this comparison as it accelerates formation of "ladder-like" structures and is thus not applicable to A-RNA.[46] The main conclusions are best illustrated by the bsc0-corrected simulations, since the bsc0 α/γ correction reduces the number of α/γ "γ-trans" flips and thus keeps the structures closer to X-ray reference structures.[37] We have also shown recently that the ff99bsc0 force field improves the behavior of RNA tetraloops relative to ff99.[46] Although the reduction of α/γ flipping in A-RNA simulations by bsc0 may be excessive, ff99 likely overpopulates the α/γ flips.[37] While the bsc0 modifications are currently essential for B-DNA simulations, their use is also starting to prevail over ff99 in RNA simulations.

We monitored mainly average values of the χ angle, sugar pucker (pseudorotation angle P according to Altona and Sundaralingam[88]), size of the major and minor grooves, and several base pair and interbase pair (base-pair step) parameters, considering them to be most relevant to A-RNA helix description. Only parameters that appeared to be sensitive to the χ angle are presented here, and the A-RNA results are summarized in Table 3 and Tables S2 and S3 in the Supporting Information. Standard deviations are shown to illustrate the distribution width.

Sensitivity of the A-RNA Structure to χ Potential. Table 3 and Tables S2 and S3 in the Supporting Information show that several structural characteristics of the A-RNA duplexes have substantial sensitivity to the shape of the χ torsion profile. Among the most sensitive parameters for A-RNA are the inclination, roll, major groove width, and propeller twist. Inclination and roll are key descriptors of the A-RNA shape and mathematically interrelated.[89,90] The magnitude of the impact of varying the χ parametrization on the structural parameters is rather unsettling; in several cases even very small changes in the χ profile, on the

Table 3. Average Structural Parameters (last 20 ns of 100 ns simulations) for the A-RNA Duplex 1QC0′ (r(GCACCGUUGG)) Obtained Using the ff99bsc0 Force Field with Various χ Corrections (values with ff99 force field in italics)[a]

parameter	X-ray	no χ correction	χ_{YIL}	$\chi_{OL\text{-}DFT}$	χ_{OL}
χ/deg	197.1 ± 4.4	203.1 ± 9.2	196.0	197.4	199.1
		209.4 ± 12.7	*194.0*	*196.3*	*196.7*
P/deg	17.7 ± 6.0	19.3 ± 13.5	15.4	19.2	17.4
		27.5 ± 16.9	*13.4*	*17.5*	*17.1*
minor groove width/Å	15.4 ± 0.1	15.3 ± 0.6	15.2	15.3	15.3
		15.0 ± 0.6	*14.9*	*15.1*	*14.8*
major groove width /Å	14.7 ± 1.5	15.9 ± 2.9	19.0	17.5	17.9
		18.9 ± 3.2	*22.1*	*19.8*	*22.3*
slide/Å	−1.70 ± 0.25	−1.69 ± 0.50	−2.07	−1.94	−1.90
		-1.89 ± 0.57	*-2.35*	*-2.11*	*-2.30*
roll/deg	8.1 ± 4.1	9.7 ± 6.1	4.6	7.1	6.7
		8.5 ± 6.2	*3.0*	*6.4*	*4.0*
propeller/deg	−12.5 ± 4.5	−13.7 ± 8.5	−6.3	−10.7	−9.7
		-12.5 ± 8.7	*-4.3*	*-9.8*	*-7.4*
X-displ./Å	−4.45 ± 1.18	−4.85 ± 1.60	−5.01	−5.07	−4.95
		-5.35 ± 2.18	*-5.50*	*-5.49*	*-5.91*
inclination/deg	15.2 ± 8.3	18.0 ± 11.0	8.8	13.4	12.7
		16.3 ± 11.7	*5.5*	*12.2*	*8.0*
helical twist/deg	32.3 ± 3.6	31.7 ± 4.1	29.7	30.5	30.4
		31.1 ± 4.9	*28.6*	*29.8*	*28.6*
rmsd/Å		1.04	1.21	1.06	1.07
		1.36	*1.85*	*1.43*	*1.90*

[a] Standard deviations are shown for the unmodified force fields for orientation, and they are very similar for the other force fields. RMSD is mass weighted for all atoms.

order of a fraction of a kcal/mol, significantly influence the simulated structure, as already noted in ref 41.

Basic Sampling of the A-RNA Conformational Space. One of the most important parameters characterizing A-RNA structure is the inclination of base pairs with respect to the A-RNA helix. In A-RNA the base pair planes are significantly inclined (typically by more than 10°) with respect to the helical axis, while in B-DNA the base pair planes are almost perpendicular to the helical axis and the inclination is close to zero. As we recently noted, the experimental values of A-RNA inclination in X-ray structures vary quite widely and do not depend on the sequence.[37,91] The average inclination value for the 1QC0′ X-ray structure is 15.2°. The ff99 and ff99bsc0 simulations give fairly similar values (18.0° and 16.3°, respectively). The χ_{YIL} parametrization, which quite strongly stabilizes the anti region, reduces the inclination to as low as 5.5° in combination with ff99 (the combination suggested by Yildirim et al.[45]) and to 8.8° when ff99bsc0 is used. This is a considerable deviation from the experimental reference. The new χ_{OL} parametrization gives values of 8.0° with ff99 and 12.7° with ff99bsc0, which represents a noticeable but still acceptable reduction of inclination, the ff99bsc0χ_{OL} combination being superior in this respect. Since the $\chi_{OL\text{-}DFT}$ parametrization consistently gives values that are quite similar to those obtained using χ_{OL}, only the latter is discussed in the following text. As noted above, the base pair parameter roll is mathematically related to inclination; thus, the roll trend mirrors that of inclination; the experimental value is 8.1°, while ff99bsc0, ff99, ff99bsc0χ_{OL}, and ff99χ_{YIL} give values of 9.7°, 8.5°, 6.7°, and 4.6°, respectively.

Another A-RNA parameter that is quite sensitive to χ parametrization is the major groove width. Major groove width varies considerably in experimental X-ray structures (it ranges from 8 to 20 Å) and seems to depend not only on the sequence but also on the crystallization conditions, as discussed in detail in refs 37 and 91. Even larger variations have been observed in published NMR studies, but these are mainly due to inaccuracies in the NMR structural refinement protocols; recent work has shown that application of the highest quality NMR methods leads to very good agreement between X-ray and NMR geometries of both A-RNA[92] and B-DNA.[93] Despite the uncertainty in target values for the major groove width it seems that it is usually overestimated by simulations. There is a marked difference in this respect between the ff99 and the ff99bsc0 force fields, primarily due to a 10−20% population of short-lived γ-trans substates with ff99, which reduce inclination and widen the major groove of A-RNA.[37] For 1QC0′ the X-ray determined major groove width is 14.7 Å, while we obtained values of 15.9, 18.9, 17.9, and 22.1 Å in simulations using ff99bsc0, ff99, ff99bsc0χ_{OL}, and ff99χ_{YIL}, respectively. Clearly, the ff99χ_{YIL} value is not only significantly larger than in the starting X-ray structure but also outside the experimentally observed ranges, while the ff99bsc0χ_{OL} values are closer to the reference.

The general trends are also well illustrated by the results obtained for the AU-rich 1RNA structure (Table S3 in Supporting Information). For inclination, the experimental value is 18.8°, while ff99bsc0, ff99, ff99bsc0χ_{OL}, and ff99χ_{YIL} give values of 25.8°, 21.4°, 19.4°, and 10.3°, respectively. In this case, the ff99bsc0χ_{OL} value is closest to the experimental data. The ff99χ_{YIL} inclination is again likely too low. The inclination trend is mirrored by roll values: experimental value is 9.96°, while ff99bsc0, ff99, ff99bsc0χ_{OL}, and ff99χ_{YIL} values are 14.1°, 12.1°,

Table 4. Average Structural Parameters (last 20 ns of 50 ns simulations) for the B-DNA Duplex 1BNA[a]

parameter	X-ray	ff99bsc0	ff99bsc0 χ_{YIL}	ff99bsc0 χ_{ODE}	ff99bsc0 $\chi_{OL\text{-}DFT}$	ff99bsc0 χ_{OL}
χ/deg	243.6 ± 14.7	243.3 ± 18.2	223.1	244.4	229.1	231.4
P/deg	129.2 ± 26.7	130.4 ± 31.6	105.1	133.5	118.4	115.6
minor groove width /Å	10.3 ± 1.0	11.5 ± 1.1	12.6	11.4	11.7	12.3
major groove width /Å	17.3 ± 0.7	19.1 ± 1.9	21.5	18.7	20.5	20.2
slide/Å	0.07 ± 0.53	−0.41 ± 0.58	−1.20	−0.36	−0.90	−0.83
roll/deg	1.98 ± 3.41	3.64 ± 5.22	2.76	3.53	3.03	4.24
propeller/deg	−13.3 ± 5.94	−12.5 ± 7.9	−8.5	−11.5	−11.1	−11.0
X-displ./Å	−0.23 ± 0.53	−1.65 ± 1.73	−2.82	−1.44	−2.19	−2.33
inclination/deg	4.0 ± 7.2	7.8 ± 10.3	5.4	6.9	5.7	8.0
helical twist/deg	35.6 ± 5.2	33.5 ± 5.7	31.5	34.2	33.0	32.6
rmsd/Å		1.58	2.52	1.46	1.95	2.15

[a] Standard deviations are only shown for the ff99bsc0 force fields because they are very similar for the other force fields. RMSD is mass weighted for all atoms.

11.1°, and 5.7°, respectively. The experimental value for major groove width is 12.3 Å, while ff99bsc0, ff99, ff99bsc0χ_{OL}, and ff99χ_{YIL} give 15.3, 17.1, 14.8, and 18.1 Å, respectively.

The trends in the structural parameters described above indicate that when the χ parameters are modified in a manner that prevents the ladder-like degradation of RNA structure associated with the original (ff99 or ff99bsc0) χ profile, A-RNA inclination and base pair roll are systematically reduced while the major groove width expands. Note that inclination, roll, and narrowing of the major groove characterize how deeply the duplex enters A-RNA conformational territory. In other words, stabilization of the anti χ region seems to counter the tendency of the simulated molecule to adopt highly compact A-RNA geometries (see Tables 3 and Tables S2 and S3 in the Supporting Information). For the sake of completeness, let us add that the anti stabilization also reduces the absolute value of propeller twist; the experimental value for this variable of 1QC0′ is −12.5°, and we obtained values of −13.7°, −12.5°, −9.7°, and just −4.3° using ff99bsc0, ff99, ff99bsc0χ_{OL}, and ff99χ_{YIL}, respectively.

Another important structural parameter is helical twist. The data presented in Table 3 and Tables S2 and S3 in the Supporting Information show that the force fields provide values for this parameter that are reasonably close to the experimental value. However, ff99bsc0 simulations usually show larger helical twists than ff99-based simulations, as the ff99 γ-trans flips, especially those with longer lifetimes, tend to reduce helical twist.[30] Note that the helical twist in RNA molecules is not as crucial as when describing the fine structure of B-DNA.

In conclusion, when suppression of the ladder-like structures formation is of primary concern, we suggest that ff99bsc0χ_{OL} is the best combination of parameters currently available for A-RNA. Its use eliminates emergence of the ladder-like structures but still allows A-RNA to adopt significant inclination, roll, and propeller twist. (The preliminary ff99bsc0$\chi_{OL\text{-}DFT}$ version provides similar results for A-RNA but overstabilizes the syn region.)

MD Simulation of B-DNA. Table 4 compares structural parameters obtained from X-ray analysis of a B-DNA dodecamer (1BNA) and simulations using the four χ parametrizations considered above in the discussion of parametrization effects on A-RNA simulations (ff99bsc0, ff99, ff99bsc0χ_{OL}, and ff99χ_{YIL}) and the parameters of Ode et al.[44] Clearly, the three new χ variants are in many respects worse than the original ff99bsc0 force field for modeling B-DNA. They reduce helical twist, which is underestimated even with ff99bsc0. Underestimation of helical twist is a notorious problem in B-DNA simulations. Another problem appears in coupling of the χ torsion with the sugar pucker. The new χ parametrizations seem to "push" the sugar pucker pseudorotation value (136° in X-ray structures) more to the east: while with ff99bsc0 the average pucker is 130°, it drops to 116° with ff99bsc0 χ_{OL} and even to 106° with χ_{YIL}. As can be seen in Table 4, these changes are reflected by shifts in other structural parameters, mostly away from the X-ray and ff99bsc0 values. The groove sizes, slide, and X-displacement increase, while propeller and helical twist slightly decrease. Both χ_{OL} and $\chi_{OL\text{-}DFT}$ parametrizations seem to provide structures that are closer, overall, to the X-ray structure than the χ_{YIL} parametrization, which also shows the largest rms error. This again indicates that χ_{YIL} overestimates the high-anti penalty, which disturbs the balance with the other force-field parameters somewhat.

In conclusion, χ_{OL} does not improve upon the original ff99bsc0 force field for the B-DNA duplex. The same holds also for $\chi_{OL\text{-}DFT}$, which was parametrized based on DNA nucleosides. We would like to reiterate that the χ angle and sugar pucker are fine tuned to complement each other in ff99bsc0 and ff99, and suitable adjustment of the sugar pucker torsions may also be beneficial for B-DNA description with the new χ parameters presented herein. This, however, is beyond the scope of this study. Our groups have attempted several times in the past to improve modeling of the helical twist of B-DNA in various ways, including pucker modification, but no convincing solution has been found to date.

CONCLUSIONS

The χ torsion angle is a challenging parameter to accurately model in the various empirical force fields for nucleic acids. Many variants of χ parametrization have been suggested in recent few years, but none of them seems to provide a fully satisfactory description. Here, we investigated whether reliable force-field parameters can be obtained based on accurate QM calculations. We studied the influence of both the level of theory on the χ profile and the applied methodology (the effects of geometry relaxation and solvation). We suggest that when deriving the torsion parameters the following three points should be considered.

(i) Using the same (usually QM-optimized) geometry for deriving the torsion parameters as differences between the QM and MM χ energies may introduce significant errors in the resulting profiles. Instead, geometry for the MM

single-point calculations should be optimized at the MM level.

(ii) Solvation-related effects considerably influence the resulting χ torsion profile. For instance, their inclusion results in stabilization of the anti region typical for A-RNA with respect to the high-anti region typical for B-DNA. It appears that appropriate balance of the anti and high-anti structures in RNA systems can only be obtained when the solvation effects are considered.

(iii) The χ torsion profile is quite sensitive to the level of theory. On the basis of comparisons with estimated reference CCSD(T)/CBS data, we suggest that the MP2/CBS method provides results of sufficient accuracy in this case, while using small basis sets such as 6-31G* with the MP2 method introduces significant errors. The PBE DFT functional does not provide sufficiently accurate results, even when a large (6-311++G(3df,3pd)) basis set is used and a dispersion correction (D-1.06-23) is applied. Results obtained with M06 and M06-2X functionals of Zhao and Truhlar are of similar quality to the PBE-D-1.06-23/LP results and also insufficiently accurate for force-field derivation. Thus, it appears that despite the impressive recent progress in DFT methodology, DFT-based calculations cannot currently match the accuracy of high-quality wave function theory calculations for modeling DNA and RNA backbone segments.

Using our parametrization model we derived new parameters for the glycosidic torsion angle, χ_{OL} ("OL" stands for the city of Olomouc in the Czech Republic), intended for use in RNA simulations. Our main goal was to correct the undesirable destabilization of the anti region with respect to the high-anti region observed with the ff99 and ff99-parmbsc0 force fields, which leads to formation of "ladder-like" structures in MD simulations of RNA molecules. The χ_{OL} parameters successfully achieve this goal.[46,84]

The ability of the χ_{OL} parameters to suppress formation of the ladder-like structures has been verified in refs 46 and 84. In these works we carried out a broad set of extended RNA simulations of UNCG and GNRA tetraloops, short A-RNA stems, and a reverse kink-turn motif with a total length of more than 15 μs. It has been shown that while use of the original ff99 and ff99bsc0 force fields leads to frequent formation of the ladder-like structures, the ff99bsc0χ_{OL} potential suppresses their emergence and keeps simulations closer to the native conformations.

In addition, in a study of UUCG tetraloop[46] we have shown that the χ_{OL} modification in connection with the ff99bsc0 force field leads to stabilization of some signature interactions present in the X-ray and NMR structures of this tetraloop. This improvement is most likely due to improved description of the syn region of χ potential, which is of key importance in this structure.

In this work we show that the χ_{OL} adjustment modestly affects helical parameters of A-RNA duplexes; nevertheless, the simulations remain in good agreement with X-ray structures. We also demonstrate that overstabilization of the anti χ region leads to excessive reductions of inclination, roll, and propeller twist in A-RNA and substantially impairs the performance of B-DNA simulations. This problem appears to occur with another recent parameter set, ff99χ_{YIL}.

We do not recommend use of the reparameterized force field for B-DNA, as adjusting the anti−high-anti balance to stabilize RNA somewhat impairs description of B-DNA. Despite substantial efforts, we have not as yet found any means, based solely on modifying the χ torsion, to stabilize A-RNA simulations while not adversely affecting B-DNA simulations. However, the χ_{OL} refinement might be useful in simulations of DNA molecules containing syn nucleotides.

Although the χ_{OL} torsion refinement can be combined with both ff99 and ff99bsc0 force-field variants, in all cases our simulations indicate that it provides better results when combined with ff99bsc0. Nevertheless, the parmbsc0 α/γ and χ_{OL} modifications are entirely independent refinements of the Cornell et al. force-field torsion space.

In summary, we recommend use of the χ_{OL} force field for RNA simulations, preferably in combination with the ff99bsc0 α/γ refinement. The main advantage of the new force field is that it eliminates formation of ladder-like structures, spurious artifacts generated by older versions of the force field. Since elimination of the ladder-like structures is a basic requirement for stabilizing RNA in simulations, the χ_{OL} parameters probably provide better RNA descriptions than other currently available parameter sets. The χ_{OL} + ff99bsc0 force field gives satisfactory descriptions of A-RNA duplexes and improves simulations of some other RNA systems, such as UNCG and GNRA tetraloops. We would like to note that although the χ_{OL} + ff99bsc0 force-field refinement brings a substantial improvement of extended RNA simulations, further reparameterizations still may be necessary.

■ ASSOCIATED CONTENT

Supporting Information. Torsion profiles of the studied ribo- and deoxyribonucleosides in vacuo and in COSMO and PB solvent models, $\chi_{OL\text{-}DFT}$ torsion parameters, and tables of structural parameters for 1RNA and 2R20′ structures. This material is available free of charge via the Internet at http://pubs.acs.org.

■ AUTHOR INFORMATION

Corresponding Author
*E-mail: petr.jurecka@upol.cz.

■ ACKNOWLEDGMENT

The authors thank F. Javier Luque for valuable discussions and suggestions regarding the continuum solvation models. This work was supported by the Academy of Sciences of the Czech Republic (grants nos. AV0Z50040507 (J.S.), AV0Z50040702 (J.S.), and GACR 203/09/1476 and P208/11/1822 (J.S.)), the Grant Agency of the Academy of Sciences of the Czech Republic (grants no. P208/10/1742 (P.J.), P301/11/P558 (P.B.), and IAA400040802 (J.S., M.O.)), the Ministry of Education of the Czech Republic (grant 203/09/H046 (P.J., M.O., J.S., and M.Z.)), the NIH R01-GM59306890 (TEC3), and NSF MCA01S027 (TEC3), Student Project PrF_2011_020 of Palacky University, Operational Program Research and Development for Innovations-European Regional Development Fund (projects CZ.1.05/2.1.00/03.0058 and CZ.1.07/2.3.00/20.0017 of the Ministry of Education, Youth and Sports of the Czech Republic), and the HPC-EUROPA2 project (project no. 228398) with the support of the European Community-Research Infrastructure Action of the FP7.

■ REFERENCES

(1) Weiner, S. J.; Kollman, P. A.; Case, D. A.; Singh, U. C.; Ghio, C.; Alagona, G.; Profeta, S.; Weiner, P. *J. Am. Chem. Soc.* **1984**, *106* (3), 765–784.

(2) Weiner, S. J.; Kollman, P. A.; Nguyen, D. T.; Case, D. A. *J. Comput. Chem.* **1986**, *7* (2), 230–252.
(3) Mackerell, A. D. *J. Comput. Chem.* **2004**, *25* (13), 1584–1604.
(4) Orozco, M.; Noy, A.; Perez, A. *Curr. Opin. Struct. Biol.* **2008**, *18* (2), 185–193.
(5) Fulle, S.; Gohlke, H. *J. Mol. Recognit.* **2010**, *23* (2), 220–231.
(6) MacKerell, A. D. *J. Phys. Chem. B* **2009**, *113* (10), 3235–3244.
(7) Foloppe, N.; Hartmann, B.; Nilsson, L.; MacKerell, A. D. *Biophys. J.* **2002**, *82* (3), 1554–1569.
(8) Cornell, W. D.; Cieplak, P.; Bayly, C. I.; Gould, I. R.; Merz, K. M.; Ferguson, D. M.; Spellmeyer, D. C.; Fox, T.; Caldwell, J. W.; Kollman, P. A. *J. Am. Chem. Soc.* **1995**, *117* (19), 5179–5197.
(9) Mackerell, A. D.; Wiorkiewiczkuczera, J.; Karplus, M. *J. Am. Chem. Soc.* **1995**, *117* (48), 11946–11975.
(10) Cheatham, T. E.; Kollman, P. A. *J. Mol. Biol.* **1996**, *259* (3), 434–444.
(11) Yang, L. Q.; Pettitt, B. M. *J. Phys. Chem.* **1996**, *100* (7), 2564–2566.
(12) Cheatham, T. E.; Kollman, P. A. *Structure* **1997**, *5* (10), 1297–1311.
(13) Cheatham, T. E.; Crowley, M. F.; Fox, T.; Kollman, P. A. *Proc. Natl. Acad. Sci. U.S.A.* **1997**, *94* (18), 9626–9630.
(14) Langley, D. R. *J. Biomol. Struct. Dyn.* **1998**, *16* (3), 487–509.
(15) MacKerell, A. D. In *Molecular Modeling of Nucleic Acids*; Leontis, N. B., SantaLucia, J., Eds.; American Chemical Society: Washington, DC, 1998; Vol. 682, p 304−311.
(16) Foloppe, N.; MacKerell, A. D. *J. Phys. Chem. B* **1998**, *102* (34), 6669–6678.
(17) Cheatham, T. E.; Cieplak, P.; Kollman, P. A. *J. Biomol. Struct. Dyn.* **1999**, *16* (4), 845–862.
(18) MacKerell, A. D.; Banavali, N. K. *J. Comput. Chem.* **2000**, *21* (2), 105–120.
(19) Foloppe, N.; MacKerell, A. D. *J. Comput. Chem.* **2000**, *21* (2), 86–104.
(20) Wang, J. M.; Cieplak, P.; Kollman, P. A. *J. Comput. Chem.* **2000**, *21* (12), 1049–1074.
(21) Cheatham, T. E.; Young, M. A. *Biopolymers* **2000**, *56* (4), 232–256.
(22) Varnai, P.; Djuranovic, D.; Lavery, R.; Hartmann, B. *Nucleic Acids Res.* **2002**, *30* (24), 5398–5406.
(23) Dixit, S. B.; Beveridge, D. L.; Case, D. A.; Cheatham, T. E.; Giudice, E.; Lankas, F.; Lavery, R.; Maddocks, J. H.; Osman, R.; Sklenar, H.; Thayer, K. M.; Varnai, P. *Biophys. J.* **2005**, *89* (6), 3721–3740.
(24) Perez, A.; Marchan, I.; Svozil, D.; Sponer, J.; Cheatham, T. E.; Laughton, C. A.; Orozco, M. *Biophys. J.* **2007**, *92* (11), 3817–3829.
(25) Svozil, D.; Sponer, J. E.; Marchan, I.; Perez, A.; Cheatham, T. E.; Forti, F.; Luque, F. J.; Orozco, M.; Sponer, J. *J. Phys. Chem. B* **2008**, *112* (27), 8188–8197.
(26) Perez, A.; Luque, F. J.; Orozco, M. *J. Am. Chem. Soc.* **2007**, *129* (47), 14739–14745.
(27) Lavery, R.; Zakrzewska, K.; Beveridge, D.; Bishop, T. C.; Case, D. A.; Cheatham, T.; Dixit, S.; Jayaram, B.; Lankas, F.; Laughton, C.; Maddocks, J. H.; Michon, A.; Osman, R.; Orozco, M.; Perez, A.; Singh, T.; Spackova, N.; Sponer, J. *Nucleic Acids Res.* **2010**, *38* (1), 299–313.
(28) Lankas, F.; Spackova, N.; Moakher, M.; Enkhbayar, P.; Sponer, J. *Nucleic Acids Res.* **2010**, *38* (10), 3414–3422.
(29) Fadrna, E.; Spackova, N.; Sarzynska, J.; Koca, J.; Orozco, M.; Cheatham, T. E.; Kulinski, T.; Sponer, J. *J. Chem. Theory Comput.* **2009**, *5* (9), 2514–2530.
(30) Reblova, K.; Lankas, F.; Razga, F.; Krasovska, M. V.; Koca, J.; Sponer, J. *Biopolymers* **2006**, *82* (5), 504–520.
(31) Blount, K. F.; Breaker, R. R. *Nat. Biotechnol.* **2006**, *24* (12), 1558–1564.
(32) Strobel, S. A.; Cochrane, J. C. *Curr. Opin. Chem. Biol.* **2007**, *11* (6), 636–643.
(33) Montange, R. K.; Batey, R. T. *Annu. Rev. Biophys.* **2008**, *37*, 117–133.
(34) Steitz, T. A. *Nat. Rev. Mol. Cell Biol.* **2008**, *9* (3), 242–253.
(35) Paulsen, R. B.; Seth, P. P.; Swayze, E. E.; Griffey, R. H.; Skalicky, J. J.; Cheatham, T. E., 3rd; Davis, D. R. *Proc. Natl. Acad. Sci. U.S.A.* **2010**, *107* (16), 7263–7268.
(36) Reddy, S. Y.; Leclerc, F.; Karplus, M. *Biophys. J.* **2003**, *84* (3), 1421–1449.
(37) Besseova, I.; Otyepka, M.; Reblova, K.; Sponer, J. *Phys. Chem. Chem. Phys.* **2009**, *11* (45), 10701–10711.
(38) Deng, N. J.; Cieplak, P. *Biophys. J.* **2010**, *98* (4), 627–636.
(39) Ricci, C. G.; de Andrade, A. S. C.; Mottin, M.; Netz, P. A. *J. Phys. Chem. B* **2010**, *114* (30), 9882–9893.
(40) Auffinger, P.; Westhof, E. *Curr. Opin. Struct. Biol.* **1998**, *8* (2), 227–236.
(41) Bosch, D.; Foloppe, N.; Pastor, N.; Pardo, L.; Campillo, M. *J. Mol. Struc.: THEOCHEM* **2001**, *537*, 283–305.
(42) Foloppe, N.; MacKerell, A. D. *J. Phys. Chem. B* **1999**, *103* (49), 10955–10964.
(43) Mlynsky, V.; Banas, P.; Hollas, D.; Reblova, K.; Walter, N. G.; Sponer, J.; Otyepka, M. *J. Phys. Chem. B* **2010**, *114* (19), 6642–6652.
(44) Ode, H.; Matsuo, Y.; Neya, S.; Hoshino, T. *J. Comput. Chem.* **2008**, *29* (15), 2531–2542.
(45) Yildirim, I.; Stern, H. A.; Kennedy, S. D.; Tubbs, J. D.; Turner, D. H. *J. Chem. Theory Comput.* **2010**, *6* (5), 1520–1531.
(46) Banáš, P.; Hollas, D.; Zgarbova, M.; Jurecka, P.; Orozco, M.; Cheatham, T.; Sponer, J.; Otyepka, M. *J. Chem. Theory Comput.* **2010**, *6* (12), 3836–3849.
(47) Fadrna, E.; Spackova, N.; Stefl, R.; Koca, J.; Cheatham, T. E.; Sponer, J. *Biophys. J.* **2004**, *87* (1), 227–242.
(48) Reblova, K.; Fadrna, E.; Sarzynska, J.; Kulinski, T.; Kulhanek, P.; Ennifar, E.; Koca, J.; Sponer, J. *Biophys. J.* **2007**, *93* (11), 3932–3949.
(49) Faustino, I.; Perez, A.; Orozco, M. *Biophys. J.* **2010**, *99* (6), 1876–1885.
(50) Foloppe, N.; MacKerell, A. D. *Biophys. J.* **1999**, *76* (6), 3206–3218.
(51) Jurecka, P.; Hobza, P. *J. Am. Chem. Soc.* **2003**, *125* (50), 15608–15613.
(52) Mladek, A.; Sponer, J. E.; Jurecka, P.; Banas, P.; Otyepka, M.; Svozil, D.; Sponer, J. *J. Chem. Theory Comput.* **2010**, *6* (12), 3817–3835.
(53) Halkier, A.; Helgaker, T.; Jorgensen, P.; Klopper, W.; Koch, H.; Olsen, J.; Wilson, A. K. *Chem. Phys. Lett.* **1998**, *286* (3−4), 243–252.
(54) Halkier, A.; Helgaker, T.; Jorgensen, P.; Klopper, W.; Olsen, J. *Chem. Phys. Lett.* **1999**, *302* (5−6), 437–446.
(55) Ahlrichs, R.; Bar, M.; Haser, M.; Horn, H.; Kolmel, C. *Chem. Phys. Lett.* **1989**, *162* (3), 165–169.
(56) Weigend, F.; Häser, M. *Theor. Chem. Acc.* **1997**, *97* (1−4), 331–340.
(57) Werner, H. J.; Knowles, P. J.; Lindh, R.; Manby, F. R.; Schütz, M.; Celani, P.; Korona, T.; Rauhut, G.; Amos, R. D.; Bernhardsson, A.; Berning, A.; Cooper, D. L.; Deegan, M. J. O.; Dobbyn, A. J.; Eckert, F.; Hampel, C.; Hetzer, G.; Lloyd, A. W.; McNicholas, S. J.; Meyer, W.; Mura, M. E.; Nicklass, A.; Palmieri, P.; Pitzer, R.; Schumann, U.; Stoll, H.; Stone, A. J.; Tarroni, R.; Thorsteinsson, T. *Molpro Version 2006.1, a package of ab initio programs*; 2006; http://www.molpro.net (accessed July 2011).
(58) Krishnan, R.; Binkley, J. S.; Seeger, R.; Pople, J. A. *J. Chem. Phys.* **1980**, *72* (1), 650–654.
(59) Clark, T.; Chandrasekhar, J.; Spitznagel, G. W.; Schleyer, P. V. *J. Comput. Chem.* **1983**, *4* (3), 294–301.
(60) Gill, P. M. W.; Johnson, B. G.; Pople, J. A. *J. Chem. Phys.* **1992**, *96* (9), 7178–7179.
(61) Frisch, M. J.; Pople, J. A.; Binkley, J. S. *J. Chem. Phys.* **1984**, *80* (7), 3265–3269.
(62) Jurecka, P.; Cerny, J.; Hobza, P.; Salahub, D. R. *J. Comput. Chem.* **2007**, *28* (2), 555–569.
(63) Schafer, A.; Huber, C.; Ahlrichs, R. *J. Chem. Phys.* **1994**, *100* (8), 5829–5835.
(64) Klamt, A.; Schuurmann, G. *J. Chem. Soc., Perkin Trans. 2* **1993**, No. 5, 799–805.
(65) Frisch, M. J.; Trucks, G. W.; Schlegel, H. B.; Scuseria, G. E.; Robb, M. A.; Cheeseman, J. R.; Montgomery, J.A.; Vreven, T.; Kudin, K. N.; Burant,

J. C.; Millam, J. M.; Iyengar, S. S.; Tomasi, J.; Barone, V.; Mennucci, B.; Cossi, M.; Scalmani, G.; Rega, N.; Petersson, G. A.; Nakatsuji, H.; Hada, M.; Ehara, M.; Toyota, K.; Fukuda, R.; Hasegawa, J.; Ishida, M.; Nakajima, T.; Honda, Y.; Kitao, O.; Nakai, H.; Klene, M.; Li, X.; Knox, J. E.; Hratchian, H. P.; Cross, J. B.; Bakken, V.; Adamo, C.; Jaramillo, J.; Gomperts, R.; Stratmann, R. E.; Yazyev, O.; Austin, A. J.; Cammi, R.; Pomelli, C.; Ochterski, J. W.; Ayala, P. Y.; Morokuma, K.; Voth, G. A.; Salvador, P.; Dannenberg, J. J.; Zakrzewski, V. G.; Dapprich, S.; Daniels, A. D.; Strain, M. C.; Farkas, O.; Malick, D. K.; Rabuck, A. D.; Raghavachari, K.; Foresman, J. B.; Ortiz, J. V.; Cui, Q.; Baboul, A. G.; Clifford, S.; Cioslowski, J.; Stefanov, B. B.; Liu, G.; Liashenko, A.; Piskorz, P.; Komaromi, I.; Martin, R. L.; Fox, D. J.; Keith, T.; Al-Laham, M. A.; Peng, C. Y.; Nanayakkara, A.; Challacombe, M.; Gill, P. M. W.; Johnson, B.; Chen, W.; Wong, M. W.; Gonzalez, C.; Pople, J. A. *Gaussian 03*, revision D.02; Gaussian, Inc.: Wallingford, CT, 2004.

(66) Case, D. A.; Cheatham, T. E.; Darden, T.; Gohlke, H.; Luo, R.; Merz, K. M.; Onufriev, A.; Simmerling, C.; Wang, B.; Woods, R. J. *J. Comput. Chem.* **2005**, *26* (16), 1668–1688.

(67) Lu, Q.; Luo, R. *J. Chem. Phys.* **2003**, *119* (21), 11035–11047.

(68) Luo, R.; David, L.; Gilson, M. K. *J. Comput. Chem.* **2002**, *23* (13), 1244–1253.

(69) Guvench, O.; MacKerell, A. D., Jr. *J. Mol. Model.* **2008**, *14* (8), 667–679.

(70) Duan, Y.; Wu, C.; Chowdhury, S.; Lee, M. C.; Xiong, G. M.; Zhang, W.; Yang, R.; Cieplak, P.; Luo, R.; Lee, T.; Caldwell, J.; Wang, J. M.; Kollman, P. *J. Comput. Chem.* **2003**, *24* (16), 1999–2012.

(71) Dockbregeon, A. C.; Chevrier, B.; Podjarny, A.; Johnson, J.; Debear, J. S.; Gough, G. R.; Gilham, P. T.; Moras, D. *J. Mol. Biol.* **1989**, *209* (3), 459–474.

(72) Drew, H. R.; Wing, R. M.; Takano, T.; Broka, C.; Tanaka, S.; Itakura, K.; Dickerson, R. E. *Proc. Natl. Acad. Sci.: Biol.* **1981**, *78* (4), 2179–2183.

(73) Timsit, Y.; Bombard, S. *RNA* **2007**, *13* (12), 2098–2107.

(74) Klosterman, P. S.; Shah, S. A.; Steitz, T. A. *Biochemistry* **1999**, *38* (45), 14784–14792.

(75) Aqvist, J. *J. Phys. Chem.* **1990**, *94* (21), 8021–8024.

(76) Jorgensen, W. L.; Chandrasekhar, J.; Madura, J. D.; Impey, R. W.; Klein, M. L. *J. Chem. Phys.* **1983**, *79* (2), 926–935.

(77) Lu, X. J.; Olson, W. K. *Nucleic Acids Res.* **2003**, *31* (17), 5108–5121.

(78) Holroyd, L. F.; van Mourik, T. *Chem. Phys. Lett.* **2007**, *442* (1−3), 42–46.

(79) Valdes, H.; Klusak, V.; Pitonak, M.; Exner, O.; Stary, I.; Hobza, P.; Rulisek, L. *J. Comput. Chem.* **2008**, *29* (6), 861–870.

(80) Jensen, F. *J. Chem. Theory Comput.* **2010**, *6* (1), 100–106.

(81) Zhao, Y.; Truhlar, D. G. *Theor. Chem. Acc.* **2008**, *120* (1−3), 215–241.

(82) Zgarbova, M.; Otyepka, M.; Sponer, J.; Hobza, P.; Jurecka, P. *Phys. Chem. Chem. Phys.* **2010**, *12*, 10476−10493.

(83) Neidle, S. In *Nucleic Acid Structure and Recognition;* Oxford University Press Inc.: Oxford, 2002.

(84) Sklenovsky, P.; Florova, P.; Banas, P.; Reblova, K.; Lankas, F.; Otyepka, M.; Sponer, J. *J. Chem. Theory Comput.* accepted for publication.

(85) Merz, K. M. *J. Chem. Theory Comput.* **2010**, *6* (4), 1018–1027.

(86) Simmerling, C.; Strockbine, B.; Roitberg, A. E. *J. Am. Chem. Soc.* **2002**, *124* (38), 11258–11259.

(87) Feig, M.; Pettitt, B. M. *Biophys. J.* **1998**, *75* (1), 134–149.

(88) Altona, C.; Sundaralingam, M. *J. Am. Chem. Soc.* **1972**, *94* (23), 8205–8212.

(89) Sponer, J.; Kypr, J. *J. Mol. Biol.* **1991**, *221* (3), 761–764.

(90) Bhattacharyya, D.; Bansal, M. *J. Biomol. Struct. Dyn.* **1989**, *6* (4), 635–653.

(91) Besseova, I.; Reblova, K.; Leontis, N. B.; Sponer, J. *Nucleic Acids Res.* **2010**, *38* (18), 6247–6264.

(92) Tolbert, B. S.; Miyazaki, Y.; Barton, S.; Kinde, B.; Starck, P.; Singh, R.; Bax, A.; Case, D. A.; Summers, M. F. *J. Biomol. NMR* **2010**, *47* (3), 205–219.

(93) Tjandra, N.; Bax, A. *Science* **1997**, *278* (5344), 1697–1697.

JCTC Journal of Chemical Theory and Computation

ARTICLE

pubs.acs.org/JCTC

Quantum Corrections to Classical Molecular Dynamics Simulations of Water and Ice

Qaiser Waheed* and Olle Edholm*

Department of Theoretical Physics, Royal Institute of Technology (KTH), AlbaNova University Center, SE-106 91 Stockholm, Sweden

ABSTRACT: Classical simulations of simple water models reproduce many properties of the liquid and ice but overestimate the heat capacity by about 65% at ordinary temperatures and much more for low temperature ice. This is due to the fact that the atomic vibrations are quantum mechanical. The application of harmonic quantum corrections to the molecular motion results in good heat capacities for the liquid and for ice at low temperatures but a successively growing positive deviation from experimental results for ice above 200 K that reaches 15% just below melting. We suggest that this deviation is due to the lack of quantum corrections to the anharmonic motions. For the liquid, the anharmonicities are even larger but also softer and thus in less need of quantum correction. Therefore, harmonic quantum corrections to the classically calculated liquid heat capacities result in agreement with the experimental values. The classical model underestimates the heat of melting by 15%, while the application of quantum corrections produces fair agreement. On the other hand, the heat of vaporization is overestimated by 10% in the harmonically corrected classical model.

1. INTRODUCTION

Structural and thermodynamic properties of water have been extensively studied with classical molecular dynamics simulations using three site models like the simple point charge (SPC) model,[1] the slightly modified SPC/E model,[2] or the TIP3P[3] model. In general, these models describe many equilibrium properties of the liquid as well as or better than models involving more than three interaction sites. There is a remarkable exception; slight reparametrizations of the classical four-site model (TIP4P[3]) have produced a couple of models, TIP4P/2005[4] and TIP4PQ/2005,[5] which reproduce ice and liquid properties including many temperature dependencies much better than the three-site models. Even, compared to much more time-consuming computer simulation methods, like Car−Parrinello molecular dynamics[6] (CPMD), which calculates the forces on the atoms directly from electron structure calculations performed at each time step, these classical models behave quite well.

There is, however, one important exception. None of these models (including the CPMD one) give reasonable heat capacities. In their original versions, the classical models have fixed bond lengths and bond angles. These degrees of freedom can be made flexible, but this will not improve results but rather make them worse since the bond length and angle potentials are stiff enough to make a quantum mechanical treatment necessary. Further, the vibration of the entire molecules in ice as well as liquid water is also quantum mechanical. Therefore, a simple classical model or even one that treats the electrons but not the nuclei by quantum mechanics is insufficient for this purpose. There is one simple way around this problem that was suggested and tried out successfully on liquid water by Berens et al.[7] in 1983. If one assumes that the vibrational motion is harmonic, one may calculate a correction to the classical heat capacity from the difference between that of a quantum and that of a classical oscillator. One, just has to integrate over all frequencies with the weight taken from the normal mode spectrum. For liquid water, this reduces the difference compared to experiment from 45% to 4%.[7] These kinds of methods are not limited to water but may be applied to much more complex systems. They have, however, since then only been applied to a few other systems. Liquid methanol[8] and solid argon[9] are two examples.

An alternative technique, path integral molecular dynamics/Monte Carlo (PIMD/PIMC), should in principle be able to produce correct heat capacities since it handles the nuclei quantum mechanically and avoids the harmonic approximation. The sparse results[5,10−13] are promising, despite some differences and that some fine-tuning of the potential parameters with respect to their classical values seems to be required.

Here, we have applied the original harmonic correction method to ordinary ice (I_h) using the SPC/E model. In this case, quantum effects are even larger than in liquid water. Bond lengths and the bond angle have been fixed as in the original SPC/E model since these degrees of freedom are rigid enough to give negligible contributions to the heat capacity. The energy fluctuations were used to calculate the classical heat capacities (see, e.g., a textbook like Allen and Tildesly[14]), while the normal mode density was calculated from the velocity autocorrelation functions.

2. THEORY

The heat capacity at constant volume, C_V, of a classical system can be calculated from the fluctuations in energy, σ_E, in a simulation at conserved volume, temperature, and particle number (NVT) as

$$C_V = \sigma_E^2/k_B T^2 \quad (1)$$

Received: May 2, 2011
Published: August 03, 2011

with k_B being the Boltzmann constant and T the absolute temperature. Alternatively, it may be obtained as a numerical derivative of the total energy with respect to the temperature. The heat capacity at constant pressure, C_p, can be obtained from the enthalpy fluctuations, σ_H, in a simulation at fixed pressure (NpT) as

$$C_p = \sigma_H^2/k_B T^2 = (\sigma_E + p\sigma_V)^2/k_B T^2 \quad (2)$$

See, e.g., refs 14 and 15 for the background. We have chosen to do the simulations at fixed volume, which gives the C_V's. Experimental heat capacities are, however, more often available as C_p's. For condensed matter systems, the difference is small, and the two types of heat capacities can readily be converted between each other using the exact thermodynamic relation (see e.g., ref 16):

$$C_p - C_V = VTK_V\alpha^2 \quad (3)$$

where the thermal expansion coefficient, $\alpha = 1/V(\partial V/\partial T)_p$, and volume compressibility modulus, $K_V = -V(\partial p/\partial V)_T$, are experimentally available. Thus, experimental C_p's can be converted into C_V's by employing this relation. The difference between the two types of heat capacities is less than 1% in the condensed water phases.

Quantum corrections to the classical heat capacities cannot easily be calculated in general without employing models or approximations. One fairly good and practical model is that of coupled harmonic oscillators, which gives an analytically solvable problem. Transformation to normal coordinates gives decoupled harmonic oscillators. The contribution of each such oscillator to the heat capacity is then

$$k_B\left(\frac{\hbar\omega}{k_B T}\right)^2 \frac{\exp(\hbar\omega/k_B T)}{[\exp(\hbar\omega/k_B T) - 1]^2} \quad (4)$$

This depends on the angular frequency, ω, of the oscillator through the dimensionless energy $x = \hbar\omega/k_B T$ (with $\hbar$ being Planck's constant divided by 2π). In the classical limit (small x or large T), we regain the Dulong–Petit result, k_B per degree of freedom. In the other (quantum) limit, the contribution to the heat capacity goes to zero. Thus, knowing the angular frequencies, ω_i ($x_i = \hbar\omega_i/k_B T$), of the normal modes, the quantum correction to the classical heat capacity per molecule is obtained as

$$\Delta c_V = k_B \sum_i \left[x_i^2 \frac{e^{x_i}}{(e^{x_i} - 1)^2} - 1\right] \approx k_B \int_0^\infty \left[x^2 \frac{e^x}{(e^x - 1)^2} - 1\right] G(x)\, dx \quad (5)$$

In the integral approximation, the integral is performed over the dimensionless variable x. The normal mode distribution, $g(\omega)$, is normalized to give the integral $\int g(\omega)\, d\omega$, equal to the number of degrees of freedom per molecule, i.e., 6 for rigid water and 9 for flexible water. As a function of the dimensionless variable x, the normal mode distribution $G(x)$ is equal to $(k_B T/\hbar)\, g(k_B T x/\hbar)$. The normal mode distribution may be obtained from the velocity spectrum as[7,15]

$$g(\omega) = N \frac{\sum_i |\hat{v}_i(\omega)|^2}{\int \sum_i |\hat{v}_i(\omega)|^2 d\omega} \quad (6)$$

were $\hat{v}_i(\omega)$ is the Fourier transform of an atomic velocity component, the sum goes over all three components of all atoms, and N is the number of degrees of freedom (6 or 9 per molecule).

The quantum corrections are negative and thus reduce the heat capacities. The SPC/E water model used here has point charges at the positions of the oxygen and the two hydrogens and Lennard-Jones interactions between the oxygens. It is usually simulated with fixed bond lengths and a fixed bond angle, but one may also perform classical simulations with harmonic vibrations in the bonds and the angle. The angular frequencies of these oscillators correspond, however, to large values of $x = \hbar\omega/k_B T$ (about 7 for the angle and 14 for the bonds at 300 K). Thus, the contribution from these degrees of freedom becomes negligible after application of quantum corrections (about $0.04k_B$ per molecule compared to the classical value $3k_B$)

The quantum correction to the energy may also be calculated as

$$\Delta u_{QM} = k_B T \int_0^\infty \left(\frac{x}{2} + \frac{x}{e^x - 1} - 1\right) G(x)\, dx = u_0 + u_e - u_{cl} \quad (7)$$

The first term, u_0, is the ground state energy of the harmonic oscillators, u_e the energy in the excited states, while u_{cl} is the classical energy (6 or 9 $k_B T$). The melting enthalpy of ice and the heat of vaporization of liquid water could thus be quantum corrected. The melting enthalpy of ice is

$$\Delta H = H_l - H_s = (U_l + pV_l) - (U_s + pV_s) = \Delta U + p\Delta V \quad (8)$$

with the $p\Delta V$ term being negligible (-1.6×10^{-4} kJ/mol) compared to ΔU (6 kJ/mol).

3. COMPUTATIONAL DETAILS

All simulations were performed using the GROMACS[17] package, version 4.0, on a local cluster in the department at Albanova University Center KTH Stockholm. All systems consisted of 360 SPC/E water molecules and were subjected to periodic boundary conditions in all directions. Liquid water was simulated at 300 K and 273 K, while ice was simulated at the temperatures of 273, 263, 243, 223, 173, 93, and 23 K. A Nose–Hoover thermostat[18,19] was used to keep the temperature constant for the system. The integration of the equations of motion was performed by using a leapfrog algorithm with a time step of 1 fs. Liquid water was simulated with fixed as well as flexible bonds and angles, but the main part of the ice simulations was done with rigid water molecules. During the equilibrations, a barostat was used to adjust the density to obtain a pressure of 1 bar. The simulations used to calculate energy fluctuations and normal mode distributions were performed at a fixed volume and temperature (NVT). The analytical SETTLE algorithm[20] was used to restrain bond lengths and angles. In simulations with flexible bonds and angles, a test with a 10-fold reduced time step did not alter any results. The classical heat capacity was calculated from the energy fluctuations over 5 ns simulations which had been equilibrated for 1 ns, while the normal mode distributions were calculated from the velocities in densely stored 500 ps trajectories. A cutoff of 1.0 nm was used for Lennard-Jones (LJ) interactions. The electrostatics were calculated using the particle-mesh Ewald (PME) method[21,22] with interactions inside 1.0 nm

Table 1. c_V's of Liquid Water and Ice Calculated from Experimental c_p's[24] Using eq 3 with Experimental Thermal Expansion Coefficients and Compressibility Modulii[23]

phase	l		s						
T [K]	300	273	273	263	243	223	173	93	23
c_V [J/mol K]	74.1	74.8	37.0	35.6	33.1	30.4	24.3	14.9	3.1
c_p [J/mol K]	75.2	75.9	38.0	36.5	33.8	31.0	24.5	14.9	3.1

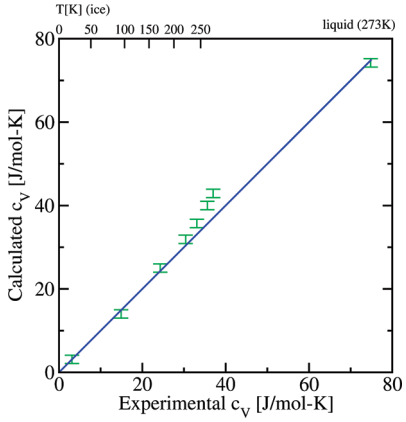

Figure 1. Calculated versus experimental heat capacities at different temperatures. The simulation figures are given with an error bar of 1 J/mol·K. The straight line ($y = x$) indicates perfect agreement.

handled in real space and those outside in Fourier space. For water and ice, the SPC/E model[1,2] was used.

4. RESULTS AND DISCUSSION

The experimental c_p's[24] are shown in the Table 1 together with the c_V's calculated using eq 3 with experimental values[23] for α and K_V. Alternatively, c_p's could be obtained by converting the c_V's from the simulations using eq 3. For this, α and K_V were determined from ice simulations at 273 K as 260×10^{-6} K^{-1} and 0.23×10^{10} N/m^2. These values deviate substantially from the experimental ones but give only a slightly lower difference of 0.8 J/mol·K instead of 1.0 J/mol·K between the heat capacities.

The heat capacities obtained after applying quantum corrections to the classical simulation data are shown versus the experimental ones in Figure 1 and in Table 2 with the quantum corrections tabulated separately. For liquid water, the rigid SPC/E model[1,2] gives an as-good (or even marginally better) heat capacity as the more complicated flexible Watts model[27] used by Berens et al.[7] The usage of flexible bonds and bond angles in the SPC/E model gives, on the contrary, a substantial overestimate of the heat capacity. The reason for this is that almost twice the energy expected from equipartition goes into these degrees of freedom. This was observed already in 1991 by Wallqvist and Teleman.[28] The deviation from equipartition decreases at lower densities and higher temperatures. We decided to stick to the rigid water model in the ice simulations. The ice simulations showed good agreement for the heat capacity at low temperatures, while the heat capacity was overestimated by about 15% (5−6 J/mol·K), close to the melting point. The classical heat capacities in Table 2 obtained from energy fluctuations were checked by numerical differentiation of the total energies

Table 2. Calculated (Classical and Quantum Corrected) and Experimental (from Table 1) Heat Capacities in J/mol·K for Liquid Water and Ice at Different Temperatures[a]

T	class c_V	QM corr.	corr. c_V	exptl. c_V
300 K (l), flex.	122.9 ± 1.4	−37.1	85.8	74.1
300 K (l), rigid	86.6 ± 0.7	−14.4	72.2	74.1
273 K (l), rigid	88.8 ± 0.7	−14.6	74.2	74.8
273 K (s)	62.2 ± 0.3	−19.3	42.9	37.0
263 K (s)	60.5 ± 0.3	−20.5	40.0	35.6
243 K (s)	58.2 ± 0.3	−22.5	35.7	33.1
223 K (s)	56.3 ± 0.3	−24.4	31.9	30.4
173 K (s)	53.9 ± 0.5	−28.9	25.0	24.3
93 K (s)	52.0 ± 0.3	−38.0	14.0	14.9
23 K (s)	50.0 ± 0.4	−47.0	3.0	3.1

[a] The total statistical error is estimated to be around ±1 J/mol·K from the statistical error in column 2 and an error in the quantum correction of ±0.5 J/mol·K due to insufficient sampling of the normal mode distribution.

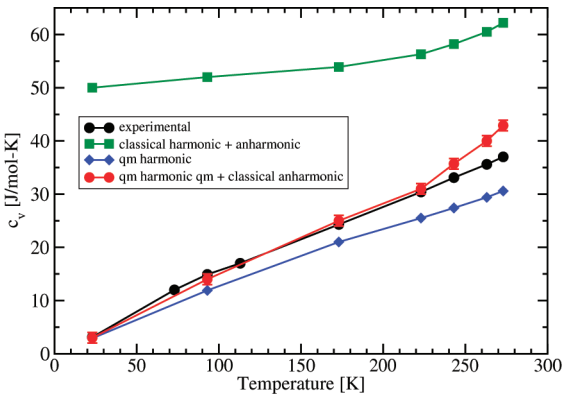

Figure 2. Experimental and calculated heat capacities versus temperature. The calculated heat capacities are (i) the classical ones containing harmonic as well as anharmonic contributions, (ii) the heat capacity from quantum mechanical harmonic oscillators, and (iii) the classical heat capacity with the harmonic part quantum-corrected.

showing no significant differences. We also checked that the larger heat capacities in ice close to the melting temperature were not due to critical fluctuations. Varying the system size (up and down) showed that the fluctuations in total energy scaled as would be expected from eq 1 ($\sigma_E \propto (N)^{1/2}$). The difference close to melting can therefore not be attributed to critical fluctuations. We also checked the sensitivity of the normal mode distribution to system size and found none.

In the Figure 2, the experimental and calculated heat capacities of ice are plotted versus the temperature. The experimental ones fit a straight line starting at zero for $T = 0$ with a slight deviation upward around 100 K. The QM corrected simulation data agree with experimental; results up to about 200 K, including the upward deviation from the straight line. At higher temperatures, the calculated heat capacities deviate upward in a way that could be described by a quadratic correction. The classical heat capacity calculated from the energy fluctuations is also shown. This is 20−50 J/mol·K larger than the experimental one, approaches the constant Dulong−Petit value, $6k_B$ = 49.9 J/mol·K at low temperatures, but is about 13 J/mol·K higher close to melting.

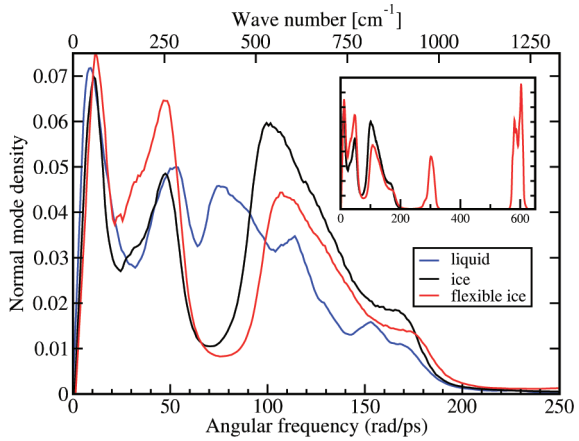

Figure 3. The normal mode distributions of ice and liquid water at 273 K with fixed bond lengths and bond angles. The normal mode distribution for ice with flexible bond lengths and angles is also shown. The inset includes the high frequency bond length and bond angle vibrations.

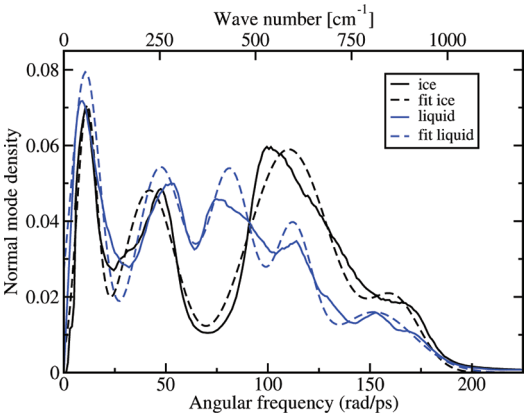

Figure 4. The normal mode distributions of ice and water at 273 K together with fits to 4 and 5 Gaussians, respectively.

This indicates that anharmonicities play an increasing role with temperature. It is, however, reassuring that experimental and calculated quantum corrected heat capacities agree at low temperatures when anharmonic contributions are expected to be small. Alternatively, one may apply a pure quantum harmonic oscillator model with the angular frequencies taken from the classical normal-mode analysis.

The heat capacities resulting from this model are also shown in Figure 2. It it clear that this model substantially underestimates the heat capacity except for very low temperatures (at which the anharmonic contribution is negligible). The quantum-corrected classical result could alternatively be viewed as the superposition of this result with the classical anharmonic contribution. This clearly reduces the error compared to when the anharmonic contribution is entirely neglected. For the highest temperatures, it does, however, overestimate the heat capacity since it misses the quantum corrections to the anharmonic contribution, which certainly would reduce the heat capacity if they could be included properly. In the liquid, the calculated heat capacity is, on the contrary, slightly on the low side, although almost within the statistical accuracy. Still, the deviation from the Dulong−Petits law is substantially larger in the liquid, indicating large anharmonic contributions to the heat capacity. These are, however, softer and thus more or less classical.

PIMD/MC methods[5,10−13] give the heat capacity without resorting to harmonic approximations. A recent study[29] employing a slightly reparametrized TIP4P/2005 model (TIP4PQ/2005) produces excellent agreement for the temperature-dependent heat capacity of ice as well as liquid water. Some of the earlier studies show less good results. The reason for that may be either that the underlying classical model is not good enough or that the fairly time-consuming simulations have not been performed long enough to produce adequate sampling.

The calculated normal mode distributions are shown in Figures 3−5. Figure 3 shows the normal mode distributions of the liquid and solid at 273 K. For ice, four broad peaks can be resolved at the angular frequencies in rad/ps or (THz) at 10(1.6), 50(8.0), 100(16), and 170(27) (corresponding to 53, 265, 530, and 900 cm^{-1} in spectroscopic units). For liquid water, the two lowest peaks are well resolved with just slight position shifts compared to ice. The pronounced minimum in the normal mode distribution of ice at 75 rad/ps is absent in the liquid, and the two broad peaks at higher frequencies are replaced by a broader distribution. Both densities of state drop to zero just above 200 rad/ps. The normal mode distribution of ice may be compared to the experimental density of states obtained from neutron scattering.[25] The pronounced minimum between 75 and 100 rad/ps in the simulated distribution agrees with a similar minimum in the experimental distribution. Otherwise, the spectra are qualitatively similar. The difference between the densities of state of H_2O and D_2O shows[26] clearly that the high-ω part of the spectrum (above the minimum) is due to rotational vibrations, while the lower part is due to translational vibrations. We verified this in simulations by increasing the mass of the hydrogens to 4 and reducing the oxygen mass to 8. Thus, the total mass of the molecule remained constant, which should result in an unaltered translational part of the spectrum. On the contrary, the rotational part should move down a factor 2 due to the 4-fold increase of the moment of inertia. We did observe (not shown) an essentially unaltered low-ω part of the density of states, while the part above 75 rad/ps was shifted down by a factor 2.

The fairly linear variation of the heat capacity with temperature shown in Figure 2 results from the broad distribution of oscillator frequencies but also from the fact that a single quantum oscillator (see eq 4) has a smooth variation of the heat capacity with the temperature. The heat capacity is half its classical value at the temperature $T_{1/2} \equiv \hbar\omega/3k_B$, with the change from 10% to 90% occurring in the fairly broad temperature interval $(0.5-3)T_{1/2}$. With the peaks in the normal mode density at frequencies corresponding to $T_{1/2}$ of 25, 120, 260, and 410 K, a considerable overlap in variation is obtained, resulting in a smooth variation of the heat capacity, which turns out to be fairly linear.

Figure 4 shows that a small number of Gaussians fit the normal mode distributions quite well. For ice, a decent fit is obtained using four Gaussians, while the liquid needs five, which still do not agree as well. Finally, the normal mode distributions of ice obtained at different temperatures are shown in Figure 5. There are fairly small but clear differences, and the distribution is shifted toward higher frequencies with more pronounced peaks at lower temperatures. This indicates that there are anharmonic parts in the potential which come out differently in normal mode distribution derived from the velocity autocorrelations at different temperatures. Still, the difference is small enough to have just minor effects on the quantum corrections. The quantum correction calculated at 273 K

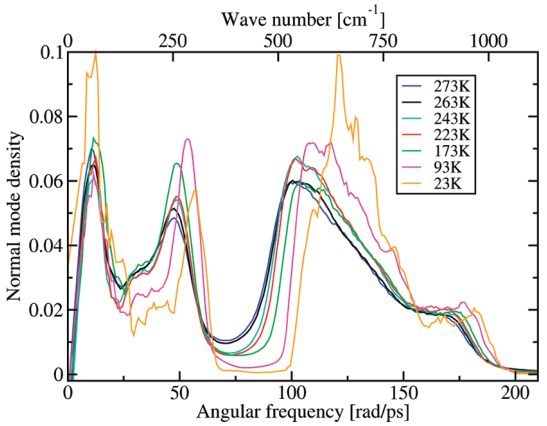

Figure 5. The calculated normal mode distributions for ice at different temperatures.

Table 3. Frequencies, ν, of the Internal Bending and Stretching (Symmetric (s) and Asymmetric (a)) Modes of Water in Different Phases in the Spectroscopic Unit, cm^{-1}[a]

	phase	bending	stretching (s)	stretching (a)
calculated	g	1592	3184	3243
experiment	g	1595	3657	3756
simulations	l	1610	3130	3220
experiment	l	1645	3280	3490
simulations	s	1600	3090	3200
experiment	s	1650	3085	3220

[a] The experimental values are based on IR and Raman spectra and are taken from refs 30 and 34 for the gas phase, from ref 23 for the liquid, and from refs 35 and 36 for the ice. The calculated values for the gas phase were obtained analytically (see, e.g., ref 32) from the geometry and force constants of the flexible SPC/E water model. The simulation values for the condensed phases were obtained from the normal mode distribution of flexible water.

from the density of states taken from the 23 K simulation is −19.8 instead of −19.3 J/mol·K as obtained with the proper distribution.

The inset in Figure 3 shows the normal mode distribution of ice with flexible and rigid molecules. In the flexible model, the angle vibrations show up as a narrow peak at 300 rad/s, while there are two overlapping peaks close to 600 rad/ps due to bond length vibrations. The area under the angle peak is approximately 1, while that under the double stretching peak deviates slightly from 2. This deviation indicates a slight mixing with the soft degrees of freedom, which is further substantiated by small differences in the low frequency part of the normal mode spectra. Table 3 shows the angular frequencies of the internal vibrational modes of water molecules in different phases as obtained from simulations using standard flexible SPC/E water. They are compared to spectroscopically determined angular frequencies in the liquid and gas phases. It is clear that the large experimental downward shift and broadening of the stretching peaks in the condensed phases are only partially reproduced in classical simulations. The standard choices of angular frequency for the bond stretching and bond angle vibrations used in the classical SPC and SPC/E water models are 3.45×10^8 J/mol nm^2 and 3.83×10^5 J/mol rad^2. As seen from Table 3, this reproduces the

Table 4. Total Classical Energies (Kinetic Plus Potential) and Harmonic Quantum Corrections for Ice, Liquid Water, and Water Vapor at 273 K[a]

energy [kJ/mol]	U_s	U_l	U_g	$U_l - U_s$	$U_g - U_l$
		intermolecular			
classical rigid model	−46.48	−41.40	6.81	5.08	48.21
QM corr.:$u_0 + u_e - u_{cl}$	6.85	5.35	0.0	−1.50	−5.35
		intramolecular			
QM ground state	47.59	50.34	53.89	2.75	3.55
quantum corrected	7.96	14.29	60.70	6.33	46.41

[a] The quantum corrections were calculated from eq 7 using the normal mode distributions in Figure 3 for the intermolecular part, while experimental bending and stretching frequencies (Table 3) were used for the intramolecular ground state energy (the excited states give negligible contributions).

experimental frequencies in the condensed phases and especially the solid phase better than those of the gas phase. The TIP3P and TIP4P water models use a slightly more stiff bond and bond angle.

The heats of melting and vaporization are easily calculated from the energy differences between the different phases. To obtain accurate values, one may have to apply quantum corrections as discussed for the liquid by Burnham and Xantheas.[37] In Table 4, we give the total energies from simulations of rigid solid and liquid water at 273 K. For the gas, we just have $3k_BT$ of kinetic energy and need no simulation. Both ice and liquid water are stable in very long time simulations at this temperature, even if the actual solid/liquid transition temperature may be different from the experimental one for the present (and other) water models. The classical intermolecular energy is now corrected by calculating the three terms in eq 7 from the normal mode distributions from Figure 3. The correction consists of two parts. The normal mode spectrum of the ice is shifted toward higher angular frequencies, which gives rise to a higher zero point energy in ice, but also to a lower average energy in the excited states in ice. The net effect from the intermolecular part will be a change of the melting enthalpy by −1.50 kJ/mol. The internal vibrational frequencies contribute through different zero point energies, smaller for ice and larger for liquid water. This gives using the experimental vibrational frequencies an additional correction of +2.75 kJ/mol to the heat of melting. When the total quantum correction, 1.25 kJ/mol, is added to the classically calculated heat of melting, 5.08 kJ/mol, a heat of melting of 6.33 kJ/mol is obtained in good agreement with experimental value of 6.01 kJ/mol.[33] The total quantum correction is smaller here than the value suggested in ref 37 of 2.75 kJ/mol. The reason for this is that we use different normal mode distributions for the intermolecular degrees of ice and liquid water (calculated from respective simulations), while Burnham and Xantheas[37] used the same normal mode distribution. For the intramolecular part, we use the same experimental vibration frequencies as they and thus have identical results. The classical TIP4P/2005 model has an energy of −49.52 kJ/mol for the liquid at 273 K,[38] while the corresponding energy for the I_h-ice is −55.84 kJ/mol at 250 K. From the latter value, we obtain −54.41 kJ/mol at 273 K using the heat capacity of classical ice (with restrained bond lengths and bond angles), 62.00 J/mol·K. Thus, this model gives the classical heat of melting, 4.89 kJ/mol. If we assume the same

quantum corrections as for the SPC/E model, we obtain 6.14 kJ/mol in slightly better agreement with experimental results.

To explore the quality of the water model and the correction scheme further, we may also calculate harmonic quantum corrections to the heat of vaporization. Originally, the classical potential energy was used to adjust the parameters of, for instance, the SPC model[1] to obtain the correct heat of vaporization. Since then, lattice summations methods for the electrostatics (instead of short cutoffs), dispersion corrections for the Lennard-Jones interactions, and other adjustments have been introduced. There are two quantum effects. First, the intermolecular energy of the liquid increases by 5.35 kJ/mol (see Table 4) as a net result of zero point energy and smaller energy in the excited states. Second, Table 3 shows that the experimental vibrational frequencies of the bond lengths are substantially larger in the gas phase compared to the liquid phase. Thus, the quantum mechanical ground state energy of the internal degrees of freedom is larger in the gas phase. On the basis of the experimental figures, we get 3.55 kJ/mol. This goes in the opposite direction of the correction to the intermolecular potential energy, and the net reduction of the heat of vaporization becomes 1.80 kJ/mol. From the quantum corrected difference in energy between the gas and the liquid, 46.41 kJ/mol, we obtain after adding the *RT* term the heat of vaporization, 48.69 kJ/mol (at 273 K). This is clearly larger than the experimental value, 45.05 kJ/mol.[33] One may note that the original SPC model, which was parametrized against the heat of vaporization, produces better agreement due to its 3.4% smaller charges. The SPC/E model has, however, other advantages. For the TIP4P/2005 model, the energy of the liquid at 273 K (see above[38]) results in a heat of vaporization (51.78 kJ/mol) which with the same quantum correction becomes 49.98 kJ/mol. The TIP4PQ/2005 model, which has 3.6% larger charges, has an even more negative energy[39] resulting in a heat of vaporization around 56.2 kJ/mol after the same quantum corrections. Different PIMD/MC studies[12,13,39] indicate a difference in energy between PIMD/PIMC and classical simulations of 4−7 kJ/mol in the liquid state. The present quantum correction to the intermolecular energy, 5.35 kJ/mol, agrees favorably with this value. It is not obvious how the different intramolecular zero-point energies of the liquid and the gas are handled in the PIMD/MC simulations. Either similar corrections to those here could be applied or flexible molecules with different force constants in the different phases could be simulated. We conclude that the SPC/E as well as the TIP4P/2005 and TIP4PQ/2005 models have on the order 10% too strong cohesive interactions to reproduce experimental heats of vaporization, while the original SPC model seems to give better agreement. Although the difference is noteworthy, we do not think that this is a serious problem for the water models.

5. CONCLUSION

Simple classical rigid three-atom models for liquid water like the SPC/E model used here (or the SPC and TIP3P models) have essentially three parameters, the dipole moment (given by the charge separation between the oxygen and hydrogens) and the two Lennard-Jones parameters. The geometry of the molecule, given by the bond length and bond angle does not leave much room for variation. Thus, these three parameters can be determined to reproduce three different properties at one given density and temperature. Still such simple models reproduce several other properties of the liquid reasonably well and also give stable ice at lower temperatures. We have shown here that even the temperature-dependent heat capacity of the ice can be reasonably reproduced after the application of quantum corrections. There is, however, still a 15% error in the heat capacity of ice close to melting that most likely is due to quantum mechanical anharmonicities. The heat of melting, which in the classical approximation is underestimated by about 15%, is on the other hand obtained very close to the experimental value after the application of quantum corrections to the SPC/E as well as the TIP4P/2005 models. The heat of vaporization is on the other hand overestimated by about 10%, even after application of the relatively small quantum corrections.

AUTHOR INFORMATION

Corresponding Author

*Phone:+46-8-55378168. E-mail: qasir2@kth.se; oed@kth.se.

ACKNOWLEDGMENT

We thank professor Göran Grimvall for helpful discussions and suggestions concerning the interpretation of the normal mode spectra of ice. Q.W. acknowledges support by a grant from the Higher Education Commission (HEC) Pakistan. O.E. acknowledges the support by a grant from the Swedish Research Council (VR).

REFERENCES

(1) Berendsen, H. J. C.; Postma, J. P. M; van Gunsteren, W. F.; Hermans, J. Interaction models for water in relation to protein hydration. In *Intermolecular Forces*; Pullman, B., Ed.; D. Reidel Publishing Company: Dordrecht, Netherlands, 1981; pp 331−342.

(2) Berendsen, H. J. C.; Grigera, J. R.; Straatsma, T. P. *J. Phys. Chem.* **1987**, *91*, 6269.

(3) Jorgensen, W. L.; Chandrasekhar, J.; Madura, J. D.; Impey, R. W.; Klein, M. L. *J. Chem. Phys.* **1983**, *79*, 926.

(4) Abascal, J. L. F.; Vega, C. *J. Chem. Phys.* **2005**, *123*, 234505.

(5) McBride, C.; Vega, C.; Noya, E. G.; Ramirez, R.; Sesé, L. M. *J. Chem. Phys.* **2009**, *131*, 024506.

(6) Marx, D.; Hutter, J. Getting started: unifying MD and electronic structure. In *Ab Initio Molecular Dynamics*; Cambridge University Press: New York, 2009; pp 27−50.

(7) Berens, P. H.; Mackay, D. H. J.; White, G. M.; Wilson, K. R. *J. Chem. Phys.* **1983**, *79*, 2375.

(8) Hawlicka, E.; Pálinkás, G.; Heinzinger, K. *Chem. Phys. Lett.* **1989**, *154*, 255.

(9) Hardy, R. J.; Lacks, D. J.; Shukla, R. C. *Phys. Rev. B* **1998**, *57*, 833.

(10) Stern, H. A.; Berne, B. J. *J. Chem. Phys.* **2001**, *115*, 7622.

(11) Shinoda, W.; Shiga, M. *Phys. Rev. E.* **2005**, *71*, 041204.

(12) Shiga, M.; Shinoda, W. *J. Chem. Phys.* **2005**, *123*, 134502.

(13) Donchev, A. G.; Galkin, N. G.; Illarionov, A. A.; Khoruzhii, O. V.; Olevanov, M. A.; Ozrin, V. D.; Subbotin, M. V.; Tarasov, V. I. *Proc. Natl. Acad. Sci U. S. A.* **2006**, *103*, 8613.

(14) Allen, M. P.; Tildesley, D. J. Statistical mechanics. In *Computer Simulation of Liquids*; Oxford University Press: New York, 1986; pp 65−68.

(15) McQuarrie, D. A. In *Statistical Mechanics*; Harper Collins Publishers: New York, 1976.

(16) Plischke, M.; Bergersen, B. In *Equilibrium Statistical Physics*, 3rd ed; World Scientific: Singapore, 1994.

(17) van der Spoel, D.; Lindahl, E.; Hess, B.; Groenhof, G.; Mark, A. E.; Berendsen, H. J. C. *J. Comput. Chem.* **2005**, *26*, 1701.

(18) Nosé, S. *Mol. Phys.* **1984**, *52*, 255.

(19) Hoover, W. G. *Phys. Rev. A.* **1985**, *31*, 1695.

(20) Miyamoto, S.; Kollman, P. A. *J. Comput. Chem.* **1992**, *13*, 952.
(21) Darden, T.; York, D.; Pedersen, L. *J. Chem. Phys.* **1993**, *98*, 10089.
(22) Essmann, U.; Perera, L.; Berkowitz, M. L.; Darden, T.; Lee, H.; Pedersen, L. G. *J. Chem. Phys.* **1995**, *103*, 8577.
(23) Eisenberg, D.; Kauzmann, W. In *The Structure and Properties of Water*; Oxford University Press: Oxford, U. K., 1969.
(24) Nhemethy, G.; Scheraga, H. A. *J. Chem. Phys.* **1962**, *36*, 3382.
(25) Li, J. C.; Londono, J. D.; Ross, D. K.; Finney, J. L.; Tomkinson, J.; Sherman, W. F. *J. Chem. Phys.* **1991**, *94*, 6770.
(26) Criado, A.; Bermejo, F. J.; Garcia-Hernandez, M.; Martinez, J. L. *Phys. Rev. E.* **1993**, *47*, 3516.
(27) Watts, R. O. *Chem. Phys.* **1977**, *26*, 367.
(28) Wallqvist, A.; Teleman, O. *Mol. Phys.* **1991**, *74*, 515.
(29) Vega, C.; Conde, M. M.; McBride, C.; Abascal, J. L. F.; Noya, E. G.; Ramirez, R.; Sesé, L. M. *J. Chem. Phys.* **2010**, *132*, 046101.
(30) Herzberg, G.; In *Molecular Spectra and Molecular Structure. II. Infrared and Raman Spectra of Polyatomic Molcules*; Van Nostrand: Princeton, NJ, 1945.
(31) Walrafan, G. E. In *Water, a Comprehensive Treatise, The Physics and Chemistry of Water*; Franks, F., Eds.; Plenum: New York, 1972; Vol 1, p 151.
(32) Landau, L. D.; Lifshitz, E. M. In *Mechanics*; Pergamon Press: London, 1976.
(33) Lide, D. R. In *CRC Handbook of Chemistry and Physics*, 88th ed.; CRC Press: Boca Raton, FL, 2008.
(34) Benedict, W. S.; Plyler, E. K.; Gailar, N. *J. Chem. Phys.* **1956**, *24*, 1139.
(35) Bertei, J. E.; Whalley, E. *J. Chem. Phys.* **1964**, *40*, 1637.
(36) Taylor, M. J.; Whalley, E. *J. Chem. Phys.* **1964**, *40*, 1660.
(37) Burnham, C. J; Xantheas, S. S. *J. Mol. Liq.* **2004**, *110*, 177.
(38) Pi, H. L.; Aragones, J. L.; Vega, C.; Noya, E. G.; Abascal, J. L. F.; Gonzalez, M. A.; McBride, C. *Mol. Phys.* **2009**, *107*, 365.
(39) Noya, E. G.; Vega, C.; Sesé, L. M.; Ramirez, R. *J. Chem. Phys.* **2009**, *131*, 124518.

JCTC Journal of Chemical Theory and Computation

ARTICLE

pubs.acs.org/JCTC

Small Molecule Solvation Free Energy: Enhanced Conformational Sampling Using Expanded Ensemble Molecular Dynamics Simulation

Andrew S. Paluch,[†] David L. Mobley,[‡] and Edward J. Maginn*[,†]

[†]Department of Chemical and Biomolecular Engineering, University of Notre Dame, Notre Dame, Indiana 46556, United States

[‡]Department of Chemistry, University of New Orleans, New Orleans, Louisiana 70148, United States

Supporting Information

ABSTRACT: We present an efficient expanded ensemble molecular dynamics method to calculate the solvation free energy (or residual chemical potential) of small molecules with complex topologies. The methodology is validated by computing the solvation free energy of ibuprofen in water, methanol, and ethanol at 300 K and 1 bar and comparing to reference simulation results using Bennett's acceptance ratio method. Difficulties with ibuprofen using conventional molecular dynamics methods stem from an inadequate sampling of the carboxylic acid functional group, which, for the present study, is subject to free energy barriers of rotation of 14−20 k_BT. While several advances have been made to overcome such weaknesses, we demonstrate how this shortcoming is easily overcome by using an expanded ensemble methodology to facilitate conformational sampling. Not only does the method enhance conformational sampling but it also boosts the rate of exploration of the configurational phase space and requires only a single simulation to calculate the solvation free energy. Agreement between the expanded ensemble and the reference calculations is good for all three solvents, with the reported uncertainties of the expanded ensemble being comparable to the uncertainties of the reference calculations, while requiring less simulation time; the reduced simulation time demonstrates the improved performance gained from the expanded ensemble method.

1. INTRODUCTION AND MOTIVATION

Knowledge of the underlying free energy (or chemical potential) of biologically active species is key to understanding their thermodynamic phase behavior and is crucial for rational drug design.[1] For example, it is well-known that the solubility of a drug is dictated by its chemical potential in a pure crystalline phase relative to the solution phase. Additionally, the ability of a drug to partition between cell membranes is governed by the relative chemical potential[2,3] and its binding with proteins by the relative free energy.[4,5] The crucial role that free energy plays in the drug discovery process is emphasized by the fact that entire monographs have been devoted to the topic.[6,7] Likewise, insight into the native structure and folding mechanism of proteins in solution may be obtained by examining the solvation free energy of individual constituent amino acid analogs.[8,9]

The free energy of a given species may be understood in terms of the fundamental molecular level details via molecular simulation. Several recent studies have highlighted the ability of molecular simulations to precisely and accurately compute the solvation free energy of amino acid analogs[10−12] and small drug and drug-like molecules.[13−15] However, the work of Hodel et al.[16] warned that even for small polypeptides, inadequate conformational sampling with molecular dynamics (MD) could lead to errors in free energy calculations in much greater excess of any other source of error. As the size and complexity of the molecule increases, the problem becomes even worse. This warning was reiterated in the recent work of Leitgeb et al.[17] for amino acids and by Klimovich and Mobley[15] for the case of small drug molecules.

It follows that extreme care must be taken to ensure that systems studied using molecular simulation are ergodic.[18,19] For complex systems, it is common that ergodicity is "broken" over the time scale of the simulation.[20,21] That is, the important regions of the configurational phase space may be separated by large free energy barriers which are not overcome during the course of conventional simulations, yielding erroneous results. While this challenge can be overcome with advanced Monte Carlo (MC) methods,[22] it is often difficult to formulate a general protocol to ensure adequate sampling by MD. Many highly efficient MD algorithms have been developed to enhance the sampling of configurational phase space;[23−30] these methods may be applied to enhance sampling when performing free energy calculations.[17,25,31,32] However, given the diversity of methods available, proper method selection poses a huge challenge when computational efficiency is important.

Recently, Paluch et al.[33] demonstrated the use of expanded ensemble (EE)[34−36] methods to increase the rate of exploration of the important regions of configurational phase space when performing free energy calculations, when MD is used to sample configurational phase space within each subensemble. Not only does EE improve the rate of exploration of configurational phase space, but the method allows for the calculation of the free energy in an efficient manner, requiring the use of a *single* simulation. Moreover, the method may be readily implemented in existing MD simulation software. The present study extends our previous work[33] by showing how EE may additionally be used to seamlessly increase the rate of conformational sampling of molecules of complex topologies within an MD framework.

Received: June 6, 2011
Published: July 27, 2011

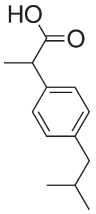

Figure 1. The chemical structure of ibuprofen.

Klimovich and Mobley[15] illustrated the inability of conventional MD-based free energy calculations to observe conformational changes of the H−O−C−O dihedral angle of carboxylic acid functional groups of small drug molecules in water and the impact this had on the computed free energy. In the present study, we have repeated the calculations of Klimovich and Mobley[15] for ibuprofen (Figure 1), which contains a carboxylic acid functional group, in water, methanol, and ethanol using MD-based EE. We will demonstrate how this technique overcomes H−O−C−O barriers of rotation of approximately 14−20 k_BT unhindered. Furthermore, akin to replica exchange (or parallel tempering) simulations,[26] ensemble average configurational properties may be calculated within each subensemble, allowing the use of EE whenever advanced conformational sampling is required. We anticipate that the technique presented in the present study, combined with previous free energy methodologies,[2,4,37,38] will aid in the rational drug design process.[1] In Section 2 we will present an overview of the EE methodology, followed by the relevant computational details in Section 3. Results and discussion are given in Section 4, followed by a summary of our findings in Section 5.

2. METHODOLOGY

An EE procedure was used to compute the free energy of solvation. The method is described in detail elsewhere,[33] so only a brief summary of the essential concepts and modification from our previous work is provided here. The basic idea behind the EE method[34−36] is to construct an augmented ensemble as a sum of $M_{\text{Total}} + 1$ subensembles. This series of subensembles connects two systems of interest by gradually performing transitions between the two systems. In the present work, the systems of interest are a noninteracting solute (ibuprofen) molecule in a pure solvent (i.e., the solute is in an ideal gas state) and a single fully interacting solute molecule in the solvent, with both states at the same temperature and pressure. The free energy difference between these two systems gives the free energy of solvation. Typically, the intermediate EE subensembles between the noninteracting and fully interacting solute subensembles serve to scale only the *intermolecular* interaction potential of the solute.[33,38−41] To improve the conformational sampling of the solute, we have additionally introduced intermediate subensembles to scale the *intramolecular* interaction potential of the solute; this addition is similar to the torsion angle potential fluctuation method of Liu and Berne[24] and the simulated scaling method of Hongzhi et al.[25] A specific subensemble is designated by index m, where the solute intermolecular Lennard-Jones (LJ) and the electrostatic interactions are regulated by the subensemble-dependent coupling parameters λ_m^{LJ} and λ_m^{elec}, respectively, and the intramolecular torsional potential of the solute is regulated by λ_m^{tors}. These coupling parameters vary from $0 \le \lambda_m^{\text{LJ}} \le 1$, $0 \le \lambda_m^{\text{elec}} \le 1$, and, in the present study, $0.1 \le \lambda_m^{\text{tors}} \le 1$.

While within a given subensemble, configurational phase space is sampled using MD within an isothermal−isobaric (NPT) ensemble. Periodically, a stochastic transition to an adjacent subensemble is attempted. The transitions are accepted using an appropriate acceptance rule.[33] However, as the free energy between subensembles increases, the probability of accepting a move decreases exponentially. This adversity is overcome by employing a biasing scheme that utilizes a combined Wang−Landau (WL)[42−44] and Bennett's acceptance ratio (BAR)[45−48] method.[33] The difference in free energy between the two end states and hence the free energy of solvation is calculated using BAR. Complete details can be found elsewhere.[33]

3. COMPUTATIONAL DETAILS

Molecular Models. For the solvents and solute (ibuprofen), nonbonded intermolecular interactions were treated using a combined LJ and fixed point charge model of the form:

$$U_{nb}(r_{ij}) = 4\varepsilon_{ij}\left[\left(\frac{\sigma_{ij}}{r_{ij}}\right)^{12} - \left(\frac{\sigma_{ij}}{r_{ij}}\right)^{6}\right] + \frac{1}{4\pi\varepsilon_0}\frac{q_i q_j}{r_{ij}} \qquad (1)$$

where r_{ij} is the site separation distance between atoms i and j, ε_{ij} and σ_{ij} are LJ parameters, and q_i and q_j are the partial charge values of atoms i and j, respectively. For interactions between unlike LJ sites, Lorentz−Berthelot[49] combining rules were employed.

To prevent instabilities in the trajectory when the solute was nearly decoupled from the system, that is when $\lambda_m^{\text{LJ}} \approx 0$, solute−solvent intermolecular nonbonded LJ interactions were modeled with a modified "soft-core" potential, $U_{\text{LJ}}^{\text{sc}}$, of the form:[11,50,51]

$$U_{LJ}^{sc}(r_{ij};m) = 4\lambda_m^{LJ}\varepsilon_{ij}\left\{\frac{\sigma_{ij}^{12}}{\left[(1-\lambda_m^{LJ})\alpha_{LJ}\sigma_{ij}^{6} + r_{ij}^{6}\right]^2} - \frac{\sigma_{ij}^{6}}{\left[(1-\lambda_m^{LJ})\alpha_{LJ}\sigma_{ij}^{6} + r_{ij}^{6}\right]}\right\} \qquad (2)$$

where r_{ij}, ε_{ij}, and σ_{ij} are the same LJ parameters as in eq 1, λ_m^{LJ} is the subensemble-dependent coupling strength of the LJ potential, and α_{LJ} is a constant, taken in this study to be 1/2. When the solute is fully coupled to the system, $\lambda_m^{\text{LJ}} = 1$, and eq 2 reduces to the normal LJ potential given by eq 1. When the solute is nearly decoupled, λ_m^{LJ} approaches 0, and eq 2 becomes a smooth interaction function that allows solvent molecules to overlap the solute with finite energy. When the solute is decoupled from the system, $\lambda_m^{\text{LJ}} = 0$, and the solute has no interaction with the solvent. Thus, the potential form in eq 2 correctly represents the limiting behavior of the solute−solvent interactions, while eliminating instabilities when $\lambda_m^{\text{LJ}} \to 0$.

Moreover, the use of eq 2 improves the configurational phase space overlap between the decoupled and nearly decoupled solute subensembles as compared to linearly scaling eq 1. This is clearly illustrated by the fact that when the solute is decoupled from the system, $\lambda_m^{\text{LJ}} = 0$, the solute will explore all regions of configurational phase space with equal probability. When the solute is nearly decoupled, $\lambda_m^{\text{LJ}} \approx 0$, a scaled form of eq 1 would perfectly exclude configurations in which the solute overlaps the solvent from the available phase space. On the other hand, use of eq 2 allows overlapping configurations to be observed with finite energy (and hence finite probability) for the nearly decoupled states, thereby increasing the regions of configurational phase

space mutual to both the decoupled and nearly decoupled subensembles. An increase in the configurational phase space overlap ultimately leads to a decrease in the bias of the calculated free energy between the decoupled and nearly decoupled subensembles.[52,53]

Solute intermolecular electrostatic interactions were decoupled in a linear fashion via the coupling parameter λ_m^{elec}; a detailed description regarding the decoupling of intermolecular interactions with Ewald summation may be found elsewhere.[33]

The same standard LJ and electrostatic interaction potential (eq 1) and combining rules were used for all intramolecular nonbonded interactions by all pairs of atoms separated by four or more bonds. For the case in which the intramolecular sites were separated by exactly three bonds, the LJ and electrostatic interactions were scaled by factors of 1/2 and 5/6,[54,55] respectively, for ibuprofen. These interactions were not necessary for the solvents studied here.

All of the molecules were modeled with flexible bonds, angles, and dihedral angles. The bond stretching and angle bending intramolecular interactions between sites separated by one and two bonds, respectively, were modeled by simple harmonic potentials of the form:

$$U_{bond}(r_{ij}) = k_{ij}(r_{ij} - r_{ij}^0)^2 \tag{3}$$

and

$$U_{angle}(\theta_{ijk}) = k_{ijk}(\theta_{ijk} - \theta_{ijk}^0)^2 \tag{4}$$

where k_{ij}, r_{ij}, and r_{ij}^0 are the force constant, distance between sites i and j, and the corresponding nominal bond length, respectively. Likewise, k_{ijk}, θ_{ijk}, and θ_{ijk}^0 are the force constant, angle between sites i, j, and k, and the corresponding nominal bond angle, respectively. The torsional potential describing the intramolecular interaction between sites separated by three bonds was modeled by a potential of the form:

$$U_{tors}(\phi_{ijkl}) = \sum_{n=0}^{5} K_n \cos^n(\phi_{ijkl} - 180^\circ) \tag{5}$$

where ϕ_{ijkl} is the dihedral angle between sites i, j, k, and l, and the K_n coefficients are constants. The same torsional potential was used to describe improper dihedral angles, meant to keep planar groups planar and to prevent unrealistic chiral inversions. The torsional potential of the solute molecule was scaled linearly via the coupling parameter λ_m^{tors}.

The molecular models for methanol and ethanol were taken from the united-atom transferable potential for phase equilibria (TraPPE-UA) force field of Siepmann and co-workers.[56,57] The TraPPE-UA models have rigid bond lengths; to avoid the use of constraints during the MD simulations, missing harmonic bond parameters were taken from the AMBER Parm94 force field.[58] For water, we employed the simple point charge[59] flexible water (SPC/Fw) model of Wu et al.[60] Parameters for ibuprofen are from the general AMBER force field (GAFF)[54,55] and were taken directly from Klimovich and Mobley.[15]

Further, to increase the MD time step of the EE simulations, we redistributed the mass of the studied molecules as suggested by Feenstra et al.;[61] the procedure involved redistributing a small amount of the mass of carbon and oxygen atoms bonded to a hydrogen to slow the corresponding vibrational frequency and to increase the simulation stability. Additionally, to slow the C═O carbonyl vibrational frequency, the mass of oxygen was redistributed such that both atoms had an atomic mass of 14 amu. Note that while redistributing the mass alters the dynamics of the system, it has no effect on the solvation free energy.[61,62] All of the force field files (which include atomic masses) used in the present study are provided in the Supporting Information.

Simulation Details. *EE.* All of the EE calculations were performed with a modified version of the MD simulation package MDynaMix 5.2.[63,64] For these simulations, LJ interactions were truncated at a distance of r_{cut} = 14 Å, and standard uniform fluid tail corrections were applied to both the energy and the pressure, assuming $g(r)$ = 1 beyond the cutoff.[22,49] Electrostatic interactions were evaluated with an Ewald summation with tin foil boundary conditions,[22,49] with real space interactions truncated at r_{cut}. A damping parameter of αr_{cut} = 3.14 was used, and the maximum number of reciprocal space lattice vectors was set by $K_{\max}$ = 7.0 for water and $K_{\max}$ = 7.3 for methanol and ethanol. Integration of the equations of motion was performed with the multiple-time step method of Tuckerman et al.[65] in Cartesian coordinates. A short time step of 0.2 fs was used for fast intramolecular degrees of freedom and nonbonded interactions within a cutoff of r_{short} = 8 Å, and a time step of 4 fs was used for all other interactions. An Andersen thermostat[66] and Andersen−Hoover barostat[66−68] were used with the collision time for the thermostat set to 0.5 ps, and the time constant for the barostat set to 1.5 ps. Modifications to MDynaMix include implementation of the Andersen thermostat, the "soft-core" potential (eq 2), separate decoupling of LJ and electrostatic solute intermolecular interactions for EE calculations, scaling of the solute torsional potential for EE calculations, WL-BAR, modification of the Ewald summation with EE fractional particles,[33] and other minor additions.

For each ibuprofen−solvent system studied, five independent simulations were performed. The systems were set up by randomly inserting a gas-phase minimized ibuprofen molecule into five previously equilibrated pure solvent boxes for each of the solvents studied. The boxes contained 1000 water, 500 methanol, or 350 ethanol molecules, which gave cubic box lengths of approximately 31−33 Å (water−ethanol). The velocities of each of the systems were initialized from a Maxwell−Boltzmann distribution with a unique seed to the random number generator. Production runs were carried out in an EE-NPT ensemble at 300 K and 1 bar for a total of 24 ns. Each of the five independent systems for each solvent was initialized with a unique random seed for the random number generator used by the thermostat and for the MC random walk. The system began in the subensemble with a noninteracting solute molecule, and attempts to change subensembles were made every 32 fs. Over the first 0.5 ns, the random walk was carried out with WL biasing, in which the WL weight factor was initially taken to be υ_{WL} = 0.5 and reduced as $\upsilon_{\text{WL}}^{\text{new}} = 0.25\upsilon_{\text{WL}}^{\text{old}}$ every 0.1 ns. During the entire course of the simulation, transition energies (in both directions) were computed each time a transition between subensembles was attempted/proposed, and new subensemble weights were computed from BAR every 0.5 ns.[33] To access the ability of EE to sample the H−O−C−O carboxylic acid dihedral angle of ibuprofen, after every proposed subensemble transition (32 fs), the current subensemble and atomic positions of ibuprofen were saved for postsimulation analysis.

In the reference subensemble (i.e., ideal gas state), m = 0, the solute is noninteracting with the rest of the system (λ_0^{LJ} = 0 and λ_0^{elec} = 0), but the intramolecular interactions are full (λ_0^{tors} = 1). The solute was taken from the reference subensemble to the

target subensemble, $m = M_{\text{Total}}$, with a fully interacting solute molecule ($\lambda^{\text{LJ}}_{M_{\text{Total}}} = 1$, $\lambda^{\text{elec}}_{M_{\text{Total}}} = 1$, and $\lambda^{\text{tors}}_{M_{\text{Total}}} = 1$) by first *reducing* the solute intramolecular torsional potential over $M^{\text{ig}}_{\text{tors}} = 3$ subensembles. For these $M^{\text{ig}}_{\text{tors}}$ subensembles, the intermolecular interactions remained off, and the torsional potential was reduced as $\lambda^{\text{tors}}_m = \{0.7, 0.3, \text{and } 0.1\}$ over the range $1 \le m \le 3$. Next, while the torsional potential was reduced, the intermolecular interactions were brought to full strength by first bringing the intermolecular LJ interaction to full strength and then adding in the intermolecular electrostatic interactions. The addition of the LJ and electrostatic interactions were performed separately in $M_{\text{LJ}} = 15$ and $M_{\text{elec}} = 4$ steps, respectively, for a total of 19 steps. First, for the M_{LJ} steps, the intermolecular electrostatic interactions were turned off, and the intermolecular LJ interactions were strengthened as $\lambda^{\text{LJ}}_m = \{0.05, 0.10, 0.20, 0.30, 0.40, 0.50, 0.60, 0.65, 0.70, 0.75, 0.80, 0.85, 0.90, 0.95, \text{and } 1.0\}$ over the range $4 \le m \le 18$. Next, the intermolecular electrostatic interactions were strengthened as $\lambda^{\text{elec}}_m = \{0.25, 0.50, 0.75, \text{and } 1.0\}$ over the range $19 \le m \le 22$; details regarding the coupling/decoupling of intermolecular interactions with Ewald summation may be found in our previous work.[33] Lastly, with the intermolecular interactions at full strength, the intramolecular torsional potential of the solute was restored (or restrengthened) over the last $M^{\text{full}}_{\text{tors}} = 3$ subensembles. For these $M^{\text{full}}_{\text{tors}}$ subensembles, the torsional potential was strengthened as $\lambda^{\text{tors}}_m = \{0.3, 0.7, \text{and } 1.0\}$ over the range $23 \le m \le 25$. Therefore there were $M_{\text{Total}} = 25$ subensembles. The intermolecular subensembles were chosen to agree with previous work of Mobley et al.[13−15] No attempt was made to optimize the intramolecular scaling; however, the employed intramolecular scaling scheme was found to be adequate to obtain full rotations of the problematic carboxylic acid dihedral angle of ibuprofen in both the reference and fully interacting (target) subensembles. All of the reported EE results are taken as the average value of the property computed by our five independent simulations, and the uncertainty is taken as one standard deviation.

Conventional MD. Reference calculations were performed using BAR with Gromacs 3.3.4[69] and directly followed the protocol of Klimovich and Mobley.[15] Generally, simulation parameters were similar for both the EE and reference calculations. Minor differences included the use of different MD integrators, a different thermostat and barostat, the use of constrained dynamics for bonds involving hydrogen for methanol, ethanol, and ibuprofen, the use of LJ and electrostatic cutoffs (r_{cut}) of 10.2, 11.25, and 11.85 Å for water, methanol, and ethanol, respectively, and a different treatment of the long-range electrostatic interactions. These differences resulted from the use of different MD simulation software and attempts to efficiently perform both the EE and reference calculations. We recently found that similar small discrepancies did not yield statistically significant differences when computing the hydration free energies of amino acid analogs.[33]

The BAR calculations were performed in 20 steps, composed of an ideal gas reference state and the same 19 (M_{LJ} and M_{elec}) steps to couple/decouple the intermolecular interactions of the solute as were used for the EE calculations. Note that the torsional potential was *not* perturbed for the reference calculations. An independent 5 ns simulation was performed for each state, for a total of 100 ns. The time step for integrating the equations of motion was 2 fs for simulations involving methanol and ethanol and 1 fs for water.

As mentioned previously, the reference simulations suffered from an inadequate sampling of the carboxylic acid dihedral angle H−O−C−O. As a result, a "confine-and-release" framework[70] was necessary to include the free energy of the conformational transformation. This was performed separately using umbrella sampling[71] to compute the potential of mean force (PMF) of the dihedral angle,[72] again following the work of Klimovich and Mobley[15] with Gromacs 3.3.4. Each PMF was constructed of 24 umbrellas. For each umbrella, a 0.5 ns simulation was conducted, for a total of 12 ns of simulation time per PMF.

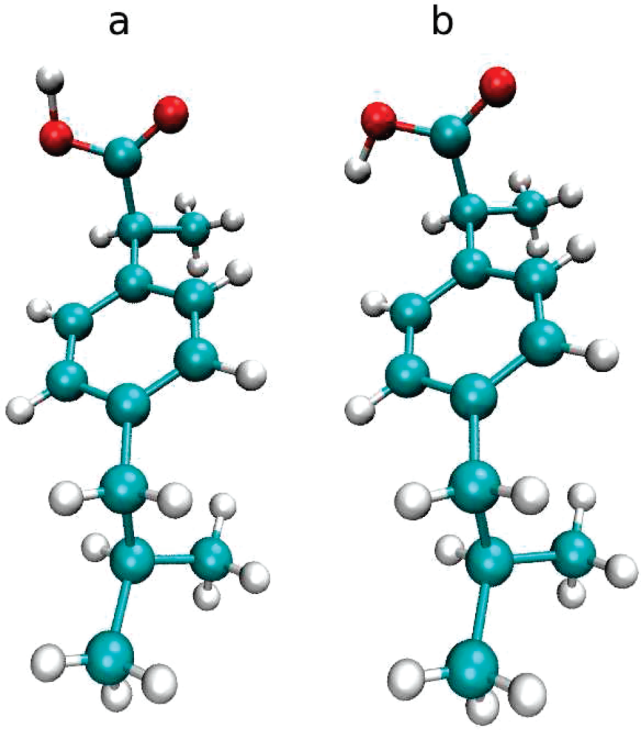

Figure 2. An illustration[81] of the conformational minima of the H−O−C−O dihedral angle of the carboxylic acid functional group of ibuprofen with: (a) the terminal H pointed toward the terminal O ($\phi = 0°$), in what we term conformation "a", and (b) the terminal H pointed away from the terminal O ($\phi = \pm 180°$), in what we term conformation "b". Note that the illustration shows only the rotation of the hydroxyl group; the rest of the molecule is left in the same conformation.

4. RESULTS AND DISCUSSION

As alluded to earlier, conventional MD simulations of ibuprofen in water, methanol, and ethanol are unable to effectively sample the H−O−C−O dihedral angle of the carboxylic acid functional group. For reference, an illustration of the conformational minima of the carboxylic acid dihedral angle is given in Figure 2. An understanding of the molecular level origin of this inefficiency may be understood by looking at the computed PMF of the dihedral angle in an ideal gas state and in solution; PMF calculations were performed using conventional MD as mentioned previously (Section 3). As illustrated in Figure 3, in the ideal gas state, the H−O−C−O dihedral angle has a strong preference to remain in the range of −90 to +90° (conformation "a"). This conformation corresponds to the terminal H pointed toward the terminal O, resulting in a strong intramolecular hydrogen bond. The strength of the interaction is emphasized by the fact that the barrier of rotation is on the order of 20 $k_{\text{B}}T$,

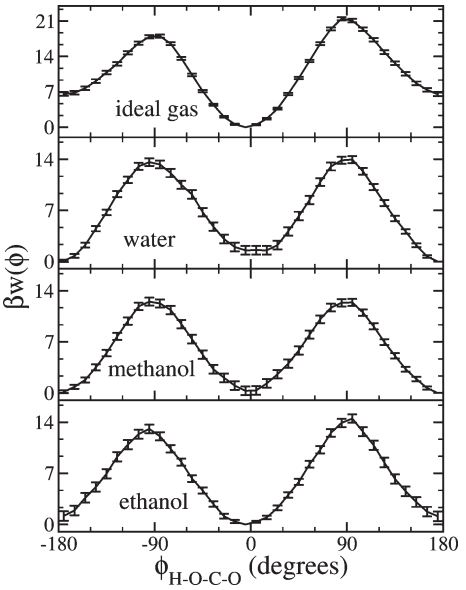

Figure 3. The PMF of rotation of the carboxylic acid dihedral angle of ibuprofen in the reference (ideal gas) subensemble and in water, methanol, and ethanol The *x*-axis corresponds to the H−O−C−O dihedral angle, and the *y*-axis is the dimensionless PMF (or relative free energy). The error bars correspond to the uncertainty of the umbrella sampling calculations.

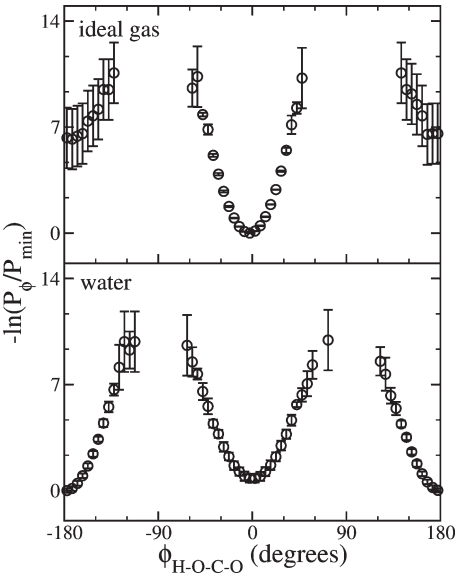

Figure 4. The visited states histogram of observing an H−O−C−O dihedral angle of ibuprofen with EE in the target (solution) and reference (ideal gas) subensemble for water. The *x*-axis corresponds to the H−O−C−O dihedral angle, and the *y*-axis is the negative logarithm of the visited states probability of observing an H−O−C−O dihedral angle relative to the minimum negative logarithm visited states probability. The error bars correspond to the uncertainty taken as the standard deviation of five independent simulations.

and the corresponding conformational minima differ by approximately 7 k_BT.

On the other hand, Figure 3 shows that for water and methanol, the H−O−C−O dihedral angle favors conformations in the range of −180 to −90 and +90 to +180° (conformation "b"). For the case of ethanol, conformation "a" is slightly favored over conformation "b". Moreover, the barrier of rotation in all of the solvents is reduced to approximately 14 k_BT, and the conformational minima differ by only approximately 1 k_BT. This change in behavior results from the presence of a hydrogen-bond accepting solvent. Whereas in the ideal gas state the strongest interaction present was the intramolecular hydrogen bond, in solution a competing hydrogen bonding scenario exists for the terminal H to hydrogen bond with the solvent. The strength of the intermolecular hydrogen bond directly influences the PMF minima of conformation "a" relative to "b" in solution. From Figure 3, we find that the difference in PMF minima between conformation "a" and "b" follows the trend: ethanol < methanol < water. As anticipated, this observation agrees with the trend of increasing strength of the hydrogen bond formed between the terminal H of the carboxylic acid group and the O of the solvent: ethanol < methanol < water.[73,74]

The inefficiencies of conventional MD simulations to compute the solvation free energy of the systems of interest are now evident. When performing free energy calculations, regardless of the employed technique, it is crucial that *all* of the important configurational phase space of the system be adequately sampled in order to obtain a meaningful result. In the present study, this condition demands that both conformations "a" and "b" of the carboxylic acid functional group be sampled in both the ideal gas (reference) and solution (target) states. This would require routinely overcoming barriers for rotation of approximately 14−20 k_BT to sample both conformations and is not realistic using conventional MD simulations. Corrections may be made to the computed free energy to compensate for the inadequate sampling postsimulation using a "confine-and-release" framework.[15,70] These corrections, however, require that the inefficiency and its cause are identified prior to calculating a solvation free energy, and subsequent umbrella sampling calculations be performed to compute the PMF along the relevant reaction coordinate. This requires human intervention and planning, so it would be highly advantageous to avoid such calculations altogether. Another key reason to solve this problem is that it may not always be clear when simulations suffer from inadequate conformational sampling. The large barrier of rotation encountered in the present study is a concerted effect of the intramolecular hydrogen bonding and the torsional potentials of both the carboxylic acid group (H−O−C−O) dihedral and the dihedral of the hydroxyl of the carboxylic acid group and the α carbon (H−O−C−C); the torsional potential of these two dihedral angles used in the present study is similar to other force fields commonly used for biological simulations.[75−77] A recent study of benzoic acid, acetylsalicylic acid, and ibuprofen (all of which contain carboxylic acid functional groups) in water assumed that a conventional NPT MD simulation of 5 ns was sufficient to sample all of the important configurational phase space;[78] the present results suggest that this may not be the case irrespective of the employed force field, motivating the present study.

Contrary to conventional MD simulations, the use of EE may alleviate the need to identify the inadequacy of sampling and the relevant reaction coordinate, dismissing the need to perform subsequent simulations to compute the relevant correction to the free energy. As seen in Figures 4−6, for EE calculations of ibuprofen in water, methanol, and ethanol, respectively, both conformations "a" and "b" of the problematic H−O−C−O dihedral angle of ibuprofen in solution are adequately sampled. This apparent gain in efficiency is a result of the introduction of

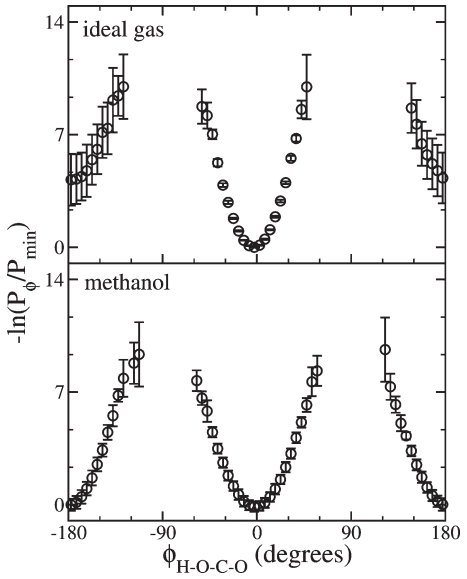

Figure 5. The visited states histogram of observing an H−O−C−O dihedral angle of ibuprofen with EE in the target (solution) and reference (ideal gas) subensemble for methanol. The *x*-axis corresponds to the H−O−C−O dihedral angle, and the *y*-axis is the negative logarithm of the visited states probability of observing an H−O−C−O dihedral angle relative to the minimum negative logarithm visited states probability. The error bars correspond to the uncertainty taken as the standard deviation of five independent simulations.

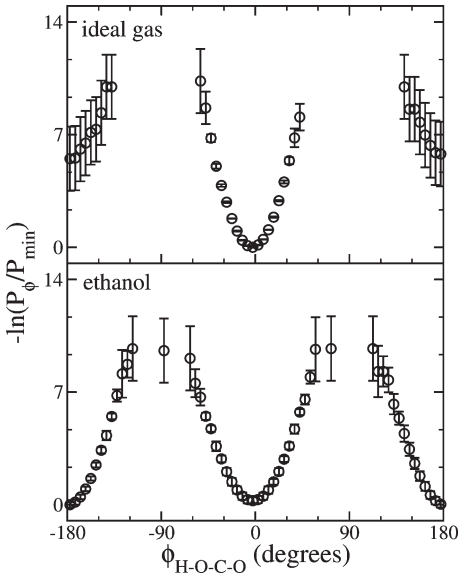

Figure 6. The visited states histogram of observing an H−O−C−O dihedral angle of ibuprofen with EE in the target (solution) and reference (ideal gas) subensemble for ethanol. The *x*-axis corresponds to the H−O−C−O dihedral angle, and the *y*-axis is the negative logarithm of the visited states probability of observing an H−O−C−O dihedral angle relative to the minimum negative logarithm visited states probability. The error bars correspond to the uncertainty taken as the standard deviation of five independent simulations.

intermediate subensembles in which the torsional barrier of rotation is reduced, greatly increasing the frequency of conformational changes in these subensembles. Analogous to replica exchange simulations, the conformations of the intermediate subensembles are then propagated between the target and reference subensembles, thereby effectively enhancing the conformational sampling. This characteristic behavior may be seen in Figure 7; we see in Figure 7 that when ibuprofen is interacting in solution with scaled torsional potentials, the reduced barrier of rotation allows for interconversion between conformation "a" and "b". These conformations are then propagated to our target subensemble. However, we should expect that the lowering of the torsional barrier of rotation in the intermediate subensembles will expand the important configurational phase space of the system. Nevertheless, as compared to conventional MD simulations, the use of EE naturally decreases the configurational correlation time, increasing the rate of exploration of phase space.[33] Ultimately, the significant increase in computational time necessary to sufficiently sample conformational changes of the H−O−C−O dihedral angle far outweighs the cost associated with the increase in the important configurational phase space of the system.

Note that in Figures 4−6, it appears that data are missing for conformations of the carboxylic acid dihedral angle near −90 and +90°, corresponding to the maximum of the PMF in the ideal gas (reference) and solution (target) states (Figure 3). However, this is an artifact of collecting data after every proposed subensemble transition (32 fs) and the propagation of conformations between subensembles. The time spent at these intermediate dihedral angles is short-lived in solution and in the ideal gas state, and as a result, they are not seen in our collected data for the corresponding subensembles. The observance of these dihedral angles is confirmed, however, by the fact that we observe transitions between conformation "a" and "b" during our EE simulations, as shown in Figure 7. Similarly, note that in Figures 4−6, while the observed distribution of conformations of the carboxylic acid dihedral angle in the ideal gas (reference) subensemble are statistically equivalent for all three systems studied, the uncertainties over the range of −90 to −180 and +90 to +180° are much larger than over than range of −90 to +90°. This results simply because these states are so improbable. The uncertainty could be reduced by running longer simulations; however, the impact of this on the computed free energy is negligible.

Having confirmed that enhanced conformation sampling is obtained with EE, we next draw our attention to the calculation of the solvation free energy.Table 1 compares the free energies computed using EE to reference calculations using BAR with additional conformational corrections.[15] The average absolute difference between EE and the reference calculations for the three systems studied is 0.5 ± 0.6 k_BT. For methanol and ethanol, agreement is excellent, with the EE and reference results being statistically equivalent. For water, the discrepancy is larger, 1.0 ± 0.7 k_BT, where the uncertainty is computed from propagation of errors and is taken as one standard deviation. This is still within two standard deviations, reaffirming confidence in the performance of the EE method.

Furthermore, Table 1 demonstrates how poor the uncorrected results are with conventional MD. If an unaware practitioner did not perform the necessary PMF corrections, then they would obtain nonsensical results. This is emphasized by the fact that the PMF correction is 10.5 and 5.6 k_BT for water and methanol, respectively; the magnitude of the PMF correction is 89 and 24% of the magnitude of the uncorrected (BAR) free energy in water and methanol, respectively. These absurd results would have an adverse effect on computed properties of biological interest.[2,4,37,38]

Additionally, two points may be made to emphasize the improved performance gained from employing EE over conventional

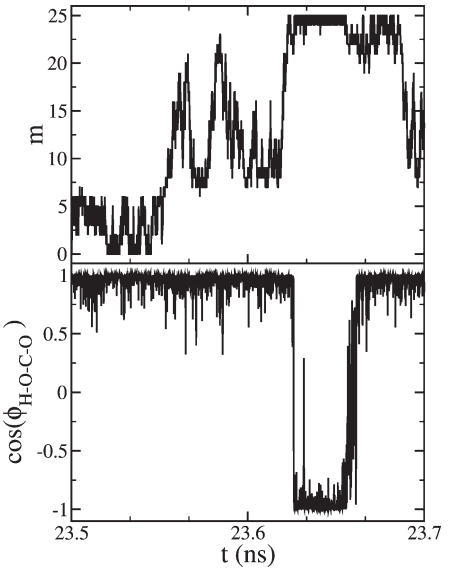

Figure 7. A sample plot of the time evolution of the EE subensemble and the cosine of the H−O−C−O carboxylic acid dihedral angle in water. The plot corresponds to 200 ps of simulation time from our first of five independent simulations of ibuprofen in water and is representative of the enhanced sampling behavior observed in each solvent.

Table 1. Comparison of the Computed Dimensionless Gibbs Free Energy of Solvation, $\Delta\beta G_{solv}$, using EE and Conventional Reference MD Simulations[a]

	EE	reference		
system	$\Delta\beta G_{solv}$	$\Delta\beta G_{solv}$	$\Delta\beta G_{solv}^{BAR}$	$\Delta\beta G_{solv}^{PMF}$
water	−12.8 ± 0.3	−11.8 ± 0.5	−22.3 ± 0.4	10.5 ± 0.3
methanol	−22.9 ± 0.3	−23.2 ± 0.3	−28.8 ± 0.1	5.6 ± 0.3
ethanol	−23.0 ± 0.2	−22.8 ± 0.3	−22.5 ± 0.1	−0.3 ± 0.3

[a] The reference results are composed of a BAR contribution ($\Delta\beta G_{solv}^{BAR}$) and a "confine-and-release" (PMF) correction ($\Delta\beta G_{solv}^{PMF}$) accounting for inadequate sampling of the ibuprofen H−O−C−O dihedral angle. Uncertainties of the EE calculations are taken as the standard deviation of the five independent simulations.

MD simulations. First, for each system studied using EE, we performed 5 independent 24 ns simulations, for a total of 120 ns of simulation time. For the conventional MD calculations, 20 independent 5 ns simulations were conducted to obtain the uncorrected solvation free energy, followed by 72 independent 0.5 ns simulations for the 3 necessary PMF corrections,[15] for a total of 136 ns of simulation time. Therefore, as seen in Table 1, for less simulation time, EE computes solvation free energies with comparable precision to the conventional MD simulations. The efficiency of free energy calculations using conventional MD is limited by the configurational correlation time of the system. On the other hand, for EE, subensemble transitions are periodically attempted. When a transition is accepted, the system begins sampling in a different subensemble. This transitioning reduces the configurational correlation time of the system and increases the rate of configurational phase space sampling, akin to replica exchange simulations, leading to the apparent improved efficiency of EE as compared to conventional MD. Note that both the EE and conventional MD simulations could have been run longer to improve the precision of the calculations; however, we anticipate that the EE calculations would remain more efficient.

However, although the net simulation time required by the EE simulations was less than the conventional MD simulations, it should be noted that with parallelization, the "wall-clock" time of the conventional MD simulations may be less than that of the EE simulations. This is because conventional MD uses more short simulations, while EE uses fewer long simulations. In practice, however, we believe the benefits of running a few simulations to get a solvation free energy directly as opposed to having to run many simulations with subsequent postprocessing corrections argues in favor of the EE method. In addition, implementation of the present EE method in a replica exchange[26] formalism would be a promising solution to reduce the "wall-clock" time.

Second, for the present study, we expect that the relative solvation free energies of ibuprofen in methanol and ethanol to be related to their relative solubility limits by the following relation:[38]

$$\Delta\beta G_{solv}^{methanol} - \Delta\beta G_{solv}^{ethanol} = \ln \frac{x_{ethanol}}{x_{methanol}} \quad (6)$$

where $\Delta\beta G_{solv}^{methanol}$ and $\Delta\beta G_{solv}^{ethanol}$ are the dimensionless Gibbs free energy of solvation of ibuprofen in methanol and ethanol, respectively, $x_{methanol}$ and $x_{ethanol}$ are the mole fraction solubility limit of ibuprofen in methanol and ethanol, respectively, and $\beta = 1/k_BT$. Experimentally,[79] we find that $\ln x_{ethanol}/x_{ethanol} = 0.33$. This is in good agreement with the EE results which give $\Delta\beta G_{solv}^{methanol} - \Delta\beta G_{solv}^{ethanol} = 0.1 \pm 0.4$ but is contrary to the results of the reference calculations which give $\Delta\beta G_{solv}^{methanol} - \Delta\beta G_{solv}^{ethanol} = -0.4 \pm 0.4$. That is, the reference calculations incorrectly predict that ibuprofen is more soluble in methanol relative to ethanol. While the results are statistically equivalent, the EE result is more accurate. Note that the Gibbs free energy of solvation for water predicted using the reference calculations is in excellent agreement with the reported experimental value of $-11.8\ k_BT$.[80] However, without further investigation, it is impossible to determine whether this is a success of the model or just a coincidence, especially since the present study does not account for dissociation of the carboxylic acid functional group in water.

5. SUMMARY AND CONCLUSION

Results have been presented that demonstrate that enhanced conformational sampling may be readily achieved via expanded ensemble molecular dynamics simulations. As a result of the ability of the carboxylic acid functional group of ibuprofen to form both intramolecular and intermolecular hydrogen bonds in the presence of hydrogen-bond accepting solvents, the H−O−C−O dihedral angle is subject to barriers of rotation of $14-20\ k_BT$. Consequently, conventional molecular dynamics simulations are unable to sufficiently observe conformational changes between conformation "a" and "b" during reasonable simulation time scales. This deficiency is particularly problematic when performing free energy calculations for which *all* of the important configurational phase space needs to be adequately sampled to obtain meaningful results. While the computed free energy may be corrected for inadequate sampling with subsequent calculations, this requires a careful practitioner to identify the problem and the relevant reaction coordinate necessary for the correction.

On the other hand, the sampling of the important regions of configurational phase space may easily be improved through use of an expanded ensemble methodology. The method not only boosts the rate of sampling of configurational phase space but also additional subensembles may be introduced to improve the conformational sampling of the solute. The additional subensembles used to enhance conformational sampling do not require an explicit definition of the relevant (burdensome) reaction coordinate. Rather, the torsional potential of all rotatable dihedral angles of the solute may be scaled without complication, while ensuring sufficient conformational sampling of the solute.

The gain obtained by using an expanded ensemble method was emphasized by calculating the solvation free energy of ibuprofen in water, methanol, and ethanol, and by comparing to reference simulation results; the reference simulation results required subsequent calculations to correct for insufficient sampling of the carboxylic acid dihedral angle. Agreement for methanol and ethanol was excellent. Deviations were larger for the results in water, but the expanded ensemble and reference results were within two standard deviations of each other. The agreement reinforced the effectiveness of the expanded ensemble method. Furthermore, the comparable precision obtained by the expanded ensemble and reference calculations, with the expanded ensemble requiring less simulation time, emphasized the enhanced computational efficiency gained. Also, the expanded ensemble calculations require performing only a single simulation and, unlike the reference results, were able to properly rank the solubility of ibuprofen in the studied solvents.

The results are extremely promising and suggest that the expanded ensemble may be used to study the solvation free energies of a wide range of molecules having complicated intramolecular potential energy surfaces. Application of the method to more complicated problems, including protein−ligand binding, is currently being successfully applied in one of our laboratories and will be described in detail in a subsequent paper.

■ ASSOCIATED CONTENT

Supporting Information. MDynaMix 5.2 and Gromacs 3.3.4 force field and topology files for water, methanol, ethanol, and ibuprofen used in this work. This material is available free of charge via the Internet at http://pubs.acs.org/.

■ AUTHOR INFORMATION

Corresponding Author

*E-mail: ed@nd.edu. Telephone: (574) 631-5687.

■ ACKNOWLEDGMENT

A.S.P. gratefully acknowledges a fellowship from the Arthur J. Schmitt Foundation, additional funding provided by the Notre Dame Sustainable Energy Initiative, and computing support provided by Notre Dame's Center for Research Computing. D.L.M. acknowledges the Louisiana Board of Regents Research Competitiveness and Research Enhancement Subprograms as well as the Louisiana Optical Network Initiative (supported by the Louisiana Board of Regents Post-Katrina Support Fund Initiative) grant LEQSF(2007-12)-ENH-PKSFI-PRS-01, and the NSF (EPS-1003897).

■ REFERENCES

(1) Chodera, J. D.; Mobley, D. L.; Shirts, M. R.; Dixon, R. W.; Branson, K.; Pande, V. S. *Curr. Opin. Struct. Biol.* **2011**, *21*, 150–160.
(2) Jorgensen, W. L.; Briggs, J. M.; Contreras, M. L. *J. Phys. Chem.* **1990**, *94*, 1683–1686.
(3) Prausnitz, J. M.; Lichtenthaler, R. N.; de Azevedo, E. G. *Molecular Thermodynamics of Fluid-phase Equilibria*, 3rd ed.; Prentice-Hall PTR: Upper Saddle River, NJ, 1999.
(4) Tembe, B. L.; McCammon, J. A. *Comput. Chem.* **1984**, *8*, 281–283.
(5) Gilson, M. K.; Zhou, H. X. *Annu. Rev. Biophys. Biomol. Struct.* **2007**, *36*, 21–42.
(6) Connors, K. A.; Mecozzi, S. *Thermodynamics of Pharmaceutical Systems: An Introduction to Theory and Applications*, 2nd ed.; John Wiley and Sons, Inc.: Hoboken, NJ, 2010.
(7) *Water-Insoluble Drug Formulation*, 2nd ed.; Liu, R., Ed.; CRC Press: Boca Raton, FL, 2008.
(8) Anfinsen, C. B. *Science* **1973**, *181*, 223–230.
(9) Dill, K. A.; Ozkan, S. B.; Shell, M. S.; Weikl, T. R. *Annu. Rev. Biophys.* **2008**, *37*, 289–316.
(10) Shirts, M. R.; Pitera, J. W.; Swope, W. C.; Pande, V. S. *J. Chem. Phys.* **2003**, *119*, 5740–5761.
(11) Shirts, M. R.; Pande, V. S. *J. Chem. Phys.* **2005**, *122*, 134508.
(12) Hess, B.; van der Vegt, N. F. A. *J. Phys. Chem. B* **2006**, *110*, 17616–17626.
(13) Mobley, D. L.; Bayly, C. I.; Cooper, M. D.; Dill, K. A. *J. Phys. Chem. B* **2009**, *113*, 4533–4537.
(14) Mobley, D. L.; Bayly, C. I.; Cooper, M. D.; Shirts, M. R.; Dill, K. A. *J. Chem. Theory Comput.* **2009**, *5*, 350–358.
(15) Klimovich, P. V.; Mobley, D. A. *J. Comput.-Aided Mol. Des.* **2010**, *24*, 307–316.
(16) Hodel, A.; Simonson, T.; Fox, R. O.; Brunger, A. T. *J. Phys. Chem.* **1993**, *97*, 3409–3417.
(17) Leitgeb, M.; Schroder, C.; Boresch, S. *J. Chem. Phys.* **2005**, *122*, 084109.
(18) McQuarrie, D. A. *Statistical Mechanics*; University Science Books: Sausalito, CA, 2000.
(19) Eckmann, J. P.; Ruelle, D. *Rev. Mod. Phys.* **1985**, *57*, 617–656.
(20) Palmer, R. G. *Adv. Phys.* **1982**, *31*, 669–735.
(21) Thirumalai, D.; Mountain, R. D.; Kirkpatrick, T. R. *Phys. Rev. A* **1989**, *39*, 3563–3574.
(22) Frenkel, D.; Smit, B. *Understanding Molecular Simulation: From Algorithms to Applications*, 2nd ed.; Academic Press: San Diego, CA, 2002.
(23) Berne, B. J.; Straub, J. E. *Curr. Opin. Struct. Biol.* **1997**, *7*, 181–189.
(24) Liu, Z.; Berne, B. J. *J. Chem. Phys.* **1993**, *99*, 6071–6077.
(25) Hongzhi, L.; Fajer, M.; Yang, W. *J. Chem. Phys.* **2007**, *126*, 024106.
(26) Earl, D. J.; Deem, M. W. *Phys. Chem. Chem. Phys.* **2005**, *7*, 3910–3916.
(27) Rosso, L.; Minary, P.; Zhu, Z.; Tuckerman, M. E. *J. Chem. Phys.* **2002**, *116*, 4389–4402.
(28) Zhu, Z.; Tuckerman, M. E.; Samuelson, S. O.; Martyna, G. J. *Phys. Rev. Lett.* **2002**, *88*, 100201.
(29) Lin, I. C.; Tuckerman, M. E. *J. Phys. Chem. B* **2010**, *114*, 15935–15940.
(30) Hansen, H. S.; Hunenberger, P. H. *J. Comput. Chem.* **2010**, *31*, 1–23.
(31) Ferguson, A. L.; Debenedetti, P. G.; Panagiotopoulos, A. Z. *J. Phys. Chem. B* **2009**, *113*, 6405–6414.
(32) Khavrutskii, I. V.; Wallqvist, A. *J. Chem. Theory Comput.* **2010**, *6*, 3427–3441.
(33) Paluch, A. S.; Shah, J. K.; Maginn, E. J. *J. Chem. Theory Comput.* **2011**, *7*, 1394–1403.
(34) Lyubartsev, A. P.; Martsinovski, A. A.; Shevkunov, S. V.; Vorontsov-Velyaminov, P. N. *J. Chem. Phys.* **1992**, *96*, 1776–1783.
(35) Lyubartsev, A. P.; Laaksonen, A.; Vorontsov-Velyaminov, P. N. *Mol. Phys.* **1994**, *82*, 455–471.
(36) Wilding, N. B.; Muller, M. *J. Chem. Phys.* **1994**, *101*, 4324–4330.
(37) Paluch, A. S.; Jayaraman, S.; Shah, J. K.; Maginn, E. J. *J. Chem. Phys.* **2010**, *133*, 124504.

(38) Paluch, A. S.; Cryan, D. D.; Maginn, E. J. *J. Chem. Eng. Data* **2011**, *56*, 1587–1595.
(39) Lyubartsev, A. P.; Jacobsson, S. P.; Sundholm, G.; Laaksonen, A. *J. Phys. Chem. B* **2001**, *105*, 7775–7782.
(40) Chang, J. *J. Chem. Phys.* **2009**, *131*, 074103.
(41) Boulougouris, G. C.; Errington, J. R.; Economou, I. G.; Panagiotopoulos, A. Z.; Theodorou, D. N. *J. Phys. Chem. B* **2000**, *104*, 4958–4963.
(42) Wang, F.; Landau, D. P. *Phys. Rev. Lett.* **2001**, *86*, 2050–2053.
(43) Yan, Q.; Faller, R.; de Pablo, J. J. *J. Chem. Phys.* **2002**, *116*, 8745–8749.
(44) Shell, M. S.; Debenedetti, P. G.; Panagiotopoulos, A. Z. *Phys. Rev. E* **2002**, *66*, 056703.
(45) Bennett, C. H. *J. Comput. Phys.* **1976**, *22*, 245–268.
(46) Lu, N.; Singh, J. K.; Kofke, D. A. *J. Chem. Phys.* **2003**, *118*, 2977–2984.
(47) Shirts, M. R.; Bair, E.; Hooker, G.; Pande, V. S. *Phys. Rev. Lett.* **2003**, *91*, 140601.
(48) Fenwick, M. K.; Escobedo, F. A. *J. Chem. Phys.* **2004**, *120*, 3066–3074.
(49) Allen, M. P.; Tildesley, D. J. *Computer Simulation of Liquids*; Oxford University Press Inc.: New York, 1987.
(50) Beutler, T. C.; Mark, A. E.; van Schaik, R. C.; Gerber, P. R.; van Gunsteren, W. F. *Chem. Phys. Lett.* **1994**, *222*, 529–539.
(51) Steinbrecher, T.; Mobley, D. L.; Case, D. A. *J. Chem. Phys.* **2007**, *127*, 214108.
(52) Wu, D.; Kofke, D. A. *J. Chem. Phys.* **2005**, *123*, 054103.
(53) Wu, D.; Kofke, D. A. *J. Chem. Phys.* **2005**, *123*, 084109.
(54) Wang, J.; Wolf, R. M.; Caldwell, J. W.; Kollman, P. A.; Case, D. A. *J. Comput. Chem.* **2004**, *25*, 1157–1174.
(55) Wang, J.; Wang, W.; Kollman, P. A.; Case, D. A. *J. Mol. Graphics Modell.* **2006**, *25*, 247–260.
(56) Martin, M. G.; Siepmann, J. I. *J. Phys. Chem. B* **1998**, *102*, 2569–2577.
(57) Chen, B.; Potoff, J. J.; Siepmann, J. I. *J. Phys. Chem. B* **2001**, *105*, 3093–3104.
(58) Cornell, W. D.; Cieplak, P.; Bayly, C. I.; Gould, I. R.; Merz, K. M.; Ferguson, D. M.; Spellmeyer, D. C.; Fox, T. F.; Caldwell, J. W.; Kollman, P. A. *J. Am. Chem. Soc.* **1995**, *117*, 5179–5197.
(59) Berendsen, H. J. C.; Grigera, J. R.; Straatsma, T. P. *J. Phys. Chem.* **1987**, *91*, 6269–6271.
(60) Wu, Y.; Tepper, H. L.; Voth, G. A. *J. Chem. Phys.* **2006**, *124*, 024503.
(61) Feenstra, K. A.; Hess, B.; Berendsen, H. J. C. *J. Comput. Chem.* **1999**, *20*, 786–798.
(62) Bennett, C. H. *J. Comput. Phys.* **1975**, *19*, 267–279.
(63) Lyubartsev, A. P.; Laaksonen, A. *Comput. Phys. Commun.* **2000**, *128*, 565–589.
(64) Lyubartsev, A. P.; Laaksonen, A. *MDynaMix: a Molecular Dynamics Program*; Stockholm University: Stockholm, Sweden; http://www.fos.su.se/~sasha/mdynamix/. Accessed February 1, 2010).
(65) Tuckerman, M.; Berne, B. J.; Martyna, G. J. *J. Chem. Phys.* **1992**, *97*, 1990–2001.
(66) Andersen, H. C. *J. Chem. Phys.* **1980**, *72*, 2384–2393.
(67) Martyna, G. J.; Tobias, D. J.; Klein, M. L. *J. Chem. Phys.* **1994**, *101*, 4177–4189.
(68) Martyna, G. J.; Tuckerman, M. E.; Tobias, D. J.; Klein, M. L. *Mol. Phys.* **1996**, *87*, 1117–1157.
(69) van der Spoel, D.; Lindahl, E.; Hess, B.; Groenhof, G.; Mark, A. E.; Berendsen, H. J. C. *J. Comput. Chem.* **2005**, *26*, 1701–1718.
(70) Mobley, D. L.; Chodera, J. D.; Dill, K. A. *J. Chem. Phys.* **2006**, *125*, 084902.
(71) Torrie, G. M.; Valleau, J. P. *J. Comput. Phys.* **1977**, *23*, 187–199.
(72) Shirts, M. R.; Chodera, J. D. *J. Chem. Phys.* **2008**, *129*, 124105.
(73) Dill, K. A.; Bromberg, S. *Molecular Driving Forces: Statistical Thermodynamics in Chemistry and Biology*; Garland Science: New York, 2003.
(74) Israelachvili, J. *Intermolecular and Surface Forces*, 2nd ed.; Academic Press: San Diego, CA, 1991.
(75) Wang, J.; Cieplak, P.; Kollman, P. A. *J. Comput. Chem.* **2000**, *21*, 1049–1074.
(76) Jorgensen, W. L.; Maxwell, D. S.; Tirado-Rives, J. *J. Am. Chem. Soc.* **1996**, *118*, 11225–11236.
(77) MacKerell, A. D.; Bashford, D.; Bellott, M.; Dunbrack, R. L.; Evanseck, J. D.; Field, M. J.; Fischer, S.; Gao, J.; Guo, H.; Ha, S.; Joseph-McCarthy, D.; Kuchnir, L.; Kuczera, K.; Lau, F. T. K.; Mattos, C.; et al. *J. Phys. Chem. B* **1998**, *102*, 3586–3616.
(78) Garrido, N. M.; Queimada, A. J.; Jorge, M.; Economou, I. G.; Macedo, E. A. *Fluid Phase Equilib.* **2010**, *296*, 110–115.
(79) Stovall, D. M.; Givens, C.; Keown, S.; Hoover, K. R.; Rodriquez, E.; Acree, W. E.; Abraham, M. H. *Phys. Chem. Liq.* **2005**, *43*, 261–268.
(80) Gaballe, M. T.; Skillman, A. G.; Nicholls, A.; Guthrie, J. P.; Taylor, P. J. *J. Comput.-Aided Mol. Des.* **2010**, *24*, 259–279.
(81) Humphrey, W.; Dalke, A.; Schulten, K. *J. Mol. Graphics* **1996**, *14*, 33–38.

JCTC Journal of Chemical Theory and Computation

ARTICLE

pubs.acs.org/JCTC

Structural Stability of V-Amylose Helices in Water-DMSO Mixtures Analyzed by Molecular Dynamics

Markus Tusch, Jens Krüger, and Gregor Fels*

Department of Chemistry, Faculty of Science, University of Paderborn, Warburger Strasse 100, D-33098 Paderborn, Germany

ABSTRACT: Computational techniques have been employed to fundamentally understand the behavior of helically structured amylose in water/DMSO mixtures. Using a computationally generated amylose helix of 55 glucose residues, we have investigated the time-dependent behavior of intra- and intermolecular hydrogen bonds, particularly between O2 and O3 of adjacent glucose molecules and between O6 and neighboring O2 and O3 groups. The helix character was defined by the total number of residually existing hydrogen bonds. Our results parallel the experimental finding that increasing the percentage of DMSO results in increasing helical stability. It can be shown that O6−O2/O3 hydrogen bonds are preferentially lost when the helix starts to unfold to a finally resulting random coil structure. While water is small enough to interact with every hydroxyl group at the helix surface and finally penetrate the helix coil, DMSO can initially only form single hydrogen bonds to part of the OH groups of the amylose molecule, thereby allowing a longer conservation of intramolecular hydrogen bonds that are necessary to maintain the helix. However, given a long enough time for interaction, the helical structure of amylose is lost in water as well as in DMSO, yielding a random orientation of the glucose strand.

INTRODUCTION

Amylose, naturally occurring as the unbranched component of starch, is a linear polysaccharide consisting of α-(1→4)-linked glucose units. Featuring a large number of rotatable glycosidic linkages, the polymer can adopt a virtually unlimited variety of possible conformations. As the actual secondary structure greatly influences the properties of a molecule, the elucidation of amylose conformations has been an objective of extensive research. Most of the available structural information has been obtained with X-ray[1−3] and electron diffraction,[4] which are restricted to the study of crystalline phases. The conformation of amylose in solution, however, still remains uncertain to some extent, as it lacks methods for direct unambiguous determination. Results from static and dynamic light scattering as well as studies of viscosity, sedimentation equilibrium, osmotic pressure, and specific optical rotation led to differing conclusions for amylose in water, ranging from a random coil without any helical character[5] to a random coil built up by helical segments[6] of more than 100 glucose units each.[7] The latter conclusion has essentially been supported by Monte Carlo studies.[8−10] The secondary structure of amylose in DMSO has also been interpreted controversially. While some authors describe it as a random coil,[6,11,12] others consider it to be rigidly or at least openly helical.[13−15] It has been pointed out that an influence of molecular weight on the global amylose structure may not be neglected in this respect.[16] On the basis of NMR spectroscopic results, the existence of intramolecular hydrogen bonds between OH2 and OH3 of amylose in DMSO has been assumed,[17,18] which as a result of a conformational analysis is supposed to be not true for aqueous solution.[19] Evidence from another more recent study contradicts the occurrence of intramolecular H bonding for the case of DMSO as well.[15] According to Cheetham and Tao,[20] who performed optical rotation, limiting viscosity, and ^{13}C NMR measurements in addition to butanol and iodine complexing experiments, the amylose conformation in water/DMSO mixtures changes from a tight helix to a looser helix and finally to a random coil with the water content increasing from 0 to 66%. Along with these transitions, the number of intramolecular OH2 to OH3 hydrogen bonds is said to diminish.[20]

With the intention of eventually studying inclusion complexes of amylose with a variety of organic compounds on a molecular basis, we have started to look into the stability of uncomplexed amylose in water and DMSO and mixtures thereof by use of force-field-based molecular modeling and molecular dynamics techniques. We find that we can reproduce the differing behavior of helical amylose in these solvents in that we can show an increasing helical stability with an increasing percentage of DMSO in DMSO/water mixtures. In the end, however, the entropy driven intermolecular interactions win over intramolecular hydrogen bonds with the result that the helical structure transforms to a random coil conformation.

MATERIALS AND METHODS

Generation of a V-Amylose Molecular Model. The molecular model of V-amylose employed in this study was derived from X-ray fiber diffraction data[1] of thin amylose−DMSO films. Following a mathematical procedure, the provided set of atomic coordinates was amplified to yield a 6-fold left-handed amylose helix comprising 55 glucose residues.

General Setup of Molecular Dynamics Simulations. All calculations were carried out with the simulation program GROMACS using the GROMOS96 force field[21,22] together with the DMSO model proposed by Geerke et al.[23] and either the simple point charge (SPC) water model,[24,25] the SPC/E

Received: July 26, 2011
Published: July 26, 2011

Table 1. Overview of the Simulated Water DMSO Systems: Number of Molecules, Water Mass Fraction ω, Water Mole Fraction χ

H_2O	DMSO	$\omega(H_2O)$	$\chi(H_2O)$
29124	0	1.00	1.00
23596	1128	0.83	0.95
17759	2400	0.63	0.88
13028	3521	0.46	0.79
6870	4903	0.24	0.58
0	6869	0.00	0.00

model,[26] or the TIP4P model.[27] The parametrization of the polysaccharide model was done in accordance with the parameters described by Lins and Hünenberger.[28]

Preparation of Solvent Mixtures. In a preliminary series of simulations, starting configurations for six solvent compositions were generated (water mass fractions ω_{water} = 0.0, 0.2, 0.4, 0.6, 0.8, 1.0), investigating the performance of three different water models: SPC, SPC/E, and TIP4P. To this end, every mixture was simulated for 25 ns with a time step of 2 fs by means of the leapfrog integrator.[29] The temperature was maintained at 298.15 K and the pressure at 1.0 bar using the V-rescale[30] and the Berendsen algorithm,[31] respectively. Isothermal compressibilities for the pure solvents were set equal to the experimental values of 8.718×10^{-4} (kJ mol^{-1} nm^{-3})$^{-1}$ for DMSO[32] and 7.51×10^{-4} (kJ mol^{-1} nm^{-3})$^{-1}$ for water,[33] while a linear combination of these values was assigned to the water/DMSO mixtures.

The LINCS procedure[34] with a fourth-order expansion of the constraint coupling matrix was applied to constrain all bond lengths and all bond angles involving H atoms. Van-der-Waals interactions were treated using a twin-range cutoff scheme.[35] Within a spherical short-range cutoff radius of 0.8 nm, the van-der-Waals energy was calculated every time step on the basis of a neighbor list updated every five time steps. The medium-range interactions up to a long-range cutoff radius of 1.4 nm were evaluated simultaneously with each neighbor list update and kept constant between re-evaluations. To account for electrostatic interactions, the reaction-field method[36] was employed with a cutoff of 0.8 nm, assigning a relative dielectric permittivity of 46[32] and 78.5[33] to pure DMSO and pure water, respectively. For the mixtures, linear combinations of these values were used.

As a measure of quality for the equilibration of the different systems, the potential energy and the density ρ were monitored during the preliminary simulations, with the latter being compared to experimental data[37] (see Figure 3). As a result, the models SPC/E and SPC were chosen to be used in all subsequent calculations.

Amylose MD Simulations. The dynamic behavior of the amylose helix was simulated in water−DMSO mixtures at six different compositions (water mass fractions ω_{water} = 0.0, 0.24, 0.46, 0.63, 0.83, 1.0; see Table 1). For this purpose, the model was centered in a dodecahedral box with a volume of approximately 885 nm^3 and solvated by means of the previously prepared solvent sets. After being subjected to short energy minimization simulations (1. steepest descent algorithm: maximum step size 0.01 nm, force tolerance 10 kJ mol^{-1} nm^{-1}; 2. conjugated gradient algorithm: maximum step size 0.001 nm, force tolerance 1 kJ mol^{-1} nm^{-1}; not more than 1000 steps either simulation), each of the systems thus generated was simulated in a series of five MD simulations for a time of 25.2 ns, employing an identical MD setup to that for the preliminary simulations (*vide supra*). This yields a total number of 55 MD simulations, with 5 × 5 simulations involving SPC/E water, 5 × 5 simulations with SPC water, and 5 simulations in pure DMSO. In addition to that, three analogous simulations were carried out over an amplified period of 100 ns, one in each of the pure solvents.

The number of hydrogen bonds was counted with the program g_hbond in GROMACS, applying cutoffs of 3.5 Å for the distance $O_{Donor}-O_{Acceptor}$ and of 30° for the angle $H-O_{Donor}-O_{Acceptor}$. Subsequently, the absolute numbers were evaluated on the basis of moving averages with subsets of 10 ps for the simulation interval between 0 and 0.05 ns, of 100 ps for 0.05 to 0.125 ns, and of 250 ps for the rest of the trajectory. In reading the calculated values, fractional numbers were rounded to the next integer; i.e., a value of 49.5 was interpreted as of 50 H bonds, for instance.

RESULTS AND DISCUSSION

Amylose Structure. In preparing our conformational studies on amylose single helices in solution, the reproduction of an idealized three-dimensional V-amylose model as a basis for our work turned out to be a nontrivial problem. The use of comparable models has been scarcely reported, including the work of Immel and Lichtenthaler on the hydrophobic topography of amylose[38] where a V-amylose helix comprising 30 glucose residues was employed. Structural data available in the literature usually are limited to the atomic coordinates of one glucose residue and specification of the space group with the respective unit cell measures.[1−4] On the basis of these data, other residues can be generated by applying the 6_5-helix symmetry operation, which of course may be accomplished by means of suitable crystallographic software. In the following, we describe an alternative mathematical procedure, that is readily doable with every spreadsheet program and which is easily adaptable to the generation of other amylose helices as well.

The molecular model of V-amylose employed in this study was derived from atomic coordinates based on X-ray fiber diffraction data.[1] Starting from the given position $\vec{x}_i$ of an atom X_i in glucose unit i, every analogous atom X_{i+1} in glucose unit $i + 1$ of the amylose chain can be localized according to the recursive mathematical sequence

$$\overrightarrow{x_{i+1}} = \begin{pmatrix} \cos(-2\pi/n) & -\sin(-2\pi/n) & 0 \\ \sin(-2\pi/n) & \cos(-2\pi/n) & 0 \\ 0 & 0 & 1 \end{pmatrix} \cdot \overrightarrow{x_i} + \begin{pmatrix} 0 \\ 0 \\ p/n \end{pmatrix} \quad (1)$$

where i is the glucose residue number, $n = 6$ is the number of repeating units per turn, and $p = 8.05$ represents the helix pitch in Ångstroms. In detail, the formula consists of a rotational matrix, generating a clockwise turn through 60° around the z axis, and a displacement vector that results in a translational movement by one-sixth of the helix pitch in the z axis direction. This amplification procedure creates the required geometry of a 6-fold left-handed helix (Figure 1). It, however, implies that adjacent monosaccharide units overlap with atoms O4 and O1. Hence, the coordinates of the redundant atoms O1, H1, and H4 were

deleted in each contemplable position, respectively, so that the generated overlapping monosaccharide units could be concatenated by glycosidic bonds.

In this manner, an amylose strand of nine 6-fold turns of overall 54 glucose residues plus one additional capping unit was generated ($C_{330}H_{552}O_{276}$; see Figure 2). The resulting helical structure measures about 5.4 Å in inner and 13.5 Å in outer diameter, respectively, and is about 73.8 Å long.

Solvent Mixtures. Six varying solvent compositions were provided for the amylose MD simulations, comprising pure water, pure DMSO, and in addition four different binary mixtures.

During the simulations for preparing the solvent starting configurations, the status of equilibration was monitored by means of the potential energy and the mass density ρ of the systems. Despite the fact that these parameters leveled off sufficiently within the first 100 ps, a total of 1 ns was provided to ensure equilibration.

In order to compare and classify the performances of the three employed water models in interaction with DMSO, the mass density ρ was evaluated over the whole simulation period of 25 ns, in this case leaving a margin of 0.2 ns for equilibration (Figure 3).

Obviously, the models generally underestimate the experimental density of the various water DMSO configurations. For pure water, the mean relative deviation is 3.3% in the case of the SPC model, while SPC/E and TIP4P obtain better approaches with 0.8% and 1.3% difference, respectively. For absolute DMSO, the simulated value averages 1.4% too low. Similar values for the DMSO model and SPC water were previously reported by Geerke et al.[23]

Correlation coefficients (Pearson's r) between the calculated data sets and the experimental record are 0.985 for SPC, 0.996 for SPC/E, and 0.991 for TIP4P. Hence, the nonlinear curvature of the experimental density graph is sufficiently well reproduced by all three of the models, with slightly better performances of SPC/E and TIP4P.

Taking into account the higher level of complexity in TIP4P and the resulting greater computational costs as compared to SPC/E and SPC, this model was ruled out for further use in this study. SPC/E, offering the best results at comparatively low computational expense, was considered to be most suitable for our purposes and was therefore employed as the main water model in all subsequent amylose MD simulations. Moreover, all simulations were also carried out with SPC water for further validation, which is closely related to SPC/E and thus does not require any additional setup procedures. For reasons of simplicity and comprehensibility, only the results obtained using the SPC/E model will be presented in the following.

Characterization of the Amylose Helix. The stability of a V-amylose helical structure essentially relies on intramolecular hydrogen bonds,[20] distinguishable into two types of hydrogen bonds that we define as interturn H bonds (O6−O2 and O6−O3) and intraturn H bonds between adjacent glucose units (O2−O3), respectively (Figure 4). The hydrogen bond O6−O3 is taken into account despite its rather weak nature in the crystal structure,[39] as the actual O−O distances within the amylose molecule are expected to fluctuate considerably in solution. Another noteworthy issue with respect to the intramolecular H-bond pattern is the effect of hydrogen bond cooperativity. As hydroxyl groups can build both accepting and donating hydrogen bonds, a continuous network can be established. The resulting mutual polarization in the functional groups leads to an enhanced stability of their hydrogen bonding network.

The idealized amylose model used in this study exhibits a total number of intramolecular hydrogen bonds N_{tot} of 152, which will be used as a reference point in the characterization of the helical content of the employed amylose (Figure 4).

Degradation of the Helical Secondary Structure. In all of the 55 amylose simulations, a continuous degradation of the helical structure can be observed. After a simulated time of 25 ns, the amylose chain independently of the solvent configuration has adopted an apparently randomly coiled conformation, and no helical content is evident anymore. This trend can numerically be tracked on the basis of the sum of intramolecular hydrogen bonds N_{tot}, which roughly speaking shows a continuous decline over the simulation time. This is true in water, as well as in DMSO and in mixtures thereof and finally results in a rather low number of intramolecular hydrogen bonds after 25 ns in each case (Figure 5).

Solvent Composition Impact on the Rate of Decomposition of the Helical Secondary Structure. A comparison of the amylose structures in DMSO and water with respect to their

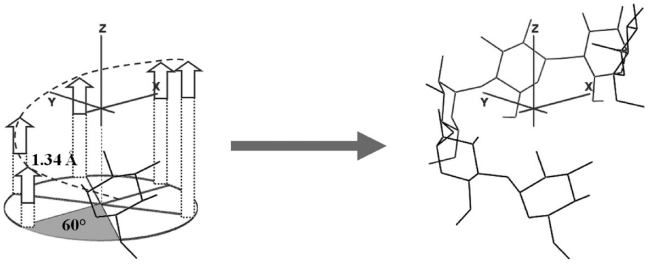

Figure 1. Schematic representation of the V-amylose modeling. By successive application of eq 1 to the atomic coordinates of one given glucose residue, a helical conformation is generated. The symmetry operation consists of a clockwise turn through 60° around the z axis and a displacement by 1.34 Å in the z axis direction.

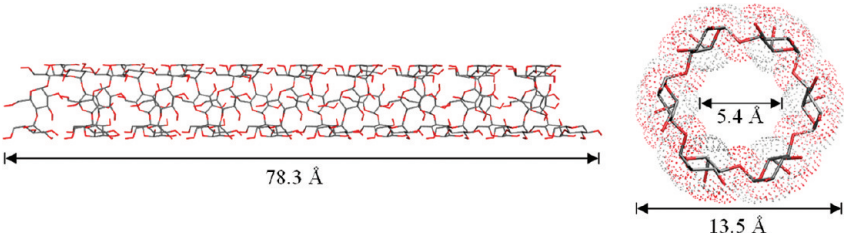

Figure 2. Views of the calculated amylose model. Lateral view and view along the helix axis (z axis) with an estimated molecular surface.

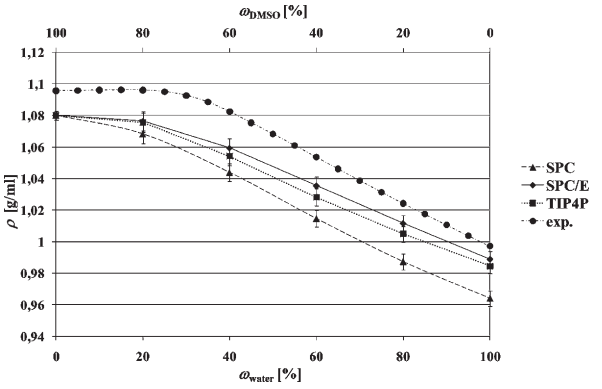

Figure 3. Density values from MD simulations and experimental data[37] versus mass fractions ω of water/DMSO in the solvent mixtures. The points were calculated as mean values of the trajectory (25 ns) of a given MD simulation, omitting an initial equilibration period of 0.2 ns. The error bars represent 2σ confidence intervals, with σ being the estimated standard deviation.

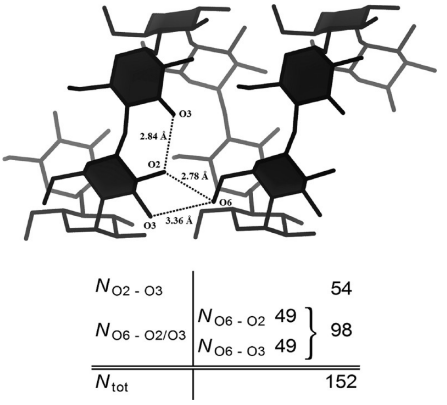

$N_{O2 - O3}$			54
$N_{O6 - O2/O3}$	$N_{O6 - O2}$	49	98
	$N_{O6 - O3}$	49	
N_{tot}			152

Figure 4. Schematic representation of the particular intramolecular hydrogen bonds in V-amylose and their respective length values. The table provides the absolute counts of the H bonds occurring in the used model structure (55 glucose residues).

time-dependent development, however, reveals significant differences. An illustration for this is shown in Figure 6, which depicts schematic snapshots of the amylose molecule at selected points in simulation time. In general, the total number of hydrogen bonds present in the amylose helix after its generation is already reduced to 80 in water and to 99 in DMSO, respectively, after initial equilibration with the steepest descent and conjugated gradient algorithms. In the following MD simulation using water, N_{tot} is reduced rather quickly after only 0.21 ns from 80 to 50 ($\equiv N_{tot}/N_{max} \approx 30\%$), resulting in a visible distortion of the helical structure, while in DMSO at the same time only a minor loss of H bonds and only slight deviations from the ideal helix can be recognized. It takes about 4.71 ns until the number of intramolecular H bonds in DMSO has reached a similar value (N_{tot} = 47). By this time, the structure in water already appears to be randomly orientated. Even after 25 ns, when the amylose model does not exhibit any obvious helix content anymore in either water or DMSO, there is still an unambiguously higher N_{tot} in the aprotic solvent DMSO as compared to water (17 versus 5). In this respect, it is noteworthy

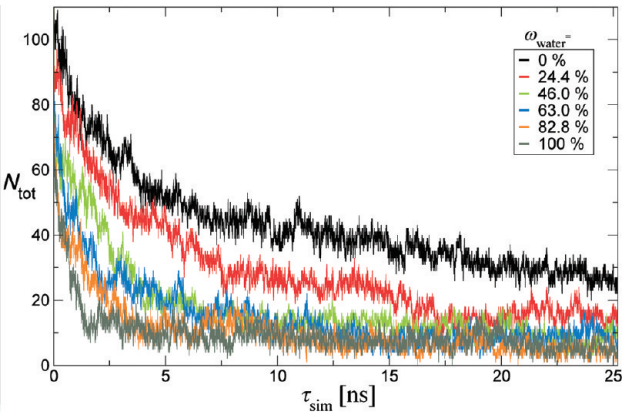

ω_{water} [%]	N_{tot} (25 ns)
0.0	21.70
24.4	14.74
46.0	10.44
63.0	7.48
82.8	9.90
100.0	7.72

Figure 5. Reduction of N_{tot} over time in one exemplary series of MD simulations in SPC/E water. The table provides values for N_{tot} after 25 ns averaged over all five simulations for each solvent mixture.

that the exemplary performed MD simulations of the systems in DMSO and water over a period of 100 ns show that even beyond 25 ns the numbers of H bonds continue to decrease, eventually leveling out near zero (Figure 7). A differentiation of amylose structures on the basis of intramolecular hydrogen bonds is then not possible anymore.

In the case of water, the substitution of intramolecular by intermolecular hydrogen bonds results in a considerable gain of Coulomb interactions for the amylose molecule (Figure 8). A comparison of the energy balances at the beginning ($\approx -11\,700$ kJ/mol) and at the end ($\approx -16\,600$ kJ/mol) of the 100 ns simulation time yields a benefit of around 4900 kJ/mol. In contrast, the unwinding of the helix in DMSO is obviously not energetically favorable in this context (deficit of 1300 kJ/mol), so there must be a considerable influence of entropic factors acting as a driving force for the decay process.

Considering the entire series of six different solvent compositions, one can detect a distinct gradual tendency in the rate of the helical decay. Essentially, the number of H bonds (N_{tot}) diminishes most rapidly in pure water and more slowly when the DMSO mass fraction ω_{DMSO} is increased. This is shown in Figure 9. Starting from pure DMSO, the simulation time τ_{sim} at which N_{tot} falls below values of 50%, 40%, and 30% of the original value N_{max} of 152 decreases with an increasing percentage of water. The shape of the three curves is very similar and indicates a gradual tendency of the decomposition

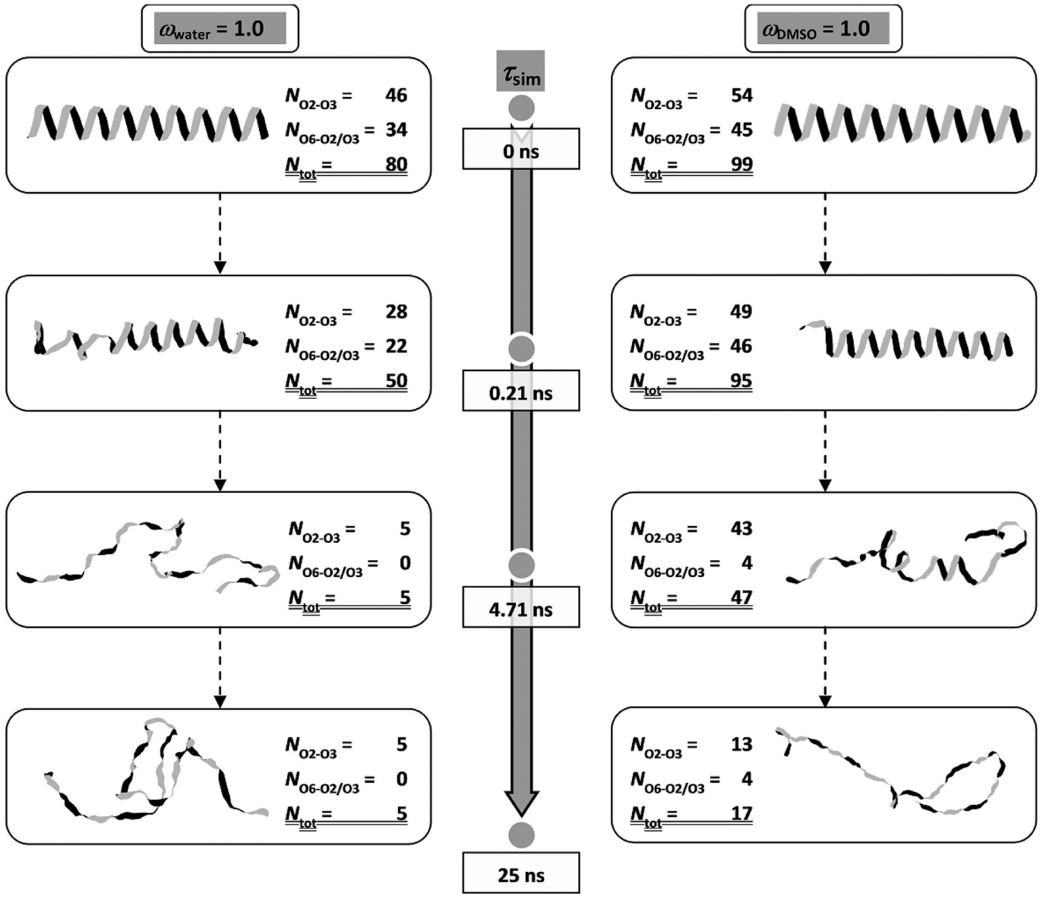

Figure 6. Corresponding snapshots of the amylose secondary structure (schematic) from two exemplary MD simulations in pure water (left) and pure DMSO (right). The depicted conformations were chosen at a point in simulation time where the ratio N_{tot}/N_{max} in the two solvents is 0.3, which is after 0.21 ns in water, while only after 4.71 ns in DMSO. In addition, the starting point is shown, i.e., after geometrical optimization using steepest descent and conjugated gradient energy minimization, as well as the end point of the simulation after 25 ns.

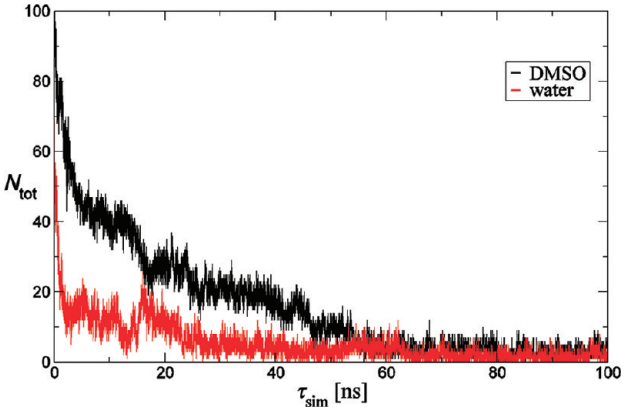

Figure 7. Development of N_{tot} over 100 ns in pure DMSO and pure water.

rate of the helical secondary structure depending on the solvent composition. Noteworthy is the change of the slope at $\omega_{water} \approx 63\%$, which resembles the discontinuities in a number of physical properties of amylose reported in the literature.[20,6] In addition, the results compare well to the experimental finding that an amylose helix is more stable in 80% to 100% DMSO than in water.[40,20]

This behavior can be explained by comparing the interaction of the two solvents, water and DMSO, with the amylose helix (Figures 10 and 11). The water molecule is strongly dipolar and is capable of forming a maximum of four hydrogen bonds at a time, two as a hydrogen donor and two as a hydrogen acceptor. Furthermore, it is small enough to deeply intrude into the polysaccharide's secondary structure, thereby weakening the intramolecular hydrogen bond network. DMSO, on the other hand, is equally polar but can only act as a 2-fold hydrogen bond acceptor. In addition, occupying a van der Waals volume about 4.5 times as high as that of water, and featuring a rather branched structure, DMSO is by far the bulkier molecule. Due to this sterical hindrance, it is impossible for DMSO to bind to each of the hydroxyl groups on the amylose surface (Figure 11). Nevertheless, it is conceivable that one DMSO molecule for instance simultaneously binds both OH2 and OH3 of one single or two adjacent glucose molecules. However, such an intensive interaction would create a rather unfavorable situation as it would lower the partial negative charge of the DMSO oxygen and thus would result in two rather weak H bonds. Instead, a more convenient situation would exist, if one DMSO molecule each attached to only one or two of the three different hydroxyl groups in the amylose chain, since this would leave two or at least one OH group per glucose residue free, which in turn would then be available for intramolecular hydrogen bonding. This results in a

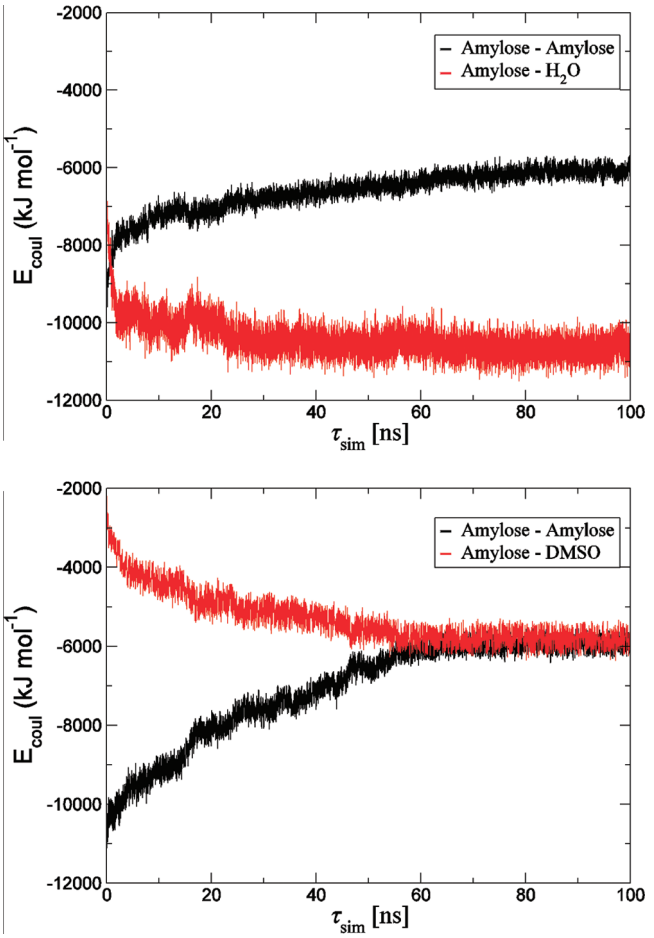

Figure 8. Intra- and intermolecular Coulomb interaction energies of amylose over 100 ns in pure DMSO and pure water.

strengthening effect of cooperative hydrogen bonding described in the literature.[40]

As a result, after equilibration of the water box including the OH groups of amylose with an otherwise constrained helical structure, we find water molecules within H bond distance to every hydroxyl group of amylose. In a representative snapshot of this simulation, shown in Figure 10, one can see that at a given time adjacent OH2 and OH3 groups can simultaneously be hydrated by water molecules, independent of being situated on adjacent glucose residues (A) or on the same residue (B). The spatial demand of water is small enough that the OH6 groups close by are at the same time also hydrated and are in some cases even coordinated by two water molecules (C).

In contrast, as DMSO molecules are about 4.5 times as voluminous as water molecules and can only act as a 2-fold direction-dependent hydrogen bond acceptor, DMSO only incompletely binds the amylose hydroxyl groups, and there are always one or two OH groups free per glucose unit. As a result, we find a lower molar density of DMSO on the helix surface as compared to that of water (Figure 11).

Interestingly, the graph in Figure 9 shows a strongly nonlinear behavior for the disruption of the helical structure, featuring a very flat slope in the region of $\omega_{water} \gtrsim 60\%$ and a rapid increase when more DMSO is added to the mixture, indicating that there is a limiting concentration of DMSO above which the decay of intramolecular hydrogen bonds in amylose is progressively

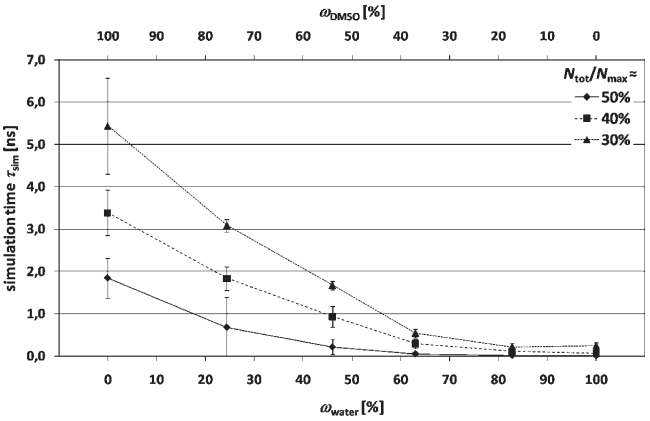

Figure 9. Average simulation period for a reduction of N_{tot}/N_{max} below values of about 50%, 40%, and 30% of the initial value as a function of solvent composition. For example, the upper line gives the results for the six solvent mixtures used from pure DMSO (left) to pure water (right) and indicates the average point in simulation time at which the total number of intramolecular H bonds of amylose N_{tot} in the given solvent mixture has decreased to 30% of its initial value (N_{max} = 152).

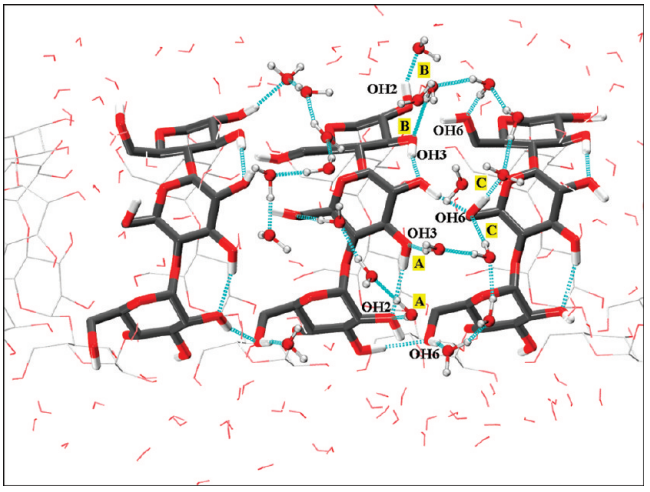

Figure 10. Orthographic snapshot of a V-amylose molecule solvated by water. Dashed lines (cyan) indicate hydrogen bonds. For the sake of clarity, only selected water molecules are drawn in CPK style. Due to their small size and ability to donate and accept hydrogen bonds in four different directions, water molecules can bind theoretically every hydroxyl group of amylose at one time. The picture shows examples for simultaneous hydration of OH2 and OH3 on adjacent glucose residues (A) as well as on the same residue (B). The respective opposing OH6 groups are also in a hydrated state, in one case even coordinated by two water molecules (C).

decelerated. Qualitatively similar discontinuities have been observed for a number of physical properties of amylose in the regarded binary system, such as limiting viscosity[20] and specific optical rotation.[6] Moreover, evidence has been presented that a minimum volume fraction of ~60% water (equivalent to $\omega_{water} \approx 0.6$) is necessary for amylose to be capable of forming detectable complexes with butanol[20] or iodine.[18,20] These observations have partially been attributed to the relative effectiveness of water and DMSO in solvating amylose, i.e., a competitive behavior of the two solvents.[18,20] Accordingly, the role of water in the

solvation of amylose and its influence on the helical structure can be considered to be predominant over that of DMSO exclusively in the region of $\omega_{water} \gtrsim 60\%$, which is equivalent to a molar ratio of water/DMSO of at least 6:1 and essentially coincides with the flat region of the curves in Figure 9.

At higher DMSO concentrations, there is presumably not enough free water present for an effective amylose hydration due to the formation of DMSO hydrates. Data on excess heat of mixing, density, and viscosity[41] as well as NMR[42] and neutron diffraction experiments[43,44] and molecular dynamics simulations[43,45−47] have revealed that these water−DMSO complexes consist of two or three water molecules attached to one single DMSO molecule strongly stabilized by hydrogen bonds. The higher basicity of the DMSO oxygen in comparison with the water oxygen makes it a better acceptor for available hydrogen bonds, consequently making the DMSO hydrates more energetically favorable than just water−water interactions. The reduced number of mobile water molecules in the mixture results in decreased stress on the intramolecular hydrogen bonding network of amylose. It is even conceivable that DMSO hydrates interact with amylose hydroxyl groups in a similar way as DMSO molecules do, thereby strengthening the remaining amylose H bonds.[40] Hence, the predefined helical conformation is degraded at a lesser rate than in pure water.

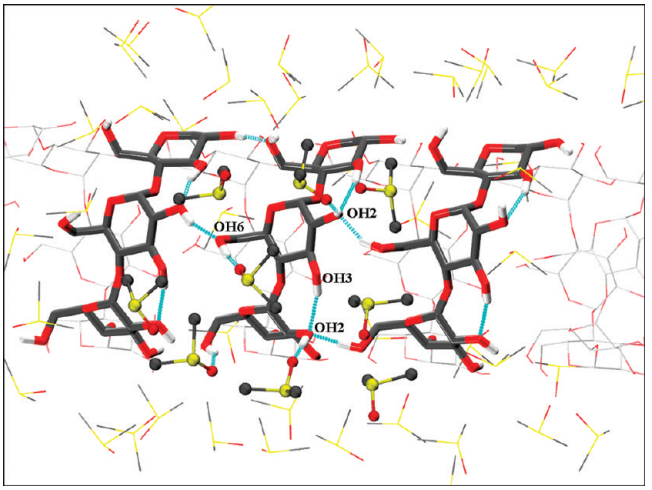

Figure 11. Orthographic snapshot of a V-amylose molecule solvated by DMSO. Dashed lines (cyan) indicate hydrogen bonds. For the sake of clarity, only selected DMSO molecules are drawn in CPK style. Note the lower molar density of DMSO on the helix surface as compared to that of water (Figure 10).

Above the threshold of $\omega_{DMSO} \approx 80\%$, which corresponds to a molar ratio of DMSO/water of about 1:1, solvation of amylose by free DMSO may be expected to predominate over solvation by water and hydrated DMSO, respectively, particularly since DMSO is the stronger hydrogen bond acceptor than water.[40] This leaves a large percentage of the amylose H-bonding network intact, which yields a further increase in conformational stability accompanied by another rise in the slope of the time graphs in Figure 9.

Differentiation of Hydrogen Bonds. The differentiation of the intramolecular hydrogen bonds was made in terms of interturn and intraturn character, referring to turns as the repetitive loops of the helical structure. O6−O2 and O6−O3 H bonds were treated as equivalent since either of them represents an interturn connection within the same pair of glucose residues (Figure 4).

Figure 6 reveals that O2−O3 and O6−O2/3 H bonds are degraded at unequal rates, in water as well as in DMSO. At the starting point (0 ns), i.e., after energy minimization, more than half of the O6−O2/3 H bonds have already been destroyed, probably in part due to the fact that one of the two bonds had to be considered weak even in the underlying crystal structure.

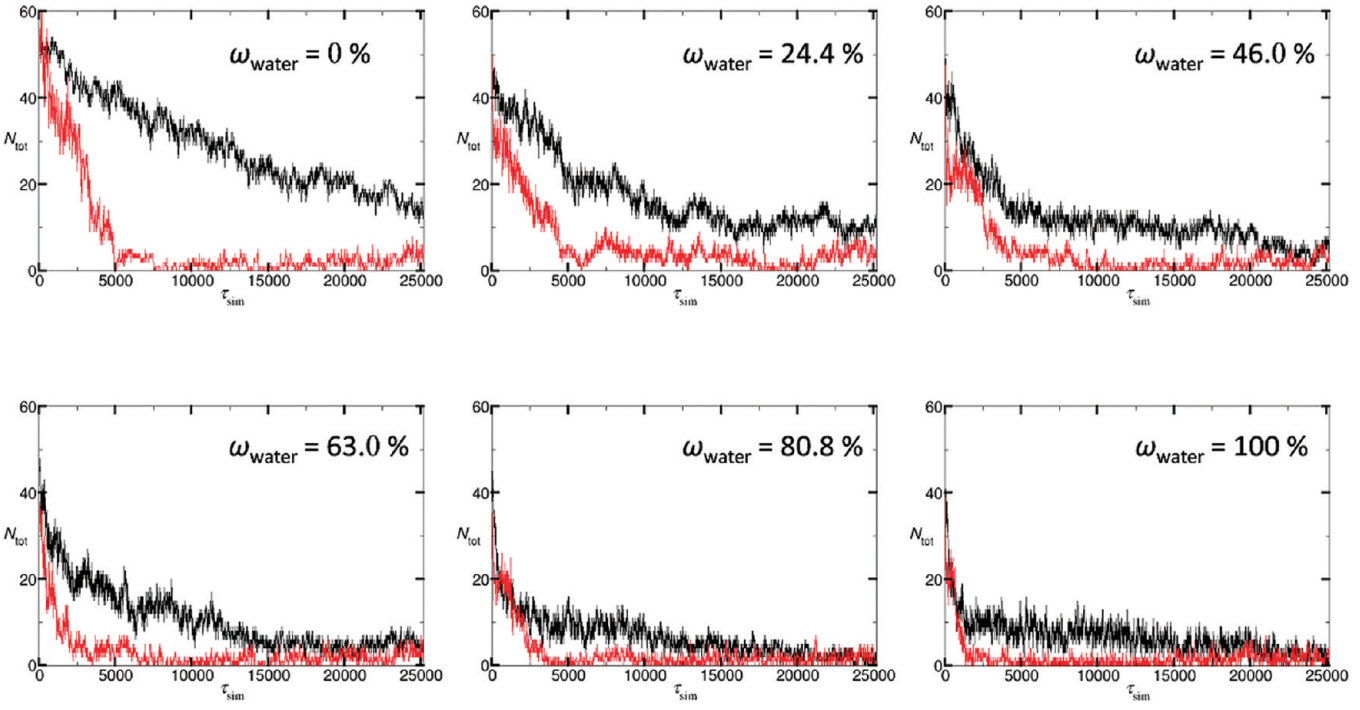

Figure 12. Total number of H bonds N_{O2-O3} (black) and $N_{O6-O2/3}$ (red) versus simulation time (ps). Each of the six solvent ratios investigated is shown as a representative graph from the series of five MD simulatons.

dx.doi.org/10.1021/ct2005159 |J. Chem. Theory Comput. 2011, 7, 2919–2928

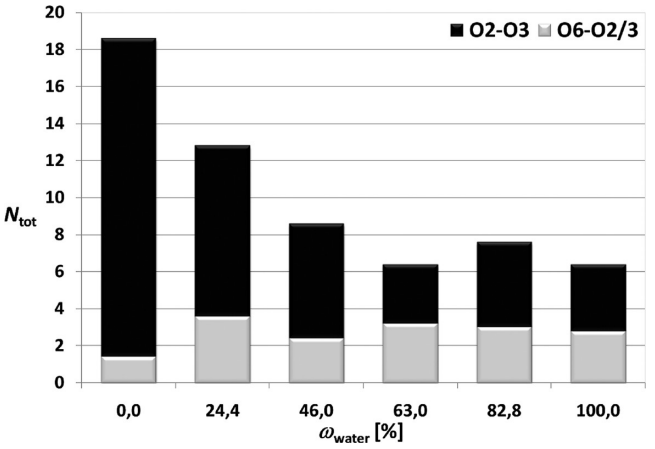

Figure 13. Average numbers of inter- and intraturn H bonds vs ω_{water} obtained after a simulation time of 25 ns.

In the following simulation period, there is a permanent dominance of intraturn over interturn H bonds. In water, this remains on the same order of magnitude, while in DMSO, it distinctly increases between 0.21 and 4.71 ns. From that point on to the end of the simulation, the difference diminishes in DMSO as the remaining number of O6−O2/3 H bonds is close to zero anyway.

The time dependence of inter- and intraturn H bonds is given in Figure 12. While each solvent system was simulated in a series of five MD simulations, the graphs show the data of only one representative exemplary simulation. Generally, the impression of a dominance of O2−O3 over O6−O2/3 H bonds is confirmed here, which implies that the intraturn H bonds are retained longer than the interturn ones. From this, it can be hypothesized that the first step of the helix degradation consists of a widening of the helical pitch by breaking the interturn H bonds directed along the z axis, meaning that the helix loses its compactness in this direction.

The degree of helical curvature depends on the orientation of subsequent glucose residues toward each other, i.e., basically on the glycosidic angles ϕ and ψ. Alterations of these angles directly influence the length and thus the stability of the O2−O3 H bond but do not implicitly break it within a certain margin. The overall conformational changes that result from the sum of many of these small torsional alterations across the amylose chain are of course much more significant. As the O6−O2/3 H bonds are situated between different turns of the helix and are therefore much more conformation dependent than the relatively fixed O2−O3 H bonds, one can expect a greater distortion for these. This explains the longer conservation of intraturn H bonds as compared to interturn ones.

The dominance of O2−O3 over O6−O2/3 H bonds as seen in Figures 6 and 13 and its chronological development is by far most significant for pure DMSO and is gradually reduced along with the increasing percentage of water. As the helical loops start to come apart, the sterically demanding DMSO molecules can first of all solvate the OH6 group, having a rather exposed location remote from the glucose ring. OH2 and OH3, in contrast, cannot be solvated simultaneously, at least not until the amylose chain becomes further unfolded and is completely surrounded by the solvent. In the process of helix degradation, this leads to an increased tendency of DMSO for breaking interturn H bonds. The smaller water molecules (free or in DMSO hydrates) on the other hand can readily solvate OH2 and

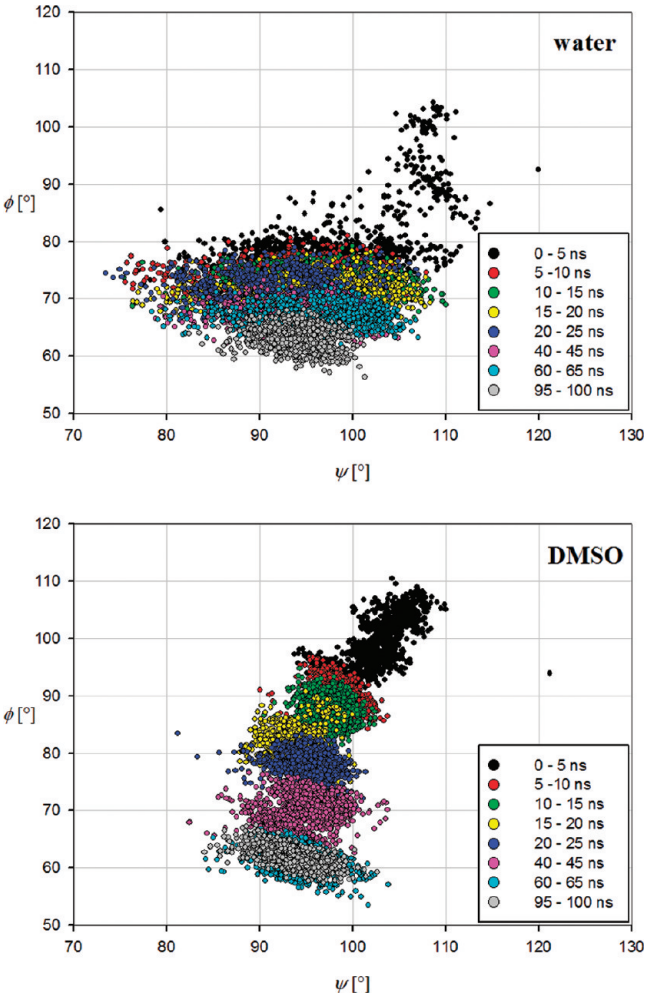

Figure 14. Time-dependent development of the glycosidic torsion angles ϕ (O5−C1−O4−C4) and ψ (C1−O4−C4−C3) in 100 ns simulations using water and DMSO as solvents, respectively. Data points are shown in differently colored time intervals of 5 ns. For the sake of clarity, only selected time intervals are shown in the region between 25 and 100 ns.

OH3 at the same time so that the preference for solvation of OH6 is not as pronounced as in pure DMSO.

Furthermore, this effect can also clearly be seen at the end of the simulation. Figure 13 shows that after a simulation period of 25 ns the average $N_{O6-O2/3}$ of each of the six solvent mixtures is not higher than 3.6. With regard to the standard deviation ranging from 1.1 for ω_{water} = 63% to 2.8 for ω_{water} = 100%, the difference of interturn H bonds between the solvent systems is statistically identical. There is, however, the expected trend in the respective N_{O2-O3} values. While there is a comparatively high average value of 17.2 for ω_{water} = 0%, it gradually decreases to values between 3 and 5 for ω_{water} = 63% to 100%. This curve shape obviously corresponds to the graphs in Figure 9 and may similarly be interpreted taking into account the specific hydrogen bonding capacities, steric features, and mixture characteristics of the two solvents, water and DMSO.

A general aspect of the parameter N_{tot} and its use in describing the helix character of amylose becomes apparent in the differentiation of hydrogen bonds as shown in Figures 6, 12, and 13. The exemplary amylose structures at 0.21 and 4.71 ns in water

and DMSO, respectively, are rated as very similar in terms of N_{tot} despite being conformationally rather different. A numerical difference only becomes visible on inspection of N_{O2-O3} and $N_{O6-O2/3}$. While in water, the numbers are on the same order of magnitude, N_{tot} in DMSO is almost exclusively based on O2−O3 H bonds. This finding demonstrates that the total number of intramolecular hydrogen bonds N_{tot} only to some extent correctly describes a generally defined "helical content" in the conformation of amylose. An exhaustive comparison of two such conformations in terms of their helix character, therefore, requires a weighting of the particular interturn and intraturn summands of N_{tot}.

This can alternatively be analyzed by evaluating the glycosidic torsion angle distribution, which is depicted in Figure 14 for the two 100 ns simulations in pure water and pure DMSO. In either case, the helical degradation is characterized by distinct changes of the dihedral angles ϕ (O5−C1−O4−C4) and ψ (C1−O4−C4−C3). Especially ϕ undergoes a pronounced decrease, namely, from an average 107° (τ_{sim} = 0 to 0.1 ns) to an average 62° (95 to 100 ns) in DMSO and from 102° to 63° in water. The major part of this development proceeds during the first 5 ns of the simulation in water, whereas the process is more extended in DMSO, which parallels the pathways of the respective number of intramolecular H bonds N_{tot} (Figure 7).

CONCLUSION

Modeling of Amylose Structures. In spite of the extensive research on structural features of V-amylose, the availability of atomic coordinates for this system is rather limited. X-ray and electron diffraction data in the literature[1−4] yield structural data of one glucose unit and do not provide atomic data for an amplified structure of monomers in either one of the known amylose conformations. Building an idealized model structure of customized length, as the one used in this study, therefore requires the utilization of adequate crystallographic software that allows performing the respective symmetry operations in order to generate a molecule coordinate file. As an alternative, the rather simple linear algebraic approach presented in this work has the advantage that it can technically be managed by a common spreadsheet program or even a programmable calculator.

Modeling of Water/DMSO Mixtures. In preparation for our studies on the behavior of an amylose helix in water, DMSO, and various mixtures thereof, we have compared the performances of three water models (SPC,[24,25] SPC/E,[26] and TIP4P[27]) in terms of their ability to reproduce an experimental density record[37] of various water DMSO mixtures by molecular dynamics procedures (Figure 3). All three models reproduce the known nonlinear density behavior of the considered series of binary solvent mixtures to a satisfactory degree. Despite its lower level of complexity as compared to TIP4P, the SPC/E model provides the best approximation to the experimental density curve. It can thus be recommended for being used in simulations of water DMSO mixtures employing the DMSO model by Geerke et al.[23]

Amylose MD Simulations. Our results suggest that with enough time given for interaction between amylose and the solvent the helix is not stable in either water or DMSO and rather unfolds to a randomly coiled structure. The intramolecular H bonds between OH2 and OH3, OH6 and OH2, and OH6 and OH3 hydroxyl groups of adjacent glucose residues, which are responsible for maintaining the helical structure, are lost in favor of intermolecular H bonds between the solvent and the OH groups of amylose combined with a gain in entropy. We can reproduce the experimentally known difference in helix stability[20,40] with a progressively faster disruption of the helical structure with an increasing percentage of water in water/DMSO mixtures, as shown in Figures 6 and 9. While Figure 6 gives a good visual impression of the different behavior of the amylose helix in water and DMSO, respectively, the strongly nonlinear behavior of the graph in Figure 9 even reflects the observed discontinuities in physical properties of the system described in the literature, such as limiting viscosity,[20] specific optical rotation,[6] and the ability to form detectable complexes with butanol[20] or iodine.[18,20] Obviously, water molecules promote the helix decay due to their small size and increased hydrogen bonding capabilities as compared with DMSO molecules. Between approximately 40% and 80% DMSO, the formation of DMSO hydrates decelerates the helix degradation by reducing the number of free water molecules, and above 80% DMSO, the excess of DMSO molecules leads to another even more distinct deceleration of the process.

Our modeling results furthermore can differentiate between the types of H bonds involved in stabilizing the helical amylose structure. We can show that there is a dominance of O2−O3 versus O6−O2/3 H bonds of adjacent glucose residues; i.e., the intraturn H bonds are more stable than the interturn ones (Figures 6, 13). This result suggests that helix degradation begins with a widening of the helical pitch by breaking the interturn H bonds directed along the z axis, accompanied by a loss of compactness in this direction. On account of the higher steric demand of DMSO molecules relative to water molecules, their preference for breaking O6−O2/3 H bonds is considerably more significant, especially as the OH6 groups are more readily accessible than the OH2 and OH3 groups close to the glucose ring.

In summary, our simulations show that, independent of the solvent, the helical structure is destroyed in water as well as in DMSO, with the distinct difference of a slower interference of DMSO with the structure preserving intramolecular H bonds of amylose. In the long run, however, the vast excess of solvent molecules substitutes the intra- with intermolecular H bonds, which is driven by entropic factors.

A stable V-helical amylose structure, therefore, requires more stabilization than can be derived from intermolecular H bonds. The most commonly known example is of course the well-known complex of iodine and starch.[48,49]

Stabilization in this case is gained from the inside of the helix as amylose and iodine form an inclusion complex. Such complexes are also known with organic compounds, even as small as butanol.[50] More prominent examples, however, are inclusion complexes from amylose and fatty acids or fatty alcohols[51] and those formed by vine-twining polymerization, when glucose is enzymatically polymerized around synthetic polymers.[52,53] These systems are of great potential industrial use, and simulations along these lines are, therefore, in progress in our laboratory.

AUTHOR INFORMATION

Corresponding Author
*E-mail: fels@uni-paderborn.de.

REFERENCES

(1) Rappenecker, G.; Zugenmaier, P. *Carbohydr. Res.* **1981**, *89*, 11–19.
(2) Winter, W. T.; Sarko, A. *Biopolymers* **1974**, *13*, 1461–1482.

(3) Murphy, V. G. *Biopolymers* **1975**, *14*, 1487–1501.
(4) Brisson, J.; Chanzy, H.; Winter, W. T. *Int. J. Biol. Macromol.* **1991**, *13*, 31–39.
(5) Brant, D. A.; Dimpfl, D. L. *Macromolecules* **1970**, *3* (5), 655–664.
(6) Dintzis, F. R.; Tobin, R. *Biopolymers* **1969**, *7*, 581–593.
(7) Elmgren, H. *Biopolymers* **1984**, *23*, 2525–2541.
(8) Jordan, R. C.; Brant, D. A.; Cesàro, A. *Biopolymers* **1978**, *17*, 2617–2632.
(9) Gagnaire, D.; Pérez, S.; Tran, V. *Carbohydr. Polym.* **1982**, *2*, 171–191.
(10) Kitamura, S.; Okamoto, T.; Nakata, Y.; Hayashi, T.; Kuge, T. *Biopolymers* **1987**, *26*, 537–548.
(11) Everett, W. W.; Foster, J. F. *J. Am. Chem. Soc.* **1959**, *81*, 3464–3469.
(12) Banks, W.; Greenwood, C. T. *Carbohydr. Res.* **1968**, *7* (4), 414–420.
(13) Cowie, J. M. G. *Makromol. Chem.* **1961**, *42*, 230–247.
(14) Fujii, M.; Honda, K. *Biopolymers* **1973**, *12*, 1177–1195.
(15) Sugiyama, H.; Nitta, T.; Horii, M.; Motohashi, K.; Sakai, J.; Usui, T.; Hisamichi, K.; Ishiyama, J. *Carbohydr. Res.* **2000**, *325*, 177–182.
(16) Nakanishi, Y.; Norisuye, T.; Teramoto, A. *Macromolecules* **1993**, *26*, 4220–4225.
(17) St-Jacques, M.; Sundararajan, P. R.; Taylor, K. J.; Marchessault, R. H. *J. Am. Chem. Soc.* **1976**, *98*, 4386–4391.
(18) Peng, Q.-J.; Perlin, A. S. *Carbohydr. Res.* **1987**, *160*, 57–72.
(19) Perez, S.; Vergelati, C. *Polym. Bull.* **1987**, *17*, 141–148.
(20) Cheetham, N. W. H.; Tao, L. *Carbohydr. Polym.* **1998**, *35*, 287–295.
(21) Van Der Spoel, D.; Lindahl, E.; Hess, B.; Groenhof, G.; Mark, A. E.; Berendsen, H. J. *J. Comput. Chem.* **2005**, *26*, 1701–1718.
(22) van Gunsteren, W. F.; Billeter, S. R.; Eising, A. A.; Hünenberger, P. H.; Krüger, P.; Mark, A. E.; Scott, W. R.; Tironi, I. G. *vdf Hochschulverlag*; ETH: Zürich, Switzerland, 1996.
(23) Geerke, D. P.; Oostenbrink, C.; Vegt, N. F.; Gunsteren, W. F. *J. Phys. Chem. B.* **2004**, *108*, 1436–1445.
(24) Berendsen, H. J.; Postma, J. P.; van Gunsteren, W. F.; Hermans, J. *Intermolecular Forces*; Pullman, B., Ed.; Reidel: Dordrecht, Holland, 1981; pp 331−342.
(25) Ferguson, D. M. *J. Comput. Chem.* **1995**, *16*, 501–511.
(26) Berendsen, H. J. C.; Grigera, J. R.; Straatsma, T. P. *J. Phys. Chem.* **1987**, *91*, 6269–6271.
(27) Jorgensen, W. L.; Chandrasekhar, J.; Madura, J. D.; Impey, R. W.; Klein, M. L. *J. Chem. Phys.* **1983**, *79*, 926–935.
(28) Lins, R. D.; Hünenberger, P. H. *J. Comput. Chem.* **2005**, *26*, 1400–1412.
(29) Van Gunsteren, W. F.; Berendsen, H. J. *Mol. Simul.* **1988**, *1*, 173–185.
(30) Bussi, G.; Donadio, D.; Parrinello, M. *J. Chem. Phys.* **2007**, *126*, 14101–14108.
(31) Berendsen, H. J.; Postma, J. P.; van Gunsteren, W. F.; DiNola, A.; Haak, J. R. *J. Chem. Phys.* **1984**, *81*, 3684–3690.
(32) Riddick, J. A.; Bunger, W. B.; Sakand, T. K. *Organic Solvents: Physical Properties and Methods of Puification*; John Wiley and Sons: New York, 1986.
(33) Kell, G. S. J. *J. Chem. Eng. Data* **1967**, *12*, 66–69.
(34) Hess, B.; Bekker, H.; Berendsen, H. J.; Fraaije, J. G. *J. Comput. Chem.* **1997**, *18*, 1463–1472.
(35) van Gunsteren, W. F.; Berendsen, H. J. *Angew. Chem., Int. Ed.* **1990**, *29*, 992–1023.
(36) Tironi, I. G.; Sperb, R.; Smith, P. E.; van Gunsteren, W. F. *J. Chem. Phys.* **1995**, *102*, 5451–5459.
(37) LeBel, R. G.; Goring, D. A. *J. Chem. Eng. Data* **1962**, *7*, 100–101.
(38) Immel, S.; Lichtenthaler, F. W. *Starch/Stärke* **2000**, *52*, 1–8.
(39) Jeffrey, G. A. *An Introduction to Hydrogen Bonding*; Oxford University Press: New York, 1997.
(40) Erlander, S. R.; Tobin, R. *Makromol. Chem.* **1968**, *111*, 194–211.
(41) Cowie, J. M. G. *Can. J. Chem.* **1961**, *39*, 2240–2243.
(42) Glasel, J. A. *J. Am. Chem. Soc.* **1970**, *92*, 372–375.
(43) Soper, A. K.; Luzar, A. *J. Phys. Chem.* **1996**, *100*, 1357–1367.
(44) Soper, A. K.; Luzar, A. *J. Chem. Phys.* **1992**, *97*, 1320–1331.
(45) Luzar, A.; Chandler, D. *J. Chem. Phys.* **1993**, *98*, 8160–8173.
(46) Vaisman, I. I.; Berkowitz, M. L. *J. Am. Chem. Soc.* **1992**, *114*, 7889–7896.
(47) Borin, I. A.; Skaf, M. S. *J. Chem. Phys.* **1999**, *110*, 6412–6420.
(48) Saenger, W. *Naturwissenschaften* **1984**, *71* (1), 31–36.
(49) Moulik, S. P.; Gupta, S. *J. Sci. Ind. Res.* **1986**, *45*, 173–178.
(50) Schoch, T. J. *Adv. Carbohydr. Chem.* **1945**, *1*, 247–277.
(51) Nimz, O.; Gessler, K.; Uson, I.; Sheldrick, G. M.; Saenger, W. *Carbohydr. Res.* **2004**, *339*, 1427–1437.
(52) Kaneko, Y.; Saito, Y.; Nakaya, A.; Kadokawa, J.-I.; Tagaya, H. *Macromolecules* **2008**, *41*, 5665–5670.
(53) Kaneko, Y.; Beppu, K.; Kadokawa, J.-I. *Biomacromolecules* **2007**, *8* (10), 2983–2985.

JCTC Journal of Chemical Theory and Computation

ARTICLE

pubs.acs.org/JCTC

Benchmarking Semiempirical Methods for Thermochemistry, Kinetics, and Noncovalent Interactions: OMx Methods Are Almost As Accurate and Robust As DFT-GGA Methods for Organic Molecules

Martin Korth* and Walter Thiel*

Max-Planck-Institut für Kohlenforschung, Kaiser-Wilhelm-Platz 1, 45470 Mülheim an der Ruhr, Germany

ABSTRACT: Semiempirical quantum mechanical (SQM) methods offer a fast approximate treatment of the electronic structure and the properties of large molecules. Careful benchmarks are required to establish their accuracy. Here, we report a validation of standard SQM methods using a subset of the comprehensive GMTKN24 database for general main group thermochemistry, kinetics, and noncovalent interactions, which has recently been introduced to evaluate density functional theory (DFT) methods (*J. Chem. Theory Comput.* **2010**, *6*, 107). For all SQM methods considered presently, parameters are available for the elements H, C, N, and O, and consequently, we have extracted from the GMTKN24 database all species containing only these four elements (excluding multireference cases). The resulting GMTKN24-hcno database has 370 entries (derived from 593 energies) compared with 715 entries (derived from 1033 energies) in the original GMTKN24 database. The current benchmark covers established standard SQM methods (AM1, PM6), more recent approaches with orthogonalization corrections (OM1, OM2, OM3), and the self-consistent-charge density functional tight binding method (SCC-DFTB). The results are compared against each other and against DFT results using standard functionals. We find that the OMx methods outperform AM1, PM6, and SCC-DFTB by a significant margin, with a substantial gain in accuracy especially for OM2 and OM3. These latter methods are quite accurate even in comparison with DFT, with an overall mean absolute deviation of 6.6 kcal/mol for PBE and 7.9 kcal/mol for OM3. The OMx methods are also remarkably robust with regard to the unusual bonding situations encountered in the "mindless" MB08−165 test set, for which all other SQM methods fail badly.

1. INTRODUCTION

Semiempirical quantum mechanical (SQM) methods are based on self-consistent-field molecular orbital theory. They employ a minimal valence basis set, integral approximations, and parametrized matrix elements that are normally fitted against experimental data. The most popular SQM methods make use of the NDDO (neglect of diatomic differential overlap) integral approximation as implemented in the MNDO (modified neglect of differential overlap) model,[1] for example, AM1,[2] PM3,[3] and PM6.[4] More recent NDDO-based approaches go beyond the MNDO model by including orthogonalization corrections into the Fock matrix. OM1[5] incorporates these corrections only in the one-center part of the core Hamiltonian matrix, while OM2[6,7] and OM3[8] include them also in the two-center part. OM3 differs formally from OM2 by neglecting some of the smaller correction terms, which results in a speedup without loss of accuracy.[8,9]

SQM methods are widely applied as an efficient tool in computational studies of large molecules, and there are several reviews that describe the underlying theory and typical applications.[10−15] In their formalism, they retain the essential physics of molecular systems by variationally optimizing the electronic wave function (thereby taking into account, for example, polarization and charge transfer effects). However, the severe approximations adopted in these methods must cause errors which can only partially be compensated for by the parametrization against (mostly experimental) reference data. Careful validation of SQM methods is thus essential to establishing their accuracy and robustness, and corresponding evaluations are available for all popular SQM methods. These evaluations normally utilize benchmark data sets assembled in the SQM community[2−4,8,9,16−19] as well as data commonly used in the ab initio and DFT communities like the G2 and G3 sets.[20−22]

Validations of existing SQM methods need to be updated when more comprehensive and/or more accurate benchmark data sets become available. In this article, we report the results of such an evaluation against the recently proposed GMTKN24 database[23] for two of the established MNDO-type methods (AM1, PM6) and three NDDO-based methods with orthogonalization corrections (OM1, OM2, OM3). AM1 is still the most widely used SQM method, PM6 is the latest and most refined parametrization of MNDO-type models, and the methods of the OMx family have been most promising in previous SQM validations.[9] In our comparisons, we include the self-consistent-charge density functional tight binding (SCC-DFTB) method,[24] which is derived within a simplified DFT formalism but shares many features with standard SQM methods.[9] Furthermore, we also address the performance of standard DFT methods (PBE,[25] B3LYP[26,27]) to put the SQM results into perspective.

2. THE GMTKN24 BENCHMARK DATABASE

Recently, Goerigk and Grimme introduced a comprehensive quantum chemistry benchmark database for general main group thermochemistry, kinetics, and noncovalent interactions named GMTKN24.[23] It consists of 24 different, chemically relevant subsets that are either taken from the literature or compiled

Received: June 22, 2011
Published: August 05, 2011

Table 1. Description of the Subsets within the GMTKN24-hcno Database[a]

set	description	no. entries (orig.[b])	av. energy	reference data
ACONF	relative energies of alkane conformers	15(15)	1.8	W1h-val
BH76RC	reaction energies of the BH76 set	17(30)	21.5	W1 and theor. est.
BH76	barriers of substitution and association reactions	38(76)	18.5	W1 and theor. est.
BHPERI	barriers of pericyclic reactions	22(26)	19.4	W1 and CBS-QB3
DARC	reaction energies of Diels−Alder reactions	14(14)	32.2	est. CCSDT/CBS
DC9	nine difficult cases for DFT	6(9)	35.7	theor. and expt.
G21EA	adiabatic electron affinities	11(25)	33.6	exptl.
G21IP	adiabatic ionization potentials	13(36)	250.8	exptl.
G2RC	reaction energies of selected G2/97 systems	12(25)	50.6	exptl.
IDISP	intramolecular dispersion interactions	6(6)	14.1	theor. and exptl.
ISO34	isomerization energies of organic molecules	34(34)	14.3	exptl.
MB08−165	decomposition energies of artificial molecules	21(165)	117.2	est. CCSD(T)/CBS
O3ADD6	energies and barriers for ozone reactions	6(6)	22.7	est. CCSD(T)/CBS
PA	adiabatic proton affinities	8(12)	174.9	est. CCSD(T)/CBS and W1
PCONF	relative energies of tripeptide conformers	10(10)	1.5	est. CCSD(T)/CBS
RSE43	radical stabilization energies	28(43)	7.5	est. CCSD(T)/CBS
S22	binding energies of noncovalently bound dimers	22(22)	7.4	est. CCSD(T)/CBS
SCONF	relative energies of sugar conformers	17(17)	4.9	est. CCSD(T)/CBS
SIE11	self-interaction error related problems	4(11)	34.0	est. CCSD(T)/CBS
W4−08woMR	atomization energies of small molecules	39(83)	237.5	W4
WATER27	binding energies of water/H^+/OH^- clusters	27(27)	82.0	est. CCSD(T)/CBS; MP2/CBS

[a] Based on a similar table in ref 23. [b] Number of entries in the full GMTKN24 database.

specifically for the purpose of benchmarking. It includes both theoretical or experimental reference values. When running the full benchmark (including multireference cases), 1049 single-point calculations are needed to determine 731 relative energies, which can then be compared with the accurate reference data. Extensive tests have shown the chemical relevance of the GMTKN24 database and its usefulness for evaluating the overall performance of theoretical methods. Goerigk and Grimme recommend validation against their benchmark data for the evaluation of the "true" performance of new quantum mechanical methods.[23]

Table 1 lists, in alphabetical order, the 21 subsets of the GMTKN24 database that contain molecules consisting only of the elements H, C, N, and O (excluding three presently irrelevant subsets without such molecules). Several subsets focus on noncovalent interactions and conformational preferences (ACONF, IDISP, PCONF, S22, SCONF, WATER27). Others address reaction, isomerization, and atomization energies (BH76RC, DARC, G2RC, ISO34, W4−08); barrier heights (BH76, BHPERI); electron affinities (G21EA); ionization potentials (G21IP); proton affinities (PA); and radical stabilization energies (RSE43), and there are two sets that collect difficult cases for DFT methods (DC9, SIE11). The MB08−165[28] subset is special in that it is based on a diversity-oriented approach. It consists of randomly generated artificial molecules which are constructed by applying systematic constraints (rather than any chemical bias) to open the narrow structural space of chemical intuition and to produce "electronically difficult" species with unusual and diverse geometries. The artificial molecules in the MB08−165 subset contain eight main-group atoms and are of single-reference character. The MB08−165 reference data are reaction energies for decomposition into small hydrides and diatomics obtained from coupled cluster [CCSD(T)] calculations with complete basis set (CBS) extrapolation.[28] The performance for the MB08−165 subset is considered to be a good indicator for general robustness in diverse chemical applications; this is supported by the finding that the performance ranking for DFT functionals is similar for the MB08−165 subset and for the whole GMTKN24 database, indicating the usefulness of this "mindless" benchmark for a quick performance assessment.[23,28]

In the original GMTKN24 publication, the authors used mean absolute deviations (MADs) in their comparisons for individual subsets and weighted total MADs (WTMADs) in their overall statistical analysis.[23] WTMADs take into account the number of entries in the test set (like a simple overall MAD would) but also subset-specific factors defined as the ratio between the corresponding MADs for the BLYP and B2PLY-D methods, in order to capture the "difficulty" of a certain subset and the importance of crucial dispersion interactions. Because of the large difference in the accuracy of BLYP and B2PLYP-D for dispersion effects, the subsets focusing on noncovalent interactions acquire particularly large weights and thus contribute prominently to the WTMAD values: the IDISP, PCONF, and S22 sets account for 38 out of 740 entries in the database and typically for almost one-fifth of the WTMAD value.[23] As a result, the inclusion of dispersion corrections in DFT methods leads to a general and rather large improvement with regard to WTMAD but to a less pronounced and less systematic improvement with regard to the overall MAD (OVMAD) for the whole database (which is available from the Supporting Information of the original GMTKN24 publication[23]). Furthermore, for DFT methods without dispersion corrections, the ranking of the different functionals is similar with respect to the WTMAD and OVMAD values. In this article, we shall present both WTMAD and OVMAD values but focus on the latter in the statistical analysis since they seem better suited for a general-purpose evaluation

Table 2. Mean Absolute Deviations (MADs) in kcal/mol for the GMTKN24-hnco and Full GMTKN24 Sets with PBE

method	PBE/(aug-)def2-QZVP[a]	PBE/TZVP[b]	PBE/TZVP[b]
sets	GMTKN24	GMTKN24	GMTKN24-hcno
ACONF	0.6	0.65	0.65
BH76	9.2	9.92	8.94
BH76RC	4.3	3.63	3.54
BHPERI	2.9	2.34	2.84
DARC	6.8	5.48	5.48
DC9	10.8	12.03	9.30
G21EA	3.4	6.43	7.17
G21IP	3.9	3.71	4.83
G2RC	6.2	9.07	7.71
IDISP	12.3	11.50	11.50
ISO34	1.8	1.68	1.68
MB08−165	9.0	9.26	9.87
O3ADD6	4.4	4.71	4.71
PA	2.1	2.29	2.47
PCONF	3.9	3.54	3.54
RSE43	3.4	3.48	3.62
S22	2.6	2.31	2.31
SCONF	0.4	0.78	0.78
SIE11	12.0	10.66	12.78
W4−08	11.0	8.65	10.41
WATER27	3.2	20.87	20.87

[a] From the Supporting Information of ref 23. Diffuse functions added to aug-cc-pVQZ for G21EA and WATER27. [b] This work.

of SQM methods (avoiding special emphasis on dispersion interactions). Regardless of this choice, it is clear that dispersion corrections are essential when noncovalent interactions play an important role, and we thus evaluate the performance of SQM methods without and with dispersion corrections.[29−33]

An extended version of the GMTKN24 database, named GMTKN30,[34] was published shortly after completion of our study. The new database contains six additional benchmark sets, three of which are made up of molecules with elements other than H, C, N, and O (ALK6, RG6, HEAVY28) and can thus not be applied here. The remaining three sets address further noncovalent interactions (ADIM), further isomerization reactions (ISOL22) for large molecules with less accurate SCS-MP3/CBS reference data, and hydrocarbon bond separation reactions (BSR36) with significant differences between the theoretical and experimental reference values. We consider these additional data in the GMTKN30 database[34] to be less crucial in the present context and thus decided to disregard them and to focus on the comparison between GMTKN24 and GMTKN24-hcno results.

3. THE GMTKN24-HCNO BENCHMARK DATABASE

Starting from the original GMTKN24 database, we have compiled the GMTKN24-hcno benchmark for SQM methods by stripping the 715 relative energies (1033 single-point energies) of the original set (excluding multireference cases) from all entries that contain elements other than H, C, N, and O, thus arriving at 370 relative energies (593 single-point energies) that are suited for all common SQM methods considered presently.

Table 1 shows the resulting number of entries for all subsets. From the original GMTKN24 database, the three subsets focusing on aluminum (AL2X), boron (NBRC), and sulfur (CYCONF) chemistry were completely skipped, as all entries contain either aluminum, boron, or sulfur. Owing to its pronounced diversity, only 21 of 165 entries of the MB08−165 benchmark could be kept. A large number of entries had to be skipped also for the G21EA, G21IP, G2RC, SIE11, and W4−08 sets (up to two-thirds) and for the BH76RC, BH76, BHPERI, DC9, PA, and RSE43 sets (up to one-half). All entries could be retained for ACONF, DARC, IDISP, ISO34, O3ADD6, PCONF, S22, SCONF, and WATER27.

Is the difficulty of the GMTKN24 benchmark greatly diminished by leaving out the entries specified above? This question can be addressed by comparing MADs from DFT calculations for the full GMTKN24 database and the reduced GMTKN24-hcno database. We have thus performed PBE/TZVP calculations for the reduced and full sets and compared the results with the published PBE/(aug-)def2-QZVP data for the full set.[23] The MADs for most subsets are obviously quite similar (see Table 2), indicating that the reduced GMTKN24-hcno subsets indeed retain the characteristic features of the full GMTKN24 subsets. Large discrepancies are found only in subsets that focus on electron affinities (G21EA) or negatively charged species (WATER27) and thus exhibit a strong basis set dependence in DFT calculations, as has been documented previously.[23]

One may also ask whether the overall performance of SQM methods can be assessed from benchmarking systems containing only H, C, N, and O. This can be checked for SQM methods that have also been parametrized for other elements, by adding to GMTKN24-hcno the corresponding reference data from the full GMTKN24 database. We tested this with PM6 for the full MB08−165 subset (165 rather than 21 entries) and found only small changes in performance (MAD 119.0 rather than 128.4 kcal/mol). In the case of the orthogonalization-corrected SQM methods (OM1, OM2, OM3), we extended the GMTKN24-hcno database by including all molecules also containing fluorine (413 instead of 370 entries), which led to only minor changes of 0.1−0.4 kcal/mol in the OVMAD values, with similar trends in performance for the fluorine-containing and other molecules (for further details see section 5.3).

In summary, these tests suggest that the GMTKN24-hcno benchmark database is well suited to serve for the purpose of evaluating SQM methods.

4. COMPUTATIONAL DETAILS

PBE[25] and B3LYP[26,27] DFT calculations with and without dispersion corrections of DFT-D2 type[35] were done using the Turbomole 5.9 software,[36] TZVP Gaussian basis sets,[37] and (in the case of PBE) the resolution-of-identity approximation[38,39] for two-electron integrals. SQM calculations were carried out with MOPAC2009[40] for AM1 and PM6; with DFTBplus[41] for SCC-DFTB; and with MNDO99[42,43] for OM1, OM2, and OM3, as well as PM3[3] and PM3-PDDG.[18] The SQM methods were enhanced with standard D2 dispersion corrections using the published parameters for AM1-D,[33] PM6-D,[33] OMx-D,[30] and SCC-DFTB-D.[31] These corrections do not involve any changes in the standard SQM parameters, unlike an alternative AM1-based approach.[29] The SQM calculations for open-shell molecules employed a restricted ROHF treatment in the case of MNDO99 and an unrestricted UHF scheme in the case of MOPAC2009. Entries involving triplets or quartets were skipped for SCC-DFTB, because the available software did not allow black-box benchmarking of such species.

5. RESULTS AND DISCUSSION

We begin with two introductory remarks. First, when calculating proton affinities with SQM methods, we follow the convention to use the experimental heat of formation for the proton since all investigated SQM methods are known to be off by several tens of kilocalories per mole for this quantity. Second, the cage/bowl isomerization of C_{20} in the DC9 subset—which is known to be problematic even for high-level *ab initio* methods because of partial multireference effects—is not described adequately by any of the investigated SQM methods, with errors exceeding 100 kcal/mol (see Table 3), which are thus much larger than the estimated uncertainty of about 10 kcal/mol in the *ab initio* reference value.[23] We therefore decided to exclude this item from the statistical analysis, thus reducing the number of entries in our GMTKN24-hcno database to 370. Removing this outlier decreases the OVMAD values for the SQM methods by 0.3−0.8 kcal/mol but does not influence our conclusions on their relative merits.

Table 3. Errors (kcal/mol) with PBE and SQM Methods for the C_{20} Cage/Bowl Isomerization, Relative to the CCSD(T)/CBS Estimate

	PBE/TZVP	PM6	AM1	OM3	OM2	OM1
C_{20} cage/bowl	−5.7	102.6	203.8	206.9	193.4	325.4

The results of our benchmarks are presented as follows: Tables 4 and 5 show SQM and DFT results for the GMTKN24-hcno benchmark database without and with empirical dispersion corrections. Table 6 summarizes the OVMAD values for several SQM and DFT methods. Table 7 shows the effect of including entries with F on the OMx MADs. Figures 1 and 2 compare the MAD values of OM3 with those of PM6 and PBE, respectively. Figure 3 shows the element-wise error of PM6 for the MB08−165 subset. We use Tables 4 and 5 and Figure 1 to compare the SQM methods with each other (subsection 5.1), Tables 4−6 and Figure 2 to compare the SQM methods with DFT (subsection 5.2), and Table 7 and Figure 3 to discuss the effect of taking other elements into account (subsection 5.3).

5.1. Comparison of SQM Methods. Perusing Table 4, the following observations regarding the different SQM methods can be made:

For most subsets, all OMx methods perform roughly similarly well. Exceptions are the PA and O3ADD6 sets where OM1 is best, whereas OM2 and OM3 are better than OM1 for the G21IP, G21EA, and WATER27 sets as well as in the description of noncovalent interactions (see for instance the IDISP set; the effect of including empirical dispersion corrections is discussed below separately). Consequently, the overall deviation (OVMAD) is substantially lower for OM2 and OM3 (8.3 and 7.9 kcal/mol, respectively) than for OM1 (10.9 kcal/mol). The differences between OM2 and the slightly faster OM3 method are small, but

Table 4. Mean Absolute Deviations (MADs) in kcal/mol for the GMTKN24-hnco Sets: PBE/TZVP, B3LYP/TZVP, and SQM Methods

set	PBE	B3LYP	OM3	OM2	OM1	PM6	AM1	SCC-DFTB
ACONF	0.65	0.77	0.86	0.63	0.52	0.56	0.44	0.23
BH76	8.94	4.82	8.69	7.58	10.42	13.81	10.88	14.82
BH76RC	3.54	2.42	6.18	4.09	5.13	17.64	12.46	12.64
BHPERI	2.84	4.42	8.82	8.79	11.31	10.36	10.59	6.98
DARC	5.48	13.65	4.91	7.25	4.10	3.91	4.65	3.55
DC9	9.30	11.36	13.20	13.60	11.40	5.18	15.68	15.22
G21EA	7.17	8.50	9.91	11.70	24.45	22.06	23.03	7.77
G21IP	4.83	4.82	12.72	12.53	22.07	40.14	24.31	15.96
G2RC	7.71	2.69	4.53	8.58	8.68	30.87	12.43	27.97
IDISP	11.50	17.04	6.67	8.19	14.17	14.27	14.01	13.13
ISO34	1.68	2.39	4.37	4.44	4.45	3.46	6.45	4.66
MB08−165	9.87	5.85	21.32	22.00	18.82	128.43	44.44	100.20
O3ADD6	4.71	1.83	10.97	12.24	4.01	2.03	10.57	7.51
PA	2.47	3.06	11.85	14.69	4.90	18.41	12.82	18.58
PCONF	3.54	3.84	1.32	1.28	3.60	2.27	5.35	1.68
RSE43	3.62	2.50	5.24	4.28	3.95	5.20	2.46	9.56
S22	2.31	3.49	3.58	3.07	5.14	3.41	6.83	3.55
SCONF	0.78	0.33	1.32	1.66	5.87	2.62	2.39	2.08
SIE11	12.78	6.53	5.00	9.38	5.15	3.29	10.65	20.83
W4−08woMR	10.41	3.46	11.82	12.79	12.08	15.57	14.35	13.90
WATER27	20.87	11.42	9.19	12.11	36.09	17.81	48.60	22.87
OVMAD	6.60	4.82	7.86	8.33	10.93	18.19	14.52	
OVMAD[a]	5.89	4.73	6.76	7.06	9.68	14.60	13.54	13.87
OVMAD*[b]	6.40	4.76	7.05	7.51	10.46	11.56	12.72	
OVMAD*[a,b]	5.78	4.80	6.21	6.68	9.51	10.04	12.17	10.26
WTMAD	5.7	5.1	6.4	6.7	9.1	13.3	11.6	

[a] Without entries involving triplets or quartets, which reduces the size of the GMTKN24-hcno benchmark database from 370 to 299 entries. [b] Overall MAD without contributions from the MB08−165 subset.

Table 5. Mean Absolute Deviations (MADs) in kcal/mol for the GMTKN24-hnco Sets: PBE/TZVP, B3LYP/TZVP, and SQM Methods with Empirical Dispersion Corrections (-D)

set	PBE-D	B3LYP-D	OM3-D	OM2-D	OM1-D	PM6-D	AM1-D	SCC-DFTB-D
ACONF	0.22	0.21	0.32	0.31	0.41	0.69	1.83	0.53
BH76	9.06	3.90	8.98	7.51	10.01	13.78	10.62	14.88
BH76RC	3.56	2.50	6.30	4.00	5.22	17.65	12.47	12.65
BHPERI	3.55	3.07	7.51	7.14	9.47	9.78	8.50	7.27
DARC	3.67	9.61	8.30	9.99	3.98	4.50	7.65	4.62
DC9	8.04	8.44	12.31	15.07	9.75	4.68	12.47	15.27
G21EA	8.85	8.45	9.92	11.71	24.46	22.06	23.03	7.77
G21IP	4.83	4.83	12.73	12.55	22.09	40.14	24.31	15.96
G2RC	7.87	2.68	4.02	8.10	8.20	30.85	12.04	28.00
IDISP	6.11	7.38	8.42	12.43	13.24	15.51	15.29	12.24
ISO34	1.60	2.08	4.43	4.44	4.37	3.42	6.54	4.60
MB08−165	9.92	5.57	21.92	21.88	18.78	128.51	45.85	100.02
O3ADD6	4.93	1.86	11.13	12.67	3.57	1.81	9.48	7.46
PA	2.62	3.05	11.66	14.76	4.98	18.40	12.67	18.54
PCONF	1.36	0.58	2.07	2.01	4.01	3.02	5.13	0.67
RSE43	3.43	2.27	4.98	4.03	3.84	5.19	2.38	9.53
S22	0.86	0.76	1.10	1.06	2.41	1.65	2.95	1.86
SCONF	0.87	0.57	1.40	1.64	5.18	2.68	1.87	2.12
SIE11	13.51	7.32	5.51	9.96	5.08	3.11	8.77	21.01
W4−08woMR	10.41	3.67	11.65	12.61	11.90	15.56	14.20	13.90
WATER27	26.19	19.43	7.80	4.24	27.58	14.92	36.78	22.21
OVMAD	6.76	4.58	7.70	7.69	9.87	17.89	13.40	
OVMAD[a]	6.05	4.60	6.57	6.31	8.42	14.23	12.14	13.72
OVMAD*[b]	6.57	4.52	6.84	6.83	9.34	11.24	11.45	
OVMAD*[a,b]	5.92	4.64	5.97	5.89	8.19	9.65	10.65	10.11
WTMAD	5.2	3.9	6.2	6.3	8.8	12.9	10.5	

[a] Without entries involving triplets or quartets, which reduces the size of the GMTKN24-hcno benchmark database from 370 to 299 entries. [b] Overall MAD without contributions from the MB08−165 subset.

Table 6. Overall Mean Absolute Deviations (OVMADs) in kcal/mol for the GMTKN24-hnco Set: DFT/TZVP and SQM Methods

method	without -D	with -D
PM6	18.2	17.9
AM1	14.5	13.4
OM3	7.9	7.7
BLYP	6.6	6.3
PBE	6.6	6.8
BP86	6.0	6.2
TPSS	5.5	5.6
B3LYP	4.8	4.6

Table 7. Mean Absolute Deviations (MADs) in kcal/mol for the GMTKN24-hnco Set and the GMTKN24-hcnof Set (Including Entries with F): OM1, OM2, and OM3

	OM1		OM2		OM3	
set	hcno	hcnof	hcno	hcnof	hcno	hcnof
BH76	10.39	10.42	7.58	9.72	8.69	10.66
BH76RC	5.28	5.13	4.09	4.29	6.18	5.37
G21EA	24.81	24.45	11.70	11.39	9.91	9.31
G21IP	22.45	22.07	12.53	12.00	12.72	11.45
G2RC	9.07	8.68	8.58	8.23	4.53	4.16
MB08−165	19.47	18.82	22.00	22.47	21.32	19.46
RSE43	3.86	3.95	4.28	4.02	5.24	4.96
SIE11	4.40	5.15	9.38	9.38	5.00	5.00
W4−08woMR	11.49	12.08	11.82	12.28	11.82	11.38
all	11.01	10.93	8.33	8.68	7.86	8.01

OM3 generally outperforms OM2 when larger differences occur (G2RC, SIE11), making OM3 overall the best OMx model in the GMTKN24-hcno benchmark.

PM6 improves upon AM1 for a number of demanding subsets (DC9, O3ADD6, SIE11) and in the treatment of noncovalent interactions (PCONF, S22, WATER27) but is less convincing than AM1 for a number of other sets with electronically complicated species (BH76RC, G21IP, G21EA, G2RC, PA, RSE43). AM1 has large problems with the MB08−165 subset (MAD 44.4 kcal/mol), but PM6 performs even worse (MAD 128.4 kcal/mol). Mostly for this reason, the overall deviation (OVMAD) is larger for PM6 (18.2 kcal/mol) than for AM1 (14.5 kcal/mol). OM3 clearly outperforms both PM6 and AM1 on a number of subsets (G21IP, G21EA, G2RC, IDISP, WATER27, and most importantly MB08−165) but fails to reach the outstanding accuracy of PM6 for DC9 and O3ADD6.

SCC-DFTB improves upon PM6 and AM1 for the G21EA, G21IP, and G2RC sets but shows large errors for SIE11 and

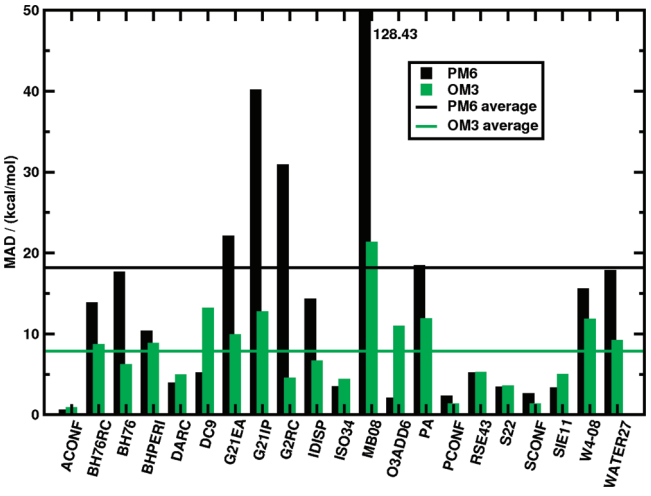

Figure 1. Comparison of OM3 and PM6 results for the GMTKN24-hcno set.

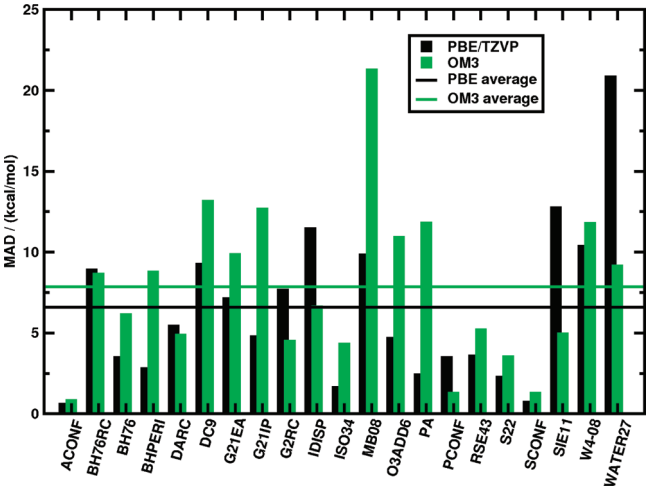

Figure 2. Comparison of OM3 and PBE/TZVP results for the GMTKN24-hcno set.

especially for the MB08−165 set (like PM6 and AM1). SCC-DFTB is inferior to OM3 for the G2RC, PA, RSE43, and WATER27 sets and even more so for SIE11 and MB08−165. As noted above (section 4), triplet and quartet species were excluded from the SCC-DFTB benchmark runs for technical reasons, and hence the overall deviation (OVMAD 13.9 kcal/mol) refers to a smaller sample. For the sake of comparison, OVMAD values for this smaller sample are given in Table 4 also for the other methods.

In addition to the methods shown in Table 4, we have also looked at the performance of the pairwise distance directed Gaussian (PDDG)[18] approach in combination with PM3[3] as implemented in MNDO99. The OVMAD value of PDDG-PM3 is 17.1 kcal/mol (12.5 kcal/mol without the MB08−165 set), about 2 kcal/mol (1 kcal/mol) higher than the value for PM3 itself (14.7 and 11.4 kcal/mol), which performs similarly to AM1 (14.5 and 12.7 kcal/mol) for our database.

Since the "mindless" MB08−165 benchmark set with its artifical molecules is particularly demanding, we also provide in Table 4 overall deviations without the MB08−165 contributions

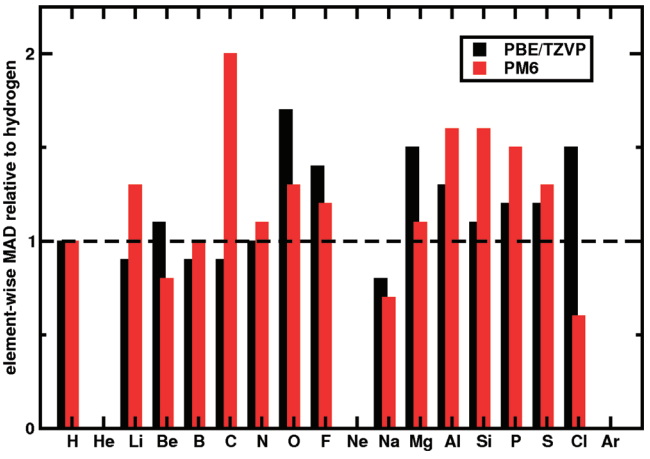

Figure 3. Element-wise MAD values relative to hydrogen for the MB08−165 set (see text for details).

(OVMAD*). These deviations decrease in the following order:

AM1 > *SCC-DFTB*≈PM6 > OM1 ≫ OM2≈OM3 > PBE > B3LYP

The OVMAD* values for AM1, PM6, SCC-DFTB, and OM1 are rather similar (ranging between 12.7 and 10.3 kcal/mol) although the performance for a specific subset may be quite different between these methods. OM2 and OM3 are distinctly more accurate (OVMAD* 7.5 and 7.1 kcal/mol, respectively) and actually approach the overall accuracy of PBE (OVMAD* 6.4 kcal/mol) while B3LYP performs best (OVMAD* 4.8 kcal/mol).

Inclusion of the artificial molecules from the MB08−165 set generally deteriorates the error statistics, but to different extents. The overall deviations (OVMAD vs OVMAD*) become much worse for PM6 and SCC-DFTB (increase by 6.6 and 3.6 kcal/mol), somewhat worse for AM1 (by 1.8 kcal/mol), and only slightly worse for the OMx methods (by 0.5−0.8 kcal/mol). The OMx methods are thus remarkably robust in this regard, again reminiscent of the performance of PBE (increase by 0.2 kcal/mol). The superior performance of the OMx methods (compared with the other SQM methods) may be viewed as support for the OMx approach of going beyond the MNDO model: including more physics in the model appears to be a better strategy for coping with the electronically demanding MB08−165 species than going for a better parametrization. On the basis of the OVMAD values, the overall deviations decrease in the following sequence:

PM6 ≫ *SCC-DFTB*≈AM1 ≫ OM1 ≫ OM2≈OM3 > PBE > B3LYP

Figure 1 illustrates the relative merits of OM3 and PM6 by plots of the overall deviations (OVMAD) and of the deviations (MAD) of the individual subsets of the GMTKN24-hcno benchmark.

Table 5 shows that the inclusion of empirical dispersion corrections into the SQM methods leads to a clear improvement for all subsets in which intermolecular noncovalent interactions play an important role (most notably S22 and WATER27), but there is also some minor deterioration for other subsets. Overall, there is a general small gain in accuracy for all SQM methods considered, with a decrease of 0.2−1.3 kcal/mol in the OVMAD and OVMAD* values. The accuracy ranking of the SQM methods in our benchmark is not affected by the inclusion of empirical dispersion corrections, since their effect on the

statistics is smaller than the underlying intrinsic differences and since all SQM methods benefit to a similar extent.

As noted above (see section 2), the use of weighted total MADs (WTMADs) emphasizes the importance of noncovalent interactions in the benchmark. These WTMADs are listed in Tables 4 and 5. They clearly reflect the gain from adding dispersion corrections to the DFT methods: Upon inclusion of these corrections, the WTMADs decrease by 0.5 kcal/mol for PBE and by 1.2 kcal/mol for B3LYP, while the OVMADs change by only 0.2 kcal/mol (increasing for PBE and decreasing for B3LYP). In the case of the SQM methods, both the WTMADs and OVMADs are generally lowered by the dispersion corrections, typically by 0.2 to 0.6 kcal/mol (for OM1 and AM1 by up to 1.1 kcal/mol). Focusing on the dispersion-corrected methods (Table 5) the WTMADs are always smaller than the OVMADs (PBE-D by 1.6 kcal/mol, B3LYP-D by 0.7 kcal/mol, OMx-D by 1.1 to 1.5 kcal/mol, other SQM-D by 2.9 to 5.0 kcal/mol), with OM2-D and OM3-D again showing the best performance among all SQM methods and approaching PBE-D accuracy. Since the emphasis of this study is not on noncovalent interactions, we will disregard dispersion corrections from now on and again employ OVMAD instead of WTMAD values in the analysis.

5.2. Comparison of SQM and DFT Methods. OM3 is the most accurate and robust of the SQM methods considered presently and has therefore been chosen for a comparison with DFT/TZVP methods. Among the available DFT functionals, we focus mainly on PBE and B3LYP, which are commonly used representatives of GGA (generalized gradient approximation) and hybrid-GGA functionals. The data in Tables 4 and 6 indicate that B3LYP (OVMAD 4.8 kcal/mol) is on average more accurate than PBE (OVMAD 6.6 kcal/mol) for organic molecules. Other common GGA functionals perform similarly to PBE (OVMAD 6.6 kcal/mol for BLYP, 6.0 kcal/mol for BP86), while at the meta-GGA level, TPSS shows an intermediate performance (OVMAD 5.5 kcal/mol). OM3 (OVMAD 7.9 kcal/mol) is surprisingly close in overall accuracy to standard DFT-GGA methods. This is visualized in Figure 2 showing the MADs for the subsets of the GMTKN24-hcno benchmark for OM3 and the PBE functional. It is obvious that PBE outperforms OM3 for several sets (BHPERI, G21IP, MB08−165, O3ADD4, PA), but there are also sets where the opposite is true (IDISP, SIE11, WATER27). These latter cases merit further comments.

The IDISP set contains molecules in which intramolecular noncovalent interactions are of crucial importance. Such intramolecular effects are partially taken into account by the OM3 parametrization (unlike intermolecular effects that are not covered), and it is therefore not surprising that the inclusion of empirical dispersion corrections actually deteriorates the OM3 results for IDISP (in contrast to the improvements for S22 where intermolecular dispersion effects are dominant). On the other hand, dispersion is generally missing at the PBE level, and the dispersion corrections in PBE-D thus yield substantial improvements both for IDISP and S22. Consequently, PBE-D has slightly lower MADs than OM3-D for both sets (IDISP, S22). This also suggests that a reparameterization of SQM methods with dispersion corrections included in the fit process is likely to be worthwhile, offering the chance for a more balanced treatment of intra- and intermolecular dispersion interactions.

The WATER27 set contains several negatively charged species. It is well-known[23] that accurate PBE calculations on these species require basis sets that are larger than the TZVP basis used presently, and extending the basis from TZVP to (aug-)def2-QZVP lowers the MAD of PBE for the WATER27 set from 20.9 to 3.2 kcal/mol (Table 2). When using a sufficiently large basis, PBE thus outperforms OM3 also for the WATER27 set (OM3 MAD 9.2 kcal/mol). On the other hand, the PBE problems related to self-interaction errors (SIE11) seem genuine since they are not alleviated by basis set extension (Table 2).

In summary, the PBE/TZVP results for the GMTKN24-hcno benchmark are somewhat more accurate than the OM3 results (OVMAD 6.6 vs 7.9 kcal/mol), which remains true after including empirical dispersion corrections (OVMAD 6.8 vs 7.7 kcal/mol). It should also be noted, that "high-end" functionals like the M0n family or double hybrids are substantially more accurate than the commonly used PBE and B3LYP methods for the benchmark sets featured in the GMTKN24 and GMTKN30 databases: The GMTKN24 WTMAD and OVMAD values for M06−2X[44] are both 2.2 kcal/mol, compared to 6.2 and 7.0 kcal/mol for PBE. The M06−2X OVMAD value for our reduced "hcno" set drops from 2.2 to 1.8 kcal/mol, well in line with the change for PBE from 7.0 to 6.6 kcal/mol, which provides further support to the transferability of our hcno results. An extensive collection of DFT data and a detailed analysis of the relative performance of a wide range of DFT functionals can be found in the original GMTKN24 and GMTKN30 publications by Grimme and Goerigk.[23,34]

5.3. Element-Specific Error Analysis. PM6 has parameters for all elements appearing in the full GMTKN24 benchmark. We can therefore use PM6 to check whether and how the errors depend on the elements that are present in the reference molecules. For this purpose, we have analyzed the performance of PM6 for the full MB08−165 benchmark set (i.e., our most demanding subset containing artificial molecules with complicated electronic structure). Figure 3 shows the element-specific errors obtained as follows: For a given entry in the MB08−165 set, each element is assigned a fraction of the error in the computed absolute reaction energy according to its occurrence (number of atoms present divided by the total number of atoms). Then, an average is taken over the resulting values for all entries and weighted with the elemental occurrence in the full set, and finally this average value is divided by the corresponding value for hydrogen for the purpose of normalization.[28] The resulting error distribution in Figure 3 looks fairly balanced both for PM6 and for the PBE functional, indicating that the quality of the PM6 results is reasonably uniform for different elements. This implies that the present GMTKN24-hcno benchmark is expected to be of general relevance and that the conclusions derived from molecules containing only H, C, N, and O may be valid in general.

In a second test, we have extended the GMTKN24-hcno database by including all species from the full database that also include fluorine atoms. The resulting GMTKN24-hcnof database contains 413 entries derived from 654 single-point calculations (compared with 371 entries and 595 single-point calculations in GMTKN24-hcno). The corresponding OMx results are shown in Table 7 for all subsets that differ in the two databases. It is obvious that the MAD values remain essentially unchanged upon the addition of fluorine-containing molecules, with variations in the overall deviations (OVMAD) for the complete benchmark database of 0.1−0.4 kcal/mol.

The outcome of both tests suggests that our GMTKN24-hcno benchmark database is indeed well suited to serve the purpose of evaluating SQM methods.

5.4. Computational Costs. The overall performance of OM3 seems satisfactory especially in view of the fact that the OM3

calculations are about 3 orders of magnitude faster than the PBE/TZVP calculations: Computation times are 4.5 s for OM3, 8296 s for PBE/TZVP, and 11865 s for B3LYP/TZVP (ratio 1:1844:2637) on one core of an Intel Xeon 5670 processor for the whole GMTKN24-hcno benchmark database. To compare the computational costs of the different SQM methods with each other, we use averages over 100 calculations of the complete database. For the systems investigated here, substantial differences are found mainly between programs and less so between methods. MNDO99 needs on average about 4 s for the complete database (AM1 3.9s, PM3 4.0s, OM2 4.2s, OM1 4.3s, OM3 4.5s); this value is roughly doubled for MOPAC2009 (AM1 8.0s, PM6 8.1s) and larger by a factor of about 9 for DFTB+ (SCC-DFTB 35.4s)

6. SUMMARY

We have presented a thorough evaluation of semiempirical QM methods based on a reduced version of the recently introduced GMTKN24 benchmark database. We find that the OMx family of methods outperforms the established SQM methods AM1, PM6, and SCC-DFTB by a significant margin. The overall differences between AM1, PM6, and SCC-DFTB are rather small, while OM2 and OM3 are substantially more accurate (by about 3 kcal/mol on average). Furthermore, the OMx family of methods is remarkably robust with regard to the unusual bonding situations in the artificial molecules from the "mindless" MB08−165 benchmark, where all other SQM methods fail badly. This provides further support to the OMx strategy of improving the adopted semiempirical model (instead of further parameter refinement). In the present GMTKN24-hcno benchmark, the OM2 and OM3 results are reasonably accurate and robust even in comparison to DFT(PBE) calculations.

AUTHOR INFORMATION

Corresponding Authors

*E-mail: korth@mpi-muelheim.mpg.de, thiel@mpi-muelheim.mpg.de.

ACKNOWLEDGMENT

M.K. was supported by Grants LPDS-2009-19 and LPDR-2009-3 from the German National Academy of Sciences Leopoldina. The authors would like to thank Lars Goerigk and Stefan Grimme for kindly supplying additional unpublished DFT data for their benchmark databases.

REFERENCES

(1) Dewar, M. J. S.; Thiel, W. *J. Am. Chem. Soc.* **1977**, *99*, 4799.
(2) Dewar, M. J. S.; Zoebisch, E. G.; Healy, E. F.; Stewart, J. J. P. *J. Am. Chem. Soc.* **1985**, *107*, 3902.
(3) Stewart, J. J. P. *J. Comput. Chem.* **1989**, *10*, 221.
(4) Stewart, J. J. P. *J. Mol. Model.* **2007**, *13*, 1173.
(5) Kolb, M.; Thiel, W. *J. Comput. Chem.* **1993**, *14*, 775.
(6) Weber, W. Ph.D. thesis, University of Zürich, Zürich, Switzerland, 1996.
(7) Weber, W.; Thiel, W. *Theor. Chem. Acc.* **2000**, *103*, 495.
(8) Scholten, M. Ph.D. thesis, University of Düsseldorf, Düsseldorf, Germany, 2003.
(9) Otte, N.; Scholten, M.; Thiel, W. *J. Phys. Chem. A* **2007**, *111*, 5751.
(10) Stewart, J. J. P. In *Reviews in Computational Chemistry*; Lipkowitz, K. B., Boyd, D. B., Eds.; VCH Publishers: New York, 1990; Vol. 1, pp 45−81.
(11) Thiel, W. *Adv. Chem. Phys.* **1996**, *93*, 703.
(12) Clark, T. J. *THEOCHEM* **2000**, *530*, 1.
(13) Thiel, W. In *Modern Methods and Algorithms of Quantum Chemistry*; Grotendorst, J., Ed.; John von Neumann Institut fur Computing: Jülich, 2000; NIC Series, Vol. 3, p 261.
(14) Bredow, T.; Jug, K. *Theor. Chem. Acc.* **2005**, *113*, 1.
(15) Thiel, W. In *Theory and Applications of Computational Chemistry*; Dykstra, C. E., Kim, K. S., Frenking, G., Scuseria, G. E., Eds.; Elsevier: Amsterdam, 2005; pp 559−580.
(16) Dewar, M. J. S.; Thiel, W. *J. Am. Chem. Soc.* **1977**, *99*, 4907.
(17) Thiel, W.; Voityuk, A. A. *J. Phys. Chem. Soc.* **1996**, *100*, 616.
(18) Repasky, M. P.; Chandrasekhar, J.; Jorgensen, W. L. *J. Comput. Chem.* **2002**, *23*, 1601.
(19) Tirado-Rives, J.; Jorgensen, W. L. *J. Chem. Theory Comput.* **2008**, *4*, 297.
(20) Curtiss, L. A.; Raghavachari, K.; Redfern, P. C.; Pople, J. A. *J. Chem. Phys.* **1997**, *106*, 1063.
(21) Curtiss, L. A.; Raghavachari, K.; Redfern, P. C.; Pople, J. A. *J. Chem. Phys.* **2000**, *112*, 7374.
(22) Redfern, P. C.; Zapol, P.; Curtiss, L. A.; Raghavachari, K. *J. Phys. Chem. A* **2000**, *104*, 5850.
(23) Goerigk, L.; Grimme, S. *J. Chem. Theory Comput.* **2010**, *6*, 107.
(24) Elstner, M.; Porezag, D.; Jungnickel, G.; Elsner, J.; Haugk, M.; Frauenheim, T.; Suhai, S.; Seifert, G. *Phys. Rev. B* **1998**, *58*, 7260.
(25) Perdew, J. P.; Burke, K.; Enzerhof, M. *Phys. Rev. Lett.* **1996**, *77*, 3865.
(26) Becke, A. D. *J. Chem. Phys.* **1993**, *98*, 5648.
(27) Stephens, P. J.; Devlin, F. J.; Chabalowski, C. F.; Frisch, M. J. *J. Phys. Chem.* **1994**, *98*, 11623.
(28) Korth, M.; Grimme, S. *J. Chem. Theory Comput.* **2009**, *5*, 993.
(29) McNamara, J. P.; Hillier, I. H. *Phys. Chem. Chem. Phys.* **2007**, *9*, 2362.
(30) Tuttle, T.; Thiel, W. *Phys. Chem. Chem. Phys.* **2008**, *10*, 2159.
(31) Elstner, M.; Hobza, P.; Frauenheim, T.; Suhai, S.; Kaxiras, E. *J. Chem. Phys.* **2001**, *114*, 5149.
(32) Rezac, J.; Fanfrlik, J.; Salahub, D.; Hobza, P. *J. Chem. Theory Comput.* **2009**, *5*, 1749.
(33) Korth, M.; Pitonak, M.; Rezac, J.; Hobza, P. *J. Chem. Theory Comput.* **2010**, *6*, 344.
(34) Goerigk, L.; Grimme, S. *J. Chem. Theory Comput.* **2011**, *7*, 291.
(35) Grimme, S. *J. Comput. Chem.* **2006**, *27*, 1787.
(36) Ahlrichs, R.; Bär, M.; Häser, M.; Horn, H.; Kölmel, C. *Chem. Phys. Lett.* **1989**, *162*, 165.
(37) Schäfer, A.; Huber, C.; Ahlrichs, R. *J. Chem. Phys.* **1994**, *100*, 5829.
(38) Eichkorn, K.; Treutler, O.; Öhm, H.; Häser, M.; Ahlrichs, R. *Chem. Phys. Lett.* **1995**, *242*, 652.
(39) Eichkorn, K.; Weigend, F.; Treutler, O.; Ahlrichs, R. *Theor. Chem. Acc.* **1997**, *97*, 119.
(40) MOPAC2009. See http://openmopac.net/MOPAC2009.html (accessed Mar 8, 2011).
(41) DFTBplus. See http://www.dftb-plus.info (accessed Mar 8, 2011).
(42) Thiel, W. *MNDO99*, version 6.1; Max-Planck-Institut für Kohlenforschung: Mülheim, Germany, 2007.
(43) The OMx methods are implemented in the MNDO99 code, which is distributed by Scienomics (http://www.scienomics.com, accessed Aug 4, 2011) and is also available from one of the authors (W.T.).
(44) Zhao, Y.; Truhlar, D. G. *Theor. Chem. Acc.* **2008**, *120*, 215.

JCTC Journal of Chemical Theory and Computation

ARTICLE

pubs.acs.org/JCTC

Solution Structure and Dynamics of Ni^{2+}(aq) from First Principles

Jiří Mareš,*,† Helmi Liimatainen,‡ Kari Laasonen,§ and Juha Vaara†

†NMR Research Group, Department of Physics, University of Oulu, P.O. Box 3000, FIN-90014, Oulu, Finland

‡Laboratory of Physical Chemistry, Department of Chemistry, University of Helsinki, P.O. Box 55 (A. I. Virtasen aukio 1), FIN-00014, Helsinki, Finland

§Laboratory of Physical Chemistry and Electrochemistry, Department of Chemistry and Materials Science, Aalto University, P.O. Box 16100, FIN-00076, Espoo, Finland

Supporting Information

ABSTRACT: The aqueous solution of Ni^{2+} was investigated using first principles molecular dynamics (FPMD) simulation based on periodic density-functional theory (DFT) calculations. The experimental structural parameters of the Ni(aq) complex are reproduced well by the simulation. An exchange event of the water molecule in the first solvation shell is observed, supporting the proposed dissociative mechanism of exchange. The calculated dynamic characteristics of the surrounding water molecules indicate too slow translational diffusion in comparison to experimental results, in agreement with other FPMD studies employing a similar level of theory. We also find that the reorientational dynamics of water are an order of magnitude slower as compared to experimental data. On the other hand, the angular momentum dynamics are in better agreement with the experimental data than the previously reported results from MD simulations employing empirical force fields. The obtained MD trajectory can supply accurate structures for the calculation of magnetic properties.

INTRODUCTION

The structure of hydrated multivalent ions is notoriously problematic to describe by classical nonpolarizable force fields. The case of the hydrated Ni^{2+} ion has been studied experimentally by neutron scattering and X-ray methods[1−3] and computationally using molecular dynamics (MD) simulations.[4−10] In the latter context, force fields have been developed that correctly model the average octahedral coordination of Ni^{2+} with six surrounding water molecules in the first solvation shell; however, the details differ among the various modeling studies. The problem originating from water polarization in the ion vicinity has been treated by an effective nonpolarizable two-body potential,[6,9] combined quantum mechanics/molecular mechanics (QM/MM) approach,[7,8,10] and, for a few different ions, accurately parametrized polarizable force fields.[11−13] As a further possible approach, first-principles molecular dynamics (FPMD) has been utilized for ion solvation.[14−20] It can be *a priori* assumed that FPMD should be superior to the other approaches, since it naturally includes polarization as well as other many-body effects. Within FPMD, one does not need to parametrize the ion−water potential and incorporate it into a particular water force field. The QM/MM approach lacks uniformity of description of the whole system, as manifested, e.g., in the practical difficulty in dealing with the exchange of molecules between the QM and MM regions. FPMD, on the other hand, treats the solvent−solvent as well as solvent−ion interactions on an equal footing. The FPMD steps require, however, either the diagonalization of the electronic Hamiltonian as well as subsequent force evaluation or an effective algorithm such as that due to Car and Parrinello[21] for approximately following the Born−Oppenheimer surface.[22] Consequently, FPMD is computationally expensive, limiting the length of the simulations as compared to parametrized empirical models. Furthermore, the underlying electronic structure method, usually density-functional theory (DFT), imposes its own restrictions on the accuracy of the intermolecular forces, as the van der Waals dispersion interaction is not well-described at standard DFT levels.[23] Properties of liquid water obtained from FPMD simulations have been discussed extensively.[24−30] Depending on the level of theory used in FPMD, primarily, the choice of the exchange-correlation functional (ECF), substantially varying structural (e.g., interatomic distances described by radial distribution functions, RDFs) and dynamical (e.g., translational and rotational diffusion) properties of water are obtained.

This work reports a very extensive FPMD simulation of the Ni^{2+} ion in aqueous solution. We investigate a variety of structural and dynamical properties. In the first part of this paper, we carefully investigate the RDFs between Ni^{2+} and the water atoms, the O−Ni−O angle distribution revealing the arrangement of ligand molecules around the Ni^{2+} ion, and the tilt angle of water molecules of the first and second solvation shells (FSS and SSS, respectively). Furthermore, we report the RDFs among the water atoms, their translational and rotational diffusion, and the angular momentum dynamics.

The six- as well as five-coordinated cases represent the prevailing situations in the solution as well as the fleeing intermediate occurring in the dissociative exchange reaction in the FSS, respectively. We were able to witness one such exchange process in our FPMD simulation, which is longer than comparable first-principles studies hitherto performed.

The paper is organized as follows: We start with a quantum-chemical (QC) study of the static structure of the unsolvated

Received: May 10, 2011
Published: July 27, 2011

hexa-aqua $Ni(H_2O)_6^{2+}$ complex, giving information on the performance of DFT ECFs against correlated *ab initio* calculations. Results from the static structure calculations are linked to the results from the FPMD simulation and compared to experimental data. Subsequently, the following sections are dedicated to the structure of the solution reported via RDFs, tilt angles, ligand−central ion−ligand angles, and dynamic properties such as self-diffusion coefficients, as well as reorientational and angular momentum correlation functions. Finally, details of the exchange process are reported.

METHODS

Quantum-Chemical Calculations. The FSS of the aqueous nickel ion, $Ni(H_2O)_n^{2+}$ (n = 5, 6), was investigated via structure optimization. For the structure optimization of the static FSS models, DFT in the ORCA program[31] was used with different ECFs (PBE, PBE0,[32,33] BLYP,[34−36] B3LYP,[35,37,38] BHandHLYP[39]). Spin-scaled second-order Møller−Plesset theory (SCS-MP2[40]) was used for comparison. Basis sets from the def2-XVP (X = S, TZ, aug-TZ, QZ) series[41] were used. The PBE functional was selected for the FPMD simulation.

First Principles Molecular Dynamics. The initial configurations of systems containing one Ni^{2+} and either 127 or 255 water molecules were prepared using empirical MD in the GROMACS 4 code.[42] The size of the cubic simulation box corresponds to experimental water density at 343 K with the side lengths of 19.8591 Å used for 255 water molecules and 15.7622 Å for 127 molecules. The boxes accommodate well both FSS and SSS; in particular, the latter has the shape of a sphere with a roughly 10 Å diameter. The two different system sizes were simulated to be able to test finite size effects on the static and dynamic characteristics important for the current and future calculations of molecular properties.

The production trajectories were run using Born−Oppenheimer MD with DFT forces calculated "on the fly", as implemented in the QUICKSTEP[43] module of the CP2K package.[44] In QUICKSTEP, a combination of the atom-centered Gaussian basis set and auxiliary plane waves (PW) is used. The PW basis is used together with the Gaussian basis to expand the electron density. The method employs a pseudopotential on each atom. For water, we tested DZVP, TZVP, TZV2P, and QZV3P valence basis sets.[43] The Ni−O distance in the $Ni(H_2O)_6^{2+}$ complex is well-converged already using the DZVP basis set, which was therefore selected for production runs. The Goedecker−Teter−Hutter pseudopotentials[45] for the PBE functional were used. For the Ni^{2+} ion, the DZV basis set available in CP2K in combination with a pseudopotential spanning 18 core electrons was used.

Furthermore, we investigated the dependence of the Ni−O distance in the $Ni(H_2O)_6^{2+}$ complex on the cutoff kinetic energy of the plane waves. Calculations using 1200, 600, 310, 280, and 250 Ry cutoffs for the larger simulation box revealed that 310 Ry yields a converged Ni−O distance. This cutoff was used for both sizes of the simulation box.

We tested the choice of the integration time-step of the equations of motion, which were propagated using the velocity Verlet algorithm.[46] Among the tested values 0.5, 0.7, 1, and 2 fs, the total energy of the Ni^{2+}/127 H_2O system within the *NVE* ensemble was well-conserved (drift 3.0×10^{-7} au/ps) using the 1 fs time-step, provided that a sufficiently tight self-consistent field (SCF) convergence criterion ($\varepsilon_{SCF} = 1 \times 10^{-7}$a.u.) was used.

The systems with 127 and 255 water molecules (both with one Ni^{2+} ion) were simulated for the total lengths of 90 and 33 ps of production trajectories, respectively. The simulation boxes, which were prepared using the classical force field in the GROMACS code, were further equilibrated in the initial phase of the FPMD simulation. The velocity scaling thermostat was used to prepare the system at the desired temperature of 343 K. Later, the production simulations continued in the *NVE* ensemble. The temperature was monitored, and the Ni−O radial distribution function (RDF) was monitored in the thermalization phase, until a stable situation was reached. The RDFs were calculated using VMD.[47] The self-diffusion coefficient D was calculated using the Einstein relation[48]

$$\langle |\mathbf{r}(\tau) - \mathbf{r}(0)|^2 \rangle = 6D\tau \quad (1)$$

where $\mathbf{r}(\tau)$ is the position of the center-of-mass of the water molecule at time τ, and the angular brackets denote averaging over molecules and time origins. Reorientational dynamics of the water molecules was investigated via the autocorrelation function of the principal axes of the moment of inertia tensor $\mathbf{I}$. For the principal axis $\hat{i}$, the relation for the unnormalized function at time offset τ is written as

$$C_{i_a}^n(\tau) = \langle P_n(\cos\theta_a) \rangle, a = x, y, z \quad (2)$$

$$\theta_a = \angle(\hat{i}_a(0), \hat{i}_a(\tau)) \quad (3)$$

where P_n is the nth order Legendre polynomial. The angular momentum correlation function was calculated in the Eckart frame[49,50] to minimize the vibrational contributions. The formula for the correlation function at time offset τ is written

$$C_{l_a}(\tau) = \langle l_a(0)\, l_a(\tau) \rangle, a = x, y, z \quad (4)$$

where l_a is the Cartesian angular momentum component along the a axis of the molecule-fixed Eckart frame.

RESULTS AND DISCUSSION

Structures of $Ni(H_2O)_6^{2+}$ and $Ni(H_2O)_5^{2+}$ Complexes. A schematic illustration of the hexa-aqua and penta-aqua complexes of Ni^{2+} is given in Figure 1. The basis-set requirements and the effect of the choice of ECF were first tested on the geometry parameters of the $Ni(H_2O)_6^{2+}$ complex, evaluated primarily via the Ni−O distance. The results are shown in Tables 1 and 2. The broad range of existing experimental data encompasses essentially all of our computational results. In the calculations using the ORCA code at the PBE level, the Ni−O distance of 2.086 Å was converged using the def2-TZVP basis set (*in vacuo*), which was then used for further tests of hexa-aqua Ni^{2+} structure. Periodic CP2K calculation of the finite $Ni(H_2O)_6^{2+}$ system using the same functional converges at a slightly longer distance, possibly due to the fact that pseudopotentials are used in CP2K. The r(Ni−O) distance and the tilt angle between the Ni−O vector and the bisector of the OH vectors of a water molecule behave systematically as functions of the exact exchange admixture in the ECF. The hybrid functionals lead to a shorter distance and smaller angle. In particular, *in vacuo*, the tilt angle using hybrid DFT or SCS-MP2 practically vanishes. With the COSMO solvation models, however, the results are brought into quantitative agreement with experimental results by the increase of the

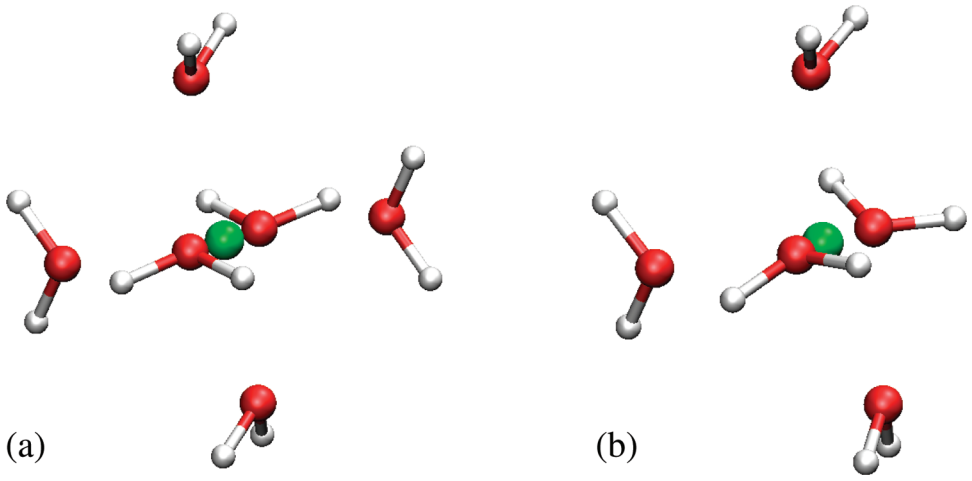

Figure 1. Structures of (a) $Ni(H_2O)_6^{2+}$ and (b) $Ni(H_2O)_5^{2+}$ obtained by geometry optimization at the SCS-MP2/def2-TZVP level using the COSMO solvation model. The positions of the water molecules are close to octahedral symmetry also in the penta-aqua complex.

Table 1. Basis-Set Dependence of the Distance (Å) between the Nickel Atom and Oxygen, r(Ni−O), in $Ni(H_2O)_6^{2+}$ [a]

program	r(Ni−O) with indicated basis sets				exptl.[b]
Orca	def2-SVP	def2-TZVP	def2-aug-TZVP	def2-QZVP	
	2.073	2.086	2.086	2.086	2.05−2.15
CP2K	DZVP	TZVP	TZV2P	QZV3P	
	2.100	2.089	2.093	2.092	

[a] The PBE functional was used in density-functional calculations *in vacuo*. For the CP2K calculation, the plane wave cutoff was set to 280 Ry in a cubic box with the side length 19.8591 Å. [b] See Table 3 for a more detailed list of values and references.

tilt angle to 33−46°. At the same time, a notable decrease of 1−2 pm in the r(Ni−O) distance takes place. Of the two tested GGA functionals (PBE and BLYP), PBE performs better for the structure as compared to the reference SCS-MP2 structure. The "optimal" amount of exact exchange appears to be somewhat below the 50% of BHandHLYP.

In general, due to error cancellation between the exact-exchange and pure DFT components, hybrid functionals lead to smaller self-interaction or, alternatively, delocalization error than pure GGAs.[51] Because of their additional computational cost, the hybrid functionals could not, however, be considered for the FPMD simulation of the required trajectory length and system size.

The structure of the 5-fold coordinated Ni^{2+} complex has also been calculated, as the $Ni(H_2O)_5^{2+}$ is the composition of the FSS of the transition structure during the exchange of coordinating water molecules. The structural parameters are listed in Table S1 (Supporting Information). Since the water molecules in $Ni(H_2O)_5^{2+}$ are not equivalent, we report values for each molecule separately. On average, however, the length r(Ni−O) is shorter compared to the 6-fold coordinated Ni^{2+} ion, whereas the average tilt angle does not differ significantly between the 5- and 6-fold structures.

Electronic Structure of $Ni(H_2O)_6^{2+}$ and $Ni(H_2O)_5^{2+}$ Complexes. In the companion article,[52] we thoroughly discuss the molecular magnetic properties obtained from the QM calculation. For the open-shell system, spin density is one such property quantitatively manifested in hyperfine coupling constants of the water nuclei. Here, we state only a few things. The discussion refers to single-point calculation on structures optimized by the corresponding method.

Comparing calculations with different DFT functionals, we see a systematic increase of the gap between the highest occupied and lowest unoccupied "α-spin" orbitals with an increasing amount of exact exchange. The same holds for the "β" orbitals. The finding is fully analogous to the commonly known trend of a HOMO−LUMO gap in closed-shell systems. The same is true for five- and six-fold coordinated complexes. In the case of the six-fold coordination, the two singly occupied molecular orbitals (SOMO) are almost exactly degenerate with energies differing by ca. 0.002−0.02 eV. The situation is different for the 5-fold coordinated complex for which the two SOMOs have an energy difference increased to the order of 0.1 eV, which in a qualitative way relates to the less symmetric structure of the five-coordinated complex.

Ni^{2+} Solvation Structure in Liquid Solution. In agreement with the accepted opinion, the Ni^{2+} complex is predominantly 6-fold coordinated in our FPMD trajectory. The main structural parameters of the hexa-aqua complex are summarized in Table 3, along with selected literature results. From the FPMD simulations, the maxima of the Ni−O and Ni−H RDF (*vide infra*) lie at 2.105 Å and 2.705 Å, respectively. The geometry optimization of $Ni(H_2O)_6^{2+}$ without dynamical corrections and using the COSMO solvation model at the PBE/def-TZVP level resulted in a Ni−O distance of 2.076 Å (Table 2). The ϕ(ONiO) angle values would in our case of octahedral geometry be expected at 90° and 180°. The ϕ(ONiO) angle of the six-coordinated ion, reported in Table 3, is very close to these values. The simulated distribution of the angle is given in Figure S1 of the Supporting Information. The 5-fold coordinated intermediate preserves to a large extent the octahedral symmetry. The same feature was observed during the optimization of the 5-fold coordinated ion (Figure 1). In the 5-fold part of the FPMD trajectory, the Ni−O and Ni−H distances are contracted by 6−7 pm as compared to the 6-fold case.

The tilt angle of water molecules around the central ion, reported in Table 3, is defined as the angle between the ion−oxygen vector and the bisector of the HOH angle. In contrast, θ is the angle between the ion−oxygen vector and the plane of the

Table 2. Dependence on the DFT Exchange-Correlation Functional of the Distance (Å) between the Nickel Atom and Oxygen, r(Ni−O), and the Tilt Angle [$\angle$(NiO,OH$_2$), (deg)] of Water Molecules in $Ni(H_2O)_6^{2+}$ [a]

solvation model	parameter	BLYP	B3LYP	BHandHLYP	PBE	PBE0	SCS-MP2	exptl.[b]
COSMO	r(Ni−O)	2.098	2.074	2.061	2.076	2.057	2.066	2.05−2.15
	$\angle$(NiO,OH$_2$)	44.1	37.7	30.7	45.7	38.4	33.0	0−50
in vacuo	r(Ni−O)	2.109	2.086	2.078	2.086	2.069	2.082	
	$\angle$(NiO,OH$_2$)	22.0	2.3	2.5	23.0	3.1	0.1	

[a] The tilt angle is illustrated in Figure S2 of the Supporting Information. Both calculations were performed with the Orca program, *in vacuo* or using the COSMO solvation model as indicated. The def2-TZVP basis set was used. For comparison, SCS-MP2 and experimental results are also given. [b] See Table 3 for a more detailed list of values and references.

Table 3. Structural Characteristics of the Aqueous Solution of Ni^{2+} [a]

	r(Ni−O) (Å)	r(Ni−H) (Å)	$\angle$(NiO,OH$_2$) (deg)	ϕ(ONiO) (deg)
FPMD(6)[b]	2.11	2.71	43.5	89−90, 172−173
FPMD(5)[c]	2.05	2.64	44.0	89−90
QM/MM[d]	2.14	2.81	∼0	89.1, 172.7
MD	2.06,[e] 2.06[e]	2.67,[f] 2.76[f]	∼35,[e] ∼0[f]	∼90[f]
exptl.	2.05−2.10(2.15),[g,h] 2.072,[i] 2.05[j]	2.77[i]	30, 40,[g,k] 0−42,[l] 42,[m] ∼0[i]	∼90, 180[i]

[a] The location (Å) of the first maxima of Ni−O and Ni−H radial distribution functions, the tilt angle of water molecules $\angle$(NiO,OH$_2$) (deg,) and the oxygen−nickel−oxygen average angle ϕ(ONiO) (deg) in the first solvation shell of Ni^{2+} are listed. [b] This work, first principles molecular dynamics using the PBE functional and the model with 128 water molecules. The part of the trajectory with a 6-fold coordinated Ni^{2+} ion. [c] As footnote *b*, but for the part of the trajectory with a 5-fold coordinated Ni^{2+} ion. [d] Ref 8. Quantum mechanics/molecular mechanics with the UHF/double-ζ/Los Alamos effective core potential (Ni) level of theory used for QM. [e] Ref 6. Empirical MD using a nonpolarizable force field. [f] Refs 3 and 9. Empirical MD using a nonpolarizable force field. [g] Reviewed in ref 1, with original literature cited therein. [h] Range of 26 experimental results from X-ray diffraction, EXAFS, and neutron diffraction. Only one report of 2.15 Å. [i] Ref 3. Extended X-ray absorption fine structure (EXAFS). [j] Ref 2. EXAFS. [k] Neutron scattering data. [l] Ref 53. Neutron scattering, 0 ± 20° at low concentration, 34 ± 8 or 42 ± 8° at 4.4 M. [m] Ref 54. Neutron scattering.

water molecule, which is defined by its normal vector. Figure S2 (Supporting Information) illustrates the two definitions as well as the simulated distributions of the two angles. In the FSS, only a small difference between θ and tilt angle exists, so they are not distinguished in further discussion. A broad range of tilt angles have been reported for the aqueous Ni^{2+} solution. Numerous older experimental data[1,53,54] show a tilted geometry, while a newer EXAFS study[3] is in agreement with angle oscillating around 0°. Inada et al.[8] reported, using the QM/MM method, a flat maximum around 0°, using the modest unrestricted Hartree−Fock level of theory for the QM part. Chillemi et al.[9] developed an empirical potential according to the experimental results of D'Angelo et al.[3] Classical MD using this potential also resulted in an around-zero tilt angle. Odelius et al.[6] obtained the angle of 35° from a classical MD simulation in a study concerning magnetic properties.

In agreement with the majority of experimental data, the current FPMD trajectories show an average tilt angle significantly distinct from zero. The average value from the 6-fold coordinated part of the FPMD trajectory is 43.5°, and the maximum of the distribution is near 47°. The same angle was observed in our simulations with both 127 and 255 solvent molecules. Static $Ni(H_2O)_6^{2+}$ structures (Table 2) obtained by optimization in implicit (COSMO) water also yielded a tilted water geometry (angle of ca. 45° at PBE level), representing very well the FPMD distribution. Hybrid functionals yield a somewhat less tilted geometry at 30−38°, however.

FPMD simulations of solvated paramagnetic ions have seldom been reported. Hence, there are very few data at the first principles level with which the present findings can be compared. As an example, in a simulation of the gadolinium ion reported by Yazyev and Helm,[55] an average tilt angle of 35° was obtained, whereas the experimental values in that case range between 10° and 24°.[1] In contrast, distribution of the tilt angle was found to be rather narrow, centered around zero degrees when using classical MD together with a polarizable force field.[11] It remains somewhat unclear how well the tilt angle distributions obtained presently for Ni^{2+} reflect the physical reality since the range of experimental results is very broad.

The distributions of the tilt and θ angles in SSS are also depicted in Figure S2 (Supporting Information). The two differently defined angles have differing distributions in SSS, in contrast to FSS. Both distributions are much broader than in FSS, reflecting the much stronger orientational bias in FSS. The SSS tilt angle distribution has two flat maxima, one around 50° where the oxygen is directed toward the central ion, reminiscent of the prevailing situation in FSS. The second maximum corresponds to the oxygen atoms pointing outward (the ∼105° local maximum in Figure S2). Distribution of the θ angle shows that there is vanishing probability for the plane of the water molecule to be perpendicular to the oxygen−ion vector.

Structure of the Surrounding Water. The parameters of the simulated RDF of the water atoms as well as published data (the latter obtained for pure water) are summarized in Table 4. It is known from the literature and also apparent from Table 4 that FPMD based on DFT tends to overstructure water. This is shown both in the O−O and H−H RDF peak locations that are found at values that are slightly smaller than in the experimental data and in the heights of the peaks that are too large. Whereas the height of the first experimental maximum of the O−O RDF falls into the range of 2.6−2.8, FPMD based on PBE typically predicts values over 3.2. Our work is well in line with the FPMD studies of pure water using the PBE functional,[26,29,28] implying a very small relative effect of the ion on the average water structure

Table 4. Comparison of the Position of the Simulated Maxima (r_{max}) and Peak Values (g_{max}) of Intermolecular Radial Distribution Functions of Liquid Water from the First Principles Molecular Dynamics Simulation of the Aqueous Solution of the Ni^{2+} Ion (This Work) and Pure Water (Literature)[a]

method	r_{max}^{OO} (Å)	g_{max}^{OO}	r_{max}^{OH} (Å)	g_{max}^{OH}	r_{max}^{HH} (Å)	g_{max}^{HH}
FPMD/PBE[b]	2.71/4.4	3.25/1.42	1.71/3.22	1.70/1.63	2.25/3.80	1.76/1.23
MD[c]	2.82/4.62	3.15/1.11	1.86/3.30	1.52/1.62	2.44/3.82	1.56/1.17
FPMD/BLYP[d]	2.82−2.84	3.12−3.24				
FPMD/BLYP-D[d]	2.80	2.78				
FPMD/PBE-D[d]	2.76	3.35				
FPMD/PBE	2.76,[d] 2.73,[e] 2.70[f]	3.28−3.54,[d] 3.25,[e] 2.99[f]				
FPMD/PBE0	2.74[f]	2.58[f]				
exptl.[g]	2.76/4.52	2.62/1.15	1.78/3.31	1.11/1.52	2.35/3.85	1.28/1.17
	2.8/4.5[h]	2.8/1.13[h]				

[a] The columns contain the properties of the first/second maximum if both are available. [b] This work; parameters extracted from the analysis of all water molecules regardless of their localization in the solvation structure of the ion. The values are identical for the smaller (127 water molecules) and larger (255) simulated systems. [c] Empirical MD using the polarizable AMOEBA force field.[56] [d] Ref 28. "D" in BLYP-D and PBE-D indicates the dispersion correction.[57,58] [e] Ref 29. [f] Ref 26. [g] Ref 59. Neutron diffraction. [h] Ref 60. X-ray scattering.

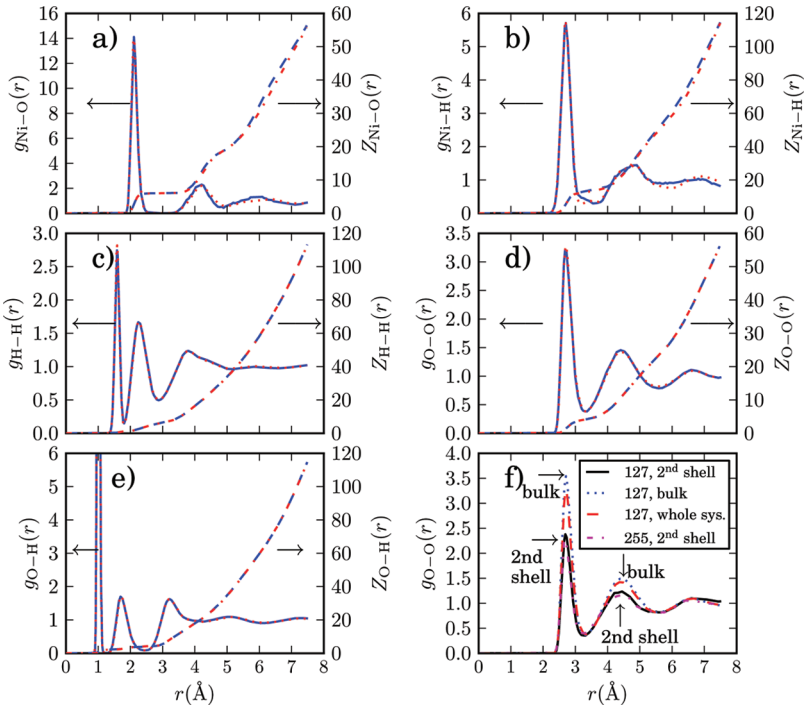

Figure 2. Radial distribution functions $g(r)$ and running coordination numbers $Z(r)$ in the first principles molecular dynamics simulations of the aqueous solution of the Ni^{2+} ion. (a) Ni−O, (b) Ni−H, (c) H−H, (d) O−O, (e) O−H, and (f) O−O RDFs. The solid blue and dotted red lines represent the RDF curves for the simulation containing 255 (33.75 ps) and 127 (90 ps) water molecules, respectively. The dashed blue (255) and dash-dotted red (127) lines represent the running coordination numbers. Panel f shows the differences in the radial distribution functions between the bulk water and the water molecules of the second coordination shell.

in our simulation. In the work of Schmidt et al.,[28] an empirical dispersion correction[57,58] is included. The best results are obtained using BLYP-D, which in a constant pressure simulation also results in a nearly experimental water density. The role of the "D" correction on the static structure may, however, be relatively small, as the PBE calculations with and without the dispersion corrections produce practically similar results. It appears that the computationally demanding hybrid DFT functionals also lead to some improvements over FPMD performed using GGA functionals.[26] The structural properties of water obtained from the classical AMOEBA[56] model, which is generally considered good for the water structure and dynamics, produces overestimated interatomic distances, in contrast to the underestimation found for FPMD. However, the RDF peak values remain too large with the empirical simulation.

The features of the intrawater O−O, O−H, and H−H RDF curves in Figure 2 are practically identical for both simulations, with 127 and 255 water molecules. In contrast, the Ni−O and Ni−H RDFs show small differences between the two simulations after the first maximum. The O−O RDF calculated separately for SSS is shifted by ca. 0.02 Å toward a shorter distance, indicating the effect of the central ion (Figure 2f). The height of the

maximum of the second shell RDF is lowered as compared to the bulk simulation by the fact that the molecules in the SSS have on average fewer neighbors than the molecules of the bulk.

We have neglected the effects of the quantum dynamics of the nuclei. Specialized simulations with path-integral treatment of quantum effects[61,62] are reported to perform better than the classical dynamics models, giving RDFs very close to the experimental results for liquid water.

Translational Diffusion in Water. In contrast to the average structural properties of water, the dynamic properties obtained by the different methods span a much broader range. Literature reports about dynamic properties of water by FPMD are by and large restricted to the coefficient of translational diffusion D. Therein, FPMD delivers results that deviate by an order of magnitude from the experimental values.[25−30] From Table 5, we can observe that the diffusion coefficients D that we obtain for water in the aqueous solution of Ni^{2+} are near the GGA-based FPMD simulations of pure water by others but are clearly too small as compared to the experimental results. D resulting from the larger simulation box is doubled with respect to the results corresponding to the smaller box. This may indicate a finite size effect due to insufficient size of the simulation cell. Indeed, the results of the corresponding FPMD simulation of pure water[29] give a still larger value, when extrapolated to an infinite box size. We have to point out, however, that the average simulation temperature of the bigger system was almost 10 K higher in our work, which influences the numerical values. It is noteworthy that hybrid DFT-based FPMD led to much improved diffusion constants,[26] in qualitative agreement with the experiment. A high-quality empirical simulation using a polarizable force field (but also other force fields not listed here) also provides better data than obtained with FPMD using the PBE functional.

Rotational Dynamics in Water. The reorientational correlation times are compared in Table 5. To be able to relate our results to the available experimental data, we calculated the rotational correlation functions associated with both the first- and second-order Legendre polynomials, eq 2. To obtain the correlation time τ, we calculated the integrals of the normalized correlation function:

$$\tau = \int_0^\infty c(t)\,\mathrm{d}t \tag{5}$$

$$c(t) = \frac{C(t)}{\langle C(0)\rangle} \tag{6}$$

in which the dominant first part was obtained by numerical integration, whereas the tail region was integrated analytically after extrapolation by a fitted biexponential function. We also report τ obtained via an alternative route, corresponding directly to a biexponential fit to the correlation function. Since the two fit parameters are sensitive to the sampling of the trajectory, we only report the longer τ corresponding to the tail region. The shorter time, corresponding to the fast-decaying exponent, reflects the initial, complex behavior of the correlation function.

Ultrafast time-resolved experimental data[66] imply that the reorientational dynamics differ from simple diffusive rotation. A jump model of water reorientation was recently described, e.g., in refs 63, 68−70. The details of the reorientational dynamics are essential, for example, for the correct evaluation of the NMR relaxation data, see, e.g., ref 71. There are, however, no other FPMD studies available for comparison with our simulation. The

Table 5. Comparison of the Self-Diffusion Coefficient D As Well As τ_1 and τ_2 Correlation Times of the Rotational Autocorrelation Functions for Pure Water (Literature Values) and an Aqueous Solution of Ni^{2+} (Present Work)

method	D (Å^2/ps)	τ_1 (ps)[a]	τ_2 (ps)[a]	temperature (K)
FPMD/PBE[b,c]	0.02	38, 34	26, 18	368
FPMD/PBE[c,d]	0.04	33, 30	21, 16	378
FPMD/PBE[e]	0.047			350
FPMD/PBE0[e]	0.28			350
FPMD/PBE[f]	0.079			300
MD	0.202[g,h]	6.6[g,i]	3.5[g,i]	298
exptl.	0.23[j]		2.5[k]	298
exptl.[l]		0.7,13		
exptl.[m]			2.07	313

[a] The correlation times τ_1 and τ_2 are simulated using first- and second-order Legendre polynomials, eq 2. [b] This work; first-principles molecular dynamics using the PBE functional, 127 water molecules. [c] Two values for both the first- and second-order correlation times τ are presented: the longer time of a biexponential fit and the "integral" time, in this order (see text). [d] As footnote *b*, but for 255 water molecules. [e] Ref 26. To be compared with ca. 0.5 Å^2/ps of 350 K for D_2O. [f] Ref 29. Result extrapolated to an infinite simulation box size. [g] Ref 56. Empirical molecular dynamics using the polarizable AMOEBA force field. [h] Ref 56. [i] Ref 63. [j] Ref 64. Diaphragm-cell technique. [k] Ref 65. Femtosecond infrared pump−probe experiment. [l] Ref 66. Femtosecond infrared pump−probe experiment, two constants of biexponential decay, temperature not reported. [m] Ref 67. ^{1}H NMR relaxation.

numbers obtained from our work are three or more times larger than the experimental values. This implies a connection to the glassy behavior of FPMD water discussed, e.g., in refs 27, 72, and 73. Slow dynamics by FPMD are therefore manifested not only in the translational diffusion as described above but also in the reorientational dynamics. Comparison of the reorientational dynamics around the different molecule-fixed axes in Figure 3 indicates relatively similar dynamics in the FSS around the direction of the molecular dipole moment as well as that of the normal of the plane of the molecule. In contrast, hindered rotation around the remaining in-plane direction is observed. Beyond FSS, a somewhat faster, isotropic reorientational motion is seen.

Angular Momentum Dynamics in Water. Further insight into the dynamical properties of water is brought by the angular velocity correlation function or, when including the moment of inertia, the angular momentum correlation function. The results from our simulations are given in Table 6. Figure 4 compares the functions for the different molecular axes and different location in solution (FSS, SSS, and bulk). See Figures S3 and S4 (Supporting Information) for an analysis of the differences between the molecule-fixed axes and effects of the simulation cell size, respectively. The literature data in Table 6 include the available empirical MD simulations[74−76] and inelastic neutron scattering data.[77] Numbers from our simulation are those for the angular momentum correlation function that are, however, identical to those of the angular velocity correlation function within the reported precision. [For test purposes, both angular momentum and an angular velocity correlation function have been calculated and compared.] Clearly, the FPMD simulation produces, albeit at higher temperatures than in the other data, the time of first minimum closest to the experimental data. Among the empirical simulations, there are large differences in τ_{min} for

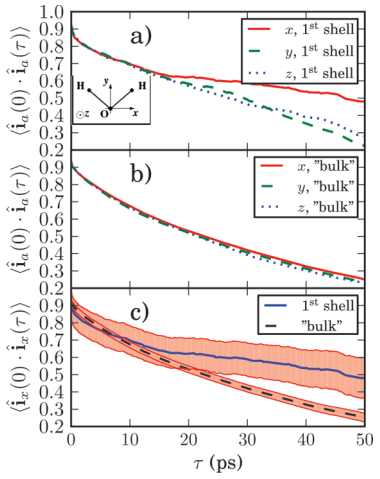

Figure 3. Reorientational correlation functions of the water molecule in aqueous Ni^{2+} from first-principles molecular dynamics simulation with 127 solvent molecules. The functions appropriate for the different molecule-fixed axes are illustrated in (a) first solvation shell and (b) bulk water as well as (c) the x direction in both. The inset of panel a indicates the choice of the molecule-fixed axis system. $\hat{\mathbf{e}}_a$ (a = x,y,z) denotes a unit vector along the molecular axis a. Panel c shows the uncertainty intervals for $a = x$ for the correlation functions of the first shell and bulk water. Here, "bulk" denotes all water molecules except those contained in the first solvation shell.

the two simulations at nearly identical temperatures using the MCYL and TIP4P force fields.[74,75] Differences between, on the one hand, the classical TIP4P model and, on the other hand, TIP4P with nuclear quantum effects appear to be of minor importance around room temperature. All of the simulations point to a slightly anisotropic behavior of the angular momentum correlation function, with the decay of the off-plane direction slightly slower than that in the two in-plane directions.

From the value of the angular momentum correlation function at its first minimum, we can reconfirm the previous observation that the intermolecular interactions within the FPMD simulation restrict the motion more than required. Nevertheless, the decay rate of the angular momentum is reproduced better than by classical force fields.

We further present a detailed analysis of the angular momentum correlation functions from our simulation in Figure 4 as well as in Figures S3 and S4 (Supporting Information). From Figure 4, it may be concluded that FSS, which interacts strongly with the metal ion, features faster fluctuations of the angular momentum than SSS and bulk water. The breakdown of the angular momentum correlation function in terms of the Cartesian components of **l** in molecule-fixed frame (Figure S3) reveals that the short time-scale dynamics are roughly isotropic, meaning that the angular momenta about the three molecular axes behave similarly. The two in-plane components l_x and l_y also behave similarly in SSS and bulk water, whereas the perpendicular component l_z exhibits the slowest time-scale.

There exists in FSS a regularly oscillating, slowly decaying angular momentum autocorrelation function, particularly in the y direction (molecular dipole moment) as compared to the more distant molecules from the ion. In Figure S4 (Supporting Information), the comparison of the smaller (127 water molecules) and larger (255) simulated systems is plotted for FSS and bulk water, here, molecules beyond FSS. From Figure S4

Table 6. Features of the Angular Velocity Correlation Function of Water Molecules in Simulated Aqueous Solution of Ni^{2+} Ion (This Work) or Pure Liquid Water (Literature)[a]

method	τ_{min} (fs)[b]	TCF_{min}[c]	temperature (K)
FPMD[d]	20, 20, 25	−0.68, −0.67, −0.68	368
MD[e]	45, 45, 55	−0.52, −0.54, −0.52	300
MD[f]	25, 29, 31	−0.59, −0.51, −0.58	298
MD[g]	25, 30, 32	−0.59, −0.48, −0.54	298
MD[h]	24, 24, 31	−0.5, −0.5, −0.5	286
exptl.[i]	14	−0.44	300

[a] Molecular axes are depicted in Figure 3a. [b] Literature numbers were extracted from published graphs. τ_{min} is the time of the first minimum corresponding to x, y, and z axes, in this order. [c] The value of the correlation function at the first minimum. [d] This work, first-principles molecular dynamics simulation of Ni^{2+} in liquid water (127 molecules, PBE functional). [e] Ref 74. *Ab-initio*-based parametrized empirical potential MCYL. [f] Ref 75. Empirical TIP4P simulation. [g] Ref 75. TIP4P with nuclear quantum effects. [h] Ref 76. MCY potential. [i] Ref 77. Inelastic neutron scattering.

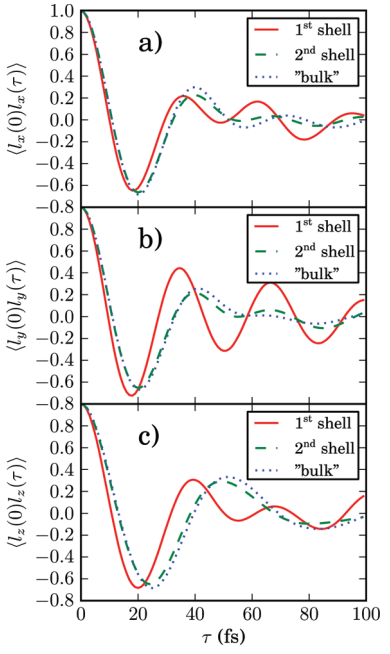

Figure 4. Angular momentum correlation functions of the water molecules in the aqueous solution of Ni^{2+} from first-principles molecular dynamics simulation with 127 water molecules. Comparison of the water property in the first and second solvation shells as well as bulk, for the different molecular axes. Here, "bulk" denotes all water molecules except those in the first and second solvation shells. See Figure 3a for the definition of the molecule-fixed axes.

(a−c), we observe that in the larger simulation box the periodic oscillations become significantly more damped for the FSS water molecules. There also exists a tiny difference in the rate of the oscillation: the smaller simulation box corresponds to slightly faster oscillations of **l**. Since this observation applies only to FSS (the bulk water is practically unaffected), the difference cannot be explained by the 10 K difference in the simulation temperature of the smaller and larger system. The finite size of the periodic box clearly exaggerates the oscillatory behavior. Hence, one should be careful in FPMD simulations that require small simulation cells,

when evaluating data that depend on the angular momentum correlation functions or related dynamical properties of FSS. Figure S5 (Supporting Information) indicates that only a small difference exists between the angular momentum autocorrelation function $\langle \mathbf{l}(0)\cdot\mathbf{l}(\tau)\rangle$ for the $\mathbf{l}$ vector as calculated in the laboratory frame and the Eckart frame, the latter enabling the above-discussed breakdown into the different molecular-fixed axes $\langle \mathbf{l}_x(0)\cdot\mathbf{l}_x(\tau)\rangle$ etc.

As an overall conclusion, the present FPMD simulations result in structural parameters, in good agreement with the current knowledge. There are better results obtained for individual properties of pure water reported in literature. In our case, selecting the PBE functional resulted in balanced properties of the more complex system featuring ion solvation. The obtained trajectory should therefore be well-suited, e.g., for the calculation of average magnetic properties.[52] As hinted by the known issues regarding the translational diffusion constant by FPMD, the reorientational dynamics are also too slow in FPMD with PBE. In contrast, FPMD for angular momentum dynamics performs significantly better. FPMD calculations of dynamical properties require particular care.

The dispersion correction[57,58] was shown to improve properties of pure water calculated by the PBE functional, though even then the problem of overstructured water is only alleviated.[28] The dynamical properties should therefore also be shifted in the required direction. In the case of the PBE functional, an improvement in gas-phase energies has been seen in more complex systems of hydrated aluminum complexes, their hydrolysis proceeding a little faster and further compared to the uncorrected PBE functional.[20] To see how the interaction between water and Ni^{2+} is affected by the *a posteriori* dispersion corrections, we ran a simple potential energy scan of the Ni^{2+} ion and one water molecule with fixed geometry. The curves are nearly identical, as the dispersion correction is very small compared to the main electrostatic forces (data not shown). The influence of the empirical dispersion corrections on dynamical properties is an interesting topic for further investigation.

Exchange in the First Solvation Shell of the Ni^{2+} Ion. The mechanisms of the exchange of water molecules in the FSS of the Ni^{2+} ion have been discussed in the literature. A MD study by Inada et al.[8] using the Ni−O force field obtained at the unrestricted Hartree−Fock level, including a three-body correction, pointed to a dissociative mechanism. This means for the Ni^{2+} complex that the exchange proceeds via a 5-fold coordinated intermediate, i.e., one molecule leaves FSS before the new molecule arrives. However, the same authors concluded in a QM/MM study[7] that mainly the associative mechanism prevails. Later on, Loffler et al.[10] applied the umbrella sampling method[79] in a classical MD simulation using the same three-body-corrected potential as in ref 8 and reconfirmed the dissociative mechanism.

During our simulation with 127 water molecules, a water exchange event in FSS was observed to proceed via a 5-fold, long-lived intermediate. At the beginning of the process, the leaving water molecule gradually increases its Ni−O distance after being expelled by collisions with the other molecules in FSS. The increase of Ni−O distance from 2.15 to 3.75 Å takes 164 fs. After 4.8 ps, another molecule approaches the 5-fold coordinated complex. The shortening of the Ni−O distance (3.75 to 2.15 Å) takes 373 fs (Figure S6, Supporting Information). The five remaining water molecules largely retain the structure of the usual 6-fold coordination, similarly to the case of static quantum-chemical structures (Figure 1). Static calculations (not shown), in which one of the water molecules was pulled away by extending the Ni−O distance (with the structure otherwise relaxed), showed that the departing water molecule started to prefer hydrogen bonding with the remaining FSS water molecules over coordination with the ion, after $r_{Ni-O} \approx 3.1$ Å.

Observation of such a FSS exchange process for a divalent ion is uncommon in FPMD simulations, and unlikely even in our simulation where the trajectory was exceptionally long (taking into account the system size). To our knowledge, a corresponding observation has not been described in the literature. The dissociative mechanism that we observe is also in accordance with a high-pressure ^{17}O NMR experiment,[80] although by observing this single exchange event, no real conclusions can be made.

A simple calculation addressing the activation energy of the water-exchange mechanism has been done using the COSMO implicit solvation model. We calculated a relaxed surface scan of one water molecule leaving the 6-fold coordinated complex at the PBE/dev2-TZVP level (Figure S7, Supporting Information). We obtained a small potential well of 1.65×10^{-2} eV as compared with $k_BT \doteq 2.58 \times 10^{-2}$ eV at 300 K. At the same level of theory, the 7-fold coordinated structure is unstable, pointing also to the dissociative mechanism of water exchange, although this simple calculation completely neglects all the effects of dynamics and other effects of explicit solvation.

CONCLUSIONS

We have investigated using first-principles computations the structure and dynamics of the aqueous solution of Ni^{2+}. Both static quantum-chemical calculations of the hexa- and penta-aqua complexes $Ni(H_2O)_n^{2+}$ (n = 5, 6), as well as first-principles molecular dynamics simulation of the aqueous solution, were performed. The investigated properties were the radial correlation functions, translational diffusion constants, and reorientational and angular momentum correlation functions. The first principles trajectory is the longest of its kind so far, for system and properties of the present type. Two different simulation cells were used with 127 and 255 water molecules and one Ni^{2+} ion.

The detailed structure of the first solvation shell including six water molecules has been found sensitive to the computational level. The optimized r_{Ni-O} distance agrees well with the experiment both in the static hexa-aqua complex and in the radial distribution functions of the simulated trajectory. The most ambiguous structural feature of the hexa-aqua Ni^{2+} complex, and also very important for subsequent calculation of the magnetic properties of the solution, is the tilt angle of the water molecules. We show that the structure of the hexa-aqua Ni^{2+} complex calculated with an implicit solvation model has a tilt angle (∼45°) close to peak of the distribution in the first-principles MD (∼47°), when the same PBE exchange-correlation functional is used. The tilt angle is larger than experimental values (ranging between 30 and 42°), and it is likely that the actual equilibrium tilt angle is close to 33° obtained for the hexa-aqua complex by the reference SCS-MP2 method.

The extensive FPMD trajectory allowed us to study the dynamics of the aqueous Ni^{2+} complex including the dynamic properties of the surrounding water. Fortuitously, an exchange event of a water molecule in the first solvation shell occurred during the simulation, and we are, for the first time, able to support by first-principles calculation the suggestion that it proceeds by a dissociative mechanism through a 5-fold

coordinated intermediate, which to a significant extent preserves the octahedral symmetry.

The computed translational diffusion constant of the water molecules has been compared to the experimental and various computational results. The diffusion constant is lower by an order of magnitude than the experimental results in pure water. This is a common finding for the combination of FPMD and the PBE exchange-correlation functional. The calculated diffusion constants feature a pronounced dependence on the simulation cell size, with the larger system leading to somewhat improved agreement with experimental results. However, qualitatively correct results have only been obtained in the literature with either expensive hybrid DFT-based FPMD or by a number of modern, empirical force fields.

We fill a gap in the literature by evaluation of the rotational dynamics of the water molecules by FPMD. The obtained τ_1 correlation time is several times longer than published experimental results. τ_2, which is obtained from experiments much more frequently, differs from our simulation by roughly an order of magnitude. The slow dynamics implies that the properties that depend on either translational or rotational diffusion must be evaluated with special care in FPMD simulations. For example, the empirical AMOEBA simulations outperform the present FPMD simulation in this respect.

Angular velocity or angular momentum correlation time of liquid water are very seldom reported in the literature. This quantity is of relevance for the spin-rotation mechanism of NMR relaxation. Comparison with results from inelastic neutron scattering indicates good performance of FPMD for this property, yielding better results than empirical force fields. Evaluation of the correlation time for the first solvation shell of the Ni^{2+} ion in the smaller and larger simulation box reveals artifacts from periodic boundary conditions, when a small cell is used. The angular momentum dynamics of the first solvation shell are overall faster than in the second shell or bulk water.

■ ASSOCIATED CONTENT

Ⓢ Supporting Information. Additional figures related to the structural and dynamical properties of $Ni^{2+}(aq)$ as well as a table of functional dependence of the distances between the nickel atom and oxygen in $Ni(H_2O)_5^{2+}$. This material is available free of charge via the Internet at http://pubs.acs.org

■ AUTHOR INFORMATION

Corresponding Author
*E-mail: jiri.mares@oulu.fi.

■ ACKNOWLEDGMENT

The authors thank Dr. Perttu Lantto and Dr. Matti Hanni (Oulu) for helpful discussions. The research leading to these results has received funding from the European Union Seventh Framework Programme (FP7/2007-2013) under grant agreement no. 254552 (J.M.). Further support was received from Swiss National Funds - project PBZHP2-125353 (J.M.), University of Helsinki Research Funds, and the University of Oulu. J.M., H.L., and J.V. belong to the Finnish Center of Excellence in Computational Molecular Science (CMS). Computational resources due to CSC (Espoo, Finland) were used.

■ REFERENCES

(1) Ohtaki, H.; Radnai, T. *Chem. Rev.* **1993**, *93*, 1157.
(2) Inada, Y.; Hayashi, H.; Sugimoto, K.; Funahashi, S. *J. Phys. Chem. A* **1999**, *103*, 1401.
(3) D'Angelo, P.; Barone, V.; Chillemi, G.; Sanna, N.; Meyer-Klaucke, W.; Pavel, N. V. *J. Am. Chem. Soc.* **2002**, *124*, 1958.
(4) Bounds, D. G. *Mol. Phys.* **1985**, *54*, 1335.
(5) Natália, M.; Cordeiro, D. S.; Ignaczak, A.; Gomes, J. A. N. F. *Chem. Phys.* **1993**, *176*, 97.
(6) Odelius, M.; Ribbing, C.; Kowalewski, J. *J. Chem. Phys.* **1995**, *103*, 1800.
(7) Inada, Y.; Loeffler, H. H.; Rode, B. M. *Chem. Phys. Lett.* **2002**, *358*, 449.
(8) Inada, Y.; Mohammed, A. M.; Loeffler, H. H.; Rode, B. M. *J. Phys. Chem. A* **2002**, *106*, 6783.
(9) Chillemi, G.; D'Angelo, P.; Pavel, N. V.; Sanna, N.; Barone, V. *J. Am. Chem. Soc.* **2002**, *124*, 1968.
(10) Loffler, H. H.; Mohammed, A. M.; Inada, Y.; Funahashi, S. *J. Comput. Chem.* **2006**, *27*, 1944.
(11) Clavaguéra, C.; Calvo, F.; Dognon, J. P. *J. Chem. Phys.* **2006**, *124*, 74505.
(12) Piquemal, J.; Perera, L.; Cisneros, G. A.; Ren, P.; Pedersen, L. G.; Darden, T. A. *J. Chem. Phys.* **2006**, *125*, 54511.
(13) Villa, A.; Hess, B.; Saint-Martin, H. *J. Phys. Chem. B* **2009**, *113*, 7270.
(14) Lyubartsev, A. P.; Laasonen, K.; Laaksonen, A. *J. Chem. Phys.* **2001**, *114*, 3120.
(15) Bakó, I.; Hutter, J.; Pálinkás, G. *J. Chem. Phys.* **2002**, *117*, 9838.
(16) Lightstone, F. C.; Schwegler, E.; Allesch, M.; Gygi, F.; Galli, G. *ChemPhysChem* **2005**, *6*, 1745.
(17) Ikeda, T.; Boero, M.; Terakura, K. *J. Chem. Phys.* **2007**, *126*, 34501.
(18) Todorova, T.; Hünenberger, P. H.; Hutter, J. *J. Chem. Theory Comput.* **2008**, *4*, 779.
(19) Petit, L.; Vuilleumier, R.; Maldivi, P.; Adamo, C. *J. Chem. Theory Comput.* **2008**, *4*, 1040.
(20) Saukkoriipi, J.; Laasonen, K. *J. Chem. Theory Comput.* **2010**, *6*, 993.
(21) Car, R.; Parrinello, M. *Phys. Rev. Lett.* **1985**, *55*, 2471.
(22) Marx, D.; Hutter, J. *Modern Methods and Algorithms of Quantum Chemistry*, 2nd ed.; John von Neumann Institute for Computing: Jülich, Germany, 2000; Vol. 3, p 329.
(23) Hobza, P.; Šponer, J.; Reschel, T. *J. Comput. Chem.* **1995**, *16*, 1315.
(24) Laasonen, K.; Sprik, M.; Parrinello, M.; Car, R. *J. Chem. Phys.* **1993**, *99*, 9080.
(25) Kuo, I. W.; Mundy, C. J.; McGrath, M. J.; Siepmann, J. I.; VandeVondele, J.; Sprik, M.; Hutter, J.; Chen, B.; Klein, M. L.; Mohamed, F.; Krack, M.; Parrinello, M. *J. Phys. Chem. B* **2004**, *108*, 12990.
(26) Todorova, T.; Seitsonen, A. P.; Hutter, J.; Kuo, I. W.; Mundy, C. J. *J. Phys. Chem. B* **2006**, *110*, 3685.
(27) Lee, H.; Tuckerman, M. E. *J. Chem. Phys.* **2007**, *126*, 164501.
(28) Schmidt, J.; VandeVondele, J.; Kuo, I. W.; Sebastiani, D.; Siepmann, J. I.; Hutter, J.; Mundy, C. J. *J. Phys. Chem. B* **2009**, *113*, 11959.
(29) Kühne, T. D.; Krack, M.; Parrinello, M. *J. Chem. Theory Comput.* **2009**, *5*, 235.
(30) Kuo, I. W.; Mundy, C. J.; McGrath, M. J.; Siepmann, J. I. *J. Chem. Theory Comput.* **2006**, *2*, 1274.
(31) Neese, F. *ORCA*; University of Bonn: Bonn, Germany, 2009.
(32) Perdew, J. P.; Burke, K.; Ernzerhof, M. *Phys. Rev. Lett.* **1996**, *77*, 3865.
(33) Perdew, J. P.; Burke, K.; Ernzerhof, M. *Phys. Rev. Lett.* **1997**, *78*, 1396.
(34) Becke, A. D. *Phys. Rev. A* **1988**, *38*, 3098.
(35) Lee, C.; Yang, W.; Parr, R. G. *Phys. Rev. B* **1988**, *37*, 785.
(36) Miehlich, B.; Savin, A.; Stoll, H.; Preuss, H. *Chem. Phys. Lett.* **1989**, *157*, 200.
(37) Becke, A. D. *J. Chem. Phys.* **1993**, *98*, 5648.

(38) Stephens, P. J.; Devlin, F. J.; Chabalowski, C. F.; Frisch, M. J. *J. Phys. Chem.* **1994**, *98*, 11623.
(39) Becke, A. D. *J. Chem. Phys.* **1993**, *98*, 1372.
(40) Grimme, S. *J. Chem. Phys.* **2003**, *118*, 9095.
(41) Weigend, F.; Ahlrichs, R. *Phys. Chem. Chem. Phys.* **2005**, *7*, 3297.
(42) Hess, B.; Kutzner, C.; van der Spoel, D.; Lindahl, E. *J. Chem. Theory Comput.* **2008**, *4*, 435.
(43) VandeVondele, J.; Krack, M.; Mohamed, F.; Parrinello, M.; Chassaing, T.; Hutter, J. *Comput. Phys. Commun.* **2005**, *167*, 103.
(44) The CP2K depelopers group. http://cp2k.berlioz.de/ (accessed Jul 27, 2011).
(45) Goedecker, S.; Teter, M.; Hutter, J. *Phys. Rev. B* **1996**, *54*, 1703.
(46) Swope, W. C.; Andersen, H. C.; Berens, P. H.; Wilson, K. R. *J. Chem. Phys.* **1982**, *76*, 637.
(47) Humphrey, W.; Dalke, A.; Schulten, K. *J. Mol. Graphics* **1996**, *14*, 33.
(48) Allen, M. P.; Tildesley, D. J. *Computer Simulation of Liquids*; Oxford University Press: New York, 1989; p 60.
(49) Eckart, C. *Phys. Rev.* **1935**, *47*, 552.
(50) Vaara, J.; Lounila, J.; Ruud, K.; Helgaker, T. *J. Chem. Phys.* **1998**, *109*, 8388.
(51) Cohen, A. J.; Mori-Sánchez, P.; Yang, W. *Science* **2008**, *321*, 792.
(52) Mareš, J.; Liimatainen, H.; Pennanen, T. O.; Vaara, J. Submitted for publication.
(53) Neilson, G. W.; Enderby, J. E. *J. Phys. C: Solid State* **1978**, *11*, L625.
(54) Newsome, J.; Neilson, G.; Enderby, J.; Sandström, M. *Chem. Phys. Lett.* **1981**, *82*, 399.
(55) Yazyev, O. V.; Helm, L. *J. Chem. Phys.* **2007**, *127*, 84506.
(56) Ren, P.; Ponder, J. W. *J. Phys. Chem. B* **2003**, *107*, 5933.
(57) Grimme, S. *J. Comput. Chem.* **2004**, *25*, 1463.
(58) Zimmerli, U.; Parrinello, M.; Koumoutsakos, P. *J. Chem. Phys.* **2004**, *120*, 2693.
(59) Soper, A. K. *Chem. Phys.* **2000**, *258*, 121.
(60) Hura, G.; Sorenson, J. M.; Glaeser, R. M.; Head-Gordon, T. *J. Chem. Phys.* **2000**, *113*, 9140.
(61) Paesani, F.; Zhang, W.; Case, D. A.; Cheatham, T. E.; Voth, G. A. *J. Chem. Phys.* **2006**, *125*, 184507.
(62) Paesani, F.; Voth, G. A. *J. Phys. Chem. B* **2009**, *113*, 5702.
(63) Laage, D.; Hynes, J. T. *J. Phys. Chem. B* **2008**, *112*, 14230.
(64) Mills, R. *J. Phys. Chem.* **1973**, *77*, 685.
(65) Rezus, Y. L. A.; Bakker, H. J. *J. Chem. Phys.* **2005**, *123*, 114502.
(66) Woutersen, S.; Emmerichs, U.; Bakker, H. J. *Science* **1997**, *278*, 658.
(67) Jonas, J. *J. Chem. Phys.* **1976**, *65*, 582.
(68) Tielrooij, K.; Petersen, C.; Rezus, Y.; Bakker, H. *Chem. Phys. Lett.* **2009**, *471*, 71.
(69) Laage, D. *J. Phys. Chem. B* **2009**, *113*, 2684.
(70) Bakker, H. J.; Skinner, J. L. *Chem. Rev.* **2010**, *110*, 1498.
(71) Grant, D. M.; Brown, R. A. In *Encyclopedia of NMR Spectroscopy*; Grant, D. M., Harris, R. K., Eds.; Wiley: New York, 1996; p 4003.
(72) Fernández-Serra, M. V.; Artacho, E. *J. Chem. Phys.* **2004**, *121*, 11136.
(73) Sit, P. H.; Marzari, N. *J. Chem. Phys.* **2005**, *122*, 204510.
(74) Evans, M.; Refson, K.; Swamy, K.; Lie, G.; Clementi, E. *Phys. Rev. A* **1987**, *36*, 3935.
(75) de la Peña, L. H.; Kusalik, P. G. *J. Chem. Phys.* **2004**, *121*, 5992.
(76) Impey, R. W.; Madden, P. A.; McDonald, I. R. *Mol. Phys.* **1982**, *46*, 513.
(77) Novikov, A.; Lisichkin, Y.; Fomichev, N. *J. Struct. Chem+.* **1990**, *31*, 574.
(78) Swart, M.; Solà, M.; Bickelhaupt, F. M. *J. Comput. Chem.* **2011**, *32*, 1117.
(79) Torrie, G. M.; Valleau, J. P. *Chem. Phys. Lett.* **1974**, *28*, 578.
(80) Ducommun, Y.; Earl, W. L.; Merbach, A. E. *Inorg. Chem.* **1979**, *18*, 2754.

JCTC Journal of Chemical Theory and Computation

ARTICLE

pubs.acs.org/JCTC

Hybrid Particle-Field Coarse-Grained Models for Biological Phospholipids

Antonio De Nicola,[†,‡] Ying Zhao,[†] Toshihiro Kawakatsu,[§] Danilo Roccatano,[∥] and Giuseppe Milano[†,‡,*]

[†]Dipartimento di Chimica e Biologia, Università di Salerno, I-84084 via Ponte don Melillo Fisciano (SA), Italy

[‡]IMAST Scarl-Technological District in Polymer and Composite Engineering, P.le Fermi 1, 80055 Portici (NA), Italy

[§]Department of Physics, Tohoku University, Aoba, Aramaki, Aoba-ku, Sendai 980-8578, Japan

[∥]Jacobs University Bremen, Campus Ring 1, D-28759 Bremen, Germany

Supporting Information

ABSTRACT: In the framework of a recently developed scheme for a hybrid particle-field simulation technique where self-consistent field theory (SCF) and molecular dynamics (MD) are combined [*J. Chem. Phys.* **2009**, *130*, 214106], specific coarse-grained models for phospholipids and water have been developed. We optimized the model parameters, which are necessary in evaluating the interactions between the particles and the density fields, so that the coarse-grained model can reproduce the structural properties of the reference particle−particle simulations. The development of these specific coarse-grained models suitable for hybrid particle-field simulations opens the way toward simulations of large-scale systems employing models with chemical specificity, especially for biological systems.

1. INTRODUCTION

Phospholipids are an important class of biomolecules. Their amphiphilic nature allows them, when they are dissolved in water, to self-assemble into a lipid bilayer with lipid tails shielded from water and polar head groups exposed to the polar environment. In living organism, lipid bilayers form cellular membranes. Biological membranes are complex structures, and despite the considerable amount of information accumulated, experimental methods able to follow their dynamics with details at the atomic level are not yet available.[1−5] For these reasons, lipid bilayers have attracted the interest of the computational biophysics community, and atomistic molecular dynamics (MD) simulations of these systems have been performed for a long time.[6−10] However, these simulations are still computationally very expensive to study processes occurring on the mesoscopic time (>μs) and length scales (>100 nm).[11] Therefore, to overcome this problem, alternative computational methods aiming to bridge the time and length scales involved in the relevant phenomena are constantly proposed. In the past few years, coarse-grained (CG) simulations became a very popular method for studying these systems. The CG approach involves the reduction of degrees of freedom in the atomic model of the simulated system by combining several atoms to a single particle ("effective bead"). CG methods have been successfully applied to several problems involving polymers,[12] biomolecules,[2] and more in general soft matter.[13]

For phospholipids, different types of CG models have been developed. For a detailed overview, the reader should refer to a recent review of Muller et al.[14] Sintes and Baumgärtner[15,16] developed a coarse-grained model for lipid bilayers where the solvent is implicitly taken into account. Later, Lenz and Schmid developed this implicit-solvent model to pure lipid bilayers composed of saturated lipids.[17] On the other hand, Goetz and Lipowsky introduced an explicit-solvent CG model for lipid membranes where a binary Lennard-Jones fluid for the solvent and a short chain of beads for the amphiphilic molecules are used.[18]

The degree of coarse-graining of a simulated system is related to the type of process that one wants to investigate. Minimalist CG models (e.g., having a very low discrimination of the chemical details of the molecule) can be successfully applied to study self-assembly phenomena involving many molecules when the structure and dynamics on atomistic length scales can be considered irrelevant for the process, and systems can be conveniently described by only a small number of key properties, e.g., the amphiphilic nature of the molecule. Usually for membrane systems, a clear separation in length, time, and energy scales assumed by this approach is often missing, and the chemical specificity of the models have to be taken into account. Furthermore, these simple models can fail to reproduce more complex phenomena involving specific interactions of membrane with other molecular systems (e.g proteins, polymers). In these cases, the generic nature of the minimal coarse-grain models limits their application.

To possibly avoid these problems, more specific CG models can be developed. These CG models usually employ several different types of beads (not just hydrophobic and hydrophilic). A successful and very widely explored example of this approach is the MARTINI CG model developed by Marrink and co-workers.[19] In the MARTINI force field, the phospholipids are described by beads having different Lennard-Jones-type interaction parameters that can smoothly modulate their hydrophobic/hydrophilic character. In addition, water molecules are treated explicitly with a coarse-grained reduction scheme of four molecules to one.

Received: February 23, 2011
Published: August 03, 2011

Despite, its simplicity, the MARTINI force field is able to reproduce with surprisingly good accuracy the properties of the self-assembly of lipid bilayers.[8,20,21] This model has been successfully extended to proteins.[22]

On the other hand, different computational approaches based on field representations have been proposed to model soft matter systems. In particular, in the framework of the self-consistent field (SCF) theory, the model systems are not represented by particles but by density fields, and the mutual interactions between segments are decoupled and replaced by an interaction between the segments and static external fields.[23] In the SCF theories, these external fields depend on the statistical average of the spatially inhomogeneous density distributions of segments of independent molecules which are interacting only with these fields. Such external fields and the particle density distributions have to be determined self-consistently. Numerous applications to block copolymers,[24−28] proteins,[29] polymer composites,[30] and colloidal particles[31,32] have demonstrated that the SCF theory is a useful and powerful method.

Several models have been reported in the literature to study mixtures of phospholipids and water using a field-based approach. Marcelja proposed the first field model. In this model, the head groups of the lipid molecules are modeled as a boundary to which the tails of the lipid molecules are anchored. The intramolecular degrees of freedom are sampled using the rotational isomeric state (RIS) model, where the segments interact through an anisotropic aligning potential.[33] The inequivalence of tail, head, and solvent segments allows the modeling of bilayers as preassembled structures, and it does not allow the study of self-assembly. Later, a fully self-consistent framework that is capable of describing stable, tensionless, self-assembled bilayers has been proposed. Both random-chain and the RIS-chain models result in membranes with qualitatively similar segment distributions and with similar thermodynamic properties.[34] Quantitatively, however, this approach underestimates the experimentally measured membrane thickness by about 50%.[14] More recently, molecular-level SCF theories that are able to treat phospholipids have been proposed.[35] The main point of these SCF techniques is to split up the calculation of multibody interactions into two procedures: i. e., to find the ensemble averaged conformation distribution and to find the segment potentials based on the segment distribution. For these purposes, differential equations have to be solved numerically using lattice approximations, and a discrete set of coordinates onto which segments can be placed has to be defined. Layers are defined imposing reflecting boundary conditions to mimic a multilamellar system. Parameters are defined so that the results of the MD simulations match those of the SCF simulations.[35] Müller and Schick[36] proposed an alternative approach developing an off-lattice representation of the field theory and obtained the single-chain partition function via a partial enumeration[37] over a large set of molecular conformations of a lipid chain with the RIS statistics. As the partition function of a single lipid in an external field cannot be obtained analytically for a realistic molecular architecture, one has to approximate the probability distributions of the conformations of noninteracting lipid molecules by a representative sample of single lipid conformations.

More recently, Müller and Smith[38] introduced a hybrid approach in the framework of SCF theory by combining it with a Monte Carlo simulation of a coarse-grained model of polymer chains to study phase separation in binary polymer mixtures. This approach has been widely and successfully applied by Müller and co-workers to coarse-grained models of diblock copolymer thin films[39] and polymer nanocomposites.[40] One of the advantages of this hybrid approach is the lack of any limitation in treating complex molecular architectures and/or intramolecular interactions. With these precedents, very recently, a hybrid particle-field approach, where the molecular dynamics (MD) method is combined with SCF description (MD-SCF), was proposed, and an implementation suitable for the treatment of atomistic force fields and/or specific coarse-grained models has been reported.[41,42]

Particle-based CG models like MARTINI are still computationally expensive compared to SCF approaches. In the following, we will refer to these models as particle−particle (PP) models. On the other hand, SCF approaches ensure accessibility to definitely larger length and time scales but at the cost of very low chemical specificity. The idea behind the combined MD-SCF method is to obtain a strategy, as far as will be possible, having the main advantages and avoiding the main disadvantages of both techniques.

In this paper, we report the development of coarse-grained specific models for biologically relevant phospholipids that are suitable for the hybrid MD-SCF techniques. In the following, we will refer to these models as particle-field (PF) models.

The paper is organized as follows: In section 2, the basis of SCF theory, which is useful for the reader to understand in regard to the present investigation, a brief description of the computational scheme for hybrid particle-field MD-SCF simulations, and simulation details are reported. In section 3, the description of the models and the strategy of the parametrization are reported. In section 4, particle-field MD-SCF simulation results of lipid bilayers are reported in comparison with classical MD simulations using the MARTINI force field, where the latter simulations are hereafter called PP simulations.

2. COMPUTATIONAL METHOD

2.1. MD-SCF Theory and Implementation. In this section, a brief exposition of the recently developed hybrid PF MD-SCF simulation scheme is reported. This section is intended to quickly guide the reader to get the basis of the methodology and to understand the framework of the present investigation. In order to obtain this approach in more detail, the reader should refer to ref 41, where the complete derivation and the implementation are described, and to ref 23 for a general review of SCF methods.

The main feature of the hybrid PF MD-SCF approach is that the evaluation of the nonbonded force and its potential between atoms of different molecules, i.e., the most computationally expensive part of MD simulations, is replaced by an evaluation of the external potential that is dependent on the local density at position $\mathbf{r}$. According to the spirit of SCF theory, a many-body problem like molecular motion in systems composed of many molecules is reduced to a problem of deriving the partition function of a single molecule in an external potential $V(\mathbf{r})$. Then, nonbonded force between atoms of different molecules can be obtained from a suitable expression of the potential $V(\mathbf{r})$ and its derivatives.

In the framework of SCF theory, a molecule is regarded as interacting with the surrounding molecules not directly but through a mean field. On the basis of this picture, the Hamiltonian of a system that is composed of M molecules can be split into two parts $\hat{H}(\Gamma) = \hat{H}_0(\Gamma) + \hat{W}(\Gamma)$, where Γ specifies a point in the phase space, which is used as shorthand for a set of positions of all

atoms in the system. Here and also in the following, the hat symbol indicates that the associated physical quantity is a function of the microscopic states described by the phase space Γ.

$\hat{H}_0(\Gamma)$ is the Hamiltonian of a reference ideal system composed of noninteracting chains but with all the intramolecular interaction terms (bond, angle, and nonbonded interactions) that are taken into account in the standard MD simulations. The term $\hat{W}(\Gamma)$ is the deviation from the reference system which is induced by the intermolecular nonbonded interactions.

Assuming the canonical (NVT) ensemble, the partition function of this system is given by

$$Z = \frac{1}{M!}\int \mathrm{d}\Gamma \exp\{-\beta[\hat{H}_0(\Gamma) + \hat{W}(\Gamma)]\} \tag{1}$$

where $\beta = 1/(k_BT)$.

From microscopic point of view, the density distribution of atoms can be defined as a sum of δ functions centered at the center of mass of each particle as

$$\hat{\phi}(\mathbf{r};\Gamma) = \sum_{p=1}^{M}\sum_{i=0}^{S(p)} \delta(\mathbf{r} - \mathbf{r}_i^{(p)}) \tag{2}$$

where M is the total number of molecules in the system, $S(p)$ is the number of particles contained in pth molecule, and $\mathbf{r}_i^{(p)}$ is the position of the ith particle in pth molecule. Several assumptions are introduced to calculate the interaction term $\hat{W}(\Gamma)$. First of all, we assume that $\hat{W}(\Gamma)$ depends on Γ only through the particle density $\hat{\phi}(\mathbf{r};\Gamma)$ as

$$\hat{W}(\Gamma) = W[\hat{\phi}(\mathbf{r};\Gamma)] \tag{3}$$

where $W[\hat{\phi}(\mathbf{r};\Gamma)]$ means that W is a functional of $\hat{\phi}(\mathbf{r};\Gamma)$. Using an identity $f[\hat{\phi}(\Gamma)] = \int D\{\varphi(\mathbf{r})\}\, \delta[\varphi(\mathbf{r}) - \hat{\phi}(\Gamma)] f[\varphi(\mathbf{r})]$ where $\delta[\varphi(\mathbf{r})]$ is the δ functional, the partition function in eq 1 can be rewritten as

$$Z = \frac{1}{M!}\int D\{\varphi(\mathbf{r})\}\int D\{w(\mathbf{r})\} \exp\left\{-\beta\left[-\frac{M}{\beta}\ln z + W[\varphi(\mathbf{r})] - \int V(\mathbf{r})\,\varphi(\mathbf{r})\,\mathrm{d}\mathbf{r}\right]\right\} \tag{4}$$

In this expression, z is the single molecule partition function, $w(\mathbf{r})$ is a conjugate field of $\varphi(\mathbf{r})$ which appeared in the Fourier representation of the δ functional, and $V(\mathbf{r})$ is the external potential that is related to $w(\mathbf{r})$ as $V(\mathbf{r}) = (i/\beta)w(\mathbf{r})$.

For evaluating this partition function approximately, the integrals over $\varphi(\mathbf{r})$ and $w(\mathbf{r})$ in eq 4 are replaced with a Gaussian integral around the most probable state that minimizes the argument of the exponential function on the right side of eq 4 (so-called saddle point approximation).

The minimization conditions in the form of functional derivatives result in

$$\begin{cases} V(\mathbf{r}) = \dfrac{\delta W[\phi(\mathbf{r})]}{\delta\phi(\mathbf{r})} \\ \varphi(\mathbf{r}) = -\dfrac{M}{\beta z}\dfrac{\delta z}{\delta V(\mathbf{r})} = \langle\hat{\phi}(\mathbf{r};\Gamma)\rangle = \phi(\mathbf{r}) \end{cases} \tag{5}$$

where $\phi(\mathbf{r})$ is the coarse-grained density at position $\mathbf{r}$.

In terms of eq 5, it is possible to acquire an expression for a density-dependent external potential acting on each segment.

Next, we assume that the density dependent interaction potential W, where each component species is specified by the index K, takes the following form:

$$W[\{\phi_K(\mathbf{r})\}] = \int \mathrm{d}\mathbf{r}\left(\frac{k_BT}{2}\sum_{KK'}\chi_{KK'}\phi_K(\mathbf{r})\phi_{K'}(\mathbf{r}) + \frac{1}{2\kappa}\Big(\sum_K \phi_K(\mathbf{r}) - \phi_0\Big)^2\right) \tag{6}$$

where $\phi_K(\mathbf{r})$ is the coarse-grained density of the species K at position $\mathbf{r}$ and $\chi_{KK'}$ represents the mean field parameters for the interaction of a particle of type K with the density fields due to particles of type K'. The second term of the integrand on the right-hand side of eq 6 is the relaxed incompressibility condition. κ is the compressibility that is assumed to be sufficiently small, and ϕ_0 is the total number density of segments (we assume that volume for all segments is the same). Then, the corresponding mean field potential is given by

$$V_K(\mathbf{r}) = \frac{\delta W[\{\phi_K(\mathbf{r})\}]}{\delta\phi_K(\mathbf{r})} = k_BT\sum_{K'}\chi_{KK'}\phi_{K'}(\mathbf{r}) + \frac{1}{\kappa}\Big(\sum_K \phi_K(\mathbf{r}) - \phi_0\Big) \tag{7}$$

Taking the case of a mixture of two components A and B as an example, the mean field potential acting on a particle of type A at position r is given by

$$V_A(\mathbf{r}) = k_BT[\chi_{AA}\phi_A(\mathbf{r}) + \chi_{AB}\phi_B(\mathbf{r})] + \frac{1}{\kappa}[\phi_A(\mathbf{r}) + \phi_B(\mathbf{r}) - \phi_0] \tag{8}$$

Thus, the force acting on the particle A at position $\mathbf{r}$ imposed by the interaction with the density field is

$$\begin{aligned} F_A(\mathbf{r}) &= -\frac{\partial V_A(\mathbf{r})}{\partial\mathbf{r}} \\ &= -k_BT\left(\chi_{AA}\frac{\partial\phi_A(\mathbf{r})}{\partial\mathbf{r}} + \chi_{AB}\frac{\partial\phi_B(\mathbf{r})}{\partial\mathbf{r}}\right) - \frac{1}{\kappa}\left(\frac{\partial\phi_A(\mathbf{r})}{\partial\mathbf{r}} + \frac{\partial\phi_B(\mathbf{r})}{\partial\mathbf{r}}\right) \end{aligned} \tag{9}$$

The main advantage of the hybrid MD-SCF scheme is that the most computationally expensive part of the MD simulations, i.e., the evaluation of the nonbonded force between atoms of different molecules, is replaced by the evaluation of forces between single molecules with an external potential. In order to connect particle and field models, for the proposed hybrid MD-SCF scheme, it is necessary to obtain a smooth coarse-grained density function directly from the particle positions Γ. Let us denote this procedure as

$$\overline{S}\{\hat{\phi}(\mathbf{r};\Gamma)\} = \phi(\mathbf{r}) \tag{10}$$

where $\overline{S}$ is a symbolic name of the mapping from the particle positions to the coarse-grained density. In order to obtain a smooth spatial density from particle positions, the simulation box is divided into several cells. In particular, particles are sorted and, according to their positions, assigned to ncell = $n_xn_yn_z$ (where n_x, n_y, and n_z are the number of cells in the x, y, and z directions, respectively). Furthermore, according to the position of each particle inside a cell, a fraction of it will be assigned to each vertex of the cell. In Chart 1, a simple two-dimensional case is used to explain the procedure. In the same chart, the structure of a phospholipid and the corresponding density field are schematized.

As shown in Chart 1B, the fraction of a particle assigned to a given lattice point is proportional to the area of a rectangle showed in the chart. For example, for a particle with coordinates x and y, a fraction $(l-x)(l-y)/l^2$ will be assigned to mesh point 1 and a fraction of xy/l^2 at mesh point 4 in Chart 1B (for simplicity, l is the length of the cell both in x and y directions). Thus, the density at every mesh point is the sum of all fractions assigned from all of the cells that share a given lattice point. According to the procedure described above, the size of the cell l is a parameter defining the density coarse-graining. The larger the value of l is, the higher the number of particles included in every cell and the coarser the calculated density will be. Once the coarse-grained density has been calculated from particle positions, the spatial derivatives of the density field can be evaluated. Spatial derivatives can be obtained by differentiation of the density lattice. In this way, the lattice where the derivatives are defined is staggered with respect to the lattice where the density is defined. As schematized in Chart 1B, the squares indicate the lattice points where the density is defined. Correspondingly, the density gradients are defined on the center of each edge (staggered lattice points indicated by crosses in Chart 1B) of the square surrounding the density lattice points.

Once both density and derivatives have been computed on their corresponding lattices, the potential energy and forces acting on the particles can be calculated using values obtained by interpolation of the density and its spatial derivatives in eqs 8 and 9.

The iteration algorithm used in the MD-SCF approach is explained in the following. According to the initial configurations of the system (at time t_0), a starting value of the coarse-grained density is obtained. The coarse-grained density is defined on a lattice, and the values of the density and density gradients at the particles positions are calculated by linear interpolation. Then, from the density gradients, forces acting on the particles at position $\mathbf{r}$ due to the interaction with the density fields are computed according to eq 9. The total force acting on the particles will be the sum of the intramolecular forces (bonds, angles, and intramolecular nonbonded forces calculated as in classical MD simulations) and the forces due to the interactions of particles with density fields. After the force calculation, a new configuration will be then obtained by integration of the equation of motion. In principle, for every new configuration, an update of the CG density calculated from the new coordinates should be performed. Test simulations have shown that, due to the collective nature of the density fields, it is possible to define an update frequency of the coarse-grained densities without a loss of accuracy.[41,42] In other words, the values of the coarse-grained density at lattice points are not updated at every time step but only at every prefixed density update time (Δt_{update}). Then, between two updates, the values of the densities on the lattice used to interpolate both density and its derivatives will be constant. When an update of density is performed, a new coarse-grained density will be obtained, and the iteration algorithm converges when the coarse-grained density and the particle-field potential become self-consistent.

Chart 1. (A) Construction of Coarse-Grained Density for a Phospholipid and (B) Criterion for the Assignment of Particle Fractions to Lattice Points

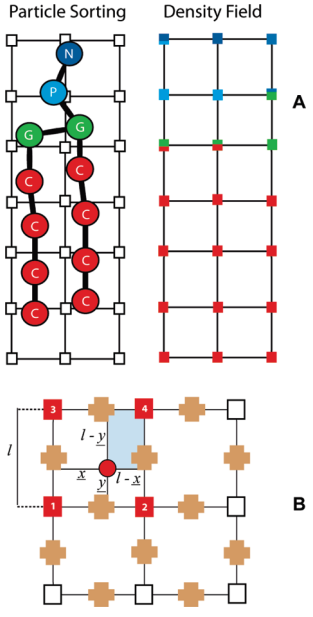

2.2. Simulations Details. Classical MD simulations used to obtain reference PP simulations have been performed using the program GROMACS (ver. 3.3).[43] The time step used for the integration of the equations of motion was 0.03 ps. The temperature and pressure were kept constant using Berendsen's weak coupling method (τ_T = 0.1 ps and τ_P = 1 ps). Target temperatures have been chosen according to the available experimental data and are listed in Table 1. A cutoff of 1.5 nm has been used to truncate nonbonded interactions. To equilibrate the system with *NPT* simulations, the target pressure was fixed to 1 bar, and semi-isotropic coupling has been employed. In order to achieve a better comparison between the results of PP and those of *NVT* PF simulations, *NVT* MD simulations have been performed using the average box lengths (see Table 1) obtained from the equilibrated *NPT* simulations. In particular, *NPT* simulations were performed for all systems for at least 120 ns. In the case of the DPPC lipid, the equilibrium area/lipid at 323 K for the PP model is 0.64 nm^2. This value was reported by Marrink et al.[44] and is in agreement with the experimental value

Table 1. Details about Simulated Systems

	box length[a] (nm)			composition			
lipid type	x	y	z	no. of lipids	no. of water	weight % lipids	T (K)
DPPC	8.17605	8.17605	6.94982	208	1600	60.9	325
DMPC	6.60390	6.60390	9.46884	208	1600	56.5	303
DOPC	7.21263	7.21263	9.62862	208	1600	64.5	303
DSPC	8.02782	8.02782	7.75874	208	1600	64.5	335

[a] Values of box length in x, y, and z directions have been fixed using averages obtained from *NPT* simulations of the reference PP models.

reported by Nagle et al.[45] and later by Kučerka et al.[46] In order to simulate systems having a correct value of area/lipid, *NVT* PF simulations have been performed using average box lengths (see Table 1) that are corresponding to those obtained in the reference PP simulations.

The molecular dynamics program OCCAM[47] was used for hybrid particle-field MD simulations. PF simulations have been performed using a time step of 0.03 ps. *NVT* simulations have been conducted keeping the temperature constant using an Andersen thermostat with a collision frequency of 5 ps^{-1}.

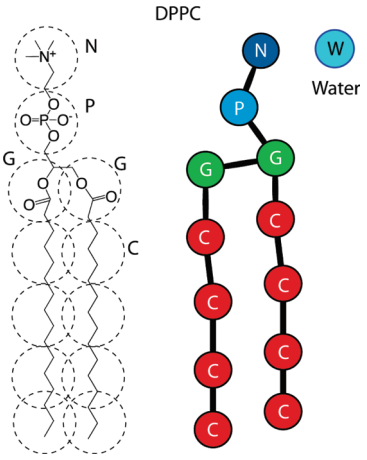

Figure 1. The adopted coarse-graining scheme for DPPC phospholipid is depicted. One coarse-grain bead corresponds to four atoms.

All density profiles, for both PP and PF simulations, have been calculated from simulations equilibrated at least for 10 ns. Density profiles have been averaged over further 2 ns after equilibration. The composition of lipid water systems has been set in the range of stability of the bilayer phase. Details about systems sizes and compositions used in the simulations reported in this paper are summarized in Table 1.

3. MODELS AND THEIR PARAMETRIZATION

As described in section 2, according to the formulation of hybrid PF models, the intramolecular bonded interactions (bond, angles) can be modeled using usual force fields suitable for molecular simulations. Our choice is to develop a hybrid PF model based on a description able to retain the chemical specificity. The coarse-graining scheme proposed by Marrink and co-workers is suitable for this purpose. The advantages of this model are that the parametrization of the interaction potentials is not tailored to a specific lipid and different phospholipids can be modeled from a small set of bead types.

In Figure 1, the MARTINI coarse-graining mapping scheme of the atomistic structures is exemplified for the phospholipid dipalmitoylphosphatidylcholine (DPPC).

According to the formulation of the MD-SCF method, bond and angle interaction potentials have the same functional form and parameters as those in the original MARTINI force field.[19] All types of nonbonded intramolecular interactions are assumed to be repulsive, while the intermolecular interactions are calculated using the assumption that each coarse-grained bead interacts with the density fields.

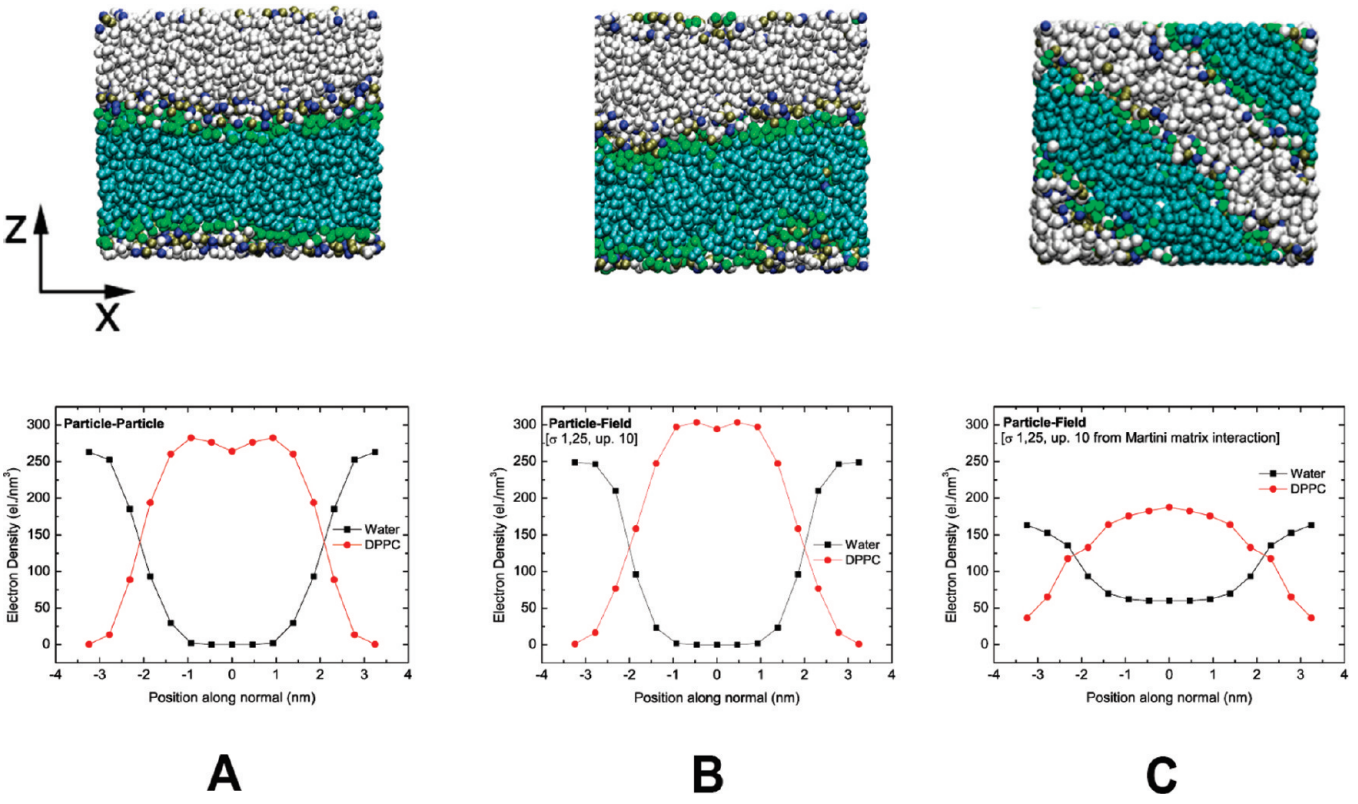

Figure 2. Water and DPPC density profiles and snapshot for (A) reference PP simulation, (B) PF simulation using a χ_{CW} parameter 2.5 times larger than the value calculated by eq 11, (C) PF simulation using the χ_{CW} parameter calculated by eq 11.

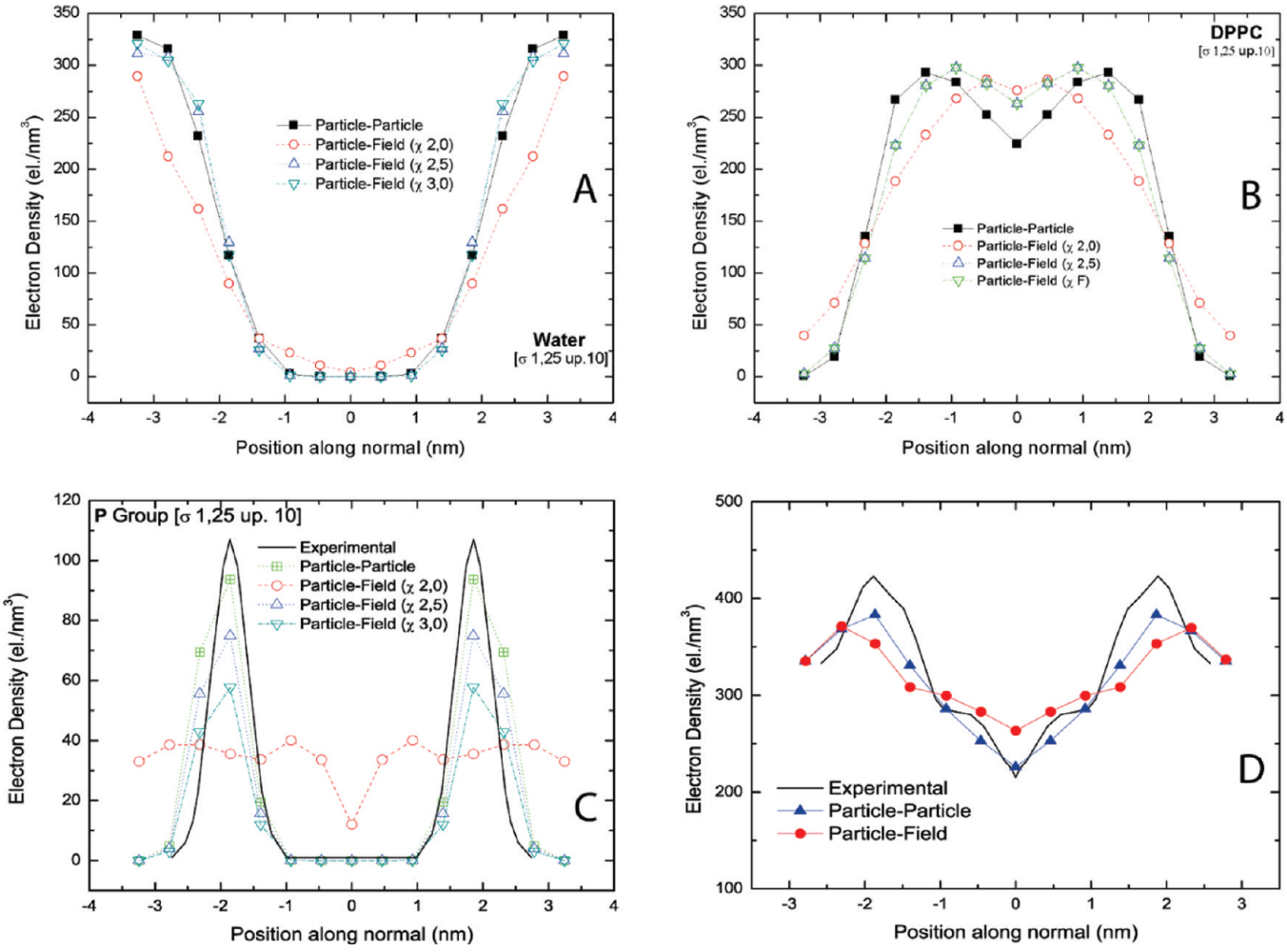

Figure 3. Comparison between reference PP and PF simulations using different values of the χ_{CW} parameter for electron density profiles of water (A), DPPC (B), and the phosphate group (C). Total density profiles for DPPC water system calculated from PP (red circles) and PF (blue triangles) simulations in comparison with experiments (black curves; D) are shown. The density profiles evaluated using the χ_{CW} parameter, which is scaled 2 to 3 times the value obtained from eq 11, are compared with those of the reference PP simulation.

According to eq 7, in order to calculate the PF potential, several mean field parameters $\chi_{KK'}$ between a particle of type K with the density field due to particles of type K' are needed. A simple choice of these parameters can be obtained by following the Flory–Huggins approach for the calculation of χ parameters for lattice models:

$$\chi_{KK'} = \frac{z_{CN}}{k_B T}\left[\frac{2u_{KK'} - (u_{KK} + u_{K'K'})}{2}\right] \quad (11)$$

where $u_{KK'}$ is the pairwise interaction energy between a pair of adjacent lattice sites occupied by the beads of types K and K'. These interaction energies have been set as $u_{KK'} = -\varepsilon_{KK'}$, where $\varepsilon_{KK'}$ is the Lennard-Jones ε parameter for the corresponding PP interactions. The parameter z_{CN} in eq 11 is the coordination number, which takes a value of 6 for a three-dimensional lattice. Another way to obtain the coordination number is from integration of the radial distribution function between all possible pairs. As the initial state for the MD simulations, we prepare a randomly mixed state of 208 DPPC and 1600 water molecules. Then, this mixture is subjected to an energy minimization procedure in order to avoid particle overlapping. This procedure gives an average number of neighbors per particle calculated at a distance equal to 1.20σ close to 6.0. With the choices described above, it is possible, given the particle–particle ε parameters and the value of z_{CN}, to obtain the corresponding PF parameters. According to our choice, the χ parameters have been obtained considering the interactions between the different particle types classified according to the four types polar, nonpolar, apolar, and charged interactions considered in the MARTINI force field.[19]

Using the models and the PF parameters described above, we simulated a system of DPPC and water using small values of both grid size (l = 0.587 nm, corresponding to 1.25σ) and update frequency (0.3 ps, corresponding to 10 time steps).

In order to determine the value of the parameter κ, which regulates the strength of the incompressibility condition imposed in eq 10, we analyzed the behavior of density fluctuations in the reference PP simulation. The criterion is the reproduction of the value of the average density fluctuations, calculated as mean square deviation between the average total density and instantaneous value averaged over all lattice points using the same grid size used in PF simulations. In particular, using values of $1/\kappa$ of about $8RT$ (where R is the gas constant and T temperature), average density fluctuations, in agreement with the reference PP simulation, are found to be smaller than 1%.

Table 2. Particle-Field Interaction Matrix[a]

	N	P	G	C	D	W
N	0.00	−1.50	6.30	9.00	7.20	−8.10
P	−1.50	0.00	4.50	13.50	11.70	−3.60
G	6.30	4.50	0.00	6.30	6.30	4.50
C	9.00	13.50	6.30	0.00	0.00	33.75
D	7.20	11.70	6.30	0.00	0.00	23.25
W	−8.10	−3.60	4.50	33.75	23.25	0.00

[a] $\chi_{KK'} \times RT$ (kJ/mol) for particles of type K interacting with density field due to particle of type K' are reported. χ parameters have been calculated using eq 11; the value of χ_{CW} is 2.5 times the one calculated by eq 11.

The system has been simulated for 60 ns; further details about simulations have been reported in section 2. In Figure 2, snapshots of the simulations together with calculated electron density profiles are reported. Here, the electron density profiles are obtained by multiplying the particle number density by the number of electrons contained in a given bead. As shown in Figure 2C, similarly to the reference PP simulation, the hybrid PF simulation leads to a successful formation of a lipid bilayer. Further comparisons between the results of PP and PF MD simulation have been used to refine the set of initial χ parameters obtained using eq 11.

In Figure 2, electron density profiles calculated by PP and PF MD simulations for the DPPC/water system (bottom panel of Figure 2) have been compared.

From a comparison of the density profiles of Figures 2A and B, it is clear that the PF model gives a weaker phase separation between DPPC and water molecules with respect to the MD simulation. Furthermore, the snapshot of Figure 2C shows that, for the system simulated with the hybrid PF method, the phospholipid plane lies along the diagonal of the simulation box. This indicates the tendency of the lipid molecules to occupy a larger area for the lipid. This tendency can be connected to a different size of the lipid molecules in the PF simulations from that of the PP simulations. To show this, the radius of gyration and the angle between two tails obtained from PP and PF simulations have been compared. In particular, histograms of these two structural quantities are very similar for both models (see the Supporting Information). As a result, both weak phase separation between the lipid and water and the tendency to occupy a larger area per lipid can be mainly ascribed to an underestimation of repulsion between the DPPC molecules and water in PF models with respect PP ones. Following this idea, several simulations were conducted to refine the interaction parameter between the hydrophobic tails of lipids and water molecules (namely the χ_{CW} parameter). Test simulations show that starting from values of χ_{CW} parameter 2.5 times larger than the value calculated by eq 11, the lipid bilayer does not occupy a larger area per lipid than the PP simulations and lies parallel to the *xy* plane of the simulation box. In Figure 3, density profiles of DPPC, water, and the phosphate group (P) obtained from simulations in which the repulsion between water and hydrophobic tail is further increased to 3 times that obtained with eq 11 are reported.

From Figure 3, it is clear that using a value of the χ_{CW} parameter that is 2.5 times larger than that evaluated by eq 11 gives electron density profiles very close to that in the reference PP simulations. In Figure 3D, the total electron density profiles of the DPPC/water system calculated from PP and PF simulations are compared with those obtained by fitting X-ray diffraction

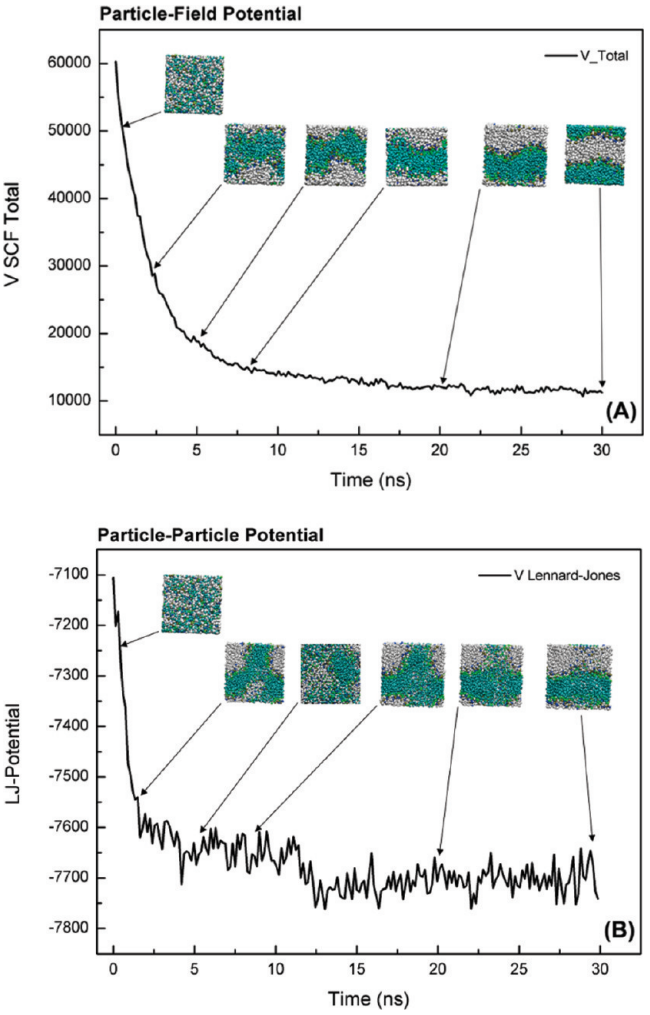

Figure 4. Comparison of the self-assembly process of DPPC and water in a bilayer phase obtained from PF (A) and PP simulations (B). In the figure, the time behavior of particle-field intermolecular potential in the PF MD simulation is compared with the behavior of the nonbonded Lennard-Jones potential in the PP MD simulation. Potential units are kilojoules per mole.

experiments of Kučerka and co-wokers.[46] The behavior of the calculated density profiles is smoother than the experimental one. In particular, in both PP and PF density profiles, the height of the peaks located at about 2 nm from the center of the bilayer is slightly underestimated. This effect, similar in PP and PF simulations, can be ascribed more to the coarse-grained nature of the models (reduction of degrees of freedom into one effective bead) than to the field description in the hybrid PF models; a similar behavior is found comparing the behavior of the calculated and experimental density profiles for the phosphate group (Figure 3C). The optimized set of χ parameters for all PF interactions is reported in Table 2.

According to eq 11, the interaction matrix is symmetric, and the χ parameter between the same type of particles is zero.

4. SIMULATIONS RESULTS

In Figure 4, self-assemblies of DPPC/water systems simulated using PP and PF models are compared. For both simulations, the initial configuration and the simulation conditions are the same

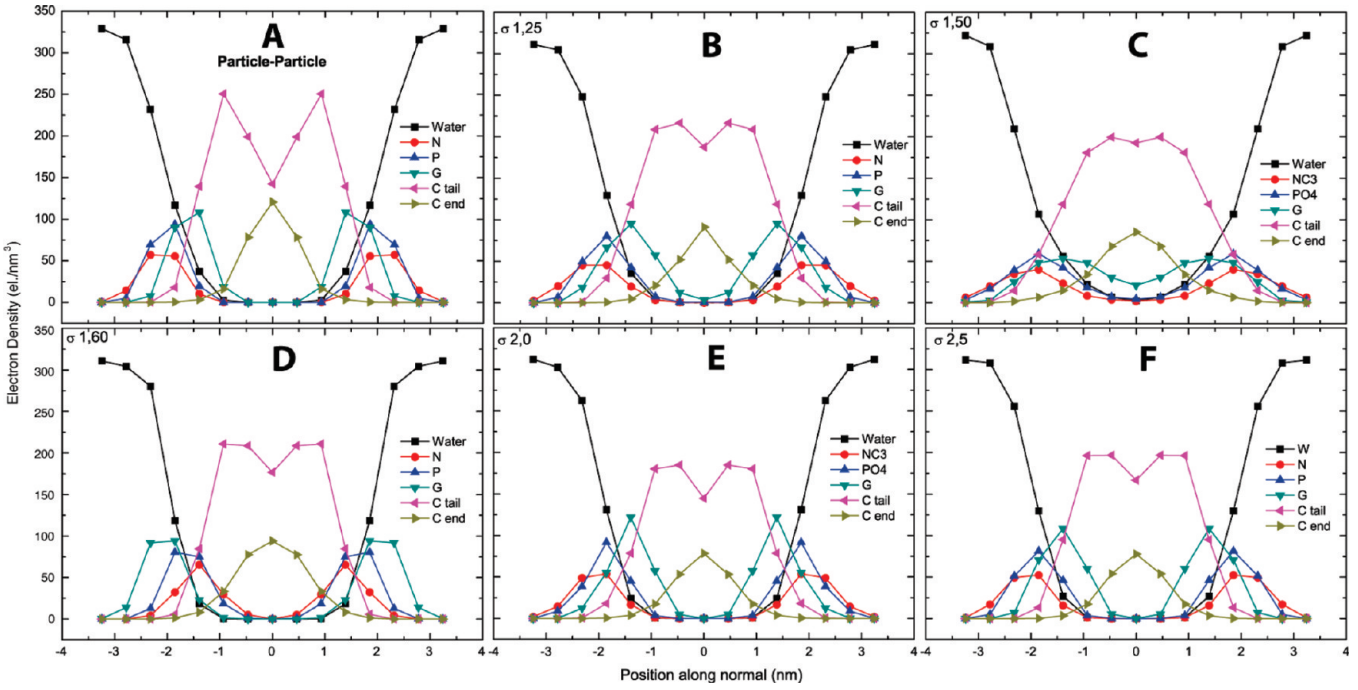

Figure 5. Partial density profiles for water and DPPC obtained from (A) PP simulations and PF simulations using l = (B) 1.25σ, (C) 1.50σ, (D) 1.60σ, (E) 2.0σ, and (F) 2.5σ. In all PF simulations, the update frequency Δt_{update} is 10 time steps.

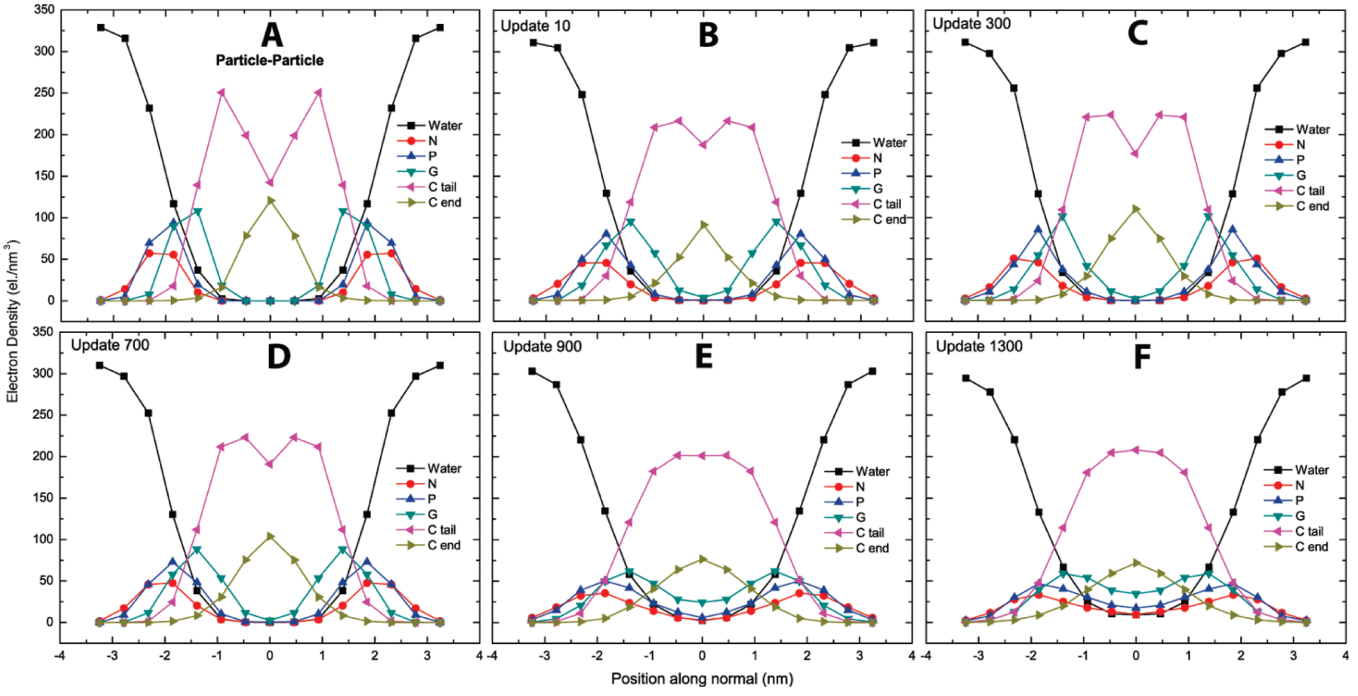

Figure 6. Partial density profiles for water and DPPC obtained from (A) PP simulations and PF simulations using Δt_{update} = (B) 10, (C) 300, (D) 700, (E) 900, and (F) 1300 time steps. In all PF simulations, the grid size l is 1.25σ.

(see Table 1). The starting configuration for both simulations is made up of randomly mixed DPPC and water molecules.

It is worth noting that in the PF simulations the formation of the lipid bilayer as stable equilibrium state, as shown by the snapshots reported in Figure 4A, is observed already after about 7 ns. From Figure 4B it can be noted that in the same time interval the PP simulation shows only an initial stage of phase separation and a stable lipid bilayer phase is formed only after 30 ns.

4.1. Influence of Density Coarse-Graining. *4.1.1. Structural Properties.* As described in section 2, coarse-grained density fields $\phi_K(\mathbf{r})$, obtained from particle positions for every particle type K, are used to calculate PF potentials and forces using eqs 8 and 9.

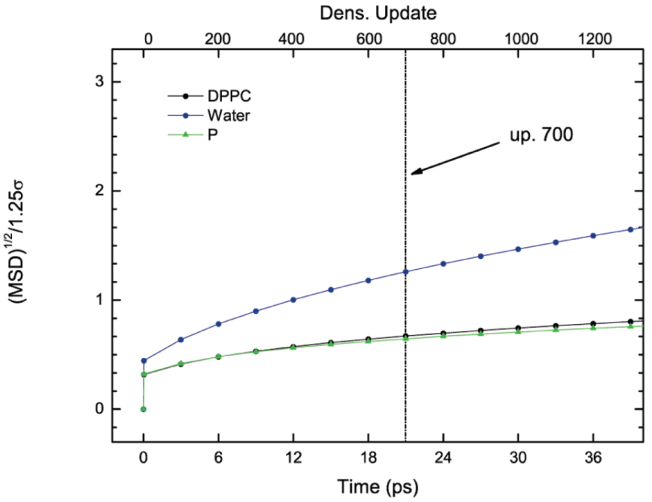

Figure 7. Normalized displacement of water, DPPC, and P beads as a function of time.

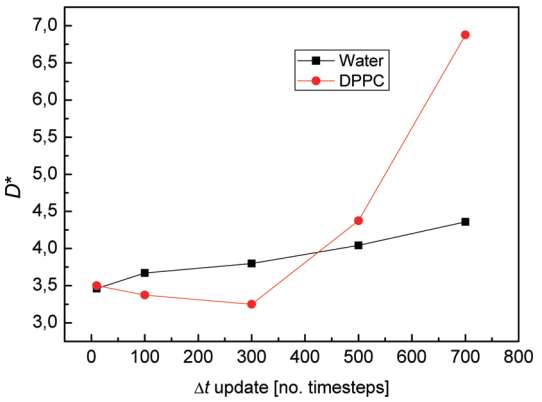

Figure 8. Ratio between PP and PF diffusion coefficients as a function of the update frequency calculated for water (black curve) and DPPC (red curve).

According to the scheme described above, two parameters, the cell size l and the update frequency Δt_{update}, regulate the degree of coarse-graining of the density fields. Larger cell sizes lead to more collective density fields. As for the value of the update frequency, it has to be chosen in a way that the approximation of slow variation of the field with respect to the particle displacement is valid between two density updates. In this section, simulation results using different density update frequencies and cell sizes will be discussed and compared with the results of reference PP simulations.

Several test simulations have been performed to understand the effect of the cell size l on the quality of calculated electron density profiles of the DPPC water bilayer. In Figure 5, partial density profiles corresponding to water and to the four different bead types (N, P, G, and C) present in DPPC obtained using l ranging from 1.25 and 2.5σ (corresponding to 0.59 and 1.17 nm) and using the same update frequency (Δt_{update} = 10 timesteps) are reported. From Figure 5 it is clear that PF simulations reproduce the structure of the lipid bilayer phase obtained from reference PP simulations well (Figure 5A). Values of l larger than 2.5σ give rise to stronger phase separation between water and DPPC with a narrowing of the density profiles. The grid size is larger, and this effect is more pronounced.

In Figure 6, electron partial density profiles for a mixture of water and DPPC molecules obtained for different values of the density update and using the same grid size (l = 1.25 σ) are compared with those obtained from reference PP simulations. In particular, the behaviors for Δt_{update} ranging from 10 (0.3 ps) to 1300 (39 ps) time steps are compared.

As expected, the agreement between PP and PF density profiles worsens as the Δt_{update} grows. For an update frequency between 10 and 700 time steps, water and DPPC density profiles are quite similar (see Figure 6B−D) and reproduce the behavior of the reference PP simulation well. Starting from update frequencies of 900 time steps (see Figure 6E), artificial undulations in the lipid bilayers are obtained. This causes a smoothing of the calculated density profiles. In particular, when large updates are used, the central depletion in the density profile of the hydrophobic beads of type C is absent (Figures 6E,F). Furthermore, the density profiles of the DPPC head groups N and P and of the bead types G are very shallow (Figure 6E,F).

The reproduction of the spatial organization of the head groups and in particular the phosphate group (type P) is important for the quality of the model. In fact, the bilayer thickness (D_{HH}), obtained by calculating the distance between the two peaks of the density profile corresponding to the phosphate group, can be compared with the values obtained from X-ray and/or neutron diffraction measurements. In the case of DPPC at 323 K (50 °C), a value of D_{HH} of 3.7 nm is obtained from PF simulations using update frequencies from 10 to 700 time steps. This value is equal to the one obtained from PP simulations and close to the experimental value of 3.8 nm measured at the same temperature.[48] For larger values of density update frequency, the electron density profile of P groups becomes broader, and a correct evaluation of D_{HH} becomes unreliable.

In order to understand the behavior of the systems as a function of the frequency of the density update, it is useful to compare the mean square displacement (MSD) of the particles as a function of time. In Figure 7, we present the behavior of the square root of the mean square displacement for water and the DPPC in units of cell length ($(MSD)^{1/2}/l$ where l is the cell length) as function of time for different values of update frequencies.

This is a direct way to understand the validity of the approximation of slow variation of the field with respect to the particle displacement between two density updates. In fact, the plot of Figure 7 quantifies how many cells a particle can cross in a given amount of simulation time. From Figure 7, it is clear that for update frequencies between 500 and 700 steps (corresponding to 15 and 21 ps) both water and DPPC beads have a displacement smaller than or equal to the cell size. For larger update time intervals, the displacement is larger than the size of a cell. This result agrees well with the good reproduction of density profiles and a bilayer thickness for update frequencies smaller than 700 steps.

This kind of analysis of PF simulations can be useful in general to set a suitable value for the update frequency also in the absence of reference simulations data.

4.1.2. Dynamical Properties. From the comparison of the self-assembly processes of a lipid bilayer obtained in the simulations shown in Figure 4, it is clear that the dynamics of the system simulated by the PF method are faster. This is due to smoother potentials and forces characterizing the PF Hamiltonian. In particular, PF models include the effect of excluded volume

Table 3. Diffusion Coefficients Calculated Using Different Update Frequencies[a]

	water [$cm^2/s \times 10^5$]				DPPC [$cm^2/s \times 10^5$]			
update frequency [timesteps]	total	x	y	z	total	x	y	z
particle−particle	1.27	1.63	1.63	0.43	0.08	0.13	0.12	0.01
10	4.40	6.5	6.6	0.04	0.28	0.45	0.43	0.03
100	4.67	7.1	6.8	0.04	0.27	0.43	0.44	0.03
300	4.82	7.3	7.1	0.04	0.26	0.38	0.38	0.04
500	5.13	7.6	7.6	0.05	0.35	0.52	0.50	0.03
700	5.53	8.4	8.4	0.05	0.55	0.079	0.078	0.09

[a] The grid size l is equal to 1.25σ for all simulations.

interactions between particles using the incompressibility condition described in eq 7. Forces acting on the particles then depend on the derivatives of the density fields that change smoothly over the length scale at larger than average distances between particle pairs.

In order to compare more quantitatively the different dynamics in PP and PF simulations, diffusion coefficients have been calculated from the MSD behaviors of water and DPPC particles as functions of time.

In Figure 8, values of the ratio D^* between the diffusion coefficients calculated from the PF simulations using different update frequencies and the one calculated from the reference PP simulation are reported. In all of the cases and for both water and DPPC, the diffusion coefficients calculated from the results of PF simulations are larger than those obtained from the results of the PP simulation. The diffusion of water is 3.5 to 4 times faster for PF simulations. The increase of the diffusion coefficient of the DPPC lipid ranges from about 3.5 to 7 times the value obtained from the reference PP simulation. This behavior is in agreement with the faster formation of a stable lipid bilayer as obtained from the comparison between PF and PP simulations reported in Figure 4.

In Table 3, the values of diffusion coefficients and their components calculated from PP and PF simulations using different density update frequencies are reported.

Results of the test simulations obtained using different grid sizes l and the same update frequency (300 timesteps) are reported in Figure 9. In particular, the values of the diffusion coefficients of water and DPPC increase according to the increase in the grid size. This is reasonable because a coarser density will give rise to smoother particle-field potentials and forces.

In the case of water, there is a small decrease in the diffusion coefficient for the largest grid sizes (2.0σ). This effect is due to the deviation from the reference density profile obtained when a larger grid size is used. As described in the previous paragraph, large grid sizes give rise to stronger phase separation between water and DPPC. The x and y components of the diffusion tensor of the water parallel to the bilayer plane show small variation as a function of the grid size, and they are practically constant within the error bar. In contrast, the z component of the diffusion tensor of water going from a grid size of 1.5 to 2.0σ is reduced by a factor of 2.

4.2. Particle−Particle and Particle−Field Correlations. The formulation of the hybrid MD-SCF method employed here is based on the interactions of single molecules with external density fields. Interactions between different molecules do not involve the evaluation of forces between particle pairs. This implies that, although the density profiles calculated with PF and

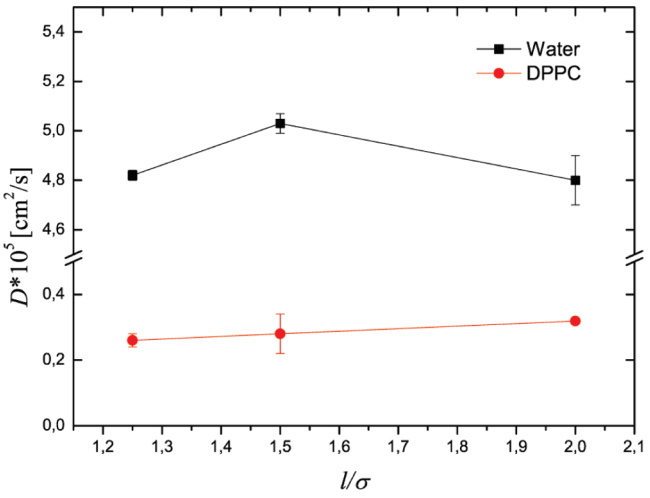

Figure 9. Behavior diffusion coefficients of water and DPPC as a function of the CG density grid size.

PP simulations are in good agreement, pair correlations between particles can be different.

In the case of PP simulations, the equilibrium structure and then the density profiles are the result of excluded volume interactions and of the different pair forces between hydrophilic and hydrophobic beads. In the case of PF simulations, the structure and the density profiles obtained from simulations are the result of the different interactions between every single hydrophilic and hydrophobic particle and the density external fields. To illustrate this point intuitively, we compare the radial distribution functions for several bead types between PP and PF simulations. Red curves in Figures 10 and 11 correspond to the radial distribution functions calculated in simulations where the short-range particle−particle repulsive interactions are explicitly included in the PF model. These simulations, named particle−particle particle−field (PPPF), will be discussed later.

In Figure 10A, radial distribution functions ($g(r)$) between the beads of water and hydrophobic tail beads (type C) calculated from PP (black curve) and PF (blue curve) simulations are shown.

For these particle pairs, the main features of $g(r)$ for the PP and PF simulations are very similar, except that the behavior of the PF is a bit smoother than that of the PP simulations.

This is due to smoother interactions between water particles and the field generated by the hydrophobic tail particles. Still similar is the behavior of the $g(r)$ between water and G type beads (Figure 10B). In this case, the radial distribution functions of the PF simulations, due to the continuous nature of the field

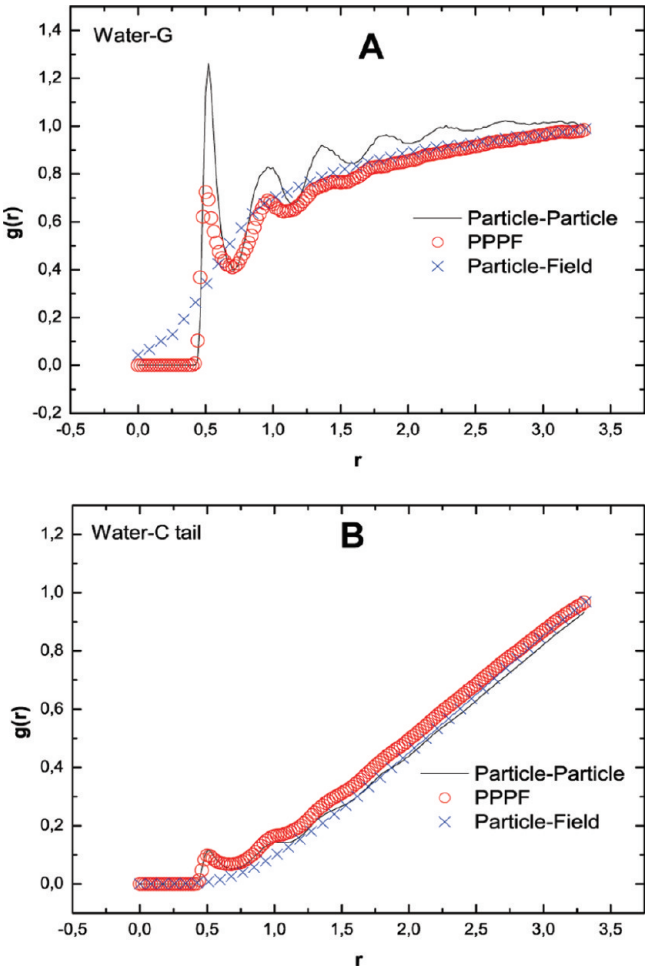

Figure 10. Radial distribution functions for (A) water−G tail and (B) water−C tail pairs.

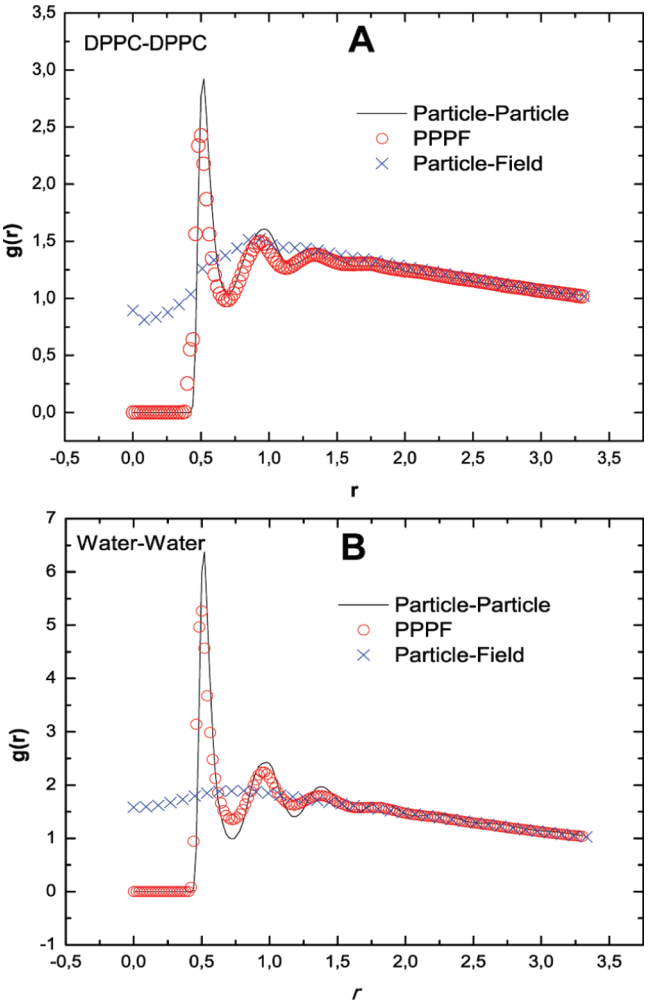

Figure 11. Radial distribution functions obtained from PP (black curve), PF (blue curve), and PPPF (red curve) simulations for (A) DPPC−DPPC and (B) water−water pairs.

representation, are characterized by the absence of peaks and a smoother behavior. Furthermore, at zero distance, the PF $g(r)$ shows a small nonzero value. Differently from PP simulations, where the overlapping between particles is strictly avoided, in the PF simulations, the excluded volume effects between different particles are taken into account in the field description by imposing the incompressibility condition in eq 7.

Different is the behavior of particle correlations in lipid and water pure phases. In particular, in Figure 11A, $g(r)$ between DPPC beads and, in Figure 11B, $g(r)$ between the water beads, both of which are obtained in PP and PF simulations, are compared.

In this case, at the PF level, the absence of correlations between particles is clear from the behavior of $g(r)$ between both water and DPPC pairs. The absence of direct correlation between particle pairs, as has been found in the radial distribution functions of Figure 11, is what is expected according to the formulation of the PF method. Differently from PP simulations, the Hamiltonian employed in PF simulations does not involve terms depending on the distance between particle pairs. The only correlation expected is between the particle and fields. In fact, this correlation has been found in the case of water and the field due to the C hydrophobic beads and partially in the case of water and the field due to G-type particles. Also in this case, due to the formulation of the PF method, although a direct correlation between the pair is still absent, the behavior of radial distribution functions is only a consequence of the repulsive interactions between water particles and density fields obtained from C or G particle types that lead to a phase separated system.

On the contrary, as shown in Figure 11, a direct correlation between particles belonging to the same hydrophilic or hydrophobic phase is absent. In the case of PP simulations, short-range correlations are dominated by excluded volume interactions due to the repulsive part of Lennard-Jones potentials between particle pairs. In contrast, in PF simulations, excluded volume interactions are modeled at the density field level by applying the incompressibility condition included in the second addend of eq 7. In this case, the density is kept homogeneous in all systems, and it is allowed to fluctuate according to the value of compressibility κ (eq 7).

In Figures 10 and 11, the behaviors of the g(r) obtained from PPPF simulations are also reported as red points.

In the simulations named PPPF, particle−field interaction potential has the form of eq 7 but without inclusion of the incompressibility condition. The excluded volume intermolecular interactions are then modeled by truncated short-range Lennard-Jones potentials. In this case, intermolecular short-range interactions are included at the particle−particle level as purely repulsive Lennard-Jones potentials truncated at $\sigma_{min} = 2^{1/6}\sigma$,

dx.doi.org/10.1021/ct200132n |J. Chem. Theory Comput. 2011, 7, 2947–2962

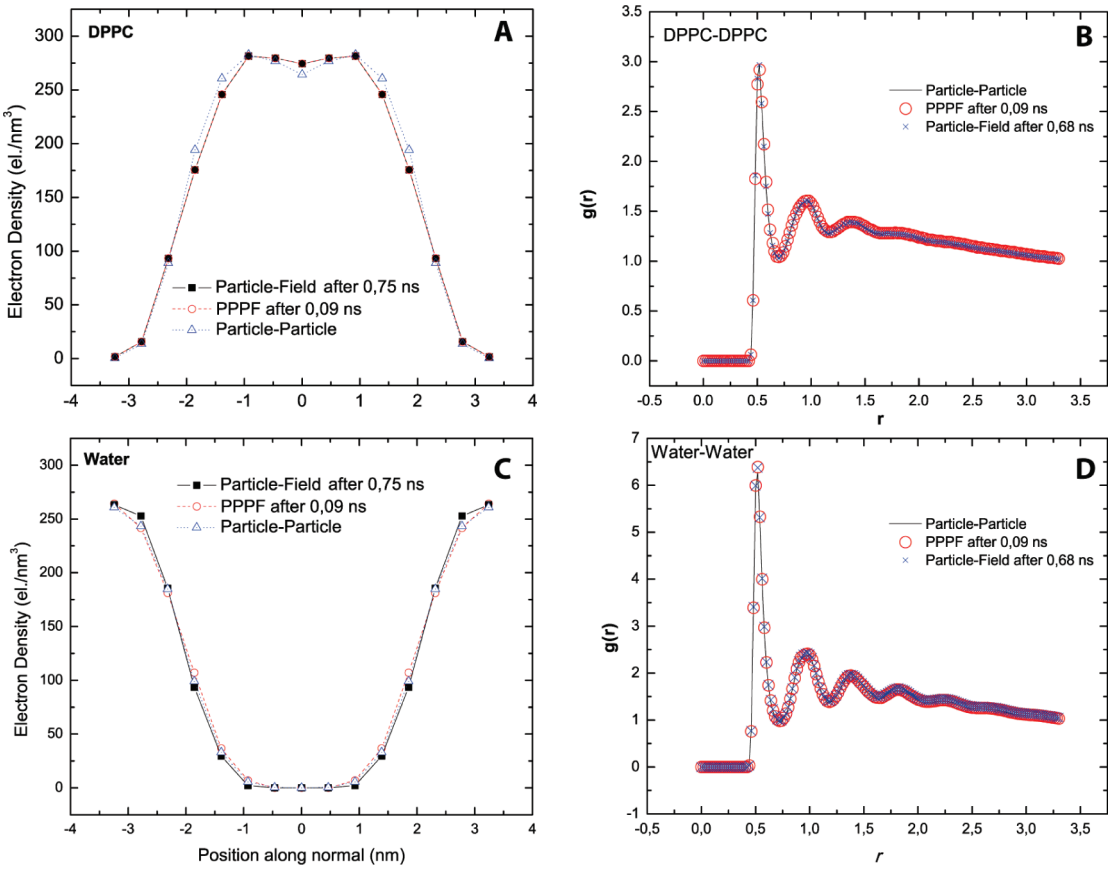

Figure 12. Comparison between PP and reverse mapped (A) DPPC and (C) water density profiles. DPPC−DPPC (B) and water−water (D) radial distribution functions. Results obtained from full equilibration at the PP level (black curves) are compared with ones obtained from reverse-mapped configurations at the PF (blue cross) and PPPF (red circles) levels.

while long-range interactions are still modeled with interactions between the particle and fields. The PPPF simulations have been run starting from equilibrium configurations obtained from PF simulations. The excluded volume pair interactions have been first gradually introduced by scaling both ε and σ from 0.001 to their full values in a few hundred steps and then running simulations with full values of ε and σ and with electrostatic interactions for about 2000 steps. From Figure 11, it is clear that short-range correlations between particles of PP simulations can be fully recovered at the PPPF level with very similar radial distribution functions.

4.3. Reverse Mapping: From PF to PP Configurations. One of the important uses of CG models is to obtain well-relaxed structures useful for generating configurations at a higher level of chemical detail. An example is the generation by local relaxation of structures of dense polymer melts at the atomistic level starting from mesoscale models.[49−51]

In the present case, the coarse-graining process operated from PP to PF models does not involve the reduction of the number of simulated particles, and shown above, the information that is average out is the direct correlation between particle pairs.

The procedure of PP simulations → derivation of a PF model; PF simulations → reverse-mapping and local relaxation of PP models can be an efficient way to obtain well-relaxed configurations of large systems suitable for full MD simulations. From this point of view, it is interesting to understand how easy it can be for the systems under investigation to reach an equilibrium structure that is indistinguishable from the one obtained by long PP simulations starting from PF or PPPF configurations. This information is useful for evaluating the feasibility of a possible reverse mapping procedure able to give systems configurations suitable for the production runs of PP simulations.

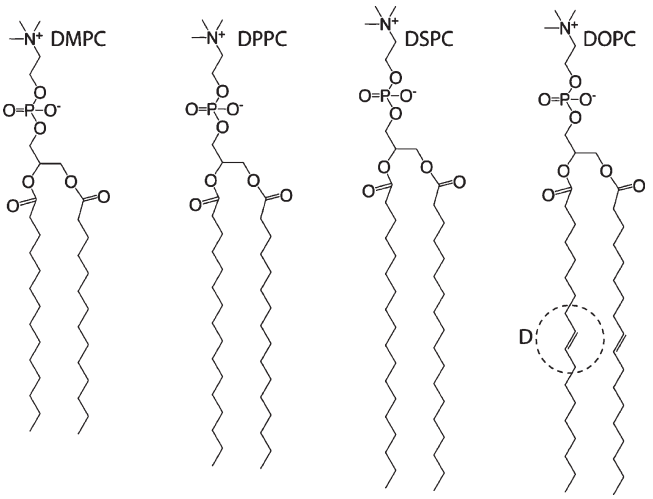

Figure 13. Structure formulas of the four phospholipids considered in the present study. The mapping scheme adopted for the CG models is the one depicted in Figure 1. For the DOPC phospholipid, the mapping for beads of type D including carbon atoms involved in double bonds is shown.

Tests using classical PP MD simulations aimed to relax configurations equilibrated at the PF (only in this case, the configurations have been previously optimized for about 300 steps) and at PPPF (no optimization has been employed in this case) levels have been conducted. These test runs show that, starting from configurations relaxed at the PF level, about 20 000 steps (corresponding to about 0.7 ns) are needed to obtain well relaxed structures equivalent to the fully equilibrated state of the PP simulations. In the case of configurations coming from PPPF, shorter simulations of about 3000 steps (corresponding to 90 ps) are required. In Figure 12, the radial distribution functions and density profiles obtained from reverse mapping procedures and the ones obtained by full equilibration at the PP level are compared. From the figure, it is clear that the structures obtained are indistinguishable, and both $g(r)$ and density profiles are practically identical.

4.4. Extension to other Phospholipids. One of the advantages of our reference PP coarse-grained model is that the parametrization of the interaction potentials is not tailored to a specific lipid, and different phospholipids can be modeled, taking into account different chemical structures, using a small set of bead types.

In this section, simulations aiming to test the transferability of the model developed for DPPC and the relative PF $\chi_{KK'}$ parameters are reported. Electron density profiles and bilayer thickness are compared between PF and PP models and with experiments.

In particular, further test simulations are conducted for three biologically relevant lipids, i.e. dimyristoylphosphatidylcholine (DMPC), distearoylphosphatidylcholine (DSPC), and dioleoylphosphatidylcholine (DOPC). In Figure 13, the chemical structures of these three phospholipids are shown along with the structure of DPPC.

The advantage of our reference PP coarse-grained models lies in the straightforward way in which the corresponding atomistic structure can be represented. The differences between lipids depend on the molecular structure on the atomistic level. For instance, the main difference between DMPC, DPPC, and DSPC is in the numbers of carbon atoms present in the hydrophobic tails. In this case, at the CG level, the PP models differ only in the number of beads of type C (see Figures 1 and 13) that compose the tails, while the parameters for the nonbonded bond and angle potentials are the same. Differently, in the case of DOPC, the presence of a double bond in each hydrophobic chain requires an extra particle type corresponding to four atoms including a double bond (see Figure 13, particle type D). For this reason, in the DOPC CG model, some of the angles and nonbonded potentials are different. In particular, the C−C−C harmonic angle potential has a minimum at 180°, while the C−D−C harmonic angle potential has a minimum at 120°. In the same way, nonbonded interactions of beads of types C and D are different.

Correspondingly, the particle−field models of DMPC, DPPC, and DSPC have the same bonded, intramolecular nonbonded, and the χ (see Table 2) parameters, and they differ only in the

Table 4. Deviations S_k (el/nm^3) between Particle−Particle and Particle−Field Density Profiles for All Considered Lipids

lipid	S_W[a]	S_P[a]	S_C[a]	average %
DPPC	8.5 (9.4%)[b]	4.3 (17%)[b]	16.5 (19.8%)[b]	15%
DMPC	18.3 (11%)[b]	7.4 (33%)[b]	12.6 (17%)[b]	20%
DSPC	7.2 (5.6%)[b]	10.9 (46%)[b]	11.4 (11%)[b]	21%
DOPC	16.9 (13%)[b]	8.9 (38%)[b]	17.3 (16%)[b]	22%

[a] Deviations have been calculated using particle−field density profiles obtained using grid size $l = 1.25\sigma$ and an update frequency of 10 time steps. [b] Deviation calculated as a percentage $S_k/\rho^{aver}_k \times 100$ of the average density of the species, where ρ_k^{aver} is the average electron density of the species k.

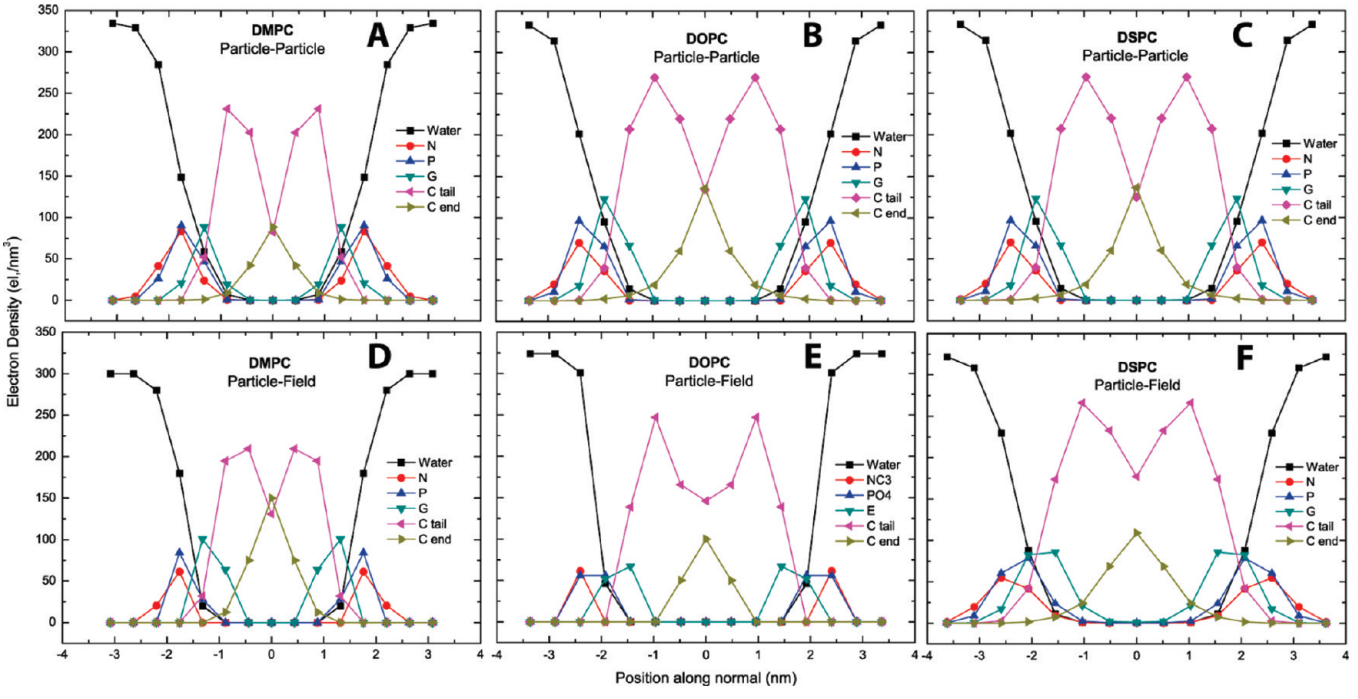

Figure 14. Electron density profiles calculated for DMPC, DOPC, and DSPC lipids with PF and PP simulations. Simulations for each lipid have been performed at the temperatures listed in Table 5.

dx.doi.org/10.1021/ct200132n |J. Chem. Theory Comput. 2011, 7, 2947–2962

number of beads. In the case of DOPC, having an extra bead type D and particle−field interactions involving only this new bead type introduces the use of different χ parameters. Of course, the interactions involving beads of type C are treated in the same manner as in DMPC, DPPC, and DSPC lipids. A complete list of parameters for the intramolecular interactions is reported in the Supporting Information.

Other details about simulated systems are reported in Table 1. Simulation temperatures have been chosen according to the available experimental data; temperatures of both experiments and simulations are listed in Table 4.

From these simulations, partial electron density profiles and bilayer thicknesses (D_{HH}) have been calculated and compared with those of the reference PP simulations and available experimental data.[45,48,52]

Partial electron density profiles compared with the corresponding ones obtained from particle−particle simulations are shown in Figure 14.

Table 5. Deviations S_k (el/nm^3) between DMPC and DOPC Density Profiles

model	S_W	S_P	S_C	average %
particle−particle	29.0 (22%)[a]	21.6 (99%)[a]	39.5 (44%)[a]	55%
particle−field[b]	30.0 (24%)[a]	16.0 (73%)[a]	30.0 (34%)[a]	49%

[a] Deviation calculated as a percentage $S_k/\rho^{aver}_k \times 100$ of the average density of the species, where ρ_k^{aver} is the average electron density of the species k. [b] Deviations for particle−field density profiles have been calculated using using grid size $l = 1.25\sigma$ and an update frequency of 10 time steps.

From Figure 14, it is possible to see that in all cases there is a good agreement between the density profiles of the reference PP and PF models. In order to evaluate quantitatively the difference between the reference density profile and the one calculated from particle−field simulations for a given bead type k, the following evaluation function can be defined:

$$S_k = \frac{1}{2l_z}\int_{-l_z}^{+l_z} |\Delta\rho_k(z)|\, dz \qquad (12)$$

where $\Delta\rho_k(z)$ is the difference between the values of the density calculated with the particle field and the reference particle−particle models for a given particle type k. According to the definition given above, in Table 4, the values of S_W, S_P, and S_C (in el/nm^3 as units) obtained by comparing PP and PF density profiles for all considered lipids are reported. The average deviation is smaller for DPPC (15%), and this is not surprising because the PP density profile of this lipid has been used for the parametrization of PF interactions. Interestingly, also the deviations between PP and PF density profiles for the other lipids are similar (around 20%). Furthermore, the main differences between the density profiles of different lipids calculated in the PP simulations can be reproduced by the PF model. For example, a comparison between DMPC and DOPC density profiles can be done using the deviations S_k. In Table 5, the deviation between density profiles of DMPC and DOPC are reported for both PP and PF simulations. It is worth noting than in this case the deviations (on the order of 50%) are much larger than the ones calculated between PP and PF density profiles of the same lipids. Furthermore, the values obtained for the deviations for single species is

Table 6. Calculated Bilayer Thickness[a]

phospholipid	D_{HH} particle−particle (nm)	D_{HH} particle−field (nm)	D_{HH} experimental (nm)
DMPC	3.7 (30 °C)	3.7 (30 °C)	3.8[b]−3.5[e] (30 °C)
DPPC	3.5 (50 °C)	3.5 (50 °C)	3.6[b] (50 °C)
DOPC	4.1 (30 °C)	4.0 (30 °C)	3.7[b]−3.6[d](30 °C)
DSPC	4.1 (60 °C)	4.4 (60 °C)	4.0[b]−4.1[c] (60 °C)

[a] Simulations have been performed at temperatures corresponding to the available experimental data. [b] From ref 48. [c] From ref 52. [d] From ref 53. [e] From ref 54.

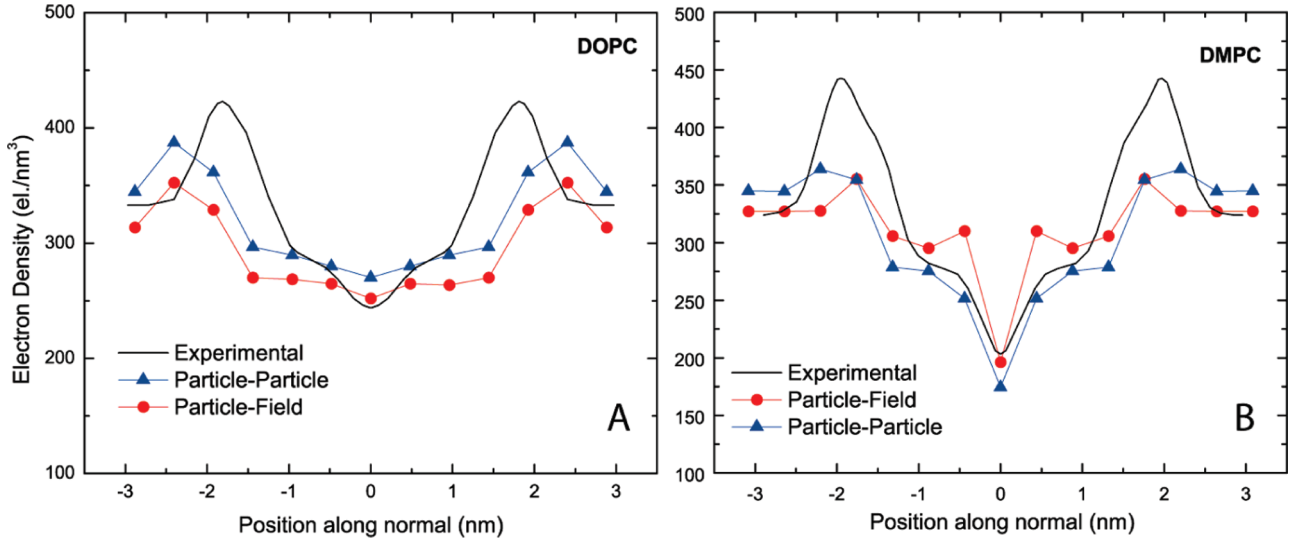

Figure 15. Total electron density profiles for DOPC (A) and DMPC (B) lipids.

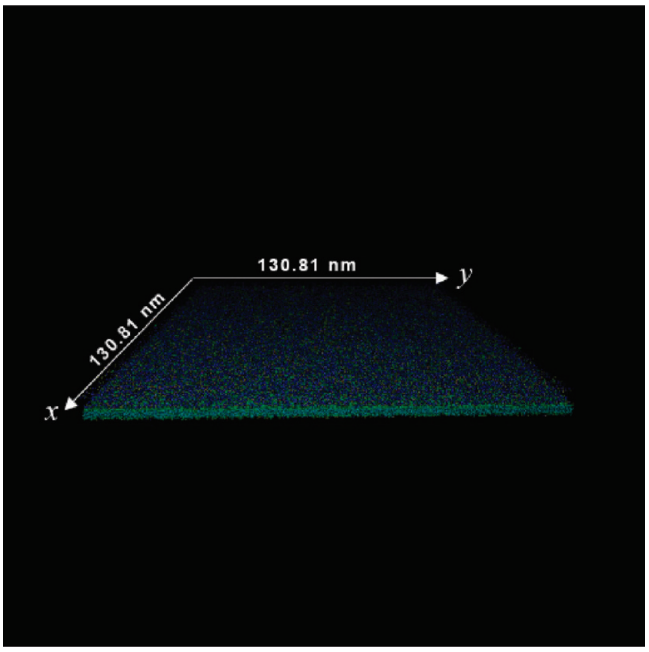

Figure 16. Snapshot of a system composed of 53 248 DPPC and 409 600 water molecules obtained by a parallel simulation. The grid size l used in the simulation was 2.5σ, and the density update frequency was 300 time steps.

very similar for PP and PF simulations. Similar conclusions can be made by comparing density profiles of any pair of two other lipids considered here, except for DOPC and DSPC. In this case, both PP and PF density profiles are very similar.

The calculated values D_{HH} are reported in Table 6 together with the reference PP and experimental values. The values of D_{HH} calculated from PF simulations are in good agreement with both PP simulations and experimental data. We want to stress that experimental values of D_{HH} lie in a very narrow range going from the smallest value of 3.6 nm for DPPC to the largest one of 4.0 nm for DSPC, and good reproduction of these values can be proof of the transferability of the chosen PF model. As previously discussed, DSPC and DOPC give very similar density profiles with both PP and PF models. This leads to the calculation of the same values of D_{HH} = 4.1 nm for these two lipids using PP models. Using PF models, according to the experimental trend, a larger value is obtained for the D_{HH} of DSPC (4.4 nm) and a smaller one for DOPC (4.0 nm).

In Figure 15, the total electron density profiles obtained by Kučerka et al. from X-ray scattering data for DOPC[53] and DMPC,[54] the ones obtained from PP and PF simulations, are plotted. In particular, the behavior of electron density of DOPC and DMPC is compared. As already found for DPPC (see Figure 3), the behavior of the calculated density profiles is smoother than the experimental ones. Furthermore, for DOPC, the position of the maximum of electron density profile of both PP and PF is shifted of about 0.5 nm. This is consistent with an overestimation of the D_{HH} (4.1 and 4.0 nm for PP and PF, respectively) with respect to the experimental value of 3.6−3.7 nm. For DMPC, the position of the maximum of the electron density profile of both PP and PF simulations is similar to the experimental one. In this case, the experimental value of D_{HH} is well reproduced (see Table 6).

CONCLUSIONS

Specific CG models for phospholipids and water suitable for hybrid particle field molecular dynamics simulations have been developed. These models and the set of parameters needed to evaluate interactions of particles with density fields are optimized to reproduce structural properties of reference PP simulations of DPPC. These parameters are transferable also to other phospholipids. The correct reproduction of the structural properties of the reference system depends on the density coarse-graining parameters. As expected, due to the smoothness of the PF interactions, the dynamics is faster in PF simulations. In particular, the ratio between diffusion coefficients calculated from PP and PF simulations goes from 3 to 7 depending on the degree of coarse-graining of the density field.

The computational efficiency of the PF approach allows one to accelerate the serial simulations by a factor of up to 10 for the considered systems. Furthermore, the peculiar formulation of the hybrid PF approach allows us a very efficient parallelization. To have an idea about the efficiency for the systems considered in this paper, 1 million steps of a simulation of a lipid bilayer system containing more than 1 million particles (a snapshot of this system containing a total of 1,048,576 particles is depicted in Figure 16) takes about 5 h on 96 processors (Intel E7330, 2.40 GHz).

In conclusion, the development of specific coarse-grained models suitable for hybrid PF simulation opens the way toward the simulation of large-scale systems employing models with chemical specificity.

ASSOCIATED CONTENT

Supporting Information. Table with bond and angle parameters, plots with histograms of the radius of gyration and the angle between tails for DPPC. This information is available free of charge via the Internet at http://pubs.acs.org

AUTHOR INFORMATION

Corresponding Author
*E-mail: gmilano@unisa.it.

ACKNOWLEDGMENT

G.M. thanks MIUR (PRIN2008 and FIRB "RETE ITALNANONET") for financial support and the HPC team of Enea (www.enea.it) for using the ENEA-GRID and the HPC facilities CRESCO (www.cresco.enea.it) in Portici, Italy. D.R. and G.M. thank Deutschen Forschungsgemeinschaft (DFG) for funding in the framework of the project "The study of detailed mechanism of polymers/biological membrane interactions using computer simulation" (RO 3571/3-1). T.K. thanks the Grant-in-Aid for Science from the Ministry of Education, Culture, Sports, Science and Technology, Japan.

REFERENCES

(1) Venturoli, M.; Sperotto, M. M.; Kranenburg, M.; Smit, B. *Phys. Rep., Rev. Sect. Phys. Lett.* **2006**, *437* (1−2), 1–54.
(2) Marrink, S. J.; de Vries, A. H.; Tieleman, D. P. *Biochim. Biophys. Acta, Biomembr.* **2009**, *1788* (1), 149–168.
(3) Gurtovenko, A. A.; Anwar, J.; Vattulainen, I. *Chem. Rev.* **2010**, *110* (10), 6077–6103.
(4) Psachoulia, E.; Marshall, D. P.; Sansom, M. S. P. *Acc. Chem. Res.* **2010**, *43* (3), 388–396.

(5) Lyubartsev, A. P.; Rabinovich, A. L. *Soft Matter* **2011**, 7 (1), 25–39.
(6) Bandyopadhyay, S.; Tarek, M.; Klein, M. L. *J. Phys. Chem. B* **1999**, *103* (46), 10075–10080.
(7) Saiz, L.; Klein, M. L. *Acc. Chem. Res.* **2002**, *35* (6), 482–489.
(8) Faller, R.; Marrink, S.-J. *Langmuir* **2004**, *20* (18), 7686–7693.
(9) Pal, S.; Milano, G.; Roccatano, D. *J. Phys. Chem. B* **2006**, *110* (51), 26170–26179.
(10) Bennett, W. F. D.; MacCallum, J. L.; Hinner, M. J.; Marrink, S. J.; Tieleman, D. P. *J. Am. Chem. Soc.* **2009**, *131* (35), 12714–12720.
(11) Brannigan, G.; Lin, L. C. L.; Brown, F. L. H. *Eur. Biophys. J. Biophys.* **2006**, *35* (2), 104–124.
(12) Muller-Plathe, F. *Chemphyschem* **2002**, *3* (9), 754–769.
(13) Peter, C.; Kremer, K. *Soft Matter* **2009**, *5* (22), 4357–4366.
(14) Müller, M.; Katsov, K.; Schick, M. *Phys. Rep.* **2006**, *434* (5−6), 113–176.
(15) Sintes, T.; Baumgaertner, A. *J. Phys. Chem. B* **1998**, *102* (36), 7050–7057.
(16) Sintes, T.; Baumgartner, A. *Biophys. J.* **1997**, 73 (5), 2251–2259.
(17) Lenz, O.; Schmid, F. *J. Mol. Liq.* **2005**, *117* (1−3), 147–152.
(18) Goetz, R.; Lipowsky, R. *J. Chem. Phys.* **1998**, *108* (17), 7397–7409.
(19) Marrink, S. J.; de Vries, A. H.; Mark, A. E. *J. Phys. Chem. B* **2003**, *108* (2), 750–760.
(20) Marrink, S. J.; Mark, A. E. *J. Am. Chem. Soc.* **2003**, *125* (49), 15233–15242.
(21) Marrink, S.-J.; Mark, A. E. *Biophys. J.* **2004**, *87* (6), 3894–3900.
(22) Monticelli, L.; Kandasamy, S. K.; Periole, X.; Larson, R. G.; Tieleman, D. P.; Marrink, S.-J. *J. Chem. Theory Comput.* **2008**, *4* (5), 819–834.
(23) Kawakatsu, T. *Statistical Physics of Polymers*; Springer: Berlin, 2004.
(24) Matsen, M. W.; Schick, M. *Phys. Rev. Lett.* **1994**, *72* (16), 2660–2663.
(25) Drolet, F.; Fredrickson, G. H. *Phys. Rev. Lett.* **1999**, *83* (21), 4317–4320.
(26) Fredrickson, G. H.; Ganesan, V.; Drolet, F. *Macromolecules* **2002**, *35* (1), 16–39.
(27) Lauw, Y.; Leermakers, F. A. M.; Stuart, M. A. C. *J. Phys. Chem. B* **2006**, *110* (1), 465–477.
(28) Ly, D. Q.; Honda, T.; Kawakatsu, T.; Zvelindovsky, A. V. *Macromolecules* **2008**, *41* (12), 4501–4505.
(29) Pinfield, V. J.; Horne, D. S.; Leermakers, F. A. M. *J. Chem. Soc., Faraday Trans.* **1997**, *93* (9), 1785–1790.
(30) Balazs, A. C.; Singh, C.; Zhulina, E. *Macromolecules* **1998**, *31* (23), 8370–8381.
(31) Roan, J. R.; Kawakatsu, T. *J. Chem. Phys.* **2002**, *116* (16), 7283–7294.
(32) Roan, J. R.; Kawakatsu, T. *J. Chem. Phys.* **2002**, *116* (16), 7295–7310.
(33) Marcelja, S. *Nature* **1973**, *241* (5390), 451–453.
(34) Leermakers, F. A. M.; Scheutjens, J. *J. Chem. Phys.* **1988**, *89* (5), 3264–3274.
(35) Leermakers, F. A. M.; Rabinovich, A. L.; Balabaev, N. K. *Phys. Rev. E* **2003**, *67* (1), 011910.
(36) Muller, M.; Schick, M. *Phys. Rev. E* **1998**, *57* (6), 6973.
(37) Szleifer, I.; Carignano, M. A. Tethered Polymer Layers. In *Adv. Chem. Phys.*; John Wiley & Sons, Inc.: New York, 2007; pp 165−260.
(38) Muller, M.; Smith, G. D. *J. Polym. Sci., Part B: Polym. Phys.* **2005**, *43* (8), 934–958.
(39) Daoulas, K. C.; Muller, M.; Stoykovich, M. P.; Park, S. M.; Papakonstantopoulos, Y. J.; de Pablo, J. J.; Nealey, P. F.; Solak, H. H. *Phys. Rev. Lett.* **2006**, *96* (3).
(40) Detcheverry, F. A.; Kang, H. M.; Daoulas, K. C.; Muller, M.; Nealey, P. F.; de Pablo, J. J. *Macromolecules* **2008**, *41* (13), 4989–5001.
(41) Milano, G.; Kawakatsu, T. *J. Chem. Phys.* **2009**, *130* (21), 214106.
(42) Milano, G.; Kawakatsu, T. *J. Chem. Phys.* **2010**, *133*, 21.
(43) Lindahl, E.; Hess, B.; van der Spoel, D. *J. Mol. Model.* **2001**, *7* (8), 306–317.
(44) Marrink, S.-J.; Risselada, H. J.; Yefimov, S.; Tieleman, D. P.; de Vries, A. H. *J. Phys. Chem. B* **2007**, *111* (27), 7812–7824.
(45) Nagle, J. F.; Zhang, R.; Tristram-Nagle, S.; Sun, W.; Petrache, H. I.; Suter, R. M. *Biophys. J.* **1996**, *70* (3), 1419–1431.
(46) Kucerka, N.; Tristram-Nagle, S.; Nagle, J. F. *Biophys. J.* **2006**, *90* (11), L83–L85.
(47) Milano, G. *OCCAM 3.0*; In University of Salerno: Salerno, Italy, 2007.
(48) Katsaras, J.; Tristram-Nagle, S.; Liu, Y.; Headrick, R. L.; Fontes, E.; Mason, P. C.; Nagle, J. F. *Biophys. J.* **2000**, *78* (1), 116Plat.
(49) Tschöp, W.; Kremer, K.; Hahn, O.; Batoulis, J.; Bürger, T. *Acta Polym.* **1998**, *49* (2−3), 75–79.
(50) Santangelo, G.; Di Matteo, A.; Müller-Plathe, F.; Milano, G. *J. Phys. Chem. B* **2007**, *111* (11), 2765–2773.
(51) Carbone, P.; Karimi-Varzaneh, H. A.; Muller-Plathe, F. *Faraday Discuss* **2010**, *144*, 25–42. 93–110. 467–81.
(52) Balgavı, P.; Dubniková, M.; Kuerka, N.; Kiselev, M.; Yaradaikin, S.; Uhríková, D. *Biochim. Biophys. Acta, Biomembr.* **2001**, *1512* (1), 40–52.
(53) Kucerka, N.; Nagle, J. F.; Sachs, J. N.; Feller, S. E.; Pencer, J.; Jackson, A.; Katsaras, J. *Biophys. J.* **2008**, *95* (5), 2356–2367.
(54) Kucerka, N.; Liu, Y.; Chu, N.; Petrache, H. I.; Tristram-Nagle, S.; Nagle, J. F. *Biophys. J.* **2005**, *88* (4), 2626–2637.

JCTC Journal of Chemical Theory and Computation

ARTICLE

pubs.acs.org/JCTC

Understanding RNA Flexibility Using Explicit Solvent Simulations: The Ribosomal and Group I Intron Reverse Kink-Turn Motifs

Petr Sklenovský,[†] Petra Florová,[†] Pavel Banáš,[†] Kamila Réblová,[‡] Filip Lankaš,[§] Michal Otyepka,[*,†] and Jiří Šponer[*,‡]

[†]Regional Centre of Advanced Technologies and Materials, Department of Physical Chemistry, Faculty of Science, Palacky University Olomouc, tr. 17. listopadu 12, 771 46 Olomouc, Czech Republic

[‡]Institute of Biophysics, Academy of Sciences of the Czech Republic, Kralovopolska 135, 612 65 Brno, Czech Republic

[§]Centre for Complex Molecular Systems and Biomolecules, Institute of Organic Chemistry and Biochemistry, Flemingovo nam. 2, 166 10 Praha 6, Czech Republic

Supporting Information

ABSTRACT: Reverse kink-turn is a recurrent elbow-like RNA building block occurring in the ribosome and in the group I intron. Its sequence signature almost matches that of the conventional kink-turn. However, the reverse and conventional kink-turns have opposite directions of bending. The reverse kink-turn lacks basically any tertiary interaction between its stems. We report unrestrained, explicit solvent molecular dynamics simulations of ribosomal and intron reverse kink-turns (54 simulations with 7.4 μs of data in total) with different variants (*ff*94, *ff*99, *ff*99bsc0, *ff*99χ_{OL}, and *ff*99bsc0χ_{OL}) of the Cornell et al. force field. We test several ion conditions and two water models. The simulations characterize the directional intrinsic flexibility of reverse kink-turns pertinent to their folded functional geometries. The reverse kink-turns are the most flexible RNA motifs studied so far by explicit solvent simulations which are capable at the present simulation time scale to spontaneously and reversibly sample a wide range of geometries from tightly kinked ones through flexible intermediates up to extended, unkinked structures. A possible biochemical role of the flexibility is discussed. Among the tested force fields, the latest χ_{OL} variant is essential to obtaining stable trajectories while all force field versions lacking the χ correction are prone to a swift degradation toward senseless ladder-like structures of stems, characterized by high-*anti* glycosidic torsions. The type of explicit water model affects the simulations considerably more than concentration and the type of ions.

INTRODUCTION

Kink-turn (K-turn) is a recurrent RNA structural motif occurring in the ribosome,[1−3] mRNA,[4,5] riboswitches,[6,7] snoRNAs,[8] and the human U4 snRNA.[9,10] K-turn plays an important role in RNA structure; for instance, it is involved in ribosome intersubunit bridges[11] and specific binding of ribosomal proteins.[12] Some K-turns are also localized in flexible segments of the ribosome which play a prominent role in the elongation. The X-ray data identified the K-turn motif as a well structured 3D RNA building block mediating a sharp bend (∼120°) of phosphodiester backbone between consecutive RNA helices. Solution experiments conducted for isolated K-turns suggested that free in solution K-turn possesses two (kinked and open) states which are in a dynamic equilibrium. The ratio of kinked/open states depends on the concentration of metal ions. At a high concentration of divalent metal ions, K-turn prefers the kinked conformation, while at low concentrations, K-turn favors the open geometry.[13−15] Besides metal ions, proteins are also able to stabilize the kinked structures.[12,16] Molecular dynamics (MD) simulations of free K-turns in their folded (kinked) topology show that K-turns are anisotropic and nonharmonic flexible structures displaying hinge-like dynamics around the folded geometry on a fast nanosecond time scale.[17−22]

Considering structural features of K-turn, a single-stranded internal bulge of K-turn forms a sharp kink between the helical axes of two consecutive RNA helices. The bulge usually contains three nucleotides, while the middle base is unstacked and flipped out. The RNA helix at the 5′ site of the bulge is a canonical stem (C-stem) consisting of Watson−Crick (WC) C═G base pairs. The second helix at the 3′ site of the bulge is a noncanonical stem (NC-stem) with two or three tandem *trans*-Hoogsteen/sugar-edge (*t*HS) A/G base pairs flanking the bulge.[23,24] Two of these *t*HS A/G base pairs neighboring the bulge are highly conserved. The structure of K-turn is stabilized by two tertiary interactions involving these two conserved *t*HS A/G base pairs of the NC-stem (see, e.g., Figure 1 in ref 16 for the annotation of the K-turn structure). The first tertiary interaction is *trans*-sugar-edge/sugar-edge (*t*SS) base pair comprising a hydrogen bond (H-bond) between the 2′-OH hydroxyl group of the 5′-most nucleotide of the bulge and N1 nitrogen of adenine of the *t*HS A/G base pair of the NC-stem adjacent to the 3′ site of the bulge. This interaction is essential for the folding of K-turns.[25,26] The second tertiary interaction is the A-minor interaction[27] between adenine of the second *t*HS A/G base pair in the NC-stem and the terminal base pair of the C-stem adjacent to the bulge. The A-minor interaction significantly contributes to the topology of K-turn and is essential for its internal structural dynamics.[20]

Received: March 24, 2011
Published: July 28, 2011

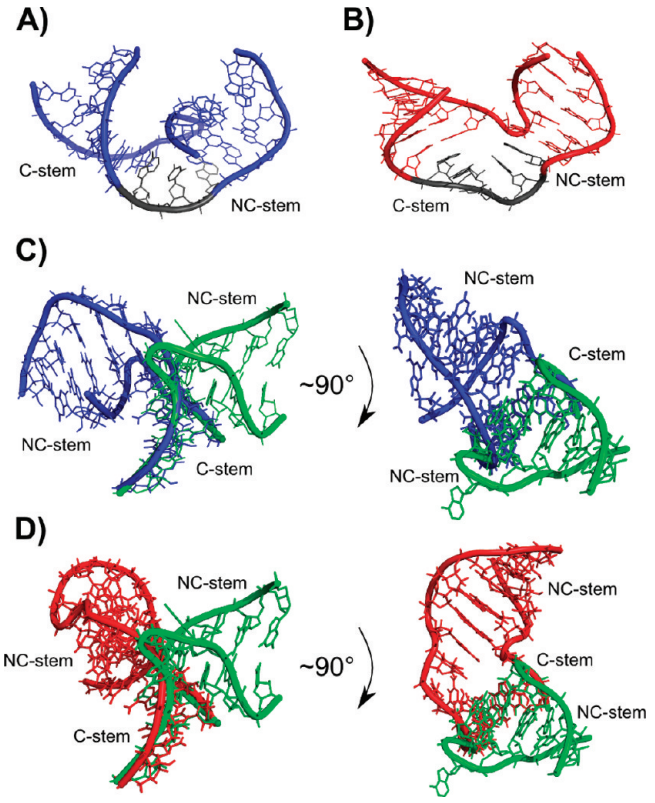

Figure 1. (A and B) The three-dimensional structures of the studied revKt-P9/9.0 (in blue) and revKt-54 (in red), respectively. Bulge regions are in gray. (C and D) The depiction of the opposite direction of revKt-P9/9.0 (blue) and revKt-54 (red) bends, respectively, in comparison to the nearly consensus ribosomal K-turn Kt-7 structure (green) from *H.m.* 23S rRNA. All systems are superimposed over their C-stems.

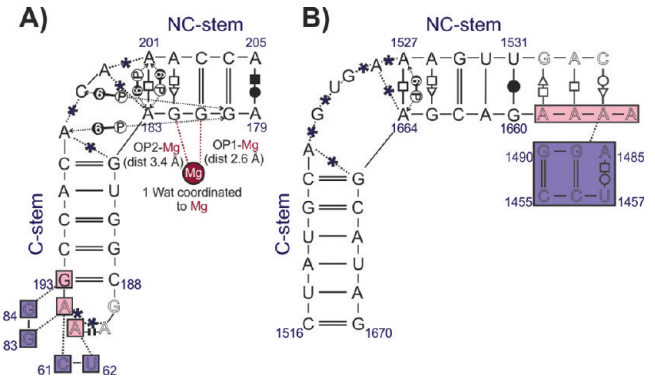

Figure 2. Secondary structures of revKt-P9/9.0 (A) and revKt-54 (B) annotated by standard classification[23,81] according to the X-ray structures (revKt-54, PDB 1S72; revKt-P9/9.0, PDB 1U6B). The dotted lines with stars in their centers highlight stacking interaction between the respective bases. Note that the coordination sphere of the Mg^{2+} is not complete in the X-ray structure due to resolution. Gray letters in panel A depict the GNRA tetraloop attached to the revKt-P9/9.0 C-stem (nucleotides 189−192; not included in MD simulations) and bases of the P5/5a intron segment (residues 61, 62, 83, and 84, not included in the simulations). In the pink squares of panel A are bases of the revKt-P9/9.0 C-stem and the GNRA tetraloop, which interact with bases of the P5/5a segment (highlighted in violet squares). Pink squares in panel B mark bases of revKt-54 NC-stem (four adenines), which interact with Helix 52 residues 1455−1457, 1485, and 1489−1490 (marked with violet rectangle). All bases colored in gray in panel B are not included in the simulations.

These two tertiary interactions bring together minor-groove sites of the two RNA stems.

The X-ray structure of the *Azoarcus* group I intron[28] revealed that the segment consisting of helices P9 and P9.0 (hereafter, revKt-P9/9.0) with almost the consensus K-turn sequence also adopts a bent conformation (the helices are mutually bent by ~90° in this particular case). The bending, however, goes in the opposite direction in comparison to the conventional K-turns (Figure 1A and C). It means that the major grooves of P9 and P9.0 stems are juxtaposed. Considering similarities to and differences from conventional K-turn (discussed below), the revKt-P9/9.0 motif is named as the reverse kink-turn (reverse K-turn). Similarly to the conventional K-turns, the bulge region is single-stranded and comprises three unpaired nucleotides: one helix is canonical (P9) containing mainly G═C WC base pairs, and the other is noncanonical (P9.0). In contrast to conventional K-turns that have a strictly conserved *t*HS A/G base pair in NC-stem adjacent to the bulge, revKt-P9/9.0 contains the *trans*-Hoogsteen/Hoogsteen (*t*HH) A201/A183 base pair at this position.[29] The second base pair of NC-stem is similar to the conventional K-turns *t*HS A202/G182 base pair (Figure 2A). The A201G mutant, having the K-turn consensual sequence, still retains the reverse K-turn fold in context of the intron structure.[29] This indicates that the fold is determined by external interactions (the overall context) rather than by local interactions and the primary sequence. Obviously, revKt-P9/9.0 lacks the A-minor interaction.[30] There is no flipped out base in the bulge between the stems, while all unpaired bases are stacked (Figure 2A). The base phosphate interactions between A198 and G180 and between C199 and G180 together with Mg^{2+} coordinated to G181 and G182 may stabilize the kinked conformation of revKt-P9/9.0 (Figure 2A).[31] There is a tertiary tetraloop−tetraloop receptor contact formed between the GNRA tetraloop adjacent to the revKt-P9/9.0 C-stem and bases of the intron P5/5a segment. The tetraloop−tetraloop receptor contact was suggested to be the leading factor in the bending of revKt-P9/9.0 toward the major groove.[29]

Another reverse K-turn was identified in the 23S rRNA of *Haloarcula marismortui* (*H.m.*).[31−33] This motif (hereafter, revKt-54) comprises helices 54 and 55 of 23S rRNA and bends again toward the major groove. The internal bulge, which bridges the helices, consists of five nucleotides, of which all are unpaired and stacked, and none is flipped out (Figures 1B,D and 2B). Helix 55 (NC-stem) contains *t*HH A1527/A1664 and *t*HS A1528/G1663 base pairs, being basically identical with the corresponding base pairs of the revKt-P9/9.0 NC-stem (cf. Figure 2A,B). Very recent automatic identification of RNA structural motifs using secondary structural alignment found another reverse K-turn motif comprising helices 55 and 56 of *H.m.* 23S rRNA.[34]

This study explores the intrinsic flexibility of two reverse K-turns (revKt-P9/9.0 and revKt-54) using an extensive set of conventional MD simulations in explicit solvent. We carried out altogether 54 simulations (typically on a 150 ns time scale) with a total simulation time of 7.4 μs (see Table 1 and Table S3, Supporting Information) under various conditions. Five variants of the Cornell et al. AMBER force field, several ionic conditions, and two explicit water models were considered. The basic purpose of this paper is two-fold. Besides characterizing the structural dynamics of reverse K-turns, we also investigate the performance and limitations of the simulation methods.

Table 1. List of MD Simulations[a]

simulated system (simulation label)[b]	water model + force field	ions	simulation length (ns)	time of "ladder like" transition (ns)[c]	RMSD (Å)[d]
revKt-P9/9.0 (INT-1)	TIP3P+*ff*99	19 Na^+, 1 Mg^{2+}	150	no transition	2.0 ± 0.6
revKt-P9/9.0 (INT-2)	TIP3P+*ff*99	19 Na^+, 1 Mg^{2+}	150	31	2.4 ± 0.6
revKt-P9/9.0 (INT-3)	SPC/E+*ff*99bsc0	40 K^+, 21 Cl^-, 1 Mg^{2+}	150	20	1.8 ± 0.3
revKt-P9/9.0 (INT-4)	SPC/E+*ff*99bsc0	40 K^+, 21 Cl^-, 1 Mg^{2+}	150	35	1.9 ± 0.3
revKt-P9/9.0 (INT-5)	TIP3P+*ff*99	21 Na^+	150	no transition	5.5 ± 1.0
revKt-P9/9.0 (INT-6)	TIP3P+*ff*99	21 Na^+	150	no transition	7.1 ± 1.5
revKt-P9/9.0 (INT-7)	TIP3P+*ff*99	21 Na^+	150	no transition	5.5 ± 2.3
revKt-P9/9.0 (INT-8)	TIP3P+*ff*99	21 Na^+	150	20	6.9 ± 1.5
revKt-P9/9.0 (INT-9)	TIP3P+*ff*99	21 Na^+	150	30	4.3 ± 1.5
revKt-P9/9.0 (INT-10)	TIP3P+*ff*99	21 Na^+	150	no transition	7.6 ± 1.5
revKt-P9/9.0 (INT-11)	SPC/E+*ff*99bsc0	42 K^+, 21 Cl^-	150	25	2.3 ± 0.8
revKt-P9/9.0 (INT-12)	SPC/E+*ff*99bsc0	42 K^+, 21 Cl^-	150	53	2.0 ± 0.6
revKt-P9/9.0 (INT-13)	SPC/E+*ff*99bsc0	42 K^+, 21 Cl^-	150	1.5	1.3 ± 0.3
revKt-P9/9.0 (INT-14)	SPC/E+*ff*99bsc0	42 K^+, 21 Cl^-	150	133	2.1 ± 0.7
revKt-P9/9.0 (INT-15)	SPC/E+*ff*99bsc0	42 K^+, 21 Cl^-	150	no transition	3.0 ± 1.1
revKt-P9/9.0 (INT-16)	SPC/E+*ff*99bsc0	42 K^+, 21 Cl^-	150	no transition	3.3 ± 1.2
revKt-P9/9.0 (INT-17)	TIP3P+*ff*94	21 Na^+	150	no transition	6.0 ± 1.9
revKt-P9/9.0 (INT-18)	TIP3P+*ff*94	19 Na^+, 1 Mg^{2+}	150	138	2.0 ± 0.6
revKt-P9/9.0 (INT-19)	TIP3P+*ff*99χ_{OL}	19 Na^+, 1 Mg^{2+}	150	no transition	4.8 ± 3.0
revKt-P9/9.0 (INT-20)	SPC/E+*ff*99bsc0χ_{OL}	40 K^+, 21 Cl^-, 1 Mg^{2+}	150	no transition	1.6 ± 0.3
revKt-P9/9.0 (INT-21)	TIP3P+*ff*99χ_{OL}	21 Na^+	150	no transition	7.7 ± 1.3
revKt-P9/9.0 (INT-22)	TIP3P+*ff*99χ_{OL}	21 Na^+	150	no transition	5.3 ± 2.4
revKt-P9/9.0 (INT-23)	TIP3P+*ff*99bsc0χ_{OL}	21 Na^+	150	no transition	5.7 ± 2.8
revKt-P9/9.0 (INT-24)	TIP3P+*ff*99bsc0χ_{OL}	21 Na^+	150	no transition	2.1 ± 0.8
revKt-P9/9.0 (INT-25)	SPC/E+*ff*99χ_{OL}	42 K^+, 21 Cl^-	150	no transition	2.3 ± 1.3
revKt-P9/9.0 (INT-26)	SPC/E+*ff*99bsc0χ_{OL}	42 K^+, 21 Cl^-	150	no transition	1.8 ± 0.5
revKt-54 (RIB-1)	TIP3P+*ff*94	25 Na^+	69	no transition	2.5 ± 0.9
revKt-54 (RIB-2)	TIP3P+*ff*94	12 Mg^{2+}, 1 Na^+	57	no transition	3.8 ± 0.7
revKt-54 (RIB-3)	TIP3P+*ff*99	25 Na^+	200	no transition	2.4 ± 0.7
revKt-54 (RIB-4)	TIP3P+*ff*99	25 Na^+	74	39	3.1 ± 0.8
revKt-54 (RIB-5)	TIP3P+*ff*99	12 Mg^{2+}, 1 Na^+	150	no transition	2.5 ± 0.7
revKt-54 (RIB-6)	TIP3P+*ff*99	12 Mg^{2+}, 1 Na^+	98	48	2.6 ± 0.7
revKt-54 (RIB-7)	TIP3P+*ff*99	23 Na^+	67	12	3.3 ± 0.9
revKt-54 (RIB-8)	TIP3P+*ff*99	23 Na^+	150	no transition	4.4 ± 0.8
revKt-54 (RIB-9)	SPC/E+*ff*99	46 K^+, 23 Cl^-	147	45	2.5 ± 0.7
revKt-54 (RIB-10)	SPC/E+*ff*99	46 K^+, 23 Cl^-	150	no transition	2.4 ± 0.5
revKt-54 (RIB-11)	TIP3P+*ff*99bsc0	23 Na^+	150	80	3.5 ± 1.0
revKt-54 (RIB-12)	TIP3P+*ff*99bsc0	23 Na^+	40	2	2.0 ± 0.5
revKt-54 (RIB-13)	SPC/E+*ff*99bsc0	46 K^+, 23 Cl^-	150	no transition	2.0 ± 0.7
revKt-54 (RIB-14)	SPC/E+*ff*99bsc0	46 K^+, 23 Cl^-	65	55	3.2 ± 1.4
revKt-54 (RIB-15)[e]	TIP3P+*ff*99	1 Mg^{2+}, 21 Na^+	150	20	2.5 ± 0.5
revKt-54 (RIB-16)	TIP3P+*ff*99bsc0χ_{OL}	23 Na^+	150	no transition	2.2 ± 0.7
revKt-54 (RIB-17)	TIP3P+*ff*99bsc0χ_{OL}	23 Na^+	150	no transition	1.9 ± 0.4
revKt-54 (RIB-18)	SPC/E+*ff*99bsc0χ_{OL}	46 K^+, 23 Cl^-	150	no transition	1.8 ± 0.4
revKt-54 (RIB-19)	SPC/E+*ff*99bsc0χ_{OL}	46 K^+, 23 Cl^-	150	no transition	2.8 ± 1.4

[a] Some additional MD simulations are listed in Table S3 in the Supporting Information. [b] The initial revKt-P9/9.0 structure in the simulations INT-9, INT-10, INT-15, and INT-16 was taken from the tenth nanosecond of the INT-18 simulation. The initial revKt-54 structure in the simulations RIB-1 to RIB-6 was taken from the *H.m.* 23S rRNA deposited under the code 1S72 while the simulations RIB-7 to RIB-19 were started from the structure taken from the *H.m.* 23S rRNA available under the code 3CC2. [c] Time at which a distorted "ladder-like" conformation of reverse K-turn occurs. [d] The mean RMSD of coordinates with respect to the X-ray structure (see the Methods section for more details concerning the RMSD calculation). The 3CC2 structure is used for revKt-54. The RMSD is strictly calculated over the trajectory portion not affected by the "ladder-like" conformations. [e] One Mg^{2+} ion was included. Its initial position was modeled via replacing the crystal water under ID 7209 in the original 3CC2 23S rRNA with Mg^{2+}. See the Methods section for discussion of the limitations of modeling Mg^{2+} by simple force fields.

Reverse K-turn substantially differs from RNA molecules studied so far by all-atom MD simulations.[35−43] Most RNA MD simulations reported to date studied molecules whose starting structures corresponded to 3D arrangements that are stable *per se*.[44] Representative examples are established autonomous RNA motifs that adopt their structures irrespective of the structural context[45−47] as well as medium-sized noncoding RNAs such as ribozymes,[35,48−51] riboswitches,[39,52] and many other RNAs.[53,54] These molecules stay locked in the starting structures in simulations. They show just local dynamics sometimes accompanied with modest rearrangements of molecular interactions. In some cases, the initial structures are trivially deformed by the surrounding elements that are not included in simulations (for example, bending of helix 44 of the small ribosomal subunit or the GTP-ase associated center RNA of the large subunit).[18,55,56] In such cases, the molecules undergo initial relaxation in simulations, which, however, does not change base pairing and tertiary interactions. Much less frequent are simulations of RNA molecules that should be intrinsically unstable since their functional 3D shapes are induced by their context. One example is the recurrent ribosomal UAA/GAN internal loop, whose 3D structure is completely remodeled by the ribosomal context.[57] This molecule is visibly locally destabilized in simulations but does not spontaneously rearrange anywhere close to the solution structure on a submicrosecond time scale.[58] Similarly, the conventional K-turns are also intrinsically unstable and unfold (unkink) in experiments with an absence of proteins or divalent ions. Nevertheless, the K-turn functional geometry is still locally stable enough so that plain simulations on a 100+ ns time scale so far did not result in any extensive K-turn perturbations or unfolding.[17−22] Considering the sequence, structure, and context of the reverse K-turns, it is obvious that functional (native) reverse K-turn structures also do not correspond to global minima of the respective isolated RNA segments. However, since reverse K-turns are less structured than the conventional K-turns, we might expect visible signs of reversible unfolding and refolding already on the presently affordable simulation time scale. This allows an analysis of force field performance during large-scale RNA rearrangements. Still, the simulations are able to characterize the flexibility of reverse K-turns pertinent to the folded structure, similarly to conventional K-turns. The simulations nevertheless also sample unfolded (or unkinked) and intermediate structures.

METHODS

Studied Systems. Two reverse K-turns were investigated. The initial geometry of revKt-P9/9.0 was taken from the X-ray structure of the *Azoarcus* group I intron with a resolution of 3.1 Å (PDB ID: 1U6B).[28] RevKt-P9/9.0 contains nucleotides 179−188 and 193−205 (23 bases in total; numbering according to the intron X-ray structure). The starting structure of revKt-54 was taken from the 50S ribosomal subunit crystal structures of *Haloarcula marismortui* (*H.m.*) deposited under the PDB codes 1S72 and 3CC2 (both determined at a resolution of 2.4 Å).[32,33] RevKt-54 from 1S72 comprises nucleotides 1516−1531 and 1660−1670 (27 bases), while that of the 3CC2 contains residues 1517−1531 and 1660−1669 (25 bases). The more recent (presumably corrected) 3CC2 structure contains G1669═C1517 and A1670−U1516 while 1S72 contains A1669−U1517 and G1670═C1516 base pairs in the C-stem. We decided to terminate the C-stem with C═G base pair to avoid terminal A−U base-pair fraying,[59] so the terminal C-stem base pair is G1669═C1517 in the case of the 3CC2 system and G1670═C1516 in the case of 1S72. We did not observe any differences between revKt-54 simulations starting from the 1S72 and 3CC2 X-ray structures, and thus we will further discuss all of these simulations as a one-simulation set of revKt-54.

The eubacterial ribosomes reveal that at positions equivalent to revKt-54 of *H.m.*, there are situated segments that bend similarly to the reverse K-turn but with a completely different sequence (hereafter, abbreviated as revKt-54-analogs; Figure S4, Supporting Information). We have carried out one 100-ns MD simulation with the revKt-54-analog from *Escherichia coli* (*E.c.*). The revKt-54-analog starting structure was taken from the X-ray structure (resolution of 3.46 Å) of the *E.c.* 50S large ribosome subunit deposited under the PDB 2AW4, while nucleotides 1405−1424 and 1574−1597 (44 bases in total) were included in the simulation (Figure S5, Supporting Information).[2]

Simulation Setup and Force Field Choice. All MD simulations were carried out using the AMBER[60] suite of programs with several force fields. The *ff*94 and *ff*99 (also known as parm94 and parm99, respectively)[61,62] can be considered as the original parametrizations which slightly differ in sugar pucker and χ torsion parameters. The *ff*99bsc0 (parmbsc0) force field is based on *ff*99 but contains a critical reparameterization of the α/γ torsion parameters, which is essential for stable simulations of DNA molecules[63] and which was recently shown to also modestly improve RNA simulations.[59,64] Until recently, all three force fields were assumed to perform equivalently for RNA systems and provide enough stable simulations on a subhundreds nanosecond time scale.[44,59] However, it has been shown that these force fields do not provide a stable minimum for A-RNA due to imbalanced description of the glycosidic torsion, which tends to adopt a high-*anti* conformation with the subsequent entire degradation of A-RNA systems on a long time scale.[50,64] In fact, some earlier simulation studies including those attempting folding of small RNAs such as stem-loop hairpins are affected by this force field artifact. Thus, complete reparameterization of the glycosidic torsion profile χ_{OL}[64] (parameters are available online at http://fch.upol.cz/en/rna_chi_ol/ (accessed Jan 25, 2010) and have also been included in the most recent *ff*10 AMBER force field as the recommended force field for RNA simulations and released in AmberTools 1.5, the parameterization procedure is in detail described in ref 103) was recently prepared and carefully tested. It prevents the ladder degradation of A-RNA by modifying the *anti* to high-*anti* balance and also improves the *syn* region description.[64] Therefore, in later stages of this reverse K-turn project, we applied the χ_{OL} modification in combination with *ff*99 (labeled as *ff*99χ_{OL}) and *ff*99bsc0 (labeled as *ff*99bsc0χ_{OL}) force fields. In fact, the inclusion of the χ_{OL} correction was entirely critical to adopting the stable trajectories of the present system. Note that although the bsc0 (α/γ) and χ_{OL} parametrizations are independent variants of the force field, our study of RNA tetraloops and short A-RNA stems strongly indicates that χ_{OL} should be combined with *ff*99bsc0 to get the optimal force field behavior.[64]

Ion and Solvent Conditions. Two different ionic (and solvent) conditions were used: the combination of Na^+ counterions (with radius 1.868 Å and well depth 0.0028 kcal/mol)[65] with the TIP3P water model,[66] modeling minimal salt conditions ($c(Na^+)$ of ∼0.25 M) and a higher ionic strength of potassium ($c(K^+)$ of ∼0.5 M, radius 1.870 Å and well depth 0.100 kcal/mol)[67] and chloride ions ($c(Cl^-)$ ∼0.25 M, radius 2.470 Å and well depth 0.100 kcal/mol)[68] in combination with the SPC/E water model[69] to simulate KCl salt excess (Table 1). The monovalent counterions were placed

using the tLEaP program according to the solute electrostatic potential. In addition, some simulations (Table 1 and Table S3, Supporting Information) comprise also divalent magnesium ion/ions coordinated to the reverse K-turn, and the following parameters for Mg^{2+} (radius 0.7926 Å and well depth 0.8947 kcal/mol)[65] were utilized. The rectangular box of explicit water solvent was set, so that a minimum distance between the box wall and the solute was 10 Å. It is to be noted that we did not have any specific reason to systematically combine TIP3P with Na^+ and SPC/E with KCl. We wanted to investigate as broad a set of conditions as possible. Obviously, the limited computer power does not allow us to investigate all possible combinations of parameters while having a statistically significant set of multiple simulations and enough robust sampling. See the Supporting Information for analyses of four simulations (600 ns in total) combining minimal salt conditions of K^+ ions with the SPC/E water model decomposing effects of the water model and salt conditions. Further studies of RNA systems with other ion and water parameters[70,71] are under way. It should, however, be noted that in general the ion/water parameters and conditions do not have a decisive effect on nucleic acids simulations, as their outcome is primarily determined by the solute force field. The present system, due to its flexibility, is assumed to be potentially more sensitive to ion/water conditions than other nucleic acids systems.

Prior to the production phase of the MD simulation, each system was minimized and subsequently warmed up to 298 K as follows. The RNA molecule was constrained, and the solvent molecules with counterions were allowed to move during a 1000-step minimization followed by 10-ps-long MD runs under $[NpT]$ conditions (p = 1 atm, T = 298.15 K). The solute was then relaxed through several minimization steps, with decreasing force constants applied to the backbone atoms. After the relaxation, each system was heated to 298.15 K within 100 ps. The particle-mesh Ewald (PME) method[72,73] was used for treating electrostatic interactions, and all simulations were performed under periodic boundary conditions in the $[NpT]$ ensemble at 298.15 K and 1 atm using a 2 fs integration step. The SHAKE algorithm with a tolerance of 10^{-5} Å was used to fix positions of all hydrogen atoms. A 10.0 Å cutoff was applied to nonbonding interactions, and coordinates were stored every picosecond. Together, 30 independent simulations (Table 1 and Table S3, Supporting Information), each 150-ns-long, were carried out with revKt-P9/9.0, and 19 simulations (Table 1) on the 40+ ns time scale were carried out with revKt-54. In addition, four independent 150 ns MD simulations were carried out with revKt-P9/9.0-A201G (revKt-P9/9.0 with A201G mutation), and one 100 ns simulation was conducted with the 23S rRNA *E.c.* revKt-54-analog (Table S3, Supporting Information). The cumulative production time amounts to ~7.4 μs.

Data Analysis and Description of Topology. MD trajectories were analyzed with the Ptraj module of the AMBER package. PyMOL[74] and VMD[75] programs were used for visualization and preparation of figures.

The RMSD vs R_g density plots were calculated using an *in-house* script. An array of 150 × 150 bins was used. The scale on the right-hand side of the density plots indicates the relative occurrence of structures in the corresponding bin. The RMSD was mass-weighted and computed over all atoms of nucleotides 180−188 and 193−204 in the case of revKt-P9/9.0 and nucleotides 1518−1530 and 1661−1668 in the case of revKt-54. The X-ray structure of revKt-P9/9.0 was used as a reference structure for the RMSD calculations. However, the simulations of revKt-54 revealed a more compact conformational substate in comparison with its X-ray structure, which may be a consequence of removing the motif from its structural context. Thus, the average structure of this more compact substate (labeled as B′ in the text, see the Results section) was used for the RMSD analysis in the case of revKt-54 (see Supporting Information, Figure S1B for the density plot in which the RMSD is calculated with respect to the X-ray structure).

The compactness of the reverse K-turns structure was described using the end-to-end distance. The end-to-end distance equals the distance between the centers of mass of selected C-stem and NC-stem terminal nucleotides of the respective reverse K-turn (Figure S2, Supporting Information). The center of mass of the revKt-P9/9.0 C-stem terminus included nucleotides G186, G187, C194, and C195, while that of the NC-stem included G180, G181, C203, and C204. The revKt-54 C-stem terminus center of mass included A1518, U1519, A1667, and U1668, while the NC-stem terminus involved G1529, U1530, A1661, and C1662. For each reverse K-turn, the lowest end-to-end distance corresponds to a highly kinked structure, while the largest value denotes an unkinked (extended) structure.

In addition, we attempted to describe the global molecule topology using two additional structural parameters: the interhelical angle and the interhelical dihedral calculated using a recently proposed algorithm.[76] The mathematical definition of both structural parameters is given in the Supporting Information (see Supporting Information, Figure S2 and Table S2). However, the opening of reverse K-turns is a rather complex structural rearrangement that cannot be fully described by these two parameters modeling the system as two (almost) rigid stems connected by a hinge. Instead, all six degrees of freedom describing mutual orientation of stems in space seem to be crucial for the description of global structural dynamics of reverse K-turns (see Supporting Information).

Qualitative analysis of energy differences among reverse K-turns substates was carried out using the MM-PBSA (Molecular-Mechanics, Poisson−Boltzmann Surface Area) module of AMBER 11.[60,77] The Gibbs energy of solvation was calculated by both Poisson−Boltzmann[78] and generalized Born[79] implicit solvent models, while the entropy contribution was estimated from normal-mode analysis. MM-PBSA allows one to estimate free energies by postprocessing explicit-solvent simulation trajectories. The energy differences should be interpreted with care, because the validity of the MM-PBSA method for RNA is compromised by the inaccuracy of implicit solvent models for the polyanionic chain of RNA, as was, e.g., demonstrated by rapid degradation of the *glmS* riboswitch in implicit solvent MD simulations.[51] The essential dynamic analysis (EDA) was carried out using the GROMACS program.[80] All atoms of revKt-P9/9.0 residues 180−188 and 193−204 and revKt-54 residues 1518−1530 and 1661−1668 were included in the EDA calculations. The projections onto the first five essential modes were computed and subsequently visualized in the PyMOL program.

RESULTS

Starting Structures. The reverse K-turns consist of an internal bulge of unpaired bases (kink region, nucleotides 198−200 for revKt-P9/9.0 and 1522−1526 for revKt-54) flanked by canonical C-stem and noncanonical NC-stem (Figures 1 and 2). The overall fold of both studied reverse K-turns is bent resembling an "L"- or "V"-shaped structural motif of K-turns.[1]

However, reverse K-turns are bent in the opposite direction of K-turns, i.e., toward major grooves (Figure 1). Furthermore, while the topology of conventional K-turns is roughly uniform, the X-ray structures of reverse K-turns substantially differ (Figure 1). The structure of revKt-P9/9.0 is more compact, showing a smaller end-to-end distance (Table 2) and base-phosphate (BPh)[81] interactions between the bulge and NC-stem (Figure 2) in comparison to the more extended revKt-54 structure.

There is one magnesium ion resolved in the revKt-P9/9.0 X-ray structure coordinated to G181 (by inner-shell contact) and G182 (an outer-shell interaction) bases, additionally forming an inner-shell contact with one water molecule (Figure 2A). Although a Mg^{2+} ion is not present directly in the kink region, it is close enough to potentially provide some electrostatic stabilization, which could compensate for the repulsion between C- and NC-stems' phosphates. In contrast, no divalent cation was resolved in the revKt-54 crystal structure, although it still does not rule out the presence of a cation in this region, since cations can be disordered and elude detection.[49,82,83]

Table 2. End-to-End Distance of Reverse K-Turn Crystal Structures and Average Structures of the Relevant Substates Obtained from MD Simulations (See Figure 5)

	end-to-end distance (Å)	
structure type	revKt-P9/9.0	revKt-54
crystal structure	20.2	26.9
substate A/A′	19.4	19.8
substate B/B′	22.9	23.0
substate C/C′	28.6	26.6
substate D/D′	31.2	29.8

The revKt-P9/9.0 contains four 6BPh interactions (6BPh interaction is a hydrogen bond between the amino group of either adenine (N6) or cytosine (N4) and the phosphate oxygen[81]). Two 6BPh contacts are formed by revKt-P9/9.0 internal bulge bases A198 and C199 with the G180 phosphate of the NC-stem (henceforth, named the bulge-helix BPh contacts), while the next two 6BPh interactions are literally cementing the *t*HH A201/A183 base pair of the NC-stem (Figure 2A). In contrast, only one 6BPh interaction occurs in the revKt-54 system, being formed between the bases A1527 and A1664 of the NC-stem (Figure 2B), i.e., again stabilizing the *t*HH base pair flanking the internal bulge.

RNA−RNA Tertiary Interactions and Structural Context of Reverse K-Turns. Neither of the studied reverse K-turns binds any proteins,[31] but both of them are affected by RNA−RNA interactions. The revKt-P9/9.0 is accompanied by the formation of a tetraloop−tetraloop receptor (TL-TLR) interaction between atoms of the GNRA tetraloop (nucleobases 189−192) flanking the revKt-P9/9.0 C-stem and the P5/5a segment of the group I intron (Figure 2A). This contact is assumed to be responsible for the bending of this reverse K-turn.[29] The 23S *H. m.* revKt-54 is not associated with any TL-TLR contact but is stabilized by the interaction between four adenines A1656−A1659 of the revKt-54 NC-stem and the minor groove of the A-RNA duplex (part of helix 52 between the UAA/GAA internal loop and adjacent four-way junction; residues 1455−1457, 1485, and 1489−1490; Figure 3). Interestingly, equivalent regions of eubacterial revKt-54-analogs show the same RNA−RNA interaction (Figure S6, Supporting Information) despite the reverse K-turn not being conserved. The sequence and the 3D structure of this tertiary interaction are strictly evolutionarily conserved in the ribosome (Figures 4A−D). This tertiary contact can play an important role in revKt-54

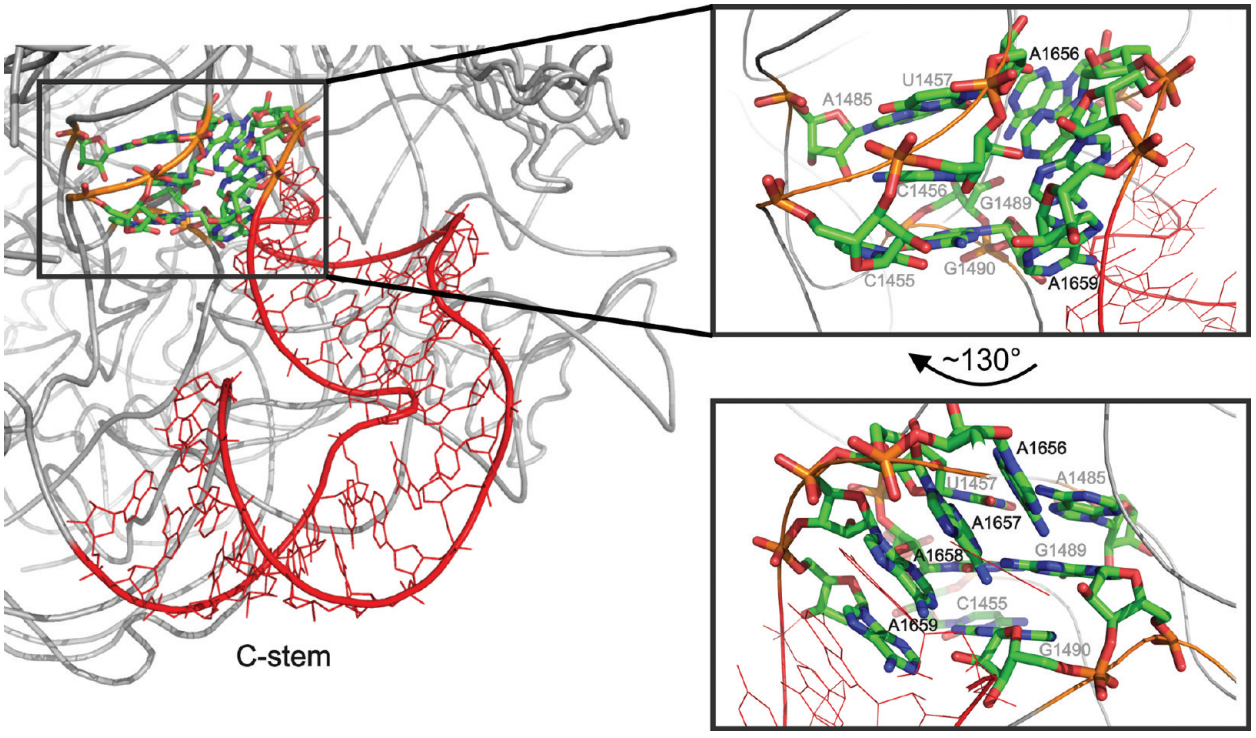

Figure 3. The tertiary RNA−RNA contact formed between the four adenines (A1656−A1659) of the revKt-54 NC-stem and part of helix 52 (base pairs *t*HW A1485/U1457, *c*WW G1489═C1456, and *c*WW G1490═C1455).

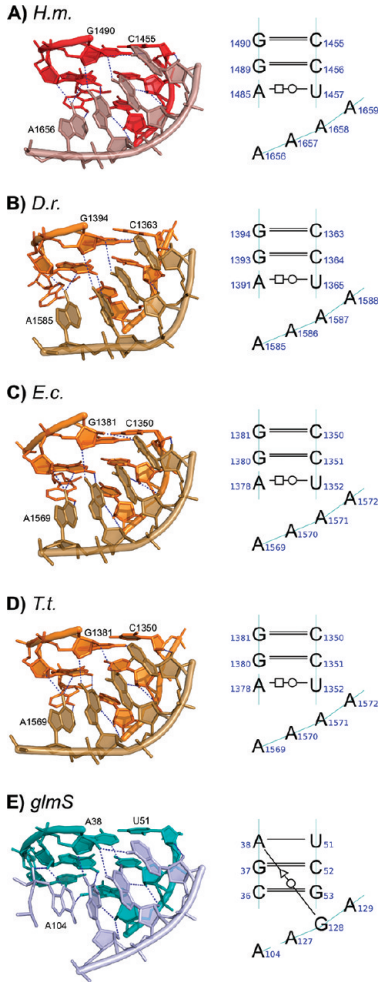

Figure 4. Three-dimensional (left) and secondary structures (right) of the new unclassified RNA interaction motif from 23S rRNAs of *Haloarcula marismortui* (PDB 3CC2) (A), *Deinococcus radiodurans* (PDB 1NKW) (B), *Escherichia coli* (PDB 2AW4) (C), and *Thermus thermophilus* (PDB 2J01) (D). (E) Depicts the motif isosteric to the rRNA motifs located in the *glmS* riboswitch (PDB 2HO7).

bending similarly to the TL-TLR interaction in revKt-P9/9.0 bending.

Transition of Reverse K-Turns' Helices into Senseless "Ladder-Like" Conformation with *ff*94, *ff*99, and *ff*99bsc0 Force Fields. MD simulations carried out with the common AMBER family force fields *ff*94, *ff*99, and *ff*99bsc0 show that both helices of each reverse K-turn undergo irreversible rearrangement to a "ladder-like" conformation (Figure S7, Supporting Information). The "ladder-like" structure was first identified as a force field artifact in extensive MD simulations of the hairpin ribozyme.[50] It was subsequently detected in simulations of short A-RNA stems and stem-loop systems.[64] The degraded "ladder-like" stem has in comparison with the A-RNA duplex a reduced twist from ∼33° to ∼10°, a base pair slide shifted from ∼−2 to ∼4 Å, and glycosidic torsions χ fluctuating around or even outside the high-*anti* region (i.e., ∼−90° while typical A-RNA χ value is ∼−165°). The shift of glycosidic torsion to a high-*anti* region is the most evident feature of the "ladder-like" structure. Considering these data and our previous simulations,[50,64] we can conclude that this artifact may be rather widespread in long *ff*94, *ff*99, and *ff*99bsc0 simulations of RNA molecules with exposed terminal stems. In fact, our unpublished simulations indicate that even folded RNA molecules sooner or later degrade toward high-*anti* structures if the simulations are long enough. The formation of "ladder-like" structures occurred stochastically, generally on a time scale of tens of nanoseconds (Table 1), and was entirely irreversible.

We did not observe any effect of ionic condition (net-neutralizing Na^+, K^+, and KCl salt excess) or the used water model (TIP3P and SPC/E) on the formation of the "ladder-like" structure, so this artifact seems to be solely a consequence of solute force field parameters. As noted above, although water/ion/salt parameters and conditions may sometimes influence NA simulations, the outcome of the simulations is overwhelmingly determined by the solute force field.

In contrast, no formation of "ladder-like" structure was observed with the new χ_{OL} parametrization of glycosidic torsion parameters, i.e., when applying the *ff*99χ_{OL} and *ff*99bsc0χ_{OL} force fields.[64] The density plot RMSD vs R_g calculated from all *ff*99χ_{OL} and *ff*99bsc0χ_{OL} productions (cumulative time of 1.1 μs for revKt-P9/9.0 and 0.6 μs for revKt-54) almost perfectly matches the RMSD vs R_g plot computed over *ff*94, *ff*99, and *ff*99bsc0 trajectory portions before the "ladder-like" degradation occurs (1.4 μs for revKt-P9/9.0 and 1.2 μs for revKt-54; Figure S8, Supporting Information). Thus, when using MD simulations carried out with *ff*94, *ff*99, and *ff*99bsc0 force fields, only trajectory portions before the "ladder-like" formation events were considered relevant for analysis of the conformational properties of reverse K-turns. Fortunately, we have accumulated enough data without this major artifact to characterize flexibility of the studied system. The "ladder-like" stem distortions are easily detectable as artificial substates in the RMSD vs R_g plots (Figure 5).

In summary, reverse K-turn simulations with corrected glycosidic torsion parameters agree with *ff*94, *ff*99, and *ff*99bsc0 simulations before the later simulations degrade, while the new parameters entirely prevent the "ladder-like" structure degradation. Thus, the reverse K-turn structures could finally be analyzed using 4.3 μs of "healthy" data.

Structures of revKt-P9/9.0 and Their Evolution over MD Simulations. The RMSD vs R_g density plot (Figure 5A) calculated from all of the 150 ns revKt-P9/9.0 simulations (2.7 μs in total) shows seven significantly populated structural substates. Yellow boxes highlight those revKt-P9/9.0 substates that are free of the "ladder-like" conformations (A−D) and which are therefore relevant for further analyses. The gray boxes mark the revKt-P9/9.0 substates with the NC-stem (substates E and G) or the C-stem (substate F) in the distorted "ladder-like" conformation.

Figure 6A illustrates the overall shape ("topology") of the average structures for the relevant substates A−D. The topology of the most compact substate A is nearly identical to that of the X-ray structure (Figure 6A and Figure S9, Supporting Information). On the other hand, substate D corresponds to a fully unfolded (unkinked) revKt-P9/9.0 (cf. Figure 6A and Table 2). The other substates B and C represent intermediate states between the native-like kinked and fully unkinked conformations (Table 2). In particular, substates B and C exhibit high flexibility corresponding to a bending movement, which is responsible for the elongated ellipsoidal shape of the corresponding regions in the density plot (see Figure 5A). Two BPh interactions supporting the *t*HH A/A base pairs remain stable during the whole simulations in all substates. In contrast, the other two bulge−helix BPh interactions observed in the X-ray structure and in substate A are much less populated in substate B and disappear in

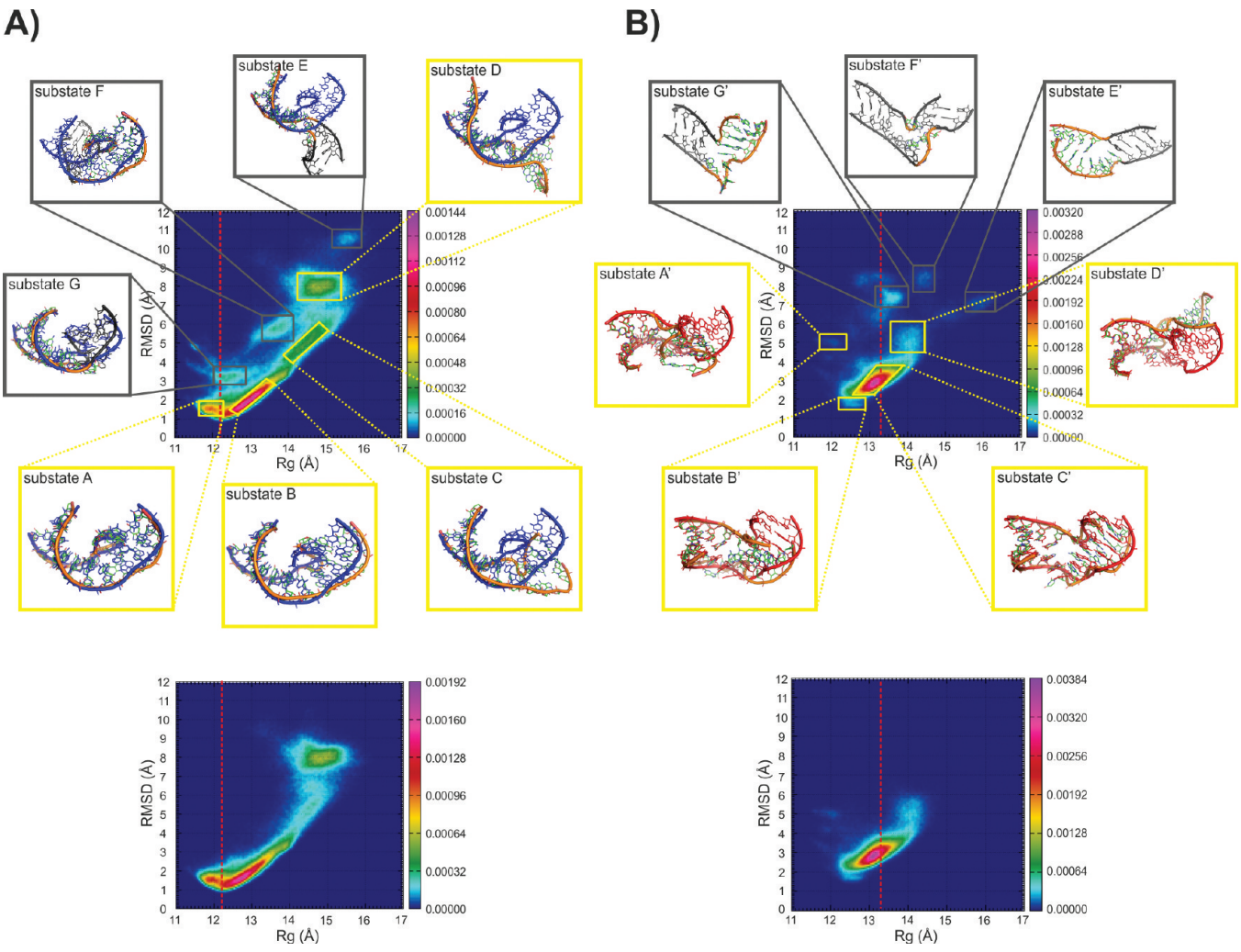

Figure 5. The upper parts of panels A and B show RMSD vs R_g density plots calculated over the entire trajectories of all revKt-P9/9.0 and revKt-54 simulations listed in Table 1, respectively. The yellow frames show densely occupied "healthy" regions of the RMSD vs R_g plots and the corresponding structure representatives (substates A−D and A′−D′). Gray boxes show substates and their representative structures bearing the degraded "ladder-like" conformation (substates E−G and E′−G′, nucleotides within the "ladder-like" conformation are colored in gray). The C-stems of each structure representative are superimposed over the C-stem of the starting structure of revKt-P9/9.0 in blue and revKt-54 in red, respectively (except of substates F and E′−G′). The vertical dashed red line highlights the radius of gyration of the crystal revKt-P9/9.0 and revKt-54 structures. In the lower part of panels A and B are the same density plots for revKt-P9/9.0 and revKt-54, respectively, but visualized without the trajectory portions affected by the "ladder-like" reverse K-turn conformations.

the more unkinked structures of substates C and D (Table 3). Besides that, the X-ray stacking pattern of bases C199 and A200 is reasonably well preserved in substates A and B, while in the substates C and D, the respective bases favor various non-native geometries (not shown).

The fully unfolded substate D almost vanishes in the MD simulations carried out with the excess KCl salt and SPC/E water model except for one MD run, INT-25, in which a reversible transition to substate D occurs, with substate D persisting for several nanoseconds (cf. Figure 7A for the time evolution of substates in all MD simulations). On the other hand, almost all MD simulations conducted with the net-neutralizing Na^+ ions and TIP3P water model sample all conformational substates A−D. This is most likely the consequence of the different viscosities of the TIP3P and SPC/E water model rather than being caused by the different ion parameters and concentrations (see the discussion about the effect of water models below). The transitions from the fully kinked substate A to the fully unkinked substate D (and vice versa) usually pass through substates B and C. The transitions between substates usually occur on the time scale of several nanoseconds. Notably, revKt-P9/9.0 fully unfolds also in the presence of Mg^{2+}.

Structures of revKt-54 and Their Evolution over MD Simulations. Seven densely populated regions were identified in the revKt-54 density plot (Figure 5B). Three of them contain "ladder-like" artificial conformations (substates E′−G′) and are not further discussed. The remaining four substates (A′−D′) exhibit relevant structures without the "ladder-like" distortion.

Substates A′ and D′ represent the most compact (kinked) and the most extended (unfolded/unkinked) revKt-54 structures, respectively (Table 2; Figures 5B and 6B). Just as for substates B and C of revKt-P9/9.0, substates B′ and C′ correspond to intermediates between the kinked and unkinked states (Figure 6B). Similarly to intermediate substates B and C of revKt-P9/9.0,

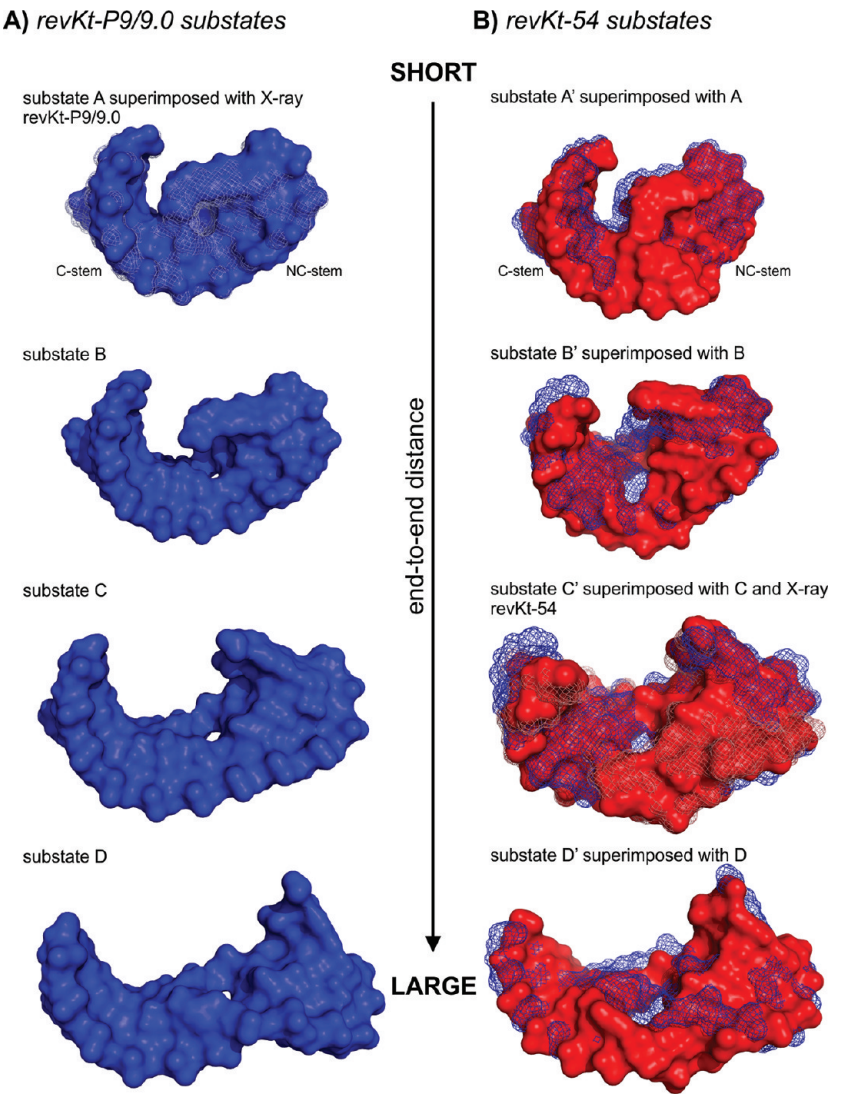

Figure 6. Average structures of revKt-P9/9.0 substates A—D (left) and revKt-54 substates A′—D′ (right) visualized using the surface representation. Blue mesh representation on the right represents revKt-P9/9.0 substates superimposed over the C-stem and NC-stem backbone atoms with corresponding revKt-54 substates. In addition, gray mesh structures superimposed over substates A and C′ of revKt-P9/9.0 and revKt-54, respectively, correspond to their X-ray structures.

Table 3. Stability of revKt-P9/9.0 BPh[81] Interactions in Substates Calculated As a Relative Population of H Bonds Involved in the BPh Interaction with a 4.0 Å for Cutoff Distance between Heavy Atoms (in %)[a]

substate	A198(N6)—G180(O1P)	C199(N4)—G180(O2P)	A201(O2P)—A183(N6)	A183(O1P)—A201(N6)
A	34.5	35.1	97.9	60.5
B	10.0	9.7	89.5	68.7
C	0.0	0.0	31.2	72.2
D	0.0	0.0	67.2	71.1
X-ray (Å)	3.3	2.9	2.7	3.2

[a] The X-ray H-bond distances are in the last line.

substate C′ of revKt-54 reveals intrinsic bending movement represented by an ellipsoidal, elongated population in the density plot (Figure 5B). The average structure of substate C′ resembles the X-ray revKt-54 topology (Figure 6B and Figure S10, Supporting Information). Similar to revKt-P9/9.0, the 6BPh interaction supporting the *t*HH A/A base pair is present in all structural substates (26%, 63%, 47%, and 73% population of direct H-bonding in substates A′, B′, C′, and D′, respectively). Substate C′ maintained well the native stacking pattern of the kink region bases, with only U1524 occasionally flipping out (data not shown), while the native conformation of kink region bases is distorted in other substates, A′, B′, and D′.

Substate C′, resembling the X-ray topology, is significantly populated over the entire time scale of most revKt-54 MD simulations (Figure 7B). In contrast, the fully kinked substate A′ is only negligibly populated in our simulations; namely, it is propagated for only several nanoseconds in the MD run RIB-19 (excess KCl salt and SPC/E water). The only substantial occupancy of substate B′ was observed in the simulation with 12 Mg^{2+} ions and TIP3P water (RIB-2). Unfolding of revKt-54 to substate D′ was detected in two simulations with Na^+ ions and the TIP3P water

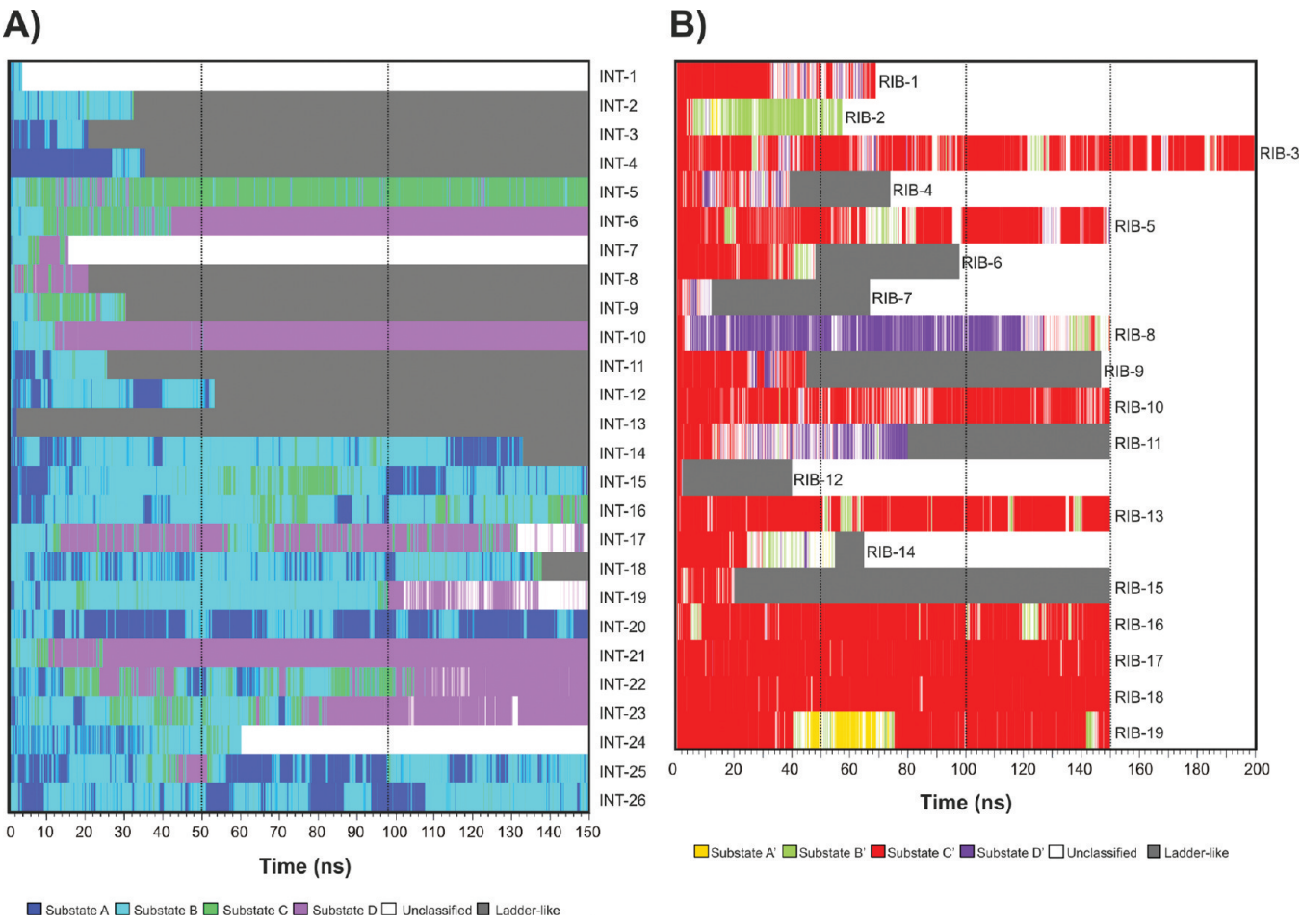

Figure 7. Time evolution of revKt-P9/9.0 (A) and revKt-54 (B) substates in individual MD simulations. The ends of individual simulations are marked by the simulation labels that correspond to Table 1.

model (RIB-8 and RIB-11; see Figure 7B). The refolding of revKt-54 from substate D′ through C′ toward B′ was observed in the RIB-8 simulation. Thus, similar to revKt-P9/9.0 simulations, the transition of revKt-54 toward more extended structures represents a fully reversible process on our simulation time scale.

Topological Similarity among the revKt-P9/9.0 and revKt-54 Substates. Although the sequence and topology in the X-ray structure of both studied reverse K-turns differ substantially, the simulations reveal profound similarity in large-scale dynamics of these motifs when they are removed from their structural context. This can be considered as a flexibility signature of the reverse K-turn. We found that both reverse K-turns share very similar structural substates (A−D and A′−D′ for revKt-P9/9.0 and revKt-54, respectively) sampled in MD simulations (Figure 6). Although the simulations of each system started from a different conformational substate due to differences between their X-ray structures (the X-ray structures of revKt-P9/9.0 and revKt-54 correspond to substates A and C′, respectively), both systems finally sample all four substates (Figure 7). Figure 6 summarizes structural similarities between conformational substates of both reverse K-turns. The most compact substates (A and A′) have small values of the end-to-end distance, while unfolded (unkinked) substates (D and D′) are characterized by the largest end-to-end distance (Table 2). The intermediate substates (substate B and C of revKt-P9/9.0 and substate C′ of revKt-54) correspond to a rather broad range of geometries with high hinge-like flexibility (see Figures 5 and 8 and the next paragraph), while the most compact or the most extended substates reveal only minor dynamics corresponding to local fluctuations around energy minimal conformation.

Both Reverse K-Turns Have Overall Hinge-Like Flexibility Similar to K-Turns. The essential dynamics analysis (EDA) reveals that the first essential motions of substates B and C of revKt-P9/9.0 and substate C′ of revKt-54 resemble the hinge-like dynamics observed in MD simulations of conventional K-turns[17−20] (Figure 8). The first essential motions dominate over the other modes, and they contribute 25.0, 34.4, and 28.5% of essential dynamics of revKt-P9/9.0 substates B and C and revKt-54 substate C′, respectively. The contributions of the subsequent essential motions progressively decrease (Table S4, Supporting Information). The hinge-like motion can be qualitatively described as a motion of two rather rigid helical arms caused by the flexible kink region. The observed motion of reverse K-turns substates B, C, and C′ exhibits anisotropic dynamics. The hinge-like dynamics of these substates is also coupled with the local dynamics of kink region bases (bases C199 and A200 in substate B, A198 in substate C, and U1524 in substate C′, see Figure 8). Substate C hinge-like dynamics is additionally coupled with *c*WW G184═C197 base pair propeller twist fluctuation. The ellipsoidal, elongated population region of these substates

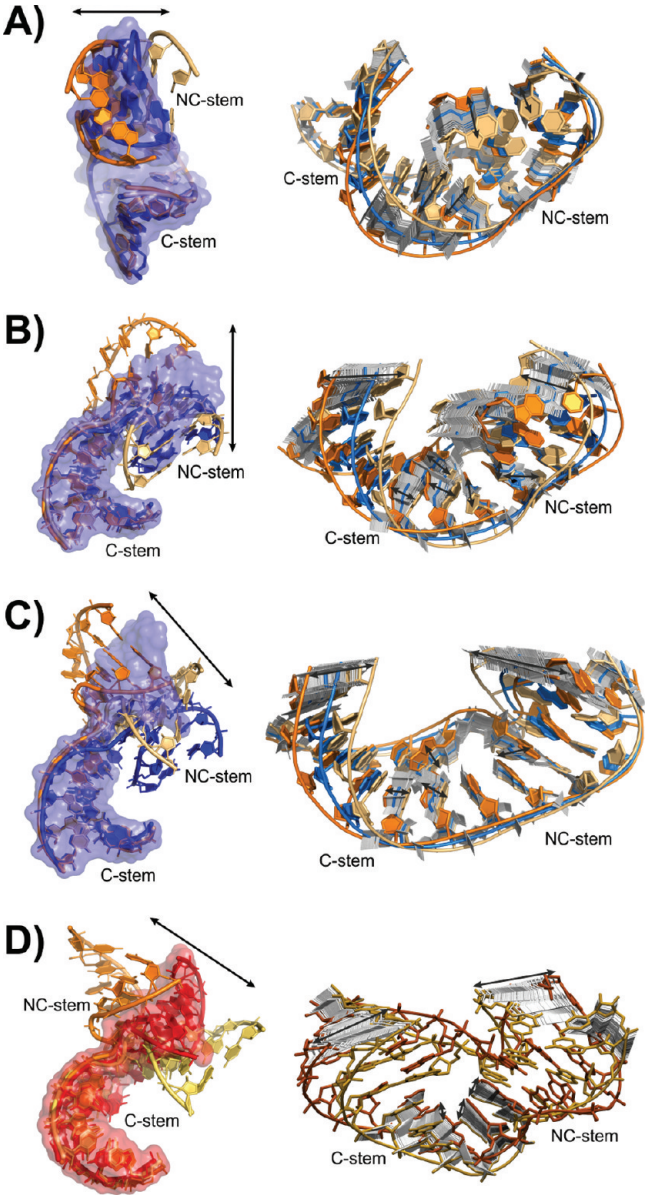

Figure 8. Essential dynamics analysis. The first essential modes of revKt-P9/9.0 substates A, B, and C (panels A, B, and C, respectively) and revKt-54 substate C′ (panel D). Figures on the left illustrate magnitudes of the hinge-like oscillations for the respective substate. The panels show superposition (over the C-stem) of the two extremes of essential mode (in orange and light-orange) with the average (surface representation) and initial reverse K-turn structure (cartoon representation). The initial and average revKt-P9/9.0 structures are colored in blue, while the initial and average structures of revKt-54 are in red. Figures on the right illustrate the coupling between the hinge-like fluctuations and local motions of bulge bases (as highlighted by the black arrows).

(Figure 5) is likely caused by this hinge-like dynamics identified by EDA. In other words, in this particular case, we were capable of identifying the movement revealed by the EDA also in the full simulation, which is not always possible due to approximations inherent to EDA.[56] A very similar hinge-like dynamics was also observed in the simulation of the *E.c.* revKt-54-analog (nucleotides 1407−1422 and 1576−1595 of 2AW4 PDB). This suggests that although the reverse K-turn is not conserved in eubacteria, the equivalent RNA segments in eubacteria still show conservation of basic RNA topological and dynamical features (Figure S11, Supporting Information).

Substates B and C of revKt-P9/9.0 and C′ of revKt-54 are similar from the flexibility point of view. However, while substate C′ fluctuates around the X-ray geometry of revKt-54, neither substate B nor substate C is the native state of revKt-P9/9.0 (Figure 8). The X-ray conformation of revKt-P9/9.0 corresponds rather to the structurally more compact substate A, which does not show much bending flexibility. Instead, there are some "side-to-side" fluctuations of revKt-P9/9.0 substate A coupled to the formation/loss of the bulge−helix BPh interactions (Figure 8A). Similarly to substate A of revKt-P9/9.0, a low flexibility was identified for structurally compact substates A′ and B′ of revKt-54, albeit they are only marginally sampled in our study (see Figure 7B). This may reflect the difference in compactness of the starting structures of both reverse K-turns, which obviously still affects sampling on the present simulation time scale. Consistent with the analogy between substates A and A′ of both reverse K-turns, we noticed a 4BPh interaction in poorly populated substate A′ of revKt-54, which is formed between the G1523 (situated in the kink region) and A1661 phosphate of the NC-stem. Thus, substate A′ reveals an internal revKt tertiary contact which seems to be analogous to the native bulge−helix BPh contacts visible in revKt-P9/9.0.

In summary, the results show that the conformational space of reverse K-turns consists of four substates ranging from compact closed to open unkinked geometries. Interestingly, while the intron molecule captures or utilizes the reverse K-turn in its most closed geometry, the ribosome utilizes the semiclosed structure, which is intrinsically the most flexible one. The archaeal ribosomal revKt-54 is replaced in eubacteria by seemingly unrelated sequences, which nevertheless adopt a similar shape and share the anisotropic flexibility.

Water Model Affects revKt-P9/9.0 Conformational Behavior. RevKt-P9/9.0 generally fully unfolds (occupies more frequently the substate D topology) in simulations carried out with TIP3P water model and net-neutralizing Na^+ ions ($c(Na^+)$ ∼0.25 M; Figure 7A and Figure S12, Supporting Information). In contrast, all MD simulations carried out with the SPC/E water model and the KCl excess salt ($c(K^+)$ ∼0.5 M; $c(Cl^-)$ ∼0.25 M) conditions maintain the kinked conformation of revKt-P9/9.0. Thus, we performed an additional set of MD simulations carried out in net-neutralizing K^+ ions ($c(K^+)$ ∼0.25 M and SPC/E water model, listed in Table S3 in the Supporting Information). We observe the same behavior in these simulations as for SPC/E KCl salt excess simulations (Figure S12, Supporting Information), explicitly suggesting that the differences in behavior are not due to different ionic conditions (K^+ net neutralizing and KCl salt excess). Further, although we have taken the Na^+ and K^+ parameters from different sets of cation parameters (see Methods), we observed that the Na^+ and K^+ ions occur at identical binding sites and with the same occupancy in the net-neutralizing (∼0.25 M) Na^+ and K^+ simulations (Figure S13, Supporting Information). This suggests that differences in behavior among revKt-P9/9.0 simulations most likely do not originate in the type of ions (Na^+ vs K^+ ions) but are driven by water models (TIP3P vs SPC/E). We can hypothesize that the effect of solvent model on the reverse K-turn flexibility can have two reasons, kinetic and thermodynamic. The TIP3P model has an approximately 2 times larger self-diffusion constant than SPC/E,[84] so the unfolding of revKt-P9/9.0 can be accelerated in TIP3P in comparison with SPC/E simulations.

Qualitative analysis of free energy differences among the substates carried out using the standard implicit solvent MM-PBSA free energy method shows that the compact states (A, B, A′, and B′) differ from the open states (C, D, C′, and D′) in Gibbs energy of solvation and the electrostatic term (Table S5, Supporting Information). The compact states are destabilized by the electrostatic term, due to repulsion of the phosphates, which is compensated by a more favorable Gibbs energy of solvation. This might indirectly support the idea that the observed differences in populations of reverse K-turn substates in explicit solvent simulations could also be caused by a different Gibbs energy of solvation between the TIP3P and SPC/E explicit water models. Nonetheless, larger time scale simulations with the SPC/E water model would be required to verify this hypothesis. Work is in progress to provide further insights into this issue. Nevertheless, it is so far apparent that selection of the water model has a much larger impact on these simulations than selection of the type and concentration of ions.

Divalent Mg^{2+} Ions Do Not Stabilize Reverse K-Turns' Kinked Topology. We carried out a set of simulations of both reverse K-turns with Mg^{2+} ions to test the influence of divalents on the flexibility of reverse K-turns. Six simulations of revKt-P9/9.0 were carried out with the TIP3P model and one Mg^{2+} ion settled near the kink region. In three out of these six simulations (INT-18, INT-19, and INT-S8), we observed unfolding of the system to substate D, i.e., similar behavior as observed in simulations with monovalent ions. The unfolding occurred on a 10 ns time scale and was entirely irreversible. Similarly, only one of four MD simulations of revKt-54 carried out with divalents revealed a stabilizing effect in the B′ substate (Figure 7B). Taken together, we did not observed any statistically relevant effect of divalent ions on the dynamic behavior of reverse K-turns. Nonetheless, it should be noted that these conclusions are limited, as classical empirical nonpolarizable force fields describe divalents inaccurately and divalents sample poorly in simulations. Thus, we generally do not recommend to include divalents in nucleic acids simulations, unless absolutely critical due to structural reasons.[44,49,55,85] The total amount of polarization and charge-transfer nonadditivities in the first ligand shell of a divalent cation (contributions entirely lacking appropriate terms in common biomolecular force fields) is about 70 kcal/mol. These effects obviously further propagate far beyond the first ligand shell, dramatically affecting the neighborhood of the divalent cation. In other words, for divalent cations such as Mg^{2+}, the force field approximation essentially breaks down completely.[86−91]

DISCUSSION AND CONCLUSIONS

Reverse K-turns are RNA motifs that possess significant sequence similarity to the conventional K-turns but have a very different mutual arrangement of the A-RNA duplexes (stems). The stems of conventional K-turns are aligned in such a way that their minor grooves are juxtaposed. The reverse K-turns display an opposite stem bending with juxtaposition of the major grooves (Figure 1). There is no significant H-bonding between stems of reverse K-turns, in contrast to K-turns that are stabilized by signature interactions.[1] To date, three unique reverse K-turns have been found in the available RNA structural data.[31,34] We studied the reverse K-turn occurring in the *Azoarcus* group I intron (revKt-P9/9.0)[28] and the reverse K-turn of helix 54 in the 23S rRNA of *H.m.* (revKt-54).[31]

We present an extensive set (7.4 μs) of explicit solvent MD simulations carried out for isolated reverse K-turns. Such simulations capture the internal flexibility of the studied RNA motifs pertinent to their starting structures, which correspond to the native folded arrangement.[44] The simulations were conducted with the traditional AMBER Cornell et al. force fields *ff*94, *ff*99, and *ff*99bsc0. Additional simulations were conducted with the recently reparameterized nucleotide N-glycosidic torsion profiles (χ_{OL}), which became available in the course of the project.[64] These simulations are labeled as either *ff*99χ_{OL} or *ff*99bsc0χ_{OL}, depending on whether the bsc0 correction is used or not (Table 1 and Table S3, Supporting Information). The simulations also compare different ion conditions (minimal concentration of Na^+ or K^+, Na^+ ions combined with Mg^{2+} divalents, and, finally, KCl excess salt). Two different explicit water models (TIP3P and SPC/E) are utilized in this study. Thus, besides the initial aim to examine the intrinsic stability and flexibility of reverse K-turns, our study also provides valuable insights into the force field dependence of RNA simulations. Due to the unique propensity of reverse K-turns to show structural transitions on the short time scale of simulations, these RNA systems are useful in such force field studies.

The Effect of the Solute Force Field on Stability of Trajectories. Without using the χ_{OL} parametrization, the stems of both reverse K-turns structurally degrade by adopting a distorted "ladder-like" conformation (Figure 5 and Figure S7, Supporting Information). The "ladder-like" conformation was recently identified as a major force field artifact which is associated with transition of the glycosidic torsion from *anti* to high-*anti* region.[50,64] The "ladder-like" transition is an irreversible process, which occurs for reverse K-turns on 10 ns time scales in *ff*94, *ff*99, and *ff*99bsc0 force fields (see Figure 7). The "toxicity" of artificial "ladder-like" rearrangement is similar to α/γ flips that were found to systematically degrade DNA simulations in *ff*94 and *ff*99 force fields.[63] However, the formation of "ladder-like" structures in RNA simulations is apparent on longer time scales, which might be the reason why the A-RNA "ladder-like" artifact has been identified almost three years after the "γ-trans" flips degradation of B-DNA.[63] Similar to α/γ flips in DNA, the "ladder-like" structure is ultimately more stable than the native A-RNA form. The transition is a textbook example of structures where the force field (without the appropriate χ reparameterization) does not provide the correct global minimum of the simulated molecule (or its part), which then sooner or later (depending on the barrier) degrades.[44,63,92,93] This degradation is entirely eliminated in simulations applying the modified χ profiles, i.e., in *ff*99χ_{OL} and *ff*99bsc0χ_{OL} force fields.[64]

It is possible (and not unlikely) that a simple force field with simple analytic function and a limited set of parameters provides a less complex (less flexible) description of structure/energy relations compared to real molecules. Then, refining the force field to reproduce the native conformations may somewhat bias sampling of less populated but still relevant regions of the conformational space. However, at the same time, any force field which has a major pathology is likely not better in sampling of less populated relevant regions. It is because it shares the same function and most parameters with the refined force field but is biased to sample completely unrealistic states as global minima. Therefore, removal of a substantial pathology as done by χ_{OL} should not be accompanied with any systematic bias of less populated nonpathological regions. In addition, the force field has not been primarily fitted to come closer to the native geometry but to reproduce reference QM data. The improvement of the simulation behavior has been achieved indirectly as a

byproduct of the genuine QM fit. The issue of biasing dynamics of less populated relevant states may be, however, a substantial concern when attempting further more subtle changes, i.e., when trying to achieve a perfect reproduction of target structures that would go beyond the principal accuracy limits of a given force field form.

Only trajectories and trajectory portions lacking any sign of the "ladder-like" structure (4.3 μs) are used to assess the dynamics of the reverse K-turns presented here. For these trajectory portions, all solute force fields provide very similar results.

The Effect of Ion and Water Treatment. Compared to the large effect of the RNA force field, the results are considerably less affected by the treatment of the ions and water. However, unkinking of the reverse K-turns is more pronounced in TIP3P in comparison with SPC/E simulations. In contrast, the type and concentration of ions do not appear to substantially affect the reverse K-turn simulations. Consistently with the present results, our earlier reference simulations of A-RNA duplexes comparing the net-neutralizing Na^+ ion ($c(Na^+) \sim 0.2$ M) conditions with the TIP3P water model and KCl excess-salt ($c(K^+) \sim 0.4$ M)) with the SPC/E water model revealed that in SPC/E salt excess the A-RNA structures were more compact, especially for some sequences.[59] Considering the present results, we suggest that the earlier reported differences in A-RNA simulations[59] were caused primarily by the water models rather than by the ionic strength or choice of counterions. Our preliminary data from additional extended MD simulations of A-RNA duplexes under various ionic strengths (data not shown) and solvent models confirm that and will be published elsewhere once completed. Thus, when the simulation conditions are ordered according to their impact on the simulated RNA structures, it appears that the most pronounced effect has the RNA force field. Considerably smaller differences are caused by the used explicit water model (the same applies also for proteins, see refs 84 and 94). Finally, the type and concentration of ions appear to be, so far, less important. This supports the view that most RNA simulations under net-neutralizing conditions are valid, of course provided that the periodic water box size is not too large to dilute the net-neutralizing ions. Further investigations of these issues are under way. It is to be noted that the above considerations are relevant for simulations executed at the presently affordable simulation time scales and with the usual box sizes used in contemporary simulations.

Reverse K-Turns Belong to the Most Flexible Nucleic Acids Molecules Simulated So Far. The X-ray structures of revKt-P9/9.0 and revKt-54 significantly differ (Figures 1 and 6); however, when removed from their structural contexts, both reverse K-turns sample similar structural substates, albeit the sampling at the present simulation time scale is still inevitably affected by the starting structures. Both reverse K-turns sample a wide variety of conformations ranging from fully kinked to fully unkinked states. We observe three types of conformational clusters (substates): (i) the compact fully kinked conformation, (ii) the fully unkinked state, and (iii) the highly flexible intermediate states that reveal hinge-like flexibility correlated with bulge region local dynamics (Figures 6 and 8). While the ribosome utilizes the revKt-54 within its structural context in a geometry corresponding to the flexible intermediate substate, the intron reverse K-turn is locked in the compact fully kinked state.

The fact that reverse K-turns are able to rearrange from fully kinked to fully unkinked substates and vice versa within a relatively short time scale of hundreds of nanoseconds indicates that these motifs are intrinsically metastable in their native conformations and that the barriers between their substates are relatively low (lower than ~7 kcal/mol, which represents the critical free energy barrier for an observable event on the 100 ns time scale). The reverse K-turn is the most flexible recurrent RNA motif studied by MD simulations until now.

Comparison of Simulation Dynamics of K-Turns and Reverse K-Turns. To date, no spontaneous unfolding of conventional K-turns has been observed on tens of nanoseconds time scales of MD simulations.[18,19] When starting from the native folded (tightly kinked) K-turn structures, the simulations reveal hinge-like fluctuations around the native structure similar to what was observed for the intermediate substates of the reverse K-turns. On the other hand, the experimental studies show that the conventional K-turns unfold (unkink) in the absence of proteins or stabilizing divalent cations.[13] Also, the recent NMR structure reveals an extended shape of an isolated K-turn.[95] In contrast to MD simulations, these experimental techniques observe conventional K-turns on much longer time scales and in thermodynamic equilibrium. Unfortunately, experimental data assessing the stability of free reverse K-turns in solution are not currently available. However, taking into account the reverse K-turn simulation data together with the current experimental as well as theoretical knowledge about the stability of conventional K-turns, we can expect that both conventional K-turns and reverse K-turns are most likely able to sample kinked and unkinked substates. The substates of conventional K-turns, however, are separated by higher free energy barriers in comparison to the reverse K-turns. In fact, taking into account the sequence similarity between K-turns and reverse K-turns, we assume that they could both prefer similar unkinked geometries in solution. We expect that both systems could in principle spontaneously attempt transitions between conventional and reverse K-turn bending, albeit this would require unstacking, flipping over, and restacking of terminal NC-stem adenine belonging to the shorter strand (see below), which is most likely a much slower process than the local dynamics of reverse and conventional K-turns.

What Might Be the Role of Reverse K-Turns? We have suggested in earlier studies that, besides their role in protein−RNA interactions, some K-turns can act as flexible molecular elbows involved in functional RNA dynamics during the elongation cycle.[17,19,20] A sufficiently long lifetime of the kinked and unkinked states (originating in the relatively high free energy barrier between both conformational states) can be important for the molecular elbow function of the K-turns, which would utilize the conformational spaces of the kinked state. In contrast, the present simulations show that the reverse K-turns are even more flexible than the conventional K-turns, with a negligible barrier between kinked and unkinked states. Their exact structure is considerably less strictly defined due to the lack of tertiary interstem interactions. Owing to this, the reverse K-turn is also much more versatile in its folded structure (disregarding its context, i.e., intrinsically). We do not have any evidence to suggest that the pronounced elbow-like flexibility of reverse K-turns contributes to large-scale RNA dynamics. Rather, the large flexibility of the reverse K-turns is utilized in RNA folding to build up static RNA 3D topologies based on RNA−RNA interactions. In contrast to conventional K-turns, reverse K-turns do not seem to interact with proteins. This again may be related to the fact that when kinked into reverse K-turn topology, the RNA molecule is still too versatile (less structured) compared to the conventional K-turn topology, due to the lack of tertiary interstem interactions.

Is There a Salient Tertiary Interaction in the Ribosome Responsible for the Reverse K-Turn Bending? The biochemical experiments for the intron revKt-P9/9.0 revealed that a remote tertiary contact is responsible for revKt-P9/9.0 bending.[29] The tertiary contact is formed between the GNRA tetraloop attached to the revKt-P9/9.0 C-stem and receptor atoms situated in the P5/5a intron part (TL-TLR contact). A part of the revKt-54 NC-stem also forms a tertiary interaction, specifically with the minor groove of helix 52. The RNA−RNA interaction does not resemble the intron TL-TLR interface and seems to be a new, as yet unclassified RNA motif or interaction pattern, since the nucleotides as well as the overall 3D topology of this motif are evolutionarily conserved in the ribosome (Figures 4A−D). Furthermore, we have identified an isosteric arrangement in the *glmS* riboswitch.[51,96,97] This motif (see Figure 4E) is the oblique stack interaction between stacked purines (four adenines in the ribosome or the AAGA stack in the *glmS* riboswitch) and the minor groove of the A-RNA stem. In *glmS* riboswitch, this motif includes the P2.1 stem and purine stacking module between P4 and P4.1 stems. It represents a very rigid motif in MD simulations and stabilizes conformation of the pseudoknot carrying the ligand binding site.[51]

We suggest that such an RNA motif stabilizes the kinked conformation of revKt-54 similarly to the intron TL-TLR interface. These interactions, which are localized in outer parts of the reverse K-turns, are most likely responsible for the bending of reverse K-turns, because without this tertiary RNA−RNA interaction both reverse K-turns easily relax to more extended structures. As the bending is imposed by external interactions with respect to the reverse K-turns, there is no direct evolutionary pressure for reverse K-turns' primary sequence conservation around the bulge. Other RNA sequences with appropriate bending capability could replace the reverse K-turn. This actually happens in the course of evolution since our simulations show that the revKt-54 structural analog from *E.c.*, which has a very different sequence in comparison to revKt-54, exhibits the same flexibility (see the Supporting Information). This strikingly resembles the evolutionary variability of the elbow segment at the base of the dynamical A-site finger of the large ribosomal subunit.[17] Also, in that case, a structured RNA motif in *H.m.* is, in bacteria, replaced by at first sight unrelated RNA segments which nevertheless adopt an identical global topology and have strikingly similar simulation behavior. Thus, evolution is capable of replacing one RNA element with another one, which looks unrelated at the level of sequence, 2D structure, as well as molecular interactions but still conserves key physical-chemistry properties (such as topology and directional flexibility) required for proper function.[17,98] These observations illustrate the modular nature of large RNA molecules, where distinct medium-sized recurrent RNA molecular building blocks are used to create large functional RNA structures. Computations can in such cases provide useful insights complementing the structural and bioinformatics data.

Why Is the First *t*HS G/A Base Pair of the NC-Stem of K-Turn Replaced by the *t*HH A/A Base Pair in Reverse K-Turn? The only significant sequence difference between K-turn and reverse K-turn structures is the (first, terminal) base pair of the NC-stem adjacent to the bulge. This base pair is critical for the bending direction, which is driven by the bend of the shorter strand, while the longer "bulge" strand passively follows (Figure 9 and Figure S14, Supporting Information). In conventional K-turns, the terminal base pair of the NC-stem must have adenine in the short strand and must be a *t*HS base pair.[30] It is due to its

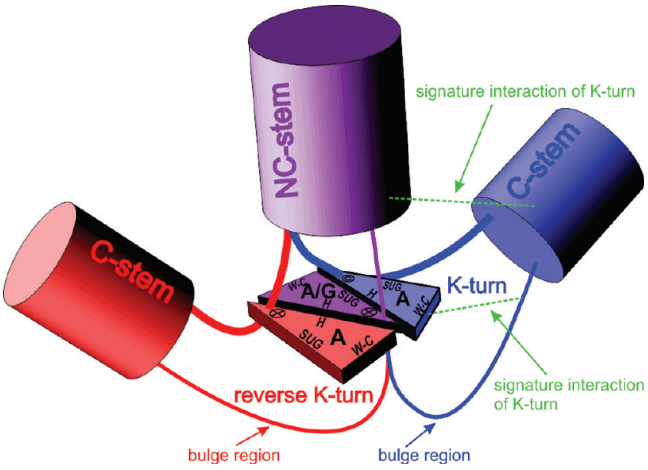

Figure 9. Scheme of the role of the flipped-over adenine (red) in reverse K-turn and the corresponding opposite bending of the K-turn (blue) and reverse K-turn (red). Both systems are superimposed over their NC-stems (the shared parts are in violet). The thick and thin lines highlight the short and long strands, respectively. The terminal base pair of NC-stem adjacent to the bulge is represented in a triangle abstraction.[102] Note that the red and blue triangles are flipped-over with respect to each other, so that they stack on the NC-stem by different nucleobase faces. The green dashed line shows the signature interactions of K-turn. The Supporting Information presents an analogical superposition of reverse K-turn revKt-54 and consensual K-turn Kt-7 structures over their NC-stem backbone atoms (Figure S14, Supporting Information).

adenine-specific N1 acceptor signature interaction with the bulge 5′-most nucleotide which firmly stacks on the C-stem.[1,30] Once this interaction is formed, only the Hoogsteen-edge of the short-strand adenine remains available (Figure S15A, Supporting Information). The first NC-stem base pair is then completed by a nucleotide from the longer strand to adopt the *t*HS arrangement (see Supporting Information for further details). The *t*HS arrangement is needed to insert the immediately following longer-strand adenine (belonging to the second base pair in the NC-stem) through its sugar edge to the minor groove of the C-stem to form the A-minor interaction between the NC- and C-stems (Figure S15B, Supporting Information). This finally fixes the overall K-turn topology (Figure S15C, Supporting Information). Among the *t*HS base pairs, the A/G base pair is energetically the most stable[99] and the most frequently realized in the naturally occurring RNAs.[100] The isosteric *t*HS A/A base pair would also be geometrically entirely compatible with the topology of conventional the K-turn but is energetically less stable[99] and also less frequent in RNAs.[100] Sequence alignments reveal that the A/A combination indeed is sometimes realized in K-turns.[14,30]

In contrast, the *t*HS base pair is incompatible with the topology of reverse K-turns. Similarly to conventional K-turns, the first nucleotide of the shorter strand in NC-stem is adenine and offers only its Hoogsteen-edge for pairing (Figure S14, Supporting Information). However, this adenine is flipped over and stacked to the NC-stem by the opposite stacking face in comparison with K-turn (and stacking in A-form RNA). Then, the shorter strand is bent in the opposite direction to that in K-turn motif (Figure 9). This rearrangement of shorter strand flips its terminal adenine of NC-stem toward the Hoogsteen-edge of the second nucleotide in the corresponding base pair, and thus the terminal base pair of NC-stem is paired in a *t*HH manner

in reverse K-turn (Figure 9). Such flip reverting strand direction was also observed in the S-turn motif of the sarcin−ricin loop, where two consequent flips form the S-shaped appearance of this motif.[101] Similarly to the sarcin−ricin loop, the flipped over adenine offers its 2′-hydroxyl group to the major groove of NC-stem forming a sugar−phosphate interaction with the *pro*-R_P nonbridging oxygen of its upstream nucleotide, in contrast to A-RNA where 2′-hydroxyl groups are exposed to the minor groove. The A/A is the most frequent *t*HH base pair in known RNAs,[100] since it is supported by the adenine-specific base−phosphate interaction. The *t*HH A/G base pair is basically absent in natural RNAs, as it does not offer a favorable combination of donors and acceptors. Thus, the difference in topology between reverse and conventional K-turns together with energetics of molecular interactions dictate the replacement of the *t*HS A/G K-turn combination with the *t*HH A/A reverse K-turn combination. While the *t*HS A/G base pair can covary with A/A, the covariation of the *t*HH A/A base pair with A/G is less likely. Despite this, the X-ray structure of the A201G mutant shows that the *t*HH A/G can be stable within the structural context of reverse K-turn within the group I intron.[29] Such covariation, however, is not expected in naturally occurring sequences.[100] Overall, the conservation of the *t*HH A/A base pair terminating the NC-stem with flipped over adenine is rather a consequence of evolutionarily conserved outlaying tertiary RNA−RNA interactions determining the direction of the reverse K-turn bend. More detailed explanation can be found in the Supporting Information.

■ ASSOCIATED CONTENT

Supporting Information. Definition of substates; mathematical definition of interhelical angle dihedral followed by a discussion of their limitations; extended discussion about the conservation of *t*HS A/G and *t*HH A/A base pairs in conventional and reverse K-turns, respectively. Figures S1−S15 and Tables S1−S5 giving the supplemental RMSD vs R_g plots; scheme of end-to-end distance, interhelical angle, and dihedral; plot of these parameters for reverse K-turns' substates; secondary and 3D structures of eubacterial revKt-54-analogs; secondary structure of *E.c.* revKt-54-analog; RNA−RNA tertiary interactions of eubacterial revKt-54-analogs; "ladder-like" conformations of both reverse K-turns; representative structures of both reverse K-turns' substates; density maps of Na^+ and K^+ around revKt-P9/9.0; NC-stem superposition of revKt-54 with the consensual K-turn Kt-7; signature interactions in K-turn Kt-7; list of RMSD and R_g intervals utilized for definition of substates; values of interhelical angles, interhelical dihedrals, and end-to-end distances for reverse K-turns' crystal structures and their substates from MD simulations; list of additional simulations; contribution of the first five essential dynamics modes in intermediate substates; absolute and relative free energies of revKt-P9/9.0 and revKt-54 substates calculated by the MM-PBSA method. This material is available free of charge via the Internet at http://pubs.acs.org.

■ AUTHOR INFORMATION

Corresponding Authors

*Tel: +420 585 634 756 (M.O.), +420 541 517 133 (J.S.). Fax: +420 585 634 761 (M.O.). E-mail: michal.otyepka@upol.cz, sponer@ncbr.chemi.muni.cz.

■ ACKNOWLEDGMENT

This work was supported by the Grant Agency of the Academy of Sciences of the Czech Republic (grants KJB400040901 and IAA400040802), by the Grant Agency of the Czech Republic (grants 203/09/H046, 203/09/1476, P208/11/1822, and P301/11/P558), by Ministry of Youth, Sport and Education of Czech Republic (grants CZ.1.05/2.1.00/03.0058, CZ.1.07/2.3.00/20.0017, LC06030, LC512, and MSM6198959216), by Student Project PrF_2011_020 of Palacky University, and by the Academy of Sciences of the Czech Republic (grants no. AV0Z50040507, AV0Z50040702, and Z40550506). F.L. gratefully acknowledges the support of the J.E. Purkyne Fellowship from the Academy of Sciences of the Czech Republic.

■ REFERENCES

(1) Klein, D. J.; Schmeing, T. M.; Moore, P. B.; Steitz, T. A. The kink-turn: a new RNA secondary structure motif. *EMBO J.* **2001**, *20*, 4214–4221.

(2) Schuwirth, B. S.; Borovinskaya, M. A.; Hau, C. W.; Zhang, W.; Vila-Sanjurjo, A.; Holton, J. M.; Cate, J. H. Structures of the bacterial ribosome at 3.5 A resolution. *Science* **2005**, *310*, 827–834.

(3) Wimberly, B. T.; Brodersen, D. E.; Clemons, W. M., Jr.; Morgan-Warren, R. J.; Carter, A. P.; Vonrhein, C.; Hartsch, T.; Ramakrishnan, V. Structure of the 30S ribosomal subunit. *Nature* **2000**, *407*, 327–339.

(4) Mao, H.; White, S. A.; Williamson, J. R. A novel loop-loop recognition motif in the yeast ribosomal protein L30 autoregulatory RNA complex. *Nat. Struct. Biol.* **1999**, *6*, 1139–1147.

(5) White, S. A.; Hoeger, M.; Schweppe, J. J.; Shillingford, A.; Shipilov, V.; Zarutskie, J. Internal loop mutations in the ribosomal protein L30 binding site of the yeast L30 RNA transcript. *RNA* **2004**, *10*, 369–377.

(6) Montange, R. K.; Batey, R. T. Structure of the S-adenosylmethionine riboswitch regulatory mRNA element. *Nature* **2006**, *441*, 1172–1175.

(7) Blouin, S.; Lafontaine, D. A. A loop loop interaction and a K-turn motif located in the lysine aptamer domain are important for the riboswitch gene regulation control. *RNA* **2007**, *13*, 1256–1267.

(8) Watkins, N. J.; Segault, V.; Charpentier, B.; Nottrott, S.; Fabrizio, P.; Bachi, A.; Wilm, M.; Rosbash, M.; Branlant, C.; Luhrmann, R. A common core RNP structure shared between the small nucleoar box C/D RNPs and the spliceosomal U4 snRNP. *Cell* **2000**, *103*, 457–466.

(9) Vidovic, I.; Nottrott, S.; Hartmuth, K.; Luhrmann, R.; Ficner, R. Crystal structure of the spliceosomal 15.5kD protein bound to a U4 snRNA fragment. *Mol. Cell* **2000**, *6*, 1331–1342.

(10) Wozniak, A. K.; Nottrott, S.; Kuhn-Holsken, E.; Schroder, G. F.; Grubmuller, H.; Luhrmann, R.; Seidel, C. A.; Oesterhelt, F. Detecting protein-induced folding of the U4 snRNA kink-turn by single-molecule multiparameter FRET measurements. *RNA* **2005**, *11*, 1545–1554.

(11) Yusupov, M. M.; Yusupova, G. Z.; Baucom, A.; Lieberman, K.; Earnest, T. N.; Cate, J. H. D.; Noller, H. F. Crystal structure of the ribosome at 5.5 angstrom resolution. *Science* **2001**, *292*, 883–896.

(12) Turner, B.; Melcher, S. E.; Wilson, T. J.; Norman, D. G.; Lilley, D. M. Induced fit of RNA on binding the L7Ae protein to the kink-turn motif. *RNA* **2005**, *11*, 1192–1200.

(13) Goody, T. A.; Melcher, S. E.; Norman, D. G.; Lilley, D. M. The kink-turn motif in RNA is dimorphic, and metal ion-dependent. *RNA* **2004**, *10*, 254–264.

(14) Schroeder, K. T.; McPhee, S. A.; Ouellet, J.; Lilley, D. M. A structural database for k-turn motifs in RNA. *RNA* **2010**, *16*, 1463–1468.

(15) Schroeder, K. T.; Lilley, D. M. Ion-induced folding of a kink turn that departs from the conventional sequence. *Nucleic Acids Res.* **2009**, *37*, 7281–7289.

(16) Spackova, N.; Reblova, K.; Sponer, J. Structural dynamics of the box C/D RNA kink-turn and its complex with proteins: the role of the A-minor 0 interaction, long-residency water bridges, and structural

ion-binding sites revealed by molecular simulations. *J. Phys. Chem. B* **2010**, *114*, 10581–10593.

(17) Reblova, K.; Razga, F.; Li, W.; Gao, H.; Frank, J.; Sponer, J. Dynamics of the base of ribosomal A-site finger revealed by molecular dynamics simulations and Cryo-EM. *Nucleic Acids Res.* **2010**, *38*, 1325–1340.

(18) Razga, F.; Koca, J.; Mokdad, A.; Sponer, J. Elastic properties of ribosomal RNA building blocks: molecular dynamics of the GTPase-associated center rRNA. *Nucleic Acids Res.* **2007**, *35*, 4007–4017.

(19) Razga, F.; Zacharias, M.; Reblova, K.; Koca, J.; Sponer, J. RNA kink-turns as molecular elbows: hydration, cation binding, and large-scale dynamics. *Structure* **2006**, *14*, 825–835.

(20) Razga, F.; Koca, J.; Sponer, J.; Leontis, N. B. Hinge-like motions in RNA kink-turns: the role of the second a-minor motif and nominally unpaired bases. *Biophys. J.* **2005**, *88*, 3466–3485.

(21) Razga, F.; Spackova, N.; Reblova, K.; Koca, J.; Leontis, N. B.; Sponer, J. Ribosomal RNA kink-turn motif--a flexible molecular hinge. *J. Biomol. Struct. Dyn.* **2004**, *22*, 183–194.

(22) Curuksu, J.; Sponer, J.; Zacharias, M. Elbow flexibility of the kt38 RNA kink-turn motif investigated by free-energy molecular dynamics simulations. *Biophys. J.* **2009**, *97*, 2004–2013.

(23) Leontis, N. B.; Stombaugh, J.; Westhof, E. The non-Watson-Crick base pairs and their associated isostericity matrices. *Nucleic Acids Res.* **2002**, *30*, 3497–3531.

(24) Sarver, M.; Zirbel, C. L.; Stombaugh, J.; Mokdad, A.; Leontis, N. B. FR3D: finding local and composite recurrent structural motifs in RNA 3D structures. *J. Math. Biol.* **2008**, *56*, 215–252.

(25) Liu, J.; Lilley, D. M. The role of specific 2′-hydroxyl groups in the stabilization of the folded conformation of kink-turn RNA. *RNA* **2007**, *13*, 200–210.

(26) Szewczak, L. B.; Gabrielsen, J. S.; Degregorio, S. J.; Strobel, S. A.; Steitz, J. A. Molecular basis for RNA kink-turn recognition by the h15.5K small RNP protein. *RNA* **2005**, *11*, 1407–1419.

(27) Nissen, P.; Ippolito, J. A.; Ban, N.; Moore, P. B.; Steitz, T. A. RNA tertiary interactions in the large ribosomal subunit: the A-minor motif. *Proc. Natl. Acad. Sci. U. S. A.* **2001**, *98*, 4899–4903.

(28) Adams, P. L.; Stahley, M. R.; Kosek, A. B.; Wang, J.; Strobel, S. A. Crystal structure of a self-splicing group I intron with both exons. *Nature* **2004**, *430*, 45–50.

(29) Antonioli, A. H.; Cochrane, J. C.; Lipchock, S. V.; Strobel, S. A. Plasticity of the RNA kink turn structural motif. *RNA* **2010**, *16*, 762–768.

(30) Leontis, N. B.; Lescoute, A.; Westhof, E. The building blocks and motifs of RNA architecture. *Curr. Opin. Struct. Biol.* **2006**, *16*, 279–287.

(31) Strobel, S. A.; Adams, P. L.; Stahley, M. R.; Wang, J. RNA kink turns to the left and to the right. *RNA* **2004**, *10*, 1852–1854.

(32) Klein, D. J.; Moore, P. B.; Steitz, T. A. The roles of ribosomal proteins in the structure assembly, and evolution of the large ribosomal subunit. *J. Mol. Biol.* **2004**, *340*, 141–177.

(33) Blaha, G.; Gurel, G.; Schroeder, S. J.; Moore, P. B.; Steitz, T. A. Mutations outside the anisomycin-binding site can make ribosomes drug-resistant. *J. Mol. Biol.* **2008**, *379*, 505–519.

(34) Zhong, C.; Tang, H.; Zhang, S. RNAMotifScan: automatic identification of RNA structural motifs using secondary structural alignment. *Nucleic Acids Res.* **2010**, *38*, e176.

(35) Xin, Y.; Hamelberg, D. Deciphering the role of glucosamine-6-phosphate in the riboswitch action of glmS ribozyme. *RNA* **2010**, *16*, 2455–2463.

(36) Fulle, S.; Christ, N. A.; Kestner, E.; Gohlke, H. HIV-1 TAR RNA spontaneously undergoes relevant apo-to-holo conformational transitions in molecular dynamics and constrained geometrical simulations. *J. Chem. Inf. Model.* **2010**, *50*, 1489–1501.

(37) Fulle, S.; Gohlke, H. Molecular recognition of RNA: challenges for modelling interactions and plasticity. *J. Mol. Recognit.* **2010**, *23*, 220–231.

(38) Freedman, H.; Huynh, L. P.; Le, L.; Cheatham, T. E., 3rd; Tuszynski, J. A.; Truong, T. N. Explicitly solvated ligand contribution to continuum solvation models for binding free energies: selectivity of theophylline binding to an RNA aptamer. *J. Phys. Chem. B* **2010**, *114*, 2227–2237.

(39) Huang, W.; Kim, J.; Jha, S.; Aboul-ela, F. A mechanism for S-adenosyl methionine assisted formation of a riboswitch conformation: a small molecule with a strong arm. *Nucleic Acids Res.* **2009**, *37*, 6528–6539.

(40) Orozco, M.; Noy, A.; Perez, A. Recent advances in the study of nucleic acid flexibility by molecular dynamics. *Curr. Opin. Struct. Biol.* **2008**, *18*, 185–193.

(41) McCrate, N. E.; Varner, M. E.; Kim, K. I.; Nagan, M. C. Molecular dynamics simulations of human tRNA Lys,3 UUU: the role of modified bases in mRNA recognition. *Nucleic Acids Res.* **2006**, *34*, 5361–5368.

(42) Cheatham, T. E., 3rd. Simulation and modeling of nucleic acid structure, dynamics and interactions. *Curr. Opin. Struct. Biol.* **2004**, *14*, 360–367.

(43) Hall, K. B. RNA in motion. *Curr. Opin. Chem. Biol.* **2008**, *12*, 612–618.

(44) Ditzler, M. A.; Otyepka, M.; Sponer, J.; Walter, N. G. Molecular dynamics and quantum mechanics of RNA: conformational and chemical change we can believe. *Acc. Chem. Res.* **2010**, *43*, 40–47.

(45) Reblova, K.; Spackova, N.; Stefl, R.; Csaszar, K.; Koca, J.; Leontis, N. B.; Sponer, J. Non-Watson-Crick basepairing and hydration in RNA motifs: molecular dynamics of 5S rRNA loop E. *Biophys. J.* **2003**, *84*, 3564–3582.

(46) Spackova, N.; Sponer, J. Molecular dynamics simulations of sarcin-ricin rRNA motif. *Nucleic Acids Res.* **2006**, *34*, 697–708.

(47) Romanowska, J.; Setny, P.; Trylska, J. Molecular dynamics study of the ribosomal A-site. *J. Phys. Chem. B* **2008**, *112*, 15227–15243.

(48) Veeraraghavan, N.; Ganguly, A.; Chen, J. H.; Bevilacqua, P. C.; Hammes-Schiffer, S.; Golden, B. L. Metal Binding Motif in the Active Site of the HDV Ribozyme Binds Divalent and Monovalent Ions. *Biochemistry* **2011**, *50*, 2672–2682.

(49) Krasovska, M. V.; Sefcikova, J.; Reblova, K.; Schneider, B.; Walter, N. G.; Sponer, J. Cations and hydration in catalytic RNA: molecular dynamics of the hepatitis delta virus ribozyme. *Biophys. J.* **2006**, *91*, 626–638.

(50) Mlynsky, V.; Banas, P.; Hollas, D.; Reblova, K.; Walter, N. G.; Sponer, J.; Otyepka, M. Extensive molecular dynamics simulations showing that canonical G8 and protonated A38H+ forms are most consistent with crystal structures of hairpin ribozyme. *J. Phys. Chem. B* **2010**, *114*, 6642–6652.

(51) Banas, P.; Walter, N. G.; Sponer, J.; Otyepka, M. Protonation states of the key active site residues and structural dynamics of the glmS riboswitch as revealed by molecular dynamics. *J. Phys. Chem. B* **2010**, *114*, 8701–8712.

(52) Villa, A.; Wohnert, J.; Stock, G. Molecular dynamics simulation study of the binding of purine bases to the aptamer domain of the guanine sensing riboswitch. *Nucleic Acids Res.* **2009**, *37*, 4774–4786.

(53) Reblova, K.; Fadrna, E.; Sarzynska, J.; Kulinski, T.; Kulhanek, P.; Ennifar, E.; Koca, J.; Sponer, J. Conformations of flanking bases in HIV-1 RNA DIS kissing complexes studied by molecular dynamics. *Biophys. J.* **2007**, *93*, 3932–3949.

(54) Bahadur, R. P.; Kannan, S.; Zacharias, M. Binding of the bacteriophage P22 N-peptide to the boxB RNA motif studied by molecular dynamics simulations. *Biophys. J.* **2009**, *97*, 3139–3149.

(55) Reblova, K.; Lankas, F.; Razga, F.; Krasovska, M. V.; Koca, J.; Sponer, J. Structure, dynamics, and elasticity of free 16s rRNA helix 44 studied by molecular dynamics simulations. *Biopolymers* **2006**, *82*, 504–520.

(56) Besseova, I.; Reblova, K.; Leontis, N. B.; Sponer, J. Molecular dynamics simulations suggest that RNA three-way junctions can act as flexible RNA structural elements in the ribosome. *Nucleic Acids Res.* **2010**, *38*, 6247–6264.

(57) Shankar, N.; Kennedy, S. D.; Chen, G.; Krugh, T. R.; Turner, D. H. The NMR structure of an internal loop from 23S ribosomal RNA differs from its structure in crystals of 50s ribosomal subunits. *Biochemistry* **2006**, *45*, 11776–11789.

(58) Reblova, K.; Strelcova, Z.; Kulhanek, P.; Besscova, I.; Mathews, D. H.; Van Nostrand, K.; Yildirim, I.; Turner, D. H.; Sponer, J. An RNA Molecular Switch: Intrinsic Flexibility of 23S rRNA Helices 40 and 68 5′-UAA/5′-GAN Internal Loops Studied by Molecular Dynamics Methods. *J. Chem. Theory Comput.* **2010**, *6*, 910–929.

(59) Besseova, I.; Otyepka, M.; Reblova, K.; Sponer, J. Dependence of A-RNA simulations on the choice of the force field and salt strength. *Phys. Chem. Chem. Phys.* **2009**, *11*, 10701–10711.

(60) Pearlman, D. A.; Case, D. A.; Caldwell, J. W.; Ross, W. S.; Cheatham, T. E.; Debolt, S.; Ferguson, D.; Seibel, G.; Kollman, P. Amber, a Package of Computer-Programs for Applying Molecular Mechanics, Normal-Mode Analysis, Molecular-Dynamics and Free-Energy Calculations to Simulate the Structural and Energetic Properties of Molecules. *Comput. Phys. Commun.* **1995**, *91*, 1–41.

(61) Cornell, W. D.; Cieplak, P.; Bayly, C. I.; Gould, I. R.; Merz, K. M.; Ferguson, D. M.; Spellmeyer, D. C.; Fox, T.; Caldwell, J. W.; Kollman, P. A. A 2nd. Generation Force-Field for the Simulation of Proteins Nucleic-Acids, and Organic-Molecules. *J. Am. Chem. Soc.* **1995**, *117*, 5179–5197.

(62) Wang, J. M.; Cieplak, P.; Kollman, P. A. How well does a restrained electrostatic potential (RESP) model perform in calculating conformational energies of organic and biological molecules? *J. Comput. Chem.* **2000**, *21*, 1049–1074.

(63) Perez, A.; Marchan, I.; Svozil, D.; Sponer, J.; Cheatham, T. E., 3rd; Laughton, C. A.; Orozco, M. Refinement of the AMBER force field for nucleic acids: improving the description of alpha/gamma conformers. *Biophys. J.* **2007**, *92*, 3817–3829.

(64) Banas, P.; Hollas, D.; Zgarbova, M.; Jurecka, P.; Orozco, M.; Cheatham, T. E.; Sponer, J.; Otyepka, M. Performance of Molecular Mechanics Force Fields for RNA Simulations: Stability of UUCG and GNRA Hairpins. *J. Chem. Theory Comput.* **2010**, *6*, 3836–3849.

(65) Aqvist, J. Ion Water Interaction Potentials Derived from Free-Energy Perturbation Simulations. *J. Phys. Chem.* **1990**, *94*, 8021–8024.

(66) Jorgensen, W. L.; Chandrasekhar, J.; Madura, J. D.; Impey, R. W.; Klein, M. L. Comparison of Simple Potential Functions for Simulating Liquid Water. *J. Chem. Phys.* **1983**, *79*, 926–935.

(67) Dang, L. X.; Kollman, P. A. Free-Energy of Association of the K +18-Crown-6 Complex in Water - a New Molecular-Dynamics Study. *J. Phys. Chem.* **1995**, *99*, 55–58.

(68) Smith, D. E.; Dang, L. X. Computer-Simulations of Nacl Association in Polarizable Water. *J. Chem. Phys.* **1994**, *100*, 3757–3766.

(69) Berendsen, H. J. C.; Grigera, J. R.; Straatsma, T. P. The Missing Term in Effective Pair Potentials. *J. Phys. Chem.* **1987**, *91*, 6269–6271.

(70) Joung, I. S.; Cheatham, T. E., 3rd. Determination of alkali and halide monovalent ion parameters for use in explicitly solvated biomolecular simulations. *J. Phys. Chem. B* **2008**, *112*, 9020–9041.

(71) Noy, A.; Soteras, I.; Luque, F. J.; Orozco, M. The impact of monovalent ion force field model in nucleic acids simulations. *Phys. Chem. Chem. Phys.* **2009**, *11*, 10596–10607.

(72) Darden, T.; York, D.; Pedersen, L. Particle Mesh Ewald - an N. Log(N) Method for Ewald Sums in Large Systems. *J. Chem. Phys.* **1993**, *98*, 10089–10092.

(73) Essmann, U.; Perera, L.; Berkowitz, M. L.; Darden, T.; Lee, H.; Pedersen, L. G. A Smooth Particle Mesh Ewald Method. *J. Chem. Phys.* **1995**, *103*, 8577–8593.

(74) DeLano, W. L. *The PyMOL Molecular Graphics System*; DeLano Scientific LLC: Palo Alto, CA, 2008.

(75) Humphrey, W.; Dalke, A.; Schulten, K. VMD: Visual molecular dynamics. *J. Mol. Graphics* **1996**, *14*, 33–38.

(76) Lankas, F.; Spackova, N.; Moakher, M.; Enkhbayar, P.; Sponer, J. A measure of bending in nucleic acids structures applied to A-tract DNA. *Nucleic Acids Res.* **2010**, *38*, 3414–3422.

(77) Case, D. A.; Darden, T. A.; Cheatham, T. E., 3rd; Simmerling, C. L.; Wang, J.; Duke, R. E.; Luo, R.; Walker, R. C.; Zhang, W.; Merz, K. M.; Roberts, B.; Wang, B.; Hayik, S.; Roitberg, A.; Seabra, G.; Kolossváry, I.; Wong, K. F.; Paesani, F.; Vanicek, J.; Liu, J.; Wu, X.; Brozell, S. R.; Steinbrecher, T.; Gohlke, H.; Cai, Q.; Ye, X.; Wang, J.; Hsieh, M.-J.; Cui, G.; Roe, D. R.; Mathews, D. H.; Seetin, M. G.; Sagui, C.; Babin, V.; Luchko, T.; Gusarov, S.; Kovalenko, A.; Kollman, P. A. *AMBER 11*; University of California: San Francisco, CA, 2010.

(78) Luo, R.; David, L.; Gilson, M. K. Accelerated Poisson-Boltzmann calculations for static and dynamic systems. *J. Comput. Chem.* **2002**, *23*, 1244–1253.

(79) Tsui, V.; Case, D. A. Theory and applications of the generalized Born solvation model in macromolecular simulations. *Biopolymers* **2000**, *56*, 275–291.

(80) Hess, B.; Kutzner, C.; van der Spoel, D.; Lindahl, E. GROMACS 4: Algorithms for highly efficient, load-balanced, and scalable molecular simulation. *J. Chem. Theory Comput.* **2008**, *4*, 435–447.

(81) Zirbel, C. L.; Sponer, J. E.; Sponer, J.; Stombaugh, J.; Leontis, N. B. Classification and energetics of the base-phosphate interactions in RNA. *Nucleic Acids Res.* **2009**, *37*, 4898–4918.

(82) Ennifar, E.; Walter, P.; Dumas, P. A crystallographic study of the binding of 13 metal ions to two related RNA duplexes. *Nucleic Acids Res.* **2003**, *31*, 2671–2682.

(83) Reblova, K.; Spackova, N.; Sponer, J. E.; Koca, J.; Sponer, J. Molecular dynamics simulations of RNA kissing-loop motifs reveal structural dynamics and formation of cation-binding pockets. *Nucleic Acids Res.* **2003**, *31*, 6942–6952.

(84) Florova, P.; Sklenovsky, P.; Banas, P.; Otyepka, M. Explicit Water Models Affect the Specific Solvation and Dynamics of Unfolded Peptides While the Conformational Behavior and Flexibility of Folded Peptides Remain Intact. *J. Chem. Theory Comput.* **2010**, *6*, 3569–3579.

(85) Banas, P.; Jurecka, P.; Walter, N. G.; Sponer, J.; Otyepka, M. Theoretical studies of RNA catalysis: hybrid QM/MM methods and their comparison with MD and QM. *Methods* **2009**, *49*, 202–216.

(86) Sponer, J.; Sabat, M.; Gorb, L.; Leszczynski, J.; Lippert, B.; Hobza, P. The effect of metal binding to the N7 site of purine nucleotides on their structure, energy, and involvement in base pairing. *J. Phys. Chem. B* **2000**, *104*, 7535–7544.

(87) Katz, A. K.; Glusker, J. P.; Beebe, S. A.; Bock, C. W. Calcium ion coordination: A comparison with that of beryllium, magnesium, and zinc. *J. Am. Chem. Soc.* **1996**, *118*, 5752–5763.

(88) Dudev, T.; Lim, C. Metal binding affinity and selectivity in metalloproteins: Insights from computational studies. *Ann. Rev. Biophys.* **2008**, *37*, 97–116.

(89) Petrov, A. S.; Bowman, J. C.; Harvey, S. C.; Williams, L. D. Bidentate RNA-magnesium clamps: on the origin of the special role of magnesium in RNA folding. *RNA* **2011**, *17*, 291–297.

(90) Gresh, N.; Sponer, J. E.; Spackova, N.; Leszczynski, J.; Sponer, J. Theoretical study of binding of hydrated Zn(II) and Mg(II) cations to 5′-guanosine monophosphate. Toward polarizable molecular mechanics for DNA and RNA. *J. Phys. Chem. B* **2003**, *107*, 8669–8681.

(91) Dudev, T.; Lim, C. Principles governing Mg, Ca, and Zn binding and selectivity in proteins. *Chem. Rev.* **2003**, *103*, 773–788.

(92) Fadrna, E.; Spackova, N.; Stefl, R.; Koca, J.; Cheatham, T. E., 3rd; Sponer, J. Molecular dynamics simulations of Guanine quadruplex loops: advances and force field limitations. *Biophys. J.* **2004**, *87*, 227–242.

(93) Fadrna, E.; Spackova, N.; Sarzynska, J.; Koca, J.; Orozco, M.; Cheatham, T. E.; Kulinski, T.; Sponer, J. Single Stranded Loops of Quadruplex DNA As Key Benchmark for Testing Nucleic Acids Force Fields. *J. Chem. Theory Comput.* **2009**, *5*, 2514–2530.

(94) Cerutti, D. S.; Freddolino, P. L.; Duke, R. E., Jr.; Case, D. A. Simulations of a protein crystal with a high resolution X-ray structure: evaluation of force fields and water models. *J. Phys. Chem. B* **2010**, *114*, 12811–12824.

(95) Falb, M.; Amata, I.; Gabel, F.; Simon, B.; Carlomagno, T. Structure of the K-turn U4 RNA: a combined NMR and SANS study. *Nucleic Acids Res.* **2010**, *38*, 6274–6285.

(96) Klein, D. J.; Ferre-D'Amare, A. R. Structural basis of glmS ribozyme activation by glucosamine-6-phosphate. *Science* **2006**, *313*, 1752–1756.

(97) Cochrane, J. C.; Lipchock, S. V.; Strobel, S. A. Structural investigation of the GlmS ribozyme bound to Its catalytic cofactor. *Chem. Biol.* **2007**, *14*, 97–105.

(98) Jaeger, L.; Verzemnieks, E. J.; Geary, C. The UA_handle: a versatile submotif in stable RNA architectures. *Nucleic Acids Res.* **2009**, *37*, 215–230.

(99) Mladek, A.; Sharma, P.; Mitra, A.; Bhattacharyya, D.; Sponer, J.; Sponer, J. E. Trans Hoogsteen/sugar edge base pairing in RNA. Structures, energies, and stabilities from quantum chemical calculations. *J. Phys. Chem. B* **2009**, *113*, 1743–1755.

(100) Stombaugh, J.; Zirbel, C. L.; Westhof, E.; Leontis, N. B. Frequency and isostericity of RNA base pairs. *Nucleic Acids Res.* **2009**, *37*, 2294–2312.

(101) Correll, C. C.; Munishkin, A.; Chan, Y. L.; Ren, Z.; Wool, I. G.; Steitz, T. A. Crystal structure of the ribosomal RNA domain essential for binding elongation factors. *Proc. Natl. Acad. Sci. U. S. A.* **1998**, *95*, 13436–13441.

(102) Leontis, N. B.; Westhof, E. Geometric nomenclature and classification of RNA base pairs. *RNA* **2001**, *7*, 499–512.

(103) Zgarbova, M.; Otyepka, M.; Sponer, J.; Mladek, A.; Banas, P.; Cheatham, T. E.; Jurecka, P. Refinement of the Cornell et al. Nucleic Acids Force Field based on Reference Quantum Chemical Calculations of Glycosidic Torsion Profiles. *J. Chem. Theory Comput.* **2011**, in press (DOI: 10.1021/ct200162x).

JCTC Journal of Chemical Theory and Computation

ARTICLE

pubs.acs.org/JCTC

Water Defect and Pore Formation in Atomistic and Coarse-Grained Lipid Membranes: Pushing the Limits of Coarse Graining

W.F. Drew Bennett[†] and D. Peter Tieleman*[,†]

[†]Department of Biological Sciences and Institute for Biocomplexity and Informatics, University of Calgary, 2500 University Drive N.W., Calgary, Alberta T2N 1N4, Canada

Supporting Information

ABSTRACT: Defects in lipid bilayers are important in a range of biological processes, including interactions between antimicrobial peptides and membranes, transport of polar molecules (including drugs) across membranes, and lipid flip−flop from one monolayer to the other. Passive lipid flip−flop and the translocation of polar molecules across lipid membranes occur on a slow time scale because of high-energy intermediates involving water defects and pores in the membrane. Such defects are an interesting test case for coarse-grained models because of their relatively small characteristic size at the level of water molecules and the complex environment of water and polar head groups in a low-dielectric membrane interior. Here we compare coarse-grained simulations with the MARTINI model with the standard MARTINI water and two recently developed coarse-grained polarizable water models to atomistic simulations. Although in several cases the MARTINI model reproduces the correct free energies, there are structural differences between the atomistic and coarse-grained models. The polarizable water model improves the free energies but only moderately improves the structures. Atomistic test simulations in which water molecules are artificially tethered to each other in groups of four, the resolution of MARTINI, suggest that the limiting factor is not the size of the coarse-grained particles but rather the simple interaction potential and/or the entropy lost in coarse graining the system. By increasing the attractive interaction between the lipids' headgroup and water, we did observe pore formation but at the expense of the correct equilibrium properties of the bilayers.

INTRODUCTION

Biological membranes form the boundaries of cells and organelles. They regulate what can enter and leave a cell, communicate signals across the membrane, provide structural support, localize distinct chemical environments, and allow electrochemical gradients, which are necessary for energy transduction and nerve propagation. The core structure of membranes, the lipid bilayer, consists of a thin (3 nm) hydrophobic slab that forms a semipermeable membrane, preventing ions, polar and charged molecules, from crossing. Several biologically important processes involve the interactions of polar or charged molecules and lipid bilayers. A few examples are electroporation, where an applied electric field induces hydrophilic pores in membranes; antimicrobial peptides, which have been shown to cause pore formation;[1] lipid translocation; and drug delivery. The interaction between a membrane and polar molecules depends on its lipid composition, which varies significantly between cell types and organelles.[2]

Lipid translocation, or flip−flop, between monolayers is an important process in cells. It involves a high free energy barrier for polar and charged lipid head groups crossing the hydrophobic bilayer interior. Flip−flop is important for the growth of membranes as well as cellular signaling.[3] The rate of passive flip−flop for PC and other phospholipids is very slow, on the time scale of hours to days.[4−6] The mechanism of PC flip−flop has been shown to involve pore formation,[4,7,8] with water and other lipid head groups entering the hydrophobic bilayer interior to prevent the dehydration of the flipping lipids headgroup. Other polar and charged molecules have been shown to disrupt the lamellar structure of the bilayer causing water defects,[9,10] where water and head groups enter the bilayer interior from only one side of the bilayer.

We are investigating the mechanism, thermodynamics, and kinetics of the process of lipid flip−flop and pore formation using computer simulations.[9,10] The standard approach uses a force field that describes interactions at the level of individual atoms (AA for all-atom). Typical trajectories on systems with ca. 20 000 atoms can reach a time scale on the order of a microsecond. More recently, a number of coarse-grained (CG) models have been developed that retain some chemical specificity but operate at a lower level of resolution. We use the MARTINI model,[11] in which typically four nonhydrogen atoms are grouped together into a single interaction site. This allows simulations on a scale that is 2−3 orders of magnitude larger than AA simulations with a comparable computational cost, but achieving a balance between detail and computational efficiency is a substantial challenge. There is a strong motivation to have a CG model that can reproduce both the energetics and the mechanism of membrane pores and defects.

MARTINI maps four water molecules to a single water bead, without a dipole or partial charge. One limitation of such a model is its inability to reproduce small-scale defects, for instance during lipid flip−flop.[11] A recently developed MARTINI water model[12] (CG-pol) combines four water molecules into three beads that represent a dipole. CG-pol simulations show pores in

Received: April 27, 2011
Published: August 04, 2011

membranes during electroporation, in agreement with AA simulations.[12] This suggests CG-pol might be better suited to study lipid translocation. The recently developed BMW water model for MARTINI uses a modified Born−Mayer−Huggins potential, which is softer than the standard Lennard-Jones potential.[13] This model was shown to reproduce the lipid interface dipole potential, which suggests it could be a useful model for heterogeneous interfacial systems.

In previous studies we have calculated atomistic potentials of mean force (PMFs) for lipid flip−flop in a number of bilayers with primarily PC lipids, including varying chain length,[8] cholesterol concentration,[14] chain unsaturation[8] and the effect of a the presence of a simple transmembrane helix on lipid flip−flop.[15] Here we describe simulations of phospholipid flip−-flop using five different models (AA, AA-bundled, CG, CG-pol, and CG-BMW) in three different membranes: dilauroylphosphatidylcholine and dipalmitoylphosphatidylcholine (DLPC and DPPC, respectively), which in MARTINI differ by one bead in each acyl chain, and the charged lipid dioleoylphosphatidylglycerol (DOPG) in a dioleoylphosphatidylcholine (DOPC) bilayer. CG-pol improves the results most for DOPG, although the structure of the defects is different between atomistic and CG models in all cases. CG simulations of flip−flop in DLPC give a much higher barrier than in atomistic simulations. To understand the possible effect of the larger size of MARTINI particles, in particular the water particles that group four water molecules into one, we simulated AA dimyristoylphosphatidylcholine (DMPC) with normal water and with water tethered in groups of four,[16] with no discernible effect on either structure or free energies. Finally, we tested different parameters for the MARTINI model to see if pore formation was possible with a CG model. By increasing the interaction between water and lipid head groups in the CG-pol model, we did observe pore formation in the DLPC bilayer. These results provide insight for future progress in refining CG lipid models.

METHODS

AA Simulations. We used the GROMACS software package.[17] For lipid parameters we used the united-atom Berger force field.[18] We use a relatively small bilayer patches of 64 lipids for DLPC, DPPC, and DOPC bilayers. We include between ca. 4000 and 5000 simple point charge (SPC)[19] water molecules for good hydration of the lipid head groups. Small bilayers are necessary for free energy calculations, which require 40−50 replicates for 10−100 ns to determine a single PMF (see Umbrella Sampling Section). To test the effect of using small bilayers for simulating large-scale changes in the bilayer structure during flip−flop, we determined a PMF for DMPC with 256 lipids and compared it to the PMF with 64 lipids (Figure S1, Supporting Information). The PMFs for the large and small bilayer were quite similar, indicating our small bilayer patches are sufficiently large for this process. All simulations were run at 323 K for comparison with DPPC, which has a high melting temperature (314 K).[20] A time step of 2 fs was used for the equations of motion. SETTLE[21] was used to constrain water bonds and angles, while LINCS[22] was used for the lipid bonds. We used periodic boundary conditions with a semi-isotropic pressure coupling algorithm with a reference pressure of 1 bar and a 4.5×10^{-5} bar^{-1} compressibility.[23] Temperature is maintained with a weak-coupling scheme and a coupling constant of 0.1 ps.[23] We use the particle mesh Ewald (PME) method for long-range electrostatic interactions with a fourth-order spline and a 0.12 nm grid spacing.[24,25]

The bundled water topology was from,[16] where four SPC waters are tethered together using harmonic distance restraints into a roughly tetrahedral geometry. A force constant of 1000 kJ mol^{-1} nm^{-2} and a distance of 0.3 nm were used. The Lennard-Jones C_{12} parameter was also increased for the interaction between all the water oxygens.

CG Simulations. For CG simulations, we use the MARTINI model[11] and the recently developed polarizable MARTINI water model (CG-pol).[12] We used a 20 fs time step and updated the neighbor list every 10 steps. Lennard-Jones interactions were shifted from 0.9 to 1.2 nm. A Coloumbic function was used for electrostatic interactions with a dielectric constant of 15 for explicit screening. For the CG-pol model, we have used mostly the same run parameters as standard MARTINI, with the exception of the dielectric coefficient, which is 2.5 instead of 15.[12] We have used the same types of lipids as the AA simulations. Small bilayer patches were used with 72 DLPCs, 72 DPPCs, and 70 DOPCs with 2 DOPGs. In the CG-pol model electrostatic interactions play a more important role, so we also tested the simulations with PME instead of the standard shifted Coulomb cutoff.

We tested the recently developed BMW water model with DLPC and DPPC MARTINI bilayers.[13] Of note, the angle potential is modified for the lipid tails for use with the BMW water model, with the force constant reduced from 25 to 10 kJ mol^{-1} rad^{-2}. BMW simulations were run with PME for long-range electrostatics with a 0.2 nm grid spacing and sixth-order spline interpolation.[24,25]

In the CG-pol model, the Lennard-Jones interaction between water beads and the choline and phosphate was reduced compared to standard MARTINI, to compensate for the increased Coulombic interactions. To try and induce pore formation, we increased the Lennard-Jones interaction between water beads and the choline and phosphate beads. For CG-pol, we increased the interaction back to the level in standard MARTINI (with ε = 5.6 kJ/mol for both interactions, compared to 5 and 4.5 kJ/mol for phosphate−water and choline−water in CG-pol). We refer to this model as CG-pol-lj*. We also increased the Lennard-Jones interaction between water and the head groups in standard MARTINI (CG-lj*) to levels beyond the range of the MARTINI force field (with ε = 6.2 kJ/mol). We then determined PMFs for DLPC and DPPC flip−flop using the CG-pol-lj* model and for DLPC using the CG-lj* model.

Umbrella Sampling. With current computers, we are able to simulate up to 1 μs for the AA model and to the 100 μs and nearly millisecond time scale for the CG model. The time scale of phospholipid flip−flop is hours to days. To simulate these slow processes, we use umbrella sampling. We run a series of ca. 50 simulations in parallel with a harmonic restraint placed on the headgroup of the translocating lipid with respect to the distance from the center of the bilayer, spaced by 0.1 nm increments. The harmonic restraint is placed on the polar or charged headgroup to ensure that the molecule samples the center of the bilayer, which is likely to be energetically unfavorable. We determine the PMF using weighted histogram analysis.[26] In each system, we pull two separate lipids, staggered by at least 4 nm, to increase computational efficiency by getting two PMFs at a time. We have determined the PMF for a single DPPC lipid, and it was within the error of the PMF calculated by pulling two DPPC lipids (Figure S2, Supporting Information). We plot the mean from the

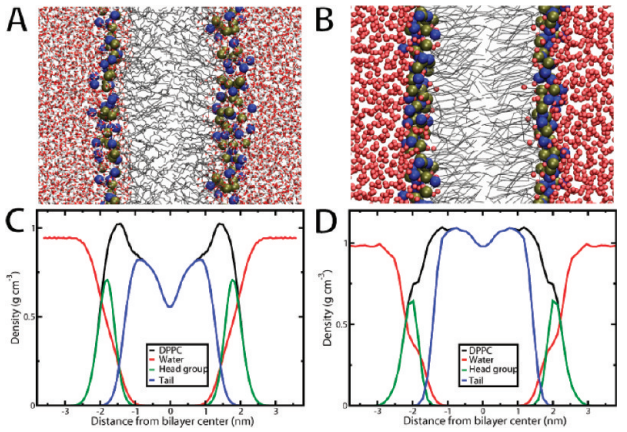

Figure 1. Snapshot and partial density profile for an AA (A and C) and CG (B and D) DPPC bilayer at equilibrium. Water is shown as small balls, head groups as thick balls, and lipid tails as thin lines. Head group includes the choline and phosphate groups, and tails include all the carbons after the carboxyl group.

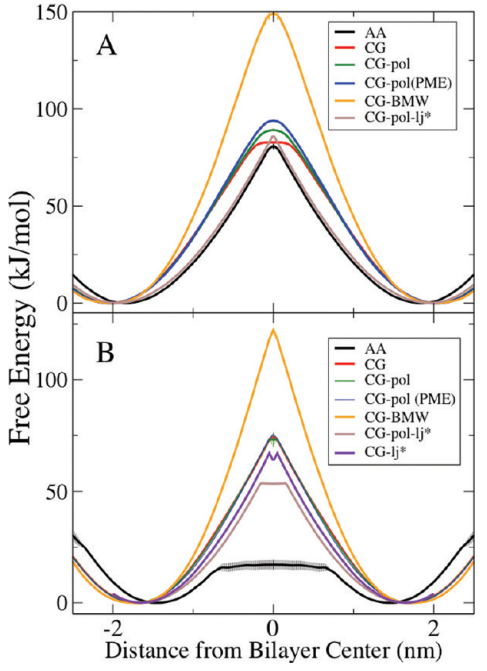

Figure 2. PMFs for phospholipid flip−flop. (A) DPPC flip−flop in a DPPC bilayer. (B) DLPC flip−flop in a DLPC bilayer. Error bars represent the standard error between two independent lipids PMFs. The PMF is mirrored at the center of the bilayer for clarity. The CG, CG-pol, and CG-pol (PME) PMFs are nearly the same, so only one curve is visible.

two independent PMFs and the standard error, after aligning the PMFs to zero at their free energy trough. In all the figures, we have shown the PMF and its mirror image that corresponds to the opposite leaflet. As the bilayers are all symmetric, the PMFs should be the same in both monolayers.

RESULTS

Phospholipid Flip−flop. Figure 1A and B shows snapshots of AA and CG DPPC lipid bilayers. Figure 1C and D shows the partial density profiles for the two bilayers. Water penetrates into the headgroup region and a small amount into the carbon tail density. This is followed by an increase in the tail density until a maximum, after which the density decreases near the center of the bilayer. The CG model reproduces the general features of the density profile, although the CG model does not have as large of a decrease near the bilayer center compared to the AA model.

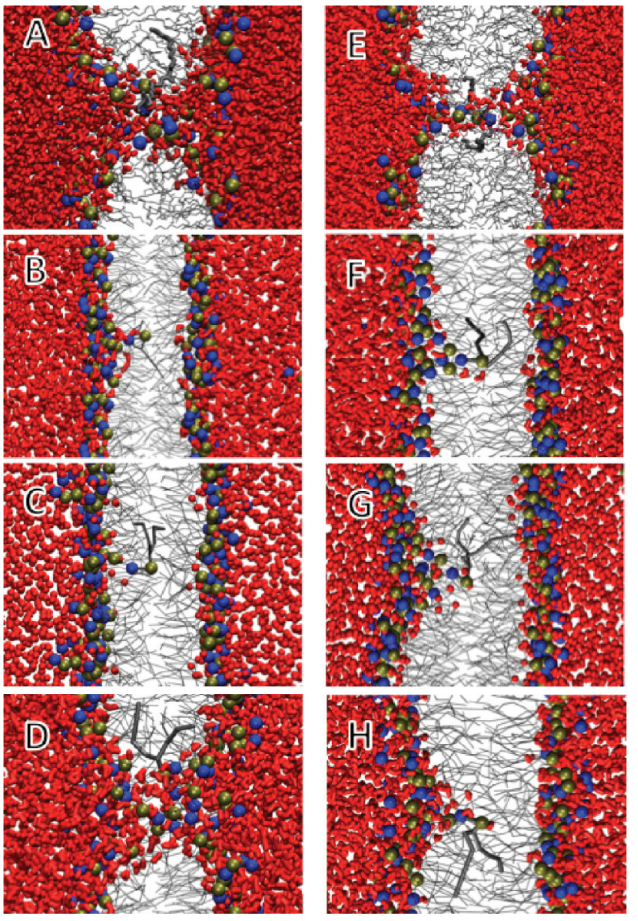

Figure 3. Snapshots for a phospholipid restrained at the center of bilayers. Water is shown as red licorice, lipid tails as gray lines, restrained lipid as thick gray lines, and headgroup phosphate (phosphorus) and choline (nitrogen) as balls. (A) and (E) are atomistic, (B) and (F) are CG-pol, (C) and (G) are CG, and (D) and (H) are CG-pol-lj* simulations. (A−D) DLPC in a DLPC bilayer and (E−H) DPPC in a DPPC bilayer.

DPPC. Figure 2A shows the PMF for AA DPPC flip−flop.[4] We used umbrella sampling (see Methods Section) to determine the free energy profile for transferring a single DPPC from equilibrium to the center of the bilayer, with umbrellas centered on the phosphate group. There is a large free energy trough corresponding to the equilibrium position of the phosphate in the bilayer (Figure 2). Moving the lipid into the bilayer has a large free energy cost.

As we move the phosphate of DPPC into the hydrophobic bilayer core, a water defect forms. Water and other PC lipid head groups move into the bilayer to prevent the DPPC from becoming desolvated. Restraining the zwitterionic headgroup of DPPC inside the bilayer significantly perturbs the lamellar structure. Similar structures and free energy slopes have been observed for other charged and polar molecules entering the interior of lipid bilayers.[7,27,28] When the phosphate is restrained

at the center of the bilayer, a pore spanning the bilayer is observed (Figure 3E). We assume this is the transition state for lipid flip−flop. Estimates for the lifetime of pores are on the order of 10−100 ns.[29] From the free energy barrier for pore formation (80 kJ/mol) and the flux of lipids across a preformed pore, a rate for DPPC flip−flop was estimated to be 4−30 h, in good agreement with experimental estimates of 1−90 h.[5,6]

The PMF for CG DPPC flip−flop shows a similar shape as the AA model (Figure 2A) and has a similar barrier for flip−flop. As the DPPC is moved into the bilayer, a small water defect does form, corresponding to a steep free energy slope. No water pore is observed when the phosphate bead is restrained at the bilayer center, although a small, unstable water defect does occasionally form (Figure 3G).

We have also determined a PMF for DPPC flip−flop using the CG-pol model (Figure 2A). Compared to the nonpolarizable model, the shape of the PMF and the free energy barrier are quite similar. Figure 3F shows that a small water defect is formed when the phosphate is at the bilayer center, although a pore is still not observed. The defects formed for CG-pol occur more often and appear slightly more stable than for CG. We determined the number of contacts (distance of less than 1 nm) formed between water beads and the phosphate bead restrained at the center of the bilayer. For CG, 98% of the time there were no contacts, 1.2% with one contact, and a maximum of 4 contacts. There were no contacts for the CG-pol model 92% of the time, 6% with one contact, 2% with two contacts, and a maximum of 7 contacts. The use of PME makes almost no difference.

To try and induce pore formation, we increased the Lennard-Jones interaction between the water bead and the choline and phosphate beads (CG-pol-lj*). Coincidentally, the PMF for CG-pol-lj* is nearly the same as the AA model, although the bilayers bulk properties were perturbed significantly. The area per lipid for the DPPC CG-pol model was 0.64 and 0.71 nm^2 for the CG-pol-lj* model. For CG-pol-lj*, the water defect was more stable, although we did not observe pore formation. When the phosphate of DPPC was restrained at the bilayer center, there were 2−5 contacts between the phosphate and the water for 80% of the simulation.

The BMW water model has a steeper slope in the PMF and a significantly higher barrier for flip−flop (150 kJ/mol), although the position of the free energy minima is the same as the other two CG models. At the center of the bilayer there was 1 contact with water and the phosphate for 49% of the time, 2 contacts for 48%, and a maximum of 5 contacts. No pores are observed for the BMW DPPC simulations.

DLPC. From the AA model, shorter lipids, such as DLPC, had lower free energy barriers for pore formation compared to DPPC. Figure 2B shows the PMF for DLPC. Similar to DPPC, there is a free energy trough at DLPC's equilibrium position and a steep slope as the PC headgroup moves into the bilayer center, corresponding to water defect formation. When the lipid was ca. 0.6 nm from the bilayer center, the water defect became a pore, causing the PMF to plateau. Once a pore forms, the lipid is able to diffuse across it at no free energy cost. This indicates that pore formation is the primary free energy barrier for flip−flop. Figure 3A shows the water pore formed at the center of the DLPC bilayer, which has many lipid head groups and water molecules in the bilayer interior. From the AA model, we calculate a free energy barrier for DLPC flip−flop of 16 kJ/mol. This low free energy barrier translates into a rate of flip−flop on the μs time scale.[8]

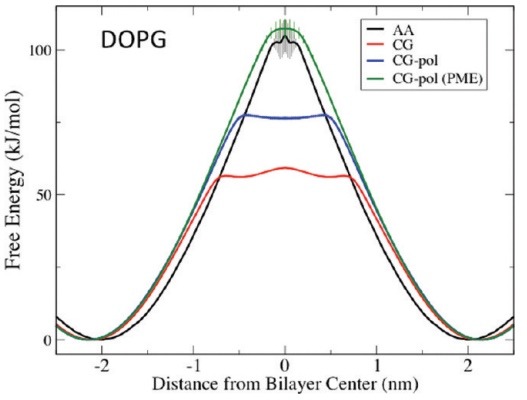

Figure 4. PMFs for DOPG flip−flop in a pure DOPC bilayer. Error bars are shown and represent the standard error between two independent lipids PMFs. The PMF is mirrored at the center of the bilayer for clarity.

Using the CG and CG-pol model, we calculated the PMF for DLPC flip−flop in a DLPC bilayer (Figure 2B). The PMFs for DLPC flip−flop are the same for the CG, CG-pol, and CG-pol with PME. There is a deep free energy minimum and a large, smooth increase in free energy to the center of the bilayer. The free energy barrier for DLPC flip−flop is 73 kJ/mol. Similar to the DPPC PMF, the BMW DLPC PMF has both a steeper slope and a higher barrier for flip−flop (122 kJ/mol). The steep slope of the PMF at the bilayer center and the snapshots (Figure 3B and C) indicate that even when the phosphate is at the center of bilayer, the lipid is still interacting with one bilayer leaflet.

The large difference between the CG models and the AA model is due to pore formation in the AA model. In contrast to the AA model, we did not observe pore formation in the CG, CG-pol, or BMW bilayers (Figure 3). At the bilayer center a small water defect forms, to keep the DLPC headgroup solvated. We did observe pore formation in the CG-pol-lj* model (Figure 3D). The structure of the pore appears similar to the AA model, with a disordered torroidal shape and multiple water and head groups within the bilayer interior. As with the AA model, once a pore formed the PMF plateaus (ca. 0.15 nm from the bilayer center), the barrier for flip−flop was reduced to 53 kJ/mol. The bulk properties of the DLPC bilayer are modified by the use of the increased interaction between water and lipid head groups, with the area per lipid increasing from 0.62 to 0.71 nm^2. We tested the CG-lj* model but did not observe pore formation, and the PMF was similar to the CG model (Figure 2B). Pores were not observed when we only increased the phosphate−water interaction, not the choline-water interaction (data not shown). Pores were not observed by increasing the charge on the phosphate and choline in DLPC to −2 and +2 (data not shown). In a subtler attempt, we increased the repulsion between the lipid tails and the lipid head groups, but pores were not observed (data not shown).

DOPG. To see the effect of a charged headgroup, we calculated PMFs for DOPG flip−flop across a DOPC bilayer (Figure 4). For the AA model, the free energy barrier for DOPG (105 kJ/mol) flip−flop in a DOPC bilayer increased compared to DOPC (87 kJ/mol) in a DOPC bilayer.[15] At the center of the bilayer, DOPG formed a water defect, and a pore was not observed (Figure 5A); this is similar to DOPC flip−flop, where we did not observe pore formation, but a water defect was present. The PMF for CG-pol DOPG flip−flop in a DOPC bilayer is shown in Figure 4. The shape of the PMF closely matches the AA PMF

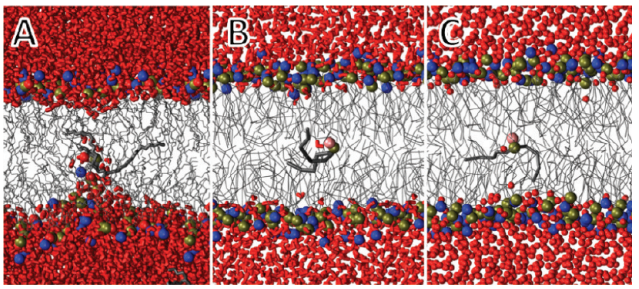

Figure 5. Snapshots for DOPG restrained at the center of a DOPC bilayer. Water is shown as red licorice, lipid tails as gray lines, restrained lipid as thick gray lines, and headgroup phosphate (phosphorus) and glycerol (oxygen) as balls. (A) AA, (B) CG, and (C) CG-pol simulations.

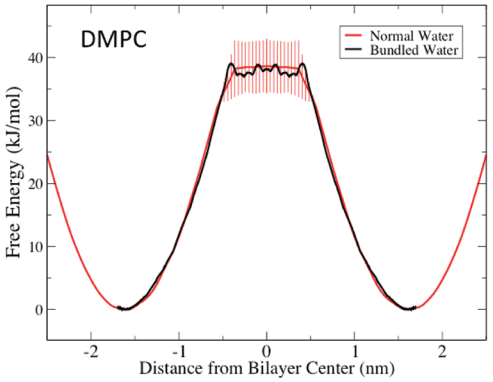

Figure 6. PMFs for DMPC flip−flop in a DMPC bilayer using normal SPC water and bundled water. Error bars for the normal water represent the standard error between two independent lipids PMFs. The bundled water PMF was only calculated once, so no error bars are shown. The PMF is mirrored at the center of the bilayer for clarity.

until ca. 0.6 nm, where the PMF suddenly flattens. A water defect was observed before this position, but near the center of the bilayer, a defect does not form (Figure 5B). In contrast to DLPC, where the PMF plateau was caused by pore formation, the plateau for DOPG is due to the lipid losing contact with either leaflet and with no net force in either direction, and the lipid almost completely desolvated. Occasionally a single water bead enters the bilayer to interact with the charged PG headgroup. The PMF for DOPG flip−flop across a DOPC bilayer using the CG model is shown in Figure 4. The PMF matches the shape of the CG-pol PMF, until ca. 0.75 nm from the center where it plateaus. Again, the plateau region corresponds to water defects breaking, exposing the DOPG to the bilayer interior along with an occasional single water bead (Figure 5C). The free energy barrier for DOPG flip−flop was closer to the AA model (104 kJ/mol) for the CG-pol model (77 kJ/mol) than for the CG model (59 kJ/mol). When PME was used with the CG-pol model, the resulting barrier is almost the same as for the AA model, although no stable water defect at the center of the bilayer is observed.

Effect of Bundling Water in AA Simulations. In all cases tested, the CG models show significantly less complex defects and in particular do not easily form pores, although the PMFs for lipid flip−flop are quite similar between CG and AA for DPPC lipids. We hypothesized that a limiting factor may be the relatively small scale of the defects: they typically involve only a small number of head groups with associated water molecules, so that the standard MARTINI water particles may be too coarse to reproduce their structure. To test this, we artificially tethered four water molecules together in atomistic simulations[16] in a tetrahedral geometry that approximates a spherical shape. With this unusual water model we calculated again the PMF for DMPC flip−flop and compared it to the result for normal atomistic water. We chose DMPC for this because it has a well-defined transition state for flip−flop with a large two-sided defect or pore.[8] The results are surprising: the tethered waters give essentially the same thermodynamics and structure as normal water. Figure 6 shows the PMFs for the normal atomistic DMPC case and the DMPC bilayer with tethered water, while Figure 7 shows two snapshots.

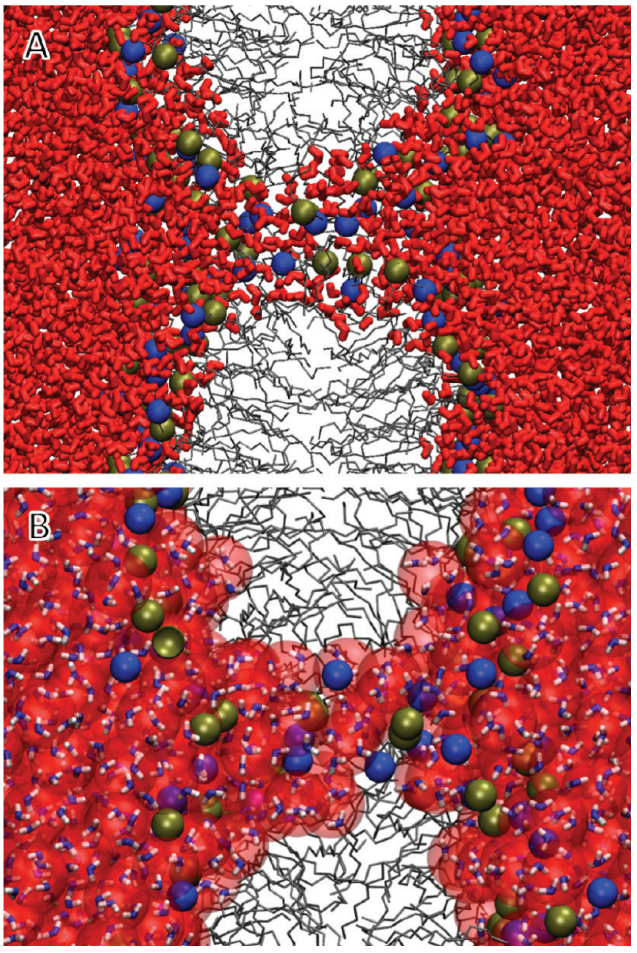

Figure 7. Snapshots of a pore formed in AA DMPC bilayer with (A) SPC water and (B) bundled water. The representation for (A) is the same as in Figure 3. For panel (B), bundled water is shown as blue and white licorice, with a red sphere around the four water molecules that comprise one bundled water.

DISCUSSION

We have studied the process of lipid flip−flop using molecular dynamics simulations with several different models. The AA model predicts that water defects or pores form as the headgroup of a phospholipid is transferred into the hydrophobic interior of a membrane. These membrane defects are hydrophilic; lined with other lipid head groups and water molecules. The free energy for

desolvating the charged or zwitterionic headgroup is higher than the cost of forming a water defect or a bilayer-spanning pore. We have observed similar behavior in the partitioning of charged and polar amino acid side chains in a DOPC bilayer.[28] The polar side chains formed water defects as they were moved into the hydrophobic interior, until the energy cost for desolvation was less than defect formation, causing the defect to break and the PMF to plateau. The charged side chains retained a water defect even at the center of the bilayer. Many other groups have observed similar behavior in the partitioning of polar and charged molecules using different force fields and methods.[27,30−32] For DPPC, the free energy barrier for lipid flip−flop was 80 (AA), 83 (CG), and 89 kJ/mol (CG-pol).

There is good agreement between the AA and CG models on the shape of the PMFs and the free energy barriers for DPPC. Both CG models observe water defects as the DPPC is moved into the bilayer core, but near the center of the bilayer, a pore does not form and the defects become unstable. The CG-pol model is more hydrated at the bilayer center, indicating an improvement over the standard MARTINI model. It is not obvious that the two models would give such similar results, and the physical properties are actually different. CG water has no dipole or polarizability, so simulations are run with a dielectric constant of 15 for implicit screening of electrostatic interactions. This means that the interaction of polar molecules is underestimated in hydrophobic environments, e.g., when a lipid headgroup is placed in the interior of a bilayer. In the AA model, with explicit water and dielectric screening, charge interactions are much stronger in an apolar medium, causing water pores to form when a DPPC is placed at the center of the bilayer. The CG-pol water model has explicit polarizability, and a dielectric of 2.5 is used, which means that the interaction between water and charged molecules is physically more realistic. Surprisingly, this has little effect on the structure of the defects, although CG-pol reproduces electroporation in a DPPC bilayer.[12] It is likely that the CG-pol will be useful for modeling phenomena where much larger pores are observed, such as the electroporation of membranes and antimicrobial peptides.[12] By increasing the Lennard-Jones interaction between the water and headgroup beads, we observed more stable water defects but still no pores in DPPC. We speculate that further increasing the interaction would cause pores to form, but changing these interactions perturbs the bilayer lamellar properties significantly.

Our results shows that water pores are still not observed during DPPC flip−flop, in contrast to AA simulations. The large size of CG-pol water beads (4 to 1 mapping) might prevent the formation of the small water pores seen in AA DPPC flip−flop, where on the order of tens of waters are involved. However, tests of tethered water in a DMPC bilayer show that the main reason is unlikely to be size related. It was suggested (in ref 12) that using a different Lennard-Jones potential (currently a 12−6 potential), particularly a less repulsive form, might improve the model. As the CG beads become more repulsive, a larger volume would be needed to from a defect or pore, which could affect the energetics of pore formation. A less repulsive model would allow beads to get closer together, possibly making defects form more easily. To this end, we tested the BMW water model, which uses a softer potential, but found that the free energy barriers for DPPC and DLPC flip−flop are significantly overestimated. There was slightly more water pulled into the center of the DPPC bilayer using the BMW model, but again no pore formation or stable water defect was observed. The high barrier for the BMW model is likely due to a high line tension, which would prevent pore formation.[33] Similarly the lack of pore formation in the CG and CG-pol model could be related to the models high bending modulus, which was shown to be nearly double atomistic and experimental values.[34] Although there is no immediate link between the bending modulus and the water/lipid line tension on the one hand and individual atomistic or MARTINI interactions on the other, it is likely that both properties are linked to the cost of defect formation. If future versions of MARTINI or other CG models improve these mechanical properties in a more integrated approach, then it will be interesting to see if this also results in an improved representation of membrane defects.

The CG and CG-pol models give similar results for DLPC flip−flop, and the use of PME had no effect on the energetics of flip−flop. There is a large discrepancy between the AA barrier for DLPC flip−flop (16 kJ/mol) and both CG models (73 kJ/mol). Intuitively, we expect defects and pores should form more readily in the thinner DLPC bilayer, compared to the DPPC. Experimental evidence has shown that pore formation in thin DLPC bilayer occurs spontaneously[35] and suggests our low free energy barrier from the AA model is realistic. Experiments on the permeation of protons and potassium ions through liposomes of monounsaturated PC lipids showed that lipids with 14 carbon tails had 2 orders of magnitude faster permeation than 18 carbon tails, which fit a pore-meditated model.[36] Increasing the interaction between the headgroup and water beads caused pore formation in the CG-pol-lj* DLPC bilayer. This suggests that neither the size of the large CG water nor the 'hard' potential for the MARTINI model prevents pore formation. As expected, increasing the water−headgroup interaction caused the area per lipid to increase, which illustrates the difficulty in parametrizing a CG force field.

We observed the largest difference between CG and CG-pol lipid PMFs for DOPG flip−flop in a DOPC bilayer. This is likely due to DOPG having a negative charge, while PC lipids are zwitterionic. The CG-pol model forms water defects to the DOPG until it is ca. 0.5 nm from the bilayer center, compared to ca. 0.75 nm for the CG model. This results in an 18 kJ/mol difference in the free energy barriers for flip−flop. Near the center of the bilayer neither model shows a water defect, although an occasional water bead does enter the bilayer to interact with the headgroup, in contrast to the AA model where a defect is present at the center. With PME, the resulting energies are very similar for both AA and MARTINI CG-pol. The use of PME with standard MARTINI has been shown to improve accurately modeling dendrimer[37] and antimicrobial peptide[38] interaction with membranes.

Given the coarseness of the MARTINI model and the complex process at length scales of a few atoms of lipid flip−flop and pore formation, the similarity in the PMFs is encouraging, although our results do suggest further refinement is necessary. These results suggest caution in using and interpreting results on polar and charged interactions with bilayer interiors, such as studies on drug partitioning, electroporation, and antimicrobial peptides, with CG models. Due to the computational demands of AA simulations and umbrella sampling calculations, it is useful to have a CG model that can used to study membrane defects and pores. It was shown that the CG-pol water model was able to form pores across bilayers and hydrophobic slabs by applying an electric field, in agreement with AA simulations.[12] We have compared standard MARTINI water, polarizable MARTINI water, and the BMW water model in their ability to model the

process of lipid flip−flop. We found good agreement in the free energy profiles for DPPC and DOPG flip−flop between the AA and CG models. This work suggests that during phospholipid flip−flop, the CG-pol model forms defects only slightly more readily than standard MARTINI, in closer agreement with AA simulations. The source of this mechanistic discrepancy is not clear, although we have ruled out two possible explanations: the size of the water beads and the use of a softer repulsive nonbonded potential. We did observe pore formation in a DLPC bilayer using the CG-pol-lj* model, which shows that pore formation is possible with CG lipids. Parameterizing a lipid force field requires a delicate balance of forces, so we do not suggest that the CG-pol-lj* is an improvement to MARTINI but rather a proof of principle. Future work into describing the molecular driving forces for AA pore formation may be necessary to fully explain the CG result. These results and similar calculations and comparisons to atomistic results could aid the parametrization of the MARTINI model and other CG lipid models.

■ ASSOCIATED CONTENT

Supporting Information. Figure S1 shows PMFs for atomistic DMPC flip−flop using a 64 lipid and 256 lipid bilayer. Figure S2 shows PMFs with one and two restrained lipids per simulation for atomistic DPPC flip−flop. This information is available free of charge via the Internet at http://pubs.acs.org/.

■ AUTHOR INFORMATION

Corresponding Author
*E-mail: tieleman@ucalgary.ca.

■ ACKNOWLEDGMENT

This work was supported by the Natural Sciences and Engineering Research Council (NSERC). W.F.D.B. is supported by studentships from NSERC, the Alberta Heritage Foundation for Medical Research (AHFMR), and the Killam Trust. D.P.T. is an AHFMR Scientist. We thank Dr. Siewert-Jan Marrink for useful comments on the manuscript.

■ REFERENCES

(1) Epand, R. M.; Vogel, H. J. Diversity of antimicrobial peptides and their mechanisms of action. *Biochim. Biophys. Acta* **1999**, *1462*, 11–28.
(2) van Meer, G.; Voelker, D. R.; Feigenson, G. W. Membrane lipids: where they are and how they behave. *Nat. Rev. Mol. Cell Biol.* **2008**, *9*, 112–124.
(3) Daleke, D. L. Regulation of phospholipid asymmetry in the erythrocyte membrane. *Curr. Opin. Hematol.* **2008**, *15*, 191–195.
(4) Tieleman, D. P.; Marrink, S. J. Lipids out of equilibrium: energetics of desorption and pore mediated flip−flop. *J. Am. Chem. Soc.* **2006**, *128*, 12462–12467.
(5) Wimley, W. C.; Thompson, T. E. Exchange and flip−flop of Dimyristoylphosphatidylcholine in Liquid-Crystalline, Gel, and 2-Component, 2-Phase Large Unilamellar Vesicles. *Biochemistry* **1990**, *29*, 1296–1303.
(6) De Kruijff, B.; Van Zoelen, E. J. Effect of the phase transition on the transbilayer movement of dimyristoyl phosphatidylcholine in unilamellar vesicles. *Biochim. Biophys. Acta* **1978**, *511*, 105–115.
(7) Gurtovenko, A. A.; Vattulainen, I. Molecular mechanism for lipid flip−flops. *J. Phys. Chem. B* **2007**, *111*, 13554–13559.
(8) Sapay, N.; Bennett, W. F. D.; Tieleman, D. P. Thermodynamics of flip−flop and desorption for a systematic series of phosphatidylcholine lipids. *Soft Matter* **2009**, *5*, 3295–3302.
(9) Marrink, S. J.; de Vries, A. H.; Tieleman, D. P. Lipids on the move: simulations of membrane pores, domains, stalks and curves. *Biochim. Biophys. Acta* **2009**, *1788*, 149–168.
(10) Gurtovenko, A. A.; Anwar, J.; Vattulainen, I. Defect-mediated trafficking across cell membranes: insights from in silico modeling. *Chem. Rev.* **2010**, *110*, 6077–6103.
(11) Marrink, S. J.; Risselada, H. J.; Yefimov, S.; Tieleman, D. P.; de Vries, A. H. The MARTINI force field: coarse grained model for biomolecular simulations. *J. Phys. Chem. B* **2007**, *111*, 7812–7824.
(12) Yesylevskyy, S. O.; Schafer, L. V.; Sengupta, D.; Marrink, S. J. Polarizable Water Model for the Coarse-Grained MARTINI Force Field. *PLoS Comput. Biol.* **2010**, *6*, e1000810.
(13) Wu, Z.; Cui, Q.; Yethiraj, A. A new coarse-grained model for water: the importance of electrostatic interactions. *J. Phys. Chem. B* **2010**, *114*, 10524–10529.
(14) Bennett, W. F.; MacCallum, J. L.; Tieleman, D. P. Thermodynamic analysis of the effect of cholesterol on dipalmitoylphosphatidylcholine lipid membranes. *J. Am. Chem. Soc.* **2009**, *131*, 1972–1978.
(15) Sapay, N.; Bennett, W. F. D.; Tieleman, D. P. Molecular Simulations of Lipid flip−flop in the Presence of Model Transmembrane Helices. *Biochemistry* **2010**, *49*, 7665–7673.
(16) Fuhrmans, M.; Sanders, B. P.; Marrink, S. J.; de Vries, A. H. Effects of bundling on the properties of the SPC water model. *Theor. Chem. Acc.* **2010**, *125*, 335–344.
(17) Van Der Spoel, D.; Lindahl, E.; Hess, B.; Groenhof, G.; Mark, A. E.; Berendsen, H. J. GROMACS: fast, flexible, and free. *J. Comput. Chem.* **2005**, *26*, 1701–1718.
(18) Berger, O.; Edholm, O.; Jahnig, F. Molecular dynamics simulations of a fluid bilayer of dipalmitoylphosphatidylcholine at full hydration, constant pressure, and constant temperature. *Biophys. J.* **1997**, *72*, 2002–2013.
(19) Berendsen, H. J. C.; Postma, J. P. M.; van Gunsteren, W. F.; Hermans, J. In *Intermolecular Forces*; Pullman, B., Ed.; D. Reidel: Dordrecht, The Netherlands, 1981, p 331−342.
(20) Biltonen, R. L.; Lichtenberg, D. The Use of Differential Scanning Calorimetry as a Tool to Characterize Liposome Preparations. *Chem. Phys. Lipids* **1993**, *64*, 129–142.
(21) Miyamoto, S.; Kollman, P. A. Settle - an Analytical Version of the Shake and Rattle Algorithm for Rigid Water Models. *J. Comput. Chem.* **1992**, *13*, 952–962.
(22) Hess, B.; Bekker, H.; Berendsen, H. J. C.; Fraaije, J. G. E. M. LINCS: A linear constraint solver for molecular simulations. *J. Comput. Chem.* **1997**, *18*, 1463–1472.
(23) Berendsen, H. J. C.; Postma, J. P. M; Vangunsteren, W. F.; Dinola, A.; Haak, J. R. Molecular-Dynamics with Coupling to an External Bath. *J. Chem. Phys.* **1984**, *81*, 3684–3690.
(24) Darden, T.; York, D.; Pedersen, L. Particle Mesh Ewald - an N. Log(N) Method for Ewald Sums in Large Systems. *J. Chem. Phys.* **1993**, *98*, 10089–10092.
(25) Essmann, U.; Perera, L.; Berkowitz, M. L.; Darden, T.; Lee, H.; Pedersen, L. G. A Smooth Particle Mesh Ewald Method. *J. Chem. Phys.* **1995**, *103*, 8577–8593.
(26) Kumar, S.; Bouzida, D.; Swendsen, R. H.; Kollman, P. A.; Rosenberg, J. M. The Weighted Histogram Analysis Method for Free-Energy Calculations on Biomolecules 0.1. The Method. *J. Comput. Chem.* **1992**, *13*, 1011–1021.
(27) Dorairaj, S.; Allen, T. W. On the thermodynamic stability of a charged arginine side chain in a transmembrane helix. *Proc. Natl. Acad. Sci. U.S.A.* **2007**, *104*, 4943–4948.
(28) MacCallum, J. L.; Bennett, W. F.; Tieleman, D. P. Distribution of amino acids in a lipid bilayer from computer simulations. *Biophys. J.* **2008**, *94*, 3393–3404.
(29) de Vries, A. H.; Mark, A. E.; Marrink, S. J. Molecular Dynamics Simulation of the Spontaneous Formation of a Small DPPC Vesicle in Water in Atomistic Detail. *J. Am. Chem. Soc.* **2004**, *126*, 4488–4489.
(30) Johansson, A.; Lindahl, E. Titratable Amino Acid Solvation in Lipid Membranes as a Function of Protonation State. *J. Phys. Chem. B.* **2009**, *113*, 245–253.

(31) Li, L.; Vorobyov, I.; Allen, T. Potential of mean force and pKa profile calculation for a lipid membrane-exposed arginine side chain. *J. Phys. Chem. B.* **2008**, *112*, 9574–9587.

(32) Yoo, J.; Cui, Q. Does arginine remain protonated in the lipid membrane? Insights from microscopic pKa calculations. *Biophys. J.* **2008**, *94*, L61–63.

(33) Wu, Z.; Cui, Q.; Yethiraj, A. A New Coarse-Grained Model for Water: The Importance of Electrostatic Interactions. *J. Phys. Chem. B* **2010**, *114*, 10524−10529.

(34) Brandt, Erik G.; Braun, Anthony R.; Sachs, Jonathan N.; Nagle, John F.; Edholm, O. Interpretation of Fluctuation Spectra in Lipid Bilayer Simulations. *Biophys. J.* **2011**, *100*, 2104–2111.

(35) Blok, M. C.; Van Der Neut-Kok, E. C. M.; Van Deenen, L. L. M.; De Gier, J. The effect of chain length and lipid phase transitions on the selective permeability properties of liposomes. *Biochim. Biophys. Acta, Biomembr.* **1975**, *406*, 187–196.

(36) Paula, S.; Volkov, A. G.; Van Hoek, A. N.; Haines, T. H.; Deamer, D. W. Permeation of protons, potassium ions, and small polar molecules through phospholipid bilayers as a function of membrane thickness. *Biophys. J.* **1996**, *70*, 339–348.

(37) Lee, H.; Larson, R. G. Coarse-grained molecular dynamics studies of the concentration and size dependence of fifth- and seventh-generation PAMAM dendrimers on pore formation in DMPC bilayer. *J. Phys. Chem. B* **2008**, *112*, 7778–7784.

(38) Rzepiela, A. J.; Sengupta, D.; Goga, N.; Marrink, S. J. Membrane poration by antimicrobial peptides combining atomistic and coarse-grained descriptions. *Faraday Discuss.* **2010**, *144*, 431–443discussion 445−481.

JCTC Journal of Chemical Theory and Computation

ARTICLE

pubs.acs.org/JCTC

Conformational Analysis of Oligoarabinofuranosides: Overcoming Torsional Barriers with Umbrella Sampling

Shahidul M. Islam,[†] Michele R. Richards,[‡] Hashem A. Taha,[‡] Simon C. Byrns,[‡] Todd L. Lowary,[‡] and Pierre-Nicholas Roy*[,†]

[†]Department of Chemistry, University of Waterloo, Waterloo, ON, Canada N2L 3G1

[‡]Department of Chemistry and Alberta Ingenuity Centre for Carbohydrate Science, University of Alberta, Edmonton, AB, Canada T6G 2G2

Supporting Information

ABSTRACT: In this report, the conformations of a series of mono- and oligoarabinofuranosides were probed through the use of umbrella sampling simulations with the AMBER force field and the GLYCAM carbohydrate parameter set. The rotamer population distribution about the exocyclic C4−C5 bonds and the puckering distributions of the rings obtained from these umbrella sampling simulations were found to be in excellent agreement with those obtained from conventional long MD simulations for small monosaccharide fragments. For larger systems, the conventional MD approach becomes impractical, and we propose the use of umbrella sampling to circumvent poor sampling of certain conformations. The same umbrella sampling simulations were used to calculate the distributions about the vicinal protons and ensemble-averaged vicinal proton−proton coupling constants ($^3J_{H,H}$). The distributions about the vicinal protons of a monomer, methyl-α-L-arabinofuranoside (**1**), were found to be very similar to those obtained from direct umbrella sampling simulations about the vicinal protons. We calculated $^3J_{H,H}$ based on DFT-based Karplus-like relationships for L-arabinofuranosides. The $^3J_{H,H}$ values were found to be very similar to those obtained with the conventional MD simulations. For **1**, the $^3J_{H,H}$ values obtained with the DFT-based Karplus equations agree very well with experimental results; the agreement is, however, not as good for the larger oligomers. An approach to determine the experimental rotamer populations from the simulations is also discussed.

INTRODUCTION

In nature, the monosaccharide arabinose is found in both possible cyclized ring forms (pyranose and furanose) and absolute stereochemistries (D and L).[1] The furanose forms are more prevalent than the pyranose forms, and the distribution of D- vs L-arabinofuranose is species-specific. D-Arabinofuranose is found predominantly in cell wall polysaccharides in mycobacteria (including the human pathogen *Mycobacterium tuberculosis*) and other members of the actinomycetes family of bacteria.[2] On the other hand, L-arabinofuranose is abundant in plant cell walls.[3,4] Regardless of their source, arabinofuranose-containing glycans play important roles in the organisms that produce them and in interactions with their environment. For example, the D-arabinofuranose-containing polysaccharides present in mycobacteria are essential for viability.[2,4] In addition, plant glycoproteins containing L-arabinofuranose moieties are believed to be essential in diverse functions such as cell division and plant−microbe interactions,[5] and these glycoconjugates have also been implicated in the response to some plant allergens.[6]

In previous studies, we have reported conformational investigations on molecules containing D-arabinofuranose rings using a combination of NMR spectroscopy and *ab initio*/density functional theory (DFT) or molecular dynamics calculations.[7−17] These studies were carried out with the expectation that a better understanding of the conformational preferences of D-arabinofuranose-containing polysaccharides (D-arabinans) would facilitate the design of molecules that would interfere with their binding to proteins. For example, such molecules targeted to enzymes involved in the biosynthesis of D-arabinans would be anticipated to be lead compounds for the treatment of mycobacterial diseases including tuberculosis and leprosy.

Having developed an understanding of the conformational preferences of D-arabinans in solution, we endeavored to study their interactions with proteins using computational methods. Access to X-ray crystal structures of proteins in complex with molecules containing D-arabinofuranose rings would greatly facilitate such investigations. Structural information of this type was, however, unavailable at the time this study was initiated.[18] We therefore turned our attention to L-arabinans, for which a larger amount of crystal structure data is available,[19−22] and focused on the structure of a mutant arabinofuranosidase, which was obtained in complex with an L-arabinofuranose trisaccharide.[23]

The present study has been carried out to better understand the conformational preferences of larger oligoarabinofuranosides (Figure 1) and relies on techniques that provide enhanced sampling of conformational space. Furanosides are highly flexible compared to their pyranoside counterparts,[24] and the rings can occupy several envelope (E) and twist (T) forms with low energy barriers.[11] According to the Altona−Sundaralingam notation,[25,26] each ring conformation can be described by a phase angle of pseudorotation (P) and a puckering amplitude (ϕ_m). Figure 2 shows the pseudorotational itinerary for the L-arabinofuranose ring.

Received: May 17, 2011
Published: August 04, 2011

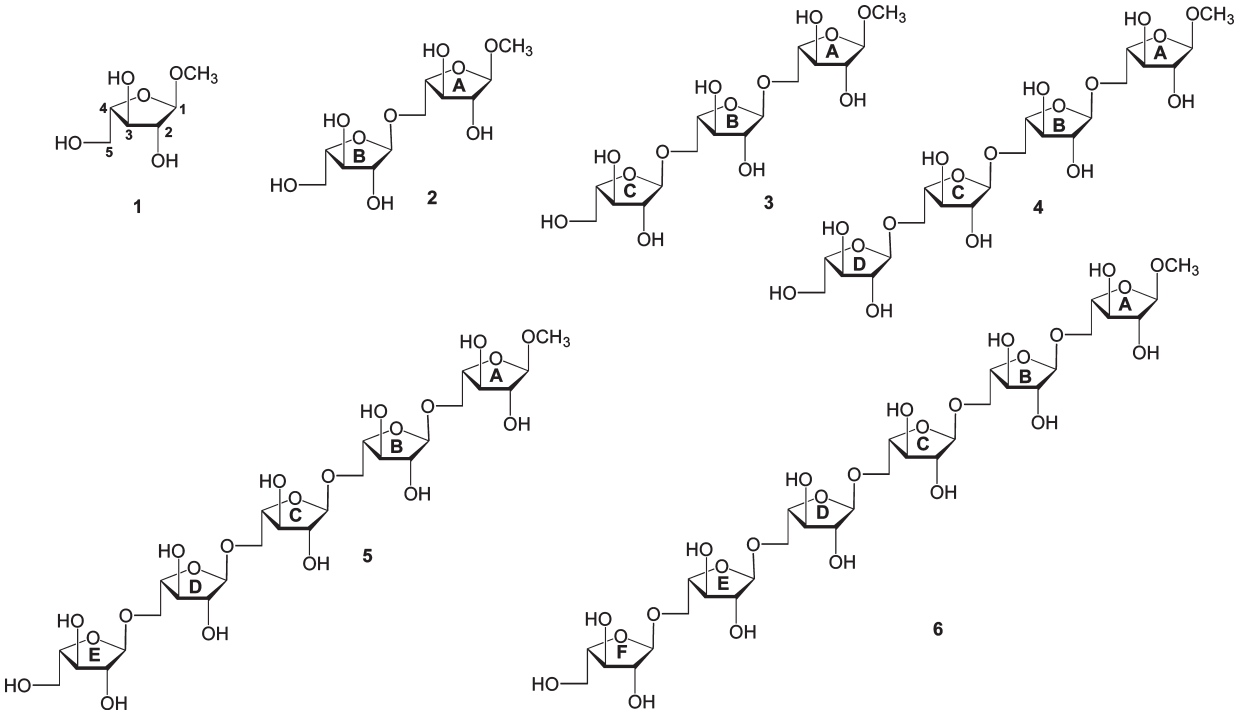

Figure 1. L-Arabinofuranosyl oligosaccharides studied in this paper.

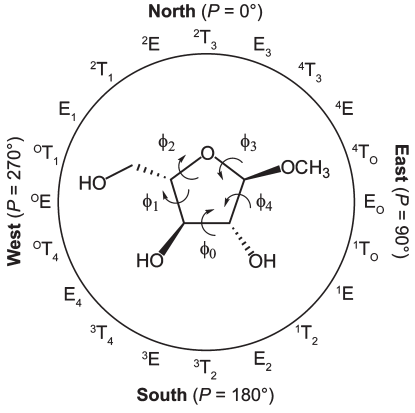

Figure 2. Pseudorotational itinerary for the L-arabinofuranose ring.

The angle P of a given conformer can be calculated from the five endocyclic torsion angles $\phi_0-\phi_4$ as defined below

$$\tan P = \frac{(\phi_2 + \phi_4) - (\phi_1 + \phi_3)}{3.077\phi_0} \quad (1)$$

The puckering amplitude, ϕ_m, which measures the maximum displacement from the planar ring form, is related to P and ϕ_0 via the relation

$$\phi_m = \frac{\phi_0}{\cos P} \quad (2)$$

Other important features that should be considered during the conformational analysis of furanosides are rotamer populations about the exocyclic C−C and C−O bonds. In the present study, we investigated rotamer populations about the C4−C5 bond, which are influenced by a combination of steric and stereoelectronic (gauche) effects.[27−31] Figure 3 shows the three staggered rotamers about the C4−C5 bond in L-arabinofuranose rings.

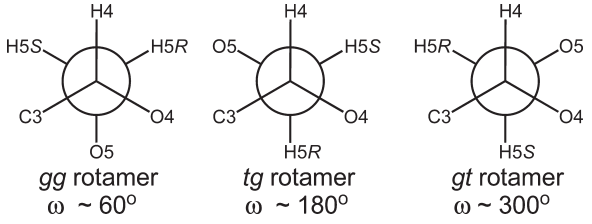

Figure 3. Definitions of the three staggered rotamers about the C4−C5 bond in L-arabinofuranosides, as shown looking down the bond from C4. The angle ω is defined as the O4−C4−C5−O5 torsion angle; see **1** in Figure 1 for the atom numbering scheme.

Because both experimental rotamer and puckering distributions can be obtained from the analysis of NMR ^{1}H−^{1}H vicinal coupling constants, $^3J_{H,H}$, a comparison with theoretically derived vicinal coupling constants allows one to assess the reliability of the simulation results. A common approach for assessing rotamer populations is to assume that a set of three discrete values of ϕ angles contains all conformational possibilities. In this case, the average coupling constant $\langle J \rangle$ is

$$\langle J \rangle = \sum_{i=1}^{3} X_i J(\phi_i), \text{with} \sum_{i=1}^{3} X_i = 1 \quad (3)$$

where X_i ($i = 1, 2, 3$) are the unknown populations of the discrete rotamers and $J(\phi_i)$ are the vicinal coupling constants between H4 and H5*R* or H5*S* for the three values of ϕ_i. The values of $J(\phi_i)$ are calculated on the basis of ϕ_i, the dihedral angle between the two coupled protons. The ϕ_i values can either represent ideally staggered rotamers (60°, 180°, and 300°) or dihedral angles having high probability obtained from MD simulations. In a

previous study,[16] we showed that the discrete approach as described above does not provide good average coupling constants when compared to experimentally obtained coupling constants or to those from a continuous approach. According to the continuous approach, $\langle J \rangle$ is measured as an average over the entire conformational space of the molecules using[32]

$$\langle J \rangle = \int_0^{360} J(\phi)\, \rho(\phi)\, d\phi \tag{4}$$

where $J(\phi)$ is a Karplus relation that correlates the vicinal nuclear spin−spin coupling constants to the dihedral angle ϕ between the coupled spins, and $\rho(\phi)$ is the probability distribution of the dihedral angles about a particular bond. This approach provides coupling constants in good agreement with experimental results, suggesting the necessity of using a method that considers all angles across the range of 0 to 360°. An improved approach is the continuous probability distribution (CUPID) method,[32] where $\rho(\phi)$ is represented as a Fourier series. In one study,[33] the CUPID method has been modified for five-member ring systems (CUPID-5). The Fourier series must be truncated, and the coefficients of the Karplus relationships must be accurate. This limits the use of this method for conformationally flexible molecules such as furanosides.

Various Karplus relationships are available in the literature to describe the dependence of the coupling constant on the dihedral angles between the coupled spins in arabinofuranosides.[7,16,17,34] Recently developed DFT-derived relationships have been found to provide the best $^3J_{H,H}$ values when compared to experimental results:[16]

$$^3J_{1,2} = 4.62 + 3.16\cos(\phi) + 4.57\cos(2\phi) \tag{5}$$

$$^3J_{2,3} = 8.04 + 8.07\cos(\phi) + 7.24\cos(2\phi) \tag{6}$$

$$^3J_{3,4} = 4.44 + 0.50\cos(\phi) + 4.25\cos(2\phi) \tag{7}$$

$$^3J_{4,5S} = 4.95 - 0.42\cos(\phi) + 4.03\cos(2\phi) \tag{8}$$

$$^3J_{4,5R} = 5.23 + 0.02\cos(\phi + 15.1°) + 4.67\cos(2\phi + 30.2°) \tag{9}$$

We present here studies directed ultimately at understanding the conformation of L-arabinofuranose-containing oligosaccharides and their interaction with proteins. In particular, we explore the use of umbrella sampling in carrying out conformational searches of these molecules, and we compare our results with experimentally obtained $^3J_{H,H}$ values and conventional MD approaches, where applicable. The umbrella sampling approach was chosen because it allows one to overcome high free energy barriers along specified reaction coordinates. The advantages of the approach are expected to become increasingly important as the size of the oligofuranoside increases. In addition, we make an effort to develop a new approach to predict experimental rotamer populations that properly takes into account thermal fluctuations and is independent of the need to experimentally measure $^3J_{H,H}$ values. Such an approach could prove valuable in large molecules where spectral overlap prohibits the measurement of these parameters.

METHODS

All molecular dynamics simulations were carried out with the AMBER 10[35] suite of programs. The AMBER ff99SB force field[36] with the GLYCAM (version 04f) parameter set for carbohydrates[37,38] was employed for the description of **1**−**6**. The additivity principle[16,39,40] was used to build the topology of the oligosaccharides. We chose this particular version of the GLYCAM parameter set for consistency with our previous simulations on these ring systems.[14−16] Note that similar C4−C5 rotamer populations and ring puckering distribution were obtained from a recently developed GLYCAM06 parameter set[41] for the monomer, methyl α-L-arabinofuranoside **1** (data not shown). For the solution simulations, **1** was solvated by 288 TIP3P[42] water molecules with a total box size of 25.816 × 24.997 × 24.007 Å. The box sizes and number of waters were then gradually increased for oligosaccharides up to 35 × 35 × 35 Å and 1325 TIP3P waters for hexasaccharide (**6**).

Long MD Simulations. Prior to long MD simulations and umbrella sampling simulations, the systems were minimized and equilibrated. First, the water molecules were minimized, keeping the geometries of the saccharides constrained. The entire system was then minimized. In both minimization steps, a steepest descent energy minimization was carried out for 50 cycles. The conjugate gradient algorithm was then used for 950 cycles. A total of 100 ps of annealing was then carried out with 50 ps each for temperature heating (5 to 300 K) and cooling (300 to 5 K). This was then followed by a short equilibration run of 250 ps. During this run, the temperature of the systems was gradually increased from 5 K to 300 K (150 ps) and then kept constant (100 ps). The production solution simulations of all compounds were performed under NPT conditions where the temperature was kept at 300 K and the pressure at 1 atm to remain consistent with experimental conditions. To assess any effect the thermostat may have on the dynamics of our systems, separate MD simulations were performed using the Langevin[43] or Berendsen[44] thermostat to control the temperature of the simulation box. A collision frequency γ of 2.0 ps^{-1} was used for the Langevin thermostat. MD simulations of 200 ns in length were carried out for compounds **1**−**3**. In all of the simulations, a 1 fs integration time step was used. Periodic boundary conditions were used, and a cutoff of 8 Å was set for nonbonded interactions. The SHAKE[45] algorithm was used to fix all hydrogen-containing bonds to their equilibrium values. Long-range electrostatic behavior was controlled with the particle mesh Ewald (PME) method.[46,47] Gas phase simulations were also performed to observe the effect of solvation. A cutoff of 18 Å was set for nonbonded interactions in the gas phase. Periodic boundary conditions and the PME method were not used in the gas phase simulations. Other parameters remained unchanged from those employed in the solution simulations.

Umbrella Sampling Simulations. The average distribution function, $\rho(\chi)$ (eq 10), along some reaction coordinate χ is defined as the Boltzmann weighted average:[48]

$$\langle \rho(\chi) \rangle = \frac{\int dq\, \delta(\chi'(q) - \chi)\, e^{-V(q)/k_B T}}{\int dq\, e^{-V(q)/k_B T}} \tag{10}$$

where $V(q)$ is the total energy of the system as a function of the conformation q and $\chi'(q)$ is the functional dependence of the reaction coordinate on the conformation. The potential of mean force (PMF) $W(\chi)$, or the change in free energy along the

coordinate χ, can be defined as[49−51]

$$W(\chi) = -k_B T \ln\langle\rho(\chi)\rangle \quad (11)$$

The accurate sampling of conformational space can, however, be hindered by the presence of large energy barriers along χ. Therefore, the calculation of $\rho(\chi)$ and the PMF by conventional MD simulations is unrealistic for large systems, especially if they require long equilibration periods for convergence. Umbrella sampling, originally proposed by Valleau and Torrie,[52,53] is a useful tool to obtain information on processes that require extremely long simulation times. In umbrella sampling, several simulations along the chosen coordinate are carried out. A biasing potential, $V_b(\chi)$, is added to the total energy to enhance the sampling of certain regions of conformational space. A harmonic form is often chosen for the biasing potential and is defined as[49,50]

$$V_b(\chi)_i = \frac{1}{2}k(\chi - \chi_i)^2 \quad (12)$$

where k is the force constant and χ_i is the target position. The separate simulations are then combined to obtain the unbiased $\rho(\chi)$ and its associated PMF. Among the various approaches to combine the simulation results,[52−56] the weighted histogram analysis method (WHAM) proposed by Kumar et al.[57] uses all of the information present in the umbrella sampling without discarding the overlapping regions. The WHAM method is a practical approach to obtaining average $\rho(\chi)$ and the PMF.

In this study, the dihedral angle about one of the exocyclic C4−C5 bonds (i.e., O4−C4−C5−O5) was taken as the reaction coordinate χ. All of the umbrella sampling simulations were performed using the final structure obtained from a short equilibration run (150 ps) of the systems. A total of 72 windows with a window width of 5° were used to cover the entire dihedral angle range from 0° to 360°. We also increased the width to 10° (with 36 windows in total) to study convergence. For monosaccharide **1**, 200 ps simulations for each window were carried out to yield a total simulation time of 14.4 ns. The simulation time for each window was increased to 1 ns for oligosaccharides **2** and **3** and 2 ns for the larger oligosaccharides **4**−**6**, with a total simulation time of 72 and 144 ns, respectively. For oligosaccharides, only one torsional sampling over 5° increments has been performed in a given window. Therefore, 72 simulations were performed for a singe torsional angle, and a total of 432 (72 × 6) simulations have been performed for **6**. A harmonic biasing potential was chosen as the biasing potential energy function, and the force constant k was set to 30 kJ mol^{-1} rad^{-2}. The Langevin[43] thermostat was used to regulate the temperature of the umbrella sampling simulations. Umbrella sampling simulations were also performed with a Berendsen thermostat for monomers to compare the behavior of the two thermostats. All of the other simulation parameters used in the umbrella sampling simulations were identical to the long MD simulations discussed above. Once the simulations were complete, the PMF and $\rho(\chi)$ were calculated as a function of dihedral coordinates about the C4−C5 bond, using the WHAM software package by Grossfield.[58] The bootstrap error analysis method[59] was utilized to obtain relative errors of the distribution of rotamer populations. During a bootstrapping procedure, some data points were randomly removed from the total ensemble; however, the total number of data points was kept constant by adding data points that were already in the ensemble. A number of such bootstrapping cycles were performed by randomly removing and duplicating the data points from the ensemble. The distributions obtained from this bootstrapping procedure were then compared to the original rotamer population distribution obtained from the umbrella sampling simulation to calculate the relative error in the original distribution. Vicinal proton−proton coupling constants ($^3J_{H,H}$) and ring puckering of the compounds were also studied using the conformational ensembles obtained from the umbrella sampling simulations. Errors in $^3J_{H4,H5R}$ and $^3J_{H4,H5S}$ were calculated from the errors in distribution obtained from the bootstrap error analysis. Errors in $\langle^3J_{H1,H2}\rangle$, $\langle^3J_{H1,H2}\rangle$, and $\langle^3J_{H1,H2}\rangle$ were calculated from the standard deviations of the simulation data points along the ring proton−proton dihedrals.

Hydrogen Bonding Analysis. An intramolecular hydrogen bonding analysis of arabinofuranosides was performed using the ptraj module of the AMBER suite. All hydroxyl hydrogen atoms were assigned as potential hydrogen bond acceptors, and all oxygen atoms were assigned as potential hydrogen bond donors. Hydrogen bonding was evaluated with a heavy atom cutoff distance of 4 Å and an angle cutoff of 120°. Percent occupancies of the hydrogen bonds throughout the simulations were also calculated.

RESULTS AND DISCUSSION

NMR Spectroscopy. The spectra for **1**, **3**, and **6** were acquired in D_2O at 300 K on a 600 MHz spectrometer. The $^3J_{H,H}$ values for **1** were determined from a 1D ^{1}H NMR spectrum and are listed in Table 2. To overcome the spectral overlap present in **3** and **6**, the variable time version of the 1D gradient-enhanced chemical shift selective filtering (ge-CSSF) TOCSY spectra[60,61] was used to provide the $^3J_{H,H}$ values (Table 3). The spectra for **3** and **6** were simulated using the program WinDNMR[62] in order to confirm the coupling constants. The spectra, as well as a table of the chemical shifts, can be found in the Supporting Information. As would be expected, the coupling constant data for all of the compounds are within ±0.1 Hz.[7] The synthesis of **3** and **6** was carried out as described previously,[7,63,64] and the details are provided in the Supporting Information

Simulations. The length of the long MD and umbrella sampling simulations required that convergence of the rotamer populations of **1** and **3** first be estimated. For monosaccaharide **1**, it was found that a 200 ns MD simulation was required to obtain converged populations of all of the rotamers with uncertainties of less than a few percentage units, while only 200 ps simulations per window were required in the case of umbrella sampling. Simulations of less than 50 ns for long MD and 120 ps for umbrella sampling produced significantly different rotamer populations with larger variances from those obtained after 200 ns and 200 ps simulations, respectively. Because a total of 72 windows were used in the umbrella sampling, the total simulation time for umbrella sampling is 14.4 ns, which is significantly lower than the 200 ns value required in the long MD simulation. We also performed umbrella sampling simulations with 36 windows with 10° intervals. These simulations required a total simulation time of 7.2 ns. The rotamer populations were found to be very similar to those obtained with the 14.4 ns simulation. Convergence studies of the rotamer populations of **3** show that a 200 ns MD simulation still provides converged rotamer populations with errors of a few percent in all three rotamers. However, simulations of less than 150 ns produce very different rotamer populations. In the case of umbrella sampling, only 1 ns for each window, which equals a total of 72 ns of simulation, was required to obtain the converged result for all rotamers. Results obtained

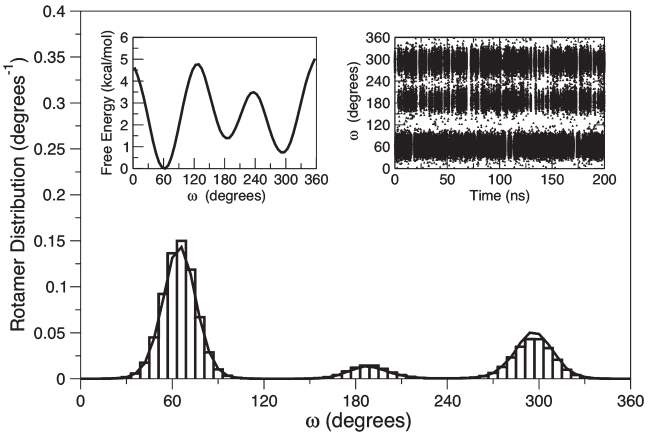

Figure 4. Comparison of the histograms obtained from the conventional MD (shown as a solid line) and umbrella sampling simulations (shown as a bar graph) of **1**. The left inset shows the PMF along the dihedral angle (ω) obtained from umbrella sampling, and the right inset shows the time dependence of ω during the long MD simulation.

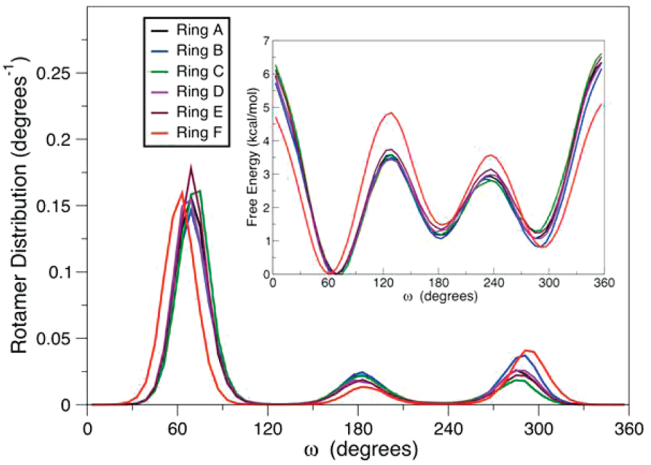

Figure 5. Comparison of the histograms of the dihedral angles (ω) obtained from the MD simulations of **6**. The inset shows the PMF along the dihedral angles (ω) obtained from umbrella sampling simulation.

from the umbrella sampling simulation are also expected to be superior because of the enhanced nature of the sampling. For larger oligomers **4**−**6**, only umbrella sampling simulations were performed with 2 ns simulations per window.

The rotamer population distribution about the C4−C5 bond of **1** obtained from both 200 ns MD simulations and 200 ps umbrella sampling simulations per window are shown in Figure 4. It is clear that both conventional MD and umbrella sampling simulations show similar distributions of rotamer populations with *gg* > *gt* > *tg*. The PMF obtained from the umbrella sampling simulations showed a 0.7 kcal mol^{-1} difference in free energy between the *gg* and *gt* rotamers. This result underscores the importance of having accurate force field torsional parameters for these systems.

The umbrella sampling-derived rotamer distribution about the C4−C5 bonds involved in the α-(1→5) linkages for the rings of the largest oligomer **6** are shown in Figure 5. Similar rotamer population distributions were also observed for oligomers **2**−**5**. The histograms show that the (1→5)-linked rotamer populations all follow the same

Table 1. Rotamer Population (%) of 1−6 in Solution (TIP3P Water) Using US Simulations[a]

structure	population	ring A	ring B	ring C	ring D	ring E	ring F
1	X_{gt}	34(2)					
	X_{tg}	9(1)					
	X_{gg}	55(2)					
2	X_{gt}	14(1)	24(1)				
	X_{tg}	15(1)	8(1)				
	X_{gg}	72(3)	67(2)				
3	X_{gt}	15(2)	11(1)	23(2)			
	X_{tg}	13(1)	15(1)	8(1)			
	X_{gg}	72(3)	74(3)	69(3)			
4	X_{gt}	11(1)	14(1)	16(1)	22(1)		
	X_{tg}	12(1)	15(1)	16(1)	7(1)		
	X_{gg}	77(3)	72(2)	68(2)	71(2)		
5	X_{gt}	10(1)	13(1)	14(1)	12(1)	23(1)	
	X_{tg}	12(1)	14(1)	14(1)	11(1)	9(1)	
	X_{gg}	78(2)	73(2)	72(2)	77(2)	69(2)	
6	X_{gt}	14(1)	20(1)	11(1)	15(1)	13(1)	22(1)
	X_{tg}	14(1)	15(1)	14(1)	12(1)	12(1)	8(1)
	X_{gg}	72(2)	66(2)	75(2)	73(2)	76(2)	70(2)

[a] Values in parentheses are relative errors obtained from the bootstrap error analysis of the distributions obtained from the umbrella sampling simulation along the O4−C4−C5−O5 dihedral angle.

trend ($X_{gg} > X_{gt} \approx X_{tg}$), while the terminal rotamer populations follow the trend $X_{gg} > X_{gt} > X_{tg}$.

The inset of Figure 5 contains the PMFs of the rotation about the torsion angle ω. It is interesting to note that the two lowest free energy barriers along ω are actually highest in the case of the terminal ring (ring F). This suggests that the internal rings more readily explore their different rotameric states (i.e., are more flexible) than the unsubstituted ring. Quantifying the simulation rotamer populations was done by integrating the distributions of Figure 5 (Table 1).

From Table 1, it is clear that the C4−C5 rotamer population (%) decreases in the order $X_{gg} > X_{gt} > X_{tg}$ for methyl-α-L-arabinofuranoside (**1**) and all of the terminal rings of **2**−**6**, while the trend for internal rings is $X_{gg} > X_{gt} \approx X_{tg}$. Similar results were also observed for **1** and **3** with conventional MD simulations. With the umbrella sampling simulations, the conformation of larger α-L-arabinofuranosides and their interactions with large biological systems can be studied. Note that we also found that the rotamer distribution about the C4−C5 bond in **1** obtained with the Langevin thermostat agrees well with that obtained using the Berendsen thermostat.

Spin−Spin Coupling Constants. Having determined the rotamer distributions from simulation, we next compared our results to experimental results. The experimental rotamer distributions can be determined from eq 3. This approach, however, assumes discrete rotamers and, as mentioned above, can lead to errors. A more appropriate approach to check the reliability of our simulation is to compare the $\langle {}^3J_{H,H} \rangle$ obtained from eq 4 directly with the experimental coupling constants. The DFT-derived Karplus relationship for α-D-arabinofuranosides, eqs 5−9, can be used for α-L-arabinofuranosides.[65] However, it should be noted that for the α-L-arabinofuranoside enantiomers, the ${}^3J_{H4,H5R}$ and ${}^3J_{H4,H5S}$ functions are exchanged. Moreover, eq 9 has a phase factor, which should be adjusted accordingly for

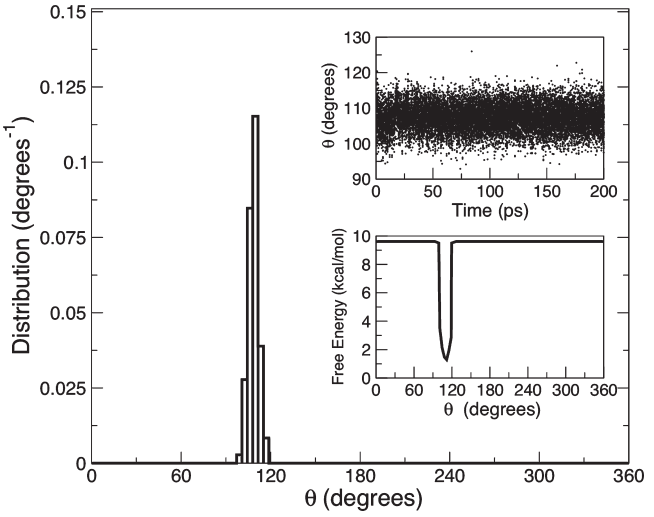

Figure 6. The distribution of the H4−C4−O4 angle (θ) obtained from the umbrella sampling simulations of **1**. The upper and lower insets show the time dependence and the PMF along the angle of θ, respectively.

$^3J_{H4,H5S}$ in α-L-arabinofuranosides. From our analysis (see Supporting Information), we found that the DFT-based Karplus relationships for $^3J_{H4,H5R}$ and $^3J_{H4,H5S}$ in α-L-arabinofuranosides are

$$^3J_{H4,H5R} = 4.95 - 0.42\cos(\phi) + 4.03\cos(2\phi) \quad (13)$$

$$^3J_{H4,H5S} = 5.23 + 0.02\cos(\phi - 15.1^\circ) + 4.67\cos(2\phi - 30.2^\circ) \quad (14)$$

Rotamer distributions along the C4−C5 bond ω were calculated using the conformational ensembles obtained from the umbrella sampling simulations. The calculation of spin−spin coupling constants requires the knowledge of rotamer distributions along the proton−proton dihedrals, i.e., the H4−C4−C5−H5*R* and H4−C4−C5−H5*S* angles, which can be obtained either from a long MD simulation or from an umbrella sampling simulation. Long MD simulations are undesirable for larger systems, and umbrella sampling simulations along each proton−proton dihedral would require additional calculations. As mentioned earlier, during the umbrella sampling simulations along the C4−C5 bond, a biasing window potential was applied at the reaction coordinate ω (i.e the O4−C4−C5−O5 angle) and later unbiased using the WHAM approach. Because the simulations were done under biased conditions and the proton−proton dihedrals are on the same C4−C5 bond, a direct calculation of the proton−proton distributions from the combined umbrella sampling simulation trajectories does not provide a reliable rotamer distribution along the proton−proton dihedral. (See the Supporting Information for the proton−proton distributions obtained from combined umbrella sampling simulation trajectories.)

A theoretically better approach is to calculate these distributions from the unbiased rotamer distributions along the C4−C5 bond obtained from the umbrella sampling simulation. This approach is feasible if significant correlations exist between the O4−C4−C5−O5, H4−C4−C5−H5*R*, and H4−C4−C5−H5*S* dihedral angles. As can be seen in Figure 3, the rotamer populations along H4−C4−C5−H5*R* and H4−C4−C5−H5*S* are related to the rotamer

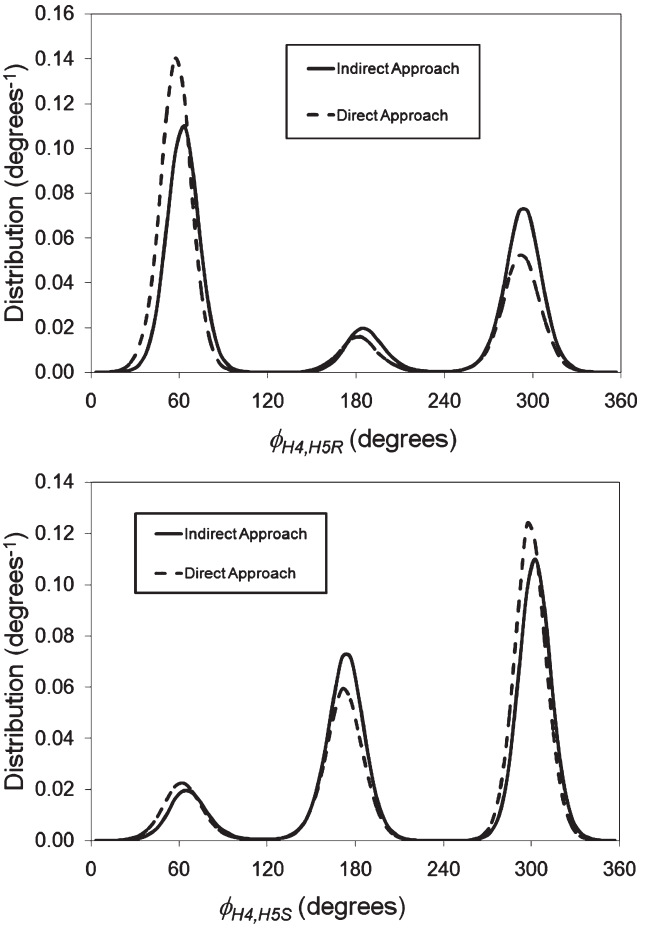

Figure 7. Comparison of the histograms obtained from indirect and direct umbrella sampling simulations about the proton−proton dihedral angles ($\phi_{H4,H5R}$ and $\phi_{H4,H5S}$) of **1**.

distribution of O4−C4−C5−O5 such that $\rho(\phi_{H4,H5R}) = \rho(\phi_{O4,O5})$ for all three rotamers and $\rho(\phi_{H4,H5S}) = \rho(\phi_{O4,O5} - 120)$, except in the case of the *gg* rotamer where $\rho(\phi_{H4,H5S}) = \rho(\phi_{O4,O5} - 120 + 360)$ for periodicity. We term the use of this assumption the "indirect approach". Such relations are expected to hold because of the relative stiffness of the bond angles involving the various protons. To support this assumption, the H4−C4−O4 bond angle distribution obtained from the umbrella sampling simulations is shown in Figure 6. It is clear that the use of a biasing potential along the dihedral angle has little effect on the H4−C4−O4 bond angle. A long molecular dynamics simulation of **1** also provides a similar population distribution along the H4−C4−O4 bond angle. We also found that the bond angles in the oligomers were rigid as expected. In fact, the three similar bond angles in **3** are found to have the same average value (∼110°). (See the Supporting Information for the distributions of bond angles in **3**.) Of course, this finding is apparent as the C4 atom forms a covalent bond with four other atoms through sp^3 hybridization. Nevertheless, our study confirms that the bond angles are more rigid than the dihedral angles along the C4−C5 bonds, and our indirect approach is feasible.

To further assess the reliability of the above assumptions, umbrella sampling simulations along the H4−C4−C5−H5*R* and H4−C4−C5−H5*S* dihedrals were also carried out for **1** (termed "direct approach"). The distributions about the

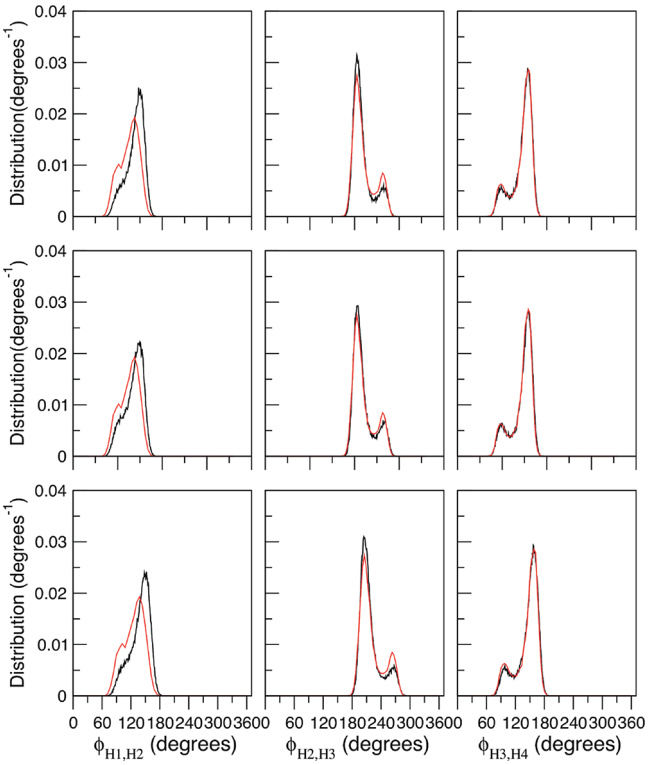

Figure 8. Comparison of the histograms obtained from umbrella sampling simulations about the proton−proton dihedral angles of rings A (upper panel), B (middle panel), and C (lower panel) of **3** (shown in black colored lines) and the ring proton−proton dihedral angles of **1** (shown in red colored lines). Due to the differences in H1−H2 dihedral angles, a ∼1 Hz difference in coupling constants compared to experimental results can be observed.

Table 2. Comparison of Experimental and Theoretical $\langle {}^3J_{H,H} \rangle$ Values (in Hz) for Monomer 1 Obtained from Umbrella Sampling Simulations

coupling	umbrella sampling	experimental
$\langle {}^3J_{H1,H2} \rangle$	2.1 (0.02)	1.7
$\langle {}^3J_{H2,H3} \rangle$	3.6 (0.02)	3.4
$\langle {}^3J_{H3,H4} \rangle$	5.4 (0.04)	5.8
$\langle {}^3J_{H4,H5R} \rangle$	3.2 (0.01)	3.3
	3.2 (0.01)[a]	
$\langle {}^3J_{H4,H5S} \rangle$	4.5 (0.02)	5.8
	4.1 (0.02)[a]	

[a] Values obtained from the umbrella sampling along the dihedrals H4−C4−C5−H5*R* and H4−C4−C5−H5*S*.

H4−C4−C5−H5*R* and H4−C4−C5−H5*S* dihedrals obtained from the indirect and direct umbrella sampling approaches are shown in Figure 7. As can be seen in Figure 7, the overall distributions are quite similar. Using these distributions, $^3J_{H4,H5R}$ and $^3J_{H4,H5S}$ values were calculated and compared to the corresponding experimental values (Table 2). The $^3J_{H4,H5R}$ obtained with the indirect approach are in excellent agreement with those obtained by the direct approach and experimentation. Similarly, the $^3J_{H4,H5S}$ obtained with the indirect approach are also in good agreement with those obtained with the direct approach; although the magnitudes of $^3J_{H4,H5S}$ calculated by both

Table 3. Comparison of Experimental and Theoretical $\langle {}^3J_{H,H} \rangle$ Values (in Hz) for Each Ring in Oligomers 3 and 6 Obtained from Umbrella Sampling Simulations[a]

	coupling	US	exptl	US	exptl	US	exptl	US	exptl	US	exptl	US	exptl
		ring A		ring B		ring C							
3	$\langle {}^3J_{H1,H2} \rangle$	3.0	1.7	2.7	1.5	2.9	1.6						
	$\langle {}^3J_{H2,H3} \rangle$	3.9	3.3	3.8	3.2	3.9	3.3						
	$\langle {}^3J_{H3,H4} \rangle$	5.4	5.8	5.4	5.9	5.5	6.0						
	$\langle {}^3J_{H4,H5R} \rangle$	2.9	3.2	3.0	3.2	3.1	3.3						
	$\langle {}^3J_{H4,H5S} \rangle$	3.4	5.8	3.4	5.8	3.7	5.9						
		ring A		ring B		ring C		ring D		ring E		ring F	
6	$\langle {}^3J_{H1,H2} \rangle$	3.0	1.7	3.1	1.6[b]	2.6	1.6[b]	2.9	1.6[b]	2.9	1.6[b]	2.8	1.5
	$\langle {}^3J_{H2,H3} \rangle$	4.0	3.2	3.9	3.2[b]	3.7	3.2[b]	4.0	3.2[b]	3.8	3.2[b]	3.8	3.3
	$\langle {}^3J_{H3,H4} \rangle$	5.5	5.8	5.4	6.0[b]	5.3	6.0[b]	5.3	6.0[b]	5.3	6.0[b]	5.3	6.0
	$\langle {}^3J_{H4,H5R} \rangle$	2.9	3.2	2.9	3.3[b]	2.8	3.3[b]	2.8	3.3[b]	2.8	3.3[b]	3.1	3.4
	$\langle {}^3J_{H4,H5S} \rangle$	3.4	5.8	3.8	5.8[b]	3.4	5.8[b]	3.4	5.8[b]	3.3	5.8[b]	3.8	5.9

[a] exptl = experimental, US = umbrella sampling simulation. Errors in theoretical coupling constants are very small within the range of 0.02−0.05 Hz. (See the Supporting Information for errors in $^3J_{H,H}$ values.) [b] The experimental $^3J_{H,H}$ values for residues B−E could not be measured individually due to spectral overlap. The average values for all four residues are shown.

approaches are lower than experimental results. It is possible that the DFT-based Karplus equation for $^3J_{H4,H5S}$ in α-L-arabinofuranosides, eq 14, provides underestimated $^3J_{H4,H5S}$ values. A more likely rationale for this discrepancy stems from undersampling of the *gt* rotamer, the largest contributor to $^3J_{H4,H5S}$ in **1**, in the MD simulations. A similar effect was observed on $^3J_{H4,H5R}$ in D-arabinofuranosides where MD simulations also underestimated the population of the *gt* rotamer and subsequently predicted a lower overall $^3J_{H4,H5R}$ value.[16,17]

Ring proton coupling constants were also calculated from the same umbrella sampling simulations. In this case, the dihedral angles between the coupled spins were calculated from the combined umbrella sampling trajectories. The distributions obtained from the dihedral angles were then used to calculate the average ring proton−proton coupling constants. We found that the distributions are in excellent agreement with those obtained from conventional MD, although an additional population in the distribution is found to be more pronounced in the umbrella sampling simulations (see Figure 8). Table 2 shows the comparison of experimental and theoretical (umbrella sampling) $^3J_{H1,H2}$, $^3J_{H2,H3}$, and $^3J_{H3,H4}$ for **1**. All three theoretically obtained coupling constants are found to be in good agreement with experimental results. The $^3J_{H1,H2}$, $^3J_{H2,H3}$, and $^3J_{H3,H4}$ obtained from the MD simulations of **1** (2.3, 3.8, and 5.7 Hz, respectively) are also very similar to that obtained from the umbrella sampling simulation. This suggests that, although this second populated region in the ring proton−proton population distributions is more pronounced in the umbrella sampling simulations, it has a minimal effect on the magnitude of the coupling constants.

The above analysis was also carried out for larger oligomers. The same Karplus-type equations were used for **3** and **6** as for **1**, even though glycosidic linkages are present. Karplus-like relationships derived for the internal and external C4−C5 bond of the α-(1→5)-linked disaccharide of D-arabinofuranose showed little difference in earlier studies (see the Supporting Information

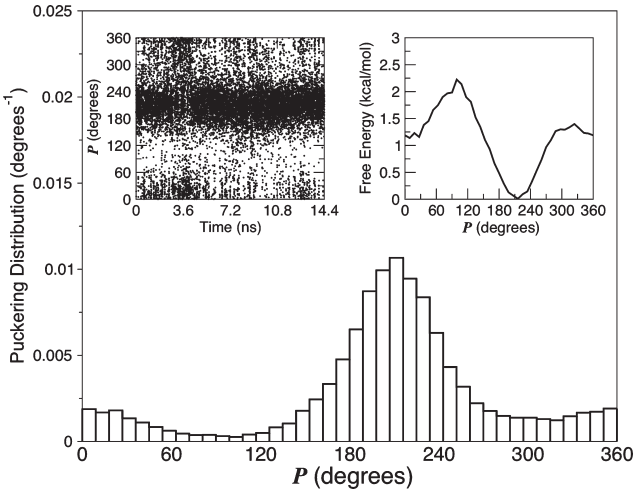

Figure 9. The distribution of the pseudorotational phase angle (P) for **1** in solution obtained from the umbrella sampling simulation. The left inset represents the time dependence of the P angle, and the right inset shows the PMF along the P of **1**.

for details). The simulation-derived $^3J_{H,H}$ values for each ring in **3** and **6** are shown in Table 3 and compared to experimental results.[66] The results demonstrate that the $^3J_{H4,H5R}$ and $^3J_{H3,H4}$ values are still in very good agreement with experimental results; on the contrary, $^3J_{H4,H5S}$, $^3J_{H1,H2}$, and $^3J_{H2,H3}$ deviate slightly when compared to those observed in the monomer (Table 2). The distributions along the H1−H2 dihedrals of **3**, as shown in Figure 8, are found to be slightly different than the corresponding H1−H2 distribution of **1**, which might be the reason for the ∼1 Hz difference in simulation $^3J_{H1,H2}$ compared to experimental results. On the other hand, we suspect that a better Karplus-like relationship is necessary to obtain better values of $^3J_{H4,H5S}$ and $^3J_{H2,H3}$ for oligosaccharides. It should be noted that the above approach is only applicable if the system explores its ring conformers relatively quickly compared to the time scale of the exocyclic torsions and if there is little correlation between the rotamers and the ring conformers. Such a correlation analysis is presented in a forthcoming section.

Distribution of Ring Conformers. The same umbrella sampling simulations were also used for the analysis of ring puckering of **1**−**6**. For each umbrella sampling trajectory, the ring puckering, P, has been calculated. The distribution of P in **1** is found to be very similar for each window (see the Supporting Information). This indicates that changes in ring puckering occur on a much faster time scale than rotation about exocyclic torsions; earlier *ab initio* and DFT calculations on methyl α-D-arabinofuranoside provided results consistent with this.[8] All of the umbrella sampling simulations corresponding to a ring were combined, and the distributions of puckering angle P and amplitude ϕ_m were then calculated. The variation of P for **1** obtained by umbrella sampling simulations is shown in Figure 9. Conventional MD also provides similar distribution of P for **1**. The umbrella sampling simulations of **1** predict that 77−84% of the conformations exist in the southern hemisphere of the pseudorotational itinerary with the area of the conformational space centered around 210−215° ($^3T_4$), although a small fraction of the conformer is also present in the northern hemisphere (Figure 9). The agreement between experimental and theoretical ring coupling constants (Table 2) suggests that the ring conformations obtained

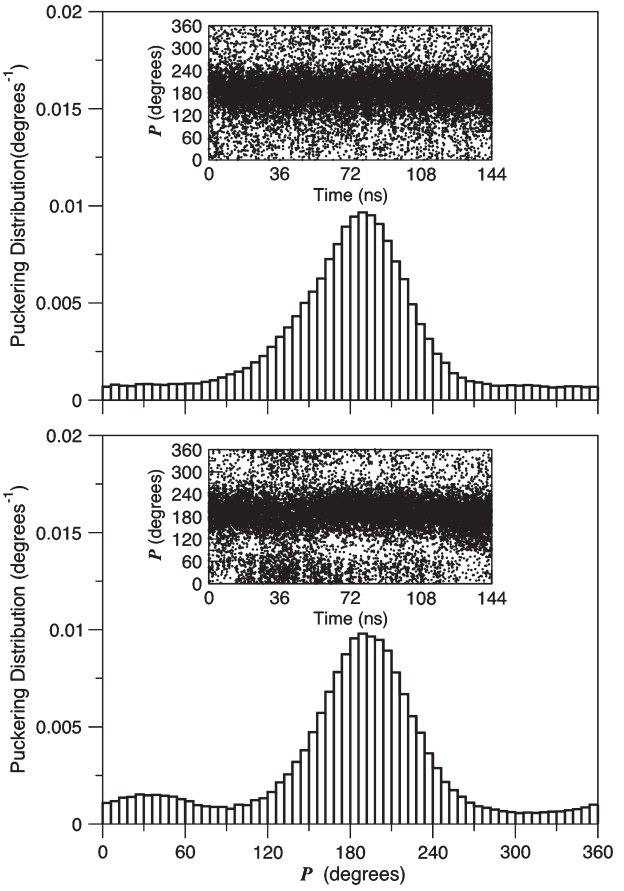

Figure 10. The distribution of the pseudorotational phase angle (P) for ring A (upper panel) and ring F (lower panel) of **6** in solution obtained from the umbrella sampling simulations. The insets represent the time dependence of the respective P angles of **6**. A minor secondary peak is also observed for the terminal ring of other oligomers with both umbrella sampling and long MD simulations.

from the simulation are accurate. The maximum free energy barrier along the P angle is about 2.2 kcal mol^{-1}, which justifies the relative ease of exploring the P compared to the ω conformational space. The distribution in ϕ_m is centered at about 36°, which agrees very well with those obtained from the crystal structure[67] and from the *ab initio* and DFT calculations.[8−12,14]

Having successfully determined the distribution of ring conformations of **1** using umbrella sampling simulations, we focused our attention on the oligomers. Figure 10 represents the distribution of puckering for rings A and F of **6** in solution obtained from the umbrella sampling simulations. It is clear that the puckering distribution in ring A has a predominantly southern conformer at P_S = 190−200° (81−86%). Rings B, C, D, and E also have similar values for P and ϕ_m. On the contrary, ring F, which contains the terminal rotamer, has a slightly different distribution of P; a second region of conformational space in the northern hemisphere, centered at P_N = 30°, of the pseudorotational wheel is populated. The ring conformations of oligomers **2**−**5** are found to be very similar to those observed in the rings of **6**. The puckering amplitude (ϕ_m) remains the same for all of the rings in **1**−**6** with ϕ_m in the range of 35−40°.

Correlation Study of Rotamers and Ring Puckering. Having successfully determined the rotamer populations about the C4−C5 bond and ring puckering from umbrella sampling simulations, we

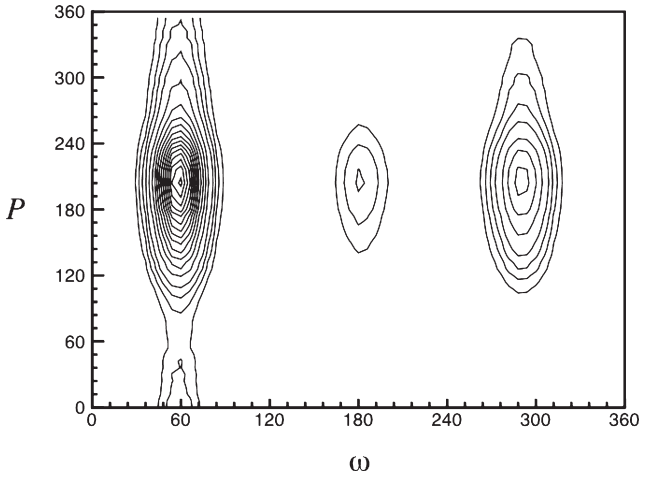

Figure 11. Joint probability distribution of the dihedral angle (ω) and the puckering angle (P) of **1** in the solution phase obtained from umbrella sampling simulation. The units of the angles ω and P are in degrees.

studied the correlation between them. The joint probability distribution ($\rho^{2D}_{\omega,P}$) of the C4−C5 torsion (ω) and puckering angle (P) for **1** and **3** calculated from umbrella sampling simulations are shown in Figures 11 and 12. Very little correlation between ω and P for **1** and **3** is observed; this is consistent with previous studies on α-D-arabinofuranoside using conventional MD simulations.[8,14] Figures 11 and 12 provide a qualitative indication of the uncorrelated behavior of ω and P for compounds **1** and **3**, respectively, but the extent of their correlation is absent. Therefore, we next endeavored to obtain a quantitative measure of this correlation.

We first define the square root or amplitude of the true 2D distribution, $\rho^{2D}_{\omega,P}$, as

$$f = \sqrt{\rho^{2D}_{\omega,P}} \tag{15}$$

and its uncorrelated counterpart as the product of the 1D distributions for each degree of freedom:

$$g = \sqrt{\rho^{1D}_{\omega}\rho^{1D}_{P}} \tag{16}$$

To study the overlap between the correlated and uncorrelated distributions, we define the inner product:

$$\int \mathrm{d}P\, \mathrm{d}\omega\, f(P,\omega)\, g(P,\omega) = \langle f|g\rangle \tag{17}$$

Because both distributions are normalized, the above inner product would equal unity in the case of the absence of correlation in the $\rho^{2D}_{\omega,P}$ distribution. If there is a correlation between ω and P, the following quantity, χ, represents the magnitude of that correlation

$$\int \mathrm{d}\tau (f-g)^2 = \chi^2 \tag{18}$$

where χ^2 ranges from 0 to 2. It can be readily shown that $\langle f|g\rangle = 1 - \chi^2/2$. Note that if $\langle f|g\rangle = 1$, χ^2 equals 0 and there is no correlation between ω and P, while if $\langle f|g\rangle = 0$, χ^2 equals 2 and there will be high correlation between ω and P. Intermediate values of $\langle f|g\rangle$ and χ^2 will indicate some correlation between ω and P. In this study, the $\langle f|g\rangle$ and χ^2 are found to be 0.99 and 0.02, respectively, for **1**, suggesting almost no correlation between ω and P. Correlation studies on oligomers also reveal that there is very little correlation between the rotamers and the respective ring conformations. The rotamer distributions show similar trends for all P values with $gg > gt > tg$ for **1**−**6**.

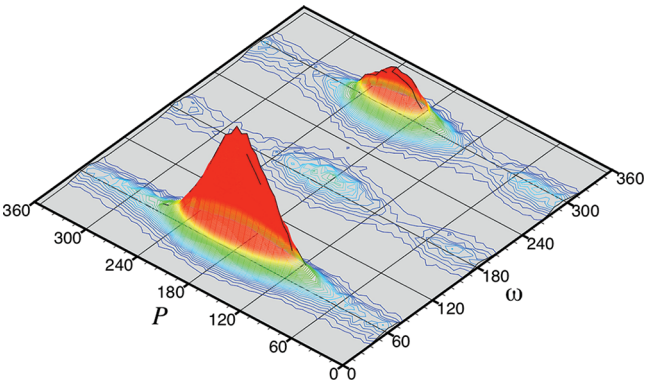

Figure 12. Joint probability distribution of the puckering angle (P) and the torsion angle (ω) for **3** in solution. All three rings have similar joint probability distributions. The units of the angles ω and P are degrees.

Determination of Experimental Rotamer Populations. We have seen that the average coupling constants for **1** obtained by using umbrella sampling simulations agree very well with experimental results (Table 2). This average coupling constant was obtained from all of the $J(\phi)$ and $\rho(\phi)$ values in the range of 0 to 360° and accounts for thermal fluctuations. When using eq 3 to determine rotamer populations from experimental results, only three discrete values of $J(\phi_i)$ and ϕ_i are used, and one, therefore, neglects these effects and assumes that each rotamer is "frozen" at some value of the dihedral angle. We propose here a simple approach to properly account for thermal fluctuations of the dihedral angle when determining experimental rotamer populations.

According to our approach, the average coupling constant $\langle J\rangle$ is given by the following sum of integrals:

$$\langle J\rangle = \int J(\phi)\, \rho_{gg}(\phi)\, \mathrm{d}\phi + \int J(\phi)\, \rho_{gt}(\phi)\, \mathrm{d}\phi + \int J(\phi)\, \rho_{tg}(\phi)\, \mathrm{d}\phi \tag{19}$$

where $\rho_i(\phi)$ is the local distribution function corresponding to rotamer i. Umbrella sampling simulations along the H4−C4−C5−H5R and H4−C4−C5−H5S dihedrals reveal three distinct Gaussian type distributions in the range of 0 to 360°. Each of these Gaussian distributions corresponds to a particular rotamer. In our approach, the mean and standard deviations were calculated from the three populations of the O4−C4−C5−O5 dihedral angle obtained from the umbrella sampling simulation. As shown above, the H4−C4−C5−H5R and H4−C4−C5−H5S dihedral angle distributions can be obtained by analysis of the O4−C4−C5−O5 dihedral angle. Therefore, the mean and standard deviations can be used to construct thermal Gaussian distributions of H4−C4−C5−H5R and H4−C4−C5−H5S of the form

$$g_i(\phi) = \frac{1}{\sqrt{2\pi\sigma^2}}\, \mathrm{e}^{-(\phi-\phi_i)^2/2\sigma^2} \tag{20}$$

for each rotamer i, where σ is the standard deviation and ϕ_i is the mean of the distribution. The experimental rotamer population

Table 4. Experimental Rotameric Distribution (%) about the C4−C5 Bond of 1, 3, and 6 in Solution Obtained Using the Gaussian Distribution Approach[a]

	1	3			6					
		A	B	C	A	B	C	D	E	F
X_{gt}	56	58	55	58	58	58	60	59	60	59
X_{tg}	14	19	19	12	19	20	21	21	20	11
X_{gg}	30	23	25	30	23	22	19	20	20	30

[a] The values obtained from the ideal and most probable dihedrals are very similar to those obtained from the Gaussian approach, and these are provided in the Supporting Information.

($X_{i=gg,gt,tg}$) is obtained by using expressions for $^3J_{H4,H5R}$ and $^3J_{H4,H5S}$ of the form below

$$\langle J \rangle = X_{gt}\int_0^{120} J(\phi)\, g_{gt}(\phi)\, d\phi + X_{tg}\int_{120}^{240} J(\phi)\, g_{tg}(\phi)\, d\phi + X_{gg}\int_{240}^{360} J(\phi)\, g_{gg}(\phi)\, d\phi \quad (21)$$

along with the restriction that the populations should add up to unity.

The experimental rotamer populations obtained for **1**, **3**, and **6** using our proposed approach are summarized in Table 4. The experimental rotamer populations for **1** and all of the terminal rotamers in **3** and **6** decrease from $X_{gt} > X_{gg} > X_{tg}$. In the case of internal rotamers in **3** and **6**, the rotamer population decreases from $X_{gt} > X_{gg} \approx X_{tg}$. The differences between X_{gg} and X_{tg} are larger for the terminal rotamers than the internal rotamers in **3** and **6**. We also determined mean and standard deviations of the populations of H4−C4−C5−H5*R* and H4−C4−C5−H5S dihedral angles of **1** using the conventional MD and umbrella sampling simulations. The mean and standard deviations were used to construct the Gaussian distributions about the H4−C4−C5−H5*R* and H4−C4−C5−H5S dihedrals, which were then used to calculate the experimental rotamer populations of **1**. The experimental rotamer population obtained from the MD (X_{gt} = 58%, X_{tg} = 13%, X_{gg} = 29%) and the umbrella sampling parameters (X_{gt} = 57%, X_{tg} = 12%, X_{gg} = 31%) were found to be very similar to those obtained from the O4−C4−C5−O5 dihedral angle (Table 4). In our opinion, the thermal Gaussian distribution approach should be used because it properly accounts for thermal fluctuations in the dihedral angles unlike earlier studies[14−17] where only either ideal dihedral angles (60°, 180°, and 300°) or the most probable dihedral values from conventional MD simulations were used to calculate the experimental rotamer population. In this study, the experimental rotamer population of **1** and **3** obtained from ideal and most probable dihedral angles were found to differ by a few percentage units when compared to the thermal Gaussian distribution approach.

A comparison of theoretical and experimental rotamer populations (Tables 1 and 4) shows that the rotamer populations obtained from simulation decrease from $X_{gg} > X_{gt} > X_{tg}$, while the experimental values decrease from $X_{gt} > X_{gg} > X_{tg}$. The experimental rotamer populations of course greatly depend on the quality of the *J* function. One explanation for the difference between experimental and theoretical rotamer populations is that the DFT-based Karplus relationship used for $^3J_{H4,H5S}$ led to an average coupling constant that differed by about 1.3 Hz from experimental results (see Table 2). One could adjust the $^3J_{H4,H5S}$ function to obtain average couplings that agree better with experimental results and subsequently use this adjusted $^3J_{H4,H5S}$ function to repeat the calculation of experimental rotamer populations. We do not attempt this sort of adjustment here.

CONCLUSIONS

Umbrella sampling simulations were carried out to accurately determine the C4−C5 rotamer populations and the distribution of ring puckering in oligoarabinofuranosides **1**−**6**. A comparison of the rotamer populations calculated with umbrella sampling and conventional MD simulations for monomer **1** reveals that umbrella sampling reproduces the results obtained from the MD simulation. For larger oligomers (e.g., **3**), converged rotamer populations were obtained after several hundred nanoseconds of conventional MD simulations, which limits the use of conventional MD simulations for even larger oligomers (e.g., **6**). On the other hand, convergence of the rotamer populations was achieved more efficiently with the umbrella sampling simulations. In general, an umbrella sampling simulation only allows one to calculate properties associated with the reaction coordinate being restrained. We have shown that for these oligofuranosides, results based on a C4−C5 dihedral reaction coordinate can also be used to obtain accurate proton−proton dihedral distributions. Vicinal proton−proton coupling constants ($^3J_{H,H}$) could therefore be calculated from the information obtained from umbrella sampling simulations and using the DFT-based Karplus relationship for methyl α-L-arabinofuranoside. For **1**, the $^3J_{H,H}$ values agree very well with those obtained directly from experimental results, while for oligomers **3** and **6** the $^3J_{H,H}$ values obtained using the umbrella sampling simulations are found to be very similar to those obtained from conventional MD simulations conducted on **3**. Ring puckering distributions and amplitudes were also calculated from the umbrella sampling simulations, and the results agree very well with those obtained from the MD simulations. We have established that the umbrella sampling simulations along a particular bond can be used to determine ring conformations, as the energy barriers for changes in the ring geometries are much lower. A correlation study showed that there is no correlation between the ring conformation and rotamer population in α-L-arabinofuranosides in solution.

Because short umbrella sampling simulations provide reliable rotamer populations and ring puckering distributions in **1**−**6**, it is a desirable and more efficient alternative to long MD simulations for the conformational study of larger oligofuranosides. The efficiency of the umbrella sampling approach also makes it possible to envisage simulations with more accurate descriptions of the electronic structure in order to capture polarization effects. The simulation of larger systems nevertheless remains a great challenge, and approaches to further improve sampling efficiency will continue to be developed.

ASSOCIATED CONTENT

Supporting Information. Synthetic details, NMR spectra, and coupling constant data (experimental and theoretical); $^3J_{H4,H5}$ coupling profiles; C4−C5 rotameric distributions and convergence plots; dihedral angle and puckering distributions; and H-bond occupancies. This material is available free of charge via the Internet at http://pubs.acs.org.

AUTHOR INFORMATION

Corresponding Author
*E-mail: pnroy@uwaterloo.ca.

ACKNOWLEDGMENT

We are grateful to the Natural Sciences and Engineering Council of Canada (NSERC), the Canada Foundation for Innovation (CFI), and the Alberta Ingenuity Centre for Carbohydrate Science for financial support as well as the SHARCNET for dedicated computational resources. M.R.R. is supported by an Alberta Innovates Health Solutions Ph.D. studentship and H. A.T by a Queen Elizabeth II scholarship.

REFERENCES

(1) Lowary, T. L. *J. Carbohydr. Chem.* **2002**, *21*, 691.
(2) Brennan, P. J.; Nikaido, H. *Annu. Rev. Biochem.* **1995**, *64*, 29.
(3) Doblin, M. S.; Pettolino, F.; Bacic, A. *Funct. Plant Biol.* **2010**, *37*, 357.
(4) Kaur, D.; Guerin, M. E.; Skovierova, H.; Brennan, P. J.; Jackson, M. *Adv. Appl. Microbiol.* **2009**, *69*, 23.
(5) Seifert, G. J.; Roberts, K. *Annu. Rev. Plant. Biol.* **2007**, *58*, 137.
(6) Leonard, R.; Petersen, B. O.; Himly, M.; Kaar, W.; Wopfner, N.; Kolarich, D.; van Ree, R.; Ebner, C.; Duus, J. O.; Ferreira, F.; Altmann, F. *J. Biol. Chem.* **2005**, *280*, 7932.
(7) D'Souza, F. W.; Ayers, J. D.; McCarren, P. R.; Lowary, T. L. *J. Am. Chem. Soc.* **2000**, *122*, 1251.
(8) McCarren, P. R.; Gordon, M. T.; Lowary, T. L.; Hadad, C. M. *J. Phys. Chem. A.* **2001**, *105*, 5911.
(9) Gordon, M. T.; Lowary, T. L.; Hadad, C. M. *J. Org. Chem.* **2000**, *65*, 4954.
(10) Gordon, M. T.; Lowary, T. L.; Hadad, C. M. *J. Am. Chem. Soc.* **1999**, *121*, 9682.
(11) Houseknecht, J. B.; Lowary, T. L.; Hadad, C. M. *J. Phys. Chem. A.* **2003**, *107*, 5763.
(12) Houseknecht, J. B.; Lowary, T. L.; Hadad, C. M. *J. Phys. Chem. A.* **2003**, *107*, 372.
(13) Houseknecht, J. B.; McCarren, P. R.; Lowary, T. L.; Hadad, C. M. *J. Am. Chem. Soc.* **2001**, *123*, 8811.
(14) Seo, M.; Castillo, N.; Ganzynkowicz, R.; Daniels, C. R.; Woods, R. J.; Lowary, T. L.; Roy, P.-N. *J. Chem. Theory Comput.* **2007**, *4*, 184.
(15) Taha, H. A.; Castillo, N.; Roy, P. N.; Lowary, T. L. *J. Chem. Theory Comput.* **2009**, *5*, 430.
(16) Taha, H. A.; Castillo, N.; Sears, D. N.; Wasylishen, R. E.; Lowary, T. L.; Roy, P.-N. *J. Chem. Theory Comput.* **2010**, *6*, 212.
(17) Taha, H. A.; Roy, P.-N.; Lowary, T. L. *J. Chem. Theory Comput.* **2011**, *7*, 420.
(18) It should be noted that structures of three related D-arabinofuranose-containing oligosaccharides in complex with an antibody Fab fragment were published recently: Murase, T.; Zheng, R. B.; Joe, M.; Bai, Y.; Marcus, S. L.; Lowary, T. L.; Ng, K. K. S. *J. Mol. Biol.* **2009**, *392*, 381.
(19) Taylor, E. J.; Smith, N. L.; Turkenburg, J. P.; D'Souza, S.; Gilbert, H. J.; Davies, G. J. *Biochem. J.* **2006**, *395*, 31.
(20) Miyanaga, A.; Koseki, T.; Matsuzawa, H.; Wakagi, T.; Shoun, H.; Fushinobu, S. *J. Biol. Chem.* **2004**, *279*, 44907.
(21) Yamaguchi, A.; Tada, T.; Wada, K.; Nakaniwa, T.; Kitatani, T.; Sogabe, Y.; Takao, M.; Sakai, T.; Nishimura, K. *J. Biochem.* **2005**, *137*, 587.
(22) Paes, G.; Skov, L. K.; O'Donohue, M. J.; Remond, C.; Kastrup, J. S.; Gajhede, M.; Mirza, O. *Biochemistry* **2008**, *47*, 7441.
(23) Nurizzo, D.; Turkenburg, J. P.; Charnock, S. J.; Roberts, S. M.; Dodson, E. J.; McKie, V. A.; Taylor, E. J.; Gilbert, H. J.; Davies, G. J. *Nat. Struct. Biol.* **2002**, *9*, 665.
(24) Angyal, S. J. *Adv. Carbohydr. Chem. Biochem.* **1984**, *42*, 15.
(25) Altona, C.; Sundaral, M. *J. Am. Chem. Soc.* **1972**, *94*, 8205.
(26) Altona, C.; Sundaralingam, M. *J. Am. Chem. Soc.* **1973**, *95*, 2333.
(27) Oleary, D. J.; Kishi, Y. *J. Org. Chem.* **1994**, *59*, 6629.
(28) Wolfe, S. *Acc. Chem. Res.* **1972**, *5*, 102.
(29) Devries, N. K.; Buck, H. M. *Carbohydr. Res.* **1987**, *165*, 1.
(30) Bock, K.; Duus, J. O. *J. Carbohydr. Chem.* **1994**, *13*, 513.
(31) Tvaroska, I.; Carver, J. P. *J. Phys. Chem. A.* **1997**, *101*, 2992.
(32) Dzakula, Z.; Westler, W. M.; Edison, A. S.; Markley, J. L. *J. Am. Chem. Soc.* **1992**, *114*, 6195.
(33) Dzakula, Z.; DeRider, M. L.; Markley, J. L. *J. Am. Chem. Soc.* **1996**, *118*, 12796.
(34) Altona, C.; Francke, R.; de Haan, R.; Ippel, J. H.; Daalmans, G. J.; Westra Hoekzema, A. J. A.; Wijk, V. *J. Magn. Reson. Chem.* **1994**, *32*, 670.
(35) Case, D. A.; Darden, T. A.; Cheatham, T. E.; Simmerling, C. L.; Wang, J.; Duke, R. E.; Luo, R.; Crowley, M.; Walker, R. C.; Zhang, W.; Merz, K. M.; Wang, B.; Hayik, S.; Roitberg, A.; Seabra, G.; Kolossváry, I.; Wong, K. F.; Paesani, F.; Vanicek, J.; Wu, X.; Brozell, S. R.; Steinbrecher, T.; Gohlke, H.; Yang, L.; Tan, C.; Mongan, J.; Hornak, V.; Cui, G.; Mathews, D. H.; Seetin, M. G.; Sagui, C.; Babin, V.; Kollman, P. A. *AMBER 10*; University of California: San Francisco, 2008.
(36) Hornak, V.; Abel, R.; Okur, A.; Strockbine, B.; Roitberg, A.; Simmerling, C. *Proteins* **2006**, *65*, 712.
(37) Woods, R. J.; Dwek, R. A.; Edge, C. J.; Fraserreid, B. *J. Phys. Chem.* **1995**, *99*, 3832.
(38) Case, D. A.; Cheatham, T. E.; Darden, T.; Gohlke, H.; Luo, R.; Merz, K. M.; Onufriev, A.; Simmerling, C.; Wang, B.; Woods, R. J. *J. Comput. Chem.* **2005**, *26*, 1668.
(39) Cieplak, P.; Cornell, W. D.; Bayly, C.; Kollman, P. A. *J. Comput. Chem.* **1995**, *16*, 1357.
(40) Cornell, W. D.; Cieplak, P.; Bayly, C. I.; Gould, I. R.; Merz, K. M.; Ferguson, D. M.; Spellmeyer, D. C.; Fox, T.; Caldwell, J. W.; Kollman, P. A. *J. Am. Chem. Soc.* **1995**, *117*, 5179.
(41) Kirschner, K. N.; Yongye, A. B.; Tschampel, S. M.; Gonzalez-Outeirino, J.; Daniels, C. R.; Foley, B. L.; Woods, R. J. *J. Comput. Chem.* **2008**, *29*, 622.
(42) Jorgensen, W. L.; Chandrasekhar, J.; Madura, J. D.; Impey, R. W.; Klein, M. L. *J. Chem. Phys.* **1983**, *79*, 926.
(43) Adelman, S. A.; Doll, J. D. *J. Chem. Phys.* **1976**, *64*, 2375.
(44) Berendsen, H. J. C.; Postma, J. P. M.; van Gunsteren, W. F.; DiNola, A.; Haak, J. R. *J. Chem. Phys.* **1984**, *81*, 3684.
(45) Ryckaert, J. P.; Ciccotti, G.; Berendsen, H. J. C. *J. Comput. Phys.* **1977**, *23*, 327.
(46) Darden, T.; York, D.; Pedersen, L. *J. Chem. Phys.* **1993**, *98*, 10089.
(47) Essmann, U.; Perera, L.; Berkowitz, M. L.; Darden, T.; Lee, H.; Pedersen, L. G. *J. Chem. Phys.* **1995**, *103*, 8577.
(48) Roux, B. *Comput. Phys. Commun.* **1995**, *91*, 275.
(49) Chandler, D. *J. Chem. Phys.* **1978**, *68*, 2959.
(50) Chandler, D. *Introduction to Modern Statistical Mechanics*; Oxford University Press Inc.: New York, 1987.
(51) Allen, M. P.; Tildesley, D. J. *Computer Simulation of Liquids*; Oxford University Press Inc.: New York, 1987.
(52) Torrie, G. M.; Valleau, J. P. *Chem. Phys. Lett.* **1974**, *28*, 578.
(53) Valleau, J. P.; Torrie, G. M. A Guide for Monte Carlo for Statistical Mechanics. In *Statistical Mechanics Part A*; Plenum Press: New York, 1977.
(54) Shen, J.; Mccammon, J. A. *Chem. Phys. Lett.* **1991**, *158*, 191.
(55) Woolf, T. B.; Roux, B. *J. Am. Chem. Soc.* **1994**, *116*, 5916.
(56) Haydock, C.; Sharp, J. C.; Prendergast, F. G. *Biophys. J.* **1990**, *57*, 1269.
(57) Kumar, S.; Bouzida, D.; Swendsen, R. H.; Kollman, P. A.; Rosenberg, J. M. *J. Comput. Chem.* **1992**, *13*, 1011.
(58) Grossfield, A. *WHAM*, version 2.0.2.; 2011.
(59) Efron, B.; Tibshirani, R. J. *An Introduction to the Bootstrap*; Chapman and Hall, CRC: Boca Raton, FL, 1994.
(60) Liu, C.; Richards, M. R.; Lowary, T. L. *Org. Biomol. Chem.* **2011**, *9*, 165.
(61) Robinson, P. T.; Pham, T. N.; Uhrin, D. *J. Magn. Reson.* **2004**, *170*, 97.

(62) Reich, H. J. In *J. Chem. Educ. Software*; 3D2: Madison, WI, 1996.
(63) Yin, H.; D'Souza, F. W.; Lowary, T. L. *J. Org. Chem.* **2002**, *67*, 892.
(64) Carapito, R.; Imberty, A.; Jeltsch, J. M.; Byrns, S. C.; Tam, P. H.; Lowary, T. L.; Varrot, A.; Phalip, V. *J. Biol. Chem.* **2009**, *284*, 12285.
(65) For compounds **2**−**6**, we used the Karplus equations derived for the monosaccharide **1**. The calculated coupling constants using Karplus equations developed specifically for (1→5)-linked disaccharide showed little difference when compared with those for the monosaccharide (Supporting Information).
(66) Given the close similarity of the coupling constants for trisaccharide **3** and hexasaccharide **6**, analgous NMR studies on oligosaccharides **2**, **4**, and **5** were not carried out.
(67) Evdokimov, A. G.; Kalb, A. J.; Koetzle, T. F.; Klooster, W. T.; Martin, J. M. L. *J. Phys. Chem. A* **1999**, *103*, 744.

JCTC Journal of Chemical Theory and Computation

ARTICLE

pubs.acs.org/JCTC

Improved Binding Free Energy Predictions from Single-Reference Thermodynamic Integration Augmented with Hamiltonian Replica Exchange

Ilja V. Khavrutskii* and Anders Wallqvist

Biotechnology HPC Software Applications Institute, Telemedicine and Advanced Technology Research Center, U.S. Army Medical Research and Materiel Command, Fort Detrick, Maryland 21702, United States

ABSTRACT: Reliable predictions of relative binding free energies are essential in drug discovery, where chemists modify promising compounds with the aim of increasing binding affinity. Conventional thermodynamic integration (TI) approaches can estimate corresponding changes in binding free energies but suffer from inadequate sampling due to the ruggedness of the molecular energy surfaces. Here, we present an improved TI strategy for computing relative binding free energies of congeneric ligands. This strategy employs a specific, unphysical single-reference (SR) state and Hamiltonian replica exchange (HREX) to locally enhance sampling. We then apply this strategy to compute relative binding free energies of 12 ligands in the L99A mutant of T4 lysozyme. Besides the ligands, our approach enhances hindered rotations of the important V111 as well as V87 and L118 side chains. Concurrently, we devise practical strategies to monitor and improve HREX-SRTI efficiency. Overall, the HREX-SRTI results agree well (R^2 = 0.76, RMSE = 0.3 kcal/mol) with available experimental data. When optimized for efficiency, the HREX-SRTI precision matches that of experimental measurements.

1. INTRODUCTION

High-quality predictions of binding free energies of small molecules to their biomolecular targets are important in drug design. The continued growth of computational power has enabled applications of statistical mechanics-based free energy perturbation (FEP) and thermodynamic integration (TI) methods to real life problems.[1−5] These advanced computational techniques are considered gold standards for binding free energy predictions, akin to isothermal titration calorimetry (ITC)—a technique that measures the binding free energies experimentally.[6,7]

Since their inception, great progress has been made in improving FEP and TI methods. Introduction of the soft-core potentials has made the calculations more reliable.[8−10] Subsequently, multiconfiguration simulation protocols[11] have laid the foundation for the application of generalized ensemble strategies such as Hamiltonian replica exchange (HREX)[12−17] which further improve the quality of the FEP and TI simulations.[18−22] Meanwhile, better postprocessing protocols have been developed that resulted in more reliable predictions of free energies and assessments of corresponding standard deviations.[4,23−27]

Despite this progress, binding free energy calculations remain challenging because of sampling limitations that are inherent in the molecular dynamics (MD) methods used in the simulations. Conventional FEP and TI free energy calculations are known to be sensitive to starting conformations of the bound complexes. For example, in a well-studied L99A mutant of T4 lysozyme, the conformation of the binding site residue V111 affects binding free energies of indene and p-xylene ligands by as much as 6 kcal/mol.[1,28−30] Other hindered residues can have a similar effect.[1] The predictions also depend on the initial orientation of the ligands in the binding pocket. These challenges are likely to be general and, therefore, need to be properly addressed.

Many enhanced sampling approaches have been devised to combat conformational challenges. It is impossible to list all of them here, but we will name a few that benefit alchemical free energy calculations. One of the earliest approaches scaled parts of the potential energy before and after an alchemical transformation to enhance sampling.[31] Recently, an approach called accelerated molecular dynamics (AMD) was combined with alchemical free energy calculations.[32−34] This approach adds a boosting potential to reduce barriers and is also independent of alchemical transformations.[35] Other methods exploited the alchemical transformations to enhance sampling. Examples include λ dynamics[36−38] or its Monte Carlo (MC) counterparts, such as chemical MC/MD[39,40] and more general simulated scaling.[41,42] In fact, these methods share important features with currently developing FEP and TI methods augmented with Hamiltonian replica exchange (HREX).[15−22,43]

Enhanced sampling will overcome dependence of FEP and TI predictions on the starting conformations and ultimately improve their accuracy and precision. Judiciously combining multiconfigurational FEP and TI methods with HREX can achieve enhanced sampling.[22,43] Previously, we presented a TI variant, called single-reference TI augmented with HREX (HREX-SRTI), which achieved convergence of solvation free energies for a challenging case of an amide system where conventional FEP and TI methods failed.[22] The amide in question had an internal barrier to cis/trans interconversion that was insurmountable in conventional MD simulations. HREX-SRTI was able to generate converged results using simulation times of only 4 ns.

In the present study, we apply HREX-SRTI to the well-studied T4 lysozyme mutant. Although this system has a simple binding

Received: June 6, 2011
Published: August 15, 2011

site—a hydrophobic cavity buried beneath the protein surface—it is sufficiently complex to render conventional FEP and TI approaches ineffective. Importantly, our binding free energy predictions for this system can be compared to the previously published independent computational and experimental values.[1,28−30]

First, we assess the variability in the free energy predictions using regular SRTI. Then, we employ SRTI with the HREX option and demonstrate that HREX efficiency is crucial to obtaining converged results. Thus, we provide practical recipes to improve the efficiency of HREX-SRTI simulations. Finally, we use one of these recipes to optimize HREX efficiency and obtain highly converged results for the most challenging of the ligands—indole.

2. METHODS

2.1. Parameters for Small Molecule Ligands. We studied 12 small molecules as follows: benzene, toluene, *o*-xylene, *p*-xylene, ethyl-benzene, *n*-propyl-benzene, *n*-butyl-benzene, *i*-butyl-benzene, phenol, indene, benzofuran, and indole. The initial coordinates of all of the small molecules in the present study were derived using the program CORINA.[44] Where applicable, we performed conformational expansion using the program ROTATE.[45] Two charge models described in sections 2.1.1 and 2.1.2 were used in combination with the GAFF force field for small molecules.[46] Each conformational ensemble was structurally refined through geometry optimization using the AM1 semiempirical quantum mechanical potential[47] as implemented in MOPAC7, version1.11.[48]

2.1.1. AM1BCC Charge Model. Partial charges from each unique conformation were accumulated using Boltzmann weighting with appropriate degeneracies by their AM1 energies at 300 K. The final AM1 charges were symmetrized where applicable and then augmented through the BCC procedure[49,50] implemented in the ANTECHAMBER program[51,52] from AMBER TOOLS, version 1.2. The resulting conformation-independent, properly symmetrized set of AM1BCC charges is expected to reproduce HF/6-31G(d) RESP charges to a good approximation.[53−56]

2.1.2. RESP Charge Model. For a select subset of molecules, we derived HF/6-31G(d) restricted electrostatic potential fit (RESP) partial charges using B3LYP/6-31G(d) optimized geometries. The geometry optimization and the electrostatic potential calculations were achieved using Gaussian 09.[57] The RESP fit[58] was performed using the ANTECHAMBER program.

2.2. Setup of Protein−Ligand Complexes. Coordinates of all of the ligands in complexes with the L99A mutant of T4 lysozyme were derived from a crystal structure (PDB: 181L) of the protein bound to benzene.[59] Initial placements of ligands other than benzene were derived using graph theory. Specifically, molecules were represented as graphs on the basis of their atom and bond types. Subsequently, association graphs were constructed, and maximal cliques were found to match atoms in the benzene rings of each molecule to those of the bound benzene.[60] There are 12 different cliques that give rise to 12 unique placements of each ligand within the binding site of the protein. Some of the cliques are degenerate depending on the symmetry of the molecule. Thus, for benzene, all 12 cliques are degenerate, yielding identical complex structures that differ only in the numbering of the carbon atoms of the ligand. However, for ligands such as benzofuran, indene, and indole, each clique yields a unique conformation of the complex.

By construction, initial protein coordinates and those of the benzene ring are identical for all of the complexes, while the atoms protruding from the benzene ring change their position. In cases with branched ligands, such as *n*-propyl-, *n*-butyl-, and *i*-propyl-benzene, the protrusions have been examined for steric clashes with protein side chains.

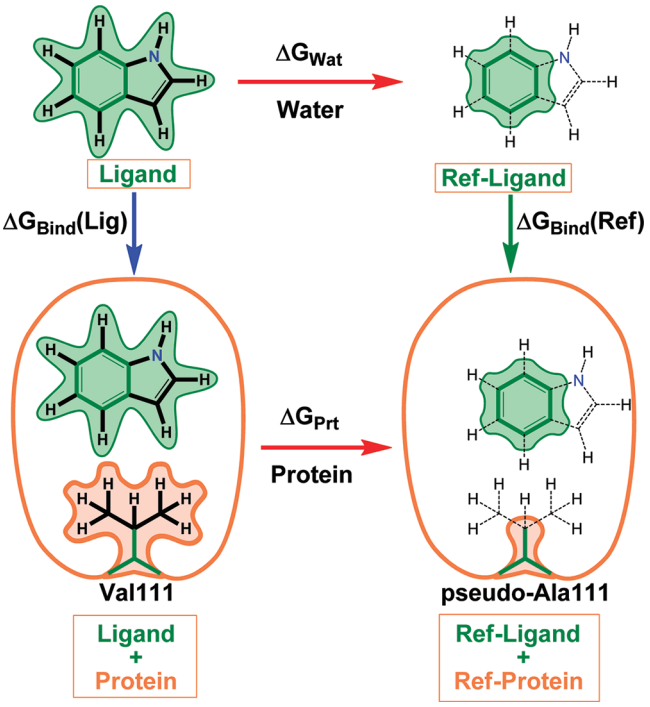

Figure 1. Thermodynamic cycle for computing binding free energies relative to an unhindered, unphysical reference state using SRTI. Horizontal arrows represent alchemical transformations of indole into the benzene core in water and the protein binding site. The protein residue V111 is alchemically converted to p-A at the same time. In the reference state, the molecular volumes of the ligand and the V111 residue (shown with green and brown shaded contours, respectively) are reduced due to disappearing atoms. The disappearing atoms interact with the rest of the system through soft-core Coulomb and vdW potentials and are connected to the reference core by dashed bonds. The torsional potentials associated with the virtual atoms are removed. These changes greatly enhance translational, rotational, and torsional degrees of freedom involved in the alchemical transformation with the help of HREX, thus activating rotation of the V111 and of the ligand in the binding site.

The protein is described by an all-atom Amber 99SB molecular mechanics force field compatible with GAFF.[61] The solvation effects were modeled using a cubic periodic box of explicit TIP3P water molecules that extended at least 10 Å beyond the solute. The protein system was neutralized by adding nine Cl^- ions.

2.3. Single Reference State. The choice of the reference states in SRTI determines which degrees of freedom of the system would be accelerated.[22] To allow for enhanced sampling of the ligands in the confines of the binding pocket, we chose the benzene core without hydrogen atoms as the reference state (Figure 1). Conveniently, our ligand reference state is independent of the charge model because the benzene core atoms have no charges by construction. Previously, we successfully employed this ligand reference state in computing free energies of hydration.[22]

Similarly, choosing an appropriate protein reference state could enhance sampling of the hindered protein side chains such as Val, Leu, Ile, and Thr. Each hindered residue could be mutated to a modified Ala residue referred to as pseudo-Ala (p-Ala).

Table 1. The L99A T4 Lysozyme Mutant Relative Binding Free Energies (Standard Deviations) to a Series of Benzene Derivatives[a]

compound	exptl	FEP	SRTI	$Diff_1$	HREX-SRTI	$Diff_2$	Wat%	Prt%
			AM1BCC Charge Model					
benzene	0.0(0.2)	0.0	0.0(0.3)	*0.0*	0.0(0.2)	*0.0*	34	29
phenol	2.5(N/A)	3.3	2.2(0.6)	*−0.3*	2.3(0.4)	*−0.2*	25	26
toluene	−0.3(0.2)	0.0	−0.1(0.3)	*0.2*	−0.2(0.2)	*0.1*	30	27
ethylbenzene	−0.6(0.2)	−1.8	−0.2(0.5)	*0.3*	−0.9(0.6)	*−0.3*	27	25
n-propylbenzene	−1.4(0.2)	−1.3	−0.4(0.5)	*0.9*	−1.5(0.4)	*−0.2*	26	23
n-butylbenzene	−1.5(0.2)	−0.3	−1.0(1.2)	*0.5*	−1.4(1.1)	*0.1*	23	21
i-butylbenzene	−1.3(0.2)	−0.5	−1.4(1.2)	*−0.1*	−1.3(0.7)	*0.1*	24	21
o-xylene	0.6(0.2)	3.3	1.0(0.4)	*0.4*	0.8(0.3)	*0.2*	28	25
p-xylene	0.5(0.2)	1.0	0.5(0.6)	*0.0*	0.4(0.3)	*−0.1*	29	26
indene	0.1(0.2)	2.8	1.3(0.4)	*1.3*	1.4(0.3)	*1.3*	21	20
indole	0.3(0.2)	4.1	2.9(1.7)	*2.6*	2.8(0.5)	*2.5*	14	21
benzofuran	−0.3(0.2)	1.0	0.4(0.5)	*0.6*	0.2(0.4)	*0.5*	24	22
RMS (cyclic)			(1.0)	*1.7*	(0.4)	*1.7*		
RMS (acyclic)			(0.7)	*0.5*	(0.5)	*0.2*		
RMS (all)			(0.8)	*1.0*	(0.5)	*0.9*		
			RESP Charge Model					
indene			−0.1(0.4)	*−0.2*	0.0(0.3)	*−0.1*	*b*	*20*
indole			0.6(1.9)	*0.3*	1.1(1.8)	*0.8*	*b*	19
benzofuran			−0.4(0.6)	*−0.1*	−0.8(0.4)	*−0.5*	*b*	*22*
RMS (cyclic)			(0.8)	*0.2*	(0.7)	*0.5*		
RMS (all)[c]			(1.1)	*0.4*	(1.1)	*0.3*		

[a] Energies are in kcal/mol relative to benzene. Averages and standard deviations are over eight (cyclic) or four (acyclic) independent simulations with distinct starting positions of the ligand in the binding site of the protein and two (all) independent simulations in water. Experimental and previously reported absolute binding free energies for benzene are −5.2 and −4.6 kcal/mol, respectively. [b] Because the effect of HREX on the simulations in water is small, regular simulations were performed. $Diff_1$ is the free energy difference between regular SRTI and experimental results; $Diff_2$ is the difference between HREX-SRTI and experimental results. The Wat and Prt columns contain acceptance ratios for the corresponding legs of the thermodynamic cycle (Figure 1). For these calculations, $p = 2$, and default values of $\alpha = 1.5$ parameters were used. Each simulation was run using 12 TI windows equally spaced in λ and 4-ns-long MD runs in the NPT ensemble at 1 atm and 300 K. The terms exptl and FEP represent previously published experimental and computational free energy perturbation benchmarks.[30] [c] Combined values with RESP@HF/6-31G(d) for cyclic and AM1BCC for acyclic compounds.

In p-Ala, hydrogen atoms of the methyl side chain are united with the Cβ carbon. A mutation of a hindered residue to p-Ala in the reference state would render its side chain atoms starting with Cβ virtual. Thus, HREX would enhance hindered rotations about bonds such as Cα−Cβ, Cβ−Cγ, and outward. In addition, the alchemical mutation of binding site residues to p-Ala can render the binding site in the reference state bigger, further aiding in the sampling of ligand transitions.

In this study, we simultaneously enhance sampling of the ligand and the protein side chains by combining the corresponding unphysical reference states.

2.4. TI Simulation Setup. In order to run the simulations, we employed GROMACS version 4.0.5 in single precision. Because the simulated system is described by Amber 99SB[61] and GAFF[46] molecular mechanical force fields that are not native to GROMACS, we used the PERL conversion script, which was described previously.[62] The script also automates setup of the alchemical transformation from the real to the reference state.

2.4.1. Soft-Core Potentials. In order to avoid the end-point catastrophe at the reference state, we employed soft-core electrostatic and LJ potentials[9,10] as implemented in GROMACS.[63−67] Earlier calculations employed a GROMOS style soft-core potential (eqs 1−3). Here, λ is the Hamiltonian coupling parameter, p is the coupling power, r is the distance between a given pair of atoms, α is the soft-core parameter, and σ is the radius of interaction computed from LJ parameters. For certain polar hydrogen atoms, σ is undefined, and in those cases a fixed value is used. Originally, we used $p = 2$, $\alpha = 1.5$, and $\sigma = 0.3$ as recommended in the user manual. Subsequently, to improve the acceptance ratio and level its distribution over TI window pairs, we used an alternative soft-core potential with $p = 1$.[10] For the latter potential, we reoptimized the value of α to arrive at $\alpha = 0.4$. The optimization of the α parameter was performed to achieve the best convergence behavior by monitoring standard deviations across independent TI runs. Other more complicated measures could be used to search for better alchemical paths, but these were not pursued in this study.[68]

$$V_{AB}^{sc}(r) = (1-\lambda)\, V_A(R_A(r,\lambda)) + \lambda V_B(R_B(r,\lambda)) \quad (1)$$

$$R_A(r,\lambda) = (\alpha\sigma_A^6\lambda^p + r^6)^{1/6} \quad (2)$$

$$R_B(r,\lambda) = (\alpha\sigma_B^6(1-\lambda)^p + r^6)^{1/6} \quad (3)$$

2.4.2. MD Simulation Parameters. The production runs were performed in the NPT ensemble at $T = 300$ K and $P = 1$ atm, following the equilibration protocol described previously.[22]

The production run employed a Langevin thermostat and a Berendsen barostat,[64−67] with identical collision frequencies of 2 ps^{-1}.

Throughout the simulations, all of the bonds containing hydrogen atoms were constrained using LINCS,[69] and the integration time step was set to 2 fs. We employed the particle mesh Ewald (PME) approach for electrostatics[64−67] with a 1 nm real space cutoff and switched off van der Waals interactions over the range of 0.8−0.9 nm. Typically, production runs were 2-ns-long for each TI window, but in some cases they were extended to 4 ns. The coordinates of the system were recorded every 1000 steps for subsequent analyses.

2.4.3. Regular SRTI Simulations. To obtain the alchemical free energies or reversible works, the real and reference states of each system corresponded to values 0 and 1 of the Hamiltonian coupling parameter λ, respectively. Each alchemical SRTI transformation employed M equally separated λ windows. The majority of the simulations used M = 12, but in some cases simulations were performed with M = 23. All λ windows of an SRTI simulation had the same initial configuration. For each λ window, we recorded $\partial V/\partial\lambda$ values at every time step. The mean values $\langle \partial V/\partial\lambda \rangle$ for all of the λ windows were assembled into the final work using the Fourier beads integration procedure, which was described previously.[22]

Averages of the final work values and their standard deviations were computed using several independent simulations. Specifically, for proteins in complex with cyclic molecules (benzofuran, indene, and indole), we performed eight simulations each with distinct starting positions of the ligand. For acyclic (not cyclic) molecules, we only performed four such simulations. Finally, for all of the ligands in water, we performed two independent simulations. The differences between the alchemical work values in water and protein environments yielded the relative binding free energies with respect to the unphysical reference state. The final relative binding free energies and their standard deviations were reported with respect to benzene.

2.4.4. HREX-SRTI Simulations. In order to run HREX-SRTI simulations, we employed an in-house PERL script interfaced with GROMACS. Replica exchanges were attempted every 1000 MD steps or 2 ps. For the majority of the simulations, we attempted exchanges a total of 2000 times resulting in 4-ns-long simulations of each window. In special cases, the number of exchange attempts was reduced to 1000, decreasing the simulation time to 2 ns per window. Following the exchanges, each λ window received a new random seed to restart its MD run. All of the other simulation details were the same as those associated with regular SRTI simulations.

2.4.5. Analysis of SRTI and HREX-SRTI Results. The analysis of real state trajectories was performed with standard GROMACS tools. Specifically, the g_angle program was used to obtain time series of dihedral angles of the hindered side chains. For the Val side chain, we gathered data on the Hα−Cα−Cβ−Hβ (κ_1) dihedral, and for the Leu side chain, data on Hα−Cα−Cβ−Cγ (κ_1) and Cα−Cβ−Cγ−Hγ (κ_2) dihedrals were collected. For HREX-SRTI simulations, the real state trajectory had to be assembled from short trajectories using an in-house PERL script that followed the state through all of the exchanges.

3. RESULTS AND DISCUSSION

In order to demonstrate the utility of the SRTI approach in computing relative binding free energies, we studied ligand binding to a well-defined binding site in the L99A mutant of T4 lysozyme. Specifically, we chose a congeneric series of 12 ligands derived from benzene that has been studied previously.[28−30] We distinguished two classes of compounds within the series according to their structure outside the common benzene motif, namely cyclic and acyclic. Thus, benzofuran, indene, and indole were considered cyclic, whereas all of the remaining compounds were considered acyclic. Because all of the ligands in the series (Table 1), with the exception of benzene, can have multiple orientations in the binding pocket, this system presents a considerable challenge for binding free energy calculations.

The cyclic and acyclic ligands behave differently when in complex with the protein. For acyclic ligands, the benzene ring can flip without an overall structural change to the complex. For cyclic ligands, the benzene flip alters the overall structure of the complex. Hence, for cyclic ligands, i.e., benzofuran, indene, and indole, we selected eight orientations (four for each of the two states resulting from the benzene flip). The degeneracy with respect to the benzene flip allowed us to reduce the number of representative orientations to four for the remaining acyclic ligands. Thus, for each ligand, we performed simulations with different initial orientations in the binding pocket.

The conformations of the active site residues are equally important and should be considered when determining binding free energies.[28−30] For the L99A mutant of T4 lysozyme, the conformational state of the V111 side chain profoundly affects the computed binding free energies. Because this residue lines the surface of the binding site, inadequate sampling of its conformations has been shown to cause discrepancies of as much as 6 kcal/mol.[28−30] Other residues in the active site may have similar effects on binding free energies.[1] Hence, we need to improve sampling of the ligand and relevant protein conformations at the same time. This combination makes the problem particularly challenging.

3.1. Regular SRTI Simulations. *3.1.1. AM1BCC Charge Model.* The average variability in the relative binding free energies from regular SRTI is 0.7 kcal/mol (Table 1). Most of the ligands have standard deviations in the range of 0.3−0.6 kcal/mol. However, the largest acyclic ligands, *n*-butyl-benzene and *i*-butyl-benzene, show increased standard deviations of 1.2 kcal/mol. Surprisingly, one of the cyclic ligands, indole, exhibits a record high standard deviation of 1.7 kcal/mol. Indole, like other cyclic ligands, is expected to have hindered flip transitions in the binding site.

In comparison to experimental values, the regular SRTI approach has an RMSE of 1.0 kcal/mol relative to and excluding benzene. Smaller ligands are in good agreement—within 0.3 kcal/mol—with the available experimental data (Table 1). It should be noted that only an upper estimate of binding free energy is available for phenol, which does not bind the T4 lysozyme mutant well. For more extended acyclic molecules, such as *n*-propyl- and *n*-butyl-benzenes, the agreement is not as favorable, with *n*-propyl-benzene demonstrating the highest deviation of 0.9 kcal/mol. The predicted binding free energy for *i*-butyl-benzene is serendipitously within 0.1 kcal/mol of the experimental value. Interestingly, the cyclic ligands exhibit the largest deviations of all compounds, diverging by as much as 2.6 kcal/mol in the case of indole.

The disagreement between computed and experimental binding free energies for the heterocyclic compounds is instructive. In particular, the results for indene and benzofuran ligands were well-converged judging by the low standard deviations (Table 1). In contrast, the binding free energy of indole exhibited a large standard deviation of 1.7 kcal/mol. These observations suggest that issues other than sampling could be responsible for the

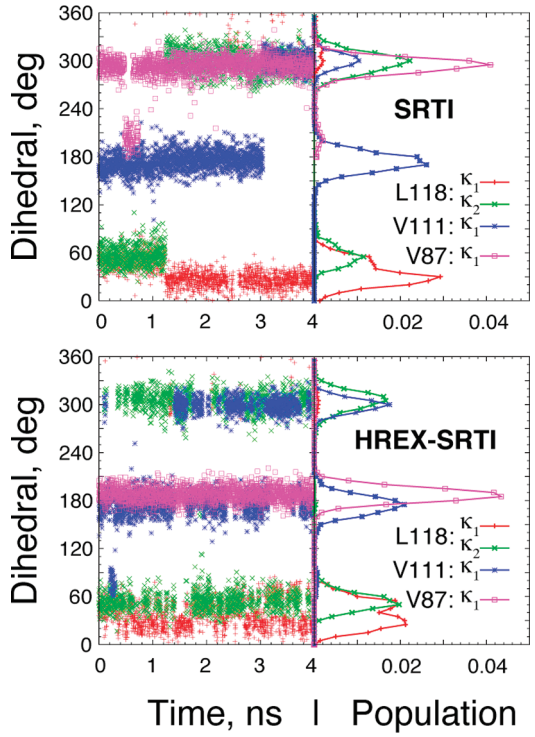

Figure 2. Side chain conformational transitions for the indole complex with the L99A mutant of T4 lysozyme using the V87p-A:V111p-A: L118p-A reference. Time series and respective histograms are presented for the κ_1 (Hα−Cα−Cβ−Hβ) torsion of V111 and V87 and for the κ_1 (Hα−Cα−Cβ−Cγ) and κ_2 (Cα−Cβ−Cγ−Hγ) torsions of L118. The bins of the histograms were 5° wide. The time series reports the corresponding values of the torsions. The top panel summarizes the regular SRTI simulation results with relatively few conformational transitions, whereas the bottom panel shows the HREX-SRTI results with numerous such transitions. The reported HREX-SRTI simulations employed 12 windows and the optimized p = 1 soft cores.

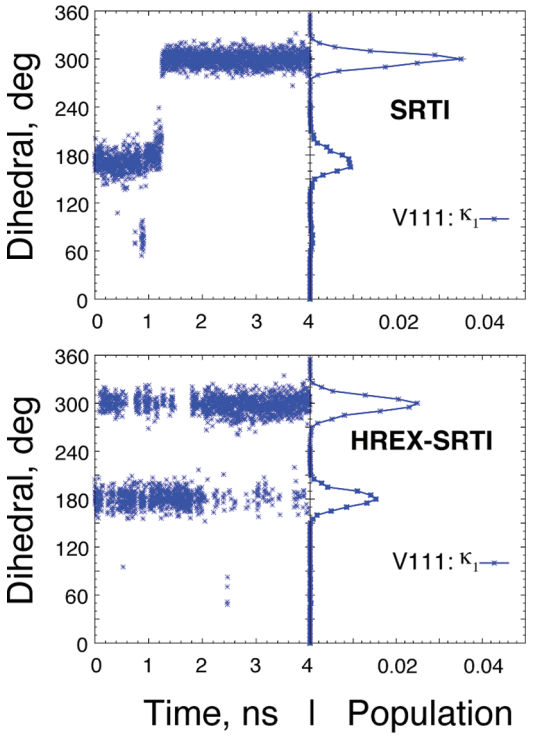

Figure 3. Side chain conformational transitions for indole complex with the L99A mutant of T4 lysozyme using the V111p-A reference. Time series and respective histograms are presented for the κ_1 (Hα−Cα−Cβ−Hβ) torsion of V111. The bins of the histograms were 5° wide. The time series report the corresponding values of the torsions. The top panel summarizes the regular SRTI simulation results with relatively few conformational transitions, whereas the bottom panel displays the HREX-SRTI results with numerous such transitions. The reported HREX-SRTI simulations employed 12 windows and the optimized p = 1 soft cores.

overall disagreement with experimental results. Because we employed the AM1BCC charge model, which approximates the RESP HF/6-31G(d) partial charges, we decided to assess the effect of the model.

3.1.2. RESP Charge Model for Cyclic Compounds. Using RESP HF/6-31G(d) charges for the cyclic compounds considerably improved the agreement of regular SRTI predictions with experimental values. Indeed, while simulations with the AM1BCC charge model systematically overestimated the binding free energies, with the RESP charges the disagreement was no longer systematic and remained within 0.3 kcal/mol. Thus, for indole, the RESP charges lowered the disagreement with experimental values by more than 2 kcal/mol. Despite the improved accuracy of the predictions, the RESP charges did not affect convergence of the cyclic ligands. Indole still had the largest standard deviation of 1.9 kcal/mol. These results suggest that a charge model can strongly affect the accuracy, but not necessarily the precision, of the computed binding free energies.

Large standard deviations in computed binding free energies identify ligands most sensitive to the initial complex configuration. The reasons for this sensitivity likely reside in hindered ligand motions. Indeed, inspecting trajectories of the ground state simulations for benzofuran using all 12 starting configurations, we found that they converge to only four metastable configurations. These metastable configurations demonstrate that the cyclic ligands do not flip freely in the binding pocket on a nanosecond time scale. Furthermore, alignment of the ligands suggests that the binding pocket has the geometry of a flattened prolate ellipsoid. Each unique configuration contributes distinctly to the binding free energy, thus, increasing the standard deviation. Therefore, enhanced sampling of the ligands in their complexes would allow the metastable configurations to rapidly interconvert, ultimately improving the quality of predictions. Because the regular SRTI approach does not have the ability to enhance these transitions alone, we need to invoke the HREX option.

3.2. Improving the SRTI Results with HREX. The use of SRTI with HREX[22] could simultaneously enhance sampling of the ligand and select protein side chains. First, we attempted to enhance motions of the ligand and the V111 side chain. Specifically, by choosing the benzene core as a ligand reference state, we intended to activate rotations of the bulkier ligands within the active site. Furthermore, by choosing a V111p-A mutant as a protein reference state (see the Methods section for definition), we expected to activate the V111 rotations that have activation barriers in the 5−8 kcal/mol range.[29,70] This strategy is expected to reduce the size of each ligand to the size of the benzene core while simultaneously enlarging the binding site around p-A111 (Figure 1) to

Table 2. Improving HREX-SRTI Efficiency for the L99A T4 Lysozyme Mutant in Complex with Indole[a]

system	N_{SRTI}	p	α	ΔG_{Pert}(SD), kcal/mol	N_{HREX}	accept, %
				V87p-A:V111p-A:L118p-A		
SRTI	*12*	*2*	*1.5*	*34.2(3.8)*		
SRTI	*23*	*2*	*1.5*	*36.9(3.3)*		
HREX-SRTI	23	2	1.5	39.5(1.4)	1000[b]	30
HREX-SRTI	12	1	0.3	29.4(0.9)	2000	17
HREX-SRTI	12	1	0.4	30.6(0.8)	2000	13
HREX-SRTI	12	1	0.5	33.6(1.2)	2000	9
				V111p-A		
SRTI	*12*	*2*	*1.5*	*−0.6(1.8)*		
HREX-SRTI	12	2	1.5	−1.0(1.8)	2000	19
HREX-SRTI	23	2	1.5	−1.6(0.5)	2000	48
HREX-SRTI	12	1	0.4	−1.7(0.2)	2000	29

[a] These results are representative of the protein leg of the thermodynamic cycle (Figure 1) using RESP@HF/6-31G(d) point charges on the ligand. N_{SRTI} and N_{HREX} refer to the number of TI windows and exchange cycles, respectively. Soft-core parameters involved in optimization are p and α (see text for description). Averages and standard deviations (SD) are over eight independent simulations with distinct starting positions of the ligand in the binding site. Two unphysical references, namely, V87p-A:V111p-A:L118p-A and V111p-A, are considered. By design, the use of the former reference with HREX should enhance side chain torsions of the V87, V111, and L118 along with rotation and flipping of the ligand. The latter reference should enhance torsions of the V111 side chain and rotations of the ligand. Unless otherwise stated, all TI windows were run in the NPT ensemble at 1 atm and 300 K for 4 ns. [b] Each window was run for 2 ns.

activate ligand flip transitions which are important in the evaluation of cyclic compounds.

Interestingly, regular SRTI simulations suggest that the V111 rotation does not significantly affect relative free energies of many ligands in the series. The free energy barrier for the valine rotation is such that it could spontaneously rotate on a time scale of several nanoseconds.[29,70] Indeed, we observed that during 4-ns-long unenhanced SRTI simulations of the ground state, V111 does spontaneously flip a few times without having a significant effect on the binding free energies of many molecules in the series (Figures 2 and 3, top panels).

The absence of the previously reported effect of V111[28−30] in cases of *p*-xylene and indene, among other ligands, is not surprising. It could be explained by the fact that SRTI computes relative binding free energies as opposed to the absolute free energies reported previously. Indeed, in the present SRTI setup, we do not need to sample an empty binding site of the protein, where V111 has a preferred conformation.[29] Nevertheless, for the largest acyclic ligands, the effect could still be significant. Therefore, we expect that enhancing the rotation of the V111 side chain through HREX would improve the overall agreement with experimental data. This approach can also be applied to enhance V111 rotation in the absolute binding free energy calculations with TI.

3.2.1. AM1BCC Charge Model and HREX-SRTI. Simply turning on the HREX option in SRTI with the V111p-A reference state produced seemingly modest improvements over the corresponding regular SRTI results (Table 1). The average standard deviation for all of the ligands decreased from 0.7 to 0.5 kcal/mol with the AM1BCC charge model. However, some of the ligands enjoyed significantly lower standard deviations versus regular SRTI. For example, *i*-butyl-benzene and indole, which had among the highest standard deviations, experienced significant drops from 1.2 to 0.7 kcal/mol and from 1.7 to 0.5 kcal/mol, respectively.

For the AM1BCC model, the overall agreement with experimental values improved only slightly, with RMSE decreasing to 0.9 kcal/mol. Most of the improvement was achieved for the acyclic ligands, which, when separated from the rest of the ligands, showed a change in RMSE from 0.5 to 0.2 kcal/mol. The cyclic compounds with AM1BCC charges are unaffected by HREX and persistently show an RMSE of 1.7 kcal/mol. Despite the improved agreement with experimental data, larger acyclic ligands still exhibit elevated standard deviations, particularly in the case of *n*-butyl-benzene.

The lack of significant improvements could indicate that other residues in the binding site might be important. Most notably, all of these simulations used 12 windows and consequently had modest acceptance ratios (Table 1). Indole in water had the lowest acceptance ratio of 14%, which increased to 21% in the protein environment with the V111p-A reference. Indole and phenol are the only two ligands in the series that have polar hydrogen atoms and an increased acceptance ratio in the protein environment.

3.2.2. RESP Charge Model and HREX-SRTI. Different charge models behave distinctly when running SRTI with the HREX option. Thus, HREX-SRTI with RESP charges for the cyclic compounds diminished the agreement with experimental results compared with that in regular SRTI. Specifically, RMSE for the three cyclic compounds increased from 0.2 to 0.5 kcal/mol. However, the average standard deviations decreased from 0.9 to 0.8 kcal/mol (Table 1). Unexpectedly, indole exhibited a sharply increased standard deviation of 1.8 kcal/mol using the RESP model compared to 0.5 kcal/mol with the AM1BCC model.

3.3. Improving HREX-SRTI Predictions. To understand the reason for poor convergence of the free energy values with HREX-SRTI and to possibly improve the results, we examined the indole system in greater detail. Specifically, we focused on the indole simulations with RESP charges that exhibited the largest disagreement with experimental values and the largest standard deviation.

3.3.1. Triple Mutant Reference State V87p-A:V111p-A:L118p-A. We hypothesized that even with the HREX option turned on, flipping of the indole might still be impeded in the V111p-A reference state. In order to test this hypothesis, we created a triple mutant reference state by mutating two additional residues, V87 and L118 to p-A. These two residues pin the benzene moiety of the ligands to the floor of the binding site. It should be noted that L118 has been experimentally shown to exhibit conformational variability similarly to V111.[1]

The triple mutant system V87p-A:V111p-A:L118p-A should completely remove the ligand flipping restriction. Moreover, this unphysical reference state could potentially open water access to the hydrophobic binding site of the L99A T4 lysozyme. In the proposed experiment, three residues would undergo alchemical transformations, making 30 atoms of the protein (nine for each valine and 12 for leucine) disappear in the reference state. While this should theoretically enhance sampling of the three residues along with the ligand, it might be difficult in practice to achieve a sufficient overall exchange rate in HREX-SRTI.[22] Hence, this test would also identify the limits of our approach in extending it to concurrent activation of multiple residues.

The triple mutant V87p-A:V111p-A:L118p-A presents a challenge for HREX-SRTI. As seen in Table 2, regular SRTI simulations with 12 and 23 windows had standard deviations of 3.8 and 3.3 kcal/mol, respectively, for just the protein leg of the thermodynamic cycle (Figure 1). The fact that the standard deviation with the triple mutant reference is more than twice as large as that with the single mutant one (1.8 kcal/mol) suggests that conformations of residues V87 and L118 may indeed affect ligand binding. The standard deviation was reduced to 1.4 kcal/mol when employing 23 windows in the HREX-SRTI simulations. The corresponding 12-window simulations did not achieve a sufficient overall exchange rate to yield results that were distinct from the regular SRTI simulations.

3.3.2. Assessing HREX Efficiency. *3.3.2.1. Round-Trip Count.* Achieving efficient exchanges is critical for obtaining converged free energies in HREX simulations.[43] The overall acceptance ratio might be inadequate to assess the efficiency of HREX simulations. While the overall acceptance ratio is a satisfactory criterion to assess the efficiency of the more widely applied temperature replica exchange (TREX) simulations in the absence of first order transitions,[71,72] the situation with HREX is different.

It is difficult to devise a universal exchange protocol for HREX simulations, because the Hamiltonian generally depends on λ nonlinearly.[15,16] One way to monitor the efficiency of HREX simulations is to examine the number of round-trips made over the simulation time.[42,71] A replica that has returned to its initial λ after visiting both $\lambda = 0$ and $\lambda = 1$ states in either order is said to have accomplished a round-trip. Although this is an excellent measure of efficiency in theory, simulations might not, in practice, be long enough to complete even a single round-trip. In addition, when increasing a number of windows, a round-trip may take longer time. Therefore, long simulation times may be required to use this measure of exchange efficiency.

Finally, we note that besides the $\lambda = 1$ window in SRTI, scaling of the dihedral and soft-core potentials can activate hindered transitions in several neighboring windows. This means that multiple windows can experience enhanced sampling. While a standard round-trip count would reflect the overall efficiency of the simulations, it may not capture diffusion of the conformations from all of the enhanced windows down to the $\lambda = 0$ window. Ultimately, we gauge the sampling gains by the reduction in the standard deviations of HREX-SRTI compared to regular SRTI, which is an independent measure of both convergence and sampling efficiency.

3.3.2.2. Acceptance Ratio Profile. Alternatively, one can generate an acceptance ratio profile for each pair of TI windows that is adjacent in λ space from the actual simulation data.[15] A flat profile would indicate equally probable exchanges between adjacent windows and, consequently, produce the largest number of round-trips possible for any given time. Therefore, we consider the acceptance ratio profile a practical alternative to the round-trip count. A simple inspection of the acceptance ratio profile could identify problems in the HREX simulations. The pair with the lowest ratio across all of the window pairs limits the round-trip rate.

3.3.2.3. Energy Difference Histograms. The acceptance ratio profile is related to the corresponding double and single energy difference histograms. Single energy difference histograms over all adjacent pairs of λ_i and λ_{i+1} involve the corresponding forward and backward energy differences. These histograms contain valuable information not only with respect to the efficiency of the simulations but also with respect to their validity.[73] Furthermore, the information from the forward and backward histograms can be used to estimate the free energy difference between the adjacent states, though such an estimator may be suboptimal.[43,73] In cases with linear dependence of the Hamiltonian on λ, the single energy difference histogram is closely related to the corresponding histogram of the energy derivative with respect to λ.[43] The double energy difference histogram comprises the energy change of the generalized ensemble that enters the Metropolis function to decide on the exchange of a particular pair.[15] These double energy difference histograms are perhaps the most informative for the purpose of the HREX. They could be computed using configurations generated by regular SRTI for a given set of λ values at an additional expense that would increase the cost of the calculation to that of HREX-SRTI.

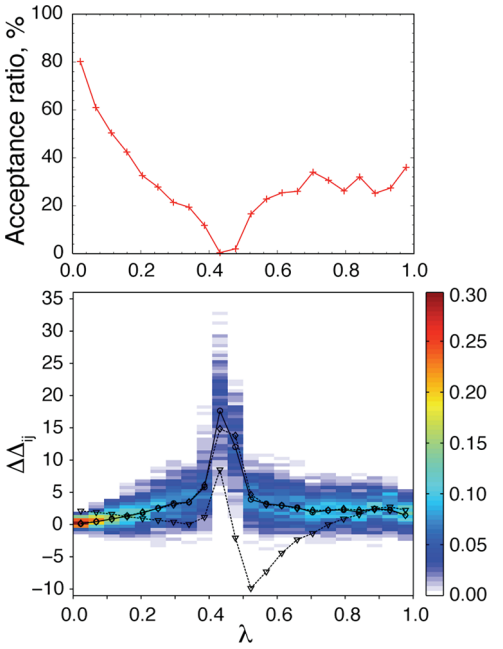

Figure 4. Monitoring efficiency of HREX-SRTI. The top panel illustrates the acceptance ratio profile for indole bound to the L99A mutant of T4 lysozyme with the V87p-A:V111p-A:L118p-A reference state. The bottom panel shows the $\Delta\Delta_{ij}$ histograms in color. On the top of the histograms is the actual profile of the mean $\Delta\Delta_{ij}$ value (solid black line with circles), its estimate from the variance (dashed black line with diamonds), and the contribution of the derivative of the $\langle\partial V/\partial\lambda\rangle$ (dashed black line with triangles), which are derived from eq 4. The HREX-SRTI simulations employed 23 windows, each run for 2 ns with $p = 2$ soft-core potentials in the NPT ensemble at 1 atm and 300 K.

3.3.3. Parameters That Influence HREX Efficiency. Predicting the dependence of the double energy difference or the acceptance ratio profile on the coupling parameter λ without actually running HREX simulations could help design more efficient simulations. Indeed, determining an optimal set of λ values that would yield a uniform acceptance ratio profile will maximize the efficiency. It is easy to show that the mean of the double energy difference histograms and the $\langle\partial V/\partial\lambda\rangle$ are related according to eq 4 (see the Appendix for derivation):

$$\langle\Delta\Delta_{ij}\rangle \approx \beta(\Delta\lambda_{ij})^2\left(\left\langle\frac{\partial^2 V}{\partial\lambda^2}\right\rangle_{(\lambda_i+\lambda_j)/2} - \frac{d}{d\lambda}\left\langle\frac{\partial V}{\partial\lambda}\right\rangle_{(\lambda_i+\lambda_j)/2}\right)$$

$$\approx \beta^2(\Delta\lambda_{ij})^2\mathrm{var}\left(\frac{\partial V}{\partial\lambda}\right)_{(\lambda_i+\lambda_j)/2} \quad (4)$$

Figure 4 shows an overlay of the $\Delta\Delta_{ij}$ distributions, their actual mean value, and its approximation using eq 4. As can be seen from Figure 4, eq 4 closely approximates the mean of the double energy difference. Furthermore, the contribution of the mean second derivative is significant and should not be neglected. Thus, eq 4 is a useful starting point for improving HREX simulation protocols.

It might be worthwhile to note that the derivative in the latter equation is related to the variance of the $\partial V/\partial\lambda$:[43,74]

$$\mathrm{var}\left\langle\frac{\partial V}{\partial\lambda}\right\rangle = \left\langle\left(\frac{\partial V}{\partial\lambda}\right)^2\right\rangle - \left\langle\frac{\partial V}{\partial\lambda}\right\rangle^2 = \beta^{-1}\left(\left\langle\frac{\partial^2 V}{\partial\lambda^2}\right\rangle - \frac{d}{d\lambda}\left\langle\frac{\partial V}{\partial\lambda}\right\rangle\right) \quad (5)$$

According to eq 5, in cases when the potential V depends on λ linearly, the variance reduces to the first derivative of the $\langle\partial V/\partial\lambda\rangle$. Because the variance is a positive quantity, the left-hand side of eq 4 would always be positive. Assuming that the value of the mean double energy difference would correspond to the most probable value of its distribution, one might expect better acceptance ratios if the mean is closer to zero. For nonlinear dependence, convexity of the potential with respect to λ would play an important role.

3.3.3.1. Increasing the Number of TI Windows. Equation 4 suggests that reducing the spacing between adjacent λ's (increasing the number of windows) would result in an increase in the acceptance probability. Indeed, similarly to our previous study,[22] increasing the number of windows from 12 to 23 in the system with the V87-pA:V111-pA:L118-pA reference state considerably improves the overall acceptance ratio from less than 10% to 30%. The reduction in standard deviation from 3.3 to 1.4 kcal/mol attests to the improved efficiency. It should be noted that the cost of the 23-window HREX-SRTI simulations was maintained similar to that of the 12-window simulation by reducing the number of exchange cycles to 1000.

The acceptance ratio profile of the HREX-SRTI simulations with V87-pA:V111-pA:L118-pA reference and 23 windows (shown in Figure 4) revealed an exchange bottleneck. Indeed, as seen in Figure 4, the acceptance ratio for the pair of windows with $\lambda_i = 0.4091$ and $\lambda_{i+1} = 0.4545$ is close to zero. In other words, our generalized ensemble was divided, with replicas sampling two independent regions of the λ space. This prevented the system from reaching a true equilibrium. Clearly, the 23-window HREX simulations, while greatly improving the overall acceptance ratio, still had the limitation of inefficient exchanges in a specific region of the λ space.

3.3.3.2. Position of Windows. Although generally applicable, simply increasing the number of windows to improve the efficiency of HREX simulations is not a viable strategy. Certainly, if successive TI windows were kept at constant λ intervals, this strategy would not remove the existing exchange bottlenecks. In addition, maintaining the number of windows at the same level as in regular SRTI simulations would be desirable from a computational cost perspective. Therefore, a better strategy would be to adjust the positions of the existing TI windows. Importantly, regular TI is sufficient for obtaining the $\partial V/\partial\lambda$ variance profile that according to eq 4 could be used to determine an optimal set of λ's for efficient HREX simulations. Alternatively, round-trip-based methods could be used to optimize placement of λ's as has been done in the context of simulated scaling.[42] However, determining the optimal set of λ's is highly system-dependent. Therefore, we did not pursue this strategy here. Fortunately, eq 4 suggests yet another strategy for improving HREX-SRTI simulations.

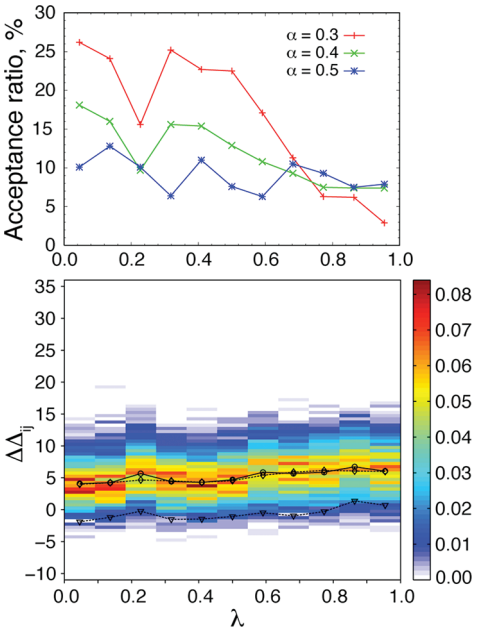

Figure 5. Optimization of HREX-SRTI efficiency by altering soft-core potential parameters. The top panel illustrates the acceptance ratio profiles for indole bound to the L99A mutant of T4 lysozyme with the V111p-A reference state. Unlike in Figure 4, these simulations employed $p = 1$ soft-core potentials with three different values for the parameter α, namely 0.3, 0.4, and 0.5. The bottom panel shows the $\Delta\Delta_{ij}$ histograms in color along with their actual mean (solid black line with circles), the estimate of the mean from the $\partial V/\partial\lambda$ variance (dashed black line with diamonds), and the contribution of the derivative of the $\langle\partial V/\partial\lambda\rangle$ (dashed black line with triangles), which are derived from eq 4. The bottom panel only shows results for the simulations with α = 0.4 that achieve the best precision. The HREX-SRTI simulations employed only 12 windows, each run for 4 ns in the NPT ensemble at 1 atm and 300 K.

3.3.3.3. Altering Mean Force Profile. Besides manipulating the number and position of TI windows, eq 4 indicates that the acceptance probability is greatly affected by the shape of the $\partial V/\partial\lambda$ variance profile. Therefore, we could improve the exchange rates by changing the shape of the profile using parameters we have at our disposal. Specifically, we can vary parameters of the soft-core potentials.

Recall the general form of the soft-core potentials available in GROMACS[9,10,63,75] (eqs 1−3). The present implementation of GROMACS supports soft-cores with $p = 1$ and $p = 2$.[9,10] The α and σ parameters have been optimized for each p using an approach that decouples Coulomb and vdW changes.[76] For the SRTI approach that simultaneously transforms Coulomb and vdW interactions, these values of parameters may be suboptimal.

Soft-core potentials with $p = 1$ are well-suited for HREX-SRTI simulations. Indeed, our earlier SRTI simulations with $p = 2$ potentials had the limitation of sharp peaks in the $\langle\partial V/\partial\lambda\rangle$ profile near $\lambda = 0$ as previously described in the literature.[9,67] These peaks are due to the hydrogen atoms with undefined σ parameters and present an obstacle to accurate integration within the Fourier beads approach.[22] In order to integrate these sharp peaks

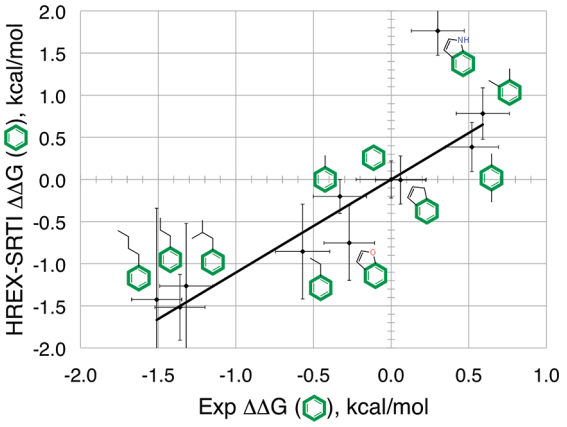

Figure 6. Comparison of the HREX-SRTI relative binding free energy predictions to experimental results. The binding free energies are relative to benzene. The best-fitted line passing through the origin is $y = 1.10x$, and the corresponding correlation coefficient is $R^2 = 0.76$. The RESP HF/6-31G(d) charge model was used for the cyclic compounds, and the AM1BCC model was used for the acyclic compounds. With the exception of indole, all of the simulations employed $p = 2$ soft-cores with default parameters. The indole prediction incorporates the results obtained with the optimized $p = 1$ soft-cores.

properly, additional TI windows have been introduced. In contrast, the profile derived using $p = 1$ soft-core potentials is devoid of such peaks.[10]

Switching to the soft-core potentials with $p = 1$ improves the acceptance ratio of the HREX-SRTI simulations. Indeed, using default parameters with only 12 windows, we obtained modest acceptance ratios of 17% in the system that had the V87-pA:V111-pA:L118-pA reference. Recall that 12-window simulations with $p = 2$ failed to achieve acceptance ratios above 10%. However, as discussed above, an improved acceptance ratio does not guarantee improved efficiency. The analysis of the acceptance ratio profile for $p = 1$ shows that windows near $\lambda = 1$ exchange poorly.

3.3.3.4. Optimization of Soft-Core Parameters for HREX. The optimization of the α parameter helps to flatten the acceptance ratio profile, rendering the HREX-SRTI more efficient. Using 12-window simulations of indole with the V87-pA:V111-pA:L118-pA reference, we varied the value of α from its default value of 0.3 to 0.4 and 0.5 at $p = 1$. Figure 5 summarizes the acceptance ratio profiles and compares predicted and actual mean $\Delta\Delta_{ij}$ for the best of them. While at $\alpha = 0.5$ we obtained the most uniform acceptance ratio profile, the overall acceptance ratio declined to 9% (Table 2). At the intermediate value of 0.4, the overall acceptance ratio was 13%, with the acceptance ratio profile demonstrating sufficient exchange probabilities near $\lambda = 1$. Clearly, one has to find a compromise between the flatness of the acceptance ratio profile and the overall acceptance ratio.

To choose the best value of parameter α, we compared the standard deviations from each set of simulations. As seen in Table 2, the intermediate value $\alpha = 0.4$ yielded the lowest standard deviations of 0.8 kcal/mol. This is a considerable improvement for the system with the triple mutant reference, in comparison to the regular 12-window SRTI simulation with $p = 2$, which had a standard deviation of 3.8 kcal/mol. Interestingly, simulations with $\alpha = 0.5$ that were associated with an almost flat acceptance ratio profile yielded a standard deviation of 1.2 kcal/mol.

3.3.3.5. Transferability of Optimized Parameters. The value of α optimized for the challenging system with the V87-pA:V111-pA:L118-pA reference state could be transferred to improve the results for an easier system with the V111-pA reference. With the latter reference state, only the V111 side chain is enhanced along with the ligand in HREX-SRTI. Indeed, as seen in Table 2, for $p = 2$, the HREX-SRTI simulations with 12 windows and the V111-pA reference achieved a standard deviation of 1.8 kcal/mol. In fact, HREX-SRTI and regular SRTI had identical standard deviations, despite the fact that the overall acceptance ratio of the former was 19%. With 23 windows, both the acceptance ratio and the standard deviation improved to 48% and 0.5 kcal/mol, respectively. To our great satisfaction, the optimized HREX-SRTI with $p = 1$ demonstrated significantly improved convergence. Remarkably, we were able to achieve an improved standard deviation of 0.2 kcal/mol using only 12 windows with an overall acceptance ratio of 29%.

Even with the optimized protocol, our predictions for indole deviate significantly from the experimental data. Figure 6 shows the comparison of our predicted binding free energies with the experimental values for all of the ligands, including the optimized results for indole. Indeed, the binding free energy of indole using the most efficient HREX-SRTI protocol is still overestimated by 1.5 kcal/mol.

3.3.3.6. Decoupling of Coulomb and vdW Transformations. As a final note on efficiency, we would like to mention that the $\langle \partial V/\partial\lambda \rangle$ profile would change radically by decoupling of the vdW and Coulomb transformations. Such a decoupling is expected to render the overall profile smoother and hence improve the acceptance ratio.[21] Indeed, HREX simulations with decoupled vdW and Coulomb transformations were recently reported.[20,21] Unfortunately, the overall acceptance ratios or acceptance ratio profiles were not provided. Since the HREX-SRTI approach was originally designed[22] to electrostatically guide ligands to better binding poses,[77,78] decoupling of the electrostatics and vdW would defeat the purpose.

3.4. HREX-SRTI As a Conformational Analysis Tool. It is instructive to analyze structural transitions in the L99A T4 lysozyme mutant in complex with indole in an attempt to explain the observed disagreement with experimental values.

3.4.1. Transitions of Hindered Residues Are Indeed Enhanced by HREX-SRTI. In order to demonstrate that HREX-SRTI enhances conformational transitions of the hindered protein side chains, we performed additional analyses of the real state trajectories ($\lambda = 0$). Figures 2 and 3 compare the dihedral angles, described in the Methods section, that characterize side chain conformations of V87, V111, and L118 where applicable. Although the histograms of the referred to dihedral angles may look similar, the time series clearly demonstrate the increased number of transitions in HREX-SRTI. In most cases, each side chain samples multiple conformational basins, supporting our earlier conclusion regarding their contributions to the binding free energies. Interestingly, the V87 side chain appears to consistently prefer a particular conformation.

3.4.2. Indole Transitions in the Binding Pocket. We also verified that indole could flip its benzene plane in HREX-SRTI simulations with triple mutant reference states. The analysis of the real state trajectories revealed multiple indole orientations in the binding pocket. In one of the orientations, the NH group of indole persistently hydrogen-bonded with the S atom of M102. In another orientation, the same NH group was involved in hydrogen bonding with the backbone carbonyl group of V87.

In the HREX-SRTI simulations with the single mutant V111p-A reference state, the ligand in-plane rotation was enhanced, but the plane flipping transitions remained hindered.

3.4.3. Water Does Not Bind T4 Lysozyme Mutant with Indole. The indole disagreement with experimental values is not attributable to a lack of water access to the binding site. Although our simulations with the V111p-A reference state are not designed to open the normally sealed active site, we have tested this hypothesis using the V87p-A:V111p-A:L118p-A reference state. By inspecting the MD trajectories, we observed that water molecules did penetrate the pocket of the triple mutant reference state ($\lambda = 1$). However, none of the configurations with water molecules inside the binding site reached the real state ($\lambda = 0$) during the HREX-SRTI simulations. This strongly suggests that water is not responsible for the observed discrepancy.

4. CONCLUSIONS

This study presented a practical application of the SRTI approach to compute relative binding free energies of small molecules to a challenging binding site in the L99A mutant of T4 lysozyme. With the HREX option, SRTI successfully enhanced sampling of the hindered transitions of protein side chains and bound ligands. Achieving efficient HREX simulations improves the quality of predictions. However, the commonly used overall acceptance ratio is not a good indicator of the efficiency of the HREX. Instead, acceptance ratio profiles should be examined and whenever possible made uniform by adjusting simulation parameters. To aid the future design of efficient simulation protocols, we have provided a useful relationship between the mean exchange energy and the corresponding $\partial V/\partial\lambda$ variance profiles. Guided by the relationship, we demonstrated that judicial changes in the soft-core potentials considerably improved HREX-SRTI simulation efficiency. Overall, the HREX-SRTI predicted relative binding free energies for a series of 12 ligands with an RMSE of 0.3 kcal/mol comparable to experimental data. Ultimately, improving efficiency of the HREX simulations may further reduce computational cost and increase the precision of the predictions.

Note, while this paper was under revision, we discovered a paper by Steiner and coauthors that used an approach identical to HREX-SRTI to compute relative free energies of a number of ligands to Plasmepsin II, albeit without accelerating any residues of the protein.[79]

APPENDIX

For a configuration R, the vertical excitation energy $\Delta_{ij}(R)$ from a Hamiltonian at λ_i to that at λ_j is calculated as follows:

$$\Delta V_{ij}(R) = V(R,\lambda_j) - V(R,\lambda_i) \tag{A1}$$

The overall potential energy change $\Delta\Delta_{ij}(R,R')$ for the generalized ensemble upon Hamiltonian exchange between two configurations R and R' from the adjacent windows λ_i and λ_j is

$$\Delta\Delta_{ij}(R,R') = \beta[\Delta V_{ij}(R)]_{\lambda_i} + \beta[\Delta V_{ji}(R')]_{\lambda_j} \tag{A2}$$

The subscripts after the square brackets indicate the Hamiltonian of the simulations used to obtain the respective configurations. Only two configurations representing each λ are involved.

The generalized ensemble average value of the double difference for a given pair of adjacent replicas is then

$$\langle\Delta\Delta_{ij}\rangle = \beta\langle\Delta V_{ij}\rangle_{\lambda_i} + \beta\langle\Delta V_{ji}\rangle_{\lambda_j} \tag{A3}$$

Using second order Taylor expansion:

$$[\Delta V_{ij}(R)]_{\lambda_i} \approx \left[\frac{\partial V(R)}{\partial\lambda}\right]_{\lambda_i}\Delta\lambda_{ij} + \frac{1}{2}\left[\frac{\partial^2 V(R)}{\partial\lambda^2}\right]_{\lambda_i}(\Delta\lambda_{ij})^2 \tag{A4}$$

where

$$\Delta\lambda_{ij} = \lambda_j - \lambda_i \tag{A5}$$

we obtain the following expression, which is equivalent to eq 4 in the main text:

$$\begin{aligned}\langle\Delta\Delta_{ij}\rangle &\approx \beta\Delta\lambda_{ij}\left(\left\langle\frac{\partial V}{\partial\lambda}\right\rangle_{\lambda_i} - \left\langle\frac{\partial V}{\partial\lambda}\right\rangle_{\lambda_j}\right) \\ &\quad + \frac{\beta(\Delta\lambda_{ij})^2}{2}\left(\left\langle\frac{\partial^2 V}{\partial\lambda^2}\right\rangle_{\lambda_i} + \left\langle\frac{\partial^2 V}{\partial\lambda^2}\right\rangle_{\lambda_i}\right) \\ &\approx \beta(\Delta\lambda_{ij})^2\left(\left\langle\frac{\partial^2 V}{\partial\lambda^2}\right\rangle_{\lambda_{(i+j)/2}} - \frac{\mathrm{d}}{\mathrm{d}\lambda}\left\langle\frac{\partial V}{\partial\lambda}\right\rangle_{\lambda_{(i+j)/2}}\right)\end{aligned} \tag{A6}$$

Recalling eq 5 from the main text we obtain the final relation.

$$\langle\Delta\Delta_{ij}\rangle \approx \beta^2(\Delta\lambda_{ij})^2\,\mathrm{var}\left\langle\frac{\partial V}{\partial\lambda}\right\rangle_{\lambda_{(i+j)/2}} \tag{A7}$$

AUTHOR INFORMATION

Corresponding Author

*E-mail: ikhavrutskii@bioanalysis.org.

ACKNOWLEDGMENT

We would like to thank Dr. In-Chul Yeh, Dr. Michael S. Lee, and Dr. Hyung-June Woo for stimulating scientific discussions. Also, we acknowledge the National Cancer Institute (NCI) for an allocation of computing time and staff support at the Advanced Biomedical Computing Center (ABCC) at National Cancer Institute, Frederick, Maryland. This work was sponsored by the U.S. Department of Defense High Performance Computing Modernization Program (HPCMP) under the High Performance Computing Software Applications Institutes (HSAI) initiative. Disclaimer: The opinions and assertions contained herein are the private views of the authors and are not to be construed as official or as reflecting the views of the U.S. Army or the U.S. Department of Defense.

REFERENCES

(1) Boyce, S. E.; Mobley, D. L.; Rocklin, G. J.; Graves, A. P.; Dill, K. A. *J. Mol. Biol.* **2009**, *394*, 747.
(2) Gallicchio, E.; Levy, R. M. *Curr. Opin. Struct. Biol.* **2011**, *21*, 161.
(3) Aleksandrov, A.; Thompson, D.; Simonson, T. *J. Mol. Recognit.* **2010**, *23*, 117.
(4) Bruckner, S.; Boresch, S. *J. Comput. Chem.* **2011**, *32*, 1303.
(5) Chodera, J. D.; Mobley, D. L.; Shirts, M. R.; Dixon, R. W.; Branson, K.; Pande, V. S. *Curr. Opin. Struct. Biol.* **2011**, *21*, 150.
(6) Leavitt, S.; Freire, E. *Curr. Opin. Struct. Biol.* **2001**, *11*, 560.
(7) Chaires, J. B. *Annu. Rev. Biophys.* **2008**, *37*, 135.
(8) Straatsma, T. P.; McCammon, J. A. *J. Chem. Phys.* **1994**, *101*, 5032.

(9) Beutler, T. C.; Mark, A. E.; van Schaik, R. C.; Gerber, P. R.; van Gunsteren, W. F. *Chem. Phys. Lett.* **1994**, *222*, 529.
(10) Shirts, M. R.; Pande, V. S. *J. Chem. Phys.* **2005**, *122*, 134508.
(11) Straatsma, T. P.; McCammon, J. A. *J. Chem. Phys.* **1991**, *95*, 1175.
(12) Kwak, W.; Hansmann, U. H. E. *Phys. Rev. Lett.* **2005**, *95*, 138102.
(13) Fukunishi, H.; Watanabe, O.; Takada, S. *J. Chem. Phys.* **2002**, *116*, 9058.
(14) Sugita, Y.; Kitao, A.; Okamoto, Y. *J. Chem. Phys.* **2000**, *113*, 6042.
(15) Hritz, J.; Oostenbrink, C. *J. Chem. Phys.* **2007**, *127*, 204104.
(16) Hritz, J.; Oostenbrink, C. *J. Chem. Phys.* **2008**, *128*, 144121.
(17) Hritz, J.; Oostenbrink, C. *J. Phys. Chem. B* **2009**, *113*, 12711.
(18) Woods, C. J.; Essex, J. W.; King, M. A. *J. Phys. Chem. B* **2003**, *107*, 13703.
(19) Woods, C. J.; King, M. A.; Essex, J. W. *Lect. Notes Comput. Sci. Eng.* **2006**, *49*, 251.
(20) Jiang, W.; Hodoscek, M.; Roux, B. *J. Chem. Theory Comput.* **2009**, *5*, 2583.
(21) Jiang, W.; Roux, B. *J. Chem. Theory Comput.* **2010**, *6*, 2559.
(22) Khavrutskii, I. V.; Wallqvist, A. *J. Chem. Theory Comput.* **2010**, *6*, 3427.
(23) Shirts, M. R.; Pande, V. S. *J. Chem. Phys.* **2005**, *122*, 144107.
(24) Shirts, M. R.; Chodera, J. D. *J. Chem. Phys.* **2008**, *129*, 124105.
(25) Shirts, M. R.; Bair, E.; Hooker, G.; Pande, V. S. *Phys. Rev. Lett.* **2003**, *91*, 140601.
(26) Bennett, C. H. *J. Comput. Phys.* **1976**, *22*, 245.
(27) Kumar, S.; Bouzida, D.; Swendsen, R. H.; Kollman, P. A.; Rosenberg, J. M. *J. Comput. Chem.* **1992**, *13*, 1011.
(28) Deng, Y.; Roux, B. *J. Chem. Theory Comput.* **2006**, *2*, 1255.
(29) Mobley, D. L.; Chodera, J. D.; Dill, K. A. *J. Chem. Theory Comput.* **2007**, *3*, 1231.
(30) Mobley, D. L.; Graves, A. P.; Chodera, J. D.; McReynolds, A. C.; Shoichet, B. K.; Dill, K. A. *J. Mol. Biol.* **2007**, *371*, 1118.
(31) Mark, A. E.; van Gunsteren, W. F.; Berendsen, H. J. C. *J. Chem. Phys.* **1991**, *94*, 3808.
(32) Wereszczynski, J.; McCammon, J. A. *J. Chem. Theory Comput.* **2011**, *6*, 3285.
(33) Fajer, M.; Hamelberg, D.; McCammon, J. A. *J. Chem. Theory Comput.* **2008**, *4*, 1565.
(34) Fajer, M.; Swift, R. V.; McCammon, J. A. *J. Comput. Chem.* **2009**, *30*, 1719.
(35) Hamelberg, D.; Mongan, J.; McCammon, J. A. *J. Chem. Phys.* **2004**, *120*, 11919.
(36) Kong, X. J.; Brooks, C. L. *J. Chem. Phys.* **1996**, *105*, 2414.
(37) Banba, S.; Guo, Z.; Brooks, C. L. *J. Phys. Chem. B* **2000**, *104*, 6903.
(38) Bitetti-Putzer, R.; Yang, W.; Karplus, M. *Chem. Phys. Lett.* **2003**, *377*, 633.
(39) Eriksson, M. A. L.; Pitera, J.; Kollman, P. A. *J. Med. Chem.* **1999**, *42*, 868.
(40) Pitera, J.; Kollman, P. *J. Am. Chem. Soc.* **1998**, *120*, 7557.
(41) Li, H.; Fajer, M.; Yang, W. *J. Chem. Phys.* **2007**, *126*, 024106.
(42) Zheng, L.; Yang, W. *J. Chem. Phys.* **2008**, *129*, 124107.
(43) Min, D.; Li, H.; Li, G.; Bitetti-Putzer, R.; Yang, W. *J. Chem. Phys.* **2007**, *126*, 144109.
(44) Sadowski, J.; Gasteiger, J.; Klebe, G. *J. Chem. Inf. Comput. Sci.* **1994**, *34*, 1000.
(45) Renner, S.; Schwab, C. H.; Gasteiger, J.; Schneider, G. *J. Chem. Inf. Model.* **2006**, *46*, 2324.
(46) Wang, J.; Wolf, R. M.; Caldwell, J. W.; Kollman, P. A.; Case, D. A. *J. Comput. Chem.* **2004**, *25*, 1157.
(47) Dewar, M. J. S.; Zoebisch, E. G.; Healy, E. F.; Stewart, J. J. P. *J. Am. Chem. Soc.* **1985**, *107*, 3902.
(48) Stewart, J. J. P. *MOPAC7*; University of Texas, Austin: Austin, TX.
(49) Jakalian, A.; Bush, B. L.; Jack, D. B.; Bayly, C. I. *J. Comput. Chem.* **2000**, *21*, 132.
(50) Jakalian, A.; Jack, D. B.; Bayly, C. I. *J. Comput. Chem.* **2002**, *23*, 1623.
(51) Wang, J. *Antechamber* **2009**, *1*, 2.
(52) Wang, J.; Wang, W.; Kollman, P. A.; Case, D. A. *J. Mol. Graphics Model.* **2006**, *25*, 247.
(53) Nicholls, A.; Mobley, D. L.; Guthrie, J. P.; Chodera, J. D.; Bayly, C. I.; Cooper, M. D.; Pande, V. S. *J. Med. Chem.* **2008**, *51*, 769.
(54) Mobley, D. L.; Bayly, C. I.; Cooper, M. D.; Dill, K. A. *J. Phys. Chem. B* **2009**, *113*, 4533.
(55) Mobley, D. L.; Bayly, C. I.; Cooper, M. D.; Shirts, M. R.; Dill, K. A. *J. Chem. Theory. Comput.* **2009**, *5*, 350.
(56) Shivakumar, D.; Deng, Y.; Roux, B. *J. Chem. Theory Comput.* **2009**, *5*, 919.
(57) Frisch, M. J.; Trucks, G. W.; Schlegel, H. B.; Scuseria, G. E.; Robb, M. A.; Cheeseman, J. R.; Scalmani, G.; Barone, V.; Mennucci, B.; Petersson, G. A.; Nakatsuji, H.; Caricato, M.; Li, X.; Hratchian, H. P.; Izmaylov, A. F.; Bloino, J.; Zheng, G.; Sonnenberg, J. L.; Hada, M.; Ehara, M.; Toyota, K.; Fukuda, R.; Hasegawa, J.; Ishida, M.; Nakajima, T.; Honda, Y.; Kitao, O.; Nakai, H.; Vreven, T.; Montgomery, J. A., Jr.; Peralta, J. E.; Ogliaro, F.; Bearpark, M.; Heyd, J. J.; Brothers, E.; Kudin, K. N.; Staroverov, V. N.; Kobayashi, R.; Normand, J.; Raghavachari, K.; Rendell, A.; Burant, J. C.; Iyengar, S. S.; Tomasi, J.; Cossi, M.; Rega, N.; Millam, N. J.; Klene, M.; Knox, J. E.; Cross, J. B.; Bakken, V.; Adamo, C.; Jaramillo, J.; Gomperts, R.; Stratmann, R. E.; Yazyev, O.; Austin, A. J.; Cammi, R.; Pomelli, C.; Ochterski, J. W.; Martin, R. L.; Morokuma, K.; Zakrzewski, V. G.; Voth, G. A.; Salvador, P.; Dannenberg, J. J.; Dapprich, S.; Daniels, A. D.; Farkas, Ö.; Foresman, J. B.; Ortiz, J. V.; Cioslowski, J.; Fox, D. J. *Gaussian 09*, Revision A.1; Wallingford, CT, 2009.
(58) Bayly, C. I.; Cieplak, P.; Cornell, W.; Kollman, P. A. *J. Phys. Chem.* **1993**, *97*, 10269.
(59) Morton, A.; Matthews, B. W. *Biochemistry* **1995**, *34*, 8576.
(60) Bron, C.; Kerbosch, J. *Commun. ACM* **1973**, *16*, 575.
(61) Hornak, V.; Abel, R.; Okur, A.; Strockbine, B.; Roitberg, A.; Simmerling, C. *Proteins* **2006**, *65*, 712.
(62) Mobley, D. L.; Chodera, J. D.; Dill, K. A. *J. Chem. Phys.* **2006**, *125*, 084902.
(63) Van Der Spoel, D.; Lindahl, E.; Hess, B.; Groenhof, G.; Mark, A. E.; Berendsen, H. J. *J. Comput. Chem.* **2005**, *26*, 1701.
(64) Berendsen, H. J. C.; van der Spoel, D.; van, D. R. *Comput. Phys. Commun.* **1995**, *91*, 43.
(65) Hess, B.; Kutzner, C.; van der Spoel, D.; Lindahl, E. *J. Chem. Theory Comput.* **2008**, *4*, 435.
(66) Van Der Spoel, D.; Lindahl, E.; Hess, B.; Groenhof, G.; Mark, A. E.; Berendsen, H. J. C. *J. Comput. Chem.* **2005**, *26*, 1701.
(67) van der Spoel, D.; Lindahl, E.; Hess, B.; Kutzner, C.; van Buuren, A. R.; Apol, E.; Meulenhoff, P. J.; Tieleman, D. P.; Sijbers, A. L. T. M.; Feenstra, K. A.; Drunen, R. v.; Berendsen, H. J. C. *GROMACS User Manual Version 4.0*; The GROMACS development team: Groningen, The Netherlands, 2006.
(68) Blondel, A. *J. Comput. Chem.* **2004**, *25*, 985.
(69) Hess, B.; Bekker, H.; Berendsen, H. J. C.; Fraaije, J. G. E. M. *J. Comput. Chem.* **1997**, *18*, 1463.
(70) Khavrutskii, I. V.; Fajer, M.; McCammon, J. A. *J. Chem. Theory Comput.* **2008**, *4*, 1541.
(71) Trebst, S.; Troyer, M.; Hansmann, U. H. E. *J. Chem. Phys.* **2006**, *124*, 174903.
(72) Yeh, I.-C.; Lee, M. S.; Olson, M. A. *J. Phys. Chem. B* **2008**, *112*, 15064.
(73) Pohorille, A.; Jarzynski, C.; Chipot, C. *J. Phys. Chem. B* **2010**, *114*, 10235.
(74) Simonson, T. *Mol. Phys.* **1993**, *80*, 441.
(75) Lange, O. F.; Schaefer, L. V.; Grubmueller, H. *J. Comput. Chem.* **2006**, *27*, 1693.
(76) Bash, P. A.; Singh, U. C.; Langridge, R.; Kollman, P. A. *Science* **1987**, *236*, 564.
(77) Sines, J. J.; Allison, S. A.; McCammon, J. A. *Biochemistry* **1990**, *29*, 9403.
(78) Tan, R. C.; Truong, T. N.; McCammon, J. A.; Sussman, J. L. *Biochemistry* **1993**, *32*, 401.
(79) Steiner, D.; Oostenbrink, C.; Diederich, F.; Zurcher, M.; van Gunsteren, W. F. *J. Comput. Chem.* **2011**, *32*, 1801.

JCTC Journal of Chemical Theory and Computation

ARTICLE

pubs.acs.org/JCTC

RI-MP2 and MPWB1K Study of π−Anion−π' Complexes: MPWB1K Performance and Some Additivity Aspects

Carolina Garau,[†] Antonio Frontera,*[,†] David Quiñonero,[†] Nino Russo,*[,‡] and Pere M. Deyà[†]

[†]Department de Química, Universitat de les Illes Balears, 07122 Palma de Mallorca, Spain

[‡]Department di Chimica, Università della Calabria, 87036 Arcavacata di Rende (CS), Italy

Supporting Information

ABSTRACT: Several sandwich complexes of hexafluorobenzene, trifluorobenzene, *s*-triazine, and trifluoro-*s*-triazine with halides, nitrate, and carbonate anions have been optimized at the RI-MP2/6-31++G** (full and frozen core), B3LYP/6-31++G**, and MPWB1K/6-31++G** levels of theory. All possible combinations of the π-systems and anions (to generate the sandwich π−anion−π' complexes) have been computed and analyzed using the aforementioned levels of theory. This allows us to evaluate the reliability and the performance of the MPWB1K functional to compute the binding energies of the anion−π complexes and to analyze the additivity of the interaction in π−anion−π' complexes where the aromatic rings are of different nature (π-acidity). We have also explored the Cambridge Structural Database and several interesting X-ray structures that support the theoretical calculations that have been found.

1. INTRODUCTION

Noncovalent interactions play a key role in many areas of modern chemistry, especially in the fields of supramolecular chemistry and molecular recognition.[1] Interactions involving aromatic rings are important binding forces in both chemical and biological systems, and they have been recently reviewed.[2] Among them, the favorable interaction of anions with π-acidic rings, namely anion−π interaction,[3] has been extensively studied theoretically.[4] Moreover, the importance of this interaction has been corroborated by a great deal of experimental work. For instance, a new family of anion receptors based on anion−π interactions has emerged.[5] In addition, the design and synthesis of highly selective anion channels[6] represents a very significant progress in this nascent field of supramolecular chemistry. In addition, the anion−π interaction has been observed in several biological systems. For instance, it participates in the inhibition of the enzyme urate oxidase by cyanide[7] or the enzymatic chlorination of tryptophan by PrnA flavin-dependent halogenase.[8] There are several excellent reviews[9] that describe different aspects of the anion−π interaction. From the physicochemical point of view, the anion−π interaction is dominated by electrostatic and anion-induced polarization forces.[3] The strength of the electrostatic component depends upon the value of the quadrupole moment of the arene. The anion-induced polarization term correlates with the molecular polarizability ($\alpha_{||}$) of the aromatic compound.[10]

This manuscript is devoted to the study of three different topics of the anion−π interaction. First, we report a computational study where we analyze the geometrical and energetic features of anion−π complexes at several levels of theory, including ab initio methods (MP2(FC), RI-MP2(FC), and RI-MP2(full)) and density functional theory (DFT) methods (B3LYP and MPWB1K). We study the performance of the MPWB1K[11] method to reproduce the MP2 results in comparison with the more popular B3LYP. It is well-known that DFT, especially with hybrid functionals, allows predicting accurately hydrogen-bonding interactions. However in case of π−π stacking interactions, DFT fails completely,[12] and the use of DFT-D (empirical London dispersion) is required.[13] However this method is less accurate than other functionals in the case of hydrogen-bonded systems. More recently, Truhlar and Zhao[11] developed the MPWB1K functional and demonstrated that it gives good results for both hydrogen-bonding and stacking interactions. Moreover, Dkhissi and Blossey[14] have confirmed the ability of this functional to describe stacking and hydrogen-bonding interactions of nucleic acid bases. They have further demonstrated that the medium basis set (6-31+G**) is sufficient to predict accurately the stacking interactions and, consequently, DFT/MPWB1K is very promising for studies of larger biomolecules (DNA/RNA bases, proteins, etc.).

Since the credibility of the MPWB1K has not been evaluated for anion−π interactions, our aim here is to demonstrate that this functional gives results that are comparable to higher level ab initio methods. On the other hand, a previous study has demonstrated that the anion−π interaction is approximately additive in a reduced number of ternary π−anion−π complexes where both π-systems are equal.[15] Furthermore, the additivity of this interaction has been recently studied using a totally different approximation.[16] That is, depending on the number of double bonds and the number of fluorine substituents, the additivity in several complexes of fluorine-substituted ethyne, ethene, butadiene, cyclobutadiene, fulvene, benzene, and [*n*]radialenes (*n* = 3−5) has been analyzed. However in the second part of this work, we have studied an unexplored aspect of the additivity of the anion−π interaction. That is, we have combined four aromatic rings and five anions (see Figure 1), in order to have a large representation of π−anion−π' complexes and with the purpose to study if the interaction is additive in these complexes

Received: June 14, 2011
Published: August 07, 2011

where the aromatic rings are different using RI-MP2 and MPWB1K methods. In the third part, we have explored the Cambridge Structural Database (CSD),[17] and we have found experimental evidence of the existence of π−anion−π assemblies in X-ray structures that have a strong influence in the crystal packing.

2. THEORETICAL METHODS

The geometry of all binary complexes included in this study was fully optimized at the MP2(FC)/6-31++G**, RI-MP2(FC)/6-31++G**, RI-MP2(full)/6-31++G**, MPWB1K/6-31++G**, and B3LYP/6-31++G** level of theory using the Gaussian 03[18] and TURBOMOLE version 5.10.[19] See Supporting Information for Cartesian coordinates of RI-MP2(FC)/6-31++G** and MPWB1K/6-31++G** optimized structures. The RI-MP2 method[20,21] applied to the study of cation−π and anion−π interactions (among others) is considerably faster than the MP2 method, and the interaction energies and equilibrium distances are almost identical for both methods.[22,23] For the ternary complexes, the optimizations and binding energy calculations were performed only at the RI-MP2(FC)/6-31++G** and MPWB1K/6-31++G** levels of theory. The binding energy was calculated with correction for the basis set superposition error (BSSE) using the Boys−Bernardi counterpoise technique.[24]

The topological analysis of the electron charge density performed for the complexes was determined using Bader's theory of "atoms-in-molecules" (AIM).[25] The electronic density analysis was performed using the AIM2000 program[26] at the RI-MP2-(FC)/6-31++G** level of theory. All complexes are stationary points apart from the fluoride complexes, where the global minimum corresponds to the nucleophilic attack of the fluoride to one carbon atom of the aromatic ring.

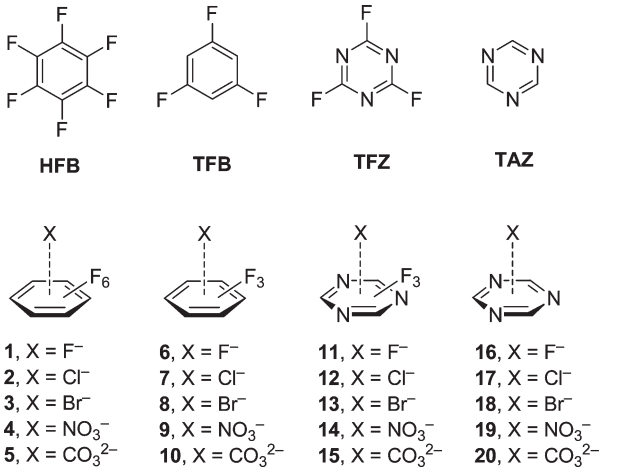

Figure 1. Aromatic rings used in this work and anion−π complexes **1**−**20**.

3. RESULTS AND DISCUSSION

3.1. Preliminary Calculations. Table 1 reports the interaction energies and equilibrium distances of binary anion−π complexes **1**−**20** at several levels of theory (see Figure 1), which have been computed using both ab initio (MP2(FC), RI-MP2(full), and RI-MP2(FC)) and DFT (MPWB1K and B3LYP) methods and the 6-31++G** basis set. In agreement with previous reports, the ab initio MP2 methods give very similar results, indicating that the frozen core and/or the resolution of the identity (RI) approximations, that significantly reduce the computational time

Table 1. Interaction Energies Using Several Methods and the 6-31++G Basis Set With the BSSE Correction (E_{BSSE}, kcal/mol) and Equilibrium Distances from the Anion to the Ring Centroid (R_e, Å) for Complexes 1−20[a]**

complex	$E_{BSSE}^{MP2(FC)}$	$R_e^{MP2(FC)}$	$E_{BSSE}^{RI\text{-}MP2(full)}$	$R_e^{RI\text{-}MP2(full)}$	$E_{BSSE}^{RI\text{-}MP2(FC)}$	$R_e^{RI\text{-}MP2(FC)}$	E_{BSSE}^{MPWB1K}	E_e^{MPWB1K}	E_{BSSE}^{B3LYP}	E_e^{B3LYP}
1 (**HFB**−F^-)	−18.31	2.570	−18.80	2.566	−18.79	2.566	−19.74	2.624	−17.48	2.656
2 (**HFB**−Cl^-)	−12.88	3.148	−13.10	3.154	−12.91	3.154	−12.99	3.297	−10.96	3.310
3 (**HFB**−Br^-)	−12.11	3.201	−12.70	3.282	−12.58	3.301	−11.92	3.412	−9.40	3.367
4 (**HFB**−NO_3^-)	−12.65	2.917	−12.70	2.927	−12.80	2.931	−10.82	2.985	−8.40	2.911
5 (**HFB**−CO_3^{2-})	−33.07	2.720	−32.10	2.750	−33.01	2.744	−32.09	2.755	−28.37	2.880
6 (**TFB**−F^-)	−7.77	2.748	−7.70	2.755	−7.70	2.758	−7.65	2.995	−6.62	2.854
7 (**TFB**−Cl^-)	−4.79	3.323	−4.81	3.336	−4.82	3.341	−4.59 (−4.77)	3.662 (3.656)	−3.31 (−3.39)	3.626 (2.569)
8 (**TFB**−Br^-)	−4.39	3.359	−4.94	3.468	−4.97	3.487	−3.72	3.422	−2.09	3.640
9 (**TFB**−NO_3^-)	−5.62	3.471	−5.72	3.043	−5.71	3.043	−4.07 (−4.39)	3.043 (3.041)	−2.59 (−2.50)	3.473 (3.421)
10 (**TFB**−CO_3^{2-})	−17.33	2.814	−17.32	2.854	−17.34	2.856	−16.47	2.853	−10.05	3.019
11 (**TFZ**−F^-)	−24.23	2.390	−24.32	2.385	−22.23	2.385	−26.30	2.327	−23.01	2.416
12 (**TFZ**−Cl^-)	−14.98	3.009	−15.05	3.008	−15.05	3.006	−15.63 (−15.69)	3.057 (3.054)	−13.00(−13.14)	3.155 (3.150)
13 (**TFZ**−Br^-)	−14.00	3.137	−14.19	3.176	−14.11	3.157	−13.72	3.156	−10.89	3.267
14 (**TFZ**−NO_3^-)	−13.01	2.805	−13.04	2.814	−13.06	2.816	−12.21 (−12.32)	2.830 (2.868)	−8.89 (−8.93)	3.047 (3.063)
15 (**TFZ**−CO_3^{2-})	−36.94	2.505	−36.95	2.520	−37.95	2.520	−40.21	2.508	−35.30	2.602
16 (**TAZ**−F^-)	−9.70	2.592	−9.76	2.584	−9.74	2.582	−11.02	2.625	−8.92	2.659
17 (**TAZ**−Cl^-)	−5.22	3.223	−5.27	3.220	−5.24	3.219	−5.57	3.475	−4.01	3.475
18 (**TAZ**−Br^-)	−5.01	3.339	−5.05	3.338	−5.22	3.402	−5.23	3.462	−2.99	3.582
19 (**TAZ**−NO_3^-)	−5.34	3.003	−5.37	3.007	−5.36	3.009	−4.21	3.016	−2.59	3.318
20 (**TAZ**−CO_3^{2-})	−16.85	2.751	−16.90	2.756	−16.90	2.758	−19.23	2.750	−12.18	2.859
rmsd	–	–	0.31	0.102	0.54	0.104	1.323	0.162	3.107	0.181

[a] The computed values using the 6-311++G** basis set are indicated in parentheses. The root-mean-square deviation (rmsd) for the different levels with respect to MP2(FC) results is also shown.

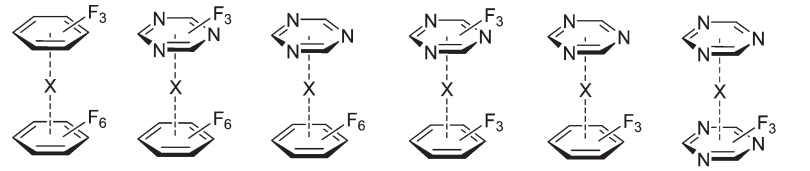

21, X = F^- **26**, X = F^- **31**, X = F^- **36**, X = F^- **41**, X = F^- **46**, X = F^-
22, X = Cl^- **27**, X = Cl^- **32**, X = Cl^- **37**, X = Cl^- **42**, X = Cl^- **47**, X = Cl^-
23, X = Br^- **28**, X = Br^- **33**, X = Br^- **38**, X = Br^- **43**, X = Br^- **48**, X = Br^-
24, X = NO_3^- **29**, X = NO_3^- **34**, X = NO_3^- **39**, X = NO_3^- **44**, X = NO_3^- **49**, X = NO_3^-
25, X = CO_3^{2-} **30**, X = CO_3^{2-} **35**, X = CO_3^{2-} **40**, X = CO_3^{2-} **45**, X = CO_3^{2-} **50**, X = CO_3^{2-}

Figure 2. Schematic representation of $\pi-$anion$-\pi'$ complexes **21**−**50**.

of calculation, are fully applicable in these systems. A more detailed analysis of Table 1 shows that when comparing the results obtained using RI-MP2(FC) with those obtained using MP2(FC), the largest difference is found in complex **8** (**TFB**−Br^-), which is overestimated in 0.6 kcal/mol using the RI approximation. This provokes the bromide complex to become more favorable than the chloride complex, in spite of having a larger equilibrium distance. A similar overestimation (0.5 kcal/mol) is observed in **HFB**−Cl^- and **HFB**−Br^- complexes, although in this case, the chloride complex is more favorable. Moreover, the differences between the interaction energies computed at the RI-MP2(full) and RI-MP2(FC) are also small, being the largest difference 2.1 kcal/mol in the **TFZ**−F^- complex (**11**). The equilibrium distances are almost equivalent for both methods; the maximum difference is 0.06 Å in complex **TAZ**−Br^- (**18**). In spite of these small differences, the utilization of the RI-MP2(FC) method is convenient, since it gives almost identical interaction energies and equilibrium distances with a significantly reduced computational cost.

In terms of energetic and geometric results gathered in Table 1, a good performance of the MPWB1K method is observed since they are comparable to MP2 results. In addition, the MPWB1K method gives much better results than the more popular B3LYP method. In general the B3LYP method underestimates the interaction energies with respect to MP2 results. For instance, the interaction energy of complex **TFB**−CO_3^{2-} at the B3LYP/6-31++G** differs in ∼6 kcal/mol with respect to the other levels of theory. In addition the interaction energies obtained using the B3LYP functional are between 2 and 4 kcal/mol less favorable than the MP2 ones for the rest of the complexes. The equilibrium distances are larger using the DFT than the MP2 methods. For the MPWB1K functional, the largest differences are found in complexes **TAZ**−Cl^- and **TFB**−Cl^- (around 0.3 Å). We have included in Table 1 the root-mean-square deviation (rmsd) between the reference method (MP2(FC)) and the other computational levels. The rmsd values for both RI-MP2 levels are very small for both energies and distances. In addition, the rmsd values obtained for the DFT calculations clearly demonstrate that the MPWB1K method is more reliable than the B3LYP method to study these complexes. Finally, for some complexes (using both MPWB1K and B3LYP functionals), we have also obtained the geometries and energies using the more flexible 6-311++G** basis set (values in parentheses, see Table 1). The geometric and energetic results are almost equivalent, indicating that the 6-31++G** basis set is of sufficient quality to perform this study.

3.2. Ternary $\pi-$anion$-\pi'$ Complexes. Once demonstrated in the previous section of the manuscript that the RI-MP2(FC) and MPWB1K methods give reliable and comparable results, we have studied the additivity of the anion$-\pi$ interaction in $\pi-$anion$-\pi'$ complexes using the four aromatic rings used so far (see Figure 1). Two of them (**HFB** and **TFZ**) are strongly π-acidic (large and positive quadrupole moment), therefore, in their complexes, the interaction will be dominated by both electrostatic and ion-induced polarization effects.[10] The other two aromatic rings (**TFB** and **TAZ**) have negligible quadrupole moments, and the interaction will be dominated only by polarization effects.[27,28] The additivity of the interaction has been analyzed in the ternary $\pi-$anion$-\pi'$ complexes using all possible combinations of **HFB**, **TFB**, **TFZ**, and **TAZ** and the five anions considered in this work (F^-, Cl^-, Br^-, NO_3^-, and CO_3^{2-}). As a result, we have optimized the complexes **21**−**50** shown in Figure 2 at both RI-MP2(FC)/6-31++G** and MPWB1K/6-31++G** levels of theory.

The energetic and geometric results are summarized in Table 2. In all cases the interaction energies are large and negative, indicating a very favorable interaction. As expected complexes **26**−**30** are more favorable than the rest because both aromatic rings (**HFB** and **TFZ**) present large and positive values of quadrupole moment (Q_{zz} = 9.50 and 8.23 B, respectively). The contrary is observed in complexes **41**−**45** because in this case both aromatic rings (**TFB** and **TAZ**) have negligible values of quadrupole moment (Q_{zz} = 0.19 and 0.99 B, respectively), and the interaction is dominated only by ion-induced polarization effects. For the rest of complexes, where one aromatic ring is electron-deficient (Q_{zz} > 8 B) and the other is neutral ($Q_{zz} \approx$ 0 B), the interaction energies are comparable for each series of anions. Therefore the interaction energies exhibit a clear trend depending on the π-acidity of the rings. For instance, for F^- the interaction energy varies from −39.9 kcal/mol in strong π-acidic rings to around −28 kcal/mol in hybrid complexes that combine high and low π-acidic rings and finally to −16 kcal/mol in weak π-acidic rings. Likewise, the interaction for Cl^-, Br^-, and NO_3^- varies from around −25 to −18 and to −10 kcal/mol for the same groups, suggesting a qualitative relationship with the π-acidic nature of the ring.

In Table 2 we also summarize the "ideal" interaction energy (E_{ideal}) that is obtained by summing the interaction energies of the two related binary complexes (see Table 1). For instance in ternary complex **21** (**HFB**−F^-−**TFB**), the E_{ideal} is the sum of the interaction energies of binary complexes **1** (**HFB**−F^-) and **6** (**TFB**−F^-). The E_{ideal} can be understood as the expected interaction energy of the ternary complex, considering the interaction is totally additive. From the results reported in Table 2, it can be observed that the difference between the E_{ideal} and the E_{BSSE} (ΔE_{ideal}) is smaller for the ab initio than for the DFT method. As a matter of fact ΔE_{ideal} is smaller than

Table 2. Interaction Energies (in kcal/mol) with the BSSE Correction for $\pi-$Anion$-\pi'$ Complexes 21−50 at RI-MP2(FC)/6-31++G** and MPWB1K/6-31++G** Levels of Theory[a]

$\pi-$anion$-\pi'$ complex	$E_{BSSE}^{RI\text{-}MP2}$	$E_{ideal}^{RI\text{-}MP2}$	$\Delta E_{ideal}^{RI\text{-}MP2}$	$R_{\pi-anion}$	$R_{anion-\pi'}$	E_{BSSE}^{MPWB1K}	E_{ideal}^{MPWB1K}	$\Delta E_{ideal}^{MPWB1K}$	$R_{\pi-anion}$	$R_{anion-\pi'}$
HFB−F^-−**TFB (21)**	−25.01	−26.50	−1.49	2.539	2.704	−25.82	−27.38	−1.56	2.631	2.683
HFB−Cl^-−**TFB (22)**	−17.68	−17.73	−0.05	3.132	3.330	−17.01	−17.59	−0.58	3.252	3.306
HFB−Br^-−**TFB (23)**	−17.28	−17.56	−0.27	3.273	3.446	−14.79	−15.64	−0.86	3.324	3.412
HFB−NO_3^-−**TFB (24)**	−17.77	−18.51	−0.74	2.917	3.020	−13.99	−14.89	−0.90	3.023	3.046
HFB−CO_3^{2-}−**TFB (25)**	−47.42	−50.34	−2.92	2.742	2.886	−44.88	−48.57	−3.68	2.766	3.020
HFB−F^-−**TFZ (26)**	−39.94	−41.02	−1.08	2.374	2.617	−41.86	−46.04	−4.17	2.642	2.368
HFB−Cl^-−**TFZ (27)**	−26.65	−27.96	−1.31	2.974	3.103	−27.20	−28.62	−1.42	3.253	3.063
HFB−Br^-−**TFZ (28)**	−25.61	−26.69	−1.08	3.182	3.277	−24.27	−25.64	−1.38	3.308	3.144
HFB−NO_3^-−**TFZ (29)**	−24.07	−25.85	−1.78	2.815	2.919	−20.99	−23.03	−2.04	3.017	2.890
HFB−CO_3^{2-}−**TFZ (30)**	−63.53	−70.06	−6.53	2.567	2.765	−63.46	−72.31	−8.85	2.778	2.563
HFB−F^-−**TAZ (31)**	−27.14	−28.53	−1.39	2.552	2.570	−28.54	−30.75	−2.22	2.633	2.570
HFB−Cl^-−**TAZ (32)**	−18.09	−18.16	−0.06	3.135	3.220	−17.92	−18.56	−0.64	3.132	3.216
HFB−Br^-−**TAZ (33)**	−17.57	−17.80	−0.24	3.279	3.380	−15.36	−17.15	−1.79	3.262	3.376
HFB−NO_3^-−**TAZ (34)**	−17.45	−18.16	−0.71	2.920	3.006	−14.14	−15.03	−0.89	3.020	3.038
HFB−CO_3^{2-}−**TAZ (35)**	−46.92	−49.91	−2.99	2.749	2.794	−46.64	−51.32	−4.68	2.769	2.787
TFB−F^-−**TFZ (36)**	−30.41	−29.93	0.48	2.724	2.378	−32.34	−33.95	−1.60	2.692	2.343
TFB−Cl^-−**TFZ (37)**	−19.56	−19.87	−0.31	3.312	3.014	−19.68 (−21.80)	−20.22 (−20.46)	−0.55 (1.34)	3.302 (3.299)	3.059 (3.063)
TFB−Br^-−**TFZ (38)**	−18.72	−19.08	−0.36	3.462	3.183	−16.79	−17.45	−0.66	3.390	3.149
TFB−NO_3^-−**TFZ (39)**	−18.07	−18.77	−0.70	3.023	2.803	−14.94 (−15.30)	−16.28 (−16.71)	−1.34 (−1.41)	3.037 (3.031)	2.867 (2.863)
TFB−CO_3^{2-}−**TFZ (40)**	−50.55	−54.39	−3.84	2.888	2.541	−51.26	−56.69	−5.43	3.017	2.525
TFB−F^-−**TAZ (41)**	−16.93	−17.44	−0.51	2.750	2.583	−17.87	−18.66	−0.79	2.683	2.570
TFB−Cl^-−**TAZ (42)**	−10.13	−10.06	0.06	3.328	3.223	−10.26	−10.16	0.10	3.319	3.398
TFB−Br^-−**TAZ (43)**	−10.32	−10.20	0.12	3.531	3.432	−8.49	−8.95	−0.46	3.413	3.476
TFB−NO_3^-−**TAZ (44)**	−10.96	−11.07	−0.11	3.027	2.995	−7.80	−8.27	−0.47	3.041	3.038
TFB−CO_3^{2-}−**TAZ (45)**	−32.54	−34.24	−1.70	2.868	2.773	−32.57	−35.70	−3.14	3.009	2.778
TFZ−F^-−**TAZ (46)**	−32.32	−31.97	0.35	2.382	2.577	−35.01	−37.32	−2.31	2.366	2.572
TFZ−Cl^-−**TAZ (47)**	−19.96	−20.29	−0.33	3.008	3.220	−20.85	−21.20	−0.34	3.063	3.387
TFZ−Br^-−**TAZ (48)**	−18.93	−19.33	−0.40	3.186	3.382	−18.07	−18.95	−0.88	3.157	3.467
TFZ−NO_3^-−**TAZ (49)**	−16.97	−18.42	−1.45	2.809	3.004	−15.47	−16.41	−0.94	2.831	3.025
TFZ−CO_3^{2-}−**TAZ (50)**	−49.85	−53.96	−4.10	2.547	2.811	−52.47	−59.45	−6.98	2.540	2.797
rmsd	-	-	-	-	-	1.93	2.48	1.27	0.111	0.086

[a] The ideal interaction energy (sum of the energies of the corresponding binary complexes, E_{ideal}) and the difference between this energy and the interaction energy (ΔE_{ideal}) are also shown. The computed values using the 6-311++G** basis set are indicated in parentheses. The rmsd for the different levels with respect to MP2(FC) results is also shown.

2 kcal/mol for all complexes apart from CO_3^{2-} complexes at the RI-MP2/6-31++G** level of theory. Therefore the interaction energy is approximately additive for all monoanionic complexes. For carbonate dianion, the ΔE_{ideal} values are greater than for the rest of complexes, ranging from −1.7 to −6.5 kcal/mol. However it should be remarked that the interaction energy in these complexes is very large, and therefore the difference between the "ideal" and "real" interaction energies increases. In addition the two negative charges of the carbonate ion may promote a larger polarization in the sandwich complex than in the two binary anion$-\pi$ complexes. In addition, in almost all complexes, the ΔE_{ideal} energies are negative, which means that the interaction energy is always less favorable than expected from the sum of the interaction energies of the binary complexes. Regarding the equilibrium distances, they are mostly unaffected by the presence of an additional anion$-\pi$ interaction. As an example, in all ternary complexes of chloride, which are represented in Figure 3, the equilibrium distances are almost equivalent with respect to the related binary complexes. For the rest of the complexes, the largest variation is found in complex **TFB**−Br^-−**TAZ (43)**, where the $\pi-$anion distance increases in 0.063 Å and the anion$-\pi'$ distance increases in 0.094 Å. Finally, the performance of the DFT method should be emphasized since it is able to reproduce the interaction energies of the ternary complexes computed at the RI-MP2(FC)/6-31++G** level of theory. The agreement of MPWB1K and RI-MP2(FC) methods is illustrated in Figure 4 and the rmsd values provided in Table 2. For two complexes, we have also validated the utilization of the 6-31++G** basis set by computing the geometries and the energies at the MPWB1K/6-311++G** level of theory and obtaining very similar results (values in parentheses in Table 2).

To further confirm the additivity of the anion$-\pi$ interaction in these systems, we have used the Bader's theory of atoms in molecules (AIM), which provides an unambiguous definition of chemical bonding,[29] using the MP2(FC)/6-31++G** wave function. The AIM theory has been successfully used to characterize anion$-\pi$ interactions and to analyze nonadditivity effects.[16] The distribution of critical points in several representative complexes is shown in Figure 5. For the anion$-\pi$ complex **12** (**TFZ**−Cl^-), the exploration of the CPs revealed the presence of three bond

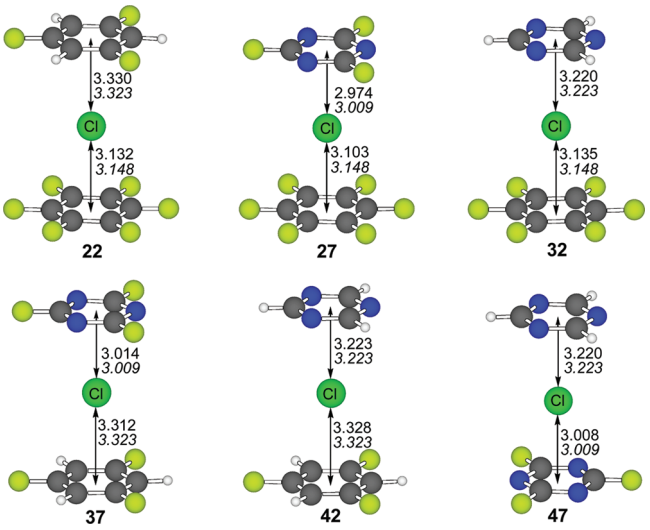

Figure 3. RI-MP2(FC)/6-31++G** optimized structures of $\pi-Cl^{-}-\pi'$ complexes. Distances (in Å) in italics correspond to the binary anion$-\pi$ complexes.

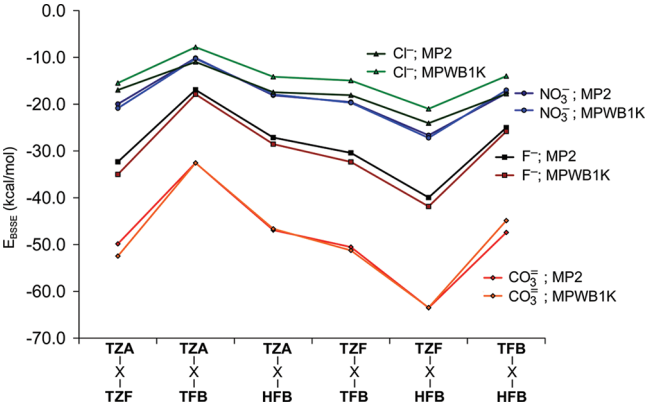

Figure 4. Plot of the interaction energies of all series of $\pi-X-\pi'$ complexes (X = F^{-}, Cl^{-}, NO_3^{-}, and CO_3^{2-}) at two levels of theory. The bromide complexes have been omitted for clarity.

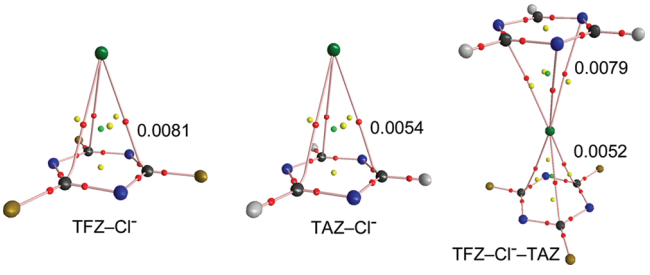

Figure 5. Schematic representation of the CPs obtained for complexes **12** (TFZ$-Cl^{-}$), **17** (TAZ$-Cl^{-}$), and **47** (TFZ$-Cl^{-}-$TAZ). Bond CPs are represented in red, ring CPs in yellow, and cage CPs in green. The values of ρ at the cage CPs are in atomic units.

and three ring CPs that connect the anion with the carbon and nitrogen atoms of the arene, respectively. The interaction is further described by the presence of a cage CP that it is located along the main symmetry axis (see Figure 5). The distribution of the CPs for complex **17** (**TAZ**$-Cl^{-}$) is identical. In the

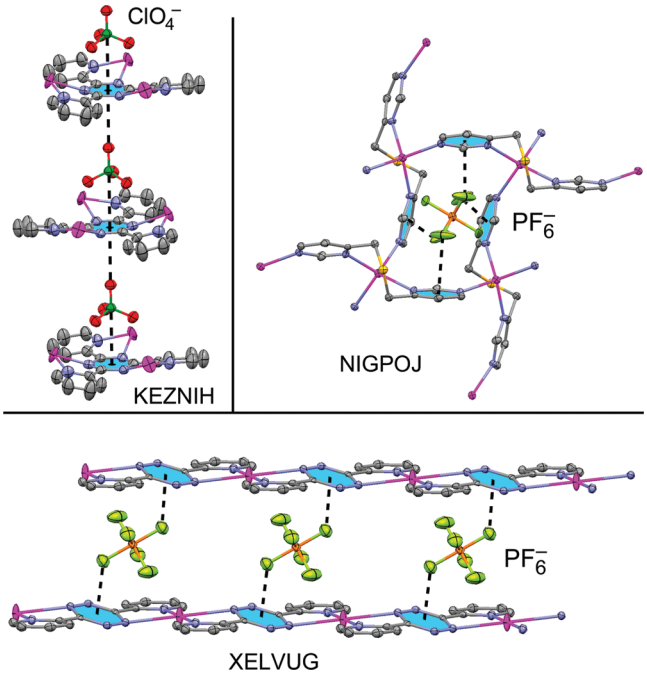

Figure 6. Selected fragments of the X-ray crystal structures of KEZNIH, NIGPOJ and XELVUG.

$\pi-$anion$-\pi'$ complex **47** (**TFZ**$-Cl^{-}-$**TAZ**) the exploration of the CPs revealed the same number and distribution than the binary complexes. A common feature of the complexes is the presence of a cage CP linking the anion with the center of the ring, as is common in the anion$-\pi$ complexes.[4] As a matter of fact, the value of the charge density (ρ) at the cage CP has been used as a measure of bond order, and it is related to the strength of the interaction.[4] In Figure 5 we have included the values of ρ at the cage CPs. It can be appreciated that the value of ρ in complex **12** is considerably greater than the one for complex **17**, in agreement with the interaction energies (see Table 1). It is interesting to compare the values of ρ obtained for the ternary complex **47** to those of the binary complexes **12** and **17**. It can be observed that the values of ρ are very similar (see Figure 5), indicating that the bond order of each anion$-\pi$ interaction in the ternary complex does not change with respect to the binary complexes. Consequently, each interaction is not affected by the presence of the second aromatic ring, thus confirming the additivity of the anion$-\pi$ interaction.

3.4. CSD Study. The CSD[17] is a convenient and reliable storehouse for geometrical information. The utility of small-molecule crystallography and the CSD in analyzing geometrical parameters and nonbonding interactions is well established.[30] We have explored the CSD searching crystallographic fragments where $\pi-$anion$-\pi$ assemblies are present in the solid state. We show in Figure 6 three selected examples (CSD reference codes: KEZNIH,[31] NIGPOJ,[32] and XELVUG)[33] that we have retrieved from the database where the $\pi-$anion$-\pi$ binding motif is very relevant and crucial in the crystal packing. The KEZNIH structure was published by Zhou et al.[31] as a part of a very interesting manuscript where the authors report the self-assembly of Ag(I) coordination networks directed by anion$-\pi$ interactions. In their study of Ag(I) metal complexes with 2,4,6-tri (2-pyridyl)-1,3,5-triazine (tpt), they found that polyatomic anions (ClO_4^{-}, BF_4^{-}, and PF_6^{-}) directed the self-assembly of Ag-tpt

coordination polymers through infinite π−anion−π interactions, as can be observed in the X-ray structure shown in Figure 6, where the anions interact with the central triazine ring of the tpt ligands in the X-ray crystal structure. Notably, the same binding motif is found in the other two X-ray structures published by Zhou et al. using BF_4^- and PF_6^- as counterions and the same ligand. In fact, in all three structures, the anions are located on the C_3-axis above and below the central triazine rings of the tpt ligands, as it is observed in KEZNIH. The XELVUG structure was reported by Dunbar and co-workers in their investigation on the role of anion−π interactions in the assembly of Ag(I) complexes using the 3,6-bis(2-pyridyl)-1,2,4,5-tetrazine (bptz) ligand.[33] This work was the first example of a comprehensive investigation of anion−π interactions as controlling elements in self-assembly reactions. They reported the formation of complexes of different structural types depending on the experimental conditions and the anion used. Interestingly the reaction of Ag(I) and bptz in a 1:1 ratio in the presence of PF_6^- ions afforded a polymer, as indicated by the single-crystal X-ray structural determination (Figure 6, bottom). Anion−π interactions are a major factor in stabilizing the structural motif where the anion is sandwiched between two central *s*-tetrazine rings of the ligands. Finally, NIGPOJ structure was published by Black et al.,[32] and it consists in a coordination polymer formed from Ag(I) ions and bis(4-pyrimidylmethyl)sulphide. It has the ability to encapsulate PF_6^- anion via a uniform mode of π−anion−π binding. The combination of this ligand with silver salts of other anions like BF_4^- and ClO_4^- in a 1:1 molar ratio gives isomorphous complexes. Anions embedded in the cavities formed by this open network are held in place by four complementary π−anion−π sandwich interactions with two pyrimidine rings (see Figure 6). These three important investigations provide strong experimental evidence for the usefulness of π-acidic rings in the design of anion receptors coordinated to transition-metal ions (that increase the π-acidity of the ring), which are bound to their counterions via multiple π−anion−π interactions, demonstrating the potential use of this binding motif in a structurally directing role.

4. CONCLUSION

The results derived from this study reveal that the interaction energies and the equilibrium distances of several anion−π complexes are well described using the MPWB1K functional. The performance of this method is considerably better than the widely used B3LYP functional in comparison to the ab initio MP2 method. In addition, the ability of the MPWB1K functional to describe the energetic and geometric parameters in π−anion−π' complexes has been demonstrated. Moreover, we have also demonstrated that the interaction is approximately additive in these complexes, especially when the anion is monoanionic. Finally, we have explored the CSD, and we have found several interesting examples where the π−anion−π assemblies are crucial to understand the architecture of the X-ray structure. Therefore, the potential of multiple anion−π interactions for the design of novel sensors, hosts, catalysts, and materials is anticipated.

■ ASSOCIATED CONTENT

Ⓢ Supporting Information. Cartesian coordinates of RI-MP2(FC)/6-31++G** and MPWB1K/6-31++G** optimized structures. This material is available free of charge via the Internet at http://pubs.acs.org.

■ AUTHOR INFORMATION

Corresponding Author

*E-mail: toni.frontera@uib.es, nrusso@unical.it.

■ ACKNOWLEDGMENT

We thank CONSOLIDER−Ingenio 2010 (CSD2010-0065) and the MICINN of Spain (project CTQ2008-00841/BQU, FEDER funds) for financial support. We thank the CESCA for computational facilities. D.Q. thanks the MICINN of Spain for a "Ramón y Cajal" contract.

■ REFERENCES

(1) Hunter, C. A.; Sanders, J. K. M. *J. Am. Chem. Soc.* **1990**, *112*, 5525.

(2) (a) Salonen, L. M.; Ellermann, M.; Diederich, F. *Angew. Chem., Int. Ed.* **2011**, *50*, 4808. (b) Meyer, E. A.; Castellano, R. K.; Diederich, F. *Angew. Chem., Int. Ed.* **2003**, *42*, 1210.

(3) (a) Mascal, M.; Armstrong, A.; Bartberger, M. *J. Am. Chem. Soc.* **2002**, *124*, 6274. (b) Alkorta, I.; Rozas, I.; Elguero, J. *J. Am. Chem. Soc.* **2002**, *124*, 8593. (c) Quiñonero, D.; Garau, C.; Rotger, C.; Frontera, A.; Ballester, P.; Costa, A.; Deyà, P. M. *Angew. Chem., Int. Ed.* **2002**, *41*, 3389.

(4) Frontera, A.; Quiñonero, D.; Deyà, P. M. *WIREs: Comput. Mol. Sci.* **2011**, *1*, 440.

(5) (a) Rosokha, Y. S.; Lindeman, S. V.; Rosokha, S. V.; Kochi, J. K. *Angew. Chem., Int. Ed.* **2004**, *43*, 4650. (b) Han, B.; Lu, J. J.; Kochi, J. K. *Cryst. Growth Des.* **2008**, *8*, 1327. (c) de Hoog, P.; Gamez, P.; Mutikainen, H.; Turpeinen, U.; Reedijk, J. *Angew. Chem., Int. Ed.* **2004**, *43*, 5815. (d) Estarellas, C.; Rotger, M. C.; Capó, M.; Quiñonero, D.; Frontera, A.; Costa, A.; Deyà, P. M. *Org. Lett.* **2009**, *11*, 1987. (e) Mascal, M.; Yakovlev, I.; Nikitin, E. B.; Fettinger, J. C. *Angew. Chem., Int. Ed.* **2007**, *46*, 8782. (f) Chifotides, H. T.; Schottel, B. L.; Dunbar, K. R. *Angew. Chem., Int. Ed.* **2010**, *49*, 7202. (g) Campos-Fernandez, C. S.; Schottel, B. L.; Chifotides, H. T.; Bera, J. K.; Bacsa, J.; Koomen, J. M.; Russell, D. H.; Dunbar, K. R. *J. Am. Chem. Soc.* **2005**, *127*, 12909. (h) Berryman, O. B.; Hof, F.; Hynes, M. J.; Johnson, D. W. *Chem. Commun.* **2006**, 506. (i) Berryman, O. B.; Sather, A. C.; Hay, B. P.; Meisner, J. S.; Johnson, D. W. *J. Am. Chem. Soc.* **2008**, *130*, 10895. (j) Gil-Ramirez, G.; Escudero-Adan, E. C.; Benet-Buchholz, J.; Ballester, P. *Angew. Chem., Int. Ed.* **2008**, *47*, 4114.

(6) (a) Mareda, J.; Matile, S. *Chem.—Eur. J.* **2009**, *15*, 28. (b) Gorteau, V.; Bollot, G.; Mareda, J.; Matile, S. *Org. Biomol. Chem.* **2007**, *5*, 3000. (c) Gorteau, V.; Bollot, G.; Mareda, J.; Perez-Velasco, A.; Matile, S. *J. Am. Chem. Soc.* **2006**, *128*, 14788. (d) Gorteau, V.; Julliard, M. D.; Matile, S. *J. Membr. Sci.* **2008**, *321*, 37. (e) Perez-Velasco, A.; Gorteau, V.; Matile, S. *Angew. Chem., Int. Ed.* **2008**, *47*, 921. (f) Dawson, R. E.; Hennig, A.; Weimann, D. P.; Emery, D.; Ravikumar, V.; Montenegro, J.; Takeuchi, T.; Gabutti, S.; Mayor, M.; Mareda, J.; Schalley, C. A.; Matile, S. *Nature Chem.* **2010**, *2*, 533. (g) Sakai, N.; Mareda, J.; Vauthey, E.; Matile, S. *Chem. Commun.* **2010**, *46*, 4225.

(7) Estarellas, C.; Frontera, A.; Quiñonero, D.; Deyà, P. M. *Angew. Chem., Int. Ed.* **2011**, *50*, 415.

(8) Estarellas, C.; Frontera, A.; Quiñonero, D.; Deyà, P. M. *Chem. Asian J.* **2011**in press.

(9) (a) Schottel, B. L.; Chifotides, H. T.; Dunbar, K. R. *Chem. Soc. Rev.* **2008**, *37*, 68. (b) Caltagirone, C.; Gale, P. A. *Chem. Soc. Rev.* **2009**, *38*, 520. (c) Robertazzi, A.; Krull, F.; Knapp, E.-W.; Gamez, P. *CrystEngComm* **2011**, *13*, 3293.

(10) Garau, C.; Frontera, A.; Quiñonero, D.; Ballester, P.; Costa, A.; Deyà, P. M. *ChemPhysChem* **2003**, *4*, 1344.

(11) Zhao, Y.; Truhlar, D. G. *J. Phys. Chem. A* **2004**, *108*, 6908.

(12) Cerny, J.; Hobza, P. *Phys. Chem. Chem. Phys.* **2005**, *7*, 1624.

(13) Elsner, M.; Hobza, P.; Frauenheim, T.; Suhai, S.; Kaxiras, E. *J. Chem. Phys.* **2001**, *114*, 5149.
(14) Dkhissi., A.; Blossey, R. *Chem. Phys. Lett.* **2007**, *439*, 35.
(15) Garau, C.; Quiñonero, D.; Frontera, A.; Ballester, P.; Costa, A.; Deyà, P. M. *J. Phys. Chem. A* **2005**, *109*, 341.
(16) Estarellas, E.; Frontera, A.; Quiñonero, D.; Deyà, P. M. *J. Phys. Chem. A* **2011**, *115*, 7849.
(17) Allen, F. H. *Acta Crystallogr., Sect. B* **2002**, *58*, 380.
(18) Frisch, M. J.; Trucks, G. W.; Schlegel, H. B.; Scuseria, G. E.; Robb, M. A.; Cheeseman, J. R.; Montgomery, J. A., Jr.; Vreven, T.; Kudin, K. N.; Burant, J. C.; Millam, J. M.; Iyengar, S. S.; Tomasi, J.; Barone, V.; Mennucci, B.; Cossi, M.; Scalmani, G.; Rega, N.; Petersson, G. A.; Nakatsuji, H.; Hada, M.; Ehara, M.; Toyota, K.; Fukuda, R.; Hasegawa, J.; Ishida, M.; Nakajima, T.; Honda, Y.; Kitao, O.; Nakai, H.; Klene, M.; Li, X.; Knox, J. E.; Hratchian, H. P.; Cross, J. B.; Bakken, V.; Adamo, C.; Jaramillo, J.; Gomperts, R.; Stratmann, R. E.; Yazyev, O.; Austin, A. J.; Cammi, R.; Pomelli, C.; Ochterski, J. W.; Ayala, P. Y.; Morokuma, K.; Voth, G. A.; Salvador, P.; Dannenberg, J. J.; Zakrzewski, V. G.; Dapprich, S.; Daniels, A. D.; Strain, M. C.; Farkas, O.; Malick, D. K.; Rabuck, A. D.; Raghavachari, K.; Foresman, J. B.; Ortiz, J. V.; Cui, Q.; Baboul, A. G.; Clifford, S.; Cioslowski, J.; Stefanov, B. B.; Liu, G.; Liashenko, A.; Piskorz, P.; Komaromi, I.; Martin, R. L.; Fox, D. J.; Keith, T.; Al-Laham, M. A.; Peng, C. Y.; Nanayakkara, A.; Challacombe, M.; Gill, P. M. W.; Johnson, B.; Chen, W.; Wong, M. W.; Gonzalez, C.; Pople, J. A. *Gaussian 03*, revision C.01; Gaussian, Inc., Wallingford, CT, 2004.
(19) Ahlrichs, R.; Bär, M.; Hacer, M.; Horn, H.; Kömel, C. *Chem. Phys. Lett.* **1989**, *162*, 165.
(20) Feyereisen, M. W.; Fitzgerald, G.; Komornicki, A. *Chem. Phys. Lett.* **1993**, *208*, 359.
(21) Vahtras, O.; Almlof, J.; Feyereisen, M. W. *Chem. Phys. Lett.* **1993**, *213*, 514.
(22) Frontera, A.; Quiñonero, D.; Garau, C.; Ballester, P.; Costa, A.; Deyà, P. M. *J. Phys. Chem. A* **2005**, *109*, 4632.
(23) Quiñonero, D.; Garau, C.; Frontera, A.; Ballester, P.; Costa, A.; Deyà, P. M. *J. Phys. Chem. A* **2006**, *110*, 5144.
(24) Boys, S. B.; Bernardi, F. *Mol. Phys.* **1970**, *19*, 553.
(25) Bader, R. F. W. *Chem. Rev.* **1991**, *91*, 893.
(26) Biegler-König, F; Schönbohm, J.; Bayles, D *J. Comput. Chem.* **2001**, *22*, 545.
(27) Garau, C.; Quiñonero, D.; Frontera, A.; Ballester, P.; Costa, A.; Deyà, P. M. *Org. Lett.* **2003**, *5*, 2227.
(28) Garau, C.; Frontera, A.; Quiñonero, D.; Ballester, P.; Costa, A.; Deyà, P. M. J. *Phys. Chem. A* **2004**, *108*, 9423.
(29) Bader, R. F. W. *J. Phys. Chem. A* **1998**, *102*, 7314.
(30) Nangia, A.; Biradha, K.; Desiraju, G. R. *J. Chem. Soc., Perkin Trans. 2* **1996**, 943.
(31) Zhou, X. P.; Zhang, X. J.; Lin, S. H.; Li, D. *Cryst. Growth Des.* **2007**, *7*, 485.
(32) Black, C. A.; Hanton, L. R.; Spicer, M. D. *Chem. Commun.* **2007**, 3171.
(33) Schottel, B. L.; Chifotides, H. T.; Shatruk, M.; Chouai, A.; Perez, L. M.; Bacsa, J.; Dunbar, K. R. *J. Am. Chem. Soc.* **2006**, *128*, 5895.

JCTC Journal of Chemical Theory and Computation

ARTICLE

pubs.acs.org/JCTC

A Failure of DFT Is Not Necessarily a DFT Failure—Performance Dependencies on Model System Choices

Heiko Jacobsen*

KemKom, 1215 Ursulines Ave, New Orleans, Louisiana 70116, United States

Supporting Information

ABSTRACT: The claim that DFT does not provide an accurate description of a weak Ru—C interaction (*J. Chem. Theory Comput.* **2007**, *3*, 665—670) is put into broader perspective. The mismatch between structures obtained from DFT (BP86) as well as DFT-D (BP86-D2) calculations of isolated molecules in the gas phase and geometries resulting from X-ray crystal structure determination is due to a dissatisfactory chemical model system. Intermolecular forces within the molecular surroundings of the crystal obtained from semiempirical lattice energy calculations emerge as likely candidates responsible for the incongruity of experimental results and computation.

INTRODUCTION

In a short article recently published in the *Journal of Chemical Theory and Computation*, Perdew and co-workers discuss some fundamental issues in ground-state density functional theory (DFT).[1] The authors forego equations and tables, and the article reads like a collection of DFT-apothegms, centered around some prime problems. When addressing the question whether or not all approximations are created equal, the authors make reference to Mel Levy, who "has stressed that, when an investigator reports a 'failure of density functional theory', he or she is typically reporting the failure of a given density functional approximation and should say that." Perdew and co-workers further suggest that users should utilize several different density functionals as a check on consistency of their results.[1]

By now, the practice to appropriate a variety of density functionals for one particular problem has found general recognition among computational chemists and users of computational chemistry tools, and it reflects the essence of many meaningful benchmark studies. For a representative review of the general performance of density functionals based on reliable proof of principle computations, we refer the reader to the recent work of Ramos and co-workers.[2] Nevertheless, a brief inspection of the current literature reveals that new work continues to be published reporting failures of density functional theory. While most of these studies pass the Levy test with flying colors, not all of them qualify as indicators of a DFT failure. When it comes to chemical quandaries, not only an improper sampling of the density functional space but also an inadequate construction of the representative model scenario is likely to result in a failure of DFT. Only if exploration of an entire verified subset of currently available functionals in conjunction with a factual chemical embodiment fails to produce reliable results might an unsuccessful density functional calculation indicate a DFT failure.

In the present work, we will revisit a case that prompted statements and speculations of a DFT failure, supposedly due to an improper chemical model system. We also suggest a simple procedure of how such a case might be identified (but not necessarily rectified). Before we present and discuss our results, we set the stage and shed some light on the chosen problem.

BACKGROUND

An article recently published in the *Journal of Chemical Theory and Computation* addresses the apparent failure of a variety of density functionals in the description of the geometry of the dicationic Ru(IV) allyl complex $[Ru(\eta^5\text{-}C_5H_5)(\eta^3\text{-}CH_2CHCHC_6H_5)(CH_3CN)_2]^{2+}$.[3] The question is posed whether the futile geometry optimization of this transition metal compound provides any evidence for a DFT failure.

It is commonly understood that the ultimate test for success of DFT is acceptable agreement with experimental results. Various gauges of comparison are conventionally utilized for entities of the realm of chemistry, but reproduction of geometric parameters remains one of the most decisive test criteria. Special attention needs to be drawn to the field of transition metal (TM) chemistry, which not only spearheaded the major success of DFT in chemistry[4] but also confronts any chemist who employs computations with a profusion of challenges. Since the problem at hand falls into the area of TM chemistry, we refer the reader to recent work of Cramer and Truhlar for an authoritative review of state of the art TM-DFT.[5]

The drawn conclusions were based on a comparison of optimized geometries of the chosen model compound with results of an X-ray structure determination of an analogous complex with permethylated cyclopentadienyl units, and the key results are reproduced in Figure 1. It was found that all density functional methods employed resulted in an unsatisfactory description of the coordination mode of the η^3-allyl unit. In particular, the Ru—C3 separation was overestimated by 20—50 pm, which gave rise to considerations of a DFT failure.

To put this result into proper perspective, one should keep in mind that molecular arrangements as obtained from crystal structure analyses are not always good representatives of the geometry of the isolated and unperturbed molecule. If the potential energy surface around relevant internal molecular coordinates exhibits a shallow profile and does not display a pronounced minimum, intermolecular dispersive forces and electrostatic interactions

Received: July 8, 2011
Published: August 15, 2011

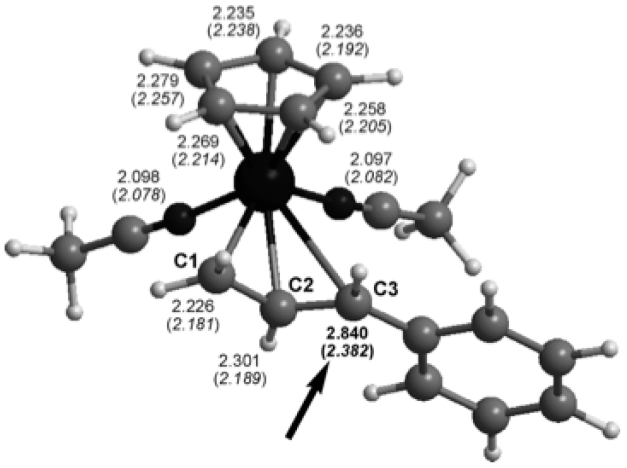

Experiment	DFT									WFT	
X-Ray	B3LYP	B3PW91	mPW1PW91	PBE1PBE	BP86	BLYP	BPW91	PW91	PBE	HF	MP2
238	279	269	264	262	274	288	276	268	268	298	231

Figure 1. Geometry of the model compound $[Ru(\eta^5\text{-}C_5H_5)(\eta^3\text{-}CH_2CHCHC_6H_5)(CH_3CN)_2]^{2+}$ and values for the Ru−C3 separation (in pm) obtained from the experiment and computations at various levels of theory (adapted from ref 3 with permission by the American Chemical Society).

might significantly influence the geometry of the molecular unit in the solid state. For this reason, Bühl and co-workers proposed a set of geometric reference data for second-row transition-metal complexes, collated from sufficiently precise gas-phase electron-diffraction experiments, as a testing ground for existing density functionals.[6] Evaluation of various density functionals in the description of 4d-TM complexes indicated that DFT only slightly overestimates the experimental bond lengths with small deviations of 2−3 pm. Further, the authors note that bond lengths involving Ru are particularly well reproduced.[6] Thus, the results of DFT calculations for the Ru model complex clearly fall short in meeting the expectations of an acceptable DFT performance.

The authors have critically analyzed their work in the search for reasons and remedies for the unsatisfactory DFT performance. For one, an exploration of the potential energy surface (PES) around the critical Ru−C3 distance revealed that a decrease in Ru−C3 separation from the B3LYP-optimized value (279 pm) to the crystal structure equivalent (238 pm) is accompanied by a destabilizing change in energy of only about 13 kJ/mol. It is concluded that "this reflects a reasonably flat PES with respect to Ru−C3 stretching, indicating a weak interaction with probably a strong component of dispersion forces".[3] It is noted that the development of DFT approaches that accurately model London dispersion interactions represents an active field of ongoing research efforts, and one straightforward approach to the problem at hand is treatment of dispersion correction as an add-on to standard density functionals either empirically[7] or semiempirically.[8] By now, density functional theory with added dispersion (DFT-D) has already found its entry into major quantum chemical computer programs, and a recent review article provides a peremptory entry to the field of dispersion DFT.[9]

Besides the limitations of the theory level, other reasons may be responsible for the mismatch between the calculated and the experimental Ru−C3 separation. One aspect concerns the adequacy of cyclopentadienyl $C_5H_5^-$ as a model for the permethylated system $C_5(CH_3)_5^-$. Additional calculations on $[Ru(\eta^5\text{-}C_5(CH_3)_5)(\eta^3\text{-}CH_2CHCHC_6H_5)(CH_3CN)_2]^{2+}$ have been carried out,[3] and the results demonstrate that the nature of the model used for the dication is not the main cause for the poor performance observed with B3LYP in particular, and by conjecture with DFT in general.

Furthermore, so-called solid-state packing effects need to be considered. The authors argue that a "close look at the X-ray structure seems to exclude the possibility that the presence of the counterions (PF_6^-) leads to a distortion of the allyl coordination geometry."[3] However, crystal effects are not always evident by close inspection alone; for the cation $[CpClZrClZrCp_3]^+$, the negative charge field of its molecular environment in the crystal has a significant influence on the Zr−Cl distances,[10] and the bent molecule $^t Bu_3PCuOSiPh_3$ ($\angle$(Cu−O−Si) = 117° in the gas phase) undergoes linearization in the solid state due to intermolecular dispersive interactions.[11] The capabilities and prospects of readily available atomistic simulation packages[12] allow one to promote "crystal packing" from the status of *deus ex machina* to a quantifiable effect.

The proper construction of a suitable model system for an extended chemical system such as the one previously discussed[3] constitutes the main focus of the present work. Dispersive interactions, not only intramolecular but also intermolecular, receive special attention.

■ COMPUTATIONAL DETAILS

DFT calculations for isolated molecules in the gas phase were carried out with the Amsterdam Density Functional suite of programs ADF, version 2008.01.[13] The general gradient approximation (GGA) constitutes the basic computational framework, and the functional employed—BP86—was chosen from the set of functionals utilized in previous work[3] guided by results of benchmark studies.[6] Within the architecture of the ADF program package, such calculations are based on the local density approximation with Slater exchange[14] and VWN-V correlation,[15] augmented by gradient corrections for exchange and correlation due to Becke[16] and Perdew,[17] respectively. DFT-D calculations include a dispersion correction added to the energy terms.[8]

Molecular orbitals were expanded in an uncontracted set of Slater-type orbitals (STOs) of polarized triple-ζ quality.[18] For TM complexes with permethylated cyclopentadienyl ligands, the basis set for H atoms was reduced to double-ζ quality. Core shells (C, N, O, F: 1s; P: 1s2s2p; Ru: 1s2s2p3s3p3d) were treated by the frozen-core approximation.[19]

Reported DFT energy values E_{DFT} refer to total bond energies (TBE), computed as an energy difference between a molecule and single atoms, which are computed as spherical symmetric and spin-restricted. For the DFT-D energy values $E_{DFT\text{-}D}$, the total bond energy is augmented by intramolecular dispersion energies (IDE).

Atomic charges were estimated by using models that are based on separation of the electron density in real space rather than on a basis-set-based partitioning. Most often, use is made of the electronic densities of the molecule $\rho(\mathbf{r})$ and of a fictitious promolecule $\rho_{promolecule}(\mathbf{r})$, the promolecule density being defined as the sum over the spherically averaged ground-state atomic densities. Such models seem to be an appropriate choice when using charges to calculate lattice energies within a crystal.

Hirshfeld atomic charges ${q_A}^H$ make use of a properly weighted molecular density, the weight function being the ratio of the charge density of the free atom to that of the promolecule (eq 1):[20]

$$q_A^H = Z_A - \int \frac{\rho_A(\mathbf{r})}{\rho_{promolecule}(\mathbf{r})}\rho_{molecule}(\mathbf{r})\,d\mathbf{r} \quad (1)$$

Voronoi atomic charges ${q_A}^V$ are based on deformation densities, $\rho_{def}(\mathbf{r}) = \rho(\mathbf{r}) - \rho_{promolecule}(\mathbf{r})$, and are obtained by direct spatial integration of the electron deformation density over an atomic domain.[21]

Lattice energies U have been estimated with the help of the General Utility Lattice Program (GULP), version 3.0.1.[22] U has been modeled as the sum of pairwise interactions within a crystal, excluding intramolecular contributions to Coulomb terms and dispersive interactions (eq 2).

$$U = \sum_{ij}(U_{ij}^{Coulomb} + U_{ij}^{dispersion}) \quad (2)$$

Coulomb interactions were based on charges obtained from Hirshfeld populations, ${U_{ij}}^{Coulomb}({q_A}^H)$, or Voronoi deformation densities, ${U_{ij}}^{Coulomb}({q_A}^V)$ (eq 3).

$$U_{ij}^{Coulomb} = \frac{q_i q_j}{4\pi\varepsilon_0 R_{ij}} \quad (3)$$

In a straightforward approach, energy contributions to dispersive interactions were obtained from a simple C_6-type dispersion potential (eq 4):

$$U_{ij}^{C_6} = -C_6^{ij}/R_{ij}^6 \quad (4)$$

C_6 coefficients for atoms were taken from the work of Grimme;[8] ${C_6}^{ij}$ combined coefficients for pairs of atoms were estimated as the harmonic mean of the corresponding atomic coefficients, a well-known combination rule for potential parameters first proposed by Fender and Halsey.[23]

A refined model takes its contributions to intermolecular dispersive interactions from a truncated damped dispersion potential, as suggested by Tang and Toennies (eq 5).[24]

$$U_{ij}^{damped-TT} = -\left[1 - \left\{\sum_{k=0}^{6}\frac{(b_{ij}R_{ij})^k}{k!}\right\}\exp(-b_{ij}R_{ij})\right]\frac{C_6^{ij}}{R_{ij}^6} \quad (5)$$

Damping coefficients b_{ij} were based on a comparison of the dispersive corrections obtained from the Tang−Toennies potential with those obtained from a Fermi-function damped potential, proposed by Wu and Yang.[7] This damping function $f_d(R)$ contains the value R_0—the sum of atomic van der Waals (vdW) radii—and it depends only on one additional parameter β. Wu and Yang determined a value of 23 for β, requiring $f_d(R) = 0.99$ at $R = 1.2R_0$. To account for the constraints of a crystal lattice, this requirement was tightened to $f_d(R) = 0.99$ at $R = 1.125R_0$, which leads to $\beta = 37$. Thus, the defining equation for the damping coefficient b_{ij} of an atom pair reads as follows (eq 6):

$$U_{ij}^{damped-TT}(R_{ref}) = -(1/(1 + \exp^{-37(R_{ref}/R_0 - 1)}))\frac{C_6^{ij}}{R_{ref}^6} \quad (6)$$

The reference distance R_{ref} was chosen as distance R_{min}—the distance at which the Fermi-function damped potential reaches its minimum—to which the harmonic mean of the atomic covalent radii was added. Following Wu and Yang, the vdW radii to construct R_0 were taken from the work of Bondi (H, C, N, O, F, P);[25] a vdW radius for Ru was reported by Batsanov.[26] Covalent atomic crystal radii[27] were chosen to build reference distances R_{ref}. Damping coefficients b_{ij} obtained from an adjustment based on the DFT-D2 dispersion potential[8] yield qualitatively the same results. The interested reader will find further information on the construction of the dispersion potentials in the Supporting Information.

Geometric analyses of crystal structures and crystal graphics utilized the program Mercury CSD, version 2.3.[28] Additional molecular graphics were created with help of the program Jmol.[29]

RESULTS

A crystal structure[30] taken from the Cambridge Structural Database (CSD) constitutes the reference system for the present and previous[3] work. Bis-acetonitrile-(η^5-pentamethylcyclopentadienyl)-(η^3-phenylallyl)-ruthenium bis (hexafluorophosphate) acetone solvate, referenced as CSD crystal structure HEQNEX, crystallizes in the space group $P\bar{1}$ with two asymmetric units per unit cell. We thus have optimized geometries of $[Ru(\eta^5\text{-}C_5(CH_3)_5)(\eta^3\text{-}CH_2CHCHC_6H_5)(CH_3CN)_2]^{2+}$ (**1**), $[PF_6]^-$ (**2**), and $(CH_3)_2CO$ (**3**) as well as of the model system $[Ru(\eta^5\text{-}C_5H_5)(\eta^3\text{-}CH_2CHCHC_6H_5)(CH_3CN)_2]^{2+}$ (**1′**). The nomenclature is such that an afterscript **x** refers to crystal structure geometries, **u** to results from DFT calculations, and **d** to results from DFT-D calculations, while **s** indicates not an optimized but a suitably adjusted geometry, to be specified later.

Isolated Molecules. The molecular framework of **1** is depicted in Figure 2. The key-problem of the present and previous work relates to the intramolecular structure relationship of the atoms Ru, C1, C2, and C3; essential geometric parameters are collected in Table 1.

The discussion centers around the distance d_{RuC} between atoms Ru and C3, laxly referred to as bond distance.[3] A closer

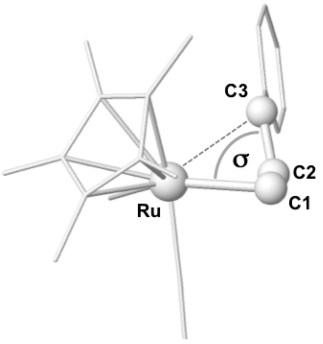

Figure 2. Molecular structure of **1** (H atoms omitted for clarity) indicating the two critical geometric coordinates: the distance d_{RuC} between atoms Ru and C3 and the significant torsion σ, which is the dihedral angle $\angle$(C3−C2−C1−Ru).

Table 1. Relevant Atomic Separations (in pm) and Angles (in deg) for the Real System 1, Obtained from Experimental Results (1x) and Calculations (1u, 1d), and for the Model System 1′, Obtained from Calculations (1′u, 1′d)

	1x[a]	1u	1d	1′u	1′d
d_{RuC} (Ru−C1)	218	221	221	223	223
d_{RuC} (Ru−C2)	219	227	223	228	224
d_{RuC} (Ru−C3)	238	267	248	278	257
σ	66.4	77.6	70.5	83.0	74.8

[a] Ref 30.

inspection of the geometry of **1** reveals that d_{RuC} is not the best choice for one of the three major internal coordinates that characterize the coordination around atom C3. If one seeks to define the internal coordinate that describes a distance between two atoms such that the chosen distance comes closest to an accepted value of a covalent bond, the distance d_{CC}(C2−C3), but not the distance d_{RuC}(Ru−C3), emerges as the best choice for one of the major internal coordinates of atom C3. It is the dihedral angle $\angle$(C3−C2−C1−Ru) that establishes a geometric relationship between the atoms Ru and C3. This internal coordinate in turn determines the separation between C3 and the transition metal center. In the present work, this angle is referred to as significant torsion σ. Values for the significant torsion σ are also listed in Table 1.

In previous work, additional calculations (B3LYP) with the Ru−C3 distance fixed at the experimental value of 238 pm have been carried out; the small change in energy going from the local minimum geometry to the adjusted structure, ΔE_{disr} = 13 kJ/mol, was interpreted as "reasonably flat PES with respect to Ru−C3 stretching."[3] It remains unclear which other internal coordinates have been affected by this change in Ru−C3 separation.

As noted above, the significant torsion σ is a suitable internal coordinate describing the coordination around C3, and we have constructed an additional set of molecules **1us**, **1ds**, **1′us**, and **1′ds**. Here, the optimized geometries of **1u**, **1d**, **1′u**, and **1′d** were described as Z matrix built upon atoms Ru, C1, C2, and C3. The dihedral angle $\angle$(C3−C2−C1−Ru) was adjusted to the experimental value of 66.4°, while the remaining internal coordinates were taken from the corresponding optimized geometry. The change in energy with respect to the local minimum structure ΔE_{disr} and the resulting value for d_{RuC} are presented in Table 2.

Table 2. Change in Energy (in kJ/mol) and Resulting Ru−C3 Separation (in pm) When the Significant Torsion σ in 1u, 1d, 1′u, and 1′d Is Adjusted to the Experimental Value of 66.4°

	1us	1ds	1′us	1′ds
ΔE_{disr}	12	4	24	10
d_{RuC}	248	241	250	242

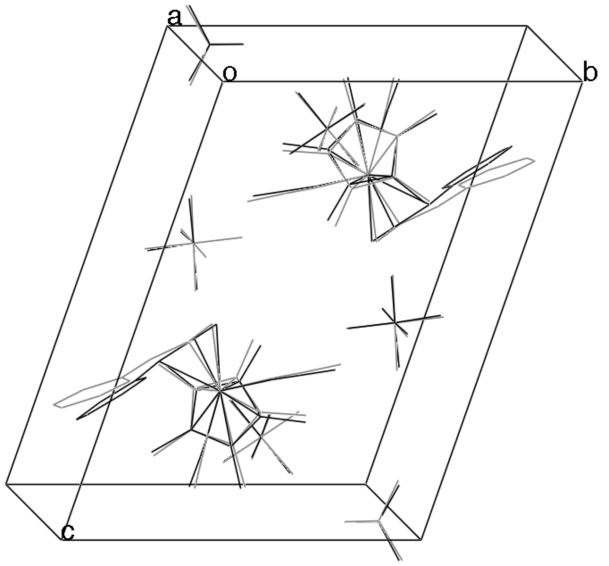

Figure 3. View along **a*** of an overlay of the unit cells of HEQNEX (black) and **IU** (gray) (H atoms omitted for clarity).

Lattice Structures and Intermolecular Energies. A series of model crystals was constructed, for which the basic structure and the molecular arrangement within the asymmetric unit {**1**, 2 × **2**, **3**} was taken from the experimental crystal structure. In other words, a model crystal was considered to have the same space group and lattice parameters as HEQNEX, and the relative orientation with respect to each other of the four independent molecules that comprise one asymmetric unit was maintained. The internal geometry and atomic charges for the individual components of the asymmetric unit were taken from DFT calculations. Four model crystals for which the chemical content of the unit cell is identical to that of HEQNEX are **IU** {**1u**, 2 × **2u**, **3u**}, **IUS** {**1us**, 2 × **2u**, **3u**}, **ID** {**1d**, 2 × **2d**, **3d**}, and **IDS** {**1ds**, 2 × **2d**, **3d**}. An exemplary overlay of crystal structures HEQNEX and **IU** is shown in Figure 3.

Inspection of Figure 3 reveals that the core molecular structures obtained from experimental results and calculation are in fair agreement. Slight differences are observed when considering the coordination geometries of the acetonitrile ligands and the orientation of the cyclopentadienyl group. Significant differences become obvious when focusing on the orientation of the phenylallyl group. This discrepancy is caused by a difference in σ of about 10°. The interested reader will find in the Supporting Information CIF data of model crystals for further examination.

A second set of model crystals, for which the chemical content of the unit cell differs from that of HEQNEX, comprises the four systems **IIU** {**1u**, 2 × **2u**}, **IIUS** {**1us**, 2 × **2u**}, IID {**1d**, 2 × **2d**}, and IIDS {**1ds**, 2 × **2d**}. Space group, lattice parameters, and the relative orientation with respect to each other of entities within

Table 3. Lattice Energy Contributions (in kJ/mol) to Coulomb and Dispersive Interactions Per Unit Cell for the Two Sets of Model Crystals IU, IUS, ID, and IDS and IIU, IIUS, IID, and IIDS

	$U^{\text{dispersion}}$ (C_6-undamped)	$U^{\text{dispersion}}$ (TT-damped)	U^{Coulomb} (q_A^H)	U^{Coulomb} (q_A^V)
IU	−719	−690	−2009	−1984
IUS	−638	−625	−2021	−1997
ID	−655	−633	−2028	−2006
IDS	−695	−650	−2028	−2006
IU	−601	−572	−1982	−1953
IUS	−501	−490	−1994	−1967
ID	−481	−466	−2005	−1978
IDS	−462	−450	−2006	−1979

Table 4. Intramolecular Energy Contributions (in kJ/mol) to Total Bond Energies and Dispersive Interactions Per Unit Cell for the Two Sets of Model Crystals IU, IUS, ID, and IDS and IIU, IIUS, IID, and IIDS

	TBE	IDE	$E_{\text{DFT/DFT-D}}$
IU	−86946	0	−86946
IUS	−86921	0	−86921
ID	−86916	−675	−87591
IDS	−86901	−682	−87583
IU	−76323	0	−76323
IUS	−76298	0	−76298
ID	−76293	−643	−76936
IDS	−76278	−650	−76928

an asymmetric unit are the same as in HEQNEX, but the solvent molecule acetone has been excluded from the unit cell.

Lattice energies U for the two sets of model crystals **IU**, **IUS**, **ID**, and **IDS** and **IIU**, **IIUS**, **IID**, and **IIDS** are collected in Table 3. The table contains entries for the contribution per unit cell of various Coulomb and dispersive interactions.

Intramolecular Energies. While the entries in Table 3 summarize essential contributions to the intermolecular lattice energy per unit cell, the content of the intramolecular crystal energy per unit cell comprises total bond energies (TBE) from DFT and DFT-D calculations, the latter one in addition containing intramolecular dispersion energies (IDE). The intramolecular energy content per unit cell for the two sets of model crystals is collected in Table 4.

DISCUSSION

The critical bond distance d_{RuC} between atoms Ru and C3 for model compound **1′u** is, at 278 pm, in fair agreement with the BP86 value formerly reported (274 pm).[3] As previously observed,[3] the substitution of hydrogen for methyl groups of the cyclopentadienyl ring causes an elongation of the critical bond distance by about 10 pm (**1u** → **1′u**: 11 pm; **1d**→ **1′d**: 9 pm). Although not negligible, the present calculations confirm that the nature of the chosen model for the transition metal complex is not the main reason for the observed mismatch in d_{RuC} when comparing experimental results and theory.

Table 5. Changes Per Unit Cell in Lattice Energy ΔU and in Crystal Energy ΔE_x (in kJ/mol) When (a) the Significant Torsion σ Is Adjusted (Entries 1 to 4), (b) Dispersion Is Included on the Intramolecular Level (Entries 5−8), and (c) the Solvent Molecule Is Omitted (entries 9−12)

		$\Delta U^{\text{dispersion}}$	$\Delta U^{\text{Coulomb}}$	ΔU	ΔTBE	ΔIDE	ΔE_x
1.	IU → IUS	59	−13	46	25	0	71
2.	ID →IDS	−11	0	−11	16	−8	−3
3.	IIU → IIUS	75	−14	61	25	0	86
4.	IID →IIDS	16	−1	15	16	−8	23
5.	IU→ID	55	−22	33	[a]	[a]	[a]
6.	IUS →IDS	−15	−9	−24	[a]	[a]	[a]
7.	IIU →IID	99	−25	74	[a]	[a]	[a]
8.	IIUS →IIDS	40	−12	28	[a]	[a]	[a]
9.	IU→IIU	118	31	149	0	0	149
10.	IUS →IIUS	134	30	164	0	0	164
11.	ID →IID	162	28	190	0	0	190
12.	IDS →IIDS	189	27	216	0	0	216

[a] Not reported.

Inclusion of intramolecular dispersion interactions during geometry optimization significantly reduces the Ru−C3 separation by about 20 pm (**1u** → **1d**: 19 pm; **1u′**→ **1′d**: 21 pm), but the best value, obtained for **1d** (d_{RuC} = 248 pm), still is off by 10 pm in comparison to the crystal structure data for **1x** (d_{RuC} = 238 pm). This discrepancy does not meet the expectations of DFT performance for 4d-TM complexes with anticipated deviations in bond lengths of about 2−3 pm.[6] Only if the significant torsion σ is adjusted to the experimental value, the Ru−C3 separation in **1ds** (d_{RuC} = 241) reaches acceptable agreement with experimental results. The fact that an adjustment of σ leads to a major improvement, signified by a reduction in d_{RuC} even for model systems where intramolecular dispersion interactions are not accounted for (**1u**, **1′u**), establishes σ as one of the three major internal coordinates that define the coordination environment of atom C3. At the same time, the σ adjustment leads to only a small increase in total bond energies, ranging from 4 to 24 kJ/mol. All of this suggests that intermolecular interactions within the crystal environment might be responsible for this unexpectedly short Ru−C3 separation as found in HEQNEX.

This becomes evident when combined intermolecular and intramolecular energies serve as basis for a comparison of different crystal arrangements. Within the context of the present work, the crystal energy per unit cell E_x is understood as the sum of the intramolecular total bond energies $E_{\text{DFT/DFT-D}}$ and the intermolecular lattice energy U per unit cell, and ΔE_x values produce a relative stability ranking for various crystal scenarios. Although the absolute value for dispersion contributions to the lattice energy depends on the chosen dispersion potential (C_6-undamped vs *TT*-damped), the energy differences obtained in comparison of different model crystals are not only qualitatively in accordance but also in fair quantitative agreement. The same holds true for Coulomb contributions to the lattice energy based on different charge models (q_A^H vs q_A^V), and we base our comparison on lattice energies based on one set of charges and one dispersion potential only, namely, Hirshfeld charges and a damped Tang−Toennies potential. Values of ΔU and ΔE_x for a comparison of various model crystal pairs are compiled in Table 5.

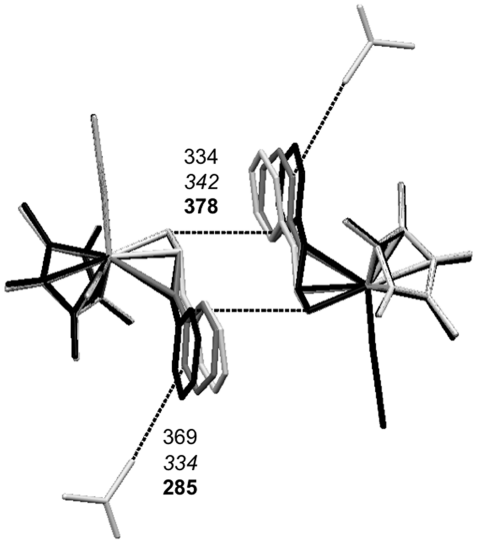

Figure 4. Overlay of model crystals **IU** (light gray), **IUS** (dark gray), and **IDS** (black) in the unit cell packing ranges $0.7 < a < 1.3$, $0.7 < b < 1.3$, and $0.0 < c < 1.0$ (H atoms omitted for clarity) and shortest intermolecular $C_{allyl}-C_{phenyl}$ and $C_{acetone}-C_{phenyl}$ distances (in pm) for **IU** (regular), **IUS** (*italics*), and **IDS** (**bold**).

The data are organized in the sense of a chemical reaction where negative energies indicate a preference for the product side.

Entries 1−4 in Table 5 examine the role of the significant torsion σ. We note that only if the adjustment of σ is carried out for a DFT-D optimized molecular system does a net stabilization in U result that is large enough to outweigh the intramolecular destabilization due to deviation from the optimized geometry. Entries 5−8 assess the indirect influence of intramolecular dispersive interactions on lattice energies. Once again, it is noted that the inclusion of dispersive interaction on the molecular level only leads to crystal stabilization when coupled with an adjustment of σ. Entries 9−12 indicate that the cocrystallizing solvent molecule too might have an influence on the crystal geometry of the transition metal cation. Entries 9−12 might be interpreted as the binding energy of two acetone molecules per unit cell. Not only do the DFT-D optimized geometries favor the inclusion of the solvent molecule by about 50 kJ/mol, the adjustment of σ too leads to additional stabilization. This in turn influences the preferred geometry of the Ru cation **1**. Neither the DFT nor the DFT-D gas-phase calculations are thus able to satisfactorily describe the crystal geometry of **1**, and the analysis of the adjusted crystal geometries reveals that intermolecular dispersive interactions are most likely responsible for the apparent failure of DFT methodologies.

A closer look at packing motifs of model crystals **IU**, **IUS**, and **IDS** illustrates the importance of intermolecular dispersive forces and the role of the cocrystallizing solvent molecule. An overlay of model crystals within a decisive unit cell packing range, $0.7 < a < 1.3$, $0.7 < b < 1.3$, and $0.0 < c < 1.0$, is presented in Figure 4.

Also reported in Figure 4 are shortest intermolecular $C_{allyl}-C_{phenyl}$ and $C_{acetone}-C_{phenyl}$ distances, and an adjustment of the significant torsion not only shortens the Ru−C3 separation but also increases the distance between two neighboring transition metal complexes. At the same time, $C_{acetone}-C_{phenyl}$ distances are reduced, an effect that is further enhanced when molecular geometries are based on DFT-D methodology. It is the value of separation between the solvent molecule and the transition metal complex that ultimately tips the balance of intermolecular dispersive interaction in favor of the shortest intramolecular Ru−C3 distance.

Although it appears that crystallization without a solvent might produce a Ru cation with a Ru−C3 distance that is more in accord with results from gas-phase calculations, the empirical nature of the present work does not support any definite conclusions. Omission of the solvent molecule might induce a reorganization of unit cell contents and produce an entirely different crystal structure. What the present work however indicates is the importance of and subtle balance between intramolecuar and intermolecular van der Waals energies. Similar conclusions can be drawn for the influence of Coulombic interactions.

CONCLUSION

It is clear that the present work does not provide a definite answer to the question as to why DFT calculations apparently are unable to satisfactorily reproduce the crystal geometry of the transition-metal cation $[Ru(\eta^5\text{-}C_5Me_5)(\eta^3\text{-}CH_2CHCHC_6H_5)(CH_3CN)_2]^{2+}$. Crystal energies have been based on an empirical model and were only included as perturbation to intramolecular energies. Recent work demonstrates that for a more reliable assessment, the periodicity of the crystal environment needs to be taken into accout,[31] and not only the molecular geometry but also the crystal lattice have to be treated variationally.[32] But, as already anticipated in the qualitative assessment of the present work, the interplay between intra- and intermolecular dispersion effects within the crystal holds the key to many counterintuitive observations. These conclusions are not restricted to the solid state but are of equal importance for solution chemistry.[33]

With the ongoing development of computational methodologies that incorporate increasingly smaller contributions to the total energy, it appears that the boundaries of suitable models for a chemical system of interest might need to be extended beyond the intramolecular regime. The simple and straightforward assessment presented here provides a first educated estimate whether, for a given problem, conventional DFT methodology might or might not be sufficient. It is advisable in cases of an apparent DFT failure not to exclude the possibility of a simple failure of DFT due to insufficiencies in the model system before expanding the computational methodology to more costly methods, as previously suggested.[3]

ASSOCIATED CONTENT

Supporting Information. Optimized geometries, final energies, convergence criteria, atomic charges, CIF data for model crystals, and details on dispersion potentials. This material is available free of charge via the Internet at http://pubs.acs.org.

AUTHOR INFORMATION

Corresponding Author
*E-mail: jacobsen@kemkom.com.

ACKNOWLEDGMENT

KemKom expresses its gratitude to Professor L. Cavallo for granting access to the MoLNaC computing facilities at Dipartimento di Chimica, Università di Salerno, Italy. The author is indebted to Professor J. T. Mague, Department of Chemistry,

Tulane University, New Orleans, for providing an entry into the Cambridge Structural Database.

REFERENCES

(1) Perdew, J. P.; Ruzsinszky, A.; Constantin, L. A.; Sun, J.; Csonka, G. I. *J. Chem. Theory Comput.* **2009**, *5*, 902–908.
(2) Sousa, S. F.; Fernandes, P. A.; Ramos, M. J. *J. Phys. Chem. A* **2007**, *111*, 10439–10452.
(3) Calhorda, M. J.; Pregosin, P. S.; Veiros, L. F. *J. Chem. Theory Comput.* **2007**, *3*, 665–670.
(4) Ziegler, T. *Can. J. Chem.* **1995**, *73*, 743–761.
(5) Cramer, C. J.; Truhlar, D. G. *Phys. Chem. Chem. Phys.* **2009**, *11*, 10757–10816.
(6) Waller, M. P.; Braun, H.; Hojdis, N.; Bühl, M. *J. Chem. Theory Comput.* **2007**, *3*, 2234–2242.
(7) Wu, Q.; Yang, W. T. *J. Chem. Phys.* **2002**, *116*, 515–524.
(8) Grimme, S. *J. Comput. Chem.* **2006**, *27*, 1787–1799.
(9) Grimme, S. *WIREs—CMS* **2011**, *1*, 211–228.
(10) Jacobsen, H.; Brackemeyer, T.; Berke, H.; Erker, G.; Fröhlich, R. *Eur. J. Inorg. Chem.* **2000**, 1423–1428.
(11) Jacobsen, H.; Fink, M. J. *Eur. J. Inorg. Chem.* **2007**, 5294–5299.
(12) Gale, J. D. *Z. Kristallogr.* **2005**, *220*, 552–554.
(13) te Velde, G.; Bickelhaupt, F. M.; Baerends, E. J.; Fonseca Guerra, C.; van Gisbergen, S. J. A.; Snijders, J. G.; Ziegler, T. *J. Comput. Chem.* **2001**, *22*, 931−967. http://www.scm.com (accessed: 11/05/2011).
(14) Slater, J. C. *Phys. Rev.* **1951**, *81*, 385–390.
(15) Vosko, S. H.; Wilk, L.; Nusair, M. *Can. J. Phys.* **1980**, *58*, 1200–1211.
(16) Becke, A. D. *Phys. Rev. A* **1988**, *38*, 3098–3100.
(17) Perdew, J. P. *Phys. Rev. B* **1986**, *33*, 8822–8824.
(18) Van Lenthe, E.; Baerends, E. J. *Comput. Chem.* **2003**, *24*, 1142–1156.
(19) Baerends, E. J.; Ellis, D. E.; Ros, P. *Chem. Phys.* **1973**, *2*, 41–51.
(20) Hirshfeld, F. L. *Theor. Chim. Acta* **1977**, *44*, 129–138.
(21) Fonseca Guerra, C.; Handgraaf, J.-W.; Baerends, E. J.; Bickelhaupt, F. M. *J. Comput. Chem.* **2004**, *25*, 189–210.
(22) Gale, J. D.; Rohl, A. L. *Mol. Simulat.* **2003**, *29*, 291–341.
(23) Fender, B. E. F.; Halsey, G. D. *J. Chem. Phys.* **1962**, *36*, 1881–1888.
(24) Tang, K. T.; Toennies, J. P. *J. Chem. Phys.* **1984**, *80*, 3726–3741.
(25) Bondi, A. *J. Phys. Chem.* **1964**, *68*, 441–451.
(26) Batsanov, S. S. *Inorg. Mater.* **2001**, *37*, 871–885.
(27) Cordero, B.; Gómez, V.; Platero-Prats, A. E.; Revés, M.; Echeverría, J.; Cremades, E.; Barragán, F.; Alvarez, S. *Dalton Trans.* **2008**, 2832–2838.
(28) Macrae, C. F.; Bruno, I. J.; Chisholm, J. A.; Edgington, P. R.; McCabe, P.; Pidcock, E.; Rodriguez-Monge, L.; Taylor, R.; van de Streek, J.; Wood, P. A. *J. Appl. Crystallogr.* **2008**, *41*, 466–470.
(29) Jmol: an open-source Java viewer for chemical structures in 3D. http://www.jmol.org/ (accessed: 11/05/2011).
(30) Fernández, I.; Hermatschweiler, R.; Breher, F.; Pregosin, P. S.; Veiros, L. F.; Calhorda, M. J. *Angew. Chem., Int. Ed.* **2006**, *45*, 6386–6391.
(31) Moellmann, J.; Grimme, S. *Phys. Chem. Chem. Phys.* **2010**, *12*, 8500–8504.
(32) Hongo, K.; Watson, M. A.; Sánches-Carrera, R. S.; Iitaka, T.; Aspuru-Guzik, A. *J. Phys. Chem. Lett.* **2010**, *1*, 1789–1794.
(33) Jacobsen, H. *Phys. Chem. Chem. Phys.* **2009**, *11*, 7231–7240.